

FEL 2017

20th - 25th August, 2017

Santa Fe Convention Center, Santa Fe, NM USA

38th International Free Electron Laser Conference



August 20 - 25, 2017

WELCOME

On behalf of the FEL2017 Organizing Committee, we would like to welcome you to the 38th International Free-Electron Laser Conference.

The Scientific Program Committee has created an exciting Conference Program, with both invited and contributed talks and extensive poster presentations. This year's Conference program highlights the impressive advances in Free-Electron Lasers over the past two years, including the first lasing results at the Pohang Accelerator Laboratory X-ray FEL in South Korea, the SwissFEL in Switzerland, the European X-ray FEL in Germany, and the Dalian VUV FEL in China. Sadly, since the last conference the FEL community lost two of its founding members, John Madey and Rodolfo Bonifacio, and a special session has been convened to honor their memories and contributions.

The FEL2017 Conference is held at the Santa Fe Community Convention Center, within walking distance of the Santa Fe Plaza and Historic District. Santa Fe, the capital of New Mexico with a large Spanish and Native American presence, is home to the oldest house in the U.S., with its foundation part of an ancient Indian Pueblo, the famed Cathedral Basilica of St. Francis of Assisi, and the Loretto Chapel with its unusual helical staircase called the "Miraculous Stairs." Santa Fe also boasts a large collection of art galleries, a variety of museums, an outdoor opera and beautiful sunset views of the Sangre de Cristo and Jemez mountains.

The nearby Los Alamos National Laboratory (LANL), located on a mesa 30 miles to the Northwest, plays host to an array of accelerator and scientific facilities such as the Los Alamos Neutron Science Center, the Dual Axis Radiographic Hydrodynamic Test facility, the National High Magnetic Field Laboratory, and the Center for Integrated Nano-Technologies. LANL has also proposed a new facility, Matter and Radiation in Extremes (MaRIE), and will host the Exascale-Class computing to advance materials science through fully characterizing materials during production and dynamic environments to attain the required material performance.

We appreciate the considerable interest from industry to showcase their products at the FEL2017 Conference. We look forward to an exciting Conference with strong participation from China, France, Germany, India, Israel, Italy, Japan, Korea, the Netherlands, Russia, Sweden, Switzerland, the UK, the USA, and other countries. We hope you will enjoy the 38th International Free-Electron Laser Conference and the beautiful city of Santa Fe.

Welcome!

Dinh Nguyen John Lewellen
Conference Chair Conference Co-Chair

FEL 2017 Committees

FEL 2017 Conference Organizing Committee

Dinh Nguyen	Conference Chair
John Lewellen	Conference Co-Chair
Cynnamon Spain	Logistics Chair
Bruce Carlsten	SPC Chair
Kip Bishofberger	Editor-in-Chief
Lucy Maestas	Conference Secretariat

International Executive Committee

I. Ben-Zvi	BNL & Stony Brook University
M.-E. Couprie	Synchrotron SOLEIL
A. Friedman	Ariel University
J.N. Galayda	SLAC
L. Giannessi	ENEA & ELETTRA-Sincrotrone Trieste
H. Hama	Tohoku University
H-S. Kang	PAL/POSTECH
K.-J. Kim	ANL & the University of Chicago
V.N. Litvinenko	Stony Brook University & BNL
E.J. Minehara	JAEA & WERC
G.R. Neil	Jefferson Lab.
D.C. Nguyen	Los Alamos National Laboratory
S. Reiche	PSI
J. Rossbach	DESY & Hamburg University
T.I. Smith	Stanford University
H. Tanaka	RIKEN Spring-8
A.F.G van der Meer	FELIX Facility, Radboud University
N.A. Vinokurov	BINP
R.P. Walker	Diamond Light Source
Z.T. Zhao	SINAP

Scientific Program Committee

Bruce Carlster(Chair)	LANL
Stephen Benson	JLAB
Simona Bettoni	PSI
Sandra Biedron	Colorado State University
John Byrd	LBNL
Simone Di Mitri	ELETTRA
Bruno Diviacco	ELETTRA
Massimo Ferrario	INFN
Gianluca Geloni	XFEL
Avraham Gover	Tel Aviv University
Ryoichi Hajima	QST
Jang-Hui Han	POSTECH
Toru Hara	SPRING8
Zhirong Huang	SLAC
Rasmus Ischebeck	PSI
Young Uk Jeong	KAERI
Heung-Sik Kang	POSTECH
Marie Labat	SOLEIL
Kexin Liu	Peking University
Alex H. Lumpkin	FNAL
Atoosa Meseck	HZB
Hideaki Ohgaki	Kyoto University
Jia QiKa	University of Science and Technology of China
Daniel Ratner	SLAC
Steve Russell	LANL
Fernando Sannibale	LBNL
Siegfried Schreiber	DESY
Evgeny Schneidmiller	DESY
Oleg Shevchenko	INP
Frank Stephan	DESY
Takashi Tanaka	SPRING8
Chuanxiang Tang	Tsinghua University
Neil Thompson	STFC
Dong Wang	SINAP
Sverker Werin	MAXLAB
Ying K. Wu	Duke University
Alexander Zholents	ANL

FEL Prize Committee

L. Giannessi, (Chair)	ENEA & ELETTRA-Sincrotrone Trieste
J.N. Galayda	SLAC
Y.U. Jeong	KAERI
T. Shintake	OIST
Z. Huang	SLAC

Contents

Preface	i
Foreword	iii
Committees	iv
Contents	vii
Papers	1
MOA01 – John Madey: A Short History of My Friend and Colleague	1
MOBA02 – Coherence Limits of X-ray FEL Radiation	5
MOC03 – Commissioning and First Lasing of the European XFEL	9
MOD02 – Status of the FLASH FEL User Facility at DESY	14
MOD04 – Status and Perspectives of the FERMI FEL Facility	19
MOD06 – Matter-Radiation Interactions in Extremes (MaRIE) Project Overview	24
MOP001 – Diamond Double-Crystal System for a Forward Bragg Diffraction X-Ray Monochromator of the Self-Seeded PAL XFEL	29
MOP003 – Concept for a Seeded FEL at FLASH2	34
MOP005 – FEL Pulse Shortening by Superradiance at FERMI	38
MOP008 – Status of the Hard X-Ray Self-Seeding Project at the European XFEL	42
MOP010 – Constraints on Pulse Duration Produced by Echo-Enabled Harmonic Generation	46
MOP011 – Strongly Tapered Undulator Design for High Efficiency and High Gain Amplification at 266 nm	49
MOP013 – Hundred-Gigawatt X-Ray Self-Seeded High-Gain Harmonic Generation	53
MOP014 – Harmonic Lasing Towards Shorter Wavelengths in Soft X-Ray Self-Seeding FELs	57
MOP016 – Comparing FEL Codes for Advanced Configurations	60
MOP017 – Echo-Enabled Harmonic Generation Results with Energy Chirp	64
MOP018 – Distributed Self-Seeding Scheme for LCLS-II	68
MOP019 – Transient Thermal Stress Wave Analysis of a Thin Diamond Crystal Under Laser Heat Load	72
MOP020 – Sideband Instability in a Tapered Free Electron Laser	76
MOP021 – Sideband Suppression in Tapered Free Electron Lasers	80
MOP023 – Two-Color Soft X-Ray Generation at the SXFEL User Facility Based on the EEHG Scheme	84
MOP024 – Simulation and Optimization for Soft X-Ray Self-Seeding at SXFEL User Facility	87
MOP026 – Study of an Echo-Enabled Harmonic Generation Scheme for the French FEL Project LUNEX5	91
MOP027 – Seeding of Electron Bunches in Storage Rings	94
MOP028 – Extraction of the Longitudinal Profile of the Transverse Emittance From Single-Shot RF Deflector Measurements at sFLASH	98
MOP031 – First Operation of a Harmonic Lasing Self-Seeded FEL	102
MOP032 – Reverse Undulator Tapering for Polarization Control and Background-Free Harmonic Production in XFELs: Results from FLASH	106
MOP033 – Baseline Parameters of the European XFEL	109
MOP035 – Optimum Undulator Tapering of SASE FEL: Theory and Experimental Results From FLASH2	113
MOP036 – Frequency Doubling Mode of Operation of Free Electron Laser FLASH2	117
MOP037 – Opportunities for Two-Color Experiments at the SASE3 Undulator Line of the European XFEL	121
MOP038 – Overview of the Soft X-Ray Line Athos at SwissFEL	125
MOP039 – Possible Method for the Control of SASE Fluctuations	129
MOP041 – Commissioning of FEL-Based Coherent Electron Cooling System	132
MOP042 – Status of Seeding Development at sFLASH	136
MOP043 – Plasma Wakefield Accelerated Beams for Demonstration of FEL Gain at FLASHForward	140
MOP044 – Commissioning Status of the European XFEL Photon Beam System	144
MOP046 – Progress of Delhi Light Source at IUAC, New Delhi	149
MOP047 – Design Calculation on Beam Dynamics and THz Radiation of Delhi Light Source	153
MOP048 – A Compact THz FEL at KAERI: the Project and the Status	156
MOP049 – Development of Compact THz Coherent Undulator Radiation Source at Kyoto University	158
MOP050 – Present Status of Infrared FEL Facility at Kyoto University	162
MOP051 – Polish In-Kind Contribution to European XFEL: Status in Summer 2017	166
MOP052 – First Observation of Coherent THz Undulator Radiation Driven by NSRRC High Brightness Photo-Injector	170
MOP053 – High Spectral Density Compton Back-Scattered Gamma-Ray Sources at Fermilab	174
Contents	vii

MOP054 – CLARA Facility Layout and FEL Schemes	178
MOP055 – SCLF: An 8-GeV CW SCRF Linac-Based X-Ray FEL Facility in Shanghai	182
MOP056 – Design of Apparatus for a High-Power-Density Diamond Irradiation Endurance Experiment for XFEL Applications	185
MOP059 – Synchronized Mid-Infrared Pulses at the Fritz Haber Institute IR-FEL	188
MOP061 – X-ray Regenerative Amplifier Free-Electron Laser Concepts for LCLS-II	192
MOP062 – X-ray FEL Oscillator Seeded Harmonic Amplifier for High Energy Photons	196
MOP064 – An Experimental Setup for Probing the Thermal Properties of Diamond Regarding Its Use in an XFEL	200
MOP066 – Free Electron Lasers in 2017	204
TUA01 – Recent FEL Experiments at FLASH	210
TUA04 – Suppression of the CSR Effects at a Dogleg Beam Transport Using DBA Lattice	216
TUB01 – Seeding Experiments and Seeding Options for LCLS II	219
TUB03 – ASU Compact XFEL	225
TUB04 – Recent On-Line Taper Optimization on LCLS	229
TUC01 – Polarization Control of Storage Ring FELs Using Cross Polarized Helical Undulators	235
TUC02 – Thermal and Mechanical Stability of Bragg Reflectors under Pulsed XFEL Radiation	240
TUC04 – Enhancement of Radiative Energy Extraction in an FEL Oscillator by Post-Saturation Beam Energy Ramping	244
TUC05 – Start-to-End Simulations for an X-Ray FEL Oscillator at the LCLS-II and LCLS-II-HE	247
TUP002 – Numerical Studies on RF-Induced Trajectory Variations at the European XFEL	251
TUP003 – First Beam Halo Measurements Using Wire Scanners at the European XFEL	255
TUP004 – Longitudinal Phase Space Optimization for the Hard X-ray Self-Seeding	259
TUP005 – Studies of the Transverse Beam Coupling in the European XFEL Injector	263
TUP009 – The Effect of Transverse Space Charge on Beam Evolution and Photon Coherence	266
TUP010 – Double-Bunches for Two-Color Soft X-Ray Free-Electron Laser at the MAX IV Laboratory	269
TUP013 – Experience and Initial Measurements of Magnetic Linearisation in the MAX IV Linac Bunch Compressors	273
TUP015 – Coherent Transition Radiation from Transversely Modulated Electron Beams	276
TUP016 – Beam-Dynamics Analysis of Long-Range Wakefield Effects on the SCRF Cavities at the Fast Facility	280
TUP022 – Modeling and Optimization of the APS Photo-Injector Using OPAL for High Efficiency FEL Experiments	284
TUP023 – Recent Developments and Plans for Two Bunch Operation with up to 1 μ s Separation at LCLS	288
TUP024 – Stochastic Effects from Classical 3D Synchrotron Radiation	292
TUP027 – Cancellation of Coherent Synchrotron Radiation Kicks at LCLS	296
TUP028 – Approximated Expressions for the Coherent Synchrotron Radiation Effect in Bending Magnets	300
TUP030 – An Emittance-Preservation Study of a Five-Bend Chicane for the LCLS-II-HE Beamline	305
TUP031 – Design of a Dogleg Bunch Compressor with Tunable First-Order Longitudinal Dispersion	309
TUP034 – Novel Aspects of Beam Dynamics in CeC SRF Gun and SRF Accelerator	313
TUP035 – CSR Wake Fields and Emittance Growth with a Discontinuous Galerkin Time Domain Method	317
TUP038 – Experiments in Electron Beam Nanopatterning	320
TUP039 – Electron Beam Requirements for Coherent Electron Cooling FEL System	323
TUP042 – Determination of the Slice Energy Spread of Ultra-Relativistic Electron Beams by Scanning Seeded Coherent Undulator Radiation	326
TUP045 – Interference-Based Ultrafast Polarization Control at Free Electron Lasers	329
TUP050 – Beam Driven Acceleration and RF Breakdown in Photonic Band Gap Travelling Wave Accelerator Structure	333
TUP053 – The ACHIP Experimental Chambers at PSI	336
TUP054 – Preparations for Installation of the Double Emittance-Exchange Beamline at the Argonne Wakefield Accelerator Facility	340
TUP057 – Measurement of Short-Wavelength High-Gain FEL Temporal Coherence Length by a Phase Shifter	344
TUP058 – Slippage-Enhanced SASE FEL	348
TUP059 – Alternative Electron Beam Slicing Methods for CLARA and X-ray FELs	352
TUP061 – Study of the Electron Transport in the COXINEL FEL Beamline Using a Laser-Plasma Accelerated Electron Beam	356
TUP062 – Electromagnetic and Mechanical Analysis of a 14 mm 10-period NbTi Superconducting Undulator	360
TUP065 – Dielectric Laser Acceleration Setup Design, Grating Manufacturing and Investigations Into Laser Induced RF Cavity Breakdowns	365
TUP066 – Luminosity Increase in Laser-Compton Scattering by Crab Crossing	368

TUP067 – Study on Cherenkov Laser Oscillator Using Tilted Electron Bunches	371
TUP069 – Simulating Beam Dynamics in Coherent Electron-Cooling Accelerator with WARP	374
TUP070 – Development of Mid-Infrared Photoacoustic Spectroscopy System for Solid Samples at Kyoto University Free Electron Laser Facility	378
TUP071 – Study on Second Harmonic Generation in SiC Using Infrared FEL	382
TUP072 – Simulation of Phase Shifters Between FEL Amplifiers in Coherent Electron Cooling	386
WEA01 – European XFEL Injector Commissioning Results	389
WEA02 – Model of Photocathode for CW Electron Gun	394
WEA04 – Novel Concepts of a High-Brightness Photoinjector RF Gun	397
WEA05 – Higher Fields and Beam Energies in Continuous-Wave Room-Temperature VHF RF Guns	401
WEB03 – R&D at SLAC on Nanosecond-Range Multi-MW Systems for Advanced FEL Facilities	404
WEB04 – Laser-to-RF Synchronization with Femtosecond Precision	407
WEC02 – Optimization of Superconducting Undulators for Low Repetition Rate FELs	411
WEP003 – Update on the Lifetime of Cs ₂ Te Photocathodes Operated at FLASH	415
WEP004 – Calculations for a THz SASE FEL Based on the Measured Electron Beam Parameters at PITZ	419
WEP005 – Coaxial Coupler RF Kick in the PITZ RF Gun	422
WEP006 – Preliminary On-Table and Photoelectron Results from the PITZ Quasi-Ellipsoidal Photocathode Laser System	426
WEP007 – Electron Beam Asymmetry Compensation with Gun Quadrupoles at PITZ	429
WEP008 – Beam Brightness Improvement by Ellipsoidal Laser Shaping for CW Photoinjectors	432
WEP009 – A Cryocooled Normal-Conducting and Superconducting Hybrid CW Photoinjector	436
WEP010 – Beam Asymmetry Studies with Quadrupole Field Errors in the PITZ Gun Section	440
WEP012 – A 2.45 GHz Photoinjector Gun for an FEL Driven by Laser Wakefield Accelerated Beam	444
WEP014 – Pulse Duration Measurement of Pico-second DUV Photocathode Driving Laser by Autocorrelation Technique Using Two-Photon Absorption in Bulk Material	447
WEP015 – Current Experimental Work with Diamond Field-Emitter Array Cathodes	450
WEP016 – Modeling of Diamond Field-Emitter Arrays for High-Brightness Photocathode Applications	454
WEP018 – Electron Beam Heating with the European XFEL Laser Heater	458
WEP019 – High Stable Pulse Modulator for PAL-XFEL*	460
WEP021 – Preliminary Results of the Dark Current Modelling for the Polfel Superconducting Lead Photocathode	463
WEP024 – Design and Research of a Micro-Pulse Electron Gun	466
WEP025 – Emittance Measurements from SRF Gun in CeC Accelerator	470
WEP026 – Inducing Microbunching in the CLARA FEL Test Facility	475
WEP027 – Numerical Study of Cherenkov Radiation From Thin Silica Aerogel	479
WEP029 – Recent Experimental Results on High-Peak-Current Electron Bunch and Bunch Trains Interacting With a THz Undulator	482
WEP030 – Large-Scale Turnkey Timing Distribution System for New Generation Photon Science Facilities	485
WEP031 – Using A Neural Network Control Policy For Rapid Switching Between Beam Parameters in an FEL	488
WEP034 – Diagnostics Upgrades for Investigations of HOM Effects in TESLA-type SCRF Cavities	492
WEP036 – Adaptive Feedback for Automatic Phase-Space Tuning of Electron Beams in Advanced XFELs	496
WEP040 – Sub-Femtosecond Time-Resolved Measurements Based on a Variable Polarization X-Band Transverse Deflecting Structures for SwissFEL	499
WEP041 – HLS to Measure Changes in Real Time in the Ground and Building Floor of PAL-XFEL, Large-Scale Scientific Equipment	503
WEP043 – Tune-Up Simulations for LCLS-II	507
WEP044 – Beam Loss Monitor for Undulators in PAL-XFEL	511
WEP048 – Coherent Undulator Radiation From a Kicked Electron Beam	515
WEP051 – Helical Undulators for Coherent Electron Cooling System	519
WEP054 – The Magnetic Field Integral Hysteresis on the European XFEL Gap Movable Undulator Systems	522
WEP055 – Tapered Flying Radiofrequency Undulator	525
WEP056 – Effect of Beam Transverse Angle Deflection in TGU on FEL Power	529
WEP057 – Design of a Compact Hybrid Undulator for the THz Radiation Facility of Delhi Light Source (DLS)	532
WEP060 – Characterizing Sub-Femtosecond X-ray Pulses from the Linac Coherent Light Source	535
WEP061 – Thermal Stress Analysis of a Thin Diamond Crystal Under Repeated Free Electron Laser Heat Load	539
WEP062 – Optical Beam Quality Analysis of the Clara Test Facility Using Second Moment Analysis	543
WEP063 – A Two-in-One Type Undulator	547

WEP064 – Tunable High-Gradient Quadrupoles for a Laser-Plasma Acceleration-Based FEL	550
WEP065 – Cryogenic Permanent Magnet Undulator for an FEL Application	554
WEP073 – Lie Map Formalism for FEL Simulation	557
WEP074 – Simulations of the Dependence of Harmonic Radiation on Undulator Parameters	560
WEP078 – Period-Averaged Symplectic Maps for the FEL Hamiltonian	563
THB02 – Non-Standard Use of Laser Heater for FEL Control and THz Generation	566
FRB01 – Time-Domain Analysis of Attosecond Pulse Generation in an X-Ray Free-Electron Laser	569
FRB03 – Dynamics of Superradiant Emission by a Prebunched E-Beam and its Spontaneous Emission Self-Interaction	572
FRB04 – Canonical Formulation of 1D FEL Theory Revisited, Quantized and Applied to Electron Evolution	576
FRB05 – Wide Bandwidth, Frequency Modulated Free Electron Laser	581
Appendices	587
List of Authors	587
Institutes List	597
Participants List	609

JOHN MADEY: A SHORT HISTORY OF MY FRIEND AND COLLEAGUE

Luis Elias, University of Hawaii, Manoa (R), Hawaii, USA



Figure 1: John Madey (1943-2016) in his Hawaii Laboratory.

BRIEF HISTORY AT STANFORD UNIVERSITY

I thank the organizing committee for inviting me to share with you some stories of my friend and colleague John Madey, who passed away on July 2016 in Honolulu, Hawaii.

I will first summarize to you the early history of John Madey's FEL at Stanford University. Then, I will try to briefly relate to you about our joint work at the University of Hawaii. Lastly, I will share with you some final thoughts on John's achievements.

I met John Madey in 1973 at Stanford University right after he and I received our respective Ph. D degrees in Physics. He from Stanford University and I from the University of Wisconsin in Madison. It was through a connection between Professors Alan Schwettman and Arthur Schawlow of Stanford University with my major professor William Yen, from the University of Wisconsin, that I was hired to assist John Madey in the demonstration of his SBR laser. Perhaps my experience with experimental vacuum synchrotron radiation spectroscopy contributed to their hiring decision.

Before arriving at SU, John's proposal goal to show "Stimulated Bremsstrahlung Radiation" had been already funded by the US Air Force Office for Scientific Research

(AFSOR). Instead of SBR, J. Madey later coined the acronym FEL (Free Electron Laser) to describe the device.

After meeting him in 1973, it did not take long for me to recognize the genius character of John Madey. During an early visit to his house in Palo Alto, I discovered that most of his house was filled with old radio electronic equipment. I then learned that John and his brother Jules had been actively involved in ham radio communications since 1956. As is well known now, when John was 13 and Jules was 16, they began relaying communications from the south pole to families and friends in the United States. I then realized that before his interest in the FEL came about, John had already accumulated a vast experience in the field of electronic devices, including his latest electronics accomplishment. It was digital communication equipment that allowed John, in Palo Alto, to communicate with his older brother Jules, in Marin County, by means of two very old teletype machines. It was a major achievement because at that time internet communication was not invented.

I remember that in 1973 there were not many scientists, including some professors at Stanford who believed that John's FEL would work. As described in his original publication [1], his physical interpretation of EM field amplification occurred because during electron radiation inside the static undulator field, the electron energy recoil can favor photon emission process over photon absorption. His quantum calculation of FEL gain was made in terms of photon energy $\hbar\omega$. I recall clearly how in one of John's presentations of his theory of the FEL to the Physics department, professors Felix Bloch and Arthur Schawlow pointed out the fact that in John's gain formula calculation \hbar mysteriously disappeared from the equation. Despite of their objection, I was quite impressed with John's valiant and intelligent defense of his theory, considering that the objections were made by Nobel Laureates in physics.

As it turned out, John's gain equation was correct and his objectors were also correct because, as we know now, quantum electrodynamics is not totally needed to explain the gain result. The theory of FEL can be satisfactorily explained in terms of classical electrodynamics.

Because of Stanford University rules professor Alan Schwettman became the principal investigator of the FEL program and consequently our boss. As director of the Superconducting Acceleration (SCA) program, he allowed us the use of the SCA in the FEL program. After my arrival at Stanford University, Alan hired Todd Smith to run the SCA. Consequently, the three of us (John, Todd and I) were charged with the responsibility of implementing the FEL program in 1973.

The Stanford FEL program was divided into three major experimental subprograms that included: (1) the electron beam system, (2) the magnetic undulator and the (3) the optics system. Todd was responsible for the electron beam,

John and I were responsible for the construction and testing of the magnetic undulator and I was responsible for the optics and signal diagnostic system.

Two 5.2-m long superconducting helical magnetic undulator were constructed for the experiment. The first undulator was wound with superconducting wire by means of a semi-automatic machine that laid a single wire along helical grooves milled on an aluminum mandrel. Unfortunately, this undulator was severely damaged because, when first energized at low temperature, an electrical short developed between the wire winding and the aluminum mandrel. This problem was eliminated in the second undulator by replacing the helical metal mandrel with a plastic one. Before potting the undulator wires, a 7-m long, 12-mm diameter copper vacuum tube was inserted along the axis of the undulator. With an inside diameter of 10 mm the copper tube served as a vacuum beamline designed to transport the electron beam and to also guide the optical beam. Low temperature testing of the new undulator was quite successful.

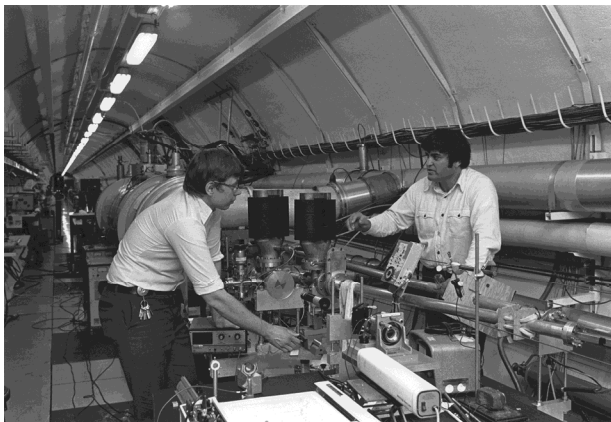


Figure 2: John Madey and Luis Elias working inside the SCA tunnel with the FEL equipment (1995).

In 1975, two years after the start of the project, the first test of FEL laser amplification was obtained using a pulsed Molelectron CO₂ laser. Running of the SCA was very costly matter. Each FEL run lasted for only a few days due to the lack of sufficient FEL financial resources. We had to work day and night to test the FEL as a light amplifier. After two or three runs we finally obtained good data on the FEL gain.

Gain was observed for optical radiation at 10.6 μm due to stimulated radiation by a relativistic electron beam in a constant spatially periodic transverse magnetic field. A gain of 7% per pass was obtained. The detail of the results was published in the following PSL article [2].

Although John's FEL gain was demonstrated at 10.6 μm. A JASON committee, was appointed by the government in 1976 to evaluate the FEL usefulness to the Department of Defense. The JASON committee central finding was that the FEL gain was too small. Perhaps their negative reaction took place because John, because of engineering background, used to described the power gain of the FEL in decibels units. In decibels, the gain of the FEL was only 0.3 dB. Compared to the gain of more than 10 dB observed

in commercial electron devices, such as microwave tubes, the FEL gain is indeed quite small. The findings by the JASON committee had the negative effect of putting in danger the continuity of FEL program funding by the AFOSR. In fact, for a period of one or two months, John used his own money to pay for my salary. I was not aware of John's generous gesture until we met again in Hawaii.

To counteract the negative aspects of the JASON committed report, John and I agreed that we needed to accelerate the next phase of the FEL program, that is we needed to show FEL oscillations without delay.

To show FEL oscillations at 10.6 μm, the plan was to install spherical vacuum mirrors, separated by about 12 m, on each end of the undulator amplifier. Because of the length of copper tube (7 m), it was not possible to establish a pure TEM₀₀ along the whole length of the copper tube.

We decided that our best chance was to transport the 10.6 μm guided mode along the copper tube. Hence, the radius of curvature of the mirrors were chosen in so that a TEM₀₀ waist was focused at each end of the undulator copper tube. The idea was to match efficiently the TEM₀₀ mode to a EH₁₁. This is dielectric mode, it is the lowest loss mode that can be transmitted along a copper waveguide because, at the CO₂ laser frequency, the copper surface behaves less as a metal and more as a dielectric. The estimated theoretical oscillator loss was about 2% per pass.

Unfortunately, as hard as we tried, we could not force to operate the FEL above threshold at 10.6 μm. After examining carefully, the inside of the copper tube, we discovered the existence of a mechanical deformation inside the pipe. We concluded that the kink in the pipe increased optical losses beyond what was required to operate the FEL above gain threshold.

After many discussions, I convinced John that we should increase the electron energy so that a higher frequency pure TEM₀₀ could clear the copper waveguide and thus diminish the losses contributed by the copper waveguide. John agreed to the suggestion provided we could accurately measure the actual optical losses of the resonator before using the electron beam. With the help of Jerry Ramian we design and constructed a pulsed intracavity helium-neon gas amplifier operating at a wavelength of 3.39 μm. When installed inside the FEL resonator, the decay time of the TEM₀₀ mode showed below 2% resonator optical losses. Encouraged by this result, we tested the operation of the FEL at 3.39 μm at the end of 1976. Almost immediately the FEL operated as an oscillator. The result was published in a PRL letter [3].

It is an underestimation to say that we were all overjoyed by the results obtained. To show his enthusiasm, the next day after the FEL operated as an oscillator, John brought down to the laboratory a case of champagne to celebrate the success of our efforts. For the benefit of those at Stanford who were not convinced that John's FEL experiment would work, we transported the output laser beam along a 24-m path out of the experimental area and showed the spot made by the beam on a thermal foil located outside lab. Many people, including professors, scientists and students

came to see the spot image. As one of the observers, I clearly remember professor Schawlow saying “Oh, this actually works!”

It took us more than a couple of weeks to realize the full implication of the FEL results. Our euphoric feelings were tempered by our paranoid thoughts that we were being watched by interested government and/or industrial agencies who wanted to misappropriate our experimental findings. Thankfully, after a couple of weeks, those feelings disappeared.

Our first contact with international scientist came about immediately after we failed to present our FEL results at the 1975 Quantum Electronics Conference in Washington, DC. My good friends Alberto Renieri and Pino Dattoli, from the Enrico Fermi Laboratory in Frascati, Italy, were present at the conference and traveled without delay to Stanford University to learn the details of the FEL experiment. We were informed that most of the participants at the conference had protested our absence noisily by stomping loudly their feet on the floor. We explained to them that we could not travel to Washington because we were in the middle of an expensive FEL run.

Later that month, my other good friend from Israel Avi Gover, who was finishing his Doctoral degree at the California Institute of California, came to Stanford to congratulate us for our FEL success. We were all delighted to meet and discuss the FEL with all our distinguished visitors.

Our first serious discussion of FEL applications took place at the Los Alamos National Laboratory in 1977. The group working with the separation of U-235 from the naturally occurring U-238 were doing it with a diode laser that generated only 6 milliwatts of power. When they heard that our FEL generated megawatts of power, we were immediately invited to present our results at LANL. Because I was not then a US citizen, the presentation was moved to the library of the lab. After the presentation, our colleagues were quite serious with the request to move the FEL equipment from Stanford University to their laboratory. John explained that their request was not possible to implement. Instead he suggested that LANL should build their own FEL, which they later did.

After the FEL oscillator experiment was completed John became interested in increasing the average power of the FEL. The use of an electron storage ring appeared then to be an appropriate device where an FEL could operate with large average power output. We all knew that during FEL amplification the energy spread of the incoming electron beam increased. John was hoping that the side of the FEL resonance curve that produces gain behaves like a force that should damp electron energy oscillations. Our computer simulations gave us the opposite result when the whole resonance curve is introduced into the simulations. At that time, John was not a computer guy. He dependent on his HP programmable calculator to carry out his simulations.

Using theoretical considerations (Liouville's theorem) Alberto Renieri confirmed that continuous energy damping could not take place in a an electron storage ring FEL.

Later, John and David Deacon collaborated with their French colleagues at the ACO electron storage ring in Orsay to test the operation of an FEL. The results confirmed that Ranieri was correct in his prediction of low average power FEL operation in an electron storage ring.

Before I moved to the University of California at Santa Barbara in 1978, I visited Richard Hechtel at nearby Litton Industries in San Carlos, CA. As a consultant, Richard was designing a depressed electron collector for an electrostatic accelerator FEL that I wanted to construct in Santa Barbara. I was explaining to him how we demonstrated FEL oscillations at Stanford University. Richard commented that the FEL appeared to like commercial electron devices. By then I had read about the Ubitron device. Richard reacted immediately and told me to come with him and meet the inventor of such a tube. It was a great pleasure to meet Robert M. Phillips. He was delighted to learn that the FEL amplifier operated very much like an extremely high voltage Ubitron tube.

At the end of my term at Stanford University, John Madey was awarded the First International FEL prize. He could not go to Jerusalem, so, he asked me to receive the accolade on his behalf. Of course, I was honored to do it.

JOHN AND MYSELF AT THE UNIVERSITY OF HAWAII IN MANOA

After nearly 7 years working with John at Stanford University, I was invited by the Physics Department of the University of California in Santa Barbara to construct and operate a far infrared FEL that could be used to study the physics of condensed mater. Eventually John moved to Duke University in Durham, North Carolina where he continued with the further developments of FELs.

Subsequently, after developing a compact far-infrared FEL at the University of Florida in Orlando, I was invited to join the faculty of Physics Department at the University of Hawaii in Manoa. I brought to Honolulu the compact far-infrared FEL. John was already there when I arrived. He offered me laboratory space inside his FEL laboratory for my FEL. Regrettably, because of the thick concrete radiation wall requirements required by the accelerators it was not possible to install my FEL inside his laboratory. Due to the high-cost of construction in Hawaii, the university did not have the funds to construct a separate far-infrared laboratory. The final disposition of my compact FEL was to ship it to the CBPF (Brazilian Center for Physics Research) located in Rio de Janeiro.

In Hawaii, John and I worked closely, for nearly 14 years in support of the Department of Defense focus on remote detection of IEDs with lasers. We also carried out discussions and calculations of EM radiation resistance problems.

JOHN MADEY: SOME OF HIS ACHIEVEMENTS

It may sound simplistic but I believe that John Madey showed us that he was a unique genius whose life was dedicated to enriching our understanding of electrodynamics and to advance technology for the benefit of humankind. His work with ham radio and his extraordinary contribution to the field of FELs and its applications to medicine are mere examples of his exemplary good character. The importance of John's scientific impact to science was stressed by the APS's selection of the two PRL publications, [2] and [3], as the most important scientific contribution of each of the years 1976 and 1976. For his scientific work John was awarded many prizes and accolades, including the *Stuart Ballantine Medal* from The Franklin Institute in 1989 and the *Robert R. Wilson Prize for Achievement in the Physics of Particle Accelerators* by the American Physical Society.

To continue with his magic scientific predictions, prepared an experimental proposal aimed at demonstrating that advanced solutions of Maxwell's equation do exist. Before he passed away, he explained to me how he and his brother Jules were ready to demonstrate instantaneous EM communication between two points in space through the detection of near-field advanced waves. As proof of the seriousness of such an experiment, they prepared a patent disclosure describing the invention. If they are right, one cannot imagine the technological impact that their discovery will have on our human society. It is up to the University of Hawaii to request a patent.

An image that is always present in my mind is the picture of John Madey permanently dressed in his black shoes, black trousers, white shirt and a blue sweater whose right side had a hole on his right side that allowed him to have direct access to his numerous keys hanging from his belt. I assumed that the hole on the sweater developed because of its daily usage. However, in one of our trips to Italy John purchased a brand new blue sweater. The next day, to my surprise, the hole appeared freshly cut.

Another Image of John was his driving an old (1960?) rusted car to work. When I asked him about buying a new

car he remarked that he himself could tune up the old clunker faster and more efficiently than a new computerized engine. To compensate for the old car, John was the pride owner of two Alfa Romeo cars. He would ride them on weekends. He told me that the only inconvenience with these cars is that he had to purchase their park plugs in Italy, the ones sold in the US did not work as well.

I remember Professor Schawlow telling me the story that that he and Professor Charles Townes had prepared a list of the ten most common applications of conventional lasers. He told me that none of their predictions were realized. Apparently, the most common commercial application of lasers is to digitally scan the price of products in supermarkets. John and I had a similar list for the FEL. None of our predictions came true. We were aware that, except for the absence of efficient mirror reflectivity FEL operation in the X-region was possible. SASE FEL radiation was not considered by us at the time. We are now all delighted by the success demonstrated by SASE FELs around the world. I am sure that the next speaker will elaborate on the important contribution that my good friend Rodolfo Bonifacio made to the theory of SASE radiation

I had the great honor of working with John Madey for more than twenty years. As a scientist, I owe him what I have accomplished, as a person I loved him like a brother. The fact that you are all here proves that John Madey also has a significant impact in so many careers. I miss him greatly.

REFERENCES

- [1] J. Madey, "Stimulated emission of Bremsstrahlung in a periodic magnetic field", *J. Appl. Phys.* 42, p. 1906 (1971).
- [2] L. Elias, W. Fairbank, J. Madey, and T. Smith, "Observation of stimulated emission of radiation by relativistic electrons in a spatially periodic transverse magnetic field", *Phys. Rev. Lett.* 36, no. 13, p. 717 (1976).
- [3] D. Deacon, L. Elias, J. Madey, G. Ramian, H. Schwettman, and T. Smith, "First operation of a free-electron laser", *Phys. Rev. Lett.* 38, no. 16, p. 892 (1977).

COHERENCE LIMITS OF X-RAY FEL RADIATION

E.A. Schneidmiller, M.V. Yurkov, DESY, Hamburg, Germany

Abstract

The radiation from SASE FELs has always limited value of the degree of transverse coherence. When transverse size of the electron beam significantly exceeds diffraction limit, the mode competition effect does not provide the selection of the ground mode, and spatial coherence degrades due to contribution of the higher order transverse modes. It is important that the most strong higher modes are azimuthally non-symmetric which leads to fluctuations of the spot size and of the pointing stability of the photon beam. These fluctuations are fundamental and originate from the shot noise in the electron beam. The effect of the pointing instability becomes more pronouncing for shorter wavelengths. We analyze in detail the case of optimized SASE FELs and derive universal dependencies applicable to all operating and planned x-ray FELs. It is shown that x-ray FELs driven by low energy electron beams will exhibit poor spatial coherence and bad pointing stability.

INTRODUCTION

Coherence properties of the radiation from SASE FELs strongly evolve during the amplification process [1–5]. At the initial stage of amplification the spatial coherence is poor, and the radiation consists of a large number of transverse modes [5–13]. In the exponential stage of amplification the transverse modes with higher gain dominate over modes with lower gain when the undulator length progresses. The mode selection process stops at the onset of the nonlinear regime, and the maximum values of the degree of the transverse coherence is reached at this point.

Gain separation of the FEL radiation modes is mainly defined by the value of the diffraction parameter B [10] describing diffraction expansion of the radiation with respect to the electron beam size. For FELs with diffraction limited beams the value of the diffraction parameter is less than or about unity, and spatial coherence at saturation reaches values of about 90%. Large values of the diffraction parameter ($B \gtrsim 10 \dots 100$) are typical for SASE FELs operating in the hard x-ray range [14–18]. Increase of the diffraction parameter results in a decrease of diffraction expansion and of relative separation of the gain of the modes. In this case we deal with the mode degeneration effect [7, 10]. Since the number of gain lengths to saturation is limited (about 10 for x-ray FELs), the contribution of the higher spatial modes to the total power grows with the value of the diffraction parameter, and the transverse coherence degrades.

The main competitor of the ground TEM_{00} mode is the first azimuthal TEM_{10} mode. When contribution of TEM_{10} mode to the total power exceeds a few per cent level, a fundamental effect of bad pointing stability becomes to be pronouncing. For optimized SASE FEL the power of the effect grows with the parameter $\hat{\epsilon} = 2\pi\epsilon/\lambda$. SASE FELs operating

at short wavelengths and low electron beam energy with the value of $\hat{\epsilon} \gtrsim 1$ suffer from the mode degeneration effect resulting in significant degradation of the spatial coherence and pointing stability of the photon beam. The effect of the photon beam pointing jitter is a fundamental one, and can not be eliminated by elimination of the jitters of machine parameters (orbit, phase, etc.).

FEL RADIATION MODES AND MODE DEGENERATION EFFECT

We consider the axisymmetric model of the electron beam. It is assumed that the transverse distribution function of the electron beam is Gaussian, so rms transverse size of matched beam is $\sigma = \sqrt{\epsilon\beta}$, where $\epsilon = \epsilon_n/\gamma$ is rms beam emittance and β is the beta-function. In the framework of the three-dimensional theory the operation of a short-wavelength FEL amplifier is described by the following parameters: the diffraction parameter B , the energy spread parameter $\hat{\Lambda}_T^2$, the betatron motion parameter \hat{k}_β and detuning parameter \hat{C} [9, 10]:

$$\begin{aligned} B &= 2\bar{\Gamma}\sigma^2\omega/c, & \hat{C} &= C/\bar{\Gamma}, \\ \hat{k}_\beta &= 1/(\beta\bar{\Gamma}), & \hat{\Lambda}_T^2 &= (\sigma_E/E)^2/\bar{\rho}^2, \end{aligned} \quad (1)$$

The gain parameter $\bar{\Gamma}$ and efficiency parameter $\bar{\rho}$ are given by:

$$\bar{\Gamma} = \left[\frac{I}{I_A} \frac{8\pi^2 K^2 A_{JJ}^2}{\lambda\lambda_w\gamma^3} \right]^{1/2}, \quad \bar{\rho} = \frac{\lambda_w\bar{\Gamma}}{4\pi}. \quad (2)$$

Here $E = \gamma mc^2$ is the energy of electron, γ is relativistic factor, and $C = 2\pi/\lambda_w - \omega/(2c\gamma_z^2)$ is the detuning of the electron with the nominal energy \mathcal{E}_0 . Note that the efficiency parameter $\bar{\rho}$ entering equations of the three dimensional theory relates to the one-dimensional parameter ρ

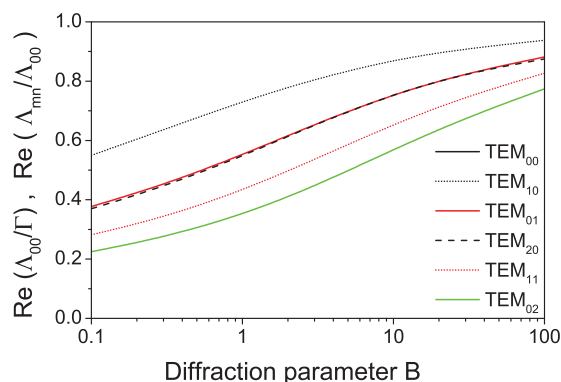


Figure 1: The ratio of the maximum gain of the higher modes to the maximum gain of the fundamental mode $Re(\Lambda_{mn})/Re(\Lambda_{00})$ versus diffraction parameter B for the case of the “cold” electron beam. Calculations have been performed with the code FAST [20].

as $\rho = \bar{\rho}/B^{1/3}$ [10, 19]. The following notations are used here: I is the beam current, $\omega = 2\pi c/\lambda$ is the frequency of the electromagnetic wave, λ_w is undulator period, K is the rms undulator parameter, $\gamma_z^{-2} = \gamma^{-2} + \theta_s^2$, $I_A = mc^3/e = 17$ kA is the Alfvén current, $A_{JJ} = 1$ for helical undulator and $A_{JJ} = J_0(K^2/2(1+K^2)) - J_1(K^2/2(1+K^2))$ for planar undulator. J_0 and J_1 are the Bessel functions of the first kind. The energy spread is assumed to be Gaussian with rms deviation σ_E .

The amplification process in SASE FELs starts from the shot noise in the electron beam. In the exponential stage of amplification the radiation consists of a large number of transverse and longitudinal modes [5–13]:

$$\begin{aligned} \vec{E} &= \sum_{m,n} \int d\omega A_{mn}(\omega, z) \Phi_{mn}(r, \omega) \\ &\times \exp[\Lambda_{mn}(\omega)z + im\phi + i\omega(z/c - t)]. \end{aligned} \quad (3)$$

Each mode is characterized by the eigenvalue $\Lambda_{mn}(\omega)$ and the field distribution eigenfunction $\Phi_{mn}(r, \omega)$ [8, 9]. The real part of the eigenvalue $\text{Re}(\Lambda_{mn}(\omega))$ is referred to as the field gain. The fundamental TEM₀₀ mode has the highest gain. Relative gain of its nearest competitors is depicted in Fig. 1 as function of the diffraction parameter. Sorting the modes by their gain results in the following ranking: TEM₀₀, TEM₁₀, TEM₀₁, TEM₂₀, TEM₁₁, TEM₀₂. The difference in the gain between the fundamental TEM₀₀ mode and higher modes is pronounced for small values of the diffraction parameter $B \lesssim 1$, but is small for large values of B . In other words, the effect of the mode degeneration takes place. Its origin can be understood with the qualitative analysis of the eigenfunctions (see Fig. 2). For small values of the diffraction parameter the field of the higher spatial modes spans far away from the core of the electron beam while the fundamental TEM₀₀ mode is more confined. This feature provides a higher coupling factor of the radiation with the electron beam and higher gain. For large values of the diffraction parameter all radiation modes shrink to the beam axis which results in an equalizing of coupling factors and of the gain.

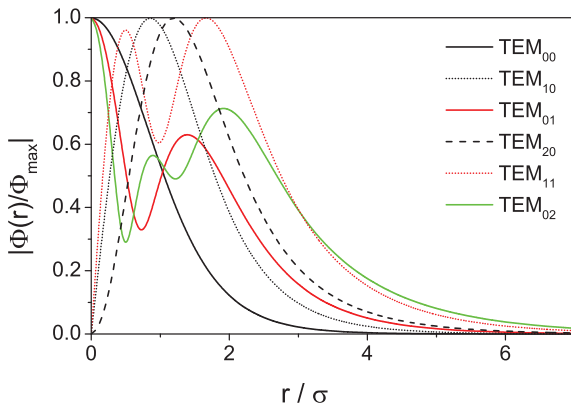


Figure 2: Amplitude of the eigenfunctions of the FEL radiation modes, $|\Phi_{mn}(r)|/|\Phi_{\max}|$ for diffraction parameter $B = 10$. The list of modes is ranked by the gain. Calculations have been performed with code FAST [20].

Asymptotically, the eigenvalues of all modes tends to the one dimensional asymptote as [3]:

$$\Lambda_{mn}/\Gamma \simeq \frac{\sqrt{3} + i}{2B^{1/3}} - \frac{(1 + i\sqrt{3})(1 + n + 2m)}{3\sqrt{2}B^{2/3}}, \quad (4)$$

where Γ is the gain parameter [10]. For x-ray SASE FELs, the undulator length to saturation is about 10 field gain lengths [1, 2, 4]. The mode selection process stops at the onset of the nonlinear regime, about two field gain lengths before saturation. For the value of the diffraction parameter $B = 1$ we get from Fig. 1 $\text{Re}(\Lambda_{10}/\Lambda_{00}) = 0.73$, and the ratio of field amplitudes of TEM₀₀ and TEM₁₀ modes exceeds a factor of 10 at the onset of the nonlinear regime. For $B = 10$ we have $\text{Re}(\Lambda_{10}/\Lambda_{00}) \simeq 0.87$, and the ratio of the field amplitudes is about a factor of 3 only. An estimate for the contribution of the higher spatial modes to the total power is about 10%. Thus, an excellent transverse coherence of the radiation is not expected for SASE FELs with diffraction parameter $B \gtrsim 10$.

OPTIMIZED SASE FELS

Target value for x-ray FEL optimization is the gain of the fundamental mode. In this case the field gain length of the fundamental mode and optimum beta function, are rather accurately approximated by [1, 2, 21]:

$$\begin{aligned} L_g &= 1.67 \left(\frac{I_A}{I}\right)^{1/2} \frac{(\epsilon_n \lambda_w)^{5/6}}{\lambda^{2/3}} \frac{(1 + K^2)^{1/3}}{KA_{JJ}} (1 + \delta), \\ \beta_{\text{opt}} &\simeq 11.2 \left(\frac{I_A}{I}\right)^{1/2} \frac{\epsilon_n^{3/2} \lambda_w^{1/2}}{\lambda KA_{JJ}} (1 + 8\delta)^{-1/3}, \\ \delta &= 131 \frac{I_A}{I} \frac{\epsilon_n^{5/4}}{\lambda^{1/8} \lambda_w^{9/8}} \frac{\sigma_\gamma^2}{(KA_{JJ})^2 (1 + K^2)^{1/8}}, \end{aligned} \quad (5)$$

where $\sigma_\gamma = \sigma_E/mc^2$, σ_E is rms energy spread, $\epsilon_n = \gamma\epsilon$ is normalized rms emittance, K is rms undulator parameter,

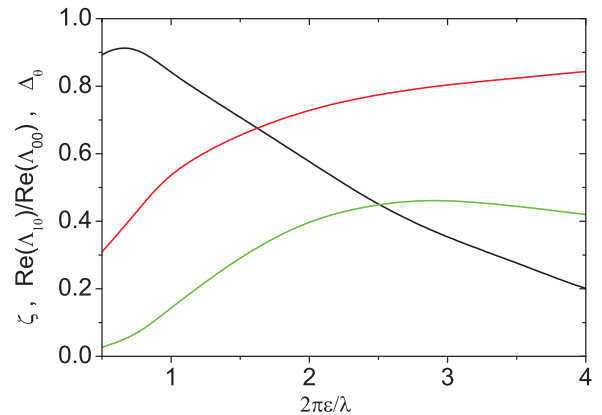


Figure 3: Optimized SASE FELs: Degree of transverse coherence ζ (black curve), ratio of the gain $\text{Re}(\Lambda_{10})/\text{Re}(\Lambda_{00})$ (red curve), and rms deviation of the photon beam center of gravity Δ_θ in terms of rms size of the photon beam (green curve). Simulations have been performed with code FAST [20].

Table 1: Parameter Space of X-Ray FELs

	LCLS	SACLA	EXFEL	SWISS FEL	PAL XFEL
Energy [GeV]	13.6	8.0	17.5	5.8	10
Wavelength [Å]	1.5	0.6	0.5	0.7	0.6
ϵ_n [mm-rad]	0.4	0.4	0.4	0.4	0.4
$\hat{\epsilon}$	1	2.7	1.5	3.4	2.1

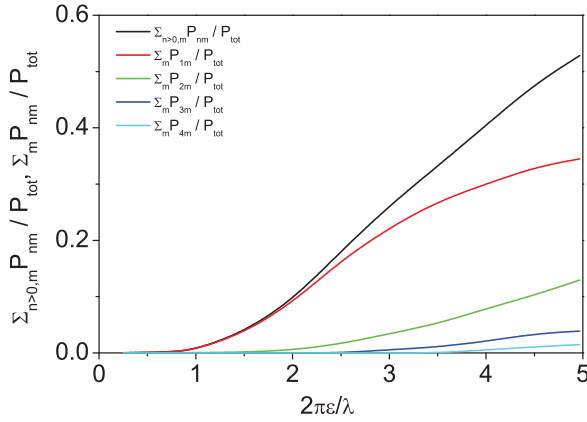


Figure 4: Optimized SASE FELs: partial contributions of nonsymmetric modes to the total power versus the emittance parameter $\hat{\epsilon} = 2\pi\epsilon/\lambda$. SASE FEL operates in the saturation. Black curve is total contribution of nonsymmetric modes, and color curves correspond to azimuthal indices from 1 to 4. Simulations have been performed with code FAST [20].

A_{JJ} is averaging factor, λ is radiation wavelength, λ_w is undulator period, I is the beam current, $I_A \approx 17$ kA is Alfven's current.

In the case of negligibly small energy spread, characteristics of SASE FEL written down in the dimensionless form are functions of two parameters, $\hat{\epsilon} = 2\pi\epsilon/\lambda$ and parameter $N_c = IL_g\lambda/(e\lambda_w c)$ defining the initial conditions for the start-up from the shot noise [1–3]. Dependence of characteristics on the value of N_c is slow, in fact logarithmic. Diffraction parameter B and parameter of betatron oscillations in the case of optimized FEL are:

$$\begin{aligned} B &= 2\bar{\Gamma}\sigma^2\omega/c \approx 12.5 \times \hat{\epsilon}^{5/2}, \\ \hat{k}_\beta &= 1/(\beta\bar{\Gamma}) \approx 0.158 \times \hat{\epsilon}^{-3/2}. \end{aligned} \quad (6)$$

Parameters of optimized x-ray FEL in saturation (saturation length, saturation efficiency, coherence time, spectrum bandwidth, degree of transverse coherence) are:

$$\begin{aligned} \hat{L}_{\text{sat}} &= \bar{\Gamma}L_{\text{sat}} \approx 2.5 \times \hat{\epsilon}^{5/6} \times \ln N_c, \\ \hat{\eta} &= P/(\bar{\rho}P_b) \approx 0.17/\hat{\epsilon}, \\ \hat{\tau}_c &= \bar{\rho}\omega\tau_c \approx 1.16 \times \sqrt{\ln N_c} \times \hat{\epsilon}^{5/6}, \\ \sigma_\omega &= \sqrt{\pi}/\tau_c, \\ \zeta_{\text{sat}} &\approx \frac{1.1\hat{\epsilon}^{1/4}}{1 + 0.15\hat{\epsilon}^{9/4}}. \end{aligned} \quad (7)$$

The diffraction parameter scales with the emittance parameter as $B \approx 12.5 \times \hat{\epsilon}^{5/2}$. Starting from $\hat{\epsilon} > 1$ the gain

of the TEM_{10} mode approaches very close to the gain of the ground TEM_{00} mode (see Fig. 3). Contribution of the TEM_{10} mode to the total power progresses with the growth of the emittance parameter (see Fig. 4). Starting from $\hat{\epsilon} > 2$ the azimuthal modes TEM_{2n} appear in the mode contents, and so on. The maximum value of the degree of transverse (which occurs in the end of the linear regime) degrades gradually with the growth of the emittance parameter (see Fig. 3).

Mode degeneration has significant impact on the pointing stability of SASE FEL. Figure 4 shows the relative contribution to the total radiation energy of the modes with higher azimuthal indices. Typical intensity distributions in the far zone are shown in Fig. 5. Transverse intensity patterns in slices have a rather complicated shape due to the interference of the fields of statistically independent modes with different azimuthal indices. These slice distributions are essentially non-gaussian when relative contribution of higher azimuthal modes to the total power approaches 10%. The shape of the intensity and phase distributions change drastically on a scale of the coherence length, and source point position and pointing jumps from spike to spike. Figure 3 represents quantitative description of this phenomena using notion of the rms deviation of the photon beam center of gravity Δ_θ expressed in terms of the rms size of the photon beam. We see that there is no perfect pointing of the photon beam, and for the values of $\hat{\epsilon} \gtrsim 2$ fluctuations of the pointing exceed 40%. Averaging of slice distributions over a radiation pulse results in a more smooth distribution. However, with limited number of longitudinal modes, the center of gravity of the radiation pulse (position) and its shape jitter from shot to shot which is frequently referred to as poor pointing stability. This effect is experimentally observed at FLASH [22], and evidently it should take place at other x-ray facilities. Only in the case of a long radiation pulse, or after averaging over many pulses, the intensity distribution approaches asymptotically to an azimuthally symmetric shape.

Table 1 presents list of parameters of the x-ray FELs compiled for the shortest design wavelength [14–18]. We assume the normalized emittance to be the same for all cases ($\epsilon_n = 0.4$ mm-mrad). Lower energy of electron beam results in larger value of the emittance parameter, and output radiation will have poor spatial coherence and poor pointing stability of the photon beam. Note that spatial jitter is of a fundamental nature (shot noise in the electron beam), and takes place even for an 'ideal' machine.

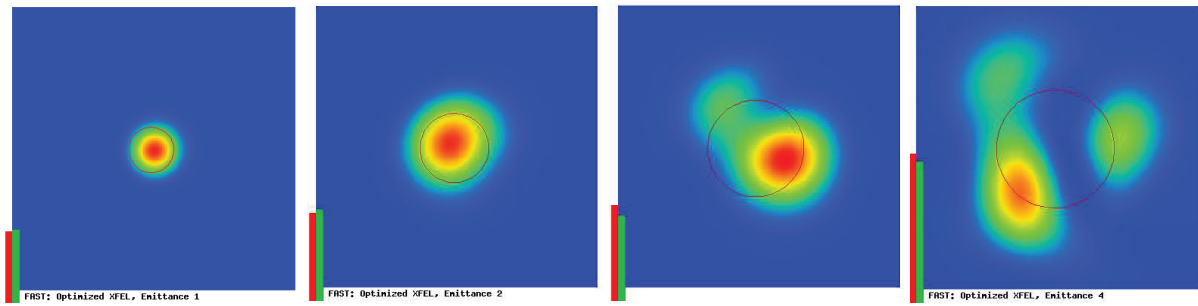


Figure 5: Typical slice distribution of the radiation intensity for optimized SASE FELs with $\hat{\epsilon} = 1, 2, 3, 4$ (from left to right). Circle denotes rms spot size. SASE FELs operates in the saturation. Simulations have been performed with code FAST [20].

There are only very limited means to suppress the mode degeneration effect by means of controlling the spread of longitudinal velocities (due to energy spread and emittance) [7, 10, 24]. Energy spread can be increased with the laser heater [25]. The price for this improvement is significant increase of the saturation length and reduction of the FEL power. Stronger focusing of the electron beam in the undulator helps to improve transverse coherence due to a reduction of the diffraction parameter and increase of the velocity spread. However, this will also result in the increase of the saturation length. Finally, with fixed energy of the electron beam, an available undulator length will define the level of spatial coherence and spatial jitter of the photon beam.

REFERENCES

- [1] E.L. Saldin, E.A. Schneidmiller, and M.V. Yurkov, *Opt. Commun.* 281 (2008) 1179.
- [2] E.L. Saldin, E.A. Schneidmiller, and M.V. Yurkov, *New J. Phys.* 12 (2010) 035010, doi: 10.1088/1367-2630/12/3/035010.
- [3] E.L. Saldin, E.A. Schneidmiller, and M.V. Yurkov, *Opt. Commun.* 281 (2008) 4727.
- [4] E.A. Schneidmiller, and M.V. Yurkov, *Proc. FEL 2012 Conference, MOPD08.pdf*.
- [5] E.L. Saldin, E.A. Schneidmiller, and M.V. Yurkov, *Opt. Commun.* 186 (2000) 185.
- [6] G. Moore, *Opt. Commun.* 52, 46 (1984).
- [7] E.L. Saldin, E.A. Schneidmiller and M.V. Yurkov, *Opt. Commun.* 97 (1993) 272.
- [8] M. Xie, *Nucl. Instrum. and Methods A* 445, 59 (2000).
- [9] E.L. Saldin, E.A. Schneidmiller and M.V. Yurkov, *Nucl. Instrum. and Methods A* 475, 86 (2001).
- [10] E.L. Saldin, E.A. Schneidmiller, and M.V. Yurkov, “The Physics of Free Electron Lasers,” Springer-Verlag, Berlin (1999).
- [11] K.J. Kim, *Phys. Rev. Lett.* 57 (1986) 1871.
- [12] J.M. Wang and L.H. Yu, *Nucl. Instrum. and Methods A* 250 (1986) 484.
- [13] S. Krinsky and L.H. Yu, *Phys. Rev. A* 35 (1987) 3406.
- [14] P. Emma *et al.* *Nature Photonics* 4, 641 (2010).
- [15] T. Ishikawa *et al.*, *Nature Photonics* 6, 540 (2012).
- [16] R. Ganter (Ed.), *Swiss FEL Conceptual Design Report, PSI Bericht Nr. 10-04*, (2012).
- [17] H.S. Kang, K.W. Kim, and I.S. Ko, *Proc. IPAC 2014 Conf., THPRO019* (2014).
- [18] M. Altarelli *et al.* (Eds.), *XFEL: The European X-Ray Free-Electron Laser. Technical Design Report, Preprint DESY 2006-097, DESY, Hamburg* (2006).
- [19] R. Bonifacio, C. Pellegrini and L.M. Narducci, *Opt. Commun.* 50 (1984) 373.
- [20] E.L. Saldin, E.A. Schneidmiller, and M.V. Yurkov, *Nucl. Instrum. and Methods A* 429 (1999) 233.
- [21] E.L. Saldin, E. A. Schneidmiller, and M.V. Yurkov, *Opt. Commun.* 235 (2004) 415.
- [22] E.A. Schneidmiller, and M.V. Yurkov, *J. Mod. Optics* (2015). DOI: 10.1080/09500340.2015.1066456.
- [23] W. Ackermann *et al.*, *Nature Photonics* 1(2007) 336.
- [24] E.A. Schneidmiller, and M.V. Yurkov, *Proc. FEL2015 Conference, Daejeon, Korea*, (2015) TUP021.
- [25] E.L. Saldin, E.A. Schneidmiller, and M.V. Yurkov, *Nucl. Instrum. and Methods, A* 528, 355 (2004).

COMMISSIONING AND FIRST LASING OF THE EUROPEAN XFEL*

H. Weise[†], W. Decking, Deutsches Elektronen-Synchrotron DESY, Hamburg, Germany
on behalf of the European XFEL Accelerator Consortium and the Commissioning Team

Abstract

The European X-ray Free-Electron Laser (XFEL) in Hamburg, Northern Germany, aims at producing X-rays in the range from 0.25 up to 25 keV out of three undulators that can be operated simultaneously with up to 27,000 pulses per second. The XFEL is driven by a 17.5-GeV superconducting linac. This linac is the world-wide largest installation based on superconducting radio-frequency acceleration. The design is using the so-called TESLA technology which was developed for the superconducting version of an international electron positron linear collider. After eight years of construction the facility is now brought into operation. First lasing was demonstrated in May 2017. Experience with the superconducting accelerator as well as beam commissioning results will be presented. The path to the first user experiments will be laid down.

INTRODUCTION

The European XFEL aims at delivering X-rays from 0.25 to up to 25 keV out of three SASE undulators [1, 2]. The radiators are driven by a superconducting linear accelerator based on TESLA technology [3]. The linac operates in 10 Hz pulsed mode and can deliver up to 2,700 bunches per pulse. Electron beams will be distributed to three different beamlines, this within a pulse. Three experiments can be operated in parallel.

The European XFEL is being realized as a joint effort by 11 European countries (Denmark, France, Germany, Hungary, Italy, Poland, Russia, Slovakia, Spain, Sweden, and Switzerland). The accelerator of the European XFEL and major parts of the infrastructure are contributed by the accelerator construction consortium, coordinated by DESY. The consortium consists of CEA/IRFU (Saclay, France), CNRS/IN2P3 (Orsay, France), DESY (Hamburg, Germany), INFN-LASA (Milano, Italy), NCBJ (Świerk, Poland), WUT (Wrocław, Poland), IFJ-PAN (Kraków, Poland), IHEP (Protvino, Russia), NIIIEFA (St. Petersburg, Russia), BINP (Novosibirsk, Russia), INR (Moscow, Russia), CIEMAT (Madrid, Spain), UPM (Madrid, Spain), SU (Stockholm, Sweden), UU (Uppsala, Sweden), and PSI (Villigen, Switzerland). DESY will also be responsible for the operation, maintenance and upgrade of the accelerator.

Construction of the European XFEL started in early 2009. The commissioning of the linear accelerator began end of 2015 with the injector, and end of 2016 with the cool-down of the main accelerator.

* Work supported by the respective funding agencies of the contributing institutes; for details please see <http://www.xfel.eu>
[†] hans.weise@desy.de

FACILITY LAYOUT

The complete facility is constructed underground, in a 5.2 m diameter tunnel about 25 to 6 m below the surface level and fully immersed in the ground water. The 50 m long injector is installed at the lowest level of a 7 stories underground building whose downstream end also serves as the entry shaft to the main linac tunnel. Next access to the tunnel is only about 2 km downstream, at the bifurcation point into the beam distribution lines. The beam distribution provides space for in total 5 undulators – 3 being initially installed. Each undulator is feeding a separate beamline so that a fan of 5 almost parallel tunnels, separated each by about 17 m, enters the experimental hall located 3.3 km away from the electron source.

The accelerator of the European XFEL starts with a photo-injector based on a normal-conducting 1.3 GHz 1.6 cell accelerating cavity [4]. A Cs₂Te-cathode, illuminated by a Nd:YLF laser operating at 1047 nm and converted to UV wavelength, produces 600 μs long bunch trains of 2,700 bunches. The photo-injector is followed by a standard XFEL superconducting (s.c.) 1.3 GHz accelerating module, and a 3rd harmonic (3.9 GHz) linearizer, also housing eight 9-cell s.c. cavities. A laser-heater, a diagnostic section and a high-power dump complete the injector.



Figure 1: First bunch compression chicane.

The European XFEL uses a three stage bunch compression scheme. All magnetic chicanes are tuneable within a wide range of R_{56} to allow for flexible compression scenarios, for instance balancing peak current and arrival time stability with LLRF performance. The tuning is achieved by means of large pole width dipole magnets and accordingly wide (400 mm) vacuum chambers (see Fig. 1). Special care was taken in the design of the vacuum chambers. There are no moving parts in order to min-

imize the risk of particle creation and transportation in the vicinity of the superconducting linac. Diagnostic stations are placed after the second and third compression stage.

The superconducting linear accelerator consists of 96 TESLA type accelerator modules [5]. Always 4 modules were fed by one 10 MW multi-beam klystron providing sufficient RF power for high gradients, including regulation reserve. The accelerator modules are suspended from the ceiling (see Fig. 2), while the complete RF infrastructure (klystron, pulse transformer, LLRF electronics) is installed below the modules. The modulators are placed in one single hall above ground, and the high-voltage pulse is fed to the pulse transformer by up to 2 km long cables. After the linac a collimation section protects down-stream hardware in case of component failure, and collimates halo particles [6].



Figure 2: View into the linac tunnel with the accelerator modules suspended from the ceiling and the RF infrastructure placed below, on the floor.

Almost 2 km of electron beam line distribute the beam to the SASE undulators SASE1 and SASE3 ('North Branch') or SASE2 ('South Branch'). The electrons are distributed with a fast rising flat-top strip-line kicker in one of the two electron beam lines. Another kicker system is capable of deflecting single bunches into a dump beam line. The distribution system allows for a free choice of the bunch pattern in each beam line even with the linac operating with long bunch trains and thus constant beam loading. Figure 3 summarizes the accelerator layout.

Electron bunch charges can be varied from 20 pC to 1000 pC [7], with resulting bunch length after compression ranging from 3 fs to 150 fs FWHM [8]. With three different linac energies (8.5, 14, and 17.5), and the variable gap undulators, photon energies from 0.25 keV to 25 keV can be covered.

COMMISSIONING RESULTS

Injector Commissioning

The injector is operated in a separate radiation enclosure, well separated from remaining tunnel installations. The beam dump at the end of the injector allows injector operation up to full beam power.

The superconducting accelerator of the injector was cooled down in December 2015 and first electrons were accelerated to 130 MeV on Dec. 18th [9]. Also at that early stage the 3rd harmonic lineariser was commissioned and from then on operated at the design gradient throughout the complete run [10]. The injector commissioning ended in July 2016, to connect the cryogenic distribution boxes of the main accelerator to the cryo-infrastructure.

Within this commissioning most of the design parameters of the European XFEL injector could be reached or even exceeded. Long bunch trains were produced and the measured slice emittance at 500 pC was between 0.4 and 0.6 mm mrad, depending on the measurement technique. Extensive emittance studies were made possible by a 4-off-axis-screen measurement stage. This enabled fast parameter scans and the study of the emittance evolution along long bunch trains [11]. Combined with a transverse deflecting structure, slice properties along the bunch train were measured.

For ultimate performance, the XFEL photo injector requires stable operation at RF power levels of about 6 MW. At these power levels the waveguide window and the cathode plug rf-contact showed reliability issues after some operating time. While solutions for these problems exist, their qualification needs long uninterrupted operation at high power levels [12]. Initially the XFEL is thus operated with a slightly reduced injector cavity gradient.

Cryogenic System

The European XFEL cryogenic system consists of two overhauled strings of the DESY HERA cryo-plant, a new distribution box and transfer line to the XFEL accelerator entrance shaft, cold compressors to reach 2K and further distribution boxes to distribute the He towards the injector. Finally, the long uninterrupted cryo-string of the linear accelerator together with its transfer and bypass-lines is also part of the cryogenic system. The cooling power was measured during the pre-commissioning. More than 1.9 kW in the 2 K circuit, 2.8 kW in the 5-8 K circuit, and 18 kW in the 40 – 80 K circuit were offered, all exceeding specifications. First cool down of the linac from room-temperature to 4 K was achieved during December 2016, with no cold leaks occurring. Start-up of the cold compressors enabled the handover of the accelerator at 2 K beginning of January. Regulation loops were optimized in the following weeks, and the pressure of the 2 K circuit can now be kept constant well below the requirement of $\pm 1\%$ [13].

Electronics and Control System

The front end electronics for LLRF, high-power RF, beam diagnostics, vacuum and cryo-control is installed in shielded and temperature controlled compartments in the tunnel. The newly developed MTCA.4 standard is used throughout the installation [14, 15]. About 250 crates in the tunnel benefit from enhanced remote monitoring and maintenance capabilities, thus reducing the need for time-consuming on the spot interventions to a minimum.

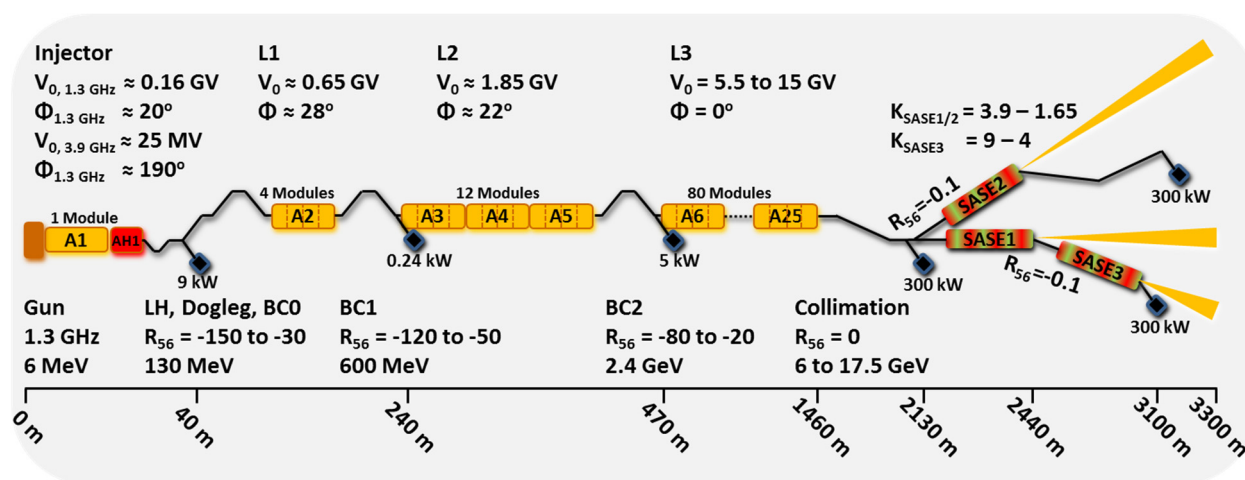


Figure 3: Schematic overview of the European XFEL accelerator. Single RF stations are named A_{nn} and feed either one module (A1) or 4 modules (A2-A25). R_{56} ranges for the bunch compressors are given in mm, and the phases of the different linac sections refer to typical compression set-ups. The maximum allowed beam power of the three commissioning dumps after the injector and the 2nd and 3rd bunch compressor (BC1 and BC2) as well as of the main dumps after the linac and each beam distribution line is given.

The accelerator's main control system is DOOCS, while some part of the infrastructure is controlled using EPICS. Photon systems and experiments use the newly developed Karabo software. Graphical user interfaces to control each subsystem are available and can easily be re-configured using the jDDD toolkit [16]. A vast suite of high-level control software integrates and automates more complex tasks like emittance measurement and optics matching. The readiness of the control software upon start-up was one of the key preconditions for the fast success of the commissioning.

Linac Commissioning

The commissioning of the XFEL accelerator started mid of January 2017. The effort was planned sequentially with the general goal to establish beam transport to subsequent sections as early as possible. The number of bunches has been kept low (<30) to lower the beam power in the initial phase of the commissioning.

LLRF commissioning was given highest priority. As of summer 2017, 22 of the 24 RF stations in the linac are available. For each of the RF stations a sequence of steps had to be performed [17]. Frequency tuning, RF signal checks, coupler tuning, coarse power-based calibration and closed-loop operation was achieved without beam, and after establishing beam transport (typical 30 bunches, 500 pC) cavity phasing and beam-based calibration followed. While the first station in L1 needed one week of commissioning, the three stations of L2 could be handed over to operations after only another week. Work in L3 then progressed in parallel on all available stations. The possibility to time shift the RF pulse of stations with respect to each other allowed parallel operation of stations on or off the beam and thus simultaneous beam commissioning. The RF commissioning went extremely smooth. Multi-pacting was observed at almost all RF stations at an accelerating gradient of 17-18 MV/m but could be condi-

tioned in all cases with an effort of a couple of hours per station.

The phase and amplitude stability was measured inner loop to be better than 0.01° and 0.01%. Preliminary beam energy jitter measurements give an upper limit for the RMS relative energy jitter of $3e-4$ after BC1 and $1e-4$ after BC2. The measured energy stability at the linac end is a factor 4 better than the specified 0.01%.

At present all stations perform at about 80% of the gradient limit obtained from previous module test results [18, 19]. Further fine-tuning of the regulation loops together with explicit verification of the individually tailored waveguide distribution will increase this in the future. The maximum energy reached so far with all available stations on the beam is 14 GeV which is the energy envisioned for first user operation.

Beamline commissioning could be performed in parallel to the LLRF commissioning, with the first beam transported to the beam dump after the linac by end of February. Trajectory response measurements proved very useful in validating the optics model and were possible right from 'Day 1' due to the excellent performing BPM system. Also other diagnostic devices like screens, toroids, beam-loss-monitors, dark current monitors were available from the beginning [20]. The BPM resolution exceeds expectations with sub-micron resolution for the cavity BPMs.

Longitudinal diagnostics commissioning is ongoing. The transverse deflecting structure after the last bunch compressor allowed beam length measurements down to about 170 fs FWHM (resolution limited). Bunch compression monitors (BCM) based on diffraction radiation allow relative bunch length measurements for shorter bunches and thus setting up bunch compression for the design 5 kA. The BCM is used in a slow feedback loop to stabilize the peak current. Newly developed beam arrival

monitors will become available soon [21, 22]. Compression factors during initial operation are set to up to 200.

Transverse beam sizes are measured with scintillating screens (LYSO) observed under an angle of 90 deg. Resolution of the screens is measured to be of the order of a few μm [23]. Typical transverse beam sizes to be resolved range from 40 to 100 μm , and are thus well above the resolution limit of the screens. Nevertheless, emittance measurements give unreasonable results at small beam sizes below about 50 μm , as they appear in the higher energy four-screen sections after BC1, BC2 and L3. Only multi-quadrupole scans with enlarged beta-functions at the screen position give reliable results. This effect is under investigation [24].

Beam Transport through SASE1 / First Lasing

After obtaining the operation permission for the ‘North Branch’ beam distribution on April 26, first beam was transported through the 1 km long beam transport line the next day. Moderate energies (10.4 GeV) were used together with a reduced 1 Hz repetition rate. The 8.8 mm by 8 mm inner aperture undulator vacuum system with a length of 235 m (SASE1) resp. 150 m (SASE3) was passed without any additional steering and moderate trajectory amplitudes of 1 mm peak. A day later all 35 undulator segments were closed to 11 mm gap ($k = 3.5$) and the phase shifters could be adjusted to the settings obtained through magnetic measurements [25].

First lasing was observed on May 2nd after some empirical tuning of the compression and the undulator trajectory. At a further reduced energy of 6.4 GeV and an undulator k of 3.5 the radiation wavelength was about 9 Å. At this moment only a fluorescent screen (25 mm by 32 mm wide YAG) was available at the beginning of the photon beamline about 170 m downstream of the last SASE1 undulator segment. Nevertheless, already spontaneous radiation from even one single undulator segment could be observed by an increase of the overall emitted light intensity.

LASING AT 2 ÅNGSTRÖM AND BELOW

Further steps to lase at shorter wavelength were required. In a common effort of both, the electron and the photon beam commissioning team, beam based alignment and more systematic tuning of longitudinal and transverse bunch properties were carried out while more and more photon beam diagnostic came into operation.

First lasing at 2 Ångström was achieved on May 24th, and only three days later an energy of 1 mJ close to saturation was reached (see Fig. 4). Further optimization including the training of new machine operators was possible since the authorization to inject photon beam into the SASE1 experimental hutch was only given June 21.

The X-ray beam was successfully guided via the respective mirrors into the experiment hutches, where a number of highly specialized instruments for characterizing the properties of the X-ray beam were meanwhile commissioned.

Directly after the first X-ray beam was guided into the hutches on 23 June, teams at European XFEL started with the characterization of the beam and started experiments for the commissioning of the instruments and started experiments for the commissioning of the instruments.

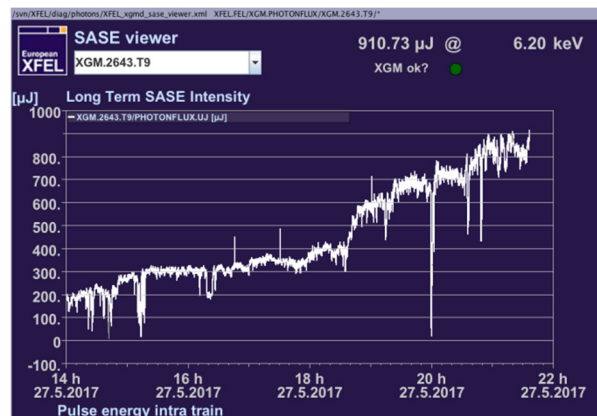


Figure 4: Long term SASE intensity measured at 2 Ångström wavelength.

One of the first diffraction patterns from European XFEL was recorded through an approximately millimeter-wide square gap at the SPB/SFX instrument (see Fig. 5). The evenly spaced, grid-like lines of the pattern show areas of interference resulting from diffraction through the gap, demonstrating that the light has very high quality laser-like properties.

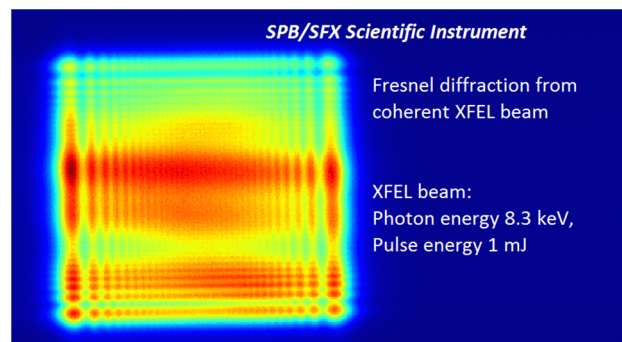


Figure 5: One of the first diffraction patterns from European XFEL. Credit: European XFEL

With a wavelength of initially two Ångström and the required peak light intensity, the X-ray light will allow the recording of atomic detail. At two experiment stations first experiments are now possible: At the instrument FXE (Femtosecond X-ray Experiments), that is designed for the research of extremely fast processes, and at the instrument SPB/SFX (Single Particles, Clusters, and Biomolecules / Serial Femtosecond Crystallography), designed for studying biomolecules and biological structures.

OUTLOOK

The European XFEL accelerator has been put into initial operation. In comparison with the published commissioning schedule, major commissioning targets were

achieved ahead of time. The initial accelerator operation is smooth, the chosen superconducting technology is convincing. The series production as well as the recent commissioning of many challenging accelerator subsystems were successful. The European XFEL is one of the worldwide visible large scale research facilities. We are looking forward to hosting highest quality user experiments with major impact on science.

First user experiments are scheduled for September 2017. In parallel the accelerator will be further developed towards higher energies and beam power. Commissioning of SASE3 and SASE2 will complete the experimental possibilities of the facility in 2018. Full operation with 4,000 user hours per year is foreseen in 2019.

ACKNOWLEDGEMENT

The European XFEL is a joint achievement of many colleagues working in different parts of the project. The Authors wish to thank all of them for their long lasting devotion and enthusiasm. In addition we would like to acknowledge the help of staff from CANDLE, ELETTRA, PSI, and SLAC during the commissioning. Collaboration is the key to success!

REFERENCES

- [1] M. Altarelli *et al.* Ed., “The European X-Ray Free-Electron Laser – Technical Design Report”, DESY, Hamburg, Germany, Rep. DESY 2006-097, July 2007.
- [2] R. Brinkmann *et al.* Ed., “TESLA XFEL Technical Design Report Supplement”, DESY, Hamburg, Germany, Rep. DESY 2002-167, March 2002.
- [3] R. Brinkmann *et al.* Ed., “TESLA Technical Design Report – Part II: The Accelerator”, DESY, Hamburg, Germany, Rep. DESY 2001-011, March 2001.
- [4] B. Dwersteg, K. Flöttmann, J. Sektuowicz, C. Stolzenburg, “RF gun design for the TESLA VUV free electron laser”, NIM A393, pp. 93-95, 1997.
- [5] H. Weise, “How to Produce 100 Superconducting Modules for the European XFEL in Collaboration and with Industry”, presented at IPAC’14, Dresden, Germany, May 2014.
- [6] V. Balandin, R. Brinkmann, W. Decking, and N. Golubeva, “Post-linac collimation system for the European XFEL”, presented at PAC’09, Vancouver, Canada, May 2009, paper TH6PFP030, pp. 3763-3765.
- [7] W. Decking and T. Limberg, “European XFEL Post-TDR Description”, European XFEL, Hamburg, Germany, Rep. XFEL.EU TN-2013-004-01, Apr. 2013.
- [8] G. Feng *et al.*, “Beam dynamics simulations for European XFEL”, DESY, Hamburg, Germany, Rep. TESLA-FEL 2013-04, 2013.
- [9] F. Brinker for the European XFEL Commissioning Team, “Commissioning of the European XFEL Injector”, in *Proc. IPAC’16*, Busan, Korea, May 2016, paper TUOCA03, pp. 1044-1047.
- [10] C. Maiano *et al.*, “Commissioning and Operation Experience of the 3.9 GHz System in the EXFEL Linac”, presented at IPAC’17, Copenhagen, Denmark, May 2017, paper MOPVA059, this conference.

- [11] B. Beutner, C. Gerth, and M. Scholz, “Phase space studies of individual bunches in an 4.5 MHz Train at the European XFEL”, presented at IPAC’17, Copenhagen, Denmark, May 2017, paper WEPAB013, this conference.
- [12] Y. Renier *et al.*, “Statistics on high average power operation and results from the electron beam characterization at PITZ”, presented at IPAC’17, Copenhagen, Denmark, May 2017, paper TUPIK051, to be published.
- [13] T. Schnautz *et al.*, „First operation of the XFEL linac with the 2K cryogenic system”, presented at CEC-ICMC 2017, Madison, U.S.A.
- [14] H. Schlarb, T. Walter, K. Rehlich, and F. Ludwig, “Novel crate standard MTCA.4 for industry and research”, presented at IPAC2013, Shanghai, China, May 2013, paper THPWA003, pp. 3633-3635.
- [15] T. Walter, M. Fenner, K. Kull, and H. Schlarb, “MicroTCA Technology Lab at DESY: Start-Up Phase Summary”, presented at IPAC’17, Copenhagen, Denmark, May 2017, paper THOAB2, to be published.
- [16] E. Sombrowski *et al.*, “jddd: A tool for operators and experts to design control system panels”, presented at ICALEPCS’13, San Francisco, USA, 2013, pp. 544-546.
- [17] J. Branlard, “Installation and First Commissioning of the LLRF System for the European XFEL”, presented at IPAC’17, Copenhagen, Denmark, May 2017, paper THOAA3, to be published.
- [18] D. Reschke *et al.*, “Performance in the vertical test of the 832 nine-cell 1.3 GHz cavities for the European X-ray Free Electron Laser”, *Phys. Rev. ST Accel. Beams*, vol. 20, p. 042004, Apr. 2017.
- [19] D. Reschke W. Decking, N. Walker, H. Weise, „The Commissioning of the European XFEL Linac and its Performance”, presented at the SRF2017 Conference, Lanzhou, China, July 2017.
- [20] D. Lipka, “Very First Experience with the Standard Diagnostics at the European XFEL”, presented at IPAC’17, Copenhagen, Denmark, May 2017, paper MOPAB045, to be published.
- [21] M. Viti *et al.*, “Recent upgrades of the bunch arrival time monitors at FLASH and European XFEL”, presented at IPAC’17, Copenhagen, Denmark, May 2017, paper MOP- IK072, to be published.
- [22] C. Sydlo *et al.*, “Femtosecond Optical Synchronization System for the European XFEL”, presented at IPAC’17, Copenhagen, Denmark, May 2017, paper THPAB108, to be published.
- [23] G. Kube *et al.*, “Transverse Beam Profile Imaging of few-micrometer Beam Sizes Based on a Scintillator Screen”, presented at IBIC’15, Melbourne, Australia, 2015, paper TUPB012, pp. 330-334.
- [24] M. Scholz and B. Beutner, “Electron Beam Phase Space Tomography at the European XFEL Injector”, presented at IPAC’17, Copenhagen, Denmark, May 2017, paper THPAB108, to be published.
- [25] Y. Li and J. Pflüger, “Phase matching strategy for the undulator system in the European X-ray Free Electron Laser”, *Phys. Rev. ST Accel. Beams*, vol. 20, p. 020702, Feb. 2017.

STATUS OF THE FLASH FEL USER FACILITY AT DESY

K. Honkavaara*, DESY, Hamburg, Germany[†]

Abstract

The FLASH facility at DESY (Hamburg, Germany) provides high brilliance FEL radiation at XUV and soft X-ray wavelengths for user experiments. Since April 2016, the second undulator beamline, FLASH2, is in user operation. We summarize the performance of the FLASH facility during the last two years including our experience to deliver FEL radiation to two user experiments simultaneously.

INTRODUCTION

FLASH [1–7], the free-electron laser (FEL) user facility at DESY (Hamburg), delivers high brilliance XUV and soft X-ray FEL radiation for photon experiments.

FLASH, originally called the VUV-FEL at TTF2, was constructed in the early 2000s based on the experience gathered from the TTF-FEL operation [8]. The user operation of the FLASH facility started in summer 2005 with one undulator beamline, which is still in use with its original fixed gap undulators (FLASH1). In order to fulfill the continuously increasing demands on beam time and on photon beam properties, a second beamline with variable gap undulators (FLASH2) has been constructed. The first lasing of FLASH2 was achieved in August 2014 [9], and since April 2016 FLASH2 is in regular user operation.

Figure 1 shows an aerial view of the north side of DESY in summer 2016. The FLASH facility with its two experimental halls is in the middle of the picture: the FLASH1 hall ("Albert Einstein") is on the right, the FLASH2 hall ("Kai Siegbahn") on the left.



Figure 1: Aerial view of the north side of DESY. The FLASH facility is in the middle of the picture: the FLASH1 experimental hall is on the right, the FLASH2 hall on the left. Next to FLASH are two experimental halls of the PETRA III synchrotron light source.

This paper reports on the status of the FLASH facility and its performance in 2016/17. Part of this material has been presented in previous conferences, most recently in [7].

THE FLASH FACILITY

Figure 2 shows a schematic layout of the FLASH facility. The seeding experiment sFLASH [10] located upstream of the FLASH1 undulators, and the FLASHForward plasma wakefield acceleration experiment [11], under construction at the FLASH3 beamline, are indicated as well.

The generation of high quality electron bunches is realized by an RF-gun based photoinjector. An exchangeable Cs₂Te photocathode is installed on the back-plane of the normal conducting RF-gun. The presently installed photocathode is in use already more than two years without any significant degradation of the quantum efficiency: the QE is still at an 8% level [12]. The photocathode laser system has three independent lasers [13], allowing a flexible operation and production of electron bunch trains with different parameters (number of bunches, bunch spacing, bunch charge).

The FLASH linac has seven TESLA type 1.3 GHz accelerating modules providing a maximum electron beam energy of 1.25 GeV. The use of superconducting RF cavities allows operation with long RF-pulses, i.e. with long electron bunch trains. The maximum length of the bunch train is defined by the RF flat top of the acceleration modules (800 μs) and of the RF-gun (presently 650 μs). The bunch train repetition rate is 10 Hz, and different discrete bunch spacings between 1 μs (1 MHz) and 25 μs (40 kHz) are possible. The train is shared between two undulator beamlines, allowing to serve simultaneously two photon experiments, one at FLASH1 and the other one at FLASH2, both at 10 Hz pulse train repetition rate.

The RF-gun and the accelerator modules are regulated by an outstanding MTCA.4 based low level RF (LLRF) system [14, 15], which allows, within certain limits, different RF amplitudes and phases for the FLASH1 and FLASH2 bunch trains. The arrival time stability down to a few tens of femtoseconds level is realized by a state of the art optical synchronization system [16].

The production of FEL radiation, both at FLASH1 and FLASH2, is based on the SASE (Self Amplified Spontaneous Emission) process. The electron beam peak current required for SASE process is achieved by compressing the electron bunches in two magnetic chicane bunch compressors at beam energies of 150 MeV and 450 MeV, respectively.

FLASH1 has six 4.5 m long fixed gap (12 mm) undulator modules, FLASH2 twelve 2.5 m long variable gap undulators. A planar electromagnetic undulator, installed downstream of the FLASH1 SASE undulators, provides, on request, THz radiation for user experiments.

* katja.honkavaara@desy.de

[†] for the FLASH team

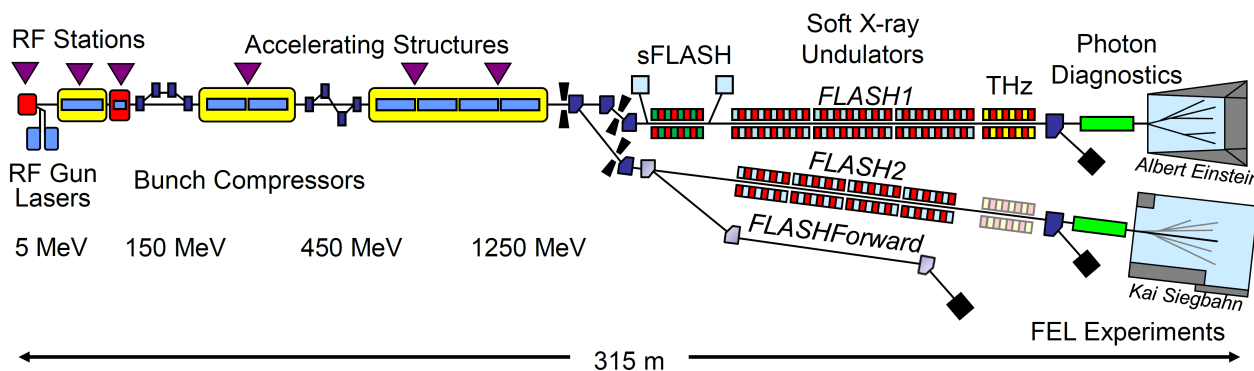


Figure 2: Layout of the FLASH facility (not to scale).

The FLASH1 experimental hall is equipped with five photon beamlines [2], including optical lasers for pump-and-probe experiments, and a THz beamline. The construction of photon beamlines in the FLASH2 hall [17] is on-going. Presently two beamlines are in operation. A pump-and-probe laser will be provided for FLASH2 experiments from early 2018 on.

Since FLASH1 has fixed gap undulators, its wavelength is defined by the electron beam energy. The minimum achievable wavelength in the present layout is 4.2 nm, the maximum one slightly above 50 nm. FLASH2 with variable gap undulators provides FEL radiation at wavelengths between 4 nm and 90 nm.

The typical single photon pulse energies at FLASH1 are from a few tens of μJ to about $100 \mu\text{J}$. At FLASH2, with its variable gap undulators, tuning for high photon pulse energies is easier: single pulse energies above $200 \mu\text{J}$ are reached routinely, and pulse energies up to 1 mJ [5] have been achieved using undulator tapering. In addition, the variable gap undulators allow fast wavelength scans, which are not possible at FLASH1.

More details of the FLASH facility are presented, for example, in [3–7]. Photon beamlines and photon diagnostics are described in [2, 17–19]. An overview of the photon science at FLASH can be found in the publication list of [20].

SIMULTANEOUS OPERATION

FLASH1 and FLASH2 beamlines are operated simultaneously with the bunch train repetition rate of 10 Hz. The separation of the bunch trains is realized by using a kicker-septum system downstream of the last accelerating module. A gap of 30 to $50 \mu\text{s}$ (kicker pulse rise time and LLRF transition time) is needed between the bunch trains.

FEL radiation parameters (photon wavelength, pulse pattern, pulse duration) need to be, as far as possible, independently tunable for FLASH1 and FLASH2 experiments.

The FLASH2 variable gap undulators can adapt to the electron beam energy, which is determined by the FLASH1 wavelength. Consequently the FLASH2 wavelength can be chosen independently of FLASH1: the wavelength range is 1 to 3 times the actual wavelength of FLASH1 [5].

In order to take full advantage of the two undulator beamlines and to allow fast wavelength changes also at FLASH1,

it is foreseen to replace the FLASH1 undulators by variable gap ones in the mid-term future.

FLASH has three photocathode lasers. Typically two of them are operated in parallel: one providing the bunch train for FLASH1 and the other one for FLASH2. This has two advantages. First of all, the bunch pattern can be determined independently for both beamlines. Secondly, FLASH1 and FLASH2 can be operated with a different bunch charge. The latter feature, combined with the possibility to use different RF phases, allows different compression of FLASH1 and FLASH2 bunches, and thus different photon pulse durations for FLASH1 and FLASH2 experiments.

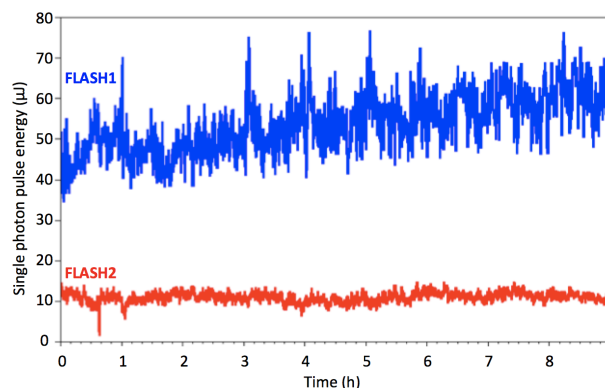


Figure 3: Single photon pulse energy (in μJ) of FLASH1 (blue) and FLASH2 (red) during 9 hours of simultaneous operation. FLASH1: 9.8 nm, 430 pulses in train with $1 \mu\text{s}$ spacing, electron bunch charge 320 pC . FLASH2: 20.6 nm, 1 pulse, electron bunch charge 70 pC .

Figure 3 shows an example of simultaneous FEL radiation delivery for FLASH1 and FLASH2 user experiments with different parameters. FLASH1 is operated with 430 bunches of 320 pC each at a photon wavelength of 9.8 nm, and FLASH2 with a single bunch of 70 pC at 20.6 nm. The FLASH2 electron bunches are produced by the special photocathode laser dedicated to short pulse operation [13]. Due to the low electron bunch charge used to obtain very short FEL pulses, the photon pulse energy in this case is at a $10 \mu\text{J}$ level.

Another example of challenging simultaneous user operation concerns FLASH1 operation with special high charge

settings to produce THz radiation combined with delivery of short FEL pulses for the FLASH2 experiment. This was realized by using very different bunch charges: 680 pC at FLASH1 and 140 pC at FLASH2. The two experiments ran in parallel more than 50 hours without interruption, demonstrating that FLASH1 and FLASH2 can be operated simultaneously with a factor five different bunch charges.

The status of simultaneous FLASH1 and FLASH2 operation, including its challenges, is discussed more in detail in [4, 5].

FLASH OPERATION 2016

In 2016 FLASH had two user periods: from January to June (Period 7) and from July to November (Period 8). The user operation of FLASH2 started in April 2016.

Similar to previous user periods, the beamtime was organized with an alternating pattern of user blocks (4-5 weeks) and study blocks (2-3 weeks). In addition, FLASH had two shutdowns: a short one (1.5 weeks) in June 2016, and a longer one (FLASH1 4 weeks, FLASH2 6 weeks) at the end of the year. Both shutdown periods were mainly scheduled for FLASHForward [11] installations.

Total 7333 operation hours were realized at FLASH1, of which 4275 hours (58.3%) were dedicated to user operation, 2284 hours (31.1%) for FEL studies and user preparation, and 774 hours (10.6%) for general accelerator R&D. During user operation, FEL radiation was delivered to experiments 80.7% of the time (3452 h), set-up and tuning of the parameters for experiment requirements took 15.8% (675 h). The downtime during user experiments due to technical and other failures was 3.5% (148 h).

In 2016, FLASH2 had 7010 hours available for beam operation, of which 5365 hours was realized. The remaining 1645 hours FLASH2 was in stand-by due to beam conditions or studies not allowing a parallel FLASH2 beam operation. In total 1570 hours were scheduled for FLASH2 user experiments. This relative low amount of user time is due to the fact that FLASH2 photon beamlines are still under construction, and thus many experiments, for example those requiring a pump-and-probe laser, could not yet take place at FLASH2, but had to be scheduled to the overbooked FLASH1 beamline.

In 2016, FEL radiation was delivered to experiments with wavelengths from 4.2 nm to 38 nm at FLASH1, and between 4.4 nm and 52 nm at FLASH2. The experiments had different demands on pulse pattern (1-500 pulses per train with various pulse spacings), and on photon pulse duration: 43% of them requested pulse durations below 50 fs, 42% 50 to 100 fs and only for 15% the pulse duration was uncritical.

Shortly after the start-up after the summer shutdown 2016, a small vacuum leak developed on the RF-gun window. The exchange of the RF-window (3 days) and its conditioning (6 days) went smoothly, and nominal operation parameters were quickly recovered. Since then the RF-gun is running stable and is routinely operated with a 650 μ s RF flat top.

FLASH OPERATION 2017

Similar to the previous year, in 2017 FLASH has two user periods. The first one (Period 9) finished middle of June, and the second one (Period 10) starts in August lasting until Christmas 2017. The shutdown in summer 2017 has been designated to two main tasks: a regular inspection of safety valves of the cryogenic system requiring a warm-up of the superconducting accelerator modules, and the installation of the FLASHForward experiment at the FLASH3 beamline. The FLASH3 beamline is located in the same building as the FLASH2 undulators.

There is no substantial change on beamtime allocation nor on beam parameters compared to the previous years. Since the upgrades of the FLASH2 photon beamlines are still ongoing, only a limited amount of FLASH2 user experiments are scheduled in 2017.

One of the 2017 operational highlights so far has been a user experiment using two FEL pulses with a tunable ns range delay [21]. This was realized by operating FLASH1 with two photocathode lasers at the same time. The experiment used pulse delays of 222 ns and 470 ns to demonstrate feasibility of liquid jet sample delivery for diffraction experiments at high pulse repetition rate.

FEL AND ACCELERATOR STUDIES

Substantial amount of the available beam time (about 30%) is allocated to improve the FLASH performance as an FEL user facility, and to prepare it for the demands of the coming user experiments. In addition, about 10% of the available time is dedicated to general accelerator physics experiments and development, like seeding (sFLASH) and plasma wakefield acceleration (FLASHForward).

In the last two years the efforts on seeding at sFLASH have been concentrated on the high gain harmonic generation (HGHG). Recently the HGHG seeding has been demonstrated of up the 9th harmonic of the seed wavelength of 266 nm [10]. Using the transverse deflecting structure, located downstream of sFLASH undulators, single-shot information of the seeded FEL photon pulse has been successfully extracted [22].

Significant amount of time has been devoted to improve the performance of the facility and to developments of advanced operation modes [21]. Thanks to the variable gap undulators, the FLASH2 performance can be optimized using undulator tapering [23]. Other developments at FLASH2 are related, for example, to reverse undulator tapering [24, 25], harmonic lasing [26–28], and frequency doubling [29].

An on-going development at FLASH1 concerns THz-XUV pump-probe experiments. In order to cope with the different length of the THz and FEL photon beamlines, two electron bunches, with 21.5 ns delay corresponding the path difference between the two beamlines, are produced by a split-and-delay unit installed at one of the standard photocathode lasers [21]. The ultimate goal is to tune the first electron bunch to produce a maximum THz pulse energy,

and at the same time optimize the second one for FEL radiation production.

Other continuing developments are, for example, the upgrade of the beam arrival time monitors [30], studies related to electron beam optics [31], and generation of ultra short photon pulses [32, 33].

SUMMARY

The FLASH facility is in regular simultaneous user operation with two undulator beamlines. The 9th user period is successfully completed in June 2017, and after a shutdown designated to a maintenance work on the cryogenic system and installations of FLASHForward, the 10th user period starts in August 2017. The scheduled operation in 2018 is similar to previous years: two 6 months user periods with short shutdowns in January and in July 2018.

FLASH2 is in user operation since April 2016. Due to ongoing construction and upgrades of the photon beamlines, so far only about a dozen of user experiments have taken place. This is foreseen to change in 2018, when pump-and-probe experiments will be possible at FLASH2.

ACKNOWLEDGMENT

We like to thank all colleagues participating in the successful operation, meticulous maintenance, and continuous upgrading of the FLASH facility.

REFERENCES

- [1] W. Ackermann *et al.*, "Operation of a free-electron laser from the extreme ultraviolet to the water window", *Nature Photonics*, **1**, 336, 2007.
- [2] K. Tiedtke *et al.*, "The soft x-ray free-electron laser FLASH at DESY: beamlines, diagnostics and end-stations", *New J. Phys.* **11**, 023029, 2009.
- [3] S. Schreiber and B. Faatz, "The free-electron laser FLASH", in *High Power Laser Science and Engineering*, **3** e20, 2015.
- [4] B. Faatz *et al.*, "Simultaneous operation of two soft x-ray free-electron lasers driven by one linear accelerator", *New J. Phys.*, **18**, 062002, 2016.
- [5] J. Roensch-Schulenburg *et al.*, "Experience with Multi-Beam and Multi-Beamline FEL-Operation", *Journal of Physics: Conf. Series*, **874**, 012023, 2017.
- [6] K. Honkavaara *et al.*, "Status of the Soft X-ray FEL User Facility FLASH", in *Proc. 37th Free-Electron Laser Conf.*, Daejeon, 2015, pp. 61-65.
- [7] M. Vogt *et al.*, "Status of the Soft X-ray Free Electron Laser FLASH", in *Proc. 8th Int. Particle Accelerator Conf.*, Copenhagen, 2017, pp. 2628-2630.
- [8] V. Ayvazyan *et al.*, "A new powerful source for coherent VUV radiation: Demonstration of exponential growth and saturation at the TTF free-electron laser", *Eur. Phys. J. D*, **20**, 149, 2000.
- [9] S. Schreiber and B. Faatz, "First Lasing at FLASH2", in *Proc. 36th Free-Electron Laser Conf.*, Basel, 2014, pp. 7-8.

- [10] J. Boedewadt *et al.*, "Experience in Operating sFLASH with High-Gain Harmonic Generation", in *Proc. 8th Int. Particle Accelerator Conf.*, Copenhagen, 2017, pp. 2596-2599.
- [11] A. Aschikhin *et al.*, "The FLASHForward Facility at DESY", *Nucl. Instr. Meth. A*, **806**, 175, 2016.
- [12] S. Schreiber *et al.*, "Update on the Lifetime of Cs2Te Photocathodes Operated at FLASH", in *These Proceedings: Proc. 38th Int. Free-Electron Laser Conf.*, Santa Fe, 2017, WEP003.
- [13] S. Schreiber *et al.*, "Simultaneous Operation of Three Laser Systems at the FLASH Photoinjector", in *Proc. 37th Int. Free-Electron Laser Conf.*, Daejeon, 2015, pp. 459-463.
- [14] M. Hoffmann *et al.*, "Operation of Normal Conducting RF Guns with MicroTCA.4", in *Proc. 6th Int. Particle Accelerator Conf.*, Richmond, 2015, pp. 841-843.
- [15] M. Omet *et al.*, "Operation Experiences with the MicroTCA.4-based LLRF Control System at FLASH", in *Proc. 6th Int. Particle Accelerator Conf.*, Richmond, 2015, pp. 844-846.
- [16] S. Schulz *et al.*, "Femtosecond all-optical synchronization of an X-ray free-electron laser", *Nature Communications*, **6**, 5938, 2015.
- [17] E. Ploenjes *et al.*, "FLASH2 Beamline and Photon Diagnostics Concepts", in *Proc. 35th Free-Electron Laser Conf.*, New York, 2013, pp. 614-617.
- [18] K. Tiedtke *et al.*, "Challenges for Detection of Highly Intense FEL Radiation: Photon Beam Diagnostics at FLASH1 and FLASH2", in *Proc. 35th Free-Electron Laser Conf.*, New York, 2013, pp. 417-420.
- [19] E. Ploenjes *et al.*, "FLASH2: Operation, beamlines, and photon diagnostics", *AIP Conference Proceedings*, **1741**, 020008 2016.
- [20] http://photon-science.desy.de/facilities/flash/publications/scientific_publications
- [21] S. Schreiber, E. Schneidmiller, and M. Yurkov, "Recent FEL Experiments at FLASH", in *These Proceedings: Proc. 38th Int. Free-Electron Laser Conf.*, Santa Fe, 2017, TUA01.
- [22] T. Plath *et al.*, "Mapping few-femtosecond slices of ultra-relativistic electron bunches", *Scientific Reports* **7**, 2431, 2017.
- [23] E. Schneidmiller, M. Yurkov, "Optimum Undulator Tapering of SASE FEL: from the Theory to Experiment", in *Proc. 8th Int. Particle Accelerator Conf.*, Copenhagen, 2017, pp. 2639-2641.
- [24] E. Schneidmiller and M. Yurkov, "Obtaining high degree of circular polarization at x-ray free electron lasers via a reverse undulator taper", *Phys. Rev. ST Accel. Beams*, **16**, 110702, 2013.
- [25] E. Schneidmiller and M. Yurkov, "Background-Free Harmonic Production in XFELs via a Reverse Undulator Taper", in *Proc. 8th Int. Particle Accelerator Conf.*, Copenhagen, 2017, pp. 2618-2620.
- [26] E. Schneidmiller and M. Yurkov, "Harmonic lasing in x-ray free electron lasers", *Phys. Rev. ST Accel. Beams*, **15**, 080702, 2012.
- [27] E. Schneidmiller *et al.*, "First operation of a harmonic lasing self-seeded free electron laser", *Phys. Rev. Accel. Beams*, **20**, 020705, 2017.

- Content from this work may be used under the terms of the CC BY 3.0 licence (© 2018). Any distribution of this work must maintain attribution to the author(s), title of the work, publisher, and DOI.
- [28] E. Schneidmiller *et al.*, "First Operation of a Harmonic Lasing Self-Seeded FEL", in *Proc. 8th Int. Particle Accelerator Conf.*, Copenhagen, 2017, pp. 2621-2624.
- [29] M. Kuhlmann, E. Schneidmiller, and M. Yurkov, "Frequency Doubler and Two-Color Mode of Operation at Free Electron Laser FLASH2", in *Proc. 8th Int. Particle Accelerator Conf.*, Copenhagen, 2017, pp. 2635-2638.
- [30] M. Viti *et al.*, "Recent Upgrades of the Bunch Arrival Time Monitors at FLASH and European XFEL", in *Proc. 8th Int. Particle Accelerator Conf.*, Copenhagen, 2017, pp. 695-698.
- [31] J. Zemella and M. Vogt, "Progress in FLASH Optics Consolidation", in *Proc. 8th Int. Particle Accelerator Conf.*, Copenhagen, 2017, pp. 211-214.
- [32] J. Roensch-Schulenburg *et al.*, "Operation of FLASH with Short SASE-FEL Radiation Pulses", in *Proc. 36th Int. Free-Electron Laser Conf.*, Basel, 2014, pp. 342-345.
- [33] F. Christie *et al.*, "Generation of Ultra-Short Electron Bunches and FEL Pulses and Characterization of their Longitudinal Properties at FLASH2", in *Proc. 8th Int. Particle Accelerator Conf.*, Copenhagen, 2017, pp. 2600-2603.

STATUS AND PERSPECTIVES OF THE FERMI FEL FACILITY

L. Giannessi[†], E. Allaria, L. Badano, F. Bencivenga, C. Callegari, F. Capotondi, F. Cilento, P. Cinquegrana, M. Coreno, I. Cudin, M. B. Danailov, G. D'Auria, R. De Monte, G. De Ninno, P. Delgiusto, A. Demidovich, M. Di Fraia, S. Di Mitri, B. Diviaco, A. Fabris, R. Fabris, W. M. Fawley, M. Ferianis, P. Furlan Radivo, G. Gaio, D. Gauthier, F. Gelmetti, F. Iazzourene, S. Krecic, M. Lonza, N. Mahne, M. Malvestuto, C. Masciovecchio, M. Milloch, N. Mirian, F. Parmigiani, G. Penco, A. Perucchi, L. Pivetta, O. Plekan, M. Predonzani, E. Principi, L. Raimondi, P. Rebernik Ribič, F. Rossi, E. Roussel, L. Rumiz, C. Scafuri, C. Serpico, P. Sigalotti, S. Spampinati, C. Spezzani, M. Svandrlik, M. Trovò, A. Vascotto, M. Veronese, R. Visintini, D. Zangrando, M. Zangrando, Elettra Sincrotrone Trieste S.C.p.A., 34149 Basovizza, Italy

Abstract

FERMI is a seeded Free Electron Laser (FEL) user facility at the Elettra laboratory in Trieste, operating in the VUV to EUV and soft X-rays spectral range; the radiation produced by the seeded FEL is characterized by a number of desirable properties, such as wavelength stability, low temporal jitter and longitudinal coherence. In this paper, after an overview of the FELs performances, we will present the development plans under consideration for the next 3 to 5 years. These include an upgrade of the linac and of the existing FEL lines, the possibility to perform multi-pulse experiments in different configurations and an Echo Enabled Harmonic Generation (EEHG) experiment on FEL-2, the FEL line extending to 4 nm (310 eV).

INTRODUCTION

FERMI is located at the Elettra laboratory in Trieste. The FEL facility covers the VUV to soft X-ray photon energy range with two FELs, FEL-1 and FEL-2, both based on the High Gain Harmonic Generation seeded mode (HG HG) [1,2]. The HG HG scheme consists in preparing the electron beam phase space in a modulator where the interaction with an external laser induces a controlled and periodic modulation in the electron beam longitudinal energy distribution. The beam propagates through a dispersive section which converts the energy modulation into a density modulation. The density modulated beam is then injected in an amplifier where the amplification process is initially enhanced by the presence of the modulation. This HG HG scheme is implemented in FERMI FEL-1, to generate fully coherent radiation pulses in the VUV spectral range [3]. The seed signal, continuously tuneable typically in the range of 230-260 nm, is obtained from a sequence of nonlinear harmonic generation and mixing conversion processes from an optical parametric amplifier. The radiation resulting from conversion in the FEL up to the 13-15th harmonics is routinely delivered to user experiments [4]. The amplitude of the energy modulation necessary to initiate the HG HG process grows with the order of the harmonic conversion and the induced energy dispersion has a detrimental effect on

the high gain amplification in the final radiator. During the past few years of operations, we have demonstrated the ability to operate the FEL at even higher harmonic orders with reduced performances, e.g., up to the 20th harmonic, but substantially higher orders can be reached with a double stage HG HG cascade, where the harmonic conversion is repeated twice. The double conversion is done with the fresh bunch injection technique [5] on FERMI FEL-2. The FEL is composed by a first stage, analogous to FEL-1, followed by a delay line, a magnetic chicane slowing down the electron beam with respect to the light pulse generated in the first stage. The light pulse from the first stage is shifted to a longitudinal portion of the beam unperturbed by the seed in the first stage. The light from the first stage functions as a short wavelength seed for the second stage. This scheme was implemented for the first time on FERMI FEL-2 [6] and was used to demonstrate the seeded FEL coherent emission in the soft-X rays, up to harmonic orders of 65, and more [7].

A first upgrade program of FERMI was completed beginning of 2016, with the installation of two new linac structures, an additional undulator segment for the radiator of the first stage of FEL-2, and a second regenerative amplifier for the seed laser system of FEL-2 [8]. After these upgrades the maximum attainable energy is 1.55 GeV for a “compressed” and “linearized” electron beam. The higher beam energy improved the performances of both the FELs, particularly for FEL-2 in the high end of the photon energy spectral range. FEL-2 has reached stable operation, with harmonic conversion factor 13 in the first stage and 5 in the second stage, at the shortest wavelength of the operating range of 4 nm. Since June 2016 the repetition rate of the source can be selected between 10 and 50 Hz. Two operation modes are foreseen: low and medium energy (electron beam energy up to 1350 MeV), at 50 Hz rep rate; high energy (1550 MeV) at 10 Hz rep rate. Harmonics of FEL-2 were measured down to 1.33 nm, as the third harmonic of the FEL tuned with the fundamental at 4 nm (this corresponds to harmonic 195 of the seed, see Fig. 2 below). In November 2016, it was possible to use at the DIPROI end-station, the 3rd harmonic of the FEL at the Cobalt L-edge, $\lambda = 1.6$ nm (778 eV).

[†] luca.giannessi@elettra.eu

Content from this work may be used under the terms of the CC BY 3.0 licence (© 2018). Any distribution of this work must maintain attribution to the author(s), title of the work, publisher, and DOI.

In the second semester of 2016 the peer reviewed user program started analysing experiments on FEL-2 and the first experiment at the carbon K-edge at about 4 nm was successfully carried out. In general, stable and reliable operating conditions have been established on both the FELs, providing high spectral quality FEL pulses to the users.

The present performance of the facility is quite mature. There is now a significant feedback from the user community about new science that could be targeted by an upgrade program focused on the next 3 to 5 years [9]. Developments are under consideration for the FEL source, addressing the possibility to produce short FEL pulses, between 15 fs and 1 fs, the extension of the wavelength reach of FEL-2 at least down to 2 nm (620 eV), thus covering, beyond the K-edge of carbon (284 eV), also the K-edges of nitrogen (410 eV) and oxygen (543 eV) at the fundamental harmonic, and the possibility to perform the quite popular two colour experiments also on FEL-2, by replacing the HGHG two-stage configuration with an EEHG one. Two-bunch operation is also being considered to allow experiments to use simultaneously the two FEL-s and other exotic multi-pulse configurations.

OVERVIEW OF FEL PERFORMANCES

Both FERMI FEL-1 and FEL-2, operating with a common linear accelerator complex, have benefited from the increase of beam energy in the high end of their respective spectral range. The VUV FEL line, FEL-1, can now be operated in the entire range at an energy per pulse larger than 100 μJ , under the condition of a single longitudinal mode spectrum, as shown in Fig. 1. The figure corresponds to harmonic 12 of the seed tuned at 260 nm.

User experiments at wavelengths in the range of 16 to 20 nm, formerly requiring the more complicated setup of FEL-2, can be now allocated on FEL-1 which may deliver similar spectral performances as the one shown in Fig. 1, at harmonic orders as high as 14 or 15 of the seed. It is worth mentioning that the seeded scheme of FEL-1 allows a wide flexibility of configurations which may be adopted to satisfy experimental demands, such as the generation of multiple pulses/multiple colours [10-14], the control of the phase and phase locking of these pulses [15,16], or the generation of modes with orbital angular momentum [17].

The performance of FEL-2 also progressed during these years of commissioning alternated to user experiments, requiring the unique spectral properties of this seeded FEL. In Fig. 2 we have summarized the energy per pulse vs. wavelength of operation in the various runs dedicated to commissioning of FEL-2. While first lasing was achieved in 2012 at 14.4 and 10.8 nm [6] the most recent data corresponding to run 26 (in Fig. 2) were acquired after the latest upgrades, with the increased beam energy, with the new laser system characterized by a minimum pulse duration in the UV of 70 fs, and with the additional undulator in the first stage amplifier.

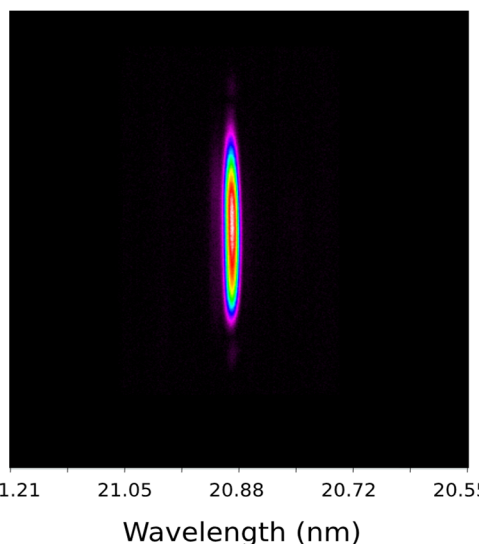


Figure 1: Spectral Line of FERMI FEL-1 at Harmonic 12.

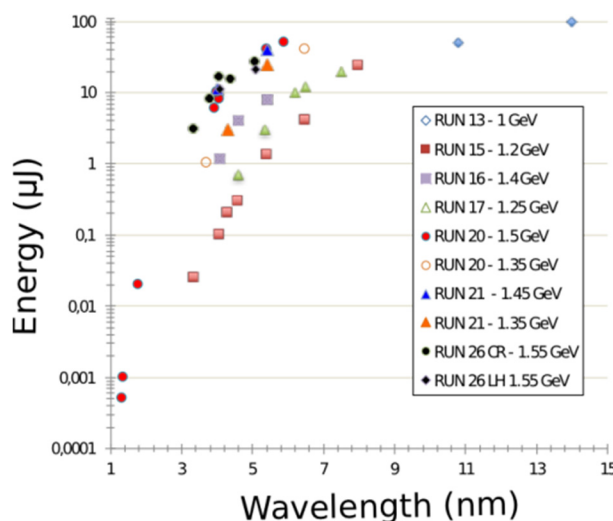


Figure 2: Energy Performances of FERMI FEL-2.

The implementation of this undulator has substantially reduced the seed energy demands, allowing us to seed the FEL in its entire spectral range (i.e. down to 4 nm) with a seed pulse energy as low as 20-25 μJ . This permits the use of the continuously tuneable OPA laser setup in the whole spectral range of FEL-2. The shorter seed pulse allows a temporal reduction of the delivered pulses down to an expected threshold of 20 fs at 4 nm, according to the expected scaling relations [18]. Notwithstanding, with the reduction in pulse duration we observed a modest increase in the energy per pulse in run 26, both in circular and in linear polarization. The spectrum in the soft-X ray at 4 nm from FEL-2 has similar features to the one of FEL-1 shown in Fig. 1. In Fig. 3, the spectral line of FERMI FEL-2 at harmonic 65, corresponding to a conversion of the seed to harmonic 13 in the first stage and to harmonic 5 in the second.

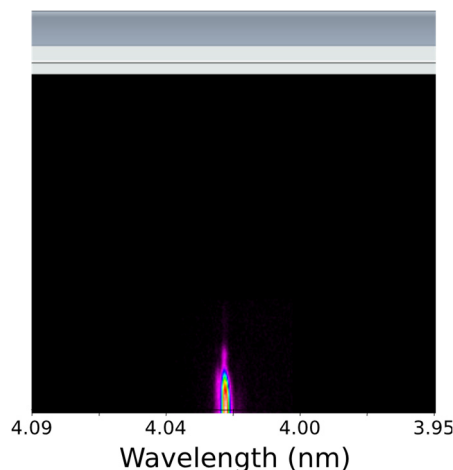


Figure 3: Spectral Line of FERMI FEL-2 at Harmonic 65.

LINAC UPGRADE

The high energy part of the linac is presently equipped with seven Backward Traveling Wave (BTW) structures with small beam apertures and nose cone geometries for high gradient operation. However, we find that these structures suffer from increased breakdown activity when operated at 25-26 MV/m and 50 Hz repetition rate.

In order to improve reliability and operability of the FERMI linac at higher energy and full repetition rate, a plan for the replacement of the seven BTW structures is under evaluation. A new accelerating module for operation up to 30 MV/m (at 50 Hz) and low wakefield contribution has thus been designed [19-21]. The module is comprised by two newly designed 3.2 meters long accelerating structures to replace each single 6.1 m long BTW structure. The new structures are designed to guarantee a reliable operation at 30 MV/m, leading to a final energy of the linac of nearly 1.8 GeV. In order to qualify the RF design and to collect statistics on the breakdown rate at full gradient, a first short (0.5 m) prototype of the structure (Fig. 4) will be fabricated in collaboration with the Paul Scherrer Institut (PSI) according to the PSI recipe.

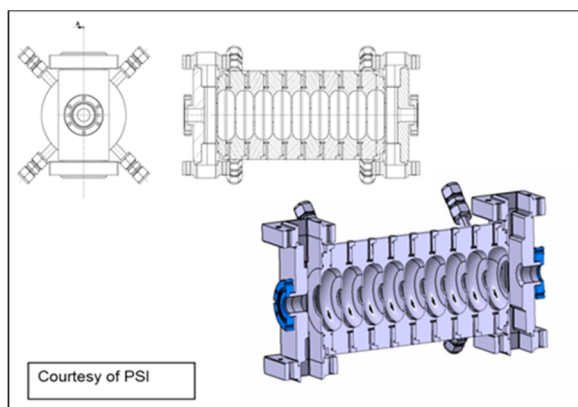


Figure 4: First Prototype.

The prototype will be a tuning free, fully brazed structure equipped with electric-coupled RF couplers [19] to lower electric and magnetic surface fields in the coupler

region. The PSI prototype will be delivered at the beginning of 2018 and high power tests at Elettra will begin in the first half of 2018.

EEHG EXPERIMENT

The recent experimental demonstration of coherent emission with EEHG at harmonics as high as the 75th [22] is an encouraging result for the future development of externally seeded FELs in the soft x-ray spectral range using only a single stage of harmonic conversion.

In order to further investigate the real capabilities of EEHG in producing fully coherent pulses in the few nm wavelength range starting from a UV laser, an experiment is planned at FERMI. The plan relies on the temporary modification of the FEL-2 layout to accommodate the installation of dedicated systems necessary for the EEHG. Main modifications include a new undulator (Fig. 5) to replace the second modulator allowing seeding with a UV laser after the delay line chicane that provides the large dispersion necessary for EEHG. The strength of the delay line chicane will be increased to reach a 2 mm dispersion required for the EEHG experiment. The user's pump and probe laser available at FERMI will be implemented as the second seed laser for the EEHG.



Figure 5: New Modulator Magnetic Array.

The main goal for the experiment is a direct comparison of the FEL performances in terms of FEL pulse quality and stability for the EEHG scheme and the already used two-stage HGHG configuration. The comparison will be focused at wavelengths in the 5-7 nm range. FEL numerical simulations show that with the proposed setup comparable results are expected using the standard FERMI electron beam [23]. Furthermore, EEHG may significantly benefit from an increase of the electron beam brightness that is possible operating the linac at higher compression rates since there is no longer the need for the fresh bunch portion on the e⁻ beam.

If numerical and theoretical predictions are confirmed by the experiment, a complete revision of the FERMI seeded FELs layout, in view of EEHG possibilities, will be planned, with the option to increase the final radiator length of FEL-2 to extend the tuning range towards 3 nm.

TWO-BUNCH OPERATION

The FERMI present layout naturally suggests investigating the possibility to operate simultaneously FEL-1 and FEL-2 by generating two electron bunches separated by few main RF buckets, i.e. multiple of 0.33 ns. This requires a new design of the transfer line from the linac to the two FEL lines. The method of splitting two bunches strongly depends upon the temporal separation ΔT between them. For ΔT of tens of ns, fast high Q-factor resonant deflecting magnets designed for the SwissFEL switch yard and actually under study are very promising [24]. However, for ΔT of few ns or sub-ns, the state of art of the magnetic-based technology is still far from being a stable and reliable solution. A second option is to consider RF deflecting cavities that are usually adopted for beam diagnostics but may find application also as fast switching devices in beam distribution systems for multiple beam lines layouts [25,26].

Beyond the issues related to a full redesign of the FERMI layout, the generation and propagation of a two-bunch system in the linac presents a series of concerns. The most important involve the wakefields excited in the linac sections by the leading bunch that affect the energy and the trajectory of the trailing bunch. It is also critical to control and steer the beam trajectory by looking at the beam position monitors (BPM) because the latter consider the two bunches as a whole with a phase factor depending on the delay. The BPM signals of two bunches indeed sum up like vectors with a response that is practically null for $\Delta T=1, 3, 5, 7, \dots$ ns. Another issue to be considered is the photo-injector double-pulse laser alignment that becomes critical for large ΔT (~ 10 ns or more).

In order to test the feasibility of the two-bunch operation we have carried out a study producing two virtually identical bunches, with separation ΔT varied between 0.66 ps and 2.33 ns [27]. The two bunches were successfully transported through the linac and the undulator line of FEL-1, up to the main beam dump, with acceptable optics and trajectory control. We have also lased at 16 nm of wavelength using alternately the first or the second bunch, without observing relevant differences between the two cases. A fine tuning of the first bunch charge and/or the time-delay has allowed to change the peak current of the trailer bunch and its longitudinal phase space in a controlled way, opening the door to novel machine configurations.

CONCLUSIONS

A first upgrade phase of FERMI has allowed us to achieve reliable, intense, and stable user operation on the whole spectral regions of FEL-1 and FEL-2. Further upgrades are presently being considered, targeting the generation of shorter pulses, of extending the spectral range to higher photon energies, and of increasing the FEL flexibility for the generation of multiple pulses also in the spectral range of FEL-2, via a single stage EEHG and

two-bunch operation. Studies, simulations, tests of prototypes, and experiments with beam during the next year have the goal to produce an upgrade proposal by the end of 2018.

REFERENCES

- [1] I. Boscolo and V. Stagno, "The converter and the transverse optical klystron", *Nuovo Cimento B* 58(2), 267–285, 1980.
- [2] L. H. Yu, "Generation of intense UV radiation by subharmonically seeded single-pass free-electron lasers", *Phys. Rev. A*, 44, 5178, 1991.
- [3] E. Allaria *et al.*, "Highly coherent and stable pulses from the fermi seeded free-electron laser in the extreme ultraviolet", *Nat. Photon.*, vol. 6, pp. 699–704, 2012.
- [4] E. Allaria *et al.*, "Tunability experiments at the FERMI@Elettra free-electron laser", *New J. Phys.*, vol. 14, 113009, 2012.
- [5] L.-H. Yu and I. Ben-Zvi, "High-gain harmonic generation of soft X-rays with the "fresh bunch" technique", *Nucl. Instrum. Methods Phys. Res. A* 393, 96–99, 1997.
- [6] E. Allaria *et al.*, "Two-stage seeded soft-X-ray free-electron laser", *Nat. Photon.*, vol. 7, pp. 913–918, 2013.
- [7] E. Allaria *et al.*, "The FERMI free-electron lasers", *J. Synchrotron Radiation*, vol. 22(3), pp. 485–491, 2015.
- [8] A. Fabris *et al.*, "FERMI upgrade plans", in *Proc. IPAC'16*, Busan, Korea, May 2016, paper MOPOW015.
- [9] L. Giannessi and C. Masciovecchio, "FERMI: present and future challenges", *Appl. Sci.* 7, 640, 2017.
- [10] G. De Ninno *et al.*, "Chirped seeded free-electron lasers: self-standing light sources for two-color pump-probe experiments", *Phys. Rev. Lett.*, 110, 064801, 2013.
- [11] B. Mahieu *et al.*, "Two-colour generation in a chirped seeded free-electron laser", *Opt. Express* 21, 022728, 2013.
- [12] E. Allaria *et al.*, "Two-colour pump-probe experiments with a twin-pulse-seed extreme ultraviolet free-electron laser", *Nat. Commun.*, 4, 2476, 2013.
- [13] E. Roussel *et al.*, "Multicolor high-gain free-electron laser driven by seeded microbunching instability", *Phys. Rev. Lett.*, 115, 214801, 2015.
- [14] E. Ferrari *et al.*, "Widely tunable two-colour seeded free-electron laser source for resonant-pump resonant-probe magnetic scattering", *Nat. Commun.* 7, 10343, 2016.

- [15] K. Prince *et al.*, “Coherent control with a short-wavelength free electron laser”, *Nat. Photonics*, 10, 176–179, 2016.
- [16] D. Gauthier *et al.*, “Generation of Phase-Locked Pulses from a Seeded Free-Electron Laser”, *Phys. Rev. Lett.*, 116, 024801, 2016.
- [17] P. Rebernik, “Extreme ultraviolet vortices from a free electron laser”, *Phys. Rev. X*, 7, 031036, 2017.
- [18] P. Finetti *et al.*, “Pulse duration of seeded free electron lasers”, *Phys. Rev. X*, 7, 021043, 2017.
- [19] C. Serpico *et al.*, “Analysis and comparison between electric and magnetic power couplers for accelerators in free electron lasers (FEL)”, *Nucl. Instr. Meth. in Phys. Res. A*, vol. 833, pp. 8–14, 2016.
- [20] C. Serpico *et al.*, “Development of a high gradient, S-band, accelerating structure for the FERMI linac”, presented at *LINAC’16*, East Lansing, MI, USA, Sep. 2016, unpublished.
- [21] N. Shafqat *et al.*, “Design study of high gradient, low impedance accelerating structures for the FERMI Free Electron Laser linac upgrade”, *Nucl. Instr. Meth. in Phys. Res. A*, to be published.
- [22] E. Hemsing *et al.*, “Echo-enabled harmonics up to the 75th order from precisely tailored electron beams”, *Nat. Photon.*, vol. 10, pp. 512–515, 2016.
- [23] P. Rebernik *et al.*, “Echo-enabled harmonic generation studies for the FERMI free electron laser” *Photonics*, vol. 4, 19, 2017, ISSN 2304-6732.
- [24] M. Paraliiev *et al.*, “High stability resonant kicker development for the SwissFEL switch yard”, in *Proc. FEL’14*, Basel, Switzerland, Aug. 2014, paper MOP039.
- [25] C. Hovater *et al.*, “The CEBAF RF separator system”, in *Proc. LINAC’96*, Geneva, Switzerland, Aug. 1996, paper MOP12.
- [26] M. Placidi *et al.*, “Compact spreader schemes”, *Nucl. Instr. Meth. in Phys. Res. A*, vol. 768, pp. 14–19, 2014.
- [27] G. Penco *et al.*, “Two-bunch operation at the FERMI FEL Facility”, presented at *IPAC’17*, Copenhagen, Denmark, May 2017, paper WEPAB037.

MATTER-RADIATION INTERACTIONS IN EXTREMES (MARIE) PROJECT OVERVIEW

R. L. Sheffield,[†] C. W. Barnes,^{*} and J. P. Tapia,[‡]
Los Alamos National Laboratory, Los Alamos, NM 87544, USA

Abstract

The National Nuclear Security Administration (NNSA) has a mission need to understand and test how material structures, defects and interfaces determine performance in extreme environments. The MaRIE Project will provide the science ability for control of materials and their production for vital national security missions. To meet the mission requirements, MaRIE must be a high-brilliance, short-pulse, coherent x-ray source with a very flexible pulse train to observe phenomena at time scales relevant to advanced manufacturing processes and dynamic events, with high enough energy to study high-Z materials. This paper will cover the rationale for the machine requirements, a pre-conceptual reference design that can meet those requirements, and preliminary research needed to address the critical high risk technologies.

MARIE MISSION

MaRIE will provide critical data to advance the state-of-art in understanding materials performance in dynamic environments and to guide advanced manufacturing. Providing this capability requires two coupled key elements: state-of-art computing platforms and advanced models, and experimental facilities which can inform these models and validate the resulting calculations. These experimental facilities must be able to perform across an extremely wide range of environmental conditions, time scales, and physical resolutions. MaRIE complements the planned National Strategic Computing Initiative by providing the data to allow resolved calculations of component manufacturing processes and system response and performance in both normal and abnormal environments. Together, MaRIE and Exascale computing will enable rapid and confident development of new materials and systems through more cost-effective and more rigorous science-based approaches.

As stated in the Basic Energy Science (BES) report on Opportunities for Mesoscale Science [1], in many important areas the functionality critical to macroscopic behaviour begins to manifest itself not at the atomic or nanoscale but at the mesoscale, where defects, interfaces, and non-equilibrium structures dominate behaviour. Microstructure is important because it determines the material's macroscopic engineering properties, such as strength, elasticity, stability under heat and pressure, and how those properties evolve with time and use. The MaRIE effort will deliver the ability to study, and thus control, time-dependent processes, structures, and properties during the manufacturing process. Experimental characterization will be complemented by capabilities in synthesis and fabrication and will be integrated with advanced

theory, modelling, and computation.

MaRIE will address this capability gap, which derives from our inability to see into and through optically opaque objects at the mesoscale, by using a coherent, brilliant x-ray source that has the required photon energy and repetition rate characteristics.

PROJECT STATUS

The MaRIE project has been in development since the late 2000s. In reviewing possible laboratory futures during the last contract transition, LANL determined that a National Security mission gap existed and a new science capability was needed. The Department of Energy has a formal process for the submission of major capabilities enhancements. The first step in this process is Critical-Decision 0, CD-0, that confirms a mission gap of national importance exists. However, CD-0 explicitly does not specify how the gap will be filled, such as what type of facilities or approaches are required. MaRIE had formal approval of Mission Need, CD-0, in March, 2016.

To understand the possible future budgetary impacts on DOE, a required part of the CD-0 submission is a schedule and budget estimate. A "plausible alternative" that will address most of the foreseen science gaps must be developed to define the required estimate of the project. The pre-conceptual reference design given later in this paper formed the basis of a schedule and budget estimate.

Following CD-0, the first step towards CD-1 is confirmation of Scientific Functional Requirements (SFRs) intended to address the mission gaps identified in CD-0. The Technical Functional Requirements (TFRs) follow from the SFRs and guide the Analysis of Alternatives (AoA). An independent review of the SFRs and TFRs by an external peer review committee was conducted in September, 2016. The AoA evaluates possible practical approaches to resolving the TFRs and does not assume the previously mentioned reference design will be the correct solution. The result of the AoA is a delineation of the facility requirements that will be addressed in a Conceptual Design. Presently, the DOE is convening a panel to conduct an independent AoA, which will be followed by the start of Conceptual Design. The remaining major Critical Decision gates after CD-1 are: Preliminary Design (CD-2), Final Design (CD-3), and Approval for Operations (CD-4).

SCIENTIFIC REQUIREMENTS

Careful assessment and analysis, based on the efforts of many working groups and the results of workshops [2], resulted in a set of Scientific Functional Requirements [3] that, if met, will provide the necessary measurements of

email addresses: [†]sheff@lanl.gov, ^{*}cbarnes@lanl.gov, [‡]john_t@lanl.gov

Table 1: The envelope formed from measurement ranges for the four representative classes of materials science listed below address the science gaps identified in the mission need documents. The highlighted cells are defining requirements that can have a major impact on the facility design. The maximum macropulse length requirement of 1 ms set by requirements to observe thermal transit effects drives the design to superconducting linac technology.

	Metals and Age Aware performance	High Explosives certification and qualification	Turbulent Materials Mixing	Casting
Spatial Resolution	<100 nm – 20 μm	< 100 nm – 20 mm	100 nm	< 1 μm – 100 μm
Field of View	100 μm – 1 mm	100 μm – 2 mm	1 mm	0.3 mm – 1 cm
# Of Frames	~ 30	~ 30	~ 30	1000 per second
Minimum Pulse Separation	< 300 ps	< 500 ps	1 ns	10 ns
Macropulse Length	5 μs	7 μs	15 μs	1 ms
Sample Thickness	> 250 μm	> 10 μm – 6 cm	1 – 10 cm	0.1 – 10 mm
Repetition Rate	< 1 Hz	< 1 Hz	10 Hz	10 Hz
Maximum Micropulse Length	< 1 ps	< 1ps	< 1 ns	< 100 ps
Lattice Measurement	0.1%	0.2%	-	0.01%
Species	Be - Pu	Typically C, H, O, N	Noble gases, Ga, Be	Actinides
Density	1%	3%	2%	1%

atomic and mesoscale phenomena to meet the mission need. Table 1 comprises four topic areas that together cover the large breadth and depth of the material science measurements that need to be addressed by MaRIE.

Following from the above requirements given in Table 1, MaRIE has to have two unique operational capabilities. First, the facility must produce high-energy x-rays to allow measuring bulk high-Z properties by maximizing elastic scattering for diffraction and minimizing absorptive heating for mesoscale measurements, and not just for thin samples, as shown in Figs. 1, 2, and 3. Note that ratio of elastic to inelastic scattering peaks between 20 to 70 keV, depending on the material. Also, the photon absorption for bulk samples, >50 grains, of higher Z materials is unacceptably high for less than 30 keV. A key design requirement, that will be central to balance of cost, risk, and performance, will be the threshold (minimum acceptable) and objective (design goal) x-ray energy.

Second, the facility must have an innovative and flexible linac pulse structure, shown in Figure 4, to make movies of phenomena on timescales ranging from electronic/ionic (sub-ps) through acoustic (ns) to shock transit (μs) to thermal (ms).

We reviewed a wide range of probe techniques that could address the expansive range of requirements given above. This preliminary analysis showed that a coherent x-ray light source is required, and an XFEL can meet the requirements for coherent brilliance, high-energy x-rays, and the very flexible temporal pulse format. Given the

complexity and flexibility of linac-driven XFELs, we determined that an XFEL is the best choice for the “bounding box” schedule and cost estimate, and so was chosen for the pre-conceptual reference design.

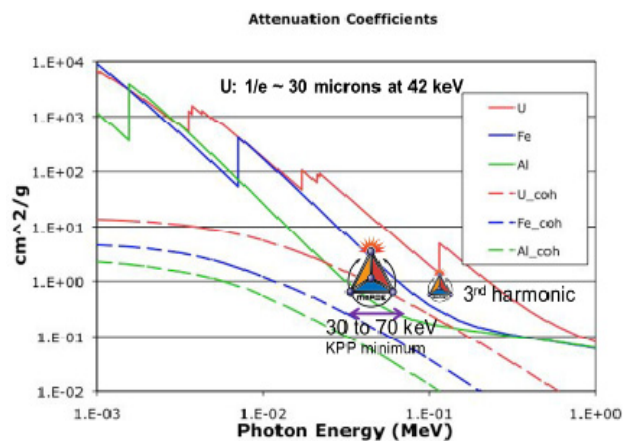


Figure 1: Plotted are inelastic (solid) and elastic (dashed) scattering [4] from 1 keV to 1 MeV for Al, Fe, and U. The Key Performance Parameters (KPP) set the operational characteristics that must be met for a determination of successful project completion. The photon energies of 30 keV to 70 keV represent a possible photon specification of the minimum acceptable operational photon energy (threshold) to the maximum planned photon energy (objective) at the fundamental XFEL photon energy.

Content from this work may be used under the terms of the CC BY 3.0 licence (© 2018). Any distribution of this work must maintain attribution to the author(s), title of the work, publisher, and DOI.

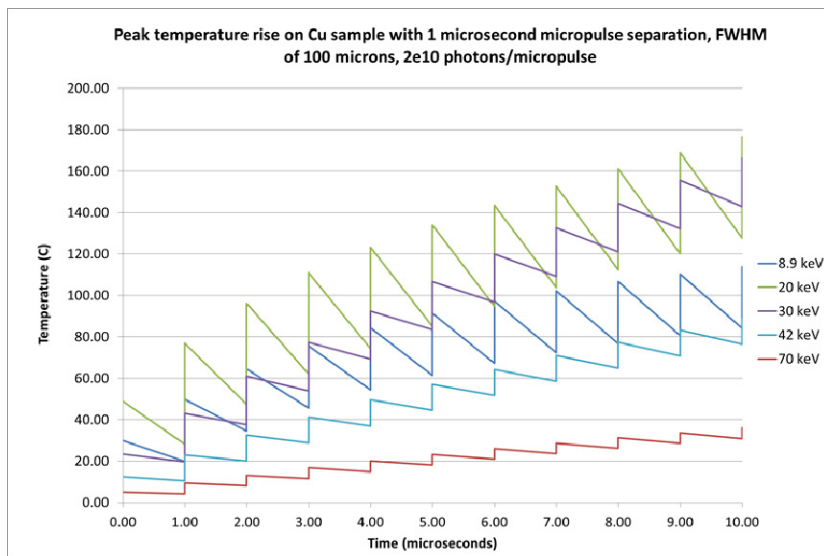


Figure 2: Graph of temperature rise for a string of closely-spaced, 1- μ s pulse separation, incident x-ray pulses on copper. Pulse-to-pulse heating quickly becomes a significant effect for photon energies less than 40 keV and for the short-pulse separations required for MaRIE measurements.

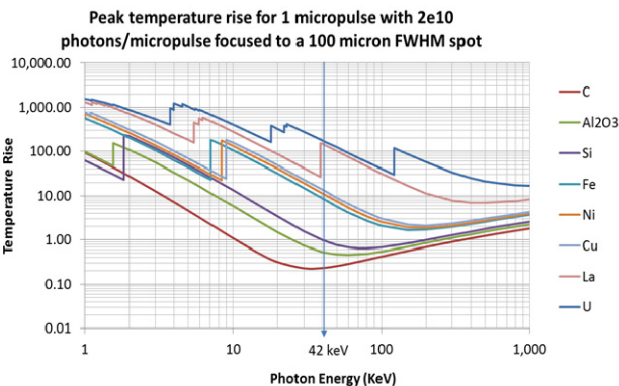


Figure 3: The plots show the fall in heating with increasing photon energy up to some minimum where the absorption flattens out and the temperature rises due to the increasing energy deposited for a fixed number of incident higher-energy photons.

PRE-CONCEPTUAL REFERENCE DESIGN

The SFR-required physical properties at the temporal and spatial scales listed above can be obtained with diagnostic techniques based on radiography, Bragg scattering, and x-ray diffraction. The pre-conceptual reference design [5-8] assumes an XFEL operating at a fundamental photon energy of 42-keV. 42-keV was chosen to allow multipulse diffractive imaging that requires greater than 10^{10} photons/image for multi-granular high-Z samples with acceptable but not insignificant heating, as compared to 10^8 photons needed for Phase Contrast Imaging (PCI). Also, operation at a 42-keV fundamental allows for the production of sufficient 3rd harmonic photons to do PCI at the K-edge of high-Z materials, such as uranium and other actinides. The maximum macropulse length requirement of 1 ms drives the choice of superconducting linac technology.

The reference design is based on an L-band 12-GeV superconducting linac similar in design to the European XFEL [9], schematically shown in Figure 6. Time-independent GENESIS simulations, Figure 5, indicate that greater than 2×10^{10} , 42-keV photons within 0.01% bandwidth can be obtained using the expected electron beam parameters. We have also included a 150 m tunnel contingency to go to 15 GeV in the future that would give ~ 2 x times the number of photons, or allow for higher photon energies. The Photon Facility Functional Requirements, given in Table 2, follow directly from the imaging requirements to achieve the SFRs, and provides the Facility Functional Requirements basis for the pre-conceptual reference design. Detailed information on the design is given in reference [5-8]. The electron beam requirements for the XFEL proper, electron driver linac, and electron radiography imaging are given in Tables 3, 4 and 5, respectively.

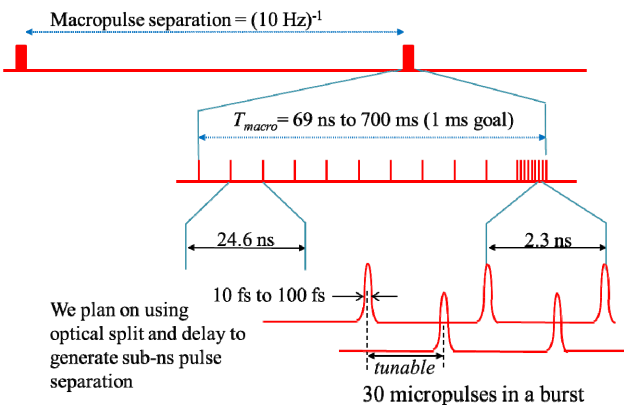


Figure 4: Pulse structure required to capture the full temporal range of dynamic events.

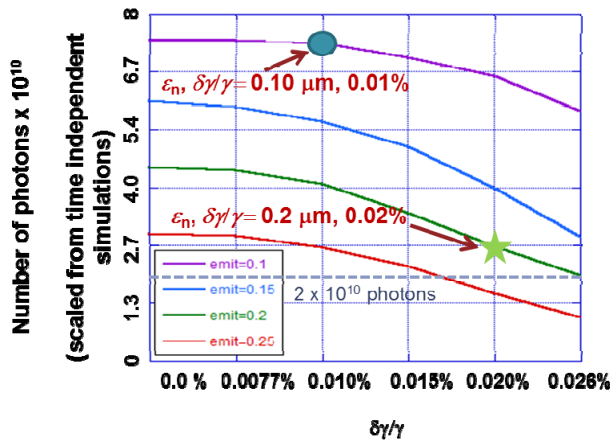


Figure 5: The blue circle shows the design goal for the electron beam of 0.1 μm emittance at 0.01% energy spread. For contingency, the XFEL calculations use the green star parameters, a factor of two higher emittance and energy spread.

Table 2: The Photon Characteristics Required to Meet the Imaging Requirements

Photon FFRs	
Design energy (keV)	5 to 42 (42 to 126 at 3 rd harmonic)
Coherent Photons per image	2×10^{10} (1×10^8 at 3 rd)
Energy Bandwidth ($\Delta E/E$)	2×10^{-4} to $< 10^{-5}$
Divergence	$< 10 \mu\text{rad}$
Pulse length	$\leq 100 \text{ fs}$

Table 3: The XFEL Electron Beam Requirements

XFEL electron beam FFRs			
Pulse charge	0.2 nC	Normalized rms slice emittance	$\leq 0.2 \mu\text{m}$
Slice energy spread	$\leq 0.02\%$	Micropulses per macropulse	30
Macropulse repetition rate	10 Hz	Minimum micropulse separation	2.3 ns

Table 4: Electron Beam Accelerator Requirements

Electron beam FFRs			
Energy	12 GeV	Electron source	Photo-injector
Linac fund. frequency	1.3 GHz	Max. macropulse duration	1 ms
Linac type	Super-conducting	Macropulse to macropulse energy variation	$\leq 0.02\%$
SC L-band cavity gradient	31.5 MV/m	Pulse energy variation within a macropulse	$\leq 0.01\%$
Maximum beamline angle	2.0 degrees @ 12 GeV	12 GeV FWHM micropulse length	33 fs

Table 5: Electron Radiography Requirements

eRad electron beam FFRs			
Pulse charge	1 nC	Normalized emittance	< 1000 microns
Microbunch energy spread	$\leq 0.02\%$	Macropulse repetition rate	10 shots per day
Micropulses per macropulse	10	Min micropulse separation	23 ns

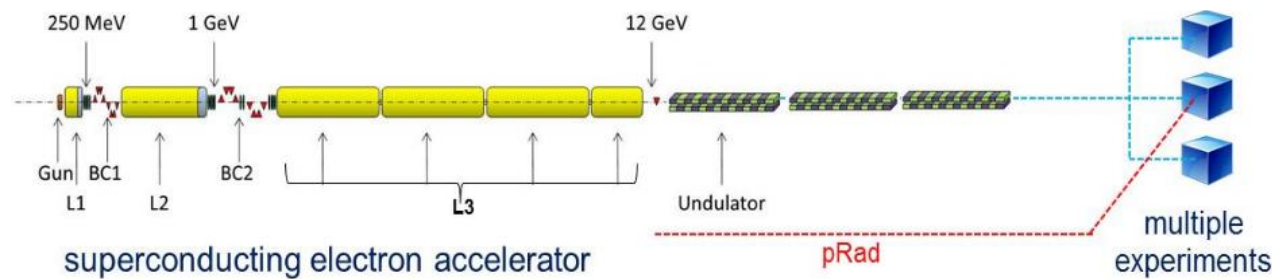


Figure 6: Pre-conceptual XFEL reference design schematic. For example, the first three major accelerator systems specified in this reference design document are: L-Band Photoinjector – Cu cathode, up to 0.2 nC, 10 ps FWHM (3 ps rms) out of gun, 1.1 ms RF macropulse, single 10 MW klystron drive, rms phase and amplitude jitter less than 0.03 degree and 0.03%. this is followed by cryomodule 1 that is based on ILC and DESY XFEL, and is: 9 cavities per cryomodule capacity, 9 cells per cavity, single 1.3 GHz multi-beam klystron (MBK) drive, RMS phase and amplitude jitter less than 0.03 degree and 0.03%, respectively, maximum cavity gradient of 31.5 MV/m, 200 kW/cavity, 18 cavities fed from a single klystron, $Q_{\text{ext}} = 3.9 \times 10^6$. this is followed by cryomodule 2, again based on ILC and DESY XFEL, 1.3 GHz (2 cavities), 3.9 GHz (6 cavities; 3rd-harmonic for linearization), 1.3 GHz cavity pair parameters and power as in CM1; 3.9 GHz single klystron drive, fields maintained to less than 0.03 degree and 0.03%, cavity gradient 20 MV/m, 3 kW/cavity, Q_{ext} for the 3.9 GHz cavities = 1.2×10^7 ; final output energy = 250 MeV when setting up for bunch compression in BC1. Also shown are x-ray-only end-stations and simultaneous, with x-ray pulses, electron and proton radiographic capabilities at an x-ray end station.

TECHNOLOGY RISK MITIGATION PLAN

The Technology Risk Mitigation Plan (TRM) is aimed at bringing the facility technologies to a technical maturity level necessary for completion of a Conceptual Design with a well-bounded cost and schedule estimate, as required by the DOE CD process. TRM also reduces risk to project success by better defining scope and requirements of programmatic equipment. For inclusion in Conceptual Design, the components and/or proposed systems had to have at least been operated in laboratory environment.

The present TRM plan [10] can be split into two categories: technologies unique to an XFEL and technologies independent of the x-ray source type. Should an XFEL be chosen as the preferred alternative then the following technology gaps must be addressed to confirm the production of 5×10^{10} photons at 42-keV with 2×10^{-4} bandwidth, and a micropulse spacing of 300 ps, as needed to base Conceptual Design:

- The photoinjector emittance must be demonstrated by a combination of relevant measurements at other facilities and then on a test stand at LANL.
- Electron beam energy spread has a major effect on XFEL performance. Energy spread source models for wakefields, Coherent Synchrotron Radiation, and microbunch instability, must be validated for inclusion in the simulation models. These models and dechirper energy correction must be demonstrated through relevant measurements at other facilities.
- Distributed seeding offers a path to attaining the required XFEL bandwidth and so relevant demonstrations at other facilities is required.
- Conceptual design requires a robust start-to-end modeling and simulation. Thus a key TRM activity is to incorporate the models from the above demonstrations and verify the codes.
- High Voltage Converter Modulator development can have a large impact on initial system cost and significantly lower operation and maintenance costs.
- TRM is also planned for on-going activities that are independent of the x-ray source, such as: High-Energy and Ultrafast Imaging Cameras, Multidimensional Dynamic Imaging techniques, Bulk Thermometry of Dynamic Materials, Development of Charged Particle Radiography for the Study of Small and Fast Physical Processes, X-ray Optics, and Long-Pulse Laser Technology Development [11].

All of the preceding TRM technologies are required to attain the full facility benefit and several will have a major impact on the facility layout.

CONCLUSION

The Project is progressing with initial funding. We are looking to fund research to identify and reduce technical risk, decrease cost, and expand performance. We are

exploring opportunities for collaborative R&D that would be relevant to MaRIE risk mitigation and conceptual design that builds on the expertise and resources at existing facilities worldwide.

In summary, the proposed MaRIE facility would offer new complementary capabilities to those at existing experimental facilities. The MaRIE capabilities will provide the tools scientists need to develop and manufacture next-generation materials that will perform predictably and with controlled functionality in extreme environments, and enable the discovery and design of advanced materials needed to meet 21st-century national security and energy security challenges.

ACKNOWLEDGMENT

The development of the MaRIE Project and the work presented in this paper is the result of the strong effort of the MaRIE team, with contributions from a large number of colleagues from across LANL, other DOE laboratories, universities, and industry.

REFERENCES

- [1] "From Quanta to the Continuum: Opportunities for Mesoscale Science," A Report for the Basic Energy Sciences Advisory Committee by the Mesoscale Science Subcommittee, September 2012.
- [2] Compendium of Workshop Reports can be found at <http://www.lanl.gov/science-innovation/science-facilities/marie/workshop-reports.php>, "Decadal Challenges for Predicting and Controlling Materials Performance in Extremes," LA-UR-10-02959.
- [3] Matter-Radiation Interactions in Extremes (MaRIE): Summary of Scientific Functional Requirements, Internal LANL Document, LA-UR 15-28325, 2015.
- [4] J. L. Barber, C. W. Barnes, R. L. Sandberg, and R. L. Sheffield, "Diffractive imaging at large Fresnel number: Challenge of dynamic mesoscale imaging with hard X-rays", *Phys. Rev. B*, 89, p. 184105, 2014.
- [5] MaRIE Electron accelerator reference design, Internal LANL document, LA-UR-15-27875.
- [6] J. W. Lewellen, *et al.*, "Status of the MaRIE X-FEL Accelerator Design", in *Proc. International PAC'15*, Richmond, VA, USA, 2015: 1894-1996.
- [7] J. W. Lewellen, *et al.*, "Technology Maturation for the MaRIE 1.0 X-FEL", in *Proc. FEL'15*, Daejeon, Korea, paper MOP062.
- [8] D. C. Nguyen, *et al.*, "Distributed Seeding for Narrow-Linewidth Hard X-Ray Free-Electron Lasers", in *Proc. FEL'15*, Daejeon, Korea, paper TUB02.
- [9] DESY Technical Design Report, http://tesla.desy.de/new_pages/TDR_CD/start.html
- [10] MaRIE Technology Risk Mitigation Plan, Internal LANL document, LA-UR-17-24477, 2017.
- [11] C. W. Barnes, *et al.*, "Technology Risk Mitigation Research and Development for the Matter-Radiation Interactions in Extremes (MaRIE) Project", 20th Biennial APS Conference on Shock Compression of Condensed Matter, St. Louis, MO, 2017.

DIAMOND DOUBLE-CRYSTAL SYSTEM FOR A FORWARD BRAGG DIFFRACTION X-RAY MONOCHROMATOR OF THE SELF-SEEDED PAL XFEL

Yu. Shvyd'ko*, S. Kearney, K.-J. Kim, T. Kolodziej, D. Shu
 Argonne National Laboratory, Lemont, IL 60439, USA

V. D. Blank, S. Terentyev

Technological Institute for Superhard and Novel Carbon Materials, Troitsk, Russian Federation

H.-S. Kang, C.-K. Min, B. Oh

Pohang Accelerator Laboratory, Gyeongbuk, Republic of Korea

P. Vodnala, Northern Illinois University, DeKalb, IL 60115, USA

J. Anton, University of Illinois at Chicago, Chicago, IL 60607, USA

Abstract

PAL XFEL (Republic of Korea) is being planned to be operated in the self-seeded mode in a 3-keV to 10-keV photon spectral range. Monochromatization of x-rays in the self-seeding system will be achieved by forward Bragg diffraction (FBD) from two diamond single crystals in the [100] and [110] orientations (one at a time). We present results on the optical and engineering designs, on the manufacturing, and on the x-ray diffraction topography characterization of the diamond double-crystal systems for the FBD monochromator.

PHYSICAL REQUIREMENTS AND OPTICAL DESIGN

Seeded x-ray free-electron lasers (XFELs) [1, 2] generate fully coherent x-rays with a well-defined spectrum and high spectral flux. A hard x-ray self-seeding scheme uses x-rays from the first half of the FEL system (electron beam in a magnetic undulator system) to generate radiation by the self-amplified spontaneous emission process and seed the electron bunch in the second half of the FEL system via an x-ray monochromator [3, 4]. PAL XFEL [5] plans the hard x-ray self-seeding system operating in the spectral range from 3 keV to 10 keV, to be installed and commissioned in 2018. The concept of the system is based on the LCLS design [1], which utilizes the one-crystal forward Bragg diffraction (FBD) x-ray monochromator proposed at DESY [4].

X-rays in Bragg diffraction from a crystal, see Fig. 1, are emitted with a time delayed t upon excitation with an x-ray pulse and subsequent multiple scattering in the crystal either at a Bragg angle θ to the reflecting atomic planes (indicated in blue) or in the forward direction (in red). The FBD time response of an x-ray-transparent crystal, such as diamond, can be presented by the analytical expression [6, 7]

$$|G_{00}(t)|^2 \propto \left[\frac{1}{2\mathcal{T}_0} \frac{J_1 \left[\sqrt{\frac{t}{\mathcal{T}_0}} \left(1 + \frac{t}{\mathcal{T}_d} \right) \right]}{\sqrt{\frac{t}{\mathcal{T}_0}} \left(1 + \frac{t}{\mathcal{T}_d} \right)} \right]^2 \quad (1)$$

with the characteristic time parameters

$$\mathcal{T}_0 = \frac{2[\bar{\Lambda}_H^{(s)}]^2 \sin(\theta + \eta)}{cd}, \quad \mathcal{T}_d = \frac{2d \sin^2 \theta}{c|\sin(\theta - \eta)|}. \quad (2)$$

where \mathcal{T}_0 is the FBD time constant, see Fig. 1(c), $\bar{\Lambda}_H^{(s)}$ is the extinction length (a Bragg reflection invariant), $\mathbf{H} = (hkl)$ is the Bragg diffraction vector, d is the crystal thickness, η is the asymmetry angle between the crystal surface and the reflecting atomic planes, c is the speed of light, and J_1 is the Bessel function of the first kind. The FBD time response is shown by the red line in Fig. 1(c) for a particular case. The FBD photons are concentrated within a spectral bandwidth,

$$\Delta E_0 = \frac{\hbar}{\pi\mathcal{T}_0}, \quad (3)$$

see Fig. 1(b), which is typically larger than $\Delta E_H = \Delta E_0 (2\pi\bar{\Lambda}_H^{(s)}/d)$, the spectral width of BD, see Fig. 1(a).

The first trailing maximum of the FBD time response appears at time delay $t_s = 26\mathcal{T}_0$, see Fig. 1(c), and its duration is $\Delta t_s = 16\mathcal{T}_0$ (assuming $t \ll \mathcal{T}_d$). The intensity, delay, duration, and monochromaticity of the x-ray photons are defined by the single parameter \mathcal{T}_0 . For efficient seeding, we require that the peak of the electron bunch is delayed by t_s , to overlap with the first trailing maximum. The optimal delay is $t_s = 20 - 25$ fs. As a result, the FBD monochromator crystal parameters d , $\bar{\Lambda}_H^{(s)}$, θ , and η should be chosen such that $\mathcal{T}_0 \approx 0.75 - 1$ fs.

An x-ray pulse emanating from the crystal in FBD is not only delayed, it experiences also a lateral shift [6, 7]

$$x = tc \cot \theta, \quad (4)$$

proportional to the time delay t schematically shown in the left graph of Fig. 1. To ensure efficient seeding, the lateral shift x_s at the time delay t_s should be much smaller than the electron beam size, which is $\approx 25 \mu\text{m}$ (rms) for PAL XFEL.

A practically important question for the fabrication of the FBD monochromator crystals is an admissible angular spread $\Delta\theta_A$ of the crystal lattice deformation due to crystal defects or mounting strain. From Bragg's law $E = E_H \sin \theta$ ($E_H = hc/2d$ is a backreflection photon energy) the variation δE of the peak reflectivity in BD and of the FBD spectral function with angle is $\delta E = E_H \delta\theta \cos \theta$. If we require that

* shvydko@aps.anl.gov

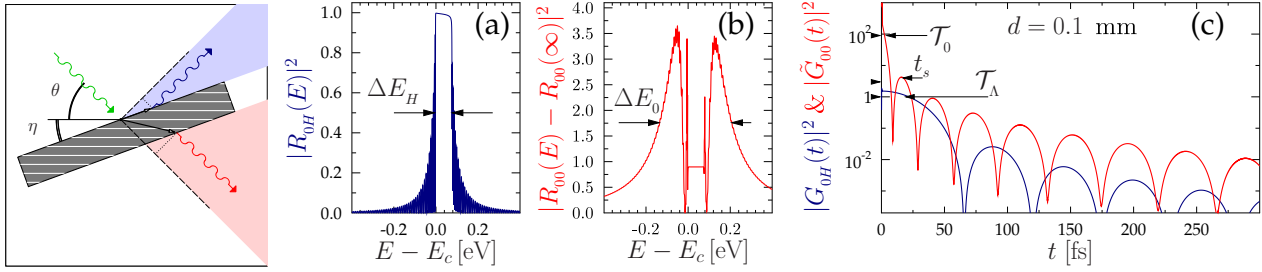


Figure 1: Schematic of Bragg diffraction (BD) and forward Bragg diffraction (FBD) of x-rays from a crystal (left). Examples of energy dependences of x-ray reflectivity $|R_{0H}(E)|^2$ in BD (a) and in FBD $|R_{00}(E) - R_{00}(\infty)|^2$ (b) from a diamond crystal in the (400) Bragg reflection, $E_c = 8.33$ keV, $\theta = 56.6^\circ$, $\eta = 0^\circ$, $d = 0.1$ mm. (c) Intensities of the corresponding time dependencies of crystal response to an excitation with an ultra-short x-ray pulse in BD $|G_{0H}(t)|^2$ (blue) and in FBD $|G_{00}(t)|^2$ (red).

C(111) $\bar{\Lambda}_{111}^{(s)} = 1.09 \mu\text{m}$ $\eta = 35.3^\circ$ $d = 30 \mu\text{m}$

$E = 3.3$ keV
 $\mathcal{T}_0 = 0.26$ fs
 $\Delta E_0 = 0.81$ eV
 $t_s = 6.7$ fs, $x_s = 0.9 \mu\text{m}$
 $\Delta\theta_A = 163.66 \mu\text{rad}$

$E = 3.6867$ keV
 $\mathcal{T}_0 = 0.26$ fs
 $\Delta E_0 = 0.79$ eV
 $t_s = 6.9$ fs, $x_s = 1.5 \mu\text{m}$
 $\Delta\theta_A = 91.33 \mu\text{rad}$

$E = 4.5$ keV
 $\mathcal{T}_0 = 0.26$ fs
 $\Delta E_0 = 0.81$ eV
 $t_s = 6.7$ fs, $x_s = 2.2 \mu\text{m}$
 $\Delta\theta_A = 48.81 \mu\text{rad}$

$E = 4.9$ keV
 $\mathcal{T}_0 = 0.25$ fs
 $\Delta E_0 = 0.83$ eV
 $t_s = 6.6$ fs, $x_s = 2.5 \mu\text{m}$
 $\Delta\theta_A = 39.52 \mu\text{rad}$

C(220) $\bar{\Lambda}_{220}^{(s)} = 1.98 \mu\text{m}$ $\eta = 0.0^\circ$ $d = 30 \mu\text{m}$

$E = 5$ keV
 $\mathcal{T}_0 = 0.86$ fs
 $\Delta E_0 = 0.24$ eV
 $t_s = 22.3$ fs, $x_s = 1.2 \mu\text{m}$
 $\Delta\theta_A = 78.87 \mu\text{rad}$

$E = 5.5$ keV
 $\mathcal{T}_0 = 0.78$ fs
 $\Delta E_0 = 0.27$ eV
 $t_s = 20.2$ fs, $x_s = 3.0 \mu\text{m}$
 $\Delta\theta_A = 29.24 \mu\text{rad}$

$E = 6$ keV
 $\mathcal{T}_0 = 0.71$ fs
 $\Delta E_0 = 0.29$ eV
 $t_s = 18.6$ fs, $x_s = 3.9 \mu\text{m}$
 $\Delta\theta_A = 20.97 \mu\text{rad}$

$E = 7$ keV
 $\mathcal{T}_0 = 0.61$ fs
 $\Delta E_0 = 0.34$ eV
 $t_s = 15.9$ fs, $x_s = 4.8 \mu\text{m}$
 $\Delta\theta_A = 14.48 \mu\text{rad}$

C(400) $\bar{\Lambda}_{400}^{(s)} = 3.63 \mu\text{m}$ $\eta = 0.0^\circ$ $d = 100 \mu\text{m}$

$E = 7$ keV
 $\mathcal{T}_0 = 0.87$ fs
 $\Delta E_0 = 0.24$ eV
 $\Delta\theta_A = 87.08 \mu\text{rad}$
 $t_s = 22.7$ fs, $x_s = 0.8 \mu\text{m}$

$E = 8.3$ keV
 $\mathcal{T}_0 = 0.74$ fs
 $\Delta E_0 = 0.28$ eV
 $\Delta\theta_A = 15.78 \mu\text{rad}$
 $t_s = 19.1$ fs, $x_s = 3.7 \mu\text{m}$

$E = 9$ keV
 $\mathcal{T}_0 = 0.68$ fs
 $\Delta E_0 = 0.31$ eV
 $\Delta\theta_A = 12.52 \mu\text{rad}$
 $t_s = 17.6$ fs, $x_s = 4.4 \mu\text{m}$

$E = 10$ keV
 $\mathcal{T}_0 = 0.61$ fs
 $\Delta E_0 = 0.34$ eV
 $\Delta\theta_A = 9.95 \mu\text{rad}$
 $t_s = 15.9$ fs, $x_s = 4.9 \mu\text{m}$

Figure 2: Bragg diffraction and forward Bragg diffraction scattering configurations shown together with diamond crystal and x-ray seed parameters in a $E = 3.3$ keV to $E = 10$ keV photon spectral range.

such variation should not exceed 5% of the FBD spectral bandwidth ΔE_0 , we obtain

$$\Delta\theta_A = 0.32 \frac{\Delta E_0}{E_H \cos \theta} \quad (5)$$

The spectral range of x-ray monochromatization from 6.9516 keV to 10 keV can be covered using the (400) Bragg diffraction from a 100 μm -thick diamond crystal in the [100] orientation. Figure 2(bottom) shows scattering geometries

for different photon energies E , and calculated values of the FBD characteristic time \mathcal{T}_0 , time delay of the first trailing maximum t_s , time-averaged spectral bandwidth ΔE_0 of the seed, lateral shift x_s at $t = t_s$, and the admissible angular broadening $\Delta\theta_A$. For all photon energies, the \mathcal{T}_0 , t_s , x_s , and $\Delta\theta_A$ values are in the desired range. Seeding at photon energies higher than 10 keV may also work, however, with lower efficiency because of too large x_s and too small $\Delta\theta_A$.

The spectral range from 4.916 keV to 7 keV can be covered using the (220) Bragg diffraction, see Fig. 2(center) from a diamond crystal in the [110] orientation. However, because of a much smaller $\bar{\Lambda}_{220}^{(s)} = 1.98 \mu\text{m}$, a much thinner crystal with $d = 30 \mu\text{m}$ has to be used to ensure the required \mathcal{T}_0 .

Using the (111) asymmetric Bragg reflection from the same crystal, see Fig. 2(top), the monochromatic seed in the spectral range from 3.3 keV to 5 keV can be generated. However, a twice smaller $\bar{\Lambda}_{111}^{(s)} = 1.09 \mu\text{m}$ for the (111) reflection, compared to that of the (220) reflection, results in \mathcal{T}_0 values out of the optimal range. Seeding may still take place, however, the electron bunch at the same delay will overlap with the radiation field having a more complex time structure (will overlap with the second and third trailing maxima) and therefore a more complex spectrum.

The above analysis suggests using two crystals (one at a time) a $100 \mu\text{m}$ -thick in the [100] orientation, for monochromatization in the 7 to 10 keV range with the (400) reflection, and a $30 \mu\text{m}$ -thick in the [110] orientation, for monochromatization in the 5 to 3.3 keV range with the symmetric (220) and the asymmetric (111) reflections.

Because manufacturing a $30 \mu\text{m}$ -thick crystal and mounting it strain-free is a challenge, a second back-up double-crystal diamond system was planned with a $90 \mu\text{m}$ -thick crystal in the [110] orientation.

ENGINEERING DESIGN AND MANUFACTURING

The mechanical design of the double-crystal system has to ensure (i) mechanically stable strain-free mount of the thin diamond crystals, (ii) a good heat transport and heat sink of the absorbed x-ray power by the crystals, and (iii) radiation-safe XFEL operations. The latter means that no metal parts are allowed within about 5 mm of the diamond crystals. A toothbrush-type mechanical design of the one-crystal FBD monochromator system for the LCLS self-seeding monochromator [8] was used as a prototype for the present design. Although it has proved to be viable, there were a few issues with the LCLS design. The diamond crystal was mounted in a graphite holder to comply with radiation safety requirements. However, the heat transport in graphite is very poor. Besides, the graphite holder does not allow easy and reliable control of the crystal mounting strain. The present design is aimed at keeping close to the LCLS standard and improving the mentioned drawbacks.

The new design features include:

1. The two diamond single-crystal plates in two different crystallographic orientations are mounted on a common base.
2. The base is manufactured from polycrystalline diamond grown with the chemical vapor deposition (CVD) method, to ensure a good heat transport through GaIn eutectic.
3. Thin graphite springs are used to press gently the diamond crystals to the base. Thin graphite springs are softer than the thin perforated diamond springs applied

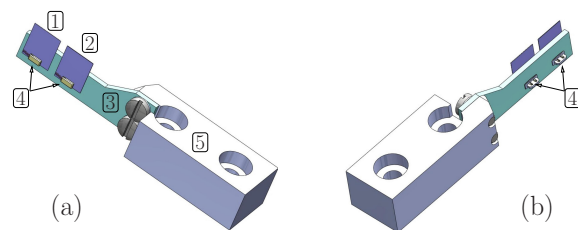


Figure 3: Drawings of the diamond two-crystal system for the FBD monochromator. Front (a) and back (b) views of the system are shown. Two diamond monochromator crystals C*[100] - 1 - and C*[110] - 2 - are mounted on the CVD-diamond base - 3 - using diamond posts and graphite springs - 4. The CVD base is attached to the graphite holder - 5.

in [9] and are still radiation safe. The pressure on the diamond crystals can be controlled by changing the springs' thickness. The diamond posts holding the springs are now firmly attached to the CVD bases as detailed in [10]. As a result, the crystals will still stay in place even if the graphite springs fall out.

4. The CVD diamond base is attached to a graphite holder, with mounting holes and dimensions equivalent to those of the LCLS design.
5. The lower narrow facet of the base can be attached to a heat sink.

Drawings of the diamond two-crystal system for the FBD monochromator are presented in Fig. 3. The system has a total length of 35.5 mm. The monochromator diamond crystals (1) and (2) are $\approx 4 \text{ mm(H)} \times 5 \text{ mm(V)}$ each. They are laser cut from the highest quality type-IIa diamond crystal grown by the high-pressure high-temperature technique (see [11] for references) and polished to a 5 nm (rms) surface micro-roughness. The $19.6 \text{ mm} \times 6 \text{ mm}$ and 0.75-mm-thick supporting CVD base (3) is machined by laser cutting. The monochromator crystals are attached to the CVD base by an assembly (4) with diamond crystal posts, graphite flat springs, and graphite wedges, as detailed in [10]. The graphite springs thickness is in the $\approx 50 - 100 \mu\text{m}$ range.

Two diamond double-crystal systems manufactured according to the design specifications and Fig. 3 drawings are shown on in Fig. 4. The systems and all their components were manufactured at Technological Institute for Superhard and Novel Carbon Materials (TISNCM, Russia).

X-RAY DOUBLE-CRYSTAL TOPOGRAPHY CHARACTERIZATION

The crystal quality of the monochromator diamond crystals has been characterized by sequential x-ray Bragg diffraction topography. The technique measures Bragg reflection images of a crystal with a pixel x-ray detector sequentially at different incidence angles to the reflecting atomic planes of well collimated x-rays. The angular dependences of Bragg reflectivity (rocking curves) measured with each detector pixel are used to calculate Bragg reflection maps of the angular widths of the rocking curves, and the maps of the center of mass (COM) of the rocking curves are shown as color

Content from this work may be used under the terms of the CC BY 3.0 licence (© 2018). Any distribution of this work must maintain attribution to the author(s), title of the work, publisher, and DOI.

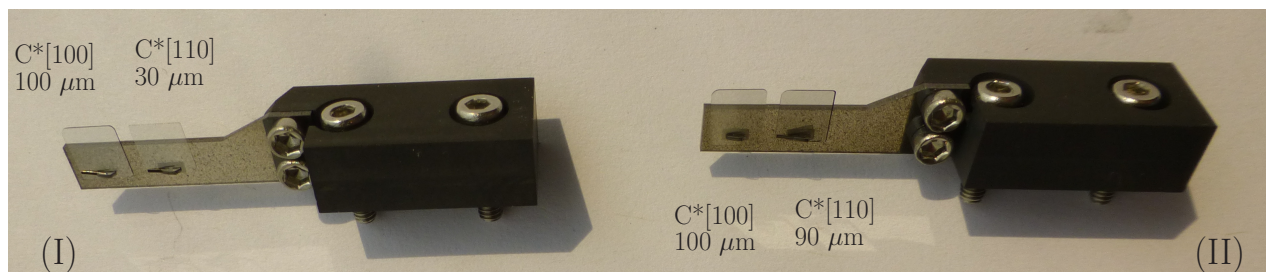


Figure 4: Photograph of the diamond double-crystal systems I and II manufactured according to the Fig. 3 drawings. The monochromator diamond single-crystal plates C^* are attached to the CVD-diamond crystal bases. Both $C^*[100]$ crystals (left in each system) are $100\ \mu\text{m}$ thick. The $C^*[110]$ crystals (right in each system) are $30\ \mu\text{m}$ and $90\ \mu\text{m}$ thick, respectively. All crystals are $\approx 4 \times 5\ \text{mm}^2$ in size.

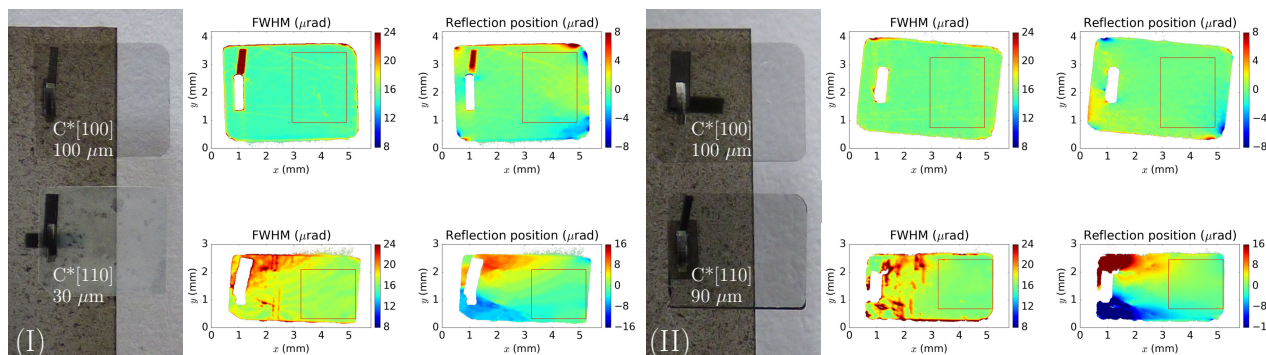


Figure 5: Photographs and Bragg reflection rocking curve color maps of the diamond FBD monochromator crystals. Shown are color maps of the reflection angular widths (FWHM) and of the reflection angular positions. The graphs in the upper row correspond to the crystals in the $[100]$ orientation, while the bottom row graphs to the crystals in the $[110]$ orientation. The graphs on the left half belong to diamond double-crystal system I, while those of system II are on the right half. Red rectangles on the maps indicate the working regions, featuring almost theoretical Bragg reflection widths and less than $1.5\ \mu\text{rad}$ (rms) reflection position angular variations.

maps in Fig. 5. Microscopic defect structure can be derived from the Bragg reflection images and Bragg reflection width maps. Mesoscopic and macroscopic defects or crystal strain can be best evaluated from the COM maps.

We have used a sequential x-ray diffraction topography setup at 1-BM X-ray Optics Testing Beamline at the Advanced Photon Source (APS, USA) [12]. The setup employs a nearly-nondispersive double-crystal $\text{Si}(531)\text{-C}^*(400)$ Bragg diffraction arrangement to characterize diamond crystals in the $[100]$ orientation, and a $\text{Si}(111)\text{-C}^*(220)$ arrangement to characterize diamond crystals in the $[110]$ orientation. In each arrangement, the first crystal is an asymmetrically cut high-quality silicon conditioning crystal, and the second one is a diamond crystal under investigation. The setup enables rocking curve mapping with a submicroradian angular and $13\ \mu\text{m}$ spatial resolution. The spatial resolution is limited by the detector pixel size.

Figure 5 shows photographs and Bragg reflection rocking curve color maps of the diamond FBD monochromator crystals. Scales on the x - and y -axis in Fig. 5 correspond to the detector coordinates. The crystals at the Bragg angle θ to the detector plane therefore appear to be contracted in the y direction by a factor of $\sin \theta = 0.85$ for the (400) Bragg reflection from the diamond crystal ($8.2\ \text{keV}$ x-rays) and by

a factor of $\sin \theta = 0.6$ for the (220) Bragg reflection. The maps were calculated using a dedicated code [13].

The double-crystal x-ray topography reveals that the crystals in working areas of $2\ \text{mm}(V) \times 2\ \text{mm}(H)$ indicated in Fig. 5 by red rectangles are almost flawless, with the reflection width close to the theoretical values and the mounting strain $\lesssim 1.5\ \mu\text{rad}$ (rms), well below the admissible $\Delta\theta_A$ values given in Fig. 2. It should be noted however, that as manufactured $30\ \mu\text{m}$ thin crystals in the $[110]$ orientation featured much larger strain. The strain has been reduced substantially by annealing the crystal for 3 hours in a muffle furnace in air at a temperature of $920\ \text{K}$, as described in [14]. Although the crystal surface became more rough and the crystal optically less transparent after annealing, no problems are expected regarding its performance as the x-ray FBD monochromator.

CONCLUSIONS

A double-crystal system composed of a $100\ \mu\text{m}$ -thick diamond crystal in the $[100]$ orientation and a $30\ \mu\text{m}$ -thick diamond crystal in the $[110]$ orientation mounted on a common CVD-diamond base was designed and manufactured for use as a forward Bragg diffraction monochromator in the $3.3\ \text{keV}$ to $10\ \text{keV}$ spectral range of the self-seeded PAL XFEL. A second back-up system was manufactured with a

thicker (90 μm) diamond crystal in [110] orientation. The crystals are mounted in a mechanically stable fashion using diamond and graphite components, ensuring proper x-ray monochromatization, heat transport, mechanical stability, and radiation-safe XFEL operations. The double-crystal x-ray topography revealed that the crystals in a working area of about $2 \times 2 \text{ mm}^2$ are almost flawless and the mounting strain is $\leq 1.5 \mu\text{rad}$ (rms), i.e., well below the admissible values. We expect that the monochromator crystals will perform close to the design specifications.

ACKNOWLEDGMENTS

Dr. Stanislav Stoupin is acknowledged for technical support at the Advanced Photon Source (APS) 1-BM beamline and making available the software for the evaluation of the x-ray topography data. Dr. Albert Macrander and Dr. Lahsen Assoufid are acknowledged for supporting this research at the 1-BM beamline. Work at Argonne National Laboratory was supported by the U.S. Department of Energy, Office of Science, Office of Basic Energy Sciences, under contract DE-AC02-06CH11357. Work at TISCNM was supported by the Ministry of Education and Science of Russian Federation: scientific project RFMEF1586114X0001 Grant No. 14.586.21.0001. Work at PAL XFEL was supported by the Ministry of Science and ICT, Republic of Korea.

REFERENCES

- [1] J. Amann, W. Berg, V. Blank, F.-J. Decker, Y. Ding, P. Emma, Y. Feng, J. Frisch, D. Fritz, J. Hastings, Z. Huang, J. Krzywinski, R. Lindberg, H. Loos, A. Lutman, H.-D. Nuhn, D. Ratner, J. Rzepiela, D. Shu, Yu. V. Shvyd'ko, S. Spampinati, S. Stoupin, S. Terentiev, E. Trakhtenberg, D. Walz, J. Welch, J. Wu, A. Zholents, and D. Zhu, "Demonstration of self-seeding in a hard-x-ray free-electron laser", *Nature Photonics*, 6, 2012.
- [2] E. Allaria, R. Appio, L. Badano, W.A. Barletta, S. Bassanese, S.G. Biedron, A. Borgia, E. Busetto, D. Castronovo, P. Cinquegrana, S. Cleva, D. Cocco, M. Cornacchia, P. Craievich, I. Cudin, G. D'Auria, and et al. "Highly coherent and stable pulses from the fermi seeded free-electron laser in the extreme ultraviolet", *Nature Photonics*, 6:699–704, 2012.
- [3] E. L. Saldin, E. A. Schneidmiller, Yu. V. Shvyd'ko, and M. V. Yurkov. "X-ray FEL with a meV bandwidth" *Nucl. Instrum. Methods Phys. Res. A*, 475:357–362, 2001.
- [4] G. Geloni, V. Kocharyan, and E. L. Saldin. "A novel self-seeding scheme for hard x-ray FELs", *Journal of Modern Optics*, 58:1391–1403, 2011.
- [5] I.S. Ko, H.-S. Kang, H. Heo, C. Kim, G. Kim, C.-K. Min, H. Yang, S.Y. Baek, H.-J. Choi, G. Mun, B.R. Park, Y.J. Suh, D.C. Shin, J. Hu, J. Hong, S. Jung, S.-H. Kim, K. Kim, D. Na, S.S. Park, Y.J. Park, Y.G. Jung, S.H. Jeong, H.G. Lee, S. Lee, S. Lee, B. Oh, H.S. Suh, J.-H. Han, M.H. Kim, N.-S. Jung, Y.-C. Kim, M.-S. Lee, B.-H. Lee, C.-W. Sung, I.-S. Mok, J.-M. Yang, Y.W. Parc, W.-W. Lee, C.-S. Lee, H. Shin, J.H. Kim, Y. Kim, J.H. Lee, S.-Y. Park, J. Kim, J. Park, I. Eom, S. Rah, S. Kim, K.H. Nam, J. Park, J. Park, S. Kim, S. Kwon, R. An, S.H. Park, K.S. Kim, H. Hyun, S.N. Kim, S. Kim, C.-J. Yu, B.-S. Kim, T.-H. Kang, K.-W. Kim, S.-H. Kim, H.-S. Lee, H.-S. Lee, K.-H. Park, T.-Y. Koo, D.-E. Kim, K.B. Lee, "Construction and commissioning of PAL-XFEL facility", *Applied Sciences*, 7(5), 2017.
- [6] R. R. Lindberg and Yu. V. Shvyd'ko "Time dependence of Bragg forward scattering and self-seeding of hard x-ray free-electron lasers", *Phys. Rev. ST Accel. Beams*, 15:050706, May 2012.
- [7] Yu. V. Shvyd'ko and R. Lindberg, "Spatiotemporal response of crystals in x-ray Bragg diffraction" *Phys. Rev. ST Accel. Beams*, 15:100702, Oct 2012.
- [8] S. Stoupin, V. D. Blank, S. A. Terentyev, S.N. Polyakov, V.N. Denisov, M. S. Kuznetsov, Yu. V. Shvyd'ko, D. Shu, P. Emma, J. Maj, and J. Katsoudas, "Diamond crystal optics for self-seeding of hard x-rays in x-ray free-electron lasers", *Diamond and Related Materials*, 33:1–4, 2013.
- [9] S. Stoupin, S. A. Terentyev, V. D. Blank, Yu. V. Shvyd'ko, K. Goetze, L. Assoufid, S. N. Polyakov, M. S. Kuznetsov, N. V. Kornilov, J. Katsoudas, R. Alonso-Mori, M. Chollet, Y. Feng, J. M. Glowina, H. Lemke, A. Robert, M. Sikorski, S. Song, and D. Zhu, "All-diamond optical assemblies for a beam-multiplexing X-ray monochromator at the Linac Coherent Light Source", *Journal of Applied Crystallography*, 47(4):1329–1336, Aug 2014.
- [10] S. Terentyev, V. Blank, T. Kolodziej, and Yu. V. Shvyd'ko, "Curved diamond-crystal spectrographs for x-ray free-electron laser noninvasive diagnostics", *Rev. Sci. Instrum.*, 87:125117, 2016.
- [11] Yu. V. Shvyd'ko, V. Blank, and S. Terentyev, "Diamond x-ray optics: Transparent, resilient, high-resolution, and wavefront preserving", *MRS Bulletin*, 62(6):437–444, 2017.
- [12] S. Stoupin, Yu. V. Shvyd'ko, E. Trakhtenberg, Z. Liu, K. Lang, X. Huang, M. Wiczorek, E. Kasman, J. Hammonds, A. Macrander, and L. Assoufid, "Sequential x-ray diffraction topography at 1-BM x-ray optics testing beamline at the Advanced Photon Source", *AIP Conf. Proc.*, 1471:050020, 2016.
- [13] S. Stoupin, "Python-DTXRD", <https://www1.aps.anl.gov/science/scientific-software/dtxrd> 2015.
- [14] T. Kolodziej, P. Vodnala, S. Terentyev, V. Blank, and Yu. V. Shvyd'ko, "Diamond drumhead crystals for X-ray optics applications", *Journal of Applied Crystallography*, 49(4):1240–1244, Aug 2016.

CONCEPT FOR A SEEDED FEL AT FLASH2*

C. Lechner[†], R. W. Assmann, J. Bödewadt, M. Dohlus, N. Ekanayake[‡], G. Feng, I. Hartl, T. Laarmann, T. Lang, L. Winkelmann, I. Zagorodnov, DESY, 22607 Hamburg, Germany
 S. Khan, DELTA, TU Dortmund University, 44227 Dortmund, Germany
 A. Azima, M. Drescher, Th. Maltezopoulos[§], T. Plath[¶],
 J. Rossbach, W. Wurth, University of Hamburg, 22671 Hamburg, Germany

Abstract

The free-electron laser (FEL) FLASH is a user facility delivering photon pulses down to 4 nm wavelength. Recently, the second FEL undulator beamline 'FLASH2' was added to the facility. Operating in self-amplified spontaneous emission (SASE) mode, the exponential amplification process is initiated by shot noise of the electron bunch resulting in photon pulses of limited temporal coherence. In seeded FELs, the FEL process is initiated by coherent seed radiation, improving the longitudinal coherence of the generated photon pulses. The conceptual design of a possible seeding option for the FLASH2 beamline envisages the installation of the hardware needed for high-gain harmonic generation (HG) seeding upstream of the already existing undulator system. In this contribution, we present the beamline design and numerical simulations of the seeded FEL.

INTRODUCTION

High-gain free-electron lasers (FELs) [1–4] generate ultrashort photon pulses of unparalleled intensities, enabling the study of fundamental processes with unprecedented temporal and spatial resolution. In a self-amplified spontaneous emission (SASE) FEL, the exponential amplification process is initiated by the shot-noise of the electron bunch, resulting in poor longitudinal coherence of the FEL radiation. Seeding techniques using external light pulses can be applied to transform the FEL into a fully coherent light source. High-gain harmonic generation (HG) [5] uses an external, longitudinally coherent, light pulse that manipulates the electron beam in a short undulator (the modulator) generating a sinusoidal energy modulation. The following chicane converts the energy modulation into a periodic pattern of microbunches. The harmonic content of this density modulation initiates longitudinally coherent FEL emission in the radiator at the desired harmonic. As the seeding process increases the energy spread of the electron beam, the achievable harmonic number is limited [6]. Single-stage HG seeding up to the 15th harmonic was demonstrated at the seeded FEL user facility FERMI [7].

Table 1: Parameters for HG seeding at FLASH2 (for operation at the 14th harmonic)

Parameter	Value
electron beam energy	1000 MeV
rms slice energy spread	150 keV
seed laser wavelength	267 nm
seed pulse energy	50 μ J
seed pulse duration	50 fs
harmonic number	14
FEL wavelength	19.0 nm
repetition rate:	
initial	10 Hz
after upgrade	(up to) 800 Hz

The FEL user facility FLASH [8] at DESY in Hamburg (see Fig. 1) has been in operation since 2005 [9], delivering high-brilliance SASE FEL radiation at wavelengths down to 4.2 nm. The superconducting linear accelerator is operated with 10 long radio-frequency pulses per second, during which trains with up to 800 high-brightness electron bunches (at a repetition rate of 1 MHz) can be accelerated to energies of up to 1.25 GeV. These bunch trains are distributed over two undulator beamlines using flat-top kickers. This enables operation at the 10-Hz bunch train repetition rate in both beamlines, the FLASH1 beamline with a fixed-gap undulator, where also the seeding experiment sFLASH [10] is installed, and the recently added FLASH2 beamline. Simultaneous SASE FEL delivery to photon user experiments at both FLASH1 and FLASH2 is now routinely achieved [11, 12] and simultaneous three-beamline SASE lasing (FLASH1, FLASH2, and sFLASH) was demonstrated [13] during machine studies.

Cascaded HG seeding was studied [14] in the conceptual planning phase of the FLASH2 undulator beamline. However, this scheme was not implemented. In the present paper, the proposed implementation of single-stage HG seeding at FLASH2 up to a maximum harmonic number of 14, corresponding to a shortest wavelength of 19 nm, is described. Table 1 lists the key parameters for HG-seeded operation at 19 nm. The initial implementation Phase 1A would provide seeding at a repetition rate of 10 Hz. Implementation Phase 1B is entered by upgrading the seed laser system to high-repetition-rate operation at a 100-kHz burst rate, matching the bunch pattern delivered by the superconducting linac. Thanks to this combination of superconducting linear accelerator and high-repetition-rate

* Work supported by Federal Ministry of Education and Research of Germany under contract No. 05K13GU4, 05K13PE3, and 05K16PEA.

[†] christoph.lechner@desy.de

[‡] present address: Michigan State University, East Lansing, MI 48824, USA

[§] present address: European XFEL GmbH, 22869 Schenefeld, Germany

[¶] present address: DELTA, TU Dortmund University, 44227 Dortmund, Germany

Content from this work may be used under the terms of the CC BY 3.0 licence (© 2018). Any distribution of this work must maintain attribution to the author(s), title of the work, publisher, and DOI.

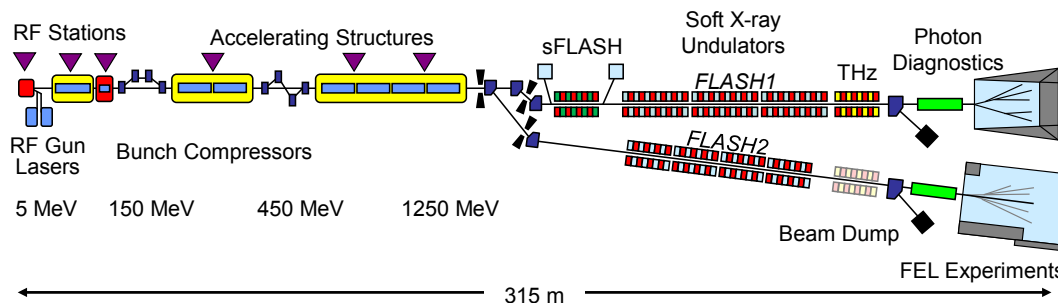


Figure 1: Layout of the FEL user facility FLASH. The superconducting linear accelerator is operated with long radio-frequency pulses and delivers trains of up to 800 electron bunches (at a repetition rate of 1 MHz). Flat-top kickers in the switchyard at the end of the linear accelerator distribute the bunches, enabling operation of both beamlines at the 10-Hz bunch train repetition rate.



Figure 2: Proposed layout of the FLASH2 undulator beamline for the implementation of HGHG seeding. The already existing variable-gap undulator system (comprising 12 2.5-m-long modules) is currently operated as a SASE FEL at wavelengths down to 4 nm. In front of this undulator, approximately 20 meter of beamline are currently partly used for electron beam diagnostics and the additional hardware would be installed there. In addition to the existing variable-gap undulator, the implementation of HGHG seeding requires a chicane, which guides the electron beam around the seed laser injection mirror, a variable-gap modulator, and a bunching chicane.

seed laser system, Phase 1B would be capable of producing up to 800 seeded FEL pulses per second. Finally, Phase 2 would be the implementation of echo-enabled harmonic generation (EEHG) [15], a seeding method enabling seeding at shorter wavelengths. See [16] for an overview of potential FLASH2 seeding options and [17] for an earlier description of the FLASH2 seeding proposal.

PROPOSED IMPLEMENTATION OF HGHG SEEDING AT FLASH2

Presently, the already existing undulator of FLASH2, which comprises 12 2.5-m-long variable-gap modules, is operated as SASE FEL at wavelengths down to 4 nm [12]. A central constraint for any proposed FLASH2 modification is that it must not compromise SASE FEL performance, thus excluding modifications of the existing undulators. An approximately 20-m-long beamline section upstream of the undulators is partly used for electron beam diagnostics and, as illustrated in Fig. 2, the additional hardware needed for the implementation of HGHG seeding would be installed here. A dedicated seed laser system generates ultraviolet seed pulses with wavelength tunable between 260 nm and 320 nm, which is required to produce continuously tunable seeded FEL radiation. For 50-fs long seed pulses, the required pulse energy at the laser system is 50 μ J (12 μ J at the modulator). The initial seed pulse repetition rate is 10 Hz. HGHG seeding at a 100-kHz burst repetition rate would

become possible after a later upgrade of the seed laser system. The design and production of a laser system meeting these very demanding parameters requires a research and development effort.

The electron beam arriving from the FLASH linear accelerator is guided around the laser injection mirror by a 4-dipole chicane allowing to inject the ultraviolet seed radiation onto the orbit. These seed pulses interact with the electron bunches in the modulator (proposed parameters: variable-gap undulator with a maximum magnetic field of 1.5 T at minimum gap, a period length of 75 mm, and 32 periods), generating a sinusoidal energy modulation. The bunching chicane, which is located between the modulator and the radiator, converts the energy modulation into periodic density modulations. The harmonics of this periodic current modulation initiate the FEL process in the seeded fraction of the electron bunch.

SIMULATIONS

For realistic simulations of the HGHG-seeded FEL, an electron distribution with an energy of 1.0 GeV was generated in start-to-end simulations [18]. The machine parameters in this simulation allow for a peak current of 1.0 kA while delivering a normalized emittance and a slice energy spread below 2 mm mrad and 150 keV, respectively. For the tracking of the electron distribution from the radio-frequency photoinjector to the entrance of the FLASH2 un-

Content from this work may be used under the terms of the CC BY 3.0 licence (© 2018). Any distribution of this work must maintain attribution to the author(s), title of the work, publisher, and DOI.

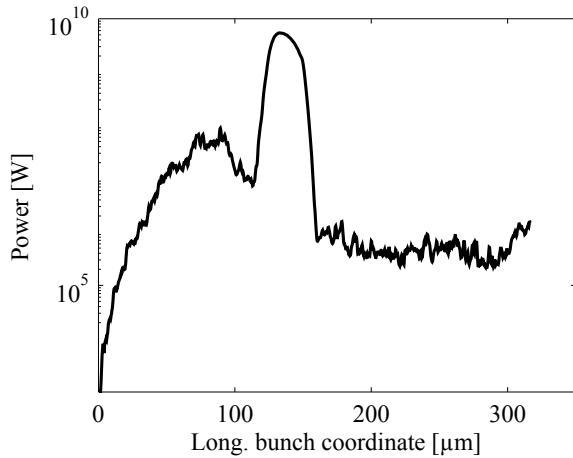


Figure 3: Temporal power profile of the photon pulse at the end of the radiator.

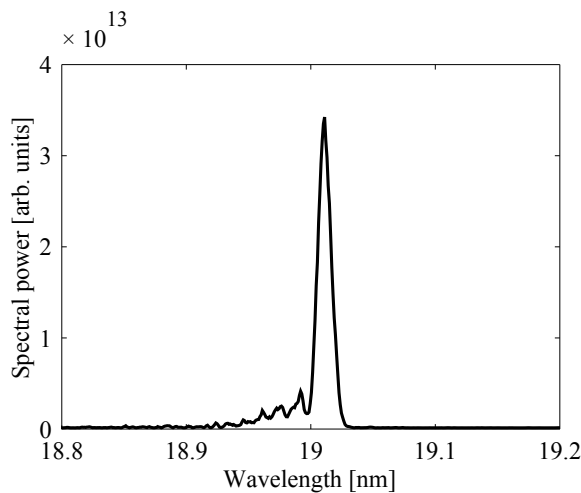


Figure 4: Spectrum at the end of the radiator.

undulator beamline, the simulation codes ASTRA [19] and CSRTRACK [20] were used.

The baseline radiator operation mode is tapered operation of all 12 modules of the FLASH2 variable-gap undulator. The studied profiles of the undulator parameter K follow the tapering law [21]

$$K(z) = K_0 \cdot \frac{a \cdot (z - z_0)^2}{1 + b \cdot (z - z_0)}, \quad (z \geq z_0)$$

with K_0 being the undulator parameter at the untapered entrance of the undulator, and a and b are numerical parameters describing the tapering profile. The tapering sets in at longitudinal position z_0 in the undulator, which should be a few gain lengths before saturation [21] of the seeded fraction of the electron bunch. At this position, the FEL gain process initiated by SASE is still in the exponential regime. The parameters a and b are determined by optimizing the contrast between the seeded signal and the SASE background for given parameters (in particular energy modulation amplitude and generated bunching factor) using so-called “time-

independent simulations” with the code GENESIS 1.3 [22]. This simulation mode is an efficient way to study the FEL process in a single slice of the electron beam under the assumption of periodicity.

Next, the seeding performance of the optimized tapering profile, which was found in the optimization procedure described above, is investigated with time-dependent FEL simulations. The simulation is split into two GENESIS 1.3 runs: The first run simulates the laser-electron interaction in the modulator and stores the resulting phase-space distribution to a file. In the second simulation run, this phase-space distribution is then further propagated through the bunching chicane and finally, the FEL process in the radiator is simulated. Figure 3 shows the temporal FEL pulse profile at the 14th harmonic (wavelength equals 19 nm) at the end of the FLASH2 undulator system and Fig. 4 shows the corresponding spectrum.

For the assumed parameters, the FEL process in the seeded fraction of the bunch saturates after 3 to 4 modules of the undulator. At this position, the power contrast between the seeded signal and the SASE background is optimal. In the following undulator modules, the seeded FEL power grows only marginally, while the FEL power in the unseeded parts of the bunch is still amplified exponentially. Consequently, the contrast between seeding and SASE deteriorates until the tapering profile begins to hamper SASE FEL amplification.

To improve the contrast, advanced operating schemes for the FLASH2 radiator, such as leaving the first undulator modules open, will be studied. For this scheme, the propagation of the already bunched electron beam along the electron beamline under seeded longitudinal space-charge effects needs to be taken into account.

SUMMARY

In this contribution, we presented a proposal for the implementation of single-stage HGHG seeding at FLASH2. The initial implementation would provide seeding at wavelengths down to 19 nm at a 10-Hz repetition rate. After an upgrade to a seed laser system supporting operation at a 100-kHz burst-mode pattern, up to 800 seeded FEL pulses per second would be generated.

ACKNOWLEDGEMENTS

We acknowledge discussions with colleagues from DESY accelerator division, DESY photon science, and University of Hamburg.

REFERENCES

- [1] W. Ackermann *et al.*, “Operation of a Free-Electron Laser from the Extreme Ultraviolet to the Water Window”, *Nat. Photonics* 1, p. 336, 2007.
- [2] P. Emma *et al.*, “First Lasing and Operation of an Ångstrom-Wavelength Free-Electron Laser”, *Nat. Photonics* 4, p. 641, 2010.

- [3] E. Allaria *et al.*, “Highly Coherent and Stable Pulses from the FERMI Seeded Free-Electron Laser in the Extreme Ultraviolet”, *Nat. Photonics* 6, p. 699, 2012.
- [4] T. Ishikawa *et al.*, “A Compact X-ray Free-Electron Laser Emitting in the sub-Ångström Region”, *Nat. Photonics* 6, p. 540, 2012.
- [5] L. H. Yu, “Generation of Intense UV Radiation by Subharmonically Seeded Single-Pass Free-Electron Lasers”, *Phys. Rev. A* 44, p. 5178, 1991.
- [6] E. Hemsing *et al.*, “Beam by Design: Laser Manipulation of Electrons in Modern Accelerators”, *Rev. Mod. Phys.* 86, p. 897, 2014.
- [7] M. Svandrlik *et al.*, “Development Perspectives at FERMI”, *Proc. 8th Intl. Particle Accelerator Conf.*, Copenhagen, 2017, pp. 2666–2669.
- [8] K. Honkavaara, “Status of the FLASH FEL User Facility at DESY”, presented at the 38th Intl. Free-Electron Laser Conf., Santa Fe, NM, USA, August 2017, paper MOD02, this conference.
- [9] K. Honkavaara *et al.*, “FLASH: First Soft X-ray FEL Operating Two Undulator Beamlines Simultaneously”, *Proc. 36th Intl. Free-Electron Laser Conf.*, Basel, 2014, pp. 635–639.
- [10] V. Grattoni *et al.*, “Status of Seeding Development at sFLASH”, presented at the 38th Intl. Free-Electron Laser Conf., Santa Fe, NM, USA, August 2017, paper MOP042, this conference.
- [11] B. Faatz *et al.*, “Simultaneous Operation of Two Soft X-Ray Free-Electron Lasers Driven by One Linear Accelerator”, *New J. Physics* 18, p. 062002, 2016.
- [12] J. Rönsch-Schulenburg, *et al.*, “Experience with Multi-Beam and Multi-Beamline FEL-Operation”, *Proc. 8th Intl. Particle Accelerator Conf.*, Copenhagen, 2017, pp. 2621–2624.
- [13] T. Plath *et al.*, “Free-electron laser multiplex driven by a superconducting linear accelerator”, *J. Synchrotron Radiation* 23, p. 1070, 2016.
- [14] A. Meseck, *et al.*, “HGHG Scheme for FLASH II”, *Proc. 33th Intl. Free-Electron Laser Conf.*, Shanghai, China, 2011, pp. 107–110.
- [15] G. Stupakov “Using the Beam-Echo Effect for Generation of Short-Wavelength Radiation”, *Phys. Rev. Lett* 102, p. 074801, 2009.
- [16] K. Hacker “A Concept for Seeding 4-40 nm FEL Radiation at FLASH2”, *Proc. 36th Intl. Free-Electron Laser Conf.*, Basel, Switzerland, 2014, pp. 286–296.
- [17] C. Lechner *et al.*, “Concept for a Seeded FEL at FLASH2”, *Proc. 8th Intl. Particle Accelerator Conf.*, Copenhagen, Denmark, 2017, pp. 2607–2610.
- [18] G. Feng *et al.*, “Seeded FEL Study For Cascaded HGHG Option For FLASH2”, *Proc. 37th Intl. Free-Electron Laser Conf.*, Daejeon, Korea, 2015, pp. 246–250.
- [19] K. Floettmann, “ASTRA”, DESY, Hamburg, <http://www.desy.de/~mpyf1o/>, 2011.
- [20] M. Dohlus, T. Limberg, “CSRtrack: faster calculation of 3D CSR effects”, *Proc. 26th Intl. Free-Electron Laser Conf.*, Trieste, Italy, 2004, pp. 18–21.
- [21] E. A. Schneidmiller and M. V. Yurkov, “Optimization of a High Efficiency Free Electron Laser Amplifier”, *Phys. Rev. ST Accel. Beams* 18, p. 030705, 2015.
- [22] S. Reiche, “GENESIS 1.3: a Fully 3D Time-Dependent FEL Simulation Code”, *Nucl. Instrum. and Meth. A* 429, p. 243, 1999.

FEL PULSE SHORTENING BY SUPERRADIANCE AT FERMI

N. S. Mirian¹, S. Spampinati¹, L. Giannessi^{1,2}

¹Elettra-Sincrotrone Trieste, 34149 Trieste, Italy

²ENEA, CR Frascati, Via E. Fermi 45, 00044 Frascati (Rome), Italy

Abstract

Explorations of saturated superradiant regime is one of the methods that could be used to reduce the duration of the pulses delivered by FERMI. Here we present simulation studies that show the possible application of a superradiant cascade leading to a minimum pulse duration below 8 fs and to a peak power exceeding the GW level in both FEL lines FEL-1 and FEL-2.

INTRODUCTION

FERMI is an externally seeded free electron laser (FEL) user facility producing photons in extreme-ultraviolet and soft x-ray spectral region, with a high degree of coherence and spectral stability [1]. FERMI hosts two FEL lines, FEL-1, which covers the wavelength range between 100 and 17 nm and FEL-2 in the range between 17 and 4 nm. The shortest pulses delivered by the FELs are expected to be in the ranges 40-90 fs on FEL-1 [2] and 20-40 fs on FEL-2, according to the seed duration and the final wavelength [1,3]. The FERMI FELs have already been exploited in fast time resolution studies, however a shorter-duration pulse, in the few femtoseconds regime, would allow resolving very fast processes as electronic rearrangements, and would increase the number of targeted experiments. One of the remarks about the implementation of ultrashort-ultraintense pulses in structural studies is that it should be possible to outrun radiation damage while collecting single-shot diffraction images with high spatial resolution [4–7].

Several techniques were proposed to obtain shorter FEL pulses at FERMI, as the chirped pulse amplification (CPA) method [8] or the manipulation of electron beam energy spread at the laser heater to longitudinally reduce the lasing portion of the beam itself [9, 10]. The method we investigate in this contribution relays on the exploration of superradiant regime in a cascaded FEL [11–16] to reduce the pulse length below the cooperation length, while preserving or even enhancing the FEL peak power beyond the saturation level ($P_{\text{sat}} \approx \rho P_{\text{beam}}$).

According to the theory [16–18], when the seed duration L_{seed} is comparable or shorter than slippage distance over a synchrotron period, slippage itself, combined with the saturation process, can shorten the pulse pushing it forward into fresh, unmodulated electrons. In this regime the pulse energy continues to grow at the expense of the electron energy and the peak power increases as $P \propto z^2$; the pulse duration δs is related to the peak power and scales as the slippage distance in half synchrotron oscillation period $2\pi/\omega_s$, i.e. proportionally to the root of the optical field amplitude, $\delta s \propto z^{-1/2}$.



Figure 1: Layout of FERMI FEL-1. The modulator (period length of $\lambda_m = 10$ cm) is tuned to the seed wavelength ($\lambda_s = 232$ nm). The amplifier is composed of two parts. Two undulators are resonant with the 5th harmonic of the seed ($\lambda_1 = 46$ nm) and the last four undulators are tuned to the 10th ($\lambda_f = 23.2$ nm) or 15th ($\lambda_f = 15.6$ nm) harmonics of the seed.

The FEL pulse is therefore temporally compressed and may become significantly shorter than the input seed.

The initial pulse formation may be induced by an external seed or may be the result of an equivalent density modulation of the electron current. In a cascaded undulator configuration, the power growth is indeed proportional to the profile of the bunching ($G(z, s) \propto b(z, s)$) at the resonant frequency in each stage of the cascade. This configuration, based on a sequence of FEL amplifiers, allows to seed an undulator at optical frequencies while inducing the growth of a superradiant pulse in the VUV range of the spectrum [16]. The scheme was investigated at SPARC, where the transition in a two stages cascade with frequency doubling at optical frequencies was studied [13]. A similar setup in the frame of the FERMI FEL-1 or FEL-2 allowing an undulator cascade made by three or four stages should enable reaching with the final wavelength the VUV or even the soft X-ray spectral range.

In this contribution we have studied via Genesis simulations [20], the applications of superradiance at FERMI FEL-1 and FEL-2 as a method to achieve extremely short pulses.

FERMI FEL-1

The superradiant cascade may be configured at FERMI by tuning the variable gap undulators defining different undulator segments resonant at the different wavelengths. The undulator line of FERMI FEL-1 is composed by a modulator resonant with the UV seed laser and a sequence of six radiators amplifying the desired harmonic order in the VUV, with harmonics typically in the range of 3-15. A superradiant cascade may be configured by tuning the undulator resonances of FEL-1 as shown in Fig. 1.

The electron beam energy at FERMI can be adjusted in the range 0.9 to 1.5 GeV. Table 1 summarizes typical electron beam parameters from the FERMI LINAC, which were used in the simulation. The electron beam profiles were retrieved

Table 1: Main Parameters of the Electron Beam

Electron beam energy	1.3 GeV
Energy spread	120 keV
Current	750 A
Normalized emittance	1.2 $\mu\text{m}\cdot\text{rad}$
Beam size in x	0.0675 mm
Beam size in y	0.0675 mm
α_x	0.1235
α_y	0.1825

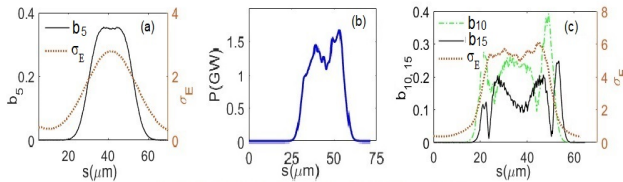


Figure 2: (a) Longitudinal distribution of the energy spread and the bunching profile at the 5th harmonic of the seed, at the entrance of the first segment of radiators tuned at $\lambda_1 = 46$ nm. (b) Pulse temporal profile of the 46-nm pulse. (c) Beam energy spread and bunching profile at the 10th and 15th harmonics, at the entrance of the third radiator.

from an Elegant beam dynamic simulation in the accelerator line [23, 24].

A UV seed laser pulse (FWHM 70 fs) imprints a periodic energy modulation on the relativistic electron beam in the modulator. This energy modulation is then converted into a current density modulation by the dispersive section ($R_{56} = 22.5 \mu\text{m}$). This microbunched electron beam emits coherent light at λ/n in the XUV to x-ray region as the electrons traverse through the periodic magnetic field of the radiators. The evolution of the bunching factors and field temporal distributions through the cascade is shown in Fig. 2.

The bunching factor at harmonic 10, or alternatively 15, at the exit of the two radiators tuned to the 5th harmonic shows a multippeak structure with the front peak slipping forward toward a region with a lower energy spread. The front peak is therefore amplified in the final radiator stage, tuned at harmonic 10 or 15 as shown in Fig. 3. In 3(a) a peak power of 3 GW, is reached in a pulse of 8 fs FWHM duration at 23.2 nm. The inset shows the pulse spectrum of width 0.094 nm (FWHM). Similarly, 3(b) shows the behavior of the cascade when the last radiator is tuned to harmonic 15. In this case the final power is reduced to about 800 MW in a pulse of 6.3 fs FWHM duration at 15.4 nm. The spectral width is 0.064 nm (FWHM).

FERMI FEL-2

This configuration of FEL-1 can be thought as a double stage cascade implementing the fresh bunch injection technique [25] via the natural slippage of radiation over the electron pulse. A similar setup may be implemented on FERMI FEL-2, which was originally designed to implement the fresh bunch injection technique, with the longitudinal

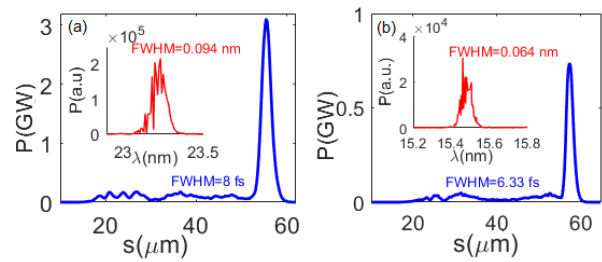


Figure 3: Pulse output power and spectrum in case of the 10th harmonic (a), or 15th harmonic (b).



Figure 4: Layout of FERMI FEL-2 in superradiant cascade mode. Similarly to the case of FEL-1, the first modulator and two radiators of the first stage are used to prepare a modulated beam with the features shown in Fig. 2 at harmonic 5. The last radiator of the first stage and the modulator of the second stage are tuned to harmonic 10 while the entire final radiator is tuned to harmonic 30 to reach the final wavelength of $\lambda = 7.7$ nm.

slippage enhanced by the delay line magnetic chicane. When operated in double stage HGHG configuration, FEL-2 is made up by a first stage similar to FEL-1 with a reduced number of radiators (three instead of six), and a second stage composed by a second modulator physically identical to the radiators of the first stage, and a final amplifier composed by six radiators with a shorter period ($\lambda_m = 3.5$ cm). The two stages are separated by the dispersive delay line used to shift the light emitted in the first stage onto fresh electrons in the second stage, to implement the fresh bunch injection technique. This large delay is not used in the superradiant cascaded configuration and the separation in different stages was rearranged as shown in Fig. 4.

Figure 5 shows the profile of the energy spread and bunching factor at harmonic 30, at the entrance of the last amplification stage. Similarly to the case analyzed on FEL-1, we have a complicated peaks structure with two narrow peaks in the head and tail region of the pulse. The energy spread in front of the trailing peak is higher than 1.3 MeV while the energy spread at the position of the leading edge peak is less than 0.51 MeV.

The slippage distance in the last amplifier is about 10 fs and the leading edge pulse has the possibility to shift over fresh electrons where the energy spread is even lower (120 keV, see Table 1). Figure 6 shows the output power and spectrum profile of the 30th harmonic. The result is that in the final amplifier this front pulse is the one giving the main contribution reaching a peak power of about 1 GW. The output pulse duration from the simulation is about 5.2 fs (FWHM) and the corresponding spectral width is 0.016 nm (FWHM).

At the end, three narrow pulses in harmonics 5, 10 and 30 with a fixed delay of few hundred are extracted. Hence this

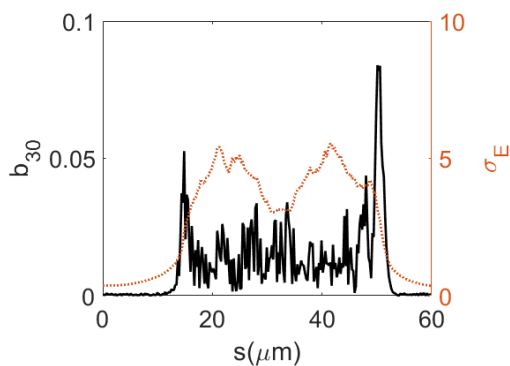


Figure 5: Bunching factor at harmonic 30 (black solid line) and energy spread (brown dotted line), vs. the longitudinal position along the electron bunch.

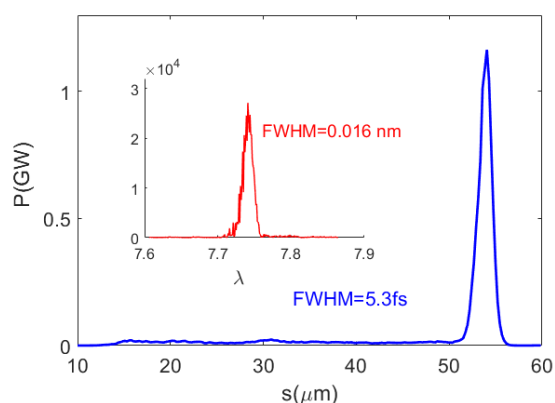


Figure 6: Pulse temporal profile and spectrum.

configuration can help to drive time resolved experiments requiring multiple ultrashort VUV pulses [26].

In Fig. 7, we show the evolution of the peak power at 7.7 nm in the final amplifier of FEL-2. In the first part of the undulator the growth is driven by the bunching factor and is quadratic. In the second part, in the last three radiators, the growth is still quadratic, but with the intensity at the saturation level the pulse is longitudinally focused as shown in the inserted plot.

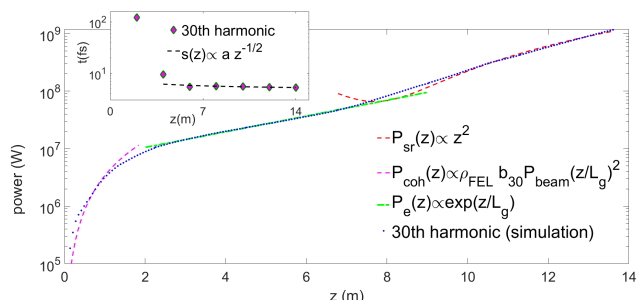


Figure 7: Growth of peak power as function of electron beam position (z) through the last radiators of the FEL-2 at the 30th harmonic radiation in different phases. Inserted plot: Evolution of time duration of the radiation pulse.

CONCLUSION

We have shown the possibility to drive the two FERMI FELs (FEL-1 and FEL-2) into a superradiant cascade regime in the VUV spectral region, leading to short pulses with duration well below 10 fs and peak power exceeding the GW level. In the specific case of FEL-2 this configuration does not require the large dispersion in the delay line between the first and second stage and therefore the region of beam used to generate the pulse has a limited extension of the order of 150 fs. The implication is that also on FEL 2 it would be possible to generate multiple pulses with a fixed delay of few hundreds of fs, to drive time resolved pump and probe experiments requiring multiple ultrashort VUV pulses. As a last remark, we remind that the presented analysis is based on the assumption of a seed duration of 70 fs, which is the shortest seed presently available at FERMI. This configuration may benefit of future developments where a reduction of the seed pulse duration to the 40-50-fs level is foreseen.

REFERENCES

- [1] E. Allaria *et al.*, “Highly coherent and stable pulses from the FERMI seeded free-electron laser in the extreme ultraviolet” *Nat. Photonics*, vol. 6, p. 699, Sep. 2012.
- [2] P. Finetti *et al.*, “Pulse duration of seeded free electron laser”, *Phys. Rev. X*, vol. 7, p. 021043, Jun. 2017
- [3] E. Allaria *et al.*, “Two-stage seeded soft- X-ray free electron laser”, *Nat. Photonics*, vol. 7, p. 913, Oct. 2013.
- [4] H. N. Chapman, *et al.*, “Femtosecond X-ray protein nanocrystallography”, *Nature*, vol. 470, p.73, Feb. 2011.
- [5] C. Caleman, *et al.*, “On the feasibility of nanocrystal imaging using intense and ultrashort X-ray pulses”, *ACS Nano*, vol. 5, p. 139, Des. 2010.
- [6] R. Neutze, *et al.*, “Potential for biomolecular imaging with femtosecond X-ray pulses”, *Nature*, vol. 406, 752, Jun. 2000.
- [7] Paola Finetti *et al.*, “Pulse duration of seeded free-electron lasers”, *Phys. Rev. X*, vol. 7, p. 021043, Jun. 2017.
- [8] D. Gauthier *et al.*, “Chirped pulse amplification in an extreme-ultraviolet free-electron laser”, *Nature Communications*, vol. 7, p. 13688, Des. 2016.
- [9] A. A. Marinelli *et al.*, “Optical shaping of X-ray free electron lasers”, *Phys. Rev. Lett.*, vol. 116, p. 254801, Jun. 2016.
- [10] V. Grattoni *et al.*, “Control of the seeded FEL pulse duration using laser heater pulse shaping” *Proc. IPAC’17*, Copenhagen, Denmark, May. 2017, paper WEPAB034, p. 2654.
- [11] T. Watanabe *et al.*, “Experimental characterization of super-radiance in a single-pass high-gain laser-seeded free-electron laser amplifier”, *Phys. Rev. Lett.*, vol. 98, p. 034802, Jan. 2007.
- [12] M. Labat *et al.*, “Pulse splitting in short wavelength seeded free electron lasers” *Phys. Rev. Lett.*, vol. 103, p. 264801, Dec. 2009.

- [13] L. Giannessi *et al.*, “Superradiant cascade in a seeded free electron laser” *Phys. Rev. Lett.*, vol. 110, p.044801 Jan. 2013.
- [14] L. Giannessi *et al.*, “High order harmonic generation and superradiance in a seeded free-electron laser”, *Phys. Rev. Lett.*, vol. 108, p. 164801, Apr. 2012.
- [15] R. Bonifacio and F. Casagrande, “The superradiant regime of a free electron laser”, *Nucl. Instrum. Methods Phys. Rev. A*, vol. 239, Num. 36, 1985.
- [16] L. Giannessi, P. Musumeci, and S. Spampinati, “Pulse evolution in seeded free-electron laser amplifiers and in free-electron laser cascades”, *J. Appl. Phys.* vol. 98, p. 043110, Jul. 2005.
- [17] R. Bonifacio, N. Piovella, and B. W. J. McNeil, “Superradiant evolution of radiation pulses in a free-electron laser”, *Phys. Rev. A*, vol. 44, p. R3441, Des. 1991.
- [18] R. Bonifacio, L. De Salvo Souza, P. Pierini, and N. Piovella, “The superradiant regime of a FEL: analytical and numerical results”, *Nuclear Instruments and Methods A*, vol. 296, p. 358, 1990.
- [19] L. H. Yu, “Generation of intense UV radiation by subharmonically seeded single-pass free-electron lasers”, *Phys. Rev. A*, vol. 44, p. 5178, Oct. 1991.
- [20] S. Reiche, “GENESIS 1.3: a fully 3D time-dependent FEL simulation code”, *Nucl. Instrum. Methods Phys. Res. A*, vol. 429, p. 243, Jun. 1999.
- [21] G. Stupakov, “Effect of finite pulse length and laser frequency chirp on HHG and EEHG seeding”, SLAC Rep. SLAC-PUB-14639, Oct. 2011.
- [22] D. Ratner A. Fry, G. Stupakov, and W. White, “Laser phase errors in seeded free electron lasers”, *Phys. Rev. ST Accel. Beams*, vol. 15, p. 030702, Mar. 2012.
- [23] M. Borland, “Elegant: A flexible SDDS-compliant code for accelerator simulation”, ANL/APS Rep. LS-287, Sep. 2000.
- [24] E. Roussel *et al.*, “New scenarios of microbunching instability control in electron linacs and free electron lasers”, *Proc. IPAC'17*, Copenhagen, Denmark, May. 2017, paper THYA1.
- [25] I. Ben-Zvi, K. M. Yang, and Yu, L. H. The “Fresh-bunch technique in FELs”, *Nuclear Instruments and Methods A*, vol. 318, p. 726, Jul. 1992.
- [26] F. Bencivenga *et al.* “Four-wave mixing experiments with extreme ultraviolet transient gratings”, *Nature*, vol. 520, p. 205, Apr. 2015.

STATUS OF THE HARD X-RAY SELF-SEEDING PROJECT AT THE EUROPEAN XFEL

X. Dong, G. Geloni*, S. Karabekyan, L. Samoylova, S. Serkez, H. Sinn,
European XFEL, Schenefeld, Germany
W. Decking, C. Engling, N. Golubeva, V. Kocharyan,
B. Krause, S. Lederer, S. Liu, A. Petrov, E. Saldin, T. Wohlenberg,
DESY, Hamburg, Germany
D. Shu, ANL, Argonne, USA
V. D. Blank, S. Terentiev, TISNCM, Troitsk, Russian Federation

Abstract

A Hard X-ray Self-Seeding setup is currently under realization at the European XFEL, and will be ready for installation in 2018. The setup consists of two single-crystal monochromators that will be installed at the SASE2 undulator line. In this contribution, after a short summary of the physical principles and of the design, we will discuss the present status of the project including both electron beam and X-ray optics hardware. We will also briefly discuss the expected performance of the setup, which should produce nearly Fourier-limited pulses of X-ray radiation with increased brightness compared to the baseline of the European XFEL, as well as possible complementary uses of the two electron chicanes.

THE HARD X-RAY SELF-SEEDING PROJECT AT THE EUROPEAN XFEL

Hard X-ray Self-Seeding (HXRSS) setups based on single-crystal monochromators [1] are active filtering systems allowing for the production of nearly Fourier-limited Hard X-ray radiation pulses at XFELs. They take advantage of the specific impulse response function of single thin crystals in transmission geometry, usually diamond crystals with a thickness around 100 μm , which is constituted by a first response similar to a Dirac δ -function followed by a long tail. The principle was first demonstrated at the LCLS [2].

A Hard X-ray Self-Seeding setup is currently under realization at the European XFEL, and will be ready for installation in 2018.

Double-Chicane Design and Performance

The specific characteristics of the European XFEL, compared to other XFELs, are the high-repetition rate and the availability of long, variable-gap undulators [3]. The latter allows for efficient tapering of the self-seeded signal, and the former for an increase of the average signal brightness, compared to low repetition-rate machines.

In order to increase the signal-to-noise ratio between seed signal and competing SASE (which constitutes, in this case, noise) we rely on a double magnetic chicane design, as sketched in Fig. 1.

We illustrate the advantages of the double-chicane design in Fig. 2, in which we show the filtering stages, Stage 2 and Stage 4, where the C004 reflection from a 100 μm -thick diamond crystal, symmetrically cut, is used. The two undulator parts in Stage 1 and Stage 3 have the same magnetic length. As it can be seen, Stage 4 suffers from poor signal-to-noise ratio. If one proceed with amplification, the seed signal would be lost due to a rapidly growing SASE signal. However, at the filtering position the signal is still almost Fourier limited and therefore the spectral density is higher than that at Stage 2. As a result, the seed signal in the time-domain is larger in Stage 4, compared to Stage 2 of a factor about equal to the ratio between the SASE and the seeded signal bandwidths. The scheme will therefore be highly beneficial in the increase of the signal-to-noise ratio of the seed.

Crystal reflections are available starting from about 3 keV, and although heat loading will likely limit the repetition rate at these very low seed energies, the double-chicane setup will help to improve the situation (see the next subsection). Simulations show that reaching to 14.4 keV should be possible on the high-energy side of the spectrum. The long undulators available at the European XFEL allow for increasing the final output power via tapering. The energy-range around 9 keV is expected to yield optimal performance. Previous studies [4] show that, for a nominal 250 pC electron beam (calculated by s2e simulations [5]) at 17.5 GeV electron energy, combining seeding and tapering one could obtain TW class beams with about 1eV bandwidth, with $7 \cdot 10^{12}$ photons per pulse. Owing to the high-repetition rate of the European XFEL, an average spectral flux of about $2 \cdot 10^{14}$ ph/s/meV can be expected.

Heat Loading Issues

The high-repetition rate of the European XFEL is also related with an increase of heat-loading of the crystals because of impinging X-rays due both to spontaneous emission and SASE/seeded radiation pulses. For both cases, the burst pattern of the European XFEL will lead to a steady temperature increase during a given bunch train, followed by a temperature decrease between one train and the next. If the temperature increase is associated to a shift of the seed frequency of the crystal well beyond a Darwin width, an overall deterioration of the bandwidth is to be expected.

* gianluca.geloni@xfel.eu

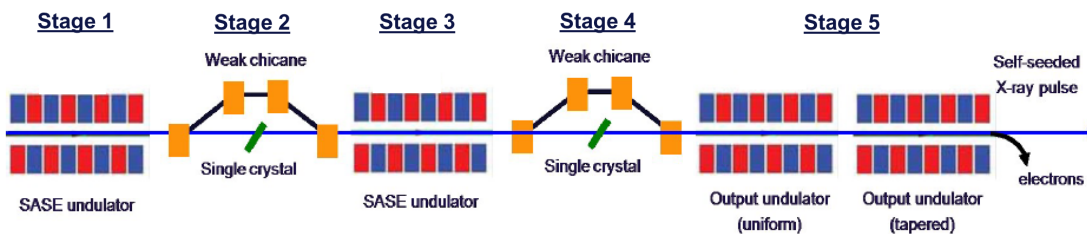


Figure 1: Layout of the HXRSS system being built at the European XFEL.

CHICANE SYSTEM

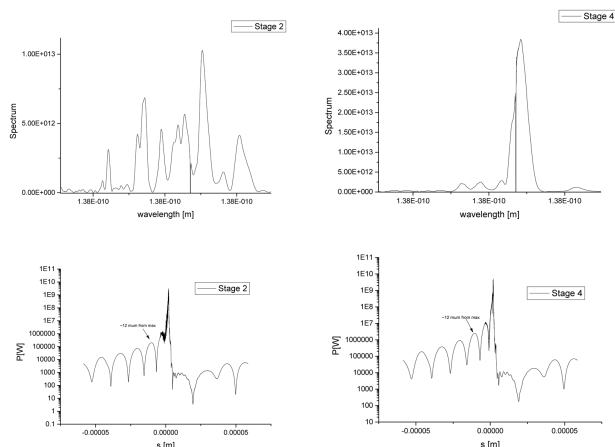


Figure 2: Illustration of the signal-to-noise ratio increase through the double-chicane design. At Stage 4, the spectrum has a bad signal-to-noise ratio, but the maximum spectral density is higher than in the SASE case in Stage 2.

The double-chicane scheme, by increasing the signal-to-noise-ratio, can be used to ease the heat-loading from the SASE/seeding signals. The SASE/seeding component of the heat load depends on the fundamental frequency. For example, for a 100 μm -thick diamond crystal, C004 symmetric reflection at a fundamental energy of 8 keV, a seed frequency-shift equivalent to the Darwin width is to be expected, after 1000 pulses at 4.5 MHz frequency, for an incident energy per pulse of about 3 μJ , corresponding to about 0.7 μJ absorbed energy. However, at 3.3 keV, the energy absorbed by the crystal increases to about 90% of the incident energy, and the same effect is to be expected for an incident pulse energy of about 0.8 μJ . The actual spectral width will be several times larger than the Darwin width so that one can tolerate impinging energies several times larger than those discussed here, i.e. up to several μJ of absorbed energy even for the lowest photon energies: under these conditions, the double-chicane scheme could allow for successful seeding even around 3 keV. However, the double-chicane cannot help dealing with the heat-loading from the spontaneous signal, which is basically independent of the fundamental, and is characterized by a broad spectrum. A pitch oscillator is under study to deal with this issue, which should compensate for the temperature cycle during the pulse train by oscillating the Bragg angle.

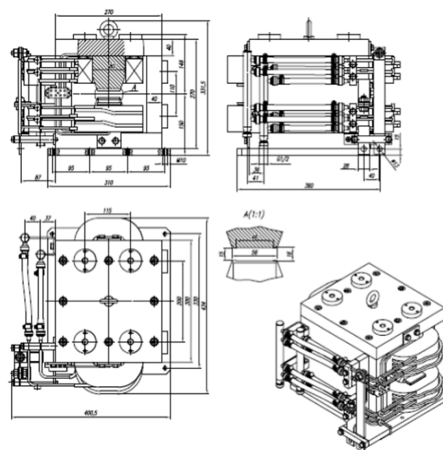


Figure 3: Schematics of the H-magnet dipole used for the HXRSS magnetic chicane.

The chicane system of the HXRSS system at the European XFEL is based on *H*-type dipole magnets, Fig. 3, which have now been fabricated. Two full chicane systems, including the girders, Fig. 4, excluding the monochromators, are presently ready for installation.

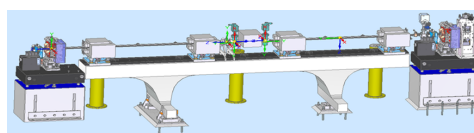


Figure 4: Illustration of the HXRSS chicane system, including girder.

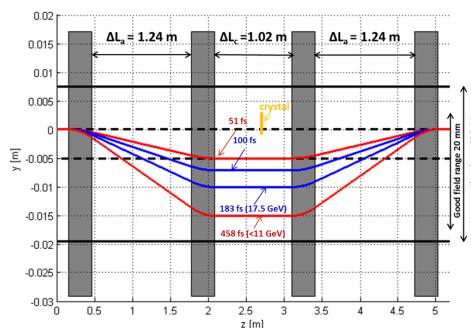


Figure 5: Relation between magnetic delay, electron trajectory and transverse offset in the HXRSS chicane system.

The chicane geometry, and the relation between magnetic delay, electron trajectory and transverse offset in the HXRSS chicane system are summarised in Fig. 5.

Content from this work may be used under the terms of the CC BY 3.0 licence (© 2018). Any distribution of this work must maintain attribution to the author(s), title of the work, publisher, and DOI.

Delay Steps and Autocorrelator Option

We designed the power supply, in terms of resolution and stability, in such a way that the minimum delay step achievable amounts to about 0.1 fs. This enables the use of the chicanes as autocorrelators [6].

Maximum Delay and Multi-Color Option

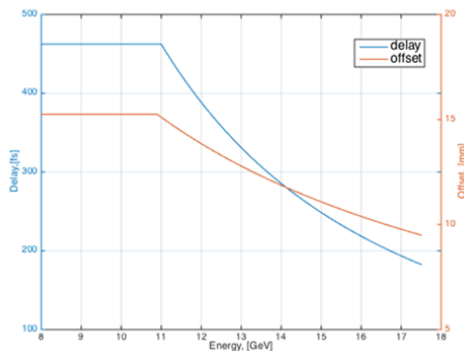


Figure 6: Maximum delay and transverse offset attainable with the European XFEL HXRSS chicane system as a function of the electron energy.

During the chicane design we took care of implementing the largest possible delay in order to enable multiple-color experiments once the HXRSS crystals are retracted [7–9]. Fig. 6 shows the dependence of maximum delay and transverse offset as a function of the electron energy. Up to about 12 GeV one chicane will be able to produce two-color pulses with a maximum temporal separation of about 460 fs.

Minimum Delay and Halo Studies

Finally, it is important to remark that the seed power level is strictly related with the minimum delay that can be achieved, which is in turn linked to the minimum offset between the crystal and the electron that can be tolerated. Beam halo studies, which were reported elsewhere [10] indicate that a minimal offset of about 2 mm is achievable, corresponding to less than 20 fs delay that is optimal for seeding.

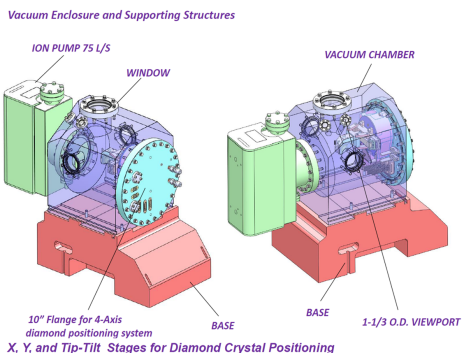


Figure 7: The monochromator system for the European XFEL HXRSS setup: vacuum enclosure and supporting structure.

4-Axis diamond positioning system for LCLS HXRSS monochromator

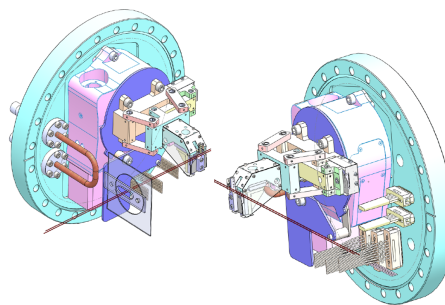


Figure 8: The monochromator system for the European XFEL HXRSS setup: 4-axis diamond positioning system

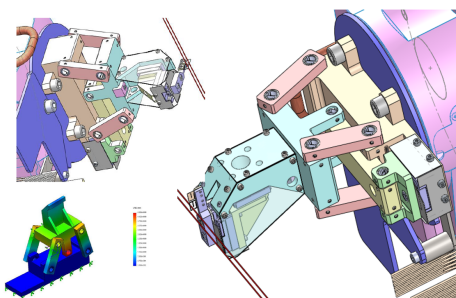


Figure 9: The monochromator system for the European XFEL HXRSS setup: X, Y and tip-tilt stages for the diamond positioning system.

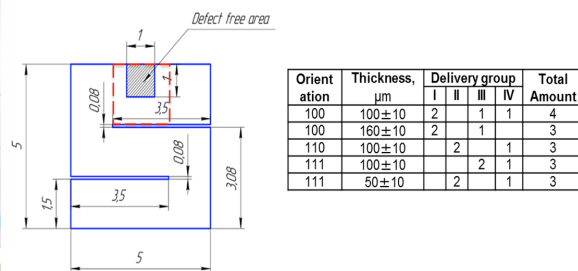


Figure 10: The monochromator system for the European XFEL HXRSS setup: crystal specifications.

MONOCHROMATOR SYSTEM AND CRYSTAL

The monochromator system for the European XFEL has been designed, and two chambers will be ready for installation by 2018. We show in graphic form the vacuum enclosure and the supporting structures, Fig. 7, the 4-axis diamond positioning system, Fig. 8, and the X, Y and tip-tilt stages for the diamond positioning system, Fig. 9. The diamond holder will be capable of hosting two crystals. Several crystals, with variable thicknesses and cuts will be available, Fig. 10.

REFERENCES

- [1] G. Geloni, V. Kocharyan, and E. Saldin, "A novel Self-seeding scheme for hard X-ray FELs", *Journal of Modern Optics*, vol. 58, issue 16, pp. 1391-1403, 2011.
- [2] J. Amann *et al.*, "Demonstration of self-seeding in a hard X-ray free-electron laser", *Nature Photonics*, vol. 6, p. 693, 2012.
- [3] M. Altarelli *et al.*, eds, "The European X-ray Free-Electron Laser: Technical Design Report" available at <http://www.xfel.eu/en/documents/>, 2006.
- [4] O. Chubar, G. Geloni, V. Kocharyan *et al.*, "Ultra-high-resolution inelastic X-ray scattering at high-repetition-rate self-seeded X-ray free-electron lasers", *J. Synchrotron Radiat.*, 23, 410-424, 2016
- [5] I. Zagorodnov, <http://www.desy.de/felbeam/s2e/xfel.html.url>
- [6] G. Geloni, V. Kocharyan, and E. Saldin, "Ultrafast X-ray pulse measurement method", DESY 10-008, available at <https://arxiv.org/abs/1001.3544>, 2010.
- [7] G. Geloni, V. Kocharyan, and E. Saldin, "Scheme for femtosecond-resolution pump-probe experiments at XFELs with two-color ten GW-level X-ray pulses", DESY 10-004, available at <https://arxiv.org/abs/1001.3510>, 2010.
- [8] A. A. Lutman *et al.*, "Experimental Demonstration of Femtosecond Two-Color X-Ray Free-Electron Lasers", *Phys. Rev. Lett.* 110, 13, 2013.
- [9] T. Hara *et al.*, "Two-colour hard X-ray free-electron laser with wide tunability", *Nat. Commun.* 4, 2919, 2013.
- [10] S. Liu, W. Decking, and L. Fröhlich, "Beam Loss Simulations for the Implementation of the Hard X-Ray Self-Seeding System at European XFEL", in *Proc. 8th Int. Particle Accelerator Conf. (IPAC'17)*, Copenhagen, Denmark, May 2017, paper WEPAB020, pp. 2611-2614.

CONSTRAINTS ON PULSE DURATION PRODUCED BY ECHO-ENABLED HARMONIC GENERATION*

G. Penn[†], LBNL, Berkeley, USA

B. Garcia, E. Hemsing, G. Marcus, SNL, Menlo Park, USA

Abstract

Echo-enabled harmonic generation (EEHG) is well-suited for producing long, coherent pulses at high harmonics of seeding lasers. There have also been schemes proposed to adapt EEHG to output extremely short, sub-fs pulses by beam manipulations or through extremely short seed lasers, but the photon flux is generally lower than that produced by other schemes. For the standard EEHG layout, it is still interesting to consider different parameter regimes and evaluate how short a pulse can be generated. EEHG at high harmonics uses a large dispersive chicane which can change the relative distance of electrons substantially, even longer than a typical FEL coherence length. We evaluate the ability to produce short pulses (in the femtosecond to 10 fs range) using a combination of theory and simulations.

INTRODUCTION

The radiation produced by free electron lasers (FELs) can be enhanced in many ways through seeding techniques. Echo-enabled harmonic generation (EEHG) [1] uses two energy modulations from external lasers to generate a much shorter output wavelength. A schematic of an EEHG beamline is shown in Fig. 1. It has several advantages over seeding schemes with a single seed laser, such as high-gain harmonic generation (HG) [2]. EEHG allows for a very large jump in photon energy in a single stage, without requiring the fresh-bunch technique. It is capable of producing narrow bandwidths by having long output pulses and it can also be less sensitive to distortions in the current or energy profile. However, short pulses with a corresponding large bandwidth are also of interest for many scientific applications. Therefore, it is worth exploring how to produce pulses shorter than 10 fs using the EEHG technique. Here, we only examine initial seeding to produce microbunches at the desired wavelength, which then radiate and amplify in a conventional FEL system. Attosecond schemes are not considered.

CONSTRAINTS ON ELECTRON BUNCH DURATION

We first consider using a very short electron bunch to limit the duration of the output radiation. In this case, the main limitation is that the EEHG scheme produces bunching over a multiple of frequency intervals. The frequency components of the electron current profile can interact with these other microbunching components to yield a combination that will

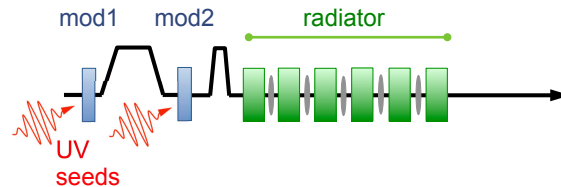


Figure 1: Schematic of an EEHG beamline, showing chicanes, modulating undulators, lasers, and radiating undulators.

either disrupt the FEL gain or introduce a large number of modes. This concern leads to an approximate constraint on the final pulse duration σ_z :

$$\sigma_z \geq \frac{\lambda_1 \lambda_2 E_{M1}}{\lambda_{\text{echo}} E_{M2}} \frac{1}{\sqrt{2} \pi (|n|^{4/3} + |n|^{2/3})}. \quad (1)$$

Here $\lambda_{1,2}$ are the wavelengths of the two incident lasers which modulation, λ_{echo} is the desired output wavelength, $E_{M1,2}$ are the amplitudes of the two energy modulations, and n is one of the mode numbers for the wave mixing. Typically, $n = -1$.

This constraint can also be viewed in terms of time. To obtain a given harmonic, the product of E_{M2} and the strength of the dispersive element after the first modulation are tightly constrained. If the second energy modulation is decreased, the dispersion, which can be quite large, has to be increased. Because the dispersion follows the first energy modulation, electrons will be displaced by an amount proportional to the amplitude of the first energy modulation. Thus, even if a very short initial bunch is used, by the time the EEHG manipulations are finished the bunch could be significantly longer, and the output pulse will match this new bunch length. For a short bunch, the induced bunching tends to reach a minimum in the center, and double-peaked pulses are the first sign that the bunch length is becoming too short for a particular EEHG configuration.

CONSTRAINTS ON DURATION OF SEEDING LASERS

Another way to produce short bunches is to use short lasers to only generate bunching over a fraction of the electron bunch. One constraint here is over the duration of the first energy modulation. If it is very short, the chicane will again spread these particles out, leaving a localized low-current hole in the electron bunch. This is the same effect used for laser slicing techniques in storage rings [4]. To

* This work was supported by the Director, Office of Science, Office of Basic Energy Sciences, U.S. Department of Energy under Contract Nos. DE-AC02-05CH11231 and DE-AC02-76SF00515.

[†] gepenn@lbl.gov

avoid this, the first laser should be kept long, and the second laser determines the duration of the microbunching. The nonlinear reduction in the duration of the seeded pulse is greatest for the second laser, so it usually determines the bunch length anyway.

Another constraint is on the duration of the electron bunch. Unseeded portions of the bunch will have a higher growth rate because the energy spread is lowest in these regions. One fix, seemingly counter to the results of Eq. (1), is to increase the first energy modulation to guarantee a large energy spread everywhere. The energy spread could also be spoiled in other ways, including blowing up the emittance or shaping either input laser to selectively increase the energy spread in regions at some distance from the nominal seeded region.

Another method is simply to end the amplification process before the self-amplified spontaneous emission (SASE) radiation has a chance to compete with the strongly seeded but slower growing main pulse. For longer output wavelengths, this can mean as little as a factor of 2 reduction in pulse energy, and a low background of unseeded radiation. At wavelengths near 1 nm, however, it is very challenging to avoid the SASE background. At 1 nm the output pulse duration is constrained to be about half of the duration of the electron bunch (or the un-spoiled portion thereof).

PARAMETERS AND BEAMLINE CONFIGURATION

Beamline parameters are modeled after expected parameters for LCLS-II [5], and are given in Table 1. The first undulator is chosen to have a period of 0.1 m for convenience. For the second modulating undulator, the large magnetic fields would induced too much energy scattering, so the period is lengthened to 0.4 m. The radiating undulators follow the design for the soft x-ray beamline of LCLS-II. To keep magnetic fields below 0.5 T in the chicanes as well, the first chicane is quite long, with a total length of 9.25 m.

Table 1: Nominal Parameters

Electron bunch:	
Energy	4 GeV
Energy spread	0.5 MeV
Peak current	800 A
Emittance	0.4 μm
Beta function	15 m
Lasers:	
Wavelength	260 nm
Undulators:	
Length	3.2 — 3.4 m
Period	0.1 m, 0.4 m, 0.039 m

SIMULATION RESULTS

Simulations were performed using the GENESIS simulation code [3] along with additional processing to incorporate

more physical effects. Scattering and resistive wall wake fields are included. The significant alteration of the longitudinal profile of the bunch by the first large chicane is also taken into account. Other effects of the chicane, in particular coherent synchrotron radiation, are not modeled.

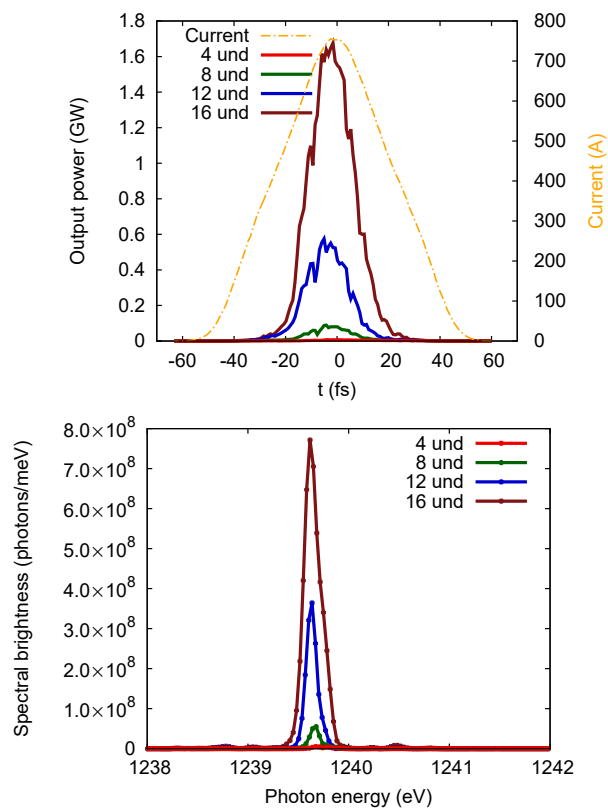


Figure 2: Radiation at 1 nm with a 50 fs bunch and long seed laser pulses. Power (overlaid against the final current profile) and spectrum are shown at various stages along the radiation undulator.

Using a 50 fs long bunch, after 16 undulator sections the pulse energy at 1 nm is $35 \mu\text{J}$ with a FWHM of 22 fs and RMS duration 8.7 fs. The spectrum has a FWHM of 200 meV. The output phase typically has a quadratic variation to it. This is typically as short as the output pulse can get using long laser seeds at 1 nm. Shorter bunches experience too much distortion. Using a 25 fs long bunch to radiate at 2 nm does yield an even shorter output pulse, saturating after 12 undulator sections. The pulse energy is $95 \mu\text{J}$ with a FWHM of 15 fs, and the FWHM bandwidth is 400 meV.

At 1 nm it is difficult to obtain significantly shorter pulses by using a short seed laser. At 2 nm this method is more effective, although it still helps to have a bunch that is not more than $10\times$ longer than the desired output pulse. After 8 undulators, the pulse energy at 2 nm is $14 \mu\text{J}$, about a factor of 2 less energy than at saturation, but the output pulse is much cleaner with a FWHM of 5 fs and RMS duration of only 3.3 fs, without any thresholds or curve fitting. The FWHM bandwidth is 700 meV, but there is a significant sideband as well.

Content from this work may be used under the terms of the CC BY 3.0 licence (© 2018). Any distribution of this work must maintain attribution to the author(s), title of the work, publisher, and DOI.

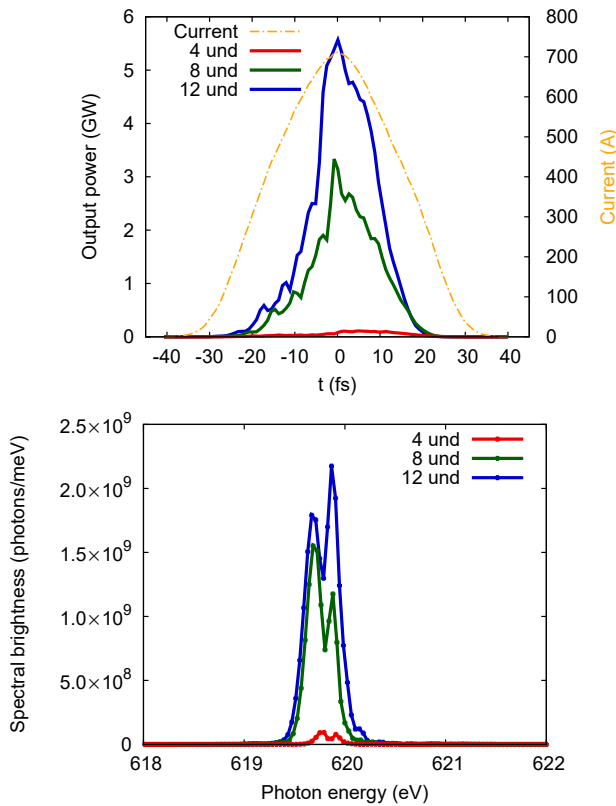


Figure 3: Radiation at 2 nm with a 25 fs bunch and long seed laser pulses. Power (overlaid against the final current profile) and spectrum are shown at various stages along the radiation undulator.

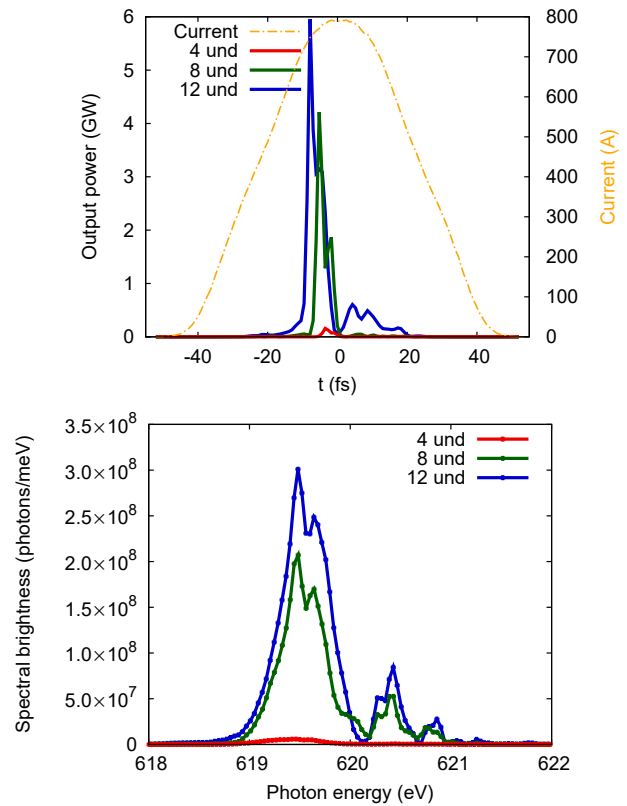


Figure 4: Radiation at 2 nm with a 50 fs bunch and a 10 fs FWHM duration for the second seed laser. Power (overlaid against the final current profile) and spectrum are shown at various stages along the radiation undulator.

CONCLUSION

It is possible to generate high-quality, soft x-rays with pulse durations below 10 fs using echo-enabled harmonic generation. The pulse duration can be selected either by the electron bunch length or the second modulating laser. However, if electron bunch is too long, then the SASE background can only be suppressed by ending the beamline before reaching saturation. This provides another option to produce short, coherent radiation in the soft x-ray regime. This method should provide stable, high-power radiation pulses, but it remains to be seen how much of an impact microbunching will have on the pulse profile.

REFERENCES

[1] G. Stupakov. Using the beam-echo effect for generation of short-wavelength radiation. *Phys. Rev. Lett.*, 102:074801, 2009. doi:10.1103/PhysRevLett.102.074801.

[2] E. Allaria, D. Castronovo, P. Cinquegrana, P. Craievich, *et al.*. Two-stage seeded soft-X-ray free-electron laser. *Nature Photonics*, 7:913–918, 2013. doi:10.1038/nphoton.2013.277.

[3] S. Reiche. GENESIS 1.3: a fully 3D time-dependent FEL simulation code. *Nucl. Instr. Meth. A*, 429:243–248, 1999. doi:10.1016/S0168-9002(99)00114-X.

[4] A. A. Zholents and M. S. Zolotarev. Femtosecond X-ray pulses of synchrotron radiation. *Phys. Rev. Lett.*, 76:912, 1996. doi:10.1103/PhysRevLett.76.912.

[5] G. Marcus, Y. Ding, P.J. Emma, Z. Huang, H.-D. Nuhn, T. Raubenheimer, L. Wang, J. Qiang, and M. Venturini. High fidelity start-to-end numerical particle simulations and performance studies for LCLS-II. In *Proc. 37th Int. Free Electron Laser Conf. JACoW*, Daejeon, Korea, 2015. TUP007.

STRONGLY TAPERED UNDULATOR DESIGN FOR HIGH EFFICIENCY AND HIGH GAIN AMPLIFICATION AT 266 nm

Youna Park, Nick Sudar, Pietro Musumeci, UCLA, Los Angeles, CA 90095, USA
 Yine Sun, Alexander Zholents, ANL, Argonne, IL 60439, USA
 Alex Murokh, RadiaBeam, Los Angeles, CA 90404, USA
 David Bruhwiler, Chris Hall, Stephen Webb, RadiaSoft, Boulder, CO 80301, USA

Abstract

Tapering Enhanced Stimulated Superradiant Amplification (TESSA) is a scheme developed at UCLA to increase efficiency of Free Electron Laser (FEL) light to above 10% using intense seed pulses, strongly tapered undulators and prebunched electron beams. Initial results validating this method have already been obtained at 10- μ m wavelength at Brookhaven National Laboratory. In this paper we will discuss the design of an experiment to demonstrate the TESSA scheme at high gain and shorter wavelength (266 nm) using the Linac Extension Area (LEA) beamline at the Advanced Photon Source of Argonne National Laboratory (ANL) to obtain conversion efficiencies around 10% depending on the length of the tapered undulator (up to 4m).

INTRODUCTION

X-ray Free Electron Lasers (FEL) have revolutionized the trajectory of science opening the door to the direct study at atomic spatial and temporal scales of fundamental systems such as chemical bond formation, motion of electrons through materials, 3D images of proteins and many more [1]. In high gain FELs the efficiency of electron beam energy conversion into radiation is typically limited to less than 1% due to the saturation effect [2]. Tapering the undulator parameters offers an opportunity to extend the interaction beyond initial saturation [3], and has been shown to provide a boost in efficiency. The Tapering Enhanced Stimulated Superradiant Amplification (TESSA) [4] method using a strongly tapered undulator an intense input seed laser and prebunched electron beams to greatly increase the conversion efficiency has been validated at Brookhaven National Laboratory (BNL) for 10 μ m wavelength and 50 cm strongly tapered undulator demonstrating efficiency greater than 35% [5].

In this paper we discuss the design of an experiment where we will demonstrate TESSA at shorter wavelength (266 nm) using the higher energy electron beam at APS linac. This experiment, which we will refer to as TESSA-266, will start with GW-level seed power and demonstrate 30 MeV/m energy exchange rates leading to a final gain of a factor of 10 in laser power. For this experiment we will use the APS injector linac at Argonne National Laboratory (ANL) which has been recently upgraded with an LCLS style photoinjector and can deliver high brightness beams to an experimental beamline where we will install the tapered undulator.

In an FEL, resonant wavelength of interaction is defined as $\lambda = (\lambda_w/2\gamma^2)(1 + K^2)$, where γ is particle energy, K undulator vector potential, and λ_w undulator period.

Table 1: Simulation Parameters of APS Linac

Electron beam energy	375 MeV
Peak current	1 kA
Seed power	< 1 GW
Normalized emittance	2 μ m

The particle energy evolution can be written as $d\gamma^2/dz = -2kK_l K \sin(\Psi_r)$ where $K_l = eE_0/km_e c^2$ laser vector potential and E_0 electric field of radiation, K undulator vector potential, and Ψ_r resonant phase. By taking the derivative of the resonance condition and using energy evolution equation we obtain the tapering equation for the normalized magnetic field amplitude along the helical undulator:

$$\frac{dK}{dz} = \frac{(1 + K^2)(dk_w/dz)}{2Kk_w} - k_w K_l \sin \Psi_r. \quad (1)$$

While period tapering is a possibility, we will limit this initial discussion to a constant period case (i.e. $dk_w/dz = 0$) and allow the gap inside the undulator to change to modify the magnetic field amplitude.

MAGNETIC SIMULATION OF UNDULATOR

Undulator Period vs. Beam Clearance

We used Radia to find the peak magnetic field for different undulator periods and gap at the center of the undulator. Figure 1 shows how the undulator vector potential K would vary as we change the undulator period. Where the resonance

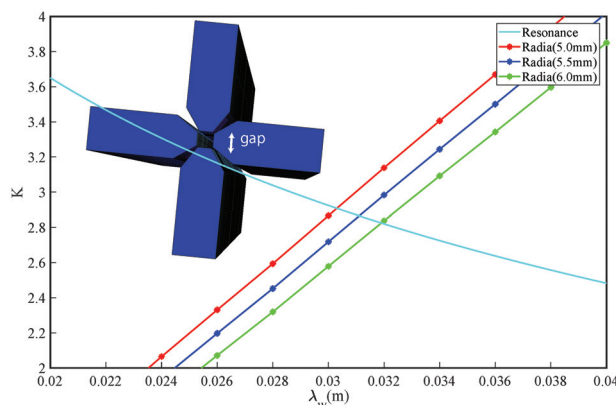


Figure 1: Undulator vector potential vs. undulator period for different gaps plotted with resonance condition.

Content from this work may be used under the terms of the CC BY 3.0 licence (© 2018). Any distribution of this work must maintain attribution to the author(s), title of the work, publisher, and DOI.

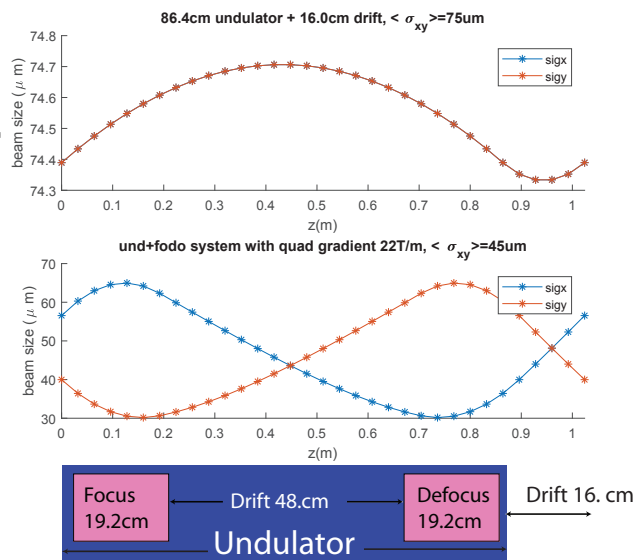


Figure 2: Top: Beam spot size for 3.2-cm period and 86.4-cm long undulator with 16-cm drift. bottom: Beam spot size for 3.2-cm period undulator with a diagram of FODO setup.

line (cyan) meets the data shows the period at resonance for different gaps of 5.0 mm, 5.5 mm, and 6.0 mm. As the thickness of the undulator and the magnet holder clearance required to assemble the undulator were not modified in the simulations, this should be considered as a rough estimate of possible undulator period. The 3.0-cm period is the bare minimum with the beam clearance of 5.1 mm (at the center of the undulator) and holder clearance of 3 mm (between the sides of undulator). We consequently decided that the best undulator period would be 3.2 cm.

The beam sizes matched to the undulator natural focusing beta-function for the period range of 3 cm–3.2 cm for 1-m long undulator were as large as 70 μm to 74 μm . Figure 2 shows that matched beam size for a 86.4 cm long undulator section followed by 16 cm drift was 74 μm with average beam size of 75 μm . This beam size would be relatively large compared to radiation spot size which will be around 100–120 μm depending on Rayleigh length and waist position and is not optimal for extraction efficiency. We consequently decided to look into installing quadrupoles around the undulator as in Figure 2 and 3 to decrease the electron beam sizes.

Quadrupole Design

Although placing quadrupoles compromises thickness of the undulator and consequently requires slightly longer period we found that the difference between the two magnetic undulator period designs was not significant (less than 1–2 mm) when considering the beam and the holder clearance so we decided that it is worthwhile to implement strong focusing in the undulator design. Figure 3 shows our preliminary undulator design of 3.2 cm period with beam clearance of 6 mm at the center and holder clearance of 4 mm around

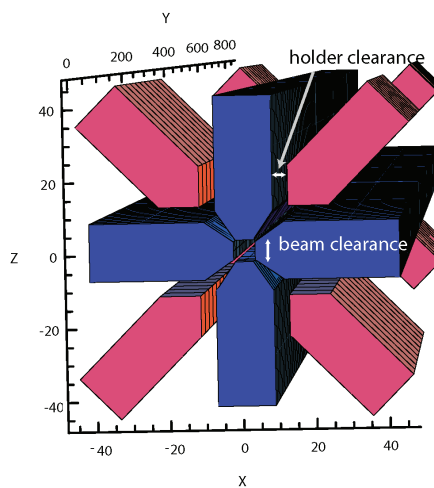


Figure 3: Radia simulation of undulator + quadrupole design for 3.2-cm undulator and 22-T/m quadrupole gradient. Blue = undulator, Red = quadrupoles. The tick marks are in 0.1-mm scale.

the sides of undulator and quadrupoles. This design gives maximum quadrupole gradient of 22 T/m which decreased average beam size to 45 μm (Figure 2). In principle it would be possible to further decrease the holder clearance around the magnets and increase overall focus and radiation power with custom design of magnets.

We studied the dynamics in the resultant FODO lattice to optimize beam size and power output given undulator period of 3.2 cm and maximum quadrupole gradient of 22 T/m. We simulated the simplest FODO system with focusing quadrupole, drift, and defocusing quadrupole to be placed inside the undulator. We varied lengths and gradients of the quadrupoles as both factors affect overall focusing strength, transverse electron propagation, and power output. Depending on the length of the undulator section it was possible to reduce average beam size upto 43 μm with quadrupole gradient of 22 T/m for undulator length of 64 cm. A more conservative design uses a 86.4 cm undulator which had greater power output due to the longer length. This 86.4 cm undulator and 16 cm drift system will have focusing and defocusing quadrupole lengths of 19.2 cm, 48.0 cm in between the two quadrupoles, and drift length of 16 cm between each undulator sections, and the system will have average beam size of 45 μm (Figure 2).

GIT SIMULATION OF 3.2-cm UNDULATOR

The beam energy is 375 MeV with a peak current of 1 kA, corresponding to 375 GW peak beam power. With approximately 10% efficiency, the peak power of the TESSA amplifier will be 20-40 GW, so that there will be considerable amount of change in the normalized field amplitude K_l along the undulator.

The system will operate in the TESSA high-gain regime. In order to optimize the tapering we used Genesis Informed

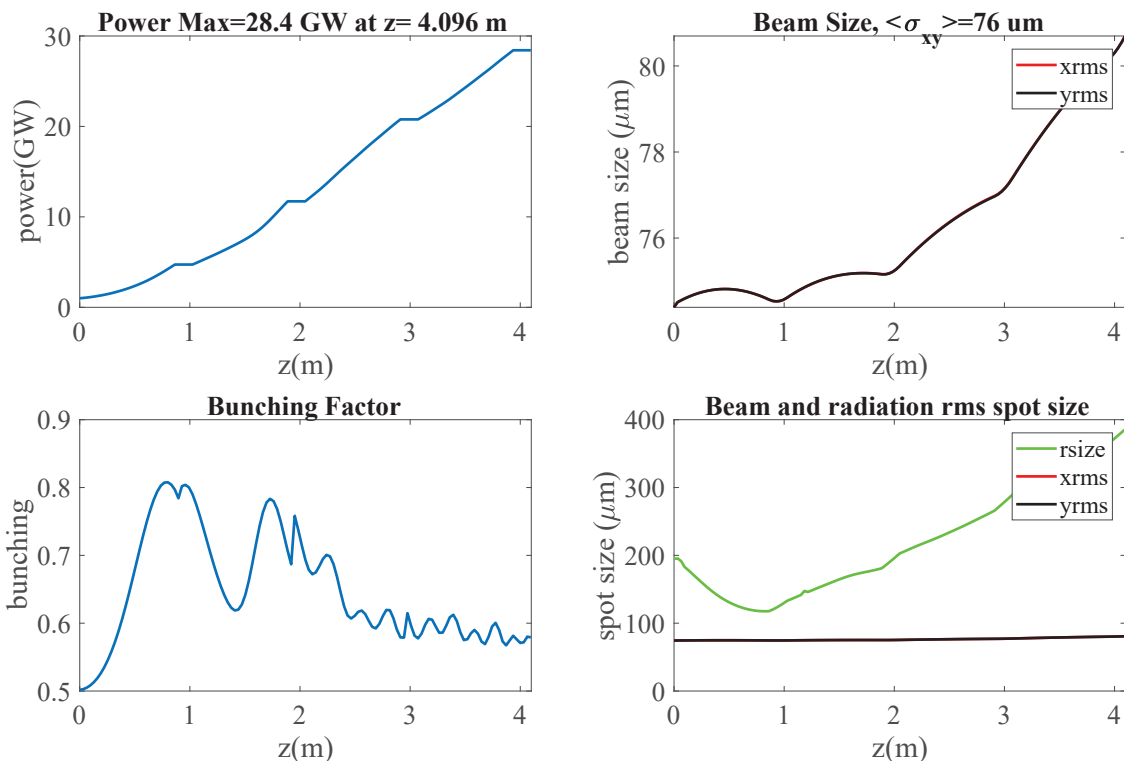


Figure 4: Power, Beam sizes, and bunching factor plots for four undulator sections of 86-cm undulator and 16-cm drift without quadrupoles.

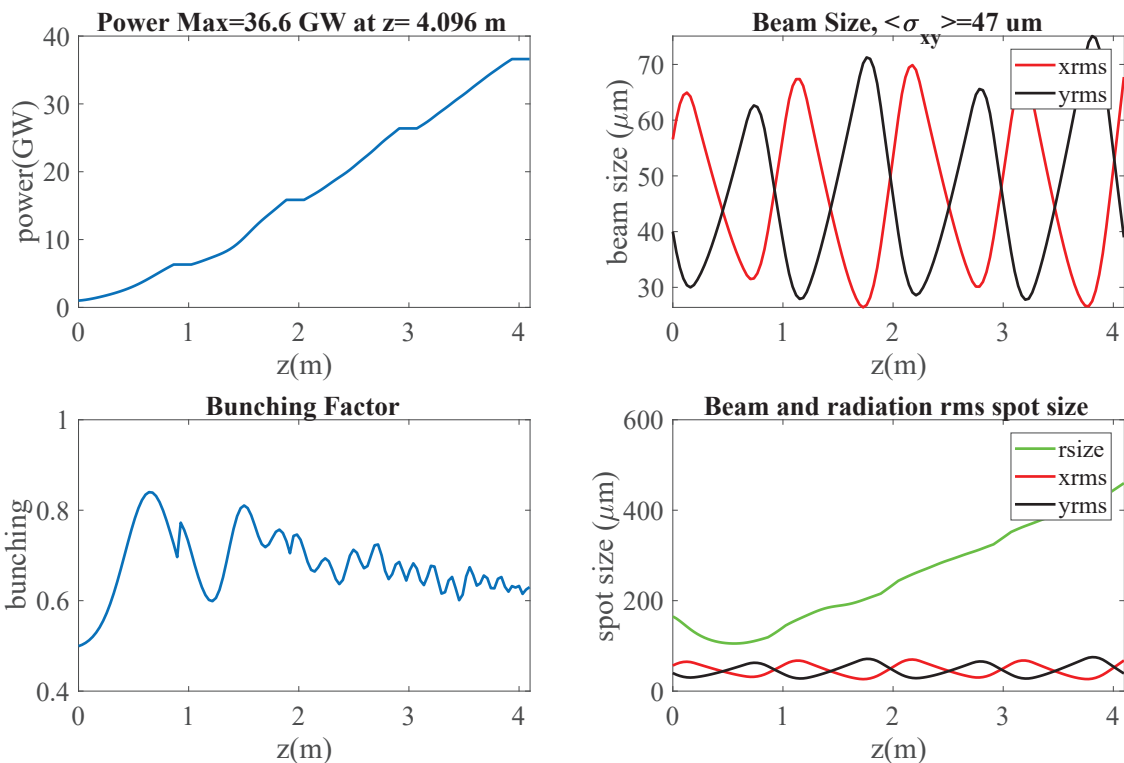


Figure 5: Power, Beam sizes, and bunching factor plots for four undulator sections of 86-cm undulator and 16-cm drift with quadrupoles.

Table 2: Simulation Parameters of Undulator

Simulation parameters of undulator	
Undulator Period	3.2 cm
Undulator gap	6 mm
Number of modules	4
Module length	4.096 m
Simulation results for undulator without FODO	
RMS beam size	76 μm
Power output	28.4 GW
Efficiency	7.6%
Simulation results for undulator with FODO	
RMS beam size	47 μm
Power output	36.6 GW
Efficiency	9.8 %

Tapering method where Genesis is called at each undulator period to simulate particle and radiation beam evolution and the tapering is varied following Equation (1) for the next period.

GIT Simulation of Undulator without Quadrupoles

Using GIT we simulated four sections 86.4-cm long undulators with 3.2-cm period. Figure (4) shows the average beam size of 76 μm and a final radiation power of 28.4 GW with an efficiency of 7.6%. For these simulations we assumed an initial bunching factor of 0.5 determined by a prebuncher with 4-cm-period undulator and a magnetic chicane located 52 cm before the entrance of the tapered undulator. The beam size slightly increases throughout longitudinal propagation due to the variation of K along the undulator.

GIT Simulation Undulator with Quadrupoles

For four sections of 86-cm undulators with FODO system of 19.2-cm long, 22-T/m gradient quadrupoles, 48.0-cm drift between the quadrupoles, and 16-cm drift between the undulators (Figure 2), we obtained average beam size of 47 μm and the final power output is 36.6 GW (Figure 5). The conversion efficiency of the system is 9.8%.

CONCLUSIONS

We show by 3D Genesis simulation that the TESSA-266 experiment could achieve an extraction efficiency of 7.6% without using strong focusing in the undulator and 9.8% with quadrupoles. This will be an order of magnitude improvement from the previous record values of efficiency at UV wavelengths [2]. The improvement has the potential for breakthrough impact in research areas such as materials synthesis, lithography, and nano-engineering where short wavelengths FELs are used [6]. The experiment will be the first time to demonstrate TESSA design at high regime taking advantage of strong focusing in the undulator.

ACKNOWLEDGMENT

This work has been supported by SBIR award DE-SC0017102.

REFERENCES

- [1] C. Bostedt *et al.*, “Linac coherent light source: The first five years,” *Rev. Mod. Phys.*, vol. 88, p. 015007, 2016. Available: <https://link.aps.org/doi/10.1103/RevModPhys.88.015007>
- [2] D. Douglas *et al.*, “High average power uv free electron laser experiments at jlab,” in *Proceedings of IPAC’12*, New Orleans, LA, USA, paper WEYB03.
- [3] N. Kroll, P. Morton, and M. Rosenbluth, “Free-electron lasers with variable parameter wigglers,” *IEEE Journal of Quantum Electronics*, vol. 17, no. 8, pp. 1436–1468, 1981.
- [4] J. Duris, A. Murokh, and P. Musumeci, “Tapering enhanced stimulated superradiant amplification,” *New Journal of Physics*, vol. 17, no. 6, p. 063036, 2015. Available: <http://stacks.iop.org/1367-2630/17/i=6/a=063036>.
- [5] N. Sudar *et al.*, “High efficiency energy extraction from a relativistic electron beam in a strongly tapered undulator,” *Phys. Rev. Lett.*, vol. 117, p. 174801, 2016. Available: <https://link.aps.org/doi/10.1103/PhysRevLett.117.174801>.
- [6] E. R. Hosler, O. R. Wood, and W. A. Barletta, “Free-electron laser emission architecture impact on EUV lithography,” *Proc. SPIE*, vol. 10143, pp. 101 431M–101 431M–12, 2017. Available: <http://dx.doi.org/10.1117/12.2260452>.

HUNDRED-GIGAWATT X-RAY SELF-SEEDED HIGH-GAIN HARMONIC GENERATION

L. Zeng[#], S. Zhao, W. Qin, S. Huang, K. Liu

Institute of Heavy Ion Physics, School of Physics, Peking University, Beijing 100871, China

Y. Ding, Z. Huang

SLAC National Accelerator Laboratory, Menlo Park, CA 94025, USA

Abstract

Self-seeded high-gain harmonic generation is a possible way to extend the wavelength of a soft x-ray free-electron laser (FEL). We have carried out simulation study on harmonic generation within the photon energy range from 2 keV to 4.5 keV, which is difficult to be achieved due to a lack of monochromator materials. In this work we demonstrate the third harmonic FEL with the fundamental wavelength at 1.52 nm. Our result shows that, by using undulator tapering technique, hundred-gigawatt narrow-bandwidth FEL output can be obtained.

*INTRODUCTION

Free-electron lasers, the so called fourth generation of light source, allow one to carry out completely new experiments in atomic and molecular physics, chemistry and many other areas. Self-amplified spontaneous emission (SASE) [1,2] is the baseline FEL operation mode in X-ray region, which has good transverse coherence. However, it starts from the shot noise of the electron beam, which leads to the poor properties in terms of a spectral bandwidth.

Several external seeding FEL schemes are proposed to obtain good longitudinal coherence. For example, directly HHG[3], HGHG[4,5], cascade HGHG[6], EEHG[7,8] and so on. Because of lacking external seeds with short wavelength, these external seeding FEL schemes have difficulty in demonstrating at hard X-ray region.

Self-seeding [9] is a way to narrow the SASE bandwidth of XFELs significantly in order to produce nearly transform-limited pulses. Last several years, self-seeding scheme has been demonstrated in both soft and hard x-ray FELs [10,11]. The monochromator for soft x-ray self-seeding FEL (the photon energy below 2 keV) is a grating-based optic system[10], while the hard x-ray self-seeding FEL (the photon energy above 4.5 keV) usually uses diamond-based monochromator[11]. However, the self-seeded FEL has not been demonstrated in the energy region between 2 to 4.5 keV. Previous study in self-seeded HGHG FEL scheme [12] can not only fill the above energy gap, but also extend the wavelength in hard X-ray self-seeding FEL. Ultra-high power FELs are more attractive for the science application like nonlinear Compton scattering[13]. In this paper, the self-seeded HGHG FEL scheme is further studied to obtain ultra-high peak power.

THE SCHEME

The schematic of the self-seeded HGHG FEL is shown in Fig. 1. At first, the electron beam goes through the undulator U_S , generating SASE radiation in the linear regime. At the exit of U_S , the SASE radiation passes through the grating-based X-ray monochromator so as to obtain a narrow-band seed for the following undulator while the electron beam goes through a bypass chicane C_{B1} . The bypass chicane C_{B1} can not only provides a proper delay to make the electron beam and the seed recombine at the entrance of undulator U_A but also help to wash out the microbunching of the electron beam built up in the SASE undulator. Then, we should notice that this seed is different to external seed of regular HGHG FEL[6]. This seed radiation from the monochromator has a much lower power, limited to a few hundred kilowatts herein because of avoiding damaging the state-of-the-art X-ray monochromator optics. As a result, we need to amplify the seed radiation. At the same time, we have to eliminate the impact of electron energy spread degradation in the seed amplification process. Consequently, an electron beam with longer bunch length is used to generate double-spike seed after monochromator. The head spike of the seed is then aligned with the tail part of the electron bunch at the entrance of the amplifying undulator U_A . Therefore only the tail part of the electron bunch is used to amplify the seed while the head part is kept undisturbed and “fresh”. After the U_A undulator, the electron bunch is delayed by a small chicane (C_{B2}), and consequently the head part is aligned with the seed radiation in the modulation undulator (U_{M2}) and gets energy-modulated. The energy modulated electron beam then goes through the dispersion chicane with proper R_{56} , getting density modulated, and radiates at the harmonic wavelength of the seed.

Compared to previous work in 2016[12], we have finished further study in this paper. (1) Further optimization in the amplifier (U_A), modulator (U_{M2}) and dispersion section (C_D), (2) Tapered radiator (U_R) study for higher output harmonic radiation FEL power. The details in both two parts will be shown in the following section.

[#]zengling@pku.edu.cn

Content from this work may be used under the terms of the CC BY 3.0 licence (© 2018). Any distribution of this work must maintain attribution to the author(s), title of the work, publisher, and DOI.

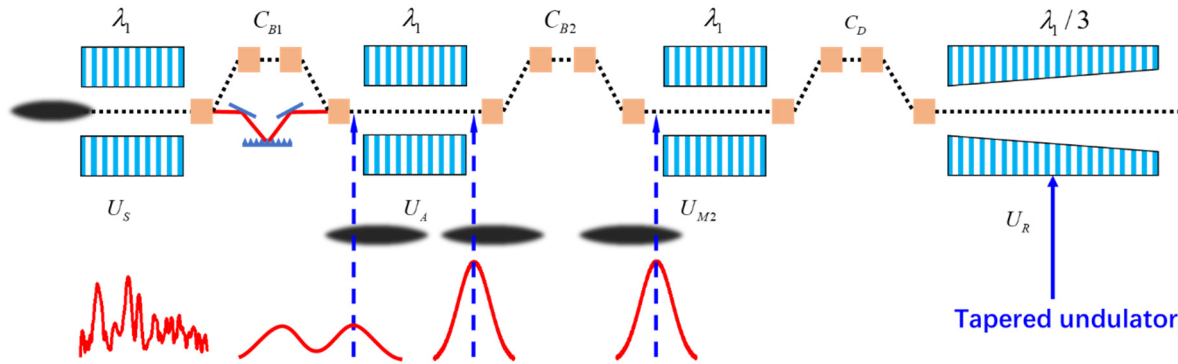


Figure 1: Schematic of tapered self-seeded HGHG FEL. U_S is a SASE undulator, U_A is a seed amplifier, U_{M2} is a modulation undulator, and U_R is a radiation undulator (radiator) of HGHG. C_{B1} and C_{B2} are bypass chicanes, while C_D is a dispersion chicane of HGHG.

FEL SIMULATION

Table 1: Parameters used for Self-seeded HGHG Simulation

Parameter	Value	Unit
Electron beam		
Energy	4.3	GeV
Peak current	2.5	kA
Energy spread	1.0	MeV
Emittance	0.5	mm-mrad
Mono / Chicane		
Resolving power	5000	
Power efficiency	0.02	
central wavelength	1.52	nm
Undulators		
undulator period	0.03	m
U_S length	19.8	m
U_S strength, a_u	2.4749	
U_{M2} strength, a_u	2.4749	
U_R strength, a_u	1.6	

Here we use the parameters of the soft X-ray self-seeding (SXRSS) FEL at LCLS for start-to-end simulations. The simulations were performed with GENESIS [14] and the parameters are shown in Table 1. Fig. 2 shows the time-dependent simulation result of radiation after monochromator. A seed with narrow bandwidth is produced for the next HGHG stage. We should notice that the seed power is about 200 kW, which is much lower than that of regular HGHG external seed.

In the amplification section, when a short undulator U_A is used, the seed could not get enough amplified. On the contrary, a long undulator U_A may obtain high seed power, but the “fresh” part of the electron bunch also may be disturbed because of the SASE process itself. Here we made optimization on the length of U_A . The evolution of the seed laser pulse and electron beam in U_A is illustrated in Fig. 3. It is clear from that, while the peak power of the radiation is amplified to about 100 MW in the U_A undulator, the head electrons in the bunch do not get disturbed and the energy spread of the tail electrons

becomes larger. After the U_A undulator, the electron bunch is delayed by the C_{B2} chicane, and the head part electrons are aligned with the seed radiation in the U_{M2} modulation undulator.

The remained part is a regular HGHG configuration. The fresh part of the electron bunch is energy modulated by the amplified seed laser at U_{M2} . Enough energy modulation is necessary for nth harmonic. However, we should avoid too much extra energy spread caused by the energy modulation process. The optimized length of U_{M2} is 8 m. Choosing $R_{56} = 0.42 \mu\text{m}$, density modulation is obtained after dispersion chicane C_D . Finally, the 3rd harmonic is generated in the radiator U_R .

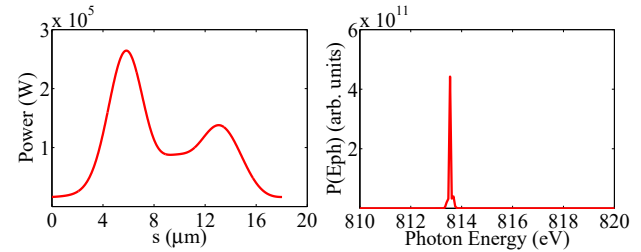


Figure 2: FEL power profile (left) and spectra (right) at the exit of monochromator C_{B1} .

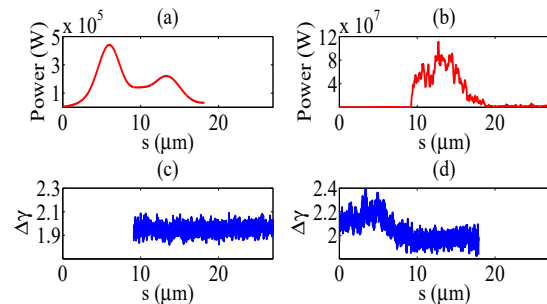


Figure 3: Simulated radiation power (top) and electron beam (bottom) evolution at the entrance to U_A (left), at and at the entrance to U_{M2} (right).

The resonance condition on the central axis of a FEL is given by the equation

$$\lambda_R = \frac{\lambda_u}{2\gamma^2} (1 + a_u^2) \quad (1)$$

For regular undulator U_R , the rms undulator parameter a_u is constant. As the FEL power of the radiation grows, the electron beam energy γ drops. Gradually, when the resonance condition can't be maintained, the FEL power reaches saturation. This severely limits the energy extraction efficiency of the FEL. When using tapered undulator U_R , a_u is a function of the axial position z so as to maintain the resonance condition continually as the electrons decelerate. The key problem is finding the proper function $a_u(z)$ or $K(z)$, the so called taper profile.

We analyse two kinds of taper profile of the radiator U_R . Fig.4 shows the common linear taper profile, z_0 is the position where the taper starts, the taper ratio is $k = (\Delta K)/K_0$. From Fig.4, the period in zigzag taper profile is z_T , and defined $\eta_{zig} = \delta K/\Delta K$. From KMR model[15] about tapered undulator, if we want more energy extraction from electron beam, two conditions are necessary. (1), make ponderomotive bucket deceleration rapid. (2), more particles should be trapped by the ponderomotive bucket. However, there is a conflict between rapid bucket deceleration and maintaining a large number of trapped particles[15]. Eventually, different kinds of taper profile have their own advantages and disadvantages. Moreover, for a given type of taper profile, we also need to optimize its key parameters. For linear taper profile, the optimized simulation parameters are: $z_0 = 13.2$ m, $k=5\%$; For zigzag taper profile, the optimized simulation parameters are: $z_0 = 13.2$ m, $z_T = 3.3$ m, $k=0.3\%$, $\eta_{zig} = 50\%$. Fig.7 demonstrates the FEL power evolution in different kinds of undulator. It's clear that by tapering, the FEL power of 3rd harmonic is enhance by about an order of magnitude. The saturation power of linear taper (65GW) is lower than that of zigzag power (75GW). The most possible reason is that the ponderomotive bucket of zigzag taper can trapped some particles which are untrapped before when the bucket moving up.

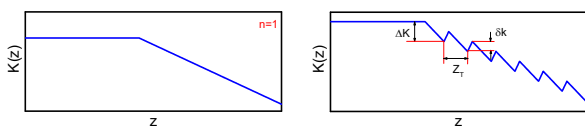


Figure 4: schematic of the linear taper profile (left) and zigzag taper profile (right) undulator

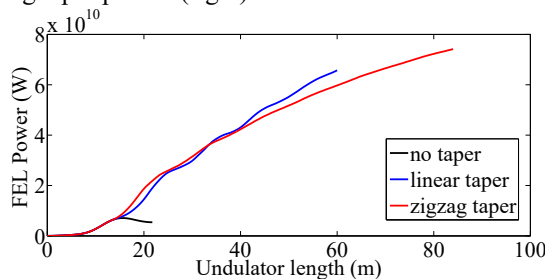


Figure 5: FEL power evolution in different kind of undulator

We have studied linear taper profile above. In addition, nonlinear taper is also important. As we know, the taper law for nonlinear taper profile can be written as

$$K(z) = \begin{cases} K_0 & (0 < z < z_1) \\ K_0 \times \left(1 - k \frac{(z - z_0)^n}{L_t^n}\right) & (z < z_1) \end{cases}$$

Here L_t is the taper length. We optimize the taper index n of normal taper profile to maximize the saturation power of the self-seeded HGHG FEL. Fig.5 shows the FEL power versus n at the exit of radiator U_R . It demonstrates that when $n=1.9$, the maximum FEL power of the 3rd harmonic is 155 GW. Fig 7 and Fig 8 demonstrate the power profile and spectra at the exit of U_R . It's obvious that a narrow-bandwidth radiation at hundred-gigawatt level is obtained.

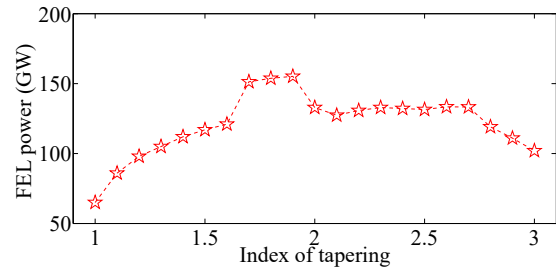


Figure 6: FEL power versus index of tapering in U_R

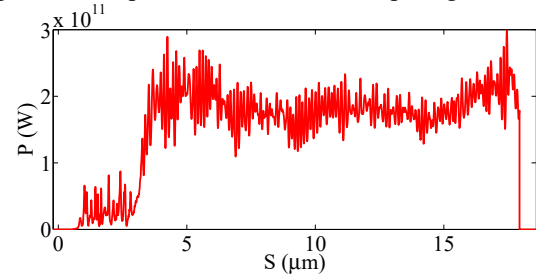


Figure 7: FEL power profile at the exit of U_R ($n=1.9$)

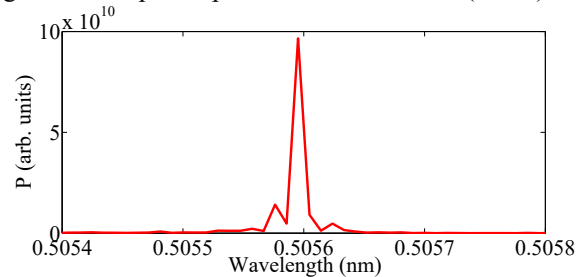


Figure 8: spectrum at the exit of U_R ($n=1.9$)

CONCLUSION

We proposed a high-peak-power self-seeded HGHG scheme, which is a promising way to extend regular self-seeded FELs to shorter wavelengths, especially within the photon energy range from 2 keV to 4.5 keV, which is difficult to achieve due to a lack of monochromator materials. The simulation result shows that hundred-gigawatt 3rd harmonic radiation (0.5 nm) is obtained by optimizing tapered undulator U_R .

REFERENCES

- [1] A. M. Kondratenko and E. L. Saldin, *Part. Accel*, vol. 10, pp. 207-216, 1980.

- Content from this work may be used under the terms of the CC BY 3.0 licence (© 2018). Any distribution of this work must maintain attribution to the author(s), title of the work, publisher, and DOI.
- [2] R. Bonifacio, C. Pellegrini, and L. M. Narducci, *Optics Communications*, vol. 50, pp. 373-378, 1984.
 - [3] G. Lambert *et al.*, *Nature Phys.*, vol. 4, pp. 296-300, 2008.
 - [4] I. Ben-Zvi *et al.*, *Nucl. Instrum. Methods Phys. Res., Sect. A* 304, pp. 181, 1991.
 - [5] L. Yu, *Phys. Rev. A*, vol. 44, pp. 5178, 1991.
 - [6] J. Wu and L. Yu, *Nucl. Instrum. Methods. A*, vol. 475, pp. 104-111, 2001.
 - [7] D. Xiang and G. Stupakov, “Echo-enabled harmonic generation free-electron laser”, *Phys. Rev. ST. Accel. Beams*, vol. 12, pp. 030702, 2009.
 - [8] M. Dunning *et al.*, A proof-of-principle echo-enabled harmonic generation FEL experiment at SLAC, Conf. Proc. 2010, C100523 (IPAC-2010-TUPE069)
 - [9] J. Feldhaus *et al.*, *Optics Communications*, vol. 140, pp. 341-352, Aug. 1997.
 - [10] D. Ratner *et al.*, *Phys. Rev. Lett.*, vol. 114, pp. 054801, 2015.
 - [11] J. Amann *et al.*, *Nature Photonics*, vol. 6, pp. 693-698, 2012.
 - [12] L. Zeng, *et al.*, *Chin. Phys. C.* vol. 40, pp. 098102, 2007.
 - [13] M. Fuchs *et al.*, « Anomalous nonlinear x-ray compton scattering », *Nat. Phys.* Vol. 11, pp. 964, 2015.
 - [14] S. Reiche, *Nucl. Instrum. Methods A*, vol. 429, pp. 243 1999.
 - [15] N. M. Kroll, P. L. Morton, and M. Rosenbluth, *IEEE J.Quantum Electron.*, vol. 17, pp. 1436, 1981.

HARMONIC LASING TOWARDS SHORTER WAVELENGTHS IN SOFT X-RAY SELF-SEEDING FELS

L. Zeng[#], S. Zhao, W. Qin, S. Huang, K. Liu

Institute of Heavy Ion Physics, School of Physics, Peking University, Beijing, China

Y. Ding, Z. Huang

SLAC National Accelerator Laboratory, Menlo Park, USA

Abstract

In this paper, we study a simple harmonic lasing scheme to extend the wavelength of X-ray self-seeding FELs. The self-seeding amplifier comprises two stages. In the first stage, the fundamental radiation is amplified but well restricted below saturation, and meanwhile harmonic radiation is generated. In the second stage, the fundamental radiation is suppressed and the harmonic radiation is amplified to saturation. We performed start-to-end simulation to demonstrate third harmonic lasing in a soft x-ray self-seeding FEL at the fundamental wavelength of 1.52 nm. Our simulations show that a stable narrow-band FEL at GW level can be obtained.

INTRODUCTION

X-ray free electron lasers (XFELs) are tunable light sources with high power, coherent radiation over a broad spectral range. Self-amplified spontaneous emission (SASE) [1,2] is a usual operation mode in single pass XFEL which has excellent transverse coherence. However, because of starting from shot noise of electron beams, SASE has poor temporal coherence.

Self-seeding [3] is a way to improve the temporal coherence of SASE which consists of two undulators and an X-ray monochromator between them. The monochromator selects a narrow band of radiation from the SASE in the first undulator as the seed. Then the seed is amplified to saturation in the second undulator. This self-seeding scheme works both for soft and hard x-rays and has been demonstrated recently [4,5]. Generally, the main material for monochromator grating when the photon energy is below 2 keV [4]. While the diamond is used for the monochromator when the photon energy is above 4.5 keV [5]. However, because of lacking proper materials, the energy gap between 2 keV to 4.5 keV for self-seeding FEL has not been achieved now.

A possible way to extend the operating range of a soft X-ray self-seeding FEL is to use nonlinear harmonic generation [6]. The odd harmonics can be radiated in the same undulator [7]. However, the intensity of harmonics is rather small because of the dominance of the interaction at the fundamental radiation [7-9]. In this paper, we study the harmonic lasing in soft X-ray self-seeding FEL which could fill the energy gap not easily achieved by regular self-seeding schemes. By suppressing the fundamental frequency, we can obtain the odd harmonic radiations with higher intensity.

HARMONIC ANALYSIS FOR THE SELF-SEEDED FEL

In a planar undulator, the resonance condition for the radiation is written as

$$\lambda_h = \frac{\lambda_u(1+K^2/2)}{2h\gamma^2} \quad (1)$$

Here h is the harmonic number, λ_h is the harmonic wavelength, λ_u is the undulator period, γ is relativistic factor, and K is the undulator parameter.

In a high-gain FEL, odd linear and nonlinear harmonics can be radiated on axis [7]. The linear amplification of harmonics is always smaller than the fundamental. The nonlinear harmonic generation occurs when a beam is strongly bunched by the fundamental frequency and the bunch spectrum develops rich harmonic contents. Especially, the growth rate of the nonlinear harmonics is h times higher than that of the fundamental. However, the dominance of the interaction at the fundamental radiation will limit the nonlinear harmonic interaction. So the intensity of harmonics is rather small. Typically, the third harmonic is at the level of a percent of the fundamental.

We study the third harmonic radiation in the soft X-ray self-seeding FEL and our simulation study is based on the LCLS parameters, which are shown in Table 1. Time-dependent simulation result by GENESIS [10] code of the soft X-ray self-seeding is shown in Fig. 1 and Fig. 2. It is clear that after the monochromator, the seed power of radiation is about 200 kW. Fig. 2 shows the evolution of the power of the fundamental and 3rd harmonic in the undulator U_2 . It's clear that the linear gain process is at $z < 15m$ and the linear harmonic grows much more slowly than the fundamental.

Table 1: Parameters Used for Soft X-ray Self-seeding FEL Simulation at LCLS

Parameter	Value	Unit
Electron beam energy	4.3	GeV
Peak current	3	kA
Energy spread	1	MeV
Emittance	0.5	mm-mmrad
Mono. central wavelength	1.52	nm
Mono. resolving power	5000	
Mono. power efficiency	0.02	
Undulator period	0.03	m
U_1 length	19.8	m
U_1 parameter K (rms)	2.4749	

Content from this work may be used under the terms of the CC BY 3.0 licence (© 2018). Any distribution of this work must maintain attribution to the author(s), title of the work, publisher, and DOI.

When $z > 15\text{m}$, the nonlinear interaction occurs and the nonlinear harmonic grows faster than the fundamental. However, the power of the 3rd harmonic is rather small, which is 0.4 GW, about 2% of the fundamental saturation power.

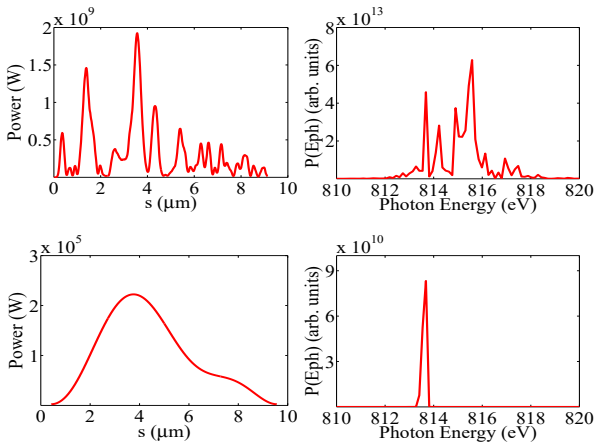


Figure 1: The FEL power at U_1 and monochromator stage in time (top) and frequency (bottom) domain. At the exit of U_s (left); At the exit of monochromator (right).

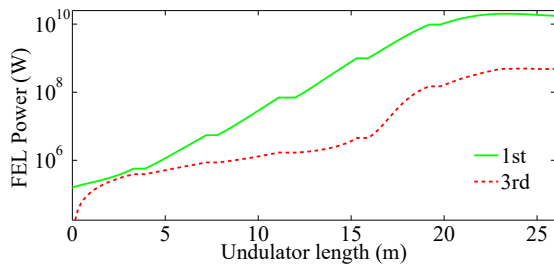


Figure 2: The fundamental (green line) and 3rd (red line) harmonic power evolution along the radiator undulator U_2

SUPPRESSION OF THE FUNDAMENTAL HARMONIC IN AMPLIFIER UNDULATOR

To achieve high output harmonic power, we could suppress the interaction at the fundamental resonance while allowing the harmonics to evolve to saturation, which is referred to as harmonic lasing [11]. The soft X-ray self-seeding harmonic lasing scheme is shown in Fig. 3. It demonstrates that the seeding undulator of normal self-seeding is segmented by a fundamental suppressor, which suppresses the radiation at the

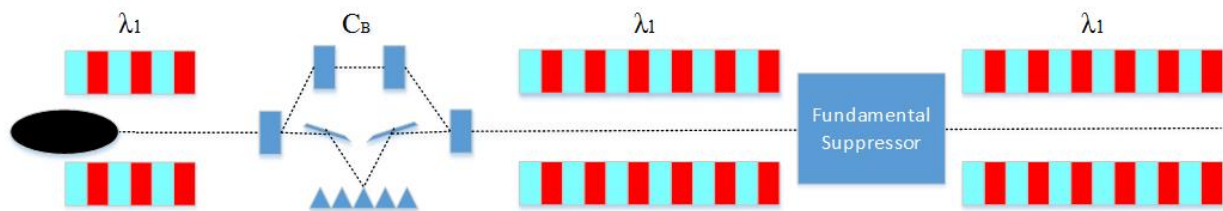


Figure 3: Soft X-ray self-seeding harmonic lasing scheme

fundamental and allow the harmonic radiation to grow in the linear regime toward saturation [4–6], so as to avoid significant nonlinear coupling to the fundamental.

One method to suppress the interaction at the fundamental resonance without affecting the third harmonic lasing is phase shifter [12]. Here we define θ_j as the phase of the electrons with respect to the ponderomotive potential of the fundamental resonant wavelength, where $j = 1, 2, \dots, N$ is the number of electrons. Then the phase of the n th harmonic is $\theta_{nj} = n\theta_j + \phi_n$, where ϕ_n is the relative phase between the ponderomotive potential of the fundamental and n th harmonic. When the phase of fundamental changes by a relative phase $\Delta\theta_j = 2\pi/k$ then the corresponding phase change for the harmonics will be $\Delta\theta_{nj} = 2\pi n/k$. Here we use $k = n = 3$, which means the phase delay is $2\pi/3$ for the fundamental and its amplification is disrupted. However, the phase delay for 3th harmonic is 2π . As a result, the fundamental can be expected to disrupt its exponential growth while the 3th harmonic should not affect its FEL interaction. It continues to get amplified without being affected by phase shifters. In Fig. 4, one can see the evolution of the 1st (at 1.5 nm) and the 3rd (at 0.5 nm) harmonics. The length of U_2 at Fig. 3 is about 11m so that the fundamental radiation is well below saturation. Then the fundamental is suppressed and the 3rd harmonic continues to get amplified to saturation. Power of the 3rd harmonic radiation at the exit is 6.5 GW.

Another method for the fundamental suppressing is intra-undulator spectral filtering [11]. Fig. 5 shows that the electron beam trajectory deviates from a straight line, and a filter is inserted. After transmitting the filter, the radiation will be absorbed in a specific frequency.

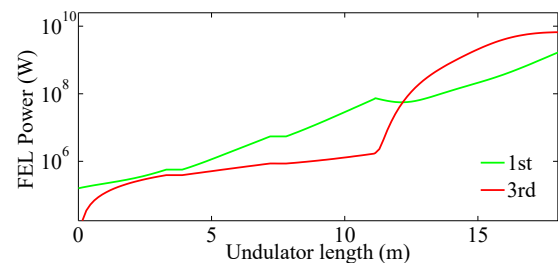


Figure 4: FEL power versus undulator length at U_2 (0~11m) and U_3 (>11m) in soft X-ray self-seeding harmonic lasing FEL.

After the filter, fundamental mode will be suppressed while the n th harmonic mode is only weakly affected.

At the same time, beam modulation will be smeared through a chicane due to R_{56} .

Figure 6 illustrates the evolution of 1st and 3rd harmonic using the intra-undulator spectral filter. Here we choose the filter which provides 10000 power attenuation for the fundamental radiation. While the 3rd still get amplified to saturation with a 4 GW saturation power.

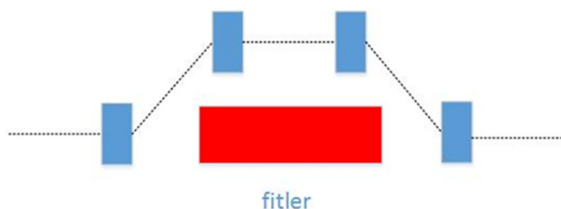


Figure 5: Schematic of intra-undulator spectral filter system.

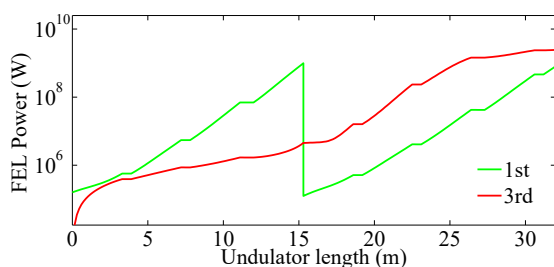


Figure 6: FEL power versus undulator length at U_2 (0~15m).

CONCLUSION

In this paper, we proposed a new simple scheme to extend the wavelength of the soft X-ray self-seeding FEL. With the help of two different ways to suppress the fundamental radiation, the harmonics will get amplified independently. The simulation shows promising results that the output power of the 3rd harmonic radiation (at 0.5 nm) reaches 6.5 GW and 4 GW according to the phase shifter method and intra-undulator spectral filter method, respectively. Further study including optimization and higher harmonic generation is ongoing.

REFERENCES

- [1] A. M. Kondratenko and E. L. Saldin, Part. Accel, 10: 207-216 (1980).
- [2] R. Bonifacio, C. Pellegrini, and L. M. Narducci, Optics Communications, 50 (6): 373-378 (1984).
- [3] J. Feldhaus, E. L. Saldin, J. R. Schneider *et al.*, Optics Communications, 140 (4): 341-352 (1997).
- [4] D. Ratner, R. Abela, J. Amann *et al.*, Phys. Rev. Lett, 114 (5):054801 (2015)
- [5] J. Amann *et al.*, Nature Photonics, 6: 693-698 (2012).
- [6] W. Ackermann *et al.*, Nature Photonics, 1, 336 (2007).
- [7] Z. Huang and K. Kim, Phys. Rev., E 62, 7295 (2000).
- [8] H. Freund, S. Biedron, and S. Milton, Nucl. Instrum. Methods Phys. Res., Sect. A 445, 53 (2000).
- [9] E. L. Saldin, E. A. Schneidmiller, and M.V. Yurkov, Phys. Rev. ST Accel. Beams 9, 030702 (2006).
- [10] S. Reiche, Nucl. Instr. Meth. Phys. Res. Sec. A 429, 243 (1999).
- [11] E.A. Schneidmiller and M.V. Yurkov, Phys. Rev. ST-AB 15 (2012) 080702.
- [12] B.W. J. McNeil *et al.*, Phys. Rev. Lett. 96, 084801 (2006).

COMPARING FEL CODES FOR ADVANCED CONFIGURATIONS

B. Garcia*, G. Marcus, SLAC, Menlo Park, California, USA
S. Reiche, Paul Scherrer Institut (PSI), Villigen, Switzerland
L. T. Campbell^{1,2}, B. W. McNeil¹, SUPA, Department of Physics,
University of Strathclyde, Glasgow, UK
¹also at Cockcroft Institute, Warrington, UK
²also at ASTeC, STFC Daresbury Laboratory, Warrington, UK

Abstract

Various FEL codes employ different approximations and strategies to model the FEL radiation generation process. Many codes perform averaging procedures over various length scales in order to simplify the underlying dynamics. As FELs are developed in more advanced configurations beyond simple SASE, the assumptions of some codes may be called into question. We compare the unaveraged code Puffin to averaged FEL codes including a new version of GENESIS in a variety of situations. In particular, we study a harmonic lasing setup, a High-Gain Harmonic Generation (HG) configuration modeled after the FERMI setup, and a potential Echo-Enabled Harmonic Generation (EEHG) configuration also at FERMI. We find the codes are in good agreement, although small discrepancies do exist.

INTRODUCTION

Numerical simulation is an important tool in assessing the performance of any X-ray FEL. While there has been significant work benchmarking numerical codes to SASE studies [1, 2], comparatively little has been done on other operation modes. In this study, we consider advanced schemes designed to extend the maximum attainable photon energy (harmonic lasing [3]) and improve the temporal coherence (beam-based seeding [4]).

The first harmonic lasing of a self-seeded X-ray FEL has recently been achieved [5], and there is considerable interest in employing this technique to XFELs. In these harmonic lasing setups, the fundamental radiation is disrupted while the higher harmonic emission is allowed to grow unfettered.

We also consider both the High-Gain Harmonic Generation (HG) [6, 7] and Echo-Enabled Harmonic Generation (EEHG) [8, 9] seeding schemes. This type of seeding potentially allows the full longitudinal coherence of conventional lasers to be transferred to an X-ray FEL.

Previous work has compared the harmonic generation capabilities of some codes for a seeded beam [10]. This was extended by work which compared the results of FAST, GENESIS, and GINGER in the cases of both artificial and phase-shifted harmonic lasing [11] starting from noise. We extend this result by adding additional simulation results from the un-averaged code PUFFIN. We then provide benchmarks for FERMI inspired HG [12] and EEHG configurations between both PUFFIN and GENESIS.

* bryantg@stanford.edu

CODE DESCRIPTIONS

The FEL simulation codes used in this study are PUFFIN [13] and GENESIS [14]. While for the harmonic lasing studies results from the codes FAST and GINGER are presented, no new simulations are performed with these codes and a description of these previous results is found in [11]. Although PUFFIN and GENESIS are both high gain FEL simulation codes, they contain some important differences so we briefly describe each in turn.

GENESIS

GENESIS is a time-dependent, 3D FEL simulation code in which both the radiation field and electron macroparticles are distributed on a Cartesian mesh. GENESIS averages over the motion of an individual undulator period, and therefore computes harmonic emission by employing an effective coupling factor [15]. Furthermore, GENESIS employs the so-called Slowly Varying Envelope Approximation (SVEA) [16] which allows one to average the radiation envelope over a radiation wavelength. While these approximations offer a large computational speedup, advanced FEL configurations may violate one or more of them.

Recent updates to GENESIS, referred to here as GENESIS V4, have made it possible to model each individual electron [17]. These so-called one4one simulations (one electron is one macroparticle) have noise statistics that are automatically correct at any wavelength. This allows for the electron beam to be re-sliced at any harmonic where the dynamics between current spikes, which result from HG or EEHG processes, can be modeled consistently. The HG and EEHG simulations shown below use this new version while the harmonic lasing simulations from 2014 use the nominal Fortran version.

PUFFIN

In contrast to GENESIS, PUFFIN does not employ the SVEA or average the electron motion. The electric field is instead discretized on a sub-wavelength scale with frequency resolution limited only by the Nyquist frequency. Similarly, the detailed electron motion resolution is limited only by the number of integration steps performed per undulator period. The cost of this is an orders of magnitude increase in computational complexity and memory requirements. While the physics captured is ostensibly more accurate as a result, one would like to benchmark the two codes in only a few

Table 1: Electron beam and undulator parameters for the various benchmarking cases.

	LCLS-I	LCLS-II	HGHG	EEHG
$E[GeV]$	11.62	4	1.24	2
$\sigma_E[keV]$	1400	500	150	1000
$\epsilon_n[\mu m]$	0.4	0.4	2	1
$I_{peak}[kA]$	3	1	0.3	0.65
$\lambda_u[cm]$	3	2.6	5.5	3
K	3.5	2.23	3.45	2.28
$\langle\beta\rangle[m]$	26	12	10	25

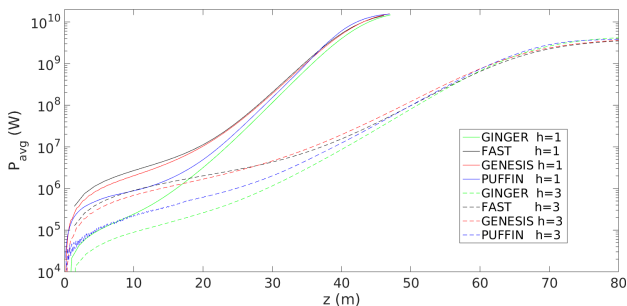


Figure 1: Growth of the fundamental (6 keV) and third harmonic (18 keV) radiation versus z for the LCLS-I like setup. The dashed curves are a separate simulation in which the fundamental is artificially suppressed.

representative cases and leave the heavy design work to the more computationally efficient GENESIS.

HARMONIC LASING BENCHMARKS

To begin, we extend the harmonic lasing benchmarks of Marcus et. al. [11] with new PUFFIN simulations. The first case is an LCLS-I like setup operating at a 6 keV fundamental radiation energy. The resulting beam parameters are listed in table 1 and the power curves for each simulation are shown in Fig. 1.

After establishing the SASE benchmark, an artificial harmonic lasing setup is studied. The averaged codes (FAST, GENESIS, and GINGER) artificially suppress the fundamental radiation by toggling its interaction off in the code. PUFFIN, however, applies a high-pass filter which allows only the 3rd harmonic to pass. The power curves for these simulations are shown as the dashed curves in Fig. 1.

The disagreement in the startup section is due to the various competing modes in the SASE process and the limit of any given code to resolve them. Since there is not significant FEL interaction with these modes, this mild disagreement does not affect the amplified fundamental.

A similar comparison can be made using a realistic harmonic lasing scheme. In this study, the FEL is now LCLS-II like (parameters in table 1) and accommodates various phase shifters and break sections along its length. The phase shifters are generally tuned to a third-multiple of the fun-

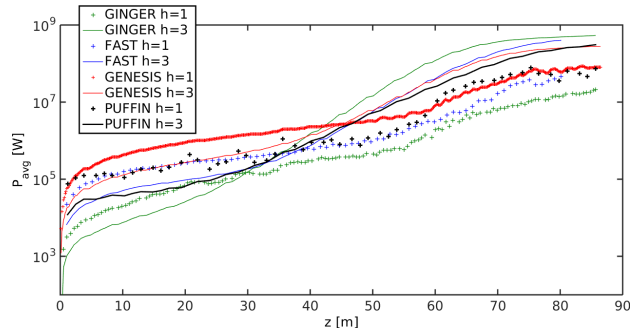


Figure 2: The power in the first and third harmonics versus z in the LCLS-II realistic harmonic lasing setup for various codes.

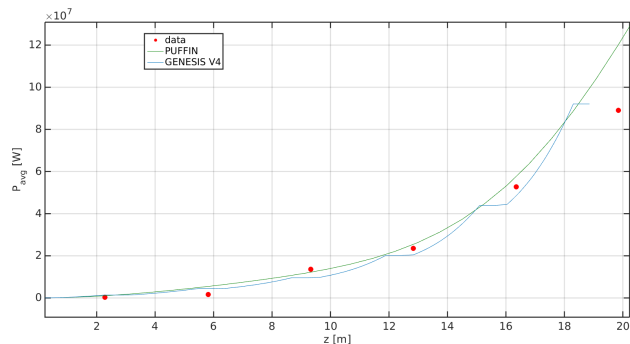


Figure 3: The average power versus z for the FERMI HGHG setup from PUFFIN, GENESIS, and measured data.

damental wavelength, i.e. $\lambda/3$ or $2\lambda/3$ to disrupt the gain in the fundamental while leaving the third harmonic unperturbed [18]. The power curves for this LCLS-II case are shown in Fig. 2.

While all codes are in general agreement, differences begin to emerge in this more realistic harmonic lasing scenario. As the physics of harmonic lasing are not the focus here, we merely remark that the averaged codes appear to be sufficient for modeling the harmonic lasing.

HIGH-GAIN HARMONIC GENERATION

We now turn towards benchmarking various beam-based seeding schemes, the simplest of which is the HGHG setup. The particular setup we consider is similar to the FERMI FEL operating in single-stage HGHG mode with 266 nm seed laser, with the parameters shown in table 1.

The HGHG settings for these simulations have scaled parameters $A = 6$ and B optimized for bunching at the eighth harmonic. The resultant gain curves for PUFFIN simulations, GENESIS V4, and the experimental data from FERMI are shown in Fig. 3. The PUFFIN simulation did not include breaks in the undulator lattice, so the distance along the undulator is scaled to approximately compensate. Good agreement in the gain curve is obtained between the simulations and experimental data. The spectrum at the end of the undulator line is also shown in Fig. 4. One clearly identifies the various harmonics produced by the HGHG

Content from this work may be used under the terms of the CC BY 3.0 licence (© 2018). Any distribution of this work must maintain attribution to the author(s), title of the work, publisher, and DOI.

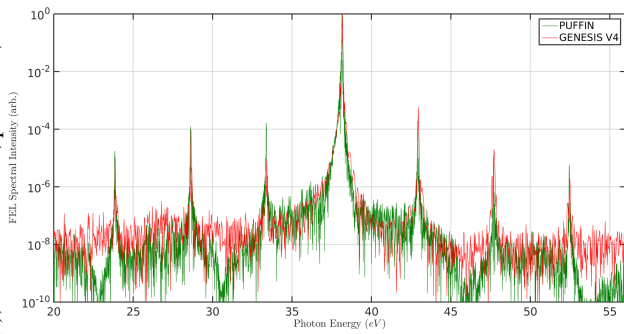


Figure 4: The FEL spectral intensity at the final undulator for the GENESIS and PUFFIN simulations for the FERMI HGHG setup.

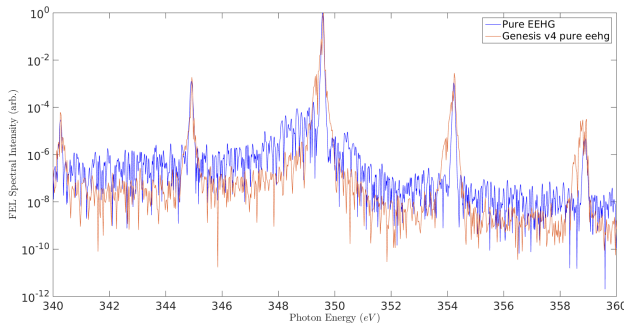


Figure 5: The saturated EEHG spectrum with both PUFFIN and GENESIS.

process, of which only the primary is significantly amplified by the FEL.

ECHO-ENABLED HARMONIC GENERATION

We turn now to the more complicated phase space manipulation of EEHG [8]. The FEL imagined in these simulations is also a rough approximation to the FERMI FEL, with slightly altered parameters as listed in table 1. As this is only a benchmark, the employed parameters differ from those quoted in FERMI's studies of potential EEHG experiments [19].

The Echo configuration is provided by two 266 nm lasers, each of which modulates the beam as perfect sinusoid by 3 MeV ($A_{1,2} = 3$). The chicanes are optimized for bunching at 3.5 nm with $B_1 = 25.95$ and $B_2 = 0.353$.

First, we compare the results in GENESIS vs PUFFIN for the case of a perfect electron beam, i.e. one with no microbunching structure; the final spectra are shown in Fig. 5. The agreement in both the central harmonic peak and the side-band harmonics is excellent between the two codes.

Energy modulations due to the microbunching instability [20] can be amplified and produce unwanted sidebands in the bunching spectrum. We compare the codes for this EEHG setup in response to a single energy modulation mode.

This modulation is applied prior to the EEHG manipulations, and is of the form $p \rightarrow p + A_0 \sin(k_\mu z + \phi)$, for amplitude A_0 , wavenumber k_μ and arbitrary phase ϕ , where

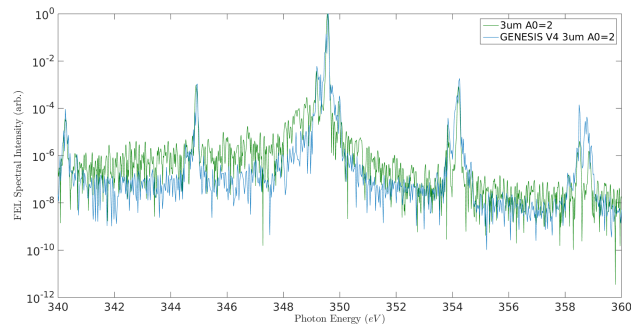


Figure 6: The saturated EEHG spectrum with an included $A_0 = 2, 3\mu\text{m}$ modulation. The extra modulation creates additional sideband structures around each of the EEHG harmonic peaks.

$p = \Delta E / \sigma_E$ is the energy deviation scaled to the slice energy spread. We select a modulation with amplitude $A_0 = 2$ and $\lambda_\mu = 2\pi / k_\mu = 3 \mu\text{m}$, which is a fairly representative mode for the instability in the LCLS [21]. The resulting FEL spectra at saturation are shown in Fig. 6. The effect of this extra energy modulation is to introduce a sideband to the main EEHG peaks, which in this case is slightly redshifted from the main peaks. The agreement between the codes on the amplitude and location of these sidebands is excellent. This confirms that GENESIS V4 is a sufficient tool for simulating EEHG beams even with high harmonic energy structure.

DISCUSSION

We have extended the previous work benchmarking against harmonic lasing to include the non-averaged code PUFFIN. While all codes are in good agreement in the artificial harmonic lasing setup, the phase-shifting induced harmonic lasing does show some disagreement. It is possible that this disagreement stems from choices in transverse gridding or how shot noise is handled, as these were not controlled for. Even a detailed study, however, of Fig. 2 could not reveal which codes are averaged and which are not, so we conclude that averaged codes are sufficiently accurate to model this harmonic lasing setup.

For the seeded cases considered, the agreement between GENESIS and PUFFIN was in general excellent. For relatively small ($\Delta E / E$) energy modulations, it seems that GENESIS is a sufficient tool for modeling both HGHG and EEHG beams. It remains possible that in more extreme settings, such as those with very large energy modulations, the assumptions of GENESIS could cause inaccurate results. Future work should continue to push this boundary and discover exactly which configurations require a more complete simulation model.

ACKNOWLEDGMENTS

This work was supported in part by the U.S. Department of Energy under Contract No. DE-AC03-76SF00515 and the Stanford University Bob Siemann Fellowship in Accelerator Physics.

REFERENCES

- [1] S. Biedron *et al.*, “Multi-dimensional free-electron laser simulation codes: a comparison study,” *Nuclear Instruments and Methods in Physics Research Section A: Accelerators, Spectrometers, Detectors and Associated Equipment*, vol. 445, no. 1, pp. 110 – 115, 2000. [Online]. Available: <http://www.sciencedirect.com/science/article/pii/S0168900200001248>
- [2] Z. Huang and K.-J. Kim, “Spontaneous and amplified radiation at the initial stage of a sase fel,” *Nuclear Instruments and Methods in Physics Research Section A: Accelerators, Spectrometers, Detectors and Associated Equipment*, vol. 507, no. 1, pp. 65 – 68, 2003, proceedings of the 24th International Free Electron Laser Conference and the 9th Users Workshop. [Online]. Available: <http://www.sciencedirect.com/science/article/pii/S0168900203008398>
- [3] E. A. Schneidmiller and M. V. Yurkov, “Harmonic lasing in x-ray free electron lasers,” *Phys. Rev. ST Accel. Beams*, vol. 15, p. 080702, Aug 2012. [Online]. Available: <https://link.aps.org/doi/10.1103/PhysRevSTAB.15.080702>
- [4] E. Hemsing *et al.*, “Beam by design: Laser manipulation of electrons in modern accelerators,” *Rev. Mod. Phys.*, vol. 86, pp. 897–941, Jul 2014. [Online]. Available: <http://link.aps.org/doi/10.1103/RevModPhys.86.897>
- [5] E. A. Schneidmiller *et al.*, “First operation of a harmonic lasing self-seeded free electron laser,” *Phys. Rev. Accel. Beams*, vol. 20, p. 020705, Feb 2017. [Online]. Available: <https://link.aps.org/doi/10.1103/PhysRevAccelBeams.20.020705>
- [6] I. Ben-Zvi *et al.*, “Proposed uv fel user facility at bnl,” *Nuclear Instruments and Methods in Physics Research Section A: Accelerators, Spectrometers, Detectors and Associated Equipment*, vol. 304, no. 1, pp. 181 – 186, 1991. [Online]. Available: <http://www.sciencedirect.com/science/article/pii/016890029190845H>
- [7] L. H. Yu, “Generation of intense uv radiation by subharmonically seeded single-pass free-electron lasers,” *Phys. Rev. A*, vol. 44, pp. 5178–5193, Oct 1991. [Online]. Available: <http://link.aps.org/doi/10.1103/PhysRevA.44.5178>
- [8] G. Stupakov, “Using the beam-echo effect for generation of short-wavelength radiation,” *Phys. Rev. Lett.*, vol. 102, p. 074801, Feb 2009. [Online]. Available: <http://link.aps.org/doi/10.1103/PhysRevLett.102.074801>
- [9] D. Xiang and G. Stupakov, “Echo-enabled harmonic generation free electron laser,” *Phys. Rev. ST Accel. Beams*, vol. 12, p. 030702, Mar 2009. [Online]. Available: <http://link.aps.org/doi/10.1103/PhysRevSTAB.12.030702>
- [10] L. Giannessi *et al.*, “Higher-order harmonics coupling in different free-electron laser codes,” *Nuclear Instruments and Methods in Physics Research Section A: Accelerators, Spectrometers, Detectors and Associated Equipment*, vol. 593, no. 1, pp. 143 – 147, 2008, fEL Frontiers 2007. [Online]. Available: <http://www.sciencedirect.com/science/article/pii/S0168900208006426>
- [11] G. Marcus *et al.*, “Fel code comparison for the production of harmonics via harmonic lasing,” in *Proceedings of the 2014 FEL Conference*, Basel, Switzerland, 2014.
- [12] E. Allaria *et al.*, “Highly coherent and stable pulses from the fermi seeded free-electron laser in the extreme ultraviolet,” *Nature Photonics*, vol. 6, no. 10, pp. 699–704, 2012. [Online]. Available: <http://www.nature.com/nphoton/journal/v6/n10/abs/nphoton.2012.233.html>
- [13] L. T. Campbell and B. W. J. McNeil, “Puffin: A three dimensional, unaveraged free electron laser simulation code,” *Physics of Plasmas*, vol. 19, no. 9, 2012. [Online]. Available: <http://scitation.aip.org/content/aip/journal/pop/19/9/10.1063/1.4752743>
- [14] S. Reiche, “{GENESIS} 1.3: a fully 3d time-dependent {FEL} simulation code,” *Nuclear Instruments and Methods in Physics Research Section A: Accelerators, Spectrometers, Detectors and Associated Equipment*, vol. 429, no. 1–3, pp. 243 – 248, 1999. [Online]. Available: <http://www.sciencedirect.com/science/article/pii/S016890029900114X>
- [15] S. Reiche, P. Musumeci, and K. Goldammer, “Recent upgrade to the free-electron laser code genesis 1.3,” in *Particle Accelerator Conference, 2007. PAC. IEEE*. IEEE, 2007, pp. 1269–1271.
- [16] F. Arecchi and R. Bonifacio, “Theory of optical maser amplifiers,” *IEEE Journal of Quantum Electronics*, vol. 1, no. 4, pp. 169–178, July 1965.
- [17] S. Reiche, “Update on the fel code genesis 1.3,” in *Proceedings of the 2014 FEL Conference*, Basel, Switzerland, 2014.
- [18] E. A. Schneidmiller and M. V. Yurkov, “A possible upgrade of flash for harmonic lasing down to 1.3 nm,” *Nuclear Instruments and Methods in Physics Research Section A: Accelerators, Spectrometers, Detectors and Associated Equipment*, vol. 717, pp. 37–43, 2013.
- [19] P. Rebernik Ribič *et al.*, “Echo-enabled harmonic generation studies for the fermi free-electron laser,” *Photonics*, vol. 4, no. 1, 2017. [Online]. Available: <http://www.mdpi.com/2304-6732/4/1/19>
- [20] Z. Huang *et al.*, “Suppression of microbunching instability in the linac coherent light source,” *Phys. Rev. ST Accel. Beams*, vol. 7, p. 074401, Jul 2004. [Online]. Available: <https://link.aps.org/doi/10.1103/PhysRevSTAB.7.074401>
- [21] D. Ratner *et al.*, “Time-resolved imaging of the microbunching instability and energy spread at the linac coherent light source,” *Phys. Rev. ST Accel. Beams*, vol. 18, p. 030704, Mar 2015. [Online]. Available: <https://link.aps.org/doi/10.1103/PhysRevSTAB.18.030704>

ECHO-ENABLED HARMONIC GENERATION RESULTS WITH ENERGY CHIRP

B. Garcia*, M.P. Dunning, C. Hast, E. Hemsing, T.O. Raubenheimer, SLAC, Menlo Park, USA
 D. Xiang, Shanghai Jiao Tong University, Shanghai, China

Abstract

We report here on several experimental results from the NLCTA at SLAC involving chirped Echo-Enabled Harmonic Generation (EEHG) beams. We directly observe the sensitivity of the different n EEHG modes to a linear beam chirp. This differential sensitivity results in a multi-color EEHG signal which can be fine tuned through the EEHG parameters and beam chirp. We also generate a beam which, due to a timing delay between the two seed lasers, contains both regions of EEHG and High-Gain Harmonic Generation (HGHG) bunching. The two regions are clearly separated on the resulting radiation spectrum due to a linear energy chirp, and one can simultaneously monitor their sensitivities.

INTRODUCTION

There has long been an interest in producing fully coherent X-ray pulses in free electron laser facilities. One promising direction is to seed the electron beam with microbunching structure at the desired wavelength. Two popular methods to do this use either a single modulator-chicane combination, as in High-Gain Harmonic Generation (HGHG) [1] [2], or a dual modulator-chicane setup as in Echo-Enabled Harmonic Generation (EEHG) [3] [4].

We report here the results from a chirped electron beam with simultaneous regions of HGHG and EEHG bunching. The two regions are clearly distinguished by their central wavelength shift [5] and sensitivity to the chirp on the electron beam.

We also directly observe the sensitivity of the different $|n|$ EEHG modes to the linear chirp. By establishing an EEHG configuration with non-negligible and simultaneous bunching at multiple $|n|$ modes, we measure the sensitivity of these modes by observing their wavelength shift as a function of electron beam chirp.

Both of these setups generate a tunable, multi-color EEHG-seeded beam. These experiments were performed in 2015 at SLAC's NLCTA facility, concurrent with work towards producing an EEHG beam capable of radiating at the 75th harmonic of a 2400 nm seed laser [6].

THE NLCTA FACILITY

The electron beam at NLCTA is generated from a 1.6 cell BNL/ANL/UCLA/SLAC S-band ($f = 2.856$ GHz) photocathode gun and is boosted by two subsequent X-band ($f = 11.424$ GHz) accelerating structures to 120 MeV. At this point, the beam has a FWHM duration of ≈ 1 ps, a

bunch charge of approximately 50 pC, and a small slice energy spread $\sigma_E \approx 1$ keV.

The beam then enters a modulating undulator (10 periods, $\lambda_u = 3.3$ cm, $K = 1.82$) where it interacts with an 800 nm (≈ 1 ps FWHM) laser. It then encounters a tunable four-dipole chicane before reaching a second modulating undulator (10 periods, $\lambda_u = 5.5$ cm, $K = 2.76$) where it interacts again with either a 800 nm or 2400 nm laser. The beam traverses a final magnetic chicane before being accelerated by a third X-band cavity which takes the energy to 160 – 192 MeV depending on the experiment. The beam finally enters a two-meter section of the VISA undulator [7] (100 periods, $\lambda_u = 1.8$ cm, $K = 1.26$) where any bunching produced by the upstream transformations is radiated as coherent radiation. This radiation is then diagnosed by a downstream EUV or VUV photon spectrometer [8].

SIMULTANEOUS EEHG AND HGHG SIGNALS

One difference between EEHG and HGHG signals is their response to a linear energy chirp. It has been shown that for the $n = -1$ EEHG mode and an HGHG configuration at the same target harmonic, the central wavelength of the HGHG setup is more sensitive to electron beam chirp than EEHG [5] [9]. This provides a powerful way of discriminating between EEHG and HGHG signals should both be present on the same electron beam.

In HGHG a single modulator produces a sinusoidal energy modulation of magnitude ΔE and at wavenumber k_1 which is converted into a density modulation by a chicane with longitudinal dispersion R_{56} . The resulting bunching is significant at integer harmonics of the laser wavenumber $k = ak_1$ and is [2],

$$b_a^{\text{HGHG}} = \left| e^{-\frac{1}{2}(B_1^2 a^2)} J_n(-aA_1 B_1) \right|, \quad (1)$$

where $A_1 = \Delta E_1 / \sigma_E$, $B_1 = R_{56}^{(1)} k_1 \sigma_E / E_0$. Notably, in order to increase the bunching at a higher harmonic, one must increase the modulation amplitude A_1 and hence the induced energy spread.

In EEHG, there are two chicanes and two separate laser modulators with possibly different laser wavenumbers and the relation $\kappa = k_2 / k_1$. This process produces bunching at wavenumbers $k_{n,m} = nk_1 + mk_2$ which is given by [3],

$$b_{n,m} = \left| e^{-\frac{1}{2}(nB_1 + aB_2)^2} J_n(nB_1 + aB_2) J_m(-aA_2 B_2) \right|, \quad (2)$$

where $a = n + m\kappa$. Analysis of this bunching spectrum reveals that the $n = -1$ harmonics can achieve the most significant bunching. The finely-spaced energy bands created

* bryantg@stanford.edu

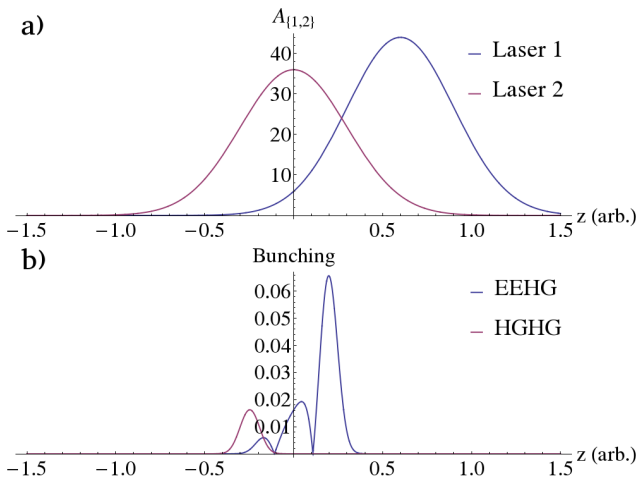


Figure 1: The EEHG and HGHG signals for Gaussian, temporally offset laser beams. Fig. a) shows the laser profiles, each of which is a Gaussian with $\sigma_z = 0.3$. Fig. b) shows the resulting bunching, both due to EEHG and HGHG showing clearly separated regions.

by the large first chicane in EEHG also allow high harmonics to be obtained with modest laser modulation amplitudes when compared with HGHG.

In order to generate a beam with both EEHG and HGHG signals, the temporal delay between the first and second modulation lasers can be adjusted. Due to this delay, there may exist a region of significant overlap between the two modulations, but also regions in which only the second laser is significant. This can create distinct regions in which the EEHG process is effective, and others in which the HGHG contribution dominates.

Since the usual definition of the bunching factor is global in nature, we instead use the notion of a local bunching factor defined as,

$$b(k, z_0, \delta_z) = \frac{1}{N_{e,z}} \left| \sum_{i=1}^{N_{e,z}} e^{ikz_i} \right|_{|z_0 - z_i| < \delta_z}, \quad (3)$$

where k is the wavenumber of interest and we are interested in a longitudinal region of size δ_z centered around the position z_0 which contains $N_{e,z}$ particles. This definition allows us to speak of a longitudinal position-dependent bunching factor, and identify the distinct regions of bunching.

We can employ the previous bunching analyses of Eqns. 1 and 2 by promoting the laser modulation amplitudes to local quantities: $A_{1,2} \rightarrow A_{1,2}(z)$, where $z = s - \beta ct$ is the intra-bunch longitudinal coordinate. Some care should be taken in interpreting this resulting bunching factor, as it assumes that the each individual subsegment at location z is infinite in longitudinal extent. However, as long as one is not concerned with the bandwidth of the resulting signals, and the typical length scale of change for $A_{1,2}(z)$ is significantly longer than the radiation wavelength it remains a reasonable approximation to consider.

To model the effect we consider a longitudinally infinite electron beam modulated by two lasers which are both Gaus-

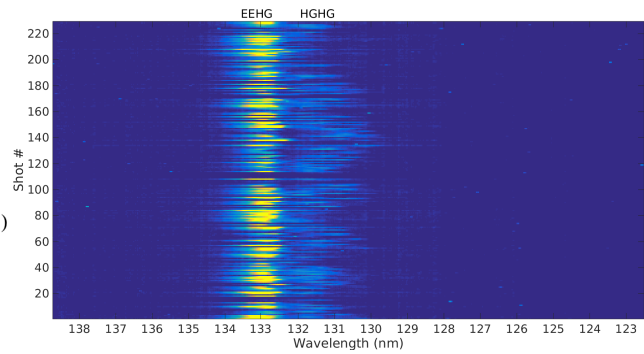


Figure 2: Simultaneous EEHG and HGHG signals in the vicinity of 133 nm. Both signals represent the 18th harmonic of the 2400 nm seed laser.

sian in temporal extent with scaled length $\sigma_z = 0.3$. The peak modulation amplitudes are $A_1 = 44$ and $A_2 = 36$, and the centers are offset by a scaled distance of $\Delta z = 0.6$. These laser profiles are shown in Fig. 1 a). The scaled dispersions are set to $B_1 = 0.818$ and $B_2 = 0.13$. The resulting bunching spectrum, both due to EEHG and HGHG contributions, is shown in Fig. 1 b). The bunching is computed assuming a laser wavenumber ratio $\kappa = 1/3$ and $n = -1$, $m = 21$.

In the region of significant laser overlap, a strong EEHG signal is established. However, in the region $z \approx -0.4$ only the second laser is relevant and this allows a pure HGHG signal to exist in there.

This situation was approximately recreated at the NLCTA with a final beam energy of $E \approx 184$ MeV and using two lasers of wavelengths $\lambda_1 = 800$ nm and $\lambda_2 = 2400$ nm. An EEHG signal was established in the neighborhood of the 18th harmonic, or 133 nm, and then the lasers de-tuned in time to create the distinct regions of bunching. The resulting spectrum across 220 separate shots (≈ 22 seconds) is shown in Fig. 2. The chicanes were set to $R_{56}^{(1)} = 12.5$ mm and $R_{56}^{(2)} = 2$ mm to give $B_1 = 0.818$ and $B_2 = 0.130$.

The magnitude of the linear chirp can be quantified by scaled parameter $h_1 = \frac{1}{k_1} \frac{dp_0}{dz} |_{z=0}$ [9]. The separation in wavelengths due to this linear chirp ($h_1 \approx -0.144$ from HGHG, $h_1 \approx 1.18$ from EEHG) imparted to the electron beam prior to modulation in one of the accelerating structures. Note the differing signs of h_1 imply that the EEHG and HGHG signals were established on the oppositely chirped sides of the electron beam. Due to the particular EEHG configuration, however, both harmonics blue shift in the presence of these chirps.

This observation is similar to the EEHG and HGHG plots shown in [10], and is an extension into the high-harmonic regime of the initial HGHG/EEHG results [11]. This result suggests the possibility of manipulating the modulation envelopes of the lasers to create and control distinct areas of bunching for potential use in multi-color FEL applications.

MULTI-COLOR EEHG EFFECTS

Multi-color operation modes are possible not only in a mixed HGHG-EEHG beam configuration, but also within

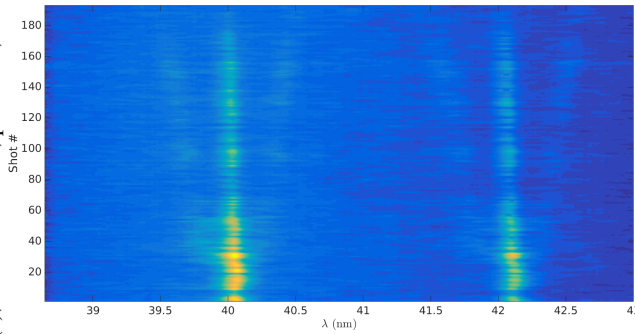


Figure 3: The splitting of the main echo peaks due to an increase in linear chirp. The shot number is correlated with RF phase increase such that the difference between shot 0 and 200 is approximately 15 degrees in RF phase (for the first RF structure).

one which is purely EEHG. This possibility again comes about due to the sensitivity to linear energy chirp on the electron beam. This linear chirp has the effect of shifting the echo harmonic a for a given echo configuration to the location [5],

$$a' = \frac{n + mk(1 + h_1 B_1)}{1 + h_1 B_1}. \quad (4)$$

This central wavelength shift is dependent on the particular mode numbers n, m . We therefore conclude that EEHG configurations with different values for $|n|$, although nominally at the same wavelength for $h_1 = 0$, will not overlap in the case of nonzero electron beam chirp. In particular, for a mode with n offset Δn ,

$$a(n + \Delta n) = a(n) - \Delta n \frac{h_1 B_1}{1 + h_1 B_1}. \quad (5)$$

It is possible to choose EEHG parameters such that there exists significant simultaneous bunching due to multiple n modes. As an electron beam chirp is applied, these initially degenerate modes will split into several sub-peaks depending on the magnitude of chirp and which $|n|$ modes are excited.

To test this idea at NLCTA, we used an EEHG configuration for Echo-20 at 40 nm. The dispersions were set as $R_{56}^{(1)} = 12.5$ mm and $R_{56}^{(2)} \approx 0.57$ mm, and the final beam energy for was 162 MeV. The RF phase in the first accelerating structure, which provides an approximate 60 MeV energy boost, was adjusted by approximately 15 degrees of phase over the course of 20 seconds, or 200 shots. The resulting spectrum in the vicinity of 40 nm is shown in Fig. 3.

Comparing the shift in the central wavelength of the $n = -1$ harmonic and Eqn. 4 gives $h_1 B_1 \approx 0.27$ by around the 170th shot. The in the shift of the $n = -1$ mode implies a positive electron beam chirp ($h_1 > 0$) for these EEHG parameters, although an optimal configuration with higher B_1 would respond oppositely to the same chirp [9].

We observe that as the RF phase is increased, two distinct sidebands form and move away from the central $n = -1$ peak. Numerical simulations of this EEHG setup show that

the approximate maximum for the $n = -1, m = 21$ echo bunching of $\approx 7.5\%$ is given when $A_1 \approx 25$ and $A_2 \approx 31$, which is consistent with the measured values of the laser modulations. In this configuration, there is nonzero bunching in the $n = -2, m = 22$ and $n = 0, m = 20$ modes at approximately the 1-2% level, while all other modes have bunching at $< 0.1\%$ and are not visible. From Eqn. 5, the $n = 0$ and $n = -2$ modes shift with opposite sign and equal magnitude away from the central peak, which gives rise to the equally spaced sidebands visible in Fig. 3. The magnitude of these shifts are consistent with the determination of $h_1 B_1 = 0.27$ from the central peak.

In this particular configuration, the magnitude of the sideband bunchings are approximately equal, however this need not be the case. For example, choosing instead $A_2 = 34$ leaves a non-negligible subsidiary bunching factor only in the $n = -2$ and $n = -1$ modes which would result in an asymmetric sideband spectrum.

DISCUSSION

The techniques demonstrated here both rely on a chirped electron beam which is then seeded via EEHG. Multicolor signals can be produced either through the simultaneous production of regions of EEHG and HGHG bunching, or through the generation of significant bunching at multiple $|n|$ modes.

While the techniques demonstrated here merely generated multi-color coherent emission, ultimately one would like to seed an FEL. In order to amplify multiple colors in an FEL the separate colors must be separated from the resonant wavelength by $\Delta\lambda/\lambda \lesssim \rho$. To take a numerical example, consider an EEHG-seeded EUV FEL with $\rho = 10^{-3}$, $\sigma_E = 100$ keV, and lasers with $\lambda_1 = \lambda_2 = 266$ nm operating at the 50th harmonic (5.32 nm). Full control of the $n = -1$ optimized wavelength within the FEL bandwidth could be obtained by a zero-crossing X-band cavity with power to provide a 100 MeV on-crest increase in beam energy.

It therefore seems plausible that the electron beam chirp could be used to create tunable, multi-color pulses at a full FEL facility. Dedicated studies with a zero-crossing RF cavity would provide an excellent test bed to examine in more depth the effects presented in this paper.

ACKNOWLEDGMENTS

This work was supported in part by the U.S. Department of Energy under Contract No. DE-AC03-76SF00515 and the Stanford University Bob Siemann Fellowship in Accelerator Physics.

REFERENCES

- [1] I. Ben-Zvi *et al.*, "Proposed uv fel user facility at bnl," *Nuclear Instruments and Methods in Physics Research Section A: Accelerators, Spectrometers, Detectors and Associated Equipment*, vol. 304, no. 1, pp. 181 – 186, 1991. [Online]. Available: <http://www.sciencedirect.com/science/article/pii/016890029190845H>

- [2] L. H. Yu, "Generation of intense uv radiation by subharmonically seeded single-pass free-electron lasers," *Phys. Rev. A*, vol. 44, pp. 5178–5193, Oct 1991. [Online]. Available: <http://link.aps.org/doi/10.1103/PhysRevA.44.5178>
- [3] G. Stupakov, "Using the beam-echo effect for generation of short-wavelength radiation," *Phys. Rev. Lett.*, vol. 102, p. 074801, Feb 2009. [Online]. Available: <http://link.aps.org/doi/10.1103/PhysRevLett.102.074801>
- [4] D. Xiang and G. Stupakov, "Echo-enabled harmonic generation free electron laser," *Phys. Rev. ST Accel. Beams*, vol. 12, p. 030702, Mar 2009. [Online]. Available: <http://link.aps.org/doi/10.1103/PhysRevSTAB.12.030702>
- [5] Z. Huang *et al.*, "Effects of energy chirp on echo-enabled harmonic generation free-electron lasers," in *Proceedings of the 31st International Free Electron Laser Conference (FEL 09)*, Liverpool, UK, STFC Daresbury Laboratory, 2009.
- [6] E. Hemsing *et al.*, "Echo-enabled harmonics up to the 75th order from precisely tailored electron beams," *Nature Photonics*, 2016.
- [7] R. Carr *et al.*, "Visible-infrared self-amplified spontaneous emission amplifier free electron laser undulator," *Phys. Rev. ST Accel. Beams*, vol. 4, p. 122402, Dec 2001. [Online]. Available: <http://link.aps.org/doi/10.1103/PhysRevSTAB.4.122402>
- [8] B. Garcia *et al.*, "Facility upgrades for the high harmonic echo program at slac's nlcta," in *Proceedings of the 2015 FEL Conference*, Daejeon, Korea, 2015.
- [9] E. Hemsing *et al.*, "Sensitivity of echo enabled harmonic generation to sinusoidal electron beam energy structure," *Phys. Rev. Accel. Beams*, vol. 20, p. 060702, Jun 2017. [Online]. Available: <https://link.aps.org/doi/10.1103/PhysRevAccelBeams.20.060702>
- [10] E. Hemsing *et al.*, "Highly coherent vacuum ultraviolet radiation at the 15th harmonic with echo-enabled harmonic generation technique," *Phys. Rev. ST Accel. Beams*, vol. 17, p. 070702, Jul 2014. [Online]. Available: <http://link.aps.org/doi/10.1103/PhysRevSTAB.17.070702>
- [11] D. Xiang *et al.*, "Demonstration of the echo-enabled harmonic generation technique for short-wavelength seeded free electron lasers," *Phys. Rev. Lett.*, vol. 105, p. 114801, Sep 2010. [Online]. Available: <http://link.aps.org/doi/10.1103/PhysRevLett.105.114801>

DISTRIBUTED SELF-SEEDING SCHEME FOR LCLS-II*Chuan Yang^{1,2†}, Juhao Wu^{1‡}, Guanqun Zhou^{1,3}, Bo Yang⁴,
Cheng-Ying Tsai¹, Moohyun Yoon^{1,5}, Yiping Feng¹, Tor Raubenheimer¹¹SLAC National Accelerator Laboratory, Menlo Park, California, USA²NSRL, University of Science and Technology of China, Hefei, Anhui, China³Institute of High Energy Physics, and UCAS, Chinese Academy of Sciences, Beijing, China⁴University of Texas at Arlington, Arlington, Texas, USA⁵Department of Physics, Pohang University of Science and Technology, Pohang, Korea**Abstract**

Self-seeding is a successful approach for generating high-brightness X-ray free electron laser (XFEL). A single-crystal monochromator in-between the undulator sections to generate a coherent seed is adopted in LCLS. However, for a high-repetition rate machine like LCLS-II, the crystal monochromator in current setup cannot sustain the high average power; hence a distributed self-seeding scheme utilizing multi-stages is necessary. Based on the criteria set on the crystal, the maximum allowed X-ray energy deposited in the crystal will determine the machine configuration for such a distributed self-seeding scheme. In this paper, a distributed self-seeding configuration is discussed for LCLS-II type projects in the hard X-ray FEL energy regime. The study is carried out based on numerical simulation.

INTRODUCTION

Linac Coherent Light Source (LCLS), the world's first hard X-ray FEL has been successfully operated in SASE mode [1]. Conventional SASE FEL has full transverse coherence, but the longitudinal coherence is limited [1,2]. In order to improve the longitudinal coherence, self-seeding scheme has been proposed [3]. A self-seeding X-ray FEL consists of two undulator sections separated in a drift section by a monochromator and an electron by-pass chicane. A grating monochromator was adopted for the soft X-ray [3], while a single crystal monochromator oriented in Bragg transmission geometry can be used for the hard X-ray [4]. The radiation generated by the first undulator section and the electron beam are separated in the drift section between the two undulator sections. The radiation passes through the monochromator, which can filter the radiation spectrum. The electron beam passes through the chicane, which washes out the micro-bunching induced by the first undulator section and delays the electron beam relative to the radiation pulse. The purified radiation and the electron beam are recombined at the entrance of the second undulator section, through which the radiation is amplified up to saturation.

The operation of self-seeding has been successfully achieved at LCLS, in which the repetition rate is 120 Hz.

However, LCLS-II FEL project is designed to operate at a higher repetition rates of 0.93MHz. In this case, the heat load on the monochromator will become an issue and limit the maximal seed power. The multi-stages self-seeding scheme can generate higher spectral purity, which can reduce the heat load of the monochromator.

For the LCLS-II hard X-ray self-seeding (HXRSS) baseline undulator system, there will be two 'missing segments' after segment 7 and 14, which are reserved for self-seeding station shown in Fig. 1. This two-stages self-seeding configuration was considered for the photon energy range of (4 keV~8 keV). In this paper, we study the two-stage self-seeding configuration for LCLS-II project with GENESIS simulation code [5] for 4 keV and 8.3 keV hard X-ray with LCLS-II parameters. All the data refer to single shot realization.

Table 1: The Relevant Parameters used in 4keV and 8.3keV Simulation.

Parameters	Value	Unit
Electron beam energy	4.0/8.0	GeV
Energy spread	0.5	MeV
Peak current	1/3	kA
Normalized emittance	0.45	mm-mrad
FEL photon energy	4/8.3	keV
Charge	100/300	pC
Undulator parameter K	0.96/1.91	-
Undulator period	2.6	cm
Number of period per undulator section	130	-
Total number of sections	32	-
Drift length	1.17	m

NUMERICAL SIMULATION*4-keV Self-Seeding Simulation*

Here we focus on 4keV self-seeding simulation to study LCLS-II HXRSS project in the low photon energy range. The baseline undulator system is shown in Fig. 1. Relevant simulation parameters are presented in Table 1. We assume that the average betatron function is 17.0 m. In the two monochromators, we choose symmetric diamond C(111) crystal to generate the wake seed, and the crystal thickness is 30 μm . The two crystal monochroma-

*The work was supported by the US Department of Energy (DOE) under contract DE-AC02-76SF00515 and the US DOE Office of Science Early Career Research Program grant FWP-2013-SLAC-100164.

†chuany@SLAC.Stanford.EDU

‡jhwu@SLAC.Stanford.EDU

tors act as bandstop filters for the radiation pulse. The modulus and the phase of the crystal transmissivity shown in Fig. 2 are calculated with the help of xop.2.4 [6] and Kramers–Kronig relations [7,8].

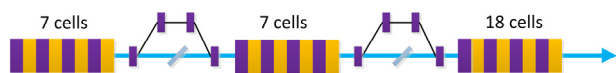


Figure 1: Design of LCLS-II hard X-ray baseline undulator system including two ‘miss undulators’ which are reserved for self-seeding operation.

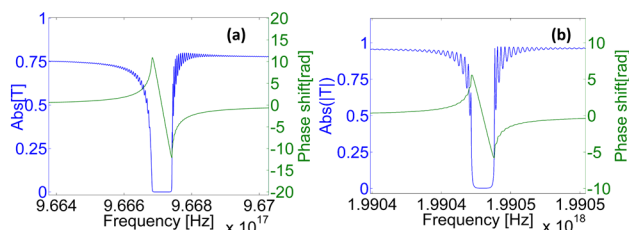


Figure 2: (a) Modulus and phase of transmissivity for symmetric C(111) Bragg reflection from perfect diamond crystal at 4keV. (b) Modulus and phase of transmissivity for symmetric C(400) Bragg reflection from perfect diamond crystal at 8.3 keV.

The spectrum and power at the end of the 7th undulator section are shown in Fig. 3 (a) and (b). Figures 3 (c) and (d) show the spectrum and the wake seed after the first crystal. The bunch, with flat top length about 28 μm , overlap with the wake seed in the red window as in the Fig. 3 (d).

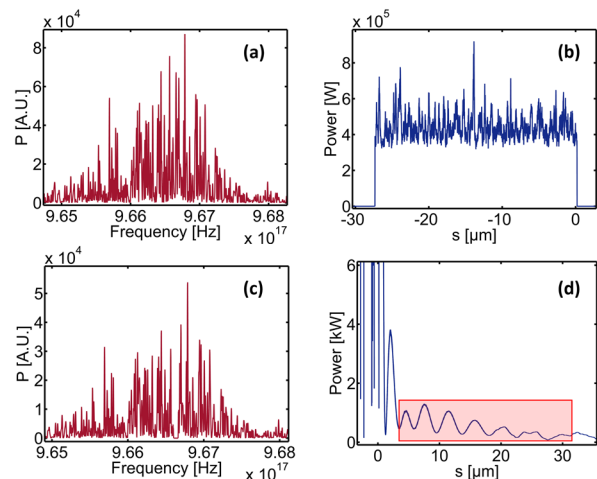


Figure 3: (a) The spectrum before the first crystal. (b) The power before the first crystal. (c) The spectrum after the first crystal. (d) The power after the first crystal. The red window is the overlap region for the electron beam and the wake seed.

The seed is amplified in the second undulator section and then impinges on the second crystal monochromator. The spectrum and power before the second crystal shown

in Fig. 5. The spectrum and power after the second crystal is shown in Fig. 6.

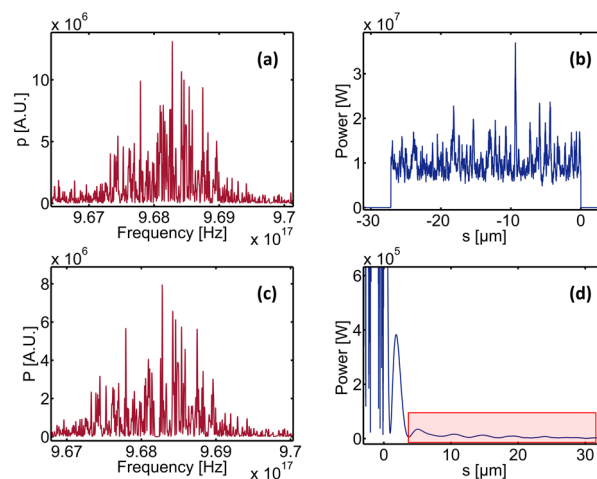


Figure 4: (a) The spectrum before the second crystal. (b) The power before the second crystal. (c) The spectrum after the second crystal. (d) The power after the second crystal. The red window is the overlap region for the electron beam and the wake seed.

After the second crystal, the seed is amplified to saturation in the final undulator section. The output spectrum and power are shown in Figure 5. The energy per pulse impinging on the second crystal is about 0.8 μJ , and the transverse rms of the electron bunch is 50 μm . The angle between the X-ray and the crystal surface is 48.8°. Therefore, the average power density is close to 80 W/mm^2 .

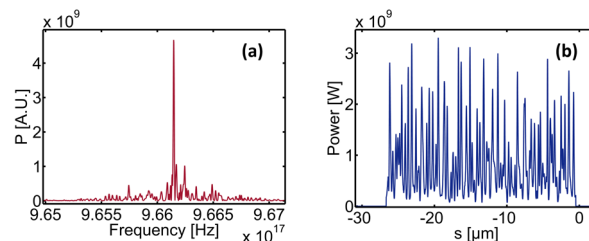


Figure 5: The spectrum (a) and power (b) at the end of the final undulator section.

According to the simulation, the seed power after the first crystal is about 1.2 kW shown in Fig. 3 (d), which is not enough to dominate over the shot noise power. In other words, the location of the first crystal may not be suitable for the 4keV case. Therefore we move the first crystal to the later locations to the end of the 13th undulator section Fig. 6. The average power density on the crystal is about 100 W/mm^2 per second [9]. This number is one order of magnitude smaller than the average power density at the first monochromator of third generation synchrotron radiation sources.

For the crystal at the new location, the spectrum and power before the crystal are shown in Fig. 7 (a), (b). The spectrum and wake seed after the crystal are shown in

Content from this work may be used under the terms of the CC BY 3.0 licence (© 2018). Any distribution of this work must maintain attribution to the author(s), title of the work, publisher, and DOI.

Fig. 7 (c), (d). The seed power is about 170 kW, now enough to dominate over the shot noise power. At the end of the final undulator section, we get a purify pulse with $\Delta\omega/\omega_0 = 7 \times 10^{-5}$ bandwidth shown in Fig. 8 (a), which has a comparable bandwidth with the two stage case.

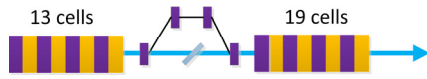


Figure 6: The assumed configuration of LCLS-II HXSS in the low photon energy range.

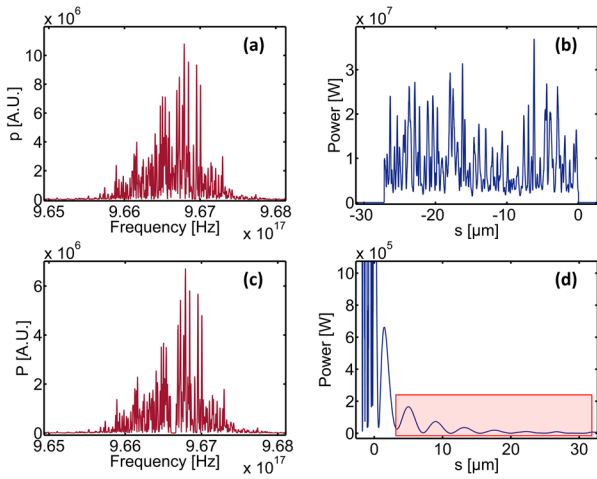


Figure 7: (a) The spectrum before the crystal. (b) The power before the crystal. (c) The spectrum after the crystal. (d) The power after the crystal. The red window is the overlap between the electron beam and the wake seed.

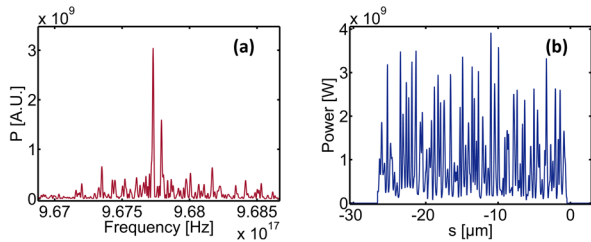


Figure 8: The spectrum (a) and power (b) at the end of the final undulator section.

8.3-keV Self-Seeding Simulation

For the high repetition rate (0.93 MHz) LCLS-II-HE high energy range, we focus on 8.3keV self-seeding simulation. The optimization of electron beam line is still on going. The assumed simulation parameters here are shown in Table 1. We assume that the average betatron function is 20.0 m. The symmetric diamond C(400) crystal is chosen to generate the wake seed, and the crystal thickness is 50 μm . The modulus and the phase of the crystal transmissivity are shown in Fig. 2 (b). The spectrum and power distribution at the end of final undulator section are shown in Fig. 9 (a), (b). The energy per pulse

impinging on the second crystal is about 50 μJ , and the transverse rms of the electron bunch is 25 μm . The angle between the X-ray and the crystal surface is 56.89° . According to the simulation result, the average power density at the second crystal is close to 11 kW/mm^2 (Fig. 10), two orders of magnitudes higher than the average power density on the crystal at third generation synchrotron radiation. This power density has exceeded the threshold. One way to resolve this heat load issue is to decrease the repetition rate to tens of kHz.

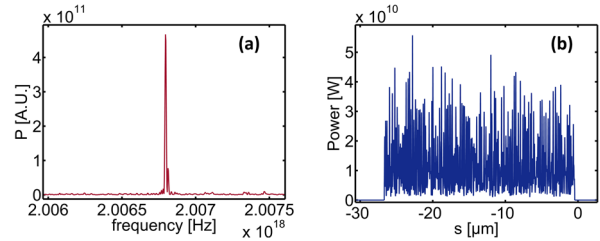


Figure 9: The spectrum (a) and power (b) at the end of the final undulator section.

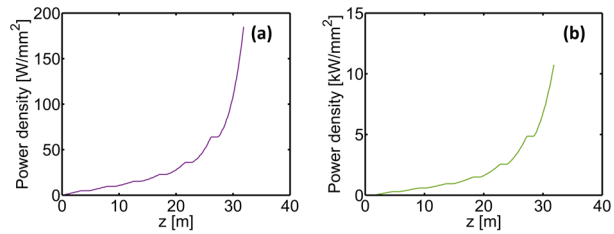


Figure 10: (a) Power density along z in the first undulator section. (b) Power density along z in the second undulator section.

SUMMARY

For the high repetition rate FEL like LCLS-II, heat load will determine the location of monochromator. For different photon energy range and different repetition machine, the optimal undulator system configuration is different. In the low energy range of LCLS-II HXRSS, from the preliminary numerical simulation above, the designed baseline of undulator system is not optimal. That is, the first monochromator after 7th undulator section is placed too early, where the seed power after the monochromator is not enough to dominate over the shot noise power within the gain bandwidth. Therefore, the location of the crystal may be after the 13th undulator section. In this new configuration, one stage self-seeding is sufficient to generate a purify spectrum. In the high-energy range of LCLS-II HXRSS, if based on the baseline design and the assumed simulation parameters in Table 1, the allowed operating repetition rate of self-seeding is in tens of kHz. We have present a preliminary simulation in this paper, more dedicated simulation work is in progress.

REFERENCES

- [1] Emma, P. *et al.*, “First lasing and operation of an angstrom-wavelength free-electron laser” *Nat. Photon.*, **4**, p. 641-647 (2010).
- [2] Altarelli, M. *et al.*, The European X-ray Free -Electron Laser, Technical Design Report, DESY 2006 -097, Hamburg (2006).
- [3] Feldhaus J. *et al.*, “Possible application of X-ray optical elements for reducing the spectral bandwidth of an X-ray SASE FEL”, *Optics. Comm.*, **140**, 341 (1997).
- [4] Gianluca G., Vitali K., and Evgeni S., “A novel self-seeding scheme for hard X-ray FELs”, *J. Mod. Opt.*, **58**, 1391(2011).
- [5] Reiche, S., *Nucl. Instrum. Methods Phys. Res., Sect. A* **429**, 243–248 (1999).
- [6] ESRF. X-ray Oriented Programs Software Package. <https://www1.aps.anl.gov/Science/Scientific-Software/XOP>
- [7] Kramers, H.A., La diffusion de la lumiere par les atomes. *Attidel Congresso Internazionale dei Fisici*; Zanichelli: Bologna, **2**, 545–557 (1927).
- [8] Kronig, R.; de, L., “On the Theory of Dispersion of X-Rays” *J. Opt. Soc. Am.* **12**, 547–557 (1926).
- [9] Gianluca G., *et al.*, “Production of transform-limited X-ray pulses through self-seeding at the European X-ray FEL”, DESY 11-165, September 2011.

TRANSIENT THERMAL STRESS WAVE ANALYSIS OF A THIN DIAMOND CRYSTAL UNDER LASER HEAT LOAD*

Bo Yang[†], Department of Mechanical & Aerospace Engineering, University of Texas at Arlington, Arlington, TX 76019, USA

Juhao Wu[‡], SLAC National Accelerator Laboratory, Menlo Park, California, 94025, USA

Abstract

When a laser pulse impinges on a thin crystal, energy is deposited resulting in an instantaneous temperature surge in the local volume and emission of stress waves. In the present work, we perform a transient thermal stress wave analysis of a diamond layer 200 μm thick in the low energy deposition per pulse regime. The layer thickness and laser spot size are comparable. The analysis reveals the characteristic non-planar stress wave propagation. The stress wave emission lasts by hundreds of nanoseconds, at a time scale relevant to the high-repetition-rate FELs at the megahertz range. The kinetic energy converted from the thermal strain energy is calculated, which may be important to estimate the vibrational amplitude of the thin crystal when excited under repeated heat loads. The transient heat transfer plays an important role in draining the mechanical energy during the dynamic wave emission process.

INTRODUCTION

Thin crystals play an important role in enabling X-ray FELs of high peak-brightness, Angstrom wavelengths, and femtosecond/sub-femtosecond pulse durations [1]. They are used as monochromator for self-seeding [2,3] and one-shot spectrometer [4-6], for example. To function properly, they must be able to sustain the ever-increasing heat load, especially from multiple pulses at high repetition rates. When a high-intensity light pulse strikes a crystal, energy is deposited through photon-electron interaction. The energy is further passed on to the lattice. It results in a temperature surge over the volume on its way of passage. It is speculated that the deposited thermal strain energy would trigger stress waves. The dynamic strain field may directly affect the optics performance. The stress wave emission may also convert a part of the deformation energy into kinetic energy. When cumulated near a resonant frequency, it may lead to severe vibration impairing the device steadiness.

In the present work, we perform a transient thermal stress wave analysis to elucidate the dynamics of stress wave emission in a thin diamond crystal under heat load of an X-ray FEL pulse. The equation of motion and the equation of energy conservation are solved together for both transient stress wave propagation and transient heat transfer. Although the mechanical deformation process does not affect much the heat transfer process, their coupling is im-

portant to reveal how the initial thermal strain energy is relaxed, i.e., partially to the kinetic energy, and partially back to the thermal energy. The case from Ref. 7 is (re-)examined. The diamond crystal thickness is 200 μm . The laser spot size is about twice the thickness. The absorption rate is adjusted such that the initial temperature rise is less than 2 K at the center of the Gaussian beam, in the low energy deposition regime. The problem is numerically solved by applying a finite volume method. The analysis reveals the characteristic non-planar stress wave propagation. While the deformation energy stored in the radial normal strain component is released in part through radial longitudinal and surface stress waves, that stored in the through-thickness normal strain component is depleted by emitting radial longitudinal stress waves due to Poisson's effect. This latter emission process lasts by hundreds of nanoseconds, at a time scale relevant to the high-repetition-rate FELs at the megahertz range. The resulting kinetic energy is calculated, which may be important to estimate the vibrational amplitude of the thin crystal when excited under repeated heat loads. The transient heat transfer plays an important role in draining the mechanical energy during the dynamic thermal stress wave emission process.

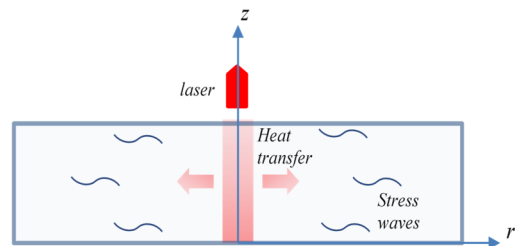


Figure 1: Schematic showing instantaneous heating and subsequent stress wave emission and heat transfer upon laser energy deposition in a thin crystal layer. The cylindrical coordinate system with axisymmetry is established.

PROBLEM FORMULATION

Consider an X-ray FEL impinging on a thin crystal, as schematically shown in Fig. 1. It interacts with the electrons and deposits a part of its energy first onto the electrons [8]. Later the energy is transferred to the lattice raising the local temperature. Then, the thermalized lattice expands dynamically emitting stress waves. The thermal diffusion begins at the same time. We aim to analyse the process of transient thermal stress wave emission. A cylindrical coordinate system (r, θ, z) is established with z -axis normal to the crystal surface. Only a laser beam perpendicular to the crystal surface is considered.

* Work supported by the US Department of Energy (DOE) under contract DE-AC02-76SF00515 and the US DOE Office of Science Early Career Research Program grant FWP-2013-SLAC-100164.

[†] boyang@uta.edu

[‡] jhwu@slac.stanford.edu

The equation of motion in the absence of body forces is given by:

$$\rho \frac{dv}{dt} = \nabla \cdot \boldsymbol{\sigma}, \quad (1)$$

where ρ is the mass density, $\mathbf{v}(=d\mathbf{u}/dt)$ is the velocity, \mathbf{u} is the displacement, $\boldsymbol{\sigma}$ is the stress tensor, and t is time. Assuming the isotropic thermoelasticity, the constitutive law is given by:

$$\boldsymbol{\sigma} = 2G \left(\boldsymbol{\varepsilon} - \frac{1}{3} \text{tr}(\boldsymbol{\varepsilon}) \mathbf{I} \right) + 3K_b \left(\frac{1}{3} \text{tr}(\boldsymbol{\varepsilon}) - \varepsilon_T \right) \mathbf{I}, \quad (2)$$

where G is the modulus of rigidity, K_b is the bulk modulus, $\boldsymbol{\varepsilon}$ is the strain tensor, ε_T is the thermal strain, \mathbf{I} is the identity matrix, and $\text{tr}(\boldsymbol{\varepsilon})$ denotes the trace of $\boldsymbol{\varepsilon}$.

The equation of energy conservation is given by:

$$\frac{d(U_T + U_\varepsilon)}{dt} = -\nabla \cdot (-\kappa \nabla T) + \boldsymbol{\sigma} : \nabla \mathbf{v}, \quad (3)$$

where T is the temperature, $U_T(= \int \rho C_v dT)$ is the thermal energy density, $U_\varepsilon(= (1/2) \boldsymbol{\sigma} : (\boldsymbol{\varepsilon} - \varepsilon_T \mathbf{I}))$ is the elastic strain energy density, κ is the thermal conductivity, C_v is the specific heat. On the right-hand side, the first term is the heat transfer according to Fourier's law. The second term is the rate of work done by the stress through a velocity field.

The initial displacement and velocity fields are both set equal to zero: $\mathbf{u}_0 = 0$, and $\mathbf{v}_0 = 0$. The initial temperature field is set at $T_0 = 300$ K. Upon a Gaussian laser pulse, the laser energy is partially absorbed raising the temperature on the way of its passage. The change of thermal energy density as a function of r and z is given by:

$$\Delta U_T(r, z) = \frac{2I_0}{\pi a^2 L} e^{-\frac{2r^2}{a^2}} e^{-\frac{z}{L}}, \quad (4)$$

where I_0 is the laser pulse energy, a is the transverse FWHM of the Gaussian beam along the radial direction, and L is the attenuation length. The corresponding temperature increase is determined from the relationship of U_T to T , which is generally a nonlinear function.

At the plate edge boundary, the fixed boundary condition is applied. The temperature is held at 300 K at all times.

In the following study, since the heat load is low, the material parameters are all nearly constant. Yet, the general nonlinear properties, including the thermal strain and specific heat [9] and the thermal conductivity [10], are used. One may refer to Ref. 11 for the details.

RESULTS AND DISCUSSION

Simulation was run for transient thermal stress wave analysis with thickness $h = 200 \mu\text{m}$, laser spot size $a = 350 \mu\text{m}$, and plate radius = 1.5 mm. Only a single pulse input is examined, with pulse energy $I_0 = 70 \mu\text{J}$ and attenuation length $L = 380 \mu\text{m}$ [7]. Fifty-one equal divisions are used to discretize the domain in the thickness direction. An adaptive mesh is used in the radial direction. 70 equal divisions are used in near $175 \mu\text{m}$ distance, and 300 unequal divisions with increasing size by gradient 1.003 in following $1325 \mu\text{m}$ distance. The time step is 0.1 ns. The stress

waves would propagate by $< 2 \mu\text{m}$ in space each time step, smaller than the spatial grid size. Since we use an implicit finite difference scheme for time integration, the solution is unconditionally stable. The simulation is terminated at $t = 400$ ns. Selected results are plotted in Figs. 2–4.

Figure 2 shows some snapshots of the fields at $t = 1, 5, 10, 20,$ and 60 ns. In the left column (a)–(e), the 3D surface plot is used to show velocity component v_z , and the contour plot with a color code at the base to indicate strain component ε_{zz} . In the right column, correspondingly velocity component v_r , and strain component ε_{rr} are shown. Figure 3 shows the time histories of the total deformation energy, $\int_V U_\varepsilon dV$, the total kinetic energy $\int_V \frac{1}{2} \rho \mathbf{v} \cdot \mathbf{v} dV$, and the change of thermal energy, $\int_V (U_T - U_{T0}) dV$, where V is the domain and U_{T0} is the initial thermal energy density upon the laser energy deposition. The r - and z -components of kinetic energy, $\int_V \frac{1}{2} \rho v_r^2 dV$ and $\int_V \frac{1}{2} \rho v_z^2 dV$, are also calculated, which represents the wave activity in the two corresponding directions, respectively. Figure 4 shows the time evolution of temperature at three different radial distances $r = 0, 175$ and $350 \mu\text{m}$ on the front and back surfaces

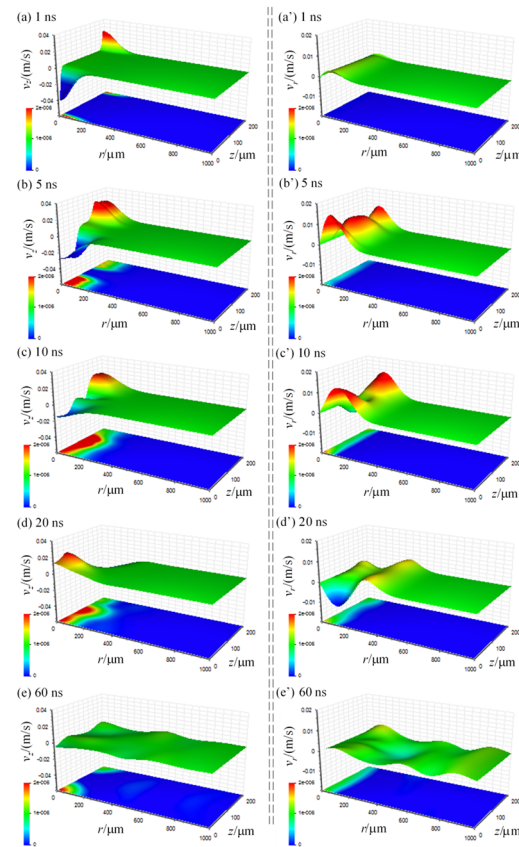


Figure 2: Snapshots of stress wave emission at various moments: (a,a') 1 ns; (b,b') 5 ns; (c,c') 10 ns; (d,d') 20 ns; (e,e') 60 ns. In the left column, the 3D profiles show the field of velocity component v_z , and the contour plots with a color code at the base indicate the field of strain component ε_{zz} . In the right column, correspondingly velocity component v_r , and strain component ε_{rr} are shown.

Content from this work may be used under the terms of the CC BY 3.0 licence (© 2018). Any distribution of this work must maintain attribution to the author(s), title of the work, publisher, and DOI.

$z = 0$ and $200 \mu\text{m}$. At $r = 350 \mu\text{m}$, the temperature change is trivial up to the time of 400 ns calculated.

In this case, about 41 % of the laser energy, i.e., $28.6 \mu\text{J}$ out of $70 \mu\text{J}$, is deposited into the diamond. Since it is over a relatively large area, the maximum temperature increase at the center of entry surface is only 1.83 K . Correspondingly, the wave fields are of low magnitude. Although the magnitudes are small, the characteristics of the transient heat transfer and stress wave emission are similar to those observed in a much concentrated case [11].

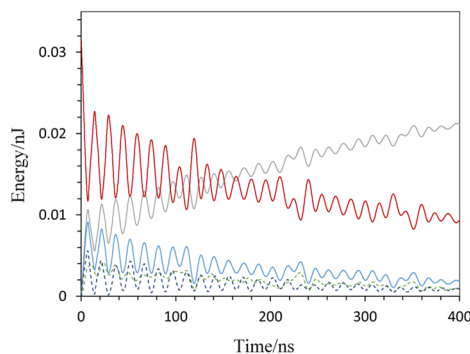


Figure 3: Time histories of thermal energy change (grey solid), deformation energy (red solid), and total (blue solid), r-portion (green dashed) and z-portion (purple dashed) of kinetic energy in a diamond plate upon a single-pulse laser input.

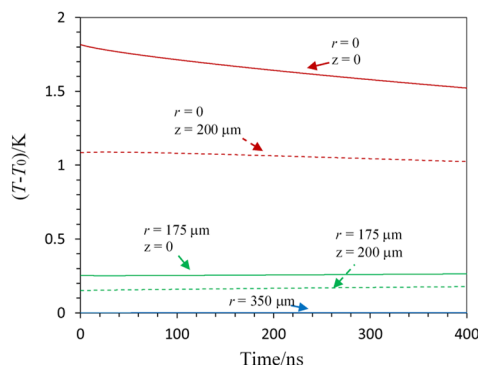


Figure 4: Time histories of temperature at three different distance $r = 0, 175, 350 \mu\text{m}$ on the front surface ($z = 0$, solid) and back surface ($z = 200 \mu\text{m}$, dashed) in a diamond plate upon a single-pulse laser input.

As seen in Fig. 2, the radial thermal strain component triggers radial dilatational waves and Rayleigh surface waves radiating away from the center. In contrast, the wave activity due to the transverse thermal strain component is much more complicated. First, this component of thermal strain induces through-thickness longitudinal stress waves bouncing back and forth between the surfaces. Second, since the heated zone is finite, this mode of wave propagation experiences constraint of particles still cool at the boundary. Due to Poisson's effect, the dynamic transverse

normal straining (i.e., a breathing mode) induces compression and tension in the radial direction, emitting radial longitudinal stress waves. This is the main mechanism depleting the energy stored in the transverse normal strain component away from the heated site. The bumps following the front wave in Fig. 2(e') are due to this mechanism.

The oscillation of an energy term in Fig. 3 is due to the transverse wave activity. Since the diamond layer is thick compared to the lateral size, the waves have reached the boundary and been reflected a few times during the period of time calculated, as seen roughly every 110 ns in Fig. 3. After 400 ns , the temperature in the center of the hot zone has dropped by about 15 %. Importantly, it is seen in Fig. 3 that a significant portion of the mechanical energy is being converted back to thermal energy. Only a small part is converted to kinetic energy, which however, if cumulated, may cause vibrational problem when the layer is excited.

SUMMARY

An exemplary case of a thin diamond layer $200 \mu\text{m}$ thick is analysed in the low energy deposition per pulse regime. The laser spot size to thickness ratio is roughly 2:1. It reveals the characteristic non-planar stress wave propagation. While the deformation energy stored in the radial normal strain component is radiated through radial longitudinal and surface stress waves, that stored in the through-thickness normal strain component is depleted in a much more complicated way. While the corresponding longitudinal stress waves bounce back and forth between the layer surfaces, they induce radial longitudinal stress waves according to Poisson's effect. Depending on the laser spot size to thickness ratio, this emission process can last a long time, for instance, hundreds of nanoseconds in the analysed case, at a time scale relevant to the high-repetition-rate FEL at the megahertz range. The transient heat transfer is found to play an important role in draining the mechanical energy during the thermal stress wave process. The resulting kinetic energy is calculated, which may be important to estimate the vibrational amplitude of the thin crystal when excited under repeated heat load.

REFERENCES

- [1] Shvyd'ko, Y., Blank, V. and Terentyev, S., "Diamond x-ray optics: transparent, resilient, high-resolution, and wavefront preserving," *MRS Bulletin* **42**, 437-444 (2017).
- [2] Geloni, G., Kocharyan, V. and Saldin, E., "A novel self-seeding scheme for hard X-ray FELs," *Journal of Modern Optics* **58**, 1391-1403 (2011).
- [3] Amann, J. *et al.*, "Demonstration of self-seeding in a hard-X-ray free-electron laser," *Nature Photonics* **6**, 693-698 (2012).
- [4] Yabashi, M. *et al.*, "Single-shot spectrometry for X-ray free-electron lasers," *Physical Review Letters* **97**, 084802 (2006).
- [5] Zhu, D. *et al.*, "A single-shot transmissive spectrometer for hard X-ray free electron lasers," *Applied Physics Letters* **101**, 034103 (2012).

- [6] Rehanek, J. *et al.*, “The hard X-ray photon single-shot spectrometer of SwissFEL—initial characterization,” *Journal of Instrumentation* **12**, A07001 (2017).
- [7] Stoupin, S. *et al.*, “Direct observation of dynamics of thermal expansion using pump-probe high-energy-resolution x-ray diffraction,” *Physical Review B* **86**, 054301 (2012).
- [8] Von der Linde, D., Sokolowski-Tinten, K. and Bialkowski, J., “Laser–solid interaction in the femtosecond time regime,” *Applied Surface Science* **109**, 1-10 (1997).
- [9] Reeber, R. R. and Wang, K., “Thermal expansion, molar volume and specific heat of diamond from 0 to 3000K,” *Journal of Electronic Materials* **25**, 63-67 (1996).
- [10] Wei, L., Kuo, P., Thomas, R., Anthony, T. and Banholzer, W., “Thermal conductivity of isotopically modified single crystal diamond,” *Physical Review Letters* **70**, 3764 (1993).
- [11] Yang, B., Wang, S. and Wu, J., “Transient thermal stress wave and vibrational analyses of a thin diamond crystal for X-ray FELs under high repetition-rate operation,” *Journal of Synchrotron Radiation* (under review).

SIDEBAND INSTABILITY IN A TAPERED FREE ELECTRON LASER*

Cheng-Ying Tsai^{1†}, Juhao Wu^{1‡}, Chuan Yang^{1,2}, Moohyun Yoon^{1,3}, and Guanqun Zhou^{1,4}

¹SLAC National Accelerator Laboratory, Menlo Park, USA

²NSRL, University of Science and Technology of China, Hefei, Anhui, China

³Department of Physics, Pohang University of Science and Technology, Pohang, Korea

⁴Institute of High Energy Physics, and UCAS, Chinese Academy of Sciences, Beijing, China

Abstract

For a high-gain tapered free electron laser (FEL), it is known that there is a so-called second saturation point where the FEL power growth stops. Sideband instability is one of the major reasons leading to this second-saturation and thus prevents from reaching hundreds of gigawatt (GW) or even terawatt (TW) level power output in an x-ray FEL. It was believed that a strong taper can effectively suppress the sideband instability and further improves the efficiency and peak power. In this paper, we give quantitative analysis of the dependence of taper gradient on the sideband growth. The study is carried out semi-analytically together with numerical simulation. The numerical parameters are taken from LCLS-like electron bunch and undulator system. The results confirm the effectiveness of strong undulator tapering on sideband suppression.

INTRODUCTION

Free electron laser (FEL) is known to be capable of generating coherent high-power radiation over a broad range of spectrum. In the x-ray FEL regime, the power efficiency is about 10^{-3} , indicating that the first saturated power can be ~ 50 GW for electron beam with peak current ~ 5 kA and energy ~ 10 GeV operating in the self-amplified spontaneous emission (SASE) mode in a ~ 100 -m-long untapered undulator. With undulator tapering, the efficiency can be improved and the power can be further increased in the post-saturation regime but eventually will reach a so-called second saturation and the radiation then approaches another equilibrium. Although numerical simulations show that the TW level of temporally integrated FEL power can be possible when the undulator tapering (of helical type) is optimized and the self-seeded scheme is employed [1], in the post-saturation regime it is the sideband instability that still limits the growth of the main signal [2–6]. Enhancing the FEL peak power can be envisioned once the sideband instability is effectively suppressed. Such instability in FELs is caused by the interaction of the electromagnetic field with the electron synchrotron motion in the ponderomotive potential well. The potential well, formed by the undulator field and the main signal, will trap electrons and result in oscillation with a synchrotron frequency (and its multiples) away from the resonance or

main-signal frequency. Once the interaction creates a positive feedback, the electron beam energy will transfer and contribute to the electromagnetic field with the synchrotron sideband frequency. Then the sideband signal will grow and usually bring about undesirable consequences. In this paper we will focus on the sideband instability in a single-pass high-gain tapered FEL in the post-saturation regime based on single-particle description in a one-dimensional (1-D) model. The validity of 1-D analysis assumes that the transverse size of the electron beam is large compared with that of the radiation field, thus ignoring the effects of diffraction and gradient of transverse electron beam density. Using a single-particle approach, we can obtain the corresponding dispersion equation, which accounts for sideband-related dynamical quantities. Then, by quantifying the so-called sideband field gain, we compare the theoretical predictions with the results from a 1-D FEL simulation and they show good agreement. We particularly focus on the effect of undulator tapering on the sideband growth and study both the gentle and strong undulator tapering, compared with the untapered case. Our numerical simulations are based on similar parameters to those of the Linac Coherent Light Source (LCLS), the LCLS-like parameters.

THEORETICAL FORMULATION

In 1-D FEL, the main signal is governed by the resonance condition, $\lambda_R = \frac{\lambda_u}{2\gamma_R^2(z)} \left(1 + \frac{K^2(z)}{2}\right)$, where λ_u is the undulator period, λ_R is the radiation wavelength of the main signal, γ_R is the electron reference energy in unit of its rest mass energy, $K \approx 0.934B_0[\text{Tesla}]\lambda_u[\text{cm}]$ is the (peak) undulator parameter, and B_0 the peak undulator magnetic field. Here λ_u is assumed constant, and K is in general a function of the undulator axis z with $B(z) = B_0 f_B(z)$ and $f_B(z)$ is the tapering profile. The 1-D FEL process can be formulated based on the following electron dynamics and wave equations [7, 8]:

$$\frac{d\theta}{dz} = \frac{\partial \mathcal{H}}{\partial \eta} = \frac{\eta - \eta_R}{f_R}, \quad (1)$$

$$\frac{d\eta}{dz} = -\frac{\partial \mathcal{H}}{\partial \theta} = -\frac{f_B}{f_R} \left(\mathcal{E} e^{i\theta} + \mathcal{E}^* e^{-i\theta} \right), \quad (2)$$

and

$$\frac{d\mathcal{E}}{dz} = \left(\frac{\partial}{\partial z} + \frac{\partial}{\partial \hat{u}} \right) \mathcal{E} = \frac{f_B}{f_R} \langle e^{-i\theta} \rangle. \quad (3)$$

In the equations, $\theta = (k_R + k_u)z - \omega_R t$ is the electron phase with respect to the radiation, and $\eta \equiv (\gamma - \gamma_R(0))/\rho\gamma_R(0)$

* The work was supported by the US Department of Energy (DOE) under contract DE-AC02-76SF00515 and the US DOE Office of Science Early Career Research Program grant FWP-2013-SLAC-100164.

† jcytsai@SLAC.Stanford.EDU

‡ jhwu@SLAC.Stanford.EDU

is the normalized energy deviation with respect to the dimensionless FEL or Pierce parameter ρ . In the case of undulator tapering, the electron reference energy is modified accordingly through the resonance condition to be $\gamma_R(z) = \gamma_{R0} f_R(z)$ where $f_R(z) = \sqrt{(1 + K^2(z)/2)/(1 + K_0^2/2)}$. $|\mathcal{E}| = |E|/\sqrt{4\pi n_0 \rho \gamma_{R0} m_0 c^2}$ is the normalized amplitude of the electric field E . Other relevant quantities are normalized as $\hat{z} = 2k_u \rho z$, $\hat{s} = 2k_u \rho (z - \beta_z ct)$ with $k_u = 2\pi/\lambda_u$, $k_R = 2\pi/\lambda_R$, $\omega_R = ck_R$, $\beta_z = v_z/c$, and $\hat{u} = \hat{s}/(1 - \beta_z)$. Equation (3) is obtained by taking the slowly varying envelope approximation and the bracket $\langle \dots \rangle$ denotes the ensemble average over the electron beam phases. Inserting $\mathcal{E} = |\mathcal{E}_0| e^{i\phi}$ into Eq. (3) and letting $\Theta = \theta + \phi$ will give two separate equations for the amplitude and phase of the radiation field to the zeroth order:

$$\frac{\partial}{\partial \hat{z}} + \frac{\partial}{\partial \hat{u}} |\mathcal{E}_0| = \frac{f_B}{f_R} \cos \Theta, \quad (4)$$

and

$$|\mathcal{E}_0| \frac{\partial \phi}{\partial \hat{z}} = -\frac{f_B}{f_R} \sin \Theta. \quad (5)$$

For the case of the untapered FEL, the field amplitude after saturation is constant (or oscillates around an equilibrium) and the radiation phase ϕ is linear in z . In what follows, the main signal is determined by the conservation of energy, where the field amplitude is given by $|\mathcal{E}_0| = \sqrt{|\mathcal{E}_0^{(0)}|^2 + (1 - f_R(\hat{z}))/\rho}$, where $\mathcal{E}_0^{(0)}$ is evaluated at the location of the first saturation and we have presumed $\cos \Theta \approx \cos \Theta_R$. Now we can study the stability of such a 1-D FEL system. Since we are interested in the sideband instability after the first saturation, we will Taylor expand the dynamical quantities around their saturation equilibria and study how the perturbation affects the system. Let us assume

$$\begin{aligned} \mathcal{E} &= (|\mathcal{E}_0| + \delta\mathcal{E}' + i\delta\mathcal{E}'') e^{i\phi}, \\ \eta &= \eta_R + \delta\eta, \\ \text{and } \theta &= \theta_R + \delta\theta, \end{aligned} \quad (6)$$

where $\theta_R = \Theta_R - \phi$. The quantities with δ ahead are considered to be small and sideband-related quantities. Linearizing Eqs. (1) and (2) using the third relation of Eq. (6) lead to the small-amplitude electron synchrotron motion with $\Omega_{\text{syn}}^2 = -2\frac{f_B}{f_R^2} |\mathcal{E}| \sin \Theta_R$. Next, we presume these perturbations do not interact with each other and behave as $(\delta\theta, \delta\eta, \delta\mathcal{E}', \delta\mathcal{E}'') \propto e^{ik\hat{z} - ik\hat{u}}$, where κ is assumed real and k can be in general complex. The real part of k represents the propagation constant, while the imaginary part indicates the growth (or damping) of the associated quantities. Inserting into Eqs.(1), (2), and (4) will result in a set of linear equations. The stability is then determined by the determinant of the corresponding coefficient matrix, i.e. the dispersion relation:

$$\left(k^2 - \Omega_{\text{syn}}^2 \right) \left[(k - \kappa)^2 - \frac{f_R^2}{4|\mathcal{E}_0|^4} \Omega_{\text{syn}}^4 \right] - \frac{f_B^2}{f_R^2 |\mathcal{E}_0|^2} \Omega_{\text{syn}}^2 = 0. \quad (7)$$

In this equation we will solve for k provided κ is given. The general behavior of the imaginary part of k , $\text{Im}k < 0$, features the growth of the sideband signal, where the maximum growth rate occurs at $\kappa \approx \Omega_{\text{syn}}(\hat{z})$, shown in Fig. 1. There exists a cutoff threshold for κ , above which the oscillating electron beam will not interact the corresponding spectral components and the corresponding signals do not exist.

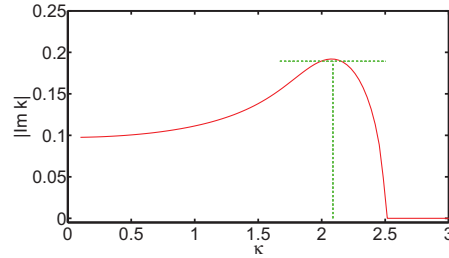


Figure 1: The growth rate $|\text{Im}k|$ as a function of κ . The dispersion curve is solved for the case of $\Omega_{\text{syn}} \approx 2$, $|\mathcal{E}_0| \approx 10$, and $f_B = f_R = 1$. The maximum growth rate $\max |\text{Im}k|$ occurs at $\kappa \approx \Omega_{\text{syn}}$.

An approximate analytical expression for the maximum growth rate can be found by looking for $k = \Omega_{\text{syn}} + \delta k$, where δk is in general a complex quantity and letting $d^2 \delta k / d\kappa^2 = 0$, giving [3, 8]:

$$\max |\text{Im}k| \approx \frac{\sqrt{3}}{2} \left[\frac{f_B^2(\hat{z}) \Omega_{\text{syn}}(\hat{z})}{2f_R^2(\hat{z}) |\mathcal{E}_0(\hat{z})|^2} \right]^{1/3}. \quad (8)$$

NUMERICAL RESULTS

In this section we will compare the numerical solutions of Eq. (7) with the full 1-D FEL simulation results [9]. Table 1 summarizes the relevant parameters for a LCLS-like hard x-ray self-seeding (HXRSS) configuration. To compare the theoretical prediction with the 1-D FEL simulation, we need to analyze the FEL output spectra. The readers are referred to Ref. [10] for the details. We define the sideband field gain as $G(\hat{z}) \equiv \left| \frac{\mathcal{E}_s(\hat{z})}{\mathcal{E}_s(\hat{z}_0)} \right| = e^{\Lambda \hat{z}}$, where \mathcal{E}_s is the sideband field around $\omega_s \approx 2\sqrt{2} c \Omega_{\text{syn}}$, \hat{z}_0 is at the first saturation, and Λ is the (z -integrated) sideband field growth rate. In what follows we are mostly interested in the third (last) section of LCLS undulator, which consists of a total of 16 undulator segments (the 17th to 32nd undulators) with the total length about 50 m. The initial saturation occurs at $z \approx 13$ m (not shown here) for all three different cases: no taper, gentle (0.8%) and strong (10%) undulator taperings. Now let us look at the effect of different undulator taperings on the sideband instability gain. Figure 2 illustrates the three different situations. From (a-c) we see that both the

Table 1: Numerical Parameters for the Beam, Undulator and Radiation Fields for the Hard X-Ray FELs

Name	Value	Unit
Electron beam energy	10.064	GeV
RMS relative energy spread	10^{-4}	
Peak current	4	kA
Normalized emittances (x, y)	0.3,0.3	$\mu\text{m-rad}$
Average beta function (x, y)	5,5	m
Undulator parameter K_0 (peak)	3.5	
Undulator period	3	cm
Input seed power	1	MW
Resonance wavelength	2.755/4.5	$\text{\AA}/\text{keV}$
First saturation power	~ 80	GW
First saturation length	~ 13	m

theoretical predictions and the 1-D FEL simulation results match reasonably well. In particular, we find that as the taper ratio increases, the sideband field gains become reduced. Comparing Fig. 2(a,b) with (c), there is also an interesting observation that the lower sideband dominates in the untapered or gentle-tapered case while the upper sideband may, but not necessarily, dominate in the strong undulator tapering. Here the theoretical prediction can not distinguish whether the lower or upper sideband will dominate because of employment of the single-particle description¹. From Fig. 2 it appears that the theoretical predictions overall match the dominant sideband very well. Moreover, the otherwise dominant sideband has always smaller growth rate and will be of less concern. Having compared the sideband field gains, let us examine the evolution of FEL output spectra for the three different undulator taperings. From Fig. 2(d-f), it can be found that the main signal with 0.8% taper ratio increases about 2.5 times of that with the untapered case. Moreover, the sideband field for the case of 0.8% undulator tapering is comparable to that of untapered case. The increase of the main signal due to undulator tapering also results in the increase of synchrotron sideband frequency. Thus the sampling synchrotron sideband frequency (marked as thin green lines) over the tapered FEL output spectrum spans a wider range than that of the untapered case. It can be even wider for larger taper ratio. The thick green lines in the figure are used to indicate the final synchrotron sideband frequency at the undulator exit (only lower sideband is shown). For the untapered case, the sampling synchrotron sideband frequency does in fact move back and forth within a certain sideband spectral range because of the periodic oscillation of the saturation power about an equilibrium. The back-and-forth sampling will result in accumulation of sideband field gain. When increasing the ratio of undulator tapering, the sideband spectrum will become broadened and the corresponding sideband field gain will reduce.

¹ Such an asymmetric sideband spectrum, either lower or upper sideband will dominate, can indeed depend on the detailed electron distribution in the phase space. More specifically, it can be possible that not the entire range of the upper or lower sideband spectrum will dominate against the other.

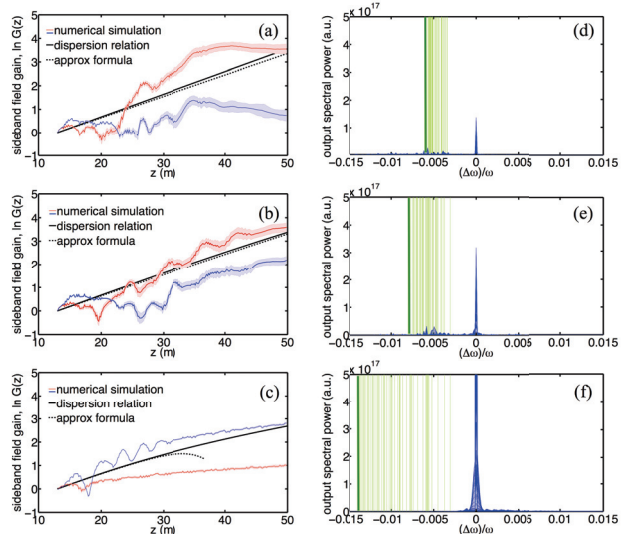


Figure 2: Sideband field gain $\ln G(z)$ as a function of z (left column) and FEL output spectra at undulator exit (right column), for (a,d) untapered, (b,e) 0.8%-tapered, and (c,f) 10%-tapered cases. For (a-c) the numerical simulations are averaged results out from 50 independent runs. For (d-f) only the lower-sideband portion is plotted; while the upper-sideband will be symmetrical should we plot it.

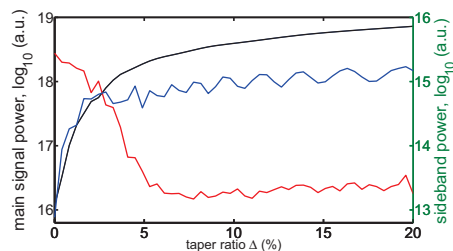


Figure 3: The main signal and the sideband power (in logarithmic scale) as a function of the taper ratio. In the axis of sideband power, the red and blue refer to the lower and upper sideband powers, respectively. The curves in this figure are obtained from the averaged results of 50 independent runs for each taper ratio.

SUMMARY AND CONCLUSION

In this work, we have derived the 1-D FEL sideband dispersion relation [7, 8] and obtained approximate analytical formulas for the maximum sideband growth rate (see Ref. [10] for more details). The instantaneous growth rate can serve as a quick estimate for the FEL sideband effect. Then we studied the FEL sideband effects based on LCLS-like parameters and have investigated the dependence of the sideband instability growth rate on the undulator taper ratio. We find that the undulator tapering can have mitigating effect on sideband growth, through the direct taper ratio, while the increase of the main signal due to the undulator tapering will make the reduction become ineffective. Using numerical simulations it can be found that 10% appears to be passable for both maximizing the main signal and reducing the lower sideband signal. In the meantime the upper sideband begins to emerge around $\Delta \approx 2\%$, at a however slightly smaller ratio than the lower sideband field being appreciably dropped.

Figure 3 shows the dependence of the main signal power and the sideband field gains as a function of the taper ratio. Not shown here but the similar conclusion is also drawn when we use 3-D numerical simulation [11].

REFERENCES

- [1] J. Wu, N. Hu, H. Setiawan, X. Huang, T. O. Raubenheimer, Y. Jiao, G. Yu, A. Mandlekar, S. Spampinati, K. Fang, C. Chu, and J. Qiang, "Multi-dimensional optimization of a terawatt seeded tapered free electron laser with a multi-objective genetic algorithm", *Nuclear Instruments and Methods in Physics Research Section A: Accelerators, Spectrometers, Detectors and Associated Equipment*, 846:56, 2017.
- [2] N. Kroll, P. Morton, and M. Rosenbluth, "Free-electron lasers with variable parameter wigglers.", *IEEE Journal of Quantum Electronics*, 17(8):1436-1468, August 1981.
- [3] Ronald C. Davidson and Jonathan S. Wurtele, "Single-particle analysis of the free-electron laser sideband instability for primary electromagnetic wave with constant phase and slowly varying phase", *The Physics of Fluids*, 30(2):557-569, 1987.
- [4] W. M. Sharp and S. S. Yu, "Two-dimensional Vlasov treatment of free-electron laser sidebands", *Physics of Fluids B: Plasma Physics*, 2(3):581-605, 1990.
- [5] Ravi P. Pilla and A. Bhattacharjee, "Elimination of the sideband instability in variable parameter free electron lasers and inverse free electron lasers", *Physics of Plasmas*, 1(2):390-397, 1994.
- [6] Spilios Riyopoulos, "Sideband suppression in tapered wiggler free electron lasers including thermal spreads", *Physics of Plasmas*, 7(5):1586-1594, 2000.
- [7] R. Bonifacio, F. Casagrande, M. Ferrario, P. Pierini, and N. Piovella, "Hamiltonian model and scaling laws for free-electron-laser amplifiers with tapered wiggler", *Optics Communications*, 66(2):133-139, 1988.
- [8] S. Isermann and R. Graham, "Suppression of the sideband instability in tapered free-electron lasers", *Physical Review A*, 45:4050, 1992.
- [9] K.-J. Kim, Z. Huang and R. Lindberg, "Synchrotron Radiation and Free-Electron Lasers: Principles of Coherent X-Ray Generation", Cambridge University Press, 2017.
- [10] C.-Y. Tsai, J.Wu, C. Yang, M. Yoon, and G. Zhou, Analysis of the sideband instability based on an one-dimensional high-gain free electron laser model, submitted to *Phys. Rev. Accel. Beams*, 2017.
- [11] S. Reiche, "GENESIS 1.3: a fully 3D time-dependent FEL simulation code", *Nuclear Instruments and Methods in Physics Research Section A: Accelerators, Spectrometers, Detectors and Associated Equipment*, vol. 429, pp. 243-248, 1999.

SIDEBAND SUPPRESSION IN TAPERED FREE ELECTRON LASERS*

Cheng-Ying Tsai^{1†}, Juhao Wu^{1‡}, Chuan Yang^{1,2}, Moohyun Yoon^{1,3}, and Guanqun Zhou^{1,4}

¹SLAC National Accelerator Laboratory, Menlo Park, California, USA

²NSRL, University of Science and Technology of China, Hefei, Anhui, China

³Department of Physics, Pohang University of Science and Technology, Pohang, Korea

⁴Institute of High Energy Physics, and UCAS, Chinese Academy of Sciences, Beijing, China

Abstract

It is known that in a high-gain tapered free electron laser (FEL) there is the so-called second saturation point where the FEL power ceases to grow. Sideband instability is one of the major reasons causing this second saturation. Electron synchrotron oscillation coupling to the sideband SASE radiation leads to the appearance of sidebands in the FEL spectrum, and is believed to prevent a self-seeding tapered FEL from reaching very high peak power or improved spectral purity without resorting to external monochromators. In this paper, we propose a simple method of using phase shifters to suppress the undesired sideband signal. This method requires no external optical device and so is applicable at any wavelength. The phase-shift method is implemented in the post-saturation regime where the main signal shall have reached its available power level. Numerical simulations based on Pohang Accelerator Laboratory x-ray FEL beam and undulator system confirm the effectiveness of this method. The results show that the sideband signals are clearly suppressed while the main signal remains a comparable level to that without employing such a method.

INTRODUCTION

Generating an intense high-power x-ray free electron laser (FEL) can be of great interest, e.g. the pulse power at the level of ~50 GW, since such power level of output radiation has stimulated numerous experiments in various scientific areas [1–3]. The output characteristics of FEL are determined by its operation modes (see, for example, Ref. [4] for introduction of short-wavelength FEL basics). In the x-ray wavelength regime a single-pass high-gain FEL can work either in the Self-Amplified Spontaneous Emission (SASE) or seeded mode, despite the lack of direct seeding source. In the SASE mode [5], the initial seeding originates from shot noise of the electron beam. Therefore the output characteristics of SASE can be chaotic in both temporal and spectral profile, although the transverse coherence can be excellent. Acting as an amplifier, the seeded mode indeed requires an input source. It has been known that utilizing higher harmonics generation, e.g. high-gain harmonics generation (HG) [6, 7] or echo-enabled harmonic generation (EEHG) [8, 9], can be an option. Another option is the so-

called self-seeding [10–12]. In the self-seeding option the FEL system starts with the first section of undulators based on SASE mode and is followed by a crystal monochromator or mirrors to select/purify the output spectrum, serving as the subsequent input signal. Then a second section of undulators proceeds, acting as an amplifier, and will amplify the (purified) signal, i.e. the main signal, up to saturation. Compared with SASE, the output characteristics of seeded FEL are in general with much narrower spectral bandwidth and better wavelength stability.

In some applications when an even higher pulse power can be desired, e.g. the femtosecond x-ray protein nanocrystallography, single molecule imaging and so on, dedicated undulator taperings are typically employed [13–16]. Recently the efficiency enhancement based on phase jump method is also proposed [17]. In other situations when the temporal coherence or spectral brightness may be benefited or even required, e.g. the resonant scattering experiment, mixing-wave experiment or those which rely on spectroscopic techniques, the seeded mode shall be considered. However, the higher spectral purity may be prevented by the so-called FEL sideband instability (see, for example, [13, 18–20]). Such instability in FEL is caused by the interaction of the radiation field with the electron synchrotron motion in the ponderomotive potential well after the first saturation of FEL. Such a potential well, formed by the undulator magnetic field and the main signal, will trap electrons and result in the oscillation with a synchrotron frequency (and its multiples) away from the resonance frequency (i.e. the frequency of the main signal). Once the interaction creates a positive feedback, the electron beam energy will continuously transfer and contribute to the electromagnetic field with the specific synchrotron sideband frequency. Then the sideband signal will grow and the output radiation spectrum will feature a main-signal peak with surrounding sideband peaks or a pedestal-like structure. This usually brings about undesirable consequences; the sideband effect can not only degrade the spectral purity but also limit the level of the saturation power of FEL. Employing a post-undulator monochromator may help clean the sideband structure. A dedicated monochromator however depends on specific wavelength range or photon energy and may limit the tunability. The method introduced here requires no external optical device and so is applicable at any wavelength.

In this paper we propose a simple method of using a set of phase shifters to suppress the undesired sideband signal. As mentioned above, because the phase shifters used for

* The work was supported by the US Department of Energy (DOE) under contract DE-AC02-76SF00515 and the US DOE Office of Science Early Career Research Program grant FWP-2013-SLAC-100164.

† jcytsai@SLAC.Stanford.EDU

‡ jhwu@SLAC.Stanford.EDU

sideband suppression will not likely enhance the main signal, they should be placed where the main signal has reached its desired power level in a prescribed undulator tapering, i.e. those phase shifters with sideband-suppression purpose should not be placed too early. It should be also noted that the phase shifters should not be placed too late, where the sideband signal would have been dominant.

THEORETICAL ANALYSIS

The study is based on 1-D FEL analysis [4], where the individual particles in an electron beam are characterized by the electron relative phase $\theta = (k_u + k_1)z - \omega_1 t$ and energy deviation $\eta = (\gamma - \gamma_R(0))/\rho\gamma_R(0)$ from a reference particle with the energy γ_R . Here t and z are the time and undulator coordinates. k_u and k_1 are the wavenumbers of the undulator and the resonant signal (or the main signal), respectively. $\lambda_{1,u} = 2\pi/k_{1,u}$, $\omega_1 = ck_1$. ρ is the usual FEL or Pierce parameter. The FEL resonance condition is $\lambda_1 = \lambda_u [1 + K^2(z)/2]/2\gamma_R^2(z)$. In a tapered FEL, $K(z) = K_0 f_B(z)$ with the taper profile $0 \leq f_B(z) \leq 1$. Correspondingly we have $\gamma_R(z) = \gamma_R(0)f_R(z)$ with $f_R(z) = \sqrt{(1 + K^2(z)/2)/(1 + K_0^2/2)}$. In the 1-D analysis the electrons are described by the following equations [13, 18, 20, 21]

$$\frac{d\theta}{d\hat{z}} = \frac{\eta - \eta_R}{f_R} \quad (1)$$

$$\frac{d\eta}{d\hat{z}} = -\frac{f_B}{f_R} (\mathcal{E}e^{i\theta} + \text{c.c.}) \quad (2)$$

where $\hat{z} = 2k_u \rho z$, \mathcal{E} is the normalized complex electric field, $\mathcal{E} = E/\sqrt{4\pi n_0 \rho \gamma_{R0} m_0 c^2}$, and c.c. denotes the complex conjugate. In the aftermath of the appreciable main signal growth, it can be shown that the main signal behaves as a low-gain FEL¹. In the post-saturation regime the low-gain enhancement by virtue of energy detuning may be limited because the phase space should have been populated by electron beam particles with appreciable energy spread, i.e. the warm beam.

Note that although the (large) main signal can follow low-gain FEL process, the (small) sideband signal after saturation can grow exponentially. The field dynamics is governed by the slowly-varying wave equation, $d\mathcal{E}/d\hat{z} = (f_B/f_R) \langle e^{-i\theta} \rangle$. For simplicity we only consider two-frequency model, i.e. $\mathcal{E} = \mathcal{E}_1 + \mathcal{E}_s = |\mathcal{E}_1| e^{i\phi_1} + |\mathcal{E}_s^\pm| e^{i\nu_\pm \phi_1}$ with $|\mathcal{E}_s^\pm| \ll |\mathcal{E}_1|$. In what follows, the subscripts 1 and s here refer to the main and the sideband signal, respectively. Here ϕ_1 is the

¹ We can Taylor expand the electron energy and phase coordinates as $\eta = \eta^{(0)} + \eta_1^{(1)} + \eta_1^{(2)} + \eta_s^{(1)} + \dots$ and $\theta = \theta^{(0)} + \theta_1^{(1)} + \theta_s^{(1)} + \dots$, respectively. To be clear, the subscripts 1 and s here refer to the main and the sideband signal, respectively. It can be shown that Madey's first theorem [22] $\langle \eta_1^{(2)} \rangle = (1/2) \partial \langle (\eta_1^{(1)})^2 \rangle / \partial \eta^{(0)}$ can be obtained (where the bracket $\langle \dots \rangle$ denotes the phase average of the electron beam macroparticles), and the low-gain function can be formulated as $G \propto -\hat{L}_u^2 \partial \left[\sin(\eta^{(0)} \hat{L}_u) / \eta^{(0)} \hat{L}_u \right]^2 / \partial \eta^{(0)}$ (where $\hat{L}_u = 2k_u \rho L_u$ is the normalized undulator segment length) in the absence of undulator tapering [4].

phase of the main signal and $\nu_\pm = 1 \pm \Delta\nu = \omega/\omega_1$ with the frequency detuning of upper sideband signal ($\Delta\nu > 0$) and the lower sideband signal ($\Delta\nu < 0$). Our analysis begins with separating the complex electric field into the main signal and the sideband signals

$$\frac{d\mathcal{E}_1}{d\hat{z}} = \frac{f_B}{f_R} \langle e^{-i\theta} \rangle \quad (3)$$

$$\left(\frac{d}{d\hat{z}} + i \frac{\Delta\nu}{2\rho} \right) \mathcal{E}_s = \frac{f_B}{f_R} \langle e^{-i\nu\theta} \rangle \quad (4)$$

We then further rewrite the main and sideband field equations into their amplitude and phase components, which lead to the following four equations

$$\frac{d|\mathcal{E}_1|}{d\hat{z}} = \frac{f_B}{f_R} \cos \Theta \quad (5)$$

$$|\mathcal{E}_1| \frac{d\phi_1}{d\hat{z}} = -\frac{f_B}{f_R} \sin \Theta \quad (6)$$

$$\left(\frac{\partial}{\partial \hat{z}} + i \frac{\Delta\nu}{2\rho} \right) |\mathcal{E}_s^\pm| = \frac{f_B}{f_R} \cos \nu_\pm \Theta \quad (7)$$

$$|\mathcal{E}_s^\pm| \frac{d\phi_s^\pm}{d\hat{z}} \pm \frac{|\Delta\nu|}{2\rho} |\mathcal{E}_s^\pm| = -\frac{f_B}{f_R} \sin \nu_\pm \Theta \quad (8)$$

where $\Theta = \theta + \phi_1$ denotes the ponderomotive phase.

In adjusting a phase shifter between two consecutive undulator segments, the relative electron phase $\Delta\theta$ is changed. Assuming the radiation pulse travels along a phase shifter with negligibly small phase change ($\Delta\phi_1 \approx \tan^{-1}(L^{PS}/z_R) \approx \tan^{-1}(1/15) \approx 4^\circ$ where L^{PS} is the section length of a phase shifter, assumed 1 m, and z_R is the Rayleigh length, typically in the range of 10 ~ 20 m), the ponderomotive phase change can be approximately quantified as $\Delta\Theta \approx \Delta\theta$. The goal is to arrange the electron beam within the phase of decelerating the sideband signal ($\cos \nu_\pm \Theta < 0$), while the main signal should remain constant ($\cos \Theta \approx 0$). Prior to a phase shifter, we assume the averaged ponderomotive phase over the electron bunch coordinate θ and beamlet slices s does not change too much, i.e. $\langle \Theta \rangle_{\theta,s} \approx 0$, during the passage in the undulator. Our numerical simulations support this assumption. A phase shifter is assumed to delay all particles of the electron beam relative to the radiation. After the phase shifter, the rate of change of the main signal is proportional to $\cos \Delta\theta$ [see Eq. (5)], while that of the sideband becomes $\cos \Delta\theta \mp |\Delta\nu| \Delta\theta \sin \Delta\theta$ [see also Eq. (7)]. Note that the detuning parameter $|\Delta\nu| \sim 10^{-3} \ll 1$. It can be easily found that $\Delta\theta \approx \pi$ (or its odd integer multiples) can meet the requirement.

NUMERICAL RESULTS

We take as an example the Pohang Accelerator Laboratory x-ray FEL (PAL-XFEL) beam and undulator system [23]. Table 1 summarizes the relevant beam, undulator and radiation parameters. The FEL operation mode is assumed to start from SASE in the first undulator section and then self-seeding in the second undulator section. It is assumed that in the second undulator section the system consists of 22 planar undulators, with 4.94 m for each undulator segment

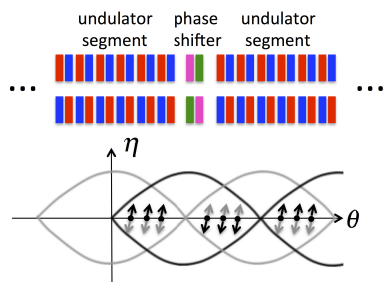


Figure 1: Two consecutive undulator segments with a phase shifter (a small by-pass chicane) in between to delay the relative electron phase to the radiation. The number and strength of the phase shifter is determined by optimizing the ratio of the main to the sideband signals. The longitudinal phase space plot above is to illustrate the purpose of our phase shift method to suppress sideband. The gray and black colors refer to the situations before and after the phase shift. The phase delay will cut out the electron synchrotron motion and therefore suppress sideband signal. The FEL field energy remains constant because the electrons first give and then absorb the energy before and after the phase change.

Table 1: The Relevant Beam, Undulator, and Radiation Parameters for PAL Hard X-Ray FEL

Name	Value	Unit
Electron beam energy	5.885	GeV
RMS fractional energy spread	1.74×10^{-4}	
Peak current	4	kA
Normalized emittances (x, y)	0.4, 0.4	μm
Average beta function (x, y)	10, 10	m
Undulator parameter K_0 (peak)	2.08	
Undulator period	2.6	cm
Input seed power	500	kW
Resonance wavelength	3.1/4	$\text{\AA}/\text{keV}$
First saturation power	~ 20	GW
First saturation length	~ 30	m

and made with variable gaps. The variable undulator gaps enable the undulator tapering up to 15%. Here we only utilize a total ratio of 7% (quadratic) tapering throughout the undulator system. A small by-pass chicane, acting as a phase shifter, is installed between two consecutive undulator segments. In what follows we will present the simulation results in the second undulator section, assuming the seeding power is 500 kW, which is achievable easily in a self-seeded FEL.

We note that the above analysis is based upon 1-D FEL model. In the following we will verify the concept of π phase shift for sideband suppression by using GENESIS [24], a three-dimensional time-dependent FEL simulation code. In GENESIS a phase shifter between two consecutive undulator segments can be modeled using a virtual undulator section. The effective undulator parameter for this section, K_{AD} , should satisfy $\frac{1+K_{AD}^2(z)}{1+K^2(z)} k_u L^{PS} = m\pi$, where m can be

an integer or a fraction. A discrete or stepwise undulator tapering is assumed and the optimized tapering profile is based on the algorithm outlined in Ref. [14]. In the above analysis we have assumed the incident ponderomotive phase $\Theta_i = 0$, i.e. assuming most of the electrons are deeply trapped in the bottom of ponderomotive potential well². Figure 2 compares both the integrated power and the main-signal power before and after employment of the π phase shifters. From Fig. 2(a) it can be seen that inserting π phase shifters will result in slight degradation of the integrated power (the black and red solid lines). This can be expected because the π phase shifting, rather than 2π for the constructive interference between FEL radiation and the electron beam, will cut out the effective interaction. The smaller deviation of the red solid and dashed lines indicate that the main-signal power, quantified as $P(\omega) \approx (dP(\omega)/d\omega) \delta\omega$, where $dP(\omega)/d\omega$ is the frequency distribution of the total power, appears to be more contributed than the usual case, in which all the phase shifters are simply set to 2π . Figure 2(b) and 2(c) respectively illustrate the resultant FEL radiation spectra for all- 2π case and the optimized π -phase-shift case. Here we note that all the π phase shifters should form as pairs, in order that the beam and the radiation can remain in phase in the downstream undulator segments of those π phase shifters.

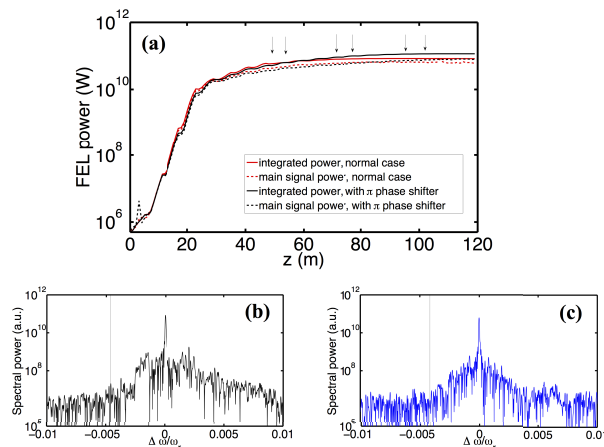


Figure 2: (a) The integrated power and the main signal power as a function of z ; (b,c) the radiation spectra for all- 2π case and the π -phase-shift case. Here the π phase shifters are inserted at the locations where the arrows in subfigure (a) are indicated.

SUMMARY AND CONCLUSION

From the analysis presented above, we have proposed a simple method of utilizing π phase shifters to effectively suppress the undesired FEL sideband instability. Such a π phase shifter should not be placed in the too-early tapered undulator segments; otherwise it will cut out the (still efficient) interaction between the main signal and the electron beam.

² In reality Θ_i may be close to 0 but does not necessarily vanish. To obtain an optimal solution for $\Delta\theta$, we numerically vary $\Delta\theta$ (i.e. K_{AD}) in the nearby value of π (or its odd integer multiples). Note that Fig. 2 presented here is not optimized yet. The numerical optimization is ongoing.

Neither should the phase shifters be employed in the too-late undulator segments, where the sideband signal would likely have become dominant. The numerical simulations based on PAL-XFEL beam and undulator parameters have confirmed the analysis. The results show that the pulse power ~50 GW with excellent spectral purity can be achieved by using this simple method.

REFERENCES

- [1] H. N. Chapman *et al.*, "Femtosecond X-ray protein nanocrystallography", *Nature* 470 (2011) 73-77. <https://doi.org/10.1038/nature09750>
- [2] M.M. Seibert *et al.*, "Single mimivirus particles intercepted and imaged with an X-ray laser", *Nature* 470 (2011) 78-81. <https://doi.org/10.1038/nature09748>
- [3] A. Fratallocchi and G. Ruocco, "Single-Molecule Imaging with X-Ray Free-Electron Lasers: Dream or Reality?", *Phys. Rev. Lett.* 106 (2011) 105504. <https://doi.org/10.1103/PhysRevLett.106.105504>
- [4] K.-J. Kim, Z. Huang, and R. Lindberg, *Synchrotron radiation and free-electron lasers: Principles of coherent x-ray generation*, Cambridge University Press, 2017.
- [5] K.-J. Kim, "Three-Dimensional Analysis of Coherent Amplification and Self-Amplified Spontaneous Emission in Free-Electron Lasers", *Phys. Rev. Lett.* 57, 1871 (1986)
- [6] L. H. Yu, "Generation of intense uv radiation by subharmonically seeded single-pass free-electron lasers", *Phys. Rev. A* 44, 5178 (1991).
- [7] L.-H. Yu, M. Babzien, I. Ben-Zvi, L. F. DiMauro, A. Doyuran, W. Graves, E. Johnson, S. Krinsky, R. Malone, I. Pogorelsky, J. Skaritka, G. Rakowsky, L. Solomon, X. J. Wang, M. Woodle, V. Yakimenko, S. G. Biedron, J. N. Galayda, E. Gluskin, J. Jagger, V. Sajaev, I. Vasserman, "High-Gain Harmonic-Generation Free-Electron Laser", *Science*, Vol. 289, Issue 5481, pp. 932-934, <https://doi.org/10.1126/science.289.5481.932>
- [8] G. Stupakov, "Using the Beam-Echo Effect for Generation of Short-Wavelength Radiation", *Phys. Rev. Lett.* 102, 074801 (2009).
- [9] D. Xiang and G. Stupakov, "Echo-enabled harmonic generation free electron laser", *Phys. Rev. ST Accel. Beams* 12, 030702 (2009).
- [10] J. Feldhaus, E. L. Saldin, J. R. Schneider, E. A. Schneidmiller, and M. V. Yurkov, "Possible application of X-ray optical elements for reducing the spectral bandwidth of an X-ray SASE FEL", *Opt. Commun.* 140, 341 (1997).
- [11] G. Geloni, V. Kocharyan, and E. Saldin, "A novel self-seeding scheme for hard X-ray FELs", *J. Mod. Opt.* 58 (2011) 1391. <https://doi.org/10.1080/09500340.2011.586473>
- [12] J. Amann *et al.*, "Demonstration of self-seeding in a hard-x-ray free-electron laser", *Nat. Photon.* 6 (2012) 693. <https://doi.org/10.1038/nphoton.2012.180>
- [13] N. Kroll, P. Morton, and M. Rosenbluth, "Free-electron lasers with variable parameter wigglers", *IEEE Journal of Quantum Electronics*, 17(8):1436-1468, August 1981.
- [14] Y. Jiao, J. Wu, Y. Cai, A. W. Chao, W. M. Fawley, J. Frisch, Z. Huang, H.-D. Nuhn, C. Pellegrini, and S. Reiche, "Modeling and multidimensional optimization of a tapered free electron laser", *Phys. Rev. ST Accel. Beams*, 15:050704, May 2012.
- [15] C. Emma, K. Fang, J. Wu, and C. Pellegrini, "High efficiency, multiterawatt x-ray free electron lasers", *Phys. Rev. Accel. Beams*, 19:020705, Feb 2016.
- [16] J. Wu, N. Hu, H. Setiawan, X. Huang, T. O. Raubenheimer, Y. Jiao, G. Yu, A. Mandlekar, S. Spampinati, K. Fang, C. Chu, and J. Qiang, "Multi-dimensional optimization of a terawatt seeded tapered free electron laser with a multi-objective genetic algorithm", *Nuclear Instruments and Methods in Physics Research Section A: Accelerators, Spectrometers, Detectors and Associated Equipment*, 846:56, 2017.
- [17] A. Mak, F. Curbis, and S. Werin, "Phase jump method for efficiency enhancement in free-electron lasers", *Phys. Rev. Accel. Beams* 20, 060703 (2017)
- [18] S. Isermann and R. Graham, "Suppression of the sideband instability in tapered free-electron lasers", *Physical Review A*, 45:4050, 1992.
- [19] S. Riyopoulos, "Sideband suppression in tapered wiggler free electron lasers including thermal spreads", *Physics of Plasmas*, 7(5):1586-1594, 2000.
- [20] C.-Y. Tsai, J. Wu, C. Yang, M. Yoon, and G. Zhou, "Analysis of the sideband instability based on an one-dimensional high-gain free electron laser model", submitted to *Phys. Rev. Accel. Beams* (2017)
- [21] R. Bonifacio, F. Casagrande, M. Ferrario, P. Pierini, and N. Piovella, "Hamiltonian model and scaling laws for free-electron-laser amplifiers with tapered wiggler", *Optics Communications*, 66(2):133-139, 1988.
- [22] J. M. J. Madey, "Stimulated Emission of Bremsstrahlung in a Periodic Magnetic Field", *Journal of Applied Physics* 42, 1906 (1971); <https://doi.org/10.1063/1.1660466>
- [23] In Soo Ko, Heung-Sik Kang, Hoon Heo, Changbum Kim, Gyujin Kim, Chang-Ki Min, *et al.*, "Construction and Commissioning of PAL-XFEL Facility", *Appl. Sci.* 2017, 7(5), 479; <https://doi.org/10.3390/app7050479>
- [24] S. Reiche, Genesis 1.3: a fully 3D time-dependent fel simulation code. *Nuclear Instruments and Methods in Physics Research Section A: Accelerators, Spectrometers, Detectors and Associated Equipment*, 429(1):243-248, 1999.

TWO-COLOR SOFT X-RAY GENERATION AT THE SXFEL USER FACILITY BASED ON THE EEHG SCHEME

Zheng Qi^{1,2}, Chao Feng¹, Wenyang Zhang¹, Bo Liu¹, Zhentang Zhao*¹

¹Shanghai Institute of Applied Physics, Chinese Academy of Sciences, Shanghai, China

²University of Chinese Academy of Sciences, Beijing, China

Abstract

We study the two-color soft x-ray generation at the Shanghai soft X-ray Free Electron Laser (SXFEL) user facility based on the echo-enabled harmonic generation (EEHG) scheme. Using the twin-pulse seed laser with different central wavelengths, an preliminary simulation result indicates that two-color soft x-ray FEL radiation with wavelengths at 8.890 nm and 8.917 nm can be obtained from the ultraviolet seed laser. The radiation power is about 600 MW and the time delay is adjustable.

INTRODUCTION

The free electron laser (FEL) has served as a prominent tool for the state-of-the-art research in many scientific frontiers ranging from physics, to chemistry and biology [1, 2]. Through the well-known pump-probe technique [3], the ultrahigh intensity, ultrashort, FEL radiation pulses can be applied to measure ultrafast phenomena inside matter. Typically, the pump-probe technique will use two laser pulses with adjustable time delay and different central wavelengths. The pump laser will give the system a perturbation to excite some reactions within the sample. The probe laser will then reach and interact within the sample after a certain time. By observing the modulation of the probe laser, one can retrieve the state of the system. Changing the time delay between the pump and probe laser pulses, the evolution of the reaction can be “filmed” as a movie while it decays back to the equilibrium state.

The FEL based pump-probe technique extends the photo energy coverage up to vacuum ultraviolet (VUV) or x-ray range, which enables the stimulation and investigation of the inner-shell electronic energy level transition [4]. Therefore it can be used to study the material structure and the ultrafast process in the atomic and molecular scale. The most important FEL based pump-probe scheme termed as the two-color FEL is based on the novel achievements developed recently in the high gain FEL research area. Basically, the two-color FEL is aiming to provide two ultrashort FEL radiation pulses with the time delay and the central wavelength could being adjusted continuously and separately.

The two-color FEL is of great interests in the scientific communities. Several schemes have been proposed and demonstrated experimentally in LCLS, SACLA and FERMI [5–8]. These schemes are generally based the self-

amplified spontaneous emission (SASE) or the high gain harmonic generation (HG) [9]. However, the SASE FEL has poor temporal coherence and power stability as the radiation initiates from the shot noise. And the HG FEL can hardly reach the x-ray wavelength range due to the limitation of the frequency up-conversion efficiency. In this paper, we study the two-color soft x-ray generation at the Shanghai soft X-ray Free Electron Laser (SXFEL) user facility based on the echo-enabled harmonic generation (EEHG) [10, 11].

LAYOUT AND MAIN PARAMETERS

The schematic layout of our design is shown in Fig. 1. It is basically a conventional EEHG configuration, consisting of a two stage energy modulation section, M1 and M2, two dispersion sections, DS1 and DS2, and a long undulator section, R. The electron bunch obtained from the LINAC upstream will interact with Seed1 in M1 to get an energy modulation with an amplitude $A1 = 2.78$. Then the electron beam is sent through the strong dispersion section DS1 with $R56 = 10$ mm to stretch the longitudinal phase space of the electron beam to form periodic structures. Seed2 will imprint another energy modulation into the electron bunch with the amplitude $A2 = 1.39$. And the second dispersion section DS2 with $R56 = 0.34$ mm will convert the energy modulation into harmonic density modulation. The bunched electron beam will then go through the radiator R to generate FEL radiation.

Seed1 is a long pulse seed laser so that it can cover the whole electron bunch during the first energy modulation process in M1. Seed2 is a twin-pulse seed laser with the two pulses of different central wavelengths and a certain time interval. Due to the principle that the FEL radiation generated in the EEHG is at the high harmonics of the seed laser, the two-color FEL radiation can be eventually obtained. The wavelength of Seed1 is 266.7 nm. The wavelengths of the two pulses in Seed2 are respectively 266.7 nm and 267.5 nm. The EEHG FEL is tuned at the 30th harmonic of the seed laser. Therefore the intended two-color soft x-ray FEL radiation is at 8.890 nm and 8.917 nm. The time delay of the two-color soft x-ray FEL can be adjusted through the time intervals between the two pulses in Seed2. According to our design of the optical system, the wavelength tunable range of the two pulses in Seed2 is $266.7 \text{ nm} \pm 2 \text{ nm}$. And the time delay can be adjusted between 0 and 1 ps. The main parameters of our design are shown in Table 1.

* zhaozhentang@sinap.ac.cn

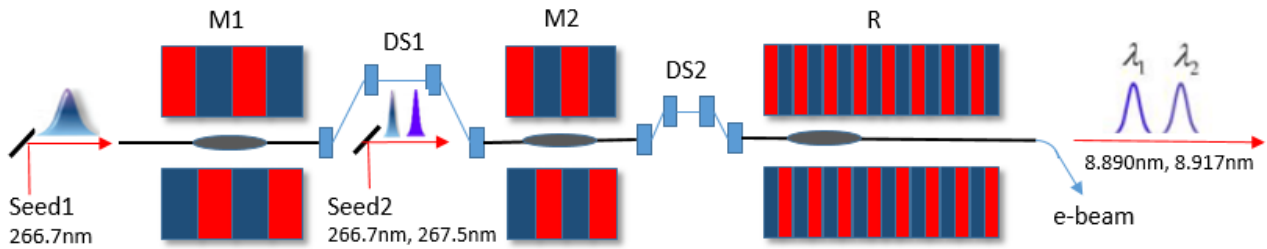


Figure 1: The schematic layout of our design.

Table 1: Main Parameters of Our Design

Parameters	Value
Beam energy [GeV]	1.6
Charge [pC]	500
Slice energy spread [%]	0.01
Normalized emittance [$\mu\text{m}\cdot\text{rad}$]	1.0
Full Bunch length [fs]	800
Peak current [A]	700
Seed1 wavelength [nm]	266.7
Seed1 pulse length [ps]	1.0
Seed1 power [MW]	100
Seed2 wavelength [nm]	266.7/267.5
Seed2 pulse length [fs]	100/100
Seed2 power [MW]	100/100
M1: $N_p \times \lambda_u$ [cm]	20×8
M2: $N_p \times \lambda_u$ [cm]	10×8
DS1: R56 [mm]	10
DS2: R56 [mm]	0.34
R: $N_s \times N_p \times \lambda_u$ [cm]	$8 \times 75 \times 4$
FEL wavelength [nm]	8.890/8.917

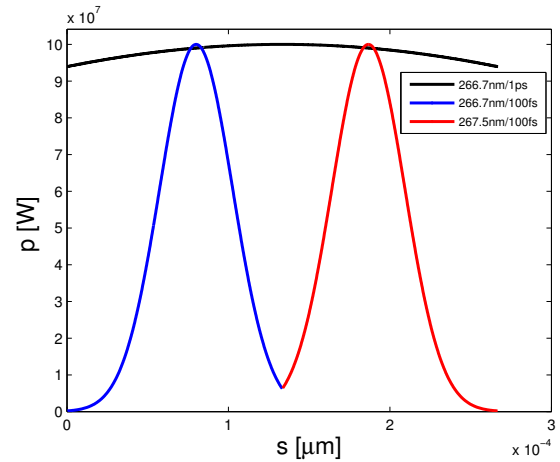


Figure 2: Seed laser pulse: Seed1 266.7 nm/ 1 ps (black). Seed2 266.7 nm/ 100 fs (blue), 267.5 nm/ 100 fs (red) and the time delay is about 400 fs here.

FEL SIMULATION

Using the typical beam parameters of the Shanghai soft X-ray Free Electron Laser (SXFEL) user facility, we present the two pulses two-color soft x-ray generation. Assuming an ideal electron beam is generated at the entrance of M1. The energy modulation processes in M1, M2 and the FEL amplification processes in R are conducted on the basis of the Genesis code.

Fig. 2 illustrates the characterization of the seed laser used in M1 and M2. The central wavelengths of the two short pulses in Seed2 are 266.7 nm and 267.5 nm. The time delay here is set to be about 400 fs. By continuously and separately adjusting the central wavelength and the time interval of this two pulses in Seed2, we can control the output FEL radiation property to be desired wavelengths and time delays.

The 30th bunching factors of the seed laser at the entrance of the radiator R are depicted in Fig. 3. Through the optimization conditions of the EEHG scheme, up to 10% bunching factor of the 30th harmonic of the seed laser can be achieved. The bunched electron beam will then be used for the sim-

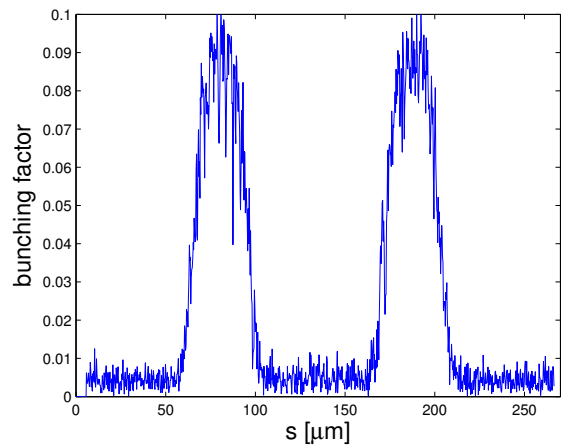


Figure 3: 30th harmonic bunching factors of the seed laser.

ulation and optimization for the final FEL radiation. The gain length of these two part bunched electrons is about 1.28 m. The total undulator length in R is 24 m. To satisfy the resonant conditions for both of the two-color radiation pulses, we give the initial electron bunch a 0.1% energy chirp. The undulator bandwidth is also enlarged and the two FEL radiation pulses can be amplified simultaneously.

CONCLUSIONS

The preliminary studies of the two-color soft x-ray generation at the SXFEL user facility based on the EEHG scheme are presented in this paper. Using the twin-pulse seed laser with different central wavelengths at 266.7 nm and 267.5 nm, about 600 MW two-color soft x-ray FEL radiation with wavelengths at 8.890 nm and 8.917 nm can be obtained eventually. The photo energy gap is about 0.4 eV and is adjustable by tuning the central wavelength of the seed laser. The time delay of the two FEL pulses is determined by the time interval of the two pulses in Seed2. The results of 200 fs and 400 fs are given. The electron beam energy chirp is optimized to satisfy the resonant conditions for both the two parts of the electron beam.

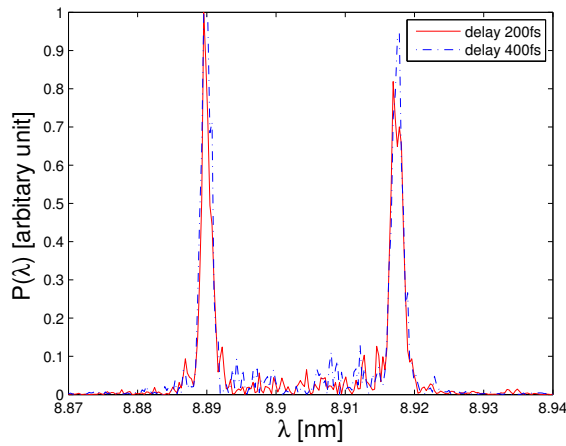
Further, we will study the dependence of the two-color FEL radiation power and spectrum on the variation of the photo energy gap. And the three-dimensional start-to-end simulation based on the SXFEL user facility is necessary for the conceivable test experiments.

ACKNOWLEDGEMENT

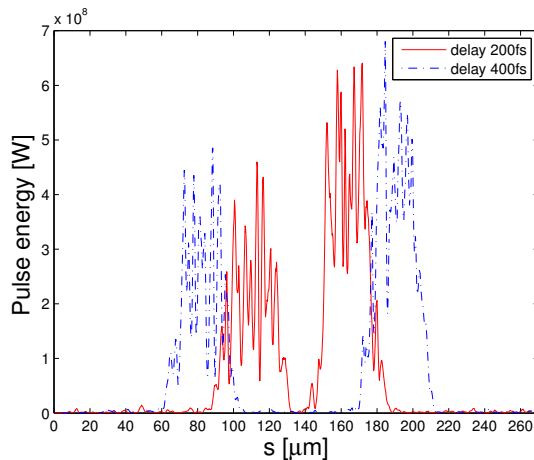
The authors would like to thank Zhen Wang, Tao Liu, and Kaiqing Zhang for helpful discussions. This work is supported by the National Natural Science Foundation of China (11475250 and 11605277).

REFERENCES

- [1] B. McNeil and N. Thompson, *Nature Photonics* 4, p. 814, 2010.
- [2] H. N. Chapman *et al.*, *Nature* 470, p. 73–77, 2011.
- [3] M. Cammarata *et al.*, *Nat. Methods* 5, p. 881–886, 2008.
- [4] S. Tanaka *et al.*, *Phys. Rev. A* 63, p. 063405, 2001.
- [5] A.A. Lutman *et al.*, *Phys. Rev. Lett.* 110.13, p. 134801, 2013.
- [6] A. Marinelli *et al.*, *Nat. Commun.* 6, p. 6369, 2015.
- [7] T. Hara *et al.*, *Nat. Commun.* 4, p. 2919, 2013.
- [8] E. Allaria *et al.*, *Nat. Commun.*, 4, p. 2476, 2013.
- [9] L. H. Yu *et al.*, *Phys. Rev. A.*, 44(8) pp. 5178-5193, 1991.
- [10] G. Stupakov *et al.*, *Phys. Rev. Lett.* 102(7), p. 074801, 2009.
- [11] D. Xiang *et al.*, *Phys. Rev. ST Accel. Beams* 12(3), p. 030702.



(a) Spectra



(b) Power

Figure 4: Two pulses two-color soft x-ray FEL radiation at the wavelengths of 8.89 nm and 8.917 nm with 200 fs (red) and 400 fs (blue) time delay. (a) Spectra. (b) Power.

The simulation results shown in Fig. 4 demonstrate the spectra and the radiation power of the two-color soft x-ray FEL radiation at the wavelengths of 8.890 nm and 8.917 nm with 200 fs and 400 fs time delay. The photo energy gap is about 0.4 eV. The radiation power is about 600 MW. The fluctuation of the radiation power may result from the in-veracious noise occurring in the simulation processes.

SIMULATION AND OPTIMIZATION FOR SOFT X-RAY SELF-SEEDING AT SXFEL USER FACILITY

Kaiqing Zhang, Chao Feng, Dong Wang, Zhentang Zhao
Shanghai Institute of Applied Physics, Chinese Academy of Sciences, Shanghai 201800, China
University of Chinese Academy of Sciences, Beijing 100049, China

Abstract

The simulation and optimization studies for the soft x-ray self-seeding experiment at SXFEL have been presented in this paper. Some critical physical problems have been intensively studied to help us obtain a more stable output and a clearer spectrum. The monochromator is optimized considering various unideal conditions such as the reflection rate, diffraction rate and the roughness of the grating and the mirrors. An integrated self-seeding simulation is also presented. The calculation and simulation results show that the properties of the self-seeding can be significantly improved by using the optimized design of the whole system and the evaluation of grating monochromator shows that the presented design is reliable for soft x-ray self-seeding experiment at SXFEL.

INTRODUCTION

The successful achievement of SASE FEL [1-3] opens a new chapter to high-brightness photon source with tunable wavelength and it provides a reliable instrument to research scientific frontier within the material, biological and chemical sciences. However, SASE FEL suffers from shot noise, poor longitudinal coherence and poor spectral bandwidth. A harmonic lasing scheme with external seeding, such as HGHG [4-5] and EEHG [6-8], can be used to generate relative short wavelength radiation with longitudinal coherence. However, it is unable to probe photon energy beyond a few hundred of eV. To improve the longitudinal coherence of SASE FEL, self-seeding [9] is proposed at DESY in 1997, after that, soft and hard X-ray self-seeding are demonstrated at LCLS separately in 2014 [10] and 2012 [11] separately. Since then, self-seeding schemes are regarded as a reliable method to obtain high brightness, longitudinal coherence and short-wavelength FEL radiation.

The self-seeding scheme separates the long radiation undulator into two parts by inserting a monochromator and a four-dipole chicane. The first undulator works on the SASE mode, the radiation and electron bunch are extracted before saturation. After that, the radiation is passed through a monochromator to purify the spectrum and the electron bunch is passed through the chicane to eliminate the beam microbunching. After that, the monochromatic radiation and the fresh electron beam are sent to the radiation undulator. In the seed undulator, the monochromatic radiation is used as a seed to interact with the electron beam. Finally, the output will be longitudinal coherent when saturation. In the previous system design, we have given preliminary design and simulation for SXFEL user facility [12]. In this paper, some critical

physical problems have been intensively studied to help us obtain a more stable output and a clearer spectrum. We give the simulation method to optimize the undulator length. The reflection and diffraction rate are calculated to get the transfer efficiency and the simulation process is more reliable considering the transfer efficiency. The monochromator is optimized considering various unideal conditions such as the roughness of the grating and the mirrors. In the previous optical simulation, we use shadow to simulate the power resolution of designed grating monochromator and the parameters of light source are not considered. In this paper, we use the calculated parameters of radiation pulse to simulate the power resolution of grating monochromator and we also give a detail simulation for designed simulation.

THE GRATING MONOCHROMATOR DESIGN

The layout of self-seeding scheme is shown in Fig. 1. The grating monochromator has five elements: a VLS toroidal grating monochromator disperses the light pulse to different transverse position as well as focuses the light pulse, a plane mirror reflects the light to horizontal direction, a slit selects out the light pulse wavelength, a spherical mirror focus the sagittal direction of pulse and another plane mirror reflects the light to the entrance of the undulator. In the previous optical system design, the layout and the parameters of optical elements have been described. Recently, some detail studies about grating monochromator have been carried out. In soft X-ray regime, the gold is generally chosen as the material of optical elemental. Based on the element material and the designed parameters, we calculate the reflection and diffraction rate of the grating monochromator. For a grating, the diffraction efficiency can be expressed as follows:

$$E_0 = \frac{R}{4} \left(1 + 2(1 - P) \cos \left(\frac{4\pi \cos(\alpha)}{\lambda} \right) + (1 - P)^2 \right),$$

where α is the incidence angle, h is the depth of the grating groove, P can be expressed as: $P = (4h \tan \alpha)/d_0$, where d_0 is the line width of adjacent grating groove and R can be expressed as: $R = \sqrt{\alpha_G \beta_G}$, where $\alpha_G = \pi/2 - \alpha$, $\beta_G = \pi/2 - \beta$, α, β is the incidence and diffraction angle separately, and the diffraction angle is related with diffraction order, here we only consider the first diffraction order. Based on the designed parameters, the diffraction efficiency can be calculated as 0.039 with gold substrate. For optical elements, the reflection efficiency can be expressed as

Content from this work may be used under the terms of the CC BY 3.0 licence (© 2018). Any distribution of this work must maintain attribution to the author(s), title of the work, publisher, and DOI.

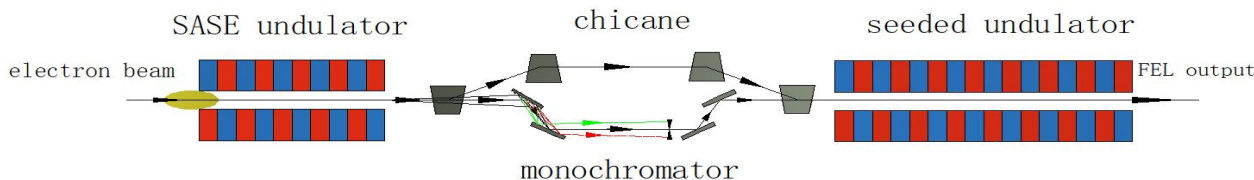


Figure 1: The layout of SXFEL user facility systems design.

$$R = \left(\frac{k_1 - k_2}{k_1 + k_2} \right)^2,$$

where k_1 can be expressed as: $k_1 = (2\pi/\lambda) \sin(\alpha)$, λ is the wavelength of diffraction pulse, k_2 can be expressed as: $k_2 = (2\pi/\lambda) \sqrt{n^2 - \cos(\alpha)^2}$, with n the atomic scattering factor, which is related to the material of optical elements. In our monochromator system design, we choose the gold as the optical elements material, the reflection efficiency can be calculated as 0.9588 for a single optical element. We consider the reflection and diffraction efficiency at the same time, the transfer efficiency of whole optical system can be calculated as 0.0329.

THE CHICANE DESIGN

In self-seeding scheme, the chicane is mainly used to eliminate the microbunching produced in SASE undulator as well as compensate the optical delay generated by the grating monochromator. The layout of designed chicane is displayed in the paper [12]. In the previous system design, the value of R_{56} of the chicane is given at the variation range from 372-446 μm , which is related to the length and the deflection angle of dipole, the relation can be expressed as: $R_{56} = L\theta^2$. Considering the actual situation, the length of dipole is chosen as 0.5 m, the variation range of deflection angle is 2.73-2.99 mrad correspondingly.

THE OPTICAL SIMULATION

In the previous optical simulation based on the shadow, we use the conventional Gaussian light and the radiation characteristic of SASE FEL is not considered. In this paper, the radiation characteristics of SASE FEL including the length, transverse size and divergence angle are considered. Based on Genesis simulations, the RMS transverse size of light pulse is 50 μm , the Rayleigh length can be calculated by:

$$Z_R = \frac{\pi\omega_0^2}{\lambda} = 6.3\text{m}.$$

Thus, the divergence angle of light pulse is:

$$\theta = \frac{0.2\omega_0}{Z_R} = 1.5\mu\text{rad}.$$

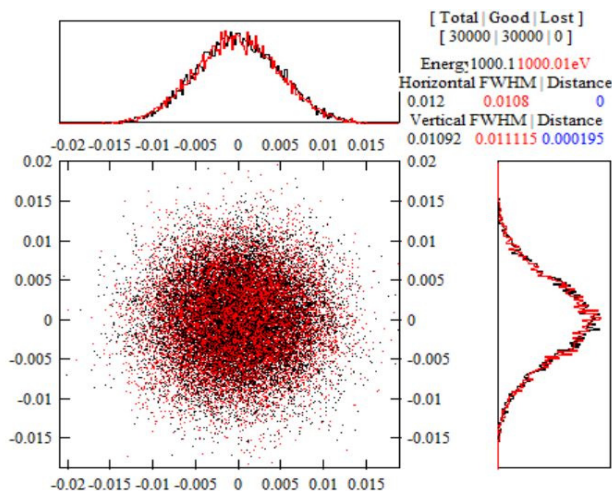


Figure 2: The transverse distribution of light source.

The RMS longitudinal depth of SXFEL user facility light pulse is 200 fs (60 μm). In the shadow simulation, the input photon energy is 1000 eV and 1000.1 eV. The transverse distribution of light source in the shadow simulation is displayed in Fig. 2. The red point is the 1000.1-eV photon and the black point is the 1000-eV photon.

In this optical system design, shadow simulation is always used to get the power resolution of monochromator. The FEL light source is passed through grating monochromator, the input parameters have been described in the paper [12]. The final transverse distribution light pulse in the shadow simulation is showed in the top figure of Fig. 3.

From Fig. 3, one can find that the photon with different photon energy is separated apparently. We can rationally point out that the resolution power is more than 1/10000. In actual situation, many unideal conditions will affect the power resolution of grating monochromator, such as the roughness of the grating surface, the variation of temperature, machining error and so on. We use the roughness of the grating surface to simulate the affection of unideal condition to grating monochromator. The final result considering the roughness is also showed on Fig. 3. One can clearly find the resolution power degree significantly comparing to the situation without roughness, it's worth mention that some photon will also lost considering roughness.

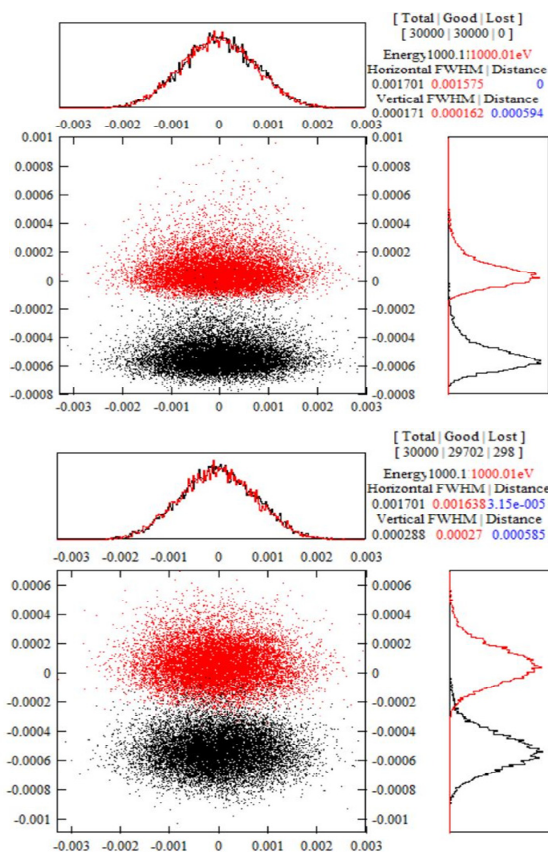


Figure 3: The transverse distribution of light pulse after the VLS toroidal grating.

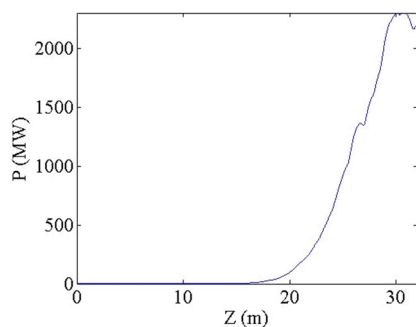


Figure 4: SASE power revolution along the undulator.

FEL SIMULATION

In the previous system design, a preliminary simulation is presented. In this paper, we present the recent simulation results based on the parameters at SXFEL user facility, the detail parameters have been displayed in the paper [12]. The SASE power revolution along the undulator, based on Genesis simulations [13], is showed in Fig. 4.

Generally, the SASE FEL radiation power in self-seeding process is two orders of magnitude lower than the saturation power, in the SASE simulation, the total SASE undulator length is chosen as 20 m. After that, the SASE radiation is purified by a monochromator. In our simulation, the transfer efficiency and power resolution of mon-

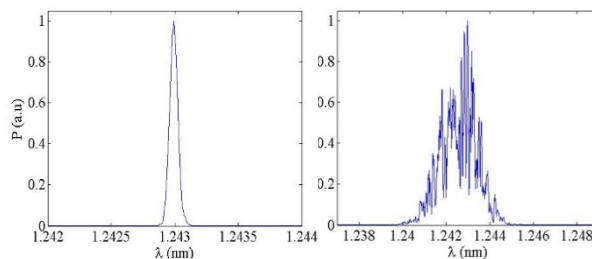


Figure 5: The spectrums before and after the monochromator.

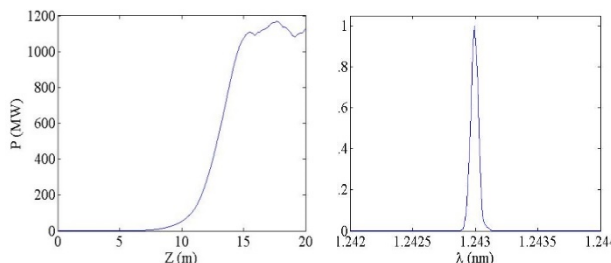


Figure 6: The power revolution along the seed undulator and the final spectrum.

ochromator are considered. Spectrums before and after the monochromator are displayed in Fig. 5.

Afterward, the purified spectrum is sent into the seed undulator to generate self-seeding radiation until saturation. At the end of the seed undulator, we can get the radiation with longitudinal coherence. The power revolution along the seed undulator and the final spectrum are displayed on Fig. 6. We can clearly find the final self-seeding radiation has longitudinal coherence completely and the radiation will get saturation at 15 m. To achieve self-seeding saturation output, the total undulator length is 35 m and the total length of whole scheme is about 40 m.

CONCLUSION

In this paper, the system design for SXFEL user facility is intensity studied. The diffraction and reflection efficiency of our designed optical system are calculated to obtain the transfer efficiency of monochromator. A concrete chicane design is also presented based on the previous chicane calculation. An optical simulation based on the shadow is presented; in this simulation, the characteristic of FEL radiation and the roughness of grating are considered. We demonstrated that the power resolution of grating monochromator is above 1/10000 and the power resolution will decrease when the roughness is considered. Finally, a detailed self-seeding simulation is given and one can easily find that the self-seeding scheme is efficient to generate FEL radiation with longitudinal coherence. We can also conclude our system design can achieve self-seeding saturation output within a distance of 40 m. Further effort will detail the system design, such as the mechanical system, thermal effect of grating monochromator and other characteristics.

REFERENCES

- [1] A. M. Kondratenko and E. L. Saldin, *Particle Accelerators* 10, p. 207, 1980.
- [2] R. Bonifacio, C. Pellegrini, and L. M. Narducci, *Optics Communications* 50, p. 373, 1984.
- [3] J. Andruszkowet *et al.*, *Phys. Rev. Lett.* 85, p. 3825, 2000.
- [4] L. Yu *et al.*, *Phys. Rev. ST - Accel. Beams* 44, p. 5178, 1991.
- [5] I. Ben-Zvi *et al.*, *Nucl. Instr. Meth. A*, 483, 1991.
- [6] D. Xiang and G. Stupakov, *Phys. Rev. ST - Accel. Beams* 12, p. 030702, 2009.
- [7] M. Dunning *et al.*, in *Proc. of IPAC'10*, Kyoto, Japan
- [8] Z. Zhao, D. Wang, *Nature Photonics* 6, p. 360, 2012.
- [9] J. Feldhaus and E.L. Saldin, *Optical Communications* 140, p. 341, 1997.
- [10] J. Amann, W. Berg, and V. Blank, *Nature Photonics* 6, p. 693, 2012.
- [11] D. Ratneret and R. Amann, *Phys. Rev. Lett* 114, p. 054801, 2015.
- [12] K. Zhang *et al.*, in *Proc. of IPAC'16*, Busan, Korea.
- [13] S. Reiche *et al.*, *Phys. Rev. ST - Accel. Beams* 429, p. 243, 1999.

STUDY OF AN ECHO-ENABLED HARMONIC GENERATION SCHEME FOR THE FRENCH FEL PROJECT LUNEX5

E. Roussel*, M. E. Couprie, A. Ghaith, A. Loulergue
 Synchrotron SOLEIL, Gif-sur-Yvette, France
 C. Evain, PhLAM/CERLA, Villeneuve d'Ascq, France
 D. Garzella, CEA, Gif-sur-Yvette, France
 on behalf of the LUNEX5 team

Abstract

In the French LUNEX5 projet (free electron Laser Using a New accelerator for the Exploitation of X-ray radiation of 5th generation), a compact advanced Free-Electron Laser (FEL) is driven by either a superconducting linac or a laser-plasma accelerator that can deliver a 400 MeV electron beam. LUNEX5 aims to produce FEL radiation in the ultraviolet and extreme ultraviolet (EUV) range. To improve the longitudinal coherence of the FEL pulses and reduce the gain length, it will operate in Echo-Enabled Harmonic Generation (EEHG) seeding configuration [1]. EEHG is a strongly nonlinear harmonic up-conversion process based on a two seed laser interaction that enables to reach very high harmonics of the seed laser. Recent experimental demonstration of ECHO75, starting from an infrared seed laser, was recently achieved at SLAC [2] and opened the way for EEHG scheme in the EUV and soft x-ray range. Furthermore, FELs are promising candidates for the next generation lithography technology using EUV light. In this work, we report a preliminary study of EEHG scheme for LUNEX5 in order to reach the target wavelength of 13.5 nm, currently expected for application to lithography.

INTRODUCTION

More than fifty years after the discovery of the laser [3], the Free-Electron Lasers (FELs) are nowadays the brightest sources in the extreme ultraviolet (EUV) and x-ray domains [4]. Thanks to the remarkable properties of the FEL pulses, like the spatial coherence, the high peak brightness, the narrow bandwidth spectrum and the ultra short duration in the sub-100 fs range, the operational FEL facilities [5–9] have opened the way to new possibilities in ultrafast dynamic of excited systems and in imaging. Besides the unprecedented capabilities of FEL lightsources, new researches are going towards the generation of even shorter FEL pulses and Fourier limits over a wide spectral range. An other trend is investigating the possibility to reduce the size of the FEL facilities by means of seeding schemes, like the echo-enabled harmonic generation (EEHG) scheme [1, 10] that enables to reach very high harmonic of the seed laser, or by replacing one of the components by an alternative, e.g. the use of cryogenic permanent magnet-based undulator (CPMU) [11, 12] or the use of new accelerator concepts like the laser-plasma acceleration (LWFA: Laser WakeField Acceleration) [13].

* eleonore.roussel@synchrotron-soleil.fr

LUNEX5 PROJECT

The LUNEX5 [14, 15] is an advanced and compact FEL demonstrator project (shown in Fig. 1) that aims at producing ultra short, coherent and intense pulses in the EUV domain. A 400-MeV electron beam will be delivered by two XFEL-type cryomodules (Fig. 1, yellow) for high repetition rate operation (see Table 1 for electron beam parameters), to a FEL line (Fig. 1, purple) composed of two modulators and four radiators based on the cryogenic permanent magnet technology for compactness. Two pilot user experiments (Fig. 1, green) in gas phase and condensed matter will qualify the FEL performance in the different cases. Measuring and controlling the temporal properties of the radiation emitted by LUNEX5 is essential for users application. A new method called MIX-FROG, based on the FROG (Frequency Resolved Optical Gating) technique, enabling to characterize these properties even in the presence of partial longitudinal coherence has been proposed and developed [16].

Table 1: Electron Beam Parameters

Beam energy	400	MeV
Bunch charge	1	nC
Bunch length	1	ps (RMS)
Peak current	400	A
Normalized slice emittance	1.5	mm.mrad
Energy spread	80	keV

The construction is not launched yet, but Research and Development programs are underway. The LUCRECE project aims at developing elementary RF cell with a 20-kW solid state amplifier. The operation at high repetition rate will also present challenges from the diagnostics point of view. This is particularly true for shot-by-shot electron bunch shape characterization. For that purpose, an original single-shot detection has been developed based on the electro-optic sampling that consists in encoding the electron bunch shape in the spectrum of a laser pulse, coupled to a photonic-time stretch strategy that slows down the signal to be detected. The feasibility of the method has been verified and applied on the detection of coherent THz pulses in synchrotron light-sources [17, 18].

An alternative accelerator line is also considered (Fig. 1) that will explore the qualification of a laser plasma acceleration process by a FEL application, using the same FEL line components and a specific transport line for handling the

Content from this work may be used under the terms of the CC BY 3.0 licence (© 2018). Any distribution of this work must maintain attribution to the author(s), title of the work, publisher, and DOI.

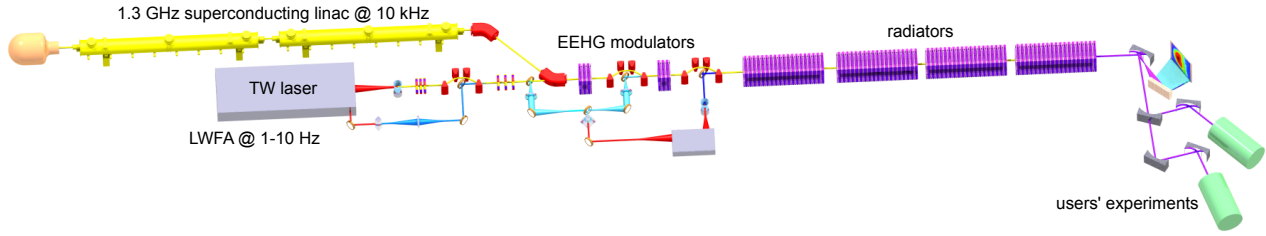


Figure 1: Layout of LUNEX5. It comprises two accelerators: a superconducting linac (yellow) and a laser-plasma accelerator (grey), and a single FEL line (purple) composed of two modulators (for EEHG seeding scheme) and four radiators. Two pilot users' experiments (green) will characterize the FEL performances from a user perspective.

plasma electron beam properties (divergence: 1 mrad, and energy spread: 1%) to enable FEL amplification [19, 20]. A test experiment with a dedicated funding (ERC), called COX-INEL (COherent Xray source INferred from Electrons accelerated by Laser), is on-going at the Laboratoire d'Optique Appliquée (LOA, France), where the laser-plasma accelerator (LPA) has been equipped with a FEL transport line designed and prepared at Synchrotron SOLEIL [21, 22]. Recently, the transport and control of the electron beam from the LPA source to the entrance of the undulator has been achieved and first spontaneous emission has been observed [12, 23].

In order to control the spectral-properties and shorten the FEL amplification process, LUNEX5 will operate in seeding configuration, either by direct seeding using a HHG (High harmonic generation in gas) source [24, 25] or by taking advantage of the highly nonlinear frequency up-conversion process of the EEHG scheme [1, 25] in order to reach short wavelengths in the tens of nm range starting from a UV seed laser.

LUNEX5 FOR EUV LITHOGRAPHY

UV lithography (EUVL) using a wavelength of 13.5 nm is a leading candidate among the next generation lithography technologies to continue the Moore's law scaling of devices, but only if the lightsource produces enough EUV photons per second to satisfy the hundreds of wafers per hour required for high volume manufacturing. The typical requirement for EUVL is a compact EUV source of 1 kW average power within 2% spectral bandwidth. The choice of FEL sources for EUVL appears to be an alternative to laser-produced plasma (LPP) EUV sources to overcome the source power limit.

CPMU Undulators

CPMUs take advantage of the enhanced field performance of permanent magnets when cooled down to low temperature, enabling shorter period with sufficient magnetic field [11, 12]. The EUV lithography community is currently focused on the wavelength of 13.5 nm. For a planar undulator, the wavelength of the FEL is given by: $\lambda_{\text{FEL}} = \lambda_u / (2\gamma^2) (1 + K^2/2)$, where γ is the relativistic factor, K is the deflection parameter, and λ_u is the undulator period. For a small beam energy,

one need an undulator with a short period to maintain a K -value closed to one. The undulator configuration considered for LUNEX5 at 13.5 nm is summarized in Table 2.

Table 2: Undulator parameters

Magnetic Period	10	mm
Number of periods	300	
Undulator type	planar	
Resonant wavelength	13.5	nm
Deflection parameter	1.14	
Peak field	1.23	T
Gap	3.17	mm

EEHG Seeding Scheme

The EEHG is based on a two-seed laser interaction that takes place in the modulators. The two modulators are followed by two dispersive sections ($R_{56}^{(1)}$ and $R_{56}^{(2)}$) and FEL amplification develops in the radiators. The two seed lasers required for the EEHG seeding scheme are "twin" seeds. The output of a Ti:Sa laser is used to produce Third Harmonic Generation (THG). The layout of the line is shown in Fig. 2.

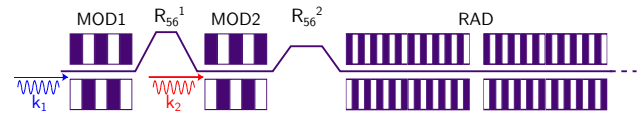


Figure 2: EEHG scheme of LUNEX5

According to [10], the bunching factor at the wavenumber $k_E = nk_1 + mk_2 = (n + Km)k_1$ is given by:

$$b_{n,m} = \left| e^{-(1/2)\xi_{n,m}^2} J_n \left[-A_1 \xi_{n,m} \right] J_m \left[-(Km + n)A_2 B_2 \right] \right|, \quad (1)$$

with

$$\xi_{n,m} = nB_1 + (Km + n)B_2. \quad (2)$$

$A_{1,2} = \Delta E_{1,2} / \sigma_E$ are the dimensionless modulation amplitudes from the first and second laser interaction, and $B_{1,2} = R_{56}^{(1,2)} k_1 \sigma_E / E_0$ are the dimensionless dispersive strengths.

It follows from the optimization of Eq. (1), that the maximum bunching at 13.5 nm is obtained for the combination

$m = 20$ and $n = -1$, that corresponds to the harmonic 19th of the seed laser. A bunching factor of 10.3% (Fig. 3a) is reached for a first energy modulation A_1 equal to 2, a first dispersive section of 2 mm and a second modulation of 1.9 and a second dispersion of 124.1 μm .

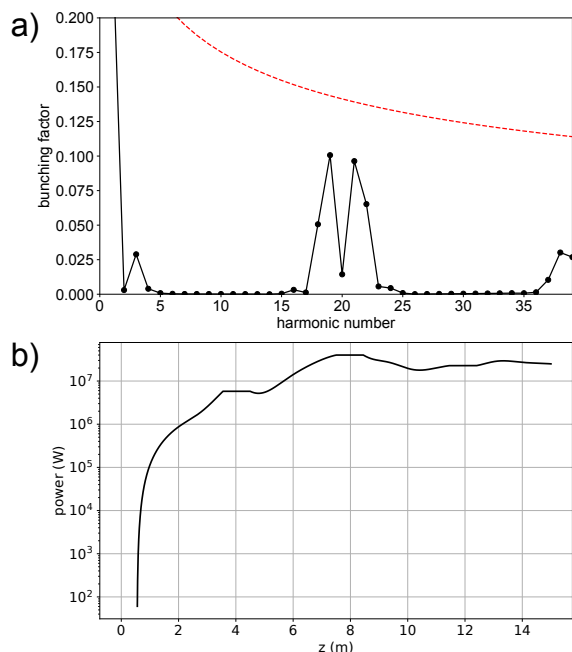


Figure 3: a) Bunching factor (black line) and maximum bunching factor (red dashed line). b) Peak power along the undulator at 13.5 nm.

A preliminary FEL simulation using GENESIS code [26] shows that the undulator radiation can reach a peak power of about 40 MW after 8 m of propagation. Thus, an average power of 0.4 kW can be obtained with a repetition rate of 10 MHz and an electron bunch length of 1 ps, that corresponds to a duty cycle of 1×10^{-6} .

The limit of the seeding schemes at high repetition rate may come from the lack of powerful laser source at this repetition rate. An alternative to single-pass seeded FELs is the FEL in oscillator configuration. Despite a still low reflectance of the mirrors in the EUV range, of the order of 70% [27], the oscillator configuration combined with an energy recovery linac will allow high repetition rate to be reached.

CONCLUSION

The LUNEX5 project is a demonstrator of advanced and compact FEL based on R&D technology. Its advanced and compact design makes it suitable for the generation of intense, coherent EUV pulses for lithography application. Moreover, the use of a superconducting linac and cryogenic undulators opens the way for FEL with high average power level.

REFERENCES

- [1] G. Stupakov, *Phys. Rev. Lett.* **102**, 074801 (2009).
- [2] E. Hemsing *et al.*, *Nat. Photonics* **10**, 512 (2016).
- [3] T. H. Maiman, *Nature*, **187**, 493 (1960).
- [4] B.W. J. McNeil and N. R. Thompson, *Nat. Photonics* **4**, 814 (2010).
- [5] W. Ackermann *et al.*, *Nat. Photonics* **1**, 336 (2007).
- [6] P. Emma *et al.*, *Nat. Photonics* **4**, 641 (2010).
- [7] T. Ishikawa *et al.*, *Nat. Photonics* **6**, 540 (2012).
- [8] E. Allaria *et al.*, *Nat. Photonics* **6**, 699 (2012).
- [9] E. Allaria *et al.*, *Nat. Photonics* **7**, 913 (2013).
- [10] D. Xiang and G. Stupakov, *Phys. Rev. ST Accel. Beams* **12**, 030702 (2009)
- [11] C. Benabderrahmane *et al.*, *Phys. Rev. Accel. Beams* **20**, 033201 (2017).
- [12] A. Ghaith *et al.*, "Cryogenic Permanent Magnet Undulator for a FEL Application", presented at FEL2017, Santa Fe, NM, USA, paper WEP065, this conference (2017).
- [13] V. Malka *et al.*, *Nat. Phys.* **4**, 447-453 (2008).
- [14] M. E. Couprie *et al.*, *Journal of Physics: Conference Series* **425**(7), 072001 (2013).
- [15] M.E. Couprie *et al.*, *Journal of Modern Optics* **63**, 4, (2016).
- [16] C. Bourassin-Bouchet and M. E. Couprie, *Nat. Comm.* **6**, 6465 (2015).
- [17] E. Roussel *et al.*, *Scientific Reports* **5**, 10330 (2015).
- [18] C. Evain *et al.*, *Phys. Rev. Lett.* **118**, 054801 (2017).
- [19] A. Loulergue *et al.*, *New J. Phys.* **17**, 023028 (2015).
- [20] M. E. Couprie *et al.*, *J. Physics B: At., Mol., Opt. Phys.* **47**, 234001 (2014).
- [21] M.E. Couprie *et al.*, "Experiment Preparation Towards a Demonstration of Laser Plasma Based Free Electron Laser Amplification", in *Proceedings of FEL2014*, Basel, Switzerland, paper TUP086 (2014).
- [22] M. E. Couprie *et al.*, *Plasma Phys. Control. Fusion* **58** 034020 (2016).
- [23] T. Andre *et al.*, "Study of the Electron Transport in the COX-INEL FEL Beamline Using a Laser-Plasma Accelerated Electron Beam", presented at FEL2017, Santa Fe, NM, USA, paper TUP061, this conference (2017).
- [24] G. Lambert *et al.*, *Nat. Phys.* **4**, 296-300 (2008).
- [25] C. Evain *et al.*, "Seeding Schemes On The French FEL Project LUNEX5", in *Proceedings of FEL2011*, Shanghai, China, paper TUPA06 (2011).
- [26] S. Reiche, *Nuclear Instruments and Methods in Physics Research A* **429**, 243 (1999).
- [27] D. B. Wu and A. Kumar, *J. Vac. Sci. Technol.*, B **25**, 1743 (2007).

SEEDING OF ELECTRON BUNCHES IN STORAGE RINGS*

S. Khan[†], B. Büsing, N. M. Lockmann, C. Mai, A. Meyer auf der Heide,
 R. Niemczyk[‡], B. Riemann, B. Sawadski, M. Suski, P. Ungelenk[§],
 Zentrum für Synchrotronstrahlung (DELTA), TU Dortmund, 44227 Dortmund, Germany

Abstract

Seeding schemes for free-electron lasers (FELs) can be adopted to generate ultrashort radiation pulses in storage rings. Creating laser-induced microbunches within a short slice of a long electron bunch gives rise to coherent emission at harmonics of the seed wavelength. In addition, THz radiation is produced over many turns. Even without FEL gain, a storage ring is an excellent testbed to study many aspects of seeding schemes and short-pulse diagnostics, given the high repetition rate and stability of the electron bunches. At DELTA, a 1.5-GeV electron storage ring operated by the TU Dortmund University in Germany, coherent harmonic generation (CHG) with single and double 40-fs seed pulses is performed at wavelengths of 800 nm or 400 nm. As a preparation for echo-enabled harmonic generation (EEHG), simultaneous seeding with 800 and 400 nm pulses in two different undulators is performed and several techniques are employed to ensure optimum timing between the seed pulses.

INTRODUCTION

Seeding of high-gain free-electron lasers (FELs) with external radiation pulses allows to control and improve spectrotemporal properties of FEL pulses at short wavelengths [1]. In electron storage rings, seeding methods can be adopted to generate femtosecond radiation pulses emitted by a short “slice” within a several 10 ps long electron bunch [2]. For pump-probe applications, another advantage of external seeding is the natural synchronization between two pulses, i.e., the seed pulse, from which a fraction is used to pump a sample, and the probe pulse resulting from the seeding process. The basic seeding mechanism is a periodic modulation of the electron energy induced by the electric field of a laser pulse co-propagating with the electrons in an undulator (the “modulator”).

In an FEL seeding scheme known as “high-gain harmonic generation” (HG) [3], a magnetic chicane converts the energy modulation into a periodic density modulation (“microbunching”) which gives rise to FEL gain at harmonics of the seed pulse wavelength in a second undulator (the “radiator”). Presently, FERMI (Trieste, Italy) is the only HG-seeded FEL in user operation [4]. The bunching factor and thus the efficiency of the seeding process decreases exponentially with increasing harmonic order. One method to reach shorter wavelengths is to use the resulting FEL pulse

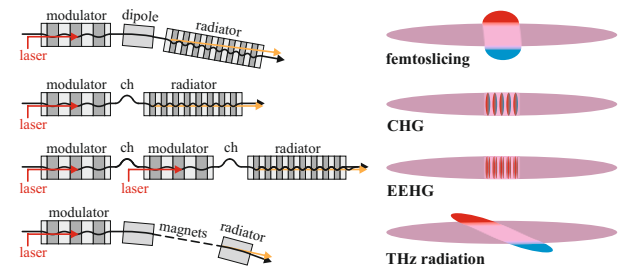


Figure 1: Applications of laser-induced energy modulation in storage rings. Left: Magnetic layout with undulators and chicanes (ch). Right: Resulting electron bunch structure (red and blue: electrons with energy gain and loss).

as seed for a second modulator. This two-stage (or cascaded) HG process has been demonstrated at FERMI [5]. Another method to obtain FEL gain at shorter wavelengths is “echo-enabled harmonic generation” (EEHG) involving a twofold laser-induced energy modulation to generate a density pattern with high harmonic content [6]. EEHG has been studied at NLCTA (SLAC, Menlo Park, USA) [7, 8] and at SDUV-FEL (SINAP, Shanghai, China) [9].

SEEDING IN STORAGE RINGS

In storage rings, the energy modulation induced by a femtosecond laser pulse applies to $\approx 1/1000$ of the bunch length and can be employed in several ways (see Fig. 1).

After passing a dipole magnet, the off-energy electrons are transversely displaced and emit a short off-axis pulse of synchrotron radiation in an undulator tuned to any wavelength [10]. Since the electrons are not microbunched, the pulse energy is proportional to the number of electrons and about 10^{-4} times lower than the energy emitted from the whole bunch. This scheme, known as “femtosing”, has been demonstrated at ALS (LBNL, Berkeley, USA) [11] and is employed in user operation at BESSY (Berlin, Germany) [12], SLS (PSI, Villigen, Switzerland) [13], and SOLEIL (Saint-Auban, France) [14].

Similar to HG, microbunching with a chicane causes coherent emission of radiation at harmonics of the seed wavelength. Without FEL gain, this process is called “coherent harmonic generation” (CHG) and was first demonstrated with ps laser pulses at ACO (Orsay, France) [15]. Short-pulse generation via CHG was performed at UVSOR (Okasaki, Japan) [16], ELETTRA (Trieste, Italy) [17], and DELTA (Dortmund, Germany) [18]. Due to coherent emission, the pulse energy is proportional to the number of electrons squared. Even for $1/1000$ of the electrons in the bunch, the CHG pulse energy exceeds that of incoherent

* Work supported by BMBF (05K15PEA, 05K15PEB), MERCUR (Pr-2014-0047), DFG (INST 212/236-1 FUGG) and the Land NRW.

[†] shaukat.khan@tu-dortmund.de

[‡] now at: DESY, 15738 Zeuthen, Germany

[§] now at: GRS gGmbH, 50667 Köln, Germany

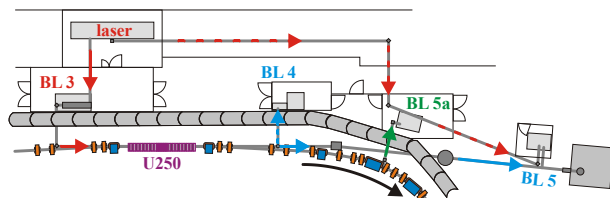


Figure 2: The short-pulse facility at DELTA comprising a laser system, a laser beamline (BL 3) guiding seed pulses to the undulator U250, a diagnostics beamline (BL 4), a soft-X-ray beamline (BL 5), and a THz beamline (BL 5a).

emission from the whole bunch. The accessible wavelengths are restricted to low harmonics ($h < 10$). Employing the EEHG scheme to reach smaller wavelengths with coherent emission in storage rings was studied for SOLEIL [19] and DELTA [20]. Performing a twofold energy modulation at successive turns was proposed for HLS (Heifei, China) [21].

In the storage ring lattice, the energy-dependence of the path lengths causes energy-modulated electrons to leave a gap in the longitudinal charge distribution which gives rise to broadband coherent emission in the (sub-)THz regime over several turns. This radiation serves as diagnostics for the laser-induced energy modulation [22] and provides information on the electron dynamics in the ring [23]. Seeding with ps intensity-modulated laser pulses allows to generate tunable narrowband THz radiation [24, 25].

Many aspects of FEL seeding can be studied in a storage ring. With a MHz revolution frequency, the laser-electron interaction rate is only limited by the laser system. Another benefit is the excellent beam stability. For a typical beam lifetime, the relative turn-by-turn decrease of the bunch charge is below 10^{-10} . Given the low electron density, space charge effects are usually negligible. Radiation damping provides stability and a homogeneous slice emittance and energy spread but also limits the freedom in manipulating the bunches. For a given radiofrequency (RF) voltage and momentum compaction factor, the bunch length is fixed and no static energy chirp can be applied. However, dynamic changes of the electron distribution can be introduced by modulating the RF phase [26] or by driving an instability.

THE SHORT-PULSE FACILITY AT DELTA

At the 1.5-GeV electron storage ring DELTA, operated by the TU Dortmund University as a synchrotron light source [27], about 50 days per year of dedicated beam time are available for seeding studies. Parameters of the ring and the CHG short-pulse facility [18] are given in Table 1. The setup is shown in Fig. 2.

Seed pulses from a titanium:sapphire laser system are focused directly through a beamline (BL 3) into the electromagnetic undulator U250 or are frequency-doubled first. The 7 upstream/downstream periods of the U250 act as modulator/radiator for CHG with a chicane between them. A diagnostics beamline (BL 4) is used to observe the spatial overlap of laser and undulator radiation on screens and to establish

Table 1: Parameters of the DELTA Short-Pulse Facility

storage ring circumference	115.2 m
electron beam energy	1.5 GeV
beam current (single/multibunch)	20/130 mA
horizontal emittance	15 nm rad
relative energy spread (rms)	0.0007
bunch length (FWHM)	100 ps
laser wavelength	800 nm
min. laser pulse duration (FWHM)	40 fs
seed pulse energy at 800/400 nm	8.0/2.8 mJ
seed repetition rate	1 kHz
modulator/radiator period length	250 mm
number of modulator/radiator periods	7
undulator periods used as chicane	3
max. modulator/radiator K parameter	10.5
max. chicane r_{56} parameter	140 μm

the temporal overlap using a streak camera. CHG radiation is characterized in air down to wavelengths of 190 nm. A soft-X-ray beamline (BL 5) operated by the Forschungszentrum Jülich is equipped with a plane-grating monochromator and a hemispherical photoelectron spectrometer. For pump-probe experiments, an evacuated beamline sends a fraction of each laser pulse to the BL 5 endstation. A dedicated beamline for THz radiation from a dipole magnet [28] is equipped with several detectors and spectrometers.

SPECTROTEMPORAL MANIPULATION

As shown in [29] for the case of FERMI, the spectrotemporal properties of HGHG/CHG pulses can be controlled by the chirp of the seed pulses and the parameter r_{56} of the magnetic chicane. Similar measurements at DELTA have been reported [30, 31]. At early experiments, CHG spectra were recorded using an avalanche photodiode while rotating the grating of a Czerny-Turner monochromator over several minutes. More recently, a gated image-intensified camera (iCCD) was used to record single-shot spectra allowing for scans of the chicane current from 0 to 700 A ($r_{56} = 140 \mu\text{m}$) in 1-A steps within a similar period of time.

For 800 nm seeding, spectra of the second and third harmonic are shown in Fig. 3 for two different compressor settings of the laser amplifier. At large r_{56} values, microbunching occurs for electrons having interacted with the head and tail of the seed pulse while electrons with maximum energy modulation are overbunched. Consequently, unchirped seed pulses result in CHG spectra with interference fringes corresponding to two successive pulses. In the case of a strong chirp, the spectra exhibit two peaks at the frequencies of the seed pulse head and tail.

The spectrotemporal properties of pulses emerging from the laser amplifier were determined using frequency-resolved optical gating (FROG) [32]), measuring a minimum pulse duration of 42 fs (FWHM) for unchirped pulses. However, these properties are not only influenced by the

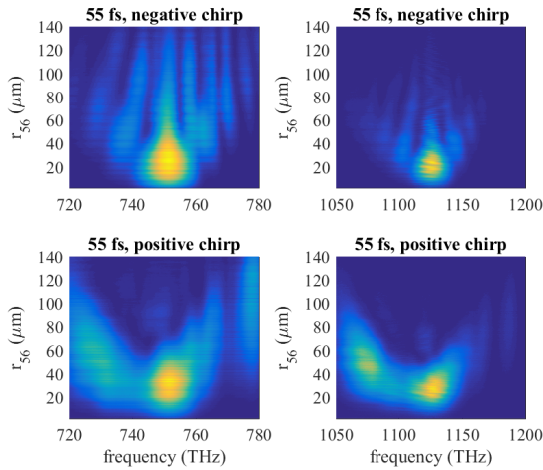


Figure 3: CHG spectra of the second (left) and third harmonic (right) of 800 nm seed pulses with negative chirp (top) and positive chirp (bottom), both with a pulse length of 55 fs, under variation of the chicane strength r_{56} .

stretcher-compressor configuration but also by the transition of the pulses through air and glass (lenses and vacuum window). Therefore, CHG spectra of pulses with 55 fs duration and negative chirp show pronounced interference fringes at large r_{56} values whereas this is not the case for pulses with similar duration and positive chirp. The asymmetry of the CHG spectra is an indication of higher-order chirp.

SEEDING WITH DOUBLE PULSES

A future application of the EEHG scheme at DELTA [20] will require a twofold energy modulation of the same electrons. To this end, first double-pulse seeding experiments were conducted (see Fig. 4). One example is seeding with two 800 nm pulses in the same modulator as described in [33], another is seeding in different modulators which corresponds to the EEHG configuration without second chicane and radiator [34]. In the latter case, one 400 nm pulse is produced by second harmonic generation (SHG), the other pulse is the residual 800 nm radiation after the SHG process. Both pulses are focused and steered independently to optimize the transverse overlap with the electron bunches. The temporal laser-electron overlap is obtained by shifting the RF input controlling the laser oscillator timing with a vector modulator. The timing between the two pulses is tuned by moving mirrors on a linear stage and fine-tuned on the sub-fs level by changing the chicane current. The delay introduced by the chicane between the two modulators is $\Delta t = r_{56}/(2c)$ with c being the speed of light. Three methods were used to verify the temporal overlap (see Fig. 5):

- (1) The THz signal as function of delay shows a symmetric interference pattern. A dip at the central maximum indicates that both radiation pulses act on the same part of the bunch thus reducing the number of electrons participating in coherent THz emission.

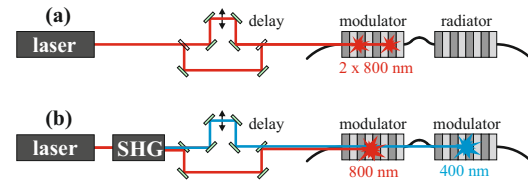


Figure 4: Seeding with 800 nm double pulses in the same modulator (a) and with 800 and 400 nm pulses in two modulators (b) with variable delay.

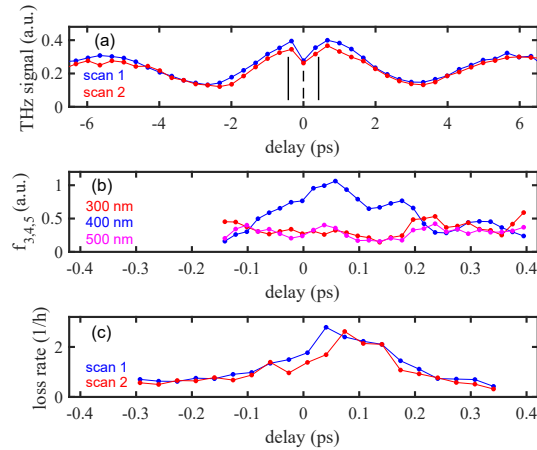


Figure 5: THz radiation (a), Fourier coefficients of the THz signal for few-fs delay variation (b), and beam loss rate (c) as function of the delay between 800 and 400 nm seed pulses. Zero delay and the delay range of (b,c) is defined in (a).

- (2) Only when both pulses act on the same electrons, the energy modulation is sensitive to their relative phase. As explained in [34], the THz signal exhibits a modulation with a periodicity of 400 nm when scanning the chicane-induced delay over several fs.
- (3) A twofold energy modulation of the same electrons results in a larger energy offset for some electrons. When reducing the RF power and thus the energy acceptance of the storage ring, the temporal overlap is indicated by an increased beam loss rate (reduced beam lifetime).

This way, an EEHG-like energy modulation can be performed and verified without radiator. In summary, spectrotemporal manipulation and double-pulse seeding were discussed as examples to show that FEL seeding methods can be studied at a storage ring benefiting from its high revolution frequency and stability. Features which are not available at linear accelerators – such as multturn coherent THz emission and the beam loss rate – provide additional diagnostics opportunities.

ACKNOWLEDGMENTS

The continuous support from our colleagues at DELTA and other institutes, particularly from DESY Hamburg, HZB Berlin, and KIT Karlsruhe is gratefully acknowledged.

REFERENCES

- [1] L. Gianessi, “Seeding and Harmonic Generation in Free-Electron Lasers”, in *Synchrotron Light Sources and Free-Electron Lasers*, edited by E. Jaeschke *et al.*, Springer Reference, 2016, pp. 195-223.
- [2] S. Khan, “Ultrashort Pulses from Synchrotron Radiation Sources”, in *Synchrotron Light Sources and Free-Electron Lasers*, edited by E. Jaeschke *et al.*, Springer Reference, 2016, pp. 51-81.
- [3] L. H. Yu, “Generation of Intense UV Radiation by subharmonically Seeded Single-Pass Free-Electron Lasers”, *Phys. Rev. A* 44, pp. 5178-5139, 1991.
- [4] E. Allaria *et al.*, “Highly coherent and stable pulses from the FERMI seeded free-electron laser in the extreme ultraviolet”, *Nat. Photonics* 6, pp. 699-704, 2012.
- [5] E. Allaria *et al.*, “Two-stage seeded soft-X-ray free-electron laser”, *Nat. Photonics* 7, pp. 913-918, 2013.
- [6] G. Stupakov, “Using the Beam-Echo Effect for Generation of Short-Wavelength Radiation”, *Phys. Rev. Lett.* 102, p. 074801, 2009.
- [7] D. Xiang *et al.*, “Demonstration of the Echo-Enabled Harmonic Generation Technique for Short-Wavelength Seeded Free Electron Lasers”, *Phys. Rev. Lett.* 105, p. 114801, 2010.
- [8] E. Hemsing *et al.*, “Echo-enabled harmonics up to the 75th order from precisely tailored electron beams”, *Nat. Photonics* 10, pp. 512-515, 2016.
- [9] Z.T. Zhao *et al.*, “First lasing of an echo-enabled harmonic generation free-electron laser”, *Nat. Photonics* 6, pp. 360-363, 2012.
- [10] A. A. Zholents, M. S. Zolotarev, “Femtosecond X-Ray Pulses of Synchrotron Radiation”, *Phys. Rev. Lett.* 76, pp. 912-915, 1996.
- [11] R.W. Schoenlein *et al.*, “Generation of femtosecond pulses of synchrotron radiation”, *Science* 287, pp. 2237-2240, 2000.
- [12] S. Khan, K. Holldack, T. Kachel, R. Mitzner, T. Quast, “Femtosecond Undulator Radiation from Sliced Electron Bunches”, *Phys. Rev. Lett.* 97, p. 074801, 2006.
- [13] P. Beaud *et al.*, “Spatiotemporal Stability of a Femtosecond Hard-X-Ray Undulator Source Studied by Control of Coherent Optical Phonons”, *Phys. Rev. Lett.* 99, p. 174801, 2007.
- [14] M. Labat *et al.*, “Commissioning Progress of the Femtoslicing at SOLEIL”, in *Proc. IPAC'14*, Dresden, Germany, 2014, pp. 206-208.
- [15] B. Girard *et al.*, “Optical Frequency Multiplication by an Optical Klystron”, *Phys. Rev. Lett.* 53, pp. 2405-2409, 1984.
- [16] M. Labat *et al.*, “Coherent harmonic generation on UVSOR-II storage ring”, *Eur. Phys. J. D* 44, pp. 187-200, 2007.
- [17] G. De Ninno *et al.*, “Generation of Ultrashort Coherent Vacuum Ultraviolet Pulses Using Electron Storage Rings: A New Bright Light Source for Experiments”, *Phys. Rev. Lett.* 101, p. 053902, 2008.
- [18] S. Khan *et al.*, “Generation of Ultrashort and Coherent Synchrotron Radiation Pulses at DELTA”, *Sync. Radiat. News* 26(3), pp. 25-29, 2013.
- [19] C. Evain *et al.*, “Study of High Harmonic Generation at Synchrotron SOLEIL using the Echo Enabling Technique”, in *Proc. IPAC'10*, Kyoto, Japan, 2010, pp. 2308-2310.
- [20] R. Molo *et al.*, “Conceptual Layout of a New Short-Pulse Radiation Source at DELTA Based on Echo-Enabled Harmonic Generation”, in *Proc. FEL'11*, Shanghai, China, 2011, pp. 219-222.
- [21] H. Li, W. Gao, Q. Jia, L. Wang, “Echo-Enabled Harmonic Generation Based on Hefei Storage Ring”, in *Proc. IPAC'13*, Shanghai, China, 2013, pp. 1208-1210.
- [22] K. Holldack, S. Khan, R. Mitzner, T. Quast, “Femtosecond Terahertz Radiation from Femtoslicing at BESSY”, *Phys. Rev. Lett.* 96, p. 054801, 2006.
- [23] C. Mai *et al.*, “Observation of Coherent Pulses in the Sub-THz Range at DELTA” in *Proc. IPAC'15*, Richmond, USA, 2015, pp. 823-826.
- [24] S. Bielawski *et al.*, “Tunable narrowband terahertz emission from mastered laser–electron beam interaction”, *Nat. Physics* 4, pp. 390-393, 2008.
- [25] P. Ungelenk *et al.*, “Continuously tunable narrowband pulses in the THz gap from laser-modulated electron bunches in a storage ring”, *Phys. Rev. Accel. Beams* 20, p. 020706, 2017.
- [26] M. A. Jebramcik *et al.*, “Coherent Harmonic Generation in the Presence of Synchronized RF Phase Modulation at DELTA”, in *Proc. IPAC'16*, Busan, Korea, 2016, pp. 2847-2850.
- [27] M. Tolan, T. Weis, C. Westphal, K. Wille, “DELTA: Synchrotron Light in Nordrhein-Westfalen”, *Sync. Radiat. News* 16(2), pp. 9-11, 2008.
- [28] M. Hoener *et al.*, “A Dedicated THz Beamline at DELTA”, in *Proc. IPAC'11*, San Sebastian, Spain, 2011, pp. 2939-2941.
- [29] D. Gauthier *et al.*, “Spectrotemporal Shaping of Seeded Free-Electron Laser Pulses”, *Phys. Rev. Lett.* 115, p. 114801, 2015.
- [30] M. Huck *et al.*, “Ultrashort and Coherent Radiation for Pump-Probe Experiments at the DELTA Storage Ring” in *Proc. IPAC'14*, Dresden, Germany, 2014, pp. 1848-1851.
- [31] S. Khan *et al.*, “Spectral Studies of Ultrashort and Coherent Radiation Pulses at the DELTA Storage Ring”, in *Proc. IPAC'16*, Busan, Korea, 2011, pp. 2851-2854.
- [32] R. Trebino, “Frequency-Resolved Optical Gating”, Kluwer, 2000.
- [33] S. Khan *et al.*, “Pilot Experiments and New Developments at the DELTA Short-Pulse Facility”, in *Proc. IPAC'17*, Copenhagen, Denmark, 2017, pp. 2578-2581.
- [34] A. Meyer auf der Heide *et al.*, “Progress towards an EEHG-Based Short-Pulse Source at DELTA”, in *Proc. IPAC'17*, Copenhagen, Denmark, 2017, pp. 2582-2585.

EXTRACTION OF THE LONGITUDINAL PROFILE OF THE TRANSVERSE EMITTANCE FROM SINGLE-SHOT RF DEFLECTOR MEASUREMENTS AT sFLASH*

T. Plath[†], S. Khan, Technische Universität Dortmund, Dortmund, Germany

Ph. Amstutz, L. L. Lazzarino, V. Miltchev, J. Roßbach, Universität Hamburg, Hamburg, Germany

Th. Maltezopoulos, European XFEL GmbH, Schenefeld, Germany

J. Bödewadt, T. Laarmann, C. Lechner, Deutsches Elektronen-Synchrotron
DESY, Hamburg, Germany

N. Ekanayake, Michigan State University, East Lansing, MI, USA

Abstract

The gain length of the free-electron laser (FEL) process strongly depends on the slice energy spread, slice emittance, and current of the electron bunch. At an FEL with only moderately compressed electron bunches, the slice energy spread is mainly determined by the compression process. In this regime, single-shot measurements using a transverse deflecting rf cavity enable the extraction of the longitudinal profile of the transverse emittance. At the free-electron laser FLASH at DESY, this technique was used to determine the slice properties of the electron bunch set up for seeded operation in the sFLASH experiment. Thereby, the performance of the seeded FEL process as a function of seed laser-electron timing can be predicted from these slice properties with the semi-analytical Ming-Xie model. The prediction is well in line with the FEL peak power observed during an experimental laser-electron timing scan. The power profiles of the FEL pulses were reconstructed from the longitudinal phase-space measurements of the seeded electron bunches that were measured with the transverse deflecting cavity.

INTRODUCTION

When starting a high-gain free-electron laser (FEL) from noise, properties of the generated photon pulses such as central wavelength and spectral shape are subject to fluctuations. Additionally, the longitudinal coherence of a SASE pulse is limited due to several longitudinal modes lasing independently from each other. One option to overcome these limitations is an FEL seeded by high-gain harmonic generation (HG). In this seeding scheme, an energy modulation is induced in the electron bunch by the interaction with an external seed laser. This sinusoidal modulation is then transferred to a density modulation when the electron bunch traverses a subsequent dispersive chicane. The electron density distribution shows micro-bunching with the periodicity of the seed laser and can efficiently start the FEL process in a downstream undulator on the seed laser wavelength and its harmonics [1].

For an HG-seeded FEL, it is essential to maintain the longitudinal and transverse overlap between the seed laser pulse and electron bunch. In the transverse plane, the laser pulse is usually larger than the electron bunch. This way, all electrons in a longitudinal slice of the electron bunch experience a similar amplitude of the electric field and a similar modulation amplitude. Longitudinally, however, the laser pulse is usually shorter than the electron bunch and the question arises which relative timing between them has to be chosen for optimum lasing performance.

While a straightforward method to optimize the longitudinal overlap is a scan of the relative timing between laser pulse and electron bunch, the optimum timing can also be determined from an analysis of single-shot measurements of the longitudinal phase-space distribution. This analysis reveals the longitudinal profile of the transverse emittance and reveals the longitudinal fraction of the electron bunch that supports best FEL performance. Here, profile refers to the physical quantity being a function that changes its value with the longitudinal coordinate in the electron bunch.

To measure the longitudinal phase-space distribution of the electron bunches, a transverse deflecting structure (TDS) is used in combination with a subsequent dispersive dipole spectrometer. While fields in the cavity kick electrons dependent on their arrival time in the vertical plane, the spectrometer deflects horizontally. On a screen downstream of the dipole, the longitudinal phase-space distribution can be measured with a time resolution below 10 fs.

At the seeding experiment sFLASH at FLASH in Hamburg the TDS is located downstream of the radiating undulator [2–4]. Here, the longitudinal phase-space distribution of seeded electron bunches can be measured. The energy drop of the seeded portion of the bunch can be used to extract seeded FEL pulse power profiles. While this method has been used before on an FEL process started from noise [5], this contribution shows its applicability to HG-seeded FEL pulses. Thus, when extracting the seeded power profiles, the seeding process can serve as a local probe to verify the emittance profile extracted from the TDS measurements and the derived performance prediction.

* Work supported by the Federal Ministry of Education and Research of Germany under contract No. 05K16PEA, 05K16GU4, 05K13PE3, and the German Research Foundation program graduate school 1355.

[†] tim.plath@desy.de

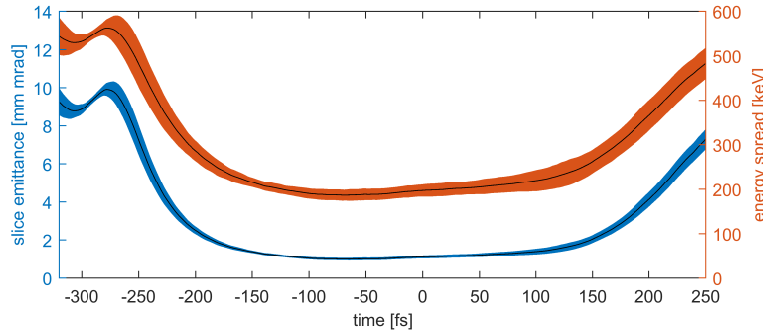


Figure 1: Longitudinal profiles of transverse slice emittance $\varepsilon_{mx} = \sqrt{\varepsilon_{n,x}\varepsilon_{n,y}}$ and measured energy spread $\sigma_{E,m}$ as a function of temporal position along the electron bunch. The colored areas show the statistical rms uncertainties of both profiles. Reprinted from [2] with permission by Scientific Reports under Creative Commons Attribution 4.0 International License.

EXTRACTION OF SLICE EMITTANCE

The energy spread $\sigma_{E,m}$ is measured on the screen of the dispersive energy spectrometer. It is a superposition of different contributions, one is the actual energy spread of the electron bunch $\sigma_{E,0}$, the other two are the heating from the deflecting fields σ_{PW} (along the lines of the Panofsky-Wenzel theorem [6]) and the transverse beam size on the screen σ_{geom} , also contributing to the width of the measured profile. Assuming that each contribution has a Gaussian profile, their widths can be added in quadrature [7]

$$\sigma_{E,m}^2 = \sigma_{E,0}^2 + \sigma_{geom}^2 + \sigma_{PW}^2. \quad (1)$$

To reconstruct the emittance of the electron bunch, an assumption on the initial energy spread $\sigma_{E,0}$ has to be made. Since, in seeded operation, the electron bunch is moderately compressed with a peak current of about 500 A to 600 A, it is assumed that the energy spread is dominated by the compression process. At FLASH, simulations show that the energy spread of the bunch is roughly given by $\sigma_{E,0} = 100 \text{ keV/kA} \cdot I_{peak}$, where I_{peak} is the peak current [8].

Both, the contribution of the heating induced by the TDS fields as well as the beam size on the screen are functions of the transverse emittance. While the heating depends on the normalized vertical slice emittance $\varepsilon_{n,y}$, the beam size on the measurement screen is a function of the normalized horizontal slice emittance $\varepsilon_{n,x}$. By defining the ratio u between both transverse emittances, these can be written as $\varepsilon_{n,x} = \varepsilon_n$ and $\varepsilon_{n,y} = u\varepsilon_n$. The Ming-Xie formalism used below to predict the FEL performance takes one normalized transverse emittance as a parameter. An estimate for the upper limit of this emittance is the geometric mean $\varepsilon_{mx} = \sqrt{\varepsilon_{n,x}\varepsilon_{n,y}} = \varepsilon_n \sqrt{u}$ of the transverse emittances [9, 10].

Equation (1) then gives the emittance:

$$\varepsilon_n(t) = \frac{\sigma_{E,m}^2(t) - \sigma_{E,0}^2(t)}{\xi}, \quad (2)$$

where $\xi = (K^2\beta_y u + A^2\beta_x)\gamma m_0^2 c^4$. Here, $K = eV_0 k / pc$ is the kick parameter of the TDS, V_0 is the effective voltage of the rf field in the TDS, k is the wave number of the rf field, p is the electron momentum, e is the elementary charge, β_y and β_x are the local beta functions, and c is the speed

of light. The parameter A is the calibration constant of the spectrometer that converts the density distribution on the screen to an energy distribution. The mean electron energy is γ and m_0 is the electron rest mass. For the moment $u = 1$ will be assumed. Any deviations will be treated later as systematic errors and will increase the uncertainties on derived emittances [2].

Figure 1 shows the longitudinal profile of the measured energy spread and the reconstructed geometrical mean of the transverse slice emittance. The emittance profile shows a minimum between -50 fs and -100 fs, where optimum FEL performance is expected.

PREDICTION OF FEL PERFORMANCE

With the extracted transverse slice emittance ε_{mx} , the estimate of the uncorrelated energy spread $\sigma_{E,0}$ and the current profile, all information to predict the gain length of the FEL is available. For this, the well established semi-analytical Ming-Xie model [11] has been used to calculate the gain length L_g and saturation power P_{sat} taking into account the HGHG-induced energy spread increase.

In an HGHG-seeded FEL, the FEL power evolution is a superposition of coherent emission of the pre-bunched beam at the beginning of the undulator and experimental FEL amplification [12]:

$$P(z) = P_{th} \left[\frac{\frac{\zeta^2}{3}}{1 + \frac{\zeta^2}{3}} + \frac{\frac{1}{2} \exp[\zeta - \sqrt{3}]}{1 + \frac{P_{th}}{2(P_{sat} - P_{th})} \exp[\zeta - \sqrt{3}]} \right], \quad (3)$$

where $\zeta = z/L_g$ is the normalized longitudinal coordinate, z is the distance traveled along the undulator and $P_{th} = \rho_{FEL} |b_n|^2 P_{beam}$ is the power threshold at which the behavior of the power gain changes from the quadratic z -dependence of coherent radiation to the exponential regime of the FEL. Here, b_n denotes the bunching factor on the n^{th} harmonic of the seed laser, which is the fundamental of the FEL process in the radiator.

As stated above, all information is available to derive which longitudinal section of the electron bunch has the shortest gain length and might run into saturation. To give an absolute prediction of the radiated power, however, the

Content from this work may be used under the terms of the CC BY 3.0 licence (<http://creativecommons.org/licenses/by/3.0/>). Any distribution of this work must maintain attribution to the author(s), title of the work, publisher, and DOI.

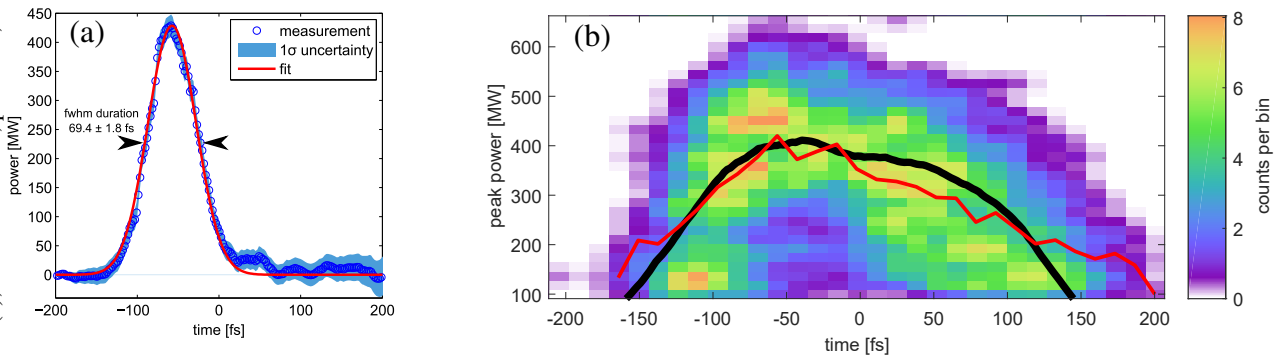


Figure 2: Measurements of FEL pulse power profiles. Panel (a) shows a single-shot power profile extracted from a TDS measurement. Panel (b) shows a two-dimensional histogram of the peak powers and longitudinal positions of FEL pulses extracted from TDS measurements smoothed by a Gaussian with an rms width of one pixel. See text for more information. Reprinted from [2] with permission by Scientific Reports under Creative Commons Attribution 4.0 International License.

initial bunching or modulation amplitude from the seed laser has to be known. In the following, this parameter will be used to fit the prediction of the FEL power to the measurements.

EXPERIMENTAL VERIFICATION

To experimentally determine the position of the electron bunch that shows best lasing performance, the FEL process is started from an initial bunching in the HGHG seeding setup. In this experiment, a 266 nm laser pulse modulates the electron bunch in a 5-period electromagnetic undulator. The radiator is tuned to the 7th harmonic of the seed laser [3].

Seeding allows to selectively start the FEL process in a longitudinally confined region of the bunch. The lasing electrons then lose energy to the radiation field. This is visible on measurements of the longitudinal phase-space distribution that can be obtained with the TDS setup at FLASH. This energy drop of the electrons due to the FEL process enables the extraction of the FEL pulse power profile as shown for a single-shot in Fig. 2a. From these reconstructions the peak power of the pulse and its longitudinal position within the electron bunch are available.

Figure 2b shows a two-dimensional, color-coded histogram of these two properties acquired in a laser-electron timing scan. The highest peak power and thus the best FEL performance is found between -50 fs and -100 fs where the emittance is minimal. While the red curve shows the mean peak power of every timing bin, the black curve shows a fit of the Ming-Xie-based prediction to the red curve.

As described above, the experimental data shown in the figure has been extracted from measurements of the longitudinal phase-space distribution after lasing has taken place. Pulses with low peak powers, however, cannot be evaluated reliably with an automatic algorithm. This is due to fluctuations in both, accelerating and TDS radio-frequency fields, that slightly change the energy profile of the electron bunch. When compared to reference bunches, this may induce false power signals below 100 MW. Thus, pulses with peak powers lower than 100 MW are omitted and the mean curve (red) above ±130 fs from the center shows a

higher value than the prediction (black). The fit parameter for the shown black curve is $\Delta\gamma = 0.777 \pm 0.001_{\text{stat}} \pm 0.154_{\text{sys}}$, corresponding to $b_7 = (3.22 \pm 0.03_{\text{stat}} \pm 1.70_{\text{sys}}) \cdot 10^{-2}$, where statistical errors originate from the fitting process and systematic errors are derived from the uncertainty of the emittance reconstruction. For a more detailed error analysis refer to Ref. [2]. Measurements of the longitudinal phase-space distribution of uncompressed electron bunches, show a modulation amplitude of $\Delta\gamma = 0.79 \pm 0.09$. Here, the impact of collective effects is minimal, since the peak current of the generated micro-bunches is small and the change of the energy spread due to longitudinal space-charge forces is small [13, 14]. This measurement, thus, gives an estimate for the modulation amplitude and is well in line with the modulation amplitude derived here.

SUMMARY AND OUTLOOK

In this contribution a simple method to extract the longitudinal profile of the transverse emittance from single-shot measurements of the longitudinal phase-space distribution is presented. The extraction was verified with a seeded FEL that is used to longitudinally resolve the FEL performance along the electron bunch. The method is well suited for moderately compressed electron bunches, where collective effects only play a minor role.

These measurements allow to predict the FEL performance along the electron bunch and enable the optimum choice of laser-electron timing in an HGHG-seeded FEL. Additionally, an on-line extraction of the emittance on a shot-by-shot basis allows the tuning of the accelerator components to generate a flat emittance profile that improves the stability of the seeded signal. A more general description of the results presented here can be found in Ref. [2].

ACKNOWLEDGEMENTS

The authors would like to thank Christopher Behrens for valuable discussions and all colleagues participating in FLASH operation.

REFERENCES

- [1] L. H. Yu, "Generation of intense uv radiation by subharmonically seeded single-pass free-electron lasers.", *Phys. Rev. A*, vol. 44, pp. 5178-5193, 1991.
- [2] T. Plath *et al.*, "Mapping few-femtosecond slices of ultrarelativistic electron bunches", *Sci. Rep.*, vol. 7, p. 2431, 2017.
- [3] V. Grattoni *et al.*, "Status of Seeding Development at sFLASH", presented at the 38th Int. Free Electron Laser Conf. (FEL2017), Santa Fe, USA, August 2017, paper MOP042, this conference.
- [4] J. Bödewadt *et al.*, "Experience in Operating sFLASH with High-Gain Harmonic Generation", in *Proc. of 8th Int. Particle Accelerator Conf. (IPAC17)*, Copenhagen, Denmark, May 2017, pp. 2596 - 2599.
- [5] C. Behrens *et al.*, "Few-femtosecond time-resolved measurements of X-ray free-electron lasers", *Nat. Commun.*, vol. 5, p. 2431, 2014.
- [6] W. K. H. Panofsky and W. A. Wenzel, "Some considerations concerning the transverse deflection of charged particles in radio frequency fields", *Rev. Sci. Instrum.*, vol. 27, pp. 967-967, 1956.
- [7] D. Ratner *et al.*, "Time-resolved imaging of the microbunching instability and energy spread at the Linac Coherent Light Source", *Phys. Rev. ST Accel. Beams*, vol. 18, p. 030704, 2015.
- [8] E.A. Schneidmiller and M.V. Yurkov, "Coherence properties of the radiation from FLASH", *J. Mod. Optic.*, vol. 63, pp. 293-308, 2016.
- [9] E. Prat and M. Aiba, "Four-dimensional transverse beam matrix measurement using the multiple-quadrupole scan technique", *Phys. Rev. ST Accel. Beams*, vol. 17, p. 052801, 2014.
- [10] J. Buon, "Multi-dimensional beam emittance and beta-functions", in *Proc. of 15th Particle Accelerator Conf. (PAC93)*, Washington DC, USA, 1993, pp. 469-471
- [11] M. Xie, "Exact and variational solutions of 3D eigenmodes in high gain FELs", *Nucl. Instrum. Meth. A*, vol. 445, pp. 59 - 66, 2000.
- [12] L. Gianessi, "Seeding and Harmonic Generation in Free-Electron Lasers", in *Synchrotron Light Sources and Free-Electron Lasers*, E. Jaeschke, S. Khan, J. R. Schneider, and J. B. Hastings, Eds., Switzerland: Springer International Publishing, 2016, p. 195.
- [13] C. Lechner, "Demonstration of SASE suppression through a seeded microbunching instability", in *Proc. of the 36th Free Electron Laser Conf. (FEL2014)*, Basel, Switzerland, 2014, pp. 177-180
- [14] E. Hemsing, "Multi-dimensional beam emittance and beta-functions", *Phys. Rev. Lett.*, vol. 113, p. 134802, 2014.

FIRST OPERATION OF A HARMONIC LASING SELF-SEEDED FEL

E.A. Schneidmiller, B. Faatz, M. Kuhlmann, J. Roensch-Schulenburg,
S. Schreiber, M. Tischer, M.V. Yurkov, DESY, Hamburg, Germany

Abstract

Harmonic lasing is a perspective mode of operation of X-ray FEL user facilities that provide brilliant beams of higher energy photons for user experiments. Another useful application of harmonic lasing is so called Harmonic Lasing Self-Seeded Free Electron Laser (HLSS FEL) that improves spectral brightness of these facilities. In the past, harmonic lasing has been demonstrated in the FEL oscillators in infrared and visible wavelength ranges, but not in high-gain FELs, and not at short wavelengths. In this paper we report on the first evidence of the harmonic lasing and the first operation of the HLSS FEL at the soft X-ray FEL user facility FLASH in the wavelength range between 4.5 nm and 15 nm. Spectral brightness was improved in comparison with Self-Amplified Spontaneous emission (SASE) FEL by a factor of six in the exponential gain regime. A better performance of HLSS FEL with respect to SASE FEL in the post-saturation regime with a tapered undulator was observed as well. The first demonstration of harmonic lasing in a high-gain FEL and at short wavelengths paves the way for a variety of applications of this new operation mode in X-ray FELs.

INTRODUCTION

Successful operation of X-ray free electron lasers (FELs) down to the Ångström regime opens up new horizons for photon science. Even shorter wavelengths are requested by the scientific community.

One of the most promising ways to extend the photon energy range of high-gain X-ray FELs is to use harmonic lasing which is the FEL instability at an odd harmonic of the planar undulator [1–5] developing independently from the lasing at the fundamental. Contrary to the nonlinear harmonic generation (which is driven by the fundamental in the vicinity of saturation), harmonic lasing can provide much more intense, stable, and narrow-band radiation if the fundamental is suppressed. The most attractive feature of saturated harmonic lasing is that the spectral brightness of a harmonic is comparable to that of the fundamental [5].

Another interesting option, proposed in [5], is the possibility to improve spectral brightness of an X-ray FEL by the combined lasing on a harmonic in the first part of the undulator (with an increased undulator parameter K) and on the fundamental in the second part of the undulator. Later this concept was named Harmonic Lasing Self-Seeded FEL (HLSS FEL) [6]. Even though this scheme is not expected to provide an ultimate monochromatization of the FEL radiation as do self-seeding schemes using optical elements [7, 8], it has other advantages that we briefly discuss below in the paper.

Harmonic lasing was initially proposed for FEL oscillators [9] and was tested experimentally in infrared and visible wavelength ranges. It was, however, never demonstrated in high-gain FELs and at a short wavelength. In this paper we present the first successful demonstration of this effect at the second branch of the soft X-ray FEL user facility FLASH [10, 11] where we managed to run HLSS FEL in the wavelength range between 4.5 nm and 15 nm.

HARMONIC LASING

Harmonic lasing in single-pass high-gain FELs [1–5] is the amplification process in a planar undulator of higher odd harmonics developing independently of each other (and of the fundamental) in the exponential gain regime. The most attractive feature of the saturated harmonic lasing is that the spectral brightness (or brilliance) of harmonics is comparable to that of the fundamental [5]. Indeed, a good estimate for the saturation efficiency is $\lambda_w / (hL_{\text{sat},h})$, where λ_w is the undulator period, h is harmonic number, and $L_{\text{sat},h}$ is the saturation length of a harmonic. At the same time, the relative rms bandwidth has the same scaling. In other words, reduction of power is compensated by the bandwidth reduction and the spectral power remains the same.

Although known theoretically for a long time [1–4], harmonic lasing in high-gain FELs was never demonstrated experimentally. Moreover, it was never considered for practical applications in X-ray FELs. The situation was changed after publication of ref. [5] where it was concluded that the harmonic lasing in X-ray FELs is much more robust than usually thought, and can be effectively used in both existing and future X-ray FELs. In particular, the European XFEL [12] can greatly outperform the specifications in terms of the highest possible photon energy: it can reach the 60–100 keV range for the third harmonic lasing. It was also shown in [13] that one can keep sub-Ångström range of operation of the European XFEL after CW upgrade of the accelerator with a reduction of electron energy from 17.5 GeV to 7 GeV. Another application of harmonic lasing is a possible upgrade of FLASH with the aim to increase the photon energy up to 1 keV with the present energy 1.25 GeV of the accelerator. To achieve this goal, one should install a specially designed undulator optimized for the third harmonic lasing as suggested in [14].

HARMONIC LASING SELF-SEEDED FEL

A poor longitudinal coherence of SASE FELs has stimulated efforts for its improvement. Since an external seeding seems to be difficult to realize in the X-ray regime, a so called self-seeding has been proposed in [7, 8]. There are alternative approaches for reducing bandwidth and increasing spectral brightness of X-ray FELs without using optical



Figure 1: Conceptual scheme of a harmonic lasing self-seeded FEL

elements. One of them [15, 16] suggests to use chicanes inside the undulator system to increase slippage of the radiation and to establish long-range correlations in the radiation pulse. Another method was proposed in [5] and is based on the combined lasing of a harmonic in the first part of the undulator (with increased undulator parameter K) and of the fundamental in the second part. In this way the second part of the undulator is seeded by a narrow-band signal generated via a harmonic lasing in the first part. This concept was named HLSS FEL (Harmonic Lasing Self-Seeded FEL) [6]. Note that a very similar concept was proposed in [17] and was called a purified SASE FEL, or pSASE.

Typically, gap-tunable undulators are planned to be used in the X-ray FEL facilities. If the maximal undulator parameter K is sufficiently large, the concept of harmonic lasing self-seeded FELs can be applied in such undulators (see Fig. 1). An undulator is divided into two parts by setting two different undulator parameters such that the first part is tuned to a h -th sub-harmonic of the second part which is tuned to a wavelength of interest λ_1 . Harmonic lasing occurs in the exponential gain regime in the first part of the undulator, also the fundamental in the first part stays well below saturation. In the second part of the undulator the fundamental is resonant to the wavelength, previously amplified as the harmonic. The amplification process proceeds in the fundamental harmonic up to saturation. In this case the bandwidth is defined by the harmonic lasing (i.e. it is reduced by a significant factor depending on its harmonic number) but the saturation power is still as high as it is in the reference case of lasing at the fundamental in the whole undulator, i.e. the spectral brightness increases.

The enhancement factor of the coherence length or, bandwidth reduction factor, that one obtains in HLSS FEL in comparison with a reference case of lasing in SASE FEL mode in the whole undulator, reads [6]:

$$R \simeq h \frac{\sqrt{L_w^{(1)} L_{\text{sat},h}}}{L_{\text{sat},1}}. \quad (1)$$

Here h is harmonic number, $L_{\text{sat},1}$ is the saturation length in the reference case of the fundamental lasing with the lower K -value, $L_w^{(1)}$ is the length of the first part of the undulator, and $L_{\text{sat},h}$ is the saturation length of harmonic lasing. We notice that it is beneficial to increase the length of the first part of the undulator. Since it must be shorter than the saturation length of the fundamental harmonic in the first section, one can consider delaying the saturation of the fundamental with

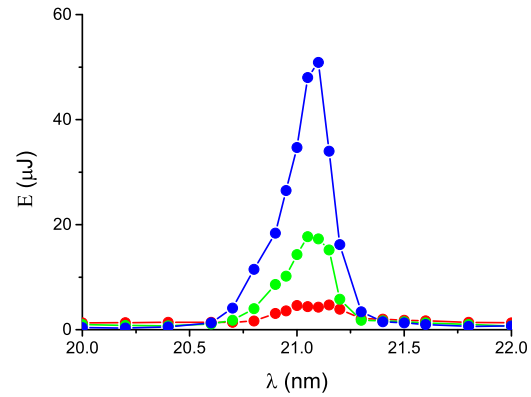


Figure 2: Scan of the resonance wavelength of the first part of the undulator consisting of one undulator section (red), two sections (green), and three sections (blue). Pulse energy is measured after the second part of the undulator tuned to 7 nm.

the help of phase shifters [4, 5] in order to increase $L_w^{(1)}$. However, for the sake of simplicity, we did not use this option in our experiments.

Despite the fact that the bandwidth reduction factor (1) is significantly smaller than that of self-seeding schemes using optical elements [7, 8], the HLSS FEL scheme is very simple and robust, and it does not require any additional installations, i.e. it can always be used in existing or planned gap-tunable undulators with a sufficiently large K -value.

One more advantage of the HLSS FEL scheme over the SASE FEL (and in many cases over a self-seeded FEL) is the possibility of a more efficient use of a post-saturation taper for an improved conversion of the electron beam power to the FEL radiation power [6, 18]. This makes us believe that HLSS FEL will become a standard mode of operation of X-ray FEL facilities.

OPERATION OF HARMONIC LASING SELF-SEEDED FEL AT FLASH

The first soft X-ray FEL user facility FLASH [10, 11] was upgraded to split the electron pulse trains between the two undulator lines so that the accelerator with maximum energy of 1.25 GeV now drives both lines. In a new separate tunnel, a second undulator line called FLASH2 with a variable-gap undulator was installed, while a new experimental hall has space for up to six experimental stations [19]. The gap-tunable undulator of FLASH2 consists of twelve 2.5 m long sections with the undulator period of 3.14 cm and the maximum rms K -value about 1.9. This makes it possible to study the HLSS FEL scheme with the 3rd harmonic seeding. The details of our measurements can be found in [20].

On May 1, 2016 we were able to successfully perform the first test of HLSS FEL at FLASH2. Electron energy was 948 MeV, charge 0.4 nC. Initially we tuned 10 undulator sections to a standard SASE, operating in the exponential gain regime at the wavelength of 7 nm (rms K parameter was 0.73); the pulse energy was 12 μJ . Then we detuned

Content from this work may be used under the terms of the CC BY 3.0 licence (© 2018). Any distribution of this work must maintain attribution to the author(s), title of the work, publisher, and DOI.

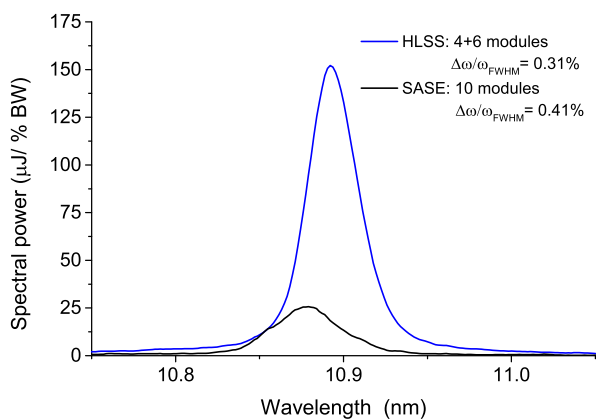


Figure 3: Spectral density of the radiation energy for HLSS FEL configuration (blue) and for SASE FEL (black).

the first section, tuned it to the third subharmonic (rms K was 1.9) and scanned it around 21 nm. We repeated the measurements with the first two sections, and then with the first three sections. Note that the fundamental at 21 nm was also in the exponential gain regime, pulse energy after three undulator sections was 40 nJ, i.e. it was far from saturation (which was achieved at the 200 μJ level). This means, in particular, that the nonlinear harmonic generation in the first part of the undulator is excluded.

One can see from Fig. 2 that the effect is essentially resonant. For example, in the case when three undulator sections were scanned, the ratio of pulse energies at the optimal tune, 21.1 nm, and at the tune of 20 nm is $51 \mu\text{J}/0.3 \mu\text{J} = 170$. We claim that there can be only one explanation of the effect that we observe in Fig. 2: FEL gain at 7 nm is strongly reduced as soon as the first part of the undulator is detuned, and then the gain is recovered (and becomes even larger) due to the 3rd harmonic lasing in the first part as soon as the resonant wavelength is 21 nm. We should stress that the pulse energy with three retuned undulator sections (51 μJ) is significantly larger than that in the homogeneous undulator tuned to 7 nm (it was 12 μJ). This is because the gain length of harmonic lasing is shorter than that of the fundamental tuned to the same wavelength [4–6, 18].

In the next runs in 2016 at different wavelengths (between 4.5 nm and 15 nm) we were able to demonstrate an improvement of the longitudinal coherence in HLSS regime with respect to SASE case as well as a better performance in the post-saturation taper regime.

In June 2016 the electron energy was different 757 MeV and we lased at 11 nm. We also used a different charge, 0.25 nC, in this experiment. The undulator settings were similar to the previous case: we used ten undulator modules, rms K-parameter was 0.73 in SASE mode and 1.9 in the first part of the undulator in HLSS mode. The difference with the previous measurements was that we detuned four undulator modules in HLSS regime.

The spectra in Fig. 3 are the results of averaging over 50 single-shot spectra in each case. One can see that HLSS FEL indeed has a smaller bandwidth, 0.31%, as compared to

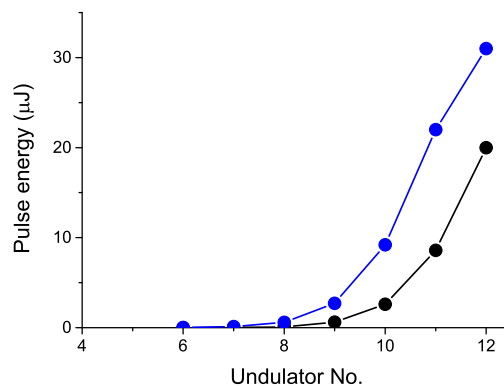


Figure 4: Radiation pulse energy versus position in the undulator for HLSS (blue) and for SASE (black) at 15 nm. Post-saturation taper was optimized for both cases.

0.41% in the case of SASE FEL. The bandwidth reduction factor is 1.3 from this measurement. The spectral power, however, differs by a factor of six due to an additional increase of pulse energy in HLSS regime. This happens because the 3rd harmonic lasing at 11 nm has a shorter gain length than lasing at the same wavelength on the fundamental. An expected bandwidth reduction factor (or coherence enhancement factor) R from formula (1) can be estimated at 1.7. The discrepancy can be explained by the energy chirp in the electron beam.

Another method of determination of an improvement of the longitudinal coherence (independent of the presence of the frequency chirp in FEL pulses) is based on statistical measurements of the FEL pulse energy along the undulator length. we obtain an estimate for the coherence enhancement factor in the end of the exponential gain regime: $R \approx 1.8 \pm 0.3$ [20]. This is in a good agreement with already presented theoretical estimate $R \approx 1.7$.

In November 2016 we set up HLSS FEL as a configuration with four first undulators tuned to 45 nm and the last eight undulators tuned to 15 nm. The electron energy was 645 MeV, the charge was 100 pC, the rms value of K was 1.9 in the first part of the undulator and 0.73 in the second part. We reached FEL saturation in SASE and HLSS modes, and applied post-saturation taper to improve FEL efficiency. The result is presented in Fig. 4 from which one can conclude that HLSS FEL indeed performs better in this operation mode than the SASE FEL. We can, therefore, forecast that HLSS may become a standard mode of operation of the X-ray FEL user facilities with gap-tunable undulators, providing an improvement of the longitudinal coherence, a reduction of the saturation length and a possibility of a more efficient post-saturation tapering.

It is also important to note that the first evidence of harmonic lasing in a high-gain FEL and at a short wavelength (down to 4.5 nm) paves the way for a variety of applications of this effect in X-ray FEL facilities [5, 6, 13, 14].

REFERENCES

- [1] J.B. Murphy, C. Pellegrini, and R. Bonifacio, *Opt. Commun.*, vol. 53, pg. 197, 1985.
- [2] R. Bonifacio, L. De Salvo, and P. Pierini, *Nucl. Instr. Meth.*, vol. A293, pg. 627, 1990.
- [3] Z. Huang and K. Kim, *Phys. Rev. E*, vol. 62, pg. 7952, 2000.
- [4] B. W. J. McNeil *et al.*, *Phy. Rev. Lett.*, vol. 96, pg. 084801, 2006.
- [5] E.A. Schneidmiller and M.V. Yurkov, *Phys. Rev. ST-AB*, vol. 15, pg. 080702, 2012.
- [6] E.A. Schneidmiller and M.V. Yurkov, "Harmonic Lasing Self-Seeded FEL", *Proc. of FEL2013*, New York, p.700, 2013.
- [7] J. Feldhaus *et al.*, *Optics. Comm.*, vol. 140, pg. 341, 1997.
- [8] G. Geloni, V. Kocharyan, and E.L. Saldin, *Journal of Modern Optics*, vol. 58, pg. 1391, 2001.
- [9] W.B. Colson, *IEEE J. Quantum Electron*, vol. 17, pg. 1417, 1981.
- [10] W. Ackermann *et al.*, *Nature Photonics* vol. 1, pg. 336, 2007.
- [11] S. Schreiber and B. Faatz, "The free-electron laser FLASH", *High Power Laser Science and Engineering*, vol. 3, e20 doi:10.1017/hpl.2015.16.
- [12] M. Altarelli *et al.* (Eds.), XFEL: The European X-Ray Free-Electron Laser. Technical Design Report, Preprint DESY 2006-097, DESY, Hamburg, 2006 (see also <http://xfel.desy.de>).
- [13] R. Brinkmann, E.A. Schneidmiller, J. Sekutowicz, and M.V. Yurkov, *Nucl. Instrum. and Methods*, vol. A 768, pg. 20, 2014.
- [14] E.A. Schneidmiller and M.V. Yurkov, *Nucl. Instrum. and Methods*, vol. A 717, pg. 37, 2013.
- [15] J. Wu, J., A. Marinelli, and C. Pellegrini, *Proceedings of the 32th International Free Electron Laser Conference*, Nara, Japan, p. 23, 2012 [<http://www.jacow.org>].
- [16] B. W. J. McNeil, N.R. Thompson, and D.J. Dunning, *Phys. Rev. Lett.*, vol. 110, pg. 134802, 2013.
- [17] D. Xiang *et al.*, *Phys. Rev. ST-AB*, vol. 16, pg. 010703, 2013.
- [18] E.A. Schneidmiller and M.V. Yurkov, *Proceedings of IPAC2016*, Busan, Korea, pg. 725, 2016 [<http://www.jacow.org>].
- [19] B. Faatz *et al.*, *New Journal of Physics*, vol. 18, pg. 062002, 2016).
- [20] E. A. Schneidmiller, B. Faatz, M. Kuhlmann, J. Roensch-Schulenburg, S. Schreiber, M. Tischer, M. V. Yurkov, *Phys. Rev. ST-AB*, vol. 20, pg. 020705, 2017.

REVERSE UNDULATOR TAPERING FOR POLARIZATION CONTROL AND BACKGROUND-FREE HARMONIC PRODUCTION IN XFELS: RESULTS FROM FLASH

E.A. Schneidmiller and M.V. Yurkov, DESY, Hamburg, Germany

Abstract

Nonlinear harmonics in X-ray FELs can be parasitically produced as soon as the FEL reaches saturation, or can be radiated in dedicated afterburners. In both cases there is a strong background at the fundamental since it is much stronger than the harmonics. One can get around this problem applying the recently proposed reverse undulator tapering. In this contribution we present recent results from FLASH where the second and the third harmonics were efficiently generated with a low background at the fundamental. We also present the results for a high-contrast operation when the afterburner is tuned to the fundamental.

INTRODUCTION

Successful operation of X-ray free electron lasers (FELs) [1–3] based on the self-amplified spontaneous emission (SASE) principle [4], opens up new horizons for photon science. One of the important requirements of FEL users in the near future will be polarization control of X-ray radiation. Baseline design of a typical X-ray FEL undulator assumes a planar configuration which results in a linear polarization of the FEL radiation. However, many experiments at X-ray FEL user facilities would profit from using a circularly polarized radiation. There are different ideas for possible upgrades of the existing (or planned) planar undulator beamlines.

As a cheap upgrade one can consider an installation of a short helical afterburner as it was done at LCLS where a so called DELTA undulator was installed behind the main undulator [5]. However, to obtain high degree of circular polarization one needs to suppress powerful linearly polarized radiation from the main undulator. A method for suppression of the linearly polarized background from the main undulator was proposed in [6] is an application of the reverse undulator taper. It was shown that in some range of the taper strength the bunching factor at saturation is practically the same as in the reference case of the non-tapered undulator, the saturation length increases moderately while the saturation power is suppressed by orders of magnitude. Therefore, the proposed scheme is conceptually very simple (see Fig. 1): in a tapered main (planar) undulator the saturation is achieved with a strong microbunching and suppressed radiation power, then the modulated beam radiates at full power in a helical afterburner tuned to resonance. This method (in combination with the spatial separation) was used at LCLS to obtain a high degree of circular polarization [7] and is routinely used now in user operation.

Obviously, the afterburner (helical or planar) can be tuned to a harmonic of the main undulator. In this case the har-

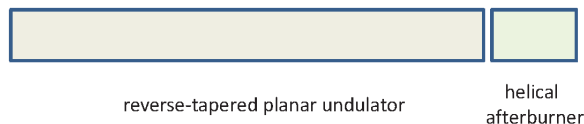


Figure 1: Conceptual scheme for obtaining circular polarization at X-ray FELs.

monics can be efficiently generated with a low background at the fundamental.

In this paper we present experimental results from FLASH [1, 8, 9] where a high contrast between the radiation from the "afterburner" (the last two undulator sections) and from the reverse-tapered undulator was demonstrated recently. Also, the results on an efficient background-free production of high harmonics from the afterburner are presented.

POTENTIAL APPLICATIONS OF REVERSE TAPER IN HIGH-GAIN FELS

Polarization Control

Undulators of X-ray FEL user facilities are usually planar, and the FEL radiation is linearly polarized. However, there is a strong interest from users in obtaining circularly polarized radiation, or, more generally, to have full polarization control. To achieve this goal one can install a short variable-polarization afterburner, and to suppress a strong linearly polarized background from the main undulator. Reverse tapering seems to be an ideal solution to this problem since it does not require any additional installations. Moreover, not only FEL power is suppressed, but also the energy modulations are strongly reduced in comparison with on-resonance operation [6]. Thus, fully bunched electron beam with small energy modulations can more efficiently radiate in the afterburner.

Efficient Background-Free Generation of High Harmonics

The afterburner can also be tuned to a harmonic of the main undulator. In this case a powerful background-free generation of this harmonic can be expected. Indeed, the modulated electron beam at saturation contains harmonics of density, and the energy modulation is small. Therefore, these density harmonics exist longer in the radiator (planar or helical), and a significant intensity can be produced at a selected harmonic. At the same time, the radiation at the fundamental and at harmonics of the main undulator is strongly suppressed (a suppression is much stronger for harmonics than for the fundamental), i.e. the background is small. In particular, if a helical afterburner is tuned to the

second or the third harmonic of the main undulator, a high degree of circular polarization should be expected. Let us note that the method of harmonics production can be used for SASE FELs as well as for seeded (self-seeded) FELs (the latter case was recently considered in [10]).

It is also worth noticing that, in principle, one does not need a dedicated afterburner for an operation of this scheme. Instead, it is sufficient to have a gap-tunable undulator with the largest part being reverse-tapered and a smaller last part tuned to a second or third harmonic. In this case one can reach a shorter wavelength than in a standard SASE mode of operation of an X-ray FEL user facility. A promising configuration could use, for example, a radiation at the third harmonic of the afterburner using the second harmonic of the beam density, produced in the reverse-tapered main undulator. Such an operation mode was recently tested at FLASH, the results will be published elsewhere.

REVERSE TAPER EXPERIMENTS AT FLASH

The first soft X-ray FEL user facility FLASH [1, 8, 9] was upgraded to split the electron pulse trains between the two undulator lines so that the accelerator with maximum energy of 1.25 GeV now drives both lines. In a new separate tunnel, a second undulator line, called FLASH2, with a variable-gap undulator was installed, while a new experimental hall has space for up to six experimental stations [9]. The gap-tunable undulator of FLASH2 consists of twelve 2.5 m long sections with the undulator period of 3.14 cm and the maximum rms K-value about 1.9.

High Contrast Radiation at the Fundamental of the Afterburner

In the experiment on January 23, 2016 we used the first ten undulator sections as a main undulator with reverse tapering, and the last two sections played the role of the afterburner, i.e. they could be tuned to a resonance with the incoming microbunched beam. In what follows we will simply call them afterburner even though they are not a dedicated device.

The electron energy during the measurements was 715 MeV, and the FEL wavelength was 17 nm. The rms value of K in the first section was 1.06 (corresponding to the undulator gap of 14.5 mm), and the depth of reverse taper over 10 undulator sections was 10% (note that the step-tapering was used, i.e. the parameter K was constant inside each section). The bunch charge was 0.3 nC, and the other parameters of electron beam (peak current, emittance etc.) were not measured due to a parallel operation with the other undulator line, FLASH1. For this reason we present here only experimental results without a comparison with simulations.

In Fig. 2 the gap scan of the two last undulator sections (afterburner) is shown. When the undulators are completely open, the pulse energy is slightly below 1 microjoule. When they are tuned to the resonance with the incoming microbunched beam, the pulse energy becomes 200 μJ (to

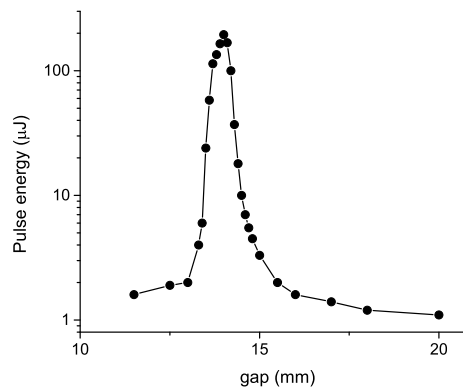


Figure 2: Gap scan of the afterburner (last two undulator sections). For a completely open gap the pulse energy is below 1 μJ .

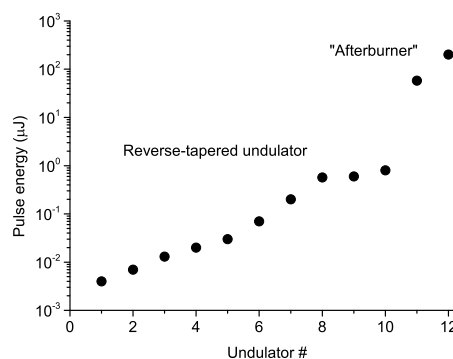


Figure 3: FEL pulse energy versus undulator number. First ten undulators are reverse-tapered, last two sections are tuned to the resonance with the incoming microbunched beam.

be compared with 260 μJ in an untapered undulator with 12 undulator sections). Note that the rms K parameter in this case is 1.11 which is the mean of the initial value, 1.06, and the final value, 1.17, of the rms K in the reverse-tapered undulator section. This result is in agreement with the predictions of the theory of an FEL with slowly varying parameters [11].

We also measured the FEL gain curve in this configuration, it is shown in Fig. 3. One can see again that the high contrast (in excess of 200) between the radiation intensity from the afterburner and from the reverse-tapered undulator is measured. The gain curve in Fig. 3 looks similar to that simulated in [6] for the European XFEL [12].

We repeated the reverse taper experiment at the same wavelength but at a higher electron energy (930 MeV) on March 12, 2016. Rms undulator parameter was 1.6, and the ten undulator sections were reverse-tapered by 5%. In this case the pulse energy was 0.25 μJ , while after tuning the 11th and the 12th sections to the resonance it reached 60 μJ , i.e. the contrast above 200 was demonstrated again.

Content from this work may be used under the terms of the CC BY 3.0 licence (© 2018). Any distribution of this work must maintain attribution to the author(s), title of the work, publisher, and DOI.

Background-Free Generation of Harmonics in the Afterburner

On March 12, 2016 we were also able to observe the generation of the second harmonic from the afterburner while the main undulator was reverse-tapered [13].

A dedicated experiment was performed on October 10, 2016 with the aim to demonstrate an efficient generation of the 2nd and the 3rd harmonics in the afterburner. The electron energy was 852 MeV, the charge was 0.3 nC, and the wavelength for the untapered case was set to 25.5 nm with the rms K parameter of 1.9. The first nine undulator sections were then 5% reverse-tapered, and the following two sections played the role of the afterburner. When the afterburner sections were completely opened, the background from the reverse-tapered main undulator was measured at the level of $0.9 \mu\text{J}$. When we tuned the afterburner sections to 26.2 nm, the pulse energy was $132 \mu\text{J}$, i.e. a contrast above 100 was measured. Then we tuned the afterburner to the second and the third harmonics of the main undulator and a wavelength scan (or, K-scan) of the undulator around the corresponding resonances was performed. The results are presented in Fig. 4 where one can see that the pulse energy reached $41 \mu\text{J}$ when the afterburner was tuned to 13.2 nm, and $10 \mu\text{J}$ for the 8.8 nm tune. Note that in the latter case the rms K-value was 0.75 only, i.e. one could have expected a better result if a dedicated optimized afterburner with a shorter period and a larger K-value had been used. We should also note the fact that a small background on the fundamental at the detectors (and, in the future, at a user experiment) from the reverse-tapered main undulator can be further reduced by using small apertures since the fundamental has a larger divergence. Thus, we have demonstrated that the reverse tapering in the main undulator can be used for an efficient, background-free, generation of harmonics in the afterburner.

ACKNOWLEDGEMENTS

We are grateful to FLASH team for technical support. We would like to thank R. Brinkmann, J. Schneider, E. Weckert and W. Wurth for valuable discussions and support of this work.

REFERENCES

[1] W. Ackermann *et al.*, *Nature Photonics*, **1**(2007)336
 [2] P. Emma *et al.*, *Nature Photonics*, **4**(2010)641
 [3] T. Ishikawa *et al.*, *Nature Photonics*, **6**(2012)540-544
 [4] A.M. Kondratenko and E.L. Saldin, *Part. Accelerators*, **10**(1980)207

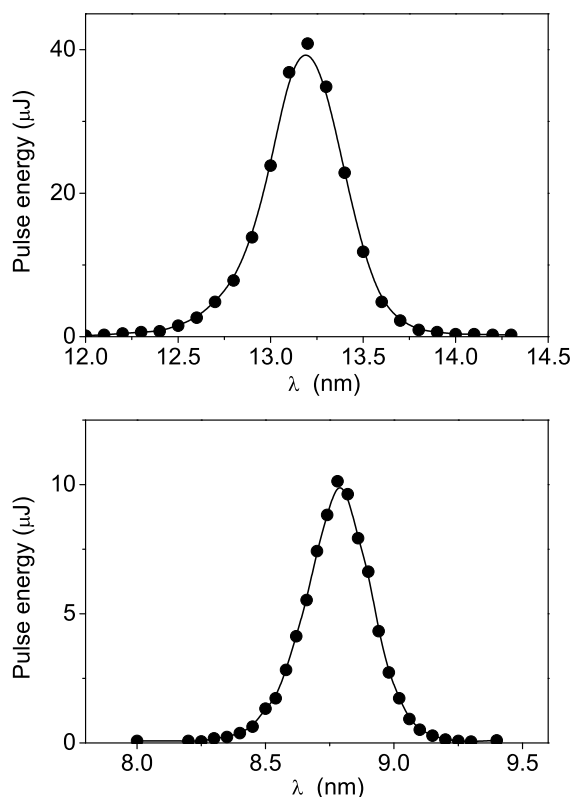


Figure 4: Radiation pulse energy of the second (left plot) and the third (right plot) harmonics radiated in the afterburner versus the resonance wavelength of the afterburner. A small background from the fundamental is subtracted.

[5] H.-D. Nuhn *et al.*, "Commissioning of the DELTA polarizing undulator at LCLS", *Proc. of FEL2015 Conf.*, Daejeon, Korea, p. 757
 [6] E.A. Schneidmiller and M.V. Yurkov, *Phys. Rev. ST Accel. Beams*, **16**(2013)110702.
 [7] A. Lutman *et al.*, *Nature Photonics*, **10**(2016)468
 [8] S. Schreiber and B. Faatz, "The free-electron laser FLASH", *High Power Laser Science and Engineering*, **3**, e20 doi:10.1017/hpl.2015.16
 [9] B. Faatz *et al.*, *New Journal of Physics*, **18**(2016)062002
 [10] K. Zhang *et al.*, *Nucl. Instrum. and Methods*, **A 854**(2017)3
 [11] Z. Huang and G. Stupakov, *Phys. Rev. ST Accel. Beams*, **8**(2005)040702
 [12] M. Altarelli *et al.* (Eds.), XFEL: The European X-Ray Free-Electron Laser. Technical Design Report, Preprint DESY 2006-097, DESY, Hamburg, 2006 (see also <http://xfel.desy.de>)
 [13] E.A. Schneidmiller and M.V. Yurkov, *Proceedings of IPAC2016*, Busan, Korea, p. 722, [<http://www.jacow.org>]

BASELINE PARAMETERS OF THE EUROPEAN XFEL

E.A. Schneidmiller, M.V. Yurkov, DESY, Hamburg, Germany

Abstract

We present the latest update of the baseline parameters of the European XFEL. It is planned that the electron linac will operate at four fixed electron energies of 8.5, 12, 14, and 17.5 GeV. Tunable gap undulators provide the possibility to change the radiation wavelength in a wide range. Operation with different bunch charges (0.02, 0.1, 0.25, 0.5 and 1 nC) provides the possibility to operate XFEL with different radiation pulse duration. We also discuss potential extension of the parameter space which does not require new hardware and can be realized at a very early stage of the European XFEL operation.

BASELINE PARAMETERS

The European XFEL is driven by a superconducting accelerator with a maximum energy of electrons of 17.5 GeV [1, 2]. It operates in the burst mode with 10 Hz repetition rate of 0.6 ms pulse duration. Each pulse brings train of up to 2700 electron bunches (up to 4.5 MHz repetition rate). Three undulators are installed in the first stage of the project: SASE1, SASE2, and SASE3 (see Table 1). SASE3 undulator is placed sequentially after SASE1 undulator in the same electron beamline. All undulators

have similar mechanical design. The length of the undulator module is equal to 5 meters. The length of the undulator intersection is equal to 1.1 m. The undulators of SASE1 and SASE2 are identical: period length is 40 mm, number of modules is 35, the range of the gap variation is 10 to 20 mm. SASE3 undulator consists of 21 modules, the period is 68 mm, the gap tunability range is 10 to 25 mm [3]. Tunability range of the undulators has been corrected on the base of magnetic measurements [3], and in terms of undulator parameter is 1.65 - 4 and 4 - 9 for SASE1/SASE2 and SASE3, respectively. The tunability range in terms of $\lambda_{\max}/\lambda_{\min}$ is 3.5 for SASE1/2 and 4.6 for SASE3.

Requirements of users are summarized and analyzed in a proper way to provide maximum opportunities for every instrument and experiment simultaneously [4–7]. The tunability ranges of the undulators are not sufficient to cover the required wavelength ranges at one fixed electron beam energy, and four electron beam energies have been defined: 8.5 GeV, 12 GeV, 14 GeV, and 17.5 GeV [4, 5]. Five operating points for the bunch charge has been fixed: 20 pC, 100 pC, 250 pC, 500 pC, and 1 nC (see Table 3). The beam formation system is designed to produce peak beam current of 5 kA with nearly Gaussian shape. Electron bunches with different bunch charges will generate radiation pulses with different radiation pulse duration. Figure 1 shows an overview of the main photon beam properties of the European XFEL for the bunch charge 1 nC. The left and right columns in these plots correspond to the SASE1/SASE2 and SASE3 undulators, and allow visual tracing of the operating wavelength bands, pulse energy, and brilliance as function of the electron energy. The general tendency is that operation with higher charges provides higher pulse energy and higher average brilliance, nearly proportional to the bunch charge.

Properties of the radiation from SASE3 are presented in Fig. 1, we assume that the electron beam is not disturbed by FEL interaction in the SASE1 undulator. Decoupling of SASE3 and SASE1 operation can be performed with an application of the betatron switcher [7, 9]. Feedback kickers can be used to test and operate this option at the initial stage. In case of positive results dedicated kickers need to be installed [6]. Operation of SASE3 as an afterburner of SASE1 is also possible, but with reduced range of accessible wavelengths and reduced power [7]. General problem is that tuning of SASE1 to higher pulse energies leads to higher induced energy spread in the electron beam, and to degradation of the SASE3 performance. For instance, operation of SASE3 at the energy of 17.5 GeV is impossible at any wavelength if wavelength of SASE1 is longer than 0.1 nm, and radiation power of

Table 1: Undulators at the European XFEL [3]

	Units	SASE1/2	SASE3
Period length	cm	4	6.8
Maximum field	T	1.11	1.66
Gap range	cm	1 – 2	1 – 2.5
K range	#	3.9 – 1.65	9.0 – 4.08
Length of module	m		5
Length of intersection	m		1.1
Number of modules	#	35	21
Total magnetic length	m	175	105

Table 2: Working Points and Tunability Ranges of the European XFEL

	SASE1/2	SASE3
Tunability, $\lambda_{\max}/\lambda_{\min}$	3.64	4.45
El. energy, GeV	Photon energy range, keV	
8.5	1.99 – 7.27	0.24 – 1.08
12.0	3.97 – 14.48	0.48 – 2.16
14.0	5.41 – 19.71	0.66 – 2.94
17.5	8.45 – 30.80	1.03 – 4.59
	Photon wavelength range, nm	
8.5	0.171 – 0.622	1.15 – 5.10
12.0	0.086 – 0.312	0.57 – 2.56
14.0	0.063 – 0.229	0.42 – 1.88
17.5	0.040 – 0.147	0.27 – 1.20

Table 3: Properties of the Electron Beam at the Undulator Entrance [6]

Bunch charge	nC	0.02	0.1	0.25	0.5	1
Peak beam current	kA	4.5	5	5	5	5
Normalized rms emittance	mm-mrad	0.32	0.39	0.6	0.7	0.97
rms energy spread	MeV	4.1	2.9	2.5	2.2	2
rms pulse duration	fs	1.2	6.4	16.6	30.6	76.6

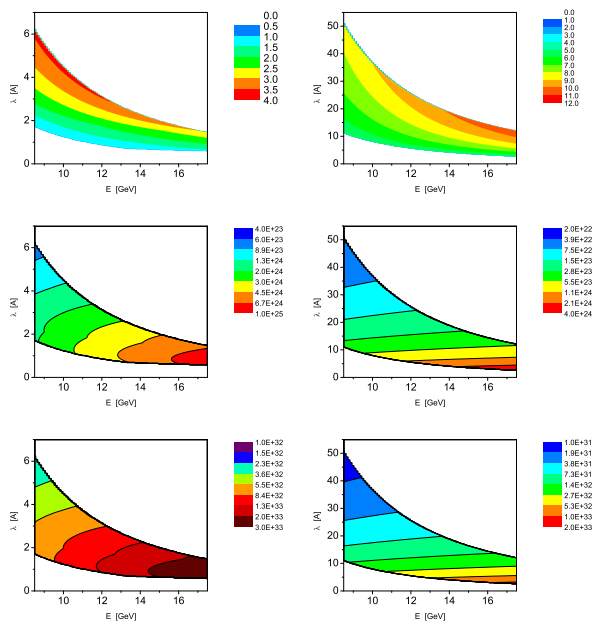


Figure 1: An overview of photon beam properties of the European XFEL for SASE1/2 (left column) and SASE3 (right column). Contour plots present pulse energy (top row), peak brilliance (middle row), and average brilliance (lower row). Units for the pulse energy and brilliance are mJ and photons/sec/mm²/rad²/0.1% bandwidth, respectively. Bunch charge is equal to 1 nC. Calculations have been performed with FEL simulation code FAST [8].

SASE1 is tuned by a factor of 1.5 above saturation power [7].

Full description of the baseline parameters is presented in a dedicated report [10]. It contains an overview and detailed saturation tables, and reference physical information for users.

The best way for planning user experiments is performing start-to-end simulations tracing radiation pulses from its origin (undulator) through a beamline (mirrors, monochromators, etc.) to a target, simulation of physical processes of the radiation interaction with a sample, and simulation of detection process of related debris (photon, electrons, ions, etc.) by detectors. We present an XFEL photon pulses simulation database (XPD) accessible through public web-server that allows the access to the data produced by time-dependent FEL simulation code FAST [8]. A web application allows for picking up selected photon pulse data in the hdf5 format for any given XFEL operation mode (electron energy, charge/photon pulse duration, active undulator range, etc.) suitable for statistical analysis, propagating through the op-

tical system, interaction with the sample, etc. The pulses post processing data, including the gain curve, time structure, source size and far field angular divergence are also provided. Detailed parameters of the radiation together with 3D field maps are being compiled in the photon data base of the European XFEL [10, 11]. Currently this data base is used for optimization of the photon beam transport and imaging experiment [12, 13]. Official web page of the European XFEL photon data base XPD is <https://in.xfel.eu/xpd/> [11].

POTENTIAL EXTENSIONS BEYOND BASELINE OPTION

There are several potential extensions beyond the baseline option which can be realized at a very early stage of the European XFEL operation without additional hardware, or by means of extension of the functions of the present hardware. Some solutions are pretty old, and some other appeared just recently. Some proposals rely on parameters of the electron beam beyond the baseline option. Several groups perform theoretical and simulation studies of different options. There is also experimental activity at FLASH and LCLS on verification of advanced concepts. Here we briefly highlight several extensions related to the European XFEL with references to the most fresh publications.

The next phase of the facility upgrade will include helical afterburner based on the reverse tapering.

Efficiency Increase by Undulator Tapering

Undulator tapering will allow significant increase of FEL power. Many studies on this subject have been performed for the parameters of the European XFEL (see [1, 7, 14, 15] and references therein). Application of the undulator tapering has evident benefits for the SASE3 FEL operating in the wavelength range around 1.6 nm. It is about a factor of 6 in the pulse radiation energy with respect to the saturation regime, and factor of 3 with respect to the radiation power at the full length. General feature of tapered regime is that both spatial and temporal coherence degrade in the nonlinear regime, but more slowly than for the untapered case. Peak brilliance is reached in the middle of the tapered section, and exceeds the value of the peak brilliance in the saturation regime by a factor of 3. The degree of transverse coherence at the saturation for the untapered case is 0.86. The degree of transverse coherence for the maximum brilliance of the tapered case is 0.66, coherence time is reduced by 15%. At the exit of the undulator the degree of transverse coherence for the tapered case is 0.6, and coherence time is reduced

Content from this work may be used under the terms of the CC BY 3.0 licence (© 2018). Any distribution of this work must maintain attribution to the author(s), title of the work, publisher, and DOI.

by 20%. Radiation of the 3rd harmonic for both the untapered and tapered cases exhibit nearly constant brilliance and nearly constant contribution to the total power. Coherence time of the 3rd harmonic for the tapered case approximately scales inversely proportional to harmonic number, as in the untapered case.

Multicolor Mode of Operation

A betatron switcher [9] can be used in long undulators for providing multi-color operation. Different parts of the undulator are tuned to different resonance wavelengths. Fast kicker and steerer force lasing of selected bunch in specific part of the undulator.

Harmonic Generation and Harmonic Lasing Self-Seeded FEL

Contrary to nonlinear harmonic generation, harmonic lasing in a high-gain FEL can provide much more intense, stable, and narrow-band FEL beam which is easier to handle if the fundamental is suppressed [16]. At the European XFEL the harmonic lasing would allow to extend operating range ultimately up to 100 keV. Currently this option is studied for implementation in the MID instrument [17]. Dedicated experimental program on harmonic generation is ongoing at LCLS [18].

A concept of a harmonic lasing self-seeded FEL (HLSS) has been proposed recently [16]. A gap-tunable undulator is divided into two parts by setting two different undulator parameters such that the first part is tuned to a sub-harmonic of the second part. Harmonic lasing occurs in the exponential gain regime in the first part of the undulator, also the fundamental stays well below saturation. In the second part of the undulator the fundamental mode is resonant to the wavelength, which was previously amplified as the harmonic. The amplification process proceeds in the fundamental mode up to saturation. In this case the bandwidth is defined by the harmonic lasing (i.e. it is reduced by a significant factor depending on harmonic number) but the saturation power is still as high as in the reference case of lasing at the fundamental in the whole undulator, i.e. the spectral brightness increases. Application of the undulator tapering in the deep nonlinear regime would allow generation of higher peak powers approaching the TW level [19]. Modification of the HLSS scheme, named purified SASE - pSASE [20], is under consideration as well by [21].

Extended Range of Electron Beam Parameters

Several options are under consideration for exploiting higher peak currents, and higher bunch charges to increase pulse energy and peak power (see [7, 22] and references therein). Dedicated activity of simulation, production, and characterization of high charge bunches in XFEL-type electron gun is ongoing at PITZ [23, 24]. Another direction of studies is production of ultrashort pulses. This activity also involves both, simulation studies for XFEL and experimental studies at FLASH (see [25–27] and references therein).

For instance, use of higher charges in combination with tapering will allow generation of sub-Joule energies in the radiation pulse [7]. Note that there can be some technical complications for operation with charges which are not in the gate of baseline parameters [6]. It is our experience of FLASH operation with small charges that limitations of the electron beam diagnostic are not stopovers, but they significantly complicate tuning, since some feedback system stop working because of noisy measurements.

“Pink” Photon Beam

Some user application require a “pink” photon beam with a spectrum width of several percent. Two options to increase the spectrum range have been considered so far: formation of the energy chirp in the bunch train [6], and formation of the energy chirp within electron bunch [28].

ACKNOWLEDGMENTS

Results presented in this paper have been discussed at the meetings devoted to revision of parameter space and discussion of potential extensions of the European XFEL. We are grateful to our colleagues from DESY and European XFEL for fruitful collaboration during this work: M. Altarelli, C. Bressler, R. Brinkmann, W. Decking, N. Gerasimova, J. Gruenert, T. Limberg, A. Madson, A. Mancuso, M. Meyer, S. Molodtsov, J. Pflueger, L. Samoylova, A. Schwarz, H. Sinn, T. Tschentscher, and H. Weise. We thank our colleagues from the Beam Dynamics Group for providing us with parameters of the electron beam: M. Dohlus, G. Feng, and I. Zagorodnov. We are grateful to M. Krasilnikov and F. Stephan for fruitful collaboration on high charge option. We thank R. Brinkmann for fruitful collaboration and support of our work.

REFERENCES

- [1] M. Altarelli *et al.*, (Eds.), XFEL: The European X-Ray Free-Electron Laser. Technical Design Report, Preprint DESY 2006-097, DESY, Hamburg, 2006. (see also <http://xfel.desy.de>).
- [2] W. Decking and F. Le Pimpec, *Proc. FEL 2014 Conference*, Basel, Switzerland, 2014, WEBO3.
- [3] J. Pflueger *et al.*, Status of the undulator systems for the European x-ray free electron laser, *Proc. FEL2013*, New York, USA, 2013, TUPS060.
- [4] T. Tschentscher, Layout of the X-Ray Systems at the European XFEL, Technical Report (2011) [10.3204/XFEL.EU/TR-2011-001] XFEL.EU TR-2011-001.
- [5] Decision of the working group of the European XFEL and DESY.
- [6] W. Decking and T. Limberg, European XFEL Post-TDR Description, XFEL.EU Technical Note 1-22 (2013) XFEL.EU TN-2013-004.
- [7] E.A. Schneidmiller and M.V. Yurkov, Preprint DESY 11-152, DESY, Hamburg 2011.

- Content from this work may be used under the terms of the CC BY 3.0 licence (© 2018). Any distribution of this work must maintain attribution to the author(s), title of the work, publisher, and DOI.
- [8] E.L. Saldin, E.A. Schneidmiller, and M.V. Yurkov, *Nucl. Instrum. and Methods A* 429 (1999) 233.
 - [9] R. Brinkmann, E.A. Schneidmiller and M.V. Yurkov, *Nucl. Instrum. and Methods A*, 616 (2010) 81.
 - [10] E.A. Schneidmiller and M.V. Yurkov, Photon beam properties at the European XFEL (September 2017 revision), in preparation.
 - [11] An activity on generation of photon data base at the European XFEL is performed by L. Samoylova, C.H. Yoon, J. Szuba, K. Wrona, *et al.*
 - [12] H. Sinn *et al.*, Technical Design Report: X-Ray Optics and Beam Transport, Technical Report (2012) [10.3204/XFEL.EU/TR-2012-006] XFEL.EU TR-2012-006.
 - [13] A.P. Mancuso *et al.*, Report (2013) Technical Design Report: Scientific Instrument Single Particles, Clusters, and Biomolecules (SPB), XFEL.EU Technical Report 1-232 (2013) [10.3204/XFEL.EU/TR-2013-004] XFEL.EU TR-2013-004.
 - [14] I. Agapov *et al.*, *Proc. FEL 2014 Conference*, Basel, Switzerland, 2014, MOP056.
 - [15] E.A. Schneidmiller and M.V. Yurkov, *Proc. FEL 2014 Conference*, Basel, Switzerland, 2014, MOP065.
 - [16] E.A. Schneidmiller and M.V. Yurkov, *Phys. Rev. ST Accel. Beams*, 15(2012)080702
 - [17] A. Madsen *et al.*, Technical Design Report: Scientific Instrument MID, XFEL.EU Technical Report 1-191 (2013) [10.3204/XFEL.EU/TR-2013-005] XFEL.EU TR-2013-005.
 - [18] D.F. Ratner *et al.*, *Proc. FEL2013 Conference*, New York, USA, 2013, WEPSO53.
 - [19] E.A. Schneidmiller and M.V. Yurkov, *Proc. FEL2013 Conference*, New York, USA, 2013, WEPSO78.
 - [20] D. Xiang *et al.*, *Phys. Rev. ST Accel. Beams*, 16 (2013)010703
 - [21] S. Serkez *et al.*, preprint DESY-13-135, DESY, Hamburg, 2013.
 - [22] S. Serkez *et al.*, *Proc. FEL 2014 Conference*, Basel, Switzerland, 2014, MOP057.
 - [23] M. Krasilnikov *et al.*, *Proc. FEL2011 Conference*, Shanghai, China, 2011, THPA08.
 - [24] G. Vashchenko *et al.*, Proc. IPAC2011, San Sebastian, Spain, 2011, THPC115.
 - [25] I. Zagorodnov, *Proc. FEL 2010 Conference*, Malmo, Sweden, 2010, WEOB12.
 - [26] B. Marchetti *et al.*, *Physica Procedia*, 52 (2014) 80.
 - [27] J. Roensch-Schulenburg, *Proc. FEL 2014 Conference*, Basel, Switzerland, 2014, TUB04.
 - [28] S. Serkez *et al.*, *Proc. FEL2013 Conference*, New York, USA, 2013, WEPSO63.
 - [29] E.A. Schneidmiller and M.V. Yurkov, *Phys. Rev. ST Accel. Beams*, 16 (2013) 110702.
 - [30] J.P. MacArthur *et al.*, *Proc. FEL 2014 Conference*, Basel, Switzerland, 2014, MOP082.

OPTIMUM UNDULATOR TAPERING OF SASE FEL: THEORY AND EXPERIMENTAL RESULTS FROM FLASH2

E.A. Schneidmiller and M.V. Yurkov, DESY, Hamburg, Germany

Abstract

In this report we present recent results of the experimental studies at FLASH2 free electron laser on application of undulator tapering for efficiency increase. Optimization of the amplification process in FEL amplifier with diffraction effects taken into account results in a specific law of the undulator tapering [1–3]. It is a smooth function with quadratic behavior in the beginning of the tapering section which transforms to a linear behavior for a long undulator. Obtained experimental results are in reasonable agreement with theoretical predictions.

UNIVERSAL TAPERING LAW

Effective energy exchange between the electron beam moving in an undulator and electromagnetic wave happens when resonance condition takes place. When amplification process enters nonlinear stage, the energy losses by electrons become to be pronouncing which leads to the violation of the resonance condition and to the saturation of the amplification process. Application of the undulator tapering [4] allows to a further increase of the conversion efficiency. An idea is to adjust undulator parameters (field or period) according to the electron energy loss such that the resonance condition is preserved. Undulator tapering has been successfully demonstrated at long wavelength FEL amplifiers [5,6], and is routinely used at x-ray FEL facilities LCLS and SACLA [7,8]. In the framework of the one-dimensional theory an optimum law of the undulator tapering is quadratic [9–15]. Similar physical situation occurs in the FEL amplifier with a waveguide [5]. Parameters of FEL amplifiers operating in the infrared, visible, and x-ray wavelength ranges are such that diffraction of radiation is an essential physical effect influencing optimization of the tapering process. In the limit of thin electron beam (small value of the diffraction parameter) linear undulator tapering works well from almost the very beginning [12]. It has been shown in [10] that: i) tapering law should be linear for the case of thin electron beam, ii) optimum tapering at the initial stage should follow quadratic dependence, iii) tapering should start approximately two field gain length before saturation.

Comprehensive analysis of the problem of the undulator tapering in the presence of diffraction effects has been performed in [1–3]. It has been shown that the key element for understanding the physics of the undulator tapering is given by the model of the modulated electron beam which provides relevant interdependence of the problem parameters. Finally, application of similarity techniques to the results of numerical simulations led to the universal law of the undulator tapering:

$$\hat{C} = \alpha_{tap}(\hat{z} - \hat{z}_0) \left[\arctan\left(\frac{1}{2N}\right) + N \ln\left(\frac{4N^2}{4N^2 + 1}\right) \right], \quad (1)$$

with Fresnel number N fitted by $N = \beta_{tap}/(\hat{z} - \hat{z}_0)$. Undulator tapering starts by two field gain length $2 \times L_g$ before the saturation point at $z_0 = z_{sat} - 2 \times L_g$. Parameter β_{tap} is rather well approximated with the linear dependency on diffraction parameter, $\beta_{tap} = 8.5 \times B$. Parameter α_{tap} is a slow varying function of the diffraction parameter B , and scales approximately to $B^{1/3}$. Analysis of the expression (1) shows that it has quadratic dependence in z for small values of z (limit of the wide electron beam), and linear dependence in z for large values of z (limit of the thin electron beam).

ANALYSIS OF TAPERING PROCESS

Seeded FEL

Red curve in Fig. 1 shows evolution of the average radiation power of seeded FEL along the optimized tapered undulator. Significant amount of particles is trapped in the regime of coherent deceleration (top plot in Fig. 2).

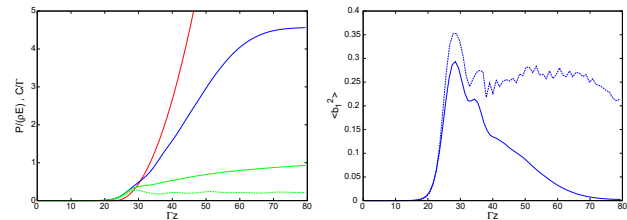


Figure 1: Left: Evolution along the undulator of the reduced radiation power $\hat{\eta} = W/(\rho W_{beam})$. Red and blue lines correspond to the case of tapered seeded and SASE FEL. Green dashed and solid lines refer the case of untapered seeded and SASE FEL. Right: Evolution along the undulator of the squared value of the bunching factor for the FEL amplifier with optimized undulator tapering. Dashed and solid line represent seeded and SASE FEL, respectively. Diffraction parameter is $B = 10$. Simulations are performed with code FAST [16].

The particles in the core of the beam are trapped most effectively. Nearly all particles located at the edge of the electron beam leave the stability region very soon. The trapping process lasts for a several field gain lengths when the trapped particles become to be isolated in the trapped energy band for which the undulator tapering is optimized further. For large values of the diffraction parameter $B \geq 10$ the trapping process is not finished even at three field gain lengths after saturation, and non-trapped particles continue to populate low energy tail of the energy distribution (see

Content from this work may be used under the terms of the CC BY 3.0 licence (© 2018). Any distribution of this work must maintain attribution to the author(s), title of the work, publisher, and DOI.

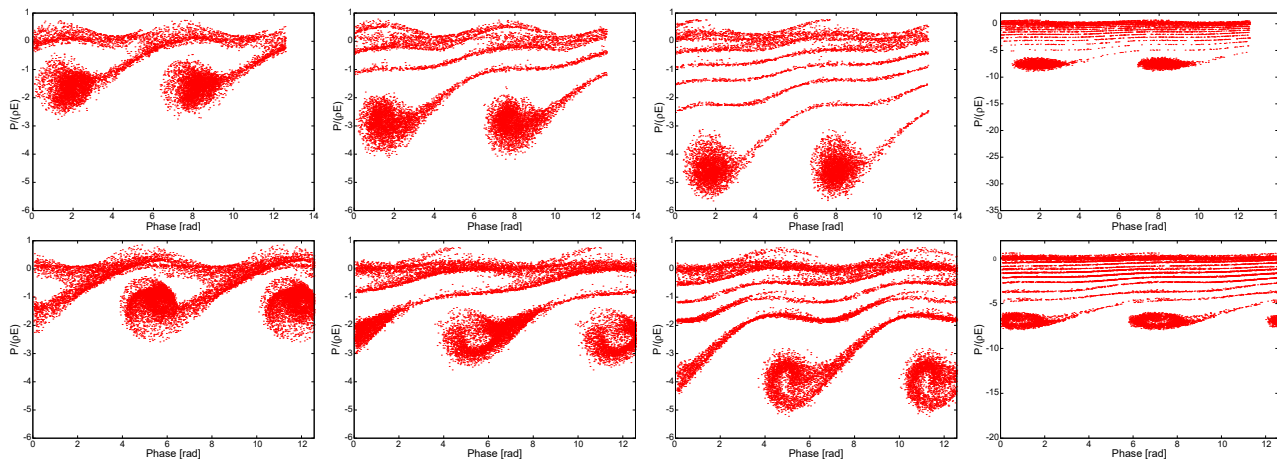


Figure 2: Phase space distribution of electrons in the tapering regime. Diffraction parameter is $B = 10$. Plots from the left to the right correspond to $\hat{z} = 36, 40, 44$ and 50 , respectively. Upper row represents seeded FEL amplifier. Lower row represents SASE FEL at the coordinate along the bunch $\hat{s} = \rho\omega t = 100$, see Fig. 4. Simulations are performed with code FAST [16].

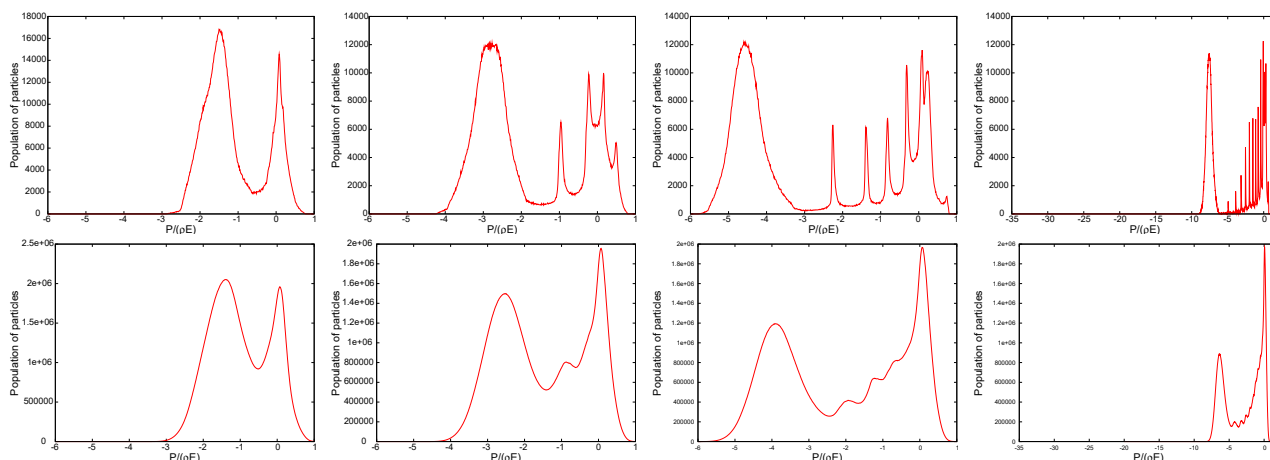


Figure 3: Population of the particles in energy at different stages of amplification. Diffraction parameter is $B = 10$. Plots from the left to the right correspond to $\hat{z} = 36, 40, 44$ and 50 , respectively. Upper and lower rows represent seeded FEL amplifier and SASE FEL, respectively. Simulations are performed with code FAST [16].

Fig. 3). There was an interesting experimental observation at LCLS that energy distribution of non-trapped particles is not uniform, but represent a kind of energy bands [17, 18]. Graphs presented in Fig. 2 give a hint on the origin of energy bands which are formed by non-trapped particles. This is the consequence of nonlinear dynamics of electrons leaving the region of stability. Note that a similar effect can be seen in the early one-dimensional studies [13, 14].

SASE FEL

The considerations on the strategy for the tapering optimization of a SASE FEL is rather straightforward. Radiation of SASE FEL consists of wavepackets (spikes). In the exponential regime of amplifications wavepackets interact strongly with the electron beam, and their group velocity visibly differs from the velocity of light. In this case the slippage of the radiation with respect to the electron beam is by several times less than kinematic slippage [15]. This feature

is illustrated with the upper plot in Fig. 4 which shows onset of the nonlinear regime. We see that wavepackets are closely connected with the modulations of the electron beam current. When the amplification process enters nonlinear (tapering) stage, the group velocity of the wavepackets approaches to the velocity of light, and the relative slippage approaches to the kinematic one. When a wavepacket advances such that it reaches the next area of the beam disturbed by another wavepacket, we can easily predict that the trapping process will be destroyed, since the phases of the beam bunching and of the electromagnetic wave are uncorrelated in this case. Typical scale for the destruction of the tapering regime is coherence length, and the only physical mechanism we can use is to decrease the group velocity of wavepackets. This happens optimally when we trap maximum of the particles in the regime of coherent deceleration, and force these particles to interact as strong as possible with the electron beam. We see that this strategy is exactly the same as we used for

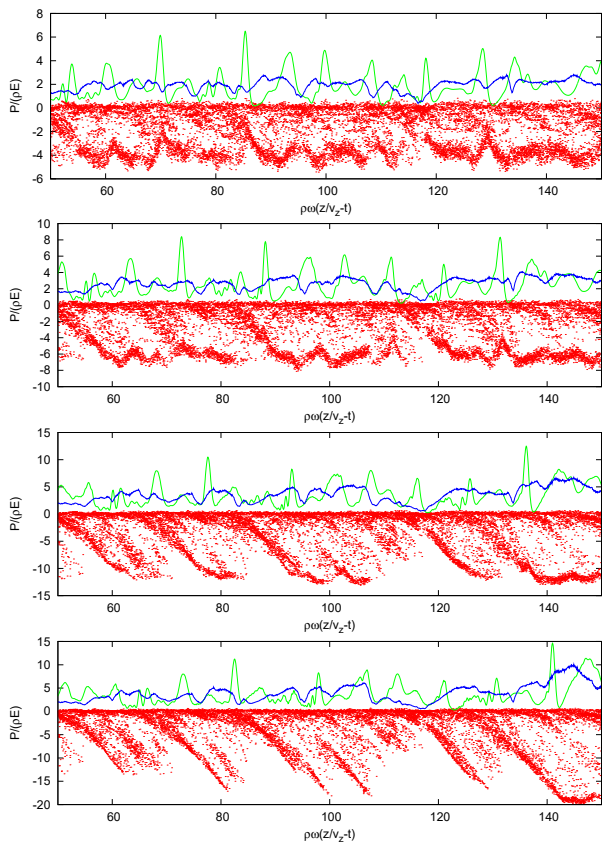


Figure 4: Phase space distribution of the particles along the bunch (red dots), average loss of the electron energy (blue line), and radiation power (green line) in the deep tapering regime. Diffraction parameter is $B = 10$. Plots from the top to the bottom correspond to $\hat{z} = 44, 50, 60$, and 70 , respectively. Simulations are performed with code FAST [16].

optimization of seeded FEL. Global numerical optimization confirms these simple physical considerations. Conditions of the optimum tapering are the same as it has been described above for the seeded case. Start of the tapering is by two field gain lengths before the saturation. Parameter β_{tap} is the same, $8.5 \times B$. The only difference is the reduction of the parameter α_{tap} by 20% which is natural if one remember statistical nature of the wavepackets. As a result, optimum detuning is just 20% below the optimum seeded case.

Figure 1 shows evolution of the average radiation power of SASE FEL along optimized tapered undulator. Details of the phase space distributions are traced with Figs. 2 and 4. Initially behavior of the process is pretty close to that of the seeded case. Initial values of the beam bunching is comparable with the seeded case (see Fig. 1). The rate of the energy growth is also comparable with the seeded case. The feature of the "energy bands" remains clearly visible in the case of SASE FEL as well (see Fig. 3). It is interesting observation that plots in Figs. 4 corresponding to the well trapped particles qualitatively correspond to experimental

data from LCLS taken with transverse deflecting cavity [17, 18].

The beam bunching gradually drop down when wavepackets travel along the bunch. As we expected, the amplification process is almost abruptly stopped when the relative slippage exceeded the coherence length. However, increase of the total radiation power with respect to the saturation power is about factor of 10.

EXPERIMENTAL RESULTS

Free electron laser FLASH is equipped with two undulator beamlines [19–21]. Fixed gap undulator (period 2.73 cm, peak magnetic field 0.48 T, total magnetic length 27 m) is installed in the first beamline, FLASH1. The second beamline, FLASH2, is equipped with variable gap undulator (period 3.14 cm, maximum peak magnetic field 0.96 T, total magnetic length 30 m). With operating range of the electron beam energies of 0.4–1.25 GeV FLASH1 and FLASH2 beamline cover wavelength range from 4–52 nm and 3.5–90 nm, respectively.

Experiment on undulator tapering has been performed at FLASH2. Undulator consists of 12 modules of 2.5 meter length separated with intersections. Two modes of undulator tapering can be implemented: step tapering and smooth tapering. Procedure of the step tapering applies step change of the undulator gap from module to module, and smooth tapering assumes additional linear change of the gap along

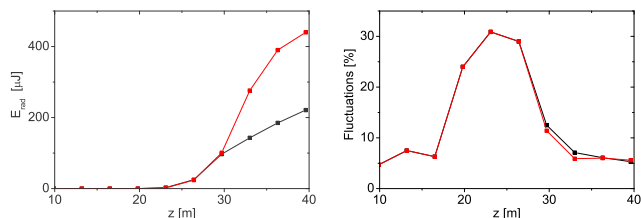


Figure 5: Pulse energy (left plot) and fluctuations of the radiation pulse energy (right plot) versus undulator length measured at FLASH2. Electron energy is 680 MeV, radiation wavelength is 32 nm, bunch charge is 300 pC. Color codes are: red for untapered case and black for optimum undulator tapering.

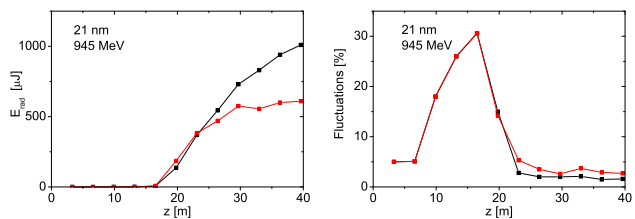


Figure 6: Pulse energy (left plot) and fluctuations of the radiation pulse energy (right plot) versus undulator length measured at FLASH2. Electron energy is 945 MeV, radiation wavelength is 21 nm, bunch charge is 400 pC. Color codes are: red for untapered case and black for optimum undulator tapering.

each module. During experiment only step tapering mode was available. Experimental procedure for tuning of the tapering parameters involves statistical measurements of the radiation energy. Optimum conditions of the undulator tapering assume the starting point to be by two field gain lengths before the saturation point corresponding to the maximum brilliance of the SASE FEL radiation [22]. Saturation point on the gain curve is defined by the condition for fluctuations to fall down by a factor of 3 with respect to their maximum value in the end of exponential regime. Then quadratic law of tapering is applied (optimal for moderate increase of the extraction efficiency at the initial stage of tapering. This experimental techniques has been successfully tested at FLASH2 as illustrated in Figs. 5 and 6. For the case shown in Fig. 6 saturation occurs at the undulator length of 20 meters, and saturation energy is about 150 μ J. Optimized tapering increases the pulse energy by a factor of 6, up to 1000 μ J. Untapered undulator delivers only 610 μ J at full undulator length of 40 meters. Thus, tapering of the FLASH2 undulator demonstrates great benefit in the increase of the radiation pulse energy.

REFERENCES

- [1] E.A. Schneidmiller and M.V. Yurkov, *Proc. FEL2014 Conference*, Basel, Switzerland, 2014, paper MOP065.
- [2] E.A. Schneidmiller and M.V. Yurkov, *Phys. Rev. ST Accel. Beams*, 18, 030705, 2015.
- [3] E.A. Schneidmiller and M.V. Yurkov, *Proc. SPIE*, 9512, 951219 (May 12, 2015); doi : 10.1117/12.2181230
- [4] N.M. Kroll, P.L. Morton, and M.N. Rosenbluth, *IEEE J. Quantum Electron*, 17, 1436, 1981.
- [5] T.J. Orzechowski *et al.*, *Phys. Rev. Lett.*, 57, 2172 (1986).
- [6] X.J. Wang, H.P. Freund, D. Harder, W.H. Miner, Jr., J.B. Murphy, H. Qian, Y. Shen, and X. Yang, *Phys. Rev. Lett.*, 103, 154801, 2009.
- [7] P. Emma *et al.*, *Nature Photonics*, 4, 641, 2010.
- [8] Tetsuya Ishikawa *et al.*, *Nature Photonics* 6, 540, 2012.
- [9] R.A. Jong, E.T. Scharlemann, and W.M. Fawley *Nucl. Instrum. Methods Phys. Res. A*, 272, 99, 1988.
- [10] W.M. Fawley, *Nucl. Instrum. Methods Phys. Res. A*, 375, 550, 1996.
- [11] W.M. Fawley, Z. Huang, K.J. Kim, and N. Vinokurov, *Nucl. Instrum. Methods Phys. Res. A*, 483, 537, 2002.
- [12] E.L. Saldin, E.A. Schneidmiller, and M.V. Yurkov, *Opt. Commun.*, 95, 141 1993.
- [13] E.T. Scharlemann, *Laser Handbook*, Volume 6, Free electron lasers, eds. W.B. Colson, C. Peilegrini and A. Renieri (North Holland, Amsterdam, 1991), p. 291.
- [14] E.L. Saldin, E.A. Schneidmiller, and M.V. Yurkov, *Physics Reports*, 260, 187 1995.
- [15] E.L. Saldin, E.A. Schneidmiller, and M.V. Yurkov, *The Physics of Free Electron Lasers*, Springer-Verlag, Berlin, 1999.
- [16] E.L. Saldin, E.A. Schneidmiller, and M.V. Yurkov, *Nucl. Instrum. and Methods A*, 429, 233 1999.
- [17] P. Krejcik, Talk WEOBB03 at IPAC 2014, June 2014, Dresden, Germany.
- [18] Y. Ding, F.-J. Decker, V.A. Dolgashev, J. Frisch, Z. Huang, P. Krejcik, H. Loos, A. Lutman, A. Marinelli, T.J. Maxwell, D. Ratner, J. Turner, J. Wang, M.-H. Wang, J. Welch, and J. Wu, Preprint SLAC-PUB-16105, SLAC National Accelerator Laboratory, 2014.
- [19] W. Ackermann *et al.*, *Nature Photonics* 1, 336 2007.
- [20] S. Schreiber and B. Faatz, *High Power Laser Science and Engineering*, e20, 1 2015. doi:10.1017/hpl.2015.16.
- [21] B. Faatz *et al.*, *New journal of physics*, 18(6), 062002, 2016.
- [22] E.L. Saldin, E.A. Schneidmiller, and M.V. Yurkov, *Opt. Commun.*, 281, 1179-1188, 2008.

FREQUENCY DOUBLING MODE OF OPERATION OF FREE ELECTRON LASER FLASH2

M. Kuhlmann, E.A. Schneidmiller, and M.V. Yurkov, DESY, Hamburg, Germany

Abstract

We report on the results of the first operation of a frequency doubler at free electron laser FLASH2. The scheme uses the feature of the variable-gap undulator. The undulator is divided into two parts. The second part of the undulator is tuned to the double frequency of the first part. The amplification process in the first undulator part is stopped at the onset of the nonlinear regime, such that nonlinear higher-harmonic bunching in the electron beam density becomes pronouncing, but the radiation level is still small to disturb the electron beam significantly. The modulated electron beam enters the second part of the undulator and generates radiation at the second harmonic. A frequency doubler allows operation in a two-color mode and operation at shorter wavelengths with respect to standard SASE scheme. Tuning of the electron beam trajectory, phase shifters and compression allows tuning of intensities of the first and the second harmonic. The shortest wavelength of 3.1 nm (photon energy 400 eV) has been achieved with a frequency doubler scheme, which is significantly below the design value for the standard SASE option.

INTRODUCTION

Free electron laser FLASH is equipped with two undulator beamlines [1]. Fixed gap undulator (period 2.73 cm, peak magnetic field 0.48 T, total magnetic length 27 m) is installed in the first beamline, FLASH1. The second beam line, FLASH2, is equipped with variable gap undulator (period 3.14 cm, maximum peak magnetic field 0.96 T, total magnetic length 30 m). With operating range of the electron beam energies of 0.4 - 1.25 GeV FLASH1 and FLASH 2 beamline cover wavelength range from 4 to 52 nm and 3.5 to 90 nm, respectively. Multiple scientific applications will benefit a lot with extension of the operating range of the facility deep into the water window spanning from 4.38 nm and 2.34 nm (K-absorption edges of carbon and oxygen).

One techniques to generate shorter wavelengths is by using the second harmonic afterburner [2–7]. Operating the afterburner at the 2nd harmonic has been tested successfully at LCLS with 5 final undulator modules retuned to the 2nd harmonic [7]. With long, variable gap undulator of FLASH2 it is possible to implement frequency doubler scheme. Here we demonstrate experimental results from FLASH2: with an appropriate optimization of undulator tuning it becomes possible to operate facility at visibly shorter wavelengths and organize two color mode of operation ($\omega + 2\omega$) with controllable radiation pulse intensities.

OPERATION OF FREQUENCY DOUBLER

The undulator is divided into two sections tuned to ω and 2ω frequencies. The plots in Fig. 1 illustrate general features of the operation of the frequency doubling scheme. Black dashed line shows evolution of the radiation power along the ω -section. The amplification process stops at some length, and then electron beam enters the 2ω -section tuned to the doubled frequency. Radiation with frequency ω does not interact with the electron beam in the 2ω -section, and just propagates forward. Radiation power produced in the ω -section at the second harmonic frequency is significantly suppressed [6, 8], thus only the beam density modulations at 2ω frequency can seed the 2ω -section.

We performed simulations of the amplification process for the full parameter space of the lengths of the ω and 2ω sections, and the results are summarized in Fig. 2. Despite the fact that simulations have been performed for specific sets of electron beam parameters, presentation of the results here is in normalized form to allow use of them for a wider range of parameters. The x-coordinate is radiation power is from the ω section normalized to the saturation power of SASE FEL operating at frequency ω . The y-coordinate is radiation power from the 2ω -section normalized to the

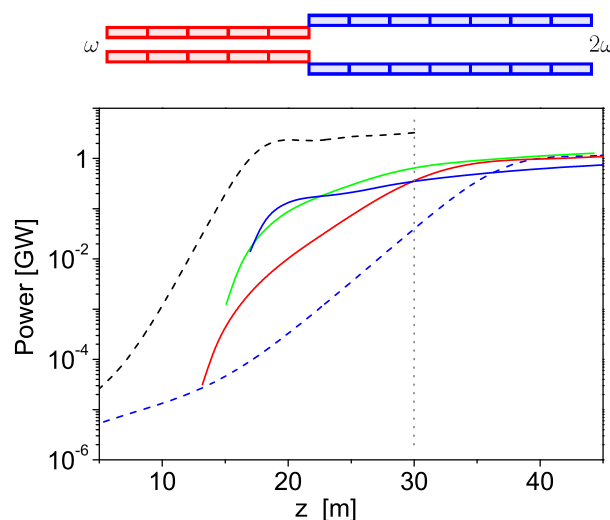


Figure 1: Top: Conceptual scheme of frequency doubler with variable gap undulator. Bottom: Evolution of the radiation power along FLASH2 undulator. Dashed curves correspond to SASE FEL operating at 8 nm (black) and at 4 nm (blue). Solid curves correspond to frequency doubler 8 nm \rightarrow 4 nm for different lengths of the ω undulator section (red, green, and blue colors). Gray dashed line at $z = 30$ m shows magnetic length of FLASH2 undulator. Electron energy is 1080 MeV, beam current is 1500 A, normalized rms emittance 1π mm-mrad, and rms energy spread 0.15 MeV. Simulations have been performed with code FAST [9].

Content from this work may be used under the terms of the CC BY 3.0 licence (© 2018). Any distribution of this work must maintain attribution to the author(s), title of the work, publisher, and DOI.

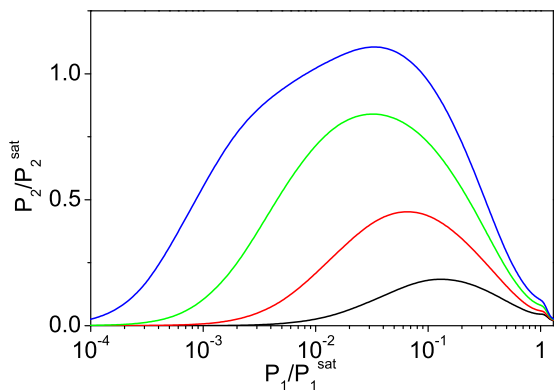


Figure 2: Parameter space of radiation powers from frequency doubler at FLASH2. P_1 is radiation power at ω at the exit of the first section, and P_2 is radiation power at 2ω at the exit of the doubling section. Radiation powers are normalized to the corresponding saturation powers of SASE FEL. Different colors (black, red, green, and blue) denote lengths of the doubling section in terms of the saturation length: $1/6 z_{\text{sat}}$, $1/3 z_{\text{sat}}$, $1/2 z_{\text{sat}}$, and $2/3 z_{\text{sat}}$. Simulations have been performed with code FAST [9].

saturation power of the SASE FEL operating at frequency 2ω . We see that with two-color mode of operation it is possible to produce simultaneously high power at both frequencies with the level of about 20% of the saturation power. When amplification process in the first undulator terminates at the onset of the nonlinear regime, it is possible to generate high radiation power at the second harmonic in the second part of the undulator.

Simple physical considerations explain operation of the frequency doubler. Indeed, for a short length of the ω -section, when the amplification process stays in the exponential gain regime, the beam density modulations at frequency 2ω remain on the level of the shot noise. Induced modulations at the frequency 2ω (and higher harmonics) occur only in the nonlinear stage of amplification. At the onset of nonlinear regime induced modulation at 2ω is small, and gradually grows when amplification process approaches saturation. At the same time we occur degradation of the electron beam quality due to interaction of the electron beam with radiation. Thus, we deal with two competing effects: growth of the beam modulation, and degradation of the electron beam quality. Lucky factor for the frequency doubling scheme is that the growth of the beam density modulation advances the degradation of the beam quality, since the radiation power should be produced first, and only then it interacts with the beam. When amplification process enters the post-saturation regime, the quality of the beam and the beam bunching degrade such that the electron beam becomes to be not appropriate for efficient radiation of higher harmonics.

EXPERIMENTAL RESULTS

Operation of frequency doubler has been successfully demonstrated during several test runs at FLASH2 in 2016. Experiments have been performed at the energy of the electron beam of 1080 MeV and 1230 MeV. Tuning of the fre-

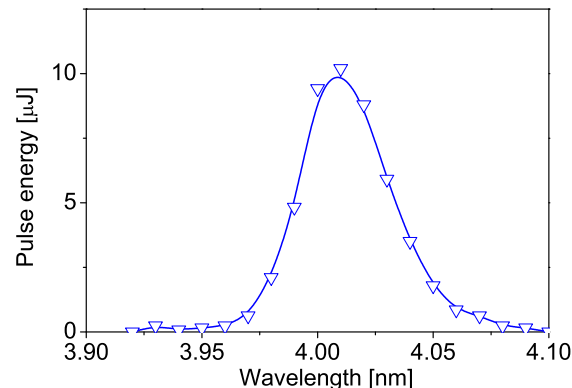
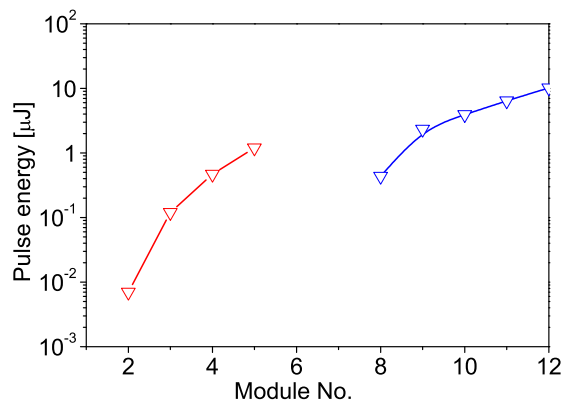


Figure 3: Frequency doubler at FLASH2 (experimental data). Left: gain curve of the frequency doubler at FLASH2. First part of the undulator (5 modules) is tuned to 8 nm, and second part (7 modules) is tuned to 4 nm. Red and blue color correspond to the radiation wavelength of 8 nm and 4 nm. Right: radiation pulse energy at the 2nd harmonic versus resonance frequency of the second part of the undulator. Electron energy is 1080 MeV, bunch charge is 300 pC.

quency doubler scheme with variable gap undulator does not require any special techniques. First, we tune maximum SASE gain in the uniform undulator tuned to frequency ω . Analysis of the gain curve and fluctuations of the radiation pulse energy allows to determine optimum length of the ω -section. Then we tune remaining sections to the frequency 2ω , and after adjustment of the phase shifters and electron beam orbit, the frequency doubler starts to generate radiation at the second harmonic.

Figure 3 shows the gain curve of the frequency doubler 8 nm \rightarrow 4 nm. First five undulator sections were tuned to 8 nm, and the last seven sections were tuned to 4 nm. Red and blue curves show radiation pulse energies at 8 nm and 4 nm. Amplification process in the second part (frequency doubler) exhibits resonance behavior on the frequency detuning (right plot in Fig. 3). Even harmonics of the radiation are strongly suppressed in the planar undulator, thus we get confirmation that the beam bunching at the second harmonic seeds the amplification process of the frequency doubling sections. One can compare experimental and simulation results presented in Fig. 1. Gain curves look pretty much similar. As for the resonance curve, the width of experimental curve is significantly wider than FEL parameter ρ . This

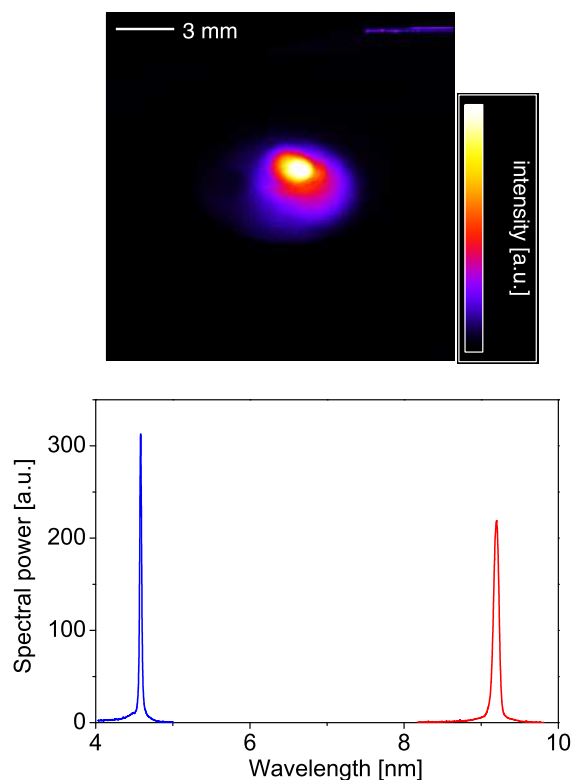


Figure 4: Photon beam image in the experimental hall (top) and radiation spectra (bottom) of the frequency doubler at FLASH2 (experimental data). Small yellow spot is 4.5 nm (2nd harmonic) radiation, pulse energy is 10 J. Larger blue/pink spot is 9 nm radiation, pulse energy is 10 μ J. Electron energy is 1080 MeV, bunch charge is 300 pC.

is typical signature of the energy chirp along the electron beam induced by the beam formation system.

Our experience shows that tuning procedure of the frequency doubler is simple and reproducible. In particular, it is possible to tune relative intensities of two colors (ω , 2ω) in a wide limits. When tuned to equal intensities, pulse energies were in the range from a few to 10 microjoules. Radiation has been transported to FLASH2 experimental hall for characterization. Figure 4 shows an example for photon beam images and spectra of two color mode of operation for the frequency doubler 9 nm \rightarrow 4.5 nm. With this first experience we can state that this operational mode can be proposed to users.

With fixed electron energy, shortening of the radiation wavelength is achieved by opening the undulator gap. Undulator field is reduced, the FEL gain falls down, and starting from some wavelength the undulator length is not sufficient to reach saturation regime. Frequency doubler scheme is capable to generate shorter wavelength radiation than standard SASE FEL. Indeed, the first part of the undulator operates at twice longer wavelength, and saturation is obtained at a half of the full undulator length. Induced beam bunching at the second harmonic is much larger than the shot noise in the electron beam, and it becomes possible to reach saturation on much shorter length of the doubling section. For fair

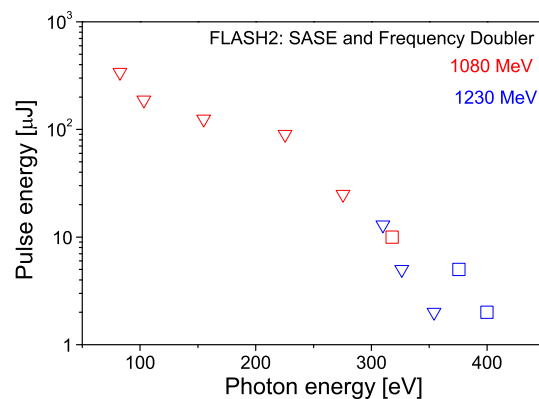


Figure 5: Radiation pulse energy versus photon energy. Experimental data from FLASH2 for electron energy of 1080 MeV and 1230 MeV, bunch charge is 300 pC. Triangles represent SASE, and squares represent frequency doubler.

comparison of two options (SASE and frequency doubler) we performed two dedicated runs at FLASH2 operating with electron energies close to the limit. First, standard SASE mode has been optimally tuned at full undulator length, and radiation pulse energy scanned versus radiation wavelength. Then frequency doubler scheme has been tuned optimally with the same electron beam, and the pulse energy scanned. Results of pulse energy measurements are compiled in Fig. 5. We see that visibly shorter wavelengths were reached with the frequency doubler. In particular, photon energies above Nitrogen K-edge have been demonstrated which significantly exceeds original specifications of FLASH2. The radiation has been successfully transported to FLASH2 experimental hall.

Analysis of experimental results obtained at FLASH2 shows that the frequency doubler scheme works in good agreement with theoretical expectations. Its tuning does not require special efforts, and it starts to work when SASE process tuned along the whole length of the undulator. Two color mode of operation is rather robust for longer wavelengths. Minimum achievable wavelength, strongly depends on the quality of the electron beam which requires dedicated tuning of the beam formation system. However, this is general problem for SASE FEL as well. Presently we reached photon energies just below Nitrogen K-edge (400 eV), and this seems to be close to the limit of the doubling frequency technique at the energy of electron beam of 1230 MeV. Additional installation of two undulator sections (2×2.5 m) may help in more reliable covering of the Nitrogen K-edge range and reaching shorter wavelengths.

ACKNOWLEDGEMENTS

We are grateful to B. Faatz, J. Rönsch-Schulenburg, S. Schreiber, and M. Tischer for fruitful collaboration, and FLASH team for technical support. We would like to thank R. Brinkmann, J. Schneider, E. Weckert, and W. Wurth for valuable discussions and interest in this work.

REFERENCES

- [1] B. Faatz *et al.*, *New journal of physics*, 18(6), 062002, 2016.
- [2] R. Bonifacio, L. De Salvo, and P. Pierini, *Nucl. Instrum. Methods Phys. Res. A*, 293, 627, 1990.
- [3] Ciocci, *et al.*, *IEEE J. Quantum Electron*, 31 1242, 1995.
- [4] W. M. Fawley *et al.*, *Proceedings of the IEEE 1995 Particle Accelerator Conference*, p. 219, 1996.
- [5] T. Aberg *et al.*, A VUV Free Electron Laser at DESY: Conceptual Design Report. TESLA FEL Report 1995-03, DESY, Hamburg, 1995.
- [6] Z. Huang and S. Reiche, *Proc. of the FEL2004 Conference*, Trieste, Italy, p. 201, 2004.
- [7] H.-D. Nuhn *et al.*, *Proc. of the FEL2010 Conference*, Malmo, Sweden, p. 690, 2010.
- [8] G. Geloni *et al.*, Preprint DESY 05-137, Hamburg, 2005.
- [9] E.L. Saldin, E.A. Schneidmiller and M.V. Yurkov, *Nucl. Instrum. and Methods A*, 429 233, 1999.

OPPORTUNITIES FOR TWO-COLOR EXPERIMENTS AT THE SASE3 UNDULATOR LINE OF THE EUROPEAN XFEL

G. Geloni*, T. Mazza, M. Meyer, S. Serkez, European XFEL, Schenefeld, Germany
V. Kocharyan, E. Saldin, DESY, Hamburg, Germany

Abstract

As is well-known, the installation of a simple magnetic chicane in the baseline undulator of an XFEL allows for producing two-color FEL pulses. In this work we discuss the possibility of applying this simple and cost-effective method at the SASE3 soft X-ray beamline of the European XFEL. We consider upgrades of this method that include the further installation of a mirror chicane. We also discuss the scientific interest of this upgrade for the Small Quantum Systems (SQS) instrument, in connection with the high-repetition rate of the European XFEL, and we provide start-to-end simulations up to the radiation focus on the sample, proving the feasibility of our concept. Our proposed setup has been recently funded by the Finnish Research Infrastructure (FIRI) and will be built at SASE3 in 2020-2021. Detailed information is available at [1].

METHOD

The simplest way currently available to enable the generation of two closely separated (on the order of 50 fs) pulses of different wavelengths (which will later result in the two-colors) at X-ray Free-Electron lasers consists of inserting a magnetic chicane between two undulator parts as suggested in [2] and experimentally proven in [3,4]. The scheme is illustrated in Figure 1-a. We propose to split the baseline SASE3 soft X-ray undulator into two parts with a magnetic chicane. Both parts act as independent undulators and will be referred further as $U1$ and $U2$. The nominal electron beam enters the first undulator $U1$, tuned to the resonant wavelength λ_1 . After passing through $U1$, both electron beam and emitted Self-Amplified Spontaneous Emission (SASE) radiation enter the chicane. This magnetic chicane has two functions: first, it introduces a suitable delay between the electron beam and the radiation generated in $U1$. Delays from zero¹ up to the picosecond level can be obtained with a compact magnetic chicane of several meters length. Second, due to dispersion, the passage of the electron beam through the magnetic chicane smears out the microbunching at wavelength λ_1 . As a result, when the -after the magnetic chicane- delayed electron beam enters the second undulator $U2$, the SASE process starts from shot-noise again. Therefore, if the undulator $U2$ is tuned to the resonant wavelength λ_2 , then at the undulator exit one obtains a first radiation pulse at wavelength λ_1 followed by a second one with wave-

length λ_2 delayed by a time interval that can be varied by changing the strength of the chicane magnets.

One must ensure that the electron beam quality at the entrance of the second undulator $U2$ is still good enough to sustain the FEL process. This poses limits on the maximum total pulse energy that can be extracted from $U1$ and $U2$. In particular, the amplification process in $U1$ should not reach saturation. Optimization of the maximum pulse energy also poses limits on the wavelengths choices. The wavelength separation between the two pulses can theoretically span across the entire range made available by the undulator system, in the case of SASE3 between about 250 eV and 3000 eV. However, the impact of the FEL process on the electron beam quality depends on the radiation wavelength. Therefore, in order to maximize the combined radiation pulse energy that can be extracted, especially at large wavelength separations, the first pulse to be produced should be at the shortest wavelength. Moreover, the magnetic chicane strength should be large enough to smear out the microbunching at λ_1 , unless the separation between λ_1 and λ_2 is larger than the FEL bandwidth.

An easy way to increase the flexibility of the scheme is to introduce a compact optical delay line to have full control on the relative temporal separation between the two pulses as shown in Figure 1-(bottom). Since the photon beam transverse size at the position of the magnetic chicane is, roughly speaking, as small as the electron beam, i.e. a few tens of microns, the length of each mirror can be as short as several centimeters. In order to simplify the design of the mirror delay line, one may fix the optical delay to a few hundred femtoseconds, thus avoiding the use of moving mirrors, and subsequently tune the delay by changing the current in the magnetic chicane coils. Therefore, the introduction of an optical delay line would allow one to sweep between negative and positive delays at a cost of a smaller delay tuneability, caused by a lower limit of the chicane magnetic field (while the optical delay is inserted).

Even the simplest way of generating two-color pulses at the SASE3 beamline of the European XFEL, in combination with the high-repetition rate capabilities of the facility is expected to enable novel exciting science at the two soft X-ray instruments: Small Quantum Systems (SQS) [5] and Spectroscopy & Coherent Scattering (SCS) [6].

Here we limit ourselves to the analysis of one science case for the SQS instrument.

SQS SCIENCE CASE

The two-color operation mode enables a large number of scientific applications based on a pump-probe excitation

* gianluca.geloni@xfel.eu

¹ In our case, due to radiation slippage in the subsequent undulators, the effective minimum delay between the two pulses of different colors is of the order of several femtoseconds.

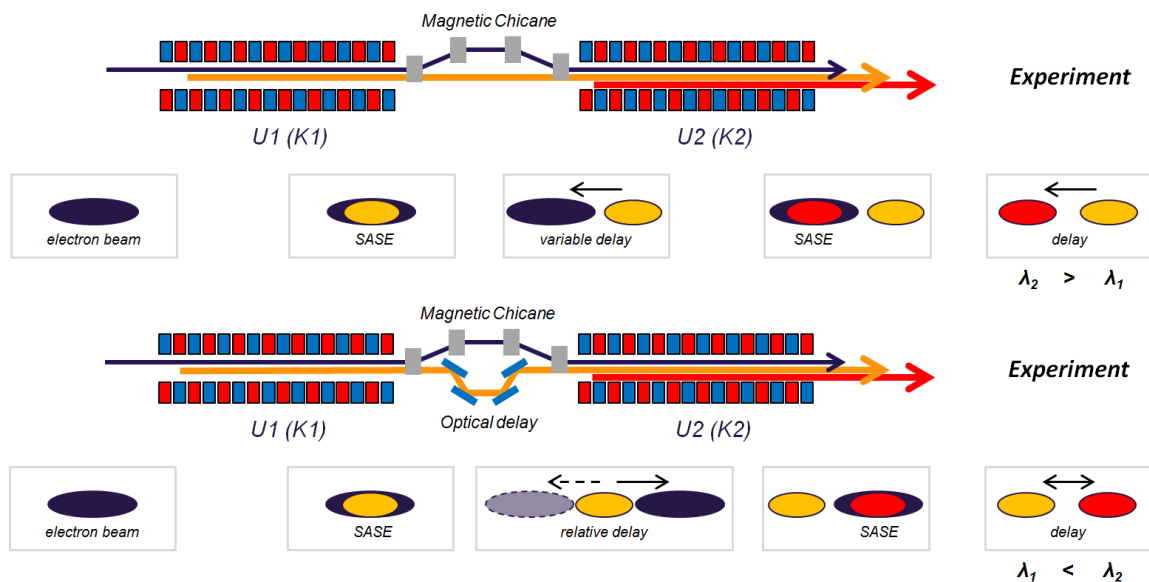


Figure 1: Schematic illustration of a simple two-color FEL technique without (top) and with (bottom) the addition of a compact optical delay line.

scheme with two individually controllable X-ray pulses. In the following a concrete example is discussed, which will make use of site-specific excitation in molecules possible at SQS scientific instrument of the European XFEL [5]. The excitation of a specific atomic site is enabled using soft X-ray pulses, since the radiation efficiently couples to the strongly bound core electrons, which are localized at the atomic site. Tuning the wavelength of the pump pulse to a specific threshold, a molecule can be excited at a well-defined atomic position. Using then the probe at another wavelength, which is connected to another core hole excitation, possible changes induced by the first pulse at a different site in the molecule are measured. Finally, the variation of the time delay between the two pulses provide access to the dynamics of this process, i.e. on the time, which is necessary to transport the information from one position in the molecule to another.

As illustrating example, we discuss charge transfer processes in a linear molecule, such as $I - C_n - H_{2n} - Cl$, composed of long carbon chain with two different halogen atoms, e.g. iodine and chlorine, at both ends. In the wavelength range accessible with the SASE3 undulator the $2p$ core electron of chlorine (threshold at 210 eV) as well as the $3d$ core electron of iodine (threshold at 630 eV) can be ionized. Considering a first pulse (pump) at a photon energy of 250 eV, the perturbation introduced by the XUV photon will be localized at the chlorine site, since core electrons of the other atoms (I and C) are still not in reach and cross section for valence ionization is weak. In the same way, choosing for the probe pulse the second photon energy at 630 eV assures that preferentially (i.e. most efficiently) the $3d$ electron at the iodine site is excited or ionized.

An efficient and informative experimental method to monitor the intramolecular processes is given by high-resolution Auger spectroscopy, ideally in combination with ion spec-

troscopy performed in a coincidence arrangement. The $3d$ Auger spectrum of iodine is located in the kinetic energy range around 400-500 eV arising mainly from the most prominent transitions to doubly charged states with electron configurations $4d^{-2}$ and $4d^{-1}4p^{-1}$ [7]. These lines are well separated from the corresponding Cl $2p$ Auger spectrum at kinetic energies between 165 and 175 eV [8] and other ionization processes taking place at the photon energies considered here.

Due to the high intensity of the FEL pulses sequential ionization processes are possible and likely to happen. As a consequence, the electron spectrum of the neutral parent molecule will be overlaid with emission lines arising from the ionization of the ionic species and of the dissociation fragments. In order to separate the emission from different species coincidences between electrons and ionic fragment can be used for a more detailed analysis. In fact, coincidence experiments will be one of the major experimental tools available at the SQS instrument, and are feasible due to the high number of X-ray pulses (up to 27 000 per second) at the European XFEL. This high repetition rate allows one to record data of high statistics for coincident measurements between electrons and ionic fragments coming unambiguously from the same molecule.

In a typical experimental scenario, first the Auger spectra would be recorded at the individual wavelength 250 eV and 630 eV, respectively, in order to obtain the one-photon reference spectra. In addition, electron-ion coincidence would provide charge and fragment resolved electron spectra would at these photon energies. In a second step, the Iodine $3d$ Auger spectrum – caused by the 630 eV photon pulse – will be monitored in the presence of the additional the 250 eV pulse. When the 250 eV pulse comes after the 630 eV pulse, the spectrum will be unchanged compared to the single color spectrum. When both pulses are overlapping or the 250 eV

comes earlier, the observation of the iodine Auger spectrum for different delays between both pulses provide the information about the intermolecular processes. Changes of the kinetic energy position and of the intensity distribution within the $I3d$ Auger spectrum are the monitor to follow charge migration processes inside the molecule, i.e. to determine e.g. the time required to transmit the information about the creation of a $2p$ core hole on the chlorine site to the iodine atom. For small molecules this time scale is in the order to a few femtoseconds [9], so probably difficult to access with pulses of about 2 fs duration each. For longer carbon chains the time scale is expected to increase to about 10 fs or more and therefore well suited to be studied with the set-up at the SQS instrument.

Furthermore, by selecting in coincidence mode a fragment containing the iodine atom or the iodine atom itself, also information on charge transfer processes is made available. Compared to earlier work using an optical laser to initiate the fragmentation [10], the pump can be used in a very selective way, changing for example between excitations of the chlorine and the carbon atom. In this way a more versatile and detailed analysis of the complex intra-molecular interaction and on the related electron and nuclear dynamics will become possible.

SIMULATIONS FOR THE SQS SCIENCE CASE

For the particular science case at the SQS instrument discussed in the previous section, two fs-order-long X-ray pulses with a tunable relative delay are required. We considered a simulation scenario where a magnetic chicane and an optical delay line are installed at SASE3, see Figure 1.

Start-to-end simulations for the electron beam through the European XFEL linac to the entrance of the SASE3 beamline based on [11] were considered. The electron beam obtained is sent through the first part of the SASE3 undulator composed of 7 segments, with the first two segments not contributing to the SASE process and the rest 5 segments tuned at 630 eV. The photon beam then passes through the fixed optical delay line, while the electron beam goes through the magnetic chicane. The delay in the magnetic chicane can be adjusted with sub-fs accuracy, and can be set to under- or over-compensate the optical delay. We dump the numerically simulated electron beam distribution at the end of undulator $U1$ and use it for the FEL simulations in $U2$, which consists of 14 segments, with the first seven switched off and the remaining seven lasing at 250 eV.

The final step consists in performing wavefront propagation simulations thorough the SQS beamline, including a pair of offset mirrors and KB mirrors up to the sample position. After passing through the entire beamline, the photon beam can be focused at the sample position. One issue concerning the optimal focusing is related to the presence of the two separate sources for the two pulses. If we decide to tune the KB mirrors to image one of the two sources at a certain location, the image of the other will not only appear

shifted in space, but will also be a subject to astigmatism. It is also possible to select an intermediate, imaginary source position between $S1$ and $S2$, which we call $S1.5$, and image it at the sample by properly tuning the KB mirror system. In this case, the images of $S1$ and $S2$ appear at positions denoted as respectively denoted as $I1$ and $I2$, while the image of $S1.5$ appears at location $I1.5$, where the sample is assumed to be introduced. This yields a good compromise in terms of beam sizes at the sample, Figure 2. Based on our simulations, the resulting photon fluxes would be sufficient to conduct the experiment proposed above.

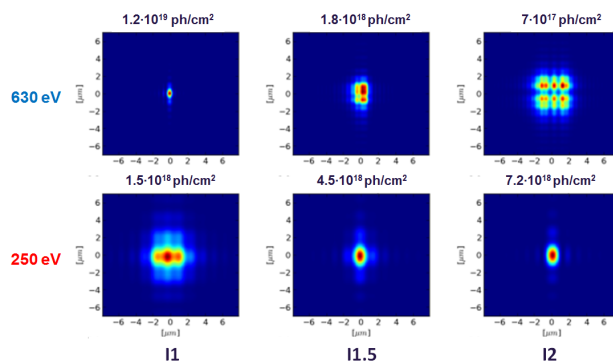


Figure 2: Radiation intensity distribution of both radiation pulses with different photon energies at various image planes. Peak photon density is provided above the plots. The method of an intermediate source reimaging would allow one to obtain comparable radiation distribution size as well as the photon flux.

While simulations presented in this paper were performed only for the purpose of illustrating the capabilities and the flexibility of the proposed setup, the same computational techniques produce results that may serve as a starting point for detailed simulation of the interaction between radiation and matter, and can be used to define and prepare experiments in great detail. Detailed information is available at [1].

ACKNOWLEDGMENTS

We thank Joachim Pflüger, Andreas Scherz and Alexander Yaroslavtsev for useful discussions and Serguei Molodtsov for his interest in this work.

REFERENCES

- [1] G. Geloni, V. Kocharyan, T. Mazza, M. Meyer, E. Saldin, and S. Serkez, “Opportunities for Two-color Experiments at the SASE3 undulator line of the European XFEL”, DESY 17-068, 2017. <https://arxiv.org/abs/1706.00423>
- [2] G. Geloni, V. Kocharyan, and E. Saldin, “Scheme for femtosecond-resolution pump-probe experiments at XFELs with two-color ten GW-level X-ray pulses”, DESY 10-004, 2010. <https://arxiv.org/abs/1001.3510>
- [3] A. A. Lutman *et al.*, “Experimental Demonstration of Femtosecond Two-Color X-Ray Free-Electron Lasers”, *Phys. Rev. Lett.* 110, 13 2013.

- [4] T. Hara *et al.*, “Two-colour hard X-ray free-electron laser with wide tunability”, *Nat. Commun.* 4, 2919, 2013.
- [5] T. Mazza, H. Zhang, and M. Meyer. “Scientific Instrument SQS”, Tech. Des. Rep. December 2012.
- [6] A. Scherz *et al.*, “Scientific Instrument Spectroscopy and Coherent Scattering (SCS)”, Concept. Des. Rep., 2013.
- [7] V. Jonauskas *et al.*, “Auger cascade satellites following 3d ionization in xenon”, *J. Phys. B At. Mol. Opt. Phys.* 36, 22, 2003.
- [8] M. Kivilompolo *et al.*, “The gas phase L_{2,3}VV Auger electron spectra of chlorine in XCl (X=H, D, Li, Na, K) molecules”, *J. Chem. Phys.* 113, 2, 2000.
- [9] N. V. Golubev and A. I. Kulek, “Control of charge migration in molecules by ultrashort laser pulses”, *Phys. Rev. A* 91, 5, 2015.
- [10] B. Erk *et al.*, “Imaging charge transfer in iodomethane upon x-ray photoabsorption”, *Science* 345, 6194, 2014.
- [11] I. Zagorodnov. DESY MPY Start-to-End Simulations page, <http://www.desy.de/felbeam/s2e/xfel.html>.

OVERVIEW OF THE SOFT X-RAY LINE ATHOS AT SwissFEL

R. Ganter[†], S. Bettoni, H.H. Braun, M. Calvi, P. Craievich, R. Follath, C. Gough, F. Loehl, M. Paraliev, L. Patthey, M. Pedrozzi, E. Prat, S. Reiche, T. Schmidt, A. Zandonella, PSI, Villigen PSI, 5232 Switzerland

Abstract

SwissFEL Athos line [1] will cover the photon energy range from 250 to 1900 eV and will operate in parallel to the hard X ray line Aramis. Athos consists of a fast kicker magnet, a dog leg transfer line, a small linac and 16 APPLE undulators. The Athos undulators follow a new design: the so called APPLE X design where the 4 magnet arrays can be moved radially in a symmetric way. Besides mechanical advantages of such a symmetric distribution of forces, this design allows for easy photon energy scans at a constant polarization or for the generation of transverse magnetic gradients. Another particularity of the Athos FEL line is the inclusion of a short magnetic chicane between every undulator segment. These chicanes will allow the FEL to operate in optical klystron mode, high brightness SASE mode, or superradiance mode. A larger delay chicane will split the Athos line into two sections such that two colors can be produced with adjustable delay. Finally a post undulator transverse deflecting cavity will be the key tool for the commissioning of the FEL modes. The project started in 2017 is expected to be completed by the end of 2020.

INTRODUCTION

Athos photon energy ranges from 250 eV to 1900 eV (or 6.5 – 49 Å) (Fig. 1) when assuming a maximum K value of 3.65. Such large range requires both a K variation and an electron energy variation. The electron energy at extraction point (270 m downstream electron source, Fig. 2) can be varied between 2.9 and 3.15 GeV. In addition, a small linac in the Athos branch can extend the beam energy range to 2.65 – 3.4 GeV.

The Athos undulator line is linked to the main linac of SwissFEL via a dogleg section (see Fig. 2). The SwissFEL injector will produce two bunches with 28 ns delay. The dogleg starts with the beam switching system, consisting of two kickers and three compensating dipoles. These kickers deflect the second beam vertically up by 1.75 mrad so that it enters a Lambertson septum magnets 10 mm above the Aramis axis [2]. The septum magnet deflects then the Athos bunch by 35 mrad horizontally. Kickers and septum deflecting angle must be very stable from bunch to bunch and a jitter of less than 0.3 μrad is expected. The rest of the dogleg should then close the vertical dispersion, collimate the beam in energy, compensate possible CSR kicks, align the beam tilt and energy acceptance by means of sextupoles and finally inject back the beam in the Athos undulator line parallel to the Aramis line at 3.75 m distance (Fig. 3). Downstream the dogleg, the beam can be accelerated / decelerated by four

C-band structures (+/- 250 MeV) followed by diagnostics (screens, wire scanner, beam arrival monitor) to characterize the beam before entering the undulator section. Sixteen undulator segments are distributed in a FODO period of 5.6 m length. Finally an X band deflecting transverse cavity [3] will be installed before the beam dump allowing a permanent monitoring of the electron energy loss when lasing [4] or to measure the slice emittance.

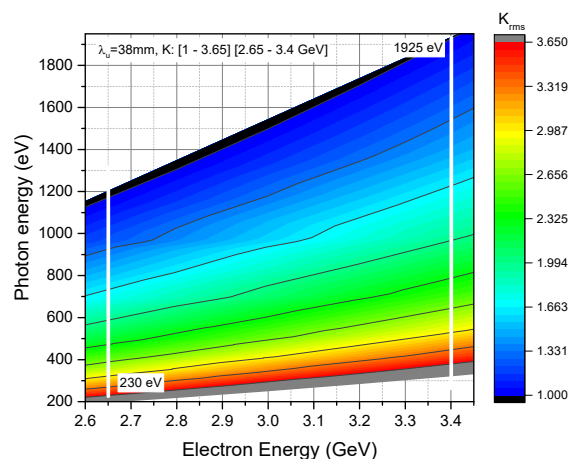


Figure 1: Photon energy range covered by the Athos FEL line (SIMPLEX [5]).

The Athos branch of SwissFEL is designed to operate in various modes of operation slightly different to standard SASE operation. The particularity of the Athos FEL lies in the permanent magnet chicanes present between every undulator segment. These chicanes allow operation in the optical klystron mode in which the microbunching process is speed up [6]. To generate terawatt – attosecond FEL pulses, a transversely tilted beam can also be shifted and delayed between every undulator segment thanks to the chicanes. In this mode, only a small portion of the beam is on the lasing trajectory and fresh electrons are supplied after a beam portion saturates [7]. The same chicanes can also be used to simply delay the bunch (without transverse shift) such that a given radiation slice (spike) will slip over a longer portion of the bunch and increase the cooperation length. This corresponds to the so called high-brightness mode [8,9] or purified SASE mode [10]. A larger magnetic chicane (2 meters length), with electromagnets, placed after the 8th undulator segment, will give the possibility to split the line and to generate two colors with adjustable time delay (0 to 500 fs). The Apple X undulator design can easily produce a transverse gradient which when used with a transversely tilted beam can produce a broadband FEL radiation of up to 10% bandwidth.

[†] romain.ganter@psi.ch

Content from this work may be used under the terms of the CC BY 3.0 licence (© 2018). Any distribution of this work must maintain attribution to the author(s), title of the work, publisher, and DOI.

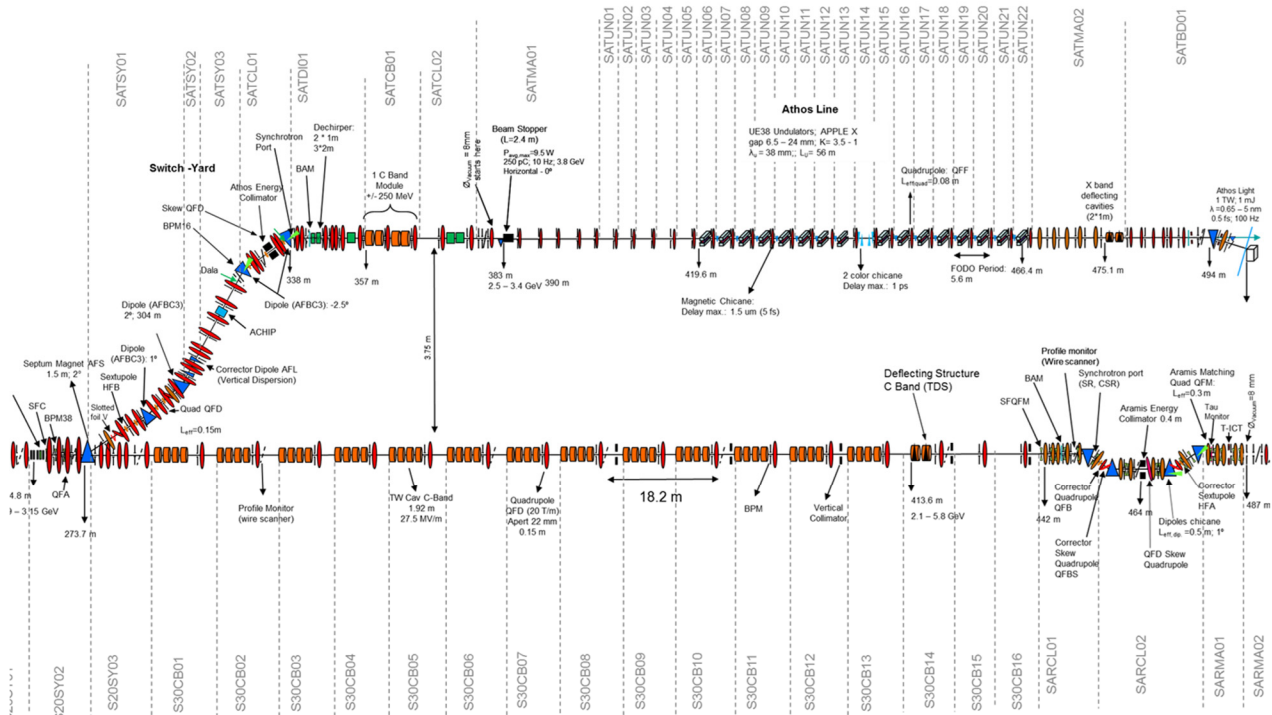


Figure 2: Layout of the Athos FEL line with the main electron beam components going from $z \sim 270\text{m}$ to $z \sim 500\text{m}$ (electron source photocathode is at $z \sim 0\text{m}$). Athos is parallel to the linac 3 of SwissFEL.



Figure 3: View of the SwissFEL tunnel with the linac 3 towards Aramis on the right and the footprint of the future Athos undulator line on the left.

ELECTRON BEAM KEY COMPONENTS

As mentioned in the introduction, beam quality corrections are foreseen in the dogleg section before entering the Athos line which is parallel to Aramis. For example, the residual beam energy chirp after bunch compressor 2 will be removed with dechirper systems.

Dechirper

The Athos dechirper consists of two adjustable (vertically and horizontally) dechirper units of one meter length each and a nominal gap of 2.5 mm followed by 3 long units of 2 meters length. The long dechirpers have a square section with a fixed aperture of 2.5 mm. In the adjustable dechirper, two parallel corrugated structures (like gratings) are used to control the wakefields generat-

ed by the beam. By properly selecting the gap and the geometry of the structure it is possible to compensate the residual energy chirp left after bunch compressor 2. The short dechirpers are shown in Figure 4. Only the gap / slit and a transverse vertical / horizontal shift can be remotely controlled. Three different corrugation geometries are available and each can be manually translated into the beam axis (during shutdown). Indeed the short dechirper units will first be used in 2018 for various test of beam manipulation on the fs time scale like deflection or dechirping [11].

Apple X Undulator UE38

The undulator segments of the Athos line have a period of 38 mm with permanent magnet situated outside vacuum. These undulators are built in the so called Apple X configuration where X comes from the possibility to move each magnet arrays radially at 45 degrees angle (see Fig. 5). In this symmetric design, gap and slit can be open simultaneously keeping the horizontal and vertical forces identical. In addition each magnet array can be moved longitudinally in order to change the polarisation from circular to linear or inclined linear. In other words, the polarisation control (shift change) is independent of the photon energy control (radial gap change). Another possible feature is to open only the left gap (or the right gap) so that the electron beam sees a transverse magnetic gradient. This offers new operation possibilities like lasing with a large bandwidth beam [12]. Permanent magnets are held in a flexible support where the position height of each half period can be adjusted to the sub micrometer level by moving a small wedge (Fig. 5). The wedge-

screw will later be automatically adjusted by a robot according to the magnetic field measured at that particular location [13].

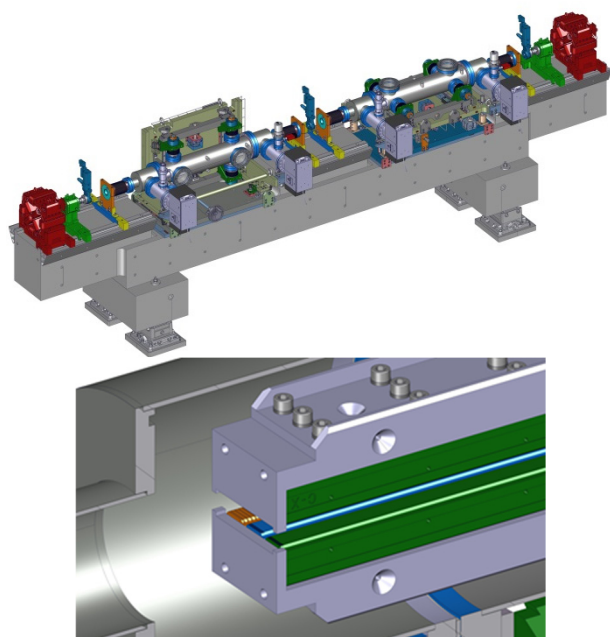


Figure 4: The vertically and horizontally adjustable dechirper on a girder (Top) Three different corrugation geometries can be installed and aligned on the axis.

Samarium cobalt will be used for the magnets since it has a permeability closer to one than NdFeB and thus less nonlinear effects. This is an important parameter for Apple undulator where the magnet field profile changes with each polarisation. Hysteresis in the magnet field leads to error in the polarisation and /or photon energy prediction. In order to boost the magnetic field near the apex of the “spade” magnets, tests of non-uniform magnetisation is currently performed by Arnold Magnetics and PSI [14]. The vacuum chamber will be produced by galvanic techniques such that the inner vacuum chamber will be 5 mm for 0.2 mm wall thickness and a minimum UE38 aperture of 6 mm.

Permanent Magnet Chicane

Most of the operation modes of Athos rely on the magnetic chicanes which will be installed between every UE38 segment. The chicane will be capable to delay the electrons by up to 8 fs (2.5 μm longitudinal delay) or to shift the beam transversally up to 350 μm . Also a combination of 5 fs (1.5 μm) delay together with a 250 μm shift will be possible. This requires however a very strong magnetic field of 2.5 T and the possibility to control each half of the chicane separately. This is achieved with the design presented in Fig. 6 where 4 motors can control the two halves of the chicane. The chicane has a magnetic length of 200 mm and a minimum gap of 6 mm. Each magnet block is an assembly of several small magnets surrounding one pole to maximize the field above this pole. The chicane should also be used as normal phase shifter when operating in normal SASE mode. In this

case, the electron beam is longitudinally delayed by less than 10 nm corresponding to a chicane gap of roughly 9 mm.

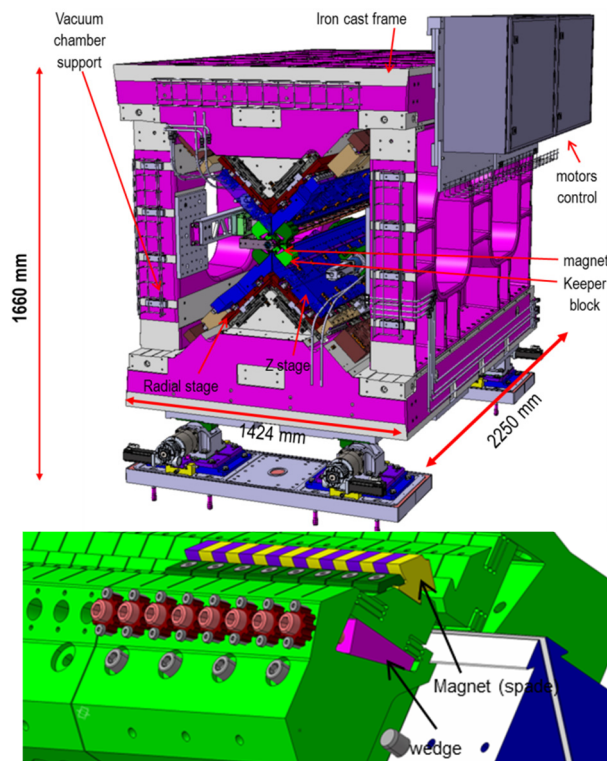


Figure 5: Apple X undulator where magnet arrays move radially along a 45-degree angle (top). Magnet keeper adjustable to sub-micrometer level (bottom).

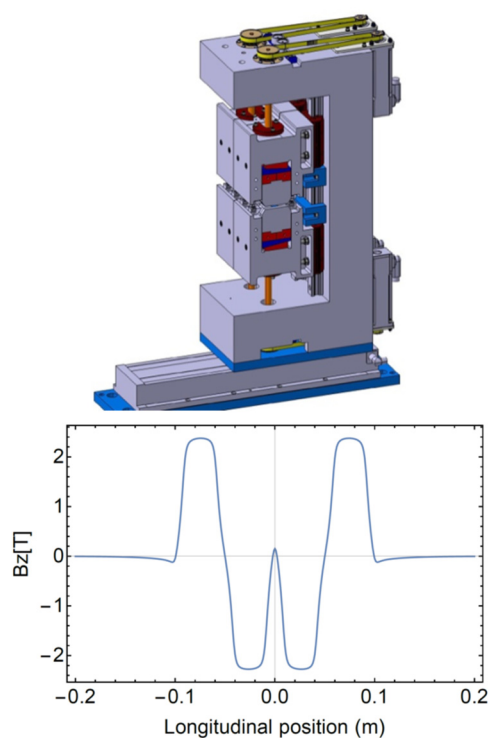


Figure 6: Magnetic chicane to shift and / or delay the electrons between every undulator segment (top) and magnetic field profile along the chicane axis (bottom).

Content from this work may be used under the terms of the CC BY 3.0 licence (© 2018). Any distribution of this work must maintain attribution to the author(s), title of the work, publisher, and DOI.

OPTICAL LAYOUT AND ENDSTATIONS

Due to the variety of the operation modes, the X ray optical component have to cope with a large range of photon beam properties. Three beamlines are foreseen for photon energies going from 170 eV to 2000 eV (see Fig. 7). To be compatible with the spatial requirements at other synchrotron facilities, especially the SLS, the height above the floor should be approximately 1400 mm at the location of the experiments. The beamline thus transports the beam from 1200 mm height at the exit of the undulator to the required 1400 mm at the experimental stations. The three endstations will share a common monochromator.

The beam transport to a height of 1400 mm above floor is accomplished by operating the grating at a higher deflection angle as the subsequent plan mirror.

The changeover from monochromatized to pink beam operation is accomplished by a roll rotation of the first mirror and a translation of the second mirror out of the beam. The photon beam divergence is varying from 5 urad to 40 urad depending on the photon energy and the mode of operation. Whenever possible, the beam transport system should accept the whole FEL beam, i.e. five times the rms-value of the beam cross section.

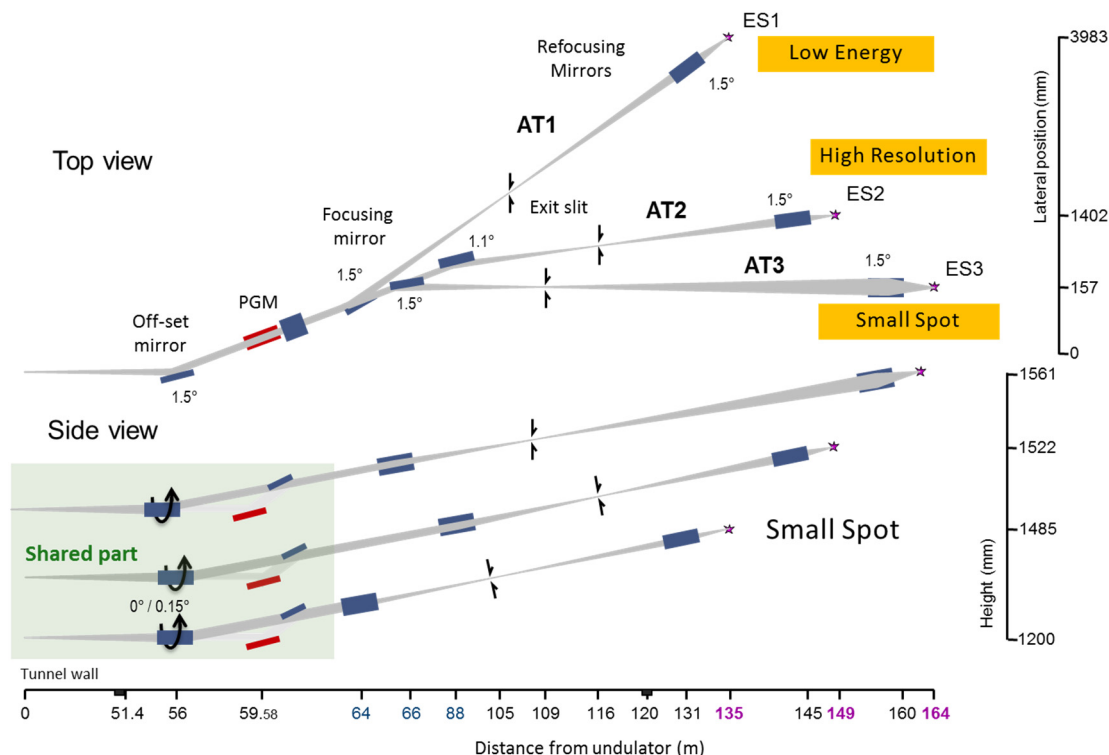


Figure 7: Optical layout of the 3 Athos photon beamlines.

The endstations are all located in the same large experimental hall for maximum flexibility. The specialty of each end station is still under discussion but as it is shown on Figure 7, ES1 should be focused more on experiment using low energy photons like in catalysis and biochemistry studies. ES2 should allow higher photon energy resolution which is more suited for spectroscopy of correlated electron systems or ultrafast magnetisation dynamics. ES3 would be dedicated to experiment requiring tight focussing.

REFERENCES

[1] J. Alex *et al.*, Athos Conceptual Design Report, in press (2017).
 [2] M. Paraliev and C. Gough, *Proc. IPAC'17*, Copenhagen Denmark (2017).
 [3] P. Craievich *et al.*, presented at FEL'17, WEP040, this conference.

[4] Y. Ding *et al.*, *Proc. IPAC'13*, Shanghai, China (2013).
 [5] T. Tanaka, *J. Synchrotron Rad.* 22, 1319 (2015).
 [6] R. Coisson, *Particle Accelerators* 11, pp. 245 (1981).
 [7] E. Prat *et al.*, *Phys. Rev. ST Accel. Beams* 18, 100701 (2015).
 [8] B. W. J. McNeil *et al.*, *Phys. Rev. Lett.* 110, 134802 (2013).
 [9] E. Prat *et al.*, *J. Synchrotron Rad.* 23, 861 (2016).
 [10] D. Xiang *et al.*, *Phys. Rev. ST Accel. Beams* 16, 010703 (2013).
 [11] S. Bettoni *et al.*, presented at FEL'17, THB04, this conference.
 [12] E. Prat *et al.*, *J. Synchrotron Rad.* 23, 874 (2016).
 [13] P. Boehler *et al.*, *Proc. MEDSI'16*, Barcelona, Spain.
 [14] Available at <http://www.arnoldmagnetics.com/en-us/Products/Shaped-Field-Magnets>.

POSSIBLE METHOD FOR THE CONTROL OF SASE FLUCTUATIONS

N. R. Thompson*

ASTeC and Cockcroft Institute, STFC Daresbury Laboratory, Warrington, United Kingdom

Abstract

It is well known that because the SASE FEL starts up from the intrinsic electron beam shot noise, there are corresponding fluctuations in the useful properties of the output pulses which restrict their usability for many applications. In this paper, we discuss a possible new method for controlling the level of fluctuations in the output pulses.

INTRODUCTION

The output of a Self-Amplified Spontaneous Emission (SASE) Free-Electron Laser [1, 2] exhibits fluctuations in the temporal and spectral domains [3] because the FEL interaction grows from an initial bunching b_0 due to the intrinsic random shot noise in the electron beam. The fluctuations can be problematic for FEL applications, although if the FEL pulse properties are recorded on a shot-by-shot basis the experimental output data can often be appropriately normalised as a mitigation strategy. This paper presents a first examination of a proposed new method for damping shot-to-shot instability. One or more dispersive chicanes are added in between the undulator modules of a SASE FEL. The longitudinal dispersion of the chicane can be set to change the amount of bunching in the electron beam in a way that is anti-correlated with the energy spread. Because the FEL-induced energy spread is itself directly correlated to the FEL power this allows a simple, passive mechanism for single pass feedback and stabilisation.

DESCRIPTION OF METHOD

Following previous work optical on klystron enhancement to SASE FELs [4] it is useful to take into account the analytical treatment originally derived for HGHG [5] to provide a simple model for the method. The bunching factor at the n th harmonic after the dispersive section in HGHG is given by

$$b_n = \left| \exp \left(-\frac{1}{2} n^2 \sigma_b^2 k_r^2 R_{56}^2 \right) J_n \left(n \frac{\Delta\gamma}{\gamma_0} k_r R_{56} \right) \right| \quad (1)$$

where σ_b is the intrinsic relative energy spread, $k_r = 2\pi/\lambda_r$ is the resonant wavenumber, R_{56} is the dispersive strength of the chicane, J_n is the n th order of the Bessel function of the first kind and $\Delta\gamma$ is the energy modulation induced by the FEL prior to the chicane.

This function is plotted in Figure 1 for $\sigma_b = 1 \times 10^{-4}$, $\lambda_r = 2\pi/k_r = 100$ nm, $n = 1$, and $R_{56} = 60$ μm . The important point to note is that there are values of $\Delta\gamma/\gamma_0$ where the gradient of this plot is negative—these are highlighted in blue. The method for SASE stabilisation takes advantage of this negative gradient to introduce a feedback into the

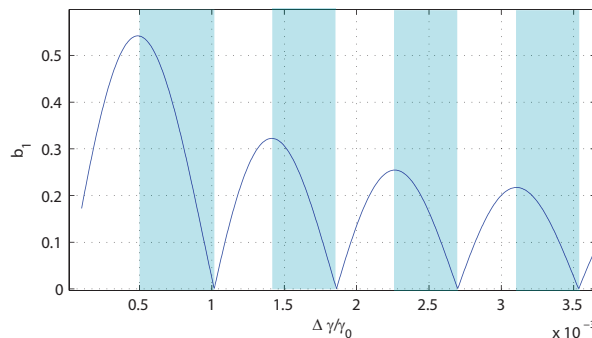


Figure 1: Plot b_n vs $\Delta\gamma/\gamma_0$ using Equation (1), for $\sigma_b = 1 \times 10^{-4}$, $\lambda_r = 2\pi/k_r = 100$ nm, $n = 1$, and $R_{56} = 60$ μm . The blue shading highlights regions where the gradient of the function is negative.

FEL growth. For example, if at the entrance to the chicane the initial bunching is small and the average induced energy spread over a number of SASE pulses is in the blue shaded region where $0.5 \times 10^{-3} \leq \Delta\gamma/\gamma_0 \leq 1 \times 10^{-3}$, then those pulses which had grown more strongly than average would have an induced energy spread higher than the average and would therefore acquire bunching after the chicane that was lower than average. Conversely, those pulses growing more weakly than average would have their bunching enhanced more than average. Overall, all the pulses would have their bunching increased in the chicane, giving stronger growth, but crucially, the weaker pulses would be boosted *more* than the stronger pulses, hence damping the shot-to-shot variation.

NUMERICAL RESULTS

The method was simulated using the three-dimensional FEL code Genesis 1.3. Two of the 240 MeV electron beam modes for the CLARA test facility [6] were used: ULTRASHORT mode which is a low charge velocity bunched mode intended to produce electron bunches suitable for lasing at 100 nm in single spike SASE regime; SHORT mode which is the default 250 pC mode for 100 nm SASE with peak current 400 A. For both modes the energy spread was set to $\sigma_b = 1 \times 10^{-4}$ and the dispersive strengths of the chicanes were within the design ranges of the facility.

ULTRASHORT Mode

The parameters of the method were empirically optimised to obtain the best stabilisation performance. The results are shown in Figure 2, which shows the pulse energy growth for a control SASE case, with 8 different shot noise seeds, and the results with the same seeds where chicanes are applied

* neil.thompson@stfc.ac.uk

Content from this work may be used under the terms of the CC BY 3.0 licence (© 2018). Any distribution of this work must maintain attribution to the author(s), title of the work, publisher, and DOI.

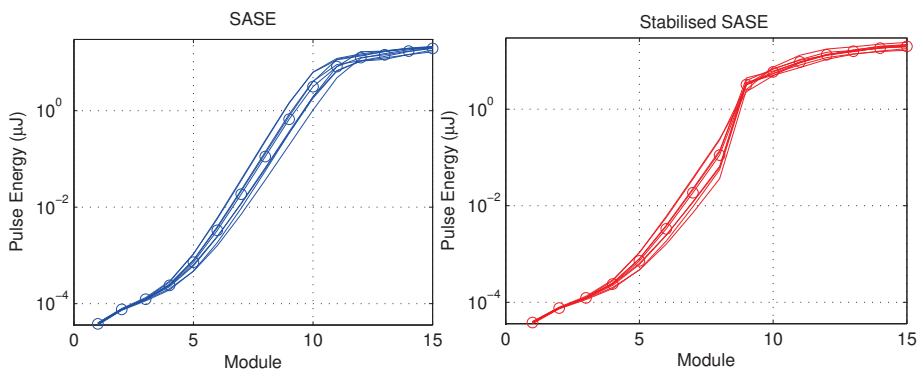


Figure 2: ULTRASHORT mode stabilisation. Top left shows the pulse energy growth for a control SASE case, with 8 different shot noise seeds. The circles mark the average. Top right shows the results where chicanes are applied before undulator modules 9, 10 and 11, with R_{56} values empirically optimised to 60 μm , 20 μm and 5 μm .

before undulator modules 9, 10 and 11, with R_{56} values 60 μm , 20 μm and 5 μm . It is seen that in undulator module 9 the variation in pulse energy over the different seeds is damped because the pulse energy plots clearly converge. After module 9 the RMS variation is reduced compared to SASE by a factor of 5.

Examination of the simulation data shows that at the entrance to undulator module 9, where the applied chicane dispersion is 60 μm , the average peak energy modulation in the electron bunch over the 8 seeds is $\Delta\gamma/\gamma_0 = 0.9 \times 10^{-3}$. From Figure 1 this means that the system is operating in the required region of negative gradient, in agreement with the simple theory.

SHORT Mode

In SHORT mode the output pulses are longer, each comprising on average 7 SASE spikes. In this case the stabilisation would be expected to work locally within the pulse, (i.e. reducing the variation in the peak powers over all the SASE spikes in each pulse) as well as over many pulses (reducing the variation in pulse energy from shot-to-shot).

Results are shown for an empirically optimised case, where chicanes are applied before undulator modules 6 to 11 inclusive, with R_{56} values 50 μm , 60 μm , 20 μm , 10 μm , 2 μm and 1 μm . This example was optimised to extend the stabilisation over as many modules as possible. In this case the number of random seeds was increased to 24 to reduce any statistical error. Figure 3 shows the RMS variation of the pulse energy over the 24 different seeds for the stabilised case, normalised to the SASE control case. The reduction in the RMS is a factor of 5 after 9 modules. It should be noted however that for the stabilised case the applied dispersion gives a reduction in the saturation length. For the SASE control, saturation (defined as the point where the radiation bandwidth and transverse size are minimised) occurs after 11 undulator modules. Here the average pulse energy is 80 μJ and the RMS variation over all seeds is 11.1%. For the stabilised case, an average pulse energy of 80 μJ is reached after only 9 undulator modules where the RMS variation is 4.6%. Therefore, if comparing output at the pulse energy

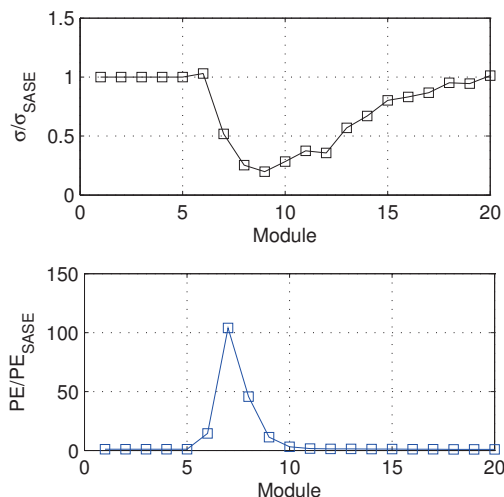


Figure 3: SHORT mode stabilisation. Top shows the RMS variation of the pulse energy over the 24 different seeds for the stabilised case, normalised to the SASE control case, and bottom right shows the normalised average pulse energy growth

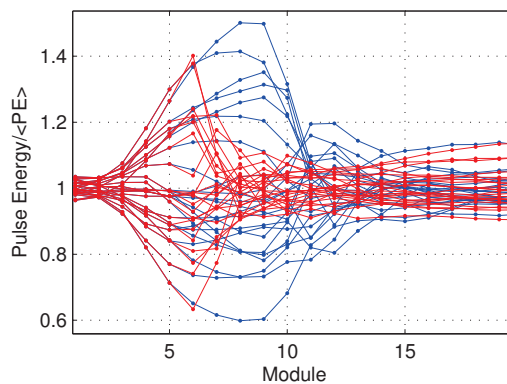


Figure 4: SHORT mode stabilisation. The blue plots show the 24 individual SASE cases, where the pulse energy at each module is normalised to the mean SASE pulse energy at that module. The red plots are for the 24 stabilised SASE cases.

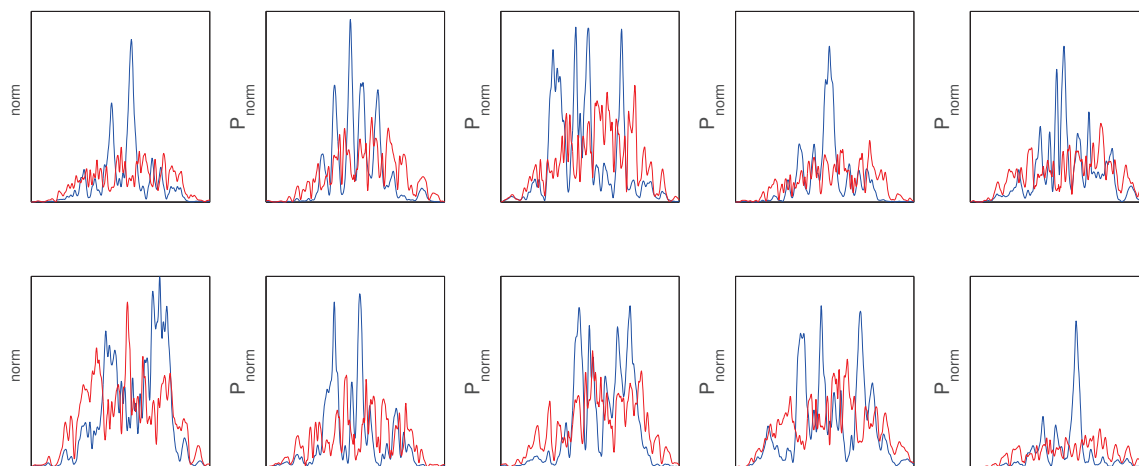


Figure 5: SHORT mode stabilisation: 10 randomly chosen examples from the 24 different shot noise seeds, showing the SASE (blue) and stabilised (red) pulse profiles at the exit of the 8th undulator module. Each pulse is normalised such that the pulse energy is unity.

of SASE saturation the improvement in stability is only a factor of 2.4.

Figure 4 shows (in blue) the 24 individual SASE cases, where the pulse energy at each module is normalised to the mean SASE pulse energy at that module, and (in red) the 24 stabilised SASE cases. It is seen that at module 7, for the stabilised cases, the pulses with higher than average pulse energy are damped (relative to the average) and those with lower pulse energy are boosted.

Finally, Figure 5 shows 10 randomly chosen examples from the 24 different shot noise seeds, with SASE (blue) and stabilised (red) pulse at the exit of the 8th undulator module. All pulses are normalised to have unity pulse energy. It is seen that with the stabilisation applied the strongest SASE spikes are damped (relatively) and the weakest SASE spikes are amplified, showing that the stabilisation method does act locally within the individual pulse as well as over many pulses.

Examination of the electron bunch data at the entrance to the 7th undulator module, where the chicane applies an R_{56} of $60 \mu\text{m}$, shows that over the whole bunch the relative energy spread varies over the range $3 \times 10^{-4} \leq \Delta\gamma/\gamma_0 \leq 1 \times 10^{-3}$. Comparing this to Figure 1 shows that this range falls mostly within the region of negative gradient and is therefore consistent with the analytic model.

CONCLUSION

A method has been proposed to stabilise the shot-to-shot variation intrinsic to SASE FELs. A simple analytic justification for the method has been given and the first simulation results are consistent with this. Two cases have been studied using the parameters of the CLARA FEL test facility: for single spike SASE operation the method is shown to reduce pulse energy fluctuations by up to a factor of five. For SASE with longer electron bunches, in which each output pulse comprises a number of SASE spikes, the method is seen to

reduce the shot-to-shot pulse energy fluctuations by a factor of five at equivalent undulator length as well as damp the variation in peak intensity for SASE spikes within an individual pulse. Comparison of the stability at equivalent pulse energy (in this case the pulse energy for SASE saturation) shows the improvement in stability is not as good - it is a factor of 2.4. Further study will fully characterise the output pulse quality of the stabilised case to compare with SASE and attempt to fully optimise the scheme to determine the stabilisation limits. The parameters used in the simulations are within the specified ranges of the parameters of the CLARA FEL Test Facility currently under construction at Daresbury Laboratory in the UK, making experimental testing of the scheme feasible in the near future.

REFERENCES

- [1] A. M. Kondratenko and E. L. Saldin, "Generation of Coherent Radiation by a Relativistic Electron Beam in an Undulator", *Particle Accelerators*, 10:207, 1980
- [2] R. Bonifacio, C. Pellegrini, and L. Narducci, "Collective Instabilities and High-Gain Regime in a Free-Electron Laser", *Optics Communications* 50:373, 1984
- [3] R. Bonifacio *et al.*, "Spectrum, Temporal Structure and Fluctuations in a High-Gain Free-Electron Laser Starting from Noise", *Physical Review Letters* 73:70, 1994
- [4] G. Penco *et al.*, "Optical Klystron Enhancement to Self-Amplified Spontaneous Emission at FERMI", *Photonics* 4, 15, 2017
- [5] L. H. Yu, "Generation of Intense UV Radiation by Subharmonically Seeded Single-Pass Free-Electron Lasers", *Physical Review A*, 44:5178, 1991
- [6] J. A. Clarke *et al.*, "CLARA Conceptual Design Report", *Journal of Instrumentation* 9 T05001, 2014 <https://doi.org/10.1088/1748-0221/9/05/T05001>

COMMISSIONING OF FEL-BASED COHERENT ELECTRON COOLING SYSTEM*

V.N. Litvinenko^{1,2,#}, I. Pinayev¹, J. Tuozzollo¹, J.C. Brutus¹, Z. Altinbas¹, R. Anderson¹, S. Belomestnykh¹, K.A. Brown¹, C. Boulware³, A. Curcio¹, A. Di Lieto¹, C. Folz¹, D. Gassner¹, T. Grimm³, T. Hayes¹, R. Hulsart¹, P. Inacker¹, J. Jamilkowski¹, Y. Jing^{1,2}, D. Kayran^{1,2}, R. Kellermann¹, R. Lambiase¹, G. Mahler¹, M. Mapes¹, A. Marusic¹, W. Meng¹, K. Mernick¹, R. Michnoff¹, K. Mihara^{1,2}, T.A. Miller¹, M. Minty¹, G. Narayan¹, P. Orfin¹, I. Petrushina², D. Phillips¹, T. Rao^{1,2}, D. Ravikumar,^{1,2} J. Reich¹, G. Robert-Demolaize¹, T. Roser¹, B. Sheehy¹, S. Seberg¹, F. Severino¹, K. Shih^{1,2}, J. Skaritka¹, L.A. Smart¹, K. Smith¹, L. Snyderstrup¹, V. Soria¹, Y. Than¹, C. Theisen¹, J. Walsh¹, E. Wang¹, G. Wang^{1,2}, D. Weiss¹, B. Xiao¹, T. Xin¹, W. Xu¹, A. Zaltsman¹, Z. Zhao¹

¹Collider-Accelerator Department, Brookhaven National Laboratory, Upton, NY, USA
²Department of Physics and Astronomy, Stony Brook University, Stony Brook, NY, USA
³Niowave Inc., 1012 N. Walnut St., Lansing, MI, USA

Abstract

An FEL-based Coherent electron Cooling (CeC) has a potential to significantly boosting luminosity of high-energy, high-intensity hadron-hadron and electron-hadron colliders. In a CeC system, a hadron beam interacts with a cooling electron beam. A perturbation of the electron density caused by ions is amplified and fed back to the ions to reduce the energy spread and the emittance of the ion beam. To demonstrate the feasibility of CEC we pursue a proof-of-principle experiment at Relativistic Heavy Ion Collider (RHIC) using an SRF accelerator and SRF photo-injector. In this paper, we present status of the CeC systems and our plans for next year.

INTRODUCTION

An effective cooling of ion and hadron beams at energy of collision is of critical importance for the productivity of present and future colliders. Coherent electron cooling (CeC) [1] promises to be a revolutionary cooling technique which would outperform competing techniques by orders of magnitude. It is possibly the only technique, which is capable of cooling intense proton beams at energy of 100 GeV and above.

The CeC concept is built upon already explored technology (such as high-gain FELs) and well-understood processes in plasma physics. Since 2007 we have developed a significant arsenal of analytical and numerical tools to predict performance of a CeC. Nevertheless, being a novel

concept, the CeC should be first demonstrated experimentally before it can be relied upon in the up-upgrades of present and in the designs of future colliders.

A dedicated experimental set-up, shown in Fig. 1, has been under design, manufacturing, installation and finally commissioning during last few years [2-4]. The CeC system is comprised of the SRF accelerator and the CeC section followed by a beam-dump system. It is designed to cool a single bunch circulating in RHIC's yellow ring (indicated by yellow arrow in Fig. 1). A 1.5-MeV electron beam for the CeC accelerator is generated in a 113-MHz SRF quarter-wave photo-electron gun and first focussed by a gun solenoid. Its energy is chirped by two 500-MHz room-temperature RF cavities and ballistically compressed in 9-m long low energy beamline comprising five focusing solenoids. A 5-cell 704-MHz SRF linac accelerates the compressed beam to 15 MeV. The accelerated beam is transported through an achromatic dogleg to merge with ion bunch circulating in RHIC's yellow ring.

In the CeC beamline, interaction between ions and electron beam occurs in the common section, e.g. a proper coherent electron cooler. The CeC works as follows: In the modulator, each hadron induces density modulation in electron beam that is amplified in the high-gain FEL; in the kicker, the hadrons interact with the self-induced electric field of the electron beam and receive energy kicks toward their central energy. The process reduces the hadron's energy spread, i.e. cools the hadron beam. Fourteen quadru-

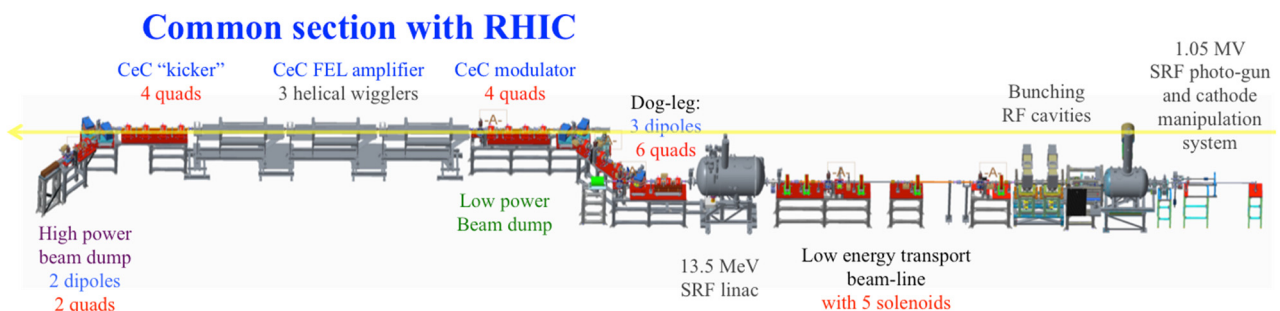


Figure 1: Layout of the CeC proof-of-principle system at IP2 of RHIC.

* Work is supported by Brookhaven Science Associates, LLC under Contract No. DEAC0298CH10886 with the U.S. Department of Energy, DOE NP office grant DE-FOA-0000632, and NSF grant PHY-1415252.

#vl@bnl.gov

Content from this work may be used under the terms of the CC BY 3.0 licence (© 2018). Any distribution of this work must maintain attribution to the author(s), title of the work, publisher, and DOI.

poles are used to optimize the e-beam interaction with the ion beam and FEL performance. Finally, the used electron beam is bent towards an aluminium high-power beam dump equipped with two quadrupoles to over-focus the beam.

COMMISSIONING OF THE CEC SYSTEM

The CeC accelerator SRF system uses liquid helium from RHIC refrigerator system, which operates only during RHIC runs, typically from February till end of June every year. Hence, the commissioning and operation of CeC accelerator is synchronized with RHIC runs.

The commissioning of the CeC accelerator was accomplished during three RHIC runs: Runs 15, 16 and 17.

During the run 15, only SRF gun and a part of the low energy beam line had been installed and commissioned. The installation of the equipment was continued during the RHIC maintenance days. We went through a steep learning curve of how to condition and operate an SRF gun with CsK₂Sb photocathode and how to prevent its QE degradation. The run was very successful and the SRF gun generated electron bunches with 1.15-MeV kinetic energy and 3-nC charge per bunch.

The major installation of the CeC system, including all common section with FEL, occurred during RHIC shutdown in 2016. We had received 5-cell SRF linac cryostat from Niowave Inc, and three helical wigglers for our FEL amplifier from BINP, Novosibirsk, Russia. The latter were assembled, magnetically measured and tuned to design performance at BNL (see [5]).

Installation of 5-cell SRF linac system suffered from two major problems. First, after installing the cryostat into the CeC system we discovered that the integrity of the linac helium system and the cryostat cooling circuits was destroyed during truck transportation from Lansing, MI to BNL. Specifically, the cavity fell from its support inside the cryostat because of the major shocks during transportation and cracks appeared in the liquid helium and nitrogen systems. The cryostat was partially taken apart and leaks repaired in situ. The second even was even more damaging – an incompetent person opened the inside of the SRF cavity to a dirty air in the tunnel. The latter resulted in excessing field emission and limited the maximum operational voltage to about 6-7 MV, instead of design value of 20 MV. The 5-cell cavity, built by Advanced Energy Systems, demonstrated voltage close to 20 MV in prior vertical tests and we decided to take the SRF linac apart and clean it after the end of the Run 16.

Nevertheless, the CeC team managed to make significant progress in CeC accelerator commissioning during RHIC run 16. Electron beam from the SRF gun was properly analysed, its emittance was measured and we had first clear indication that the SRF gun is generating electron beam of exceptionally high quality.

We also were discovering complexity of operating SRF quarter-wave gun with CsK₂Sb photocathode. We discovered that while in a normal (high 1 MV scale voltage) mode of operation the SRF gun naturally has excellent vacuum,

at low voltage it has a number multipacting (MP) zones. One of these zones, in the range of 28 kV to 40 kV of the gun accelerating voltage, was very strong, frequently preventing us from passing to operational voltage using 2 kW power amplifier. In addition to the frustrating incapability of achieving the operational voltage, MP was spoiling the gun vacuum and was destroying photocathode's QE. Lastly, this process was also enhancing the strength of MP, presumably by depositing high second-emission-yield (SEY) material from the photocathode to the surrounding surfaces. More details about our findings can be found in Refs. [6-7].

As the result of our experiences we increased the power of our transmitter to 4 kW and also developed a dedicated LLRF procedure providing for a single-shot pass through the most dangerous 40-kV multipacting barrier. After the passing the barrier, the gun was kept at operation voltage all the time and was intentionally turned down only for access to the RHIC IP2, where the gun is located. Accidental turning off the gun voltage – either by operator errors or system failures – were infrequent. If, by a chance, the gun was caught at MP level (mostly because of operator mistakes) and the MP barrier went above 4 kW of available power, keeping the gun idle for about 30 minutes was solving the problem.

During CeC run 17 (February-June 2017) the CsK₂Sb photocathodes QE ~ 3-4% was stable for months of operation. We used only two cathodes for five month of continuous operation and the change was done simply to explore an additional cathode. Our SRF gun had generated electron beam with charge up to 4 nC per bunch and extremely high quality. The best measured normalised emittance of the 1.56-MeV, 0.5-nC bunch was 0.32 mm-mrad [8].

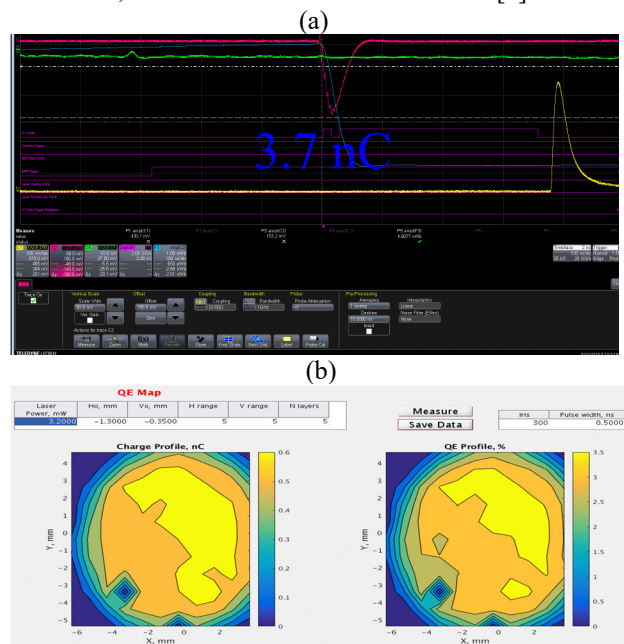


Figure 2: (a) A typical digital scope trace showing the electron bunch pulse (from integrated current transformer, red trace) and delayed trace of laser pulse (from a slow photo-diode sensor); (b) a measured QE map of CsK₂Sb photocathode after two months of operating in the SRF gun.

Content from this work may be used under the CC BY 3.0 licence (© 2018). Any distribution of this work must maintain attribution to the author(s), title of the work, publisher, and DOI.

The main efforts during the shutdown period between Runs 16 and 17 were dedicated to complete disassembly of the SRF linac cryostat (done by the SRF group at BNL), re-cleaning of the 5-cell cavity system (which was performed at ANL SRF facility), to reassemble the cryostat (at BNL) and to install it back onto CeC accelerator system. Unfortunately, the SRF linac could operate only at voltage below 13.5 MV and exhibited typical hard-quench behaviour above this level. The quenching characteristics are typical for a cavity defect near its equator, which cannot be repaired. Hence, this setback with the SRF linac limited the

energy of electron beam from CeC accelerator to about 15 MeV. This created a major obstacle in commissioning of the CeC FEL system by shifting its wavelength from 13 μm to 30 μm and rendering all our IR diagnostics practically useless: its vacuum out-coupling window had cut off above 16 μm .

Nevertheless, we had fully commissioned the CeC accelerator and propagated CW beam through the entire CeC system – including FEL system - to the high-power dump with very low losses. Table 1 summarizes the main parameters of the CeC system and its electron beam.

Table 1. Main Parameters of the CeC system

Parameter	Design	Status	Comment
Species in RHIC	Au ⁺⁷⁹ , 40 GeV/u	Au ⁺⁷⁹ 26.5 GeV/u	To match e-beam
Particles/bucket	$10^8 - 10^9$	$10^8 - 10^9$	✓
Electron energy	21.95 MeV	15 MeV	SRF linac quench
Charge per e-bunch	0.5-5 nC	0.1- 4 nC	✓
Peak current	100 A	50 A	Sufficient for this energy
Pulse duration, psec	10-50	12	✓
Beam emittance, norm	<5 mm mrad	3 - 4 mm mrad	✓
FEL wavelength	13 μm	30 μm	New IR diagnostics
Rep-rate	78 kHz	26 kHz**	Temporary**
e-beam current	Up to 400 μA	40 μA	Temporary**
Electron beam power	< 10 kW	600 W	Temporary**

The second consequence of the electron beam's low energy was a mismatch between the frequency of the SRF and revolution frequency of 26.5 GeV/u gold ions, f_{rev} . The nearest of the harmonics of the revolution frequency was outside of the available tuning range provided by movable gun's FPC [11,12].

In order to test the interaction of the electron beam with the ion beam circulating in RHIC, we had tuned the gun to the frequency $(n+1/3) f_{\text{rev}}$, resulting in the e-beam rep-rate of 26 kHz. This problem will be fixed before the next RHIC run by mechanically retuning the gun frequency. Using this set-up, we synchronised the electron beam with the ion bunch circulated in RHIC's yellow ring and scanned electron beam energy. In this case, the ion beam was overlapping with electron bunch at each third turn. Beams were overlapped both the temporarily and spatially. The recorded beam parameters during the scan are shown in Fig. 3. Without IR diagnostics we did not had chance to CeC cooling – it would require scan of 10 parameters, but we managed to detect weak energy-dependent interaction between the beams.

PLANS FOR RUN 18

Currently, RHIC is in shutdown mode and we are pursuing a program of modifications and small repairs to the CeC system. The main advances to the CeC capabilities will come from new IR diagnostic system, which would be

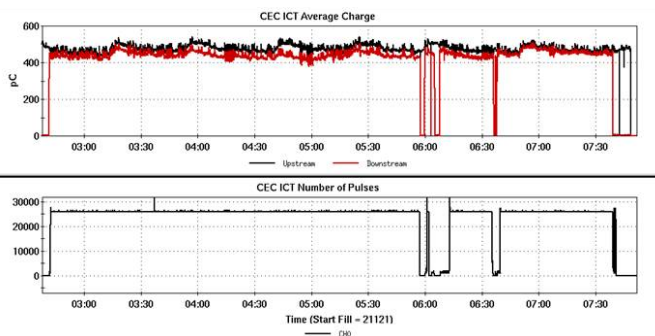


Figure 3: The charge per bunch and repetition rate during the interaction experiment.

coupled, to FEL via an SVD diamond window transparent in the entire IR spectrum. Other modifications are aimed to improving accuracy of SRF controls and orbit correction in low-energy transport beamline.

We expect to start CeC operation in January 2018 and finish the run, which is determined by RHIC operation schedule, in mid-June 2018. First, we plan to establish a stable phase, amplitude and timing operation of RF and laser system to reliably deliver a stable electron beam. After that we plan to commission our new IR diagnostics and establish FEL operation/amplification. This will be followed by synching electron beam with 26.5 GeV/u gold ion beam, aligning them transversely and synchronizing the ion and

electron beams energies using IR diagnostics. Specifically, we will observe energy-dependent increase in the intensity of FEL radiation. Finally, we plan to test and characterize Coherent electron Cooling.

CONCLUSION

We successfully commissioned SRF-based CeC electron accelerator with beam parameters sufficient for CeC demonstration experiment [11-12]. We plan to undertake the challenging task of experimentally demonstrating coherent electron cooling during next RHIC run.

REFERENCES

- [1] V.N. Litvinenko, Y.S. Derbenev, *Physical Review Letters*, **102**, 114801 (2009).
- [2] V.N. Litvinenko *et al.*, “Proof-of-principle experiment for FEL-based coherent electron cooling”, *Proc. of PAC’11*, New York, NY, USA, paper THOBN3.
- [3] I. Pinayev *et al.*, “Present status of coherent electron cooling proof-of-principle experiment”, *Proc. of COOL’13*, paper WEPP014.
- [4] I. Pinayev *et al.*, “First results of the SRF gun test for CeC PoP experiment”, *Proc. of FEL 2015*, paper TUD03.
- [5] I. Pinayev *et al.*, “Helical undulators for coherent electron cooling system”, presented at FEL’17, Santa Fe, NM, USA, paper WEP051, these proceedings.
- [6] I. Petrushina *et al.*, “Novel aspects of beam dynamics in CeC SRF gun and SRF accelerator”, presented at FEL’17, Santa Fe, NM, USA, paper TUP034, these proceedings.
- [7] I. Petrushina *et al.*, “Mitigation of multipacting in 113-MHz superconducting RF photo-injector”, in preparation for submission to PRST-AB.
- [8] K. Mihara, Y. Jing, V.N. Litvinenko, I. Pinayev, G. Wang, and I. Petrushina, “Emittance measurements from SRF Gun in CeC accelerator”, presented at FEL’17, Santa Fe, NM, USA, paper WEP025, these proceedings.
- [9] G. Wang, Y. Jing, V.N. Litvinenko, J. Ma, “Electron beam requirements for coherent electron cooling FEL system”, presented at FEL’17, Santa Fe, NM, USA, paper TUP039, these proceedings.
- [10] Y. Jing, V.N. Litvinenko, and I. Pinayev, “Simulation of phase shifters between FEL amplifiers in coherent electron cooling”, presented at FEL’17, Santa Fe, NM, USA, paper TUP072, these proceedings.
- [11] T. Xin *et al.*, *Review of Scientific Instruments*, **87**, 093303 (2016).
- [12] I. Pinayev *et al.*, “High-gradient high-charge CW superconducting RF gun with CsK2Sb photocathode”, arXiv:1511.05595, 2015.

STATUS OF THE SEEDING DEVELOPMENT AT sFLASH

V. Grattoni*, R. Assmann, J. Bödewadt, I. Hartl, T. Laarmann, C. Lechner,
M. M. Kazemi, A. Przystawik, DESY, Hamburg, Germany
S. Khan, N. M. Lockmann, T. Plath, TU Dortmund, Dortmund, Germany
A. Azima, M. Drescher, W. C. A. Hillert, L. L. Lazzarino,
V. Miltchev, J. Rossbach, University of Hamburg, Hamburg, Germany

Abstract

sFLASH is the experimental free-electron laser (FEL) setup producing seeded radiation installed at FLASH. Since 2015 it has been operated in the high-gain harmonic generation (HGHG) mode. A detailed characterization of the laser-induced energy modulation, as well as the temporal characterization of the seeded FEL pulses is possible by using a transverse-deflecting structure and an electron spectrometer. In this contribution, we present the status of the sFLASH experiment, its related studies and possible developments for the future.

INTRODUCTION

Since 2005, the free-electron laser (FEL) facility in Hamburg, FLASH, at DESY has been operated as a user facility [1]. The wavelength range was upgraded in several steps to cover an interval from about 4.2 nm to 45 nm at the beamline FLASH1. Recently, a second undulator beamline, called FLASH2, was built and commissioned to serve simultaneously two user end stations [2]. Both the beamlines are operated in the self-amplified spontaneous emission (SASE) mode [3, 4].

As a SASE FEL starts up from the random shot noise in the electron beam, the FEL radiation has poor spectral stability and limited longitudinal coherence. Seeding the FEL with a fully coherent source such as a laser, offers an option to overcome these limitations as experimentally demonstrated in the FERMI FEL in Trieste, Italy [5].

At DESY, an experimental setup for seeding developments has been installed upstream of the FLASH1 main SASE undulator in 2010 [6]. After successful demonstration of direct-HHG seeding [7] at 38 nm in 2012 [8], the focus of the seeding R&D at FLASH has turned on HGHG [9] and echo-enabled harmonic generation (EEHG) [10] seeding [11, 12].

The results obtained at the sFLASH seeding experiment guide the design process of the proposed FLASH2 seeding option [13].

In this contribution, the performance of HGHG seeding at sFLASH is described and we present the current status of the FEL seeding developments at DESY.

EXPERIMENTAL SETUP

The sFLASH seeding experiment is installed at the FEL user facility FLASH [14]. Figure 1 shows the schematic layout of the sFLASH experiment.

The electron bunches arrive from the FLASH linear accelerator with a repetition rate of 10 Hz, a typical charge of 0.4 nC and an energy between 680 MeV and 700 MeV. At the exit of the energy collimator, the sFLASH section starts with two electromagnetic undulators (called modulators, labelled MOD1 and MOD2 in Fig. 1) with 5 full periods of period length $\lambda_u = 0.2$ m and orthogonal polarization [15], each followed by a magnetic chicane (labelled as C1 and C2). In the HGHG experiment, MOD1 and C1 are not used and the interaction of the seed laser pulse with the electron bunch takes place in MOD2. Here, the seed pulse generates a sinusoidal energy modulation in the electron bunch that afterwards is converted into a density modulation by chicane C2.

The Seed Laser

The 266 nm seed pulses are generated by third-harmonic generation (THG) of near-infrared (NIR) Ti:sapphire laser pulses. The maximum energy of these UV seed pulses at the entrance of the vacuum transport beamline to the modulator undulator is 500 μ J. At the interaction point with the electron beam, the Rayleigh length of the UV beam is between 1.5 and 3 m depending on the focus of the laser.

A single-shot cross-correlator for NIR and UV pulses in the laser laboratory enables to measure the UV pulse duration, that is typically between 250 and 280 fs FWHM. The NIR pulse duration is simultaneously measured with a single-shot auto-correlator and it is about 50 fs FWHM. The longitudinal position of the beam waist can be adjusted by changing the NIR focusing into the THG setup. Before and after MOD2, the seed beam position and size are measured using Ce:YAG fluorescence screens. In the configuration in which the beam waist coincides with the center of the modulator module, a characteristic value for the rms beamsize at the screen positions is $\sigma_r = 0.33$ mm.

Latest upgrades Until the end of 2016, the THG setup was installed in the FLASH tunnel, limiting maintenance access. Now, this setup is installed in the seed laser laboratory and can be accessed when needed which facilitates the optimization of the UV seed beam quality. In particular, thanks to the more generous spaces inside the laser laboratory, a second THG setup has been installed next to the existing one and the NIR laser transport system has been modified in order to obtain two properly focused pulses that enter each in one of the two triplers. The new UV beam is focused into MOD1 by a Galilean telescope that has been installed in the FLASH tunnel before MOD1 in July this year. The

* vanessa.grattoni@desy.de

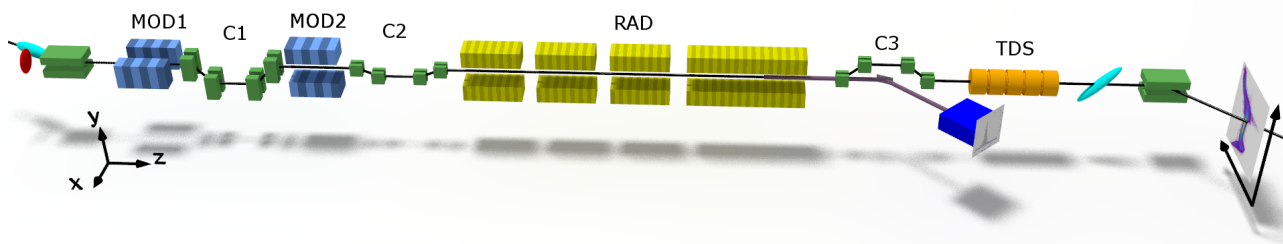


Figure 1: Layout of the sFLASH seeding experiment.

already existing UV seed source continues to be focused into MOD2 through a telescope in the laser laboratory. This setup enables experimental EEHG studies as presented in [16].

Radiator section

Four variable-gap undulators modules (labeled RAD in Fig. 1) with a total effective length of 10 m act as the FEL radiators. These undulators are tuned at an harmonic of the seed laser in order to make the current-modulated electron bunch initiate the FEL process. Downstream of the sFLASH radiator, the electron beam is guided around the radiation extraction mirrors by chicane C3 and it enters into the transverse-deflecting structure (TDS). The TDS is followed by a dispersive dipole spectrometer that deflects the electron bunch into a beam dump. An observation screen is installed in the dispersive section between the dipole spectrometer and the beam dump on which the longitudinal phase space distribution of the electron bunch can be observed. From these measurements, the parameters of the electron bunch such as current and slice emittance are obtained [17, 18]. When operated with uncompressed electron bunches (in order to exclude FEL gain), the uncorrelated energy spread of the electron bunch can be extracted by analysing coherent harmonic generation (CHG) emission at several harmonics [19]. The energy resolution of this technique significantly surpasses that of the TDS setup.

FEL Diagnostics

The seeded FEL pulses are transported to an in-tunnel photon diagnostics section, where different detectors are available: fluorescence screens for transverse beam diagnostics, a photon energy monitor based on a microchannel plate, and a high-resolution spectrometer for wavelengths from 4 to 40 nm [20].

Alternatively, the seeded FEL beam can be transported to a dedicated diagnostics hutch outside the radiation shielding of the accelerator. Here, the temporal profile of the FEL pulse can be studied utilizing a THz-streaking technique [21, 22]. A second, non-invasive method to obtain the power profile of the photon pulses is to extract this information from longitudinal phase space distributions of the electron bunch [17, 18, 23].

Table 1: Experimental Parameters for HGHG.

Parameter		Value
Modulator	period length λ_u^{MOD}	0.2 m
	N_u^{MOD}	5
	K_{MOD}	2.77
Radiator	period length λ_u^{RAD}	31.4 mm
	N_u^{RAD}	318
	K_{RAD}	2.61
Chicanes	R_{56} C1	not used
	R_{56} C2	50-200 μm
	R_{56} C3	190 μm
Electron Beam	energy	680-700 MeV
	charge	0.4 nC
	bunch duration	>500 fs (FWHM)
	besmsize	100 μm
Seed Beam	wavelength	267 nm
	NIR pulse duration	\sim 50 fs (FWHM)
	UV pulse duration	250-280 fs (FWHM)
	UV Rayleigh length	1.5-3 m
	UV waist w_0	660 μm

PERFORMANCE OF HGHG SEEDING

Since 2015, the sFLASH experiment has been dedicated to the HGHG seeding scheme. Future experiments will focus not only on HGHG, but also on the more advanced scheme of EEHG [24]. In the following, the performance of HGHG at the sFLASH experiment are presented. The typical parameters used during the HGHG seeding are reported in Tab 1. The energy spread of the uncompressed electron beam after the interaction with the seed laser can be measured for different seed laser pulse intensities and the maximum experimentally achievable modulation amplitude was found to be (350 ± 50) keV. Figure 2(a) shows a recorded TDS measurement of the (uncompressed) electron bunch longitudinal phase space distribution. From this, the energy spread profile along the electron bunch is extracted and fitted with a Gaussian (Fig. 2(b)).

In Fig. 3, consecutive single-shot spectra of the FEL at the 8th harmonic are presented. The resulting central wavelength is $\lambda_8 = 33.47$ nm and the spectral width is $\Delta\lambda/\lambda_8 = 3.02 \times 10^{-4}$ in FWHM. At the 7th ($\lambda_7 = 38$ nm) the FWHM spectral

Content from this work may be used under the terms of the CC BY 3.0 licence (© 2018). Any distribution of this work must maintain attribution to the author(s), title of the work, publisher, and DOI.

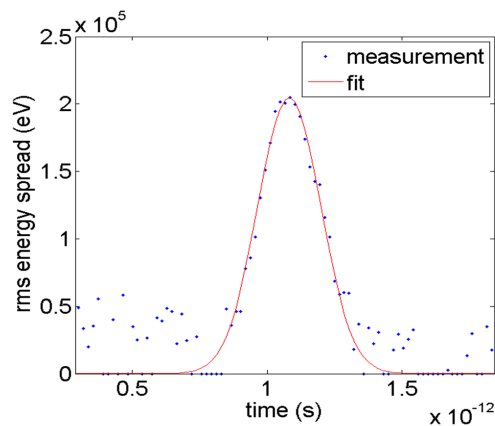
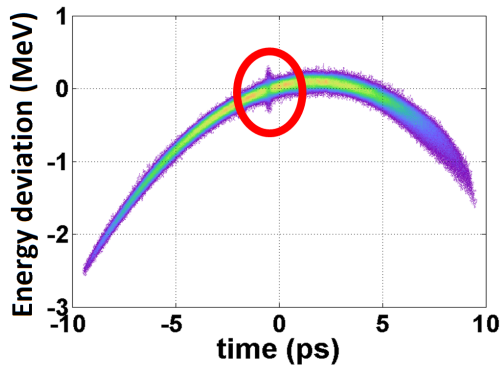


Figure 2: Extraction of modulation amplitude from longitudinal phase-space distribution: (a) Measured longitudinal phase space distribution of an uncompressed electron beam and radiator off. Energy-modulated region is highlighted with a red circle. (b) Extracted rms energy spread along the electron bunch from the measurement shown in (a).

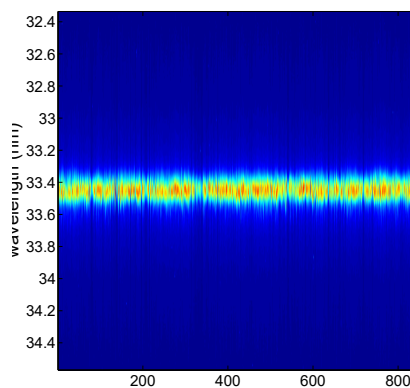


Figure 3: Series of consecutive single-shot FEL spectra taken in HGHG operation at the 8th harmonic.

width is $\Delta\lambda/\lambda_7 \leq 1.4 \times 10^{-3}$. In Fig. 4, a Gaussian is fitted to a single-shot FEL power profile at the 7th harmonic. From a statistical analysis of a set of profiles at the same harmonic, the duration of the FEL pulse is found to be $\sigma_{t,FEL} = (28.4 \pm 5.6)$ fs.

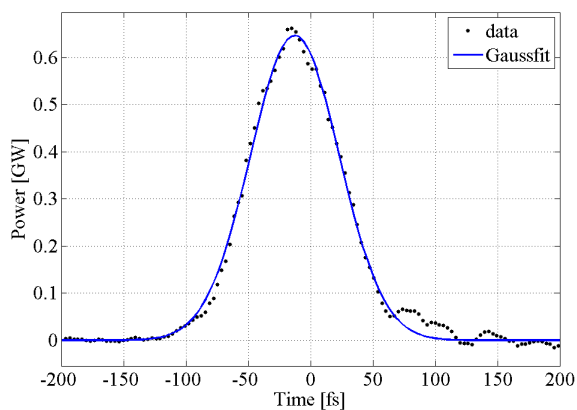


Figure 4: FEL power profile at the 7th harmonic extracted from TDS measurement.

At sFLASH, seeded FEL radiation up to the 11th harmonic of the 266 nm seed laser has been observed.

Considerations on EEHG seeding

As reported in [16], an EEHG experiment is currently prepared at sFLASH. After the laser upgrade, two UV-seed laser pulses are available, and by proper configuration of the telescopes the laser pulses can be focussed independently, which enables optimum laser-electron coupling in both modulators.

Presently, further simulations are on-going in order to find the experimental parameters that will give the best performance for the parameters of the sFLASH experiment.

ACKNOWLEDGMENTS

Without the help from many groups at DESY, the preparation and commissioning of all components of the seeding experiment would not have been conceivable. Their support is gratefully acknowledged. This work is supported by the Federal Ministry of Education and Research of Germany within FSP-302 under FKZ 05K13GU4, 05K13PE3, and 05K16PEA and the German Research Foundation within GrK 1355.

REFERENCES

- [1] W. Ackermann *et al.*, “Operation of a free-electron laser from the extreme ultraviolet to the water window”, *Nature Photon.*, vol. 1, pp. 336-342, June 2007.
- [2] B. Faatz *et al.*, “Simultaneous operation of two soft x-ray free-electron lasers driven by one linear accelerator”, *New J. Phys.*, vol. 18, p. 062002, Jun. 2016.
- [3] A. M. Kondratenko and E. L. Saldin, “Generation of coherent radiation by a relativistic electron beam in an undulator”, *Part. Accel.*, vol. 10, pp. 207-216, Jan. 1980.
- [4] R. Bonifacio, C. Pellegrini, and L. M. Narducci, “Collective instabilities and high-gain regime in a free electron laser”, *Opt. Commun.*, vol. 50, pp. 373-378, Jul. 1984.

- [5] E. Allaria *et al.*, “Highly coherent and stable pulses from the FERMI seeded free-electron laser in the extreme ultraviolet”, *Nature Photon.*, vol. 6, pp. 699-704, Sept. 2012.
- [6] S. Khan *et al.*, “sFLASH: An experiment for seeding VUV radiation at FLASH”, in *Proc. 30th Int. Free-Electron Laser Conf. (FEL’08)*, Gyeongju, Aug. 2008, paper TUPPH072, pp. 405-408.
- [7] M. Ferray *et al.*, “Multiple-harmonic conversion of 1064 nm radiation in rare gases”, *J. Phys. B: At. Mol. Opt. Phys.*, vol. 21, no 3, pp. L31-L35, 1988.
- [8] S. Ackermann *et al.*, “Generation of coherent 19- and 38-nm radiation at a free-electron laser directly seeded at 38 nm”, *Phys. Rev. Lett.*, vol. 111, p. 114801, Sept. 2013.
- [9] L.-H. Yu *et al.*, “High-gain harmonic-generation free-electron laser”, *Science*, vol. 289, p. 932, Aug. 2000.
- [10] G. Stupakov, “Using the beam-echo effect for generation of short-wavelength radiation” *Phys. Rev. Lett.*, vol. 102, p. 074801, Feb. 2009.
- [11] J. Bödewadt *et al.*, “Results and perspectives on the FEL seeding activities at FLASH”, in *Proc. 35th Int. Free-Electron Laser Conf. (FEL’13)*, New York, Aug. 2013, paper WEPSO02, pp. 491-495.
- [12] K. Hacker, “A concept for seeding 4-40 nm FEL radiation at FLASH2”, in *Proc. 36th Int. Free-Electron Laser Conf. (FEL’14)*, Basel, Aug. 2014, paper MOP097, pp.53-57.
- [13] C. Lechner *et al.*, “Concept for a seeded FEL at FLASH2”, presented at 38th Int. Free-Electron Laser Conf. (FEL’17), Santa FE, NM, USA, Aug. 2017, paper MOP003, this conference.
- [14] K. Honkavaara *et al.*, “Status of the FLASH FEL user facility at DESY”, presented at 38th Int. Free-Electron Laser Conf. (FEL’17), Santa FE, NM, USA, Aug. 2017, paper MOD02, this conference.
- [15] G. Angelova *et al.*, “Installation of the optical replica synthesizer in FLASH”, in *Proc. 29th Int. Free-Electron Laser Conf. (FEL’07)*, Novosibirsk, Aug. 2007, paper WEPPH039, p. 438.
- [16] J. Bödewadt *et al.*, “Parameter optimization for operation of sFLASH with echo-enabled harmonic generation”, in *Proc. 1st Int. Particle Accelerator Conf. (IPAC’17)*, Copenhagen, Denmark May 2017, paper WEPAB015, p. 2592.
- [17] T. Plath *et al.*, “Mapping few-femtosecond slices of ultra-relativistic electron bunches”, *Scientific Reports*, vol. 7, no 2431, May 2017.
- [18] T. Plath *et al.*, “Extraction of the longitudinal profile of the transverse emittance from single-shot-RF deflector measurements at sFLASH”, presented at 38th Int. Free-Electron Laser Conf. (FEL’17), Santa FE, NM, USA, Aug. 2017, paper MOP028, this conference.
- [19] J. Bödewadt *et al.*, “Determination of the slice energy spread of ultra-relativistic electron beams by scanning seeded coherent undulator radiation by coherent harmonic generation”, presented at 38th Int. Free-Electron Laser Conf. (FEL’17), Santa FE, NM, USA, Aug. 2017, paper TUP042, this conference.
- [20] F. Curbis *et al.*, “Photon diagnostic for the seeding experiment at FLASH”, in *Proc. 31st Int. Free-Electron Laser Conf. (FEL’09)*, Liverpool, Aug. 2009, paper THOB05, p. 754.
- [21] U. Frühling *et al.*, “Single-shot terahertz-field-driven X-ray streak camera” *Nature Photon.*, vol. 3, p. 523, Sep. 2009.
- [22] W. Helml *et al.*, “Measuring the temporal structure of few-femtosecond free-electron laser X-ray pulses directly in the time domain”, *Nature Photon.*, Vol. 8, p. 950, Nov. 2014.
- [23] C. Behrens *et al.*, “Few femtosecond time-resolved measurements of X-ray free-electron lasers”, *Nat. Comm.*, vol.5, p. 3762, Apr. 2014.
- [24] E. Hemsing *et al.*, “Echo-enabled harmonics up to the 75th order from precisely tailored electron beams”, *Nature Photon.*, vol. 10, pp. 512–515, Jun. 2016.

PLASMA WAKEFIELD ACCELERATED BEAMS FOR DEMONSTRATION OF FEL GAIN AT FLASHFORWARD *

P. Niknejadi[†], A. Aschikhin, C. Behrens¹, S. Bohlen¹, J. Dale, R. D'Arcy, L. Di Lucchio, B. Foster¹, L. Goldberg¹, J.-N. Gruse¹, Z. Hu, S. Karstensen, A. Knetsch, O. Kononenko¹, K. Ludwig¹, F. Marutzky, T. Mehring, C. A. J. Palmer, K. Poder, P. Pourmousavi¹, M. Quast¹, J.-H. Röckemann¹, L. Schaper, J. Schaffran, H. Schlarb, B. Schmidt, S. Schreiber, S. Schroeder, J.-P. Schwinkendorf¹, B. Sheeran¹, M.J.V. Streeter, G. Tauscher¹, V. Wacker¹, S. Weichert¹, S. Wesch, P. Winkler¹, S. Wunderlich, J. Zemella, J. Osterhoff, Deutsches Elektronen-Synchrotron DESY, Hamburg, Germany
V. Libov, A. Martinez de la Ossa, M. Meisel
Institut für Experimentalphysik, Universität Hamburg, Germany
A. R. Maier¹, Center for Free Electron Lasers, Hamburg, Germany
C. Schroeder, Lawrence Berkeley National Laboratory, California, USA
¹ also at Institut für Experimentalphysik, Universität Hamburg, Germany

Abstract

FLASHForward (FF▶▶) is the Future-ORiented Wakefield Accelerator Research and Development project at the DESY free-electron laser (FEL) facility FLASH. It aims to produce high-quality, GeV-energy electron beams over a plasma cell of a few centimeters. The plasma is created by means of a 25 TW Ti:Sapphire laser system. The plasma wakefield will be driven by high-current-density electron beams extracted from the FLASH accelerator. The project focuses on the advancement of plasma-based particle acceleration technology through the exploration of both external and internal witness-beam injection schemes. Multiple conventional and cutting-edge diagnostic tools, suitable for diagnosis of short electron beams, are under development. The design of the post-plasma beamline sections will be finalized based on the result of these aforementioned diagnostics. In this paper, the status of the project, as well as the progress towards achieving its overarching goal of demonstrating FEL gain via plasma wakefield acceleration, is discussed.

PLASMA WAKEFIELD ACCELERATORS

As opposed to conventional particle accelerators, where the accelerating electric gradients are generated by radio waves in superconducting (SRF) or nonsuperconducting (RF) structures, plasma wakefield accelerators (PWFA) employ a charged particle beam to create a charge-density "wake" in a plasma. With accelerating gradients on the order of 10-100 GeV/m, about three orders of magnitude greater than those produced by SRF methods, plasma wakefield accelerators allow for significant reduction of length, ultimately scaling down the size of future high energy accelerators for future light sources and colliders [1, 2]. Hence, PWFA is a promising alternative to conventional accelerators, worthy of further investigation.

FLASHFORWARD FACILITY

FLASHForward [3] is one of the few facilities in the world that is dedicated to studying and overcoming the technical and scientific challenges of beam-driven plasma wakefield acceleration. FLASHForward has as its main feature a new electron beamline in the FLASH2 tunnel, which consists of beam extraction, beam matching and focusing, a plasma cell, beam diagnostics, and undulator sections. This beamline is shown in Fig. 1. The first three sections of the beamline leading to the plasma cell are currently being installed. The project is planned in two phases so that progress and understandings gained in the first phase can benefit the second phase. Demonstration of high-quality electron beams, with small emittance and energy spread, is the goal of this first phase of the FLASHForward project. This phase will conclude with measurements of the longitudinal phase space of plasma-accelerated beams with femtosecond resolution via an X-band transverse deflecting cavity (XTDC) [4]. The design for the sections beyond the plasma cell, the diagnostics and undulator section, will be finalized after demonstration and characterization of PWFA beams. The commissioning of the second phase is expected to begin in 2020.

As previously mentioned, FLASHForward is an extension to the FLASH facility, to be operated in parallel with FLASH1 and FLASH2. As such, FLASHForward already benefits from features that are unique to linear accelerators designed for high-gain single-pass FEL sources. These features include a beam of sufficient quality to drive an FEL (up to 1.25 GeV energy, ~ 0.1% energy spread, ~ 2 μm transverse normalized emittance) with a peak current of 2.5 kA and variable current profile.

Through the use of FLASH bunches, which are already used to generate FEL pulses, the efficiency of a PWFA stage as an energy booster for FELs will be explored. In this scheme the FLASH beam will receive an energy boost via plasma acceleration while its qualities are preserved to produce FEL gain. Preservation of beam quality during accel-

* Work supported by Helmholtz ARD program and VH-VI-503

[†] pardis.niknejadi@desy.de

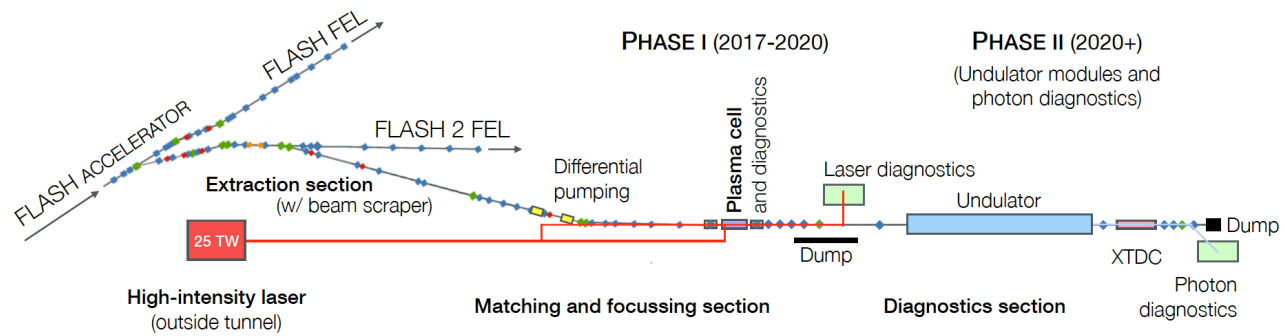


Figure 1: Outline of the FLASHForward beamline. The distance from the extraction unit to the dump is ~ 100 m. The space allocated to the undulator modules would be between 15-20 meters.

eration, extraction of the beam from the plasma stage, and transportation to the diagnostics and FEL regions all present challenges.

Furthermore, the L-band superconducting cavities at FLASH are capable of generating beams at MHz repetition rates. This is an important feature for high-average-power and high-average-brilliance applications of PWFA. Through the use of a pulsed kicker magnet, two bunches within one FLASH bunch train may be extracted to FLASHForward. An example of such a FLASH bunch train scheme is shown in Fig 2. This will allow the stability of the plasma-acceleration process at μs time intervals between two acceleration events to be tested; this is a crucial test for the future of PWFA in applications requiring high average power.

The ultimate scientific goal of FLASHForward is to demonstrate FEL gain. However, to achieve this end, a broad range of scientific milestones need to be reached before future FEL facilities can benefit from this technology. The development and testing of plasma cells, plasma-based beam optics, and femtosecond phase-space measurement [4] are among some of the challenges currently under investigation. Details of planned and achieved milestones can be found in [3] and [5].

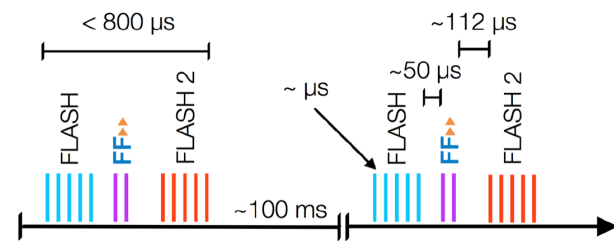


Figure 2: An example of a possible timing scheme for FLASH1, FLASH2 and FF bunch-train.

PLANNED INJECTION MECHANISMS FOR FLASHFORWARD

Injection mechanisms for PWFA can be divided into two main categories: external and internal injection. External injection is a two-bunch scheme, in which a drive bunch excites a wake while a second trailing witness bunch "surfs"

the wake. If the witness is placed in the accelerating phase of the wake it will accelerate. PWFA via external injection is also referred to as a Plasma Booster. At FLASHForward, longitudinal bunch selection by means of a beam scraper [6] is being studied for the production of the double bunch. Internal injection, on the other hand, uses one bunch only. In this scheme, the drive-bunch generates wakefields that trap and accelerate a witness beam composed by electrons either from the background plasma or from a neutral dopant species coexisting with the plasma. Several internal injection mechanisms were studied by particle-in-cell (PIC) simulations using OSIRIS [7]: beam-induced ionization injection [8, 9], wakefield-induced ionization injection [10, 11], density-downramp (DDR) injection [12, 13] and laser-induced ionization injection (Trojan horse) [14]. Of these methods, DDR has been shown to be the most suitable candidate for demonstrating FEL gain by an internal injection scheme at FLASHForward. PWFA via internal injection is also referred to as Plasma Cathode. Beam parameters from the PIC simulations for both external injection and DDR are compared to the FLASH beam in Table 1.

DEMONSTRATION OF FEL GAIN FROM PWFA

For Phase II of the FLASHForward project, a demonstration of FEL gain will be defined as a 100-fold magnification of the self-amplified spontaneous emission (SASE) signal. Therefore, a FLASHForward FEL would operate in the exponential regime. To satisfy the conditions for exponential power growth, it is important that the electron-beam emittance is less than the photon beam emittance and that beam energy spread is less than the FEL bandwidth. Minimizing both of these parameters will minimize the FEL gain length. A number of modules of Tesla Test Facility (TTF) undulators will be available for use. A preliminary scan of the parameter space via the Xie formalism [15] for the TTF undulators ($K = 1.27$, $\lambda_u = 27.3$ mm, 4.5 m long with upper bound of ~ 3 meters for FEL gain length) and PWFA beams from the PIC simulations have been performed. These show that PWFA beams are suitable for demonstration of FEL gain, particularly if strong focusing [16] is implemented (Fig. 3).

Table 1: Comparison Between the FLASH Beam Parameters and the Predicted FLASHForward Beams

Beam Parameter	Symbol	FLASH Driver Bunch	FF►► Internal Injection Witness Bunch (DDR)	FF►► External Injection Shaped Witness Bunch (w/ Scraper)	Unit
Energy	E	0.6-1.25	~1.6-2.0	>1.6	GeV
Sliced Energy spread	ΔE	~0.1	0.3-0.5	~0.2	%
Normalized emittance	ϵ_n	<2	0.3-0.5	~2	mm-mrad
Peak current	I_p	1-2.5	~0.5-1.0	>2	kA
Bunch duration	σ_b	100-500	~20-40	~10	fs

The contour plot in Fig. 3 is a generalized parameterization via Xie formalism. The vertical axis shows the average β -function for the undulator beam line. For a natural-focusing undulator beamline, the average β function is close to the undulator length. An alternating gradient (FODO) lattice can be used to provide strong focusing along the undulator line. The region meeting the 3 meter gain-length requirement in Fig. 3 falls around the contour lines for the 2 GeV beam and an average beta function of 2 meters. In addition to the 3D effects considered via Xie formalism, strong slippage effects must be avoided. Therefore the PWSA bunch lengths must be longer than the slippage length. For external injection parameters, the minimum bunch length is ~ 5 fs and for DDR parameters, ~ 9 fs. These initial criteria have been met in the preliminary studies. Full 3D simulations are planned to further investigate this scheme. Additionally, since the slice energy spread is the most critical parameter for minimizing FEL gain length, precise measurements of longitudinal phase space—planned in 2018 after the installation of the X-band transverse deflecting cavity—will be the final determining factor for FLASHForward undulator beamline design. The ultimate objective of Phase II will be to investigate the possibility of FEL gain at shorter wavelengths than that of FLASH, which will demonstrate the utility of a PWSA stage.

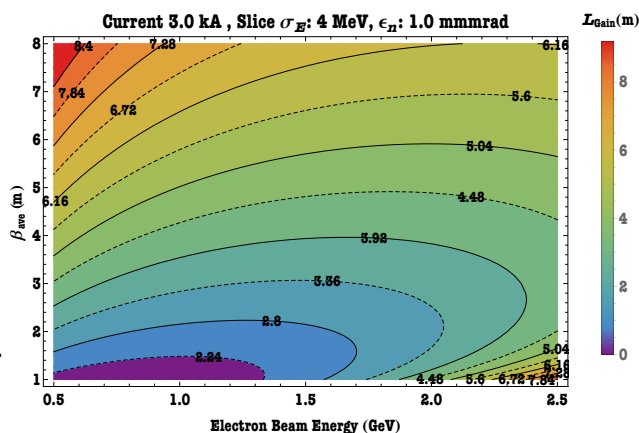


Figure 3: Initial FEL parameter study using the Xie formalism shows that the TTF undulators would be a suitable candidate for the predicted beams from the PIC simulations.

START-TO-END SIMULATIONS

To understand the effects of the beamline components on the quality of generated electron beams, as well as performance and operation of the FEL, complete start-to-end simulations are being performed. At present, the majority of these studies consider an idealized beam. However, as future experimental measurements at FLASH are made, more realistic features of the beam will be included. The final start-to-end simulations will include coherent synchrotron radiation, space-charge, and wakefield effects. In addition to the studies of the conventional accelerator sections of FLASH, the plasma-wakefield acceleration of the electron beams is simulated by OSIRIS [7] and HiPACE [17], while the transport and diagnostics of the electron beam is simulated by elegant [18]. Finally, the passage and interaction of the electrons through the undulator modules and the FEL radiation are modeled by GENESIS [19] and Puffin [20].

OUTLOOK AND SUMMARY

The FLASHForward beamline will be the third beamline at the existing FLASH accelerator facility and will benefit from the unique characteristics of FLASH electron beams that are suitable for PWSA investigations. Installation of the electron and laser beamlines up to and including the experimental chamber and the plasma cell is ongoing and will be completed by the end of 2017. Of the various injection techniques that have been studied, DDR and external injection have been selected for the first experiments in 2017 and 2018. Full parameter optimization by means of start-to-end simulation is ongoing and will benefit from the forthcoming experimental results. The first demonstration of an FEL, driven by electron beams from PWSA, is planned for the period beyond 2020.

ACKNOWLEDGMENT

The authors would like to thank the Helmholtz ARD program and the HGF Virtual Institute VH-VI-503 for their funding and support.

Content from this work may be used under the terms of the CC BY 3.0 licence (© 2018). Any distribution of this work must maintain attribution to the author(s), title of the work, publisher, and DOI.

REFERENCES

- [1] W. P. Leemans *et al.*, *Nature Physics* 2, (2006) 696.
- [2] A. Buck *et al.*, *Nature Physics* 7, (2011) 543.
- [3] A. Aschikhin *et al.* *Nuclear Instruments and Methods in Physics Research Section A* 806, (2016) 175-183.
- [4] R. D’Arcy *et al.*, *Proc. of IBIC’16, Barcelona, Spain*, (2016) WEPG51.
- [5] R. D’Arcy *et al.*, *Proc. of IPAC’17, Copenhagen, Denmark*, (2017) TUPIK006.
- [6] P. Muggli *et al.*, *Phys. Rev. Lett.* 101 (2008) 054801.
- [7] R. A. Fonseca *et al.*, *Computational Science—ICCS 2002 (Lecture Notes in Computer Science vol 2331)* edited by P. Sloot, *et al.* (Springer Berlin Heidelberg, 2002) 342–351.
- [8] E. Oz *et al.*, *Phys. Rev. Lett.* 98, (2007) 084801.
- [9] A. Martinez de la Ossa *et al.*, *NIM A* 740, (2014) 231.
- [10] A. Martinez de la Ossa *et al.*, *Phys. Rev. Lett.* 111, (2013) 245003.
- [11] A. Martinez de la Ossa *et al.*, *Physics of Plasmas* 22, (2015) 093107.
- [12] J. Grebenyuk *et al.*, *NIM A* 740, (2014) 246.
- [13] A. Martinez de la Ossa *et al.*, “Optimizing density down-ramp injection for beam-driven plasma wakefield accelerators”, accepted in *Phys. Rev. AB*, 2017.
- [14] B. Hidding *et al.*, *Phys. Rev. Lett.* 108, (2012) 035001.
- [15] M. Xie, *IEEE Proc. PAC95*, 95CH3584, (1996) 183.
- [16] J. Pflüger and Y. M. Nikitina, *Nuclear Instruments and Methods in Physics Research A* 381, (1996) 554.
- [17] T. Mehrling *et al.*, *Plasma Phys. Control. Fusion* 56, (2014) 084012.
- [18] M. Borland, “Elegant: A flexible SDDS-compliant code for accelerator simulation,” *Advanced Photon Source LS-287*, September 2000.
- [19] S. Reiche, *NIM A* 429, (1999) 243-248.
- [20] L. Campbell and B. McNeil, *Physics of Plasmas* 19, (2012) 9.

COMMISSIONING STATUS OF THE EUROPEAN XFEL PHOTON BEAM SYSTEM

F. Le Pimpec*, European XFEL, Schenefeld, Germany

Abstract

The European XFEL located in the Hamburg region in Germany, has finished its construction phase and is currently being commissioned. The European XFEL facility aims at producing X-rays in the range from 260 eV up to 24 keV out of three undulator beam lines that can be operated simultaneously with up to 27000 pulses/second. The FEL is driven by a 17.5 GeV linear accelerator based on TESLA-type superconducting accelerator modules. The accelerator has finished its first commissioning phase and is currently delivering photon beam to the experimental areas for commissioning in view of the user operation. This paper presents the status of the photon beam system from the undulators to the three experimental areas, as well as the status of the instruments.

INTRODUCTION

The European XFEL accelerator, operated by the DESY staff, has lased after 6 months of commissioning time [1, 2] and has reached the first set of design parameter as described in [3]. This success allows for the official start of the operation phase of the European XFEL. Although the machine would benefit of more time for a thorough commissioning of all its subsystems; the accelerator must provide x-ray (XR) laser type beam to the two instruments FXE (Femtosecond X-ray experiments) and SPB/SFX (Single Particles, clusters and Biomolecules /Serial Femtosecond Crystallography) located in the SASE 1 branch (see Fig.1). The technical commissioning of these two instruments, with and without beam, is in full swing in order to be ready to receive their first users in September 2017. The tight schedule allows a start of the exploitation phase with external users with a set of limited parameters for the electron and for the XR photon beams. The two other photon beamlines SASE 2 and 3 should be ready to receive beam in early 2018 and the instruments located at their end for user operation sometimes in late 2018.

ACCELERATOR OPERATION STATUS

The layout of the entire superconducting based Linear accelerator, including the 3 undulator sections and their respective electron beam dumps can be found in Figure 3 in the following reference [1]. Some of the design parameters of this machine and the value achieved at the beginning of August 2017 are given in Table 1. The normalized slice emittance measured with a bunch charge of 500 pC was 0.6 mm/mrad. The machine is now providing and tuning around a photon energy of 9.1 keV hence adjusting the gap

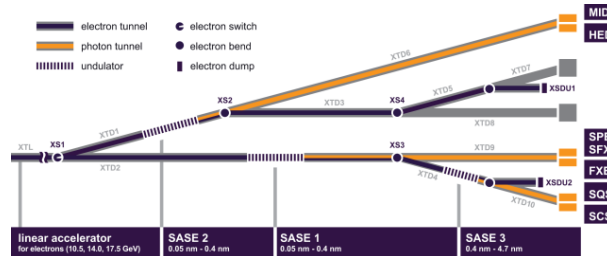


Figure 1: Photon beam system layout underlined by the orange color for the X-ray optics, diagnostics and beam transport

of the undulators according to needs based on the electron energy.

Table 1: European XFEL Design Parameters and Target Parameters Achieved at the Beginning of August 2017 [1].

Parameter		Design	Achieved
Energy	GeV	17.5	14.6
Bunch Charge	pC	20 - 1000	100-500
Macro Pulse Repetition Rate	Hz	10	10
Macro Pulse RF length	μ s	600	600
Inner pulse bunch frequency		1-2700	1-30
Max. beam power at LINAC end	kW	473	1.8
Peak Current	kA	3-5	5
Compression Factor		200-2000	200
Operating Temperature	K	1.9	1.9

It must be mentioned that the injector itself which finished its commissioning in 2016 could produce and drive to the injector dump (160 MeV) 2700 bunches per train at 10 Hz. The complex pattern of the European XFEL is reproduced in Fig.2. The warm RF gun could produce bunches with a charge varying from 20 pC to 1 nC [1].

In order to qualify the European XFEL facility to be ready to enter the operation phase, a set of parameters had to be achieved:

1. Photon Wavelength: < 0.2 nm
2. Peak brilliance: $> 10^{30}$ photons/s/mm²/mrad²/0.1 % BW
3. Dimension at sample: < 1 mm² (FWHM)
4. Positional stability: $< 50\%$ of beam size (RMS)
5. Photon energy stability: $< 0.1\%$
6. Shot-to-shot intensity fluctuation: $< 10\%$

* frederic.le.pimpec@xfel.eu

Content from this work may be used under the terms of the CC BY 3.0 licence (© 2018). Any distribution of this work must maintain attribution to the author(s), title of the work, publisher, and DOI.

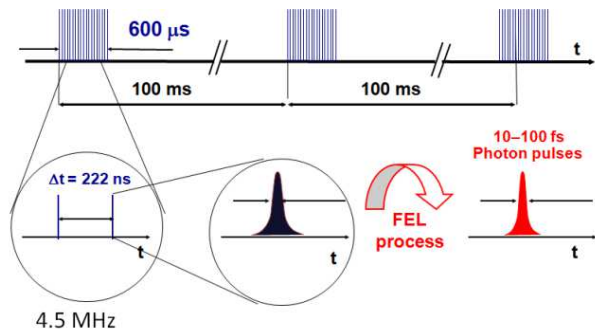


Figure 2: Electron beam pattern and FEL pulse length per bunch.

Those parameters were demonstrated by the European XFEL commissioning team (European XFEL and DESY staff) and endorsed by the Machine and Scientific Committee Chairs.

This success is commendable but more work is still to come for the machine in order to reach the nominal design parameters as displayed in Table 1. In addition the machine will enter 2 modes of functioning, an operating mode to serve users and a commissioning mode to finish its own commissioning but also provide a stable beam to commission the photon systems and the remaining 4 instruments located in the SASE 2 and 3 tunnels and experimental areas. Finally the machine is expected to be fully commissioned in 2019 and to operate 5800 hrs with 4000 hrs reserved for user runs and 1800 hours reserved for Accelerator and X-Ray development.

PHOTON BEAM SYSTEM

The responsibility of the photon beam system (PBS) starts, and is shared at the undulator sections and ends inside the experimental hutches. The layout of these sections and the SASE (Self Amplified Spontaneous Emission) FEL radiation energy expected are shown in Fig. 1,3 [3].

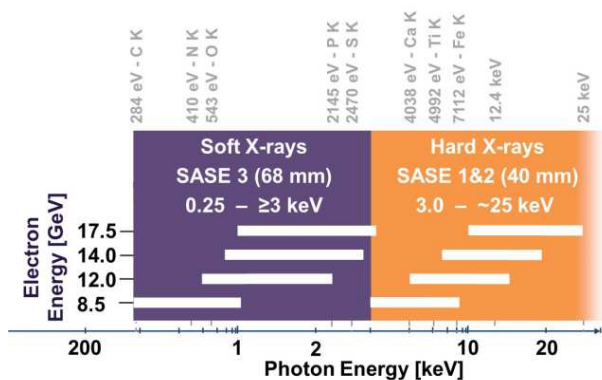


Figure 3: Photon Energy Range produced by the variable gap undulators depending on the electron beam energy

The first electron/photon and photon beam line to be commissioned is labeled SASE 1. It encompasses two series of tunnels XTD2 and XTD9 as represented in Fig. 1.

In XTD2 the electron beam and the FEL light will co-propagate and two control systems will be used to direct them to their respective end destination, either to XTD9 and the SASE 1 experimental area for the photons or in the SASE 3 section for the electrons. The DOOCS system is used to control the accelerator and the electron beam optics while Karabo [4, 5] is used for the photon beam system, the control of the instruments and to cope with the deluge of data the detectors, installed at the instruments Fig. 4, will produce. A bridge between the two control systems is still under development to, at term, authorize the control of the undulators by the users using the Karabo control system. With this bridge the machine will be able to read, in DOOCS, all the photon diagnostics installed in the tunnels but also installed in the experimental hutches, for better tuning. The control room is equipped with consoles running both systems.

SASE 1	Single Particles, Clusters and Biomolecules (SPB)	AGIPD	Gotthard V2	Fast CCD
	Materials Imaging & Dynamics (MID)	AGIPD	Gotthard V2	
SASE 2	Femto Second X-ray Experiments (FXE)	LPD	Gotthard V2	Gotthard V1
	High Energy Density Matter (HED)		Gotthard V2	
SASE 3	Small Quantum Systems (SQS)	DSSC	Fast CCD	MCP
	Spectroscopy and Coherent Scattering (SCS)	DSSC	Fast CCD	MCP, Small pnCCD

Figure 4: Various photon detectors needed at the soft and Hard X-ray beamlines. Most of them are capable of operating at the intra-bunch frequencies (4.5 MHz). A Gotthard type detector is also used by the diagnostic group as a photon arrival time monitor.

Photon source and beam transport

A thorough description of the capabilities of the undulators, the phase shifters, and the properties of the B₄C coated XR mirrors are available in [6–8]. All undulators have been installed allowing for the feeding of all the experimental stations in the three SASE areas, Fig.1. The transport mirrors, 2 offset mirrors (X,Y) and a distribution mirror, are installed on SASE 1 beam line. SASE 3 and 2 will have their mirrors installed by the end of this year.

The undulator parameters are summarized in Table.2 [7]. It has to be noted that the beam transport system does not allow the propagation of the 1.99 keV and 30.8 keV radiation in SASE 1 & 2 and the 4.6 keV radiation for SASE 3.

The commissioning of the SASE 3 & 2 photon systems will be happening during the first quarter of 2018.

In SASE 1, the undulator system and its control software is in general well operational. Amelioration of the control system is ongoing to be able to perform for example in a single click a photon energy scan. Such scans, using variable gap undulators, require that the gap of the undulators and the

Table 2: FEL Undulator Source Parameters

Parameter	SASE1 SASE2	SASE3
Period length (mm)	40	68
Maximum B-field (T; @10 mm)	1.11	1.68
Number of poles per segment	248	146
Number of segments	35	21
Total system length (m)	205	121
Gap range (mm)	10 - 20	10 - 25
K-parameter range	1.65 - 3.9	4 - 9
Photon energy range (keV; @8.5 GeV)	1.99 - 7.2	0.243 - 1.08
Photon energy range (keV; @12 GeV)	3.97 - 14.5	0.485 - 2.16
Photon energy range (keV; @17.5 GeV)	8.44 - 30.8	1.031 - 4.6

phase shifters are moving in sync. The undulator group will test this implemented feature in a dedicated machine development run. The undulator group is also carefully monitoring the electron beam losses as radiation dosing will cause demagnetization of the permanent magnets (poles per segment as in Table 2) constituting each undulator. The wavelength of the photons (λ_{photon}) produced by the undulators is highly dependent on knowing reliably the K parameter of each undulator, it is given by:

$$\lambda_{\text{photon}} = \frac{\lambda_{\text{undulator}}}{2\gamma^2} \left(1 + \frac{K^2}{2} \right) \quad (1)$$

with

$$K = \frac{e B_{\text{undulator}} \lambda_{\text{undulator}}}{2\pi m_e c} \quad (2)$$

where $\lambda_{\text{undulator}}$ is the period of the undulator, $B_{\text{undulator}}$ is the magnetic field at a given gap, see Table 2, γ is the Lorentz factor, e the electron charge and c the speed of light. In the current absence of the K monochromator spectrometer, the machine relies on the K tables produced by the undulator group. The commissioning parameters, as described in the first section, reflects the care taken to protect the sensitive equipment.

As stated previously, the super polished mirrors have been installed in their vacuum chambers and can deflect the beam from the straight line to SPB/SFX to the FXE experimental station. The mirror can also be inserted half way such that both instruments can commission some of their uncritical elements with FEL beam. During installation it was found that a mechanical collision with the water cooling system of the mirrors existed. The cooling system has been removed allowing for the free translation of the mirror in or out of the beam. In consequence the mirrors cannot take, for the moment, the full load of the nominal parameters that the machine shall provide. To protect those long lead delivery

items, the machine will run longer with reduced number of bunches and charge. An upper limit in term of heat load and deformation has already been evaluated by the optics group.

Photon Beam Diagnostics

The tuning and characterization of the SASE FEL beam (quality of the photon beam (wavefront), pulse energy, position, wavelength, spectrum and bandwidth, polarization) depends on available XR diagnostics. A full set of invasive (imagers (or screens), K spectrometer ...) and online diagnostics (X-Ray gas monitor (XGM), high resolution x-ray spectrometer (HIREX)...) have been installed in the appropriate tunnels [6, 7]. The search for SASE and the tuning of the FEL energy was done first using the various imagers installed along the photon beamline. The energy of the photon beam was then measured using the calibrated XGM, Fig.5. A FEL energy of 1 mJ has been achieved at a wavelength of 1.5 Å. The energy of the photon beam provided by the XGM relies on the operation at a pressure of 10^{-5} mbar partial pressure of the following gases Xenon, Krypton, Neon, Argon or Nitrogen. Xenon is for the commissioning time the selected gas as it provides the largest signals thanks to its largest cross-sections in the hard X-ray domain. With both elements available (Imagers and XGM) one can first easily integrate the intensity of the light on a screen to provide a quick quantitative value for the XR beam energy. Those values can be cross calibrated using the XGM to produce an absolute photon beam energy using solely a screen. The XR photon diagnostics group is now concentrating its effort in commissioning the K spectrometer. The K spectrometer is now necessary in order to cross check the validity, after a few months of operation, of the K of the SASE 1 undulator beam line.



Figure 5: SASE intensity measured with the XGM during a 30 bunch operation per train (0.5 nc, 10 Hz, 12.7 GeV) at 8.27 keV (1.5 Å).

EXPERIMENTAL AREA

Past the photon beam shutter the XR will enter the experimental zones where the 6th instruments are located, Fig.1. The science addressed by the instruments are summarized in Table 3.

The SASE 1 instruments are under commissioning while SASE 3 and SASE 2 instruments will be commissioned during the second and third quarter of 2018, respectively. The SASE 1 instruments (FXE and SPB/SFX) are scheduled to welcome their first users on 14th of September 2017. Both instruments will carry out pump probe experiments and depends on the availability of the lasers [6]. Due to delays in the laser hutches and laser lab infrastructure the lasers will be available toward the end of 2017.

Readiness of SPB/SFX

The SPB/SFX instrument [7] is the most complex of the two instruments. SPB/SFX experiments are dependant of the in-vacuum detector AGIPD (Adaptive Gain Integrating Pixel Detector). The full performances of SPB/SFX will be achieved when its 4 Kirkpatrick-Baez (KB) mirrors and an additional 2 KB mirror systems for focusing the XFEL beam to micron-scale and 100 nm-scale focii, respectively, will be installed. For its first experiments the instruments has commissioned its focusing Beryllium compound refractive lenses (CRL). The first AGIPD detector is currently being installed on the beamline. The delivery sample system [6] is installed, see Fig.6. The whole experimental beamline including the optic hutch is now being commissioned with FEL type beam, Fig.7. The commissioning is done in shifts of 12 hours 24/7 over a few days. The beam alternates between the SPB/SFX instrument and the FXE instrument.

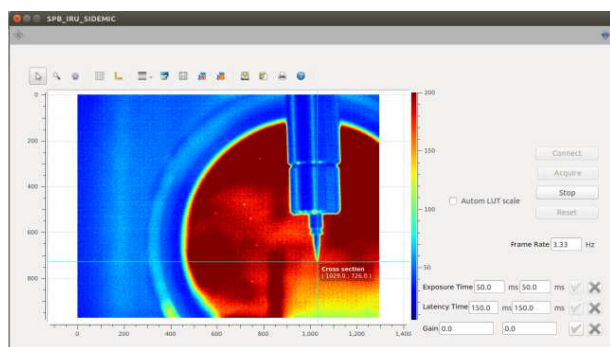


Figure 6: Liquid Jet delivery sample system in the SPB experimental chamber. Shot taken using Karabo.

Readiness of FXE

The FXE beamline [7] depended for most of its components on an in-Kind Contribution (IKC) from Denmark through DTU. This IKC was very successful and all components were delivered in time. The main focusing elements for FXE are also a set of CRLs.

FXE first test with the FEL beam was done using calibrated LaB₆ powder. Fig.8 presents the diffraction rings

Table 3: Science Addressed by the Six Instruments at European XFEL

Scientific Instrument	nm-scale structures	Ultra-fast Processes	Extreme States
SPB/SFX: Single Particles, clusters and Biomolecules / Serial Femtosecond crystallography Structure determination of single particles: atomic clusters, bio-molecules, virus particles, cells	X	X	
FXE: Femtosecond X-ray Experiments Time-resolved investigations of the dynamics of solids, liquids, gases		X	
MID: Materials Imaging & Dynamics Structure determination of nano-devices and dynamics at the nanoscale.	X	X	
HED: High Energy Density Matter Investigation of matter under extreme conditions using hard X-ray FEL radiation, e.g. probing dense plasmas		X	X
SQS: Small Quantum Systems Investigation of atoms, ions, molecules and clusters in intense fields and non-linear phenomena	X	X	X
SCS: Soft x-ray Coherent Scattering/Spectroscopy Electronic and real structure, dynamics of nano-systems and of non-reproducible biological objects	X	X	

from the LaB₆ powder recorded via Karabo on 2-tile prototype of the LPD, using 2 bunches per train with an unfocused XR beam. The LPD was set to measure 32 images and Fig.8 proves the single shot detection capability of LPD when running at 4.5 MHz and the performances of Karabo.

Content from this work may be used under the terms of the CC BY 3.0 licence (© 2018). Any distribution of this work must maintain attribution to the author(s), title of the work, publisher, and DOI.

First diffraction pattern at SPB/SFX 29.6.2017

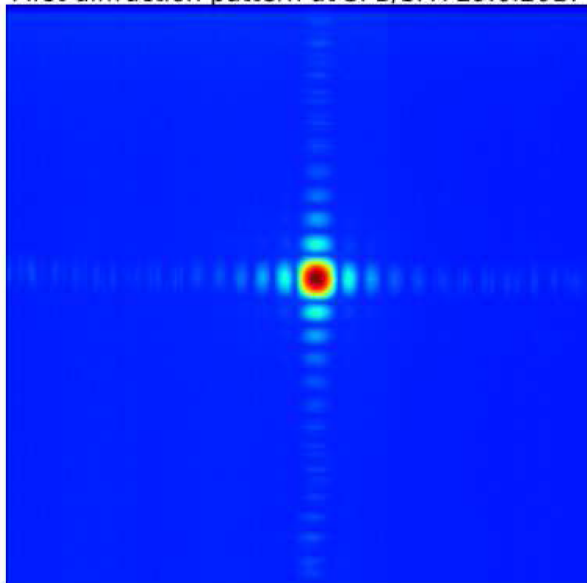


Figure 7: First Diffraction pattern recorded by SPB/SFX team, 1 bunch per train, 8.3 keV.

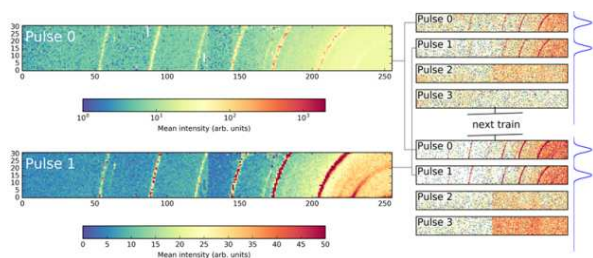


Figure 8: Diffraction ring pattern recorded via Karabo on 2 tiles of the LPD detector. LaB₆ calibration powder, 2 bunches per train, 8.3 keV, few hundred μJ FEL energy

Since then, three detectors are being commissioned, LPD Fig.9, the Van Hamos and Johan spectrometers. FXE strength lies in the so call pump-probe type experiments. As noted earlier, they depend strongly on the availability of a pump laser lasing in the IR, VUV regions, depending on the needs. The FXE team will use a Tangerine[®] laser [9] from Amplitude technology to ensure the first experiments by its users.

CONCLUSION

The European XFEL facility is finishing its first phase of commissioning which will allow for a first user run on the SASE 1 beam line from September 2017 on. In 2018 parallel operation of the 3 beamlines are foreseen. SASE 1 will see its second user run with the full availability of the pump-probe laser, while SASE 2 and 3 will commission their photon systems and their instruments. It is expected that a user run in the second semester of 2018 will be possible for SASE 3 and for MID (SASE 2). The sharing of the 6000 hours of machine run, between user runs, machine and XR system development in 2019, will have to be reviewed in due time.



Figure 9: Large Pixel Array detector in the FXE experimental hutch.

ACKNOWLEDGMENT

This paper could not be written without the information, pictures, provided by the European XFEL and DESY team. The author would like to thank in particular the help of C. Bressler and the FXE team, A. Mancuso and the SPB/SFX team, F. Wolff-Fabris from the undulator team, J. Liu and T. Maltezopoulos from the diagnostic team and the detector group for the detector suite schematics; W. Decking for its latest update on the accelerator operation

REFERENCES

- [1] W. Decking and H. Weise. Commissioning of the European XFEL Accelerator. In *IPAC 2017, Copenhagen, Denmark*, 2017.
- [2] H. Weise. First Lasing of the European XFEL. In *FEL17, Santa Fe, NM, USA*, 2017.
- [3] M. Altarelli *et al.*, editor. *European XFEL Technical Design Report*. DESY 2006-097. DESY-European XFEL, 2007.
- [4] B. Heisen *et al.*, Karabo: An Integrated Software Framework Combining Control, Data Management, and Scientific Computing Tasks. In *ICALEPS2013, San Francisco, USA*, 2013.
- [5] B. Heisen, M. Teichmann, K. Weger, and J. Wiggins. Karabogui: The multi-purpose graphical front-end for the karabo framework. In *ICALEPS2015, Melbourne, Australia*, number PUBDB-2016-01111. European XFEL, 2015.
- [6] W. Decking, F. Le Pimpec. European XFEL Construction Status. In *FEL14, Basel, Switzerland*, 2014.
- [7] T. Tschentscher, C. Bressler, J. Grünert, A. Madsen, A. Mancuso, M. Meyer, A. Scherz, H. Sinn, U. Zastra. Photon Beam Transport and Scientific Instruments at the European XFEL. *Applied Sciences*, 6(6):592, 2017.
- [8] F. Wolff-Fabris, Y. Li, J. Pflüger. The Magnetic Field Integral Hysteresis on the European XFEL Gap Movable Undualtor Systems. In *FEL17, Santa Fe, NM, USA*, 2017.
- [9] http://www.amplitude-systemes.com/client/document/tangerine_2.pdf.

PROGRESS OF DELHI LIGHT SOURCE AT IUAC, NEW DELHI*

S. Ghosh[†], B. K. Sahu, P. Patra, J. Karmakar, B. Karmakar, S. R. Abhilash, D. Kabiraj,
V. Joshi, N. Kumar, S. Tripathi, G. K. Chaudhari, A. Sharma, A. Pandey,
S. Kumar, G. O. Rodrigues, R. K. Bhandari, D. Kanjilal,
Inter University Accelerator Centre (IUAC), New Delhi, India
A. Aryshev, S. Fukuda, M. Fukuda, N. Terunuma, J. Urakawa,
High Energy Accelerator Research Organization, KEK, Tsukuba, Japan
U. Lehnert, P. Michel, Helmholtz Zentrum Rossendorf Dresden (HZDR), Dresden, Germany
V. Naik, A. Roy, Variable Energy Cyclotron Center, Kolkata, India
M. Tischer, Deutsches Elektronen-Synchrotron (DESY), Germany
T. Rao, Brookhaven National Laboratory, USA

Abstract

The first phase of the pre-bunched Free Electron Laser (FEL) based on the RF electron gun, has been initiated at Inter University Accelerator Centre (IUAC), New Delhi. The photoinjector-based electron gun made from OFHC copper was fabricated and tested with low power RF. The beam optics calculation by using ASTRA and GPT codes are performed and radiation produced from the pre-bunched electron bunches are being calculated. The high-power RF system was ordered and will be commissioned at IUAC by the beginning of 2018. The design of the laser system is being finalised and assembly/testing of the complete laser system will be started soon in collaboration with KEK, Japan. The initial design of the photocathode deposition system has been completed and its procurement/development process is also started. The first version of the undulator magnet design is completed and its further improvements are underway. The initial design of the DLS beam line have been worked out and various beam diagnostics components are being finalised. Production of the electron beam and THz radiation is expected by 2018 and 2019, respectively.

INTRODUCTION

A typical Free Electron Laser (FEL) accelerator is either based on the principle of oscillator or seeded amplifier or Self Amplified Spontaneous Emission. The length of most FEL facilities is extended to a few tens of metres which make the system complex as well as expensive. To reduce the length of the machine and, hence, to minimise the cost and complexity, the pre-bunched FEL [1,2] based on the photoinjector RF electron gun was planned to be developed at Inter University Accelerator Centre (IUAC), New Delhi. The name of the project is Delhi Light Source (DLS) [3] and it is divided into three phases. In the first phase, a photocathode based electron gun will produce low emittance electron beam with maximum energy of ~ 8 MeV which will be injected in to a compact, variable gap undulator

magnet to produce the coherent THz radiation in the range of 0.15 to 3.0 THz. During the second phase, a superconducting RF photo-injector will be developed and the electron beam will produce THz radiation with higher average power by an undulator magnet. In the third phase, the energy of the electron beam will be increased from 8 to 40 MeV and it will be injected in to longer undulator magnets to produce far-infrared and infrared radiation. The electron beam will be also used to produce soft X-rays by colliding it with a laser beam. Presently, the first stage of the DLS project is about to be commissioned at IUAC.

DEVELOPMENTAL STATUS OF MAJOR COMPONENTS OF PHASE-I OF DLS

A class 10000 clean room has been commissioned to accommodate the Phase-I of DLS. In addition to that, the photocathode deposition mechanism and all the experimental stations to perform experiments with electron and THz beam will be also installed inside the clean room. The stages of developments for various subsystems of the compact FEL is given in the following sections:

Simulation of Beam Optics and Radiation Production from the Undulator

The beam optics simulations are performed with the help of ASTRA [4] and GPT [5] code. In the first phase of DLS, the single laser pulse responsible to produce electron bunches will be split in to 2, 4, 8 or 16 micropulses. The maximum separation between 2, 4, 8 or 16 micropulses of laser and hence electrons will be ~ 6.6 ps, 2.2 ps, 950 fs or 333 fs respectively so that the total span of the microbunch train will occupy less than about 6.6 ps in an RF cycle of 2860 MHz. If the RF pulse width is adjusted to be at 3 μ sec, then 15 electron microbunch trains, each separated by 200 ns containing 2, 4, 8 or 16 micro-bunches will be accommodated within a RF pulse whose repetition rate is ~ 80 msec. For the case of 16 laser micro-bunches, a total number of 3000 electron micro-bunches ($16 \times 15 \times 12.5$) will be produced. If 15-pC electron charge can be accommodated inside a micro-bunch, the total charge of a macro-

[†] ghosh64@gmail.com

* The work is supported by Board of Research in Nuclear Science, India and Inter University Accelerator Center, India

Content from this work may be used under the terms of the CC BY 3.0 licence (© 2018). Any distribution of this work must maintain attribution to the author(s), title of the work, publisher, and DOI.

bunch will be 240 pC. The beam optics calculation is done to cover the desired range of radiation frequency (0.15 to 3 THz) and the parameters like charge per microbunch, electron bunch width, solenoid field, position and field of the quadrupole singlet, laser spot size, etc. are adjusted to restore the beam quality and to avoid the overlapping of the microbunch structure. The important parameters of the beam optics calculation are tabulated in Table 1.

Table 1: Parameters of the Beam-Optics Calculation [6].

Range of radiation frequency (THz)	0.15	3
Accelerating field (MV/m)	58.5	110
Launching phase (deg)	30	30
Electron Energy (MeV)	4.1	8.1
Energy spread (%)	1.1	0.43
e-beam FWHM @ cathode (fs)	200	200
Total charge (pC)/microbunch	15	15
Number of microbunches	2	16
Av. microbunch separation at undulator's entrance (ps)	6.6	0.345
Peak Current (A) at und. entrance	20	75
$\sigma_{x,y}$ (mm) at undulator's entrance	0.25, 0.19	0.27, 0.17
Emittance (x, y) π mm-mrad at undulator's entrance	3.5, 0.04	0.2, 0.01

The simulation of the radiation produced from the undulator is calculated by the analytical formula by using Lienard-Wiechert's equation [6]. The total photon energy from a single 16 microbunch train for the frequency of 3 THz has been calculated as 12 μ J [6] on a square area of 30 mm \times 30 mm at a distance of 0.5 metre from the exit of undulator.

The Copper Cavity as the Electron Gun

The electron gun of the FEL will be a 2.6 cell copper cavity with a resonance frequency of 2860 MHz. This cavity has been fabricated and tested in collaboration with KEK, Japan and a quality factor of $\sim 15,000$ has been measured during the low power RF test. The field profile of the cavity was measured by the bead pull method. The picture of the cavity and the match between its field profile from simulation and bead pull data is shown in Figure 1. The cavity is waiting to be installed in the beam line of DLS and currently under evacuation at IUAC inside a clean room of class 100.

The RF System of DLS

The RF system of DLS comprises of a Low-Level RF section and high power RF system consisting of klystron and modulator to power the RF cavity. Specifications of the high-power system are summarised in Table 2.

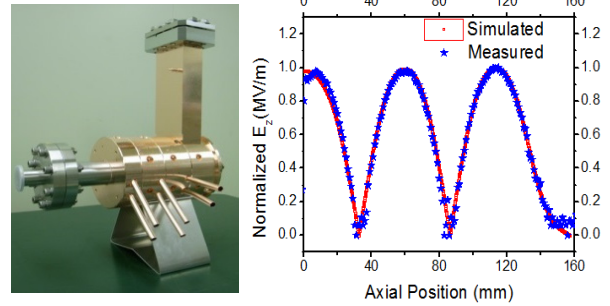


Figure 1: 2860 MHz copper cavity and its field profile.

Table 2: Main Parameters for Klystron & Modulator.

	Parameter – RF system	Value
1	Peak output power	≥ 25 MW
2	Average output power	≥ 5 kW
3	Operating frequency	2860 MHz
4	Bandwidth (-1 dB)	± 1 MHz
5	RF pulse duration	0.2 μ s to 4 μ s
6	Pulse repetition rate	1-50 Hz
7	Pulse top flatness	$\pm 0.3\%$
8	Rate of rise and fall of modulator output voltage	200-250 kV/ μ s
9	Long term stability	$\pm 0.05\%$

The Photocathode Deposition System to Produce Photocathode Plug

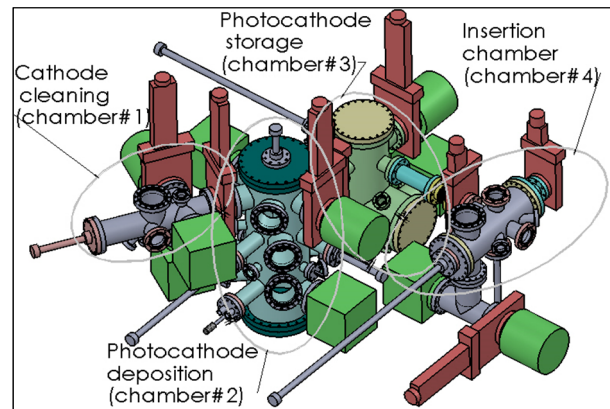


Figure 2. The photocathode deposition mechanism

In the photocathode based RF gun, initially, electrons will be produced from the copper photocathode by illuminating it with the laser beam. The copper photocathode has been fabricated along with the cavity and is ready to be installed inside the copper cavity. An ultra-high vacuum chamber with a few vacuum manipulators to insert the copper photocathode inside the copper cavity has been designed and presently is being fabricated. However, to increase the electron yield from the accelerator, semiconductor photocathode e.g. Cs₂Te and K₂CsSb will be used in future. To develop the deposition facility of the semiconductor photocathode on metal substrate, the complete de-

sign of the deposition system consisting of four dedicated vacuum chambers along with numerous accessories is frozen (Figure 2) and the initiative to fabricate the device has been started. In this deposition system, while preparing the thin film of Cs₂Te, the metal substrate will be loaded in the cathode cleaning chamber and the surface to be deposited will be cleaned by the laser beam. After cleaning, the substrate will be brought to the deposition chamber and it will be deposited first by Tellurium and then by Caesium with a constant measurement of Quantum efficiency (Q.E.). Then the photocathode will be shifted to the storage chamber where there will be a provision to store six photocathode plugs and any one of them can be inserted in to the cavity through the insertion chamber. The complete system will be working at an expected vacuum level of 5×10^{-11} mbar and the movement of the photocathode plugs will be done by various load locks and vacuum manipulators.

The Laser System to Produce Electrons from the Photocathode

The oscillator frequency of the Yb doped fiber laser system (Table-3) will have 130 MHz to produce 1030 nm as fundamental mode which will be synchronised with the master clock (2860 or 1300 MHz). The repetition rate will be reduced by AOM to 5 MHz to avoid laser pulse loading (Figure 3). Then after stretching and amplification through the PCF fiber, the laser pulses will be transported through the pulse picker to pick up the pulses in the ~3 microsecond RF window with 12.5 Hz rep rate. Two burst amplifiers will be added subsequently to increase the pulse energy. After amplification, the splitting mechanism will split each laser into 1-16 pulses but it's location is still uncertain and can be placed before amplification. Finally, after fourth harmonic conversion, the UV laser will be delivered to the photocathode. With 0.1- μ J pulse energy, we can produce maximum of 200-pC charge from Cs₂Te photocathode. The pulse energy in the UV can be increased up to 10 μ J if the laser system is operated at transient amplification region which can be used mainly due to lower quantum efficiency of Cu photocathode.

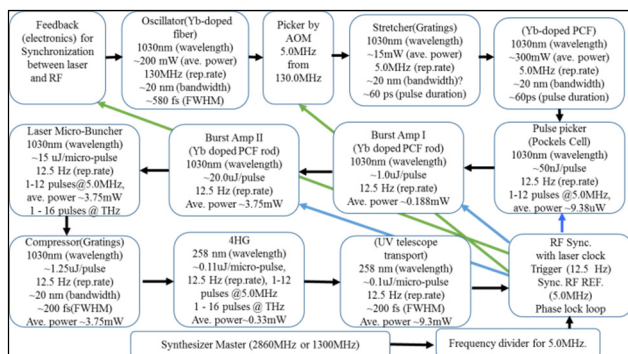


Figure 3: Block diagram of the fiber laser system.

Table 3. A Few Specifications of the Fiber Laser System

Energy/Pulse @ 258 nm @cathode	Number of micro-pulses	Pulse-width micro-pulses	Photo-cathode & expected Q.E.	Charges produced from each micro-pulses	MaxCurrent 15x16 bunch structure at 12.5Hz rate)
10 μ J, transient amp. state	1	200fs	Copper, 0.0014%	20 pC	3.8 nA
0.1 μ J, steady state	1-16	200fs	Cs ₂ Te, 1%	200 pC	600 nA

The Design of the Compact Undulator

To produce the THz radiation in the range of ~0.15 to 3 THz, a compact hybrid Undulator magnet consisting vanadium-permendur poles with a period length of 50 mm has been designed [7] with the code RADIA [8]. Initial beam optics calculation suggested that the device length will be 1.5 meter. The end-field termination is designed to follow 1: 3/4 : 1/4 configuration. There will be 28 full periods (56 poles and 56 magnets) and the end structure will consist of 2 poles and 2 magnets on both sides. The working gap range of the undulator is 20–45 mm corresponding to the range of magnetic field of 0.61–0.11 T. The undulator with full five periods and its magnetic field plots is shown in Figure 4.

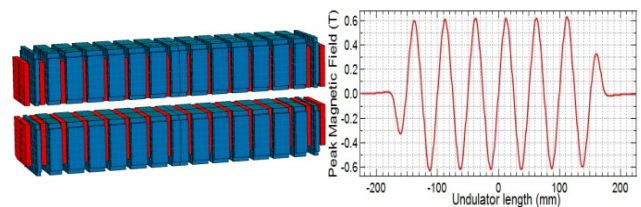


Figure 4: Miniature model of the 16-pole undulator (asymmetric structure) and its field plot at the gap of 20 mm.

PRESENT STATUS

A project to develop a compact THz radiation facility in the range of 0.15 to 3 THz based on pre-bunched FEL has been initiated at IUAC, New Delhi. The electron gun to produce 8 MeV of electron beam has been fabricated and tested. The suitable RF system to power the electron gun will be installed and operated at the beginning of 2018. The state of the art fiber laser system is going to be developed in collaboration with KEK, Japan. The design of the photocathode deposition system to produce the semiconductor photocathode is frozen and will be developed or procured

shortly. The first phase of the design of the undulator is done and it is going to be developed in collaboration with a reputed magnet company. The solenoid to focus the electron beam is ordered and will be delivered to IUAC within a few months. The design and development of the other electromagnets, e.g. dipole, quadrupole and steering magnets will be started soon.

The beam line design of the THz facility is almost frozen and the various components of the beam line are being procured or developed. The demonstration of the electron beam and THz radiation are expected to happen by the end of 2018 and 2019.

REFERENCES

- [1] S. Liu and J. Urakawa, in *Proc. FEL'11*, Shanghai, China, 2011, pp. 92-95.
- [2] M. Boscolo *et al.*, *NIMA* vol. 577, p. 409-416, 2007.
- [3] S. Ghosh *et al.* *NIM-B* vol. 402, p. 358-363, 2017.
- [4] K. Flöttmann, ASTRA, www.desy.de/~mpyflo
- [5] General Particle Tracker, available at: <http://www.pulsar.nl/gpt/index.html>
- [6] V. Joshi *et al.*, presented at FEL'17.
- [7] S. Tripathi *et al.*, presented at FEL'17.
- [8] RADIA, available at: <http://www.esrf.eu/Accelerators/groups/Insertion Devices/Software/Radia>

DESIGN CALCULATION ON BEAM DYNAMICS AND THz RADIATION OF DELHI LIGHT SOURCE*

V. Joshi[†], J. Karmakar, N. Kumar, B. Karmakar, S. Tripathi, S. Ghosh, D. Kanjilal, R. Bhandari,
Inter University Accelerator Centre (IUAC), New Delhi, India
U. Lehnert, Helmholtz Zentrum Dresden Rossendorf (HZDR), Dresden, Germany
A. Aryshev, High Energy Accelerator Research Organization (KEK), Ibaraki, Japan

Abstract

The development of a compact light source facility, Delhi Light Source (DLS), based on pre-bunched Free Electron Laser has been initiated at Inter University Accelerator Centre (IUAC) [1-3]. A photocathode based normal conducting RF gun will generate a low emittance 'comb' electron beam with a maximum energy of ~ 8 MeV, which when injected into a 1.5 metre compact undulator magnet ($\sim 0.4 < K_{rms} < \sim 2$) will produce intense THz radiation in the frequency range of 0.15 to 3.0 THz. There will be provision to vary the spatial separation between the successive microbunches of the electron beam so that by varying the Undulator magnetic field and/or electron energy, the THz frequency can be tuned. The detailed information of the radiation to be generated from the facility along with the optimized beam optics results will be presented in the paper.

INTRODUCTION

Delhi Light Source (DLS) is a project initiated by Inter University Accelerator Centre to develop a compact THz radiation facility based on the principle of prebunched Free Electron Laser [1-3]. The facility will consist of a fibre laser system to generate 'comb' laser pulses with variable separation in frequency range of 0.15 to 3 THz which will be incident on the photocathode (Cu or Cs₂Te) to generate the electron micro-bunches. The electron beam generated from the photocathode will be accelerated by the normal conducting 2.6-cell copper cavity to produce an electron energy of ~ 8 MeV.

In this paper, we discuss the simulation results of generation of e-beam microbunches from the photocathode and its evolution through the beam line. General Particle Tracer [4] was used to track the electron beam from the photocathode to the exit of the undulator. The characteristics of the THz radiation to be produced from the wiggling electrons through the undulator was studied numerically by solving the Lienard-Wiechert fields for ensemble of charged particles, moving relativistically under the combined influence of the interaction fields and the undulator fields.

PRINCIPLE OF OPERATION OF DLS

The first phase of DLS is intended to produce THz radiation in the wavelength range of 0.15 to 3 THz. To reduce the cost and complication of the project, it was decided to design a compact facility with maximizing the peak elec-

tron current and peak intensity of radiation within a time width of a few hundreds of femtoseconds. This challenging goal can be achieved by producing thin slices of electrons called microbunches and then producing a train of those microbunches with a variable separation equal to the wavelength of the frequency range by varying the separation of the laser pulses. If the bunch length of the individual microbunches in the electron beam is extremely small with respect to the radiation wavelength, then the emitted radiation from individual electrons is added up in phases resulting in maximum radiation intensity and the bunches are called "super-radiant" [5]. Further, if each microbunch is super-radiant and inter microbunch separation is maintained at one radiation wavelength, then the radiation from each microbunch will be coherently added and the intensity will be proportional to the square of the total number of electron in e- beam. The total electric field [6] from the train of microbunches will be given by the following summation where k is the microbunch number, N_m is the total number of the microbunches, t_0 is the observation time for the radiation pulse from first microbunch and t_k is the temporal separation of the k th microbunch from the first microbunch. Since $\exp(-i\omega(t_0 + t_k))$ is a periodic function and $\exp(-i\omega(t_0 + t_k)) = \exp(-i\omega t_0)$ if $t_k = T_{\text{radiation}}$; therefore; the equation for total electric field will be reduced to $E_{\text{total}} = E_0 N_m N_e B_w$ where B_w is called bunching factor and the intensity will scale as $I \sim E_0^2 N_m^2 N_e^2 B_w^2$. Thus, pre-bunching should result in enhancement of the emission spectral energy for the frequency to be generated [5].

BEAM OPTICS SIMULATIONS

The beam optics simulations have been performed by using the GPT code and it includes the generation of the electron beam at the photocathode, its acceleration through the 2.6 cell RF cavity, transportation of the beam from the exit of the RF cavity up to the undulator exit with help of a solenoid magnet and a quadrupole magnet. To improve the quality of the e-beam, the simulation calculations have been performed a) to reduce the size, energy spread and emittance of the beam b) to maximize the bunching factor of the beam and c) to avoid the overlapping of the microbunch structure of the beam bunches starting from undulator entrance to exit. The beam optics calculations have been done with radial beam and important simulation parameters are given in Table 1.

The e- beam profile in x and y direction for the two extreme frequencies of 0.15 and 3THz from the photocathode

*This work is supported by Board of Research in Nuclear Sciences (BRNS) and IUAC.

[†] vipuljoshi92@gmail.com

Content from this work may be used under the terms of the CC BY 3.0 licence (© 2018). Any distribution of this work must maintain attribution to the author(s), title of the work, publisher, and DOI.

up to the exit of undulator is shown in Figure 1. The microbunch structures at the entrance of the undulator for 16 and 2 microbunches (corresponding to 3 and 0.15 THz respectively) are shown in Figure 2. The bunching factor for 16 microbunches (3 THz) is shown in Figure 3. During simulation calculations, the parameters of the electron beam, the solenoid and quadrupole field are adjusted to maximize the bunching factor and to reduce the merging effect of the electron microbunches at the undulator's entrance.

Table 1: Parameters for DLS at Undulator's Entrance

Radiation Frequency (THz)	0.15	3
No. of microbunches	2	16
Charge per microbunch (pC)	15	15
Accelerating field (MV/m)	58.5	110
Energy (MeV)	4	8
Energy spread (%)	1.1	0.43
FWHM (fs)	~750	~200
$\sigma_{y,x}$ (mm)	0.19, 0.25	0.175, 0.275
Emittance, $\epsilon_{x,y}$ (π mm-mrad)	3.7, 0.04	0.2, 0.01
Avg. separation	6.6 ps	345 fs
Peak current (A)	20	75

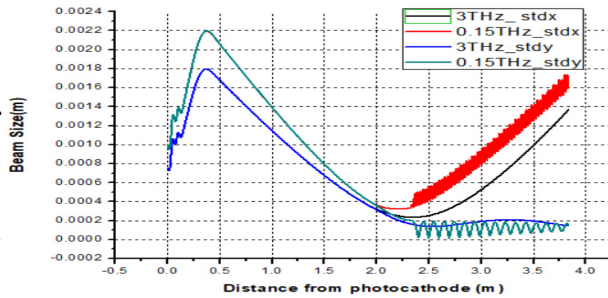


Figure 1: Electron-beam size from photocathode to undulator's exit.

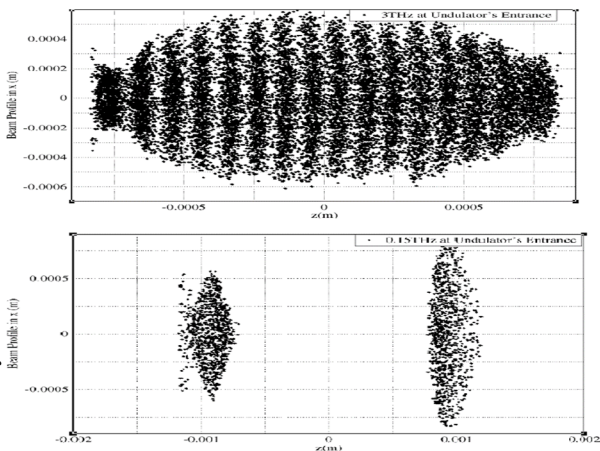


Figure 2: Beam profile for 3 THz (top) & 0.15 THz (bottom) at undulator's entrance.

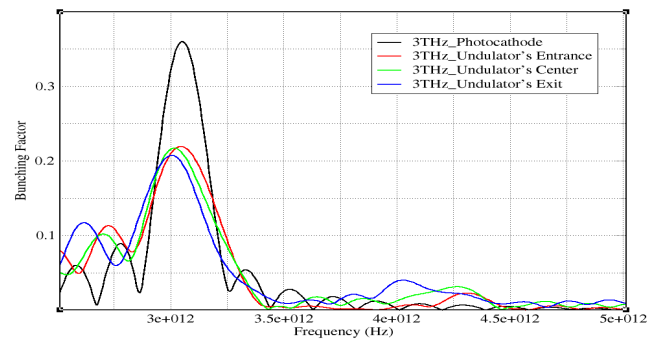


Figure 3: Bunching factor at different beamline positions.

SIMULATION CALCULATIONS OF TERAHERTZ RADIATION

The simulated electron bunch structure at the undulator entrance obtained from GPT code was used to simulate the radiation fields. An in-house code based on C++ was developed to perform the radiation simulation. In this code, the radiation fields are simulated by solving the Lienard-Wiechert fields for a point particle, given by the following equations [7]:

$$E(r, t) = \frac{q}{(4\pi\epsilon_0)} \left(\frac{n - \beta}{\gamma^2(1 - n \cdot \beta)^3 |\mathbf{r} - \mathbf{r}_s|^2} + \frac{n \times ((n - \beta) \times \dot{\beta})}{c(1 - n \cdot \beta)^3 |\mathbf{r} - \mathbf{r}_s|} \right)_{t_r}$$

$$B(r, t) = \frac{n(t_r)}{c} \times E(r, t),$$

where n , β , $\dot{\beta}$, $\mathbf{r} - \mathbf{r}_s$, are the unit vector pointing from source of radiation to the observation point, velocity of the particle, acceleration of the particle and the distance of the observation point from the source of radiation respectively. In the code, the particles are loaded and tracked through the undulator's field using Vay Algorithm [8]. The entire history of the trajectory and information like velocity, momentum, acceleration and position of the particles are recorded. In order to calculate the fields, firstly the retarded time at which the radiation was emitted is calculated and then the relative distance (between source of radiation and observation point), velocity and acceleration of the particle are evaluated at that retarded time. In present simulations, the interaction between the electrons and the electron-radiation have been ignored.

Table 2: Undulator Parameters Used for THz Calculations

undulator		freq. (THz)	e-energy (MeV)	K	Bu (T)
length (m)	period (mm)	0.15	4	2.802	0.69
1.5	50	3	8	0.467	0.1

The radiation wave train was calculated for on-axis distance of 3.5 m from the exit of the undulator (Table 2) and the growth of the radiation emitted from the 16 microbunches is shown in Figure 4. The scope of the paper limits the discussion to 3 THz only. As explained earlier, the linear growth in the field amplitude is because of the in-phase addition of the radiation wave packets from different microbunches. The growth in the first few period is slow because the first few microbunches in the microbunch structure (see Figure 2) is “washed out”; resulting in incoherent emission from these bunches. Figure 5 shows the spectrum obtained after doing a Fast Fourier Transform of the field obtained in Figure 4 with a sharp peak at 3 THz.

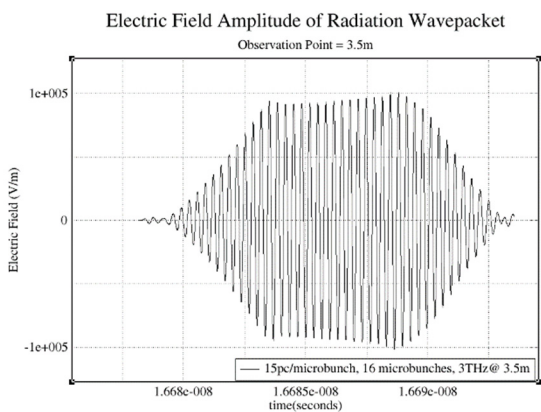


Figure 4: Electric field variation in a radiation wave packet observed on axis at 3.5 m from undulator's exit.

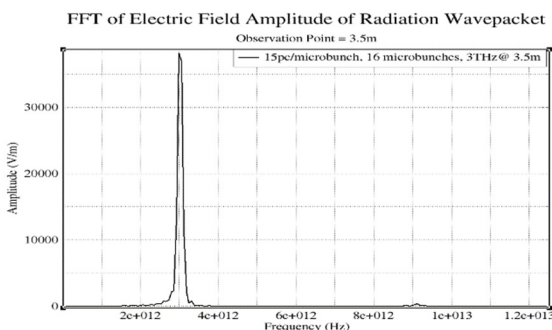


Figure 5: Spectrum of the radiation wave train emitted by 16 microbunches.

An important point to consider for DLS system is the transverse radiation beam profile. The radiation beam profile for 3 THz was evaluated at 0.5 m away from the undulator's exit, a transition point between the smaller size of beam pipe to a larger size where the radiation propagation can be treated as a free space propagation. The beam pipe to be installed inside the undulator will be 40 mm(x) × 20 mm(y). In order to cover the entire frequency range, the minimum gap required between the two jaws of undulator is 20 mm; which limits the maximum size of rectangular beam pipe in y-dimension. However, Figure 6 (left) suggests that the beam size will be comparable to the beam-pipe dimensions. Therefore, it is expected that the radiation envelope will undergo multiple reflections on the walls of

the beam pipe. This effect was simulated and it was observed that due to the reflections from the wall, the radiation envelope at the exit of undulator's beam pipe will be somewhat “squeezed” in the y-dimension (see Figure 6-right). Radiation beam profile obtained on the 30 mm × 30 mm grid was used to first find the Poynting vector and then integrated with respect to time and area to find the total pulse energy. The calculation shows that the total energy contributed from 16 microbunch train at 0.5 m from the undulator's exit is 12 micro-joules for 3 THz.

CONCLUSION

In the paper, the feasibility study of generating pre-bunched e-beam by manipulating the laser pulses incident on the photocathode is reported. For the case of 3THz, the simulation calculation shows that a bunching factor of the 16 microbunch train can be maintained to a value of ~ 0.2 from the entrance to the exit of the undulator. The output radiation waveform for 3THz shows that the radiation wave packet emitted from trailing microbunches interfere constructively with the radiation wave packets emitted by leading microbunches and the radiation field grows linearly (Figure 4). The study of the transverse beam profile and the effect of beam-pipe inside the undulator on the beam profile suggests that there will be some distortion due to the beam pipe. It is expected that this effect will be dominant for longer wavelength.

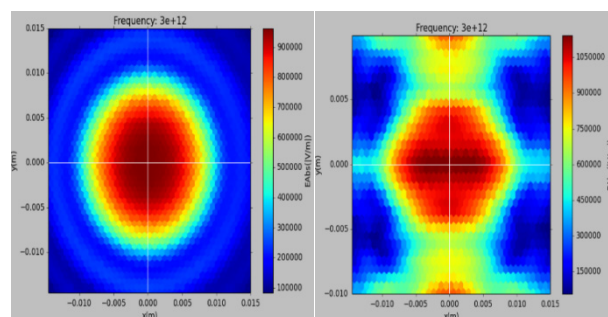


Figure 6: 3 THz: Transverse beam profile (left) and effect of beam pipe on the beam profile (right).

REFERENCES

- [1] S. Ghosh *et al.*, *Nuclear Instruments and Methods in Physics Research B*, vol. 402, p. 358-363.
- [2] S. Ghosh *et al.*, in *Proc. of FEL'14*, Basel, Switzerland, p. 596.
- [3] S. Ghosh *et al.*, in *Proc. of IPAC'16*, Busan, Korea, p. 748.
- [4] General Particle Tracker, www.pu1sar.n1/gpt/index.html
- [5] A. Gover, *Physical Review Special Topics-Accelerators and Beams* 8, 030701 (2005).
- [6] P. Schmuser, M. Dohlus, J. Rossbach, *Ultraviolet and Soft X-ray Free-Electron Lasers*, STMP 229, Springer, Berlin Heidelberg (2008).
- [7] J. D. Jackson, *Classical Electrodynamics*, Wiley, New York, NY, 3rd ed. edition, (1999).
- [8] J.-L. Vay, *Physics of Plasma* 15, 056701 (2008).

A COMPACT THz FEL AT KAERI: THE PROJECT AND THE STATUS

S. Miginsky^{†1}, S. Bae, B. Gudkov, K. H. Jang, Y. U. Jeong, K. Lee, J. Mun, S. Saitiniyazi,
 Korea Atomic Energy Research Institute, Daejeon, Korea
 S. H. Park, Korea University Sejong Campus, Sejong, Korea
¹also at Budker Institute of Nuclear Physics, Novosibirsk, Russia

Abstract

A new compact THz free electron laser driven by a microtron is being developed recently at KAERI. It uses a hybrid electromagnetic undulator. A novel scheme of injection/extraction/outcoupling is developed. The machine is partially assembled and commissioned. Characteristic features and current state are described in the paper.

INTRODUCTION

About twenty years ago the first compact THz FEL at KAERI has been commissioned [1]. Since then a huge number of experiments using this FEL have been conducted [2, 3]. In addition, its parameters have been improved during this intensive operation. A number of user stations have been built at this machine. It operates now, but its resource is almost consumed and operation is not so stable. In this regard, a development of a new machine seems to be a good idea. Finally, technological progress over these years is significant, so a new FEL could provide much better characteristics. Thus, it was decided to develop a new FEL several years ago.

PROJECT

The basic scheme of the new FEL has been chosen similar to that of the previous one. It consists of a microtron, a beamline, and a FEL structure, as shown in Fig. 1.

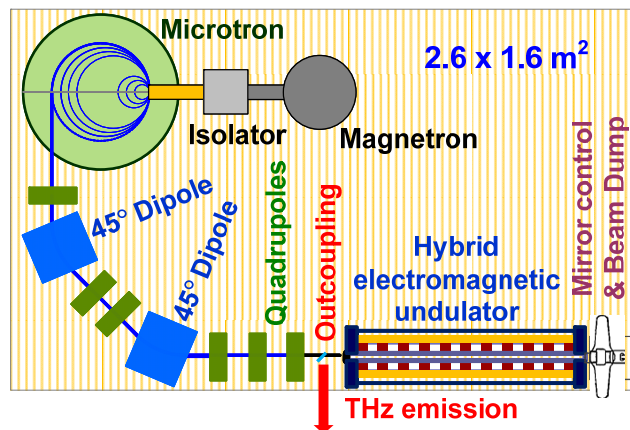


Figure 1: Schematic top view of the FEL.

The A microtron is an RF resonance electron accelerator with constant frequency and leading magnetic field, and variable harmonics number [4]. RF power is supplied by a magnetron in our case. A modulator for it is based on

storage capacities, solid state switches, and a high-voltage transformer. This combination seems to be the cheapest source of a comparably high quality electron beam of the energy of several MeV. Its basic parameters in our case are as follows:

- Electron kinetic energy 4.9 MeV
- Macropulse current 40 mA
- Macropulse duration 5 μ s
- Repetition rate up to 100 Hz
- Typical emittance x: 2 mm·mrad
y: 0.1 mm·mrad
- Typical energy spread $4 \cdot 10^{-3}$

The electron beam comes further through a beamline to the FEL structure. The beamline is used for matching the beam parameters to the optimal ones for the undulator. The matter is that the beam dispersion function and its derivative are not zero at the microtron exit while both should be zero in the undulator. Also, vertical and horizontal α - and β -functions are also far enough from the optimal ones in the undulator. Thus, one should match 6 parameters, so we used the very minimum number of quadrupoles. Two dipoles (but not one) were used to make the beamline more compact and avoid too big bending angles. This beamline provides the optimal beam parameters in the undulator at all expected entrance ones and the whole range of the undulator strengths.

A hybrid electromagnetic scheme has been selected for the undulator. This device contains magnetically soft poles and both permanent magnets and coils with electric current. Its design is similar to that of the existing machine. The strength is controlled by current in the coils. The main advantage of this design over the conventional hybrid one (without coils) is absence of moving parts. It means absence of heavy loaded precision mechanics (~ 1 ton) and permits to fasten a waveguide of an optical resonator precisely and reliably. In addition, compensation of the 1st and 2nd integrals of magnetic field at the entrance seems to be much easier in the chosen design.

There is no horizontal focusing in a perfectly planar undulator. In this case, it is impossible to conduct an electron beam through a narrow waveguide. To compensate for this, the poles were appropriately shaped to provide significant focusing. The two utmost poles were reshaped to compensate the integrals. The basic parameters of the undulator are as follows:

[†] email address Miginsky@gmail.com

- Geometry planar
- Length 1 m
- Period 25 mm
- Clearance 5.5 mm
- K 1.77...2.66
- Horizontal focusing 38...44 m⁻²

The latter parameter belongs to the beam energy.

The peak current of the beam in our case is comparably small and the wavelength is long enough, so it is a problem to get lasing in free space. The reason is that the transverse size of the fundamental mode of an open resonator is too big, so an undulator of a reasonable period and a huge clearance is too weak and the beam-to-wave interaction is insufficient. So we chose a waveguide scheme for our FEL to reduce the mode size. The main problem in this case is wave attenuation. A lenticular shape and dielectric coating are used to solve it, as shown in Fig. 2. Some details are in [5]. In this case the power attenuation coefficient decreases by 10–17 times compared to a rectangular waveguide of similar sizes. Also the effective mode area decreases twice, so the total efficiency increases by 20–34 times. We expect the power attenuation coefficient $\alpha = 0.01...0.02 \text{ m}^{-1}$ at $\lambda = 0.4...0.6 \text{ mm}$ and the effective mode area $\approx 6 \text{ mm}^2$, so the estimated gain $K_p - 1 \approx 2.9...4.1$. This waveguide is also much more effective than a parallel-plate one, as in the previous machine.



Figure 2: Cross-section of FEL waveguide.

Injection of an electron beam into and extraction from a waveguide, and emission outcoupling are interrelated and sophisticated problems. We consider combining a blind mirror of the optical resonator and a beam dump, so the extraction is not necessary. Injection and outcoupling are implemented through a mesh mirror. Another tilted mirror with a hole is necessary to separate an electron beam and THz emission, like in Fig. 3. This is possible as the THz emission divergence is significantly bigger than one of the electron beam. A mesh mirror is thin enough and does not disturb a beam significantly. For first experiments we need a mesh of 10...15% transparency in THz to ease lasing, and we should optimize it further for better efficiency.

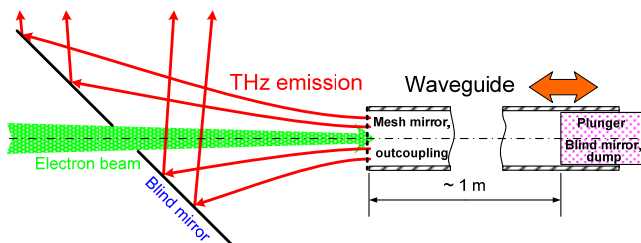


Figure 3: Outcoupling scheme.

We expect the following basic parameters of the FEL:

- Wavelength tuning range 0.4...0.6 mm
- Spectral width 1%
- Peak power 5 kW
- Macropulse average power 600 W
- Macropulse duration & repetition rate as for microtron

STATUS

At present time, the scheme and the composition of equipment for the FEL are determined. Each part has been simulated and optimized. Thus, both the conceptual and technical designs are ready. The microtron has been commissioned, and is being optimized now. Some typical signals during commissioning are presented in Fig. 4. The undulator has been manufactured and is being assembled. All the magnets for the beamline has been manufactured and tested. The following parts are to be mechanically designed and manufactured: the optical resonator, a vacuum chamber for the beamline, and supports. After that the whole machine can be assembled and commissioned.

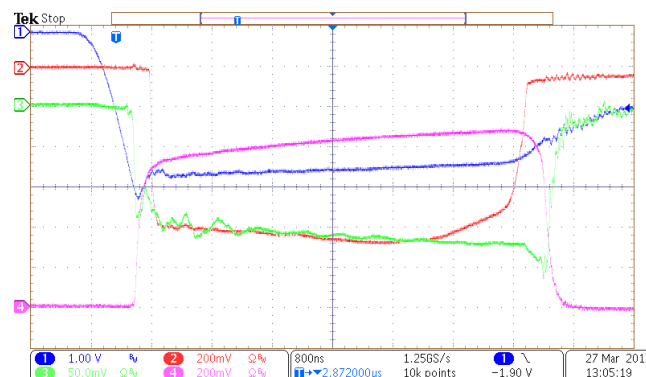


Figure 4: Microtron commissioning: (1) Modulator voltage ($/1.22 \cdot 10^4$), (2) target current (25 Ω), (3) reflected RF power, (4) emission current (0.808 Ω).

REFERENCES

- [1] Y. U. Jeong *et al.*, "First lasing of the KAERI compact far-infrared free-electron laser driven by a magnetron-based microtron", *Nucl. Instr. and Meth.*, vol. 475, pp. 47-50, Dec. 2001.
- [2] Y. U. Jeong *et al.*, "Application of a wide-band compact FEL on THz imaging", *Nucl. Instr. and Meth.*, vol. 543, pp. 90-95, May 2005.
- [3] Y. U. Jeong *et al.*, "Demonstration of a wide-band compact free electron laser to the THz imaging of bio samples", *Nucl. Instr. and Meth.*, vol. 575, pp. 58-62, May 2007.
- [4] S. P. Kapitza and V. N. Melekhin, *The Microtron*, London, UK: Harwood Academic Publishers Ltd., 1978.
- [5] S. Miginsky *et al.*, "HE₁₁ mode in a waveguide THz FEL", *Bulletin of the Russian Academy of Sciences. Physics.*, vol. 79, no. 1, pp. 31-35, Jan. 2015.

DEVELOPMENT OF COMPACT THz COHERENT UNDULATOR RADIATION SOURCE AT KYOTO UNIVERSITY*

Siriwan Krainara[†], Heishun Zen, Toshiteru Kii, Hideaki Ohgaki, Institute of Advanced Energy, Kyoto University, Gokasho, Uji, Kyoto 611-0011, Japan

Sikharin Suphakul, Department of Physics and Materials Science, Faculty of Science, Chiang Mai University, Chiang Mai 50200, Thailand

Abstract

A new THz Coherent Undulator Radiation (THz-CUR) source has been developed to generate intense quasi-monochromatic THz radiation at the Institute of Advanced Energy, Kyoto University. The system consists of a photocathode RF gun, bunch compression chicane, quadrupole magnets, and short planar undulator. The total length of this system is around 5 meters. At present, this compact accelerator has successfully started giving the THz-CUR in the frequency range of 0.16 - 0.65 THz. To investigate the performance of the source, the relationship between the total radiation energy, peak power and power spectrum as a function of bunch charge at the different undulator gaps were measured. The results are reported in the paper.

INTRODUCTION

At present, there are several THz sources such as quantum cascade lasers, solid state oscillators, optically pumped solid state or gas devices, electron tubes and accelerator based sources. They have been developed as the useful tools in many scientific fields [1]. At the Institute of Advanced Energy, Kyoto University, a THz Coherent Undulator Radiation (THz-CUR) source (Fig. 1), which consists of a photocathode RF gun, bunch compression chicane, quadrupole magnets, and short planar undulator, has been developed [2]. It is expected to generate a quasi-monochromatic THz beam with high peak power. This project has been started since 2008 and the construction was started in end of 2013. The 1.6-cell S-band BNL-type photocathode RF-gun designed and manufactured by KEK has been installed in 2014. The electron beam was firstly generated in 2015 with the electron beam energy of 4.6 MeV with the energy spread of 1.3% [3]. And the RMS normalized transverse emittance with the bunch charge of 50 pC was reported to be 6 and 8 mm-mrad for horizontal and vertical axis, respectively [4]. The first THz-CUR in this source was observed in August 2016.

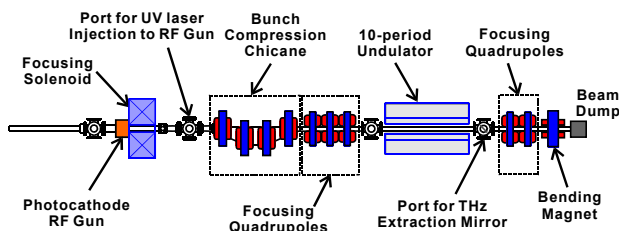


Figure 1: Layout of THz-CUR source at Kyoto University.

To investigate the performance of the THz-CUR source, the measurements of total radiation energy, the radiated peak power, and power spectrum were conducted as functions of bunch charge and the undulator gap. The results are presented and discussed.

THz-CUR PROPERTIES

The coherent undulator radiation (CUR) can be emitted when the electrons are propagating in undulator. The energy of CUR can be expressed in the formula [5]

$$W_{\text{coh}} = W_{1e} N_e^2 f(\omega, \sigma_z),$$

where W_{1e} is the total energy radiated by the single electron ($W_{1e} = \pi e^2 N_u K^2 \gamma^2 / 3 \epsilon_0 \lambda_u$), N_u is the number of undulator period, γ is the Lorentz factor. The undulator strength parameter K is $0.934 B_0 [T] \lambda_u [\text{cm}]$. B_0 is the magnetic field and λ_u is the period length of undulator. The bunch form factor $f(\omega)$ is defined as the square of the Fourier transform of the normalized longitudinal particle distribution. For a Gaussian bunch with the RMS width of σ_z , the form factor can be given as $f(\omega, \sigma_z) = \exp(-\omega^2 \sigma_z^2)$. The pulse energy is proportional to the square of electron number in the bunch. In order to have CUR, the longitudinal bunch length must be shorter than the radiation wavelength.

Up to now, the bunch length has not been measured, but it can be estimated by using General Particle Tracer (GPT) code [6]. The longitudinal bunch length is 1.0 ps in FWHM after compressing the electron bunch by using chicane magnets. As shown in Fig. 2, the bunch form factor gradually decreases to zero if the resonance frequency is higher than 0.8 THz and 0.5 THz for the bunch length of 1.0 ps and 1.5 ps, respectively.

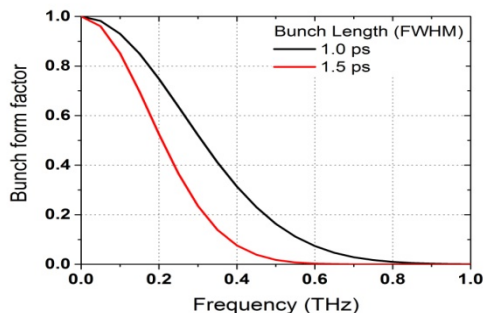


Figure 2: The bunch form factor with two bunch lengths of 1.0 and 1.5 ps in FWHM.

*This work supported by the MEXT/JSPS KAKENHI 26706026.

[†]siriwan.krainara.82r@st.kyoto-u.ac.jp

Content from this work may be used under the terms of the CC BY 3.0 licence (© 2018). Any distribution of this work must maintain attribution to the author(s), title of the work, publisher, and DOI.

MACHINE OPERATION FOR MEASUREMENTS

As shown in Fig. 1, the system starts from the photocathode RF-gun. The photocathode is driven by a 266-nm UV laser [7]. The photocathode drive laser and electron beam parameters used in this measurement are listed in Table 1. The solenoid field was adjusted from 0.14 to 0.16 Tesla for focusing the beam. To optimize the bunch compression condition, the values of the first order momentum compaction factor (R_{56}) of chicane magnet were varied in between -44 to -48 mm. The injection phase of photocathode drive laser should be adjusted nearly 20 degrees to have suitable longitudinal phase-space for the bunch compression by the chicane. At each measurement condition, the electron beam optics and positions were optimized to have the maximum intensity of THz beam and bunch charge at the beam dump.

Table 1: Electron-Beam Parameters Used in the Measurement

Laser pulse duration:	6	ps
Laser pulse energy:	< 200	uJ
Number of laser pulse:	1- 4	pulses
Bunch charge:	< 200	pC
Beam energy:	4.6	MeV
Energy spread:	1.3	%

The undulator installed in this source is a planar Halbach type one. The gap can be manually adjusted between 30 mm to 90 mm. The period length and number of period of the undulator are 0.07 meters and 10, respectively. The peak magnetic field and undulator strength parameter as a function of undulator gap are plotted in Fig. 3.

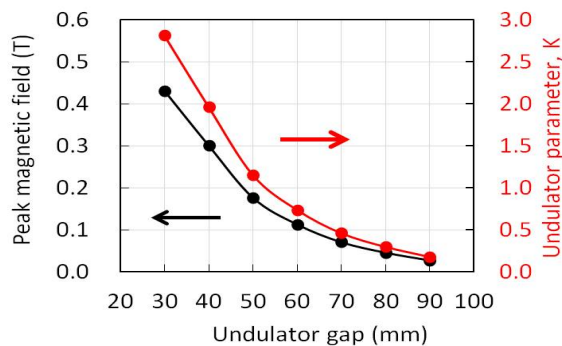


Figure 3: The peak magnetic field and undulator parameter K .

EXPERIMENTAL SETUP

When the short electron bunch passes through the undulator, the CUR radiation was generated. Just after the undulator, THz radiation was reflected by titanium foil with 50- μm thickness inside the vacuum chamber and traveled through a fused silica window with the transmission of 75%. Then, it went to the experimental setup [8].

Total radiation intensity: The layout is presented in Fig. 4. We used two parabolic mirrors for focusing THz beam. Two pyroelectric detectors were used for this measurement; one was a calibrated thin-film pyroelectric detector (THz10 and VPA amplifier module, Sensor und Lasertechnik) and the other is a highly sensitive pyroelectric detector (PYD-1, PHLUXi). The THz10 detector, whose detector size is 10 mm and sensitivity is 7.95 MV/J, was used for absolute intensity measurement. The PYD-1 detector, whose detector size is 1 mm, is used for spatial distribution measurement.

Power Spectrum: The Michelson interferometer shown in Fig. 4 was used to measure the power spectrum. A parabolic mirror with the focus length of 50 mm was placed 50-mm downstream of the focusing point instead of the THz10 detector used for total radiation intensity measurement. The transported beam was separated into two beams by a beam splitter. The reflected beam was injected to fixed mirror and returned. The transmitted beam was injected to a movable mirror and reflected back. Both beams were combined and focused on the PYD-1 detector by a parabolic mirror.

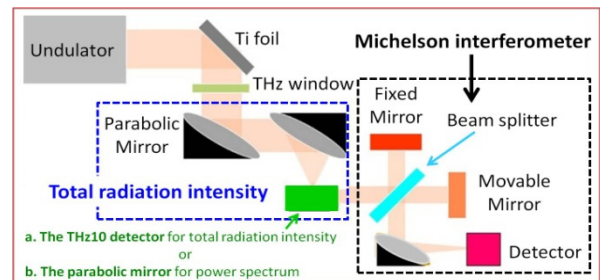


Figure 4: Experimental setup for measuring the total radiation energy and power spectrum.

RESULTS AND DISCUSSION

Total radiation energy

Firstly, the spatial distribution of THz beam with the undulator gap of 30 mm was measured by the PYD-1 detector to find the focusing point and to know the size of the radiation. The measured distribution at the focus point is shown in Fig. 5. The overlap factor between the THz10 detector and the THz beam can be determined by the ratio of integration of the measured distribution inside the 10 mm aperture and whole measured area.

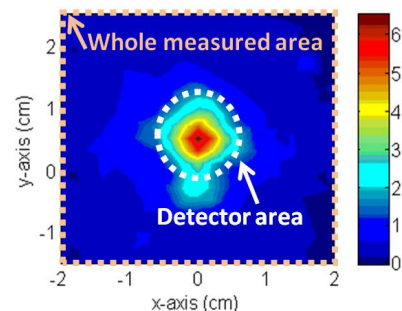


Figure 5: Spatial distribution (whole radiation area is in the orange box while the detector area is in white circle).

Content from this work may be used under the terms of the CC BY 3.0 licence (© 2018). Any distribution of this work must maintain attribution to the author(s), title of the work, publisher, and DOI.

The integration of the detector signal inside in the 10 mm aperture was $0.9548 \text{ V}\cdot\text{cm}^2$ while that of the whole measured area was $1.9564 \text{ V}\cdot\text{cm}^2$. Therefore, the overlap factor estimated from this result is 0.485. It means that around half of the total radiation would be measured by the calibrated detector.

Next, at the focus point and undulator gap of 30 mm condition, the dependence of the total radiation energy on the bunch charge was measured with the THz10 detector. The results are presented in Fig. 6. The curve of micro-pulse energy with the bunch charge seems to have the quadratic function prior to the saturation. The saturation was obvious when the bunch charge got higher than 80 pC. At the bunch charge condition of 160 pC, the total radiation energy was around 1300 nJ. Accordingly, the radiated peak power was evaluated to be higher than 20 kW with the assumption of 10-cycle pulse duration and 0.16-THz radiation frequency. The expected peak power obtained by theoretical calculated is approximately $\sim 5 \text{ MW}$ which is estimated from the proportion of the total radiated energy and radiation pulse width. It can be defined by $W_{\text{coh}}/(N_u \lambda_r/c)$, where λ_r is radiation wavelength $\lambda_u(1+K^2/2)/2\gamma^2$ and c is the speed of light. The experimentally determined peak power is much lower than the calculated value.

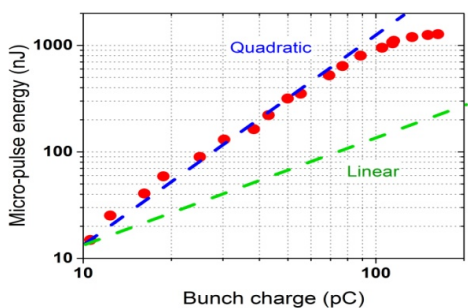


Figure 6: The total radiation energy as a function of the bunch charge at the undulator gap of 30 mm.

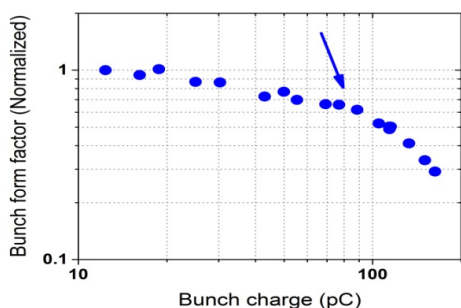


Figure 7: The normalized bunch form factor estimated from the measured total radiation energy and square of bunch charge.

From the measured result of total radiation energy, we estimated the change of the bunch form factor. Normally, the bunch form factor is proportional to the total radiation energy divided by the square of the bunch charge, $f(\omega, \sigma_z) \propto W_{\text{coh}}/Q^2$, where Q is the bunch charge. Figure 7 presents the decreasing in the normalized value of bunch form factor with the increasing of bunch charge. It is shown that the value of bunch form factor reduces promptly when

the bunch charge is raised up more than 80 pC. The result can lead to bunch lengthening, due to the effect of the electron space charge.

Power Spectrum

The intensity signals as a function of the path difference of two beams in the interferometer (so called interferogram) were measured. Then the power spectra of the radiation were obtained by Fast Fourier Transform (FFT) of the interferograms. The power spectrum measurements were performed at the undulator gap conditions of 30, 40, 50 and 60 mm with two different bunch charges of 160 and 60 pC. The measured results are shown in Fig. 8. It is worth noting that the THz-CUR can be generated in the range of frequency from 0.16 – 0.65 THz with the 60-pC bunch charge by changing the gaps of undulator. While with the bunch charge of 160 pC, the frequency of 0.65 THz cannot be generated.

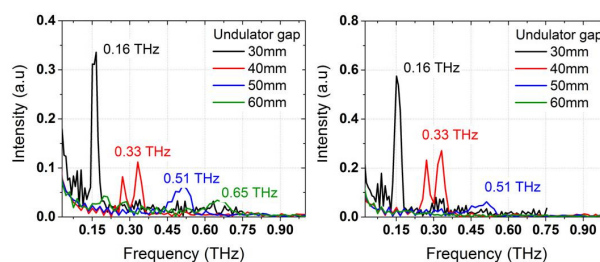


Figure 8: Power spectrum as a function of undulator gap with the bunch charges of 60 (left) and 160 pC (right).

CONCLUSION

A THz-CUR source based on photocathode RF gun has been developed at the Institute of Advanced Energy, Kyoto University. Some commissioning experiments to check the performances of the THz-CUR source have been performed. As the results show, the saturation of total radiation energy has been observed when the bunch charge was higher than 80 pC, because of the bunch lengthening. It can be confirmed that our THz-CUR source can generate the THz radiation with the total radiated energy and the radiated peak power of about 1300 nJ and higher than 20 kW, respectively at the resonance frequency of 0.16 THz and the bunch charge of 160 pC. Moreover, the source can cover the frequency range from 0.16 - 0.65 THz when the bunch charge was 60 pC. Due to the space charge effect, the frequency of 0.65 THz cannot be generated when the bunch charge was 160 pC. The performance of the source could be improved by mitigating the space charge effect.

REFERENCES

- [1] T. Ping *et al.*, “Terahertz radiation sources based on free electron lasers and their applications”, *Sci China Inf Sci* 55, Issue 1 (2012).
- [2] S. Suphakul *et al.*, “Development of compact TH-FEL system at Kyoto University”, in *Proc. FEL'14*, paper TUP057 (2014).
- [3] S. Suphakul *et al.* “Generation of short bunch electron beam from compact accelerator for terahertz radiation”, in *Proc. IPAC'16*, paper TUPOW008 (2016).

Content from this work may be used under the terms of the CC BY 3.0 licence (© 2018). Any distribution of this work must maintain attribution to the author(s), title of the work, publisher, and DOI.

- [4] K. Damminsek *et al.*, “Electron beam properties from a compact seeded terahertz FEL amplifier at Kyoto University”, in *Proc. FEL'15*, paper MOP025 (2015).
- [5] D. Bocek *et al.*, “Observation of coherent undulator radiation from sub-picosecond electron pulses”, AIP conference series, 367 (1996).
- [6] S.B. van der Geer *et al.*, “General Particle Tracer: A 3D code for accelerator and beam line design”, in *Proc. EPAC'96*, paper THP18F (1996).
- [7] H. Zen *et al.*, “Development of Photocathode Drive Laser system for RF Guns in KU-FEL”, in *Proc. FEL'14*, paper THP045 (2014).
- [8] S. Krainara *et al.*, “THz coherent undulator radiation generated from compact accelerator based on photocathode RF gun”, in *Proc. PASJ'17*, paper WEOM02 (2017).

Content from this work may be used under the terms of the CC BY 3.0 licence (© 2018). Any distribution of this work must maintain attribution to the author(s), title of the work, publisher, and DOI.



PRESENT STATUS OF INFRARED FEL FACILITY AT KYOTO UNIVERSITY*

H. Zen[†], J. Okumura, S. Tagiri, S. Krainara, S. Suphakul^{††}, K. Torgasin, T. Kii, K. Masuda,
and H. Ohgaki, Institute of Advanced Energy, Kyoto University, Uji, Japan

Abstract

A mid-infrared Free Electron Laser (FEL) named KU-FEL has been developed for promoting energy related research at the Institute of Advanced Energy, Kyoto University. KU-FEL can cover the wavelength range from 3.5 to 23 μm and routinely operated for internal and external user experiments. Recently a THz Coherent Undulator Radiation (CUR) source using a photocathode RF gun has been developed as an extension of the facility. As the result of commissioning experiment, it was confirmed that the CUR source could cover the frequency range from 0.16 to 0.65 THz. Present statuses of these infrared light sources are reported in this paper.

INTRODUCTION

An oscillator type Mid-Infrared Free Electron Laser (MIR-FEL) named as KU-FEL has been developed at the Institute of Advanced Energy, Kyoto University for promoting energy related research [1]. The FEL succeeded in its first lasing [2] and power saturation [3] in 2008. At that time, the tunable range of the FEL was not so wide (only 10 to 14 μm) because of the limited gain of the FEL and macro-pulse duration of the electron beam. In order to extend tunable range, the optical cavity mirrors and the undulator have been replaced in January 2012. Then the tunable range of KU-FEL has been extended to 5 – 15 μm [4]. The narrowest undulator gap has been reduced from 20 to 15 mm by replacing the vacuum duct of undulator section in 2013. As the result of commissioning experiment, it was confirmed that KU-FEL could cover the wavelength range from 5 to 21.5 μm [5]. After the replacement of the vacuum duct of the undulator, some efforts to optimize the operation parameter of KU-FEL have been made and now the tunable range was extended 3.5 – 23 μm .

Now, KU-FEL is routinely operated for internal and external user experiments. The layout of KU-FEL facility is shown in Fig. 1. There are three user stations available. The user station #1 is the FEL beam diagnostics and simple irradiation station. In this station, an MIR-monochromator, MIR-detectors, pyroelectric energy meters and some focusing optics are available. The user station #2 is the pump-probe experiment station. In the pump-probe station, ns-Nd:YAG laser (1064, 532 and 266 nm), ps-Nd:YVO₄ laser (1064 and 532 nm), and a closed-cycle cryostat with optical windows are available. Users

can perform the pump-probe experiment of solid samples with the lowest sample temperature of 12 K with various combinations of MIR-FEL and those solid state lasers. At this station, MIR induced mode-selective phonon excitation experiments of solid samples have been performed [6-8]. The station #3 is intended for multi-purpose application. There is an optical table and users can construct their experimental setup on the table.

In order to satisfy the user who wants to perform some nonlinear spectroscopy in MIR region, the photocathode operation of the KU-FEL has been demonstrated [9]. It was confirmed that the peak power of the FEL can be significantly increased by the photocathode operation with a significant reduction of the average power.

Recently, a THz Coherent Undulator Radiation (THz-CUR) source using a photocathode RF gun has been developed as an extension of the facility [10]. When the electron bunch length is shorter than the radiation wavelength, the radiations from each electron are coherently superposed. In the condition, the radiation intensity can be intense and the radiation has good longitudinal coherence. This radiation is called as “coherent” radiation. In the case of undulator radiation, it is called as CUR. In the THz region, some CUR sources have been developed so far [11-13]. Our THz-CUR source consists of a 1.6-cell photocathode RF gun, a bunch compression chicane, and 0.7-m Halbach type undulator. The total length of the machine is about 5 m. The THz-CUR source shares a photocathode driving laser system [14] and an RF source with a 4.5-cell RF gun of KU-FEL. The construction and commissioning of THz-CUR source were finished in August 2016. The layout of THz-CUR source is also shown in Fig. 1.

MIR-FEL

The oscillator type MIR-FEL named as KU-FEL consists of a 4.5-cell thermionic RF gun with a LaB₆ thermionic cathode which generates multi-bunch electron beams with the energy of 8.4 MeV, a dog-leg energy filtering section, a 3-m traveling-wave type accelerating structure, a bunch compressing 180-deg. arc section, a 1.8-m hybrid undulator, and a 5-m optical cavity. The typical characteristics of KU-FEL under the thermionic cathode operation are listed in Table 1. The available macro-pulse energies of KU-FEL measured at the user station #1 are shown in Fig. 2.

The shortest wavelength of KU-FEL (3.5 μm) is limited by the maximum available electron beam energy and the undulator period length which are 40 MeV and 33 mm, respectively. We can generate FEL with bit shorter wavelength by increasing available electron beam energy of the facility. The reason why the longest wavelength is

* This work was partially supported by the MEXT/JSPS KAKENHI Grant Number 26706026

[†] e-mail address zen@iae.kyoto-u.ac.jp

^{††} present affiliation Department of Physics and Materials Science, Faculty of Science, Chiang Mai University, Chiang Mai, Thailand

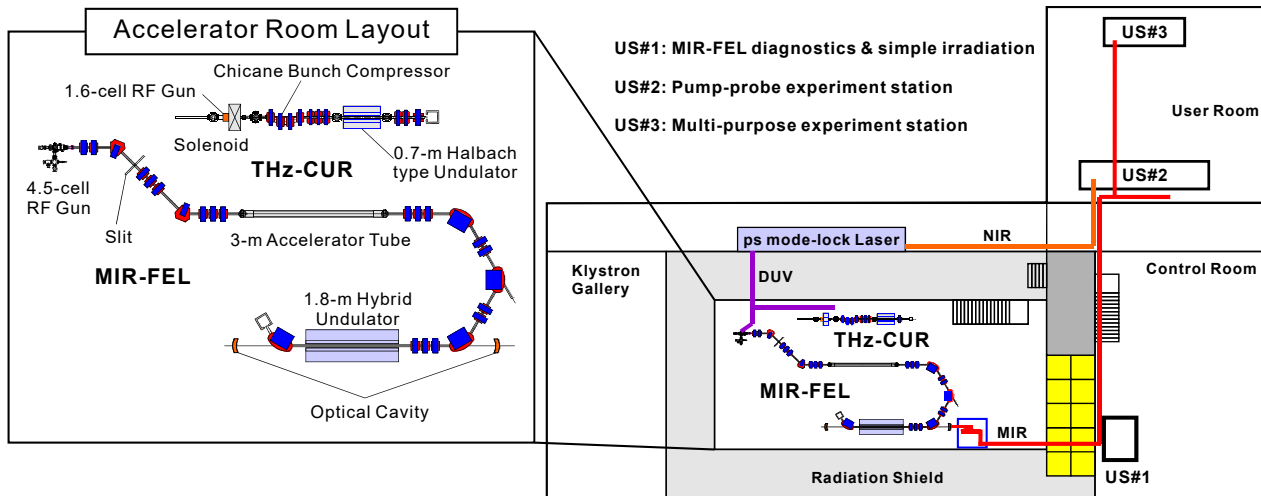


Figure 1: Layout of the infrared FEL facility in August 2017.

limited to 23 μm is not well understood. The resonant wavelength of the undulator and KU-FEL can be longer when the electron beam energy is reduced. We have tried several times to achieve FEL lasing at the wavelength of 24 μm by reducing the electron beam energy. However, we could not observe FEL lasing at this wavelength. For further investigation of the reason, a fast pyroelectric detector (ELTEC, Model 420) was introduced for measuring the round-trip loss of the optical cavity. The measured temporal evolution of FEL macro-pulse at the wavelength of 19.5 and 23 μm are shown in Fig. 3. The decaying slopes of the measured waveforms were analyzed and the optical cavity losses were determined as 6% and 8% for 19.5 and 23 μm , respectively. As one can see in the figure, the waveform of 23- μm condition has faster-rising slope than that of 19.5- μm . It implies that the FEL gain of 23- μm condition was higher than that of 19.5- μm condition. The round-trip loss of the optical cavity tends to increase as the wavelength of the FEL gets longer. However, this slow increase of the round-trip loss of the optical cavity seems to be not the critical factor which limits the tunable range of KU-FEL.

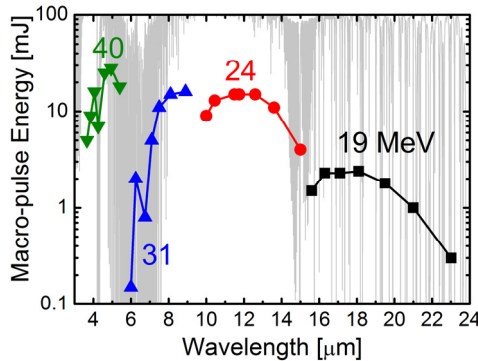


Figure 2: The available macro-pulse energy of KU-FEL at the user station #1.

In other facilities, it was reported that the FELs with an optical cavity having partial waveguide have specific wavelength where the phase difference of two transverse optical modes is π and the FEL lasing gets difficult [16]. The shortest specific wavelength λ_0 can be given by:

$$\lambda_0 = \frac{b^2}{2L}, \quad (1)$$

where b and L denote the height and longitudinal length of vacuum duct inserted in the undulator, respectively. At KU-FEL, the height b is 11 mm and length L is 2 m. Then using Eq. (1), the specific wavelength is 30.25 μm . The specific wavelength calculated was not so different from the longest wavelength limit of KU-FEL. This might be the reason why the KU-FEL cannot achieve lasing at 24 μm . Some efforts to understand the reason for the longest wavelength limit are being undertaken.

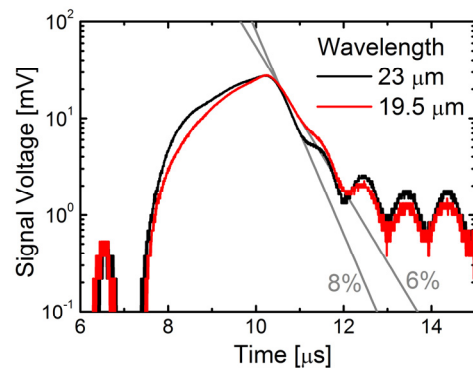


Figure 3: Temporal evolution of FEL macro-pulse at the wavelength of 19.5 and 23 μm .

Photocathode operation

A LaB₆ single crystal is used as the thermionic cathode installed in the 4.5-cell RF gun. The cathode can also be used as a photocathode. A multi-bunch ps-DUV laser system [14] has been developed for the photocathode operation of the 4.5-cell RF gun and KU-FEL. In 2015,

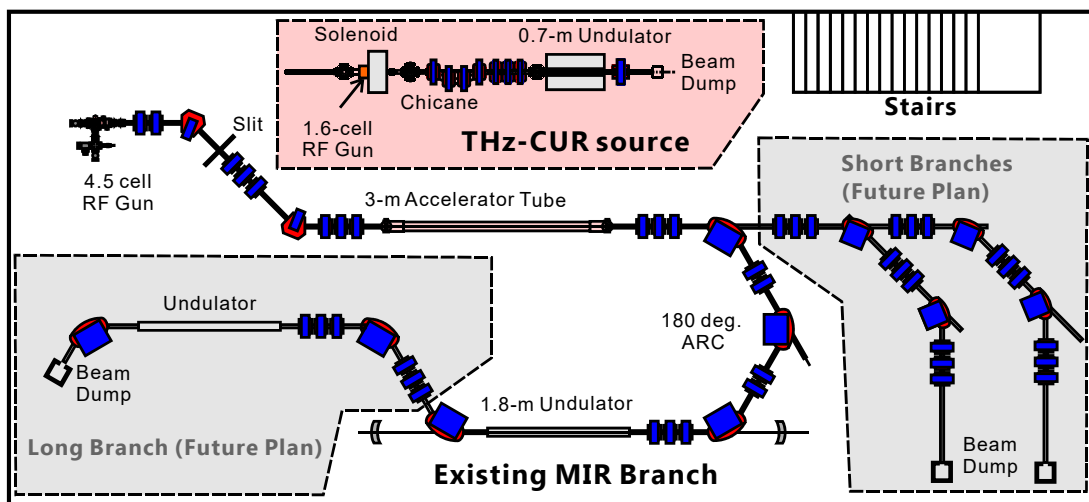


Figure 4: Possible arrangement of new beamlines in the infrared FEL facility at the Institute of Advanced Energy, Kyoto University.

we conducted some commissioning experiments and achieved the photocathode operation of KU-FEL [9].

Under the photocathode operation condition, the bunch charge was approximately 150 pC, which was three times as high as that of thermionic operation. Then the micro-pulse energy was increased from 2 to 13 μ J at the FEL wavelength of 11.7 μ m. At that time, the macro-pulse energy of KU-FEL with photocathode operation was around 0.8 mJ, which is much smaller than that of thermionic operation (13 mJ). It is because of the difference

of micro-pulse repetition rate; 29.75 MHz for photocathode operation and 2856 MHz for thermionic operation. The photocathode operation can realize the condition of FEL with low average power and high peak power. This condition is good for nonlinear optical experiments where the peak fluence of the laser beam is important.

THz-CUR SOURCE

Since a more detailed report will be available in these proceedings [17], here we only show some brief results obtained by the commissioning experiments of THz-CUR source. As the result of the commissioning experiments, it was confirmed that the THz-CUR source could cover the frequency range from 0.16 to 0.65 THz by using short bunch electron beam with the energy of 4.6 MeV. The peak power of the THz-CUR source was measured to be higher than 20 kW. The THz-CUR intensity dependencies on the electron bunch charge were measured at various undulator gap conditions. As a result, saturation of THz-CUR intensity was observed. The saturation could be caused by the bunch lengthening and emittance degradation due to strong space charge effect. For real user experiments, a THz transport line should be constructed.

FUTURE PERSPECTIVE

The MIR-FEL can now cover the wider range than its initial target wavelength range (5–20 μ m). Although there

are some remained study subjects such as the limitation of the longest wavelength, introduction of photocathode operation to user experiments, and further optimization of the operation conditions, it is reasonable to mention the future upgrade of the facility. The possible arrangement of additional beamlines is shown in Figure 4. A similar configuration has been reported in the previous report [18] but some descriptions are updated. As shown in the figure, there is some space to install a long branch and two short branches. An undulator can be installed in the long branch. The target wavelength could be THz region. There are two possible schemes to generate monochromatic THz beam; one is the CUR and the other is the oscillator FEL. The CUR does not require optical cavity and is much simpler in operation and realization than the oscillator FEL. So, we may start from CUR. One of the short branches can be used for coherent THz generation using various schemes such as coherent transition radiation [19, 20], Vavilov-Cherenkov radiation from a grating pair [21], and resonant coherent diffraction radiation [22]. The other short branch can be used for electron beam irradiation and other interesting applications.

REFERENCES

- [1] T. Yamazaki *et al.*, *Proc. of 23rd Int. Free Electron Laser Conference*, pp.II-13-14 (2002).
- [2] H. Ohgaki *et al.*, *Jpn. J. Appl. Phys.* 47, pp.8091-8094 (2008).
- [3] H. Ohgaki *et al.*, *Proc. of FEL2008*, pp.4-7 (2008).
- [4] H. Zen *et al.*, *Proc. of FEL2012*, pp.449-452 (2013).
- [5] H. Zen *et al.*, *Proc of FEL2013*, pp.711-714 (2013).
- [6] K. Yoshida *et al.*, *Appl. Phys. Lett.* 103, pp. 182103 (2013).
- [7] M. Kagaya *et al.*, *Jpn. J. Appl. Phys.*, 56, pp. 022701 (2017).
- [8] T. Katsurayama *et al.*, *Proc. of IRMMW-THz 2016* (2016) DOI: 10.1109/IRMMW-THz.2016.7758848.
- [9] H. Zen *et al.*, *Proc. of IPAC2016*, pp.754-756 (2016).
- [10] S. Sikhari *et al.*, *Proc. of IPAC2016*, pp.1757-1759 (2016).
- [11] B. Green *et al.*, *Scientific Reports*, 6, pp. 22256 (2016).
- [12] A. Doria *et al.*, *Phys. Rev. Lett.* 93, pp. 264801 (2004).
- [13] X. Wen *et al.*, *Nucl. Instrum. Meth. A*, 820, pp.75-79 (2016).

Content from this work may be used under the terms of the CC BY 3.0 licence (© 2018). Any distribution of this work must maintain attribution to the author(s), title of the work, publisher, and DOI.

- [14] H. Zen *et al.*, *Proc. of FEL2014*, pp.828-831 (2015).
[15] Y. Qin *et al.*, *Optics Letters*, 38, pp.1068-1070 (2013).
[16] R. Prazeres *et al.*, *Phys. Rev. ST Accel. Beams*, 12, pp. 010701 (2009).
[17] S. Krainara *et al.*, "" presented at FEL'17, Santa Fe, USA, 2017, paper MOP049, this conference.
[18] H. Zen *et al.*, *Physics Procedia*, 84, pp.47-53 (2016).
[19] U. Happekk *et al.*, *Phys. Rev. Lett.* 67, pp.2962-2965 (1991).
[20] Y. Shibata *et al.*, *Phys. Rev. A*, 45, R8340 (1992).
[21] V.A. Smirnov *et al.*, *Phys. Rev. ST Accel. Beams*, 18, pp. 090703 (2015).
[22] Y. Honda *et al.*, *Proc. of FEL2015*, pp.547-549 (2015).

POLISH IN-KIND CONTRIBUTION TO EUROPEAN XFEL: STATUS IN SUMMER 2017*

J. A. Lorkiewicz[#], K. Chmielewski, Z. Golebiewski, W. C. Grabowski, K. Kosinski, K. Kostrzewa,
P. Krawczyk, I. M. Kudla, P. Markowski, K. Meissner, E. Plawski, M. Sitek, J. Szewinski,
M. Wojciechowski, Z. Wojciechowski, G. Wrochna,
National Centre for Nuclear Studies (NCBJ), 05-400 Otwock-Swierk, Poland
J. Sekutowicz, Deutsches Elektronen Synchrotron (DESY), 22-607 Hamburg, Germany
M. Duda, M. Jezabek, K. Kasprzak, A. Kotarba, K. Krzysik, M. Stodulski, M. Wiencek,
J. Swierblewski,
Institute of Nuclear Physics, Polish Academy of Sciences (IFJ PAN), 31-342, Krakow, Poland
P. Grzegory, G. Michalski, Kriosystem, 54-424 Wroclaw, Poland
P. Borowiec, Jagiellonian University, 30-392 Krakow, Poland
M. Chorowski, P. Duda, J. Fydrych¹, A. Iluk, K. Malcher, J. Polinski, E. Rusinski,
Wroclaw University of Science and Technology (WUST), 50-370 Wroclaw, Poland
J. Glowinkowski, M. Winkowski, P. Wilk, Wroclaw Technology Park, 54-424 Wroclaw, Poland
¹ also at European Spallation Source, 221 00 Lund, Sweden

Abstract

In the years 2010-2017 some of the Polish research institutes - members of the European-XFEL consortium, took responsibility for production and delivery of components, test infrastructure and procedures for the superconducting (sc) linear electron accelerator (LINAC) and PLC units of slow control system for the first experimental instruments of the European XFEL at DESY (Hamburg). The paper briefly summarizes the output of these works.

INTRODUCTION

European X-ray Free Electron Laser (Eu-XFEL) is dedicated to advanced studies of the structure of matter. It is based on a linear sc electron accelerator (LINAC) constructed by DESY (Deutsches Elektronen Synchrotron) and its partners of international XFEL consortium. The LINAC in its final version is composed of 97 modules. Each module contains 8 sc, nine-cell niobium cavities based on TESLA technology, placed in a liquid helium vessel and a single magnet package with a sc, super-ferric quadrupole magnet and two dipole magnets inside it [1]. The magnet packages are placed in liquid helium bath too. Every cavity is equipped with two high order mode (HOM) couplers. Parasitic high order modes (HOMs) in RF field are excited by e⁻ beam. They have to be coupled out by coaxial HOM couplers and sent

via cables to loads outside the module [1]. In addition a single beam line absorber (BLA) is installed in interconnectors between the modules to absorb the travelling HOMs. Each cavity is equipped with a pick-up (PU) antenna – a field probe in RF control system to regulate the amplitude and phase of the accelerating field. The activities of Polish groups which contributed in-kind to the project are briefly described below.

Wroclaw University of Science and Technology (WUST) was in charge of design and Wroclaw Technology Park (WPT) with its subcontractors were responsible for manufacturing and installation of a 165 m long XATL1 cryogenic transfer line for supercritical helium transport from the HERA refrigerator at DESY to Accelerator Module Test Facility (AMTF) hall and of two vertical cryostats for low power acceptance tests of cavities.

A group of National Centre for Nuclear Research (NCBJ) was in charge of design, production, testing and delivery of 1648 HOM couplers, 824 PU antennae with output lines and 108 HOM beam-line absorbers (BLAs).

A team of Institute of Nuclear Physics (IFJ-PAN, Krakow) was responsible for preparation and performance of acceptance tests for XFEL-type cavities, complete accelerator modules, sc magnets and their current leads.

Another group of NCBJ now contributes to the production of programmable logic controller (PLC) units for slow control system of the first experimental instruments to be installed at the ends of XFEL photon lines. The status of these tasks on the eve of XFEL facility startup is presented in the following sections.

*Supported by Polish Ministry of Science and Higher Education

[#]email address: jerzy.lorkiewicz@ncbj.gov.pl

CRYOGENIC LINE AND TWO VERTICAL CRYOSTATES

A vacuum-isolated cryogenic transfer line XATL1 is composed of external vacuum envelope housing a thermal shield and four processing tubes [1]. It is destined for the transport of cooling media at two temperature levels in two different circuits: at 4.5 K (supercritical helium) and gaseous helium at 40/80 K. The latter is used to maintain a sufficiently low temperature of the shield, whereas the supercritical helium is further cooled and delivered to test stands inside the AMTF hall. WUST was also engaged in design of the two vertical test cryostats.

A vertical cryostat consists of a liquid helium vessel with an “insert” structure to install four cavities to be tested and a thermal shield surrounding it. They are placed in a vacuum tank which contains valves and tubing for cold circuits, a recuperative heat exchanger and cold terminals for transfer lines connection. 4.7 K liquid helium from a redistribution system in ASTM (subcooler) is pre-cooled in the heat exchanger to 2.2 K and further cooled down to its working temperature of 2 K inside the vessel by expansion on a Joule-Tomson (J-T) valve.

Before manufacturing all the cryogenic components were modelled to analyze thermal stresses and heat loads. In particular, a detailed analysis of design parameters of the transfer line [2], insert [3] and vertical cryostats [4] has been performed. Both, cryogenic line and the cryostats were certified by TUEV Nord company based in Germany. They were produced in the years 2010-2012 by WPT with its subcontractors: Kriosystem and KATES. The transfer line was mounted on a tube bridge (Fig.1a) and connected to the HERA cryoplant on the one end and to the subcooler on the other the cryostats were installed in the hall inside concrete radiation shields (Fig. 1b) and commissioned in 2013 (see Fig. 2). The installations have been functioning flawlessly for the next three years till the end of admission tests of the sc cavities and LINAC cryomodules.

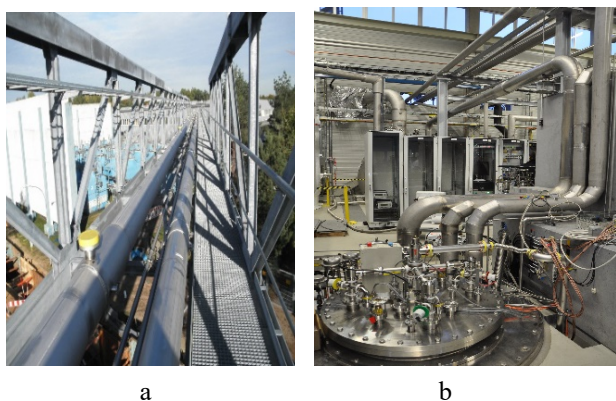


Figure 1: General views of XATL1 cryogenic line (a) and a vertical cryostat in AMTF hall (b), DESY in 2013.

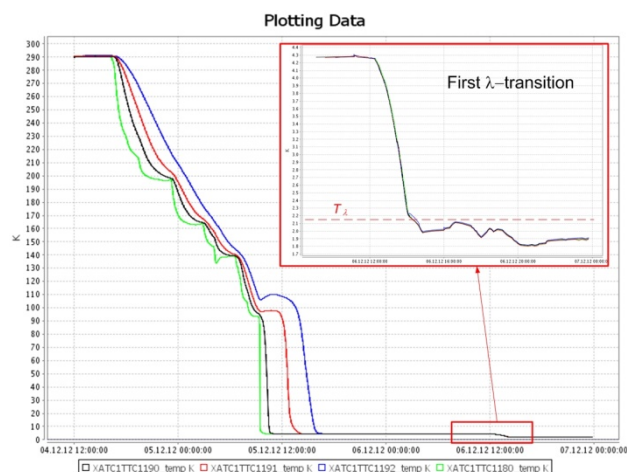


Figure 2: Cooling curves of four cavities in a vertical cryostat. λ - transition to superfluid HeII is shown.

HOM COUPLERS AND BLAs

The HOM couplers and PU antennae were developed for TESLA-type cavities in the previous decade (see eg. [5]). Specific choice of the coupler type for XFEL was agreed on between NCBJ, DESY and Kyocera company (NCBJ subcontractor). NCBJ team performed RF matching of external circuits and resistive loads [1]. BLAs design completion at NCBJ required, certain structure modifications based on computation of fatigue resistance of compensation bellows and precise materials selection. In particular, the choice of the material of ceramic rings for travelling HOM absorption was based on measurements of high order modes attenuation (at 300 K and at 70 K) and dc resistivity. The obtained results led to the choice of AlN-based lossy ceramic rings produced by Sienna Technologies Inc. (USA). The quantities of HOM couplers (1700) and PU antennae (850) delivered to DESY till May 2015 exceeded the contractual obligations of NCBJ. Of the 110 beam-line absorbers (BLAs) delivered together with auxiliaries till the end of 2016, 97 were installed in XFEL LINAC after admission tests at DESY comprising leak check, residual gas analysis and magnetic permeability of their walls. One of the BLAs that have successfully passed the tests is shown in Fig. 3.



Figure 3: BLA after admission tests at DESY.

TESTS OF SC MAGNETS, CAVITIES AND LINAC CRYOMODULES

Before performing the tests the IFJ PAN team at DESY elaborated the documents: quality plans, risk assessment and nearly 200 detailed test procedures. The latter included development of measuring software, hardware and local databases as well as their communication with user interfaces. The written procedures and documents were loaded to Engineering Data Management System – a central documentation and collaboration platform at DESY [1]. The test procedures are characterized in some detail in [6] including eg the rules of input and output inspection or vacuum and cryogenic systems operation.

In brief: tests of sc magnets are aimed at measuring field quality, magnetic axis, roll angle, or saturation effects [1, 6-8]. They comprise check procedures of feedthrough flanges and current leads and measurements of the magnets at 300 K and 2 K (see Fig. 4). Tests include harmonics and harmonic hysteresis measured with rotating coil or stretched-wire measurements used to determine the field angle and offset between magnetic and mechanical axes. Those tests were performed in collaboration with a German group of DESY.

Cavities tests in a vertical cryostat (Fig. 5a) are aimed at determining their performance, maximum available electric field (accelerating gradient) and its dependence of radiation level, cavity quality factor Q_0 on the gradient. An important validation demand for the

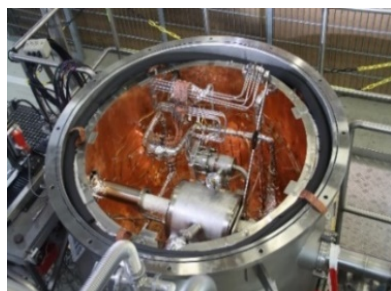


Figure 4: Sc magnet with current leads in a test cryostat.

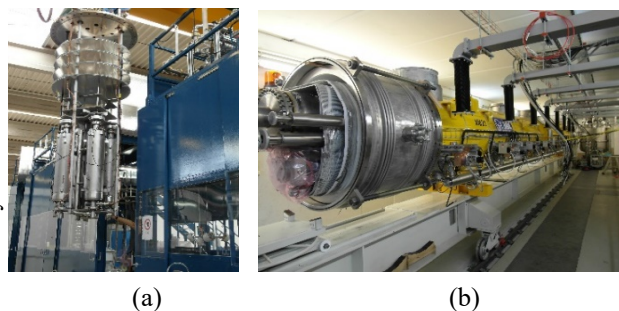


Figure 5: Four cavities in a transportation frame (insert) on their way to a cryostat (a) and a complete LINAC module prepared for high power RF tests (b).

cavities assumes that Q_0 of more than 10^{10} is obtained for the field gradient up to 23.6 MV/m. The contracted number of tested and approved cavities (816) was reached in March 2016.

Low- and high power RF measurements of cavities installed inside a module were performed with Vector Network Analyzer and a klystron as power sources, respectively (Fig. 5b). This final check of the LINAC components results in cavities tuning and determination of external quality factors of input RF couplers, HOM couplers and pick-up antennae. HOM spectra are measured to verify if the parasitic higher modes are attenuated. Maximum and usable field gradients are measured for a single cavity. Finally heat load measurement is done to calculate cavity Q_0 [6]. All the planned tests of 100 LINAC modules were finished and documented till Aug. 2016.

MANUFACTURING OF PLC UNITS

The newest NCBJ engagement into Eu-XFEL facility refers to manufacturing of Beckhoff programmable logic control units for slow-control systems of the first six experimental instruments in XFEL facility. For each of these instruments rough estimates of the equipment to be controlled include 300 motors and 60 valves and pumps which call for 200 PLC units in total. Out of this number, 187 units have been manufactured till July 2017 (Fig. 6). The remaining quantity should be completed till the end of August 2017.



Figure 6: Assembly of a PLC module at NCBJ.

SUMMARY

Implementation of the cryogenic installation by the end of 2012 and reaching the readiness for serial tests and serial production of HOM couplers and absorbers enabled other teams of DESY and CEA Saclay to start assembly of the modules and the entire LINAC. Continuous research and upgrading of the test procedures in many aspects (see [9-19]) allowed testing of long cavities and modules series in a tight time schedule since 2014 (on average: 8 cavities and one module per week). The cryogenic installations and the beam line absorbers were positively assessed and certified in the light of design criteria.

REFERENCES

- [1] E. Plawski et al., "Polish in-kind contribution to European X-ray Free Electron Laser (XFEL): Status in spring 2013", *Synch. Rad. In Natural Scien.*, vol. 12, pp. 1-5, 2013.
- [2] E. Rusinski, M. Chorowski, A. Iluk, J. Fydrych and K. Malcher, "Selected aspects related to the calculations and design of a cryogenic transfer line", *Archives of Civil and Mechanical Engineering*, vol. 14, issue 2, pp. 231-241, 2014.
- [3] J. Schaffran et al., Design parameters and commissioning of vertical inserts used for testing the XFEL superconducting cavities", *AIP Conf. Proc.*, vol 1573, pp. 223-228, 2014.
- [4] J. Polinski et al., "Design and Commissioning of Vertical Test Cryostats for XFEL Superconducting Cavities Measurements", *AIP Conf. Proc.* vol. 1573, pp. 1214-1221, 2014.
- [5] G. Devanz et al., in *Proc. EPAC'02*, pp. 230-232 and the references therein.
- [6] A. Kotarba et al., "Tests of the Superconducting Magnets, Cavities and Cryomodules for the European XFEL", *Proc. of SPIE*, vol. 8903, p. 890329, 2013.
- [7] H. Brueck et al., "First results of the magnetic measurements of the superconducting magnets for the European XFEL", *IEEE T. Appl. Supercond.*, vol. 24, p. 4101204, 2014.
- [8] H. Brueck et al., "Results of the magnetic measurements of the superconducting magnets for the European XFEL", *IEEE T. Appl. Supercond.*, vol. 26, p. 4902204, 2016.
- [9] A. Sulimov et al., "Efficiency of High Order Modes Extraction in the European XFEL LINAC", in *Proc. LINAC2014*, Geneva, Switzerland, 31 Aug.-5 Sept. 2014, paper THPP022, pp. 883-885.
- [10] K. Kasprzak et al., "Automated Quench Limit Test Procedure for serial Serial Production of XFEL RF Cavities", in *Proc. IPAC2015*, Richmond, VA, USA, May 2015, paper WEPMN031, pp. 2994-2996.
- [11] K. Przygoda, et al., "Testing Procedures for Fast Frequency Tuners of XFEL Cavities", in *Proc. IPAC2015*, Richmond, VA, USA, May 2015, paper WEPMN030, pp. 2991-2993.
- [12] K. Kasprzak and M. Wienczek, "Fundamental mode spectrum measurements of RF cavities with RIC equivalent circuit", in *Proc. 16th Int. Conf on RF Superconductivity (SRF2013)*, Paris, France, Sept. 2013, paper THP093, pp.1141-1143.
- [13] J. Shaffran, B. Petersen, D. Reschke and J. Świerblewski, "Test sequence for superconducting XFEL cavities in the accelerator module test facility (AMTF) at DESY", *Phys. Proc.*, vol. 67, pp. 874-878, 2015.
- [14] J. Świerblewski et al., "Improvements of the mechanical, vacuum and cryogenic procedures for European XFEL cryomodule testing", in *Proc. 17th Int. Conf. on RF Superconductivity (SRF2015)*, Whistler, Canada, Sept. 2015, paper TUPB115, pp. 906-909.
- [15] K. Kasprzak et al., "First cryomodule test at AMTF Hall for the European X-Ray Free Electron Laser", in *IPAC2014*, Dresden, Germany, June 2014, paper WEPRI032, pp. 2546-2548.
- [16] M. Wienczek et al., "Update and status of test results of the XFEL series accelerator modules", in *Proc. 17th Int. Conf. on RF Superconductivity (SRF2015)*, Whistler, Canada, Sept. 2015, paper MOPB080, pp. 319-323.
- [17] M. Wienczek et al., "Improvements of RF test procedures for European XFEL cryomodule testing", in *Proc. 17th Int. Conf. on RF Superconductivity (SRF2015)*, Whistler, Canada, Sept. 2015, paper TUPB118, pp. 914-918.
- [18] V. Anashin et al., "Experience with cryogenic operation of Accelerator Module Test Facility during testing of one third of XFEL cryomodules", *IOP Conf. Series: Mat. Scien. Eng.*, vol. 101, p. 012139, 2015.
- [19] K. Wienczek, K. Krzysik, J. Świerblewski and J. Chodak, "Cavities and cryomodules managing system at AMTF", in *Proc. 17th Int. Conf. on RF Superconductivity (SRF2015)*, Whistler, Canada, Sept. 2015, paper TUPB117, pp. 910-913.

FIRST OBSERVATION OF COHERENT THZ UNDULATOR RADIATION DRIVEN BY NSRRC HIGH BRIGHTNESS PHOTO-INJECTOR

M. C. Chou[#], K. T. Hsu, S. Y. Hsu, N. Y. Huang, C. S. Hwang, J. Y. Hwang, J. C. Jan,
 C. K. Kuan, W. K. Lau, A. P. Lee, C. C. Liang, G. H. Luo, I. C. Sheng
 NSRRC, Hsinchu, Taiwan
 Y. H. Wen, NTHU, Hsinchu, Taiwan

Abstract

Generation and characterization of coherent undulator radiation (CUR) in the THz region using the NSRRC S-band photo-injector linac system is achieved. The system consists of a laser-driven photocathode rf gun and one 5.2-m long S-band accelerating linac. Electron bunches in the linac can be accelerated and compressed simultaneously by velocity bunching. In this work, narrow-band tunable fully-coherent THz radiation can be produced from a U100 planar undulator when it is driven by a 100-pC electron bunch with effective bunch length of 90 fs. The experimental setup and the measurement of the power and the frequency spectrum of the coherent THz undulator radiation are reported.

INTRODUCTION

Terahertz (THz) radiation has recently attracted a lot of attention in the scientific applications, such as spectroscopy, imaging, communications and elementary excitations (e. g. excitation of phonons in solids). The THz frequency which is defined as 0.1 to 10 THz (wavelengths of 3 mm to 30 μm) covers the gap between microwaves and infrared light. Development of THz technologies is hindered by the so-called “THz-gap” which reflects the lack of THz sources in the electromagnetic wave spectrum. Over the past decade, the fruitful development of laser-based THz sources as well as nonlinear optics leads to a partial fill up of the THz-gap.

Accelerator-based THz radiation sources attract much attention in recent years [1, 2]. It is well-known that a relativistic electron beam emits temporal coherent synchrotron radiation when its bunch length is much shorter than the radiation wavelength [3]. For example, recalled that the wavelength of a 1 THz wave is 300 μm , a 100-fsec electron bunch can be used to generate coherent radiation in the THz regime such that the radiation intensity is proportional to the square of electron number in the bunch. Realization of a fully coherent THz light is possible if an ultrashort and simultaneously a low-emittance electron beam is available. For modern photo-injector, the beam transverse emittance is usually much smaller than that of the photon beam and therefore, radiation with excellent spatial coherence can be achieved.

A high brightness photo-injector equipped with a laser-driven photocathode rf gun and a 2998-MHz, 5.2-m-long

traveling-wave rf linac has been developed at NSRRC several years ago. In this report design of tunable narrow-band THz coherent undulator radiation (CUR) with this photoinjector and a 10-cm period length planar permanent magnet undulator (U100) has been studied. In addition, first observation of the THz CUR driven by this machine is also reported.

COHERENT UNDULATOR RADIATION

It is well known that relativistic electrons moving in a magnetic field emit synchrotron radiation as they are accelerated by the magnetic force which is always perpendicular to the electron orbits. Undulators can be used to produce synchrotron radiation with significantly higher brightness at narrow spectral bandwidth. Coherent synchrotron radiations (CSR) from bending magnets and undulators are possible as long as the bunch length is much shorter than the radiation wavelengths. When the electron beam emittance is smaller than the radiation photon emittance, a spatially coherent beam or diffraction limited radiation can be produced. Furthermore, a temporal coherent radiation can be achieved when the radiation fields from electrons that are randomly distributed in the bunch of length σ_t add up constructively when $c\sigma_t \leq \lambda$.

In general, the radiation spectrum of the electron bunch can be described as

$$\left. \frac{d^2W}{d\Omega d\omega} \right|_{\text{multi}} = \{N[1 - F(\omega)] + N^2F(\omega)\} \left. \frac{d^2W}{d\Omega d\omega} \right|_{\text{single}},$$

where N is the number of electrons in the bunch and $F(\omega)$ is the form factor which is the Fourier transform of

Table 1: Predicted Performance of THz CUR from U100

CUR from U100		
Electron charge	100 pC	100 pC
E-beam energy (MeV)	18.3 – 33.5	33.5
bunch length (fs, rms)	90 – 223	90
Undulator strength K	4.6	3.2 – 4.6
THz frequency (THz)	0.67 – 2.2	2.2 – 4.3
Bandwidth	5.6%	5.6%
THz pulse energy (μJ)	0.5 – 2.7	0.1 – 2.7
Repetition rate (Hz)	10	10
Average power (μW)	5 – 27	1 – 27
Peak power (MW)	0.02 – 0.32	0.02 – 0.32

[#]chou.mc@nsrc.org.tw

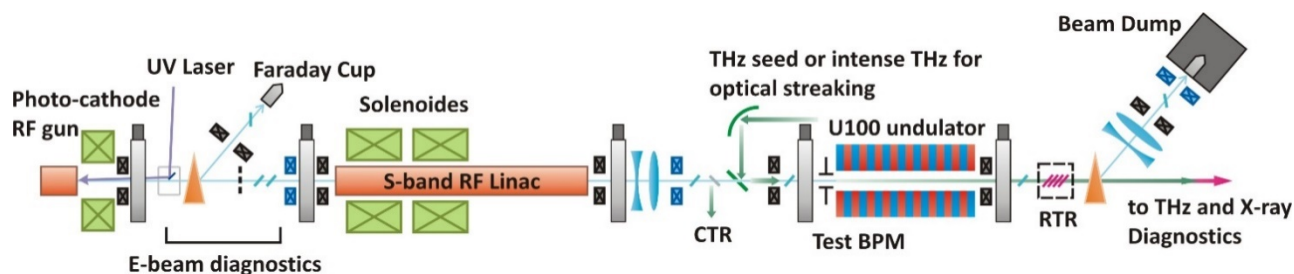


Figure 1: Layout of the NSRRC high brightness photo-injector and THz CUR source.

the temporal distribution of the electrons in the bunch. In comparison with the case of a single electron, the coherent undulator radiation of N electrons is enhanced by a factor of N^2 but the spectrum is enveloped by the form factor. Narrow-band coherent THz radiation with frequency adjustable from 0.7 to 4.0 THz can be generated from the U100 undulator (18-period undulator of 10-cm period length) when it is driven by the ultrashort electron beam. Performance of the radiation is calculated and listed in Table 1, which the transmission loss in the undulator chamber has been included in the calculation.

GENERATION OF ULTRASHORT ELECTRON BUNCHES

Magnetic bunch compressors are commonly used to enhance beam brightness in many advanced accelerator facilities. The concept of rf compression in photo-injector by velocity bunching was first suggested by Serafini and Ferrario in 2001 [4]. This alternative method is a one-step scheme that beam acceleration and rectilinear compression are accomplished simultaneously in the accelerating structure. Propagation of microwave in a typical traveling wave linac has a constant phase velocity equal to the speed of light. An electron moving slower than the phase velocity slips in phase with respect to the rf wave until it is accelerated to higher energy. In general, the amount of electron phase slippage depends on the injection phase. Therefore, it is possible that a bunch of electrons with different initial phases being injected into the linac at certain nominal rf phase will slip backward to the crest of the accelerating field such that bunch compression can be achieved.

Velocity bunching is attractive because less space is required in comparison with the magnetic bunching scheme. Since no dipole magnets are used, deterioration of beam emittance due to CSR effect can be avoided. However, it should be noted that velocity bunching is effective only for lower energy electron beams (< 10 MeV) and the transverse beam emittance and beam size has to be controlled carefully.

With GPT simulation, a 3 ps, 100 pC electron beam generated from the laser-driven photo-cathode rf gun is injected into the rf linac at 15 MV/m accelerating field gradient for velocity bunching. A compressed beam with energy of ~ 33.6 MeV, bunch length of ~ 65 fs can be obtained

at the linac exit. However, it is found that there is a moderate growth in beam size as well as a slight degradation of transverse beam emittance during the acceleration/compression process. This can be fixed by introducing solenoid magnetic field to the frontier section of the linac. The transverse growth of beam size for accelerated beam can be limited with the assistance this solenoid magnetic field.

PHOTO-INJECTOR AND THz CUR SYSTEM

High Brightness Photo-Injector

The commissioning of the high brightness photo-injector, aims to develop a 100 MeV photo-injector system for light source R&D, has been carried out at the beginning of April in 2016 [5]. The layout of the photo-injector is shown in Fig. 1.

The photo-injector is composed by a BNL/UCLA/SLAC type gun, operating at 2998 MHz with peak accelerating gradient of 70 MV/m on the copper photocathode. The gun is followed by a solenoid which is used to compensate space charge induced emittance growth. A commercial Ti:sapphire laser system, delivering 800 nm, 100 fs pulses with energy of 3.5 mJ, is used as a drive laser system to produce the 266 nm UV light required for the photocathode through a third harmonic generation unit. A pulse stretcher capable of adjustable range of 0.8 – 14 ps is used to stretch the UV laser pulses. A synchrolock system ensures that the laser is synchronized with the 40th subharmonic (74.95 MHz) of the master clock at 2.998 GHz. A 156-cell, DESY-type constant gradient traveling wave linac is used as rf compressor. Two solenoid coil sets embedding this linac provide additional magnetic focusing to control the beam envelope and reduce the emittance growth under velocity bunching. Both the gun and the linac are powered by one 35-MW klystron. A tunable power splitter and phase shifter will allow us to tune the power and the phase independently.

A diagnostic beam line is installed at downstream of the linac to characterize the electron beam. Charge and current are measured using integrating current transformers (ICT). Beam energy is measured using the dipole magnet spectrometer, and the beam position is measured at various positions along the beam line using YAG:Ce screen imaging systems.

Content from this work may be used under the terms of the CC BY 3.0 licence (© 2018). Any distribution of this work must maintain attribution to the author(s), title of the work, publisher, and DOI.

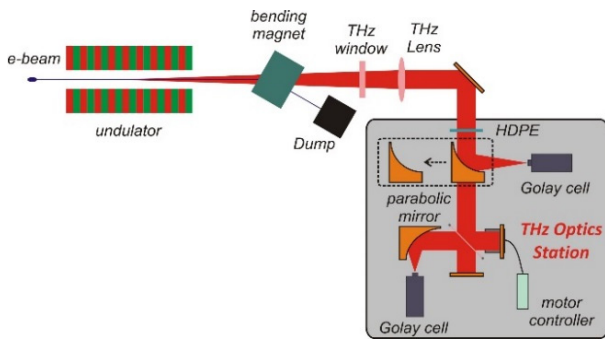


Figure 2: Schematic of the THz CUR source and the optical system for measurement.

NSRRC U100 Undulator

The planar undulator U100 with 18 periods, 10 cm period length and physical length 2.2-m was designed and fabricated by NSRRC. It was installed after the photon-injector system for the generation of THz radiation. The undulator gap can be varied from 24 mm to 120 mm. The maximum peak B field is 0.945 T which corresponds to a K value of 8.8 when the gap is set at the minimum value of 24 mm.

Coherent THz Undulator Radiation Source

Figure 2 shows a schematic of the THz CUR source and the optical system for measuring the THz output signals. The ultrashort electron beam from the photo-injector and the THz photon beam coexist in the undulator vacuum chamber. While the THz radiation goes straight ahead to the THz output window, a dipole magnet bends the electron beam to the dump. A THz Tsurupica window (Broadband Inc.) is used to separate the optical system which is installed in the atmospheric environment from the vacuum. A THz diagnostic system for characterizing the CUR has been installed at downstream of the dipole magnet.

The system includes: (1) a THz Tsurupica lens (Broadband Inc.) with 2.5-m focal length is used to collimate the THz radiation into a parallel beam, (2) three mirrors coated with gold are used to transport the THz radiation, (3) an off-axis parabolic mirror (OAP) with 15-cm focal length which is mounted on a translation stage is used to focus the signal onto the THz detector and (4) the THz detector is a Goly cell detector (Tydex, GC-1P) with the responsivity of 86.7 kV/W at 10 Hz modulation rate. An HDPE plate is inserted in front of the OAP to filter out the unwanted light.

Once the OAP is moved away, the THz radiation can be directed into a bunch length interferometer system. The interferogram of the recombined signal coming from two optical arms can be detected by another Goly cell detector. The bunch length and the frequency spectrum of THz radiations can be derived by analysing the interferograms. The THz diagnostic system including the THz optics and the interferometer is purged with dry air to prevent the propagation loss of THz radiation in air.

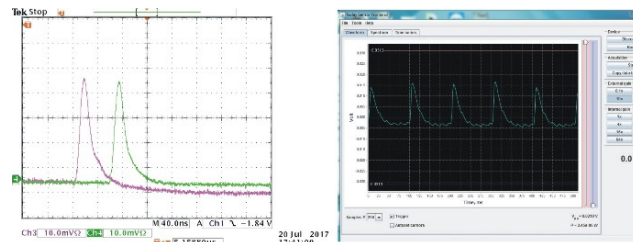


Figure 3: Left: ICT signals, the purple curve is at the linac entrance and the green one is at the linac exit; Right: the measured CUR THz signal.

EXPERIMENTAL RESULTS

A 3.5-MeV electron beam with bunch charge of 100 pC is generated from the photocathode rf gun operated at the peak rf accelerating gradient of 70 MV/m while the laser injection phase is 23° respect to the rf field. Then the electron beam is accelerated to the energy of 43.7 MeV through the linac. The bunch charge measured by the ICTs at the linac entrance and exit is almost the same as shown in the left part of Fig. 3. After that, the electron beam passed through the U100 undulator, installed at 1.52-m downstream from the linac exit, with a gap of 40 mm, corresponding to undulator constant K of 4.6, to produce the THz CUR.

The THz CUR signal was measured by the Goly cell detector, as shown in the right part of Fig. 3. Excluding the energy loss caused by the response of the Goly cell detector, HDPE transmittance, and throughput of all optics, the approximate THz pulse energy is 38.7 nJ at the exit of the undulator vacuum chamber. Parameters of the THz CUR experiment are summarized in Table 2.

In our experiment, the time jitter between the drive laser and microwave and the phase jitter of the microwave result in shot-to-shot fluctuations of bunch charge and the beam energy. Since we did not optimize the operating condition of the photo-injector, the energy of THz radiation is much lower than the predicted value. Besides, the inner height of the undulator vacuum chamber is 28 mm, different from the design value of 36 mm. We believe that the THz output power is strongly limited by the smaller chamber height. The optimization of the status of the photo-injector will be the next step to get higher THz CUR pulse energy.

Table 2: Parameters of the THz CUR experiment

Electron beam energy	43.7 MeV
Bunch charge	90 ± 10 pC
Bunch repetition rate	10 Hz
Undulator period	100 mm
Number of undulator period	18
Undulator gap	40 mm
Undulator constant, K	4.6
Inner height of undulator vacuum chamber	28 mm
THz pulse energy	38.7 nJ @ undulator chamber exit

CONCLUSION

A laser-driven photo-injector system has been developed at NSRRC for R&D of future light sources such as free electron lasers, inverse Compton sources etc. A THz CUR source (or THz superradiant FEL) has been installed to demonstrate the capability of this injector. First THz light has been observed with the Golay cell detector installed at downstream of the U100 undulator. Considered the power loss of the THz optics, the radiation pulse energy at the exit of the undulator chamber is 38.7 nJ (interception of THz energy by the undulator vacuum chamber has not been taken into account yet). Optimization of bunch form factor by velocity bunching for higher THz pulse energy and measurement of spectral distribution are in progress. Improvement of the photo-injector for lower emittance and higher repetition-rate is under consideration.

REFERENCES

- [1] N. Stojanovic and M. Drescher, "Accelerator- and laser-based sources of high-field terahertz pulses", *J. Phys. B: At. Mol. Opt. Phys.* **46**, 192001, 2013.
- [2] S. Benson, *et al.*, "The 4th generation light source at Jefferson Lab", *Nucl. Instrum. Methods A*, **582**, 14, 2007.
- [3] T. Nakazato, *et al.*, "Observation of coherent synchrotron radiation", *Phys. Rev. Lett.* **63**, 2433, 1989.
- [4] L. Serafini and M. Ferrario, "Velocity bunching in photo-injectors", in *Physics of, and Science with, the X-ray Free Electron Laser*, *AIP Conf. Proc.* 2001, No.581.
- [5] A. P. Lee, *et al.*, "First beam test of the high brightness photo-injector at NSRRC", TUPOW025, IPAC'16.

HIGH SPECTRAL DENSITY COMPTON BACK-SCATTERED GAMMA-RAY SOURCES AT FERMILAB *

D. Mihalcea¹, B. Jacobson², A. Khizhanok³, A. Murokh², P. Piot^{1,4}, and J. Ruan⁴

¹ Department of Physics and Northern Illinois Center for Accelerator & Detector Development, Northern Illinois University, DeKalb, USA

² Radiabeam Technologies, Santa Monica, USA

³ Department of Mechanical Engineering, Northern Illinois University, DeKalb, USA

⁴ Fermi National Accelerator Laboratory, Batavia, USA

Abstract

A ~ 1.2 MeV gamma-ray source is planned to be built at Fermilab following the completion of the ~ 300 MeV superconducting linac. The high energy photons are back-scattered from the interactions between electrons and high intensity IR laser pulses. In this contribution we discuss some of the experiment design challenges and evaluate the performances of the *gamma*-ray source. We expect the peak brilliance to be of the order of 10^{23} photons/[s-(mm mrad)² 0.1% BW] and the spectral density of the radiation in excess of 2×10^5 photons/s/eV.

INTRODUCTION

Gamma-ray sources are extensively used in various fields from biomedical and fundamental research applications to industry and national defense. The required performances of the γ -ray sources are dictated by the application, but for most cases, large values of peak brightness, photon flux, and a small energy bandwidth are desired. Typically, high precision experiments would require high brightness sources and others, like biomedical and industrial applications, would mostly benefit from higher beam fluxes.

Gamma-ray sources consisting of back-scattered radiation resulting during the collisions of energetic electrons and laser pulses [1], process also known as Inverse Compton Scattering (ICS), became attractive due to the progress in producing high quality GeV-class electron beams and very high intensity lasers. The size and the cost of these γ -sources are mostly driven by the electron beam accelerator. Recent progress in the field of laser plasma wakefield accelerators (LPWA) [2] made possible building compact γ -ray sources with very high brightness [3, 4] but with relatively low photon flux due to the low operating frequency (~ 10 Hz). To overcome this problem our approach is to use the superconducting 300 MeV Fermilab injector to be built at FAST facility, which can deliver up to 15,000 electron pulses per second.

In this paper we present the design of the proposed γ -ray source and the expected performances based on simulations.

* This work was sponsored by the DNDO award 2015-DN-077-ARI094 to Northern Illinois University. Fermilab is operated by Fermi Research Alliance, LLC, for the U.S. Department of Energy under contract DE-AC02-07CH11359.

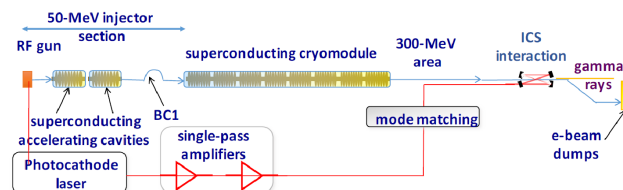


Figure 1: Linac layout at FAST facility.

ICS EXPERIMENT SETUP

The most relevant components of the FAST linac are shown in Fig. 1. The electrons are extracted by photoemission from a CsTe₂ cathode illuminated with picosecond long UV laser pulses. The acceleration is performed by a normal conducting RF gun, two superconducting TESLA cavities and a superconducting cryomodule consisting of eight TESLA cavities. The operating RF frequency is 1.3 GHz the final electron energy is up to 300 MeV and the charge of each electron pulse is up to 5 nC. More details about the linac and beam dynamics simulations can be found in Refs. [5, 6]. The low energy section of the linac, consisting of the gun and the two booster cavities, was successfully tested in the summer of 2016 and the full completion, testing and some experiments are expected to take place in the summer of 2017.

The laser system, already functional, can produce up to $10 \mu\text{J}$ IR pulses at 3 MHz sampling rate. The IR laser pulses are split in two components: the first component contains about 10% of the total energy and it is sent to the photocathode via two stages of frequency doubling crystals. The second component is further amplified to about 0.5 mJ/pulse and sent to the ICS experimental area. Up to five equally spaced RF macropulses are generated each second. The duration of each macropulse is 1 ms and trains of about 3,000 electron bunches can be emitted during this time.

The LINAC components most relevant for this experiment are those used for the final focus of the electron beam. Thirty centimeters upstream of the interaction point (IP) there are three permanent magnetic quadrupoles (PMQs) (Fig. 2) manufactured by Radiabeam. They are hollow cylinders with outer radius 15 mm, inner radius 4 mm and lengths 3 cm, 6 cm, and 3 cm respectively. The spacing between them is 5 cm. The lens strengths of the PMQs in the preliminary design are -150 m^{-1} , 150 m^{-1} and -150 m^{-1} . Symmetrically, there are three more identical PMQs downstream of

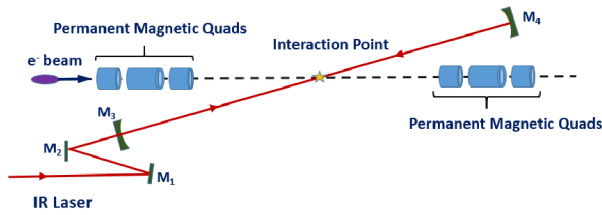


Figure 2: Simplified view of the interaction region. PMQs are symmetrically located 30 cm upstream and downstream of the interaction point (IP). Fabry-Perot (FB) high finesse enhancement cavity consists of the concave mirrors M_3 and M_4 . The angle between electron beam direction of propagation and FB axis is about 5° . Optical elements for laser beam matching, feed-back components and the additional Herriott cell are not shown.

the IP. The final focus region also includes four adjustable quadrupoles located upstream of the first set of PMQs. These quadrupoles allow matching the beam into the PMQs such that certain requirements on the beam at IP are met.

Before its arrival at the interaction region, the IR laser beam travels through a delay stage to ensure the synchronization with the electron beam at IP. The delay stage is driven by the electrical signal provided by a photoconductive THz antenna inserted into the beamline [7].

The IR beam is directed to a Fabry-Perot (FB) resonator, see Fig. 2, where beam intensity is amplified by a factor of at least 10 due to coherent addition of the laser pulse which bounces inside the cavity and the incoming pulses produced by the laser system [8]. To match the eigenfrequencies of the ≈ 1 m long resonator with the 3 MHz laser sampling rate, the FB cavity is coupled to a Herriott cell [9] which extends the total propagation distance inside the resonator. With this addition we estimate that the amplification factor is at least 50.

FINAL FOCUS OPTIMIZATION

The electron beam quality is critical to the overall performance of the γ -ray source. Electron beam transverse emittance (ϵ_\perp), transverse spot size at IP (σ_e), bunch duration (τ_e), charge (eN_e), energy ($W = \gamma m_e c^2$), beam divergence (σ'_e), and repetition rate in addition to laser pulse energy (proportional with IR photon number N_l) and laser beam waist (w_0) completely determine the most important parameters of the scattered radiation [10, 11]: brightness (B_x), photon flux (N_x) and γ -ray bandwidth (BW).

$$B_x \propto \frac{N_l}{w_0^2} \gamma^2 \frac{N_e}{\tau_e \epsilon_\perp^2} \quad (1)$$

$$N_x \approx \frac{N_e N_l \sigma_T}{2\pi \left(\sigma_e^2 + \frac{w_0^2}{4} \right)} \quad (2)$$

$$BW \equiv \frac{\delta\omega_x}{\omega_x} \approx 2\gamma^2 \sigma_e'^2 \quad (3)$$

where σ_T in Eqn. 2 is the total Thompson cross section and ω_x in Eqn. 3 is the scattered radiation frequency.

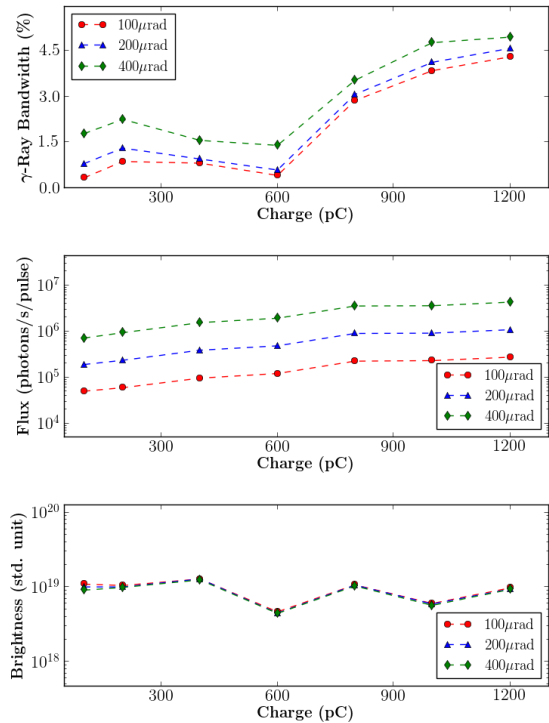


Figure 3: Scattered radiation bandwidth, flux and brightness as functions of electron beam charge and for three values of collimator opening angle.

The validity condition for Eqn. 2 requires that the transverse size of the two beams at IP are about the same. In this experiment the scattered photon flux is mostly constrained by the laser beam waist which in our design is $w_0 = 30 \mu\text{m}$. The expression of the scattered radiation bandwidth in Eqn. 3 is valid when electron beam transverse emittance is the dominant contributor to the γ -ray energy spread. The contributions from electron beam energy spread ($< 0.1\%$) and laser bandwidth ($< 0.2\%$) are negligible in comparison with at least 0.5% we expect from electron beam emittance. Energy spread due to the opening angle of the collimator that captures the scattered radiation should also be considered. Equation 3 shows that electrons with angular spread of about $100 \mu\text{rad}$ (rms) and beam energy close to 250 MeV generate scattered radiation with energy spread of 0.5% provided only beam emittance is considered.

To maximize the scattered photon flux the electron beam spot size at IP should be close to the laser beam waist. Also, to minimize the γ -ray bandwidth, the angular spread of the electrons should be at a minimum. Since the transverse emittance does not change much in the final focus region and spot size at IP is constrained ($\sigma_e = \frac{w_0}{2}$), electrons angular spread minimization can be achieved by reducing the correlation between the transverse position and the divergence that is the electron beam Twiss parameter $\alpha_e \approx 0$. The two conditions are:

$$\sigma_e = \frac{w_0}{2}, \quad \text{and} \quad \alpha_e = 0. \quad (4)$$

Content from this work may be used under the terms of the CC BY 3.0 licence (© 2018). Any distribution of this work must maintain attribution to the author(s), title of the work, publisher, and DOI.

Figure 3 shows brightness, bandwidth, and photon flux as functions of electron beam charge and the three values of the collimator opening angle: 100 μrad , 200 μrad , and 400 μrad . Larger electron beam charge leads to larger transverse emittance, higher bandwidth and higher photon flux. The weak dependence of bandwidth with opening angle shows that electron beam emittance has by far the largest contribution to the scattered radiation energy spread increase. Table 1 summarizes the scattered radiation parameters, evaluated with the code described in [10], and Table 2 contains the relevant parameters of the electron beam and IR laser.

Table 1: γ -ray Parameters for Different Collimator Opening Angles Generated by the Collision Between a Single Electron Bunch of Charge 100 pC and Energy 259 MeV and an IR Laser Pulse. The Last Column Corresponds to the Whole Scattered Radiation.

Opening angle	100 μrad	200 μrad	> 10 mrad
Brightness (std. units)	1.1×10^{19}	1.0×10^{19}	1.1×10^{18}
Flux (photons)	5.0×10^4	1.9×10^5	1.4×10^7
Bandwidth (%)	0.34	0.80	49.8

Table 2: Electron Beam and Laser Main Parameters.

Electron beam		Laser pulse	
Beam energy (MeV)	259.0	wavelength (nm)	1053
Beam charge (pC)	100	pulse energy (J)	0.5
Energy spread (%)	0.06	bandwidth (%)	0.2
Duration (ps)	5.0	Duration (ps)	3.0
Beam size x/y (μm)	12/13	waist (μm)	30
Emittance (μm)	0.34		

As suggested in Ref. [12], an important figure of merit of the γ -ray source is spectral density defined as $\delta \equiv \frac{N_{ph}}{\delta E \delta t}$. Assuming scattered radiation bandwidth lower than 1 % the spectral density we can achieve from a single electron bunch collision is $\delta \approx 19.8$ photons/s/eV, when beam charge is 100 pC and opening angle 200 μrad . Since about 15,000 electron bunches can be generated each second we expect the spectral density to be above 2×10^5 /photons/s/eV. Higher spectral density can be obtained by increasing the collimator opening angle and electron bunch charge. In this case the photon dose becomes significantly larger at the expense of slightly higher bandwidth (Fig. 3).

The conditions on electron beam at IP stated in Eqn. 4 can only approximately be fulfilled with the four adjustable quadrupoles in the final focus region. The "tails" of the electron beam angular distributions at IP, see Fig. 4, increase the scattered radiation bandwidth. One way (not tested yet) to decrease the electron beam divergence at IP is to also use

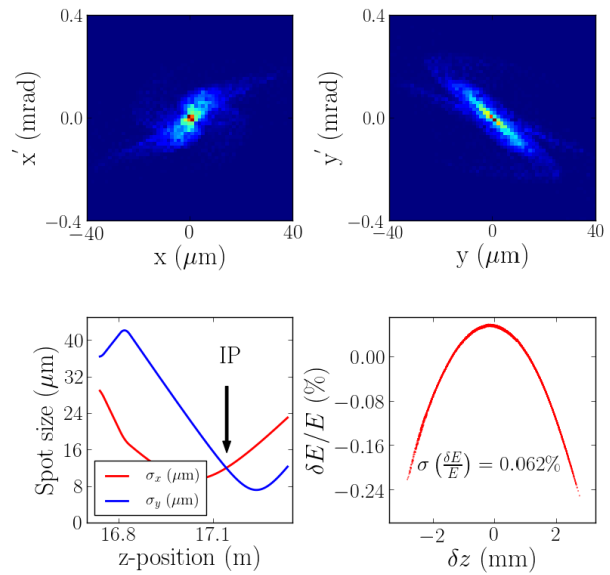


Figure 4: Top: $x-x'$ and $y-y'$ distributions at IP for a 100 pC electron beam. Bottom: σ_x and σ_y values upstream of IP (left) and longitudinal electron beam energy spread (right).

some of the quadrupoles located upstream of the final focus region.

CONCLUSIONS

Beam simulations from cathode to IP were performed to determine the realistic electron bunch distribution just prior to the collision with the IR laser pulse. The final focus region contains four medium strength adjustable quadrupoles and six small ultra-high strength permanent magnetic quadrupoles. The laser pulse energy is enhanced with a Fabry-Perot optical cavity coupled to a Herriott cell to match resonator eigenfrequencies with laser sampling rate.

The electron beam transverse size is matched with the laser beam waist at IP, $\sigma_e = \frac{w_0}{2} \approx 15 \mu\text{m}$ and electrons divergence is minimized by setting the Twiss parameter $\alpha \approx 0$. The scattered radiation brightness is of the order of 10^{19} photons/[s-(mm-mrad)²-BW(0.1%)], and photon flux 1.9×10^5 photons/s from a single 100 pC electron bunch and collimator opening angle of 200 μrad . The γ -ray photons have energy of 1.2 MeV bandwidth of 0.8 % and spectral density 19.8 photons/s/eV from a single bunch. Photon flux, brightness and spectral density are enhanced by a factor of 15,000 representing the electron beam repetition rate.

REFERENCES

- [1] O. Kulikov, Y. Telnov and M. Yakimenko, *Phys. Lett.*, **13**, 344, 1964.
- [2] E. Esarey, C. B. Schroeder, and W. P. Leemans, Physics of laser-driven plasma-based accelerators, *Rev. Mod. Phys.*, **81**, 12291285, 2009.
- [3] K. Ta Phuoc, S. Corde, C. Thaury, V. Malka, A. Tafzi, J. P. Goddet, R. C. Shah, S. Sebban, and A. Rousse, All-optical

- Compton gamma-ray source, *Nat. Photonics*, **6**, 308311, 2012.
- [4] S. Chen, *et al.*, MeV-energy X rays from Inverse Compton Scattering with laser-wakefield accelerated electrons, *Phys. Rev. Lett.* **110**, 155003, 2013.
- [5] J. Leibfritz *et al.*, in *Proceedings of the PAC11*, New York, USA, 2011.
- [6] P. Piot, Y.-E. Sun, and M. Church, in *Proceedings of the IPAC10*, Kyoto, Japan, 2010.
- [7] B. Jacobson, Fermilab IOTA Workshop, June 15, 2016.
- [8] H. Shimizu, A. Aryshev, Y. Higashi, Y. Honda, and J. Urakawa, *NIMA*, **745**, 63-72, 2014.
- [9] D. R. Herriott, H. Kogelnik, and R. Kompfner, *Appl. Opt.*, **3**, 523, 1964.
- [10] W. J. Brown and F. V. Hartemann, *Phys. Rev. ST Accel. Beams*, **7**, 060703, 2004.
- [11] W. J. Brown and F. V. Hartemann, *AIP Conference Proceedings*, **737**, 839, 2004.
- [12] A. Bacci, *et al.*, *J. of Applied Physics*, **113**, 194508, 2013.

CLARA FACILITY LAYOUT AND FEL SCHEMES

D. J. Dunning* on behalf of the CLARA team
STFC Daresbury Laboratory and Cockcroft Institute, Daresbury, UK

Abstract

CLARA is a new FEL test facility being developed at STFC Daresbury Laboratory in the UK. Commissioning has started on the front-end (photo-injector and first linac) while the design of the later stages is still being finalised. We present the latest design work, focusing on the layout and specification of components in and around the undulator sections. We give an overview of the design and modelling of the FEL schemes planned to be tested.

INTRODUCTION

The UK is constructing a new FEL test facility called CLARA [1] which will be a dedicated accelerator R&D facility focused around demonstrating FEL schemes that can be applied to enhance the capabilities of X-ray FEL facilities - including a potential UK XFEL [2]. It will operate with 250 MeV maximum energy and $\lambda_r=100\text{-}400$ nm fundamental FEL wavelength (see Fig. 1 for layout). The front end (up to 50 MeV) is being commissioned and the second phase (up to 150 MeV) is being assembled while design of the later stages continues - aiming for FEL lasing in 2022.

While CLARA will serve as a test-bed for various accelerator technologies, the focus of this paper is on the FEL schemes and the implications for the layout of the FEL section. The design of the FEL section will be finalised in September 2017 prior to initiating purchasing of the undulators. The main aims dictating design choices for the CLARA FEL section are:

- To demonstrate novel FEL capabilities that could be applied at X-ray FEL facilities, specifically ultra-short pulses, improved pulse quality, stability and synchronisation. For ultra-short pulses the aim is for pulse durations in the 1-100 fs range, which would correspond to 1-100 as when translated from the 100 nm minimum wavelength of CLARA to ~ 0.1 nm facilities.
- To gain experience with schemes for a future UK XFEL including those already demonstrated elsewhere.
- To produce a flexible design that can accommodate new ideas and future upgrades.

Given the above we aim to keep the focus on energy/wavelength-independent aspects of the FEL concepts and so minimise energy/wavelength-specific difficulties so far as possible. Key drivers for the wavelength choice were therefore the availability of single-shot diagnostic techniques for the characterisation of the output and availability of suitable seed sources for interacting with the electron beam. To suit single-shot temporal diagnostics it is proposed to study short pulse generation for FEL wavelengths in the range 250-400 nm, where suitable

non-linear materials are available. For schemes requiring only spectral characterisation the operating wavelength range will be 100-266 nm. While it was previously planned to use seed/modulating laser sources throughout the range from 800 nm-100 μm [1], on further consideration it is more straightforward (i.e. requires less laser R&D) to avoid the range from $20 \mu\text{m} \lesssim \lambda_{\text{mod}} \lesssim 70 \mu\text{m}$ and to cluster FEL schemes around a few select wavelengths.

FEL SCHEMES

The CLARA FEL team maintains an ongoing review of FEL schemes that have been proposed and demonstrated worldwide and assesses their compatibility with the aims and layout of CLARA. Some of these are listed below, categorised into what is foreseen to be the initial/major CLARA projects and others that impact the layout through maintaining as options of high interest.

Initial Projects

Schemes under consideration for the early stages of CLARA are those that are expected to be relatively less demanding at least in not requiring external laser modulation or synchronisation. This includes single-spike SASE [3], tapering (assessed for CLARA in [4]), two-colour schemes via undulator tuning and testing novel undulator technology [5] in a designated afterburner section.

Major Projects

These are listed in a potential running order where elements of the layout would be introduced incrementally:

High-brightness SASE The high-brightness SASE scheme [6] employs chicanes between undulator modules to increase the slippage of the radiation relative to the electron bunch and so improve the temporal coherence of the emitted radiation pulse. In simulations the scheme has been shown to perform more effectively for undulator modules shorter than the FEL gain length. It requires no laser seeding/modulation.

Mode-locked FEL The mode-locked FEL concept [7] uses chicane delays between undulator sections to allow pulses with duration much shorter than the FEL co-operation length, $l_c = \lambda_r/4\pi\rho$ (where the FEL parameter $\rho \approx 10^{-4} - 10^{-3}$), which is a lower limit for many schemes. The number of cycles per pulse can be reduced from hundreds to approximately the number of periods in an undulator module, N . For demonstration on CLARA the number of periods per undulator module should therefore be minimised, without negatively impacting other schemes: this has been set to 27 periods. While preliminary results could be achieved

* david.dunning@stfc.ac.uk

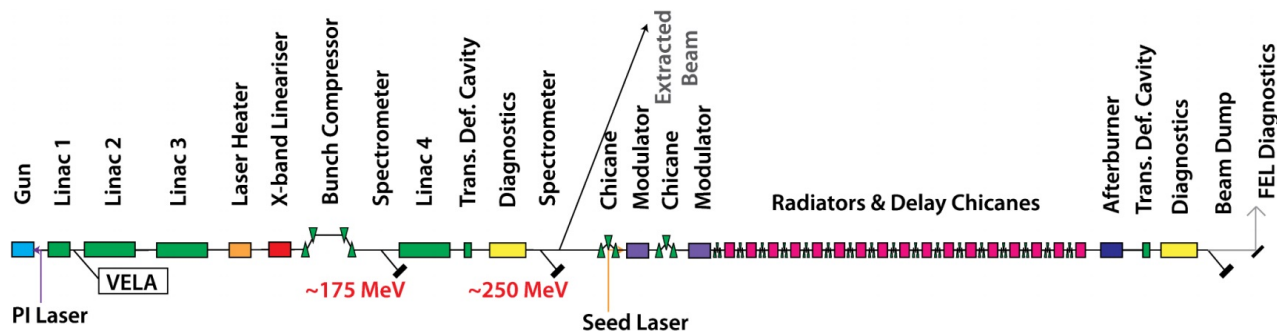


Figure 1: Schematic layout of CLARA. The total length is ~ 90 m.

without interaction with an external laser, the scheme ultimately requires the electron beam energy to be modulated with period $\lambda_{\text{mod}} = S_e N \lambda_r$, where the slippage enhancement factor [7] $S_e \sim 4 - 8$ has commonly been used in modelling. Latest studies indicate that a $20 \mu\text{m}$ source would be suitable.

Mode-locked afterburner The mode-locked afterburner [8] differs from the above by requiring chicane delays and short undulator modules only in a short afterburner section, without the constraint of maintaining performance of other schemes. N can therefore be reduced to ~ 8 periods and the modulation period can be reduced, e.g. to $3 \mu\text{m}$ at $\lambda_r = 100 \text{ nm}$ [9] or $\sim 8 \mu\text{m}$ at $\lambda_r = 266 \text{ nm}$.

Energy chirp with tapered undulator The energy chirp with tapered undulator scheme [10] uses a few-cycle laser pulse to modulate the electron beam energy and a tapered undulator to select a short region of the beam with a specific chirp for FEL lasing. In [10] a hard x-ray resonant FEL wavelength of $\lambda_r = 0.15 \text{ nm}$ is used with an 800 nm modulating laser pulse to generate an isolated SASE spike with 200 fs FWHM duration, corresponding to sub-cycle scale of the 800 nm modulation. For CLARA with $\lambda_r = 266 \text{ nm}$ the optimum modulating wavelength should be approximately $40 \mu\text{m}$ [1], so operation with $\lambda_r = 400 \text{ nm}$ and $\lambda_{\text{mod}} \approx 70 \mu\text{m}$ may be preferable to deliver a suitable modulating laser.

Other Schemes Impacting the Layout

Variable polarisation The relative advantages of planar undulators versus helical (with variable polarisation) undulators for CLARA has been considered in depth [11]. Given that the priority is not for significant investment in complex polarisation-preserving transport and diagnostics, the conclusion is that the flexibility and higher growth rate of helical undulators does not justify the increased complexity and cost. Nevertheless some flexibility is desirable to provide an extra degree of freedom for future developments. Hence the option of rotating the undulators about the beam axis has been specified provided the cost increase is not substantial. An example of a scheme enabled by this has been studied [12] and more complex variants can be envisaged.

EEHG Echo-enabled harmonic generation (EEHG) [13] is not presently a major project because

detailed experimental studies have been carried out elsewhere. Nevertheless because of its utility and flexibility for a range of schemes it is considered essential to include components to allow this. EEHG on CLARA has been studied assuming 800 nm seed wavelength [1].

Frequency modulation Frequency modulation in FELs is a topic of research aiming to deliver output with very broad bandwidth [14]. Undulator tapering within modules is specified for CLARA to enable studies such as this.

Summary of Requirements

The conclusion from analysis of potential schemes is that the design of the FEL section should be suitable for the major projects but also flexible to enable a large number of other options. This can be achieved by choosing a layout that is fairly universal in the sense that it will feature a short modulation section, then a long radiator, then an afterburner region, with several features to maximise flexibility: (1) Including two modulator undulators with chicanes of suitable R_{56} to allow EEHG and to increase modulation amplitude applied in the first modulator by the optical klystron effect [15]. Upgrades to add extra modulators could be achieved by removing radiators. (2) Allowing sufficient transverse aperture to inject a large range of wavelengths from external lasers (up to $100 \mu\text{m}$). (3) Utilising short radiator modules with chicanes between modules to study HB-SASE and mode-locking. (4) Using rotatable planar undulators to give a degree of freedom on polarisation, together with variable gap and tapering within modules. (5) Leaving space to interchange afterburner sections to test e.g. novel undulators, mode-locked afterburner. (6) Engineering approaches to ease re-configuring the layout (e.g. rail-mounting) have been proposed and will be considered in more detail.

OTHER FACTORS IMPACTING LAYOUT

Upstream of FEL Section

A number of electron beam operating modes, corresponding to FEL research topics, have been specified [16], with short-bunch and long-bunch modes both specified as 250 pC Gaussian bunches with target 0.5 mm-mrad normalised emittance and 25 keV energy spread but with differing peak currents (400 A versus 125 A) and nominal energies (240 MeV

Content from this work may be used under the terms of the CC BY 3.0 licence (© 2018). Any distribution of this work must maintain attribution to the author(s), title of the work, publisher, and DOI.

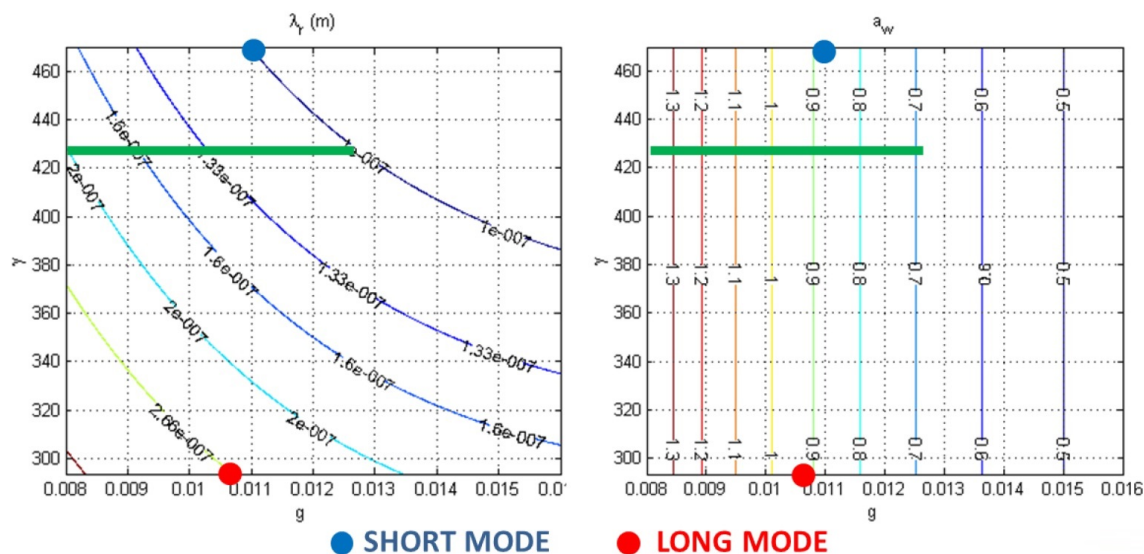


Figure 2: Wavelength and undulator parameter (a_w) tuning ranges for the CLARA radiator with $\lambda_u = 2.5$ cm, in terms of undulator gap, g [m] and beam energy, γ . The green line shows a factor of 2 wavelength tuning from 100–200 nm. The maximum λ_r is 400 nm.

versus 150 MeV). The lower energy of the long-bunch mode brings the wavelength range in line with the temporal diagnostics (for short pulse schemes) and eases the seed laser power requirements by more than a factor of two compared to 240 MeV. Ultra-short and flat-top modes are also planned. The latest details of the accelerator layout to deliver the required beams for CLARA is given in [17]. The option of manipulating the beam using e.g. a dielectric wakefield element will be included in the layout to allow dechirping [18] and potentially more advanced FEL schemes [19]. While studies indicate that a laser heater will not be required for FEL lasing, space is reserved to add this as a future upgrade to enable e.g. microbunching studies [20].

Modulation Section

It has been concluded that the chosen FEL schemes can be achieved with a few selected seed/modulation wavelengths, listed in a potential order of implementation according to the FEL schemes above: 20 μm for mode-locking, 800 nm for EEHG and general purpose, 3–8 μm for the mode-locked afterburner, ~ 70 –100 μm for chirp + taper. The transverse apertures have therefore been specified for a maximum 100 μm wavelength and it was identified that a seeding chicane would be preferable to a dog-leg for this [17]. To enable the chosen FEL schemes the modulators should be tuneable from 800 nm–100 μm , with sufficient transverse aperture and suitable modulator designs have been produced. Alternative modulation methods are presently under consideration that could potentially replace some of the functionality of the longer wavelength sources with e.g. an 800 nm source [21].

Radiator

A hybrid planar undulator type is chosen for the radiator modules, giving stronger on-axis field than a permanent

magnet device. The choice of undulator period, λ_u , depends on the minimum operating gap (dependent on vacuum and wakes) and the required wavelength tuning range. Analysis of the former shows that for CLARA the vacuum benefits of NEG coated vessels are less important than the minimisation of wakefield effects by using aluminium or copper vessels [22], with 6 mm diameter aluminium/copper vessel specified (therefore 8 mm minimum undulator gap). For the tuning range we specify a factor of two in wavelength tuning at a fixed electron beam energy to enable e.g. harmonic cascade schemes. The combination of factors results in $\lambda_u = 2.5$ cm, with tuning range as shown in Fig. 2.

While short undulator modules in the radiator are preferred for mode-locking and HB-SASE, there must also be consideration of the impact on normal FEL operation. The nominal module length of 0.75 m [15] has been compared against other options and found to be suitable in terms of transverse beam quality [23]. The break sections between modules are specified to be 0.5 m and the specifications of the break section components are being defined. Details of the FEL section beam-based alignment strategy using cavity BPMs are given in [24].

Radiation Extraction/Afterburner

Given the wavelength and expected transverse properties of the FEL light [23] it will be necessary to extract it before the afterburner section. Latest details of the mode-locked afterburner are given in [9].

SUMMARY

Design choices for the CLARA FEL section have been outlined and will be finalised in an upcoming internal review to initiate purchasing of the undulators.

REFERENCES

- [1] J. A. Clarke *et al.*, “CLARA conceptual design report,” *Journal of Instrumentation*, vol. 9, no. 05, p. T05001, 2014, <https://doi.org/10.1088/1748-0221/9/05/T05001>.
- [2] Science & Technology Facilities Council (UK), “Free-Electron Laser (FEL) Strategic Review,” 2016, <https://www.stfc.ac.uk/files/fel-report-2016/>.
- [3] Y. Ding, A. Brachmann, F.-J. Decker, D. Dowell, P. Emma, J. Frisch, S. Gilevich, G. Hays, P. Hering, Z. Huang, R. Iverson, H. Loos, A. Miahnahri, H.-D. Nuhn, D. Ratner, J. Turner, J. Welch, W. White, and J. Wu, “Measurements and Simulations of Ultralow Emittance and Ultrashort Electron Beams in the Linac Coherent Light Source,” *Phys. Rev. Lett.*, vol. 102, p. 254801, Jun 2009, <https://doi.org/10.1103/PhysRevLett.102.254801>.
- [4] I. P. S. Martin, R. S. Bartolini, D. Dunning, and N. Thompson, “Studies of undulator tapering for the CLARA FEL,” in *Proc. of FEL2015*, 2015, pp. 412–416, <http://jacow.org/FEL2015/papers/tup025.pdf>.
- [5] J. A. Clarke *et al.*, “Optimisation of Superconducting Undulators for Low Repetition Rate FELs,” 2017, presented at FEL2017, Sante Fe, NM, USA, paper WEC02, this conference.
- [6] B. W. J. McNeil, N. R. Thompson, and D. J. Dunning, “Transform-Limited X-Ray Pulse Generation from a High-Brightness Self-Amplified Spontaneous-Emission Free-Electron Laser,” *Phys. Rev. Lett.*, vol. 110, p. 134802, Mar 2013, <https://doi.org/10.1103/PhysRevLett.110.134802>.
- [7] N. R. Thompson and B. W. J. McNeil, “Mode locking in a free-electron laser amplifier,” *Phys. Rev. Lett.*, vol. 100, p. 203901, May 2008, <https://doi.org/10.1103/PhysRevLett.100.203901>.
- [8] D. J. Dunning, B. W. J. McNeil, and N. R. Thompson, “Few-cycle pulse generation in an x-ray free-electron laser,” *Phys. Rev. Lett.*, vol. 110, p. 104801, Mar 2013, <https://doi.org/10.1103/PhysRevLett.110.104801>.
- [9] C. L. Shurvinton, D. J. Dunning, and N. R. Thompson, “Design Study for the Generation of Few-Cycle FEL Pulses Using Mode-Locked Afterburner Scheme at CLARA,” in *Proc. of IPAC2017*, 2017, pp. 2783–2786, <https://doi.org/10.18429/JACoW-IPAC2017-WEPAB089>.
- [10] E. L. Saldin, E. A. Schneidmiller, and M. V. Yurkov, “Self-amplified spontaneous emission FEL with energy-chirped electron beam and its application for generation of attosecond X-ray pulses,” *Phys. Rev. Spec. Top. Accel. Beams*, vol. 9, no. 5, pp. 1–6, May 2006, <https://doi.org/10.1103/PhysRevSTAB.9.050702>.
- [11] N. Thompson, “Radiator Undulator Specification,” 2016, CLARA technical note 1168-fel-rpt-1002.
- [12] D. Bultrini, D. J. Dunning, L. T. Campbell *et al.*, “Modelling two-colour FEL with wide wavelength separation and individual polarisation tuning,” in *Proc. of IPAC2017*, 2017, pp. 2808–2811, <https://doi.org/10.18429/JACoW-IPAC2017-WEPAB097>.
- [13] G. Stupakov, “Using the Beam-Echo Effect for Generation of Short-Wavelength Radiation,” *Phys. Rev. Lett.*, vol. 102, p. 074801, 2009.
- [14] L. T. Campbell *et al.*, “Frequency Modulation in the Free Electron Laser,” 2017, presented at FEL2017, Sante Fe, NM, USA, paper FRB05, this conference.
- [15] J. A. Clarke *et al.*, “The status of CLARA, a new FEL test facility,” in *Proc. of FEL2015*, 2015, pp. 49–53, <http://jacow.org/FEL2015/papers/mop011.pdf>.
- [16] P. H. Williams *et al.*, “Developments in the CLARA FEL Test Facility Accelerator Design and Simulations,” in *Proc. of IPAC2016*, 2016, pp. 797–800, <https://doi.org/10.18429/JACoW-IPAC2016-MOP0W037>.
- [17] P. H. Williams, D. J. Dunning, and N. R. Thompson, “Developments in the CLARA FEL Test Facility Accelerator Design and Simulations,” in *Proc. of IPAC2017*, 2017, pp. 2787–2789, <http://jacow.org/ipac2017/papers/wepab090.pdf>.
- [18] T. H. Pacey, G. Xia, Y. Saveliev, and D. J. Dunning, “Phase space manipulation of sub-picosecond electron bunches using dielectric wakefield structures,” in *Proc. of IPAC2017*, 2017, pp. 3302–3304, <https://doi.org/10.18429/JACoW-IPAC2017-WEPVA021>.
- [19] A. A. Lutman *et al.*, “Fresh-slice multicolour X-ray free-electron lasers,” *Nature Photonics*, vol. 10, p. 745, 2016, <https://doi.org/10.1038/NPHOTON.2016.201>.
- [20] A. D. Brynes *et al.*, “Inducing Microbunching in the CLARA FEL Test Facility,” 2017, presented at FEL2017, Sante Fe, NM, USA, paper WEP026, this conference.
- [21] D. J. Dunning *et al.*, “Alternative Electron Beam Slicing Methods for CLARA and X-ray FELs,” 2017, presented at FEL2017, Sante Fe, NM, USA, paper TUP059, this conference.
- [22] O. Malyshev, K. Marinov, K. Middleman, N. R. Thompson, R. Valizadeh, and P. H. Williams, “The Applicability of NEG Coated Undulator Vessels for the CLARA FEL Test Facility,” in *Proc. of IPAC2017*, 2017, pp. 3181–3183, <https://doi.org/10.18429/JACoW-IPAC2017-WEPIK100>.
- [23] H. M. C. Cortes, D. J. Dunning, M. D. Roper, and N. R. Thompson, “Optical Beam-Quality Analysis of the CLARA Test Facility Using Second Moment Analysis,” 2017, presented at FEL2017, Sante Fe, NM, USA, paper WEP062, this conference.
- [24] J. K. Jones and N. R. Thompson, “Beam Based Alignment Studies for the CLARA FEL Test Facility,” in *Proc. of IPAC2017*, 2017, pp. 1971–1974, <https://doi.org/10.18429/JACoW-IPAC2017-TUPIK108>.

SCLF: AN 8-GEV CW SCRF LINAC-BASED X-RAY FEL FACILITY IN SHANGHAI

Z.Y. Zhu¹, Z.T. Zhao^{2†}, D. Wang², Z. Liu¹, R.X. Li³, L.X. Yin² and Z.H. Yang² for the SCLF Team

¹ShanghaiTech University, Shanghai 201210, China

²Shanghai Institute of Applied Physics, CAS, Shanghai 201800, China

³Shanghai Institute of Optics and Fine Mechanics, CAS, Shanghai 201800, China

Abstract

The Shanghai Coherent Light Facility (SCLF) is a newly proposed high repetition-rate X-ray FEL facility, based on an 8-GeV CW superconducting RF linac. It will be located at Zhangjiang High-tech Park, close to the SSRF campus in Shanghai, at the depth of ~38m underground and with a total length of 3.1 km. Using 3 phase-I undulator lines, the SCLF aims at generating X-rays between 0.4 and 25 keV at rates up to 1MHz. This paper describes the design concepts of this hard X-ray user facility.

INTRODUCTION

We are currently witnessing a rapid progress in X-ray free electron laser (XFEL) development across the globe, among which the superconducting RF (SCRF) linac based high-repetition-rate XFELs are leading ones. European XFEL [1] achieved its first lasing in early May 2017, and started operational phase in early July 2017. The LCLS-II [2] construction is now under way, and is scheduled to become operational in 2020. An energy upgrade proposal to LCLS-II, the LCLS-II-HE project, has also been initiated [3]. Considering this international context, and in response to the rapidly growing demands from Chinese science community on the high peak and high average brightness X-ray sources, and the needs from Zhangjiang Comprehensive National Science Center in Shanghai, a high repetition-rate XFEL, the Shanghai Coherent Light Facility (SCLF), was proposed.

SCRF linac. As shown in Fig. 1, it will be located at the Zhangjiang High-tech Park of Shanghai Pudong, closely connected to the campuses of the Shanghai Synchrotron Radiation Facility, the Shanghai Advanced Research Institute and the ShanghaiTech University. The SCLF major facility will be installed in the tunnels at the depth of ~38m underground and with a maximum length of 3.1 km.

The SCLF will have five shafts, one accelerator tunnel and three parallel undulator tunnels and the following three beamline tunnels, with each undulator tunnel capable to accommodate two undulator lines. In its initial phase, the SCLF consists of an 8 GeV CW SCRF linac, three undulator lines, three following FEL beamlines, and ten experimental end-stations. The end-stations are distributed in the near experimental hall (NEH) in Shaft 4 and the far experimental hall (FEH) in Shaft 5. The initial three undulator lines will be located in two undulator tunnels. Using these three undulator lines, the SCLF aims at generating brilliant X-rays between 0.4 and 25 keV at pulse repetition rates up to 1 MHz.

The proposed SCLF project is planned to start its civil construction within one year immediately after its preliminary design report is approved by the central government. The whole SCLF project is expected to be completed in 7 years, and then the user experiments can start right after the completion of the beamline and experimental station commissioning.

MACHINE LAYOUT AND MAIN PARAMETERS

Figure 2 shows the layout of the SCLF. The SCLF accelerator complex comprises the following two parts: a photo-injector which generates a bright electron beam with repetition rate up to 1 MHz and accelerates it to ~100 MeV; The main SCRF linear accelerator, where the electron beam is accelerated to about 8 GeV and longitudinally compressed to about 1.5 kA with two compressors working at energies of 270MeV and 2.1GeV respectively.

The photo-injector is based on the VHF photocathode gun similar to that developed at LBNL [4]. On the basis of LCLS-II experience, the design draws heavily to produce a 10ps (FWHM) long pulse with 100 pC bunch charge and a RMS normalized transverse emittance of 0.4 mm-mrad at 90-120 MeV. The bunch repetition rate is designed up to 1 MHz during the operation. The SCLF injector includes a 216 MHz photocathode VHF gun, a 1.3 GHz buncher, a 1.3 GHz single 9-cell cavity cryomodule, a 1.3 GHz eight 9-cell cavities standard cryomodule, a laser heater, and the beam diagnostics. A laser heater system is employed to

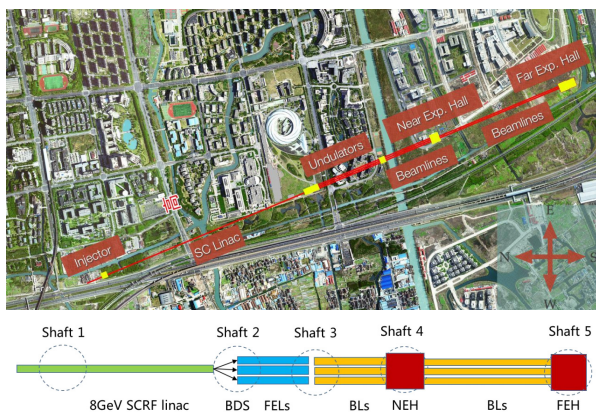


Figure 1: Aerial view of the SCLF project.

This proposal was officially approved by the central government of China in April 2017. The SCLF is an X-ray FEL facility based on an 8 GeV continuous-wave (CW)

† zhaozt@sinap.ac.cn

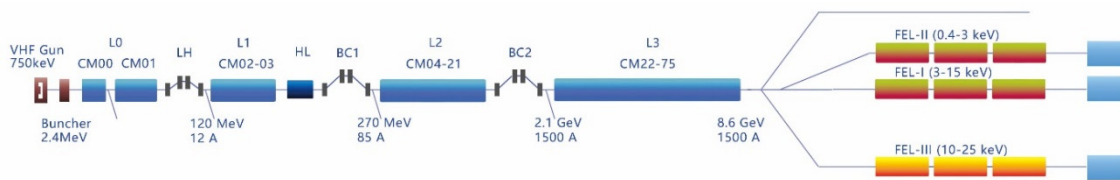


Figure 2: Machine layout of the SCLF.

suppress the micro-bunching instability and control the RMS deviation and the distribution shape of sliced beam energy spread by choosing the laser spot and the peak power. Moreover, the injector also includes photocathode system, drive laser system, solid state RF power sources, power supplies, vacuum and mechanic support systems.

The function of the SCRF linear accelerator system is to accelerate the 10 ps long electron bunch exiting the photo-injector to 8 GeV and to compress the beam to its final duration and peak current. Depending on the FEL lasing requirements, an electron bunch length of 70 fs (FWHM) and a peak current of 1.5 kA or higher can be provided with 100 pC of charge. The horizontal and vertical normalized emittances at the end of the linac should not exceed 0.4 mm-mrad to achieve the desired photon throughput.

At the exit of the photo-injector, the ~100 MeV electrons enter the L1 linac section (2 cryomodules) where they are accelerated to 326 MeV. Off-crest acceleration creates the correlated energy spread along the bunch needed to compress it in the first compressor BC1. Two 3.9 GHz SCRF cryomodules tuned at the 3rd harmonic of 1.3 GHz are placed right before the first bunch compressor BC1. The function of the harmonic cavities is to provide cubic corrections of the correlated momentum distribution along the bunch in presence of the photo-injector and the magnetic compressors non-linearity.

The L2 linac section (18 cryomodules) is located between the first and second bunch compressor, which accelerates the electron beam from 270 MeV to 2.1 GeV. They also provide the residual energy chirp needed for the second compressor BC2. After BC2 the beam is accelerated to its final 8 GeV energy in the L3 linac section (54 cryomodules). The baseline parameters for the cavity unloaded quality factor Q_0 and the CW accelerating gradient of the standard cryomodule are 2.7×10^{10} and 16 MV/m respectively.

As shown in Fig. 2, the beam distribution system (BDS) starts from the end of linac tunnel, passes through the Shaft 2 and ends in the undulator tunnels. The first three undulator lines, referred to as the FEL-I, FEL-II and FEL-III, will be installed in two of the three undulator tunnels. The FEL-I will deliver X-rays with photon energies from 3 keV to 15 keV; The FEL-II will cover the photon energy range of 0.4-3 keV; And the FEL-III will cover the photon energy range of 10-25 keV.

All the undulators of SCLF have been chosen to be variable gap one. The wavelength can be tuned by changing the undulator gap at constant electron beam energy. The FEL-I and FEL-II lines are based on out vacuum planar, hybrid permanent magnets type undulators. The magnetic lengths of the individual undulator are 5.0 m

(26 mm undulator period) for the FEL-I and 4.0 m (68 mm undulator period) for the FEL-II, respectively. FEL-III undulator is designed to be superconducting undulator with period of 16mm to cover 10-25 keV photon energy range with the 8 GeV electron beam energy. Cavity beam position monitors, quadrupoles, correctors and quadrupole movers are installed between the undulator segments to monitor and correct the electron trajectory.

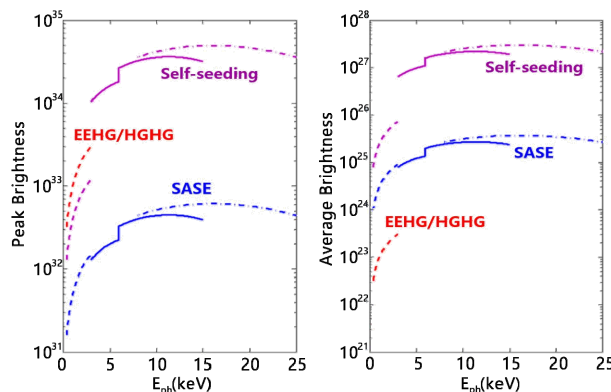


Figure 3: Peak and average brightness of the SCLF in units of photons/mm²/mrad²/s/0.1%BW. The repetition rate of the external seeding and self-seeding is assumed to be 10 kHz and 1 MHz in the calculation.

At the hard X-ray wavelength, the FEL process requires the straightness of the electron trajectory in the undulators to stay within 1 μ m (RMS value over the undulator length). This requirement is beyond the state-of-the-art of present surveying techniques, a beam based alignment [5] procedure will be required to achieve the desired performance.

The accessible SCLF photon brightness are plotted in Fig. 3 versus the photon energy accessible from the FEL-I, FEL-II and FEL-III. The main parameters of the SCLF project are summarized in Table 1.

Both the FEL-I and the FEL-III will run in the SASE mode, with self-seeding option [6, 7]. The high brightness SASE (HB-SASE) mode [8] will also be implemented in FEL-I. In FEL-II, several operation schemes will be made possible, e.g. SASE, self-seeding, cascaded EEHG [9, 10], and polarization control with EPUs as an afterburner.

In the initial phase, the SCLF project will provide three X-ray beam paths, one for each undulator line. These beam paths, shown schematically in Fig. 4, include the components necessary to filter, attenuate and collimate the X-ray beam. Ten experimental end-stations, distributed in the NEH and the FEH, covering the research fields of physics, chemistry, materials, life science, and extreme environment science, are planned.

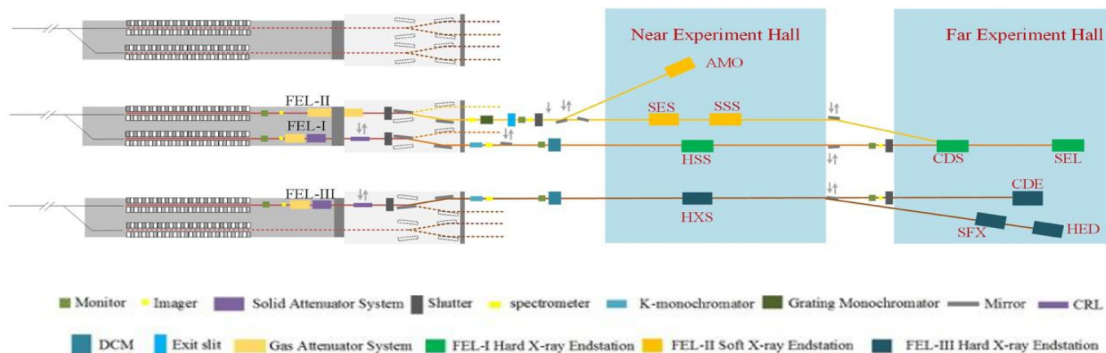


Figure 4: Initial FEL beamlines and the ten end-stations. AMO: atomic, molecular, and optical physics; CDE: Coherent Diffraction End-station; CDS: Coherent diffraction end-station for single particle and biomolecules; HED: High Energy Density science; HSS: Hard X-ray Scattering Spectrometer; HXS: Hard X-ray Spectroscopy; SEL: Station of Extreme Light; SES: Spectrometer for Electronic Structure; SFX: Serial Femtosecond Crystallography End-station; SSS: Soft X-ray Scattering Spectrometer.

Table 1: Main Parameters of the SCLF

Parameters	Nominal	Objective
Beam energy/GeV	8	4-8.5
Bunch charge/pC	100	10-300
Peak current/kA	1.5	0.5-3
Slice emittance/ $\mu\text{m-rad}$	0.4	0.2-0.7
Max repetition rate/MHz	1	1
Beam power/MW	0.8	0-2.4
Photon energy/keV	0.4-25	0.4-25
Pulse length/fs	66	3-600
Peak brightness*	5×10^{32}	10^{31} - 10^{33}
Average brightness*	5×10^{25}	10^{23} - 10^{26}
Total facility length/km	3.1	3.1
Total tunnel length/km	5.7	5.7
Tunnel diameter/m	5.9	5.9
2K Cryogenic power/kW	12	12
RF power/MW	2.28	3.6

* Photons/ $\mu\text{m}^2/\text{rad}^2/\text{s}/0.1\% \text{BW}$

The SCLF scientific instruments will enable the probing of structural dynamics of materials, including the physical and chemical behaviours in biomaterials and condensed matters, in the fundamental length ($\sim \text{\AA}$) and temporal ($\sim \text{fs}$) scales.

As shown in Fig. 4, a variety of advanced techniques are employed in the initial 10 end-stations, including Coherent Diffraction Imaging (CDI), time-resolved photoelectron spectroscopy/microscopy, ultrafast x-ray absorption/emission scattering spectroscopy, Serial Femtosecond Crystallography (SFX), etc. These ten end-stations in the first installation phase are decided as the results of the demanding from the wide scientific user communities. Among these 10 end-stations, the Station of Extreme Light (SEL), which combines the hard X-ray FEL with a 100 PW laser, is aimed at pioneering cutting-edge researches on strong field QED physics.

SUMMARY

The rapid development of new XFEL user facilities around world has opened up a new paradigm for X-ray sciences. The proposed Shanghai Coherent Light Facility is aimed to join this exclusive club as one of the most advanced user facilities by delivering fs-scale X-ray pulses from 0.4 keV to 25 keV, up to million pulses per second. The 8 GeV SCRF linac based SCLF will enable the probing of structural and functional properties of materials, including the physical and chemical behaviours in condensed matters and biomaterials, in the fundamental length ($\sim \text{\AA}$) and temporal ($\sim \text{fs}$) scales. In addition, SCLF will work together with a 100PW laser facility to serve for a dedicated end-station for strong field QED physics.

REFERENCES

- [1] M. Altarelli, R. Brinkmann, M. Chergui *et al.*, The European X-Ray free-electron laser, Technical Design Report, DESY, 2007.
- [2] J. N. Galayda, *Proc. of IPAC'14*, 2014: 935.
- [3] T. Raubenheimer, Workshop on Scientific Opportunities for Ultrafast Hard X-rays at High Rep. Rate, 2016.
- [4] K. Baptiste, *et al.*, *Nucl. Instr. Methods Phys. Res. Sect. A*, 599, 9-14, 2009.
- [5] P. Emma, *et al.*, *Nucl. Instr. Methods Phys. Res. Sect. A*, 429, 407-413, 1999.
- [6] J. Feldhaus, *et al.*, *Opt. Commun.* 140, 341-352, 1997.
- [7] G. Geloni, *et al.*, DESY 10-033, 2010.
- [8] B.W. McNeil, *et al.*, *Phys. Rev. Lett.*, 110, 134802, 2013.
- [9] Z.T. Zhao, *et al.*, *Science bulletin*, 61, 720-727, 2016.
- [10] Z.T. Zhao, *et al.*, *Nuclear Science and Techniques*, 28, 117, 2017.

Content from this work may be used under the terms of the CC BY 3.0 licence (© 2018). Any distribution of this work must maintain attribution to the author(s), title of the work, publisher, and DOI.

DESIGN OF APPARATUS FOR A HIGH-POWER-DENSITY DIAMOND IRRADIATION ENDURANCE EXPERIMENT FOR XFEL APPLICATIONS

S. P. Kearney*, D. Shu, T. Kolodziej, K.-J. Kim, R. Lindberg, S. Stoupin†, D. A. Walko, J. Wang, Y. Shvyd'ko, Argonne National Laboratory, Lemont, IL 60439, USA

Abstract

We have designed apparatus for an irradiation setup capable of achieving greater than 10 kW/mm^2 power density of x-rays on a diamond single crystal under ultra-high-vacuum conditions. The setup was installed at the 7-ID-B beamline at the Advanced Photon Source (APS) for an irradiation experiment, demonstrating the capability of diamond to endure x-ray free electron laser oscillator (XFEL) levels of irradiation ($\geq 10 \text{ kW/mm}^2$) without degradation of Bragg reflectivity [1]. Focused white beam irradiation ($50 \mu\text{m} \times 20 \mu\text{m}$ spot size at 12.5 kW/mm^2 power density) of a diamond single crystal was conducted for varying durations of time at different spots on the diamond in a vacuum environment of 1×10^{-8} Torr and an additional irradiation spot in a “spoiled” vacuum environment of 4×10^{-6} Torr. Here we present the apparatus used to irradiate the diamond consisting of multiple subassemblies: the fixed masks, focusing optics, gold-coated UHV irradiation chamber, water-cooled diamond holder, chamber positioning stages (with sub-micron resolution), and the scattering detector.

DIAMOND IRRADIATION APPARATUS

A type IIa single crystal diamond in the [100] orientation was irradiated with focused white beam x-rays ($50 \mu\text{m} \times 20 \mu\text{m}$ spot size at 12.5 kW/mm^2 power density) to demonstrate the capability of diamond to endure XFEL levels ($\geq 10 \text{ kW/mm}^2$) of irradiation without degradation of Bragg reflectivity [1]. The diamond was irradiated at different spots on the diamond for varying durations and environments, which required scanning stages. In addition, two vacuum environments were tested, 1×10^{-8} Torr and a single irradiation spot with a “spoiled” vacuum environment of 4×10^{-6} Torr.

Figure 1(a) shows the entire apparatus, which was temporarily installed at the 7-ID-B beamline at the Advanced Photon Source (APS) [2]. The main components of the apparatus are identified in Fig. 1(a) and will be discussed in detail. Figure 1(b) is a diagram of the entire beamline layout showing the distances of the main components from the x-ray source.

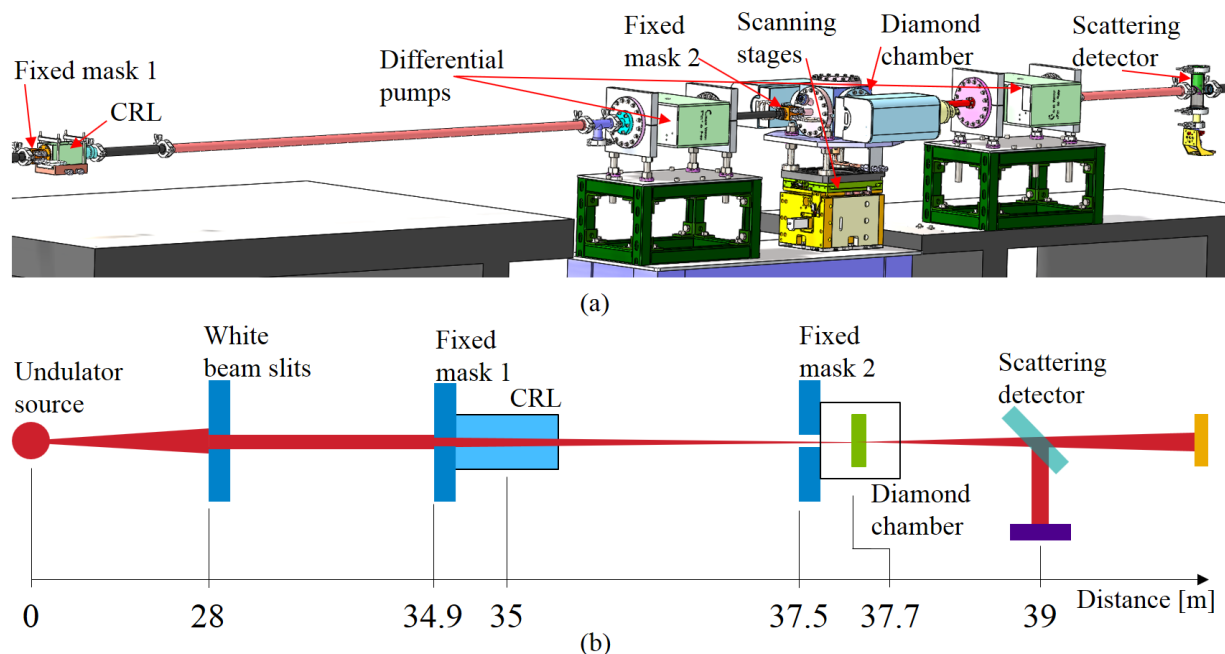


Figure 1: (a) Model of the diamond irradiation apparatus. The beam direction is from left to right and the main components are identified. (b) Diagram of the setup showing the distances from the source of the main components.

* skearney@aps.anl.gov

† Now at Cornell High Energy Synchrotron Source, Cornell University, Ithaca, NY 14853, U.S.A.

Content from this work may be used under the terms of the CC BY 3.0 licence (© 2018). Any distribution of this work must maintain attribution to the author(s), title of the work, publisher, and DOI.

Water Cooled Fixed Masks and CRL

Figure 2 shows the two water cooled fixed masks, and the compound refractive lens (CRL) holder. Both masks were made from Glidcop™ and the mask apertures were machined using wire electrical discharge machining (EDM). The first water cooled mask (3) in Figure 2, has a minimum 1 mm diameter aperture and 4° sloped wall to protect the entrance aperture of the CRL holder (2). Standard Kwik-Flange™ flanges were machined into the mask. The CRL holder, which was directly mounted to the first mask, was also water cooled by an oxygen free high conductivity (OFHC) copper mounting base (1). The second fixed mask (4) is mounted to the vacuum chamber and had an aperture 1 mm larger than the diamond profile to protect the apparatus during diamond scanning process. Knife edge flanges were machined into the single Glidcop™ piece.

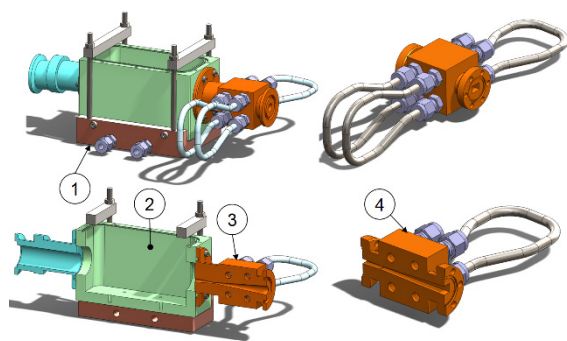


Figure 2: On the left is the CRL holder and first fixed mask and on the right is the second fixed mask, section views are shown on the bottom row. The listed components are: 1) CRL water cooled mounting base, 2) CRL holder, 3) first fixed mask, and 4) second fixed mask.

Gold Coated Diamond Irradiation Chamber

Figure 3 shows the diamond irradiation chamber (2) with an isometric view on the top and a section view on the bottom. The entire chamber was designed to move, eliminating the need for UHV compatible stages for the diamond scanning. The chamber assembly was mounted using spherical washers (3) to level and align the height. Two (75S, Gamma Vacuum) ion pumps (1) were positioned on the sides of the irradiation chamber and used to reach 1×10^{-8} Torr, compared to 4×10^{-6} Torr without these pumps (to provide a comparison of diamond's endurance in a lower-quality vacuum). In addition, differential pumps (100 L, Gamma Vacuum) were positioned upstream and downstream of the chamber, to protect the chamber from the lower vacuum of the CRL and scattering detector chambers. The chamber internal walls (5) were coated with a 50 μm thick gold layer to avoid carbon contamination from scattered x-rays hitting the stainless steel components of the vacuum chamber [3]. The diamond holder (4) was water cooled using an OFHC copper cooling finger (6), which was brazed to a stainless steel flange.

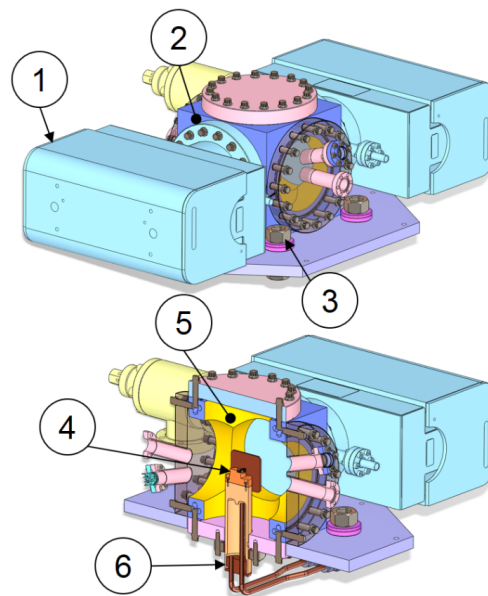


Figure 3: On the top is an isometric view of the diamond irradiation chamber and on the bottom is a section view along the beam vertical plane. The listed components are: 1) 75 L ion pump, 2) diamond irradiation chamber, 3) spherical washers, 4) diamond holder, 5) inner chamber wall gold coating, and 6) water cooled cooling finger.

Diamond Holder

Figure 4 shows the OFHC copper diamond holder (2). It was mounted to the cooling finger with 100 μm thick silver foil (1) in-between to decrease thermal contact resistance. A strain limited clamp was used to hold the diamond (3). The diamond also had 100 μm thick silver foil on either side to reduce strain as well as decrease thermal contact resistance. An OFHC copper shield (4) was placed on either side of the diamond to stop x-ray scattering towards components that were not gold coated (the outboard shield was removed from the image for clarity).

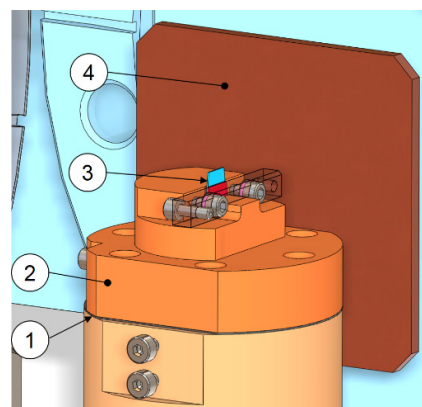


Figure 4: The diamond holder components: 1) Silver foil, 2) OFHC copper diamond holder, 3) CVD diamond, and 4) OFHC copper shield.

Scanning Stages

For scanning the sample during irradiation the entire assembly is designed to move in the plane perpendicular to the beam. Moving the entire assembly rather than the sample greatly reduces the complexity inside the chamber and again assures a cleaner UHV environment by reducing the number of internal wires, metallic objects, and screw hardware. The scanning stages can be seen in Figure 5, and consisted of a vertical (1) and horizontal stage (3) with sub-micron resolution, 12.7 mm travel range, and 90 kg load capacity; in addition, a manual rotation stage (4) was used to align the diamond surface perpendicular to the beam. The vertical and horizontal stages were driven by stepper motors with 50:1 harmonic drives (PK523HPB-H50S, Oriental Motor Corp.). Closed loop control of the diamond scans was performed using EPICS experiment-control software and two (MicroE MII6000, Celera Motion) linear optical grating encoders (2).

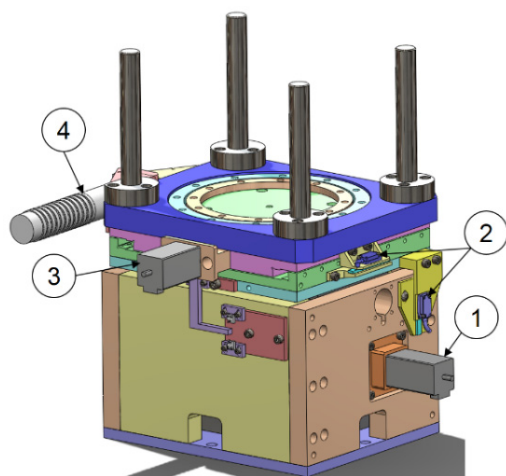


Figure 5: The scanning stages: 1) vertical stage, 2) MicroE optical encoders, 3) horizontal stage, and 4) manual rotation stage.

Scattering Detector

Figure 6 shows the scattering detector. It used a thin aluminium foil sheet (1) mounted at 45° to the beam plane and a calibrated photo diode (3) next to a beryllium window (2) to measure x-ray flux.

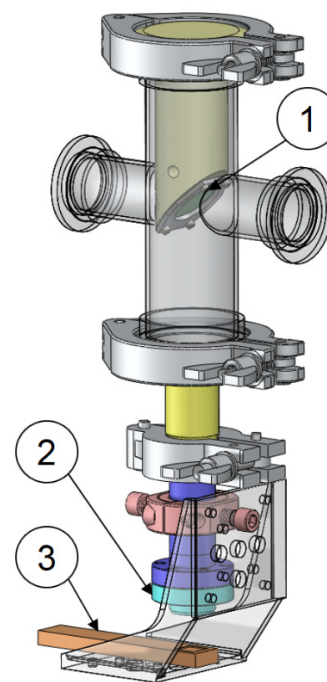


Figure 6: The scattering detector: 1) thin aluminium foil mounted at 45°, 2) beryllium window, and 3) pin diode detector.

CONCLUSION

A diamond irradiation setup was designed to handle high power density x-rays. The experiment used 8 keV x-rays with a power density of 12.5 kW/mm² and a 50 μm x 20 μm spot size. The diamond was irradiated in 1x10⁻⁸ Torr and 4x10⁻⁶ Torr vacuum environments. During irradiation, the diamond was scanned over an area of 50 μm x 60 μm for 12 hours in each environment. This resulted in an equivalent 4-hour irradiation over the x-ray spot size.

REFERENCES

- [1] T. Kolodziej, *et al.*, *Free Electron Laser Conf.* 2017.
- [2] D.A. Walko *et al.*, *AIP Conf. Proc.* 1741, 030048 (2016).
- [3] H. Ohashi, *et al.*, *AIP Conf. Proc.* 1741, 040023 (2016).

SYNCHRONIZED MID-INFRARED PULSES AT THE FRITZ HABER INSTITUTE IR-FEL

R. Kießling, S. Gewinner, W. Schöllkopf, M. Wolf, A. Paarmann
Fritz-Haber-Institut der Max-Planck-Gesellschaft, Berlin, Germany

Abstract

The combined application of FEL radiation and femtosecond table-top lasers for two-color spectroscopy demands an accurate pulse synchronization. In order to employ the infrared FEL at the Fritz Haber Institute for non-linear and time-resolved experiments, an RF-over-fiber-based timing system has been established. Using a balanced optical cross-correlation scheme, we determined an FEL micro-pulse timing jitter of 100 - 200 fs (rms). The long-term timing drift was found to be well correlated to the energy fluctuations of the accelerated electron bunches.

By means of sum-frequency generation cross-correlation, we directly measure the FEL pulse shape at different cavity detunings. For large cavity detuning, narrowband IR radiation ($\sim 0.3\%$ FWHM) can be generated and utilized for high-resolution non-linear spectroscopy. On the other hand, sub-picosecond pulses are provided at small detuning, which are well-suited for time-resolved measurements. At intermediate detuning values, we observe the build-up and dynamics of multipulses that result in the well-known limit-cycle power oscillations.

INTRODUCTION

Vibrational excitations are a fundamental property of molecules, clusters and solids and therefore contain material-specific information. Modes of vibrations carry kinetic energy of few meV, consequently optical excitation demands infrared (IR) wavelengths. Since its first demonstration, free-electron lasers are an ideal tool for infrared spectroscopy due to the frequency-tunable narrow-bandwidth radiation output. So far, the infrared FEL at the Fritz Haber Institute (FHI) has been used to investigate (static) vibrational spectra of gas-phase ions, bio-molecules, metal-clusters and polar dielectrics. Further investigations will employ the intense FEL IR radiation also for non-linear and time-resolved two-color spectroscopy experiments. To that end, an accurate synchronization of FEL and table-top laser pulses is required for sub-ps resolved measurements. In the following, the concept, timing stability and first application of the synchronized laser system is presented.

EXPERIMENTAL SYSTEM

Free-Electron Laser

Since the start of user operation in 2013, the mid-IR free-electron laser oscillator at the FHI provides intense, pulsed radiation in the wavelength region from 3 to 50 μm [1]. The electron bunches emitted from a thermionic cathode are accelerated by two subsequent normal-conducting linacs to

kinetic energies between 15 and 50 MeV, depending on the desired IR spectral range. The master oscillator (MO), an 2.99 GHz RF source, drives the electron gun at the third sub-harmonic, producing few-ps short micro-bunches of 1 GHz repetition rate within $\sim 10\ \mu\text{s}$ long macro-bunches at a 10 Hz rate. The following electron wiggling in a planar hybrid-magnet undulator with parameter $K = 0.5 - 1.6$ generates linearly polarized, ps-long IR pulses with a gap-scan tunable wavelength. Besides a 1 GHz micro-pulse rate, reduced repetition modes of 27.8 MHz and 55.5 MHz are available that are required for time-resolved studies. Adjustment of the optical cavity length is an additional degree of freedom to set the spectrum bandwidth as low as 0.3 %.

Synchronization Setup

As table-top laser we employ a high-power Terbium-doped fiber oscillator (FO) providing ~ 100 fs, near-infrared ($\lambda = 1055$ nm) pulses with up to 50 nJ pulse energy. The repetition rate of 55.5 MHz is matched to a reduced electron micro-bunch rate, corresponding to two FEL pulses circulating in the 5.4 m long FEL cavity simultaneously. For high-precision synchronization, the MO signal of 2.99 GHz is distributed from the FEL vault to the user lab via a stabilized RF-over-fiber link approximately 100 m long. This reference clock transfer system is a low-jitter (rms < 7 fs [10 Hz-10 MHz]) and low-drift (< 40 fs/day) RF transmission turn-key solution utilizing optical fiber connections [2].

The FO is locked to the MO using the 54th harmonic of the table-top laser output. Adjustment of the FO repetition-rate is done by temperature control of the fiber cage for coarse tuning and a piezo motor for fine setting of the fiber cavity length. In order to manage multiple synchronized situations due to phase-locking of the table-top laser to a higher frequency reference clock, a phase-shifter of the 2.99 GHz signal is added using the photodiode signal of the FO and a separately fiber-link transferred 55.5 MHz RF signal from the FEL machine (superperiod-lock). The shifter is used to adjust the temporal overlap of the optical pulses in the experimental setup. The fiber cables of the synchronization system going along the beamline from the FEL vault to the user lab are subject to ambient temperature and humidity fluctuations, which are compensated by the system.

Balanced Optical Cross-Correlation

Characterization of the synchronization stability of the FEL-table-top laser system is performed by two-color balanced optical cross-correlation (BOC) [3]. Utilizing a non-linear crystal (GaSe) for sum-frequency generation (SFG), the FEL and fiber oscillator pulses are overlapped twice within the same crystal, but with slightly different temporal

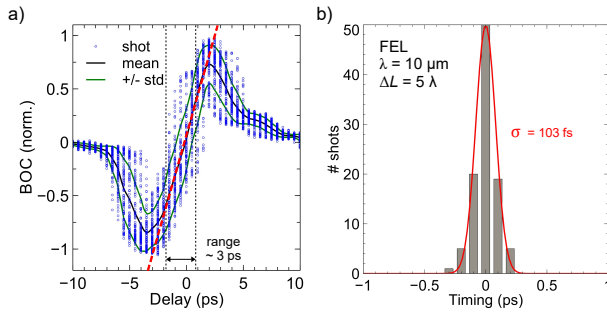


Figure 1: Jitter determination by balanced optical cross-correlation. (a) Measured BOC curve by scanning the FEL-table-top laser pulse delay τ with 100 FEL macro-pulses per delay point. The linear dynamic range of the tool is about 3 ps. Analysis of the delay value at zero BOC crossing informs about the timing, which is shown in the histogram plot in (b). By fitting a Gaussian distribution, a jitter value of $\sigma \sim 100$ fs (rms) is extracted.

overlap Δt . After separation of both SFG signals from the fundamental pulses, the balanced cross-correlation value is obtained by normalizing and subtraction of the SFG1 and SFG2 intensity. Scanning the relative delay τ between FEL and table-top laser pulse gives the BOC curve. In contrast to a single cross-correlation, the absolute delay between the pulses is determined without sign ambiguity. For a properly chosen fixed time delay Δt , the BOC signal is linear within a certain range around $\tau = 0$. By statistical analysis, the FEL shot-to-shot micro-pulse timing jitter can be extracted from the shift of the zero-crossing position. The slope of a linear fit near the zero-crossing provides the calibration coefficient of the BOC curve. Setting the time τ to a constant value within the center of the linear range and converting the BOC value measured over a long period of time into a temporal information offers the timing drift of the FEL micro-pulses with respect to the FO pulses. Results shown below were obtained at a FEL wavelength of $10 \mu\text{m}$ with $\sim 1 \mu\text{J}$ micro-pulse energy at a repetition rate of 27 MHz (or 1 GHz, respectively) and ~ 5 nJ FO pulse energy. Since phase-matched SFG is used, standard photodiodes are sufficient for signal detection.

TIMING CHARACTERISTICS

A typical shot (i.e. macro-pulse)-resolved BOC curve is shown in Fig. 1a. Analyzing 100 subsequent shots, the root mean square value of the timing shift is about $\sigma = 200 - 300$ fs in the case of 1 GHz FEL micro-pulse rate and $\sigma \sim 100$ fs in 27 MHz low-repetition mode (Fig. 1b). No (significant) dependence of the optical pulse jitter on FEL wavelength (different undulator gap size for given electron energy) or FEL cavity length (mirror translation) was found. Considering that the synchronization relies on electronic phase-locking, a high timing stability is achieved that is suitable for sub-ps resolved FEL-table-top experiments.

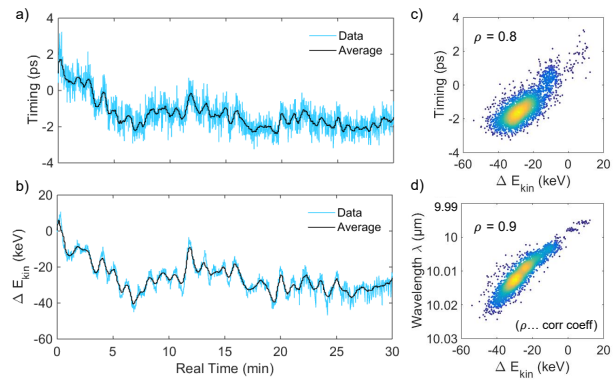


Figure 2: Drift of FEL pulse timing and energy. (a) Micro-pulse timing fluctuations measured by BOC and moving average with half minute window and (b) corresponding changes in kinetic energy of electron bunches as determined by beam-position monitoring. Nominal electron energy is 36.5 MeV. Also shown are correlation plots of kinetic energy vs. timing (c), and vs. FEL radiation wavelength (d), respectively.

The long-term temporal shift is determined to be 3 ps per 15 min peak-to-peak (Fig. 2a). Simultaneously, the kinetic energy of the accelerated electron bunches was monitored (Fig. 2b). As depicted in Fig. 2c, a clear linear correlation (coefficient $\rho = 0.8$) consists between changes of the electron energy after the two linacs (up to 0.1 %) and the timing drift. Since the magnetic undulator field is fixed during this measurement, the kinetic energy fluctuations are directly reproduced in the shift of the FEL center wavelength (Fig. 2d). Consequently, the drifting temporal overlap is mainly caused by amplitude and/or phase fluctuations in the accelerating fields of the linacs; thermal drifts in the system are of minor impact.

FEL PULSE BEHAVIOR

An application of the low-jitter synchronized laser is to study the evolution of the FEL micro-pulse shape within the macro-pulse. The measurement is done by recording the

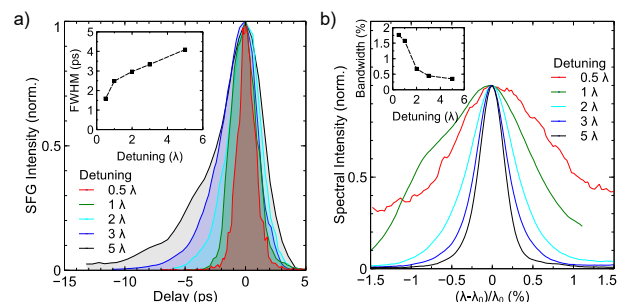


Figure 3: Cavity detuning dependence of FEL micro-pulse. (a) Temporal shape measured by SFG cross-correlation and extracted FWHM duration, (b) Spectral structure and bandwidth.

Content from this work may be used under the terms of the CC BY 3.0 licence (© 2018). Any distribution of this work must maintain attribution to the author(s), title of the work, publisher, and DOI.

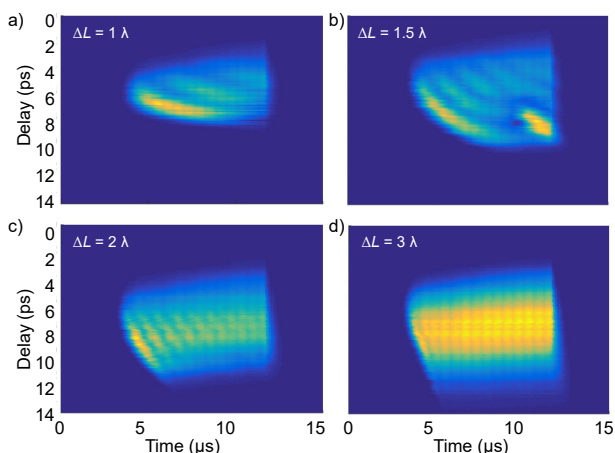


Figure 4: Evolution of the micro-pulse shape within a macro-pulse of the FEL oscillator for different cavity detunings ΔL . Data are measured by SFG cross-correlation. The optical macro-pulse is about 10 μs long, ending at around 12 μs .

(single) sum-frequency cross-correlation intensity during a complete macro-pulse while scanning the delay between FO pulse and FEL micro-pulse. Since the temporal duration of the FO pulse is much shorter than that of the FEL micro-pulse, the SFG signal resembles the actual intensity envelope of the FEL pulse. The dependence of the pulse shape on the cavity detuning is depicted in Fig. 3a. While the electron macro- and micro-bunch durations are unchanged, the length of the optical micro-pulses increases for larger detuning values. The corresponding narrowing of the spectral bandwidth can be observed in Fig. 3b. Additionally, there is a transition from a Gaussian to an asymmetric micro-pulse shape with an exponential leading edge. This behavior is caused by a change of the temporal overlap between the short optical pulses and electron bunches [4]. Shorter cavity lengths shift the free electron gain medium to the edge of the IR pulse that is amplified.

Further details of the pulse evolution are revealed by analyzing the completely delay- and time-resolved SFG cross-correlation data, shown in Fig. 4 and 5a, where the FEL cavity detuning is a highly sensitive parameter. At the beginning of the macro-pulse, optical micro-pulses begin to develop until a steady-state duration and intensity saturation is reached after a number of undulator passes. The temporal end of the macro-pulse lasing is mainly determined by the electron macro-bunch switch-off, but also dependent on the cavity quality factor. For small detunings, pronounced power oscillations within a macro-pulse appear. Period and strength of the intensity modulation (up to 50%) diminish with increasing cavity detuning.

The power oscillations result from the formation of equally-spaced sub-pulses within a micro-pulse as can be seen in cross-correlation (Fig. 5b) as well as auto-correlation delay scans (Fig. 6). These so-called 'limit-cycle' oscillations (Fig. 5c) were previously observed also at another IR FEL oscillator as a consequence of the short optical and elec-

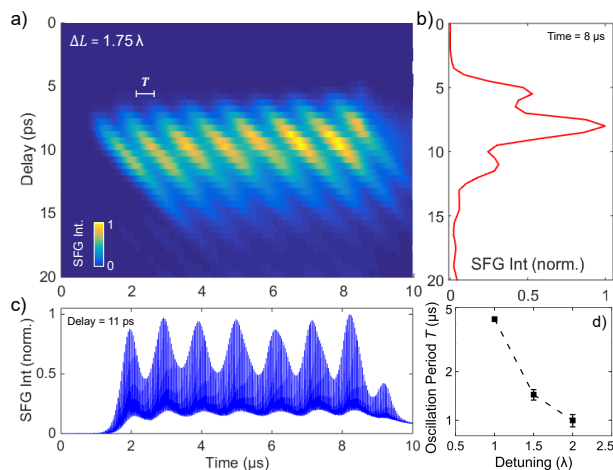


Figure 5: FEL pulse shape in the case of limit-cycle oscillations obtained by cross-correlation measurement. The cross-sections from the 2D plot in (a) along a constant time of 8 μs within the macro-pulse (b) and a constant delay of 11 ps (c) clearly show the sub-pulse structure of the micro-pulses and power oscillations within the macro-pulse, respectively. The dependence of the oscillation period on the cavity detuning is depicted in (d).

tron pulses [5]. Due to a velocity difference the optical pulse at saturation loses temporal overlap with the electron bunch. Only at the trailing edge the optical micro-pulse undergoes amplification, resulting in the growth of a sub-pulse. The repeated modulation of the optical group velocity results in the periodic sub-pulse formation as long as there is net gain. Larger detuning values result in lower saturated power so that the modulation depth decreases until a stable output regime with a uniform single long micro-pulse is settled (Fig. 6d).

In contrast to previous experimental investigations of limit-cycle oscillations based on power or auto-correlation measurements (e.g., [5, 6]), the cross-correlation study presented here allows one to follow the evolution of the sub-pulses during subsequent cavity round-trips (i.e., along the macro-pulse timescale). It can be clearly seen how the sub-pulse structure initiates on the trailing edge of the optical micro-pulse and is shifted through the pulse envelope over many passes. The agreement with simulations based on Maxwell-Lorentz theory [6] is apparent.

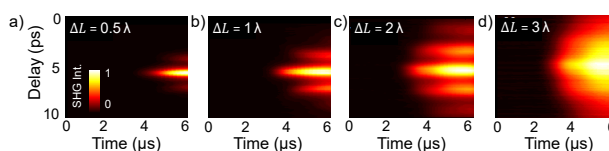


Figure 6: Sub-pulse structure measured by second-harmonic generation (SHG) auto-correlation of the FEL micro-pulses for different detunings ΔL . For shorter cavity lengths, more sub-pulses are formed until their overlap results in a single-peaked long micro-pulse.

CONCLUSION

We implemented a low-jitter ($\sigma \sim 100$ fs) synchronization of a NIR femtosecond table-top laser oscillator to the MIR FEL operating in the wavelength region of 3 to 50 μm at 27 MHz, 55 MHz or 1 GHz repetition rate. This enabled us to study the optical micro- and macro-pulse intensity shape and duration of the FEL by cross-correlation measurements in great detail. In particular, our observations confirm the strong dependence on the cavity detuning. The high-resolution scans clearly resolve the occurring limit-cycle oscillations and sub-pulse formation. Furthermore, the study provides useful information for our ongoing efforts to utilize the short-pulsed FEL radiation for time-resolved spectroscopy.

REFERENCES

- [1] W. Schöllkopf *et al.*, in *Proc. SPIE* 9512, 95121L (2015).
- [2] S. Zorzut *et al.*, in *Proc. FEL2015*, paper MOP043, p.126 (2015).
- [3] S. Schulz *et al.*, *Nat. Commun.* 6, 5938 (2015).
- [4] G. M. H. Knippels *et al.*, *Phys. Rev. Lett.* 83, 1578 (1999).
- [5] D. A. Jaroszynski *et al.*, *Phys. Rev. Lett.* 70, 3412 (1993).
- [6] D. A. Jaroszynski *et al.*, *Nucl. Instr. Meth. Phys. Res. A* 331, 52 (1993).

X-RAY REGENERATIVE AMPLIFIER FREE-ELECTRON LASER CONCEPTS FOR LCLS-II

G. Marcus, Y. Ding, J. Duris, Y. Feng, Z. Huang, J. Krzywinski, T. Maxwell, D. Ratner,
T. Raubenheimer, SLAC, Menlo Park, USA

K.-J. Kim, R. Lindberg, Y. Shvyd'ko, ANL, Argonne, USA

D. Nguyen, LANL, Los Alamos, USA

Abstract

High brightness electron beams that will drive the next generation of high repetition rate X-ray FELs allow for the possibility of optical cavity based feedback. One such cavity based FEL concept is the Regenerative Amplifier Free-Electron Laser (RAFEL). This paper examines the design and performance of possible RAFEL configurations for LCLS-II. The results are primarily based on high-fidelity numerical particle simulations that show the production of high brightness, high average power, fully coherent, and stable X-ray pulses at LCLS-II using both the fundamental and harmonic FEL interactions.

INTRODUCTION

XFELs such as the LCLS, based primarily on Self-Amplified Spontaneous Emission (SASE), are capable of producing extremely bright, transversally coherent, ultra-short pulses suitable for the investigation of ultra-fast chemical and physical processes that operate on the time and length scales of atomic and molecular motion [1, 2]. A characteristic feature of single-pass SASE FELs, however, is poor longitudinal coherence, which results from the initial amplification of incoherent radiation shot-noise [3, 4]. Improvement of the longitudinal coherence is of great practical importance and has been the subject of many recent investigations. Longitudinal coherence can be obtained by seeding the FEL amplifier with sufficiently narrow bandwidth radiation well above the effective shot noise power in the electron beam. Examples of this include self-seeding [5], which has been successfully implemented at LCLS in both the hard [6] and soft X-ray [7] spectral regimes and externally seeded schemes, which are currently being vetted as possible upgrade paths for LCLS-II soft X-rays [8]. Self-seeding, however, nominally suffers from low seed power in an attempt to preserve the electron beam properties important for lasing and is fundamentally still dependent on the noisy SASE process leading to large (100%) seed power fluctuations. External seeding necessarily requires high-harmonic conversions that have inherent challenges [9]. The RAFEL concept, studied here, offers an alternative pathway to the production of stable, fully coherent, high brightness, and high average power X-ray radiation.

Similar to an XFEL oscillator [10], a RAFEL consists of a high repetition rate electron beam, a short undulator and an X-ray crystal cavity (in the case of hard X-rays) to provide optical feedback (see, for example, Fig. 1). However, unlike an oscillator, which operates as a low-gain FEL in a

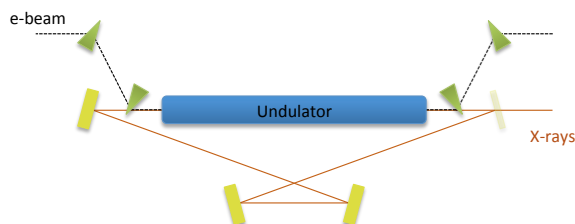


Figure 1: RAFEL concept where the X-ray cavity is wrapped around the entire undulator.

low output coupling cavity, the RAFEL is a high-gain FEL that reaches saturation in only a few round trips in a high output coupling cavity. The RAFEL concept exhibits many additional distinct advantages over an oscillator when considering challenges associated with potential cavity design. The high-gain FEL should be less sensitive to X-ray induced cavity optics degradation and the small number of cavity passes should relax the longitudinal alignment tolerances relative to what is expected with an oscillator cavity. In addition, the RAFEL cavity does not serve the function of defining the transverse radiation mode since the dominant amplified mode is gain guided. This substantially relaxes the cavity opto-mechanical stability and crystal positioning requirements. The main responsibility of the cavity is to recirculate the radiation, which, in turn, seeds successive electron bunches. This optical feedback also allows for a reduced undulator length relative to SASE and can ultimately produce longitudinally coherent X-ray pulses close to the Fourier Transform limit.

This paper reports the results of preliminary RAFEL studies within the context of the LCLS-II project. Numerical particle simulations using the FEL code GENESIS [11] are used to explore, in an ideal sense, possible RAFEL performance at LCLS-II in both the soft and hard X-ray spectral regimes. Results from lasing at both the fundamental FEL resonance wavelength as well as harmonics, using harmonic lasing [12–14], are presented.

SIMULATION STRATEGY

The high repetition rate LCLS-II FEL has been thoroughly studied and the challenges associated with generating, accelerating, and transporting high brightness electron beams to the undulators are well understood and documented (e.g. see [15–17] and references therein). Global optimizations of the electron beam delivery system and SASE FEL performance for charge distributions that span the planned opera-

tional range are ongoing. However, seeded FELs can suffer from pedestal growth caused by microbunching-instability induced energy and density modulations on the electron beam [18]. Running hundreds to thousands of full start-to-end simulations in order to capture these effects for a single RAFEL simulation is untenable. Therefore, the start-to-end simulations were used to define the slice properties of an ideal electron beam that was used in the FEL simulations. The electron beams used in the simulations below had a flat-top current profile and gaussian distributions in energy as well as the transverse dimensions.

Electron beams both with and without the effects of the space charge driven microbunching-instability are included below where only energy modulations on the beam longitudinal profile are included. For simulations with microbunching modulations, the spectrum of the energy structure is modeled to mimic the general microbunching gain spectrum due to longitudinal space charge and has the form

$$p_0 = p + C \sum_i^N \left(\frac{\lambda_0}{\lambda_i} \right)^2 \exp \left(\left(\frac{\lambda_0}{\lambda_i} \right)^2 \right) \sin \left(\frac{2\pi}{\lambda_i} s + \phi_i \right), \quad (1)$$

where p is the momentum, N is the number of individual modulations (typically around 100), λ_0 is the peak wavelength of the microbunching spectrum (here around $2\mu m$), λ_i is a particular microbunching wavelength within the spectral envelope, ϕ is a random phase, and C is an amplitude chosen to adjust the integrated energy spread.

Optical cavity design challenges and constraints, which can be significant, are not considered here. As such, optical propagation through potential cavity geometries was not considered in the simulations, although implementation would be straightforward [19]. The fields are assumed to be re-imaged at the entrance to the undulator in the transverse planes while the various cavity detunings that were studied served to shift the field in time with respect to the arrival of the electrons.

HXR SIMULATION RESULTS

Harmonic lasing was used in order to both increase the performance at the high end of the hard X-ray undulator tuning range (5 keV) and to extend the photon energy reach beyond this limit (9 keV). We present the results from simulation below.

5 keV

The results of high-fidelity start-to-end simulations for the low charge (20 pC) operational mode at LCLS-II were used to define the slice properties of the ideal electron beam that were used in the HXR RAFEL simulations. The slice properties as well as the undulator parameters used for this study can be found in Table 1. For simplicity, the nominal LCLS-II undulator parameters are used here. The X-ray crystal Bragg mirrors that would nominally compose the recirculating optical cavity would provide some frequency filtering due to their limited reflectivity bandwidth [20]. This is modeled in

Table 1: Nominal 20(100) pC Electron Beam and Undulator Parameters for the Baseline LCLS-II Scenario.

Parameter	Symbol	Value	Unit
e-beam energy	E	4.0	GeV
emittance	ϵ	0.15(0.4)	μm
current	I	0.5(1)	kA
energy spread	σ_E	400	keV
beta	$\langle \beta \rangle$	15	m
undulator period	λ_u	26(39)	mm
segment length	L_u	3.4	m
break length	L_b	1.0	m

a very simple way here where a Gaussian filter with resolving power $R = 15,000$ is used to model a reflectivity curve and is applied once before interaction with a fresh electron beam. This filter is also used to model the high output coupling associated with a RAFEL cavity by returning only 10% of the FEL power per round trip. It should be noted that the bandwidth and reflectivity associated with this filter is much larger and less efficient than typical Bragg mirrors. However, it was useful to use these parameters to establish and learn about the RAFEL output dependencies on the various knobs available (gain length, undulator length, cavity detuning, output coupling, etc.). The results of 10 passes through the RAFEL system are shown in Fig. 2, which compares the spectrum of the RAFEL tuned to produce 5 keV radiation at the 3rd harmonic to SASE at the fundamental.

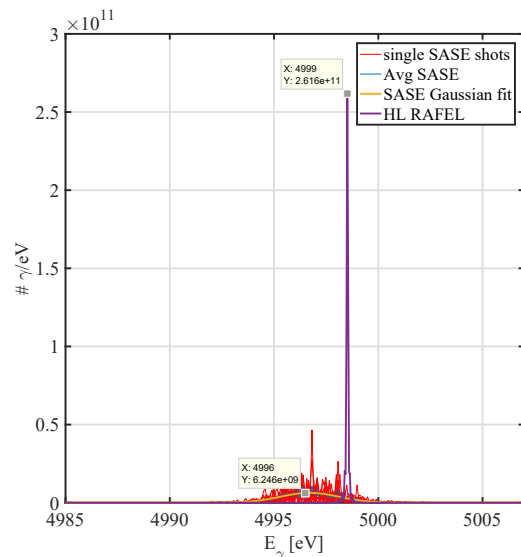


Figure 2: Comparison of the spectral brightness at 5 keV from SASE at the fundamental resonant wavelength to the RAFEL using the 3rd harmonic.

simulations show that a RAFEL can increase the peak spectral brightness of the baseline LCLS-II performance at 5 keV by greater than a factor of 20 at saturation (the electron

Content from this work may be used under the terms of the CC BY 3.0 licence (© 2018). Any distribution of this work must maintain attribution to the author(s), title of the work, publisher, and DOI.

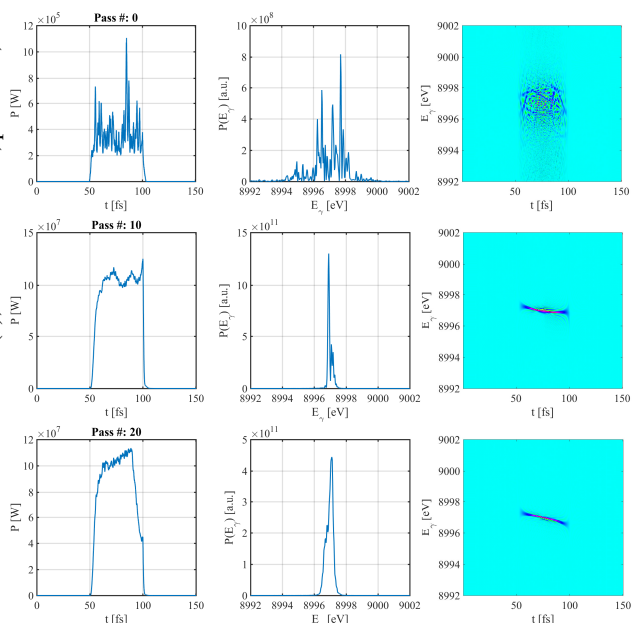


Figure 3: Results for 3rd harmonic lasing at 9 keV in the RAFEL for three passes starting from noise. Top row: pass 0. Middle row: pass 10. Bottom row: pass 20. The first column is the temporal profile of the radiation at the exit of the undulator, the second column is the spectrum and the third column is the Wigner profile.

beam used in the RAFEL simulations was twice as long as the beam used in SASE simulations).

9 keV

The procedure for frequency and amplitude filtering described above is used to investigate the possibility of using a RAFEL at the 3rd harmonic to produce radiation far above the nominal reach of SASE at the fundamental using the 4.0 GeV energy LCLS-II electron beam. Figure 3 shows the results, after optimizing the cavity detuning and undulator length for a 90% output coupling, at various passes during the RAFEL amplification starting from noise. Full three-dimensional coherence is reached with significant power after only 20 passes.

SXR SIMULATION RESULTS

Much progress is being made in the development of high quality optics in the soft X-ray spectral range [21]. While the demonstration of optics possessing the properties necessary for a RAFEL optical cavity are probably far off, it is still instructive to establish a baseline performance to compare against other seeding techniques [8]. To this end, the RAFEL performance at a 1 nm resonance wavelength and 90% output coupling was investigated using the fundamental FEL interaction for LCLS-II like parameters. The ideal electron beam used in these simulations was defined using the slice properties of a typical 100 pC start-to-end beam, which can be found in Table 1. Along with these ideal simulations, as mentioned above, the microbunching induced energy mod-

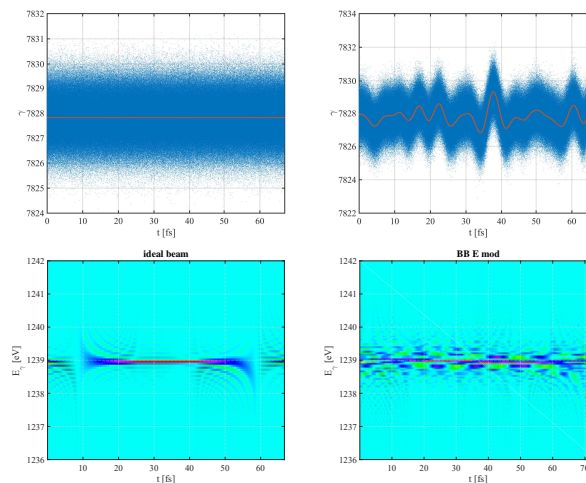


Figure 4: Longitudinal phase space of a typical ideal electron beam (top left) and an electron beam with broadband energy modulations (top right) used in simulation. Below are the corresponding normalized on-axis Wigner distributions of the X-rays after 100 passes (bottom left) and 145 passes (bottom right).

ulations that are reflected in typical start-to-end beams are modeled to investigate their effect on the spectral properties of the RAFEL output.

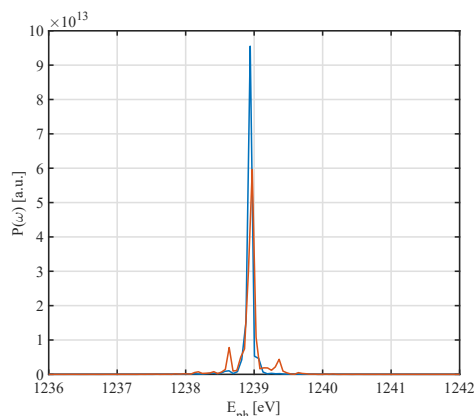


Figure 5: Spectral comparison for a 1 nm RAFEL driven by an ideal electron beam (blue) and an electron beam with broadband energy modulations (red).

1 nm

Figure 4 shows the longitudinal phase space of electron beams that have been used in simulation to investigate the RAFEL performance at 1 nm as well as the Wigner distributions of the amplified light after 100 passes (ideal electron beam, left) and 145 passes (broadband energy modulations, right).

While the ideal electron beam produces light with full longitudinal coherence, the broadband energy modulations create some structure on the pulse. This is clearly seen as the

amplification of sidebands in Fig. 5, which shows a spectral comparison between the two scenarios.

The peak spectral brightness, however, does not suffer significantly and compares well with other externally seeded scenarios [8]. It should be noted that no spectral filtering has been applied in these cases. The FEL, which is a group-velocity dispersion medium, cleans up the spectrum through continuous slippage. The cavity detuning and undulator length have to be carefully chosen to keep the amplification in the exponential gain regime just up to saturation and to allow the phase information to be propagated from the back of the beam forward over many passes.

CONCLUSION

Preliminary simulations show that various RAFEL configurations can boost the performance of the LCLS-II at the high end of the tuning range in the HXR undulator, can extend the tuning range far beyond the nominal 5 keV limit, and compare well with externally seeded schemes in the SXR spectral range at the high end of the tuning range. Harmonic lasing, which works well with seeded schemes as opposed to the more difficult SASE case, can be leveraged in many cases. Detailed optical cavity designs, as well as their associated challenges, have not been considered here but are an ongoing effort. The performance boost experienced in the SXR spectral range relative to externally seeded schemes could potentially warrant additional investigations into optics suitable for a RAFEL cavity where current limitations, including being limited to large angle, or grazing incidence, reflections, and inefficient and narrow reflectivity bandwidth, are prohibitive.

ACKNOWLEDGMENT

This work was supported by the U.S. Department of Energy under contract No. DE-AC02-76SF00515.

REFERENCES

- [1] P. Emma *et al.*, "First lasing and operation of an Ångstrom-wavelength free-electron laser", *Nature Photonics* vol. 4, no. 641, 2010.
- [2] C. Bostedt *et al.*, "Ultra-fast and ultra-intense x-ray sciences: first results from the Linac Coherent Light Source free-electron laser", *Journal of Physics B: Atomic, Molecular and Optical Physics*, vol. 46, no. 16, p. 164003, 2013.
- [3] R. Bonifacio, C. Pellegrini, and L. M. Narducci, "Collective instabilities and high-gain regime in a free electron laser", *Opt. Commun.*, vol. 50, no. 373, 1984.
- [4] R. Bonifacio, L. De Salvo, P. Pierini, N. Piovella, and C. Pellegrini, "Spectrum, temporal structure, and fluctuations in a high-gain free-electron laser starting from noise", *Phys. Rev. Lett.*, vol. 73, no. 70, 1994.
- [5] J. Feldhaus, E. Saldin, J. Schneider, E. Schneidmiller, and M. Yurkov, "Possible application of x-ray optical elements for reducing the spectral bandwidth of an x-ray SASE FEL", *Opt. Commun.*, vol. 140, no. 341, 1997.
- [6] J. Amann *et al.*, "Demonstration of self-seeding in a hard-x-ray free-electron laser", *Nature Photonics*, vol. 6, no. 693, 2012.
- [7] D. Ratner *et al.*, "Experimental demonstration of a soft x-ray self-seeded free-electron laser", *Phys. Rev. Lett.*, vol. 114, p. 054801, 2015.
- [8] E. Hemsing, "Seeding experiments and seeding options for LCLS II", presented at FEL'17, New Mexico, USA, paper TUB01, this conference.
- [9] E. Allaria *et al.*, "Two-stage seeded soft-x-ray free-electron laser", *Nature Photonics*, vol. 7, no. 913, 2013.
- [10] K.-J. Kim, Y. Shvyd'ko, and Sven Reiche, "A proposal for an x-ray free-electron laser oscillator with an energy-recovery linac", *Phys. Rev. Lett.*, vol. 100, p. 244802, 2008.
- [11] S. Reiche, "GENESIS 1.3: a fully 3D time-dependent FEL simulation code", *Nucl. Instr. Meth. Phys. Res. Sect. A*, vol. 429, p. 243, 1999.
- [12] B. W. J. McNeil, G. R. M. Robb, M. W. Poole, and N. R. Thompson, "Harmonic lasing in a free-electron-laser amplifier", *Phys. Rev. Lett.*, vol. 96, p. 084801, 2006.
- [13] E. A. Schneidmiller and M.V. Yurkov, "Harmonic lasing in x-ray free electron lasers", *Phys. Rev. ST Accel. Beams*, vol. 15, p. 080702, 2012.
- [14] G. Marcus, Y. Ding, Z. Huang, T.O. Raubenheimer, and G. Penn, "Harmonic lasing options for LCLS-II", in *Proceedings of the 36th International Free Electron Laser Conference*, Basel, Switzerland, August 2014, paper MOP054, pp. 148-152.
- [15] G. Marcus *et al.*, "High fidelity start-to-end numerical particle simulations and performance studies for LCLS-II", in *Proceedings of the 37th International Free Electron Laser Conference*, Daejeon, Korea, August 2015, paper TUP007, pp. 342-346.
- [16] J. Qiang *et al.*, "Start-to-end simulation of the LCLS-II beam delivery system with real number of electrons", in *Proceedings of the 37th International Free Electron Laser Conference*, Daejeon, Korea, August 2015, paper WEP070, pp. 714-717.
- [17] T.O. Raubenheimer, "LCLS-II: Status of the CW x-ray FEL upgrade to the SLAC LCLS facility", in *Proceedings of the 37th International Free Electron Laser Conference*, Daejeon, Korea, August 2015, paper WEP014, pp. 618-624.
- [18] Z. Zhang *et al.*, "Microbunching-instability-induced sidebands in a seeded free-electron laser", *Phys. Rev. Accel. Beams*, vol. 19, p. 050701, 2016.
- [19] G. Marcus "Spatial and temporal pulse propagation for dispersive paraxial optical systems", *Optics Express*, vol. 24, p. 7752, 2016.
- [20] Z. Huang and R.D. Ruth, "Fully coherent x-ray pulses from a regenerative-amplifier free-electron laser", *Phys. Rev. Lett.*, vol. 96, p. 144801, 2006.
- [21] N. Ghafoor *et al.*, "Impact of B₄C co-sputtering on structure and optical performance of Cr/Sc multilayer x-ray mirrors", *Optics Express*, vol. 25, p. 18274, 2017.

X-RAY FEL OSCILLATOR SEEDED HARMONIC AMPLIFIER FOR HIGH ENERGY PHOTONS

W. Qin*, IHIP, Peking University, Beijing 100871, China
K.-J. Kim, R. R. Lindberg, ANL, Argonne, IL 60439, USA
J. Wu, SLAC, Menlo Park, CA 94025, USA

Abstract

High power, high energy X-ray pulses in the range of several tens of keV have important applications for material sciences. The unique feature of an X-ray FEL Oscillator (XFEL) makes it possible to seed a harmonic amplifier to produce such high energy photons. In this paper, we present simulation studies using 14.4-keV output pulses from an XFEL to generate harmonics at 43.2 keV (third harmonic) and 57.6 keV (fourth harmonic). Techniques such as undulator tapering and fresh bunch lasing are considered to improve the amplifier performance.

INTRODUCTION

High power, high energy hard X-ray free-electron lasers (XFELs) have important applications for exploring the dynamic properties of materials under extreme conditions. Generation of such high energy photons can be realized using conventional self-amplified spontaneous emission (SASE) [1, 2] scheme and advanced harmonic lasing [3] and fresh-slice technique [4] to improve the performance. An alternative way is to use the proposed XFEL [5], which successively amplifies X-ray pulse trapped in a low loss cavity, to produce coherent, stable hard X-ray as the seed for a high gain harmonic generation (HGHG) [6] type FEL, which is possible to generate stable pulses with high intensity and narrow bandwidth. This concept was studied for third harmonic of 14-keV XFEL and fourth harmonic of 15-keV XFEL using ideal beam [7, 8] for the Matter-Radiation Interactions in Extremes (MaRIE) [9]. Here we use the output from a start-to-end simulated 14.4-keV XFEL operating in fundamental mode [10] to investigate the harmonic performance at third harmonic (43.2 keV) and fourth harmonic (57.6 keV).

LAYOUT

The layout of the proposed scheme is illustrated in Fig. 1, where two photoinjectors are used to generate high brightness interleaved electron bunches for the XFEL and the harmonic amplifier, respectively. Electron beams are kicked from the linac at 8 GeV into the XFEL to generate a 14.4-keV seed. With a proper delay, the seed is sent into a modulator to modulate the 12-GeV, 3.4-kA electron beam. The energy modulation can be converted to density modulation via a small magnetic chicane or a detuned undulator. In a subsequent radiator tuned at third or fourth harmonic of

the modulation wavelength, high energy photons are emitted. Fresh bunch technique, where a fresh electron bunch is delayed to interact with the FEL radiation generated in the first part of the radiator, is used to reduce the effect of the increased energy spread after modulation on the FEL performance. The fresh bunch can be provided by accelerating two bunches in one RF bucket, as in Ref. [11], and the delay between two bunches is tens of femtosecond, which can be reached using a small magnetic chicane. Although the XFEL pulse is much longer than the delay of the two bunches, one of the two bunches can be tuned to off resonant in the modulator through energy difference between the two bunches due to wakefields, so that one bunch is modulated and the other remains fresh. Bunch charge is 100 pC for all cases. Normalized emittance is 0.2 μm for 12-GeV ideal Gaussian beam. For the XFEL simulation, the emittance is 0.25 μm . More machine parameters used in this study are listed in Table 1.

Table 1: Electron beam and FEL parameters. Bunch charge is 100 pC for all cases. Normalized emittance is 0.2 μm for 12 GeV ideal Gaussian beam. For the XFEL simulation, the emittance is 0.25 μm .

Parameter	XFEL	Mod.	43.2 keV	57.6 keV
FEL K	1.48	2.79	1.44	1.03
E_b [GeV]	8	12	12	12
I_{pk} [A]	120	3400	3400	3400
σ_s [fs]	317	12.5	12.5	12.5
σ_E [MeV]	0.2	1.8	1.8	1.8
λ_u [cm]	2	1.94	1.55	1.55
L_u [m]	20	8	70	70
harmonic	1	1	3	4

THE XFEL

The XFEL uses high reflectivity, narrow spectral bandwidth crystals as mirrors for the X-ray pulses. In this study we adopt the four crystal configuration as proposed in Ref. [12] to allow for wavelength tunability and C(733) is used for 14.4-keV radiation. GINGER [13] simulation is conducted to evaluate the XFEL performance, with its temporal profile and spectrum shown in Fig. 2. The power of the XFEL output reaches about 37 MW after saturation and the FWHM bandwidth is about 3.4 meV, which is two orders narrower than hard X-ray self-seeding machine.

* qinweilun@pku.edu.cn, also at SLAC.

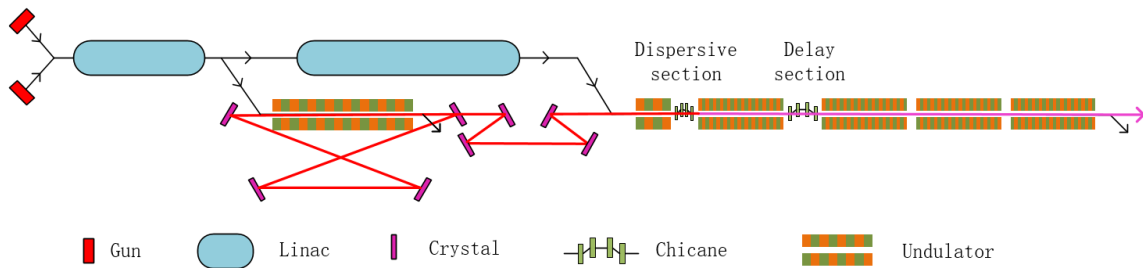


Figure 1: Layout of the proposed XFEL driven high gain harmonic generation scheme.

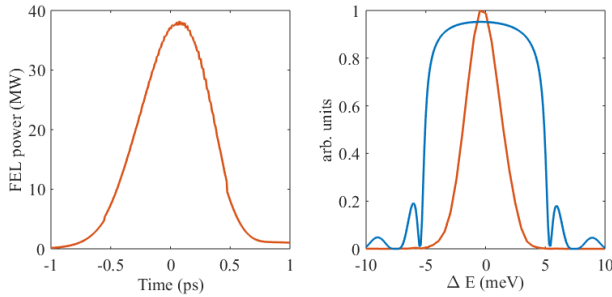


Figure 2: Output pulse temporal profile and spectrum of the 14.4-keV XFEL.

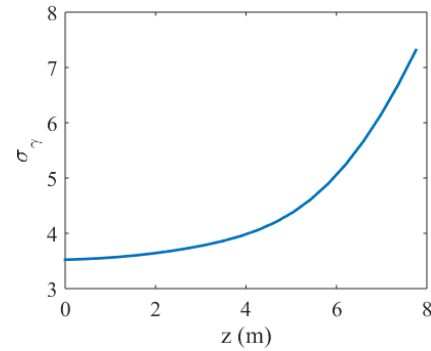


Figure 3: Electron beam rms energy spread evolution along the modulator.

HARMONIC GENERATION

Modulator

The XFEL output is converted to GENESIS [14] input as radiation description file for harmonic generation simulation. An 8 m undulator with 1.94 cm period is used to introduce sufficient energy modulation in the beam. To obtain sufficient bunching after dispersive section with R_{56} , an energy modulation amplitude of $h\sigma_E$ is favorable for the h^{th} harmonic. The energy modulation also increases the beam energy spread, which should be smaller than the FEL ρ to ensure sufficient FEL gain. For the 12-GeV beam in this study, the beam energy spread is 1.5×10^{-4} and the Pierce parameter ρ is about 4×10^{-4} for third harmonic and 3.2×10^{-4} for fourth harmonic. As is shown in Fig. 3, the beam rms energy spread is almost doubled at the end of the modulator, with the corresponding electron beam longitudinal phase space shown in Fig. 4. The R_{56} needed to convert the energy modulation into density modulation is about 10 nanometers, which can be achieved with either small magnets (bend angle 1×10^{-4} and length 2.5 cm) or a detuned undulator. The bunching factor reaches about 9% with $R_{56} = 1.4 \times 10^{-8}$ m for third harmonic and 4% with $R_{56} = 1.2 \times 10^{-8}$ m for fourth harmonic.

Third Harmonic

To explore the FEL performance at the third harmonic in the radiator, four cases are simulated using GENESIS: 1) non-fresh bunch, 2) non-fresh bunch, with undulator taper, 3) with fresh bunch and 4) with fresh bunch and undulator taper. The radiator length is 70 m for non-fresh bunch cases

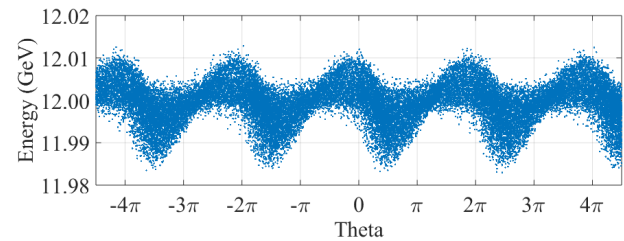


Figure 4: Electron beam longitudinal phase space at the end of the modulator.

and (5 + 65) m for fresh bunch cases. FEL pulse energy evolution along the undulator is shown in Fig. 5. The standard HGHG scheme produce about 100- μ J X-ray pulse at the end of the undulator. After a proper taper, the pulse energy is increased to 500 μ J, corresponding to 7.2×10^{10} photons per pulse. Using the fresh bunch method along with undulator taper, the pulse energy reaches 750 μ J at 70 m, corresponding to 1.1×10^{11} photons per pulse. Compared with non-fresh cases, the improvement of pulse energy using fresh bunch method is less than a factor of two, indicating that the increased energy spread in the modulator is well within favorable range for third harmonic. The temporal profile and spectrum for the case with both fresh bunch and taper are shown in Fig. 6. FEL pulse with 45 GW power and 17 fs FWHM pulse duration is generated. The pulse spectrum is clean and the FWHM bandwidth is about 0.38 eV.

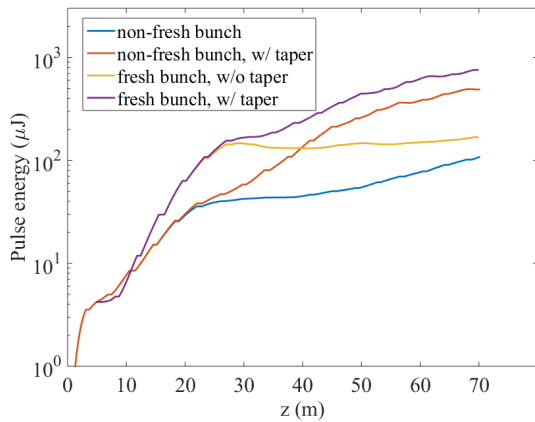


Figure 5: FEL pulse energy evolution in the radiator for 43.2-keV X-rays.

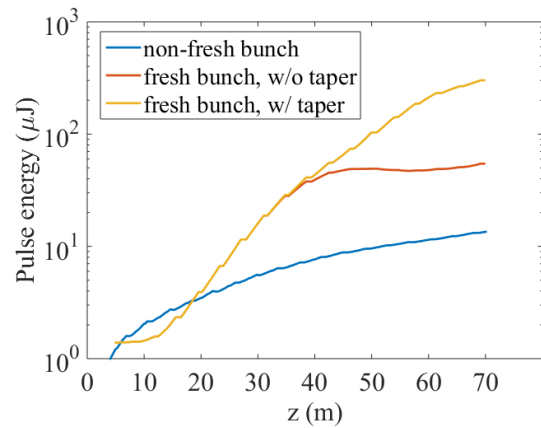


Figure 7: FEL pulse energy evolution in the radiator for 57.6-keV X-rays.

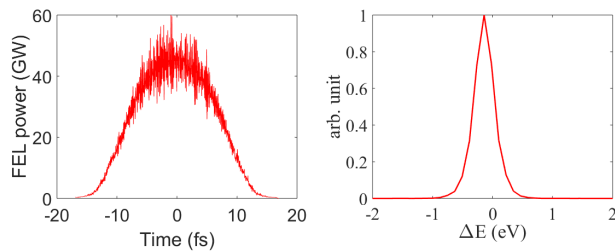


Figure 6: Temporal profile and spectrum for the 43.2-keV X-rays with fresh bunch and undulator taper.

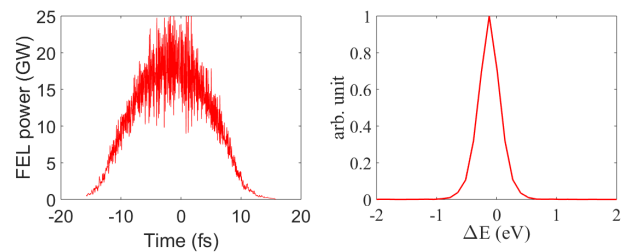


Figure 8: Temporal profile and spectrum for the 57.6-keV X-rays with fresh bunch and undulator taper.

Fourth Harmonic

For the fourth harmonic radiation, it can be seen in Fig. 7 that the increased energy spread after modulation is limiting the FEL performance in the radiator, with only 13- μ J pulse energy at the end of the undulator. With the help of fresh bunch, the output pulse energy is increased to 55 μ J. Undulator taper further increases the pulse energy to 300 μ J, corresponding to 3.3×10^{10} photons per pulse. Temporal profile and spectrum for the case with fresh bunch and undulator taper for the fourth harmonic are shown in Fig. 8. The temporal and spectral characteristics are similar to those of the third harmonic, with 19-GW power, 16-fs FWHM pulse duration and 0.4-eV FWHM bandwidth.

CONCLUSION

We studied the FEL performance of an HGHG-type harmonic amplifier driven by a 14.4 keV XFEL to generate coherent high energy photons for scientific applications under extreme conditions. This scheme takes full advantage of the high-power, narrow-bandwidth hard X-rays from the XFEL. Simulations show that, with the help of fresh bunch and undulator taper, 750 μ J and 300 μ J pulse energy can be generated for third harmonic at 43.2 keV and fourth harmonic at 57.6 keV, respectively. The generated high energy X-ray pulses have $10^{10} - 10^{11}$ photons per pulse and narrow bandwidth down to 10^{-6} . More detailed study should be conducted in several aspects of the proposed scheme, for example, the accelerator system that can deliver two high-

energy, interleaved electron bunch streams with large current difference, the optimization of the undulator taper, the non-linear harmonic generation in the radiator to produce even higher photon energies.

ACKNOWLEDGEMENT

W. Qin would like to thank L. Zeng and G. Zhou for helpful discussions on HGHG simulations. This work is supported by the U.S. Department of Energy under Contract No. DE-AC02-76SF00515 and U.S. Department of Energy under Contract No. DE-AC02-06CH11357.

REFERENCES

- [1] A. Kondratenko and E. Saldin, "Generation of coherent radiation by a relativistic electron beam in an undulator", *Part. Accel.* 10, 207 (1980).
- [2] R. Bonifacio *et al.*, "Collective instabilities and high-gain regime in a free electron laser", *Opt. Commun.* 50, 373 (1984).
- [3] E. A. Schneidmiller *et al.*, "First operation of a harmonic lasing self-seeded free electron laser", *Phys. Rev. Accel. Beams* 20, 020705 (2017).
- [4] C. Emma *et al.*, "Demonstration of fresh slice self-seeding in a hard X-ray free electron laser", *Proc. of NAPAC'16*, Chicago, IL, USA, TUB3CO03.
- [5] K.-J. Kim *et al.*, "A proposal for an X-ray free-electron laser oscillator with an energy-recovery linac", *Phys. Rev. Lett.* 100, 244802 (2008).

Content from this work may be used under the terms of the CC BY 3.0 licence (© 2018). Any distribution of this work must maintain attribution to the author(s), title of the work, publisher, and DOI.

- [6] L. Yu, "Generation of intense UV radiation by subharmonically seeded single-pass free-electron lasers", *Phys. Rev. A* 44, 5178 (1991).
- [7] K.-J. Kim, "XFEL Seeded Amplifier" (talk), *MaRIE workshop*, Santa Fe, NM, USA (2016).
- [8] L. Gupta *et al.*, "Performance of a Combined System Using an X-Ray FEL Oscillator and a High-Gain FEL Amplifier", *Proc. of NAPAC'16*, Chicago, IL, USA, WEPOB32.
- [9] J. W. Lewellen *et al.*, "Technology maturation for the MaRIE 1.0 X-FEL", *Proc. of FEL'15*, Daejeon, Korea, TUP030.
- [10] W. Qin *et al.*, "Start-to-end simulations for an X-ray FEL Oscillator at the LCLS-II and LCLS-II-HE", presented at FEL'17, TUC05, these proceedings.
- [11] A. Marinelli *et al.*, "High-intensity double-pulse X-ray free-electron laser", *Nat. Commun.* 6, 6369 (2015).
- [12] K.-J. Kim *et al.*, "Tunable optical cavity for an x-ray free-electron-laser oscillator", *Phys. Rev. ST Accel. Beams* 12, 030703 (2009).
- [13] W. M. Fawley, "A user manual for GINGER-H and its post-processor XPLOTGINH", Version 2.0k, June 2012.
- [14] S. Reiche, "GENESIS 1.3: a fully 3D time-dependent FEL simulation code", *Nucl. Instr. Meth. A* 429 (1999) 243.

AN EXPERIMENTAL SETUP FOR PROBING THE THERMAL PROPERTIES OF DIAMOND REGARDING ITS USE IN AN XFELO*

C. P. Maag, I. Bahns, J. Rossbach, P. Thiessen[†], Universität Hamburg, Hamburg, Germany
H. Sinn, European XFEL GmbH, Hamburg, Germany
J. Zemella, Deutsches Elektronen Synchrotron (DESY), Hamburg, Germany

Abstract

This work presents an optical pump-probe setup for measuring the thermal evolution of diamond crystals at cryogenic temperatures under the heat load conditions of an X-ray free-electron laser oscillator (XFELO). As an XFELO is based on a cavity using diamond Bragg reflectors and these reflectors are subjected to intense heat loads during operation, the correct understanding of the thermal evolution in diamond plays a major role in the correct modeling of an XFELO. *Stoupin et al.* [1] did a room temperature x-ray diffraction measurement on the nanosecond transient thermal response of diamond to an optical pulse. The measurements presented in this paper for the first time incorporate effects due to the very short penetration depth of only a few μm of an XFELO pulse in combination with the high mean free path in diamond at cryogenic temperatures. While at room temperature the heat equation based on Fourier's law accurately fits the measured results, this vastly changes due to the onset of ballistic processes at cryogenic temperatures. These changes, which are hard to predict theoretically, show the necessity of measurements of the thermal evolution in diamond with special regard to a correct mimicking of the heat load in an XFELO.

INTRODUCTION

Current hard X-ray free-electron laser (FEL) facilities all use the self-amplified spontaneous emission (SASE) scheme for operation. While these sources produce very brilliant femtosecond X-ray pulses with excellent transverse coherence, they suffer from a lack of longitudinal coherence. A promising approach for reaching full longitudinal coherence in the hard X-ray regime proposed by *Kim et al.* in 2008 [2] is the X-ray free-electron-laser oscillator (XFELO). This scheme is based on using a rather short undulator with a length of less than 15 m and a highly reflective cavity based on very pure diamond crystals serving as Bragg reflectors. As these Bragg reflectors also act as spectral filters an XFELO promises a spectral bandwidth in the order of the crystals bandwidth ($\Delta\omega/\omega \approx 10^{-5} - 10^{-7}$) and therefore orders of magnitude better than SASE-FELs. Furthermore, as the radiation field is built up over many cavity round trips, very low shot-to-shot fluctuations can be expected, even making the XFELO a promising candidate for X-ray quantum optics (XQO) [3]. With the recently commissioned European XFEL the realization of an XFELO becomes in reach. This is due to the facility's excellent electron beam

properties and especially due to its very high bunch repetition rate of 4.5 MHz in pulsed-mode [4] which enables resonator lengths of only 33 m.

A major issue one needs to address when dealing with an XFELO is the effect of the light-matter interaction between the X-ray field and the Bragg reflectors. This is due to the high requirements for the angular and spatial stability [5,6] as well as the necessity of very stable Bragg conditions.

As shown by *Zemella et al.* in 2012 [7] even an XFELO with a designedly limited saturated pulse energy of $\approx 250 \mu\text{J}$ circulating with a rate of 4.5 MHz leads to a considerable heating of the Bragg reflectors and thereby to their thermal expansion. This thermal expansion may lead to vibrations of the crystal, change of the wavelength satisfying the Bragg's law [7] and the generation of ultrasonic pulses [1,8]. The last effect is studied by *Bahns et al.* [9] also at this conference.

Owing to the importance of keeping these effects as low as possible, it has already been concluded that diamond at cryogenic temperatures is the ideal candidate for an XFELO [10,11], due to its very high thermal conductivity, its low thermal expansion coefficient as well as high radiation hardness and a Bragg reflectivity over 99%. Nonetheless, even with diamond at 50 K, heating of the crystals does not seem negligible [7]. Consequently, in order to properly predict the behavior of an XFELO at the European XFEL and the effect of the thermal load, the diamond reflectors' thermal response need to be understood and especially measured as will be shown in the following. Our approach is to mimic an XFELO by a UV laser which deposits roughly the same energy into a diamond crystal at the same penetration depth as an saturated XFELO pulse. Such an experimental setup is presented in this work.

QUASI-BALLISTIC HEAT TRANSPORT

As discussed above, diamond is the ideal candidate for Bragg reflectors in an XFELO. However, when treating thermally highly conductive materials, especially at low temperatures where the phonon-phonon Umklapp scattering is freezing out, one has to take into account size effects which lower the predictive power of the heat equation based on Fourier's law. The latter is based on the assumptions of local thermal equilibrium and time- and length scales of interest larger than the typical scattering time or mean free path of a phonon, respectively. As the mean free path in diamond is of the order of hundreds of microns at $T = 50 \text{ K}$ and still of the order of tens of microns at $T = 100 \text{ K}$, these assumptions begin to fail and size dependent ballistic processes begin to occur.

* Work supported by BMBF (FKZ 05K13GU4 + FKZ 05K16GU4)

[†] patrick.thiessen@desy.de

There are two different size effects to consider. The first is the so called "Gradient Effect": When a temperature gradient ∇T is varying quickly on length scales comparable to the mean free path, ballistic effects begin to have an considerable influence. Traditionally one would simulate these effect by the use of the computationally expensive Boltzmann-Transport equation or the simplified McKevley-Shockley flux method (MSM) yielding comparable results [12]. But as has been pointed out by *Maassen and Lundstrom* in 2015 [13, 14], the MSM for the heat transport can be rewritten as computationally much cheaper diffusion equations. This is under the premise one knows the physically correct boundary conditions as well as the energy dependence of the scattering parameter $\tau(\epsilon)$. These boundary equations as well as the exact $\tau(\epsilon)$ are very hard to estimate theoretically, as will be shown in the following paragraph. While in the stationary case Fourier's law

$$\mathbf{q} = -\lambda_{th} \nabla T,$$

with the thermal heat flux density \mathbf{q} and the thermal conductivity λ_{th} , and the corresponding heat equation hold true [13], they begin to fail in the transient case of the gradient effect [14] for the reasons discussed above. In this case, which also describes the situation in an XFELo, Fourier's law can still be applied. But one has to keep in mind, that the thermal conductivity in the formula is physically incorrect and Fourier's law only apparently holds. Nonetheless in this work we use it, as the deviation of the derived $\lambda_{th}^{(app)}$ from the literature bulk values gives a good estimate of the significance of ballistic processes.

The other size effect is the boundary-scattering at the crystal surfaces, which lead to a reduction of the phonons' mean free path. Consequently Fourier's law would also yield a reduced apparent thermal conductivity. As the temperature dependent energy ϵ spectrum of the mean free path $l_{mfp}(\epsilon)$ or scattering time $\tau(\epsilon)$ of the phonons can span orders of magnitude, it is hard to predict how the individual phonon modes are scattered at the surface [15, 16], making an accurate estimate of the effect hard to achieve. This effect is important for an XFELo, especially when one plans to couple out the radiation by using a very thin ($\sim 40 \mu\text{m}$) and therefore partly transmissive diamond crystal [7]. But it is of no significance at the temperatures experimentally probed in this paper.

EXPERIMENTAL SETUP

As one can see from the discussion in the previous section, it is of great importance to conduct thermal measurements when it comes to properly modeling the heat transport under conditions given for the XFELo. For this purpose an optical pump-probe experiment displayed in Fig. 1 was developed. In particular, a nanosecond 213 nm UV laser with a pulse energy of $2.5 \mu\text{J}$ - which is about the absorbed pulse energy in a saturated XFELo [7] - is being absorbed by a diamond crystal, which causes a time dependent distortions of the temperature T inside the solid.

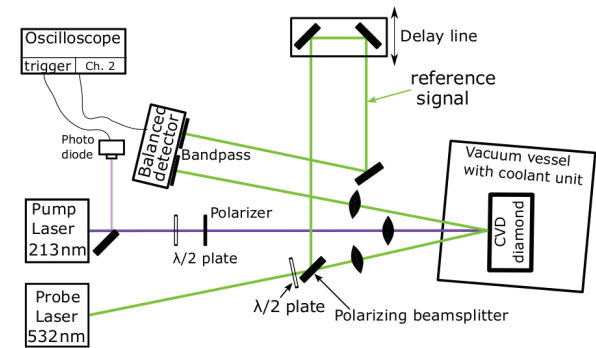


Figure 1: Scheme of the experimental setup. A nanosecond UV pump laser providing the pulse energy characteristics of an XFELo introduces a change in temperature in the sample, a $300 \mu\text{m}$ thick CVD diamond single crystal. The change in temperature is probed by the reflection of a green cw laser. A balanced photo detector amplifies the difference between the reflected signal and a reference signal. A fast oscilloscope averages the signal's time evolution over many pump pulses.

The temperature couples to the refractive index $\tilde{\eta} = \eta' + i\eta''$ and therefore to the diamond optical properties. One can directly relate a change in reflectivity [17]

$$\frac{\Delta R}{R} = \frac{4(\eta'^2 - \eta''^2 - 1)\Delta\eta' + 8\eta'\eta''\Delta\eta''}{[(\eta' + 1)^2 + \eta''^2][(\eta' - 1)^2 + \eta''^2]} \approx \underbrace{\left(\frac{1}{R} \frac{\delta R}{\delta \Delta T}\right)}_{k_T} \Delta T$$

to a change in the refractive index $\Delta\tilde{\eta} = \Delta\eta' + i\Delta\eta''$ and therefore to a change in temperature ΔT . The above linear approximation is valid for temperature changes of a few degree. In this work, a green 532 nm cw-laser is used to measure the change in reflectivity and with the knowledge of $k_T \Delta T$ induced by the UV pump laser can be determined. The physical time resolution is mainly determined by the photo diode's rise time and the bandwidth of the detection system.

As the thermal gradient resulting from the pump pulse is long compared to the probe lasers' wavelength, the probe signal does not notice abrupt changes in the temperature dependent refractive index, which would be a premise for reflection. Consequently no internal reflections occur and the measured change in reflectivity is directly proportional to the temperature at the sample surface.

A challenge in this experimental setup is the rather bad signal to noise ratio. This is caused by a low thermorefectance calibration coefficient k_T relating a big change in ΔT to a comparably low ΔR . To overcome this bad signal to noise ratio each $\Delta R(t)$ curve has to be averaged over many pump pulses.

In order to get information on the thermal evolution at cryogenic temperatures, the sample is located in a vacuum chamber attached to a helium pulse tube cooler. With this cooling unit, temperatures down to $\sim 50 \text{ K}$ can be reached.

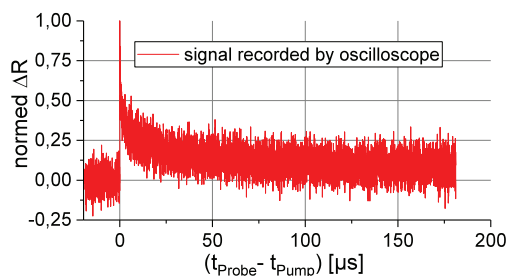


Figure 2: Time evolution of the change in reflection at $T_0 = 297$ K showing a slow μ s to ms long contribution to the crystals recovery back to its initial state. This contribution results from excitations of long living electron states by the pump laser. The bad signal to noise ratio comes from a low number of averages.

RESULTS

Figure 2 displays an exemplary measurement for the long time evolution of the change in reflectivity after the pump pulse at $T_0 = 297$ K. The measurement shows a slow decline of the reflectivity on the scale of approximately 100μ s after the absorption of the pump pulse. This is much slower than the expected thermal response on the timescale of a few hundred nanoseconds. The effect can probably be traced back to the excitation of long living electronic states in the diamond after the absorption, which also changes the sample's refractive index \tilde{n} . In order for it not to disturb the analysis of the thermal response, in the following an offset is subtracted from the measurement signal. This is justified as the slow decay appears constant on the much shorter timescale of the thermal processes. Also one has to note, that these long living electronic states do not disturb the XFEL operation, as Bragg reflection is much less sensitive to the electronic structure than optical reflection.

Figure 3 displays measurements at two different temperatures: (a) $T_0 = 297$ K and (b) $T_0 = 150$ K. In addition, a plot of the derived thermal conductivities versus the temperature is shown (c). In both measurements (a) and (b) the signals are cleared from an offset as discussed above. Both measurements (a) and (b) still exhibit a noisy background, but a clear evolution of the reflectivity on the nanosecond scale is apparent. This evolution is fitted to a model derived from Fourier's law. For the room temperature case (a) and $T_0 = 250$ K the derived λ agrees well with the literature value (see Fig. 3(c)). This can be seen as a proof of principle measurement for the validity of the experimental setup, as one would not yet expect ballistic effects to play a role at these temperatures. However, the measurements at lower temperatures, especially at $T_0 = 150$ K begin to show strong deviations from the literature bulk values. This is in agreement with the discussion of the "gradient effect", as for $T = 150$ K the middle mean free path $l_{mfp} \approx 15 \mu$ m is of the same order as the pump pulse's penetration depth.

Another important consideration is that at room temperature a significant portion of the thermally induced shift in reflectivity remains after 220 ns, while at $T_0 = 150$ K,

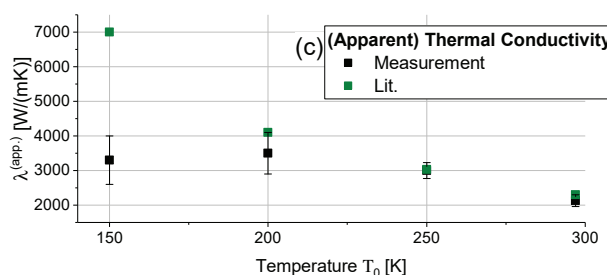
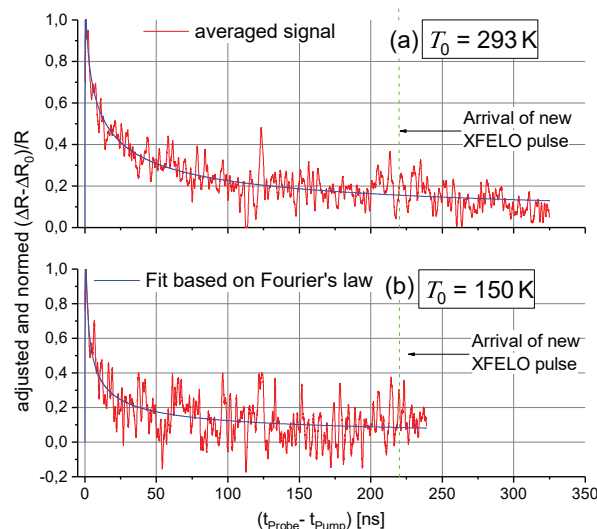


Figure 3: Nanosecond scale time evolution of the change in reflectivity for (a) $T_0 = 297$ K and (b) $T_0 = 150$ K. Following the discussion regarding Fig. 2 the results are corrected by a constant offset. Because of a shorter measurement time, (b) exhibits a noisier background. The signals are each fitted to a model based on Fourier's law. A plot of the derived thermal conductivities against the temperature (c) is displayed together with their bulk literature values [18].

ΔR has declined significantly more. This shows the usefulness of cooling for avoiding consecutive heating of the Bragg reflectors and the resulting disturbances in operation [7] in an XFEL with a repetition rate of 4.5 MHz.

CONCLUSION AND OUTLOOK

An tabletop setup for measuring the effect of thermal load on diamond Bragg crystals in an XFEL was developed. The validity of the measurement method was demonstrated by proof of principle measurements at room temperature and $T_0 = 250$ K, which yield thermal conductivities λ_{th} agreeing well with bulk literature values. However, with decreasing temperature the calculated $\lambda_{th}^{(app.)}$ from Fourier's law begin to differ considerably from the respective bulk values. This can be traced back to the growing contribution of ballistic processes to the heat conduction at decreasing temperatures. This supports the necessity of experimentally measuring diamonds' thermal properties at low temperatures under XFEL conditions. Also, the measurement exhibited a not fully declined thermal excitation after 220 ns, confirming the idea of a pile up of thermal energy in a 4.5 MHz XFEL.

Content from this work may be used under the terms of the CC BY 3.0 licence (© 2018). Any distribution of this work must maintain attribution to the author(s), title of the work, publisher, and DOI.

In the future measurements at crystals with varying thickness and at additional temperatures need to be conducted, especially at $T_0 = 50$ K and $T_0 = 100$ K, where additionally effects due to boundary scattering are expected. Finally, these results need to be implemented into the modeling of an entire XFEL.

ACKNOWLEDGEMENT

We would like to thank Franz Kärtner for providing us with the pump laser for our measurement setup, Ingmar Hartl, Axel Ruehl and Lutz Winkelmann for their support and the helpful discussions. We would also like to thank the DESY and European XFEL GmbH for their financial and technical support.

REFERENCES

- [1] S. Stoupin *et al.*, “Direct observation of dynamics of thermal expansion using pump-probe high-energy-resolution x-ray diffraction,” *Phys. Rev. B*, vol. 86, p. 054301, Aug 2012.
- [2] K.-J. Kim, Y. Shvyd’ko, and S. Reiche, “A proposal for an x-ray free-electron laser oscillator with an energy-recovery linac,” *Physical Review Letters*, vol. 100, jun 2008.
- [3] B. Adams and K.-J. Kim, “X-ray comb generation from nuclear-resonance-stabilized x-ray free-electron laser oscillator for fundamental physics and precision metrology,” *Physical Review Special Topics - Accelerators and Beams*, vol. 18, mar 2015.
- [4] “European XFEL,” located at http://www.xfel.eu/overview/facts_and_figures/.
- [5] S. Stoupin *et al.*, “Nanoradian angular stabilization of x-ray optical components,” *Review of Scientific Instruments*, vol. 81, no. 5, p. 055108, 2010.
- [6] C. Maag, J. Zemella, and G. J. Rossbach, “Numerical studies of the influence of the electron bunch arrival time jitter on the gain process of an XFEL-oscillator for the European XFEL,” in *Proc. of FEL’15*, Daejeon, Korea, TUP032.
- [7] J. Zemella, J. Rossbach, C. Maag, M. Tolkiehn, and H. Sinn, “Numerical simulations of an XFEL for the European XFEL driven by a spent beam,” in *Proc. of FEL’12*, Nara, Japan, WEPD29.
- [8] C. Thomsen, H. T. Grahn, H. J. Maris, and J. Tauc, “Surface generation and detection of phonons by picosecond light pulses,” *Phys. Rev. B*, vol. 34, pp. 4129–4138, 1986.
- [9] I. Bahns *et al.*, “Thermal and mechanical stability of Bragg reflectors for an XFELP,” presented at FEL’17, Santa Fe, USA, TUC02, this conference.
- [10] Y. V. Shvyd’ko, S. Stoupin, A. Cunsolo, A. H. Said, and X. Huang, “High-reflectivity high-resolution x-ray crystal optics with diamonds,” *Nature Physics*, vol. 6, pp. 196–199, Jan 2010.
- [11] S. Stoupin and Y. V. Shvyd’ko, “Thermal expansion of diamond at low temperatures,” *Phys. Rev. Lett.*, vol. 104, p. 085901, Feb 2010.
- [12] J.-H. Rhee and M. S. Lundstrom, “Drift-diffusion equation for ballistic transport in nanoscale metal-oxide-semiconductor field effect transistors,” *Journal of Applied Physics*, vol. 92, no. 9, pp. 5196–5202, 2002.
- [13] J. Maassen and M. Lundstrom, “A simple Boltzmann transport equation for ballistic to diffusive transient heat transport,” *Journal of Applied Physics*, vol. 117, no. 13, p. 135102, 2015.
- [14] J. Maassen and M. Lundstrom, “Steady-state heat transport: Ballistic-to-diffusive with Fourier’s law,” *Journal of Applied Physics*, vol. 117, no. 3, p. 035104, 2015.
- [15] D. P. Sellan, J. E. Turney, A. J. H. McGaughey, and C. H. Amon, “Cross-plane phonon transport in thin films,” *Journal of Applied Physics*, vol. 108, no. 11, p. 113524, 2010.
- [16] G. Chen, “Thermal conductivity and ballistic-phonon transport in the cross-plane direction of superlattices,” *Physical Review B*, vol. 57, no. 23, p. 14958, 1998.
- [17] M. Farzaneh *et al.*, “Ccd-based thermoreflectance microscopy: principles and applications,” *Journal of Physics D: Applied Physics*, vol. 42, no. 14, p. 143001, 2009.
- [18] *The element six CVD diamond handbook*, Element Six Technologies US Corporation.

FREE ELECTRON LASERS IN 2017

P. J. Neyman*, W. B. Colson, S. C. Gottshalk, A. M. M. Todd
Compass Scientific Engineering, Fremont CA 94539 USA

J. Blau, K. Cohn

Physics Department, Naval Postgraduate School, Monterey CA 93943 USA

Abstract

Forty-one years after the first operation of the free electron laser (FEL) at Stanford University, there continue to be many important experiments, proposed experiments, and user facilities around the world. Properties of operating and proposed FELs in the terahertz (THz), infrared (IR), visible, ultraviolet (UV), and X-ray regimes are tabulated and discussed.

LIST OF FELS IN 2017

The following tables list existing (Tables 1 and 2) and proposed (Tables 3 and 4) relativistic free electron lasers (FELs) in 2017. Some FELs in Tables 1 and 2 may not be currently operating, but are still included until we have been notified they are decommissioned. Tables 2 and 4, denoted as “Short Wavelength”, contain FELs that are designed to operate in the UV and X-ray regimes (400-nm or shorter wavelength), while Tables 1 and 3, denoted as “Long Wavelength”, contain all other FELs. The first column lists a location or institution, and the FEL’s name in parentheses. References are listed in Tables 5 and 6; another useful reference is the following website: http://sbfel3.ucsb.edu/www/v1_fel.html.

The second column of each table lists the operating wavelength λ , or wavelength range. The longer wavelength FELs are listed at the top and the shorter wavelength FELs at the bottom of each table. The seven orders of magnitude of operating wavelengths indicate the flexible design characteristics of the FEL mechanism.

In the third column, t_b is the electron bunch duration (FWHM) at the beginning of the undulator, and ranges from almost continuous-wave to short sub-picosecond time scales. The expected optical pulse length in an FEL oscillator can be several times shorter or longer than the electron bunch depending on the optical cavity Q, the FEL desynchronization and gain. The optical pulse can be many times shorter in a high-gain FEL amplifier, or one based on self-amplified spontaneous emission (SASE). Also, if the FEL is in an electron storage ring, the optical pulse is typically much shorter than the electron bunch. Most FEL oscillators produce an optical spectrum that is Fourier-transform limited by the optical pulse length.

The electron beam kinetic energy E and peak current I are listed in the fourth and fifth columns, respectively.

* pneyman@ccicms.com

The next three columns list the number of undulator periods N , the undulator wavelength λ_0 , and the rms undulator parameter $K = eB\lambda_0/2\pi mc^2$ (cgs units), where e is the electron charge magnitude, B is the rms undulator field strength, m is the electron mass, and c is the speed of light. For an FEL klystron undulator, there are multiple undulator sections as listed in the N-column; for example, 2x7. Some undulators used for harmonic generation have multiple sections with varying N , λ_0 , and K values as shown. Some FELs operate at a range of wavelengths by varying the undulator gap as indicated in the table by a range of values for K . The FEL resonance condition, $\lambda = \lambda_0(1+K^2)/2\gamma^2$, relates the fundamental wavelength λ to K , λ_0 , and the electron beam energy $E = (\gamma - 1)mc^2$, where γ is the relativistic Lorentz factor. Some FELs achieve shorter wavelengths by using coherent harmonic generation (CHG), high-gain harmonic generation (HG), or echo-enabled harmonic generation (EEHG).

The last column lists the accelerator types and FEL types, using the abbreviations listed after Table 4.

The FEL optical power is determined by the fraction of the electron beam energy extracted and the pulse repetition frequency. For a conventional FEL oscillator in steady state, the extraction can be estimated as $1/(2N)$; for a high-gain FEL amplifier, the extraction at saturation can be substantially greater. In a storage-ring FEL, the extraction at saturation is substantially less than this estimate and depends on ring properties.

In an FEL oscillator, the optical mode that best couples to the electron beam in an undulator of length $L = N\lambda_0$ has a Rayleigh length $z_0 \approx L/12^{1/2}$ and has a fundamental mode waist radius $w_0 \approx (z_0\lambda/\pi)^{1/2}$. An FEL typically has more than 90% of its power in the fundamental mode.

At the 2017 FEL Conference, new lasings were reported at DESY, PSI, SACLAL, Pohang, and SINAP. These are all large X-ray FEL facilities, showing there is significant worldwide interest in short wavelength FEL applications. Various other facilities reported updated parameters for existing FELs, and there are several newly proposed short-wavelength FELs around the world.

ACKNOWLEDGMENT

The authors are grateful for the support of Compass Scientific Engineering.

Content from this work may be used under the terms of the CC BY 3.0 licence (© 2018). Any distribution of this work must maintain attribution to the author(s), title of the work, publisher, and DOI.

Table 1: Existing Long Wavelength Free Electron Lasers (2017)

LOCATION (NAME)	$\lambda(\mu\text{m})$	$t_b(\text{ps})$	E(MeV)	I(A)	N	$\lambda_0(\text{cm})$	K(rms)	Type
Ariel (EA-FEL)	3000	5×10^7	1.4	0.5-3	26	4.44	0.8	EA,O
Frascati (FEL-CATS)	430-760	15-20	2.5	5	16	2.5	0.5-1.4	RF
UCSB (mm FEL)	340	25000	6	2	42	7.1	0.7	EA,O
Dresden (TELBE)	100-3000	0.15	15-34	15	8	30	≤ 5.7	RF,SU
Nijmegen (FLARE)	100-1400	3	10-15	50	40	11	0.5-3.3	RF,O
KAERI (THz FEL)	100-1200	20	4.5-6.7	0.5	80	2.5	1.0-1.6	MA,O
Novosibirsk (FEL1)	90-240	100	12	10	2×32	12	0-0.9	ERL,O
Osaka (ISIR, SASE)	70-220	20-30	11	1000	32	6	1.5	RF,S
Himeji (LEENA)	65-75	10	5.4	10	50	1.6	0.5	RF,O
UCSB (FIR FEL)	60	25000	6	2	150	2	0.1	EA,O
Osaka (ILE/ILT)	47	3	8	50	50	2	0.5	RF,O
Novosibirsk (FEL2)	37-85	20	22	50	32	12	0-1.1	ERL,O
Osaka (ISIR)	25-150	20-30	13-20	50	32	6	≤ 1.5	RF,O
Tokai (JAEA-FEL)	22	2.5-5	17	200	52	3.3	0.7	RF,O
Bruyeres (ELSA)	20	30	18	100	30	3.2	0.8	RF,O
Dresden (ELBE U100)	18-250	1-25	15-34	30	38	10	0.5-2.7	RF,O
Osaka (iFEL4)	18-40	10	33	40	30	8	1.3-1.7	RF,O
Novosibirsk (FEL3)	9	10	42	100	3×28	6	0.3-1.8	ERL,O
Darmstadt (FEL)	6-8	2	25-50	2.7	80	3.2	1.0	RF,O
Osaka (iFEL1)	5.5	10	33.2	42	58	3.4	1.0	RF,O
Nijmegen (FELICE)	5-100	1	18-50	50	48	6.0	1.8	RF,O
Dresden (ELBE U37)	5-40	0.8-4	15-34	60	54	3.7	0.5-1.34	RF,O
Beijing (BFEL)	5-25	4	30	15-20	50	3	0.5-0.8	RF,O
Kyoto (KU-FEL)	5-21.5	< 1	20-36	17-40	52	3.3	0.7-1.56	RF,O
Daresbury (ALICE)	5-11	~ 1	27.5	80	40	2.7	0.35-0.9	ERL,O
Tokyo (MIR-FEL)	4-16	2	32-40	30	43	3.2	0.7-1.8	RF,O
Orsay (CLIO)	3-150	10	12-50	100	38	5	≤ 1.4	RF,O
Nijmegen (FELIX)	3-150	1	15-50	50	38	6.5	1.8	RF,O
Berlin (FHI MIR FEL)	2.9-50	1-5	15-50	200	50	4	0.5-1.5	RF,O
Hawaii (MkV)	2-10	2-5	30-45	30-60	47	2.3	0.1-1.3	RF,O
Osaka (iFEL2)	1.88	10	68	42	78	3.8	1.0	RF,O
Nihon (LEBRA)	1.5-6.5	1	58-100	10-20	50	4.8	0.7-1.4	RF,O
JLab (IR upgrade)	0.7-10	0.35	120	300	30	5.5	3.0	ERL,O

Content from this work may be used under the terms of the CC BY 3.0 licence (© 2018). Any distribution of this work must maintain attribution to the author(s), title of the work, publisher, and DOI.

Table 2: Existing Short Wavelength Free Electron Lasers (2017)

LOCATION (NAME)	λ (nm)	t_b (ps)	E(GeV)	I(kA)	N	λ_0 (cm)	K(rms)	Type
Osaka (iFEL3)	300-700	5	0.155	0.06	67	4	1.4	RF,O
Duke (OK-5)	250-790	5-20	0.27-0.8	0.01-0.05	2x30	12	3.18	SR,O,K
JLab (UV demo)	250-700	0.35	0.135	0.2	60	3.3	1.3	ERL,O
Okazaki (UVSOR-II)	200-800	6	0.6-0.75	0.028	2x9	11	2.6-4.5	SR,O,K
DELTA (U250)	200	100	1.5	0.04	2x7	25	7.3-10	SR,K,H
Duke (OK-4)	190-400	50	1.2	0.035	2x33	10	4.75	SR,O,K
ELETTRA (SR-FEL)	90-260	70	1	0.150	2x19	10	4.2	SR,A,K,H
Frascati (SPARC)	66-800	0.15-8	0.08-0.177	0.04-0.38	450	2.8	0.5-1.55	RF,A,S,H
DESY (sFLASH)	38	0.5	0.7	0.5-2	180 120	3.14 3.3	1.9 2.1	RF,S,H
ELETTRA (FERMI-1)	20-100	0.7-1.2	0.9-1.5	0.3-0.7	252	5.5	1-3	RF,A,H
SINAP (SXFEL-TF)	8.8	0.5	0.84	0.5	760	2.35	1.012	RF,H,E
SACLA (BL1 SX)	8-62	1	0.3-0.8	0.3	777	1.8	1.5	RF,S
DESY (FLASH2)	4-90	0.03-0.2	0.5-1.25	2.5	768	3.14	0.5-2	RF,S
DESY (FLASH1)	4-50	0.03-0.2	0.35-1.25	2.5	981	2.73	0.87	RF,S
ELETTRA (FERMI-2)	4-20	0.7-1.6	0.9-1.5	0.3-0.7	396	3.5	0.85-1.6	RF,A,H
Pohang (PAL SXFEL)	1.0-4.5	0.03-0.18	2.6-3.15	1-3	980	3.50	1.5-3.3	RF,S
DESY (European XFEL)	0.13-0.9	0.1	6-14	5	4375	4	1.65-3.9	RF,S
SLAC (LCLS)	0.12	0.07	15.4	3.5	3696	3	2.5	RF,S
PSI (SwissFEL Aramis)	0.1-0.7	0.002-0.015	2.1-5.8	1.5-2.7	3192	1.5	0.5-1.3	RF,S,SS
Pohang (PAL HXFEL)	0.06-0.7	0.02-0.09	4-10	2-4	3770	2.60	1.2-2.0	RF,S
SACLA (BL3 HX) (BL2 HX)	0.06-0.3 0.06-0.3	0.01-0.02 0.01-0.02	8.3 8.3	10 10	5817 4986	1.8 1.8	2.0 2.0	RF,S RF,S

Table 3: Proposed Long Wavelength Free Electron Lasers (2017)

LOCATION (NAME)	λ (μ m)	t_b (ps)	E(MeV)	I(A)	N	λ_0 (cm)	K(rms)	Type
KAERI (Table-top THz)	400-600	20	6.5	1	28	2.3-2.6	2.1-2.4	MA,O
Tokyo (FIR-FEL)	300-1000	5	10	30	25	7	1.5-3.4	RF,O
Ariel (THz FEL)	75-300	0.3	3-6	1000	20	2.5	0.47	RF,A
India (CUTE-FEL)	50-100	1000	10-15	20	50	5	0.57	RF,O
Berlin (FHI FIR FEL)	40-500	1-5	20-50	200	40	11	1-3	RF,O
Beijing (PKU-FEL)	4.7-8.3	1	30	60	50	3	0.5-1.4	ERL,O
Turkey (TARLA U90) (TARLA U25)	18-250 3-20	0.4-6 0.4-6	15-40 15-40	12-155 12-155	40 60	9 2.5	0.7-2.3 0.25-0.7	RF,O
Tallahassee (Big Light)	2-1500	1-10	50	50	45	5.5	4.0	ERL,O

Content from this work may be used under the terms of the CC BY 3.0 licence (© 2018). Any distribution of this work must maintain attribution to the author(s), title of the work, publisher, and DOI.

Table 4: Proposed Short Wavelength Free Electron Lasers (2017)

LOCATION (NAME)	λ (nm)	t_b (ps)	E(GeV)	I(kA)	N	λ_0 (cm)	K(rms)	Type
Daresbury (CLARA)	100-400	0.5	0.25	0.4	500	2.5	0.7-1.4	RF,A
Dalian (DCLS)	50-150	1	0.3	0.3	360	3.0	0.3-1.6	RF,A,H
Soleil (LUNEX 5)	4-40	1	0.4	0.4	800	1.5	<2.6	PW,H,E,SS
Glasgow (ALPHA-X)	2-300	0.001-0.005	0.10-1.0	1	200	1.5	0.5	PW,A
SINAP (SXFEL-UF)	3	0.35	1.5	0.7	1200	2.35	1.09	RF,H,E
	2	0.35	1.5	0.7	2500	1.6	1.074	RF,S
Groningen (Z FEL)	0.8	0.1	1-2.1	1.5	2600	1.5	0.85	RF,S,H
ASU (CXFEL)	0.15-1	0.001-0.01	0.05	0.2	300	0.0001	0.25	RF,OU,SU
PSI (SwissFEL Athos)	0.7-7	0.002-0.015	2.5-3.4	1.5-2.7	1200	4	0.7-3.5	RF,S,SS
SLAC (LCLS-II SXR) (LCLS-II HXR)	1.0-6.2	0.01-0.1	2.0-4.0	0.5-1.5	1827	3.9	1.4-3.9	RF,S,SS
	0.05-1.2	0.01-0.1	2.5-15.0	0.5-4	4160	2.6	0.36-1.7	RF,S,SS
DESY (European XFEL)	0.4-5	0.002-0.18	8-17.5	5	1544	6.8	4-9	RF,S
	0.05-0.4				4375	4	1.65-3.9	
SINAP (SCLF)	0.4-3	0.066	8	1.5	2352	6.8	1.37-4.5	RF,H,E,SS
	0.08-0.4	0.066	6-8	1.5	6538	2.6	0.75-1.8	RF,S,SS
	0.05-0.12	0.066	8	1.5	10000	1.6	0.69-1.64	RF,S,SS
LANL (MaRIE)	0.03	0.03	12	3.4	5600	1.86	0.86	RF,S,H,E

Facility type:

TF – Test Facility
 UF – User Facility

Accelerator type:

MA - Microtron Accelerator
 ERL - Energy Recovery Linear Accelerator
 EA - Electrostatic Accelerator
 RF - Radio-Frequency Linear Accelerator
 SR - Electron Storage Ring
 PW- Laser Plasma Wakefield Accelerator

FEL type:

A - FEL Amplifier
 K - FEL Klystron
 O - FEL Oscillator
 OU – Optical Undulator
 S - Self-Amplified Spontaneous Emission (SASE)
 H - Harmonic Generation (CHG, HGHG)
 E - Echo-Enabled Harmonic Generation (EEHG)
 SS - Self-Seeded Amplifier
 SU - Super-radiant FEL

Content from this work may be used under the terms of the CC BY 3.0 licence (© 2018). Any distribution of this work must maintain attribution to the author(s), title of the work, publisher, and DOI.

Table 5: References and Websites for Existing FELs

LOCATION (NAME)	Internet Site or Reference
Ariel (EA-FEL)	http://www.ariel.ac.il/research/fel
Beijing (BFEL)	http://www.ihep.ac.cn/english/BFEL/index.htm
Berlin (FHI MIR)	http://fel.fhi-berlin.mpg.de
Bruyeres (ELSA)	P. Guimbal <i>et al.</i> , <i>Nucl. Inst. and Meth. A</i> 341, 43 (1994).
Daresbury (ALICE)	http://www.stfc.ac.uk/ASTeC/Alice/projects/36060.aspx
Darmstadt (FEL)	M. Brunken <i>et al.</i> , <i>Nucl. Inst. and Meth. A</i> 429, 21 (1999).
DELTA (U250)	H. Huck <i>et al.</i> , <i>Proceedings of FEL 2011</i> , Shanghai, China. http://accelconf.web.cern.ch/AccelConf/FEL2011/papers/mooa5.pdf
DESY (FLASH, sFLASH, European XFEL)	http://xfel.desy.de
Dresden (ELBE)	http://www.hzdr.de/FELBE
Duke (OK-4, OK-5)	http:// https://www.phy.duke.edu/duke-free-electron-laser-laboratory
ELETTRA (SR-FEL)	http://www.elettra.trieste.it/elettra-beamlines/fel.html
ELETTRA (FERMI)	http://www.elettra.trieste.it/FERMI
Frascati (FEL-CATS)	http://www.frascati.enea.it/fis/lac/fel/fel2.htm
Frascati (SPARC)	http://www.roma1.infn.it/exp/xfel
Hawaii (MkV)	M. Hadmack, Ph.D. Dissertation, University of Hawaii, December 2012.
Himeji (LEENA)	T. Inoue <i>et al.</i> , <i>Nucl. Inst. and Meth. A</i> 528, 402 (2004).
JLab (IR upgrade)	G. R. Neil <i>et al.</i> , <i>Nucl. Inst. and Meth. A</i> 557, 9 (2006).
JLab (UV demo)	S. V. Benson <i>et al.</i> , <i>Proceedings of FEL 2011</i> , Shanghai, China. http://accelconf.web.cern.ch/AccelConf/FEL2011/papers/weoci1.pdf
KAERI (THz FEL)	Y. U. Jeong <i>et al.</i> , <i>Nucl. Inst. and Meth. A</i> 575, 58 (2007).
Kyoto (KU-FEL)	H. Zen <i>et al.</i> , <i>Proceedings of FEL 2013</i> , New York, NY, USA http:// https://accelconf.web.cern.ch/accelconf/FEL2013/papers/wepso84.pdf
Nihon (LEBRA)	K. Hayakawa <i>et al.</i> , <i>Proceedings of FEL 2007</i> , Novosibirsk, Russia. http://accelconf.web.cern.ch/AccelConf/f07/papers/MOPPH046.pdf
Nijmegen (FELICE, FELIX, FLARE)	http://www.ru.nl/felix
Novosibirsk (FEL1)	N. G. Gavrilov <i>et al.</i> , <i>Nucl. Inst. and Meth. A</i> 575, 54 (2007).
Novosibirsk (FEL2)	N. A. Vinokurov <i>et al.</i> , <i>Proceedings of FEL 2009</i> , Liverpool, UK. http://accelconf.web.cern.ch/AccelConf/FEL2009/papers/tuod01.pdf
Novosibirsk (FEL3)	G. Kulipanov <i>et al.</i> , <i>IEEE Trans. Terahertz Sci. Technol.</i> no. 5, 798 (2015).
Okazaki (UVSOR- II)	H. Zen <i>et al.</i> , <i>Proceedings of FEL 2009</i> , Liverpool, UK. http://accelconf.web.cern.ch/AccelConf/FEL2009/papers/wepc36.pdf
Orsay (CLIO)	http://clio.lcp.u-psud.fr
Osaka (iFEL4)	T. Takii <i>et al.</i> , <i>Nucl. Inst. and Meth. A</i> 407, 21 (1998).
Osaka (iFEL1,2,3)	H. Horiike <i>et al.</i> , <i>Proceedings of FEL 2004</i> , Trieste, Italy. http://accelconf.web.cern.ch/AccelConf/f04/papers/THPOS17/THPOS17.pdf
Osaka (ILE/ILT)	N. Ohigashi <i>et al.</i> , <i>Nucl. Inst. and Meth. A</i> 375, 469 (1996).
Osaka (ISIR)	R. Kato <i>et al.</i> , <i>Proceedings of IPAC 2010</i> , Kyoto, Japan. http://accelconf.web.cern.ch/accelconf/IPAC10/papers/tupe030.pdf
Pohang (PAL XFEL)	http://pal.postech.ac.kr/paleng/
PSI (SwissFEL Aramis)	http://www.psi.ch/swissfel
SACLA (BL1,2,3)	http://xfel.riken.jp/eng/users/
SINAP (SX-FEL)	Z. Zhao <i>et al.</i> , Status of the SXFEL Facility. <i>Applied Sciences</i> 7(6), 607 (2017).
SLAC (LCLS)	http://lcls.slac.stanford.edu
Tokai (JAEA-FEL)	R. Hajima <i>et al.</i> , <i>Nucl. Inst. and Meth. A</i> 507, 115 (2003).
Tokyo (MIR-FEL)	http://www.rs.noda.tus.ac.jp/fel-tus/English/E-Top.html
UCSB (mm, FIR FEL)	http://sbfel3.ucsb.edu

Content from this work may be used under the terms of the CC BY 3.0 licence (© 2018). Any distribution of this work must maintain attribution to the author(s), title of the work, publisher, and DOI.

Table 6: References and Websites for Proposed FELs

LOCATION (NAME)	Internet Site or Reference
Ariel (THz FEL)	A. Friedman <i>et al.</i> , <i>Proceedings of FEL 2014</i> , Basel, Switzerland, http://accelconf.web.cern.ch/AccelConf/FEL2014/papers/tup081.pdf
ASU (CXFEL)	W. S. Graves <i>et al.</i> , <i>Proceedings of FEL 2017</i> , Santa Fe, NM, USA, TUB03.
Beijing (PKU-FEL)	Z. Liu <i>et al.</i> , <i>Proceedings of FEL 2006</i> , Berlin, Germany. http://accelconf.web.cern.ch/AccelConf/f06/papers/TUAAU05.pdf
Berlin (FHI FIR)	http://fel.fhi-berlin.mpg.de
Dalian (DCLS)	T. Zhang <i>et al.</i> , <i>Proceedings of IPAC2013</i> , Shanghai, China http://accelconf.web.cern.ch/accelconf/IPAC2013/papers/weodb102.pdf
Daresbury (CLARA)	J. A. Clarke <i>et al.</i> , <i>Proceedings of IPAC 2012</i> , New Orleans, LA, USA. http://accelconf.web.cern.ch/AccelConf/IPAC2012/papers/tuppp066.pdf
DESY (European XFEL)	http://xfel.desy.de
Glasgow (ALPHA-X)	http://phys.strath.ac.uk/alpha-x/
Groningen (ZFEL)	J. P. M. Beijers <i>et al.</i> , <i>Proceedings of FEL 2010</i> , Malmo, Sweden. http://accelconf.web.cern.ch/AccelConf/FEL2010/papers/mopc22.pdf
India (CUTE-FEL)	S. Krishnagopal and V. Kumar, <i>Proceedings of FEL 2007</i> , Novosibirsk, Russia. http://accelconf.web.cern.ch/accelconf/f07/papers/MOPPH074.pdf
KAERI (Table-top THz)	Y. U. Jeong <i>et al.</i> , <i>J. Korean Phys. Soc.</i> 59, no. 5, 3251 (2011).
LANL (MaRIE)	http://marie.lanl.gov
PSI (SwissFEL Athos)	http://www.psi.ch/swissfel
SINAP (SCLF)	Z. Zhu <i>et al.</i> , <i>Proceedings of FEL 2017</i> , Santa Fe, NM, USA, MOP055
SINAP (SX-FEL)	Z. Zhao <i>et al.</i> , Status of the SXFEL Facility. <i>Applied Sciences</i> 7(6), 607 (2017).
SLAC (LCLS-II)	http://lcls.slac.stanford.edu
Soleil (LUNEX 5)	M. E. Couprie <i>et al.</i> , <i>Journal of Physics: Conference Series</i> 425 (2013)
Tallahassee (Big Light)	http://www.magnet.fsu.edu/usershub/scientificdivisions/emr/facilities/fel.html
Tokyo (FIR-FEL)	http://www.rs.noda.tus.ac.jp/fel-tus/English/E-Top.html
Turkey (TARLA U25,U90)	http://www.tarla.org.tr

Content from this work may be used under the terms of the CC BY 3.0 licence (© 2018). Any distribution of this work must maintain attribution to the author(s), title of the work, publisher, and DOI.

RECENT FEL EXPERIMENTS AT FLASH

Evgeny A. Schneidmiller, Siegfried Schreiber*, and Mikahil V. Yurkov, DESY, Hamburg, Germany

Abstract

The FLASH free-electron laser user facility at DESY (Hamburg, Germany) provides high brilliance SASE FEL radiation in the XUV and soft X-ray wavelength range. With the recent installation of a second undulator beamline (FLASH2), variable gap undulators are now available. They now allow various experiments not possible with the FLASH1 fixed gap undulators. We report on experiments on tapering, harmonic lasing, reverse tapering, frequency doubling at FLASH2 and experiments using double pulses for specific SASE and THz experiments at FLASH1.

INTRODUCTION

Since summer 2005, FLASH, the free-electron laser (FEL) user facility at DESY (Hamburg), delivers high brilliance XUV and soft X-ray FEL radiation for photon experiments [1, 2]. In 2013/14, the facility has been upgraded with a second undulator beamline (FLASH2), being the first FEL facility worldwide operating simultaneously two undulator lines [3, 4]. The FLASH2 beamline is equipped with modern variable gap undulators allowing now a variety of FEL experiments which have not been possible before. The 12 planar undulators have a period of 31.4 mm, a length of 2.5 m each with an adjustable $K_{\text{rms}} = 0.7$ to 1.9.

A planar electromagnetic undulator, installed downstream of the FLASH1 SASE undulators, provides THz radiation for user experiments [5, 6]. In order to facilitate THz-XUV pump-probe experiments, double pulse lasing has been developed to provide SASE and/or THz pulses with a variable and shorter delay in the nanosecond scale than the usual 1 μs .

More details of the FLASH facility are described in [3, 4, 7, 8] and references therein. An overview on photon science at FLASH can be found in the publication list of [9].

The amplification process in a free-electron laser (FEL) can be effectively controlled by means of changing its resonance properties along a gap tunable undulator with integrated phase shifters. Novel schemes for the generation of FEL radiation with improved properties based on the use of variable gap undulators have been developed at DESY and demonstrated at FLASH2. In particular, we report on the first operation of the Harmonic Lasing Self-Seeded (HLSS) FEL [10–13] that allows to improve longitudinal coherence and spectral power of a SASE FEL. We were able to successfully demonstrate the validity of the reverse tapering concept [14–16] that can be used to produce circularly polarized radiation from a dedicated afterburner with strongly suppressed linearly polarized radiation from the main undulator. This scheme can also be used for an efficient background-free production of harmonics in an afterburner. We performed

experiments on the frequency doubling scheme [17, 18] and were able to extend the photon energy range of FLASH down to Nitrogen K-edge (400 eV), far below original design parameters. The described FEL schemes can easily be implemented at large scale X-ray FEL facilities [19–22], and the scientific community will definitely benefit from these innovative extensions.

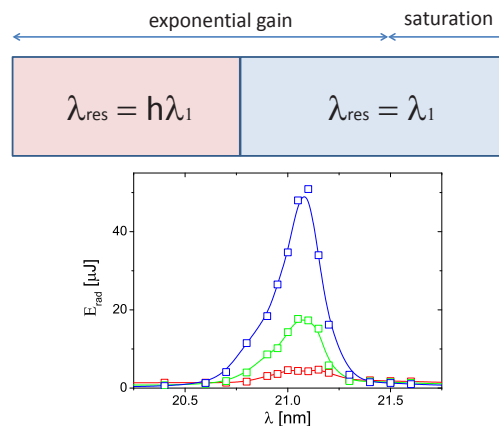


Figure 1: Top: conceptual scheme of a harmonic lasing self-seeded FEL. Bottom: operation of HLSS at FLASH2. Scan of the resonance wavelength of the first part of the undulator consisting of one undulator section (red), two sections (green), and three sections (blue). Pulse energy is measured after the second part of the undulator tuned to 7 nm.

HARMONIC LASING SELF-SEEDED FEL

In addition to well-known seeding and self-seeding techniques with enhanced spectral brightness [23–25], there are schemes without using optical elements. One of them is based on the combined lasing on a harmonic in the first part of the undulator with increased undulator parameter K , and on the fundamental in the second part [11]. In this way the second part of the undulator is seeded by a narrow-band signal generated via harmonic lasing in the first part (top plot in Fig. 1). This concept was named HLSS FEL (Harmonic Lasing Self-Seeded FEL). The enhancement factor of the coherence length (or, bandwidth reduction factor), that one obtains in an HLSS FEL in comparison with a reference case of lasing in SASE FEL mode in the whole undulator, is $R \approx h[L_w^{(1)}L_{\text{sat},h}]^{1/2}/L_{\text{sat},1}$ [11]. Here h is harmonic number, $L_{\text{sat},1}$ is the saturation length in the reference case of the fundamental lasing with the lower K -value, $L_w^{(1)}$ is the length of the first part of the undulator, and $L_{\text{sat},h}$ is the saturation length of harmonic lasing. Despite that the bandwidth reduction factor is significantly smaller than of traditional self-seeding schemes [23–25], the HLSS FEL scheme is very simple and robust, and it does not require any addi-

* siegfried.schreiber@desy.de

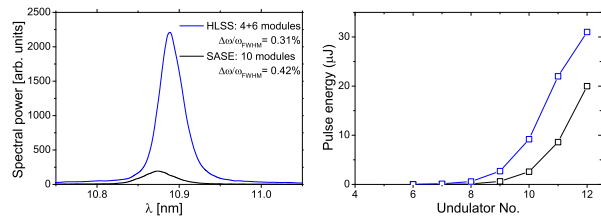


Figure 2: Comparison of SASE FEL and HLSS FEL operation at FLASH2. Left: Spectral density of the radiation energy for HLSS FEL configuration (blue) and for SASE FEL (black). Right: Radiation pulse energy versus position in the undulator for HLSS (blue) and for SASE (black) at 15 nm. Post-saturation taper was optimized for both cases.

tional installations. It can always be used in gap-tunable undulators with a sufficiently large K -value range.

On May 1, 2016 we demonstrated the first operation of HLSS FEL at FLASH2. Initially we tuned 10 undulator sections to standard SASE, operating in the exponential gain regime at a wavelength of 7 nm ($K_{\text{rms}} = 0.73$); the pulse energy was 12 μJ . Then we detuned the first section and tuned it to the third subharmonic ($K_{\text{rms}} = 1.9$) and scanned it around 21 nm (see Fig. 1). We repeated the measurements with the first two sections, and then with the first three sections. The fundamental at 21 nm was in the exponential gain regime with a pulse energy of 40 nJ after three undulator sections, far away from the saturation level of 200 μJ . This means that nonlinear harmonic generation in the first part of the undulator is excluded. It is seen from Fig. 1 that the effect is essentially resonant. The ratio of pulse energies at the optimal tune (21.1 nm) and at the tune of 20 nm away from the resonance is equal to 170.

In the following runs at different wavelengths (between 4.5 nm and 15 nm) we were able to demonstrate an improvement of the longitudinal coherence and brilliance of HLSS with respect to SASE, and also a better performance using post-saturation tapering (see Fig. 2). Both configurations use the same electron beam and the same undulator length. The left plot in Fig. 2 shows the averaged spectra for two study cases: SASE FEL with ten undulator modules, and HLSS FEL with four modules tuned to 33 nm plus six modules tuned to 11 nm. The spectral powers differ by a factor of six due to an increase of the pulse energy in the HLSS regime by a factor of five, and of the bandwidth reduction by a factor of 1.3 (0.31% for HLSS versus 0.41% for SASE). Note that the spectral width has been visibly widened due to an energy chirp along the electron beam. The coherence time has been improved by a factor 1.8 with respect to SASE. As a result, undulator tapering works more effectively in the case of HLSS FEL due to the improved longitudinal coherence (right plot in Fig. 2).

REVERSE UNDULATOR TAPER

Most X-ray FEL facilities are equipped with planar undulators generating linearly polarized radiation. Circularly polarized radiation is generated in a short helical afterburner

installed after the main undulator. To obtain a high degree of circular polarization, one needs to suppress the powerful linearly polarized radiation from the main undulator. The most effective suppression technique is reverse tapering of the main undulator [14–16] (see Fig. 3). At optimum taper strength, the bunching factor at saturation is practically the same as in a non-tapered undulator. The saturation length increases only moderately while the saturation power in the reverse tapered case is suppressed by orders of magnitude. The strongly modulated electron beam now radiates at full power in the afterburner.

The reverse tapering scheme has been successfully tested at FLASH2. The radiation energy from the afterburner sections exhibit a clear resonance behavior, and reaches its maximum value when the resonance frequency of the afterburner matches the frequency of the electron beam modulation in the main undulator (see Fig. 3).

An important figure of merit of the afterburner scheme is contrast, the ratio of the radiation power from the afterburner and from the main undulator. We could demonstrate in this experiment that a contrast of 200 is achievable for planar undulators.

In the case of helical afterburners, the contrast will increase up to 400. This means that the degree of circular polarization from a helical afterburner is expected to reach the value of 99.8%.

The density modulation of the electron beam driving a SASE FEL in saturation and in the post-saturation regime

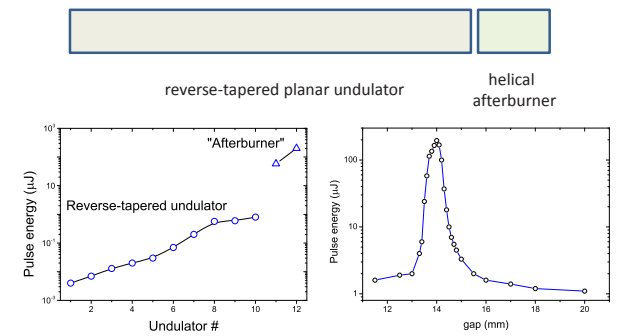


Figure 3: Top: Conceptual scheme to obtain circular polarization at X-ray FELs. Bottom: operation of the reverse tapering scheme at FLASH2. Left: FEL pulse energy versus undulator number. The first ten undulators are reverse-tapered, the last two sections are tuned to resonance to the incoming microbunched beam. Right: gap scan of the afterburner (last two undulator sections). For a completely open gap the pulse energy is below 1 μJ .

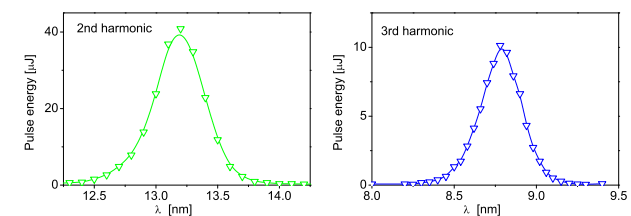


Figure 4: Generation of harmonics in the reverse tapering scheme at FLASH2: radiation pulse energy of the 2nd and the 3rd harmonics versus the resonance wavelength of the afterburner.

Content from this work may be used under the terms of the CC BY 3.0 licence (© 2018). Any distribution of this work must maintain attribution to the author(s), title of the work, publisher, and DOI.

contains a rich spectrum of higher harmonics. The radiation of a SASE FEL with a planar undulator contains higher odd harmonics as well. However, their intensity is pretty low, the 3rd harmonic intensity is in the one per cent level, and the 5th harmonic is on a level of a fraction of a per mille of the fundamental. This is because of debunching of the electron beam at higher harmonics due to the strong interaction of the electron beam with the fundamental harmonic. Another important problem is a strong background of the radiation from the main undulator.

An important feature of reverse tapering in the main undulator is to reach high values of the beam bunching at higher harmonics with very low radiation background from the main undulator. The afterburner tuned to higher harmonics is capable of generating much higher radiation energies than in the untapered case. Relevant experimental results from FLASH2 are presented in Fig. 4. Ten undulator sections (main undulator) have been tuned to the radiation wavelength of 26.5 nm with a reverse undulator tapering of 5%. The two remaining undulator sections have been tuned to the maximums of the power around the fundamental, the 2nd, and the 3rd harmonics. Radiation pulse energies of 150 μJ at the fundamental, 40 μJ at the 2nd, and 10 μJ at the 3rd harmonics have been obtained. We note that the pulse energy of the 2nd harmonic is comparable with the pulse energy of the fundamental, and the pulse energy of the 3rd harmonic exceeds by an order of magnitude the level of the 3rd harmonic from a SASE FEL.

FREQUENCY DOUBLER

In this section we discuss the generation of second harmonic allowing 2-color lasing simultaneously (ω and 2ω) as well as operation at shorter wavelengths [17, 18]. The frequency doubler scheme is conceptually simple (Fig. 5). The first part of the undulator is tuned to the frequency ω . In this part, the amplification process develops up to the onset of saturation when notable beam modulation at the fundamental and higher harmonics occurs, but the radiation power does not reach saturation yet. Then the modulated electron



Figure 5: Conceptual scheme of a frequency doubler.

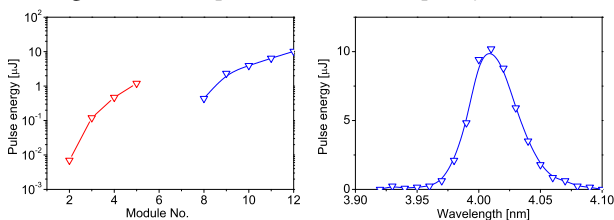


Figure 6: Left: gain curve of the frequency doubler at FLASH2. The first part of the undulator (5 modules) is tuned to 8 nm, the second part (7 modules) to 4 nm. Red and blue colors correspond to the radiation wavelength of 8 nm and 4 nm, respectively. Right: radiation pulse energy of the 2nd harmonic versus the resonance wavelength of the second part of the undulator.

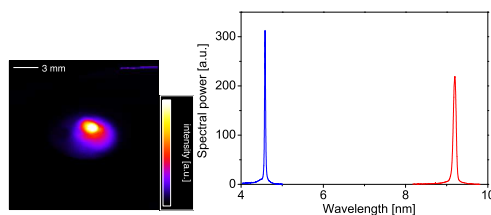


Figure 7: Photon beam image in the experimental hall (left) and radiation spectra (right) of the frequency doubler at FLASH2 showing 2-color lasing. The small yellow spot is 4.5 nm (2nd harmonic) radiation, the pulse energy is 10 μJ . The larger blue/pink spot is 9 nm radiation with a pulse energy of 10 μJ . The electron beam energy is 1080 MeV, the bunch charge 300 pC.

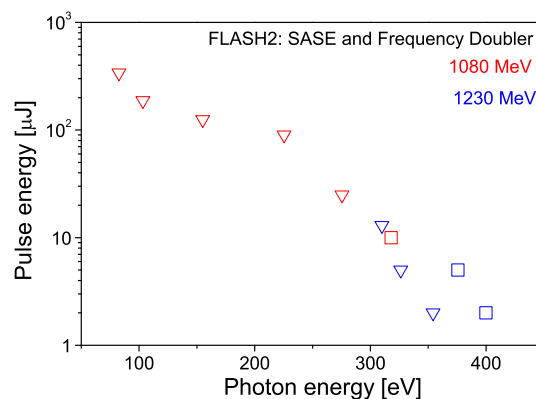


Figure 8: Radiation pulse energy of SASE (triangles) and frequency doubler (squares) obtained for various photon energies. The data are plotted for an electron beam energy of 1080 MeV and 1230 MeV resp.

beam enters the second part of the undulator tuned to the frequency 2ω . Now the beam modulation corresponding to the 2nd harmonic seeds the amplification process.

The operation of a frequency doubler has been successfully demonstrated at FLASH2. Figure 6 shows the gain curve of a frequency doubler 8 nm to 4 nm. The first five undulator sections are tuned to 8 nm, and the last seven sections to 4 nm. Scanning the gap and thus the wavelength of the second part exhibits a clear resonance behavior in the amplification process at the 2nd harmonic frequency (right plot in Fig. 6). This result clearly shows, that the beam bunching at the second harmonic seeds the amplification process of the frequency doubling section. Note, that seeding with the 2nd harmonic of SASE is excluded, since even harmonics are strongly suppressed in planar undulators.

The tuning procedure of the frequency doubler is simple and reproducible. In particular, it is possible to tune the relative energies of two colors ω and 2ω in a wide range. When tuned to equal pulse energies, a few to ten microjoules are obtained. Figure 7 shows a photon beam image and spectra as an example for 2-color lasing at FLASH2. With this first experience we can state that this operational mode can be proposed to users.

The frequency doubler scheme is also capable to generate shorter wavelength radiation than standard SASE. The first

part of the undulator operates at twice the wavelength, and saturation is obtained at half of the full undulator length. The induced beam bunching at the second harmonic is much larger than the shot noise in the electron beam, and it becomes possible to reach saturation on a much shorter length of the doubling section.

We performed two dedicated runs at FLASH2 with electron energies close to the limit of the accelerator. Both, SASE and the frequency doubler are optimized for maximum radiation pulse energy with the same electron beam. The results of pulse energy measurements are compiled in Fig. 8. We could reach shorter wavelengths with the frequency doubler, down to a record of 3.1 nm (400 eV) demonstrating photon energies above the Nitrogen K-edge. This significantly exceeds the original specification of the lowest wavelength of 4 nm for FLASH2.

DOUBLE PULSE OPERATION

FLASH is an accelerator based on superconducting technology which allows the acceleration of many bunches in a so-called burst with a length of up to 800 μ s (10 Hz repetition rate). FLASH uses a laser driven photo-injector to generate high brilliance electron bunches. The distance of the bunches in a burst is given by the present laser design to 1 μ s; a few longer distances are possible as well (2, 4, 5, 10, 20, and 25 μ s).

A variety of experiments would profit from an operation mode with two bunches closer than the usual bunch distance of 1 μ s. The split & delay method allows to generate very closely spaced double bunches of a few picoseconds up to a few tenth of nanoseconds. The split & delay method becomes unpractical for larger distances. To extend the double pulse spacing for large distances, two laser systems are used simultaneously.

Double Pulses with Close Spacing

A unique feature of FLASH is a planar electromagnetic undulator installed downstream of the FLASH1 SASE undulators [5]. It provides THz radiation for user experiments in the wavelength range from a few micrometers to 200 μ m (300 THz to 1.5 THz). An important feature is the precise synchronization of the THz pulses with the XUV and soft-X ray pulses, since both are produced by the same electron beam. Together with an optical laser, this arrangement allows THz-XUV-optical pump-probe experiments.

However, due to the specific THz beamline design [6], the THz pulses arrive much later (about 20 ns) at the experimental station than the XUV-pulses. A solution is to let the XUV-pulses propagate over the interaction point by 10 ns and back-reflect the radiation by special coated high-reflective mirrors. The disadvantage of this scheme is, due to the usually very small bandwidth of the mirror coating, that only one single XUV-wavelength can be used.

An elegant solution with the advantage that the XUV-wavelength is not fixed by the XUV-mirror is the use of double pulses with an appropriate distance to cancel the

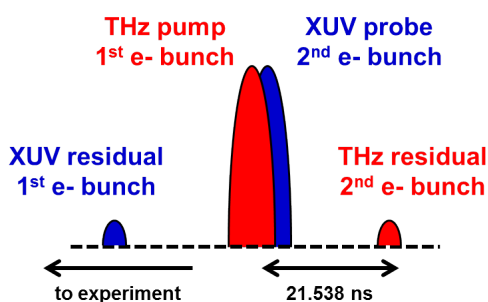


Figure 9: Principle of the THz-Doubler. Two electron bunches are generated with a delay of 21.538 ns (28 RF-buckets). The first one generates a good THz-pump pulse (red) while SASE is suppressed. The second one generates a good XUV-probe SASE pulse (blue) while THz is suppressed. The THz-pump and XUV-probe pulses are overlapping in the experiment.

THz/XUV path difference. In this scheme, the first electron bunch is tuned to provide a good THz radiation pump-pulse, and at the same time the second pulse is optimized for SASE radiation providing the XUV-probe pulse. Figure 9 shows the principle idea of this method.

The distance of the pulses must fit into an integer multiple of an 1.3 GHz RF-bucket, the frequency of the accelerator. One RF-bucket corresponds to 769.2 ns, 28 RF-buckets corresponds to 21.538 ns. The doubler electron pulses are generated with a split & delay unit at one of the three photo-injector laser (laser 1). The split & delay unit is a copy of the one already built in 2006 for a similar purpose [26]. Note, that with this arrangement, the complete burst of up to 800 pulses is automatically doubled.

Three laser knobs are available for tuning the two pulses independently: the phase in respect to the RF, pulse energy, and position on the cathode. All other parameters, especially the accelerating amplitude and phase of the accelerator cannot change within the 21 ns. The phase of pulse 1 is set with the phase of an 1.3 GHz RF-signal used to synchronize the laser oscillator. The phase pulse 2 is adjusted with a remote controlled delay stage in the delayed arm of the split & delay unit. The laser pulse energy is adjusted with variable attenuators realized with a remote controlled half wave plate together with a polarizer independent for both pulses allowing different bunch charges for pulse 1 and 2. To slightly correct the orbit in the accelerator, the position of both pulses on the cathode is slightly corrected remotely. The THz-doubler is permanently installed in the laser beamline [27], pulse 2 is switched in by simply opening a shutter.

First experiments with the THz-doubler have been performed to set-up THz and XUV-radiation for both pulses and to suppress XUV for the first and THz for the second. Some pump-probe experiments may not accept THz and XUV for both pulses.

Since the THz radiation is generated by the same electron bunch than the corresponding XUV signal, both are inherently synchronized to the few femtosecond level (< 5 fs). The question is, whether this is also the case for pulse 1 and

Content from this work may be used under the terms of the CC BY 3.0 licence (© 2018). Any distribution of this work must maintain attribution to the author(s), title of the work, publisher, and DOI.

2? Since the split & delay unit is built with fixed mirrors, and acceleration parameters in a distance of 20 ns should be the same, we expect a similar stability. A measurement using spectral decoding has been set-up to determine the arrival time jitter between pulse 1 and 2. Preliminary results show a jitter of less than 50 fs limited by the resolution of the set-up [28]. Next steps are an improvement of the experiment and a construction of an experimental set-up using the new double pulse scheme..

For completeness, we would like to mention that a similar split & delay unit is used by the FLASHforward experiment [29]. It is installed in the second laser system and provides a very short delay of the second pulse by a few picoseconds only for plasma acceleration experiments in the third beamline of FLASH.

Double Pulses With Large Spacing

On the request of a user experiment (AG Chapman) a new scheme has recently been developed to generate XUV double-pulses with an arbitrary variable delay.

The FLASH photoinjector has three drive lasers to produce electron bunches. All three lasers can be sent simultaneously in any beamline [27]. Usually one laser serves FLASH1, the second one the FLASH2 beamline.

In the new double pulse scheme, two lasers are sent simultaneously into one FLASH beamline while the third laser is used for the second beamline. The lasers are delayed in respect to each other to the requested distance.

In order to have equal beams for both pulses, it is important that the double pulse distance is an integer multiple of an RF-bucket of the accelerator. Even though arbitrary delays can be realized, for the sake of easy use, the user interface allows to set the delay in steps of 9.2 ns (the FLASH beam diagnostics use 108 MHz ADC boards). Once set-up, the delay can be changed at any time. At every delay step, the laser is kept exactly at the same phase in respect to the RF of the accelerator within 100 fs. This is guaranteed by active mode-locking of the laser oscillator to the 1.3 GHz RF-frequency of the accelerator.

In order to achieve the same XUV-radiation properties for both pulses, still a few adjustments have to be done. Tuning knobs are similar to the THz-doubler: the laser energy, laser phase, and position on the cathode. A slight tuning of the orbit, and a slight change in compression is required as well. Note, that in contrast to the small delay of the THz-doubler, large delays may exhibit slightly different amplitude and phase of the accelerating structures which need to be corrected.

The specific user experiment set-up at FLASH1 used a delay of 221.5 ns and 470 ns respectively to study the recovery time of a liquid jet hit by a XUV pulse [30]. The experiment has been performed with a SASE wavelength of 4.29 nm. The first pulse was tuned to an energy of 18 μ J, the second pulse to 10 μ J running stable for the duration of the experiment of several hours. Figure 10 shows an example of a liquid jet hit by the double pulses. Pulse 1 disrupts the flow of the liquid. When pulse 2 arrives with a delay of 221.5 ns,

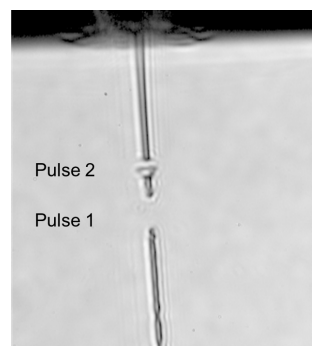


Figure 10: Example of a liquid jet hit by the double XUV-pulses (4.29 nm). Pulse 1 disrupts the flow of the liquid. When pulse 2 arrives with a delay of 221.5 ns, the jet has already recovered. Courtesy Max Wiedorn, CFEL, Hamburg, Germany.

the jet has already recovered. This shows, that experiments with liquid jets are feasible for high repetition rate beams as the European XFEL provides.

ACKNOWLEDGEMENTS

We are grateful to B. Faatz, M. Kuhlmann, J. Rönsch-Schulenburg, M. Tischer and R. Treusch for fruitful collaboration and to the FLASH team for technical support. The THz-doubler spectral decoding experiment has been performed by the DESY THz-team: E. Zapolnova, R. Pan, T. Golz, and N. Stojanovic. The split & delay unit has been set-up by K. Klose and one of the authors (S.S.). The liquid jet experiment has been performed by the research team of Henry Chapman, CFEL. We would also like to thank R. Brinkmann, J. Schneider, E. Weckert and W. Wurth for valuable discussions and interest in this work.

REFERENCES

- [1] W. Ackermann *et al.*, “Operation of a free-electron laser from the extreme ultraviolet to the water window”, *Nature Photonics* **1**, 336 (2007).
- [2] K. Tiedtke *et al.*, “The soft x-ray free-electron laser FLASH at DESY: beamlines, diagnostics and end-stations”, *New J. Phys.* **11**, 023029 (2009).
- [3] B. Faatz *et al.*, “Simultaneous operation of two soft x-ray free-electron lasers driven by one linear accelerator”, *New J. Phys.* **18**, 062002 (2016).
- [4] S. Schreiber and B. Faatz, “The free-electron Laser FLASH”, In: *High Power Laser Science and Engineering*, **3**, e20 (2015).
- [5] J. Feldhaus *et al.*, “The infrared undulator project at the VUV-FEL”, in *Proc. 27th Free-Electron Laser Conf.*, Stanford, USA, 2015, p. 183, MOPP055.
- [6] M. Gensch *et al.*, “New infrared undulator beamline at FLASH”, *Infr. Phys. & Techn.* **51**, 423 (2008).
- [7] J. Roensch-Schulenburg *et al.*, “Experience with Multi-Beam and Multi-Beamline FEL-Operation”, *Journal of Physics: Conf. Series* **874**, 012023 (2017).
- [8] K. Honkavaara *et al.*, “Status of the FLASH FEL User Facility at DESY”, presented at the 38th Int. Free Electron Laser Conf., Santa Fe, NM, USA, 2017, MOD02, this conference.

- [9] http://photon-science.desy.de/facilities/flash/publications/scientific_publications
- [10] E.A. Schneidmiller and M.V. Yurkov, "Harmonic lasing in x-ray free electron lasers", *Phys. Rev. ST Accel. Beams* **15**, 080702 (2012).
- [11] E.A. Schneidmiller and M.V. Yurkov, "Harmonic lasing self-seeded FEL", in *Proc. 25th Free-Electron Laser Conf.*, New York, USA, 2013, p. 700, WEP5078.
- [12] E.A. Schneidmiller and M.V. Yurkov, "Studies of harmonic lasing self-seeded FEL at FLASH2", in *Proc. 7th Int. Particle Accelerator Conf.*, Busan, Korea, 2016, p. 725, MOPOW009.
- [13] E.A. Schneidmiller *et al.*, "First operation of a harmonic lasing self-seeded free electron laser", *Phys. Rev. Accel. Beams* **20**, 020705 (2017).
- [14] E.A. Schneidmiller and M.V. Yurkov, "Obtaining high degree of circular polarization at x-ray free electron lasers via a reverse undulator taper", *Phys. Rev. ST Accel. Beams* **16**, 110702 (2013).
- [15] E.A. Schneidmiller and M.V. Yurkov, "Reverse undulator tapering for polarization control at XFELs", in *Proc. 7th Int. Particle Accelerator Conf.*, Busan, Korea, 2016, p. 722, MOPOW008.
- [16] E.A. Schneidmiller and M.V. Yurkov, "Background-Free Harmonic Production in XFELs via a Reverse Undulator Taper", in *Proc. 8th Int. Particle Accelerator Conf.*, Copenhagen, Denmark, 2017, p. 2618, WEPAB022.
- [17] M. Kuhlmann, E.A. Schneidmiller, and M.V. Yurkov, "Frequency doubler and two-color mode of operation at free electron laser FLASH2", in *Proc. SPIE Advances in X-ray Free-Electron Lasers Instrumentation IV*, Prague, Czech Republic, 2017, **10237**, p. 10237-10.
- [18] M. Kuhlman, E.A. Schneidmiller, and M.V. Yurkov, "Frequency doubler and two-color mode of operation at Free Electron Laser FLASH2", in *Proc. 8th Int. Particle Accelerator Conf.*, Copenhagen, Denmark, 2017, p. 2635, WEPAB027.
- [19] P. Emma *et al.*, "First lasing and operation of an Ångström-wavelength free-electron laser", *Nature Photonics* **4**, 641 (2010).
- [20] A.A. Lutman *et al.*, "Polarization control in an X-ray free-electron laser", *Nature Photonics* **10**, 468 (2016).
- [21] T. Ishikawa *et al.*, "A compact X-ray free-electron laser emitting in the sub-Ångström region", *Nature Photonics* **6**, 540 (2012).
- [22] M. Altarelli *et al.* (Eds.), "The European X-Ray Free-Electron Laser. Technical Design Report", DESY 2006-097, DESY, Hamburg, 1-646 (2006).
- [23] J. Feldhaus *et al.*, "Possible application of X-ray optical elements for reducing the spectral bandwidth of an X-ray SASE FEL", *Optics. Comm.* **140**, 341 (1997).
- [24] E.L. Saldin, Y.V. Shvyd'ko, E.A. Schneidmiller, and M.V. Yurkov, "X-ray FEL with a meV bandwidth", *Nucl. Instrum. and Methods A* **475**, 357 (2001).
- [25] G. Geloni, V. Kocharyan, and E.L. Saldin, "A novel self-seeding scheme for hard X-ray FELs", *Journal of Modern Optics* **58**, 1391 (2011).
- [26] O. Grimm, K. Klose, and S. Schreiber, "Double-pulse generation with the FLASH injector laser for pump/probe experiments", in *Proc. 10th European Particle Accelerator Conf.*, Edinburgh, UK, 2006, p. 3143, THPCH150.
- [27] S. Schreiber *et al.*, "Simultaneous Operation of Three Laser Systems at the FLASH Photoinjector", in *Proc. 37th Free-Electron Laser Conf.*, Daejeon, Korea, 2015, p. 459, TUP041.
- [28] E. Zapolnova *et al.*, submitted to be published.
- [29] A. Aschikhin *et al.*, "The FLASHForward Facility at DESY", *Nucl. Instr. Meth. A* **806**, 175 (2016).
- [30] The experiment has been performed by the research team of Henry Chapman, CFEL, Hamburg, Germany.

SUPPRESSION OF THE CSR EFFECTS AT A DOGLEG BEAM TRANSPORT USING DBA LATTICE

Toru Hara[†], Takahiro Inagaki, Kazuaki Togawa, Hirokazu Maesaka, Yuji Otake, Hitoshi Tanaka
 RIKEN SPring-8 Center, Sayo-cho, Hyogo 679-5198, Japan
 Chikara Kondo, Kenji Fukami
 JASRI, Sayo-cho, Hyogo 679-5149, Japan
 Shingo Nakazawa, Taichi Hasegawa, Osamu Morimoto, Masamichi Yoshioka
 SPring-8 Service Co., Ltd., Tatsuno-shi, Hyogo 679-5165, Japan

Abstract

Multi-beamline operation is an important issue of linear accelerator based XFELs to improve usability and efficiency of a facility. At SACLA, the multi-beamline operation had been tested since 2015 using two XFEL beamlines, BL2 and BL3. But the CSR effects at a 3-degree dogleg beam transport of BL2 caused projected emittance growth and instability of the electron beam orbit due to a high peak current of 10 kA and short bunch duration of SACLA. Consequently, stable lasing was obtained only for elongated electron bunches with low peak-currents below 3 kA. To suppress the CSR effects, the beam optics of the BL2 dogleg was replaced to that based on two DBA structures. In the new beam optics, the transverse effects of CSR are cancelled out between four bending magnets. To avoid the bunch length change, the electron beam passes an off-center orbit at the quadrupole magnets

of DBA. After the modification of the beam optics, stable lasing has been successfully obtained with 10-kA electron bunches. The parallel operation of the two beamlines will be started in autumn 2017 for user experiments.

INTRODUCTION

To meet the increasing demands from XFEL (X-ray Free-Electron Laser) users, the parallel operation of multiple beamlines is an important issue for improving the usability and efficiency of a facility [1].

Figure 1 is a schematic layout of SACLA (SPring-8 Angstrom Compact free-electron LASer) [2]. The undulator hall of SACLA can accommodate up to five undulator beamlines, and three of them have been installed so far. BL1 is a soft x-ray FEL beamline driven by a dedicated linear accelerator, SCSS+, which was originally build as a prototype of SACLA [3, 4]. BL2 and BL3 are XFEL

[†] toru@spring8.or.jp

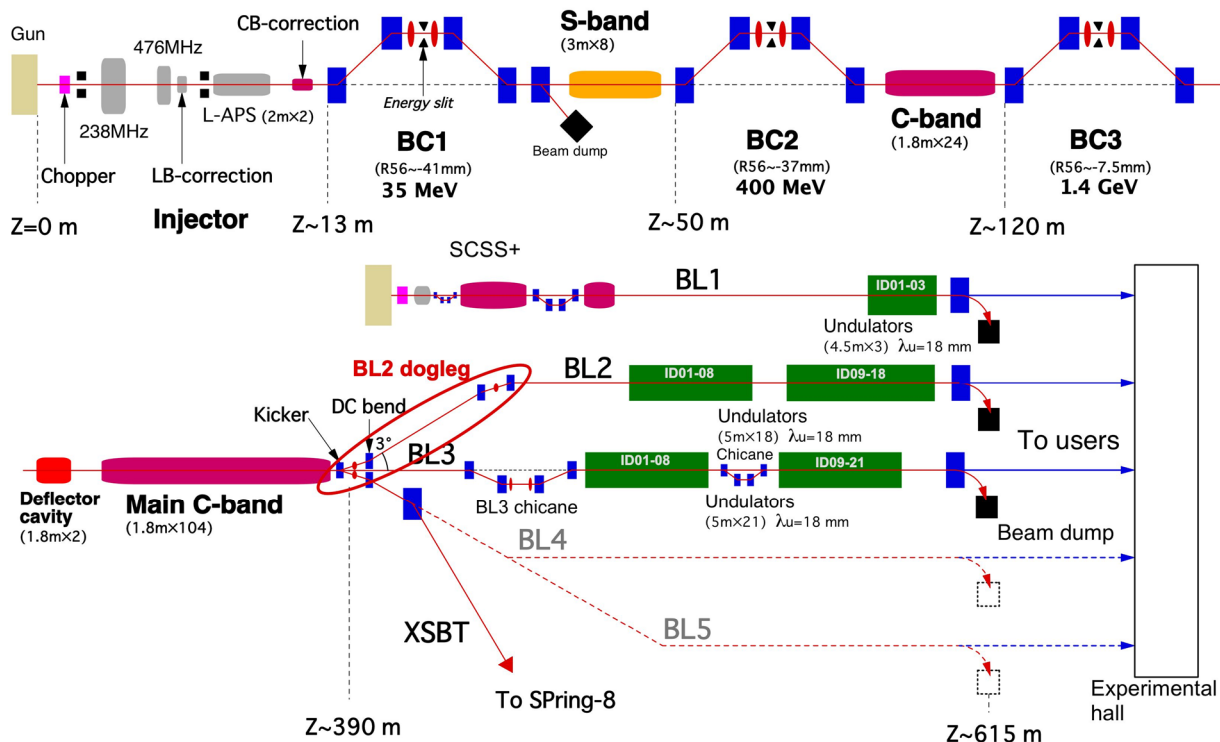


Figure 1: Schematic layout of SACLA.

Content from this work may be used under the terms of the CC BY 3.0 licence (© 2018). Any distribution of this work must maintain attribution to the author(s), title of the work, publisher, and DOI.

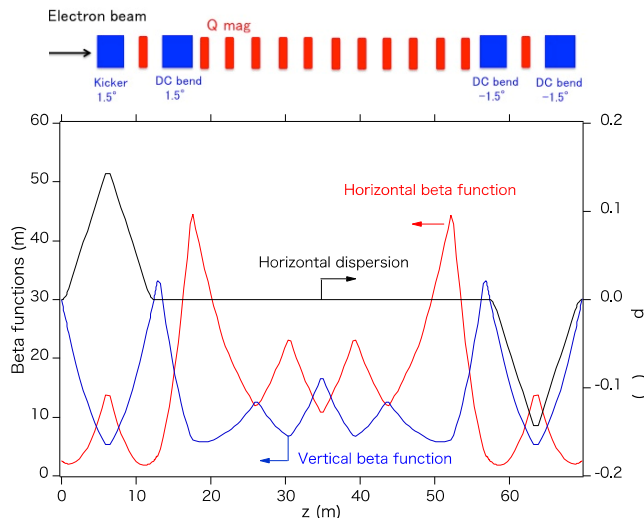


Figure 2: Magnet configuration (up) and beam optics functions (bottom) of the BL2 dogleg beam transport.

beamlines and a kicker magnet at the end of the SACLA linear accelerator switches the beamlines. The parallel operation of the two XFEL beamlines had been tested since 2015. However, the peak current of the electron beam was limited to below 3 kA due to the effects of CSR (Coherent Synchrotron Radiation) at a 3-degree dogleg electron beam transport to BL2 [1].

In order to suppress the CSR effects at the BL2 dogleg, the electron beam optics of the dogleg was changed to a new lattice based on DBA (Double Bend Achromat) structures. In this paper, the suppression of the CSR effects at the dogleg and the multi-beamline operation of SACLA are reported.

NEW BEAM OPTICS OF BL2 DOGLEG

Figure 2 shows the magnet configuration and beam optics functions of the new BL2 dogleg. Two DBA structures are placed at the entrance and exit of the dogleg to deflect the electron beam by 3 degrees. All four bending magnets, including a kicker magnet, are made identical with a deflection angle of 1.5 degrees. To suppress transverse CSR effects on the electron beam, such as projected emittance growth and orbit instability, the betatron phase advance between the two DBA is set to π [5, 6].

For the cancellation of the CSR effects, the longitudinal electron bunch profile should be the same at the four bending magnets. For the electron bunches used for the daily operation of SACLA having a peak current of more than 10 kA with 10~20 fs duration (FWHM), R_{56} of the dogleg, which is about 200 μm , is not negligible. In order to make R_{56} zero, the electron beam orbit is off-centered at the quadrupole magnets of the DBA structures.

Figure 3 shows a horizontal phase space distribution of the electron bunch after the dogleg calculated by ELEGANT [7]. A 10 kA-10 fs (FWHM) Gaussian bunch with 0.8 mm-mrad initial normalized emittance is assumed for figure 3. With a former optics of the dogleg, the horizon-

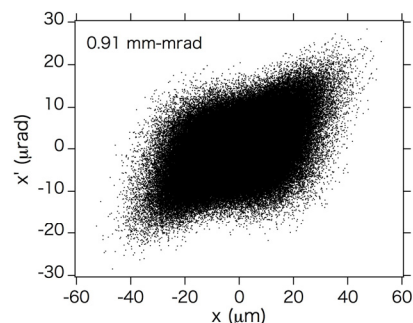


Figure 3: Horizontal phase space distribution of the electron bunch at the end of the BL2 dogleg. The initial conditions of the electron bunch are 8 GeV, 10 kA, 10 fs (FWHM) and 0.8 mm-mrad.

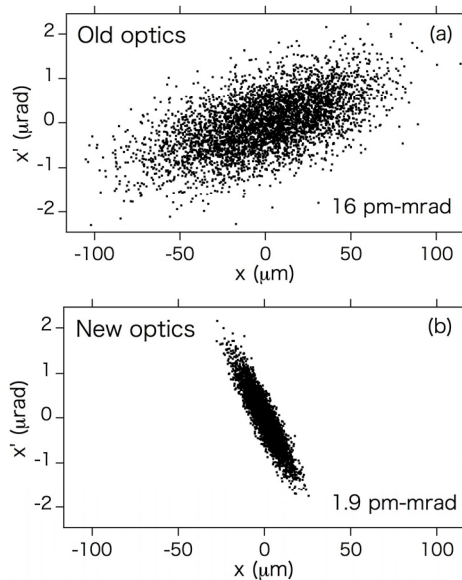


Figure 4: Stability of the horizontal electron beam orbit measured after the BL2 dogleg, before (a) and after (b) the replacement of the beam optics.

tal beam emittance becomes 8 mm-mrad after the dogleg, while the emittance of the new optics is 0.9 mm-mrad.

Since the deflection angle of the kicker magnet becomes three times larger in the new beam optics, the development of a pulsed power supply was a challenge [1]. By using SiC MOSFETs as switching elements, the new power supply achieves a targeted stability of 10 ppm (full width), which is small enough compared with an intrinsic orbit stability of SACLA [8] (see figure 4).

The beam optics of the BL2 dogleg was replaced in January 2017. Figure 4 is a comparison of the beam orbit stability before and after the replacement. The horizontal positions of the electron beam after the BL2 dogleg are measured and plotted in the phase space. The peak current of the electron beam is about 10 kA. From figure 4, the horizontal orbit stability is improved by an order of magnitude and the CSR effects are successfully cancelled with the new beam optics. The high peak current bunches are now stably transported to BL2 without serious emittance growth.

MULTI-BEAMLINE OPERATION

Figure 5 shows the XFEL output in the multi-beamline operation. The repetition of the electron beam is 60 Hz and the electron bunches are alternately deflected to BL2 and BL3 by the kicker magnet. The laser pulse energies are increased by 2~3 times compared with those before the optics replacement due to the higher peak currents.

Since spectral tunability is one of the important features of FEL light sources, it should be maintained also for the multi-beamline operation. In figure 5, the beam energy is changed for BL2 and BL3 in addition to the undulator K-values. By running twenty C-band accelerating structures at 30 Hz, which is half of the beam repetition, the electron bunches are alternately accelerated to 6.5 GeV and 7.8 GeV [9]. Then the kicker magnet deflects the lower energy bunches to BL2 and the higher energy bunches to BL3. Together with the K-values, the difference of the photon energies between the two beamlines reaches a factor of two, and wide spectral tunability of XFEL is ensured for the multi-beamline operation.

When operating the two beamlines in parallel, the optimum condition of the electron bunch compression with respect to the laser output might slightly differ for the two beamlines. At SACLA, this is mainly due to the different R_{56} of BL2 and BL3. As mentioned previously, R_{56} of the BL2 dogleg is adjusted to zero to suppress the CSR effects, while a chicane, whose R_{56} is about $-800 \mu\text{m}$, is installed in front of the BL3 undulators to measure the final beam energy and remove dark currents from the C-band accelerator.

Figure 6 shows the laser pulse energies of BL2 and BL3 as a function of CSR monitor signals installed at BC3 [10]. The optimum condition of the bunch compression is different for the two beamlines. At SACLA, the electron bunch compression parameters, namely RF phases, can be changed from bunch to bunch to obtain the maximum laser pulse energy simultaneously at both beamlines.

SUMMARY

The new beam optics of the BL2 dogleg beam transport based on two DBA structures successfully suppresses the CSR effects. As a result, the laser pulse energy of BL2 is increased by a factor of 2~3 due to the higher peak current of the electron bunches.

In the multi-beamline operation of SACLA, the beam energy and the bunch compression parameters can be controlled from bunch to bunch and independently optimized for the two beamlines. Thus, the laser pulse energies can be maximized for the two beamlines and wide spectral tunability of XFEL is maintained.

The multi-beamline operation will be open to users in Autumn 2017, which expands the opportunity of user experiments.

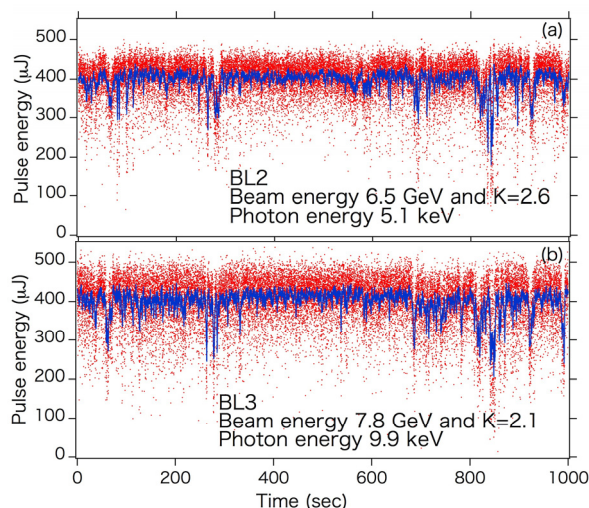


Figure 5: XFEL pulse energies obtained in the multi-beamline operation, (a) BL2 and (b) BL3. Red dots represent single-shot results and blue lines show averaged values over one second. The bunch repetition is 60 Hz. The electron beam energies and K-values are 6.5 GeV and 2.6 for BL2, and 7.8 GeV and 2.1 for BL3.

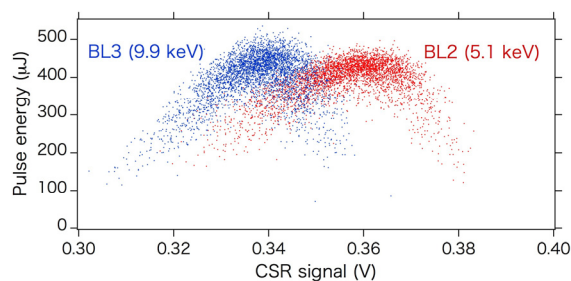


Figure 6: XFEL pulse energies of BL2 and BL3 plotted as a function of the CSR signal of BC3. The beam energies of BL2 and BL3 are 6.5 GeV and 7.8 GeV. Red and blue dots represent the pulses of BL2 and BL3, respectively.

REFERENCES

- [1] T. Hara *et al.*, *Phys. Rev. Accel. Beams*, **19**, 020703 (2016).
- [2] T. Ishikawa *et al.*, *Nat. Photon.*, **6**, 540 (2012).
- [3] S. Owada *et al.*, to be published in *J. Synchrotron Radiat.*
- [4] K. Togawa *et al.*, in *Proceedings of IPAC'17*, Copenhagen, May 2017, 1209 (2017).
- [5] D. Douglas, Thomas Jefferson National Accelerator Facility, Technical note, JLAB-TN-98-012 (1998).
- [6] S. Di Mitri, M. Cornacchia and S. Spampinati, *Phys. Rev. Lett.*, **110**, 014801 (2013).
- [7] M. Borland, *Phys. Rev. ST Accel. Beams*, **4**, 070701 (2001).
- [8] C. Kondo *et al.*, in *Proceedings of IPAC2017*, Copenhagen, May 2017, 3404 (2017).
- [9] T. Hara *et al.*, *Phys. Rev. ST Accel. Beams*, **16**, 080701 (2013).
- [10] Y. Otake *et al.*, *Phys. Rev. ST Accel. Beams*, **16**, 042802 (2013).

SEEDING EXPERIMENTS AND SEEDING OPTIONS FOR LCLS II

E. Hemsing[†], R. Coffee, G. Dakovski, W. Fawley, Y. Feng, B. Garcia, J. Hastings,
 Z. Huang, G. Marcus, D. Ratner, T. Raubenheimer, and R. W. Schoenlein
 SLAC National Accelerator Laboratory
 G. Penn

Lawrence Berkeley National Accelerator Laboratory

Abstract

We discuss the present status of FEL seeding experiments toward the soft x-ray regime and on-going studies on possible seeding options for the high repetition soft x-ray line at LCLS-II. The seeding schemes include self-seeding, cascaded HGHG, EEHG, and possible hybrid methods to reach the 1-2 nm regime with the highest possible brightness and minimal spectral pedestal. We describe relevant figures of merit, performance expectations, and potential issues.

INTRODUCTION

The general motivation for FEL seeding arises from the need for control over the longitudinal coherence. At soft x-rays, the ability to trade-off time-resolution (10-60 fs) and spectral resolution (180-30 meV) at close to the Fourier transform limit will open new dimensions in X-ray science.

Many seeding methods have been proposed to produce transform limited pulses down to soft x-rays. The three leading candidates are soft x-ray self seeding (SXRSS), Cascaded high gain harmonic generation (HGHG), and Echo Enabled Harmonic Generation (EEHG). SXRSS uses the monochromatized output from an upstream section of the FEL to seed the downstream section to saturation. It is currently the most mature technology in the 1-2 nm regime, as it has been demonstrated and delivered to users at LCLS for several years [1]. Cascaded HGHG uses external lasers to generate harmonic bunching and is in regular use at the FERMI FEL at Sincrotrone Trieste on the FEL-2 line where it is used to reach the 4-nm water window with peak fluences of order 10 μ J [2]. FERMI is currently operating as a user facility and has proved to be attractive for experiments that require wavelength tunability, multicolor pulses, polarization tunability, and higher coherence than is generally available from SASE-based FELs. EEHG also uses external lasers [3-8] and has been experimentally tested at wavelengths down to 32 nm [9], but has yet to demonstrated at soft x-rays, though efforts are underway [10, 11].

We have recently conducted studies on seeding for the high repetition soft x-ray line at LCLS-II. We find that the most promising candidates at this stage are SXRSS and EEHG as judged by anticipated performance, sensitivity, and flexibility, though there are clear challenges with both schemes. We show and compare their expected performance both in the case of ideal beams and more realistic start-to-end (S2E) beams. Other seeding methods like cascaded HGHG

[†] ehemsing@slac.stanford.edu

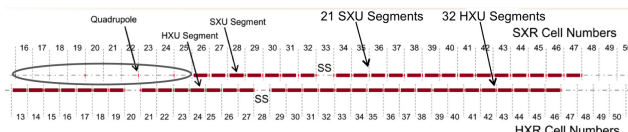


Figure 1: Layout of LCLS-II soft x-ray (top) and hard x-ray (bottom) undulators.

or even direct high harmonic generation (HHG) seeding are not among the most promising candidates at this stage due to anticipated poor performance or lack of current technical maturity. For example, we find through detailed simulations that cascaded HGHG is highly sensitive to the electron beam phase space distribution and that the spectral quality is comparable to SASE at the 1-2 nm level. The HHG technique is even more limited in its ability to access the required performance criteria due to poor ($\lesssim 10^{-6}$) harmonic conversion efficiency at shorter wavelengths. Upcoming proof-of-principle experiments on hybrid schemes like cascaded EEHG or EEHG/HGGH combinations, or on alternate techniques like coherent inverse Compton scattering may provide key information on their use as potential options, but currently these concepts are only in the preliminary experimental stages.

PERFORMANCE GOALS

The expectation for any seeding scheme in LCLS-II is the production of temporally coherent pulses with sufficient spectral brightness to address the photon science requirements. These requirements include several features that favor a seeded FEL with many characteristics inherent to optical laser systems:

- **Enhanced Control:** Precision control of the central wavelength well within the SASE bandwidth, as well as the ability to control the coherent bandwidth.
- **Minimal Spectral Pedestal:** The microbunching instability (MBI) is predicted to be a significant effect at the LCLS-II. It is believed to be responsible for the limited resolving power (roughly 2000-5000) of the SXRSS at LCLS [1, 12, 13]. Recent studies indicate that EEHG has a reduced sensitivity to MBI under certain conditions [14].
- **Coherent Two/Multi Color Operations:** Several different schemes to produce two-color x-ray pulses with variable pulse energy separations and timing delay have

Content from this work may be used under the terms of the CC BY 3.0 licence (© 2018). Any distribution of this work must maintain attribution to the author(s), title of the work, publisher, and DOI.

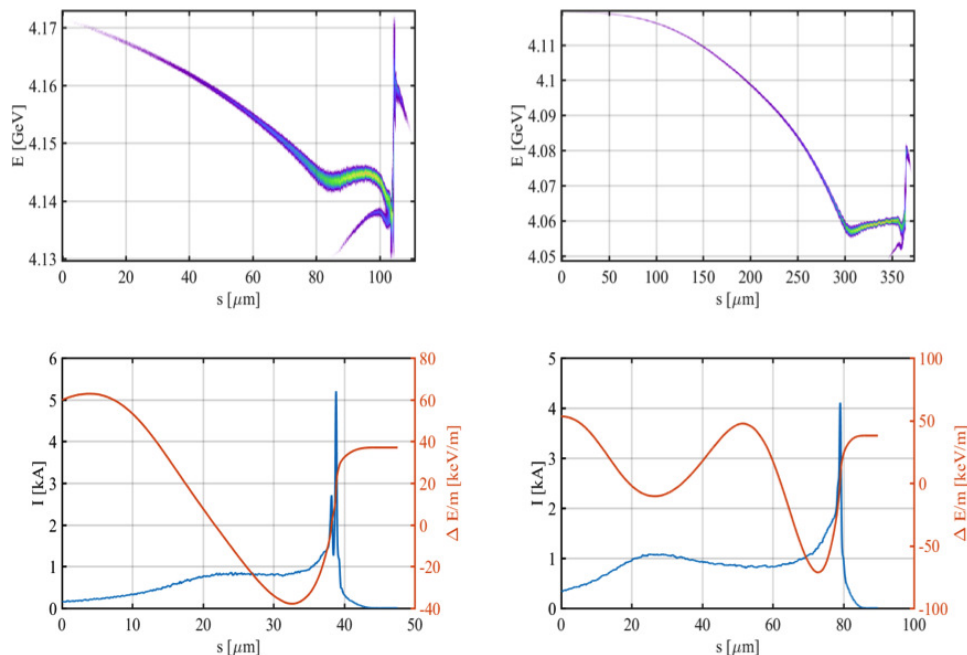


Figure 2: 100 pC and 300 pC electron beams from start-to-undulator IMPACT optimizations used for LCLS-II FEL simulations (head is to the right of the figures). Top left: Longitudinal phase space of 100 pC electron beam. Bottom Left: Current profile of the head and core of the 100 pC electron beam as well as the time-dependent energy loss per meter of distance in the undulator due to resistive wall wakefields. Top Right: Longitudinal phase space of 300 pC electron beam. Bottom Right: Current profile of the head and core of the 300 pC electron beam as well as the time-dependent energy loss per meter of distance in the undulator due to resistive wall wakefields.

recently been demonstrated at LCLS [15–17]. Multiple colors can be seeded at hard x-rays with the crystal monochromator, but such techniques do not translate to the SXRSS grating monochromator. Multicolor pulses have been produced at the FERMI FEL via the single stage HGHG configuration [18], and similar such methods could be extended to soft x-rays with EEHG.

LCLS-II LAYOUT

The layout of the LCLS-II undulators is shown in Figure 1. There is ~40 m of space available upstream of the soft x-ray line (circled) that could be used for external seeding infrastructure. Each of the 21 soft x-ray undulator segments have a $\lambda_u=39$ mm period and are variable gap. The total length is 96 m, with each segment is 3.4 m long and separated by a 1 m break. LCLS-II electron beam parameters are listed in Table 1.

QUANTIFYING PERFORMANCE

The measures of performance that aid in comparing different schemes are the peak photon density (photons/meV), the “FWHM-equivalent” bandwidth, ΔE_e , and the dimensionless brightness B_e . The ΔE_e is useful in capturing the contribution of the pedestal and is defined by the minimum spectral extent that contains 76% of the total pulse energy

E . This corresponds to the fraction that a 1-D Gaussian contains in the FWHM central region. From this we can define a dimensionless brightness $B_e = 0.76 * E/\Delta E_e$, which is the number of photons contained within the FWHM-equivalent bandwidth.

START-TO-END BEAMS

The IMPACT code was used to track both a 100 pC and a 300 pC electron beam (two standard configurations as of early 2017) from the cathode to the LCLS-II SXR undulator. The upper panels of Fig. 2 show the predicted longitudinal phase space of each beam. Note the apparent energy oscillations developed from MBI growth, the curvature in the beam core, and the long tails. We stress that these

Table 1: LCLS-II SXR Electron Beam Parameters

Parameter	Value
Energy	4 GeV
Charge	100-300 pC
Peak Current	1 kA
Emittance	0.45 mm-mrad
Energy Spread	500 keV
Beta Function	12 m

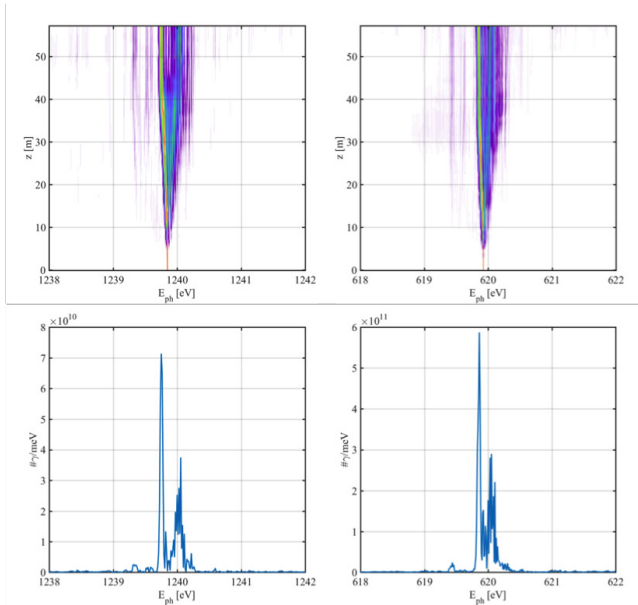


Figure 3: 300 pC beam SXRSS simulation results at 1 nm (left) and 2 nm (right).

beams are optimized primarily for low transverse emittance and high current, and are thus not necessarily optimized for seeding. Beams that are optimized better for seeding are currently under study. Figure 2 also shows the current profile of the head and core of each electron beam as well as the predicted time-dependent electron energy loss (in keV) per meter of distance travelled in the undulator due to the resistive wall wakefield. These long wavelength energy modulations broaden the bandwidth of a seeded FEL spectrum even in the absence of MBI-driven energy or density modulations.

SXRSS S2E

Figure 3 shows the spectra and normalized spectral evolution of the 1 and 2 nm cases with the 300 pC beam. An ideal seed is assumed from the SXRSS monochromator. In both cases, the spectrum has a clear bifurcation around $z = 30$ m (measured from the SXRSS section) due primarily to the long wavelength energy modulation imprinted on the electron beam from the resistive wall wakefield. The lower panels of Figure 3 show the spectra at the peak of the spectral brightness, which is at the end of the undulator. Clear spectral splitting is evident from the two dominant peaks, the largest of which has a FWHM of 55 meV. However, the splitting leads to a $\Delta E_e = 600$ meV at 1 nm and $\Delta E_e = 400$ meV at 2 nm. Less prominent but still evident are the effects of MBI-induced energy modulations, which drive the amplification of pedestal photon energies.

Figure 4 shows the spectra for the 100 pC LCLS-II beam. The performance is much better than the 300 pC case, due primarily to the shorter bunch length ($20\mu\text{m}$ compared to $80\mu\text{m}$) which is not as susceptible to resistive wall wakefield-driven bandwidth splitting. While MBI-driven modulations still serve to amplify frequency content in the pedestal, the

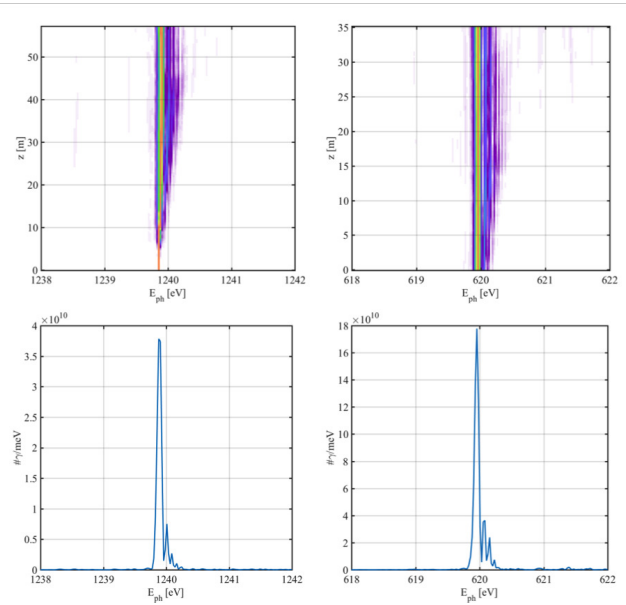


Figure 4: 100 pC beam SXRSS simulation results at 1 nm (left) and 2 nm (right).

spectrum is essentially a single spike. The FWHM of the spike is 80 meV in both cases, with $\Delta E_e = 115$ meV at 1 nm and $\Delta E_e = 180$ meV at 2 nm. It should be noted that the peak photon density with the 100 pC electron beam at 1 nm is only 50% of the value from the corresponding 1 nm simulation of the 300 pC beam, even though it has one third of the charge.

EEHG S2E

The EEHG modulator and chicane specifications used in simulations are listed in Table 2. As with the SXRSS simulations, undulator tapering is also used to optimize performance. Where applicable, benchmarking between Genesis v2 [19], Genesis v4 and with Puffin [20] was performed, with all codes showing similar results. The two 260 nm input lasers are taken to have the same 400 fs FWHM gaussian pulse duration. While this is not essential, with shorter seed lasers it can be difficult to maintain good contrast against SASE from the unseeded portions of the bunch. EEHG simulations were also performed using a variety of lasers and chicane configurations, with similar results.

Recent simulations and analytic studies [14] indicate that moderate initial energy modulations will not affect the EEHG scheme much as long as they do not generate significant current spikes or folding over of the beam phase space. This is because the large initial dispersion in EEHG acts like an effective damping for small modulations with wavelength $\lambda_0 < a\lambda_1/4\pi A_2$, where A_2 is the second energy modulation scaled to the slice energy spread (here $A_2 \approx 6$). In the case of the S2E LCLS-II beams, however, the large tails and strongly chirped regions of phase space combined with the strong first EEHG dispersion lead to significant folding of the the phase space. An example is shown in Figure 5. The result is a beam that is significantly less optimal for clean radiation than the original distribution.

Table 2: EEHG Specifications

Element	Strength: 1(2.3) nm	Length
Mod 1	K=25 $\Delta E_1 \approx 1(1.5)$ MeV	3.2 m, $\lambda_u=10$ cm
Mod 2	K=12.5 $\Delta E_2 \approx 2(3)$ MeV	3.2 m, $\lambda_u=40$ cm
Chic 1	$R_{56}=14.4(9.8)$ mm	9.25 m, $L_m=2$ m
Chic 2	$R_{56}=53(85)$ μm	2.25 m, $L_m=25$ cm

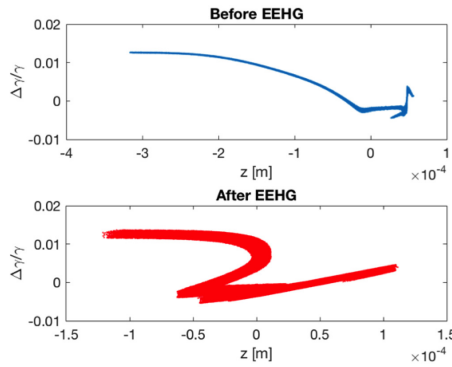


Figure 5: EEHG 300 pC phase space at 1 nm.

The consequences on the FEL spectra are shown in Fig. 6. The full spectral width of the 300 pC beam 2nm spectrum is 2x narrower than the 300 pC SXRSS spectrum due to the smaller pedestal and lack of strong spectral splitting from resistive wakefields. The FWHM of the narrow spike is 60 meV and 45 meV for the 2.3 nm and 1 nm cases, respectively. This is comparable to the 50 meV FWHM with SXRSS, but for EEHG there are 15 times fewer photons within the spike at 1 nm, and 2 times fewer at 2 nm.

The EEHG spectra for the shorter 100 pC beam are also shown in Fig. 6. At 1 nm, the FWHM of the spike is 170 meV, and contains $3e11$ photons; a factor of 20 smaller photon

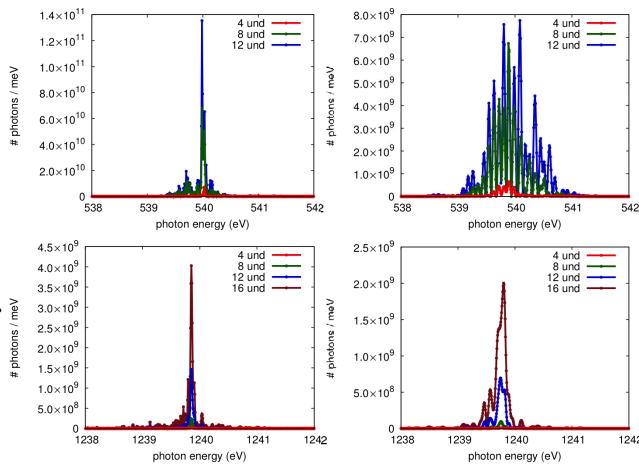


Figure 6: EEHG spectra with 300 pC beam (left) and 100 pC beam (right).

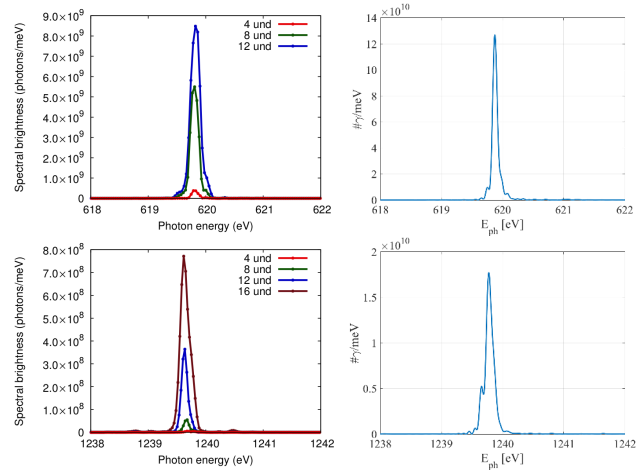


Figure 7: EEHG (left) and SXRSS spectra (right) with ideal 100 pC, 50 fs beam.

density than for SXRSS. At 2.3 nm, the EEHG spectrum has multiple spikes that together cover 500 meV. These are the result of interference between the head and tail current spikes in the e-beam that produce two temporally separated FEL pulses. Such a feature may be useful for phase locked multicolor operations, but this arrangement does not readily produce a single spectral spike.

IDEAL BEAMS

Given the seeding performance of the S2E beams, simulations with ideal, flat-top current profile, 50 fs beams were performed to establish the baseline expectations of EEHG and SXRSS. Beams longer than 50 fs tend to perform worse for both schemes due to the resistive wall wakefields in the LCLS-II undulators, which add nonlinear structure to the otherwise ideal linear e-beam phase space that fragments the spectrum. For beams shorter than 50 fs, the effect of the wake is to introduce a nearly linear chirp in the FEL output.

SXRSS

SXRSS results with an ideal 100 pC beam are shown in Figure 7, seeded from an ideal grating monochromator. The output FEL spectra are single spikes, though the effect of the resistive wall wakefields is revealed in the steady reduction in resolving power from 10k near the grating to around 5k near saturation.

EEHG

The 1 and 2 nm output EEHG spectra are also shown in Figure 7 from two ideal $\lambda_1=260$ nm lasers, corresponding to the $a = 130^{th}$ and 260^{th} harmonics. Like the SXRSS spectra, the EEHG spectra are also somewhat broadened by the wakefield-induced chirp, but are still single spike. The EEHG spectra are broader, however, due to two effects. First, there is a harmonic compression effect that shortens the pulse length. Second, the initially flat current profile transforms into a trapezoidal profile after the large chicane.

As such, the current at the head and the tail is reduced leaving only a shortened region to lase. Fewer of the total electrons thus participate, so the output power is also less than for SXRSS.

Issues for LCLS-II SXRSS

- **Spectral Purity:** The SXRSS spectrum is susceptible to pedestal formation and spectral splitting due to long wavelength electron beam phase space modulations, particularly in the longer 300 pC beams.
- **Mechanical Inflexibilities and Optical Coupling:** In contrast to the existing LCLS SXRSS system, an optimized LCLS-II SXRSS design will include extra mechanical flexibility including rotatable and movable mirrors to better optimize the e-beam/seed beam overlap over 1-4 nm range.
- **Heating of compact optical elements:** The footprint of the SASE beam on the VLS grating is a few millimeters, and requires cooling of the grating and focusing mirrors to handle the high average power x-ray load (some tens of Watts). Preliminary analysis assuming steady-state conditions indicates that with water cooling, the VLS grating with 5k resolving power would remain within specs for repetition rates up to 100 kHz.

Issues for EEHG

The S2E beams are clearly not well-optimized for external seeding due to the strong non-linear phase space distortions, particularly the large tails. We are currently pursuing beams that can perform much closer to the ideal case. Even so, there are several known issues under consideration for EEHG implementation at soft x-rays:

- **Laser Spectral Phase:** Spectral phase of the input laser gets multiplied by the large harmonic upconversion factor, but the noise is also filtered by the finite bandwidth of the modulators and FEL. Even orders of spectral phase have the most deleterious effects (ie, linear frequency chirp), but may be mitigated by laser pulse stretching.
- **MBI Growth:** Strong modulators ($K=12-25$) increase effect of longitudinal space charge by $1+K^2/2$ factor in drift length. The effect is the worst in 2nd modulator, and can be amplified by chicanes.
- **ISR-driven energy spread growth:** ISR in second modulator can wash out fine-grained energy structure. This is minimized in current lattice design, but probably precludes slippage-boosted spectral cleaning schemes (ie, harmonic coupling in modulator).
- **Large chicane:** First chicane ($R_{56} \approx 15$ mm) folds long tails in phase space, and can also generate CSR energy structures that reduce long range coherence of bunching.

Table 3: SXRSS/EEHG Brightness Comparison $B_e [10^{16}]$

Beam	1 nm	2 nm
300 pC	1.0/0.1	5.5/2.6
100 pC	2.4/0.1	3.7/0.2
Ideal	1.1/0.05	7.8/0.8

CONCLUSION

High-resolution numerical simulations with recent S2E 100 & 300 pC beams for LCLS-II indicate that SXRSS delivers pulses with $\sim 2 - 20$ times higher brightness than EEHG, depending on the tune. This is due to the increased energy spread of the laser modulated EEHG beam and the strong phase space deformation of the non-linear S2E beams in EEHG. SXRSS has the obvious advantage of simplicity of setup, (assuming cooling is adequate), but lacks some of the potential for multipulse and multicolor FEL operations enabled by external seeding. Thus, these seeding options appear to be complementary, given available space in the current LCLS-II beam line design (See Figure 1), as well as expectations with user demand and FEL performance. The performance of these schemes with S2E beams that are better optimized for seeding is currently under study.

REFERENCES

- [1] D. Ratner, R. Abela, J. Amann, C. Behrens, D. Bohler, G. Boucharde, C. Bostedt, M. Boyes, K. Chow, D. Cocco, et al., Phys. Rev. Lett. **114**, 054801 (2015a), URL <http://link.aps.org/doi/10.1103/PhysRevLett.114.054801>.
- [2] E. Allaria, D. Castronovo, P. Cinquegrana, P. Craievich, M. Dal Forno, M. Danailov, G. D'Auria, A. Demidovich, G. De Ninno, S. Di Mitri, et al., Nature Photon. **7**, 913 (2013).
- [3] G. Stupakov, Phys. Rev. Lett. **102**, 074801 (2009).
- [4] D. Xiang and G. Stupakov, Phys. Rev. ST Accel. Beams **12**, 030702 (2009).
- [5] D. Xiang, E. Colby, M. Dunning, S. Gilevich, C. Hast, K. Jobe, D. McCormick, J. Nelson, T. O. Raubenheimer, K. Soong, et al., Phys. Rev. Lett. **105**, 114801 (2010).
- [6] D. Xiang, E. Colby, M. Dunning, S. Gilevich, C. Hast, K. Jobe, D. McCormick, J. Nelson, T. O. Raubenheimer, K. Soong, et al., Phys. Rev. Lett. **108**, 024802 (2012).
- [7] E. Hemsing, M. Dunning, C. Hast, T. O. Raubenheimer, S. Weathersby, and D. Xiang, Phys. Rev. ST Accel. Beams **17**, 070702 (2014), URL <http://link.aps.org/doi/10.1103/PhysRevSTAB.17.070702>.
- [8] Z. T., WangD., C. H., C. H., D. X., D. G., FengC., GuQ., H. M., L. H., et al., Nat Photon **6**, 360 (2012), URL <http://dx.doi.org/10.1038/nphoton.2012.105>.
- [9] E. Hemsing, M. Dunning, B. Garcia, C. Hast, T. Raubenheimer, G. Stupakov, and D. Xiang, Nat Photon **10**, 512 (2016), URL <http://dx.doi.org/10.1038/nphoton.2016.101>.
- [10] Z. Zhao, C. Feng, J. Chen, and Z. Wang, Science Bulletin **61**, 720 (2016), ISSN 2095-9281, URL <http://dx.doi.org/10.1007/s11434-016-1060-8>.

- Content from this work may be used under the terms of the CC BY 3.0 licence (© 2018). Any distribution of this work must maintain attribution to the author(s), title of the work, publisher, and DOI.
- [11] P. Rebernik Ribič, E. Roussel, G. Penn, G. De Ninno, L. Giannessi, G. Penco, and E. Allaria, *Photonics* **4**, 19 (2017), ISSN 2304-6732.
- [12] D. Ratner, C. Behrens, Y. Ding, Z. Huang, A. Marinelli, T. Maxwell, and F. Zhou, *Phys. Rev. ST Accel. Beams* **18**, 030704 (2015b).
- [13] Z. Zhang, R. Lindberg, W. M. Fawley, Z. Huang, J. Krzywinski, A. Lutman, G. Marcus, and A. Marinelli, *Phys. Rev. Accel. Beams* **19**, 050701 (2016), URL <http://link.aps.org/doi/10.1103/PhysRevAccelBeams.19.050701>.
- [14] E. Hemsing, B. Garcia, Z. Huang, T. Raubenheimer, and D. Xiang, *Phys. Rev. Accel. Beams* **20**, 060702 (2017), URL <https://link.aps.org/doi/10.1103/PhysRevAccelBeams.20.060702>.
- [15] A. A. Lutman, R. Coffee, Y. Ding, Z. Huang, J. Krzywinski, T. Maxwell, M. Messerschmidt, and H.-D. Nuhn, *Phys. Rev. Lett.* **110**, 134801 (2013), URL <http://link.aps.org/doi/10.1103/PhysRevLett.110.134801>.
- [16] A. Marinelli, A. A. Lutman, J. Wu, Y. Ding, J. Krzywinski, H.-D. Nuhn, Y. Feng, R. N. Coffee, and C. Pellegrini, *Phys. Rev. Lett.* **111**, 134801 (2013), URL <http://link.aps.org/doi/10.1103/PhysRevLett.111.134801>.
- [17] A. Marinelli, D. Ratner, A. A. Lutman, J. Turner, J. Welch, F. J. Decker, H. Loos, C. Behrens, S. Gilevich, A. A. Miahnahri, et al., *Nature Communications* **6**, 6369 EP (2015), URL <http://dx.doi.org/10.1038/ncomms7369>.
- [18] E. Ferrari, C. Spezzani, F. Fortuna, R. Delaunay, F. Vidal, I. Nikolov, P. Cinquegrana, B. Diviacco, D. Gauthier, G. Penco, et al., *Nature Communications* **7**, 10343 EP (2016), URL <http://dx.doi.org/10.1038/ncomms10343>.
- [19] S. Reiche, *Nuclear Instruments and Methods in Physics Research A* **429**, 243 (1999).
- [20] L. T. Campbell and B. W. J. McNeil, *Physics of Plasmas* **19**, 093119 (2012), URL <http://scitation.aip.org/content/aip/journal/pop/19/9/10.1063/1.4752743>.

ASU COMPACT XFEL*

W. S. Graves[†], J. P. J. Chen, P. Fromme, M. R. Holl, R. Kirian, L. E. Malin, K. E. Schmidt,
J. C. H. Spence, M. Underhill, U. Weierstall, N. A. Zatsepin, C. Zhang,
Arizona State University, Tempe, USA
P. D. Brown, K. H. Hong, D. E. Moncton, MIT, Cambridge, USA
E. A. Nanni, C. Limborg-Deprey, SLAC, Menlo Park, USA

Abstract

Arizona State University (ASU) is pursuing a concept for a compact x-ray FEL (CXFEL) that uses nanopatterning of the electron beam via electron diffraction and emittance exchange to enable fully coherent x-ray output from electron beams with an energy of a few tens of MeV. This low energy is enabled by nanobunching and use of a short pulse laser field as an undulator, resulting in an XFEL with 10 m total length and modest cost. The method of electron bunching is deterministic and flexible, rather than dependent on SASE amplification, so that the x-ray output is coherent in time and frequency. The phase of the x-ray pulse can be controlled and manipulated so that new opportunities for ultrafast x-ray science are enabled using attosecond pulses, very narrow line widths, or extremely precise timing among multiple pulses with different colors. These properties may be transferred to large XFELs through seeding with the CXFEL beam. Construction of the CXFEL accelerator and laboratory are underway, along with initial experiments to demonstrate nanopatterning via electron diffraction. An overview of the methods and project are presented.

INTRODUCTION

ASU has embarked on a multiphase effort to develop powerful compact x-ray sources, beginning with the compact x-ray light source [1] (CXLS) that is now under construction and will be operational by end of 2017. CXLS uses an x-band photoinjector, standing wave linac, and high power lasers to produce x-rays via inverse Compton scattering (ICS) with projected flux of about 10^8 photons per shot at the high repetition rate of 1 kHz. The 35 MeV linac is expected to produce photon energies in the range 1-35 keV with pulse length of 100 fs to 1 ps. CXFEL is the planned second phase of development and is closely based on CXLS equipment. CXFEL will transform the incoherent ICS emission of CXLS into a fully coherent x-ray laser by creating ‘nanobunches’ using a combination of methods including diffraction of the electron beam from a patterned silicon crystal [2–5] at energy of 4-10 MeV and transformation of the resulting spatial pattern, or density modulation, into the longitudinal dimension using emittance exchange (EEX) [6]. CXLS is designed to be easily upgraded to CXFEL by reconfiguring the bunch compression chicane into a double dogleg EEX

line. All of the electron optics and equipment needed to pattern the electron beam, with the exception of the EEX line, are included in the phase 1 CXLS, enabling preliminary experiments to study and understand the generation and manipulation of patterned electron beams.

TECHNICAL DESCRIPTION

The CXFEL components are shown in Figure 1. Beginning at the right end of the figure is the 4.5 cell x-band photoinjector [7] that accelerates the beam to 4 MeV. Following ports for the cathode laser is the first of three short 35 cm long linac sections, each of which is an innovative 20-cell standing-wave linac [8] adapted to our 9.3 GHz RF frequency. SLAC spinoff company Tibaray LLC is producing the photoinjector and linac. The first linac section L1 can accelerate the beam up to 12 MeV and/or adjust the time-energy chirp for optimum diffraction in the thin silicon crystal that sits just downstream of it. After the crystal the two linac sections L2 and L3 are jointly powered and phased to accelerate the beam to a maximum of 35 MeV. The photoinjector and linac L1 are powered by one RF transmitter with high power waveguide attenuator and phase shifter to arbitrarily split RF amplitude and phase among the two devices. A second RF transmitter powers L2 and L3 as well as the deflector cavity in the downstream EEX line. The RF transmitters are Scandinova solid-state K1A modulators driving L3 L6145-01 9.3 GHz klystrons capable of 6 MW output power in 1 microsecond pulses at repetition rates up to 1 kHz. The transmitters are now in final testing at the vendor and have demonstrated better than 100 ppm RMS voltage stability.

Following L3 is a set of 4 quadrupoles (Q1-Q4) arranged as a variable demagnification telescope to image the electron beam at the crystal plane to a downstream point. For electron microscopy studies the beam is spatially imaged onto a profile monitor PRO6 in the EEX line. The imaging requirement is different to generate nanobunches at the output of the EEX line. In this case the spatial image of the silicon grating is never formed, but rather a matching condition with tilted ellipses [2] is generated at the entrance to the EEX line so that the original modulation created by the crystal is transferred to the longitudinal dimension at the EEX output. The EEX line consists of the 4 bend magnets B1-B4, an RF deflector cavity and accelerator cavity that are independently phased and powered, along with sextupoles S1-S3 and octopole O1 for aberration correction. Following the EEX line is a quadrupole triplet (Q5-Q7) that focuses

* This work was supported by NSF Accelerator Science award 1632780, NSF BioXFEL STC award 1231306, DOE contract DE-AC02-76SF00515, and ASU.

[†] wsg@asu.edu

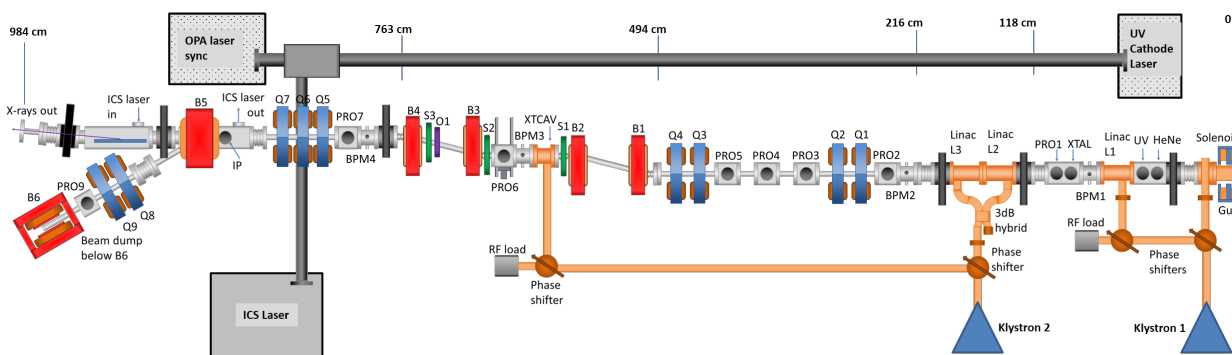


Figure 1: Major components of CXFEL. The photoinjector is at the right end. A short linac (L1) modifies the electron beam energy and chirp before diffraction into a nanopattern. The beam is further accelerated in linacs L1 and L2, then a telescope demagnifies the pattern and matches to the emittance exchange line before the laser interaction point. The entire assembly is 10 m long.

the electron beam to micron size at the ICS interaction point (IP) where the patterned electron bunches radiate coherently in the ICS laser field. Downstream of the IP the beam is deflected 30 degrees horizontally (B5) and then 90 degrees vertically (B6) into a beam dump. Nominal charge per pulse is 1 pC so that the average power into the dump is <1 W.

The photocathode laser is a Lightconversion Pharos Yb:KGW amplifier with integral UV conversion generating up to 1.5 mJ at 1030 nm, and 150 μJ at 4th harmonic 258 nm, in 180 fs pulses. The Pharos also contains the laser oscillator running at 72.6 MHz, the 128th subharmonic of the 9300 MHz RF frequency. The Pharos is located in local shielding adjacent to the photoinjector to present a short beam path to the cathode and to facilitate synchronization with the electron beam and ICS laser. The ICS laser is a Trumpf Dira 200-1 Yb:YAG amplifier generating 200 mJ in 1.5 ps pulses. Both lasers operate at 1 kHz to match the accelerator repetition rate. The Dira is located in a laser room adjacent to the ICS interaction point.

Timing synchronization of the electron beam, lasers, and x-rays is a critical performance parameter for linac-based light sources. Our initial goal is sub-100 fs timing synchronization of the beams, and eventually sub-10 fs synchronization. The low-level RF (LLRF) and laser oscillator are locked to a Wenzel MXO RF master oscillator with -176 dBc/Hz intrinsic phase noise. The laser oscillator uses a Menlo Systems custom SYNCHRO RRE with fast and slow piezo loops to lock to the MO and control the Pharos timing. The Dira ICS laser is synchronized to the Pharos by splitting a small portion of the Pharos output to white light generation for seeding an optical parametric chirped pulse amplifier (OPCPA) that measures and corrects the Dira timing. This method has demonstrated sub-10 fs timing [9]. The LLRF that drives the RF transmitters is being adapted from the LCLS upgrade in collaboration with SLAC, and has demonstrated RMS phase jitter <0.01 RF degrees [10] (3 fs at 9300 MHz). The compact size of the facility and high degree of care taken with the laboratory construction are expected to contribute to ultrastable timing.

In addition to timing stability, the source demands stability in pointing, energy, and flux, which in turn depend on stability of all power supplies and the laboratory environment. All magnet power supplies have stability in current ripple and drift of <100 ppm, and the solid-state RF modulators have demonstrated the best possible stability. Initial tests of the Dira laser indicate pointing stability less than 5 μrad and power stability of 0.3% over 12 hour long term tests.

LABORATORY FACILITIES

ASU is constructing a new Biodesign C building that contains 25,000 sq.ft. of laboratory space on the basement level to house CXLS and CXFEL (Figure 2). There are two mirror-image laboratories to house independent light sources. The phase 1 construction will finish the CXLS lab. The labs are highly customized to provide the optimum environment needed for stable operation. The slab floor is 6 ft thick and is mechanically isolated from the surrounding building to avoid vibration. The labs are rated at vibration criterion VC-E, equivalent to state-of-the-art electron microscopy labs. The accelerator vaults and x-ray hutches are ISO class 8 cleanrooms with non-turbulent airflow. The laser labs are ISO class 7 cleanrooms. During construction the iron rebar that was used in the accelerator areas was hand-selected for low magnetic field, and degaussed where needed. Background fields were repeatedly measured with the result that the ambient magnetic field in the labs is at Earth's background. The RF room containing the RF transmitters is a sealed aluminum Faraday cage with special penetrations for waveguide and other signals in order to isolate electromagnetic noise emitted by the pulsed transmitters. Air temperature control is ±0.5°C in the vault, RF room, and x-ray hutch, and ±0.25°C with relative humidity 35-40% in the laser room. All equipment racks are actively cooled. The relatively small space and equipment needs of CXFEL makes this precise environmental control practical and cost effective.

Content from this work may be used under the terms of the CC BY 3.0 licence (© 2018). Any distribution of this work must maintain attribution to the author(s), title of the work, publisher, and DOI.

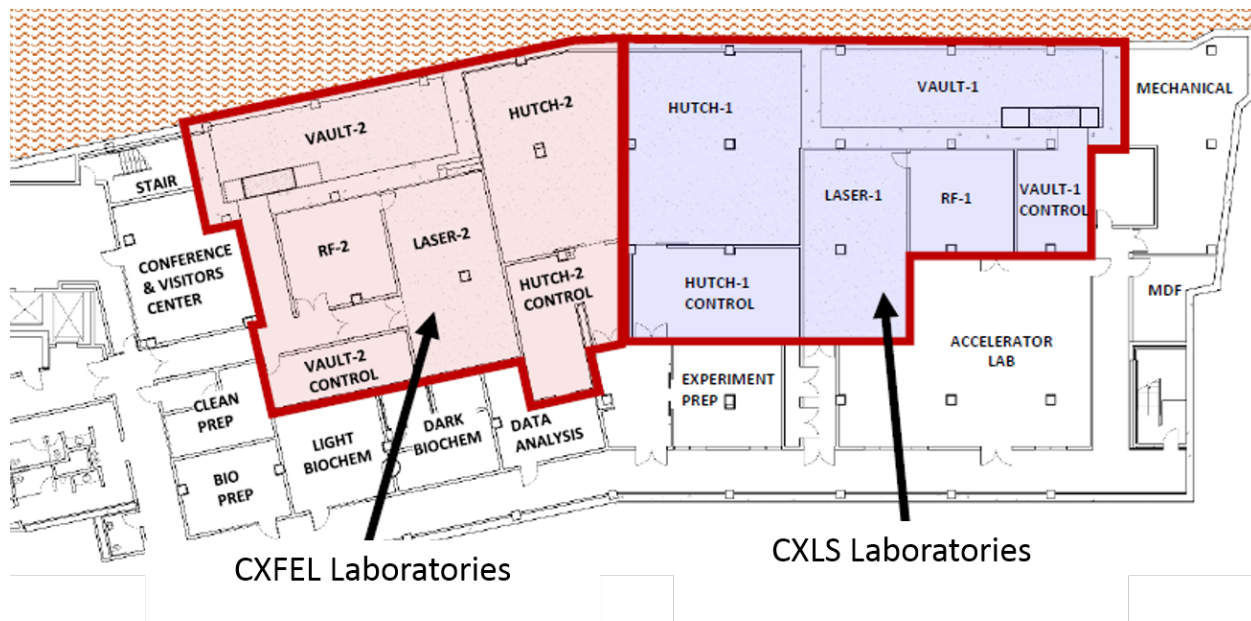


Figure 2: ASU laboratories under construction in new Biodesign C building to house CXLS and CXFEL. Vault, laser room, and x-ray hutch are on slabs isolated from surrounding building meeting VC-E vibration criteria.

ESTIMATED PERFORMANCE

CXFEL will have fully coherent output, unlike the large XFELs that lack temporal coherence, with properties that can be manipulated in novel ways. Frequency chirps can be reproducibly programmed and x-ray optics used to compress the few fs long pulses to below 1 fs. The method allows for coherent control of the phase, frequency, bandwidth, pulse length and amplitude of the x-ray pulses, and enables a variety of 2-color or multi-color experiments with precisely tunable femtosecond delays for pump-probe experiments, and perhaps even sub-cycle phase-locking of the multiple colors. The CXFEL can transfer many of these properties to beams at large XFELs by providing a coherent seed with power orders of magnitude above the SASE startup noise.

The electron beam must meet criteria in emittance, energy spread, and peak current. In order for good coupling of electron emission into the fundamental x-ray mode the emittance ϵ_n should satisfy $\frac{\epsilon_x}{\gamma} \leq \frac{\lambda_x \beta_x}{4\pi L_G}$ (eq. 73 of [11]) where $\beta_x \approx 1$ mm is the accelerator lattice beta function at the interaction point. This is an example where the extremely short gain length $L_G < 100 \mu\text{m}$ enabled by using a laser undulator is advantageous because the ratio $\beta_x/L_G \approx 20$ in the emittance equation rather than unity for a conventional FEL enables CXFEL to meet the emittance requirement. Taking example beam parameters for 8 keV photons where $\lambda_x = 0.155$ nm, and electron energy of 22 MeV ($\gamma = 45$) the emittance requirement becomes $\epsilon_n \leq 11$ nm. While this is a very low emittance, it can be achieved at low charge of 1 pC by reducing the cathode spot size. The emittance varies linearly with spot size so that a laser spot with RMS radius $20 \mu\text{m}$ ($80 \mu\text{m}$ diameter) will produce an initial emittance of 10 nm. Simulations [2] show that 10 nm emittance can

be maintained through the 8 m of transport from cathode to interaction point. These simulations show that the peak current is 3 A at the gun exit for a 300 fs bunch length.

One result of the nanopatterning method is that the transverse emittance upstream of the EEX line determines the energy spread and current at the IP downstream. The relative energy spread $\delta = \frac{\Delta y}{y}$ must be lower than the FEL parameter $\rho_{\text{FEL}} \approx 5 \times 10^{-4}$, and the peak current should be as high as possible. Because EEX results in an exact swap of transverse and longitudinal emittances we can predict that downstream of EEX, $\delta \times c\tau = \epsilon_n/\gamma$. Our nominal design is for 10,000 periods of 0.155 nm x-rays, thus the bunch length at the IP is $c\tau = 1.55 \mu\text{m}$ or 5 fs. For 1 pC of charge this results in 200 A peak current, and, conserving emittance, $\delta = 1.5 \times 10^{-4} < \rho_{\text{FEL}}$. We note that the longitudinal emittance upstream of the EEX must be equal to or better than the transverse emittance 10 nm, which simulations show is satisfied at the low charge and current generated by the photoinjector. Summarizing this section, the electron beam parameters at the interaction point are $\epsilon_n = 10$ nm, $\delta = 1.5 \times 10^{-4}$, peak current = 200 A, bunch length = 5 fs, $Q = 1$ pC, lattice parameter $\beta_x = 1$ mm to produce rms beam size of 0.3 microns. Using these parameters we find that indeed $\rho_{\text{FEL}} = 4.7 \times 10^{-4}$ for 8 keV photons, similar to large XFELs, and a surprising result for such a modest charge, energy, and current. The gain length for 8 keV photons produced by a 22 MeV beam is just $72 \mu\text{m}$. An electron beam with this set of parameters is very well matched to the coherent x-ray mode. We predict the CXFEL output properties from this beam will be a peak power of 2 MW with transform-limited bandwidth of 0.01% and pulse length 5 fs that can be chirped to 0.1% bandwidth and then compressed with multilayer optics to 0.5 fs.

ACKNOWLEDGMENT

We thank Vinod Bharadwaj, Sergio Carbajo, Mitch D'Ewart, Valery Dolgashev, Joe Frisch, Ernie Ihloff, Arvinder Sandhu, Sami Tantawi, and Andrew Young for many helpful technical discussions. This work was supported by NSF Accelerator Science award 1632780, NSF BioXFEL STC award 1231306, DOE contract DE-AC02-76SF00515, and ASU.

REFERENCES

- [1] W. S. Graves *et al.*, “Compact x-ray source based on burst-mode inverse Compton scattering at 100 kHz,” *Phys. Rev. ST Accel. Beams*, vol. 17, p. 120701, Dec 2014.
- [2] E. A. Nanni, W. S. Graves, and D. E. Moncton, “Nano-modulated electron beams via electron diffraction and emittance exchange for coherent x-ray generation,” arXiv:1506.07053, 2015.
- [3] E. Nanni *et al.*, “Measurements of transmitted electron beam extinction through Si crystal membranes,” in *Proc. of Int. Particle Accel. Conf (IPAC2016)*, no. 7 in International Particle Accelerator Conference, (Busan, Korea), pp. 1611–1614, May 2016.
- [4] L. Malin *et al.*, “Comparison of theory, simulation, and experiment for dynamical extinction of relativistic electron beams,” in *Proc. of Int. Particle Accel. Conf (IPAC2017)*, (Copenhagen, Denmark), p. THPAB088, May 2017.
- [5] C. Zhang *et al.*, “Experiments in electron beam nanopatterning,” in *Proc. of 2017 Int'l Free Electron Laser Conference (FEL2017)*, (Santa Fe, USA), p. TUP038, August 2017.
- [6] E. A. Nanni and W. S. Graves, “Aberration corrected emittance exchange,” *Phys. Rev. ST Accel. Beams*, vol. 18, p. 084401, Aug 2015.
- [7] W. S. Graves *et al.*, “Design of an x-band photoinjector operating at 1 kHz,” in *Proc. of Int. Particle Accel. Conf (IPAC2017)*, (Copenhagen, Denmark), p. TUPAB139, May 2017.
- [8] M. H. Nasr, Z. Li, C. Limborg, S. Tantawi, and P. Borchard, “High power tests of a novel distributed coupling linac,” in *Proc. of Int. Particle Accel. Conf (IPAC2017)*, (Copenhagen, Denmark), p. TUPAB131, May 2017.
- [9] S. Prinz, M. Häfner, M. Schultze, C. Y. Teisset, R. Bessing, K. Michel, R. Kienberger, and T. Metzger, “Active pumpseed-pulse synchronization for OPCPA with sub-2-fs residual timing jitter,” *Opt. Express*, vol. 22, pp. 31050–31056, Dec 2014.
- [10] M. D'Ewart *et al.*, “Performance of ATCA LLRF system at ICLS,” in *Proc. of Int. Particle Accel. Conf (IPAC2017)*, (Copenhagen, Denmark), p. THPVA152, May 2017.
- [11] Z. Huang and K.-J. Kim, “Review of x-ray free-electron laser theory,” *Phys. Rev. ST Accel. Beams*, vol. 10, p. 034801, Mar 2007.

RECENT ON-LINE TAPER OPTIMIZATION ON LCLS*

Juhao Wu^{1†}, Kun Fang^{1‡}, Xiaobiao Huang¹, Guanqun Zhou^{1§}, Axel Brachmann¹,
 Claudio Emma^{1¶}, Chunlei Li^{1||}, Eric Li², Haoyuan Liu³, Weihao Liu^{4,1}, Alberto Lutman¹,
 Tim Maxwell¹, Claudio Pellegrini¹, Weilun Qin^{1**}, Tor O. Raubenheimer¹, Alexander Scheinker⁵,
 Cheng-Ying Tsai¹, Bo Yang⁶, Chuan Yang^{1††}, Moohyun Yoon^{1‡‡}, Brandon W. Zhang⁷
¹SLAC, Stanford University, Stanford, USA, ²Palo Alto High School, Palo Alto, USA,
³Boston University, Boston, MA, USA, ⁴NSRL, University of Science and Technology of China,
 Hefei, Anhui, China, ⁵LANL, Los Alamos, USA, ⁶Dept. of Mechanical & Aerospace Engineering,
 University of Texas at Arlington, Arlington, USA ⁷Lakeside School, Seattle, USA

Abstract

High-brightness XFELs are in high demand, in particular for certain types of imaging applications. Self-seeding XFELs can respond to a heavily tapered undulator more effectively, therefore seeded tapered FELs are considered a path to high-power FELs in the terawatt level. Due to many effects, including the synchrotron motion, the optimization of the taper profile is intrinsically multi-dimensional and computationally expensive. With an operating XFEL, such as LCLS, the on-line optimization becomes more economical than numerical simulation. Here we report recent on-line taper optimization on LCLS taking full advantage of nonlinear optimizers as well as up-to-date development of artificial intelligence: deep machine learning and neural networks.

TAPERED FEL TO REACH HIGH POWER

Ultra-fast hard X-ray Free electron laser (FEL) pulse providing atomic and femtosecond spatial-temporal resolution [1,2] makes it a revolutionary tool attracting world-wide interests for frontier scientific research. Among these, single particle imaging is one of the applications demanding terawatts (TW) level peak power [3]. To reach TW FEL peak power, using a tapered undulator to keep the FEL further extracting kinetic energy from the high energy electron bunch is an active research direction [4]. However, the FEL after exponential growth saturation has to have good temporal coherence to better respond to a heavily tapered undulator [5]. While the SASE FEL provides high spatial coherence, the

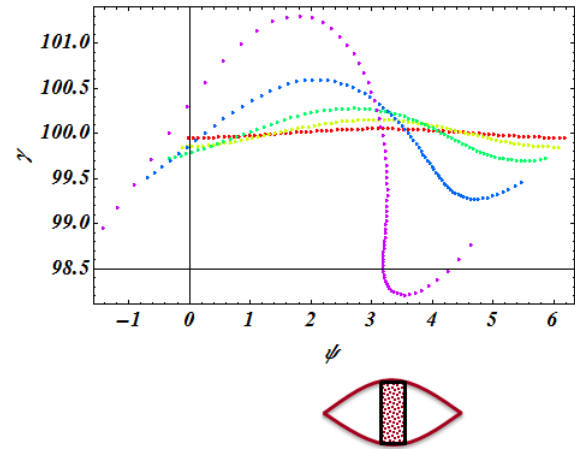


Figure 1: The electrons experience a quarter of a synchrotron motion period and microbunch with a central phase of $\psi \sim \pi$.

temporal coherence is rather poor at exponential growth saturation point. To improve the temporal coherence, seeding approaches: both external [6, 7] and self-seeding [8, 9] and Slippage-enhanced SASE (SeSASE) [10–13] can produce an FEL pulse with good temporal coherence at the exponential growth saturation region. In this paper, we conduct our study with a self-seeding tapered FEL [14–17].

The physics changes from high-gain to low-gain FEL after the exponential growth saturates. In the high-gain region, the FEL power grows exponentially [18]:

$$P_{\text{FEL}}(z) = P_0 \exp[z/L_G], \quad (1)$$

where P_0 is the start-up power, L_G is the power gain length, and z is the coordinate along the electron forward traveling direction in the undulator. The electrons experience a quarter of a synchrotron motion period from red, yellow, green, blue, and purple; they eventually microbunch with a central coordinate of $\psi \sim \pi$ as shown in Fig. 1. The electrons together with the FEL bucket are illustrated in the lower part of Fig. 1 indicating microbunching at $\psi \sim \pi$.

After the exponential growth saturation, the FEL system evolves into coherence emission. Assuming a transversely round electron beam, a constant bunching factor b_1 , and no

* Work supported by the US Department of Energy (DOE) under contract DE-AC02-76SF00515 and the US DOE Office of Science Early Career Research Program grant FWP-2013-SLAC-100164.

† jhwu@SLAC.Stanford.EDU

‡ now at Wells Fargo & Co., San Francisco, CA, USA

§ Ph.D. student from Institute of High Energy Physics, and UCAS, Chinese Academy of Sciences, Beijing, China

¶ Ph.D. student from UCLA, Los Angeles, USA

|| now at Shanghai Institute of Applied Physics, Chinese Academy of Sciences, Shanghai, China

**Ph.D. student from Peking University, Beijing, China

††Ph.D. student from NSRL, University of Science and Technology of China, Hefei, Anhui, China

‡‡on sabbatical leave from Department of Physics, Pohang University of Science and Technology, Pohang, Korea

beam loss, so that the peak current I_{pk} is also a constant, the coherent radiation power is [16]:

$$P_{\text{coh}} = \frac{Z_0 K^2 [JJ]^2 I_{pk}^2 b_1^2 z^2}{32\sqrt{2}\pi\sigma_x^2 \gamma^2}, \quad (2)$$

where Z_0 is the vacuum impedance, K is the peak undulator parameter, $\sigma_x (= \sigma_y)$ is the rms transverse round electron bunch size, γ is the relativistic factor, and

$$JJ = J_0 \left[\frac{K^2}{4(1+K^2/2)} \right] - J_1 \left[\frac{K^2}{4(1+K^2/2)} \right], \quad (3)$$

with J_0 and J_1 are the zeroth-order and first-order Bessel function.

Due to energy conservation, the resonance energy γ_r evolves according to:

$$\frac{d\gamma_r}{dz} = -\mathcal{A} \frac{K^2 z}{\gamma_r^2}, \quad (4)$$

with

$$\mathcal{A} = \frac{e [JJ]^2 Z_0 I_{pk} b_1}{2^{11/4} m c^2 \pi w_0 \sigma_x} \sin(\psi_r), \quad (5)$$

ψ_r is the synchronous phase of the electrons, e is the electron charge, m electron static mass, and w_0 the waist size of the FEL beam.

To maintain the resonance condition for a z -dependent energy, the taper profile is then z -dependent as [16]

$$K(z) \approx K_0 \left[1 - \frac{\mathcal{A} \mathcal{B}^2 \gamma_{r0}}{2K_0^2} (z - z_0)^2 \right] \text{ for } z > z_0, \quad (6)$$

where $\gamma_{r0}^2 = \gamma_r(z_0)^2$, $K_0 = K(z_0)$, and

$$\mathcal{B} = \frac{4\lambda_r}{\lambda_w}. \quad (7)$$

At this point, we want to make some comments. According to Eq. (4) with Eq. (5), the overall energy exchange between the electrons and the FEL bucket will be almost zero, if we set $\psi_r \sim \pi$. Unfortunately, when the electrons microbunched during the high-gain region, they are microbunched around $\psi \sim \pi$. Indeed, when we do FEL simulation with Genesis code [19], we do find that the electron evolves to a different central phase away from $\psi_r \sim \pi$ when the electrons initially microbunched at the end of the exponential growth region. The details of a particular example are shown in Fig. 2 where the red, green, blue, magenta, cyan, and brown dots stand for the electrons 30, 60, 80, 100, 110, and 120 m into the tapered undulator.

Besides the common feature that the central phase is away from $\psi \sim \pi$, the electrons' central phase is evolving as well as shown schematically as the electron together with the FEL bucket in the right column in Fig. 2. At $z = 120$ m in this particular case, the electron (shown as brown dots) detrapped from the FEL bucket and the FEL reaches the taper

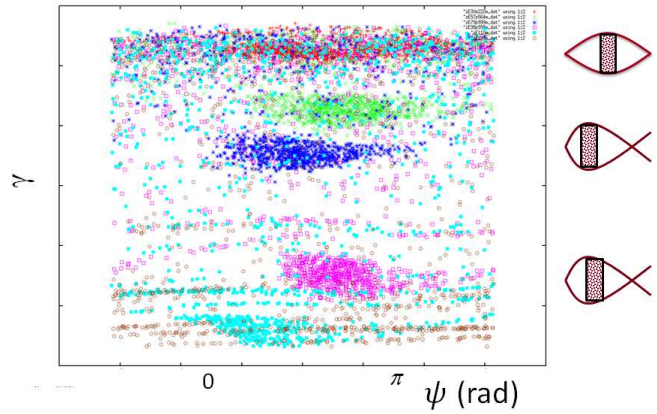


Figure 2: The electrons evolve to a different central phase away from $\psi \sim \pi$ during the post-saturation tapered region.

saturation point, the so-called the second saturation point, to be distinguished from the exponential growth saturation point, the first saturation point.

During the transition region from high-gain (before first saturation) to low-gain in the tapered undulator, the microbunched electrons will have to migrate from $\psi_r \sim \pi$ away to a new phase to achieve best efficiency. In addition, according to Fig. 2, the electron will be doing 2-D motion even in a tapered undulator.

TAPER OPTIMIZATION

For the original LCLS configuration, there were 33 planar undulator sections. Right now, the 9th and the 16th undulator section were removed and replaced with a by-pass chicane together with a grating-based monochromator in section 9 for Soft X-Ray Self-Seeding (SXRSS) and a by-pass chicane with a thin diamond crystal monochromator for Hard X-Ray Self-Seeding (HXRSS) in section 16. Also, the 33th planar undulator is now replaced with a helical undulator. So, the layout is shown in Fig. 3 with each yellow bar standing for one undulator section, the two gaps for two self-seeding station, and the last long yellow bar for the helical undulator.

Taper Profile

Continuous Taper Based on the analysis in the previous section, the taper should be approximately quadratic [16]. In the on-line optimization, we add the quartic term based on the simulation results analyzed in Ref. [16] to have:

$$K(z) = K_0 \left[1 - b_2 \left(\frac{z - z_2}{L_w - z_2} \right)^2 - b_4 \left(\frac{z - z_4}{L_w - z_4} \right)^4 \right], \quad (8)$$

where L_w is the undulator length, b_2 and b_4 stand for the strength of the taper ratio; while z_2 and z_4 for the starting point of the quadratic and quartic taper.

Discrete Taper In this case, we optimize piecewise for the 17th to the 32nd undulator sections.

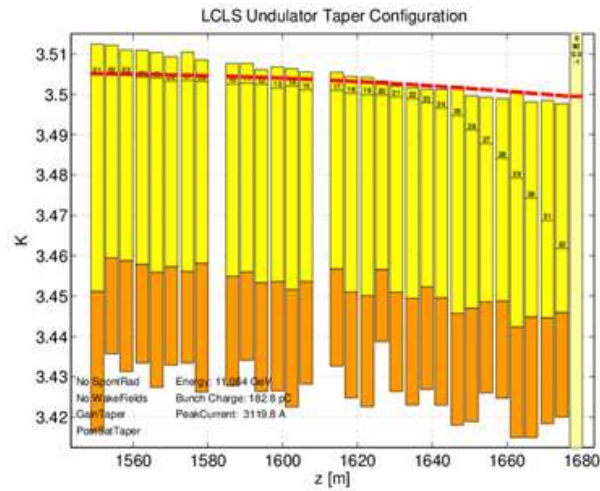


Figure 3: The schematics of the LCLS undulator system. Each yellow bar stands for an undulator section. The two gaps at the 9th and 16th slot host the two monochromators for self-seeding operation.

Optimizer

For the past few years, our team has been working on the following algorithms: Robust Conjugate Direction Search (RCDS) [20], Multi-Object Genetic Algorithm (MOGA) [16], Particle Swarm Optimization (PSO) [21], Extreme Seeking (ES) [22], Simulated Annealing (SA) [23], Reinforcement Learning (RL), and Markov Chain Monte Carlo (MCMC).

Experiment Details in Setting Up the Undulators

In the experiments, we separate the undulator system into three sessions.

Session I Session I consists of sections 1 to 8 for SASE mode, or sections 4 to 8 for 4.5-keV self-seeding mode. The reason why we do not use the first three sections 1 to 3 for the 4.5-keV self-seeding mode is because in the self-seeding mode, the same electron bunch which generates the SASE FEL before the monochromator will be used to amplify the coherent seed in the undulator sections after the monochromator. So, we do not want the slice energy spread of the electron bunch gets too large. In the SASE FEL sections before the monochromator, the electron bunch must not lase too much and maintains a relatively small slice energy spread for later amplification purpose. For a 4.5-keV FEL, the undulator is set up as:

$$K_j = K_{1(,4)} \left[1 - b_1 \frac{j - 1(,4)}{8 - 1(,4)} \right] \quad (9)$$

where $j \in [1, 8]$ in SASE mode or $j \in [4, 8]$ for self-seeding.

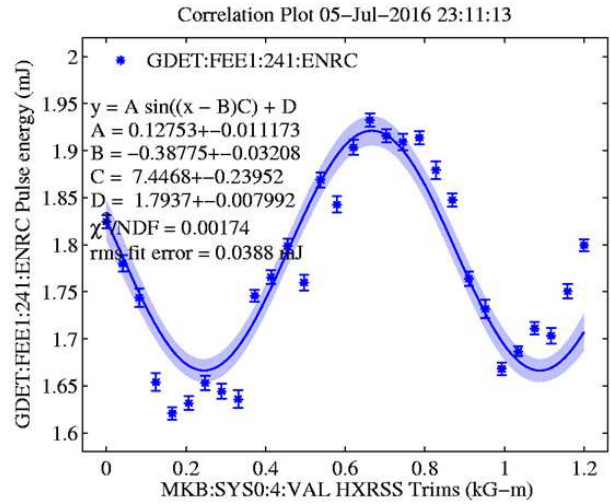


Figure 4: Temporal (phase) matching between the seed and the electron bunching by adjusting the chicane magnet trim coils.

Session II Session II consists of undulator sections 10 to 15. For $j \in [10, 15]$, the undulator setup is:

$$K_j = (K_8 + \Delta K_{10}) \left[1 - b_1 \frac{j - 10}{5} \right]. \quad (10)$$

Session III Session II consists of undulator sections 17 to 32. For $j \in [17, 32]$, the undulator setup is:

$$K_j = (K_{15} + \Delta K_{17}) \left[1 - b_1 \frac{j - 17}{15} - b_2 \left(\frac{j - j_2}{32 - j_2} \right)^2 - b_4 \left(\frac{j - j_4}{32 - j_4} \right)^4 \right]. \quad (11)$$

In the above setup for the undulator strength, b_1 takes care of the spontaneous emission and the wakefield effect. This is a linear taper. We introduce ΔK_{10} and ΔK_{17} for detuning and phase matching. j_2 and j_4 stand for the starting point for the quadratic and quartic taper.

Additional Experiment Details

Besides the details of setting up the undulator system as mentioned above, some additional details have to be carefully taken care of.

Seeding Phase Matching Even though, in principle, the SASE microbunching should be washed out to have a temporally uniform distribution when the electron bunch traverses the by-pass chicane; there is still an overall temporal (phase) matching to be performed as shown in Fig. 4 using the chicane magnet trim coils.

Orbit and Beta-Matching The by-pass chicane is relative weakly; yet, the orbit of the electrons after traversing the chicane has to be carefully adjusted to make sure the electron

Content from this work may be used under the terms of the CC BY 3.0 licence (© 2018). Any distribution of this work must maintain attribution to the author(s), title of the work, publisher, and DOI.

- Self-seeding with the monochromator at U16; U17 – U32 for amplification
- Use Diamond [-1,1,1] plane to configure self-seeding at **4.5 keV**
- Electron bunch: 150 pC, 3 kA, U4-U15 → SASE FEL, seed FEL > 1 mJ

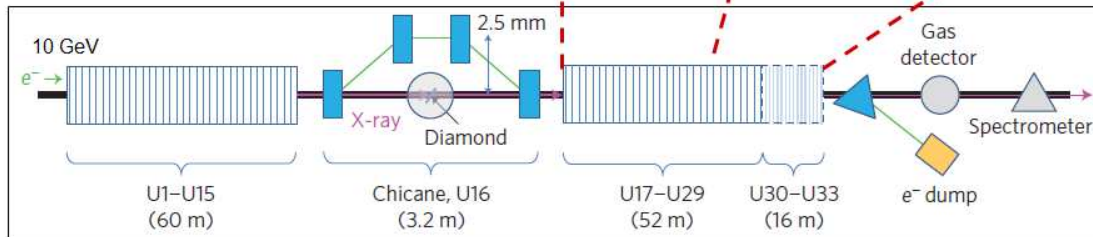
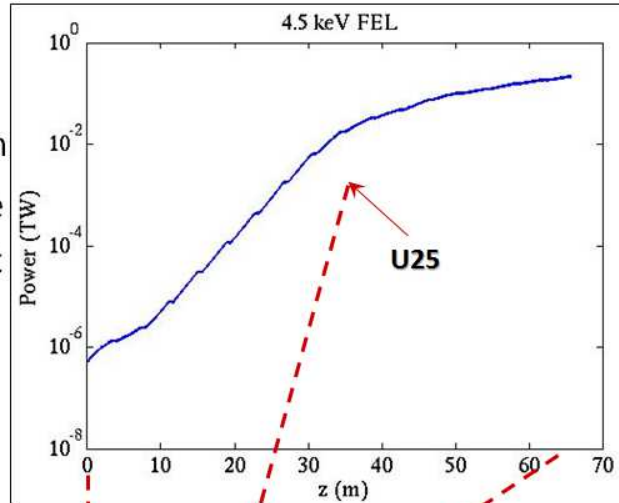


Figure 5: Details of the experiment setup for the 4.5-keV self-seeding tapered FEL.

- 4.5 keV FEL > 1 mJ in 10 fs → > 100 GW
- FWHM Bandwidth: ~ 1 eV → 2E-04

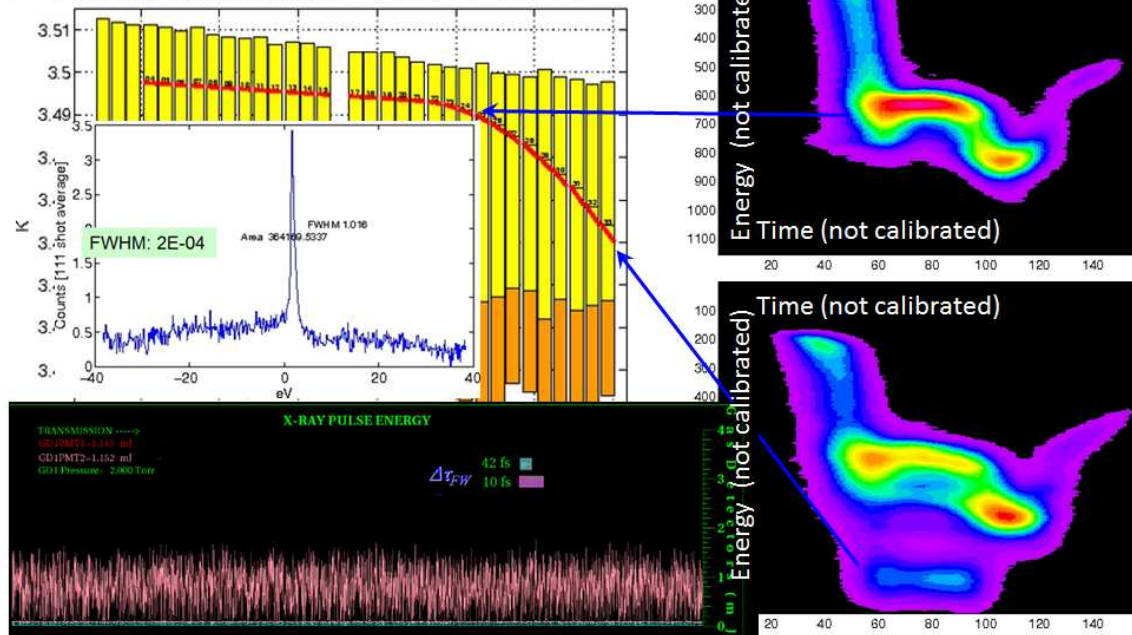


Figure 6: Experimental results from the 4.5-keV self-seeding tapered FEL.

➤ 5.5 KeV Self-Seeding Tapered FEL

- Doubled FEL pulse energy
- Zig-zag taper profile: ~ 1 mJ in 10 fs

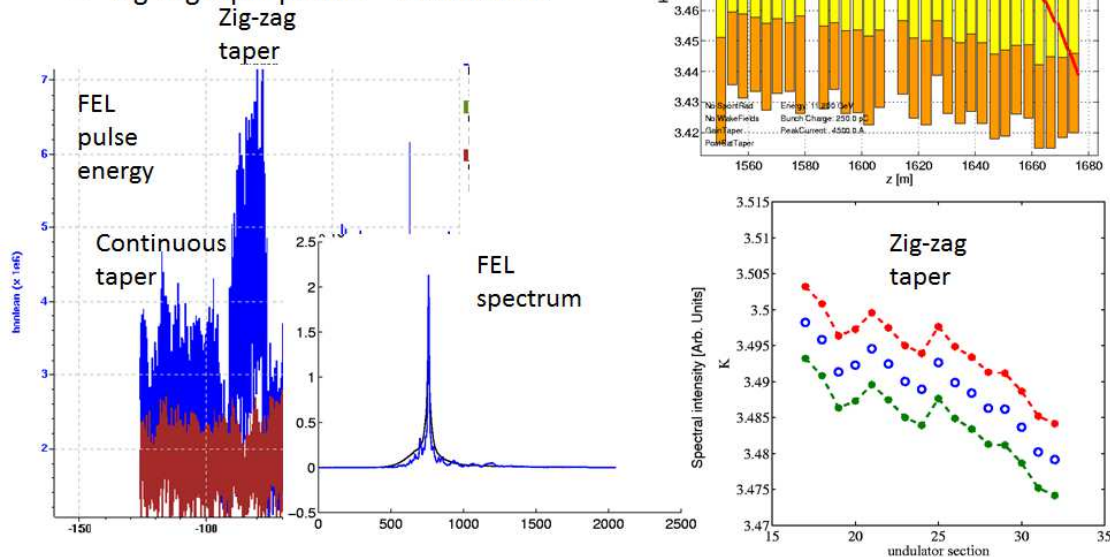


Figure 7: Experimental results from the 5.5-keV self-seeding tapered FEL.

bunch and the seed can spatially best overlap with each other. In addition, rematching the beta-function is important with the by-pass chicane turned on.

Overall Residual Chirp For a self-seeding tapered FEL to have good efficiency, the electron bunch longitudinal phase space should be flat. With an X-band Transverse deflecting cavity (XTCAV), fine tuning of the electron bunch longitudinal phase space is important and necessary.

4.5-keV FEL REACHING 100 GW

With the above mentioned details of theoretical thinking as well as the experimental set up, we here report a 4.5-keV self-seeding experiment generating 100-GW peak power with the LCLS undulator system which provides a maximum of 0.8% taper ratio, *i.e.*, $[K_0 - K(L_w)]/K_0 \leq 0.8\%$. The details of this experiment setup is shown in Fig. 5. In this experiment, the monochromator is configured with the diamond (-1,1,1) plane as the reflection plane and works in the Bragg condition. The electron bunch has 150-pC charge and a peak current of 3 kA. Undulator sections 1 to 3 were turned off to keep the electron bunch slice energy spread to be relatively small.

The coherent seed at 4.5 keV after the monochromator is about 500 kW in peak power. It is then amplified in the undulator section 17 to 32. The seeded FEL exponential growth saturates at the 25th undulator. After that the optimum taper is on-line obtained. In this case, a continuous

taper model was adopted as shown in Fig. 6. Using the XTCAV, the electron-bunch phase space is clearly shown in the two subplot in the right column in Fig. 6. At the 25th undulator, the electrons does not lose much energy yet as shown in the upper right subplot. Due to the tapered undulator, the trapped electrons keep losing energy to the FEL, so as shown in the lower right subplot, there is clearly a band of electrons well separated form the others. These electrons in the capture band are the ones who keep giving their kinetic energy to the FEL. This finally leads to an FEL pulse about 10-fs FWHM duration with 1-mJ pulse energy. This indicates that the FEL peak power reaches $P_{FEL} \sim 100$ GW. The FEL FWHM bandwidth is about 1 eV, or $\Delta\omega/\omega \sim 2 \times 10^{-4}$.

5.5-keV FEL: MACHINE LEARNING

With more and more simulation as well as experimental results, we conducted deep machine learning for the taper optimization. In details, we adopt reinforcement learning for LCLS tapered FEL optimization. Using a Clustering technique, we characterize the XTCAV image as *state* information. Spectrometer and Gas detector measure the FEL pulse energy and give the system *reward*. The undulator K adjustment is then the *action*. With this setup, and a discrete taper setting, the result is a zig-zag taper profile as shown in Fig. 7. In this experiment, we worked with 5.5-keV self-seeding tapered FEL. We started with a continuous taper profile and optimized to get the optimal profile shown as the red curve in the upper right subplot. The corresponding FEL

pulse energy is shown as the blue dots in the lower left subplot. With the optimal zig-zag taper, the FEL pulse energy is doubled as shown in the lower left subplot of Fig. 7. In this experiment, for a 5.5-keV self-seeding tapered FEL, we also reached - mJ FEL pulse energy in about 10-fs duration.

CONCLUSION

Over the past a few years, we conducted extensive theoretical and numerical studies, and created on-line optimization packages with these optimizers (both local and global) including reinforcement learning. For the 4.5-keV and 5.5-keV self-seeding tapered FEL at LCLS, the FEL pulse energy can reach 1 mJ with 10-fs duration, generating a peak power of $P_{\text{FEL}} \sim 100$ GW.

REFERENCES

- [1] P. Emma *et al.*, “First lasing and operation of an Ångstrom-wavelength free-electron laser”, *Nature Photonics* **4**, 641-647 (2010).
- [2] T. Ishikawa *et al.*, “A compact X-ray free-electron laser emitting in the sub-ångstrom region”, *Nature Photonics* **6**, 540-544 (2012).
- [3] A. Aquila *et al.*, “The Linac Coherent Light Source single-particle imaging road map”, *Structural Dynamics* **2**, 041701 (2015).
- [4] N. Kroll, P. Morton, and M. Rosenbluth, “Free-electron lasers with variable parameter wigglers”, *IEEE Journal of Quantum Electronics* **17**(8), 1436 (1981).
- [5] W. Fawley, Z. Huang, K.-J. Kim, and N. Vinokurov, “Tapered undulators for SASE FELs”, *Nuclear Instruments and Methods in Physics Research Section A: Accelerators, Spectrometers, Detectors and Associated Equipment* **483**, 537 (2002).
- [6] L.-H. Yu *et al.*, “High-gain harmonic-generation free-electron laser”, *Science* **289**, 932-934 (2000).
- [7] G. Stupakov, “Using the beam-echo effect for generation of short-wavelength radiation”, *Phys. Rev. Lett.* **102**, 074801 (2009).
- [8] J. Feldhaus *et al.*, “Possible application of X-ray optical elements for reducing the spectral bandwidth of an X-ray SASE FEL”, *Opt. Commun.* **140**, 341-352 (1997).
- [9] G. Geloni, V., Kocharyan, and E. Saldin, “A novel self-seeding scheme for hard X-ray FELs”, *J. Mod. Opt.* **58**, 1391-1403 (2011).
- [10] B. McNeil, N. Thompson, and D. Dunning, “Transform-limited X-ray pulse generation from a high-brightness self-amplified spontaneous-emission free-electron laser”, *Phys. Rev. Lett.* **110**, 134802 (2013).

- [11] J. Wu, A. Marinelli, and C. Pellegrini, “Generation of longitudinally coherent ultra-high power X-ray FEL pulses by phase and amplitude mixing”, in *Proceedings of FEL'12*, Nara, Japan, p. 237.
- [12] J. Wu *et al.*, “X-Ray spectra and peak power control with iSASE”, in *Proceedings of IPAC'13*, Shanghai, China, p. 2068.
- [13] D. Xiang, Y. Ding, Z. Huang, and H. Deng, “Purified self-amplified spontaneous emission (pSASE) free-electron lasers with slippage-boosted filtering”, *Phys. Rev. ST Accel. Beams* **16**, 010703 (2013).
- [14] Y. Jiao *et al.*, “Modeling and multidimensional optimization of a tapered free electron laser”, *Phys. Rev. ST Accel. Beams* **15**, 050704 (2012).
- [15] C. Emma, K. Fang, J. Wu, and C. Pellegrini, “High-efficiency, multi-terawatt x-ray free-electron lasers”, *Phys. Rev. Accel. Beams* **19**, 020705 (2016).
- [16] J. Wu *et al.*, “Multi-dimensional optimization of a terawatt seeded tapered free-electron laser with a multi-objective genetic algorithm”, *Nuclear Instruments and Methods in Physics Research Section A: Accelerators, Spectrometers, Detectors and Associated Equipment* **846**, 56 (2017).
- [17] A. Mak, F. Curbis, and S. Werin, “Phase-jump method for efficiency enhancement in free-electron lasers”, *Phys. Rev. Accel. Beams* **20**, 060703 (2017).
- [18] A. Bonifacio, C. Pellegrini, and Narcucci, “Collective instabilities and high-gain regime in a free-electron laser”, *Opt. Commun.* **50**(6), 373 (1984).
- [19] S. Reiche, “Genesis 1.3: a fully 3d time-dependent FEL simulation code”, *Nuclear Instruments and Methods in Physics Research Section A: Accelerators, Spectrometers, Detectors and Associated Equipment*, **429**(1), 243-248 (1999).
- [20] X. Huang, J. Corbett, J. Safranek, and J. Wu, “An algorithm for online optimization of accelerators”, *Nuclear Instruments and Methods in Physics Research Section A: Accelerators, Spectrometers, Detectors and Associated Equipment* **726**, 77-83 (2013).
- [21] K. Fang, C. Pellegrini, J. Wu, S. Hsu, and C. Emma, “Recent study in iSASE”, in *Proceedings of FEL'15*, Daejeon, Korea, p. 393.
- [22] A. Scheinker, X. Huang, and J. Wu, “Minimization of betatron oscillations of electron beam injected into a time-varying lattice via extremum seeking”, *IEEE Transactions on Control Systems Technology* 2017, DOI. 10.1109/TCST.2017.2664728.
- [23] L. Gupta, K. Fang, and J. Wu, “Optimization of an improved SASE (iSASE) FEL”, pp. 1881, in *Proceedings of IPAC'15*, Richmond, VA, USA.

POLARIZATION CONTROL OF STORAGE RING FELS USING CROSS POLARIZED HELICAL UNDULATORS *

J. Yan^{1,†}, H. Hao¹, S. Mikhailov¹, V. Popov¹, S. Huang², J. Y. Li³,
V. N. Litvinenko⁴, N. A. Vinokurov⁵, Y. K. Wu^{1,‡}

¹DFELL/TUNL, and Department of Physics, Duke University, Durham, NC, USA

²Institute of Heavy Ion Physics, Peking University, Beijing, China

³Institute of High Energy Physics, Chinese Academy of Sciences, Beijing, China

⁴Department of Physics and Astronomy, Stony Brook University, Stony Brook, USA

⁵Budker Institute of Nuclear Physics, Novosibirsk, Russia

Abstract

For more than two decades, accelerator researchers have been working to gain control of polarization of synchrotron radiation and FELs using non-optical means. In 2005, using mixed linear and helical undulators, the first experimental demonstration of polarization control of an FEL beam was realized with the Duke storage ring FEL. With the recent upgrade of the undulator system, the Duke FEL can be operated with up to four helical undulators simultaneously. Using two sets of helical undulators with opposite helicities, for the first time, we have demonstrated full control of the polarization of a storage ring FEL, including helicity switching and rotatable linear polarization. The helicity switching of the FEL beam has been realized with good lasing up to a few Hertz. The generation of a linearly polarized FEL beam using a set of cross polarized helical undulators has been demonstrated with a high degree of polarization ($P_{\text{lin}} > 0.95$). The FEL polarization direction can be fully controlled using a buncher magnet. Furthermore, the use of non-optical means to control the FEL polarization allows us to extend polarization control to γ -ray beams via Compton scattering. For the first time, we have produced linearly polarized Compton γ -ray beams with the rotatable polarization direction using helical undulators.

INTRODUCTION

Control of the polarization of light is of great importance to certain scientific research. For example, in the optical regime, a circularly polarized radiation source with switchable handedness can be used for magnetic dichroism experiments [1, 2]. In addition, some polarization-dependent spectroscopy techniques require the radiation sources to have switchable linear polarizations (typically two orthogonal linear polarizations). Polarization of light can be manipulated using polarizing optics in the visible regime. However, for the short wavelength regions such as vacuum ultraviolet (VUV) or extreme ultraviolet (EUV) where polarizing optics are either not available or have very limited capabilities, controlling polarization without the need of using polarizing optics is critical. In fact, non-optical polarization control

of the accelerator based light sources was proposed about 30 years ago, initially for the third-generation storage ring based synchrotron sources. A common approach to realize polarization control is to employ an undulator with multiple arrays of mechanically movable permanent magnets [3–5]. A specific polarization state can be obtained by translating one or more arrays of the magnets to a specific configuration. However, the manufacturing of such an undulator is typically very complicated and costly. Another method to obtain variable polarization is based upon the coherent superposition of two orthogonal polarization states. This idea (referred to as the crossed undulator configuration) was first proposed for planar undulators [6], where two identical planar undulators are used with the first one aligned to produce horizontally polarized radiation and the second one rotated by 90° to produce the vertically polarized radiation. The phase delay between two orthogonally polarized radiation beams is varied using a phase retarder positioned between two undulators, and elliptical polarization with arbitrary ellipticity can be obtained after a monochromator.

Polarization control is also a critical feature for FELs. Since the idea of the crossed undulator configuration was first introduced to the FEL field in the early 2000s [7], FEL polarization control was first experimentally demonstrated on a storage ring FEL at Duke University [8]. Later on, the development of polarization control using crossed undulators was proposed for several linac based FEL projects [9, 10]. In the past few years, some have experimentally realized polarization control using either variable-polarization undulators [11, 12] or crossed planar undulators [13, 14]. In Ref [7], Kim also proposed to use crossed helical undulators to produce linearly polarized radiation with controllable direction of the linear polarization. Its feasibility was theoretically confirmed by Dattoli *et al.* soon after [15, 16]. However, since most FELs do not have the configuration of crossed helical undulators, no experimental demonstration was done until the recent work at FERMI, a linac based high-gain FEL, in 2015 [14].

In 2005, the Duke storage ring FEL achieved polarization control using two planar undulators and two helical undulators [8]. By mixing the linearly polarized radiation from the OK-4 undulators and circularly polarized radiation from the OK-5 undulators with their relative FEL gains controlled by

* Work supported in part by the US DOE grant no. DE-FG02-97ER41033.

† junyan@fel.duke.edu, 1-919-660-2667.

‡ wu@fel.duke.edu, 1-919-660-2654.

Content from this work may be used under the terms of the CC BY 3.0 licence (© 2018). Any distribution of this work must maintain attribution to the author(s), title of the work, publisher, and DOI.

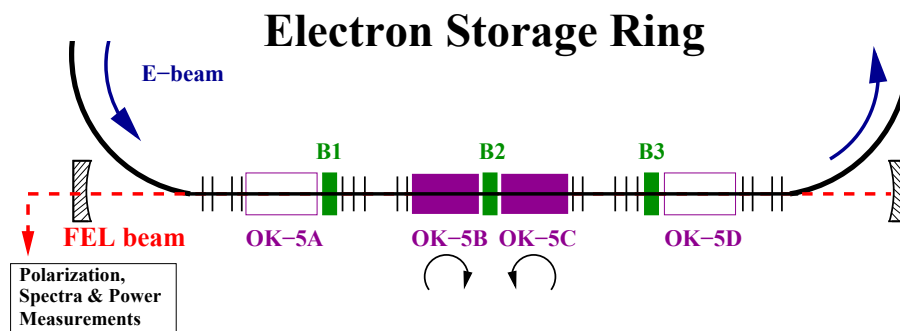


Figure 1: The undulator configuration for the polarization control of FEL beams used for this experimental work. The two helical undulators in the middle of the FEL straight section are turned on with OK-5B and OK-5C operated in normal helicity and reversed helicity, respectively.

buncher magnets, the polarization state of the FEL beams can be continuously tuned between linear and elliptical. However, using this approach, the orientation of the polarization ellipse cannot be independently adjusted. In addition, at that time only two outboard helical undulators (OK-5A and OK-5D) could be used, which unfortunately, were too far apart, and they could not form an effective crossed undulator configuration. Since 2012, with the installation of two additional helical undulators (OK-5B and OK-5C) on an undulator switchyard system in the middle of the FEL straight section [17], up to four helical OK-5 undulators became available for FEL operations (see Fig. 1). This opened up opportunities for the FEL to operate in some novel configurations with variable polarization. To realize control of the FEL beam polarization, two downstream undulators (OK-5C and OK-5D) have been configured with switchable helicity (using a solid-state based dc current switch to change the polarity of current in the vertical coils of the undulators) so that they can produce circularly polarized radiation with either handedness. The two upstream undulators (OK-5A and OK-5B) have a fixed helicity, producing right-handed circularly polarized radiation. Crossed helical undulators can be realized using either two undulators (OK-5B in normal helicity and OK-5C in reversed helicity) or four undulators (OK-5A and OK-5B in normal helicity, and OK-5C and OK-5D in reversed helicity). In this paper, we mainly report the experimental results for the two-undulator configuration, as shown in Fig. 1. Using this configuration, we have achieved the first experimental demonstration of a storage ring FEL with fully controllable polarization, including (1) helicity switching of circularly polarized radiation, and (2) generation of linearly polarized radiation with controllable polarization direction. Using a carefully calibrated polarization diagnostic system, the FEL beam with a high degree of linear polarization can be realized using two cross polarized helical undulators.

HELICITY SWITCHING OF AN FEL BEAM

For the helicity switching, OK-5B (normal helicity) and OK-5C (reversed helicity) undulators, powered by two independent power supplies, are used to produce right- and left-handed circularly polarized FEL beams, respectively (see Fig. 1). The lasing wavelength is typically set to the wavelength which has the minimum round-trip loss of the FEL cavity. Helicity switching is realized by alternately producing lasing of one undulator while preventing the other undulator from lasing. To stop the lasing of a particular undulator, its current is lowered by a few percent so that the center wavelength of the undulator is tuned away from the cavity loss is higher. Meanwhile, the current of the other undulator, which was parked at a lower current, is ramped up to produce FEL lasing. This simultaneous current ramping of two undulators leads to the lasing of one undulator while suppressing the lasing of the other undulator. Using this approach, the helicity switching can be realized at a reasonably fast rate, as high as 5–10 Hz depending on operational parameters. Using a 600 MeV electron beam, helicity switching of circular polarization was experimentally studied with the FEL lasing around 458 nm.

An optical measurement system, as shown in Fig. 2, was developed to characterize FEL beams. A beamsplitter (BS1) was used to split the FEL beam into two arms, with the regular FEL diagnostics lying in its transmission arm and the individual power measurements of the two beams with different circular polarizations located in its reflection arm. To minimize changes of the polarization state of the incident FEL beam due to beamsplitter BS1, this beamsplitter was aligned almost normal to the FEL beam with a small angle ($\sim 7.5^\circ$), which is the minimum angle permitted by the available space on the optical table (Fig. 2). In the reflection arm of BS1, a quarter-wave plate with its fast axis aligned

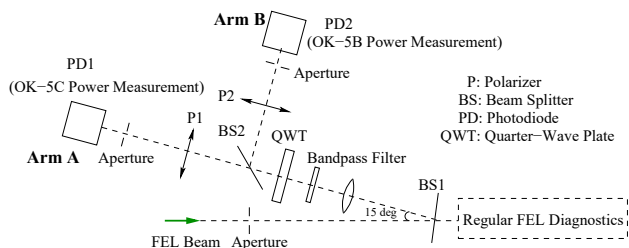


Figure 2: Optical diagnostics to study helicity switching. Power measurement for a particular helicity beam is carried out by selecting a beam of a particular polarization using a quarter-wave plate and a linear polarizer.

horizontally was employed to transform the incoming circularly polarized FEL beams into the linearly polarized ones, with the left-handed (right-handed) circular polarization converted to the 135° (45°) linear polarization. A polarizer in each arm after beamsplitter BS2 was then used to allow the beam of a particular polarization state to pass. Arm A and arm B were chosen to measure the FEL power produced by OK-5C and OK-5B undulators, respectively. The polarizing axis of each polarizer was aligned to minimize intensity leakage when the other undulator was used for lasing.

Helicity switching of a circularly polarized FEL beam was first characterized with a low switching frequency (2.5 mHz). Figure 3 shows a dc power measurement for two cycles of helicity switching during 13.6 minutes. The measured FEL powers produced by two undulators are cross-calibrated using the measured electron beam bunch lengthening. As shown in Fig. 3, the FEL powers are stable without tuning any knobs between two adjacent switchings with a relative rms variation of 0.5% for the right-handed circular beam (OK-5B) and that of 0.6% for the left-handed circular beam (OK-5C). In addition, the average power of the left-handed circular beam is about 7% lower than that of the right-handed circular beam. This may be attributed to the less optimal alignment between the electron beam trajectory and the optical path in OK-5C undulator, compared to that in OK-5B undulator. The tracking of the lasing spectra over the measurement period also shows a good spectral stability with the central wavelength kept nearly constant at 458.06 ± 0.07 nm with the rms spectral width of 0.89 ± 0.02 nm. Furthermore, as shown in the inset of Fig. 3, lowering the undulator current by 8% is sufficient to alternately stop lasing for the detuned undulator. Such a small amount of detuning allows helicity switching to be completed in a very short period of time. With this capability, the lasing processes for fast helicity switching (> 1 Hz) have also been investigated. It is found that as the helicity switching frequency increases, the FEL beam tends to show a more irregular pulsing structure. Therefore, in order to obtain reasonable stability with helicity switching FEL operation, the switching rate should be no greater than 2.5 Hz (for a 600 MeV electron beam), which is limited by the energy damping time of the electron beam circulating in the storage ring.

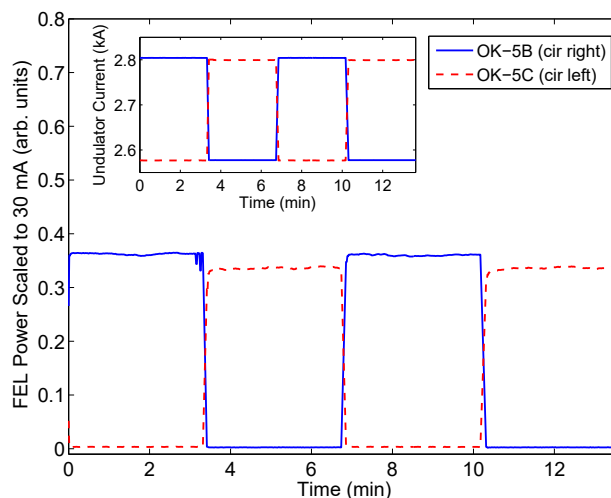


Figure 3: FEL helicity switching using cross polarized helical undulators. The beam current is kept between 29.50 mA and 31.15 mA with top-off injection. The injection occurred once (around $t = 3.2$ min) during the entire measurement. The measured FEL power is linearly scaled to 30 mA for the alternate lasings of OK-5B and OK-5C undulators. The inset shows the undulator currents as a function of time.

LINEARLY POLARIZED FEL BEAM GENERATED USING CROSSED HELICAL UNDULATORS

For the generation of linearly polarized radiation, independently powered OK-5B (normal helicity) and OK-5C (reversed helicity) undulators are used to lase simultaneously at the same wavelength (Fig. 1). With equal intensity, the two circularly polarized FEL beams of opposite handednesses are superposed to result in a linearly polarized beam. As usual, the lasing wavelength of each undulator is mainly tuned by varying the respective undulator magnetic field strength, with the fine adjustments of the wavelength realized by tuning buncher B2 (see Fig. 1). On the other hand, the requirement of equal intensity for the two circularly polarized beams to generate linearly polarized radiation can be met by balancing the FEL gains of the two undulators. The gain balancing is also achieved by tuning the undulator strengths and buncher B2. Furthermore, the direction of the generated linear polarization is determined by the phase difference between the two circularly polarized beams. This phase difference can also be controlled by tuning the field strengths of the two undulators and buncher B2, and consequently, any direction of the linear polarization can be obtained by tuning these three knobs properly. Therefore, in this experiment the strengths of OK-5B and OK-5C undulators and the setting of buncher B2 are three key knobs, which can be used not only to adjust the lasing wavelength, but also to balance the gain between two undulators as well as to manipulate the direction of linear polarization. The other knobs for optimizing the linear polarization of the FEL beam include the FEL mirror settings and the storage ring

Content from this work may be used under the terms of the CC BY 3.0 licence (© 2018). Any distribution of this work must maintain attribution to the author(s), title of the work, publisher, and DOI.

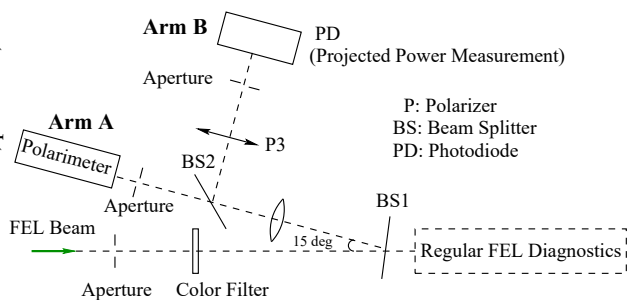


Figure 4: Optical setup for measuring FEL polarization. A polarimeter with a rotating quarter-wave plate is used to measure the polarization ellipse of the FEL beam in arm A. A more precise projection measurement is set up in arm B to measure the degree of linear polarization of the FEL beam.

rf frequency detune. The experimental results reported in this work were obtained using a 550 MeV electron beam and FEL lasing around 548 nm.

As shown in Fig. 4, the optical diagnostics in this work is similar to that shown in Fig. 2 for helicity switching, except for the setup in the reflection arm of beamsplitter BS1, which is modified to characterize the FEL beam polarization by measuring Stokes parameters. In the reflection arm of BS1, the FEL beam is split by a second beamsplitter (BS2) so that one beam is sent to a polarimeter in arm A and the other beam to a polarizer (P3) followed by a photodiode (PD) in arm B. The polarimeter used is Model PA510 from Thorlabs, a device to measure Stokes parameters using the technique of a rotating quarter-wave plate. However, the workable wavelength range of this polarimeter is limited to 450–700 nm. The precision of the polarimeter measurements highly depends on the intensity stability of the incident optical beam. Because the intrinsic power fluctuation of the FEL beam has time constants related to certain harmonics of the polarimeter signal, the polarimeter has been modified to reject FEL beam fluctuation. However, the polarimeter after being modified still has some issues under certain operational conditions. Therefore, we have also developed an independent optical setup to precisely measure the degree of linear polarization using a polarizer and a photodiode. This setup is installed in arm B. The degree of linear polarization can be experimentally obtained by measuring the maximum and minimum intensities of the incoming FEL beam by rotating the polarizer. This setup can be used for a wide spectral range with a properly chosen polarizer.

By scanning the setting of buncher B2 (N_{B2} , representing the relative phase delay between the laser and electron beams), the linear polarization of the FEL beam can be continuously rotated. Figure 5 shows a 360° rotation of the linear polarization (a complete two-period rotation) with N_{B2} varied from 0.33 to 2.33. In the figure, the polarization direction θ_1 (relative to the horizontal direction) and the degree of linear polarization P_{lin} are measured using the polarizer and the photodiode in arm B (Fig. 4). In order to take into account the change of the polarization state caused by the effect of the optics, the whole optical system is care-

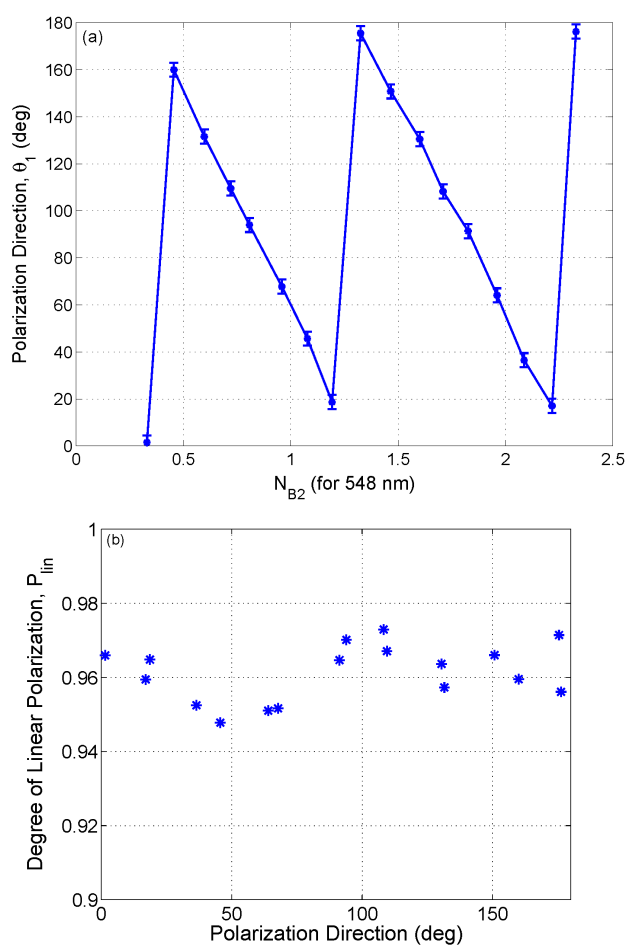


Figure 5: Rotation of the linear polarization by continuously varying buncher B2. (a) The dependency of the polarization direction θ_1 on N_{B2} . All directions (θ_1) have been projected into the range of 0–180°. (b) The measured degree of linear polarization of the FEL beam at the FEL exit window, P_{lin} .

fully calibrated using the Mueller matrix formalism [18], and the measured quantities are corrected accordingly. As shown in Fig. 5(b), with the fine tuning of the operational parameters (N_{B2} , undulator currents, FEL cavity mirrors, ring rf frequency etc.), a high degree of linear polarization has been achieved for all measured polarization directions with $P_{lin} = 0.94\text{--}0.98$. In addition, throughout the process of rotating the direction of the linear polarization, the FEL power is maintained reasonably stable with a relative power variation of 6.8% (rms), and the lasing spectra is also steady with the central wavelength kept at 547.81 ± 0.10 nm.

SUMMARY

Using two closely placed helical undulators with opposite helicities and independent power supplies, we have achieved full polarization control for a storage ring FEL. By simultaneously ramping the currents of the two undulators in opposite directions between a lower parking setting and the operational setting, we have realized helicity switching of the circularly polarized FEL beam. In addition, operating

these two cross polarized helical undulators to lase simultaneously with well balanced gains, we have experimentally demonstrated the generation of the linearly polarized FEL beam with a high degree of linear polarization (0.94–0.98). The direction of this linear polarization can be rotated by tuning the buncher magnet between the two undulators.

The Duke FEL is mainly used as a laser driver to produce Compton γ -ray beams at the High Intensity γ -ray Source [19, 20]. Since the backscattered γ -rays inherit the polarization of the laser photons, both new capabilities to control FEL polarization can be readily transferred to γ -ray production. The ability to produce γ -ray beams with full polarization control and flexibility will open up a variety of opportunities for experimental nuclear physics research [20, 21]. Using the crossed helical undulator configuration, the production of linearly polarized γ -ray beams with the rotatable polarization direction has been recently demonstrated, and further optimization will be carried out as our future work.

ACKNOWLEDGMENT

We would like to thank G. Swift for designing and building the mechanical system for polarization diagnostics, P. Wallace for useful discussions, and the engineering and technical staff at DFEL/TUNL for their support. This work was supported by DOE Grant DE-FG02-97ER41033.

REFERENCES

[1] L. Baumgarten *et al.*, *Phys. Rev. Lett.* **65**, 492 (1990).
[2] A. Agui *et al.*, *Rev. Sci. Instrum.* **72**, 3191 (2001).
[3] S. Sasaki *et al.*, *Nucl. Instr. and Meth. in Phys. Res. A* **331**, 763 (1993).

[4] S. Sasaki *et al.*, *Nucl. Instr. and Meth. in Phys. Res. A* **347**, 87 (1994).
[5] T. Tanaka, K. Shirasawa and H. Kitamura, *Rev. Sci. Instrum.* **73**, 1724 (2002).
[6] K. J. Kim, *Nucl. Instr. and Meth. in Phys. Res. A* **219**, 425 (1984).
[7] K. J. Kim, *Nucl. Instr. and Meth. in Phys. Res. A* **445**, 329 (2000).
[8] Y. K. Wu *et al.*, *Phys. Rev. Lett.* **96**, 224801 (2006).
[9] H. Geng, Y. Ding, and Z. Huang, *Nucl. Instr. and Meth. in Phys. Res. A* **622**, 276 (2010).
[10] Y. Li, B. Faatz and J. Pflueger, *Nucl. Instr. and Meth. in Phys. Res. A* **613**, 163 (2010).
[11] E. Allaria *et al.*, *Phys. Rev. X* **4**, 041040 (2014).
[12] A. A. Lutman *et al.*, *Nat. Photon.* **10**, 468 (2016).
[13] H. Deng *et al.*, *Phys. Rev. ST Accel. Beams* **17**, 020704 (2014).
[14] E. Ferrari *et al.*, *Sci. Rep.* **5**, 13531 (2015).
[15] G. Dattoli, P. L. Ottaviani, and L. Bucci, *Optics Comm.* **195**, 419 (2001).
[16] G. Dattoli, and P. L. Ottaviani, *Nucl. Instr. and Meth. in Phys. Res. A* **479**, 668 (2002).
[17] Y. K. Wu *et al.*, *Proceedings of the 2013 International Particle Accelerator Conference* 267 (2013).
[18] D. Goldstein, *Polarized Light*. New York: Marcel Dekker, Inc., second edition, 2003.
[19] V. N. Litvinenko *et al.*, *Phys. Rev. Lett.* **78**, 4569 (1997).
[20] H. R. Weller *et al.*, *Prog. Part. Nucl. Phys.* **62**, 257 (2009).
[21] B. E. MacGibbon *et al.*, *Phys. Rev. C* **52**, 2097 (1995).

THERMAL AND MECHANICAL STABILITY OF BRAGG REFLECTORS UNDER PULSED XFEL-RADIATION*

I. Bahns^{1†}, P. Thiessen, C. Maag, J. Rossbach, Universität Hamburg, Germany
J. Zemella, DESY, Hamburg, Germany
V. Sleziona, H. Sinn, European XFEL, Hamburg, Germany

Abstract

Free-electron laser (FEL) x-ray radiation can deliver pulses with a huge amount of energy in short time duration. X-ray optics like Bragg reflectors therefore must be chosen in a way that they can withstand radiation-material interaction without getting damaged so that they can maintain their technical functionality. Therefore thermal and mechanical reactions of Bragg reflectors to the radiation induced thermal strain and force (radiation pressure) have been considered in this study. The theory of thermoelasticity has been used to simulate the strain conditions at saturation of the amplifying process in an X-ray free-electron laser oscillator (XFELO). One aim of this study was to investigate, if the radiation pressure could be an effect that gives a considerable contribution to the strain propagation. The results of the simulations have shown that, if Bragg backscattering of the X-ray pulse by a diamond crystal with 99% reflectivity and 1% absorptivity is assumed, the value of the thermally induced strain is about two magnitudes higher than the radiation pressure induced strain. Also a measurement method which could be used to detect the simulated strain is shortly discussed at the end of this document.

INTRODUCTION

The European XFEL is under commissioning, the first lasing was achieved in May 2017. The facility provides radiation with high peak brilliance on the order of 10^{33} photons $[(s^{-1} mm^{-2} mrad^{-2}) / (0.1\% BW)]$, with up to 27000 photon pulses s^{-1} , which are delivered in 600 μs long pulse trains with a repetition rate of 10 Hz [1]. These conditions give the possibility for the realization of an X-ray free-electron laser oscillator (XFELO) [2]. With the integration of an XFELO at the European XFEL longitudinally full coherent pulses and an increase of the peak brilliance by one order magnitude should be achievable. The bandwidth would reduce to a value of $\frac{\Delta E}{E} = 1.6 \cdot 10^{-6}$. The amount of energy in saturation of these photon pulses would be about 300 μJ to 1 mJ. The small bandwidth is in the order of the Darwin width and therefore nearly the whole amount of energy per photon pulse would be Bragg reflected. Shvyd'ko et al have shown that nowadays diamond crystals are available, which have reflectivity of more than 99% in case of Bragg reflection [3]. Hence, by considering such a Bragg reflector for saturated XFELO radiation the maximum amount of pulse energy which is absorbed inside the penetration depth (extinction length) can be at most 1%.

Under these radiation conditions the thermal and mechanical stability of Bragg-reflectors, which are necessary for the XFELO, have to be considered in detail. Therefore simulations of the strain induced by X-ray radiation in a diamond crystal have been performed in this study. Strain has a direct influence on the lattice parameter and therefore changes the Bragg reflection conditions, which can influence the stability of an XFELO.

When energy of electromagnetic radiation is interacting with a solid body in the timespan of femtoseconds, the system moves out of thermal equilibrium. Theoretical and experimental studies [4] [5] have shown that the dynamics of this thermal expansion, apart from heat transfer, can be explained as a mechanical disturbance. The absorbed energy creates thermal stress which is propagating as a longitudinal wave with the speed of sound into the irradiated material [6].

Besides the creation of a thermally induced strain wave, the radiation pressure could also create such a strain propagation. This could be important in cases where the amount of reflected energy is large and the absorbed portion is small. These conditions exist for Bragg reflected radiation that a saturated XFELO would deliver, because the thermal expansion is directly influenced by the amount of energy that is absorbed whereas radiation pressure occurs for absorption as well as for reflection. However, the force which is induced by radiation pressure is very small due to the small impulse of a photon and therefore the thermal effects are normally dominating this effect.

Mechanical deflection of micro beams caused by the radiation pressure have been investigated theoretically and experimentally by several authors [7–10]. However, in the present study the strain propagation and not the deflection is the parameter of interest. To the best knowledge of the authors this kind of strain propagation has not been considered by any other theoretical or experimental investigation so far.

PROBLEM FORMULATION

Stoupin *et al.* [11] have done experimental studies on the strain propagation caused by a ≈ 8 ps laser pulse in diamond. The strain has been assumed to propagate only along the z direction (Fig. 2 a), which is valid for $\sqrt{A} \gg d$, where A is the radiated area of a crystal with the thickness d . In case of a low-flux laser pulse the heat dissipation can be neglected for the first tens nanoseconds after the radiation-material interaction and the formulas of thermoelasticity [12] yields:

* Work supported by BMBF FKZ 05K16GU4

† immo.bahns@desy.de

$$\sigma_{zz} = Y \frac{\partial u(z,t)}{\partial z} - \alpha Y \Delta T(z), \text{ and} \quad (1)$$

$$\frac{\partial \sigma_{zz}}{\partial z} + F(z,t) = \rho \frac{\partial^2 u(z,t)}{\partial t^2}, \quad (2)$$

where Y is the Young's modulus, α is the linear thermal expansion coefficient and ρ is the mass density. u is the displacement and its derivative is the strain $\epsilon_{zz} = \frac{\partial u(z,t)}{\partial z}$ and $F(z,t)$ the body force.

The Dirichlet boundary conditions are that the stress σ_{zz} vanishes at the crystal boundaries and the initial conditions at $t=0$ are that the spatial and temporal derivative of the displacement is zero.

Absorption and reflection of saturated XFEL X-ray radiation at a diamond Bragg reflector

In this study a Bragg reflection under the following conditions is considered: a diamond crystal C 444 in backscattering $\Theta = 90^\circ$ configuration, FEL radiation with $E = 12.04 \text{ keV}$ ($\lambda = 1.03 \text{ \AA}$), a beam radius of $r \approx 40 \mu\text{m}$, a pulse duration of $t_p \approx 70 \text{ fs}$, an amount of energy per pulse of $E_p = 1 \text{ mJ}$, a bandwidth of $\approx 20 \text{ meV}$ equal to the Darwin width ($\approx 20 \text{ meV}$ for C 444), a reflectivity of 99%, an absorptivity of 1%, an extinction length $l_{ext} \approx 20 \mu\text{m}$ and a crystal thickness of $150 \mu\text{m}$.

Following the work of Thomson *et al.* [5] the temperature rise can be described by

$$\Delta T(z) = \Delta T_{0,R} e^{-z/l_{ext}}, \text{ where} \quad (3)$$

$$\Delta T_{0,R} = \frac{0.01 E_p}{A \rho c_v l_{ext}}. \quad (4)$$

In this Formula c_v is the specific heat capacity which is 509 J/(kg K) for diamond.

The body force $F(z,t)$ which is induced by radiation pressure [10] is

$$F(z,t) = F_{0,R} e^{-z/l_{ext}} \cdot tri(t), \text{ where} \quad (5)$$

$$F_{0,R} = \frac{0.99 \cdot 2 E_p}{t_p c_0 A l_{ext}}, \quad (6)$$

and c_0 is the speed of light. Unlike the thermal gradient $\Delta T(z)$ the body force $F(z,t)$ must be time dependent, because it only exists when the photons interact with the material. To consider this, a triangular function $tri(t)$, whose full width half maximum (FWHM) is the photon pulse duration, has been multiplied to the equation.

Another point that has to be considered in case of radiation pressure induced body force is, that the energy transferred to the lattice will cause a constant velocity of the entire considered system due to Newtons laws. To consider this the boundary conditions for the stress have been modified in this study to be:

$$\sigma_{zz}|_{z=0} = D \cdot u \text{ and } \sigma_{zz}|_{z=d} = -D \cdot u, \quad (7)$$

where, u is the displacement and D is a spring constant the value of which depends on the clamping of the crystal. Using the assumptions of the Euler–Bernoulli beam theory the spring constant for a cantilever beam yields:

$$D = \frac{3YI_y}{L^3}. \quad (8)$$

In this study a rectangular crystal with $I_y = b \cdot d^3/12$ is considered, where $d = 150 \mu\text{m}$ is the thickness and b is the width with a value of 0.5 mm . The length L is 5 mm , so D becomes 4.1 kN/m .

RESULTS OF THE SIMULATED STRAIN PROPAGATION

Simulations of the stress propagation are calculated by solving Eq. 2 with the finite element (FEM) software COMSOL Multiphysics®. A FEM calculation of the strain in the case where the body force $F(z,t)$ in Eq. 2 is zero, is compared to an analytical solution which is presented in the study of Stoupin *et al.* [11]. Calculations using the same system parameters are show in Fig. 1. Both calculations give the same results for the strain values and the temporal function. However, the FEM solution shows some minor oscillations on the main signal which could be reduced by using a smaller mesh size, but this would significantly prolong the calculation time.

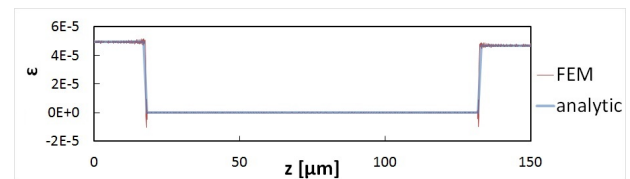


Figure 1: Comparison of numerical and analytical calculation of strain for a fixed time value

The heat expansion and the body force induced by the radiation pressure will create a longitudinal strain wave that is assumed to propagate with the speed of sound in z direction (illustration Fig. 2 a). The diagram that is used to illustrate the strain propagation can be explained by Fig. 2 b. The strain will propagate with the speed of sound between the boundaries of the crystal. In this study only a time duration of a strain wave that travels through the crystal once (back and forth) is considered.

The results of the discussed situations of the section “Problem Formulation” are show in Fig. 3. The maximum value to the strain caused by dynamical thermal expansion is about two magnitudes higher than the one due to radiation pressure in the considered case. However, the propagation of radiation pressure could be a considerable effect if the situation would be created were the absorption is even smaller than

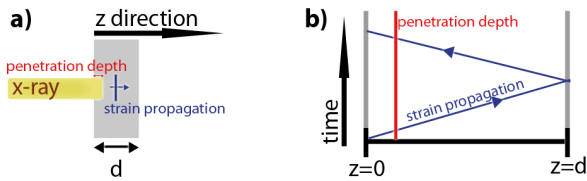


Figure 2: a) Illustration of the radiation-material interaction with a penetration depth smaller than the crystal thickness b) description of the plots used in the present study

1%. For example this could be the case if Bragg reflection of a diamond crystal far from backscattering would be chosen where the reflectivity is up to 99.9% [3]. Also the clamping of the crystal could perhaps increase the value of the strain. To find situation where the radiation pressure is the dominating effect and therefore a direct measurement would be feasible, further simulations are necessary.

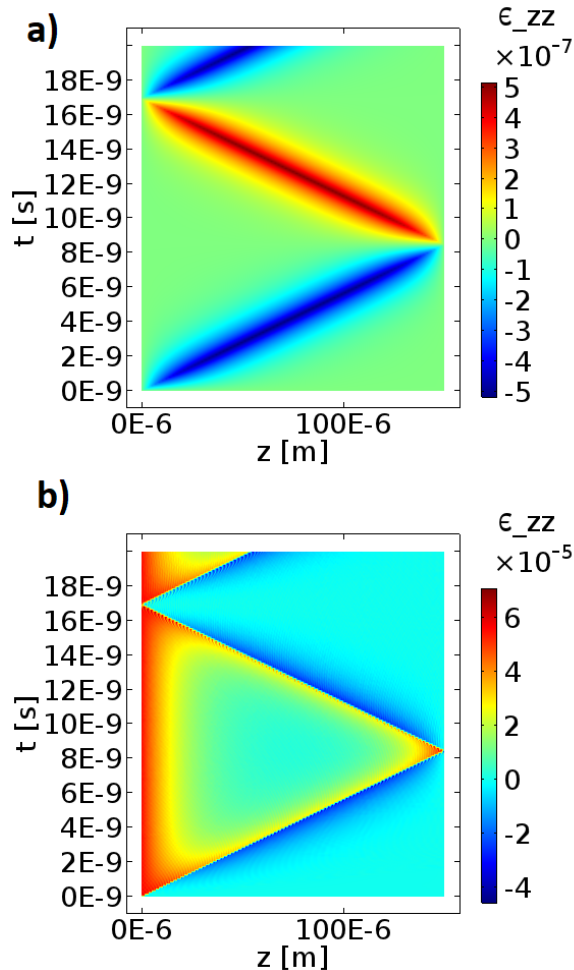


Figure 3: FEM calculations of the cases discussed in section “Problem Formulation” a) strain propagations due to body force induced by radiation pressure b) strain propagation due to dynamical thermal expansion.

A general problem that has to be mentioned in the presented simulation is that the considered beam radius is so

small that a 1D simulation would not be exact anymore. However, the results give a first estimation on the order of magnitude of the strain induced by an XFEL pulse.

Investigation of the strain during the first nanoseconds as presented in this paper provides information about the important physics at the creation of strain and its initial propagation in diamond. The relaxation of this strain taking place on larger time scales was not part of the present study. However, it is of paramount relevance for the operation of an XFEL since it determines the amount of strain remaining after a round trip in the oscillator. This aspect is experimentally investigated by Maag *et al.* [13].

Experimental setup for strain detection

Stoupin *et al.* [11] have measured the transient strain by observing the temporal change of Bragg reflection. The strain has a direct effect on the local lattice parameters and therefore changes a diffraction pattern the shape of which can be simulated with the dynamical diffraction theory and can then be compared with the measured signal. A great advantage of this method is that the strain, which is the value of interest, has a direct influence on the measured signal. However, this method needs coherent x ray radiation which can only be created with monochromatised synchrotron or FEL radiation. A different method to measure the strain is proposed by Thomson *et al.* [5] and is based on the change of reflectivity ΔR of an optical probe laser after absorption of a pump laser. This is caused by the change of the optical constants as a result of the propagating strain ($\Delta n(z, t) = \frac{\partial n}{\partial \epsilon_{zz}} \epsilon_{zz}$ and $\Delta \kappa(z, t) = \frac{\partial \kappa}{\partial \epsilon_{zz}} \epsilon_{zz}$) induced by the pump pulse. Here $\Delta n(z, t)$ and $\Delta \kappa(z, t)$ are the changes of the real and imaginary parts of the complex index of refraction, respectively, from their values n and κ in the absence of strain. The problem with this method is that values of $\frac{\partial n}{\partial \epsilon_{zz}}$ and $\frac{\partial \kappa}{\partial \epsilon_{zz}}$ have to be known. One possibility would be a calibration measurement of the reflectivity for a fixed wavelength for a material of interest. If such a measurement would be done, the presented experimental setup build up by Maag *et al.* [13] could be used to measure the strain propagation simulated in this study.

CONCLUSION

The results of the strain simulations in this study have shown, that for the considered XFEL setup the strain which is induced by dynamical thermal expansion is about two magnitudes higher than the strain induced by radiation pressure. However, for X-ray radiation with a bandwidth similar to the Darwin width and even smaller values of absorptivity, the radiation induced strain may become a considerable and experimentally measurable effect in strain propagation.

ACKNOWLEDGEMENT

We like to thank the DESY and European XFEL GmbH for their financial and technical support.

Content from this work may be used under the terms of the CC BY 3.0 licence (© 2018). Any distribution of this work must maintain attribution to the author(s), title of the work, publisher, and DOI.

REFERENCES

- [1] M. Altarelli, and A. P. Mancuso, "Structural biology at the European X-ray free-electron laser facility", *Phil. Trans. R. Soc. B* 369.1647 (2014): 20130311.
- [2] K-J. Kim, Y. Shvyd'ko, and S. Reiche. "A proposal for an X-ray free-electron laser oscillator with an energy-recovery linac", *Physical review letters* 100.24 (2008): 244802.
- [3] Shvyd'Ko, Yuri, *et al.*, "Near-100% Bragg reflectivity of X-rays", *Nature Photonics* 5.9 (2011): 539-542.
- [4] D. W. Tang, *et al.*, "Dynamic thermal expansion under transient laser-pulse heating", *Applied physics letters* 59.24 (1991): 3113-3114.
- [5] C. Thomsen, *et al.*, "Surface generation and detection of phonons by picosecond light pulses", *Physical Review B* 34.6 (1986): 4129.
- [6] C. Rose-Petruck, *et al.*, "Picosecond-milliangstrom lattice dynamics measured by ultrafast X-ray diffraction", *Nature* 398.6725 (1999): 310.
- [7] D. Kleckner, and D. Bouwmeester, "Sub-kelvin optical cooling of a micromechanical resonator", *Nature* 444.7115 (2006): 75.
- [8] D. Ma, J. L. Garrett, and J. N. Munday, "Quantitative measurement of radiation pressure on a microcantilever in ambient environment", *Applied Physics Letters* 106.9 (2015): 091107.
- [9] H. Rokhsari, *et al.*, "Radiation-pressure-driven micro-mechanical oscillator", *Optics Express* 13.14 (2005): 5293-5301.
- [10] D. R. Evans *et al.*, "Laser actuation of cantilevers for picometre amplitude dynamic force microscopy", *Scientific reports* 4 (2014): 5567.
- [11] S. Stoupin, *et al.*, "Direct observation of dynamics of thermal expansion using pump-probe high-energy-resolution x-ray diffraction", *Physical Review B* 86.5 (2012): 054301.
- [12] T. Furukawa, and T. Sueyoshi. "Thermal stress analysis of thin films in the context of generalised thermoelasticity", *International Journal of Theoretical and Applied Multiscale Mechanics* 2.1 (2011): 72-81.
- [13] C. Maag, *et al.*, "An experimental setup for probing the thermal properties of diamond regarding its use in an XFEL", *FEL Conference 2017* (2017) MOP064.

Content from this work may be used under the terms of the CC BY 3.0 licence (© 2018). Any distribution of this work must maintain attribution to the author(s), title of the work, publisher, and DOI.

ENHANCEMENT OF RADIATIVE ENERGY EXTRACTION IN AN FEL OSCILLATOR BY POST-SATURATION BEAM ENERGY RAMPING

H. S. Marks[†], A. Gover, Tel Aviv University, Tel Aviv, Israel
 Yu. Lurie, E. Dyunin, Ariel University, Ariel, Israel

Abstract

We present results of experiments and simulations showing a greater than 50% increase in post-saturation radiation power extraction from a Free Electron Laser oscillator based on an electrostatic accelerator. Electrostatic accelerator free electron laser oscillators have the potential for CW operation. Present day operating oscillators rely on long pulses of electrons, tens of microseconds in duration, they generate correspondingly long radiation pulses, at a single longitudinal mode after a mode competition process. The post-saturation power extraction enhancement process is based on temporal tapering (up-ramping) of the beam energy, enabling a large synchrotron oscillation swing of the trapped electron bunches in passage along the interaction length. We further discuss the theoretical limits of the temporal tapering efficiency enhancement process.

INTRODUCTION

Of the FEL oscillators operating in the world [1], few operate with an electrostatic accelerator [2-6], one of them is the Israeli Electrostatic Accelerator FEL (EA-FEL). Generally, in FEL only a small proportion of the electron kinetic energy is extracted in the form of radiation. One way of increasing the efficiency of extraction is use of a tapered wiggler. That is, when the undulator period and or magnetic field are modified [7-10]. This ensures that as electrons lose kinetic energy their interaction with the radiated electric field remains strong [11]. Spatial undulator tapering has been proved already in experiments with an amplifier FEL [12-13]. All these works are connected to single-pass Self-Amplified Spontaneous Emission (SASE) amplifier FELs.

Oscillator FELs are multi-pass radiation systems. The out-coupling of the resonator can be modified until the optimum energy balance with the resonator internal losses is found for maximum radiative output power [14]. Pre-bunching the electron beam has also been shown to increase the extraction efficiency of radiative power [15].

Another way to increase the extraction of useful radiative energy is to positively-ramp the kinetic energy of the electron beam entering the resonator post-saturation. This temporal tapering of the electron parameters serves to raise the electrons, in terms of their potential to radiate, onto a more energetically favourable synchrotron oscillation path. Such a scheme was demonstrated via experiment and simulation for the first time [16].

Figure 1 shows a schematic of the Israeli Tandem EA-FEL. A thermionic cathode e-gun is biased to -40 kV and provides electron beam pulses with currents in the range 0.7-3 A and up to 100- μ s duration. These electron beam pulses are accelerated up to around 1.4 MeV where they enter an equipotential region where they are focused by quadrupoles for optimal entrance into the resonator (which is encompassed by a planar Halbach wiggler [17]). After passing through the resonator the electrons are again focused by quadrupoles before entry into the deceleration tube, at the end of the deceleration tube they are collected. Under regular operation the resonator and wiggler are at the same potential as the sections with the quadrupoles between the acceleration and deceleration tubes. The main properties of the EA-FEL are summarised in Table 1, and described in a previous publication [14].

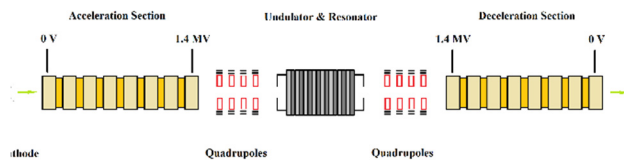


Figure 1: Schematic of the Israeli EA-FEL based on a Tandem Van-der-Graaf generator.

Table 1: Properties of the EA-FEL

Beam Current	0.7-3 A
Beam Energy	1.35-1.45 MeV
Wiggler Period	44.4 mm
Effective No. of Wiggler Periods	24
Wiggler field Amplitude	1.93 kG
Waveguide Fundamental Mode	HE11
Radiation Frequency	95-110 GHz
Optical Length of Resonator	1.514 m
Free Spectral Range of Resonator	100 MHz

A voltage ramping device (VRD) was built to compensate for falling accelerating voltage due to electrons hitting the walls of the beam line. The VRD is an electronic circuit composed of a 20-kV bipolar power supply that is remotely triggered to charge a capacitive load through selectable resistors producing an exponential pulse of rise time $\tau = RC$ that is nearly linear for time $t < \tau$. The first purpose of the

device was to stabilise the lasing frequency and increase lasing time with its use. The VRD is connected directly between the electrically short-circuited resonator and undulator and the high voltage terminal metallic baseplate. The undulator sits on ceramic mounts to isolate it from the high voltage equipotential region of the terminal. The isolated resonator/wiggler acts as one surface of a capacitor and is charged by the VRD synchronously with the start of the electron-beam from the cathode. The charging rate is controlled through different resistors. As the resonator is isolated from the high voltage terminal, voltage ramping relative to the terminal increases the kinetic energy of the electrons upon entry to the wiggler to compensate or over-compensate the potential energy drop of the terminal.

INCREASING EXTRACTION FROM THE ELECTRON BEAM

As we do not have precise control over the accelerating voltage due to the inherently limited pulse to pulse voltage stability of the electrostatic accelerator, there is some variability from pulse to pulse in the radiation output power. However, by comparing the output power data of a series of pulses it is possible to see the effect of voltage ramping on the peak output power from the resonator. Three cases were tested in a series of 75 lasing shots (see Fig. 2). During this entire series of experiments the accelerating voltage was dropping by 2.26 kV/ μ s during each pulse. The distribution of the first 25 lasing shots of Fig. 2, marked as stars were without voltage ramping. Then 25 lasing pulses with 20 kV voltage ramping and $\tau = 8 \mu$ s are marked with diamonds, and finally another 25 lasing pulses with 20 kV voltage ramping and a rise time of $\tau = 2 \mu$ s are marked with circles. The average peak power for each of the three cases is marked on the graph with a horizontal bar. From left to right in Fig. 2 the averages are 1690 W, 2260 W, and 2505 W. It is seen that the average peak power of the $\tau = 2 \mu$ s case was on average 50% higher than without. Even though the same electron beam current of 1.13 A was being used in all cases. The transmission of the resonator output was $\sim 5\%$.

The rate of increase in voltage in the two cases is only a factor because the ramping is counteracting the falling accelerating potential and there is an optimal increment above the initial beam energy. So, in the case of $\tau = 8 \mu$ s the beam energy increment is just compensating for the voltage drop, when the rate of ramping is increased to $\tau = 2 \mu$ s the beam energy rises above the beam energy that corresponds to the maximum of the small signal gain, this results in a significantly increased extraction efficiency. This increase is the main point of interest. It means that post-laser-saturation, the maximum gain point is shifted from the point before the build-up process. The experiment described just checked two very limited cases with fixed resonator transmission.

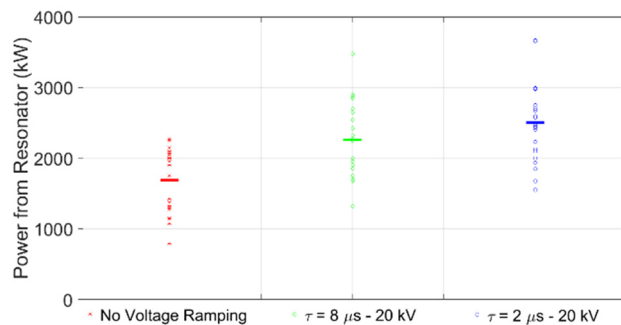


Figure 2: Summary of the results of the initial peak power obtained from 75 lasing pulses. Of the 75, 25 were carried out without voltage ramping (leftmost stars), 25 with a compensating voltage ramping pulse of rise time $\tau = 8 \mu$ s - centre diamonds), and 25 with an overcompensating pulse of rise time $\tau = 2 \mu$ s - rightmost circles). The averages of the markers are shown with a horizontal marker.

FINDING THE MAXIMUM ENHANCEMENT FROM BEAM ENERGY RAMPING

To simulate the effect of falling or rising beam energy, the electron-radiation interaction dynamics code FEL3D was used. The simulation code is a steady state, single frequency, and single pass (amplifier) program, considering three-dimensional effects due to a finite beam size and a non-uniform profile of the undulator magnetic field.

The results of the FEL3D simulation of extracted power for a given beam energy ramp with a 1.13-A current (and the parameters in Table 1) are depicted in three sets of graphs in Fig. 3. We demonstrate the effect of voltage ramping here at three different ramping levels, 0 kV (top), 10 kV (graph), and 20 kV (bottom), for roundtrip reflectivity levels of 0.35, 0.45, 0.55, and 0.61. The initial beam energy in each of the graphs is that for the maximum of the small signal gain at the frequency oscillating in the resonator. The top graph is the power developed in the resonator with no change in beam energy. The middle graph shows the effect of an abrupt 10-keV increment in the beam energy.

It is interesting to note that the increase in resonator power is not uniform for different levels of roundtrip reflectivity. Indeed, in the bottom graph, whilst a 20-kV ramp causes a 60% increase in power for $R_{rt} = 0.61$, for $R_{rt} = 0.35$, this causes an end to lasing. For $R_{rt} = 0.61$ there is more stored power in the resonator than for $R_{rt} = 0.35$, so when the beam energy is raised 20 keV, for the $R_{rt} = 0.61$ case the electrons are moved to a more favourable synchrotron oscillation trajectory from the point of view of energy extraction, whereas for $R_{rt} = 0.35$ the electrons become de-trapped (for a more detailed discussion, see [16]).

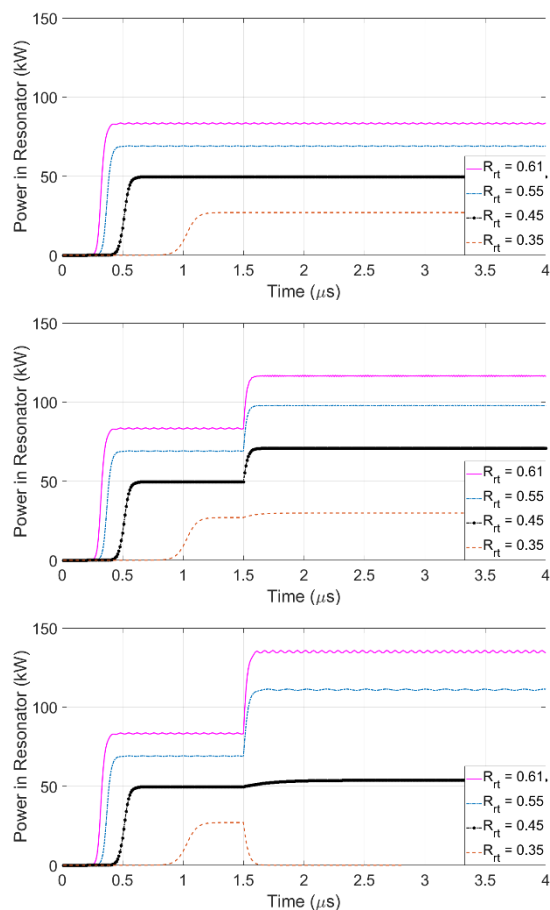


Figure 3: Power stored in the resonator as a function of time. The beam energy is that for maximum small signal gain. No change is made to the beam energy in the top graph. In the middle and bottom graphs an abrupt increase of 10 and 20 keV respectively is made at 1.5 μ s.

CONCLUSION

Via simulation and experiment, the importance of post-saturation changes in electron beam energy to output power has been demonstrated. This is the first experimental demonstration for an FEL oscillator of efficiency enhancement of energy extraction from an un-bunched continuous electron beam using voltage ramping where 50% more radiation power has been obtained.

REFERENCES

[1] G. R. Neil, "FEL oscillators", *Proceedings of PAC'03*, pp. 181-185, 2003.
 [2] L. R. Elias, J. Hu, and G. Ramian, "The UCSB electrostatic accelerator free electron laser: First operation", *Nucl. Instr. Meth.*, vol. 237, no. 1, pp. 203-206, 1985.

[3] A. G. A. Verhoeven *et al.*, "First microwave generation in the FOM free-electron maser", *Plasma physics and controlled fusion*, vol. 40, no. 8A, p. 139, 1998.
 [4] W. Bongers, "Millimeter-wave aspects of the FOM fusion free electron laser", Doctoral Thesis, 2004.
 [5] B. C. Lee, S. K. Kim, Y. U. Jeong, S. O. Cho, B. H. Cha, and J. Lee, "First lasing of the KAERI millimeter-wave free electron laser", *Nucl. Instr. Meth.*, vol. 375, no. 1, pp. 28-31, 1996.
 [6] A. Amir, L. R. Elias, R. J. Hu, and G. Ramian, "Spectral characteristics of the UCSB free-electron laser", *Technical Symposium Southeast. International Society for Optics and Photonics*, pp. 20-22, Sept. 1987.
 [7] P. Sprangle, Cha-Mei Tang, and W. M. Manheimer. "Non-linear theory of free-electron lasers and efficiency enhancement", *Phys. Rev. A*, vol. 21, no. 1, p. 302, 1980.
 [8] E. A. Schneidmiller and M. V. Yurkov, "Optimization of a high efficiency free electron laser amplifier", *Phys. Rev. ST Accel. Beams*, vol. 18, no. 3, p. 030705, 2015.
 [9] F. J. Bahman and B. Maraghechi, "Efficiency enhancement in free-electron laser amplifier with one dimensional helical wiggler and ion-channel guiding", *Physics of Plasmas*, vol. 19, no. 1, p. 013107, 2012.
 [10] H. P. Freund, "Comparison of free-electron laser amplifiers based on a step-tapered optical klystron and a conventional tapered wiggler", *Phys. Rev. ST Accel. Beams*, vol. 16, no. 6, p. 060701, 2013.
 [11] N. M. Kroll, P. L. Morton, and M. N. Rosenbluth, "Free-electron lasers with variable parameter wigglers", *IEEE J. Quantum Electron.*, vol. 17, no. 8, 1981.
 [12] X. J. Wang *et al.*, "Efficiency and spectrum enhancement in a tapered free-electron laser amplifier", *Phys. Rev. Lett.*, vol. 103, no. 15, p. 154801, 2009.
 [13] Y. Hidaka *et al.*, "Experimental investigation of superradiance in a tapered free-electron laser amplifier," *Proceedings of PAC'11*, New York, USA, THP148, pp. 2396-2398.
 [14] H. S. Marks *et al.*, "Radiation power out-coupling optimization of a free electron laser oscillator", *IEEE Trans. Microwave Theory and Techniques*, vol. 64, no. 3, pp. 1006-1014, 2016.
 [15] A. Abramovich, Y. Pinhasi, H. Kleinman, A. Eichenbaum, Y. M. Yakover, and A. Gover, "Efficiency enhancement of a pre-bunched free-electron maser oscillator by locking to a single eigen frequency of the resonator", *Nucl. Instr. Meth.*, vol. 429, no. 1, pp. 107-110, 1999.
 [16] H. S. Marks, Y. Lurie, E. Dyunin, and A. Gover, "Enhancing electron beam radiative energy extraction efficiency in free-electron laser oscillators through beam energy ramping", *IEEE Trans. on Microwave Theory and Techniques*, 2017.
 [17] H. S. Marks *et al.*, "Wiggler improvement based on single axis magnetic measurement, synthesized 3-D field simulation of trajectories and sorting of lateral focusing magnets," *Nucl. Instr. Meth.*, vol. 660, no. 1, pp. 15-21, 2011.

Content from this work may be used under the terms of the CC BY 3.0 licence (© 2018). Any distribution of this work must maintain attribution to the author(s), title of the work, publisher, and DOI.

START-TO-END SIMULATIONS FOR AN X-RAY FEL OSCILLATOR AT THE LCLS-II AND LCLS-II-HE

W. Qin*, S. Huang, K. X. Liu, IHIP, Peking University, Beijing, China
 K.-J. Kim, R. R. Lindberg, ANL, Argonne, USA

Y. Ding, Z. Huang, T. Maxwell, K. Bane, G. Marcus, SLAC, Menlo Parck, USA

Abstract

The proposed high repetition-rate electron beam from the LCLS-II and LCLS-II High Energy (LCLS-II-HE) upgrade are promising sources as drivers for an X-ray FEL Oscillator (XFEL) operating at both the harmonic and fundamental frequencies. In this contribution we present start-to-end simulations for an XFEL operating at the fifth harmonic with 4 GeV LCLS-II beam and at the fundamental with 8 GeV LCLS-II-HE beam. The electron beam longitudinal phase space is optimized by shaping the photoinjector laser and adjusting various machine parameters. The XFEL simulations show that high-flux output radiation pulses with 10^{10} photons and 3 meV (FWHM) spectral bandwidth can be obtained with the 8 GeV configuration.

INTRODUCTION

X-ray free-electron lasers (XFELs) such as the LCLS [1] in self-amplified spontaneous emission (SASE) [2, 3] mode are now generating unprecedentedly bright X-ray pulses for wide range of applications. Reaching fully coherent, stable hard X-ray pulses is still challenging due to the stochastic nature of the SASE process. Hard X-ray self-seeding [4] improved the temporal coherence and brightness but still relies on a SASE seed. The transition to the era of high repetition rate XFELs provides promising opportunities for the linac based X-ray FEL oscillator (XFEL) [5–8], which is characterized with full coherence, ultra narrow bandwidth, and stable X-ray pulses. The XFEL relies on successive low gain amplification of X-ray pulses trapped in an optical cavity with crystal mirrors. Since the spectral acceptance of the crystal mirror is about ~ 10 meV, high quality electron beams with low emittance, low energy spread are required.

Feasibility study of the 5th harmonic XFEL utilizing the LCLS-II [9] was carried out with an ideal 4 GeV beam for 14.4 keV photon energy [10, 11]. The proposed high energy upgrade of LCLS-II to 8 GeV LCLS-II-HE [12] enables driving the same wavelength in the fundamental mode. The performance of XFEL is strongly affected by the longitudinal phase space flatness due to the narrow spectral acceptance of the crystals. Linearizing longitudinal phase space via current shaping was studied [13]. Here, we present the start-to-end simulations for an XFEL based on both 4 GeV LCLS-II beam and 8 GeV LCLS-II-HE beam.

LAYOUT

The layout of the proposed linac-XFEL is sketched in Fig. 1. A photoinjector is used to generate high-brightness electron beams, and the 1.3 GHz superconducting linac cavities accelerate the beam to 4 GeV for LCLS-II and 8 GeV for LCLS-II-HE. Since the XFEL usually operates at lower current compared with high gain FELs, two stages of bunch compression are used to compress the beam to 100 A level current. A 3.9 GHz harmonic cavity is located before the first compressor to linearize the longitudinal phase space. The accelerated beam is transported for 2 km to the Beam Switch Yard (BSY) and directed to End Station A (ESA), a possible location for the XFEL. Since there is a beam energy chirp after the transport, a passive, parallel-plate corrugated dechirper [14, 15] is employed to cancel the energy chirp before entering the XFEL. The X-ray cavity is in the four crystal configuration as proposed in Ref. [6]. Diamonds are used as high reflectivity mirror for X-rays. For the harmonic setup, phase shifters are used to suppress the fundamental wavelength [7].

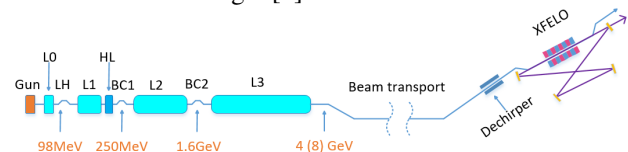


Figure 1: Layout of the proposed XFEL at the LCLS-II.

INJECTOR SIMULATION

Baseline of the LCLS-II injector [16] is based on the Advanced Photoinjector Experiment (APEX) [17] design, consisting of a normal conducting rf (NCRF) gun at 186 MHz with up to 20 MV/m gradient, one 1.3 GHz 2-cell buncher, two emittance compensation solenoids and one standard cryomodule with eight 9-cell superconducting cavities. Laser pulses of 40 ps flat-top are irradiated to a semiconductor cathode to generate 100 pC electrons bunches. The beam energy exiting the gun is 750 keV and reaches about 100 MeV at the exit of the injector. Genetic optimization based on NSGA-II algorithm was applied in the design of the injector to minimize the beam emittance [18]. Figure 2 shows the ASTRA [19] simulated electron longitudinal phase space, current, slice energy spread, and slice emittance of the 100 pC baseline case at the exit of the injector. The beam emittance is about $0.3 \mu\text{m}$. The electron beam exhibits a Gaussian-like current profile.

To get flat final longitudinal phase space, one approach is to shape the beam current by shaping the drive laser pulse profile at the injector. Since the NCRF gun setup compresses

* qinweilun@pku.edu.cn, also at SLAC.

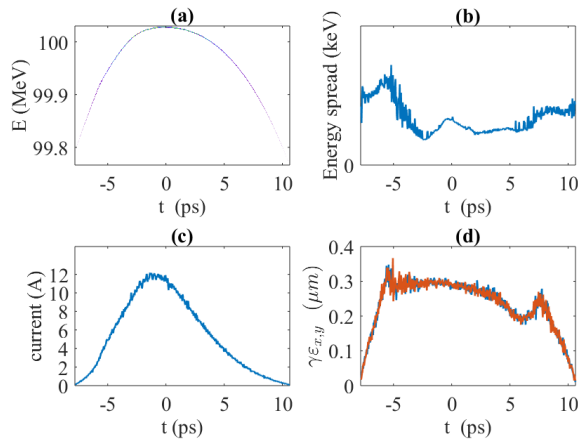


Figure 2: Electron longitudinal phase space, beam current, slice energy spread and slice emittance at injector exit for NCRF gun setup.

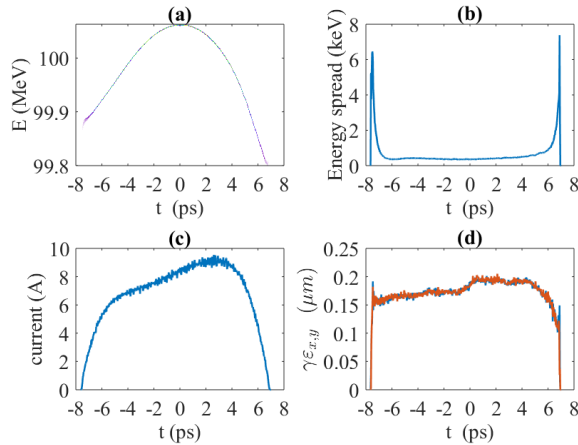


Figure 3: Electron longitudinal phase space, beam current, slice energy spread and slice emittance at injector exit for SCRF gun setup.

the beam from 40 ps to 10 ps at relatively low beam energy of 750 keV, shaping the initial current strongly affects the envelope oscillation in the injector, leading to an increase in the projected beam emittance.

An alternative injector setup begins with one superconducting rf (SCRF) gun like the Wisconsin gun [20], which allows higher gun gradient up to 40 MV/m and the beam energy at the gun exit is near 4 MeV. The initial laser pulse is also reduced to 20 ps to reduce the bunch compression factor at low energy. The basic layout is kept the same as the NCRF setup except that the buncher is replaced with a 9-cell superconducting cavity, which requires a separate cryomodule. Figure 3 shows the final electron beam phase space distribution, current, slice energy spread, and slice emittance for the case of the SCRF gun setup. The projected emittance is about $0.25 \mu\text{m}$. The current profile is shaped to a ramped form with relatively sharp edges compared with the NCRF results.

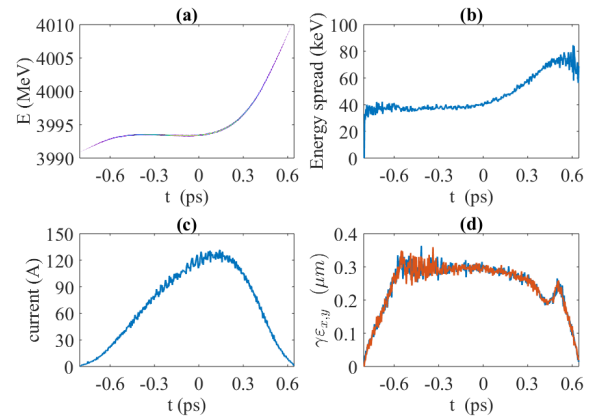


Figure 4: Electron longitudinal phase space, beam current, slice energy spread, and slice emittance after linac optimization, using NCRF injector beam.

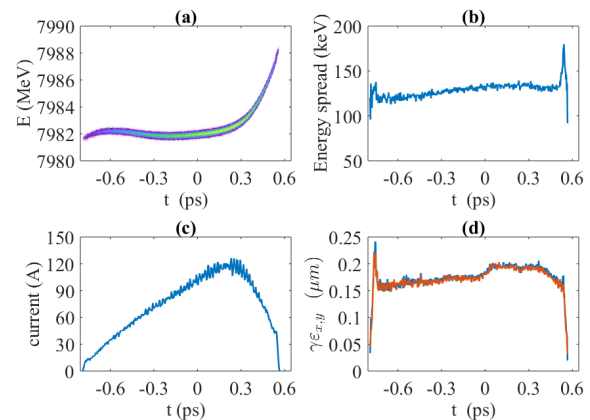


Figure 5: Electron longitudinal phase space, beam current, slice energy spread, and slice emittance after linac optimization, using SCRF injector beam.

LINAC SIMULATION

Several factors in the linac beam dynamics contribute to the final longitudinal phase space distribution, such as curvatures from the RF fields, nonlinearity from bunch compression, and bunch wakefields from the linac, long transport as well as the dechirper structure. We employ genetic algorithm with LiTrack [21] to optimize the linac parameters, including the gradient and the phase of the three main linacs as well as the harmonic cavity, the R_{56} of both bunch compressors and the parameters of the dechirper. For simplicity, beam energy at L1 end, L2 end and L3 end are fixed. The optimization objectives are set as the length of the flat part in the longitudinal phase space, defined as the bunch length within a specific energy spread, and the average beam current within the flat part. The optimized solution is then simulated using ELEGANT [22] with 1 million macroparticles.

Figure 4 and Fig. 5 show the ELEGANT simulated final beam phase space distribution, current, slice energy spread and slice emittance before the undulator for NCRF injector beam and SCRF injector beam, respectively. For the NCRF gun setup beam, the flat part of the beam is 400 fs,

Table 1: XFELO Simulation Parameters and Output Pulse Properties, the Repetition Rate is Assumed to be 1 MHz).

Parameter	4.9 keV	10 keV	14.4 keV	14.4 keV	14.4 keV	20 keV	24.2 keV
Electron gun	SCRF	SCRF	NCRF	NCRF	SCRF	SCRF	SCRF
FEL K	3.2128	2.0125	1.4304	1.4837	1.4837	1.0125	1.1539
E_{beam} [GeV]	7.982	7.982	3.994	7.982	7.982	7.982	7.982
Q [pC]	15	50	100	100	100	100	100
ϵ_n [μm]	0.25	0.25	0.35	0.35	0.25	0.25	0.25
σ_E [keV]	130	130	70	70	130	130	130
λ_u [cm]	2	2	2.6	2	2	2	1.5
N_u	1000	1000	1250	1000	1000	1000	2000
harmonic number	1	1	5	1	1	1	1
Z_R [m]	10	10	10	10	10	10	15
Bragg crystal	C(220)	C(440)	C(733)	C(733)	C(733)	C(880)	C(888)
Output coupling	4%	4%	4%	4%	4%	4%	5%
Pulse energy [μJ]	3.1	21	0.3	7	28	11	4.4
Spectral FWHM [meV]	10.9	5.4	5.8	3.9	3.4	2.7	1.3
Temporal FWHM [fs]	138	530	400	557	693	905	1989
$\sigma_\tau\sigma_\omega$ (FWHM)	2.27	4.37	3.52	3.26	3.58	3.67	4.06
# of Photons/pulse	3.9×10^9	1.3×10^{10}	1.3×10^8	3.1×10^9	1.2×10^{10}	3.4×10^9	1.1×10^9
Spectral flux [ph/s/meV]	3.6×10^{14}	2.4×10^{15}	2.2×10^{13}	7.9×10^{14}	3.6×10^{15}	1.3×10^{15}	8.5×10^{14}

almost doubled compared with Ref. [10]. For the SCRF gun setup beam, the overall beam chirp is reduced and the flat part extends over 600 fs. The slice energy spread for both setup are well within 200 keV and the low slice emittance is maintained during the acceleration and transport.

FEL SIMULATION

With the electron beam from ELEGANT, we conducted GINGER [23] simulation to evaluate the XFELO performance. The XFELO adopts the proposed geometry in [6] with four high-reflectivity diamond crystals to allow tuning of the central photon energy. Two sets of compound refractive lenses (CRLs) are used to provide focusing for the XFELO cavity. One of the four crystal is made thinner to allow for 4% output of the X-ray power.

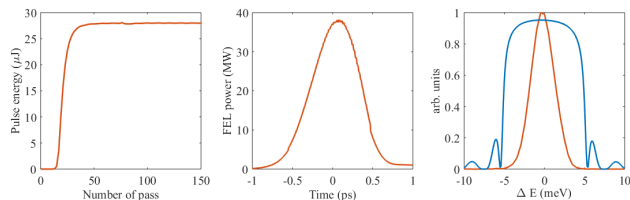


Figure 6: XFELO performance for 14.4 keV using 0.25 μm emittance, 130 keV slice energy spread and over 500 fs flat part beam with the SCRF gun setup.

XFELO parameters and performance are summarized in Table 1. For the 4.9 keV and 10 keV case, only part of the whole bunch is simulated to avoid spiky output of the spectra since the spectral acceptance is relatively large and the useful part of beam is long enough. For the NCRF gun setup, XFELO operating in 5th harmonic mode at 14.4 keV

can generate X-rays with about 1.3×10^8 photons/pulse. XFELO operating in fundamental mode can generate much higher pulse energy than 5th harmonic mode thanks to higher single pass gain, reaching 3×10^9 photons/pulse. With higher gain, longer part of the beam contributes to lasing and the bandwidth is decreased. With the SCRF gun setup, the smaller emittance and the longer flat part of the beam result in a factor of four increase of output pulse energy. High flux X-rays with 1.2×10^{10} photons/pulse at 14.4 keV can be reached, corresponding to 3.6×10^{15} photons/s/meV spectral flux assuming 1 MHz repetition rate. The corresponding pulse energy evolution, temporal profile as well as spectrum for this case are shown in Fig. 6. It should be noted that if the emittance of the SCRF gun setup is the same as the NCRF gun setup (0.35 μm), the output photons drop to about 6.5×10^9 photons/pulse, still a factor of 2 better than the NCRF gun setup. XFELO performance at higher photon energy up to 24.2 keV can also generate 10^9 photons/pulse with narrower bandwidth.

CONCLUSION

We performed the start-to-end simulations for XFELO driven by high repetition rate electron beams at the LCLS-II and the LCLS-II-HE. Two injector setup, one based on normal conducting APEX design and one based on superconducting gun design of the Wisconsin gun, are optimized using a genetic optimizer to obtain low emittance for the XFELO. The drive laser distribution of the SCRF setup is also shaped to obtain current ramp for phase space linearization. The parameters of the acceleration and beam manipulation components, *i.e.*, the linac, bunch compressor and the dechirper, are optimized with a genetic algorithm based LiTrack optimizer to obtain flat phase space distribution over

the length of 500 fs. The XFEL performance with various beam parameters in a photon energy range of 5-25 keV are evaluated with the start-to-end simulation. In the case of 8 GeV beam with the APEX type injector, about 10^9 photons per pulse with meV level bandwidth can be generated. With low emittance SCRF gun setup and drive laser shaping, the output at 14.4 keV is 1.2×10^{10} photons/pulse with 3.4 meV spectral bandwidth, corresponding to 3.6×10^{15} photons/s/meV spectral flux. The high flux and wide photon energy coverage makes the XFEL an unique source complementary to the high gain XFELs for exciting scientific applications.

ACKNOWLEDGEMENT

The authors would like to thank W. M. Fawley for helpful discussions on XFEL simulation, and C. Mitchell, F. Zhou and R. K. Li for injector simulations. This work is supported by the U.S. Department of Energy under Contract No. DE-AC02-76SF00515 and U.S. Department of Energy under Contract No. DE-AC02-06CH11357.

REFERENCES

- [1] P. Emma *et al.*, "First lasing and operation of an ångstrom-wavelength free-electron laser", *Nature Photonics* 4, 641 (2009).
- [2] A. Kondratenko *et al.*, *Part. Accel.* 10, 207 (1980).
- [3] R. Bonifacio *et al.*, "Collective instabilities and high-gain regime in a free electron laser", *Opt. Commun.* 50, 373 (1984).
- [4] J. Amann *et al.*, "Demonstration of self-seeding in a hard-X-ray free-electron laser", *Nature Photonics* 6, 693 (2012).
- [5] K.-J. Kim *et al.*, "A proposal for an X-ray free-electron laser oscillator with an energy-recovery linac", *Phys. Rev. Lett.* 100, 244802 (2008).
- [6] K.-J. Kim *et al.*, "Tunable optical cavity for an x-ray free-electron-laser oscillator", *Phys. Rev. ST Accel. Beams* 12, 030703 (2009).
- [7] J. Dai *et al.*, "Proposal for an X-ray free electron laser oscillator with intermediate energy electron beam", *Phys. Rev. Lett.* 108, 034802 (2012).
- [8] R. R. Lindberg *et al.*, "Performance of the x-ray free-electron laser oscillator with crystal cavity", *Phys. Rev. ST Accel. Beams* 14, 010701 (2011).
- [9] SLAC National Accelerator Laboratory, *Linac Coherent Light Source II Conceptual Design Report*, No. SLAC-R-978 (2011).
- [10] T. J. Maxwell *et al.*, "Feasibility study for an X-ray FEL oscillator at the LCLS-II", IPAC'15, Richmond, VA, USA, TUPMA028.
- [11] J. Zemella *et al.*, "Time dependent study for an xray FEL oscillator at LCLS-II", FEL'15, Daejeon, Korea, TUP030.
- [12] LCLS-II-HE "First Experiments" Meeting: Chemistry and Materials Physics, available: https://portal.slac.stanford.edu/sites/conf_public/lclsiihe2017/Pages/default.aspx.
- [13] W. Qin *et al.*, "Beam Optimization Study for an X-ray FEL Oscillator at the LCLS-II", IPAC'16, Busan, Korea, WE-POY019.
- [14] K. Bane and G. Stupakov, "Corrugated pipe as a beam dechirper", *Nucl. Instru. and Methods A*, 690: p. 106-110. (2012).
- [15] Z. Zhang *et al.*, "Electron beam energy chirp control with a rectangular corrugated structure at the Linac Coherent Light Source" *Phys. Rev. ST Accel. Beams* 18, 010702 (2015).
- [16] J. F. Schmerge, *et al.*, "The LCLS-II Injector Design", FEL'14, Basel, Switzerland, THP042.
- [17] D. Filippetto *et al.*, "APEX: A photo-injector for high average power light sources and beyond", FEL'14, Basel, Switzerland, TUA01.
- [18] C. F. Papadopoulos *et al.*, "RF injector beam dynamics optimization for LCLS-II" IPAC'14, Dresden, Germany, WE-PRO015.
- [19] K. Flottmann, "ASTRA: A Space Charge Tracking Algorithm", user's manual available at http://www.desy.de/~mpyflo/Astra_dokumentation.
- [20] J. Bisognano *et al.*, NAPAC'13, Pasadena, USA, p622.
- [21] K.L.F. Bane *et al.*, PAC'05, Knoxville, Tennessee, FPAT091 (2005).
- [22] M. Borland, "Elegant: A flexible SDDS-Compliant Code for Accelerator Simulation", Advanced Photon Source Report No. LS-287, (2000).
- [23] W. M. Fawley, "A User Manual for GINGER-H and its Post-Processor XPLOTGINH", Version 2.0k, June 2012.

NUMERICAL STUDIES ON RF-INDUCED TRAJECTORY VARIATIONS AT THE EUROPEAN XFEL

T. Hellert, B. Beutner, N. Walker, W. Decking, DESY, Hamburg, Germany

Abstract

At the European X-Ray Free-Electron-Laser, superconducting TESLA-type cavities are used for acceleration of the driving electron bunches. Due to the high achievable duty cycle, a long radio frequency (RF) pulse structure can be provided, which allows to operate the machine with long bunch trains. The required pointing stability of the FEL radiation places stringent restrictions on the acceptable trajectory variations of individual electron bunches. Therefore a transverse intra-bunch-train feedback system (IBFB) is located upstream of the undulator section. However, intra-bunch-train variations of RF parameters and misalignments of RF structures induce significant trajectory variations that may exceed the capability of the IBFB. In this paper we give an estimate of the expected RF induced intra-bunch-train trajectory variation for different machine realizations and investigate on methods for their limitation.

INTRODUCTION

The European X-Ray Free-Electron Laser (EuXFEL) Facility [1–3] is built in Hamburg and is currently undergoing commissioning [4]. It will provide FEL radiation with wavelengths from 0.05 nm to 5 nm. Acceleration of the driving electron bunches is achieved by using superconducting TESLA-type [5] cavities. The long RF pulse structure allows to provide long bunch-trains adapted to the needs of the experiments. Up to 2700 bunches are accelerated within one RF pulse with a pulse repetition rate of 10 Hz and a bunch spacing down to 222 ns, thus 27000 bunches per second can be used for the experiments.

The designated pointing stability of the photon beam leads to a stability requirement of 3 μm maximum trajectory spread within one bunch-train in the undulator section. A conservative estimate predicts worst case beam trajectory perturbations, e.g. from magnet vibrations or spurious dispersion, of about $\pm 100 \mu\text{m}$ assuming a beta function of 30 m [6]. This magnitude of amplitude can be corrected for individual bunches at the entrance to the undulator section by the transverse intra-bunch-train feedback system (IBFB) [7]. However, RF-induced trajectory variations have not been considered in the design studies of the IBFB.

At EuXFEL, several cavities with individual operational limits [8] are supplied by one RF power source. Within the bunch-train, the low-level-RF system (LLRF) [9, 10] is able to restrict the variation of the vector sum of the accelerating gradient of one RF station sufficiently [11]. However, individual cavities have an intrinsic variation of RF parameters within one bunch train, caused by the effects of beam loading and Lorentz force detuning [12]. Misaligned cavities in combination with variable RF parameters induce

intra-bunch-train trajectory variations [12]. Coupler kick variations caused by variations of the detuning are additional beam dynamics perturbations within one bunch train. In this paper we investigate their magnitude for different machine realizations and present methods for their limitation.

MODEL SETUP

A detailed description of the utilized beam dynamics model can be found in Ref. [12]. We use a combination of axially symmetric beam transport matrices [13] and discretized coupler kicks [14]. Misalignments are modeled by coordinate system transformations. The EuXFEL linear accelerator increases the electron beam energy up to 17.5 GeV in three separate sections: L1, L2 and L3, each consisting out of 4, 12 and 84 accelerating modules, respectively. Each module contains eight cavities and a quadrupole magnet, providing a FODO lattice in the accelerating sections. Initial beam energy is 150 MeV for L1, 600 MeV for L2 and 2.4 GeV for L3. If not stated differently, for each machine seed the following model parameters are randomly created within their range: variation of amplitude $\Delta V = 2 \text{ MV m}^{-1}$ and phase $\Delta\phi = 4^\circ$ of the accelerating field and the detuning $\Delta f = 20 \text{ Hz}$ of individual cavities within the bunch train. Furthermore the offset $\Delta u_{\text{cav}} = 0.5 \text{ mm}$ and tilt $\Delta u'_{\text{cav}} = 0.25 \text{ mrad}$ of cavities and modules, $\Delta u_{\text{mod}} = 0.5 \text{ mm}$ and $\Delta u'_{\text{mod}} = 0.2 \text{ mrad}$, respectively. The above values are expected for nominal machine operation.

BEAM DYNAMICS SIMULATIONS

Before conducting a statistical analysis of each accelerating section, tracking results of one random machine realization are presented. Figure 1 shows the intra-bunch-train trajectory variation for the horizontal and vertical plane as it could be recorded at the beam position monitors at each module at EuXFEL. Mean bunch train offsets are subtracted. The lower row of Figure 1 additionally shows the normalized trajectory variation $\Delta\tilde{u}$. It will be defined as the maximum possible offset variation at a point with zero divergence and $\beta_u = 30 \text{ m}$, where u stands for x and y , respectively. The normalized trajectory variation evolves non-monotonically throughout the machine. The correlation of particular misalignments of cavities and their RF parameters can affect the initial trajectory variation at the entrance of the cavity constructively or destructively. An accurate consideration must involve statistical methods.

The accumulated normalized intra-bunch-train trajectory variation $\Delta\tilde{u}$ is calculated for L1, L2 and L3 independently. 10^5 random sets of misalignments and RF parameters are evaluated. Figure 2 shows a histogram of $\Delta\tilde{u}$, as induced in each linac. Critical trajectory variation is defined as the

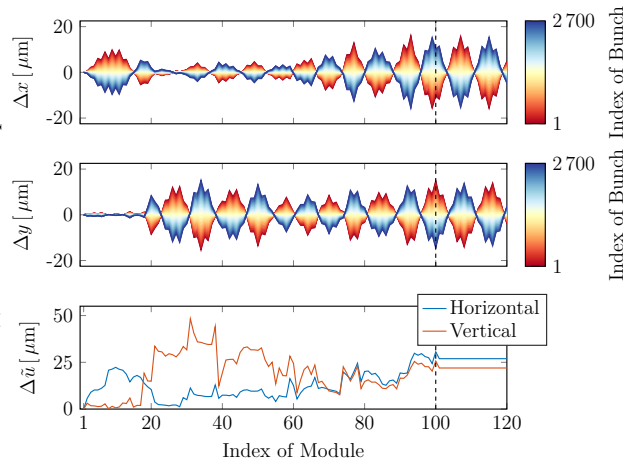


Figure 1: Simulated intra-bunch-train trajectory variation at EuXFEL. The horizontal (up) and vertical (mid) intra-bunch-train offsets are plotted, evaluated at each BPM. The red line corresponds to the first bunch, the blue line to the 2700th bunch of one bunch train. The bottom row shows the normalized trajectory variation. After module 100, a FODO section is appended for visualization purposes.

value which exceeds 90% of the evaluations and is marked as circles in Fig. 2. It's values are $\Delta\tilde{x}_c = 63 \mu\text{m}$ and $\Delta\tilde{y}_c = 41 \mu\text{m}$ for the horizontal and vertical plane, respectively, in L1, $\Delta\tilde{x}_c = 33 \mu\text{m}$ and $\Delta\tilde{y}_c = 20 \mu\text{m}$ in L2 and $\Delta\tilde{x}_c = 13 \mu\text{m}$ and $\Delta\tilde{y}_c = 9 \mu\text{m}$ for L3. The decreasing difference between the transverse planes from L1 to L3 points out the decreasing impact of coupler kicks at higher beam energy.

Influence of gradient slopes: The slope of the amplitude of the accelerating field within one bunch train, ΔV , is key in the creation of trajectory variations. For typical machine operation at EuXFEL, the amplitude slope is determined mainly by the interaction of a common loaded quality factor Q_L with dissimilar operational gradients of the cavities [12]. LLRF simulations show that these beam loading induced amplitude slopes are proportional to the beam current and can reach up to 4 MV m^{-1} for the design beam current of 4.5 mA without further Q_L -correction.

The left side of Figure 3 shows the critical trajectory variation $\Delta\tilde{u}_c$ at the end of 100 modules as a function of the

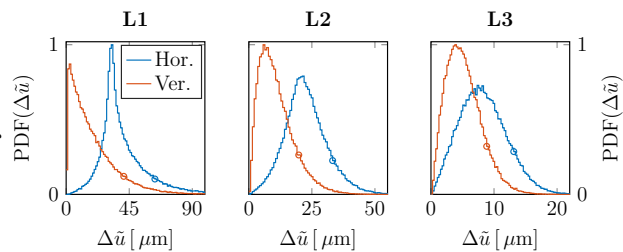


Figure 2: Histogram of the normalized intra-bunch-train trajectory variation $\Delta\tilde{u}$ induced in L1 (left), L2 (mid) and L3 (right) for the horizontal (blue) and vertical (red) plane.

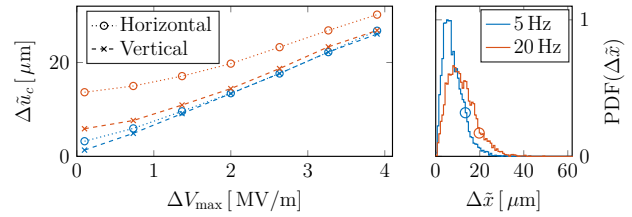


Figure 3: Critical trajectory variation $\Delta\tilde{u}_c$ at the end of L3 as a function of the maximum amplitude slope ΔV_{max} (left) for the horizontal (circles) and vertical (crosses) plane. The two colors correspond to a maximum detuning of $\Delta f = 20 \text{ Hz}$ (red) and $\Delta f = 5 \text{ Hz}$ (blue). The right plot shows the histogram of the horizontal trajectory variation for $\Delta V = 2 \text{ MV m}^{-1}$ for both detuning scenarios.

maximum amplitude slope ΔV_{max} , evaluated for both planes and two detuning scenarios. The blue and red color correspond to a maximum detuning of 5 Hz and 20 Hz, respectively. The right plot shows a histogram of the horizontal trajectory variation for both detuning scenarios. For small detuning and high amplitude slope the trajectory variation is proportional to the amplitude slope and the influence of coupler kicks vanishes. For high beam currents, a limitation of beam loading induced amplitude slopes by changing the Q_L -setup is advised.

Influence of the beam trajectory: In this section two methods for minimizing the intra-bunch-train trajectory variation for a given machine realization are discussed. The effect of a misaligned structure on the trajectory variation depends on the beam trajectory through the structure and the phase advance between individual perturbations. At first, the phase advance is studied. The strength of the horizontally focussing and defocusing quadrupole, k_F and k_D , can be set independently from each other. It is therefore possible to vary the horizontal and vertical phase advance in the accelerating sections independently. For reasons of simplicity only periodic solutions are assumed, meaning that all k_F and k_D , respectively, have the same strength.

Figure 4 shows exemplarily tracking results at the end of a string containing 100 modules for one machine realization, thus RF- and misalignment seed. The accumulated normalized trajectory variation $\Delta\tilde{u}$ is plotted for both transverse planes. The upper two plots show a contour of $\Delta\tilde{x}$ (left) and $\Delta\tilde{y}$ (right) as a function of the horizontal and vertical phase advance, μ_x and μ_y , respectively. The lower plot shows $\Delta\tilde{x}$ and $\Delta\tilde{y}$, evaluated at phase advances which correspond to the dashed line in the upper plots. Obviously individual perturbations cancel remarkably at a certain phase advance while they add up in other cases. This result can be used to improve the multi-bunch performance of the XFEL. During setup of the machine the dependence of the intra-bunch-train trajectory variation on the phase advance can be scanned.

Changing the quadrupole magnets linearly in a way that $k_F + k_D = \text{const}$, the whole range of phase advance in both planes can be covered (cf. the dashed line in Figure 4) and

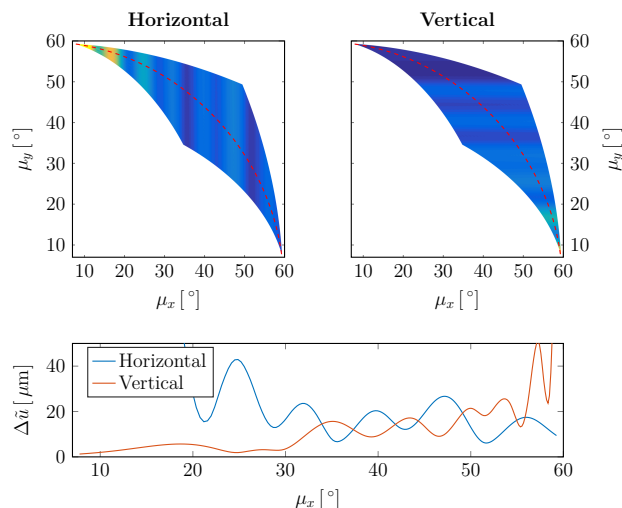


Figure 4: Impact of the phase advance in the FODO-lattice on the accumulated normalized intra-bunch-train trajectory variation $\Delta\tilde{u}$. The upper plots illustrate qualitatively the horizontal (left) and vertical (right) plane as a function of the horizontal and vertical phase advance, μ_x and μ_y , respectively. Bright yellow corresponds to $110\ \mu\text{m}$ and dark blue to $0\ \mu\text{m}$. The lower plot shows $\Delta\tilde{u}$ evaluated at phase-advances according to the dashed line in the upper plots.

an optimal working point can be chosen. In order to quantify the reduction for any given realization of misalignments and RF parameters, 10^4 machine seeds are randomly created. For each seed, the strength of the quadrupoles is varied and the pair of phase advances is found at which the mean trajectory variation $\langle\Delta\tilde{u}\rangle$, averaged over both transverse planes, is minimized. The range of k -values is $k_i \in [0.05, 0.07]$.

Figure 5 illustrates the results. The black histogram in the left plot shows the distribution of $\langle\Delta\tilde{u}\rangle$ as calculated for $k_F = k_D = 0.065\ \text{m}^{-2}$. This corresponds to a phase advance of about 45° in both planes and reflects the design lattice. The blue line corresponds to the distribution of tracking results with a tune that minimizes $\langle\Delta\tilde{u}\rangle$. The right histogram shows the relative amount of trajectory variation reduction. For most machine realizations the intra-bunch-train trajectory variation can be decreased significantly. In average, a reduction of 73 % is possible. In 90 % of the cases the achievable reduction is larger than 49 %. Note that a reduction of 66 % reflects a final trajectory variation three times smaller than its initial value.

So far, the beam entered the first accelerating module on axis. The impact of a variation of the initial beam trajectory on the accumulated intra-bunch-train trajectory variation is considered in the following. This scenario reflects steering the beam at the entrance of L1. Note that no initial intra-bunch-train trajectory variation and only one pair of steerers are considered. 10^4 machine realizations are evaluated. Analog to the previous method, the beam trajectory angle at the entrance of the first module is changed for each machine seed. The pair of horizontal and vertical trajectory angles

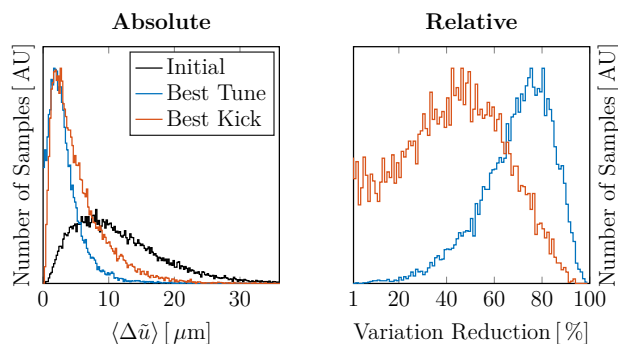


Figure 5: Absolute (left) and relative (right) reduction of normalized intra-bunch-train trajectory variation $\langle\Delta\tilde{u}\rangle$, averaged over both transverse planes. The black histogram in the left plot reflects the distribution as calculated for the design values. The blue curve corresponds to the remaining trajectory variation after choosing an optimal phase advance. The red curve corresponds to the remaining trajectory variation after choosing an optimal trajectory angle at the entrance of the first module. The right plot shows the relative trajectory variation reduction of both methods.

is found at which the mean accumulated trajectory variation $\langle\Delta\tilde{u}\rangle$ is minimized. The considered range of trajectory angles is ± 3 mrad. The results are shown in Fig. 5 in red. In average, a reduction of 44 % is possible. In 90 % of the cases the achievable reduction is larger than 11 %. The rms value of the trajectory angle with best reduction is 1 mrad. The reduction is less noticeable than by changing the optical functions. However, steering the beam is significantly less time-consuming. Note that in this simplified example only one pair of steerers at the entrance of the first module was considered. An automated optimizer including several steerers throughout the accelerator should be implemented and run by default when setting up the machine.

CONCLUSION

Intra-bunch-train trajectory variations which are caused by a variation of RF parameters of individual cavities within one bunch train at EuXFEL have been analyzed systematically. Different accelerating sections and ranges of machine parameter were discussed and methods for reducing the accumulated trajectory variation for a given machine realization were presented. Future studies on limiting the variation of RF parameters by means of a Q_L -correction are advised.

ACKNOWLEDGMENTS

We would like to thank Martin Dohlus, Klaus Flöttman and Julien Branlard for their help in valuable discussions.

REFERENCES

- [1] M. Altarelli *et al.*, "XFEL: The European X-Ray Free-Electron Laser - Technical Design Report", DESY-06-097, July 2006.

- Content from this work may be used under the terms of the CC BY 3.0 licence (© 2018). Any distribution of this work must maintain attribution to the author(s), title of the work, publisher, and DOI.
- [2] Winfried Decking and Torsten Limberg, "European XFEL Post-TDR Description", Technical Report XFEL.EU TN-2013-004, 2013.
 - [3] T. Tschentscher. "Layout of the X-Ray Systems at the European XFEL", Technical Report XFEL.EU TR-2011-001, 2011.
 - [4] M. Bousonville *et al.*, "Planning and Controlling of the Cold Accelerator Sections Installation in XFEL", in *Proceedings of IPAC'16*, Busan, Korea, 2016, pages 716–718, paper MOPOW006.
 - [5] B. Aune *et al.*, "Superconducting TESLA cavities", *Phys. Rev. ST Accel. Beams*, 3:092001, Sep 2000.
 - [6] B. Keil *et al.*, "Design of an Intra-Bunch-Train Feedback System for the European X-Ray FEL", in *Proceedings of DIPAC'07*, Venice, Italy, May 2007, paper WEPB02.
 - [7] B. Keil *et al.*, "Status of The European XFEL Transverse Intra Bunch Train Feedback System", in *Proceedings of IBIC'15*, Melbourne, Australia, 2015, paper TUPB064.
 - [8] D. Reschke, V. Gubarev, J. Schaffran, L. Steder, N. Walker, M. Wenskat, and L. Monaco, "Performance in the vertical test of the 832 nine-cell 1.3 GHz cavities for the european x-ray free electron laser", *Phys. Rev. Accel. Beams*, 20:042004, Apr 2017.
 - [9] T. Schilcher, "Vector Sum control of pulsed accelerating fields in Lorentz Force Detuned Superconducting Cavities", PhD thesis, University of Hamburg, 1998.
 - [10] J. Branlard *et al.*, "The European XFEL LLRF System", in *Proceedings of IPAC'12*, New Orleans, USA, 2012, page 55, paper MOOAC01.
 - [11] M. Omet *et al.*, "Operation Experiences with the MICRO-TCA.4-based LLRF Control System at FLASH", in *Proceedings of IPAC'15*, Richmond, Virginia, USA, 2015, page 844, paper MOPHA029.
 - [12] T. Hellert, "Intra-Bunch-Train Transverse Dynamics in the Superconducting Accelerators FLASH and European XFEL", PhD thesis, University of Hamburg, 2017.
 - [13] J. Rosenzweig and L. Serafini, "Transverse particle motion in radio-frequency linear accelerators" *Phys. Rev. E*, 49:1599–1602, Feb 1994.
 - [14] M. Dohlus, I. Zagorodnov, E. Gjonaj, and T. Weiland, "Coupler Kick for Very Short Bunches and its Compensation", in *Proceedings of EPAC'08*, Genoa, Italy, 2008, page 582, paper MOPP013, JACoW.

FIRST BEAM HALO MEASUREMENTS USING WIRE SCANNERS AT THE EUROPEAN XFEL

S. Liu[†], V. Balandin, B. Beutner, W. Decking, L. Fröhlich, N. Golubeva, T. Lensch, DESY, Hamburg, Germany

Abstract

Beam halo measurements and collimations are of great importance at the European XFEL, especially for the operation at high repetition rates (27000 pulses/s). First beam halo measurements have been performed during the commissioning using the wire scanners installed before and after the ~200 m long post-linac collimation section. We present the measurement results and the comparison of beam halo distributions before and after the collimation section.

INTRODUCTION

The European XFEL [1] is driven by a ~1.7 km long superconducting linear accelerator followed by three undulator systems called SASE1, SASE2 and SASE3 with 35, 35 and 21 undulator segments (each 5 m long), respectively. It operates in bunch train mode with 10 Hz of repetition rate and a maximum number of 2700 electron bunches can be generated per macro pulse with a spacing of 220 ns. The maximum beam power can be generated is more than 500 kW. It is well known that, a common issue for high power machines is the control of beam losses, since the beam losses can cause damages to different components of the machine. In the case of European XFEL, the main concern is the damage to the undulators. Therefore, a ~200 m long post-linac collimation (CL) section is designed to collimate the beam halo and dark current before the undulator section [2].

The CL section has two arcs and one straight section in between as phase shifter. The betatron functions at the collimator locations can be varied by tuning the quadrupoles in the matching sections before and after the collimation section, and in the phase shifter. This tuning includes also the possibility of FODO-like transport through the whole collimation section. This feature brings the flexibility to operate the collimation section in different optics modes. At the beginning of the commission, the FODO-like mode is used. Recently, another two optics modes have also been tested. One is the mode A optics: the standard collimation optics with beta functions (of about 200m) at the collimator locations, and the other is the mode B optics (see Fig.1): the relaxed optics with smaller beta functions (of about 100m) at the collimator locations.

The efficiency of beam halo collimation has been studied in simulations during the design of the collimation section [2] and also for the implementation of Hard X-ray self-seeding, where a diamond crystal will be inserted close to the beam in the undulator sections [3]. For the experimental study, different instruments can be used to

measure the beam halo (e.g. YAG:Ce screen [4], diamond detector [5] and wire scanners [6]). At the European XFEL, the wire scanners (WS's) [7] installed before and after the collimation section can be used. In this paper, we present the design and commissioning of the WSs followed by the first beam halo measurements using the WSs with the collimation optics mode B.

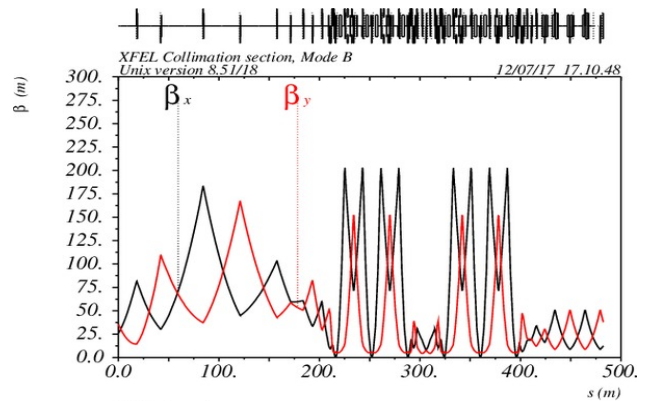


Figure 1: Betatron functions in the collimation section for optics mode B.

WIRE SCANNERS AT THE EUROPEAN XFEL

At the European XFEL, there are in total 4 sets of WSs installed in L3 (before CL), TL (after CL), T1 (before SASE2) and T4 (before SASE3), respectively. Each set of WS consists of three WS units, and each unit has one horizontal and one vertical WS stage. The WSs are installed in the optics matching sections, this allows for emittance measurement and optics matching purposes (especially at high repetition rate) in complementary to the measurements using the scintillation screens [5] (usu-

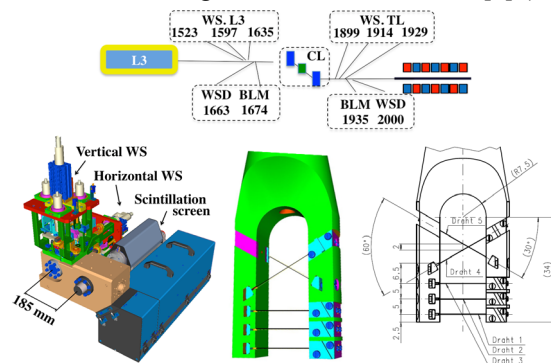


Figure 2: Two WS sets before and after CL section and their detectors (top), the number indicates their location from the gun in meters. Layout of WS stations with scintillation screen layout (bottom-left) and the wire scanner fork with tungsten wires (bottom-right).

[†] shan.liu@desy.de

ally only for single bunch) installed on the same stages at around 185 mm in front of the WS (see Fig. 2).

On one WS stage, there are in total 5 tungsten wires mounted on one fork with the orientations as indicated in Fig. 2. The diameters of the first three wires are 50 μm , and 20 μm , respectively. The vacuum chamber diameter is 40.5 mm, so a well-aligned beam center should be located at around 20 mm. Since we have observed halos even at more than 10 mm away from the beam core (see Fig. 4 lower-left), and the spacing between each wire is 5 mm, so the measured signal can be biased by the background (BG) generated by the halo hitting on the other wires or even on the supporting fork itself. Therefore, in our measurements, we used only the first wire (50 μm) for the beam halo measurements.

The WSs are designed to operate in the fast scan mode with the maximum speed of 1 m/s to minimize the influence on the beam. Meanwhile, they can also be operated in slow scan mode. For the first measurements, we used only the slow scan mode.

WS detectors and the beam loss monitors

The WS detectors (WSDs) are made of plastic scintillating fibers optically coupled to photomultipliers (PMT). They are rolled on the beam pipes downstream of the WSs to detect the showers generated in the beam pipes by the scattered electrons and the bremsstrahlung photons. The locations of the detectors are chosen to maintain a good signal to noise ratio (SNR). There are two WSDs for each set of WS. In addition to the WSDs, the beam loss monitors (BLMs) [6] can also be used to detect the losses generated by the wires passing through the beam. Since the BLMs are more sensitive to low losses, they are more suitable for beam halo measurements than the WSDs¹.

Commissioning of the WSs

Beam size measurements have been performed using the WSs during the commissioning of the WSs (with 500 pC, compressed beam). The measured beam sizes have been compared with the measured beam sizes by the scintillating screens installed on the same stages (see Fig. 2 left). One example of the comparison is shown in Fig. 3. is a discrepancy in the beam size measured by the WS and the

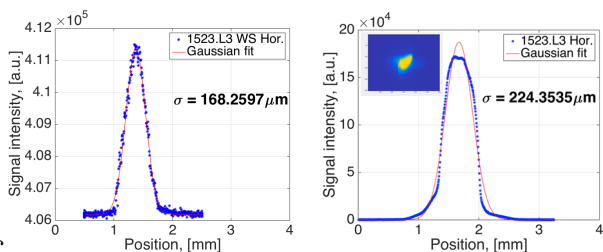


Figure 3: Horizontal beam size measured by the wire scanner (left) and the screen (right).

¹ For the beam core scan, however, the BLM signals are saturated, so only WSD signals can be used. Meanwhile, the WSD pedestal level is apparently too high to measure the beam halo.

² We assume this is due to the saturation of the scintillator, however, there might be COTR effect also.

screen. By measuring with different stages of WS and screens, we have observed an increase in discrepancy with the decrease of beam sizes. Meanwhile, we can see in Fig. 3 that the signal on the screen in the beam core region seems to be saturated², while on the WS it is well fitted to the Gaussian distribution. Therefore, we think the WS measured beam sizes are more reliable than the screen.

FIRST BEAM HALO MEASUREMENT RESULTS

First beam halo measurements have been performed with the collimation optics mode B (see Fig. 1) using one WS in front of the CL section (1523.L3) and two WSs after CL section (1899.TL and 1914.TL) (see Fig. 2, top). The beam charge is ~ 500 pC and the beam is compressed with nominal compression. During the measurements, three of the four collimators were set to 4 mm diameter aperture and the third main collimator was set to 6 mm diameter aperture.

Before scanning the beam, we registered the pedestal level of the BLMs, and scanned the dark current³. Then, the beam core is scanned and beam size is extracted from the Gaussian fit of the beam core measured by the WSD. After the beam core scan, a larger range ($> \pm 10 \sigma$) scan is performed to measure the beam halo using several downstream BLMs. The beam halo measurement results are presented in Fig. 4. Only the signal from the BLM with the highest SNR is shown. The pedestal is subtracted from the distributions.

Since the BLMs are saturated in the beam core region, we reconstructed the beam core based on the beam sizes measured by the WSD. In the reconstruction, we try to keep at least two points, which overlap with the Gaussian beam core. However, the saturation level of the BLMs is unknown⁴. Besides, there is a constant BG from the beam losses without the wire (or from the electronics), and the beam halo below this BG level cannot be detected. Therefore, when the halo is below the BG level, we can only set an upper limit on the halo level with respect to the beam core intensity.

From Fig. 4 (lower-left) we can see that before the CL section at 1523.L3, there is a rather long tail of vertical halo lasting up to -17 mm away from the beam core. This tail continues to increase on the right side (lower side) of the beam core, which indicates that the signal is strongly affected by the BG generated by other wires or the fork. This effect can also be observed in the horizontal measurement, as shown in Fig. 4 (upper-left). The visible horizontal and vertical beam halo level before the CL section at -10σ is around 10^{-3} and 10^{-2} of I_{peak} , respectively.

In Fig. 4 (middle and right) one can also see that the

³ The averaged absolute readout of the pedestal from BLM.1674.CL is $\sim 3 \times 10^{-3}$, and from BLM.1935.TL is $\sim 5 \times 10^{-3}$. During the measurements, the dark current level is below the pedestal level, therefore, we couldn't see it.

⁴ The BLMs signals are not calibrated, so the saturation level can differ from one BLM to another.

Content from this work may be used under the terms of the CC BY 3.0 licence (© 2018). Any distribution of this work must maintain attribution to the author(s), title of the work, publisher, and DOI.

beam halo shapes measured by the two WSs after the CL section are quite similar, and the halo levels are also quite consistent. The visible horizontal and vertical beam halo level at -10σ are both below 10^{-4} of I_{peak} , and beyond 10σ the beam halo is below the pedestal level. Meanwhile, we can see that the horizontal beam halo distribution is asymmetric (more halos are measured on the left side than on the right side) and the vertical beam halo is more or less symmetric. This is maybe due to the horizontal misalignment of the beam with respect to the collimators. Besides, this also indicates that there is less beam halo left after collimation and the measurements are less (or almost not) affected by the BG generated by the other wires.

By looking at the distributions (see Fig. 4) and comparing the upper limit of halo level with respect to the I_{peak} (see Table.1), we can conclude that the halo are significantly collimated in the collimation section. The halo intensity at -10σ position decreased at least by factor 10 horizontally and factor 100 vertically after the CL section.

Table 1: Comparison of visible halo level at $-10\sigma_{x,y}$ before and after CL.

	Before CL	After CL	
	1523.L3, [I_{peak}]	1899.TL, [I_{peak}]	1914.TL, [I_{peak}]
X	$\sim 10^{-3}$	$< 10^{-4}$	$< 10^{-4}$
Y	$\sim 10^{-2}$	$< 10^{-4}$	$< 10^{-4}$

SUMMARY AND PROSPECTS

We have demonstrated the first beam halo measurements at the European XFEL with mode B collimation optics using the WSs before and after the CL section. In order to cover a large dynamic range, we have used the WSD for beam core measurement and the BLMs for

beam halo measurement. By reconstructing the beam core using the WSD measured beam size, we can set the upper limits of the beam halo levels, which allows us to compare the beam halo level before and after the CL section. According to the comparison, we can conclude that the beam halo is significantly collimated by the collimators. The first measurements show that the horizontal and vertical beam halo are at least factor 10 and 100 less at -10σ after the CL section.

There are several ways to improve the precision and dynamic range of the measurement. Firstly, according to the first measurement results, the position of the WSD and the BLMs can be optimized to enlarge the SNR. Secondly, the WSD pedestal level can be lowered down to enable halo measurement using the WSD by changing the HV on the PMT. Last but not the least, the WS hardware can also be improved. To minimize the BG from other wires, one can kick the beam close to the edge of the vacuum chamber, where the first wire enters. However, it is better to have a single wire system for beam halo measurements. With these improvements, more detailed beam halo collimation study can be carried out to compare different collimation schemes with the simulations. The measured beam halo distributions can be used in the tracking simulations for future implementations with tight aperture requirements (e.g. HXRSS and corrugated structure).

ACKNOWLEDGEMENTS

The authors would like to thank the DESY colleagues: D. Nölle, T. Wamsat, M. Scholz for their help in experiment planning and data taking; O. Hensler for software development; A. Delfs, M. Pelzer, A. Ziegler, V. Gharibyan, H. Tiessen, I. Krouptchenkov for WS design and installation. Thanks to P. Krejcik (SLAC) for helpful discussion.

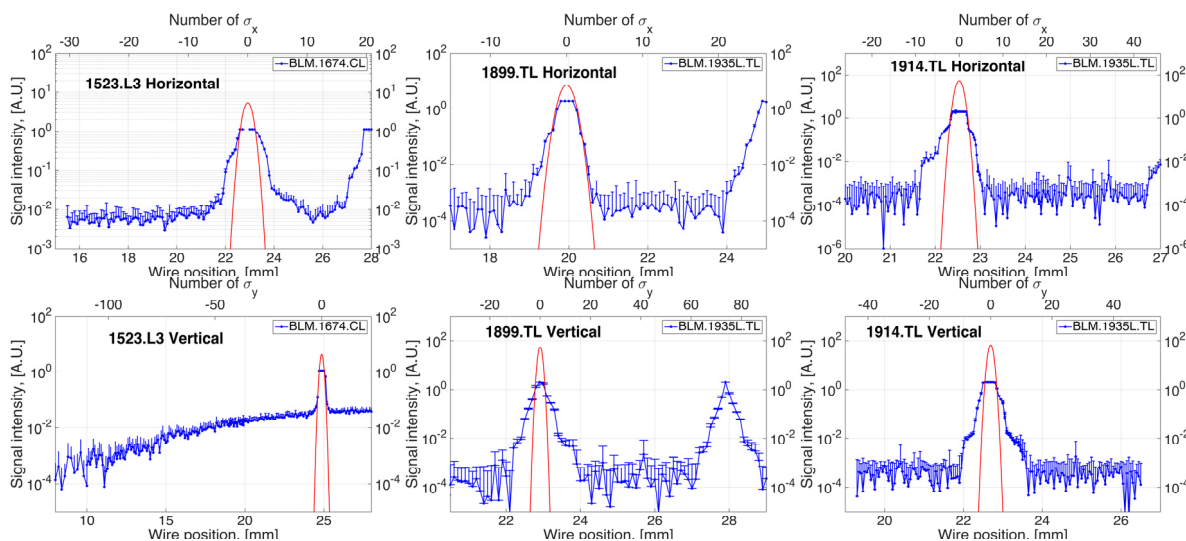


Figure 4: Horizontal (upper) and vertical (lower) beam halo measured using the WSs located before CL at 1523.L3 (left), and after CL at 1899.TL (middle) and 1914.TL (right). The blue line shows the measured distribution by the BLMs (only upper error bar is shown in log scale) and the red line shows the reconstructed Gaussian beam core.

REFERENCES

- [1] M. Altarelli, R. Brinkmann *et al.*, “XFEL: The European X-Ray Free-Electron Laser Technical Design Report”, DESY, Hamburg, Germany, DESY 2006-097, 2006.
- [2] V. Balandin, R. Brinkmann, W. Decking, and N. Golubeva, “Optics Solution for the XFEL Post-Linac Collimation Section”, DESY, Hamburg, Germany, TESLA-FEL Report 2007-05, 2007.
- [3] S. Liu, W. Decking and L. Fröhlich, “Beam Loss Simulations for the Implementation of the Hard X-Ray Self-Seeding System at European XFEL”, in *Proc. 8th Int. Particle Accelerator Conf. (IPAC'17)*, Copenhagen, Denmark, May 2017, paper WEPAB020, pp. 2611-2614.
- [4] N. Takashi, and T. Mitsuhashi, “Beam halo measurement utilizing YAG: Ce screen”, in *Proc. of 4th International Beam Instrumentation Conference IBIC'15*, Melbourne, Australia, Sept. 2015, paper TUPB024, pp.373-376.
- [5] S. Liu *et al.*, “In vacuum diamond sensor scanner for beam halo measurements in the beam line at the KEK Accelerator Test Facility”, *Nucl. Instr. Meth. A*, vol. 832, pp. 231-242, 2016.
- [6] S. Liu *et al.*, “Measurements of beam halo transverse distribution using wire scanners at ATF2” Rep. ATF-14-01, 2014.
- [7] T. Lensch *et al.*, “Wire Scanner Installation into the MicroTCA Environment for the European XFEL”, in *Proc. of IBIC'14*, Monterey, USA, Sept. 2014, paper MOPF13, pp. 73-76.
- [8] C. Wiebers *et al.*, “Scintillating screen monitors for transverse electron beam profile diagnostics at the European XFEL”, in *Proc. of IBIC2013*, Oxford, UK, Sept. 2013, paper WEPF03, pp. 807-810.
- [9] A. Kaukher *et al.*, “XFEL Beam Loss Monitor System”, in *Proc. of BIW 2012*, Virginia, USA, April 2012, paper MOPG007, pp. 35-37.

LONGITUDINAL PHASE SPACE OPTIMIZATION FOR THE HARD X-RAY SELF-SEEDING

S. Liu[†], W. Decking, G. Feng, V. Kocharyan, I. Zagorodnov, DESY, Hamburg, Germany
 G. Geloni, S. Serkez, European XFEL, Schenefeld, Germany

Abstract

For the implementation of Hard X-Ray Self-Seeding (HXRSS) at European XFEL, short electron bunches (FWHM ≤ 50 fs) are preferred to mitigate spatio-temporal coupling effect and to fit to the seeding bump width. Therefore, operations with low charges (< 250 pC) are of interest. Longitudinal phase space optimization has been performed for the 100 pC case by flattening the current distribution. Start-to-end simulations show that, with the optimized distribution, for the photon energy of 14.4 keV, the HXRSS output power, pulse energy and spectral intensity can be increased by a factor of two compared to the nominal working point.

INTRODUCTION

The European XFEL [1] is driven by a superconductive linear accelerator operated with three bunch compressors (see Fig. 1 top) to enable operation with high peak current (~ 5 kA) and low transverse emittance at different charges (20 pC – 1 nC). Since the injector laser pulse length is the same for all the charges, the smaller the charge is, the larger compression is required to keep the same peak current. Different compression scenarios have been studied for the European XFEL to maximize the RF tolerances and minimize collective effects [2-4].

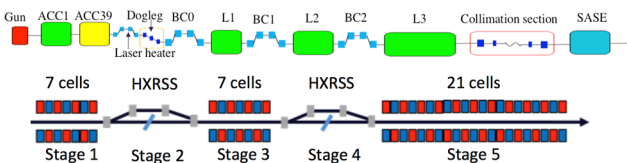


Figure 1: Schematic layout of European XFEL beam line (top) and HXRSS in SASE2 (bottom).

Hard X-ray Self-Seeding (HXRSS) is a well-known scheme to increase the X-ray longitudinal coherence and brightness simultaneously [5]. It has been successfully demonstrated at LCLS in 2012 [6]. The HXRSS at the European XFEL is planned to be implemented in the SASE2 beam line in 2018 (see Fig.1 bottom) [7, 8]. For the implementation of HXRSS at European XFEL, short electron beam bunches (FWHM ≤ 50 fs) are preferred to mitigate spatio-temporal coupling effect [9] and to fit to the seeding bump width. HXRSS simulations have been performed for several cases with different electron beam charges (100 pC and 250 pC) and output photon energies (9 keV-14.4 keV) [10, 11]. In these simulations, the input electron beam distributions used were, however, not fully optimized for self-seeding.

[†] shan.liu@desy.de

One example of the current profile and longitudinal phase space obtained from start to end (S2E) simulation is shown in Fig. 3 (top right, before undulator) for the 100 pC case with the nominal compression parameters. One can see a relatively narrow spike (FWHM ≈ 12 fs) with a peak current of ~ 5 kA. This spike is much more pronounced for lower charges than for higher charges due to the larger compression. Due to this spike, the lower charges suffer more from CSR effects in the bunch compressors, especially in BC2 and in the collimation section, which causes a nonlinear energy distribution along the bunch. The nonlinearity in the longitudinal phase space can seriously deteriorate the HXRSS performance. It results in multi-peaks in the final output power (if tapering is not applied) and in the spreading in photon spectrum. Thus, for the HXRSS, it is preferable to have a “flat top” current distribution, which mitigates the CSR energy loss in the bunch compressors and avoids long head or tails to obtain both higher spectral intensity and pulse energy. In the following sections, we present the study of the longitudinal phase space optimization for the 100-pC case with beam dynamics simulations including HXRSS.

OPTIMIZATION PROCEDURES

At the European XFEL, a third harmonic RF cavity ACC39, which is installed in the injector right after the booster cavity ACC1 (see Fig.1, top), is used to linearize the energy profile and to control the shape of the current profile. The combination of RF parameters of ACC1 and ACC39 defines the 1st derivative p' (chirp), the 2nd derivative p'' (curvature) and the 3rd derivative p''' (skewness) of the momentum p before the first bunch compressor BC0 as follows [3]:

$$\begin{bmatrix} 1 & 0 & 1 & 0 \\ 0 & -k & 0 & -(nk) \\ -k^2 & 0 & -(nk)^2 & 0 \\ 0 & k^3 & 0 & (nk)^3 \end{bmatrix} \cdot \begin{bmatrix} V_{1,1} \cos \phi_{1,1} \\ V_{1,1} \sin \phi_{1,1} \\ V_{1,3} \cos \phi_{1,3} \\ V_{1,3} \sin \phi_{1,3} \end{bmatrix} = \begin{bmatrix} 1 \\ p_0^{(1)} \\ p_0^{(2)} \\ p_0^{(3)} \end{bmatrix} \quad (1)$$

where k is the wave number of the fundamental RF, n is the harmonic number (in our case, $n=3$), $V_{1,1}$, $V_{1,3}$, $\phi_{1,1}$, $\phi_{1,3}$ are the voltage amplitude and phase of fundamental and third harmonic RF, respectively.

The parameter that plays the main role in our optimization is the skewness p''' , since it changes the ratio of compression in different parts of the bunch (i.e. the flatness). After changing p''' , one can adjust the curvature p'' to control the symmetry of the current distribution. Since the goal is to add more compression to the head and tail particles. In the new configuration, we significantly decreased the 3rd derivative p''' from -226.3 to -5.05×10^4 ,

Content from this work may be used under the terms of the CC BY 3.0 licence (© 2018). Any distribution of this work must maintain attribution to the author(s), title of the work, publisher, and DOI.

and the 2nd derivative p'' is changed from 463.05 to 437.06. Figure 2 (top-left) shows the resulting RF sum voltage of A1 and AH1 in comparison with the nominal configuration. In the zoomed plot (Fig. 2 bottom-left), one can see that, the chirp in the center is not changed, however, in the head and tail region, the chirp is increased. This means that the head and tail particles can be compressed more forming a “flat top” current profile.

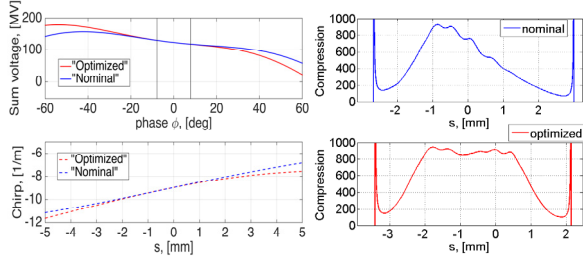


Figure 2: Left: sum voltage of ACC1 and ACC39 (top), the black lines indicate the edge of the bunch and this region is zoomed in (bottom) showing the energy chirp; Right: compression factor along the bunch for the nominal (blue) and the optimized (red) configuration.

The optimized RF parameters are shown in Table 1. Since the compression factor (C) at each stage has been optimized in the design to maximize the RF tolerance [4], in our optimization, we kept the chirp and R56 at the first stage unchanged and modified only slightly the chirp at stage 2 and stage 3 to obtain ~5 kA peak current. The simulation procedure and codes used are the same as presented in Ref. [12]. RF tweak 5 [13] is used for the calculation of RF parameters, which are taken as the initial input for the S2E simulations. A total number of 10⁶ particles have been used in the simulation. Several iterations have been performed and the RF parameters have been adjusted at each iteration until we get the “flat top” current profile with ~5 kA peak current. Figure 2 (right) shows the global compression along the bunch with the nominal and optimized configurations calculated from S2E simulation. Once can see that, in both cases, a maximum compression factor of ~870 is achieved. However,

in the optimized case, the compression is more flat in the bunch center. Similar optimizations have been performed before, for the energy dechirper studies with 250 pC and 500 pC charges [14]. In the next section, we present the optimization results for 100 pC and the HXRSS simulations with the optimized beam profile.

Table 1: The RF Parameters for the Nominal and the Optimized Configurations

	$V_{1,1}$ MV	$\phi_{1,1}$ deg	$V_{1,3}$ MV	$\phi_{1,3}$ deg	P' m^{-1}	P'' m^{-2}	P''' m^{-3}
Nominal	156.7	18.0	25.6	184.1	-8.98	463.05	-226.3
Optimized	173.1	30.9	29.3	211.5	-8.98	437.06	-5.05e4
	V_2 MV	ϕ_2 deg	P_2' m^{-1}	V_3 MV	ϕ_3 deg	P_3' m^{-1}	V_4 MV
Nominal	639.6	27.2	-11.4	1.832e3	21.5	-7.6	1.51e4
Optimized	641.7	27.6	-11.6	1.832e3	21.5	-7.6	1.51e4

OPTIMIZATION RESULTS

Figure 3 shows the comparison of the current distribution and the longitudinal phase space before and after the optimization. Since the main parameter change is in the injector, one can already see the difference in the current profile after BC0. Due to more compression on the head particles, in the optimized case, the current distribution is asymmetric with respect to the reference particle position (at 0 mm) after BC0. However, later on, due to the space charge effect in the linac L1, the distribution becomes more symmetric and more flat after BC1. After BC2, one can see a significant improvement in the compression of the head and the tail particles (4% of the head and tail particles, which are in the over compressed region, are excluded from the particle distributions after BC2 and before the undulator).

Comparing with the nominal profile, the optimized one is more flat in the top and the current FWHM increased from 12 fs to 15 fs. Meanwhile, the distortion in phase space is less pronounced after optimization. However,

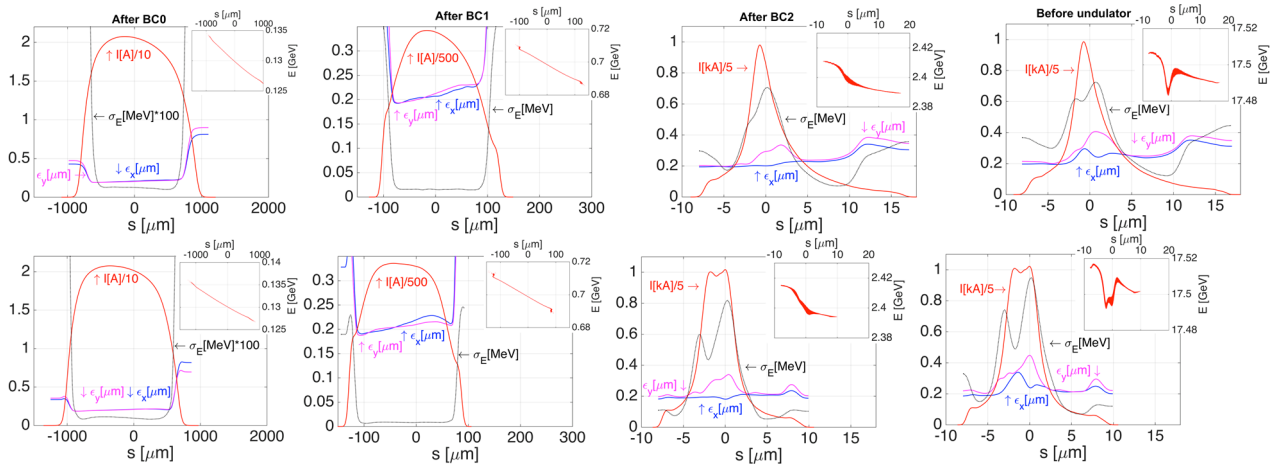


Figure 3: Current distribution, slice emittance and energy spread with longitudinal phase space (up-right plot in each subplot) for 100 pC before (top) and after (bottom) optimization. From left to right: after BC0, BC1, BC2 and before undulator.

since the chirp in the head and the tail is larger than in the beam center (see Fig. 2), a small double-horn structure is formed in the current distribution after BC2 (more tuning in the skewness is required to get rid of the double-horn). The double-horn structure continues to affect the longitudinal phase space, and due to space charge effect in L3 and CSR effect in the collimation section, the longitudinal phase space ended up with a double-valley structure (see Fig. 3, before undulator). However, both the double-horn and the double-valley are not very pronounced and can not affect the HXRSS performance according to the following HXRSS simulations.

HXRSS SIMULATIONS

HXRSS simulations have been performed using OCELOT [15] which relies on GENESIS [16] for SASE calculations. The spatio-temporal coupling effect is included in the simulations. The input beam distributions used are from the S2E simulation as presented in Fig. 3 (before undulator). The simulation is divided into 5 stages, the HXRSS system is located at 2nd and 4th stage (8th and the 16th undulator section) and the other stages are undulator beam lines (see Fig. 1, bottom). Simulations have been performed with the crystal surface C400 for the 14.4 keV photon energy (highest energy of interest for HXRSS).

Figure 4 shows the simulation results for the “nominal” and the “optimized” distributions with and without uniform tapering of the undulator parameter K at stages 3 and 5. Uniform tapering is applied to compensate the large energy losses upstream. Without uniform tapering, the lasing in the peak current slices would be suppressed due to large energy loss and lasing at the neighbouring slices would be enlarged due to smaller energy losses. The K value is therefore scanned for the “nominal” and “optimized” cases separately, and the optimal K is chosen to get maximum pulse energy and spectral density at the end of stage 5. At stage 5, the simulation is performed up to 12 undulator sections (5-m long segments with 1.1-m intersections).

The increment of pulse energy along stage 5 is shown in Fig. 4 (top-left). The reference point for HXRSS performance comparison is taken at the saturation point of the pulse energy (after ~ 9 undulators). The energy and energy spread distribution at the saturation point are shown in Fig. 4 (top-right). As mentioned before, the valley in the phase space, formed by collective effects, became more flat for both the “nominal” and “optimized” configurations after lasing. However, the “optimized” distribution lases in a wider range longitudinally than the “nominal” case since the FWHM of current distribution is larger and the valley in energy distribution is also wider. The radiation power is also higher for “flat top” as shown in Fig. 4 (bottom-left). One can also see that by applying the uniform tapering in stage 3 and stage 5, the radiation power increases of about factor 2 in both cases. Meanwhile, as shown in Fig. 4 (bottom-right), the spectral intensity also increased by factor 2 for the “optimized” case after uniform tapering. However, in the “nominal” case, the spectral density didn’t increase significantly and

a second peak appeared due to the lasing amplified in the region with slightly different energy and smaller energy spread (on the two sides of the peak current).

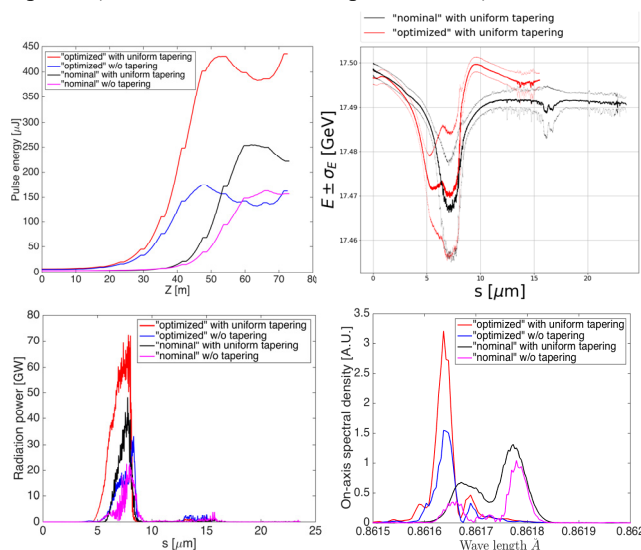


Figure 4: Top-left: pulse energy along the undulator beam line (at stage 5 with 12 undulators); top-right: energy and energy spread distribution at saturation (after 9 undulators); radiation power (bottom-left) and on-axis spectral density (bottom-right) at saturation for the “nominal” and the “optimized” cases with and w/o uniform taper.

SUMMARY AND DISCUSSIONS

We have performed longitudinal phase space optimization for the 100-pC case for the HXRSS application. We added more compression to the head and tail particles by significantly decreasing the 3rd derivative of momentum after the third harmonic RF cavity, which flattened the current distribution. S2E simulations have been performed taking into account the collective effects. The FWHM of current distribution is increased from 12 fs to 15 fs and the total bunch length is decreased from 80 fs to 60 fs. With the flattening of the peak current, the valley in the longitudinal phase space formed by the collective effects also gets wider. By applying a uniform tapering in stage 3 and stage 5 in the HXRSS simulations, the pulse energy, peak power and the spectral density have been increased by factor 2 at the saturation point. Further increase of power and spectral density is expected by applying tapering to the rest of the undulator beam line (12 undulators in our case).

The optimized distribution is particularly interesting for higher photon energy operation (e.g. 14.4 keV), since the higher the photon energy, the longer gain length is required to obtain the seed power required. However, since the RF tolerance for 100 pC operations is much higher than for higher charges [17], an experimental demonstration and stability study for the optimized setup is essential, and will be the subject of further investigations.

ACKNOWLEDGEMENTS

The authors would like to thank B. Beutner, M. Dohlus, M. Scholz and T. Limberg for helpful discussions.

REFERENCES

- [1] M. Altarelli *et al.*, “XFEL: The European X-Ray Free-Electron laser technical design report”, DESY, Hamburg, Germany, DESY 2006-097, 2006.
- [2] G. Feng *et al.* “Beam Dynamics Simulations for European XFEL”, DESY, Hamburg, Germany, TESLA-FEL Report 2013-04, 2013.
- [3] M. Dohlus and T. Limberg, *Proc. IPAC’05*, SLAC, Stanford, p. 250.
- [4] I. Zagorodnov and M. Dohlus, “Semianalytical modeling of multistage bunch compression with collective effects”, *PRST-AB*, vol. 14.1, p. 014403, 2011.
- [5] G. Geloni, V. Kocharyan and E. Saldin, “A novel self-seeding scheme for hard X-ray FELs”, *Journal of Modern Optics*, 58(16), pp.1391-1403, 2011.
- [6] J. Amann *et al.*, “Demonstration of self-seeding in a hard-X-ray free-electron laser”, *Nature Photonics*, 6 (10), pp. 693-698, 2012.
- [7] G. Geloni, V. Kocharyan and E. Saldin, “A Cascade self-seeding scheme with wake monochromator for narrow-bandwidth X-ray FELs”, DESY, Hamburg, Germany, DESY 10-080, June 2010.
- [8] X. Dong *et al.*, “Status of the Hard X-ray Self-seeding project at the European XFEL”, presented at FEL’17, MOP008.
- [9] R. R. Lindberg and Y. V. Shvyd’ko, “Time dependence of Bragg forward scattering and self-seeding of hard x-ray free-electron lasers”, *PRST-AB*, vol. 15(5), p. 050706, 2012.
- [10] G. Geloni, V. Kocharyan and E. Saldin, “Scheme to increase the output average spectral flux of the European XFEL at 14.4 keV”, DESY, Hamburg, Germany, DESY 15-141, August 2015.
- [11] O. Chubar *et al.*, “Ultra-high-resolution inelastic X-ray scattering at high-repetition-rate self-seeded X-ray free-electron lasers”, *Journal of Synchrotron Radiation*, vol. 23.2, pp. 410-424, 2016.
- [12] I. Zagorodnov, G. Feng and T. Limberg, “Corrugated structure insertion for extending the SASE bandwidth up to 3% at the European XFEL”, *Nucl. Instr. Meth. A*, vol. 837, pp. 69-79, 2016.
- [13] B. Beutner, “RF Tweak 5 Tool for FLASH and XFEL. RF Tweak 5 Tool for FLASH and XFEL”, FEL Seminar, DESY, Hamburg, Germany, Feb. 2015.
- [14] G. Feng, “Beam Energy Dechirping Study for EXFEL”, Beam Dynamics Group Meeting, DESY, Hamburg, Germany, Nov. 2015, http://www.desy.de/fel-beam/s2e/talks/2015_11_16/feng.pdf
- [15] I. Agapov *et al.*, “OCELOT: A software framework for synchrotron light source and FEL studies”, *Nucl. Instr. Meth. A*, vol. 768, pp. 151-156, 2014.
- [16] G. Reiche, “GENESIS 1.3: a fully 3D time-dependent FEL simulation code”, *Nucl. Instr. Meth. A*, vol. 429.1, pp. 243-248, 1999.
- [17] I. Zagorodnov, “Ultra-short low charge operation at FLASH and the European XFEL”, *Proc. FEL’10*, Malmö, Sweden.

STUDIES OF THE TRANSVERSE BEAM COUPLING IN THE EUROPEAN XFEL INJECTOR

M. Scholz*, B. Beutner, DESY, Hamburg, Germany

Abstract

Coupling between the transverse planes leads to an increase of the horizontal and vertical electron beam emittances. The coupling can be measured with dedicated multi quadrupole scans while the correlations of the beam are observed on a screen. In this paper we show the results from first coupling studies in the European XFEL injector.

INTRODUCTION

SASE FELs like the European XFEL [1] depend strongly on the emittance, thus it is significant to investigate and optimize this parameter. Earlier multi quad scans revealed hints for transverse coupling of the electron beam thus we started further investigations. The technique how to measure the coupling between the transverse planes with multi quadrupole scans was e. g. demonstrated at the SwissFEL Injector Test Facility (SITF) [2]. This method was also used for the coupling measurements in the injector. Additional information can be found in [3]. In this paper, we present measurements of the transverse coupling in the European XFEL injector.

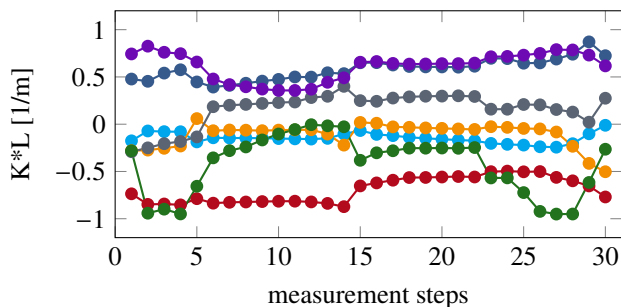


Figure 1: Normalized integrated strength of all quadrupole magnets used for the scan.

EUROPEAN XFEL INJECTOR

A schematic layout of the European XFEL injector is presented in Fig. 4. Two superconducting accelerating modules are installed in the linac, a 1.3 GHz module and the third harmonic module, which operates with 3.9 GHz, to linearize the longitudinal phase space of the particle distributions. The design beam energy downstream these modules is 130 MeV. A subsequent diagnostic section including a transverse deflecting cavity as well as four screens [4] and a spectrometer allow to study the electron beam quality. All quads in the diagnostics section are equipped with individual bipolar power supplies.

* matthias.scholz@desy.de

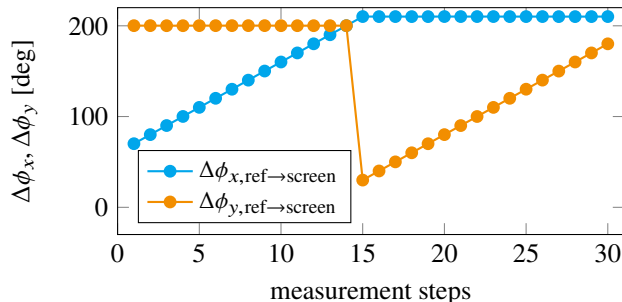


Figure 2: Phase advances in horizontal and vertical plane between optics reference position and the screen plotted for all scan steps.

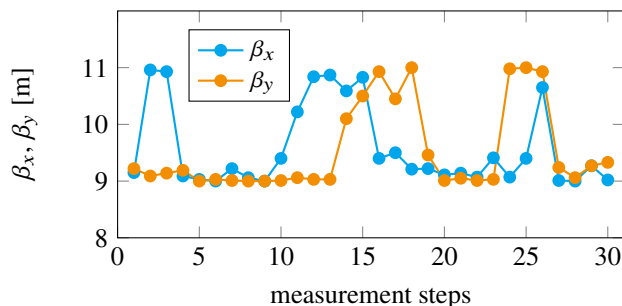


Figure 3: Horizontal and vertical beta functions at the screen for all steps of the phase scan.

MULTI-QUADRUPOLE SCANS

The basic requirements on the quad scan for these measurements is to scan the phase advance between the optics reference position and the measurement screen in one plane over 180 degree (if possible) and keep it constant in the second one. Then the second plane has to be scanned while phase advance in the first plane is constant. In addition, the beam sizes should be kept preferably constant on the screen in order to ensure the same resolution for all measurement steps. A list with $k \times n$ entries of quadrupole strengths, fulfilling the described requirements mentioned above, has to be prepared. The number of measurement steps is k , here $k = 30$, and the number of quads is n , here $n = 7$. All k quadrupole settings are then applied one by one to the machine. For each setting, the transverse particle distribution at the measurement screen is saved for evaluation. For the quad scan discussed in this paper, all 7 quadrupole magnets between the laser heater chicane and the last screen in the diagnostics section were used. Figure 1 shows the integrated strengths of all seven quads and for all 30 measurement steps. The phases advances of the quad scan are shown in Fig. 2.

Content from this work may be used under the terms of the CC BY 3.0 licence (© 2018). Any distribution of this work must maintain attribution to the author(s), title of the work, publisher, and DOI.

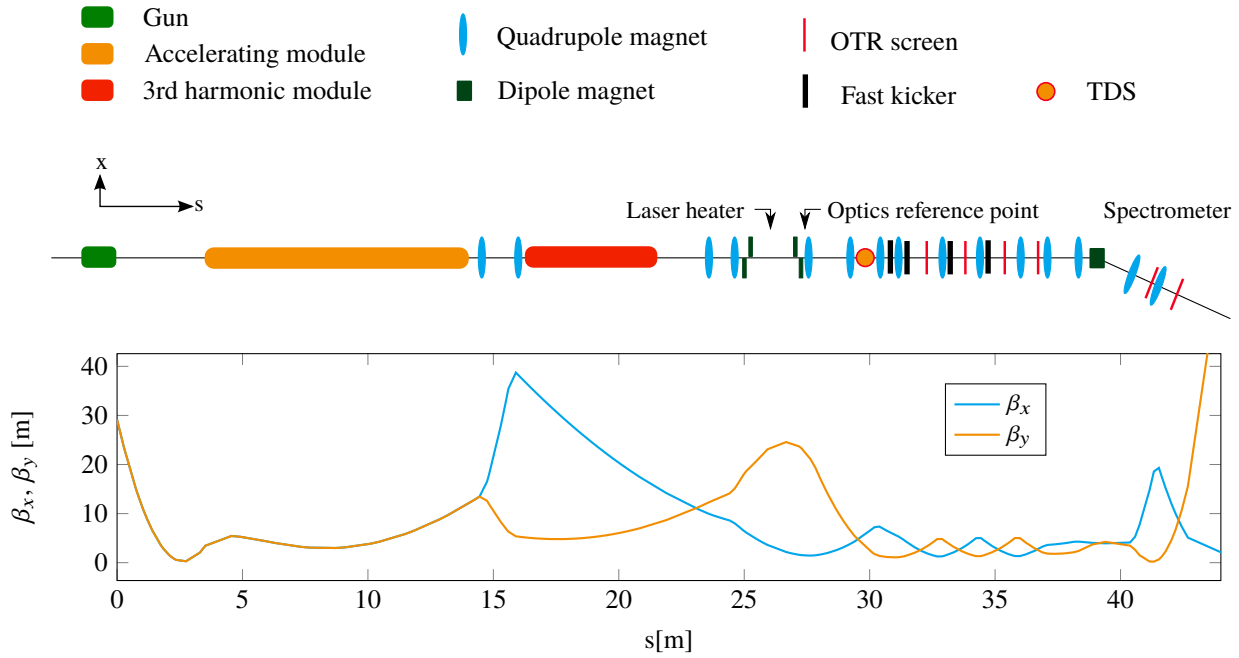


Figure 4: The default beta functions in the XFEL injector starting at the photo cathode and ending in the injector dump. Above the plot one can find a schematic layout of the XFEL injector. The last screen in the diagnostics section upstream the spectrometer dipole was the measurement position. All quadrupole magnets between the laser heater and the measurement screen were used for the scan of the phase advances.

It shows the data for both planes and for all 30 measurement steps. The large number of quads gives enough flexibility to keep the beta function on the screen almost constant during the scan as it is shown in Fig. 3.

EVALUATION METHOD

The 4D beam matrix σ^{4D} describes the full transverse distribution of the beam [2, 3]:

$$\sigma^{4D} = \begin{pmatrix} \langle x^2 \rangle & \langle xx' \rangle & \langle xy \rangle & \langle xy' \rangle \\ \langle xx' \rangle & \langle x'^2 \rangle & \langle x'y \rangle & \langle x'y' \rangle \\ \langle xy \rangle & \langle x'y \rangle & \langle y^2 \rangle & \langle yy' \rangle \\ \langle xy' \rangle & \langle x'y' \rangle & \langle yy' \rangle & \langle y'^2 \rangle \end{pmatrix}. \quad (1)$$

The horizontal plane is described with x and x' , the vertical plane respectively with y and y' . All mixed matrix elements describe the transverse coupling of the beam.

The particle distribution at a position s can be calculated from the starting distribution at position s_0 with the transport matrix $R_{s \rightarrow s_0}$,

$$\sigma_s^{4D} = R_{s \rightarrow s_0} \sigma_{s_0}^{4D} R_{s \rightarrow s_0}^T \quad (2)$$

Thus $\langle x^2 \rangle_{k,s}$, $\langle y^2 \rangle_{k,s}$ and $\langle xy \rangle_{k,s}$ can be described as follows:

$$\begin{aligned} \langle x^2 \rangle_{k,s} &= R_{k,11}^2 \langle x^2 \rangle_{s_0} + R_{k,12}^2 \langle x'^2 \rangle_{s_0} + 2R_{k,11}^k R_{k,12}^k \langle xx' \rangle_{s_0} \\ \langle y^2 \rangle_{k,s} &= R_{k,33}^2 \langle y^2 \rangle_{s_0} + R_{k,34}^2 \langle y'^2 \rangle_{s_0} + 2R_{k,33}^k R_{k,34}^k \langle yy' \rangle_{s_0} \\ \langle xy \rangle_{k,s} &= R_{k,11} R_{k,33} \langle xy \rangle_{s_0} + R_{k,12} R_{k,33} \langle x'y \rangle_{s_0} \\ &\quad + R_{k,11} R_{k,34} \langle xy' \rangle_{s_0} + R_{k,12} R_{k,34} \langle x'y' \rangle_{s_0} \end{aligned}$$

where $R_{k,ij}$ is the ij -element of the transfer matrix $R_{s \rightarrow s_0}$ for the k^{th} measurement step.

The same parameters can be obtained from the measurements data as follows:

$$\langle uv \rangle_{k,s} = \frac{\sum v_i w_i q_{s,k,i}}{\sum q_{s,k,i}} \quad (3)$$

with u and v referring either to x or y . The sum is taken over all pixels i and $q_{s,k,i}$ is the intensity of the respective pixel as measured at the screen (position s and measurement step k). A noise cut procedure [5] was used before the picture evaluation in order to reduce impact from beam halo. The beam moments at position s_0 can then be obtained fitting the data of the $k=30$ different measurements of the quad scan.

All scripts for these measurements and data reconstruction were tested with simulations. We were able to reconstruct the coupling terms from various simulated initial particle distributions using the same transfer matrices as for the quad scan in the injector.

MEASUREMENTS AND EVALUATION

Quadrupole scans as described above were carried out with a beam of 500 pC bunch charge and 130 MeV beam energy. Ten data sets were taken for each setup. For each measurement step one exemplary beam spot taken on the screen is shown in Fig. 5. Figure 6 shows the horizontal and vertical beam sizes ($\langle x^2 \rangle_{k,s}^{1/2}$ and $\langle y^2 \rangle_{k,s}^{1/2}$) as measured. The data shown in Fig. 7 shows the coupling term $\langle xy \rangle_{k,s}$ for each measurement step. All reconstructed parameters like

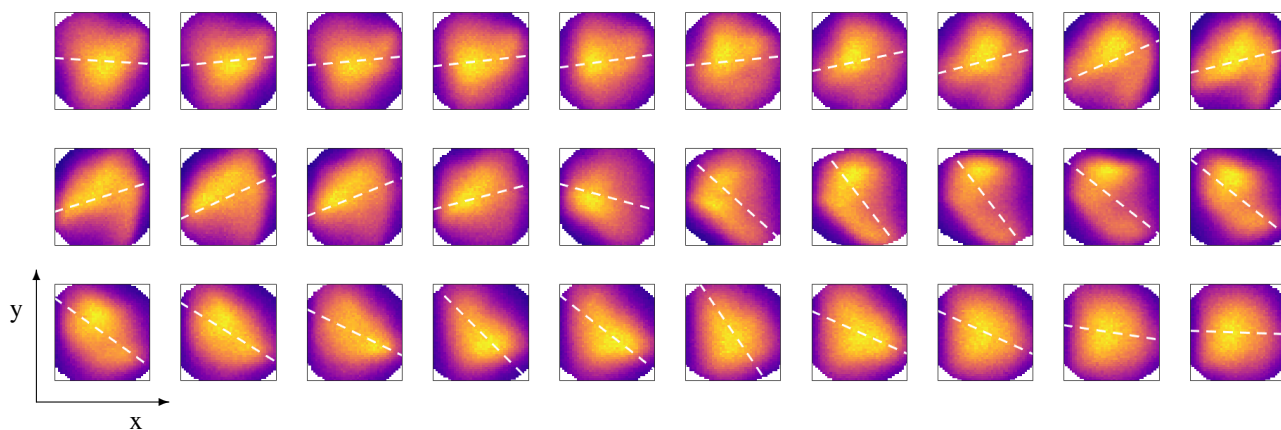


Figure 5: Beam spots on the screen for all 30 steps of the measurement. The first one is shown top left, the last one bottom right. The dashed lines show the detected slope of the correlation between horizontal and vertical plane.

the emittances as well as the coupling parameters $\langle xy \rangle_{s_0}$, $\langle x'y \rangle_{s_0}$, $\langle xy' \rangle_{s_0}$ and $\langle x'y' \rangle_{s_0}$ can be found in Table 1.

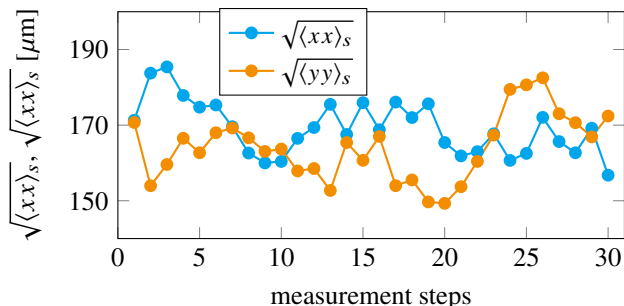


Figure 6: Horizontal and vertical beam sizes at the screen for all steps of the measurement.

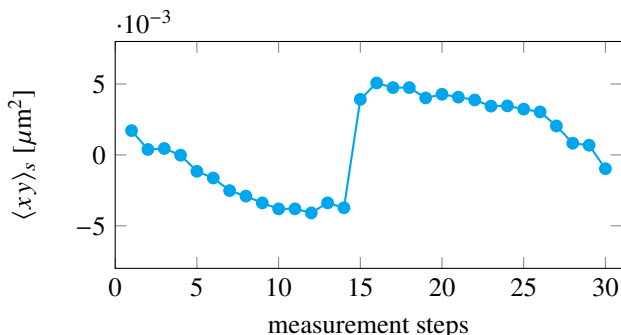


Figure 7: The coupling parameter $\langle xy \rangle_s$ for all measurement steps.

CONCLUSIONS

We established a method to measure the transverse beam coupling between x and y plane for the injector of the European XFEL. First measurements and evaluations could be carried out. Recently installed quadrupole and skew-quadrupole magnets on the main solenoid of the electron

Table 1: Reconstructed Parameters

ϵ_x	=	0.77 mm mrad
ϵ_y	=	0.71 mm mrad
$\langle xy \rangle_{s_0}$	=	$51.14 \cdot 10^{-9} \text{ m}^2$
$\langle x'y \rangle_{s_0}$	=	$-52.26 \cdot 10^{-9} \text{ m}$
$\langle xy' \rangle_{s_0}$	=	$-11.57 \cdot 10^{-9} \text{ m}$
$\langle x'y' \rangle_{s_0}$	=	$11.51 \cdot 10^{-9}$

gun can be used to change the transverse coupling of the beam [6]. Future measurement can then be used to minimize those effects.

ACKNOWLEDGMENT

We like to thank all colleagues who have been involved in the construction, building and commissioning of the European XFEL.

REFERENCES

- [1] M. Altarelli *et al.*, “The European X-Ray Free-Electron Laser, Technical design report”, DESY 2006-097 July 2007.
- [2] E. Prat and M. Aiba, “Four-dimensional transverse beam matrix measurement using the multiple-quadrupole scan technique”, *Physical Review Special Topics - Accelerators and Beams* 17, 052801, 2014.
- [3] F. Löhl, “Measurement of the transverse emittance at the VUV-FEL”, *TESLA-FEL* 2005-03, 2005.
- [4] Ch. Wiebers *et al.*, “Scintillating screen monitors for the transverse electron beam profile diagnostics at the European XFEL”, WEPF03, in *Proceedings of IBIC'13*, Oxford, UK, 2013.
- [5] B. Beutner and E. Prat, “Considerations about optics-based phase-space measurements at linac-based FEL facilities”, in *Proceedings of FEL'11*, TUPA18, 2011.
- [6] M. Krasilnikov *et al.*, “Electron beam asymmetry compensation with gun quadrupoles at PITZ”, presented at FEL'17, WEP007, 2017.

THE EFFECT OF TRANSVERSE SPACE CHARGE ON BEAM EVOLUTION AND PHOTON COHERENCE

Q. Marksteiner, Los Alamos National Laboratory, Los Alamos, USA

Abstract

An electron beam experiences a transverse electric field which tests to act like a defocusing force on the beam. This defocusing force will act with different strengths at different locations in the electron beam because the current varies along the beam. A single, quasi-analytic method is presented to calculate the impact of this force on beam projected emittance.

INTRODUCTION

The effect of transverse space charge on the transverse emittance of the beam in the MaRIE [1] accelerator is estimated. The dominant effect of transverse space charge is that it causes an extra defocusing term in the electron beam transverse evolution. This defocusing is different at different locations along the electron beam, because electron current is different at different locations of the beam. This will cause the beam to go through different betatron oscillations along the accelerator, which will increase the projected emittance.

THE MaRIE ACCELERATOR

Figure 1 shows a schematic of the MaRIE accelerator [2]. The accelerator consists of three accelerator sections, L1, L2, and L3, with two bunch compressors, BC1 and BC2. The initial current after the photocathode is 15 A. After BC1, the current is compressed to 150 A, and after BC2, the current is compressed to 3 kA. The final energy of the electron beam is 12 GeV. The accelerating gradients of the three sections are all slightly different, with the accelerating gradient in L2 being much lower than the accelerating gradient in the other two accelerator sections. The gradient in L2 is lower because the beam is accelerating off crest in order to provide a chirp for the BC2 bunch compressor.

The effect of the transverse space charge decreases as the beam accelerates, but increases with current. Because of this, the effect of the transverse space charge is strongest right after the bunch compressors.

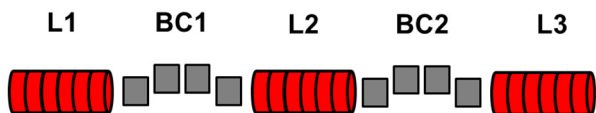


Figure 1: A simple schematic of the MaRIE accelerator.

EQUATIONS OF MOTIONS

Beam Evolution

In order to examine the effect of transverse space charge, we must first look at the transverse dynamics of a single

electron that is being accelerated at a constant rate. The time derivative of the radial component of an electron under the force of a radial electric field is given by $d/dt(\gamma m \dot{r}) = (eE_{r,l})/\gamma^2$. Here \dot{r} is the time derivative of the electron's radial coordinate, $E_{r,l}$ is the radial field, as described in the lab frame of reference, and γ is the relativistic factor.

For a long bunch ($\gamma l \gg a$) with a constant radial current density, given in the lab frame by $\rho_l(z)$ (z is the location along the electron bunch) we can estimate the radial electric field using Gauss's law. Then we have

$$d/dt(\gamma m \dot{r}) = e r \rho_l(z) / (2\epsilon_0 \gamma^2).$$

Next, we expand out the derivative, replace \dot{r} with $\beta c r'$, substitute in the Alven current $I_A = (4\pi\epsilon_0 m c^3)/e$, replace the current density with the total line current ($\rho_l(z) = I(z)/(\pi R^2 \beta c)$), and rearrange to get:

$$r'' = \frac{2 I(z)}{\beta^3 \gamma^3 R^2 I_A} r - \frac{\gamma'}{\gamma} r'. \quad (1)$$

Equation (1) describes the motion of a single electron under acceleration, with no external focusing. We next want to solve for the evolution of the rms value of the radius of the electron beam: $R^2 = \langle r^2 \rangle$, when the electron beam is under constant acceleration. We use the radial envelope equation (3):

$$R'' = \frac{\langle r r'' \rangle}{R} + \frac{\epsilon_r^2}{R^3}. \quad (2)$$

Next, we solve for $\langle r r'' \rangle$. Using equation 1, we get:

$$\langle r r'' \rangle = \frac{2 I(z)}{\beta^3 \gamma^3 I_A} - \frac{\gamma'}{\gamma} R R'. \quad (3)$$

Then we can use the approximation that the normalized slice emittance remains constant in an accelerator: $\epsilon_n = \gamma \epsilon$. Plugging this and equation (3) into equation (2) gives:

$$R'' = \frac{2 I(z)}{I_A} \frac{1}{R \beta(s)^3 \gamma(s)^3} - \frac{\gamma'(s)}{\gamma(s)} R' + \frac{\epsilon_{nr}^2}{\gamma(s)^2 R^3}. \quad (4)$$

Here s represents the distance along the accelerator. Equation (4) can be used to calculate the evolution of electron beams with different values of electron current $I(z)$.

Beam Evolution

In this paper, we analyse the evolution of the transverse size of the electron beam at different locations of the electron beam. We assume that the electron current profile is a Gaussian, given by $I(z) = I_0 \exp(-z^2/(2\sigma^2))$.

Content from this work may be used under the terms of the CC BY 3.0 licence (© 2018). Any distribution of this work must maintain attribution to the author(s), title of the work, publisher, and DOI.

A MATLAB [4] code was written to solve equation (4) in order to calculate the evolution of the electron beams rms size for different values of $I(z)$. Figures 2-4 show various solutions of equation (4) with different starting and accelerator parameters (see IV).

By solving $R[I(z)]$ up to the point at the end of an accelerator section, the growth in electron beam projected emittance can be calculated in terms of $R(z)$ and $R'(z)$. Figures 5-7 show plots that include both the beam current, and the final values of $R(z)$ and $R'(z)$ at the end of one of the accelerator sections, calculated using equation (4).

The projected emittance is defined as:

$$\epsilon_p = \sqrt{\langle r^2 \rangle_p \langle (r')^2 \rangle_p - \langle rr' \rangle_p^2} \quad (5)$$

The projected values $\langle r^2 \rangle_p$ and $\langle rr' \rangle_p^2$ can easily be calculated using once $R(z)$ and $R'(z)$ are known:

$$\langle r^2 \rangle_p = \frac{\int I(z)R^2(z)dz}{\int I(z)dz} \quad (6)$$

$$\langle rr' \rangle_p^2 = \frac{\int I(z)R(z)R'(z)dz}{\int I(z)dz} \quad (7)$$

In order to calculate $\langle (r')^2 \rangle_p$, the slice value $\langle (r')^2 \rangle_s$ must first be calculated:

$$\langle (r')^2 \rangle_s = \frac{\epsilon_r^2 + (RR')^2}{R^2} \quad (8)$$

Then the projected $\langle (r')^2 \rangle_p$ is just:

$$\langle (r')^2 \rangle_p = \frac{\int I(z)\langle (r')^2 \rangle_s dz}{\int I(z)dz} \quad (9)$$

In order to calculate emittance, equations (7-9) are integrated down to the point where the electron current has decreased to 1/3 of the peak current. This is done in order to make the emittance calculate relevant for free electron lasers [5], where there is little photon generation at low electron currents.

RESULTS

We analyse the evolution of the electron beam after BC1 and BC2, to look for an increase in the projected emittance due to transverse space charge. The electron beam is assumed to emerge from each chicane at a waist, with a projected and a slice emittance of $\epsilon_x = \epsilon_y = 0.2 \mu\text{m}$.

Emittance Growth in L2

Figures 2 and 3 show the evolution of R and R' for an electron beam slice with different values of current in L2, for an electron beam with a starting R of $100 \mu\text{m}$. Figure 4 shows the current profile of the electron beam in and the final values of R at different locations of the beam. Figure 5 shows the current profile and the final values of R' .

The final projected emittance at the end of L2 is $\epsilon_x = \epsilon_y = 0.220 \mu\text{m}$ when the initial rms size coming out of BC1 is $100 \mu\text{m}$, and is $0.285 \mu\text{m}$ when the initial rms size is 1mm . The emittance increase can be decreased by making the beam small coming out of the bunch compressor.

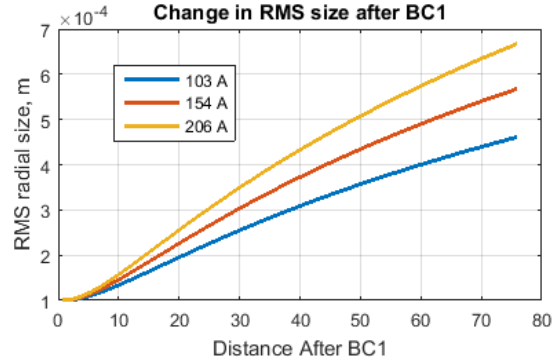


Figure 2: The evolution of rms beam size R in L2 for different slice current values.

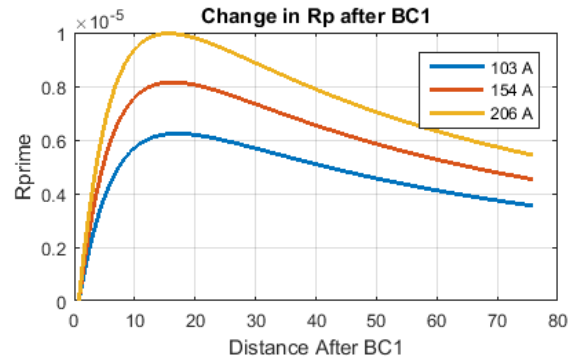


Figure 3: The evolution of R' in L2 for different slice current values.

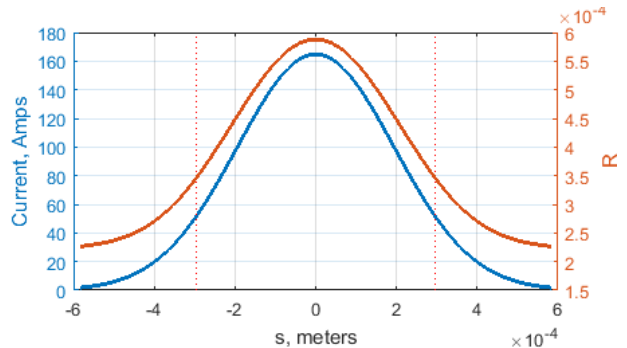


Figure 4: The beam current profile (blue, left), and the final values of R at the end of L2 (red, right), for a beam with initial rms size of $100 \mu\text{m}$.

Content from this work may be used under the terms of the CC BY 3.0 licence (© 2018). Any distribution of this work must maintain attribution to the author(s), title of the work, publisher, and DOI.

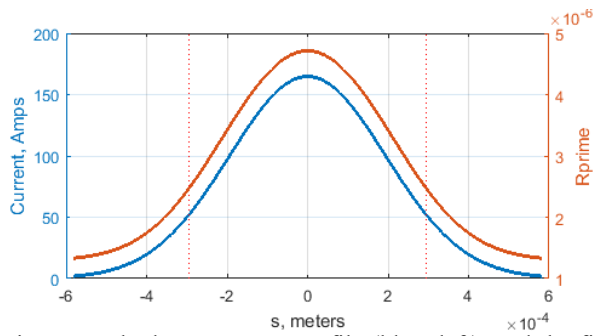


Figure 5: The beam current profile (blue, left), and the final values of R' at the end of L2 (red, right), for a beam with initial rms size of $100 \mu\text{m}$.

Emittance Growth in L3

Figures 6 and 7 show the evolution of R and R' for an electron beam slice with different values of current in L3, for an electron beam with a starting R of $100 \mu\text{m}$. Figure 8 shows the current profile of the electron beam in L3, and the final values of R at different locations of the beam. Figure 9 shows the current profile and the final values of R' .

The final projected emittance at the end of L2 is $\epsilon_x = \epsilon_y = 0.255 \mu\text{m}$ when the initial rms size coming out of BC1 is $100 \mu\text{m}$, and is $0.405 \mu\text{m}$ when the initial rms size is 1 mm . The emittance increase is more dramatic in L3 than in L2.

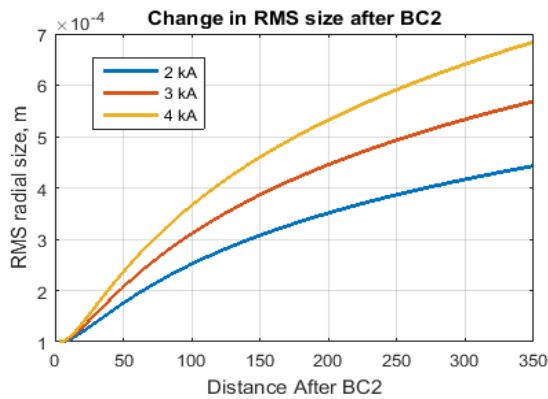


Figure 6: The evolution of rms beam size R in L3 for different slice current values.

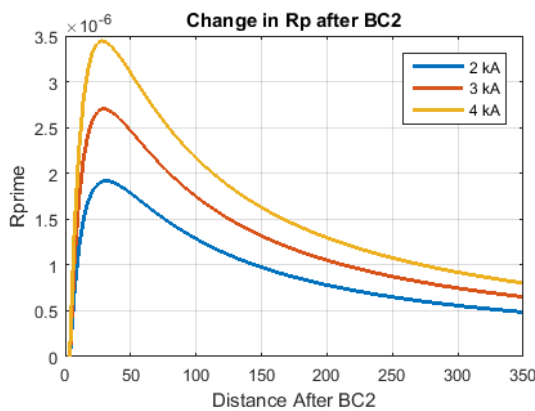


Figure 7: The evolution of R' in L3 for different slice current values.

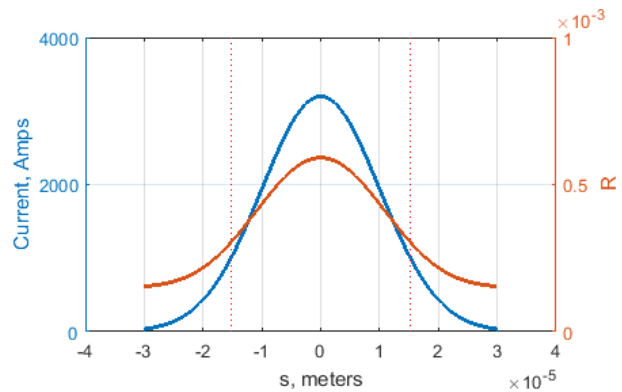


Figure 8: The beam current profile (blue, left), and the final values of R at the end of L3 (red, right), for a beam with initial rms size of $100 \mu\text{m}$.

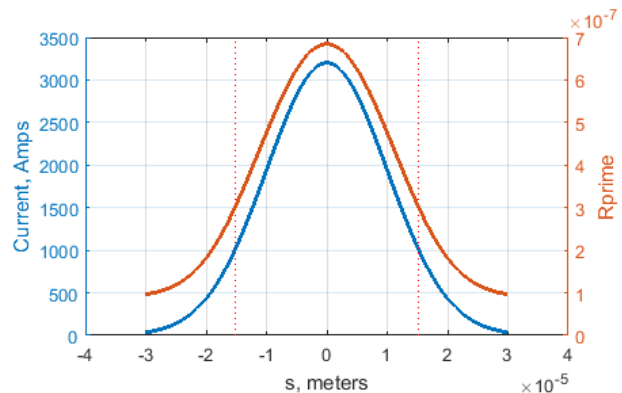


Figure 9: The beam current profile (blue, left), and the final values of R' at the end of L2 (red, right), for a beam with initial rms size of $100 \mu\text{m}$.

CONCLUSION

Modest increases in the projected emittance were found in both L2 and L3 as a results of transverse space charge. This effect can be reduced by making the electron beam have a smaller transverse size at the locations of the chicanes. The increase in projected emittance was greater in the final stage of the accelerator, L3, than in the central stage.

ACKNOWLEDGMENT

I gratefully acknowledge the United States Department of Energy for funding this research.

REFERENCES

- [1] LANL online MaRIE reference: <http://www.lanl.gov/science-innovation/science-facilities/marie/>.
- [2] J. W. Lewellen, private communication, 2015.
- [3] B. E. Carlsten, USPAS notes, unpublished.
- [4] MATLAB Release 2012B, The MathWorks, Inc. Natick, Massachusetts, United States
- [5] P. Emma, *et al.* "First lasing and operation of an angstrom-wavelength free-electron laser." *Nature Photonics* 4, p. 641-647, 2010.

DOUBLE-BUNCHES FOR TWO-COLOR SOFT X-RAY FREE-ELECTRON LASER AT THE MAX IV LABORATORY

J. Björklund Svensson*, O. Lundh, Department of Physics, Lund University, Sweden
J. Andersson, F. Curbis, M. Kotur, F. Lindau, E. Mansten,
S. Thorin, S. Werin, MAX IV Laboratory, Lund, Sweden

Abstract

The ability to generate two-color free-electron laser (FEL) radiation enables a wider range of user experiments than just single-color FEL radiation. There are different schemes for generating the two colors, the original being to use a single bunch and two sets of undulators with different K-parameters. An alternative scheme was recently shown, where two separate bunches in the same RF bucket are used for lasing at different wavelengths in a single set of undulators. We here investigate the feasibility of accelerating and compressing a double-bunch time structure generated in the photocathode electron gun for subsequent use in a soft X-ray FEL at the MAX IV Laboratory.

INTRODUCTION

The MAX IV Linear Accelerator \mathbb{T} is a warm S-band electron accelerator serving as full-energy injector for the 1.5 and 3 GeV storage rings [2] as well as the Short Pulse Facility (SPF) [3], where the electron bunches are compressed to 100 fs at an emittance of $\lesssim 1$ mm mrad and a bunch charge of 100 pC. A compact overview of the linac is shown in Fig. 1. The layout of the MAX IV facility is such that the SPF houses three available slots, located downstream of the transfer line to the 3 GeV storage ring. The end of the linac, from the second bunch compressor and downstream, is shown in Fig. 2, with the existing sections and possible extensions on white and orange background, respectively. Simulations indicate that it is possible to compress the bunches to well below 100 fs and still keep the emittance low [4].

The Soft X-ray Laser (SXL) project, currently in the early conceptual design phase, is a collaboration between many Swedish research groups with experience from both user and accelerator sides [5]. The idea is to use one of the SPF beamlines to house a soft X-ray free-electron laser (FEL) operating in the 0.25-1 keV energy range at pulse lengths below 100 fs, paired with unique pumping, detection and imaging schemes. Strong scientific interest has also been expressed towards a two-color radiation operation mode.

Two-color FEL radiation pulses are a way of extending the experimental range at an FEL by producing two radiation pulses with a certain variable separation in energy and time. The original implementation [6] of the concept for X-rays used a single electron bunch and two differently tuned undulator sections to achieve lasing at two different wavelengths, while a more recent development [7, 8] uses two electron bunches, accelerated in the same RF period, and only one

undulator section. Benefits of using the double-bunch technique include allowing both colors to reach saturation intensity and a simpler undulator setup. Double electron bunches can be obtained in a few different ways, but we will focus on generation by tailored laser pulses in the photo-cathode electron gun.

Generating the double-bunch time structure in the photocathode gun at MAX IV would require some additional work on the laser system [9, 10], but no further addition to the accelerator or lattice seems necessary, potentially making this technique a cost-effective extension of the operational capabilities of the SPF. Because of the layout of the facility, see Fig. 2, this could synergetically enable experiments on beam-driven plasma-wakefield acceleration (PWFA) [11]. We have used the particle tracking code `elegant` [12] to simulate the acceleration and compression of a double-bunch beam in the MAX IV Linear Accelerator.

BUNCH COMPRESSION

Compression and Linearization

To compress the bunches longitudinally, the MAX IV linac employs two double achromat compressors, see e.g. [4], which have a positive first-order momentum compaction, R_{56} . This means that a positive chirp, with respect to longitudinal coordinate z , is required for compression. This is achieved with a positive off-crest phase in the RF voltage. The naturally positive second-order momentum compaction, T_{566} , has been optimized with sextupoles in such a way that it cancels out the longitudinal phase-space curvature imposed by the RF field. This means that the phase space linearization is done using the optics alone; no higher-order harmonic cavity is employed. This compressor scheme is simple, reliable and economical.

One effect of this compression scheme is that the first bunch, which arrives closer to the peak of the RF voltage, will in many cases obtain a smaller (and less linear) chirp than the second bunch, particularly in the first linac section, L0-L1b (see Figure 1). This can lead to weaker compression of the first bunch, yielding a beam where the second bunch is shorter than the first. The second bunch curvature can also become over-compensated, leading to asymmetric compression. Part of the tuning process involves minimizing these effects.

Wakefields and Coherent Synchrotron Radiation

Short-range geometric longitudinal wakefields can influence the bunch chirp in the linac [13]. The effects of these wakefields increase with both bunch charge and degree of

* jonas.bjorklund@fysik.lth.se

Content from this work may be used under the terms of the CC BY 3.0 licence (© 2018). Any distribution of this work must maintain attribution to the author(s), title of the work, publisher, and DOI.

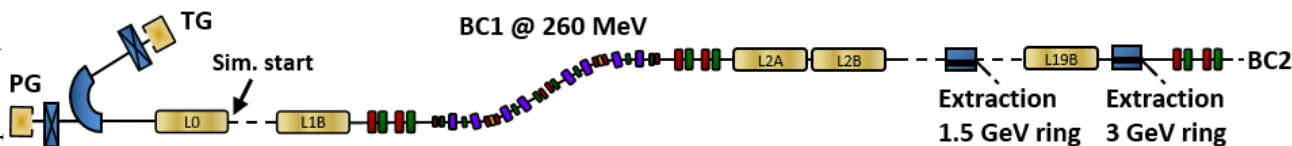


Figure 1: Compact layout of the MAX IV Linac. Yellow denotes radiofrequency (RF) structures, red/green are focusing/defocusing quadrupole magnets, purple are dipole magnets, orange are sextupole magnets and blue are special magnets. PG and TG are photo-cathode and thermionic RF guns, respectively, L are the linac sections and BC1 is the first bunch compressor. This view is cut right before BC2, which is shown in Fig. 2.

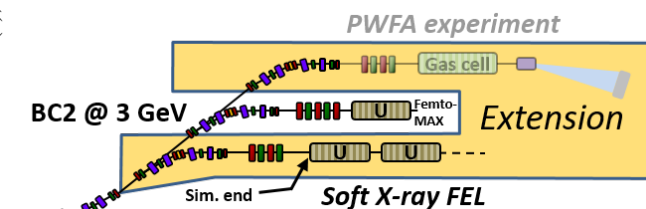


Figure 2: End of the linac and SPF (see Fig. 1) with the 3 possible beamlines, of which FemtoMAX is the only existing to date. U denotes undulator. Possible extensions are within the orange field.

compression. Since the energy chirp is positive with respect to z , and the wakefields cause a progressive decrease in particle energy going backwards in the bunch, the total energy chirp of the bunches increases, which leads to a stronger compression. This was studied in Refs. [14, 15] for single bunches in the MAX IV linac.

Also of concern is coherent synchrotron radiation (CSR), where the bunch irradiates itself with coherent low-frequency radiation, leading to an emittance growth in the compressors. Typically, the tail of the bunch irradiates the head of the bunch, but in the case of two bunches with short length and separation, there is also a risk that the second bunch could irradiate the first bunch.

SIMULATION RESULTS

Tracking of the particles is done from after the pre-injector [16], see Fig. 1, to after a preliminary matching section constructed with 4 quadrupoles, see Fig. 2, using *elegant*, with both wakefields and CSR enabled and 250k particles per bunch. A preliminary double-bunch structure is created using Gaussian distributions for the transverse sizes and divergences, while it is parabolic in time (Beta distribution with shape parameters $\alpha = \beta = 2$) with longitudinal momentum coordinates accounting for different longitudinal phase space curvature of the bunches. The results presented here are found with initial bunch lengths of 2.7 ps full width at half-maximum (FWHM), separation of 4 ps peak-to-peak and with the first bunch 10 degrees off-crest out from the pre-injector, see Fig. 3a. The normalized emittance is 0.3 mm mrad in both directions and for both bunches and they are set to contain 50 pC each.

The main variables for controlling the final time structure are the RF phases in the linac. The phase in the first linac section is mainly used to control the energy separation of the bunches, since the degree of compression in BC1 de-

termines how far apart the bunches sit in the RF wave in the second linac section (L2-L19). The second linac phase is then used to get the peak current sufficiently high without sacrificing too much emittance. Both must be varied together to achieve a certain end result, as the variables are not completely independent.

An example is shown in Fig. 3b, which displays the longitudinal phase space and current of the beam at the end of the preliminary matching stage. The first (second) bunch horizontal normalized emittance, $\epsilon_{n,x}$, is 0.5 (0.5) mm mrad, the bunch length, τ , is 10.1 (13.5) fs fwhm with a peak current, I_p , of 4.7 (3.4) kA, and the bunch separation, Δt , is 80 fs. This is achieved by placing the centroid RF phases in L1 and L2-L19 (see Fig. 1) at 29.75 and 6 degrees off-crest, respectively. As a result, the final energy spread is $\leq 0.05\%$ rms around each current peak and the energy separation is $\sim 0.35\%$ between the average energy of each bunch.

CONCLUSIONS AND OUTLOOK

Firstly, because of the fact that the wakefields increase the bunch chirp imposed by the RF, it is at present not possible to simultaneously have a short pulse and a very narrow energy spread of the individual bunches. This problem is exacerbated greatly by inclusion of CSR effects, which spoil the electron beam spectrum in BC2, as seen in Fig. 3b. In the figure, it also appears that the first bunch exhibits larger CSR modulations than the second, possibly meaning that the second bunch has irradiated both itself and the first bunch. It is also evident that the second bunch, unlike the first, is not compressed symmetrically, which is due to over-compensation of the phase space curvature in the compressors. This lowers the peak current somewhat, compared to a symmetric compression.

The nearest future step in this investigation include simulating the pre-injector with ASTRA [17], to use more realistic beams as input for the tracking simulations. Simulations of the FEL dynamics using Genesis [18] will also be performed. A parameter space for varying the time and energy separation, while keeping the peak current constant, also needs to be mapped out. For this at least a third variable is needed, besides the two linac phases. Since parameters such as laser pulse separation at the cathode and bunch charge will affect the beam emittance out from the pre-injector, it might be more practical to change e.g. R_{56} and/or T_{566} in BC2, as suggested in [8]. As there are currently no linac sections after BC2, the beam energy at BC2 is the final beam energy, which disables the beam energy at BC2 as a tuning param-

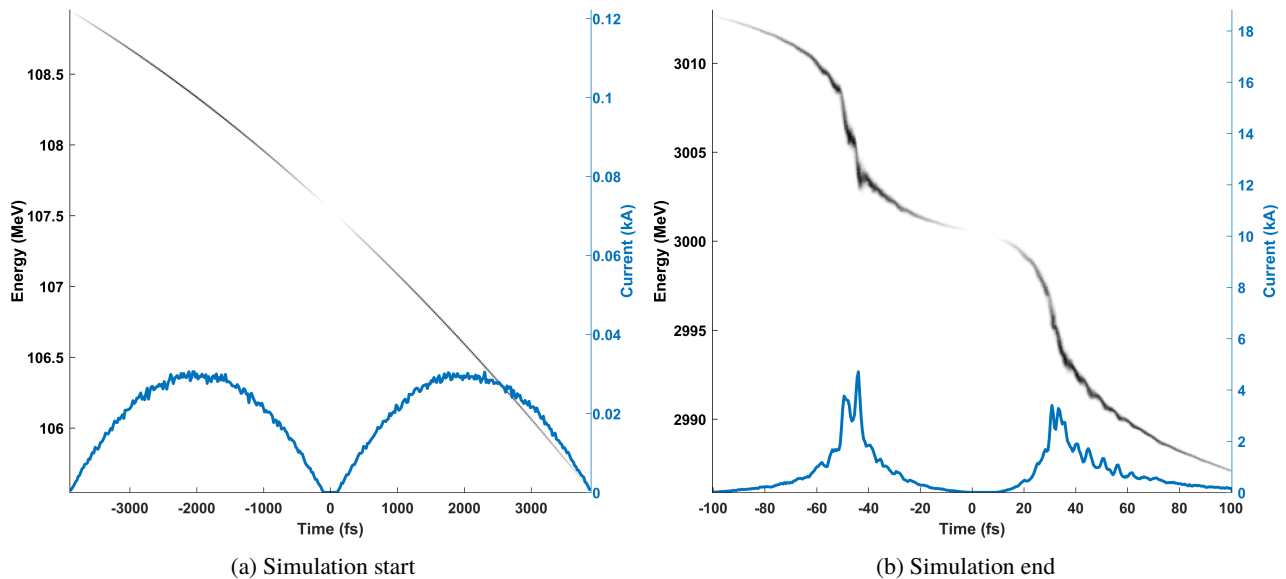


Figure 3: 2D histograms of the longitudinal phase spaces (greyscale) and the corresponding currents (blue) at the start and end of the simulation. The histogram density ranges from white (minimum) to black (maximum). The first bunch is to the left in the figures. Parameters from this particular simulation are given in the text.

eter even if the linac is capable of reaching up to 3.6 GeV. A passive (de-)chirper placed before BC2 could, however, provide practical tuning of the individual bunch chirps using the wakefields, particularly for low-charge bunches.

Better control of the slice Twiss parameters is also needed. At present, the Twiss parameters vary over the bunch lengths and between the bunches, something that causes a slight mismatch throughout the linac. As the total beam energy spread at BC1 is $\geq 1.7\%$ rms, some higher-order dispersion is also transmitted through the compressors, which needs to be addressed. Also making the compression of the second bunch more symmetric would equalize the peak currents.

However, the results from these early simulations are very similar to the results presented in [8], with a ~ 4 kA peak current and ≤ 100 fs time separation at 3 GeV and $\sim 0.35\%$ energy separation, even when including CSR in the simulations. With the presented values for peak currents and emittances, it is not unreasonable to assume that these two bunches can achieve lasing. Thus, we conclude that it appears feasible to accelerate and compress a double-bunch beam with FEL quality in the MAX IV Linear Accelerator.

REFERENCES

- [1] S. Thorin *et al.*, “The MAX IV Linac”, in *Proc. LINAC’14*, Geneva, Switzerland, August 2014, paper TU10A03, pp. 400-403.
- [2] S. Leemann *et al.*, “Beam dynamics and expected performance of Sweden’s new storage-ring light source: MAX IV”, *Phys. Rev. ST Accel. Beams*, vol. 12, no. 12, pp. 120701, 2009.
- [3] S. Werin *et al.*, “Short pulse facility for MAX-lab”, *Nucl. Instr. Meth. Phys. Res. A*, vol. 601, no. 1-2, pp. 98-107, 2009.
- [4] S. Thorin *et al.*, “Bunch compression by linearising achromats for the MAX IV injector”, in *Proc. FEL’10*, Malmö, Sweden, August 2010, paper WEPB34, pp. 471-474.
- [5] S. Werin *et al.*, “The Soft X-ray Laser Project at MAX IV”, in *Proc. IPAC’17*, Copenhagen, Denmark, May 2017, paper WEPAB077, pp. 2760-2762.
- [6] A. A. Lutman *et al.*, “Experimental Demonstration of Femtosecond Two-Color X-Ray Free-Electron Lasers”, *Phys. Rev. Lett.*, vol. 110, no. 13, pp. 134801, 2013.
- [7] A. Marinelli *et al.*, “High-intensity double-pulse X-ray free-electron laser”, *Nat. Commun.*, vol. 6, no. 6369, 2015.
- [8] Z. Zhang *et al.*, “Longitudinal dynamics of twin electron bunches in the Linac Coherent Light Source”, *Phys. Rev. ST Accel. Beams*, vol. 18, no. 3, pp. 030702, 2015.
- [9] F. Lindau *et al.*, “MAXIV Photocathode Gun Laser System Specification and Diagnostics”, in *Proc. IPAC’17*, Copenhagen, Denmark, May 2017, paper TUPAB097, pp. 1544-1546.
- [10] M. Kotur *et al.*, “Pulse Shaping at the MAX IV Photoelectron Gun Laser”, in *Proc. IPAC’17*, Copenhagen, Denmark, May 2017, paper TUPAB096, pp. 1541-1543.
- [11] J. Björklund Svensson *et al.*, “Driver-witness-bunches for plasma-wakefield acceleration at the MAX IV linear accelerator”, in *Proc. IPAC’17*, Copenhagen, Denmark, May 2017, paper TUPIK031, pp. 1743-1746.
- [12] M. Borland, “elegant: A Flexible SDDS-Compliant Code for Accelerator Simulation”, Advanced Photon Source LS-287, September 2000.
- [13] P. B. Wilson, “Introduction to wakefields and wake potentials”, SLAC PUB-4547, January 1989.
- [14] O. Karlberg *et al.*, “Characterization of Longitudinal Wakefields in the MAX IV Linac”, in *Proc. IPAC’14*, Dresden, Germany, May 2014, paper THPRO074, pp. 3050-3052.
- [15] O. Karlberg *et al.*, “Short Range Wakefields in the MAX IV and FERMI Linac”, in *Proc. IPAC’12*, New Orleans, USA, May 2012, paper WEP060, pp. 3063-3065.

- [16] J. Andersson *et al.*, "Beam performance of the photocathode gun for the MAX IV linac", in *Proc. FEL'14*, Basel, Switzerland, 2014, paper THP037, pp. 799-802.
- [17] K. Floettmann, "ASTRA user manual", 2000.
- [18] Genesis, genesis.web.psi.ch/index.html

EXPERIENCE AND INITIAL MEASUREMENTS OF MAGNETIC LINEARISATION IN THE MAX IV LINAC BUNCH COMPRESSORS

S. Thorin, J. Andersson, M. Brandin, F. Curbis, L. Isaksson, M. Kotur,
F. Lindau, E. Mansten, D. Olsson, R. Svärd, S. Werin, MAX IV Laboratory, Lund, Sweden
J. Björklund Svensson, Lund University, Lund

Abstract

The MAX IV Linac is now in routine operation for injection into two storage rings, and as a high-brightness driver for a Short Pulse Facility (SPF). In short-pulse mode the electron bunch is created in a photo cathode gun and compressed in two double achromat bunch compressors that also linearise longitudinal phase space with the second order transfer matrix element T566. T566 in the compressors can be tweaked with weak sextupoles located at high dispersion. In this paper we present the current experience from operating the bunch compressors at MAX IV and results from initial measurements of longitudinal phase space using our version of the the zero-crossing method.

BACKGROUND

The MAX IV facility [1] is the successor of the MAX-lab accelerators at Lund University and include two storage rings, a full energy linac and a Short Pulse Facility (SPF) [2]. The rings are operated at 1.5 and 3 GeV. The SPF is a single pass linac lightsource, producing sub-ps spontaneous X-ray pulses. The linac injector is flexible enough to drive both injection and top-up for the storage rings, and produce high brightness pulses for the SPF. Recently plans for a soft X-ray FEL has developed [3] and the long term strategic plan for the facility include an X-ray FEL. The linac was developed to be fully prepared to handle the high demands for an FEL driver.

The MAX IV linac is now operating mainly to deliver beam to both storage rings and to the Short Pulse Facility. Some commissioning work still remains, to the most part concerning bunch compression.

MAX IV LINAC GENERAL DESIGN

For injection and top up to the storage rings a thermionic gun with a pulse train chopper system is used [4]. In high brightness mode we use a 1.6 cell photo cathode gun capable of producing an emittance of 0.4 mm mrad at a charge of 100 pC [5]. The gun is operated together with a kHz Ti:sapphire laser at 263 nm [6].

The acceleration is done in 39 warm S-band linac sections together with 18 RF units, each consisting of a 35 MW klystron and a solid state modulator. The klystrons are operated at the lower power of 25 MW which reduces the operational cost and gives a total redundancy in energy of 0.6 GeV. The RF power is doubled with a SLED.

The beam is kicked out for injection into the storage rings at 1.5 and 3 GeV. Bunch compression is done in double achromats [7] at 260 MeV and at full energy, 3 GeV, after

extraction to the storage ring. A schematic view of the linac layout can be seen in Figure 1.

Linearising double achromat compressors

The magnetic double achromats used as bunch compressors in the MAX IV injector has a positive R56 unlike the commonly used magnetic chicane which has a negative R56. We have thus to work on the falling slope of the RF voltage. Both types of bunch compressors naturally have a positive T566 and a positive T566 has a linearising effect in the achromat case. We can thus choose the optical parameters in the achromat to get optimal linearisation without needing to have a harmonic linac for this purpose. A sextupole is needed to minimize the second order dispersion at the end of the achromat. This sextupole, positioned at the achromat middle, is rather weak and could be compared with the chromaticity compensating sextupoles in a storage ring.

The natural T566 of the double achromats is actually over-linearising the RF induced curvature and the sextupoles work in the opposite direction of the natural T566, to compensate for the over-linearisation. To achieve full linearisation of longitudinal phase space, the sextupole strength has to be increased. This can be done in such a way that second order dispersion is still closed at the end of the BC, but the energy derivative of dispersion becomes large, leading to increased emittance. For a spontaneous source like the SPF this is however not a problem. But even without over-tuning the sextupoles, a satisfying linearisation can be achieved to produce low emittance pulses, although at a lower peak current.

Table 1: Electron Bunch and Measurement Parameters

Compression energy	265 MeV
Final energy	9.98 GeV
Compression phase	0-50°
Initial electron bunch length rms	3 ps
Charge	100 pC
Dispersion at the screen	0.34 m
Sextupole strength	18/35 m ⁻³

BUNCH LENGTH MEASUREMENT USING A VARIANT OF THE ZERO-CROSSING METHOD

One single achromat will also induce some other second-order effects acting in the transverse direction. Many of the relevant ones are energy-dependent and thus linear in angle or position. The introduction of a double achromat, the

Content from this work may be used under the terms of the CC BY 3.0 licence (© 2018). Any distribution of this work must maintain attribution to the author(s), title of the work, publisher, and DOI.

MAX IV linac layout

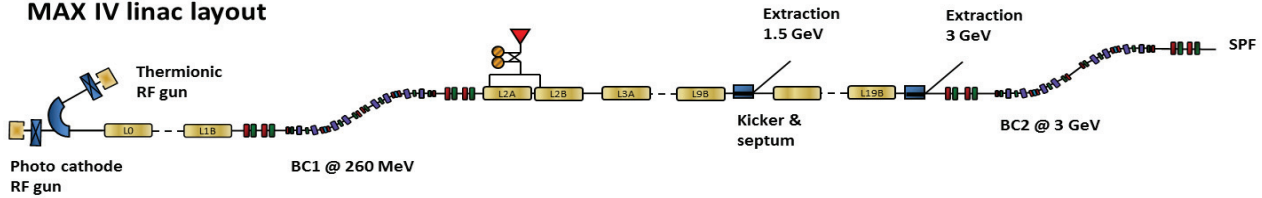


Figure 1: Layout of the MAX IV linac.

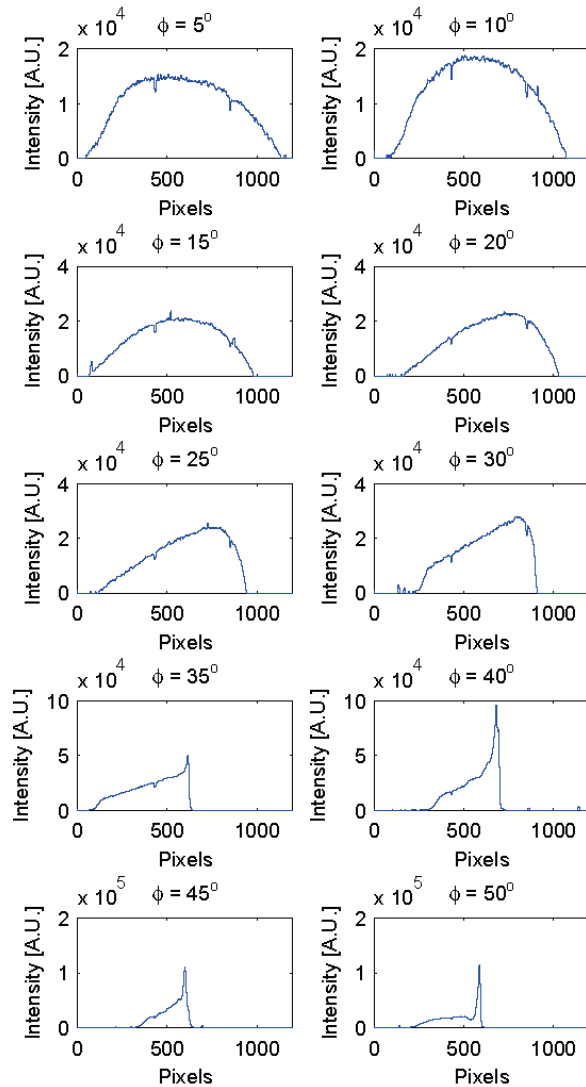


Figure 2: The x-projection of the electron bunch measured on a screen in BC2 while scanning the compression phase before BC1.

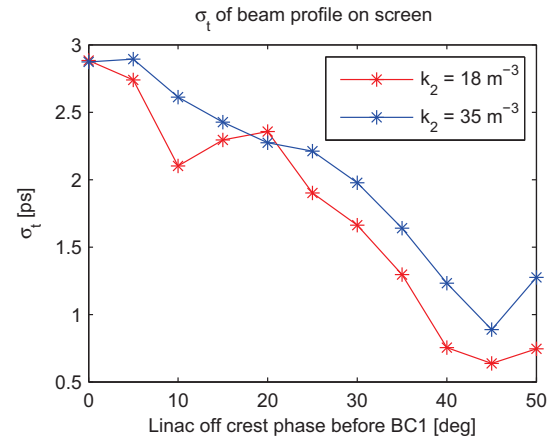


Figure 3: The RMS bunchlength of the electron bunch when the compression phase is scanned from 0 to 50°.

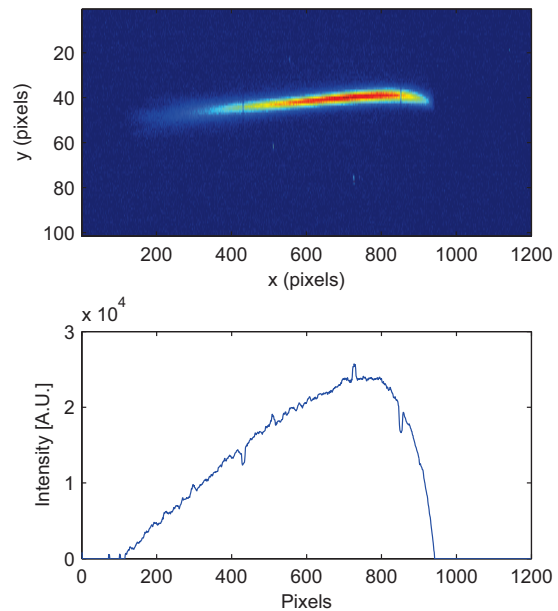


Figure 4: Ramped current shape with a compression factor of 3 and sextupole value 35 m⁻³.

achromats bending in opposite directions, will cancel these terms. We will also effectively get a translation of the beam instead of a change of angle, which eased the construction of the linac hall. Since the R56 of the double achromats is fixed, the off crest RF phase is used to vary the compression factor. By optimizing the combination of sextupole settings and compression RF phase the longitudinal profile of the

beam can be shaped to give both a very high spike of peak current or a ramped triangular shaped current profile.

The nature of the MAX IV compressors has also shown useful for letting double pulses with in one RF bucket to be simultaneously compressed giving two short bunches with around 100 fs separation [8].

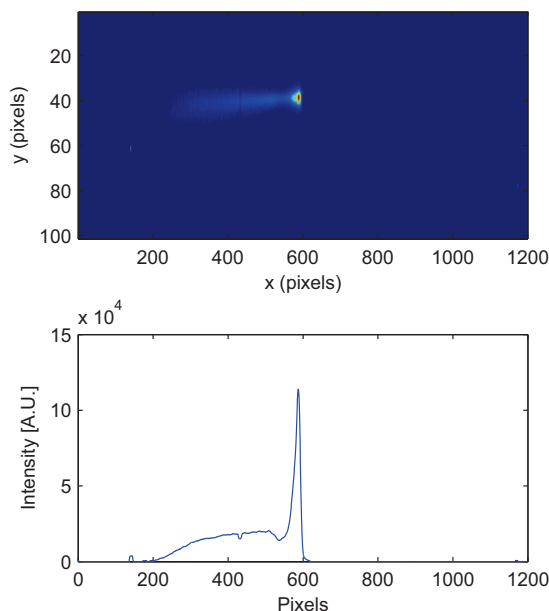


Figure 5: FWHM bunch length of the beam is 160 fs in the narrow peak.

Lacking a transverse deflecting cavity, measurements of longitudinal phase space has been made using our version of the zero-crossing method [9]. The beam was accelerated 20° off crest in the main linac, between BC1 and BC2, and viewed on a screen at maximum dispersion in BC2 [10]. This induces a correlated energy spread in the beam, and the dispersive region in BC2 will streak the beam horizontally, making the profile along the x -axis on the screen proportional to the longitudinal profile of the beam. The phase of the linacs before BC1 was scanned between 0 and 50° off crest. With the known dispersion of 0.32 m at the screen the width of the pulse on the screen could be related to the energy spread of the beam. With the known off crest phase in the main linac, this could then be converted to bunch length. Beam and compression parameters for the measurement can be found in table 1. Images from the screen and the projection along the x -axis for a sextupole setting of 35 m $^{-3}$ can be seen in figure 2. In figure 3 the RMS bunch lengths for sextupole strength 18 and 35 m $^{-3}$ are plotted.

Using this method we could see that the current profile of the beam will get a triangular shape for certain sextupole

settings and compression factors (see figure4). It is also possible to achieve a very high peak current at full compression where even though the RMS bunch length is in the order of 500 fs due to a charge plateau, the fwhm bunchlength in the peak comes down to 160 fs (see figure5). This results was obtained using only one bunch compressor.

SUMMARY AND OUTLOOK

The MAX IV linac uses 2 double achromat bunch compressors where the linearisation of longitudinal phase space is done through the T566 in the compressors. Weak sextupoles can be used to tweak the linearisation and with that also the shape of the electron bunch. By accelerating the electron bunch off crest in the main linac after compressing it in BC1 we could use a screen at high dispersion in BC2 to image the longitudinal bunch distribution. Using this method we were able to measure bunch lengths down to 160 fs in the sharp peak of a fully compressed bunch.

REFERENCES

- [1] *Detailed Design Report-MAX IV facility* (2010) Lund, Sweden.
- [2] S. Werin, *et al.*, "Short pulse facility for MAX-lab", *Nucl. Instr. and Meth. in Phys. Res. A* 601, pp. 98- 107, (2009).
- [3] S. Werin *et al.*, "The Soft X-ray Laser Project at MAX IV", WEPAB077, IPAC2017.
- [4] D. Olsson *et al.*, *Nuclear Instruments and Methods in Physics Research A*, 759, p. 29–35 (2014).
- [5] E. Elafifi *et al.*, "An Electron Gun Test Stand to Prepare for the MAX IV Project", TUPPD065, IPAC2012.
- [6] F. Lindau *et al.*, "MAXIV Photocathode Gun Laser System Specification and Diagnostics", TUPAB097, IPAC2017.
- [7] S. Thorin *et al.*, "Bunch Compression by Linearising Achromats for the MAX IV Injector", WEPB34, FEL2010.
- [8] J. Björklund Svensson *et al.*, "Double-Bunches for Two-Color Soft X-Ray Free-Electron Laser at the MAX IV Laboratory", TUP010, These proceeding.
- [9] WANG, D. X *et al.*, "Measurement of femtosecond electron bunches using a rf zero-phasing method", *Physical Review E*, 1998, 57.2: 2283.
- [10] F. Curbis *et al.*, "Prospects for Longitudinal Phase-space Measurements at the MAX IV Linac" THPME170, IPAC14.

COHERENT TRANSITION RADIATION FROM TRANSVERSELY MODULATED ELECTRON BEAMS

A. Halavanau^{1,2}, D. Mihalcea¹, P. Piot^{1,2}, S. P. Antipov^{3,4}, J. G. Power³, W. Liu⁴,
 E. Wisniewski³, C. Whiteford³, N. Neveu^{3,5}, A. Benediktovitch^{6,7}, A. V. Tyukhtin⁸, S. N. Galyamin⁸

¹ Department of Physics and Northern Illinois Center for Accelerator & Detector Development, Northern Illinois University DeKalb, IL, USA

² Fermi National Accelerator Laboratory, Batavia, IL, USA

³ Argonne Wakefield Accelerator, Argonne National Laboratory, Lemont, IL, USA

⁴ Euclid Techlabs LLC, Bolingbrook, IL, USA

⁵ Illinois Institute of Technology, IL, USA

⁶ Belarusian State University, Department of Theoretical Physics and Astrophysics, Minsk, Belarus

⁷ Center for Free Electron Laser Science, DESY, Hamburg, Germany

⁸ Saint Petersburg State University, Saint Petersburg, Russia

Abstract

A transverse laser-shaping optical setup using microlens arrays (MLAs), previously developed and employed at Argonne Wakefield Accelerator (AWA), allows the formation of both highly uniform and modulated (patterned) beams. In the latter case, transverse modulation is imposed in the sub-millimeter scale. In the present study, we report the simulations of backward coherent transition radiation (CTR) emitted from a transversely modulated beam. We compare the case of a uniform round beam against different transverse modulation wavelengths by generating CTR on a steel target and measuring the autocorrelation function of the resulting radiation with an interferometer. We particularly focus on the differences between round and patterned beam distributions and discuss possible future applications of this setup in THz radiation generation.

INTRODUCTION

Microlens arrays (MLAs) are commonly known in laser technology as light condensers and are often used for transverse laser beam homogenization. An alternative application of the MLAs is the generation of patterned beams that can be used in photoinjectors for multiple purposes [1].

Microlens array consists of periodically placed lenses forming a rectangular, honeycomb, or circular pattern. The resulting modulated light distribution mimics the microlens array geometry. The modulated pattern generated at the photocathode can be preserved and propagated downstream of the accelerator, while the spacing between the beamlets is controlled via solenoid and quadrupole lenses. Such an experimental setup was recently established at Argonne Wakefield Accelerator (AWA) facility [1], see Fig. 1.

Coherent transition radiation (CTR) is commonly used in temporal profile diagnostics [2–8]. An experimental setup usually consists of a retractable metallic screen and radiation diagnostics operating in the THz regime. Such a setup is depicted in Fig. 1 (a) and was recently built at AWA facility.

The goal of this study is to utilize MLA setup to introduce transverse modulation in the electron beam and observe its effect on the resulting CTR spectrum.

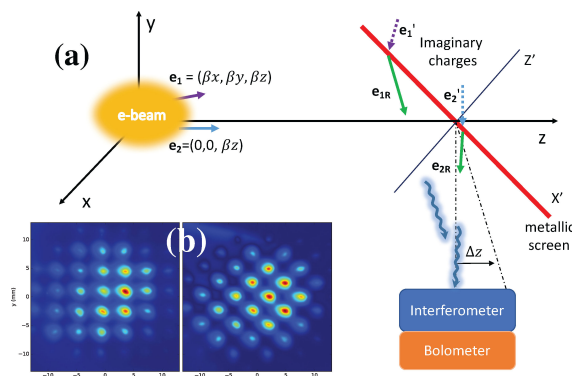


Figure 1: (a) Schematic of the experiment: an electron beam is incident on a metallic screen positioned at 45 deg. The resulting transition radiation photons are received in bolometer via interferometer transport to perform an auto-correlation scan. (b) An example of MLA-formed electron beam patterns observed at $\gamma = 100$.

SIMPLIFIED ANALYTICAL CALCULATION

A detailed analytical derivation of the transition radiation from a point charge as a solution of Maxwell's equations between two media can be found in classical textbooks [9, 10]. The electromagnetic field of a point charge falling onto a metallic plate can be calculated using the “method of images” [11], where for every charge incident on an infinite plane (q, \mathbf{e}_i) there is a “mirror” charge (q', \mathbf{e}'_i) behind the plane forming a pair of real and image charges. When a virtual pair of charges approaches the plane, it emits radiation that is mathematically equivalent to the transition radiation from a point charge [10]¹.

¹ Additionally, an analytical expression for a TR EM-field in case of a finite metallic plane can be found in [12].

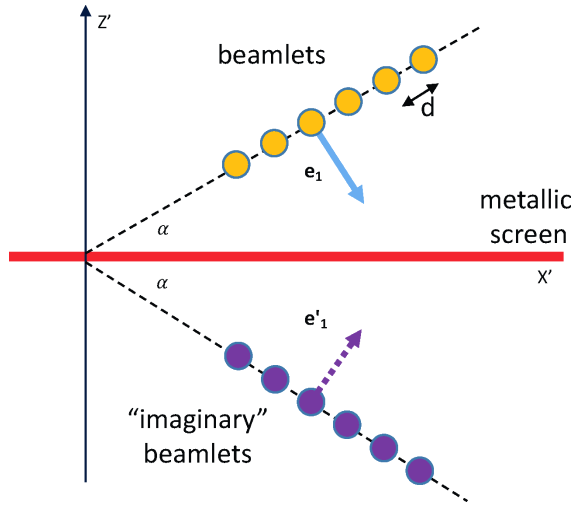


Figure 2: Simplified schematics of the “line” charge arrangement with spacing d . Axes correspond to Figure 1 notations.

Assume a “line” formation of point charges with spacing d arriving in parallel at the infinite metallic screen. Figure 2 illustrates such an arrangement for both “real” and “imaginary” charges.

A magnetic component of a TR EM-field can be written as [10]:

$$\vec{H}_\omega = \frac{q}{2\pi c} \sum_{i=1}^N \left(\frac{\vec{e}_{iR} \times \vec{e}_i}{1 - \vec{e}_{iR} \cdot \vec{e}_i} - \frac{\vec{e}'_{iR} \times \vec{e}'_i}{1 - \vec{e}'_{iR} \cdot \vec{e}'_i} \right) \times \frac{\exp(i\omega R_i/c + i\omega t_i)}{R_i}, \quad (1)$$

where N is the number of charges q , \vec{e}_i is the velocity vector, \vec{e}_{iR} is the vector from the point of incidence to the detector, R_i is the distance from the point of incidence to the detector, t_i is the time of arrival of i -th charge at the metallic plate, ω is the radiation frequency. The spectral density of the radiation can then be computed as [10]:

$$\frac{d^2W}{d\omega d\Omega} = cR^2 |\vec{H}_\omega|^2 \quad (2)$$

Assuming the detector is far from the plate, Eq. 1 can be rewritten as:

$$\vec{H}_\omega \approx \frac{q}{2\pi cR} \vec{f} \sum_{i=1}^N \exp(i\omega R_i/c + i\omega t_i), \quad (3)$$

where $\vec{f} = \left(\frac{\vec{e}_R \times \vec{e}}{1 - \vec{e}_R \cdot \vec{e}} - \frac{\vec{e}'_R \times \vec{e}'}{1 - \vec{e}'_R \cdot \vec{e}'} \right)$ and the term under summation can be referred as a bunching factor:

$$F = \left| \sum_{i=1}^N \exp(i\omega R_i/c + i\omega t_i) \right|^2 \quad (4)$$

Note, if the detector is located in the far-zone, the particles with the same t_i will have almost the same contribution to the resulting spectrum. Nevertheless, the path difference

ΔR_i is finite, therefore has to be accounted for. The resulting spectral density can be then rewritten in a shorter form:

$$\frac{d^2W}{d\omega d\Omega} \approx \frac{q^2}{4\pi^2 c} f^2 F \quad (5)$$

NUMERICAL SIMULATIONS

To perform numerical simulations, a code that computes radiation spectral density (Eq. (2)) with exact expression for \vec{H}_ω (Eq. (1)) and approximation (Eq. (3)) was developed. The results were found to be very close, therefore hereafter we will refer to the calculations via Eq. (3). $N = 8000$ particles were used in simulations of both transverse Gaussian bunches and beamlets arranged in a vertical “line” with a spacing of $d = 1$ mm. The longitudinal bunch length was assumed to be Gaussian with $\sigma_z \ll d$. The detector was assumed to be in a far-zone meaning $R \gg 8$ mm. In the simulations, the electron beam was assumed to have a waist at the location of the metallic screen and transverse emittance was set to 0.

TR is known to have a “double-horn” structure, which is independent of transverse electron distribution and attributed to the fact that there is no radiation emitted along the direction perpendicular to the charge velocity [9, 10]. Such a spectrum is displayed in Fig. 3 for the case of a Gaussian and modulated transverse distribution. The simulation was done for the same number of particles in both cases and the 3σ size of the Gaussian distribution was matched by the beamlet array size.

The spectral content of the radiation generated by a Gaussian bunch and 8 beamlets arranged in a “line” is depicted in Fig. 4. The beamlet pattern possesses a peculiar spectral structure in the THz regime. As it can be seen in Fig. 4, additional radiation peaks emerge at detector offsets of about 2° , while the maximum of the radiation is contained around 0.57° . The first harmonic seems to be relatively narrow-band, therefore motivating the experimental attempt.

The numerical study with realistic beam distributions will be performed in the near future and reported elsewhere.

EXPERIMENTAL SETUP

A numerical model of the AWA-DB beamline was established in OPAL-T, IMPACT-T, GPT and ASTRA [13–16]. Electron beam simulations were performed to achieve necessary beam parameters at the location of the metallic screen [17, 18].

In the experimental setup we use two MLA plates of a rectangular spacing with $300 \mu\text{m}$ pitch and $f = 5$ mm focal length. The MLAs are illuminated with mJ-energy 248 nm laser pulses. Such a configuration provides very flexible spatial shaping technique, therefore it is routinely employed in various AWA electron beam experiments [1]. The electrons are accelerated to 7 MeV in an L-band RF gun and further transported through 6 L-band linacs to a final energy of up to 72 MeV; see [19].

A stainless steel mirror is installed in the beamline at $\alpha = 45^\circ$ after the last accelerating structure with an interferometer and bolometer on the side; see Fig 1. For a detailed

Content from this work may be used under the terms of the CC BY 3.0 licence (© 2018). Any distribution of this work must maintain attribution to the author(s), title of the work, publisher, and DOI.

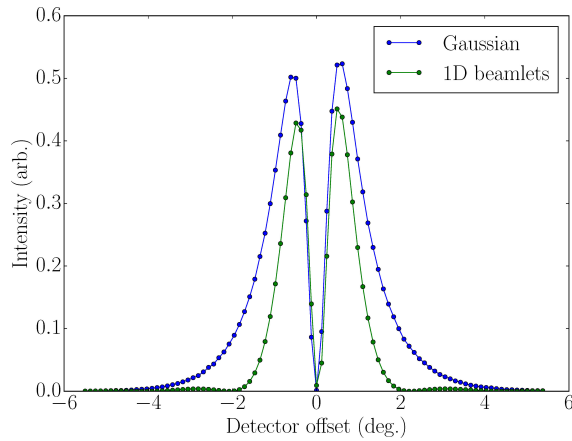


Figure 3: Simulated “double-horn” TR spectrum calculated at $\omega = 6$ THz for the detector configuration shown in Fig. 1. Beamlet “line” arrangement consisted of 8 beamlets with spacing $d = 1$ mm.

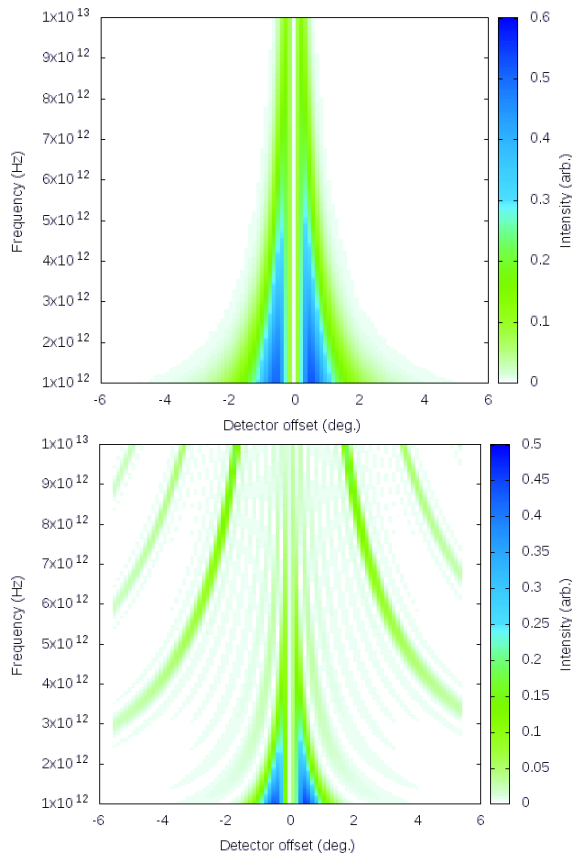


Figure 4: Spectral content of the Gaussian (top) and 8 beamlets “line” arrangement (bottom) with spacing of $d = 1$ mm.

description of the interferometer please see [8]. A IR-Labs general purpose LN-6/C 4.2 K bolometer [20] is installed downstream of the interferometer.

Such a setup allows autocorrelation scans of the electron beam, revealing it’s spectral content. Additionally, the MLAs were placed on a rotatable stage to compensate the Larmor rotation in the RF gun solenoids and allow for different pattern angles at the CTR mirror; see Fig 1 (b).

EXPERIMENTAL PLAN

The experiment will be performed as follows. A transversely homogenized laser distribution will be created in the MLA setup and transferred onto photocathode. The beamline will be tuned to provide the beam waist at the location of the metallic screen. An interferometer will be used for an autocorrelation scan with the CTR signal registered in bolometer. This data will be used for the bunch length measurement. The MLA setup will then be switched to the beamlet mode and the electron beamlet distribution will be propagated onto the screen. The same measuring technique will be used to compare the spectral contents between the two cases. A mechanical scanning slit will be used to introduce detector offset, allowing for measurement of the narrow-band part of the spectrum. The beamlet spacing will be determined by the bunch length, and imposed by using quadrupole magnets upstream of the screen.

CONCLUSIONS

We demonstrated via numerical simulations the possibility of generating THz coherent transition radiation via electron beam transverse shaping. The resulting spectral content is different from the Gaussian transverse distribution, with narrow-band harmonics present in the THz range. The limiting factor is found to be the bunch length which has to be significantly shorter than beamlet spacing. The particle distribution along the vertical axis has a leading effect in generating transverse CTR, while the distribution along the horizontal axis is a second-order effect. A preliminary experiment confirmed the difference in CTR spectrum due to transverse beam modulation. A follow-up experiment is scheduled at AWA facility and the results will be reported shortly.

REFERENCES

- [1] A. Halavanau, G. Qiang, G. Ha, E. Wisniewski, P. Piot, J. G. Power, and W. Gai, "Spatial Control of Photoemitted Electron Beams using a Micro-Lens-Array Transverse-Shaping Technique", arxiv:1707.08448, submitted to PRAB, (2017).
- [2] U. Happek, A. J. Sievers, and E. B. Blum, "Observation of coherent transition radiation", *Phys. Rev. Lett.*, 67:2962–2965, (1991).
- [3] W. Barry, "Measurement of subpicosecond bunch profiles using coherent transition radiation", *AIP Conference Proceedings*, 390(1):173–185, (1997).
- [4] Y. Shibata, T. Takahashi, T. Kanai, K. Ishi, M. Ikezawa, J. Ohkuma, S. Okuda, and T. Okada, "Diagnostics of an electron beam of a linear accelerator using coherent transition radiation", *Phys. Rev. E*, 50:1479–1484, (1994).
- [5] C. Settakorn, "Generation and use of coherent transition radiation from short electron bunches", PhD thesis, Stanford University (2001).
- [6] T. J. Maxwell, "Measurement of Sub-Picosecond Electron Bunches via Electro-Optic Sampling of Coherent Transition Radiation", PhD thesis, Northern Illinois U. (2012).

- [7] S. Antipov, C. Jing, M. Fedurin, W. Gai, A. Kanareykin, K. Kusche, P. Schoessow, V. Yakimenko, and A. Zholents, "Experimental observation of energy modulation in electron beams passing through terahertz dielectric wakefield structures", *Physical review letters*, 108(14):144801, (2012).
- [8] D. Mihalcea, C. L. Bohn, U. Happek, and P. Piot, "Longitudinal electron bunch diagnostics using coherent transition radiation", *Phys. Rev. ST Accel. Beams*, 9:082801, (2006).
- [9] D. J. Jackson, *Classical Electrodynamics*. Wiley, 1998. New York.
- [10] V. L. Ginzburg and V. N. Tsytovich, *Transition Radiation and Transition Scattering*. Hilger, 1990. London.
- [11] V. N. Krasilnikov and A. V. Tyukhtin, "Reflection theorems for some anisotropic media", *Radiophysics and Quantum Electronics*, 27, 717-723 (1984).
- [12] S. Casalbuoni, B. Schmidt, P. Schmüser, V. Arsov, and S. Wesch, "Ultrabroadband terahertz source and beamline based on coherent transition radiation", *Phys. Rev. ST Accel. Beams*, 12:030705 (2009).
- [13] A. Adelman, A. Gsell, V. Rizzoglio, C. Metzger-Kraus, Y. Ineichen, X. Pang, S. Russell, C. Wang, J. Yang, S. Sheehy, C. Rogers, and D. Winklehner, "The opal framework", PSI-PR-08-02.
- [14] J. Qiang, *IMPACT-T reference manual*, LBNL-62326, (2007).
- [15] S.B. van der Geer *et al.*, "3d space-charge model for gpt simulations of high brightness electron bunches", *Institute of Physics Conference Series*, 175:101, (2005).
- [16] K. Flöttmann, *ASTRA reference manual*, DESY (2000).
- [17] N. Neveu, J. Larson, J. G. Power, and L. Spentzouris, "Photoinjector optimization using a derivative-free, model-based trust-region algorithm for the argonne wakefield accelerator", *Journal of Physics: Conference Series*, 874(1):012062, (2017).
- [18] N. Neveu *et al.*, "Benchmark of RF Photoinjector and Dipole Using ASTRA, GPT, and OPAL", in *Proc. of NAPAC'16*, Chicago, USA, paper THPOA46, (2016).
- [19] M.E. Conde *et al.*, in *Proceedings of IPAC'10*, Kyoto, Japan, paper THPD016, (2010).
- [20] IR Labs, <http://www.infraredlaboratories.com/home.html>

BEAM-DYNAMICS ANALYSIS OF LONG-RANGE WAKEFIELD EFFECTS ON THE SCRF CAVITIES AT THE FAST FACILITY*

Young-Min Shin[#], Northern Illinois Univ., Dekalb, IL, and FNAL, Batavia, IL, USA

Randy M. Thurman-Keup, Jinhao Ruan, Alex H. Lumpkin, FNAL, Batavia, IL, USA

Frank L. Krawczyk, Kip A. Bishofberger, Bruce E. Carlsten, LANL, Los Alamos, NM, USA

Abstract

Long-range wakefields in superconducting RF (SCRF) cavities create complicated effects on beam dynamics in SCRF-based FEL beamlines. The driving bunch excites effectively an infinite number of structure modes (including HOMs) which oscillate within the SCRF cavity. Couplers with loads are used to damp the HOMs. However, these HOMs can persist for long periods of time in superconducting structures, which leads to long-range wakefields. Clear understanding of the long-range wakefield effects is a critical element for risk mitigation of future SCRF accelerators such as XFEL at DESY, LCLS-II XFEL, and MaRIE XFEL. We are currently developing numerical tools for simulating long-range wakefields in SCRF accelerators and plan to experimentally verify the tools by measuring these wakefields at the Fermilab Accelerator Science and Technology (FAST) facility. A particle-in-cell (PIC) simulation model for the FAST 50 MeV beamline indicates strong bunch-by-bunch variations of beam parameters with the operating conditions at 9 MHz bunch rep-rate along a macro-pulse and 500 pC, 1 nC, and 2 nC per bunch. This paper previews the experimental conditions at the FAST 50 MeV beamline based on the simulation results.

INTRODUCTION

An ILC type cryomodule, consisting of nine 1.3 GHz, 9-cell SCRF cavities, is considered standard for future SCRF accelerators. The XFEL at DESY in Germany and the LCLS-II XFEL in USA are being constructed with these cryomodules with only minor modifications and the same cryomodule is included in the pre-conceptual design of the MaRIE XFEL. In such SCRF cavities, the driving bunch excites effectively an infinite number of structure modes (including higher-order modes (HOMs)) which oscillate within the superconducting cavity, with some even propagating into other cavities. Couplers with loads are used to damp the HOMs. However, these HOMs can persist for long periods of time in superconducting structures, which leads to long-range wakefields. The signals measured via a HOM-detector [1] indicated that the ILC HOM dampers do not act fast enough to damp out the long-range wake-fields and their effects need to be considered for closely spaced electron bunches. Energy in the HOMs clearly persists for at least a few μ secs, and is particularly large over the first few 10^3 's of nanosecs after

the drive bunch, which is the time scale for the bunch spacing within burst pulses of high rep-rate X-Ray FELs, e.g. MaRIE XFEL.

Particle tracking simulations with the numerical code Lucretia [2] indicated that HOM couplers are not capable of damping all HOMs: while some are well damped, a limited number of modes remain poorly damped. In this calculation, only the five modes most destructive to the beam are damped to the level of $Q = 10^5$, with the rest of modes having $Q = 10^6$. A train of 500 bunches was injected at a 3 MHz repetition rate and with an offset of 6 μ m. Tracking this beam through the linac indicated that a single 9-cell cavity would generate 3 - 5 % of emittance growth for the bunches at the end of the train, which is catastrophic, given that there are on the order of a thousand cavities in a linac for an XFEL and even more for a collider. The duration of the HOM power and its possible effect on an electron bunch from this scoping calculation strongly indicate that more detailed analysis and measurements are needed. Importantly, the alignment of individual cavities in the ILC cryomodules is limited to about 0.2 mm due to the fabrication technique, far larger than the offset used in this scoping calculation.

The experiment to verify the long-range wake effect for the first time was planned at the FAST facility. The beamline consisting of two SCRF capture cavities and a full 8-cavity ILC cryomodule is designed to operate with up to 3000 bunches per macro-pulse, up to 9 MHz in bunch repetition rate, and up to 3 nC per bunch at beam energies from 50 MeV to 300 MeV with several high-resolution beam diagnostics tools, including BPMs and a streak camera. The facility fits well for the long-range wakefield experiment. The experiment is currently scheduled for the 2017 FAST runtime.

As a part of the plan, we have been developing simulation tools for accurately assessing SCRF long-range wakefield effects on beam dynamics and comparing it to the diagnostic capabilities at the FAST 50 MeV beamline. Bunch-to-bunch deviations of the longitudinal and transverse beam profiles are analyzed for the current FAST beamline setup. In this paper, the simulation results are discussed with the measurable range of the instruments installed in the 50 MeV beamline.

OVERVIEW

In the FAST beamline (Fig. 1), the two capture cavities (CC1 and CC2) are ILC superconducting cavities. Last year beam commissioning was conducted through the diagnostic stations after CC2 (with up to a 50-MeV electron beam). The 9-cell cavities, operating with 25

* Work supported by the subcontract (contract No: G2A62653) of LANL-LDRD program and DOE contract No. DEAC02-07CH11359 to the Fermi Research Alliance LLC.

[#] yshin@niu.edu

MV/m gradient at a liquid helium temperature (2 K), boost the beam energy up to 55 MeV with a few mm-mrad of rms emittance. The time structure of the bunch train, e.g. number of bunches per macro-pulse and bunch-to-bunch spacing, are controllable depending on charge per bunch. A series of corrector- and quadrupole-magnets are employed to control the transverse beam position/size.

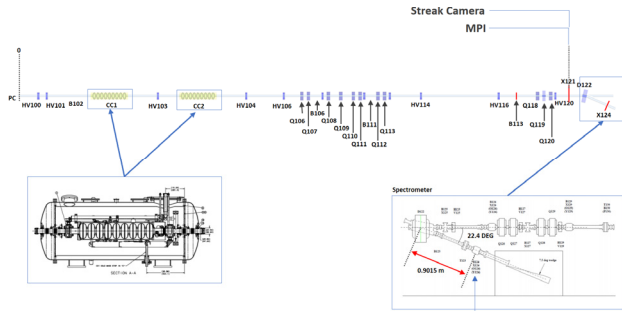


Figure 1: Layout of FAST 50 MeV beamline with the beamline components (HV: H- and V-correctors, Q: quadrupoles, D: dipole, B: BPMs, X: image-screens).

The measured BPM resolutions downstream of the gun are 25 μm at 2 nC, which is increased to 290 μm at 250 pC. Prior to the actual measurements, RF-BPM resolution and beam emittance will be re-measured at various bunch charges. Also, CC1/CC2 gradient-drop from beam-loading loss for a bunch train will be measured at X124 and it will be compensated by adjusting the RF-feedforward. The transverse beam position in CC1/CC2 will be adjusted with correctors until the CC1/CC2 HOM detector-signals are minimum (to minimize transverse HOMs). After the pre-setup, we will measure the bunch-by-bunch deviations of longitudinal and transverse beam parameters, including centroid beam-energy, energy spread, transverse beam position/size, etc, with BPMs (B121/122/123/124), streak-camera, and dipole spectrometer. The measurement will be repeated with various conditions in bunch charge (0.5 – 2 nC), number of bunches (10 – 200), and bunch rep-rate (1, 3, and 9 MHz). For this test plan and experimental conditions we analyzed the bunch-by-bunch dynamics of beam parameters with particle-in-cell (PIC) and wake simulation models based on 2D- (ECHO-2D) and full 3D- (CST-PS) codes.

PIC-SIMULATION ANALYSIS

The PIC models use 5 bunches (500 pC per bunch) equally spaced with 110 ns and each bunch in order was compared with the single-bunch case under the same condition (RF-fields/phase of CC1/CC2). In the model, CC1 and CC2 used a SCRF surface-resistivity ($\sigma = 10^9 [\Omega^{-1}\text{m}^{-1}]$), leading to $Q \sim 10^{10}$, while the beampipe along the beamline used a lossy metal ($\sigma = 7.69 \times 10^6 [\Omega^{-1}\text{m}^{-1}]$). The beam injected in the beamline model has 4 MeV centroid beam energy, 1.5 % energy spread, 1.9 mm beam size, and 0.1 mm-mrad geometric emittance. The amplitude and matching-phase of individual RF-pulses in CC1 and CC2 were adjusted until the output beam energies after CC2 reach 50 MeV on-crest. The field maps of the acceleration mode (TEM₀₁₀) in CC1 and CC2 were obtained from a

separate eigenmode simulation and then imported to the cavities in the PIC model. The driving power is adjusted until the output energy reaches 50 MeV. Collective effects, including space charge effects and potential depression, are intrinsically reflected in the PIC model.

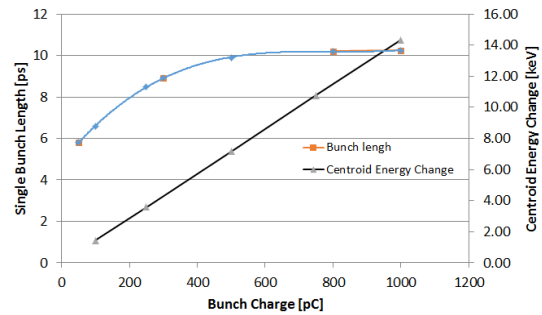


Figure 2: Bunch lengths and centroid energy losses of a single-bunch per bunch charge (wakes for different charges ~ 10 keV maximum).

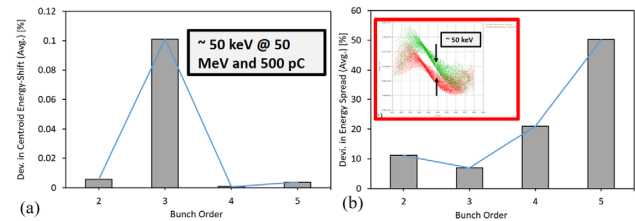
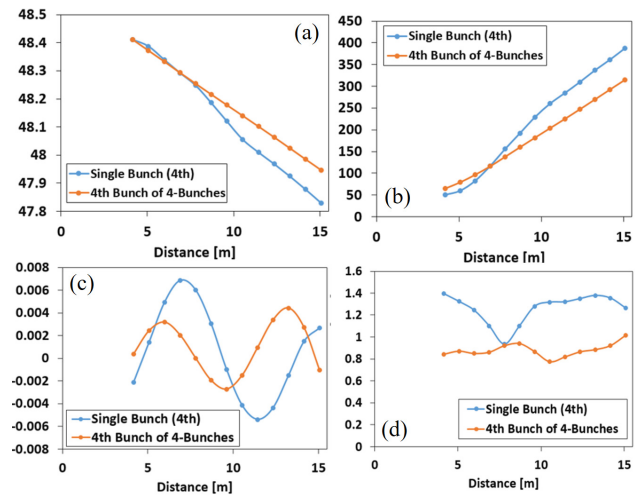


Figure 3: Bunch-by-bunch deviations (single-bunch versus multi-bunch – 2nd, 3rd, 4th, and 5th) in (a) centroid energy and (b) energy spread (inset: bunch charge-distribution in energy versus time (3rd bunches with (green) and without (red) 1st and 2nd bunches)).

We first identified a short wakefield effect on a single bunch prior to multi-bunch simulations. Figure 2 shows the bunch lengths and energy-spreads of a single bunch with various bunch charges, estimated by ECHO-2D in comparison with measured data at FAST beamline. The simulation indicated that the maximum energy spread out of the wake for the 2-cavity system is about 10 keV. Monitoring right after CC2, one sees that the 3rd bunch has the largest shift (~ 50 keV) in centroid beam energy from a single-bunch, while its energy spread is minimum (Figs. 3(a) and (b)) for the 500 pC case.



Content from this work may be used under the terms of the CC BY 3.0 licence (© 2018). Any distribution of this work must maintain attribution to the author(s), title of the work, publisher, and DOI.

Figure 4: Beam parameters, (a) centroid energy (MeV), (b) energy spread (keV) (c) beam position (mm), (d) beam size (mm), versus distance plots of a single (blue) and multiple (red) bunches of (4th) after CC2 with $I = 0$ A for H101.

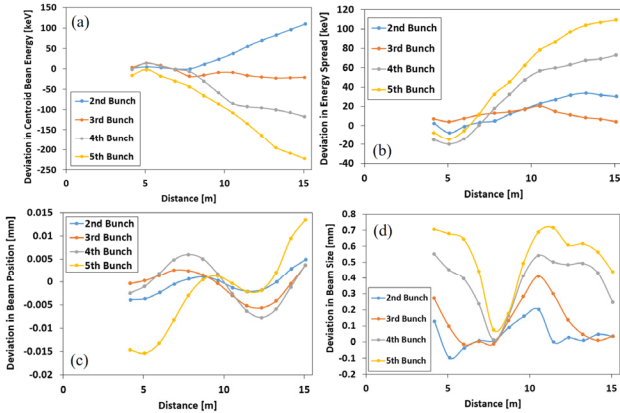


Figure 5: Bunch-by-bunch deviation versus distance plots (single-bunch versus multi-bunch – 2nd, 3rd, 4th, and 5th) in (a) centroid beam energy (b) energy spread (c) transverse beam position and (d) beam size with $I = 0$ A for H101.

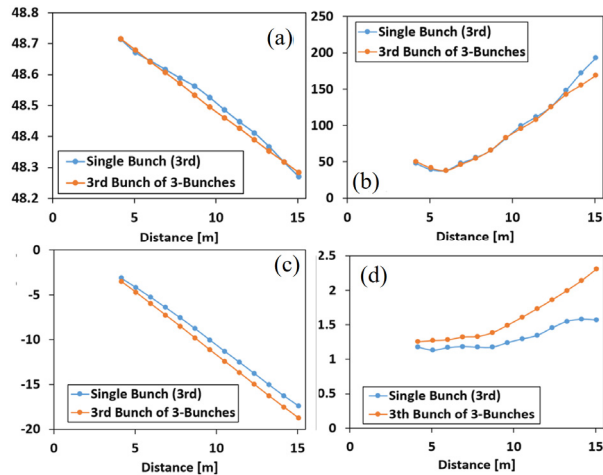


Figure 6: Beam parameters, (a) centroid energy (MeV), (b) energy spread (keV) (c) beam position (mm), (d) beam size (mm), versus distance plots of a single (blue) and multiple (red) bunches of (3rd) after CC2 with $I = 0.4$ A for H101.

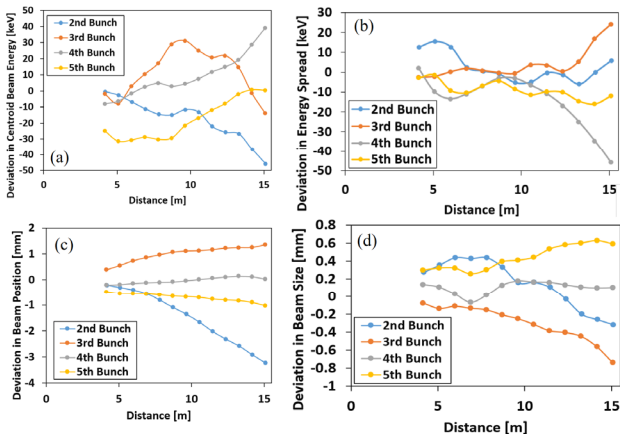


Figure 7: Bunch-by-bunch deviation versus distance plots (single-bunch versus multi-bunch – 2nd, 3rd, 4th, and 5th) in

(a) centroid beam energy (b) energy spread (c) transverse beam position and (d) beam size with $I = 0.4$ A for H101.

The deviations vary from bunch to bunch under the influence of wakefield interferences. The shift would be more prominent when the periodically excited wakefields are constructively superposed.

The beam parameters and their deviations (single-bunch vs bunch-trains) are also traced along the beampipe after CC2 with different corrector currents (H/V101), $I = 0$ A and 0.4 A. Under the current setup of FAST 50 MeV injector beamline, the horizontal beam position injected into CC1 can be controlled by H101 (or H100). The beampipe is lossy (a few orders of magnitude more than the cavities) and it is an additional source of "resistive wakefields", which add longitudinal and transverse wake potentials to the beam. The transverse and longitudinal effects appear in the centroid beam energy (Fig. 4, (a)) and transverse beam position (Fig. 4 (c)). The energy loss and correlated energy spread of a single-bunch along 10 m long beampipe downstream of CC2 are about 300 keV and 150 keV. For the bunch-train, the numbers fluctuate ($\pm 150 - 200$ keV in centroid-energy and $\sim \pm 120$ keV in energy spread) due to wake-potentials accumulated from each bunch in CC1 and CC2, as shown in Figs. 5(a) and (b).

The centroid beam position also oscillates within $5 \mu\text{m}$ due to the transverse wakefields in the beampipe (Fig. 4 (c)), which is increased up to $15 \mu\text{m}$ with the bunch-train (Fig. 5(c)). For I (H101) = 0.4 A (Fig. 6), which is the case of off-axis injection, the transverse effects (transverse wake-potentials in CC1 and CC2) are more dominant. Therefore, the deviations (single-bunch vs bunch-train) in centroid energy and energy spread (Figs. 7 (a) and (b)) get rather decreased from the case of I (H101) = 0 A, but those in transverse beam position reach a few mm 10 m away from CC2 (Fig. 7(c)). Their transverse beam positions, especially of the 2nd and 3rd bunch are substantially changed beyond the estimated BPM resolution, $\sim 100 \mu\text{m}$ at 500 pC, due to strong transverse wakefields from off-axis beam injection. The shift is thus measurable by BPMs. In the case that the beam size changes bunch by bunch, which most likely occurs, the streak camera operating in framing mode can more clearly measure the effect.

SUMMARY AND PLAN

The experiment to identify long-range wakefield effects in ILC type cryomodules is being planned at FAST facility for 2017. As a part of the plan, we have been developing simulation tools to estimate long-range wakefield effects on beam dynamics and to lay out the experimental conditions. Our plan is to experimentally benchmark and verify the simulation model, which will have relevance for all current and future projects using ILC SCRF cavities.

ACKNOWLEDGMENT

The authors would like to thank FAST Department staff for the helpful discussion.

REFERENCES

- [1] A. Lumpkin, Y.-M. Shin, D. Edstrom, J. Ruan, R. Thurman-Keup, and P. Prieto, presentation at the LANL/FNAL planning meeting, Fermilab, Nov. 2, 2016.
- [2] P. Tenenbaum *et al.*, The Lucretia Project. <http://www.slac.stanford.edu/accel/ilc/codes/Lucretia>

MODELING AND OPTIMIZATION OF THE APS PHOTO-INJECTOR USING OPAL FOR HIGH EFFICIENCY FEL EXPERIMENTS*

C. C. Hall[†], D. L. Bruhwiler, S. W. Webb, RadiaSoft LLC., Boulder, USA
Y. Sun, A. Zholents, Argonne National Laboratory, Argonne, IL, 60439, USA
P. Musumeci, Y. Park,

Department of Physics and Astronomy, UCLA, Los Angeles, California 90095, USA
A. Murokh, RadiaBeam Technologies Inc., Santa Monica, CA 90404, USA

Abstract

The Linac Extension Area (LEA) is a new beamline planned as an extension of Argonne's APS linac. An S-band 1.6-cell copper photo-cathode (PC) RF gun has been installed and commissioned at the APS linac front end. The PC gun will provide a beam to the LEA for accelerator technology development and beam physics experiments, in interleaving with a thermionic RF gun which provides a beam for APS storage ring operations. Recently an experiment was proposed to demonstrate the TESSA high-efficiency concept at LEA. In support of this experiment, we have begun simulating the photo-injector using the code OPAL (Object-oriented Particle Accelerator Library). In this paper, we first benchmark OPAL simulations with the established APS photo-injector optimization using ASTRA and ELEGANT. Key beam parameters required for a successful high-efficiency TESSA demonstration are discussed.

OVERVIEW

The Advanced Photon Source (APS) linac provides electrons at up to 500 MeV for operation of the APS storage ring. The end of the APS linac beamline has been extended to create a new beamline called the Linac Extension Area (LEA) that will be fed by an alternate photo-injector operating in-between top-up cycles for the synchrotron. The LEA beamline will serve as an area for performing a variety of experiments requiring flexible, high-brightness electron beams.

* Work supported by the United State Department of Energy, Office of Scientific Research, under SBIR contract number DE-SC0017161.

[†] chall@radiasoft.net

The Tapering Enhanced Stimulated Superradiant Amplification (TESSA) concept [1] is a novel FEL scheme that allows for extremely high extraction efficiencies (as much as 50%). Design of an undulator to test the TESSA concept at 266 nm is underway, with plans to perform a proof-of-principle experiment at the LEA beamline.

We will discuss simulation studies of the photo-injector and APS linac to ensure that sufficient beam quality can be achieved to meet requirements for TESSA. We first show comparisons between the code ASTRA, previously used for the injector modeling, and OPAL, which is now being used. We then look at the electron beam requirements for TESSA and some of the challenges to meeting these requirements.

LEA and the APS Linac

The APS linac, shown in Fig. 1, serves as the start of the accelerator chain feeding the APS light source. When operating in this capacity a thermionic rf gun (RG2) is used, electron bunches are accelerated to 450 MeV in the linac and fed into the booster. During normal top-up operation the linac is only used for twenty seconds every two minutes. During the downtime on this interval the linac will be used to feed electron bunches from the photocathode gun (PCG) to the Linac Extension Area (LEA). The timing structure for LEA/APS operation is shown in Fig. 2.

Beam from the PCG will reach the L2 linac at 40 MeV where it will then be using the same lattice as beam from thermionic guns. Previous efforts at APS have optimized lattice settings that can accommodate the disparate properties of both PCG and RG2 beams [2]. From L2 the beam is

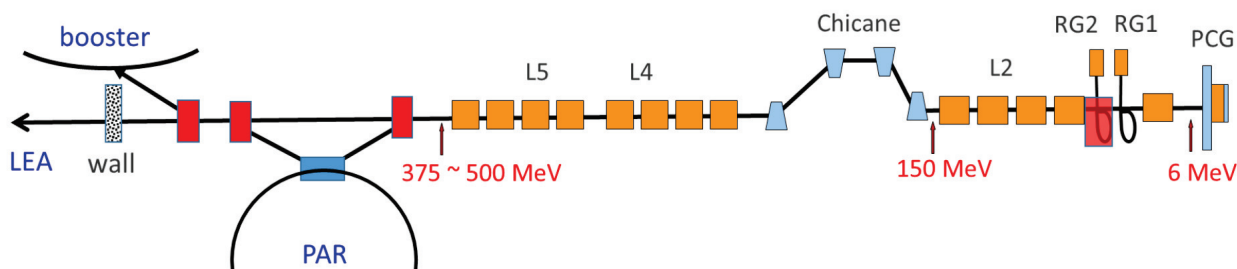


Figure 1: Schematic of the APS beamline showing the thermionic rf guns (RG1 and RG2), photocathode gun (PCG), accelerating sections (L2, L4 and L5), and Linac Extension Area (LEA) at the end of the beamline.

accelerated up to 150 MeV before reaching the compression chicane and followed by the L4 and L5 linacs sections which can provide a final energy of 375 MeV to 500 MeV. Beam from the PCG will bypass the PAR and Booster and enter the LEA beamline section at the end of the linac. There will be a several meter space for experimental device setup upstream of a dipole spectrometer and beam dump. Expected parameters for the electron beam at LEA are shown in Table 1.

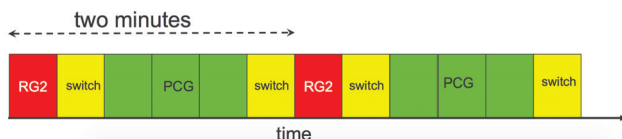


Figure 2: Timing structure for photocathode gun (PCG) and thermionic gun (RG) interleaving operation.

Table 1: Beam Parameters of the LEA Beamline

Property	Value
Energy	< 500 MeV
Energy Spread	250 keV to 500 keV
Bunch Charge	50 pC to 500 pC
Emittance (Normalized)	0.5 μm to 1.5 μm
Bunch Length	100 fs to 1000 fs

MODELING THE PHOTO-INJECTOR

The photocathode injector is an S-band, LCLS-type gun [3], capable of a peak field of 120 MV/m. It is powered by Nd:glass laser which provides pulses with an rms length of 2 ps to 4 ps. Nominal beam energy out of the injector is ~ 5 MeV, immediately following the injector is an accelerating section that brings the beam up to ~ 40 MeV. In this initial portion of the beamline, where space charge effects are particularly important simulations have previously been performed in ASTRA [4]. In the following section we discuss implementation of the injector in OPAL and show compare to the previous ASTRA model.

OPAL

The Object-Oriented Parallel Accelerator Library (OPAL) is a framework for modeling charged particle optics in particle accelerators [5]. Though OPAL comes in several flavors, we use version 1.4.0 of OPAL-T in all work shown here. OPAL-T is time based tracking code that includes a fully 3D particle-in-cell implementation of space charge, with an integrated Green's function Poisson solve. Space charge is calculated in the electrostatic approximation in a comoving frame with the bunch.

Many common accelerator elements are included in the code and beamlines may be constructed using a MAD-like syntax. Electrostatic, magnetostatic, and electrodynamic

fields may be specified in several 1D or 2D formats. Especially important for the work shown here, OPAL-T includes a 1D coherent synchrotron radiation model, based on Saldin *et al.* [6]. While this model is only valid in the ultra-relativistic approximation this should not pose an issue for modeling the APS linac, as the chicane is at a beam energy greater than 100 MeV. Wakefunctions may be imported in SDDS format for calculation of short-range, transverse and longitudinal wakefields.

Benchmarking OPAL-T with ASTRA

Our initial work required conversion of the prior ASTRA model of the injector and L1 accelerating section over to OPAL-T. The benchmark shown here begins at the photo-injector and run to the entrance of L2 in Fig. 1. To provide an equivalent comparison an externally defined 1000-macroparticle bunch was used in both simulation versions. The space charge solve in OPAL-T was carried out on a $32 \times 32 \times 32$ grid with open boundaries in all dimensions.

The beam energy gain through the injector and L1 accelerating section are shown in Fig. 3. It should be noted a $\sim 20\%$ adjustment of the L1 phase specified in ASTRA was required to bring the two results in agreement. This adjustment also corrected previously observed differences in curvature in the longitudinal phase space. The normalized transverse emittances and rms sizes along the accelerator are shown in Fig. 4. Because ASTRA provides emittance calculated with the canonical momentum while OPAL-T does not by default there is large discrepancy between the two in the injector solenoid field. Finally, Fig. 5 compares the bunch length and rms energy spread.

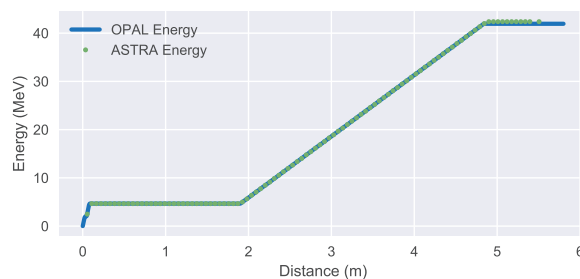


Figure 3: Average bunch energy along the beamline from OPAL and ASTRA.

Overall, extremely good agreement between the two codes is seen in all parameters. This provides confidence in the transition from ASTRA to OPAL-T moving forward with start-to-end studies. As part of this effort work is currently underway to extend the OPAL-T model past the end of the bunch compression chicane. This will allow modeling that fully captures any lingering space charge effects. Because the linac does not include any correction for longitudinal curvature, compression will likely yield a non-uniform current with a large spike at the head. This will exacerbate CSR [7] and together with longitudinal space charge effects may produce energy fragmentation [8].

Content from this work may be used under the terms of the CC BY 3.0 licence (© 2018). Any distribution of this work must maintain attribution to the author(s), title of the work, publisher, and DOI.

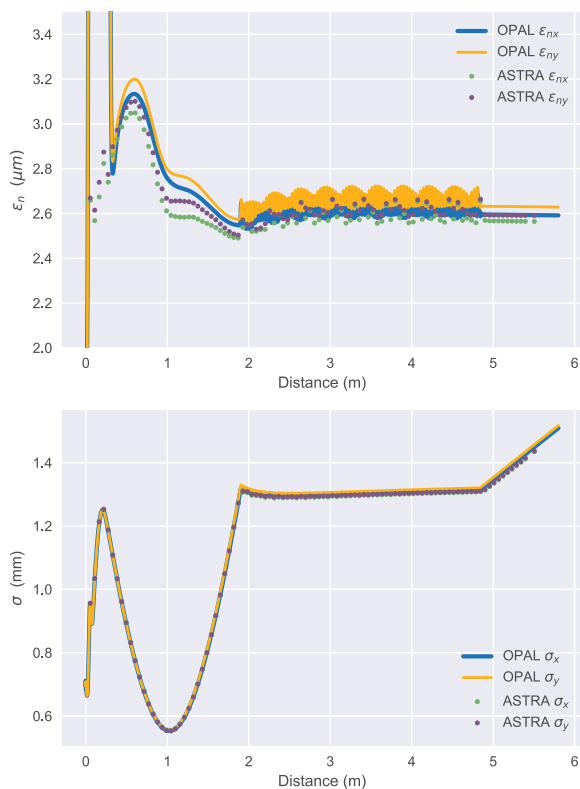


Figure 4: Top: The normalized transverse emittance along the beamline from OPAL and ASTRA. Bottom: The rms spot size of the bunch.

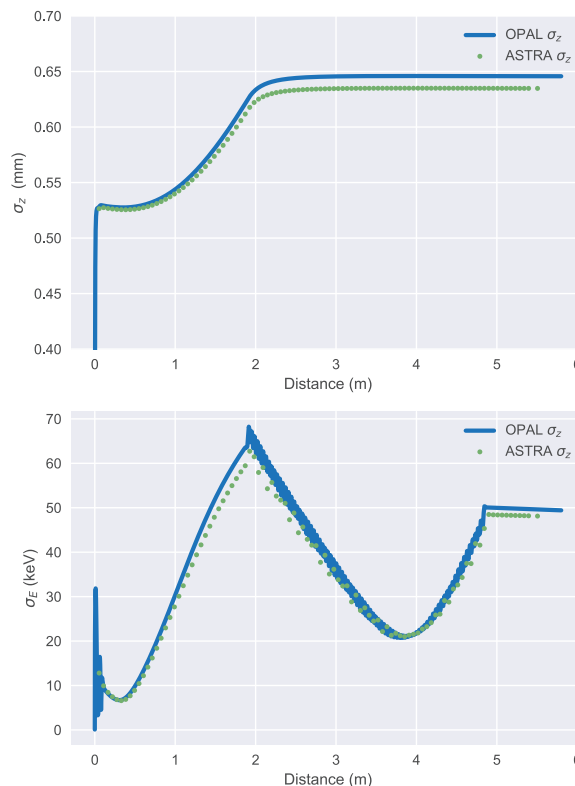


Figure 5: Top: The rms bunch length along the beamline from OPAL and ASTRA. Bottom: The rms energy spread of the bunch.

ELECTRON-BEAM REQUIREMENTS FOR TESSA

The nominal electron beam parameters from the LEA photo-injector should be able to easily achieve requirements, shown in Table 2, necessary for the 266-nm TESSA experiment. Even with degradation from effects such as CSR the transverse emittance at the undulator should remain below the 2- μm requirement.

Table 2: Beam-Quality Requirements at the Undulator Entrance for the TESSA Experiment at LEA

Property	Value
Energy	300 MeV
Energy Spread	0.02 % to 0.1 %
Peak Current	1 kA
Emittance (Normalized)	2 μm
spot size (rms)	30 μm to 40 μm
$\beta_{x,y}$	0.54 m to 1 m

The biggest foreseeable challenge is meeting the required peak current with a sufficient fraction of the bunch and min-

imal adverse effects to the energy distribution of the bunch. Because the APS linac does not have a linearizer, nonlinear effects – T_{655} from the rf and T_{566} in the chicane – will create a curved longitudinal phase space distribution with a large spike in the current, as exhibited in Fig. 6. This will result in larger uncorrelated energy spread at the high-current portion of the bunch. Furthermore, collective effects from this short, high-current region may spoil the energy distribution and interfere with the prebunching required for TESSA. Modeling of the linac in OPAL-T past the end of the compressor is underway in order to better understand what may be done to mitigate these problems.

CONCLUSION

Planning is underway to use the new LEA beamline area at the APS linac to test the high efficiency FEL concept TESSA. In preparation for this experiment start-to-end modeling of the linac and LEA beamline is underway. As part of this effort modeling of the linac photo-injector is being performed with the code OPAL. Comparisons of OPAL to previous simulations in ASTRA have shown excellent agreement. Work is now being carried out to further extend the OPAL beamline model and optimize the accelerator optics to negate possible adverse effects resulting from bunch compression.

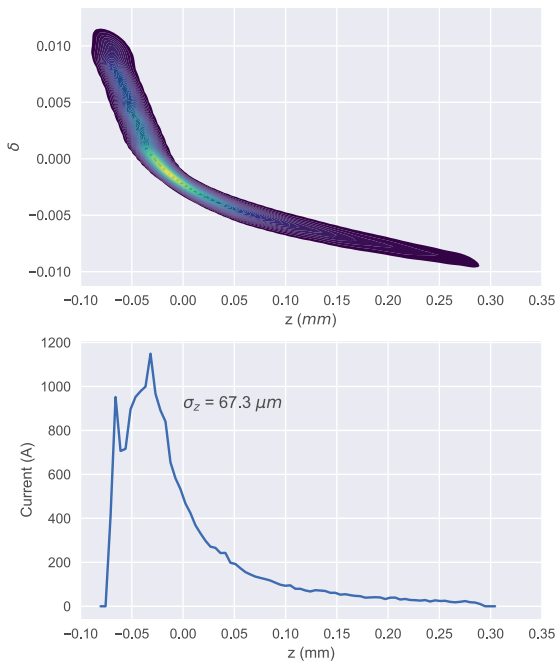


Figure 6: Top: The simulation of the longitudinal phase space of a bunch at the LEA beamline. Bottom: The current distribution of the same bunch.

ACKNOWLEDGMENT

We would like to thank A. Adelman for his assistance with setting up and running OPAL.

REFERENCES

- [1] J. Duris, A. Murokh, and P. Musumeci, “Tapering enhanced stimulated superradiant amplification,” *New Journal of Physics*, vol. 17, no. 6, p. 063036, 2015.
- [2] S. Shin, Y. Sun, and A. Zholents, “Interleaving lattice design for APS linac,” in *Proc. of NAPAC’17*, Chicago, USA, pp. 713–715, Oct. 2017.
- [3] Y. Sun *et al.*, “Commissioning of the photo-cathode rf gun at APS,” in *Proc. of FEL’14*, Basel, Switzerland, pp. 803–806, 2014.
- [4] K. Flöttmann, “Astra user manual.” www.desy.de/~mpyflo/Astra_documentation.
- [5] A. Adelman *et al.*, “The OPAL (Object-Oriented Parallel Accelerator Library) framework,” Tech. Rep. PSI-PR-08-02, Paul Scherrer Institut, (2008–2014).
- [6] E. Saldin, E. Schneidmiller, and M. Yurkov, “On the coherent radiation of an electron bunch moving in an arc of a circle,” *Nuclear Instruments and Methods in Physics Research Section A: Accelerators, Spectrometers, Detectors and Associated Equipment*, vol. 398, no. 2, pp. 373–394, 1997.
- [7] R. Li, “Sensitivity of the CSR self-interaction to the local longitudinal charge concentration of an electron bunch,” *Nucl. Instrum. Methods Phys. Res., Sect. A*, vol. 475, no. 1, pp. 498–503, 2001.
- [8] C. C. Hall *et al.*, “Measurement and simulation of the impact of coherent synchrotron radiation on the jefferson laboratory energy recovery linac electron beam,” *Phys. Rev. ST Accel. Beams*, vol. 18, p. 030706, Mar 2015.

RECENT DEVELOPMENTS AND PLANS FOR TWO BUNCH OPERATION WITH UP TO 1 μs SEPARATION AT LCLS*

F.-J. Decker, K.L.F. Bane, W. Colocho, A.A. Lutman, J.C. Sheppard, SLAC, Menlo Park, USA.

Abstract

Two electron bunches with a separation of up to 1 μs at the Linac Coherent Light Source (LCLS) is important for LCLS-II developments. Two lasing bunches with up to 220 ns separation have been demonstrated. Many issues must be solved to get that separation increased by a factor of 5. The typical design and setup for one single bunch has to be redressed for many devices. RF pulse widths must be widened, BPM diagnostics can see only one bunch or a vector average, feedback systems must be doubled, the main Linac RF likely needs to be un-SLEDED, and special considerations must be done for the Gun and L1X RF.

INTRODUCTION

Since the first two bunch test in 2010 [1], many photon experiments have been performed in recent years [2,3]. They can be categorized into pump-probe and probe-probe experiments. The first typically excites the sample and then probes it, using different photon energies for the two bunches, the first above and the second below an absorbing K-edge. Probe-probe experiments have identical bunches only differentiated by arrival time. They study the natural time evolution of the sample without disturbing it with the first pulse.

SHORTER BUNCH SEPARATION

Operation up to about 25-ns bunch separation is already considered “standard” procedure. However, attention is needed as different experiments require special setups. A typical setup for probe-probe experiments is described followed by a description of pump-probe setups, wherein the first bunch typically has a higher photon energy above a K-edge and is absorbed while the lower energy second bunch goes through and its scattering pattern is detected.

Same Bunch Performance, Just Delayed

To make two bunches with different time separation, two pulses from independent lasers are combined on the cathode, typically in S-band bucket intervals (0.35 ns). When they overlap in time, an interference pattern is generated on the gun cathode (see Fig. 1 in Ref. [4]); the temporal overlap reduces the total charge emitted from cathode by 10%. The BPM response for different delays shows a beating, determined to be an artefact of the BPM processing frequency (1/140 MHz = 7 ns) (see Fig. 2 in Ref. [4]) [5].

RF Setup The RF timing must be set up so that the two bunches have a flat energy gain versus time, this is especially problematic for long separations (over 100 ns).

Wakefield Kicks It was observed that at certain bunch separations the second bunch did not lase (Fig. 1). The rms beam trajectory in the undulator must be less than 40 μm to produce significant FEL energy.

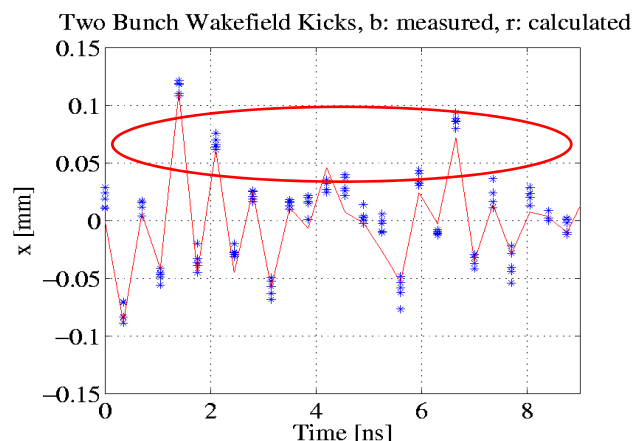


Figure 1: Timing scan of the second bunch. At certain bunch separations, the second bunch gets kicked by wake-fields and has therefore enough transverse displacement in the undulator so that it does not produce FEL radiation.

A two-mode wakefield calculation predicted a too simplistic picture of the transverse kick which slowly increases up to 2.5 ns, then decoheres around 5 ns, and recoheres afterwards [6]. The observed behaviour was consistent with the 5-ns decoherence where both bunches typically lase. But the kicks are more complicated (see Fig. 3 in Ref [4]). With a two-bucket separation, both bunches always lase since the second bunch does not get kicked. A new time-domain wakefield calculation revealed that modes 3, 6 and 10 are important and produce the observed kicks. The peak wakefield at 1.4 ns is $W_x = -2\text{V}/(\text{pC}\cdot\text{m}\cdot\text{mm})$ for an S-band structure. The X-band cavity, L1X, has 16 times larger transverse wakefields, which decohere faster; the only significant effects are at one and two bucket separation ($W_x = +38$ and $-16 \text{ V}/(\text{pC}\cdot\text{m}\cdot\text{mm})$).

* Work supported by U.S. Department of Energy, Contract DE-AC02-76SF00515.

Content from this work may be used under the terms of the CC BY 3.0 licence (© 2018). Any distribution of this work must maintain attribution to the author(s), title of the work, publisher, and DOI.

X-Ray Diagnostics

It was understood early on that it is important that the intensity of each of the two bunches is known separately.

Gas Detector The gas detector raw signal is analysed and fitted for the two bunch intensities (see Fig. 3 in Ref [4]). Intensities can be therefore equalized by the operators fine tuning. At lower soft x-ray energies or shorter delays, this method fails since the signal response is too slow. It also only partially useful when the X-rays are monochromatized making their intensities sensitive to different photon energies and statistically dependent on the pulse duration.

Fast Diode, Microchannel Plate A fast photodiode at high photon energies or a microchannel plate at low photon energies can resolve the separate bunch intensities down to few buckets (~ns) separation. A fast code was written to deal with the issues of timing jitter, amplitude noise, and ringing of the raw signals. Even a fast signal with significant ringing can see the two bunches. In this case, the second bunch had on average about 50% more intensity. An example of signal analysis for a 4.5-ns separation can be found in Fig. 5 in Ref [4].

Different Bunch Parameters

For pump-probe experiments the two bunches might be quite different in intensity, photon energy, and transverse offset at the target.

Intensity The two bunch intensities might need to be set up so that the first just excites a change, while a stronger probe is tuned for the best signal to noise response. Typically, this is set by the laser intensity at the cathode, or by mistuning the first bunch.

Energy Different photon energies can be set up by sitting on the rising or falling slope of the SLED RF pulse (Fig. 2). This works sufficiently when the bunch separation is 8.4 ns or greater. For shorter separations, the two bunches must start at different times (around 10 ps) at the gun, which then causes them to have different energies at Bunch Compressor 1 (BC1) and beyond. This makes the standard horn-cutting at BC1 not possible. A different injector optimization is required. This second mode is typical for twin-bunches with up to 100 fs separation [7] but has not yet been tried for ns-separations.

Transverse Offset Different transverse positions at the target of the experiment are the most difficult requirement. This can be done in two different ways. Since the electron bunches have different energies a vertical dispersion in the undulator will separate them and therefore the photon beams. The maximum separation should be at the source point which gets imaged onto the target. If it is not perfectly at that location, the two bunches will be more separated on the guiding and focussing mirrors and might be differently collimated. Since the dispersion will also separate the different energies inside a bunch, the following setup is pre-

ferred. The two bunches get different kicks by TCAV3 (transverse deflecting cavity) after BC2. For this method to work best the betatron phase advance must be adjusted so it is $90^\circ + n \cdot 180^\circ$ from the source point. Both methods will result in a much lower photon intensity since the two bunches will make betatron oscillations inside the undulator.

LONGER BUNCH SEPARATION

For longer bunch separation above about 100 ns, additional effects need to be considered. The RF pulse is not flat for most RF stations which are SLEDED (SLAC Linac Energy Doubler) wherein a 4- μ s pulse gets compressed into 825 ns, which corresponds to the accelerator fill time. Figure 2 shows the effective energy gain for Linac 3 (L3, the Linac section after BC2). For up to 1- μ s bunch separation, two choices can be made.

SLEDED Mode

The first is to run with the typical SLED pulse mode and run with the two bunches ± 500 ns off the peak. This will reduce the L3 energy gain from 10 to 7 GeV, or scaled for the whole Linac the maximum photon energy will reduce from 13 to about 6 keV. In this configuration, the two bunches will experience different RF kicks since for the first bunch the accelerator structure is barely half-filled with RF, while for the second pulse the main RF pulse is already gone and only some left in the second half of the structure. This can be avoided by running unSLEDED. This reduces the energy by a factor of about 1.65. The maximum photon energy will be about 4.5 keV ($= 0.36 \cdot 13$ keV) under perfect conditions.

Up to 210-ns separation in the SLEDED mode lasing was achieved with both bunches lasing (Fig. 3).

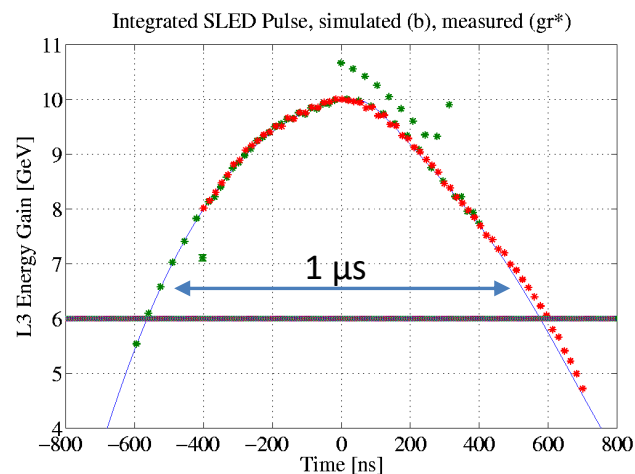


Figure 2: Energy gain in L3 due to the SLED pulse. Green and red are scaled measurements, while blue is the simulated curve. The flat line at 6 GeV indicates the energy for running unSLEDED.

Content from this work may be used under the terms of the CC BY 3.0 licence (© 2018). Any distribution of this work must maintain attribution to the author(s), title of the work, publisher, and DOI.

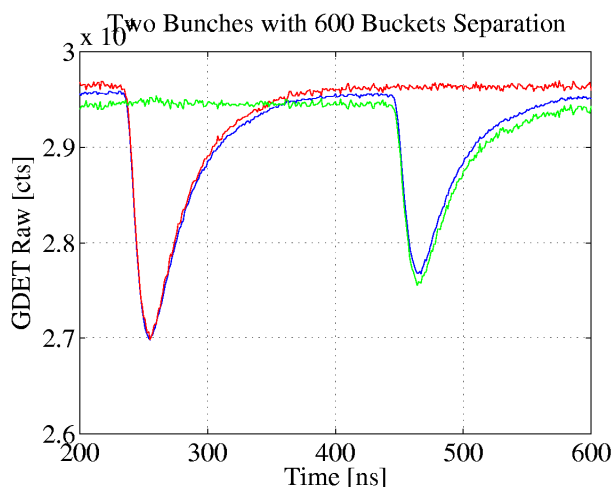


Figure 3: Gas Detector raw waveform for 600 buckets delay (210 ns). The two bunches can easily be separated (red and green out of the combined blue).

UnSLEDed Mode

It seemed difficult to achieve longer separations with the SLEDed mode above 220 ns. Since we thought it was due to RF kicks, we decided to run unSLEDed. As it turned out this was also problematic until we discovered that one trigger (of two) for the sub-boosters were not adjusted with the “PSK” timing knob. After fixing this, we achieved two bunches with a 2000-bucket (700-ns) separation having the same energy all the way through the undulator (there was not any beam time remaining for tuning lasing).

Special RF Setups

Besides the SLEDed, or unSLEDed setups there are a few RF stations which require special setups.

Special RF Stations The injector stations (L0A, L0B and L1S) run typically unSLEDed. Their pulse lengths were widened to 2 μ s (minimum: 1 μ s + 825 ns for fill time) and the timing is set so that the first bunch is close to the time when the structure is just filled and the flat part starts. The high voltage pulse of the modulator must be reasonably flat over 2 μ s.

LIX The X-band linearizer (LIX) needed a special treatment. Its fill time is only 100 ns, and its RF pulse was raised to 300 ns (from 200 ns) to have room for short delays. For separations exceeding 200 ns, a wider pulse would be necessary, but since the RF average power would be too high, a different solution was chosen. The RF is double-pulsed, utilizing two 150-ns pulses, where the second pulse can be adjusted in amplitude and phase. Initially the phase for the second bunch was adjusted so that it went through the middle of BC1. It turned out the bunch phase was about -40° incorrect (-220° instead of -160°) and the bunch was not being compressed (no charge reduction due to the horn-cutting collimators). Because the high voltage pulse of LIX is not flat but has a more rounded top, the

phase of the second RF pulse was adjusted by $+65^\circ$ (see Fig. 9 in Ref [4]).

Gun The gun RF setup is special on many fronts. First it is a standing wave setup, which reaches its highest field for a flat RF pulse exponentially. To get a flat RF amplitude in the 1.6-cell structure for a period of time after the initial rise, the incoming RF pulse has to be lowered to a value which is right for the steady state condition. But the real world is more complicated. Just after the time for the first bunch (1.4 μ s) the initial RF reflection starts to be seen reaching the gun. This must be counteracted by a much lower RF pulse with a certain phase offset. After that we got a reasonable flat pulse over 500 ns. But the second part changes daily by about $\pm 2\%$ probably due to temperature changes of the waveguide for the reflected part.

XTCAV The transverse deflecting cavity XTCAV after the undulator must run unSLEDed too. The phase of the waveform was adjusted so both bunches were close on the screen.

RF Kicks

The transverse RF kicks can be measured by taking the difference trajectory between RF off and RF on. The measurements for all RF stations revealed that the klystron station 21-3 right after BC1 caused a significant kick in the horizontal (x).

A \sim mm accelerator structure misalignment was confirmed by looking at the wakefield kicked orbit. The main kick in x starts at BPM number 20, which is the same location like the RF kick. To quantify the misalignment a betatron oscillation was fitted with kicks at different locations. At three locations of BPM #25, 30, and 35 a 2-mm offset each would “explain” the strange oscillation, but only a 1-mm offset was necessary to get the big initial kick at BPM #20. The induced non-linear oscillation looks as if caused by an offset and is probably increased by the addition of the wakefield tail of the bunch being kicked. After making a local 1-mm orbit bump, the wakefield and RF kick were reduced by an order of magnitude.

MULTIPLE BUNCHES

After the successful run of several photon experiments with two bunches, people are interested in multiple bunches. We are currently setting up a split and delay and combine system for the injector lasers to get two times four bunches, each of the four separated by two buckets [8].

CONCLUSION

Two bunches with many ns separation has opened many different scientific fields.

ACKNOWLEDGMENT

We would like to thank the laser group for all the special laser setups to make two and multi bunch scenarios possible.

REFERENCES

- [1] F.-J. Decker *et al.*, “A demonstration of multi-bunch operation in the LCLS”, *Proc. of FEL’10*, Malmö, Sweden, WEPB33.
- [2] M. H. Seaberg *et al.*, “Nanosecond x-ray photon correlation spectroscopy on magnetic skyrmions”, *Phys. Rev. Letters*, accepted 10 July 2017.
- [3] Y. Feng *et al.*, “Direct experimental observation of the gas filamentation effect using a two-bunch x-ray FELK beam”, arXiv:1706.02352, May 2017.
- [4] F.-J. Decker *et al.*, “Recent developments and plans for two bunch operation with up to 1 μ s separation at LCLS”, Report No. SLAC-PUB-17128, SLAC, 2017.
- [5] F.-J. Decker *et al.*, “Two bunches with ns-separation with LCLS”, *Proc. of FEL’15*, Daejeon, Korea, WEP023.
- [6] K. L. F. Bane, “Wakefield calculations for the LCLS in multi-bunch operation”, *Proc. of IPAC’11*, San Sebastian, Spain, MOPS085.
- [7] A. Marinelli *et al.*, “High-intensity double-pulse X-ray free-electron laser”, *Nat. Commun.* 6, p. 6393. (2015).
- [8] J. Cryan, P. Bucksbaum, and R. Coffee, “Field-free alignment in repetitively kicked nitrogen gas”, *Phys. Rev. A* 80 p. 063412 (2009).

STOCHASTIC EFFECTS FROM CLASSICAL 3D SYNCHROTRON RADIATION

B. Garcia*, T. O. Raubenheimer, SLAC, Menlo Park, USA
 R. Ryne, Lawrence Berkeley National Laboratory, Berkeley, USA

Abstract

In most cases, the one-dimensional coherent synchrotron radiation wakefield gives an excellent approximation to the total coherent effect due to classical synchrotron radiation in bend magnets. However, full particle Liénard-Wiechert simulations have revealed that there is non-numerical, stochastic noise which generates fluctuations about the approximate 1D solution. We present a model for this stochastic term in which this noise is due to long-range interaction with a discrete number of synchrotron radiation cones. The nature of this noise and how it depends on the 3D dimensions of the beam are explored.

INTRODUCTION

Much study has focused on the so-called Coherent Synchrotron Radiation (CSR) effect in bend magnets [1] [2] [3] [4]. Radiation from the tail of the electron bunch catches up with the head electrons where it exchanges energy with them. This leads to a well-known, one-dimensional wakefield which is a deterministic function of the longitudinal distance along the bunch.

While this wakefield is often undesirable and can lead to emittance growth in bend magnets [5], it is a deterministic function and can therefore in principle always be removed. Other effects which can cause emittance degradation are stochastic in nature, and thus provide an irreversible heating of the beam. Two effects are especially important in the context of bending magnet systems: Incoherent Synchrotron Radiation (ISR) [6] and Intra-Beam Scattering (IBS) [7]. ISR is caused by the quantum nature of the synchrotron radiation emission process, and its effect on the beam grows strongly with electron beam energy. By contrast, IBS is caused by multiple small-angle Coulomb scattering events and increases with electron beam density.

Computational results in the past few years have suggested that the CSR wakefield result also contains a stochastic component [8] [9]. Recently, an analytical model has been developed which explains this stochastic noise term [10]. The goal of this paper is to compare the analytical theory with computational results obtained from full 3D Liénard-Wiechert simulations.

THEORY OVERVIEW

The full theory on the stochastic origin of the CSR noise is presented in [10], so we first briefly present the main results. The analytical theory is based on a 3D extension of the steady state two-dimensional CSR model developed

by Huang, Kwan, and Carlsten [11]. In this work they noticed a long-ranged, narrow cone of longitudinal synchrotron radiation trailing behind the electron. It is this feature of the radiation profile which is ultimately responsible for the noise.

We describe the electron bunch and radiation via the scaled coordinates $\alpha = s/R$, $x = \chi/R$, and $y = \Upsilon/R$, where s is the arclength along a circular trajectory of radius R , χ is the physical radial displacement, and Υ the physical vertical displacement. It is found that this long-ranged longitudinal radiation component has magnitude $E_s^T \approx \frac{-q\beta^2\gamma^4}{\pi\epsilon_0 R^2}$ for a beam with relativistic factor γ . The net effect of this region integrated over a uniform electron beam is found to be zero. However, counting statistics on the number of particles contained within this region leads to a stochastic variation in the total field.

This field region does not decay in the radial dimension but opens up in the vertical plane. This leads to two distinct regimes characterized by the parameter $\Xi \equiv \frac{\gamma^4\sigma_y^4}{\sigma_x^2}$, where $\sigma_{x,y}$ are the (scaled) rms beam sizes for a Gaussian electron distribution. The case of $\Xi \ll 1$ is essentially a 2-D beam, while for $\Xi \gg 1$ the beam's vertical size is much larger than the radiation extent.

The probability f that an electron in a group of N_p electrons will be contained within the trough can be computed analytically. There will therefore be a variance in the total (longitudinal) field due to this finite number of contained electrons which can be expressed as,

$$\sigma_{E_s} = g E_s^T \sqrt{f N_p}, \quad (1)$$

where g is an $O(1)$ geometric factor related to the non-constant value of the field across the trough ($g = 4/9$ for a parabolic profile, for example). While the exact expression is complicated, the scaling of this field variance with energy can be written down in the two Ξ regimes as,

$$\sigma_{E_s} \sim \begin{cases} \gamma^2 & \Xi \gg 1 \\ \gamma^{2.5} & \Xi \ll 1 \end{cases}. \quad (2)$$

The above result is derived for the variations in the field at the center of the electron bunch. However, one can easily generalize the electron fraction f for an off-radial electron with displacement $a = x/\sigma_x$. The resulting ratio of f factors

* bryantg@stanford.edu

is given by the more complicated expression,

$$\frac{f(a)}{f(a=0)} = \begin{cases} e^{-\frac{a^2}{2}} \left({}_1F_1 \left[\frac{3}{4}; \frac{1}{2}; \frac{a^2}{2} \right] \right. \\ \left. + \frac{\sqrt{2}a\Gamma\left(\frac{5}{4}\right)}{\Gamma\left(\frac{3}{4}\right)} {}_1F_1 \left[\frac{5}{4}; \frac{3}{2}; \frac{a^2}{2} \right] \right) & \Xi \gg 1 \\ \operatorname{erf}\left(\frac{a}{\sqrt{2}}\right) + 1 & \Xi \ll 1 \end{cases}, \quad (3)$$

where ${}_1F_1$ is the generalized hypergeometric function.

These results are true for an electron bunch in a bend magnet at a single instance. We must also understand how this field variation evolves in time, or distance, through the bend of length z .

In a simple (zero-emittance) model, off-center electrons simply travel on displaced circular trajectories. As a result, they drift slightly in relative position with respect to the central particle and traverse the trough region of radiation. After a short evolution distance \bar{z} , all electrons which were previously contained in this region have left and a new cohort has entered. This distance \bar{z} can be considered as the step size in a fixed-time random walk. This geometric motion gives,

$$\bar{z} = \frac{4R}{\sqrt{2\pi}3\gamma^3\sigma_x} \left(-\gamma_E + \log 2 - \log \frac{b}{\sigma_x} \right), \quad (4)$$

where $b = 4/(3\gamma^3\Theta)$ for a total evolution angle of Θ , and $\gamma_E \approx 0.577$ is the Euler-Mascheroni constant. These variations in longitudinal field lead to a diffusion in energy according to,

$$\sigma_E = q\sigma_{E_s} \sqrt{z\bar{z}}. \quad (5)$$

This diffusion of energy is therefore proportional to $\gamma^{0.5 \sim 1}$, depending on Ξ , and inversely proportional to the electron beam density (through both the factors f and \bar{z}). These are the essential scaling results we wish to compare with numerical simulations.

LIÉNARD-WIECHERT SOLVER

The Liénard-Wiechert code used in this study is a massively parallelized Liénard-Wiechert solver designed to simulate a realistic ($> 10^9$) number of electrons [8]. By simple superposition, then, one computes the total electric field by summing the individual Liénard-Wiechert contributions. This allows the modeling of realistic discrete particle effects, one manifestation of which is the above-derived noise about the deterministic solution.

This model is steady state in that it assumes the trajectories of the particles to be perfect circles which can be traced arbitrarily far back in time. Practically, this means that it is only a good model once the electron bunch is sufficiently deep within the bend magnet ($z > \sqrt[3]{24\sigma_z R^2}$) [4].

As an evolution code which can step the particle distribution through a finite bend angle, the simulation is not self consistent. Although the fields are computed at each time

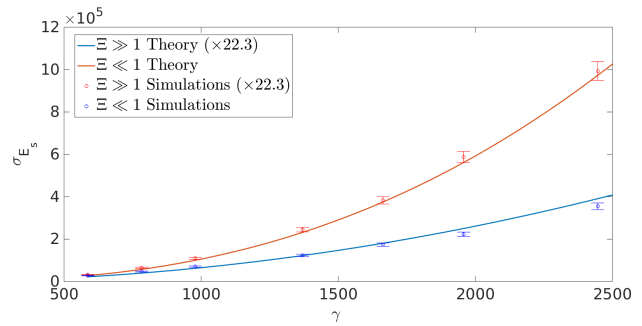


Figure 1: Comparison between theory and simulation for the variation in the longitudinal CSR field with γ for both $\Xi \gg 1$ and $\Xi \ll 1$ bunches.

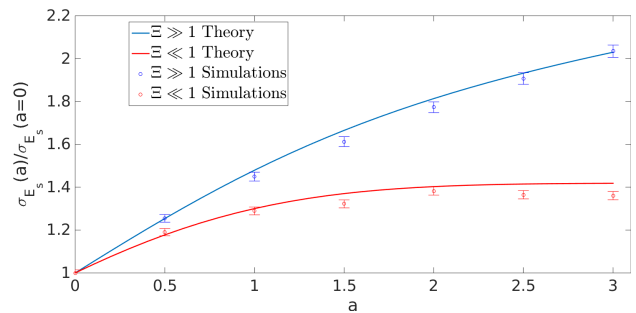


Figure 2: A comparison of the off-axis field variation $\sigma_{E_s}(a)$, normalized to its central value $\sigma_{E_s}(a=0)$ for both $\Xi \gg 1$ and $\Xi \ll 1$ bunches.

step, they do not interact back on the electrons. This is equivalent to maintaining the electron distribution shape which distorts only geometrically. Future study may illuminate whether or not this restriction turns out to be overly limiting.

COMPARISON WITH LIÉNARD-WIECHERT SIMULATIONS

The first result to compare is the γ dependence of the variation in the longitudinal field. The electron beam used has a charge of 10 pC, and is therefore composed of 6.25×10^7 electron macroparticles. The bend radius is taken to be one meter in all studies. We compare the results from the analytical theory for the field at bunch center (Eqn. 1) and 500 separate simulations in Fig. 1.

The simulation with $\Xi \ll 1$ has $\sigma_x = 1 \times 10^{-5}$, $\sigma_y = 5 \times 10^{-7}$, and $\sigma_z = 1 \times 10^{-5}$, while the $\Xi \gg 1$ has $\sigma_x = 5 \times 10^{-7}$, $\sigma_y = 1 \times 10^{-4}$, and $\sigma_z = 1 \times 10^{-4}$. The error bars in the simulation data points represent the finite simulation sample size. A value of $g = 0.33$ is assumed for the each analytical calculation. The agreement between simulation and theory is remarkably good with the adjusted value of g , confirming the γ dependence of Eqn. 2.

We also simulate the field in off-axis locations to test the radial dependence of Eqn. 3. The results are shown in Fig. 2 for 5000 simulations of both a $\Xi \gg 1$ and $\Xi \ll 1$ beam. Both simulations have $E = 500$ MeV with 6.24×10^6 particles and $\sigma_x = \sigma_r = 10^{-5}$. The $\Xi \ll 1$ simulation has

Content from this work may be used under the terms of the CC BY 3.0 licence (© 2018). Any distribution of this work must maintain attribution to the author(s), title of the work, publisher, and DOI.

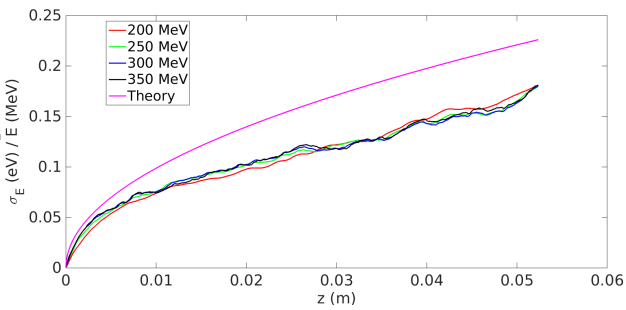


Figure 3: The cumulative diffusion in energy, normalized to the mean electron energy, due to the longitudinal field through the bend. The four averaged simulation curves are shown for each energy are each computed from 100 separate realizations of the electron beam. The 200 MeV analytic curve is shown in magenta.

$\sigma_y = 5 \times 10^{-7}$ while the $\Xi \gg 1$ case has $\sigma_y = 4 \times 10^{-5}$. The agreement between simulation and theory is quite good here as the theoretical uncertainty of the g factor of Eqn. 1 is normalized out.

Having established agreement between theory and simulation for the static field result, we turn to the evolution of this field and resulting diffusion. Again, we are primarily interested in two aspects of this diffusion: its scaling with energy and beam density.

For these simulations, we take the electron beam to have an energy 200-350 MeV and low charge 1 pC, which then evolves through three degrees of a 1 m bend magnet. The evolution proceeds in discrete steps of size $\delta z \approx 25 \mu\text{m}$, which is sufficient to resolve the noise structure at these low energies. The electron beam for this study has $\sigma_\alpha = \sigma_x = 10^{-5}$, and $\sigma_y = 10^{-6}$. For each beam energy, 100 separate runs are performed and compared with the analytical results in Fig. 3.

While the normalization of the analytical result is in slight disagreement, this is not entirely unexpected. The definition of \bar{z} as computed in Eqn. 4, and the \bar{z} which represents the fixed-time random walk step size are not necessarily identical. Nevertheless, Fig. 3 supports both the γ^{-1} dependence (in this $\Xi \ll 1$ regime), as well as the $\sqrt{\bar{z}}$ random walk character of the cumulative energy change.

In order to investigate the dependence on the radial beam size σ_x , we fix the energy and simulate beams with several different values for σ_x . Evolution curves for various values of σ_x are plotted in Fig. 4. These simulations have $E = 200\text{MeV}$, $\sigma_\alpha = 5 \times 10^{-5}$, and $\sigma_y = 10^{-6}$, and 6.24×10^6 electrons. The scaled curves represent the $\sigma_x = 5 \times 10^{-5}$ curve scaled according to the theoretical prediction for \bar{z} of Eqn. 4. As before, the normalization is off due to the ambiguity in converting between the differing values for \bar{z} . However, the scaled curves accurately reproduce the σ_x dependence, supporting the logarithmic dependence of Eqn. 4.

Given the myriad of assumptions that enter into ultimately obtaining Eqn. 5, the agreement between simulation and

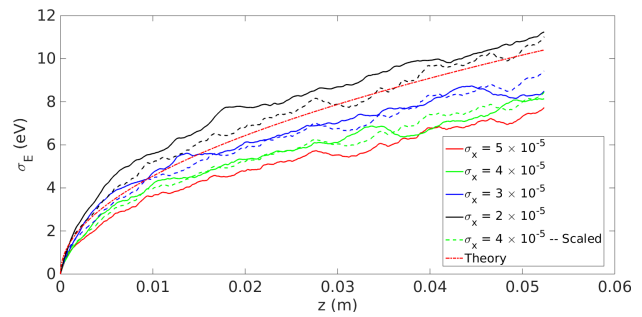


Figure 4: The cumulative diffusion in energy for various values of σ_x . Each computational curve is the result of 100 separate simulations. The dashed scaled curves are taken from the $\sigma_x = 5 \times 10^{-5}$ and scaled according to Eqn. 4 and 5. The theory curve is the pure result from Eqn. 5.

theory, especially in the scaling with various parameters, is remarkable. This suggests that the essential physics encapsulated in Eqn. 5 is more or less correct.

DISCUSSION

We have provided a comparison of the analytical theory of stochastic synchrotron radiation effects to full particle simulations. In all the various scaling parameters compared, the agreement is quite good, although there is an $O(1)$ ambiguity in the absolute normalization of the theory. There are however two main limitations on the results of this study.

The first is that only the longitudinal field E_s has been computed in detail and compared with simulations. The full theory predicts that there should be a similar noise term in both the radial and vertical synchrotron radiation fields [10]. It may be the case that the direct contribution to emittance growth via radial and vertical fields is more important than the dispersion-induced growth from the noisy longitudinal field. Further work should therefore explore the other dimensions of the field in simulation and theory.

The second main limitation is that neither the analytical theory nor the simulation model the reaction of the electron distribution to the radiation. Further work should develop, if not a self consistent model, at least an analytically guided result for how this bunch distortion would take place. This might begin with, for example, a z -dependent bunch profile which distorts under the influence only of the 1D-CSR mean field result. Such a study will illuminate the effect, if any, to which a self-consistent model would differ from the one derived and simulation in this work.

ACKNOWLEDGMENTS

This work was supported in part by the U.S. Department of Energy under Contract No. DE-AC03-76SF00515 and the Stanford University Bob Siemann Fellowship in Accelerator Physics.

REFERENCES

- [1] G. Schott, "Electromagnetic radiation," 1912.
- [2] J. Schwinger, "On the classical radiation of accelerated electrons," *Physical review*, vol. 75, no. 12, p. 1912, 1949.
- [3] J. Murphy, R. Gluckstern, and S. Krinsky, "Longitudinal wake field for an electron moving on a circular orbit," *Part. Accel.*, vol. 57, no. BNL-63090, pp. 9–64, 1996.
- [4] E. L. Saldin, E. A. Schneidmiller, and M. Yurkov, "On the coherent radiation of an electron bunch moving in an arc of a circle," *Nuclear Instruments and Methods in Physics Research Section A: Accelerators, Spectrometers, Detectors and Associated Equipment*, vol. 398, no. 2-3, pp. 373–394, 1997.
- [5] P. Emma and R. Brinkmann, "Emittance dilution through coherent energy spread generation in bending systems," in *Proceedings of the 1997 Particle Accelerator Conference*, vol. 2. IEEE, 1997, pp. 1679–1681.
- [6] J. D. Jackson, *Classical electrodynamics*, 3rd ed. New York, NY: Wiley, 1999.
- [7] J. Bjorken and S. Mtingwa, "Intrabeam scattering," *Particle Accelerators*, vol. 13, no. 3-4, pp. 115–143, 1983.
- [8] R. Ryne *et al.*, "Large scale simulation of synchrotron radiation using a liendard-wiechert approach," *Proc. IPAC*, 2012.
- [9] "Using a liendard-wiechert solver to study coherent synchrotron radiation effects," in *Proceedings of the 2013 FEL Conference*, 2013, pp. 17–23.
- [10] B. Garcia, T. Raubenheimer, and R. Ryne, "Stochastic coherent synchrotron radiation effects," *Phys. Rev. Lett.*, In Prep.
- [11] C. Huang, T. J. T. Kwan, and B. E. Carlsten, "Two dimensional model for coherent synchrotron radiation," *Phys. Rev. ST Accel. Beams*, vol. 16, p. 010701, Jan 2013. [Online]. Available: <https://link.aps.org/doi/10.1103/PhysRevSTAB.16.010701>

CANCELLATION OF COHERENT SYNCHROTRON RADIATION KICKS AT LCLS

D. Z. Khan[†], T. O. Raubenheimer, SLAC, Menlo Park, USA

Abstract

In this paper, we look at a phase advance manipulation technique used for the Coherent Synchrotron Radiation (CSR) emittance growth cancellation pioneered by D. Douglas [1]. The idea was then further developed by R. Hajima in the matrix formalism and later extended in the Courant-Snyder formalism by S. Di Mitri [2,3]. With the ever-growing demands of high energy, short wavelength Electron Storage Rings (ESR) and Free Electron Laser (FEL) drivers, the CSR effect has proven to be a detrimental factor in emittance stability. Under linear approximation, it has been shown that the CSR induced dispersive kicks in successive bending magnet systems can, with careful balancing of the linac optics, cancel each other to nullify the bend plane emittance growth. This technique of optics balancing in the constant bunch length regime is the focus of this paper. We will present our findings, analytically and numerically, of the emittance measurements for the current Linac Coherent Light Source (LCLS) dogleg system (DL2).

INTRODUCTION

Bending systems in linear accelerators are essential for beam transport and bunch compression. When electrons travel in curved orbits in the bending magnets of an accelerator they emit synchrotron radiation [4]. For longer bunches, the electrons radiate independently and the radiation is incoherent with a power scaling of N , the number of electrons in the bunch. The situation is vastly different when the bunch length becomes ultra-short and comparable to the radiation's wavelength; the electrons begin to radiate as a unit and the radiation is coherent with a power scaling of N^2 . The dramatic increase in radiation power for the coherent case has the ability to induce a sizable energy chirp along the beam which will, consequently, dilute the transverse emittance of the beam as its transported through the linac [5]. Conserving the transverse emittance is essential in delivering high brightness electron beams. The CSR radiation induces a variation of the electron energy that is correlated along the longitudinal bunch coordinate (barring transverse effects). It is in this correlation that we may manipulate and attempt to suppress the CSR driven transverse emittance dilution.

The LCLS at the Stanford Linear Accelerator Center (SLAC) is one of the world's premiere X-ray free-electron laser (XFEL) facilities. It is the source of the brightest coherent radiation in the sub-nanometer wavelength regime and has remarkable capabilities in the bio-

logical, chemical, material science and the molecular research fields [6-8]. After injection, the beam transport line consists of a two-stage bunch compression system with three accelerating sections, as shown in Figure 1. The bunch length at the second bunch compressor is short ($\sim 10 \mu\text{m}$) and the radiation emitted in the dipoles is coherent for the wavelengths comparable to the electron bunch length.

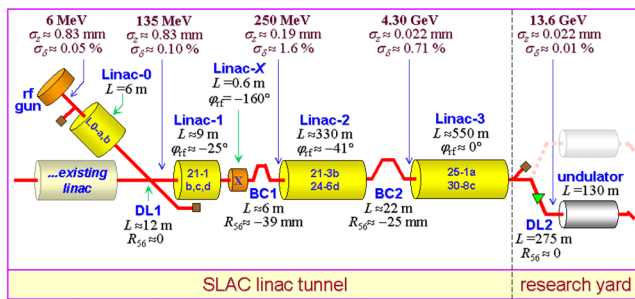


Figure 1: LCLS beamline schematic.

At the end of the 3rd linac section is a dogleg (DL2) bending system implemented to transport the electron bunch to the undulator beamline. It is at this location where we will conduct our studies of CSR emittance growth cancellation via optics balancing. As we will see, with careful balancing of the optics in between the dispersive CSR kicks in BC2 and DL2, we can orient the kicks to cancel each other and preserve transverse emittance along the beam line.

OPTICS BASED BALANCING OF CSR DISPERSIVE KICKS

We first acquaint ourselves with Hajima's first order matrix approach to the analysis of CSR induced transverse emittance growth [3]. To the first order, the bend plane space coordinates can be written as $x(s) = (x, x', \delta_0, \kappa L_B, \kappa)^T$ where x is the deviation from the on energy path, x' is derivative of the deviation with respect to the ideal path, δ_0 is the initial relative energy deviation, L_B is the magnet length, and κ is the normalized CSR wake potential in a bend magnet measured in [eV/m]. In this formalism, the CSR energy deviation is found by $\delta_{\text{CSR}} = \kappa L_B$. When a particle gains or loses energy within a bending system, its transverse coordinates are altered with respect to the on-energy path as $\Delta x = R_{16}\delta$ and $\Delta x' = R_{26}\delta$, where the matrix terms R_{16} and R_{26} are the first order dispersion and its slope. The corresponding bend magnet matrix can then be constructed via the Green's function method to include the effect of CSR [9]:

*Work supported by the U.S. Department of Energy under contract No. DE-AC03-76SF00515

[†] donish@SLAC.stanford.edu

Content from this work may be used under the terms of the CC BY 3.0 licence (© 2018). Any distribution of this work must maintain attribution to the author(s), title of the work, publisher, and DOI.

$R_{\text{BEND}} =$

$$\begin{pmatrix} \text{Cos}(\theta) & \rho \text{Sin}(\theta) & \rho(1 - \text{Cos}(\theta)) & \rho(1 - \text{Cos}(\theta)) & \rho^2(\theta - \text{Sin}(\theta)) \\ -\frac{1}{\rho} \text{Sin}(\theta) & \text{Cos}(\theta) & \text{Sin}(\theta) & \text{Sin}(\theta) & \rho(1 - \text{Cos}(\theta)) \\ 0 & 0 & 1 & 0 & 0 \\ 0 & 0 & 0 & 1 & \rho\theta \\ 0 & 0 & 0 & 0 & 1 \end{pmatrix}$$

where ρ is the bending radius and θ is the bending angle of the dipole magnet. This is an extension of the dispersion matrices used in beam transport, but with the addition of a CSR dispersive kick element. Combining the matrices for a simple bend-drift-bend system, as is the case with the LCLS DL2, we can compile a system where the CSR spatial and angular kicks are explicitly written and a cancellation scheme can be quantified.

Alternatively, S.D. Mitri extended this matrix approach to the Courant Snyder (C-S) formalism [10]. For a particle with the reference energy, the invariant, bend-plane deviation and angle are $J = x = x' = 0$. Upon traversing a bending magnet, the particle will receive a CSR energy kick, which will instantaneously alter the particle's invariant and bend plane phase space coordinates with respect to the ideal path:

$$\begin{aligned} X &= \sqrt{2J\beta} \text{Cos}(\phi) = \eta \delta_{\text{CSR}} \\ X' &= -\sqrt{\frac{2J}{\beta}} (\alpha \text{Cos}(\phi) + \text{Sin}(\phi)) = \eta' \delta_{\text{CSR}} \\ 2J &= \gamma X^2 + 2\alpha X X' + \beta X'^2, \end{aligned} \quad (2)$$

where β and α are the Twiss optics functions, γ is $(1 + \alpha^2)/\beta$, and ϕ is the phase advance. Subsequent magnets result in the same addition to the transverse deviation, angle and invariant. The ensemble average of each particle's invariant in the beam is the representative transverse emittance, $\langle J_i \rangle = \epsilon_x$. The results are equivalent as those derived in the Hajima matrix approach though achieved in a different way. Each method has their strengths and merits depending on the situation in which they are to be implemented.

Both methodologies assume that the bunch length is constant between successive bending magnets and therefore the CSR RMS energy spread induced on the beam is identical for each bend. This assumption greatly simplifies the mathematics of the system. Although, these methods are still valid in systems where the bunch length is evolving, such as bunch compressors, the mathematics is quite rigorous adding an extra variable for each CSR energy spread term of each bend involved in the system.

LCLS DOGLEG2

The LCLS DL2, sketched in Figure 2, is a bending system consisting of 4 dipole magnets which form two double-bend achromats [11]. The parameters of the system are such that the dispersion function is symmetric and its

derivative is anti-symmetric across a single achromat. The Twiss parameters are roughly symmetric across the two achromats, and the phase advance between the two magnets in each achromat is roughly π , as shown in Table 1.

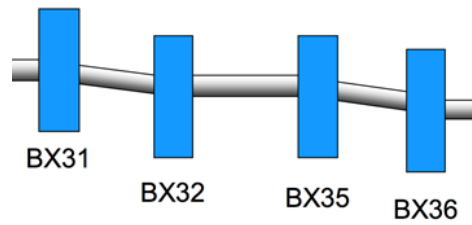


Figure 2: Cartoon of the dipole layout of DL2 of LCLS-I.

In the nominal operation of the LCLS, there are two prominent sources of CSR transverse emittance growth located at BC2 and DL2 as can be seen in Figure 3 of the normalized (dispersion corrected) transverse emittance along the beamline. The CSR energy kick experienced by the beam will be constant in each of the magnets of DL2 due to the fact that the bunch length is not changing and is a prime candidate for the aforementioned CSR emittance growth cancellation via optics balancing techniques. We apply the principles of Douglas, Hajima and Mitri to develop a configuration where the dispersive CSR kicks of BC2 and DL2 cancel each other to minimize the cumulative transverse emittance growth of the beam.

Table 1: Various Twiss parameters for DL2

Magnet	β_x	α_x	η_x	η'_x
BX31	33.5 m	2.3	0.01 m	0.0087
BX32	48.1 m	-3.3	0.01 m	-0.0087
BX35	38.0 m	2.6	-0.01 m	-0.0087
BX36	54.5 m	-3.75	-0.01 m	0.0087

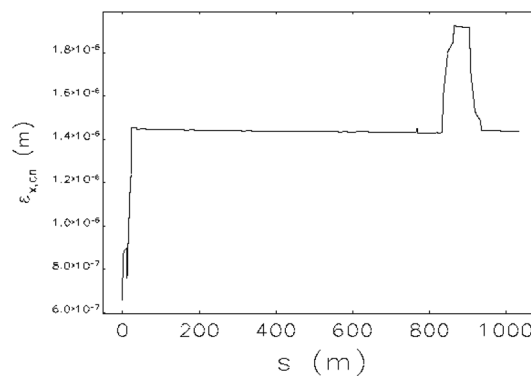


Figure 3: Map of the dispersion-corrected transverse emittance along the LCLS (to shortly past DL2) under nominal settings.

Content from this work may be used under the terms of the CC BY 3.0 licence (© 2018). Any distribution of this work must maintain attribution to the author(s), title of the work, publisher, and DOI.

For this, we follow Mitri's routine in modelling the CSR kicks under the C-S formalism. As a particle exits BC2 (S_0), it leaves with some transverse invariant growth, ΔJ , resulting from the CSR effect from the four bending magnets of the chicane. The CSR induced invariant growth from BC2, J_0 , will have some associated transverse phase space coordinates:

$$X_{BC2}(S_0) = \sqrt{2J_0\beta(S_0)}\cos(\phi(S_0)),$$

$$X'_{BC2}(S_0) = -\sqrt{\frac{2J_0}{\beta(S_0)}}\left(\alpha(S_0)\cos(\phi(S_0)) + \sin(\phi(S_0))\right). \quad (3)$$

The particle continues along the beamline, while undergoing betatron oscillations, until it encounters the first magnet of DL2 (BX31), in which another CSR dispersive kick is added to its transverse phase space coordinates. The new coordinates are as follows:

$$\begin{aligned} X_{BX31} &= X_{BC2}(\phi(S_1)) + \eta_{BX31}\delta_{DL2} \\ X'_{BX31} &= X'_{BC2}(\phi(S_1)) + \eta'_{BX31}\delta_{DL2}, \end{aligned} \quad (4)$$

where $\phi(S_1)$, η_{BX31} , η'_{BX31} , δ_{DL2} is the phase advance (relative to BC2), dispersion and its slope, and normalized CSR energy kick at the location of BX31, S_1 , respectively. After the CSR kick, the particle's invariant is changed to $2J = \gamma X_{BX31}^2 + 2\alpha X_{BX31}X'_{BX31} + \beta X_{BX31}'^2$. Again, at BX32 the particle receives another CSR dispersive kick for each bending magnet and the process reiterates for the calculation of the transverse phase space coordinates and invariant as the particle travels through the entire system.

The goal now is to find the phase advance in the L3 linac section and the drift space separating the two achromats of DL2 (from BX32 to BX35) that will achieve optimal cancellation of the CSR kicks. Since we do not know the parameters and details of the CSR kick from BC2 (it is a superposition of the CSR kicks from each of the 4 bending magnets of the chicane, though with different strengths at each bend due to evolving bunch length in the system) we must employ numerical techniques to achieve this optimization.

SIMULATION STUDIES

We can compare our analytical findings with that of simulation studies of the system using the particle tracking code ELEGANT [12]. For this we have developed a phase advance shifter (postscript deriving the phase advance matrix for given Twiss parameters) in L3 and the drift space between the two achromats in DL2, which can be used to scan the phase advance in each section to see its effect on the transverse emittance growth at the exit of

DL2. The phase advance shifter is implemented in ELEGANT as a theoretical, zero-length matrix element that shifts only the phase advance at that particular location while preserving all other parameters. For completeness, we scanned the phase advance at each location from 0 to 360 degrees in increments of 10 degrees. The results of the phase advance scans are shown in Figure 4 and demonstrate significant transverse emittance preservation with an additive phase advance of 170 and 190 degrees in L3 and the middle drift section in DL2, respectively.

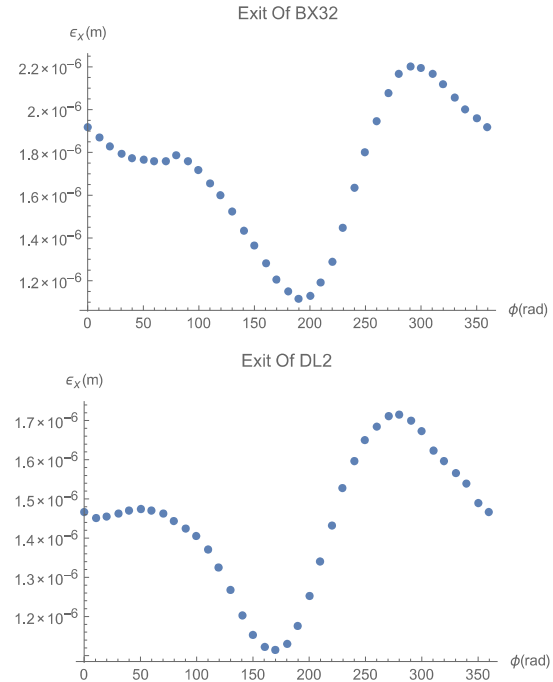


Figure 4: Phase advance scan using theoretical phase advance matrix element in ELEGANT. Top: Transverse emittance plotted at the exit of BX32 for phase advance scans of L3. A minimum is found at 190 degrees. Bottom: Phase advance scan of middle drift in DL2 with a transverse emittance minimum found at 170 degrees.

To actually vary the phase advance in the LCLS machine for demonstration, we would need to configure the quadrupole settings in the linac sections. We can emulate this procedure in ELEGANT by solving for the correct quadrupole configuration in L3 and the drift section of DL2 to achieve the appropriate phase advance conditions. The transverse emittance along the accelerator with the new quadrupole configuration for the optimal phase advance solution is shown in Figure 5. The emittance preservation is considerable when comparing it to the nominal settings in Figure 3.

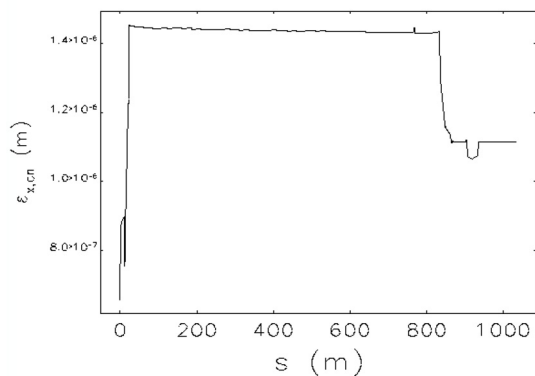


Figure 5: Transverse emittance plot of the LCLS beamline up to the undulator with the altered quad settings.

A POSSIBLE EXPERIMENTAL PROPOSAL AT LCLS

In the previous section, we have shown that there exists a configuration based simply on the optical functions of a multi-bend system that can successfully suppress the CSR emittance growth. To experimentally verify such a phenomenon with the actual LCLS machine we are required to manipulate the phase advance in L3 and the drift space in DL2 by altering the strength of the quadrupoles. The challenge in this task comes from adjusting the quads to meet our specific phase advance requirement while ensuring that matching of the optic functions is preserved so as not to generate emittance dilution due to optics mismatch [13-15]. For this, we will be creating a “tuning knob” for the phase advance that could be programmed into the main controls of the LCLS accelerator to vary the quadrupole strengths with the ability to scan a full 2π phase advance to study the optics-balance effect on the transverse emittance.

CONCLUSION

In this paper, we have demonstrated an application of the Twiss optics balance technique for mitigation of the CSR induced emittance growth between bending systems. The technique relies on de-constructively aligning the CSR spatial and angular kicks in phase space between successive bending magnets. This is achieved by properly tuning the Twiss parameters and phase advance between the sources of CSR. In the case of the LCLS, it was numerically shown that with the proper phase advance condition between BC2 and DL2 the cumulative CSR emit-

tance growth can be suppressed. This technique promotes a simple method of beam optimization that may be used in today’s operating linacs and FELs.

ACKNOWLEDGMENT

We would like to thank Simone Di Mitri for helpful communications. This work was supported by the U.S. Department of Energy under Contract No. DE-AC03-76SF00515.

REFERENCES

- [1] D. Douglas, “Thomas Jefferson National Accelerator facility report”, no. JLAB-TN-98-012, 1998.
- [2] S. Di Mitri, M. Cornacchia, and S. Spampinati, *Phys. Rev. Lett.* vol. 110, pp. 014801, 2013.
- [3] R. Hajima, *Jpn. J. Appl. Phys.*, vol. 42, pp. L974-L976, 2003.
- [4] J. D. Jackson, *Classical Electrodynamics* 3rd Ed., Wiley, August 10, 1998.
- [5] K. L. F. Bane *et al.* “Measurements of coherent synchrotron radiation and its impact on the LCLS electron beam”, no. SLAC-PUB-13391. Stanford Linear Accelerator Center (SLAC), 2008.
- [6] N. Rohringer *et al.*, *Nature*, vol. 481, pp. 488, 2012.
- [7] H. N. Chapman *et al.*, *Nature*, vol. 470, pp. 73, 2011.
- [8] M. M. Seibert *et al.*, *Nature*, vol. 470, pp. 78, 2011.
- [9] H. Wiedemann, *Particle Accelerator Physics* vol. 314. Berlin: Springer, 2007.
- [10] E. Courant and S. Hartland, “Theory of the alternating-gradient synchrotron”, *Annals of Physics* 3.1 pp. 1-48, 1958.
- [11] Linac Coherent Light Source Conceptual Design Report, SLAC-R-593, UC-414.
- [12] M. Borland, “Elegant: a flexible SDDS-compliant code for accelerator simulation,” Advanced Photon Source LS-287, September 2000.
- [13] R. Capi and M. Giovannozzi, “Computation of betatron mismatch and emittance blow-up for multi-turn extraction”, no. CERN-PS-2002-083-AE. 2002.
- [14] J. Seeman, F. Decker, and I. Hsu. “The introduction of trajectory oscillations to reduce emittance growth in the SLC linac.” XV Int. Conf. on High Energy Accelerators, Hamburg. 1992.
- [15] F. Decker *et al.* “Dispersion and betatron matching into the linac.” *Proc. of PAC’91*, San Francisco, CA.

APPROXIMATED EXPRESSIONS FOR THE COHERENT SYNCHROTRON RADIATION EFFECT IN BENDING MAGNETS

D. Z. Khan[†], T. O. Raubenheimer, SLAC, Menlo Park, California, USA

Abstract

In today's X-ray free-electron laser (XFEL), the ultra-bright radiation's strict dependence on emittance has motivated research on advanced electron accelerator techniques. Understanding mechanisms borne in the linac that could jeopardize FEL radiation is important to ensure maximal potential of the machine. One such mechanism, is the Coherent Synchrotron Radiation (CSR) effect. The effect is prominent in latter stages of the linac where the bunch length is short, the peak current is high and the synchrotron radiation emitted in curved sections is temporally coherent. Though, the CSR effect has been comprehensively studied, it still must be quantified for any accelerator system, and requires care in circumventing [1-9].

In this paper, we describe the development of simple and compact analytic expressions for the relative CSR RMS induced energy spread resulting from two typical bending magnet situations in electron particle accelerators. The expressions are compared with the CSR wake field integral expressions derived for a electron bunch with arbitrary linear density, λ_s [10, 11]. Then, the accuracy of each expression is compared against ELEGANT's CSR computational algorithm with the simulation of several idealized examples [15].

INTRODUCTION

The standard derivation of the CSR wakefield begins with the Liénard-Wiechert fields for two electrons traveling along the *same* circular trajectory, ignoring any transverse extent of the beam [10]. The energy transfer due to the electric field of the trailing electron onto the advancing electron is simply given by $dE/d(ct) = e\vec{\beta} \cdot \vec{E}$. The wakefield is inversely proportional to the distance between the two electrons and contains a singularity when the electron separation approaches zero. The singularity is removed by the "normalization process" developed by Saldin *et al.* [10] by subtracting off the contribution of two electrons along a straight-line trajectory. The resulting two electron kernel for the CSR wakefield can then be integrated over any longitudinal bunch distribution to give the collective effect under a wide range of scenarios one might find in a typical accelerator environment. In particular, we concern ourselves with two highly prominent cases found in XFEL applications: First, a linearly chirped electron bunch entering a bending magnet and compressing into the steady-state regime, and second, an electron bunch exiting a bend into the subsequent drift section, both cases of which, are in the ultra-relativistic regime ($\gamma \rightarrow \infty$). The complete mathematical expressions

for the two situations under the 1-D projected model are as follows [10]:

$$\frac{dE}{dz} \Big|_{\text{bend}} = \frac{4}{R\phi} (\lambda(s - S_L) - \lambda(s - 4S_L)) + \dots \frac{2}{(3R^2)^{\frac{1}{3}}} \int \frac{d\lambda(s')}{ds'} \left(\frac{1}{(s-s')^{\frac{1}{3}}} \right) ds' \quad (1)$$

$$\frac{dE}{dz} \Big|_{\text{drift}} = \frac{4}{R} \left(\frac{\lambda(s-S_M)}{\theta_B + 2x} \right) + \dots \frac{4}{R} \left[\int \frac{d\lambda(s')}{ds'} \left(\frac{1}{\phi + 2x} \right) ds' \right] , \quad (2)$$

where R is the bending radius, θ_B is the total bend angle, x is the subsequent drift coordinate, ϕ is the bend angular displacement, λ_s is the normalized longitudinal distribution of the bunch, s and s' are the internalized bunch coordinate of the front and back electron, respectively, and S_L , S_M are the slippage conditions inside the bend and in the subsequent drift, respectively [11]. In the ultra-relativistic regime, the slippage conditions reduce to:

$$S_L = s - s' = \frac{R\phi^3}{24} \quad (3)$$

$$S_M = s - s' = \frac{R\phi^3}{24} \frac{R\phi + 4x}{R\phi + x} . \quad (4)$$

The RMS energy deviation (normalized to the beam energy) that the CSR induces onto the bunch is an important parameter in beam dynamics. Let us now look at the induced CSR energy spread for the specific case of an electron bunch traversing a bending magnet. In this case, when the bunch is fully contained in the magnet, all trailing electron fields will catch-up and interact with advancing electrons (for a given "s" coordinate) and the slippage condition effectively approaches infinity, $S_L \rightarrow \infty$. Under this condition, the first two terms on the right of eq. 1, the "transient" terms, tend to zero and the lower bound of the integral spans the entire bunch tail domain i.e. the energy transfer is constant along the trajectory dz . In this steady-state regime, the relative CSR RMS energy spread induced on a beam with a Gaussian longitudinal distribution was derived to be [12]:

$$\sigma_{CSR} = 0.22 \frac{r_e N L_B}{\gamma \rho^{2/3} \sigma_s^{4/3}} . \quad (6)$$

The above expressions can also take into account the evolution of the longitudinal profile of the electron bunch in compression scenarios assuming that the bunch length is short compared to the slippage. We substitute the constant σ_s terms with one that evolves via the R_{56} of the system and energy chirp, h , of the beam to incorporate

*Work supported by the U.S. Department of Energy under contract No. DE-AC03-76SF00515

[†] donish@SLAC.stanford.edu

compression [13]. No such calculation, to date, has been published for the relative CSR RMS induced energy spread in the subsequent drift section.

CSR INTEGRAL APPROXIMATIONS

The mobility of the CSR integral expressions, eqs. 1 and 2, are limited when quick estimates are desired (they require a knowledge of the exact longitudinal distribution of the electron beam which demands numerical integration). Deriving analytically accessible expressions, such as eq. 6, in place of the CSR integrals is of great utility for accelerator and FEL applications. In this section, we develop expressions for the relative CSR RMS energy spread induced on a beam in a bend transitioning to steady-state and the subsequent drift in lieu of eqs. 1 and 2. Both derivations take advantage of situational approximations that can be assumed for FEL applications. Both models assume a Gaussian longitudinal distribution.

CSR Energy Spread in Transition to Steady-State for a Bend

The aforementioned σ_{CSR} expression, eq. 6, was derived in the steady-state regime. In actuality, steady-state is not always (sometimes never) achieved in typical FEL bending magnet settings. During bunch compression, for instance, the electron bunch commonly begins out of steady-state ($\sigma_s > S_L$) and compresses into steady-state ($\sigma_s < S_L$) while still in the bend. We would like to have a more comprehensive expression to describe the RMS energy gain/loss of this transitional state to compliment the current σ_{CSR} expression.

To start, we provide a simple conceptual model of the CSR dynamics for this situation. First, we recognize that a key feature of the steady-state regime lies in the integration limits of eq. 1 i.e. the amount of trailing electrons contributing to the wake field. The lower bound is described by the slippage condition in ultra-relativistic limit, $S_L = R\emptyset^3/24$, where we remind the reader that \emptyset is the angular displacement of the observing electron, with internal bunch coordinate s , within the bend. Once the slippage condition exceeds σ_z , the integration bounds virtually encompasses the entire tail-end of the bunch, and the integral is constant; steady-state is achieved. This process is heavily affected if the beam is being compressed and the σ_s is evolving. Second, we incorporate the two transient terms outside of the integral in eq. 1 to properly describe the energy transfer as the steady-state expression neglects them both. The transient terms come about from the entrance wake (case A in [11]) and from the integration-by-part derivation's surface/stationary term of the bend magnet wake (case B in [11]). Both terms will eventually dissipate and slip out of range as the electron bunch traverses the bend. The full description of the transient wakes will take into account the angular dependence, \emptyset , of the slippage and compression, but the solution will be non-analytical. For our purposes, we assume the compression of the bunch ($\propto \emptyset$) is negligible

relative to the slippage of the wake ($\propto \emptyset^3$) before steady-state is achieved. This will allow us to use the entrance bunch length, σ_{si} , and ignore compression completely to ease the mathematical cost of the RMS calculation. So, our amended model of the σ_{CSR} should reflect this approach to steady-state and take into account the aforementioned assumptions.

To begin, we introduce a normalization factor, A_{bend} , in the σ_{CSR} expression to model the beam transitioning into the steady state regime:

$$\begin{cases} A_{\text{bend}} = \frac{\sigma_{ss}}{\sigma_{si}(1 + hR_{56})}, & \sigma_s > \sigma_{ss} \\ A_{\text{bend}} = 1, & \sigma_s \leq \sigma_{ss} \end{cases}$$

where σ_{ss} is steady-state bunch length defined by the slippage condition, σ_{si} is the bunch length at the entrance of the bend, h is the longitudinal energy chirp, and R_{56} is the momentum compaction of the bend. Now, we can modify the expression for the relative CSR RMS energy spread with the normalization factor for a bunch is being compressed into the steady-state regime:

$$\begin{aligned} \sigma_{CSR} &= \frac{\sigma_{ss}}{\sigma_{si}(1 + hR_{56})} \left(0.22 \frac{Nr_e L_B}{\gamma \rho^{\frac{2}{3}} (\sigma_{si}(1 + hR_{56}))^{\frac{4}{3}}} \right) \\ &= 0.22 \frac{Nr_e L_B \sigma_{ss}}{\gamma \rho^{\frac{2}{3}} (\sigma_{si}(1 + hR_{56}))^{\frac{7}{3}}}. \end{aligned} \quad (7)$$

The above expression is the relative CSR RMS energy spread for a non-steady-state electron bunch undergoing linear compression of its RMS bunch length. It should be noted that the normalization factor, A_{bend} , assumes a linearity towards the bunch approaching steady-state when, in actuality, the correct behaviour is a dictated by the third power of $z^3/24R^2$ taken from the slippage condition. This assumption is only valid for small z excursions which is nearly always satisfied in the short bending magnets of FELs.

Next, we incorporate the transient wake terms [10, 11]:

$$\frac{dE}{dz} \Big|_{\text{transient}} = \frac{4}{R\emptyset} (\lambda(s - S_L) - \lambda(s - 4S_L)),$$

under the assumption that there is no compression of the bunch length and that the wake is only valid for small angles, \emptyset . This will permit a small angle expansion of \emptyset , and cause the nested RMS integration over the path length ($Rd\emptyset$) and internal bunch coordinate, s , to be analytical. Computing the RMS energy spread gives:

$$\sigma_{\text{transient}} = 2.9169 \frac{Nr_e L_B \theta_B^2}{\gamma \sigma_{si}^2}. \quad (8)$$

Therefore, the cumulative CSR RMS energy spread induced onto the beam while in transition to steady-state in a bend is simply the sum of eqs. 7 and 8:

Content from this work may be used under the terms of the CC BY 3.0 licence (© 2018). Any distribution of this work must maintain attribution to the author(s), title of the work, publisher, and DOI.

$$\sigma_{\text{transient}} = \frac{Nr_e L_B \theta_B^2}{\gamma} \left(2.9 \frac{1}{\sigma_{si}^2} + \left(7.7 \times 10^{-7} \frac{L_B \theta_B^2}{(\sigma_{si}(1+hR_{56}))^7} \right)^{1/3} \right), \quad (9)$$

where the unit of the energy spread is in percent(s). The above expression is only valid when the bunch length has not reached the steady-state condition as dictated in the A_{bend} boundary conditions i.e. the σ_{CSR} steady-state expression (eq. 6) can be used in post.

CSR Energy Spread for a Drift

The CSR RMS energy spread induced on the beam due to the subsequent drift section is typically more detrimental than that produced solely in the bend. The reason is that the CSR wake in the drift has much more distant over which sustained energy transfer to the beam can occur. The difficulty in solving the drift space CSR integral (eq. 2) is in its requiring of numerical methods for even simple bunch distributions e.g. a Gaussian distribution. Again the utility of a simple expression to describe the CSR RMS energy spread in a drift is desired.

To begin, we conceptually map a set of simple assumptions that will ease the mathematical complexity of the CSR integral. First, we recognize that the wake in the drift section (with drift coordinate x) after a bend is essentially the CSR wake from the bend co-propagating with the beam. We can assume the beam reached steady-state in the bend prior to entering the drift so that transient effects are not present in the co-propagating CSR wake. In essence, if the bunch has achieved steady-state the slippage condition, eq. 4, will drop its \emptyset dependence and only depend on x . The x -dependence of the slippage will effectively contain the entire tail-end of the bunch for any x value and we can equivalently allow the integration lower bound to negative infinity. Second, while the CSR wake propagates further into the drift, its power decreases as radiating electrons leave the bend, which will amount to a x^{-1} decay of the wake. Integrating over the drift distance x , the energy transfer should tend as the natural log and will contain a singularity at $x = 0$. To circumvent the singularity, we restrict the integration limits over drift intervals where the entire bunch has transitioned out of the bend and completely into the drift section ($\sigma_s < x \leq d$, where d is the entire drift distance).

With these simplifications in place, we begin to calculate the CSR integral from a slightly different approach than previously published [10]. Standard derivation of eq. 2 is obtained via integration by parts that incorporates the derivative of the longitudinal bunch distribution. Instead, we opt to not employ the integration by parts routine and simply integrate the two-electron kernel with the longitudinal bunch distribution:

$$\frac{dE}{dz} \Big|_{\text{drift}} = \int_{-\infty}^s \frac{-32e^2(R\emptyset+x)^2}{\emptyset^2(R\emptyset+2x)^4} \lambda(s') ds',$$

where the two-particle wake is taken from Stupakov and Emma in the ultra-relativistic regime [11]. From here, we are able to integrate over the bend angle using $ds' = \frac{-R\emptyset^2 (R\emptyset+2x)^2}{8 (R\emptyset+x)^2} d\emptyset$ derived from the slippage condition:

$$\frac{dE}{dz} \Big|_{\text{drift}} = \int_{-\infty}^0 \frac{-32e^2(R\emptyset+x)^2}{\emptyset^2(R\emptyset+2x)^4} \times \lambda(s - S_M) \left(\frac{-R\emptyset^2 (R\emptyset+2x)^2}{8 (R\emptyset+x)^2} d\emptyset \right).$$

This integral is non-analytical. To make the integral solvable for the RMS energy spread we employ one last simplification to the bunch length and expand it about small bunch coordinates s . For any given order, we have:

$$\frac{dE}{dz} \Big|_{\text{drift}} = \int_{-\infty}^0 \frac{4e^2 R}{(R\emptyset+2x)^2} \frac{N}{\sqrt{2\pi}\sigma_z} e^{-\frac{s^2}{2\sigma_s^2}} \times \left(1 + \frac{sR\emptyset^3}{6\sigma_s^2} - \frac{sR^2\emptyset^3}{8x\sigma_s^2} + \dots \right) d\emptyset.$$

Taking only the zeroth order term, we can solve for the total energy transfer by integrating over the drift distance (under our second assumption's bounds $[\sigma_s, d]$), and solve for the relative CSR RMS energy spread analytically given by:

$$\sigma_{CSR} = \frac{Nr_e}{\gamma\sqrt{\pi}\sigma_s} \sqrt{\left(\frac{2}{\sqrt{3}} - 1\right) \log\left(\frac{24d}{R\theta_B^3}\right)}. \quad (10)$$

This expression is valid for short bunches, as it will justify the steady-state condition in the bend ($\sigma_s < S_L$) and the expansion about small bunch positions, s .

SIMULATION STUDIES

The 6-D particle tracking code, ELEGANT, has been used extensively in the simulation of charged particle beams for FEL applications [14]. ELEGANT also includes a computationally low cost evaluation of the CSR energy kicks a charged particle beam will experience while traversing a bend magnet and coasting into a subsequent drift section based on the projected longitudinal model [15]. This makes ELEGANT an ideal candidate for testing the accuracy of our newly formed CSR RMS expressions.

The simulation study will consist of benchmark tests for both relative CSR RMS energy spread expressions, eqs. 9 and 10. For this, we simulate a 100-pC Gaussian electron bunch ($\beta_{x,y} = 100 m$, $\gamma\epsilon_{x,y} = 0.5 \mu m$, $E_0 = 1.6 GeV$) to inject into an idealized bend-drift ($L_B = 0.55 m$) system while scanning through prominent parameters: initial bunch length σ_{si} , bend angle θ_B , and drift distance d .

CSR Energy Spread in Transition to Steady-State for a Bend

To test eq. 9, we impose a linear energy chirp along the beam's longitudinal dimension and inject the beam into a typical second-stage 4-bend chicane bunch compressor ($R_{56} \approx 37 \text{ mm}$). The third bend is where the majority of the compression cycle occurs, and typically, where the beam will compress into the steady-state regime (compresses from $\sim 100 \mu\text{m}$ to $\sim 10 \mu\text{m}$) making it an ideal location to test our first expression.

The bending angle and incoming bunch length at the third bend are systematically and independently varied while never allowing the beam to achieve steady-state. Figure 1 plots the bunch length's approach to the steady-state condition for the angle and bunch length scans, respectively.

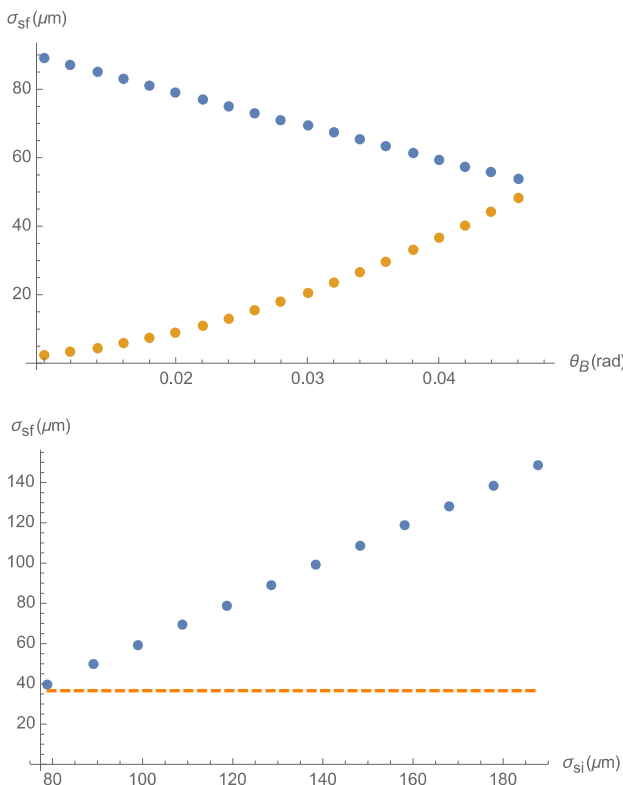


Figure 1: Top: The exiting bunch length of the beam after compression (blue marker) and steady-state bunch length (orange marker) for various bending angles. Bottom: The exiting bunch length of the beam (blue marker) and the steady-state condition (orange dashed line) for various initial bunch lengths.

The relative CSR RMS energy spread is measured at the exit of the bend and compared with that of equations 1 and 9. The results are compared in Figure 2.

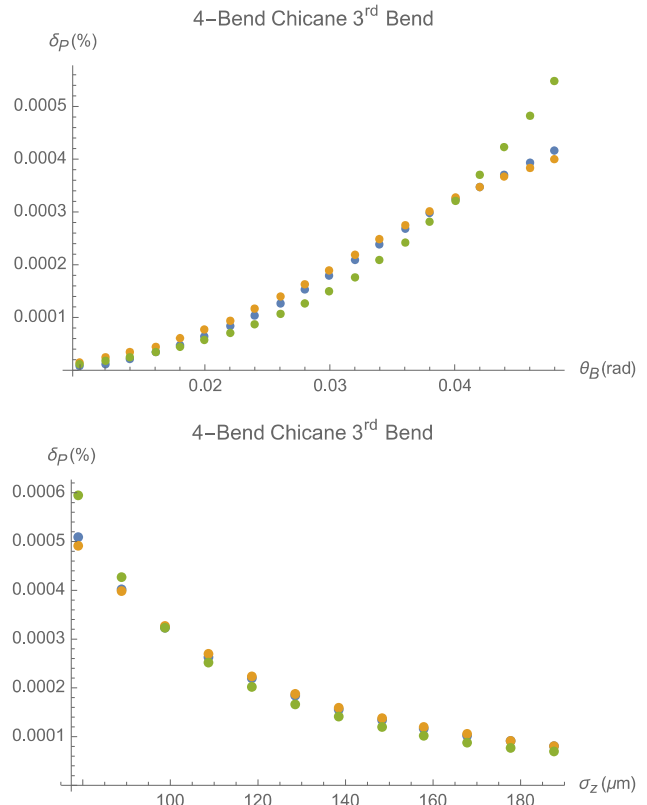


Figure 2: Top: The CSR RMS energy spread calculated by ELEGANT (blue marker), full CSR integral in eq. 1 (orange marker), and the newly derived approximate expression in eq. 9 (green marker) for various bending angle values. Bottom: The CSR RMS energy spread calculated by ELEGANT (blue marker), full CSR integral in eq. 1 (orange marker), and the newly derived approximate expression in eq. 9 (green marker) for various initial bunch lengths. In both plots, the ELEGANT and CSR integral markers mostly overlap.

Equation 9 shows strong agreement in both scans, but tends to stray when steady-state is being approached. This is seen in the large bend angles of Figure 2 (top) and the small bunch lengths of the Figure 2 (bottom). These are the regions where the beam is closest to steady-state and are corroborated in Figure 1.

CSR Energy Spread for a Drift

To test eq. 10, we inject the mono-energetic ($\sigma_\delta = 0$) Gaussian beam into a 0.55 m, 0.04 radian bending magnet and allow the beam to coast into a drift section. We systematically scan the incoming bunch length, drift length, and bend angle while measuring the relative CSR RMS energy spread at the end of the drift section. The results are displayed in Figure 3.

Content from this work may be used under the CC BY 3.0 licence (© 2018). Any distribution of this work must maintain attribution to the author(s), title of the work, publisher, and DOI.

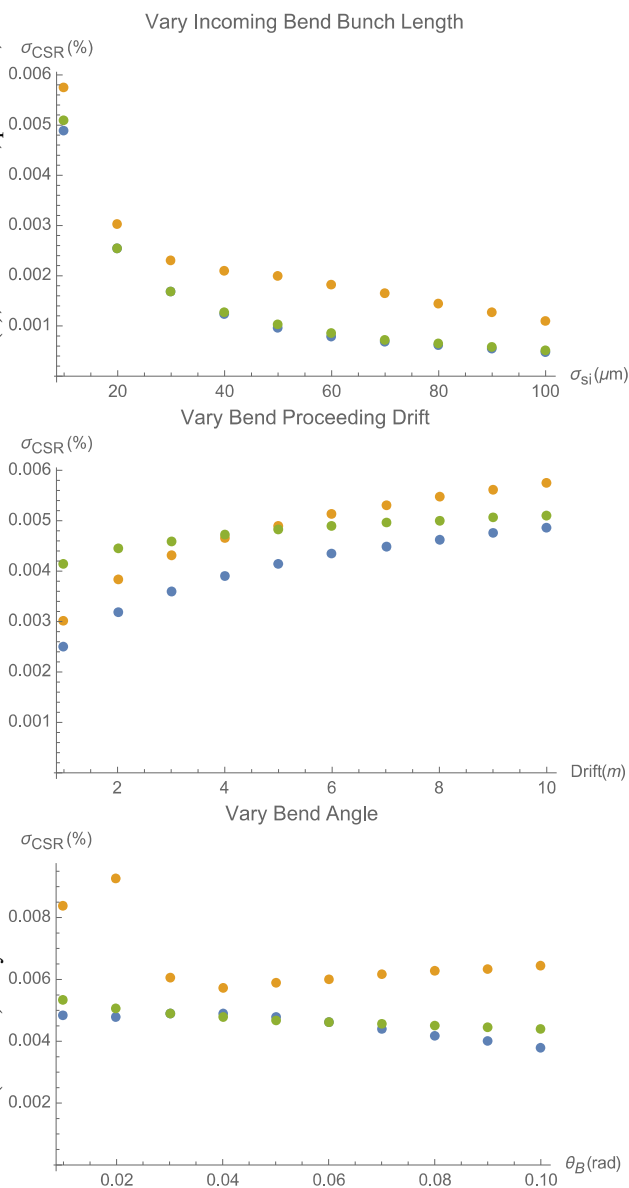


Figure 3: The relative CSR RMS energy spread measured at the end of the bend-drift system. ELEGANT (blue marker), the full CSR integral in eq. 2 (orange marker), and eq. 10 (green marker) are plotted together while varying the incoming bunch length (top), the subsequent drift length (middle), and bend angle values (bottom). In the top plot, the ELEGANT and the relative CSR RMS energy spread expression markers mostly overlap.

CONCLUSION

We have demonstrated, through simple mathematical approximations, that the relative CSR RMS energy spread for a beam transitioning into steady-state and a beam propagating in a post-bend drift section can be simply modelled. The expressions serve well for performing quick estimates of the CSR effect that is commonly found in FEL bending magnets, and in particular, bunch compressor chicanes. The utility of such expressions can be

used to highlight, and thereby circumvent, features of the CSR effect that may lead to potential degradation of the beam phase space quality.

ACKNOWLEDGMENT

This work was supported by the U.S. Department of Energy under Contract No. DE-AC03-76SF00515.

REFERENCES

- [1] D. Douglas, “Thomas Jefferson National Accelerator Facility,” Report No. JLAB-TN-98-012, 1998.
- [2] R. Hajima, *Japanese Journal of Applied Physics* 42 (2003): 974.
- [3] F. Stulle, A. Adelman and M. Pedrozzi, *Physical Review Special Topics—Accelerators and Beams* 10 (2007): 031001.
- [4] Y. Jing, *et al.*, *Physical Review Special Topics—Accelerators and Beams* 16 (2013): 060704.
- [5] C. Mitchell, J. Qiang, and P. Emma, *Physical Review Special Topics—Accelerators and Beams* 16 (2013): 060703.
- [6] S. Di Mitri, M. Cornacchia, and S. Spampinati, *Physical Review Letters* 110 (2013): 014801.
- [7] S. Di Mitri and M. Cornacchia, *Nuclear Instruments and Methods in Physics Research Section A: Accelerators, Spectrometers, Detectors and Associated Equipment* 735 (2014): 60.
- [8] D. Khan and T. Raubenheimer, “LCLS-II bunch compressor study: 5-bend chicane,” *Proc. of FEL’14*, Basel, Switzerland.
- [9] Y. Jiao *et al.* “Generic conditions for suppressing the coherent synchrotron radiation induced emittance growth in a two-dipole achromat,” *Physical Review Special Topics-Accelerators and Beams* 17.6 (2014): 060701.
- [10] E. L. Saldin and E. A. Schneidmiller, and M. V. Yurkov, *Nuclear Instruments and Methods, Sec. A* 398, (1997): 373.
- [11] G. Stupakov and P. Emma. “CSR wake for a short magnet in ultra-relativistic limit,” Report No. LCLS-TN-01-12, SLAC, Dec. 2001.
- [12] Y. Derbenev *et al.* “Microbunch radiative tail-head interaction,” Report No. TESLA-FEL-95-05. SCAN-9511114, DESY, 1995.
- [13] C. Mayes and G. Hoffstaetter, “Exact 1D model for coherent synchrotron radiation with shielding and bunch compression,” *Physical Review Special Topics – Accelerators and Beams* 12.2 (2009): 024401.
- [14] M. Borland, “Elegant: a flexible SDDS-compliant code for accelerator simulation,” Report No. LS-287, September 2000.
- [15] M. Borland, “Simple method for particle tracking with coherent synchrotron radiation,” *Physical Review Special Topics-Accelerators and Beams* 4.7 (2001): 070701.

AN EMITTANCE-PRESERVATION STUDY OF A FIVE-BEND CHICANE FOR THE LCLS-II-HE BEAMLINE

D. Z. Khan[†], T. O. Raubenheimer, SLAC, Menlo Park, CA, USA

Abstract

The Linac Coherent Light Source II (LCLS-II) is an upgrade intended toward advancing on the great success of its predecessor, LCLS, to maintain its position at the forefront of X-ray science. The introduction of a niobium metal superconducting linac for LCLS-II not only increases the repetition rate to the MHz level (from 120 Hz) but also boasts an average brightness many orders higher ($\sim 10^4$) than that of LCLS. Though, these improvements do not come without a price: the peak brightness suffers by a factor of 10 in part due to the impact of Coherent Synchrotron Radiation (CSR) diminishing the peak current of the beam in the second bunch compressor (BC2) [1]. In this paper, we discuss the impact of implementing a plug-compatible 5-bend chicane for BC2 on the beam's emittance dilution for a high energy, low emittance configuration of LCLS-II (LCLS-II-HE). The results are compared with that of a standard 4-bend chicane under various settings in ELE-GANT and CSRTrack [2, 3].

INTRODUCTION

The detrimental effects of CSR in the accelerator environment is one of most challenging problems to study, let alone counter, for current free electron laser (FEL) facilities. The CSR energy chirp induced by the beam onto itself from traveling along arced sections of the beam line has direct consequences on the beam's bend-plane emittance. The issue is exacerbated by the push to produce even shorter and more compact electron bunches for ultra-brilliant FEL radiation in the X-ray regime at facilities such as the European XFEL at DESY, Spring-8 Angstrom Compact Free Electron laser (SACLA), Pohang Accelerator Laboratory X-ray Free Electron Laser (PAL-XFEL) and the LCLS-II, which is currently being construction. The ceiling of producing such radiation is in the painstaking details of the beam transport line, in particular, the latter stage bunch compression systems [4]. Many techniques have been researched and developed but, as the limits are continually pushed, new solutions are needed to adjust with the demand.

LCLS-II HIGH ENERGY (HE)

The LCLS-II high-rate FEL can generate X-ray pulses from 200 eV to 5 keV at MHz repetition rates [5]. The electron beam for the FEL is generated in an RF gun and accelerated in a superconducting RF (SCRF) linac to a beam energy of 4 GeV. While the beam is accelerated, it is compressed to a peak current of 400 to 1000 Amps,

depending on the bunch charge. Over much of the photon energy range, the LCLS-II electron beam will generate X-rays with peak powers of roughly 10 GW [6].

While the average brightness of the LCLS-II X-ray laser will be many orders-of-magnitude higher than that of the LCLS operating at 120 Hz, the peak brightness will be a factor of 10 or more lower. For comparison, the LCLS routinely produces X-ray pulses with over 200 GW using a 5 kA electron bunch and beam shaping techniques [7].

There are two reasons for the relatively poor peak performance of the LCLS-II: first, the peak current of the LCLS-II electron bunch is 5 to 10 times lower than that in the LCLS and, second, the beam energy is a factor of 2 to 3 times lower than that in the LCLS. The reduced peak current is largely due to the impact of Coherent Synchrotron Radiation (CSR) and Longitudinal Space Charge (LSC) which are exacerbated by a lower beam energy at the second bunch compressor (BC2) of 1.6 GeV versus roughly 5 GeV. These effects are further amplified in the 2-km long bypass transport line which, at the 4 GeV beam energy, lead to a significant micro-bunching instability [8].

To extend the photon energy range to upwards of 20 keV and improve the X-ray pulse performance, the LCLS-II-HE was proposed with a high energy upgrade from 4 to 8 GeV and a possible lower beam emittance where the gun emittance is reduced from 0.4 to 0.1 μm . The upgrade will increase the beam energy in the 2 km Bypass line from 4 to 8 GeV, significantly reducing the impact of the largest LSC contribution. However, the energy of BC2 will be roughly the same, increasing from 1.6 to 1.9 GeV, leaving the impact of CSR on the beam comparable and diluting the beam emittance significantly. In December 2016, the LCLS-II-HE concept received CD0 from the DOE. Further details on the upgrade can be found in the supporting documentation at https://portal.slac.stanford.edu/sites/conf_public/lclsiihe2017/Pages/default.aspx.

LCLS-II Bunch Compressor 2 (BC2)

The LCLS-II second stage bunch compressor, BC2, is a standard 4-bend chicane with its main features listed in Table 1. It is responsible for the final compression of the beam before its transported to the undulators. It is here that the peak current reaches its maximum value thus making BC2 a salient area for CSR driven emittance growth.

Current methods for mitigating BC2's CSR emittance growth are centered on linac optics optimization. First method of which, balances the RF chirp, $h = (1/E_0) (dE/dz)$, and the compression factor amongst the bunch compressors to find a minimization of the CSR induced emittance growth. Generally, allocating the linac's R_{56} , so that much of the compression work can be done

*Work supported by the U.S. Department of Energy under contract No. DE-AC03-76SF00515

[†] donish@SLAC.stanford.edu

Content from this work may be used under the terms of the CC BY 3.0 licence (© 2018). Any distribution of this work must maintain attribution to the author(s), title of the work, publisher, and DOI.

earlier in BC1, allows BC2 to have smaller bending angles and consequently less contribution from CSR due to its $\theta^{2/3}$ dependence [9]. The second method focuses the beam to a waist ($\alpha_x = 0$, $\beta_x = \beta_{\min}$) toward the final bend of a chicane, where the bunch length is the shortest and the CSR is the greatest, to suppress the CSR induced emittance growth via the \mathcal{H} -function minimization [10]. These two methods are among many that have been shown to be successful in partially suppressing the CSR induced emittance dilution for a 4-bend chicane bunch compressor.

Table 1: Various Design Parameters of BC2 in LCLS-II

Parameter	Symbol	BC2	Unit
Electron Energy	E_0	1.6	GeV
Momentum Compaction	$ R_{56} $	39.5	mm
Chicane Total Length	L_T	23.7	m
Bend Angle Per Dipole	$ \theta $	0.04	Rad
Eff. Length of Each Bend	L_B	0.55	m
Dispersion at Center	$ \eta_x $	458	mm

THE FIVE-BEND CHICANE BUNCH COMPRESSOR

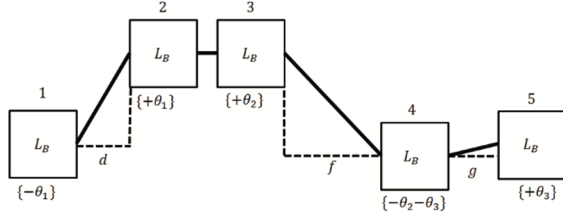


Figure 1: Diagram of a five-bend chicane. Not to scale.

The 5-Bend chicane (Fig. 1) is a dual-polarity dispersive bunch compressor intended for the final-stage bunch compression where an electron bunch reaches its shortest length and where CSR is most detrimental [11]. The 5-bend chicane would be largely plug-compatible with the present LCLS-II 4-bend BC2 design. It would be situated in the same space that will be occupied by the 4-bend chicane and it would reuse much of the LCLS-II BC2 hardware. One additional bending magnet would be added, the supports would be relocated, and the vacuum system would be modified for the different bending magnet spacing. The 5-bend chicane's various features are listed in Table 2.

The plug-compatibility of the 5-bend chicane relies on the fact that it can maximally preserve the beam emittance while minimally reconfiguring the existing BC2 hardware

(and engineering cost). To do this, we solved for a 5-bend chicane configuration which can be accommodated in the existing 4-bend chicane space. The design will require only a longitudinal shift of the apparatus housing magnets 2 and 3 and a permanent placement of the additional magnet in between bends 3 and 4 (both, with respect to the 4-bend chicane configuration). In addition, the 5-bend chicane design would have to be able to be turned off i.e. allow a direct line of motion for the beam to travel through. This sets a requirement on the permanent placement of the 4th additional magnet (it cannot be displaced too far from the chicane's axis), and therefore sets a strict requirement on the absolute dispersion value in the 4th bend. Under these engineering guidelines, the robust performance of the 5-bend proves to be a low-cost and simple upgrade to the standard 4-bend chicane.

Table 2: Characteristic Parameters of the Five-Bend Chicane for BC2

Parameter	Symbol	5-Bend Chicane	Unit
Electron Energy	E_0	1.6	GeV
Momentum Compaction	$ R_{56} $	39.5	mm
Chicane Total Length	L_T	23.7	m
First Chicane Drift Length	L_D	7.3	m
Second Chicane Drift Length	L_F	11.1	m
Third Chicane Drift Length	L_G	0.8	m
Angle 1	$ \theta_1 $	0.052	Rad
Angle 2	$ \theta_2 $	0.037	Rad
Angle 3	$ \theta_3 $	0.018	Rad
Eff. Length of Each Bend	L_B	0.54	m
Dispersion After Magnet 2	$ \eta_x $	410	mm
Dispersion After Magnet 4	$ \eta_x $	19	mm

The 5-bend chicane has several distinct features that distinguishes itself from the standard 4-bend chicane with regards to CSR induced emittance growth suppression. Firstly, the additional bend allows the ability to allocate the R_{56} amongst the five bends (the R_{56} of a 4-bend is predominantly constrained into the two middle magnets). This additional flexibility is likened to an optics-like tuning of the CSR energy kicks in each of the bending magnets. Additionally, the dual-polarity dispersion of the chicane opens the possibility of locally cancelling path/angle excursions caused by the CSR energy kicks [12]. To the first order, a CSR energy kick translates to a final spatial/angular devi-

ation of

$$\Delta x_{\text{exit}} = \eta_{\text{bend}} \delta_{\text{CSR}} \quad (1)$$

$$\Delta x'_{\text{exit}} = \eta'_{\text{bend}} \delta_{\text{CSR}}, \quad (2)$$

where Δx_{exit} and $\Delta x'_{\text{exit}}$ are the spatial and angular deviations at the exit of the chicane (where the dispersion closes), η_{bend} and η'_{bend} are the dispersion and its slope at the location of the CSR energy kick and δ_{CSR} is the CSR energy kick normalized to the beam energy. So, for a 5-bend chicane, the dual-polarity of the dispersion opens the opportunity to have the path/angle excursions at the end sum to zero; a feature not present in the 4-bend chicane.

SIMULATION STUDIES

Preliminary simulation studies have been conducted for the present LCLS-II-HE 4-bend BC2 design and the proposed 5-bend BC2 chicane design. The transverse emittance has been studied for moderate and high peak currents (0.8 and 1.5 kA, respectively) in the LCLS-II-HE at 100-pC bunch charge and low-emittance configurations (0.27 μm and 0.10 μm , respectively). The emittance comparison studies between the 4 and 5-bend chicanes were conducted using ELEGANT and CSRTrack.

ELEGANT Simulation Results

ELEGANT was used as the lead simulation software in optimizing the 5-bend chicane and comparing its results with that of a 4-bend chicane.

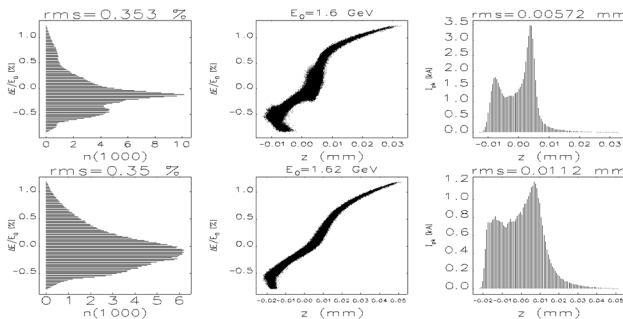


Figure 2: Top: The longitudinal phase space plots, from left to right, respectively, of the energy spread distribution, the $z - \delta_E$ phase space, and current profile for an electron bunch compressed to ~ 0.8 kA. Bottom: The longitudinal phase space plots for an electron bunch compressed to ~ 1.5 kA. Both plots are for the 4-bend chicane (the 5-bend's plots are identical) and the 0.27 μm low-emittance case (again, the low-emittance, 0.10 μm case produces visually similar results).

Table 3: LCLS-II-HE X-plane Emittance Measurements

Configuration	4-Bend	5-Bend
	$(\gamma\epsilon_{xf}, \Delta\gamma\epsilon_x, \Delta\gamma\epsilon_x/\gamma\epsilon_{xi})$	$(\gamma\epsilon_{xf}, \Delta\gamma\epsilon_x, \Delta\gamma\epsilon_x/\gamma\epsilon_{xi})$
0.8 kA, 0.27 μm	(0.33 μm , 0.06 μm , 22%)	(0.30 μm , 0.03 μm , 11%)
1.5 kA, 0.27 μm	(0.62 μm , 0.35 μm , 130%)	(0.33 μm , 0.06 μm , 22%)
0.8 kA, 0.10 μm	(0.16 μm , 0.06 μm , 60%)	(0.12 μm , 0.01 μm , 12%)
1.5 kA, 0.10 μm	(0.41 μm , 0.31 μm , 310%)	(0.16 μm , 0.06 μm , 60%)

CSRTrack Simulation Results

CSRTrack was used as a post verification check of the results obtained in ELEGANT for thoroughness of our study. CSRTrack employs a 2.5-D modelling of the electromagnetic forces an electron beam would experience in an accelerator bending system (though we suspect no transverse coherence of overtaking fields as $R^{1/3}\sigma_s^{2/3} > \sigma_x$).

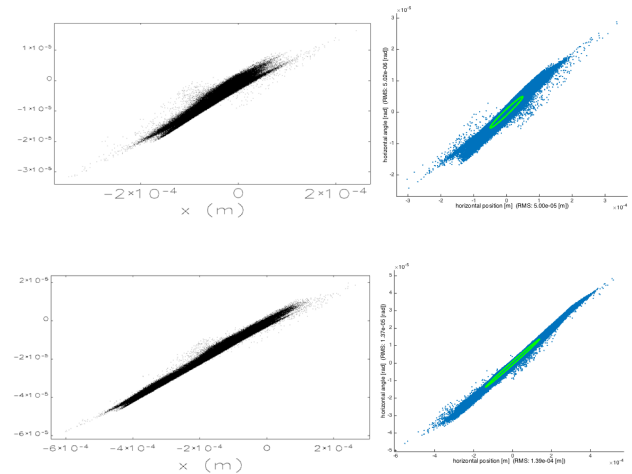


Figure 3: The bend-plane projected emittance at the exit of the nominal 4-bend chicane in ELEGANT (left) and CSRTrack (right) for the low-emittance 0.10- μm beam. The top row of plots is compression to ~ 0.8 kA and the bottom to ~ 1.5 kA.

Table 4: LCLS-II-HE X-plane Emittance Measurements

Configuration	4-Bend	5-Bend
	$(\gamma\epsilon_{xf}, \Delta\gamma\epsilon_x,$ $\Delta\gamma\epsilon_x/\gamma\epsilon_{xi})$	$(\gamma\epsilon_{xf}, \Delta\gamma\epsilon_x,$ $\Delta\gamma\epsilon_x/\gamma\epsilon_{xi})$
0.8kA, 0.27 μm	(0.32 μm , 0.05 μm , 19%)	(0.29 μm , 0.02 μm , 7%)
1.5kA, 0.27 μm	(0.64 μm , 0.37 μm , 137%)	(0.34 μm , 0.07 μm , 26%)
0.8kA, 0.10 μm	(0.16 μm , 0.06 μm , 60%)	(0.13 μm , 0.03 μm , 30%)
1.5kA, 0.10 μm	(0.42 μm , 0.32 μm , 320%)	(0.15 μm , 0.05 μm , 50%)

The 5-bend chicane shows strong CSR emittance growth suppression in all cases, more notably when the peak current is increased as in the 1.5kA cases.

CONCLUSION

The expectation is that the 5-bend modification of BC2 would be a cost-effective approach to maximize the capability of the LCLS-II-HE. It would allow operation with low emittance beams as might be required to generate ~20 keV X-rays and/or operate with higher peak beam currents and thereby increase the peak brightness and peak power of the LCLS-II-HE FEL.

ACKNOWLEDGMENT

We would like to thank Ji Qiang for sharing the IMPACT simulation results used in our initial comparison studies.

This work was supported by the U.S. Department of Energy under Contract No. DE-AC03-76SF00515.

REFERENCES

- [1] M. Venturini *et al.*, in *Proc. IPAC'15*, Richmond, VA, USA, TUPMA003.
- [2] M. Borland, "Elegant: a flexible SDDS-compliant code for accelerator simulation," Advanced Photon Source LS-287, September 2000.
- [3] M. Dohlus and L. Torsten, "CSRtrack: faster calculation of 3D CSR effects", in *Proc. FEL'14*.
- [4] K. L. F. Bane *et al.*, "Measurements of coherent synchrotron radiation and its impact on the LCLS electron beam", SLAC-PUB-13391. Stanford Linear Accelerator Center (SLAC), 2008.
- [5] G. Marcus *et al.*, *ICFA Beam Dynamics Newsletter*, May 2016.
- [6] G. Marcus and J. Qiang, LCLS-II unpublished Technical Note, TN-17-04, (2017).
- [7] Y. Ding *et al.*, in *Proc. PRAB'19*, 100703 (2016).
- [8] M. Venturini *et al.*, *IPAC'15*, paper TUPMA003, Richmond, VA (2015).
- [9] Y. S. Derbenev *et al.*, "Microbunch radiative tail-head interaction", TESLA-FEL-95-05, 1995.
- [10] S. Di Mitri and M. Cornacchia, "Merit functions for the linac optics design for colliders and light sources", *NIMA* 735, pp. 60-65, 2014.
- [11] D. Z. Khan and T. O. Raubenheimer, "LCLS-II bunch compressor study: 5-bend chicane", in *Proc. FEL'14*, Basel, Switzerland, 2014.
- [12] M. Borland, "Design and performance simulations of the bunch compressor for the APS LEUTL FEL", arXiv physics/0008112, 2000.

DESIGN OF A DOGLEG BUNCH COMPRESSOR WITH TUNABLE FIRST-ORDER LONGITUDINAL DISPERSION

W.K. Lau, N.Y. Huang, M.C. Chou, A.P. Lee, NSRRC, Hsinchu, Taiwan
 J. Wu, SLAC National Accelerator Laboratory, Menlo Park, CA 94025, USA

Abstract

A nonlinear bunch compressor has been designed for the proposed NSRRC VUV FEL facility. It is a double dog-leg configuration that provides a first order longitudinal dispersion function (i.e. R_{56}) with a sign opposite to that of a conventional four-dipole chicane. A large variation in the bunch length or the peak current for various operation conditions can be done by tuning R_{56} . This can be realized by changing the longitudinal positions of the outside dipoles and adjusting the quadrupoles and sextupoles settings for desired bunch compression. Residual energy chirp left after bunch compression as revealed from ELEGANT simulation can be corrected by a capacitive dechirper structure when the bunch is slightly over-compressed.

INTRODUCTION

A high brightness S-band injector system equipped with a laser-driven photocathode rf gun has been developed in house at NSRRC [1]. This system has been operated regularly in the Accelerator Test Area (ATA) for light source R&D. Recently, the possibility of establishing a free electron laser facility which delivers high intensity tunable coherent VUV radiation in the range of 66.5-200 nm is being investigated. The baseline design is a 4th harmonic high gain harmonic generation (HGHG) FEL driven by a 325 MeV driver linac system [2]. By making maximum use of existing hardware, a driver linac system has been designed [3]. One unique part of this design is that the bunch compressor is a single-stage double dogleg, which allows a control of nonlinear beam dynamics for efficient bunch compression. In this report, the analysis of nonlinear bunch compressors is recalled and the design this dogleg compressor for the 325 MeV high brightness linac system is studied. Tunability of bunch length and peak current by controlling R_{56} of this compressor is also discussed.

NONLINEAR BEAM DYNAMICS IN BUNCH COMPRESSORS

Consider an electron moving in the traveling-wave field of a constant-gradient linac structure. The energy gain of this electron is

$$\Delta E = eV_0 \cos(\omega t - kz + \varphi_0), \quad (1)$$

where V_0 , ω , k , φ_0 are the peak voltage, frequency, wave vector and initial phase of the wave which is propagating

in the $+z$ direction with phase velocity of $V_p = \omega/k = c$ respectively. The electron is also moving in the $+z$ direction with velocity $v_e = \beta c$.

When an electron enters the linac structure at $\phi_0 = 0$, acceleration of electron is maximized as it rides on the crest of the wave. It is worth noting that if an electron in a bunch passes a fixed location in space earlier (later) than all other electrons in time, it must be at the very front (end) of this bunch and it defines the location of bunch head (tail). For a bunch of electrons moving with the traveling wave in a linac along the direction of the $+z$ axis, the bunch head always has a positive value with respect to the bunch center.

Nonlinear Energy Chirps

Generally speaking, in a split photo-injector configuration, the associated rf linac structure is operated at a phase (i.e. the rf crest) to minimize beam energy spread and a subsequent chirper linac is used to produce the required energy chirp for the bunch compression in the dispersive section located downstream. Therefore, it is reasonable to assume the correlated energy spread of the electron beam at the entrance of the chirper linac is small and the energy deviation of an electron from the designed value at chirper linac exit (i.e. $\delta(z) = (E_f(z) - E_{f0})/E_{f0}$) can be expressed by means of Taylor series expansion as

$$\delta(z) = a\delta_i + h_1 z + h_2 z^2 + h_3 z^3 + \dots \quad (2)$$

where $E_f(z)$ is the central beam energy at the entrance of chirper linac, δ the deviation of electron energy from the designed value with initial uncorrelated energy spread, z the particle's initial longitudinal coordinate relative to the bunch center. E_{f0} is the central beam energy after the chirper linac, $a = E_{i0}/E_{f0}$ is the damping factor and

$$\begin{cases} h_1 = \frac{keV_0}{E_{f0}} \sin \varphi_0, \\ h_2 = -\frac{k^2 eV_0}{2E_{f0}} \cos \varphi_0, \\ h_3 = -\frac{k^3 eV_0}{6E_{f0}} \sin \varphi_0, \end{cases} \quad (3)$$

are the first, second and third order energy chirps respectively. It is clear that the signs of the 1st order and the 3rd

energy chirp depends on the linac phase. The 2nd-order energy chirp, however, is always negative if the linac is operated for electron acceleration (i.e. $-\pi/2 < \phi_0 < \pi/2$).

Bunch Compression

If δ is kept unchanged after passing through a dispersive section, the longitudinal position of an electron at the exit of the section z_f can be expressed as

$$z_f = z_i + R_{56}\delta + T_{566}\delta^2 + U_{5666}\delta^3 + \dots \quad (4)$$

where z_i is the initial longitudinal position before entering the dispersive section, R_{56} , T_{566} and U_{5666} are the first, second and third order longitudinal dispersion functions of the dispersive beamline respectively. Neglecting the initial uncorrelated energy spread in the high order terms of the right hand side of Eq. (2) and combining Eq. (2) and Eq. (4), the longitudinal position of an electron after regrouping is given as

$$z_f(z_i) = C_0 + z_i/C_1 + z_i^2/C_2 + z_i^3/C_3 + \dots, \quad (5)$$

where C_0 , C_1 , C_2 , C_3 , ... are the corresponding coefficients defined as

$$\begin{cases} C_0 = aR_{56}\delta_i, \\ C_1 = (1 + h_1R_{56})^{-1}, \\ C_2 = (h_2R_{56} + h_1^2T_{566})^{-1}, \\ C_3 = (h_3R_{56} + 2h_1h_2T_{566} + h_1^3U_{5666})^{-1}. \end{cases} \quad (6)$$

Since the rms electron bunch length is defined as the expectation value of electron longitudinal position in a given distribution. Assuming that the electron bunch preserves a Gaussian distribution after passing through the dispersive beamline, we can therefore neglect the odd order terms in the expansion of the square of longitudinal position and we have

$$z_f^2 = C_0^2 + C_1^{-2}z_i^2 + \left[C_2^{-2} + 2(C_1C_3)^{-1} \right] z_i^4 + \dots \quad (7)$$

As implied by the first term on the R.H.S. of Eq. (7), the compressed bunch length is obviously limited by the initial uncorrelated energy spread of the beam. If we ignore the initial energy spread, C_1 can be interpreted as the linear compression factor. The compressor system can be designed by targeting the linear compressor factor and bunch length according to Eq. (7) and minimizing the quadratic term when the coefficient of the first order term is small. If we neglect the third order term in Eq. (5), the design of a nonlinear bunch compressor involves the design of a beamline with R_{56} and T_{566} such that

$$\begin{cases} R_{56} = -1/h_1, \\ T_{566} = -h_2R_{56}/h_1^2. \end{cases} \quad (8)$$

In order to have large linear bunch compression factor, h_1 and R_{56} should have opposite signs. Once h_1 , h_2 and R_{56} have been determined, the value of T_{566} is known. The signs of R_{56} and T_{566} should be the same as each other so that the second order term in Eq. (5) is minimized. It is well known that R_{56} for a conventional four-dipole chicane is always positive. That is, higher-energy electrons take shorter path while crossing the chicane. It is obvious to let lower-energy electrons at the bunch head of a chirped beam by setting the chirper linac phase. The second order longitudinal dispersion of a four-dipole chicane ($T_{566} = -1.5R_{56}$) is, however, always negative. Therefore, it does not match the requirements as stated in Eq. (8). One method to resolve this problem is to add a higher harmonic rf section operating at decelerating phase to flip the sign of h_2 [4].

DOGLEG COMPRESSOR FOR THE NSRRC VUV FEL DRIVER LINAC

An alternative method is to flip the sign of R_{56} so that both T_{566} and R_{56} have the same sign [5,6]. However, in this case, the chirper linac phase has to be set for positive h_1 . By introduction of quadrupole and sextupole magnets into the compressor, the longitudinal dispersion function can be adjusted by controlling the transverse dispersion functions according to the following relations:

$$\begin{aligned} R_{56} &= - \int \frac{R_{16}}{\rho} ds, \\ T_{566} &= - \int \left[\frac{T_{166}}{\rho} + \frac{1}{2}R_{26}^2 + \frac{1}{2} \left(\frac{R_{16}}{\rho} \right)^2 \right] ds. \end{aligned} \quad (9)$$

Since the dominant (second and third) terms in the integrand of the second expression of Eq. (9) are always positive, T_{566} will be negative in most cases. This forces us to consider a compressor with negative R_{56} . As implied in the first expression of Eq. (9), R_{56} is the path integral of the product of transverse dispersion function R_{16} and beam curvature ρ^{-1} , one can design a beamline with negative R_{56} by placing the horizontal quadrupoles in the region where transverse dispersion function is nonzero. And the quads help to focus the beam to the point of anti-symmetry of the dogleg.

Our goal is to design a 325-MeV high-brightness sub-100-fsec electron beam at the end of the driver linac system. However, the design is limited by availability of space as well as the existing and affordable hardware. This is the main reason to employ nonlinear magnet compressor and avoid using higher harmonic rf linac and its corresponding pulsed klystron system. In order to fit the whole facility into the 38-m ATA tunnel, the compressor

under consideration is a single-stage, 130-MeV design at about 5 m in length. Although the beam energy is not too high, deterioration of beam quality due to CSR is considered to be severe. In order to reduce this effect, we considered employing the double dog-leg scheme as illustrated in Figure 1.

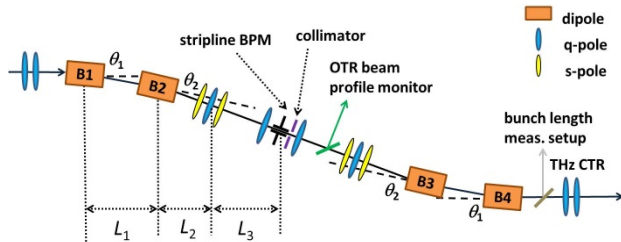


Figure 1: Layout of the double dogleg bunch compressor for the NSRRC VUV FEL driver linac system.

Tunability of R_{56}

A large variation in the bunch length or the peak current for various operation conditions can be done by the tuning of R_{56} . This can be realized by changing the longitudinal positions of the outside dipoles, B1 and B4, and adjust the quadrupoles and sextupoles settings for appropriate bunch compression. Since our nominal C_1 is about 50 when the electron distribution is almost upstood in longitudinal phase space, a small tuning of the R_{56} (in this case, -55 mm) is able to provide a large variation in the bunch length or the peak current.

For example, over-compressing the bunch slightly by changing R_{56} from -55 mm to -56 mm is accomplished simply by translating B1 and B4 longitudinally by approximately 10 cm in the opposite direction will. However, unlike a four-dipole chicane, which requires only simple tuning of the dipole field strength, the dogleg compressor will need retuning of each element from B1 to B4.

Beam Dynamics in the Driver Linac

In simulation study, the electron beam from cathode surface to exit of the photoinjector system is tracked by GPT with 3D space charge effects included. The output beam data at the photoinjector exit ($E \sim 100$ MeV) is then transferred to ELEGANT for particle tracking so that the effects of wake fields in the linacs and CSR can be included. We assumed the gun field is 70 MV/m and charge from cathode surface is 100 pC. The beam is accelerated near rf crest by the photoinjector.

When the chirper is operated at $\phi_0 = 45^\circ$ with accelerating gradient of 18 MV/m, h_1 and h_2 according to Eq. (3) are 18 m^{-1} and -569 m^{-2} respectively. To compress the electron bunch with $C_1 > 20$ in one stage, R_{56} of -55 mm is required for an upstood bunch. The horizontal dispersion functions are matched to zero at both ends of compressor to avoid the emittance growth. The sign of the first order longitudinal dispersion function has been

flipped to have the same sign as second order dispersion, and the required value T_{566} is -258.6 mm. Beam optics of the compressor has been verified with the MAD.

Electron distribution in transverse phase space has been adjusted carefully to an orientation such that the contribution of CSR kicks to emittance growth is minimized [7]. We have considered operating the compressor in the slightly under compression regime to preserve good quality beam. In this case, a compressed bunch with rms bunch length of $\sigma_t \sim 120$ fs in a near-Gaussian current profile can be obtained at the compressor exit.

With consideration of wake fields in the main rf linac, a 319 MeV, ~ 97 fs beam with sliced rms energy spread of ~ 98 keV and the peak current of 1.1 kA is obtained at the exit of the linac system (Fig. 2). The normalized horizontal and vertical slice emittances in this case are 0.62 and 0.48 mm-mrad respectively.

It may be desirable to operate the dogleg for a slightly over-compressed bunch to reduce energy spread, there is still a residual energy chirp which causes shorten FEL pulses. Since the wakefield in the main linac is not strong enough to reduce this energy chirp, a dechirper is needed. Furthermore, since the dog-leg compressor has a negative R_{56} , the higher energy electron will take a longer path in the compressor. In other words, the electrons in the bunch head will have higher energy for an under-compressed bunch. The capacitive LCLS-type dechirper [8], however, will enhance the energy chirp. Therefore, if we use a LCLS-type dechirper (capacitive), we will have to run the electron bunch in the over-compression mode.

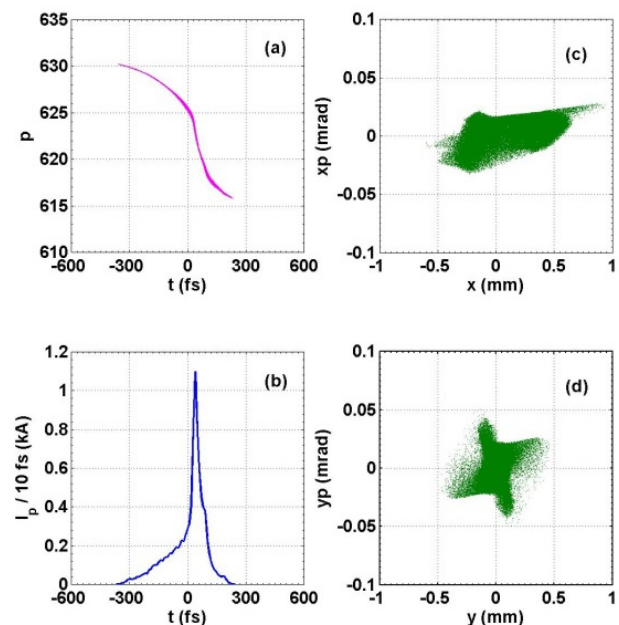


Figure 2: (a) electron distribution in longitudinal phase space, (b) current profile, electron distributions in (c) x - x' phase space and (d) y - y' phase space at the main linac exit.

CONCLUSION

Beam dynamics in this linac system has been studied by particle tracking simulation including collective effects such as space charge, wake fields and coherent synchrotron radiation. We demonstrated a 319 MeV high brightness electron beam can be generated from the linac for the proposed 4th harmonic HGHG FEL operation. R_{56} of the dogleg is tunable by changing the longitudinal positions of the outside dipoles in opposite directions and adjust the quadrupoles and sextupoles settings for appropriate bunch compression. Further study includes other tuning schemes and the tolerances of parameter variations of this compressor.

REFERENCES

- [1] A.P. Lee *et al.*, in *Proc. IPAC'14*, Dresden, Germany, p. 2974, 2014.
- [2] L. H. Yu *et al.*, *Science* 289, p. 932 2000.
- [3] N. Y. Huang *et al.*, in *Proc. IPAC'14*, Dresden, Germany, p. 2980.
- [4] P. Emma, Technical Note SLAC-TN-05-004, LCLS-TN-01-1, November 14, 2001.
- [5] Y. Sun *et al.*, *Phys. Rev. ST Accel. Beams* 17, p. 110703, 2014.
- [6] R. England *et al.*, *Phys. Rev. ST Accel. Beams* 8, p. 012801, (2005).
- [7] M. Shimada *et al.*, in *Proc. ERL'07*, Daresbury, UK, p. 108.
- [8] M. W. Guetg *et al.*, Technical Note SLAC-PUB-16834, March 6, 2017.

NOVEL ASPECTS OF BEAM DYNAMICS IN CEC SRF GUN AND SRF ACCELERATOR

I. Petrushina*¹, T. Hayes, Y. Jing, D. Kayran, V.N. Litvinenko¹, G. Narayan,
I. Pinayev, F. Severino, K.S. Smith, G. Wang¹, K. Shih¹, K. Mihara¹
Brookhaven National Laboratory, Upton, NY 11973, USA
¹ also at Stony Brook University, Stony Brook, NY 11794, USA

Abstract

A 15 MeV CW SRF accelerator has been commissioned at Brookhaven National Laboratory to test the Coherent electron Cooling concept. The accelerator consists of an SRF 113 MHz photoemission gun, two 500 MHz bunching cavities and a 704 MHz 5-cell SRF linac. In this paper, we describe our experience with this system with focus on unusual phenomena, such as multipacting in the SRF gun. We also discuss issues of wakefields in the CeC accelerator.

CEC ACCELERATOR

Coherent electron Cooling (CeC) is an advanced method of beam cooling which is based on electrostatic interactions between electron and ion beams amplified by a high-gain free electron laser (FEL) [1]. This promising method would significantly reduce cooling time of a hadron beam compared to the other known techniques. The CeC Proof of Principle (PoP) experiment is currently undergoing commissioning at Brookhaven National Laboratory, and the layout of the CeC beamline is illustrated in the figure at the top of the next page [2]. The accelerating section of the system consists of a 113 MHz superconducting photo-injector followed by the first focusing solenoid, two 500 MHz normal conducting bunching cavities, a transport section with 5 solenoids, and a 704 MHz superconducting accelerating 5-cell cavity. After the electron beam is accelerated to the velocity matching the velocity of the hadron beam circulating in RHIC, it is directed by the dogleg into the common section, where the beams co-propagate. In this paper, we present the observations during the system commissioning alongside with the simulation results, and we discuss our future plans for the wakefields and beam dynamics simulations.

113 MHz SRF PHOTO-INJECTOR

The 113 MHz photo-injector is based on a quarter-wave resonator which provides 1.05 MV of accelerating voltage, and can generate an electron bunch with charge up to 4 nC (see Fig. 1) [3–5]. This year, the gun was generating an electron beam at the third subharmonic of the RHIC revolution frequency, which is 26 kHz for the hadron's energy of 26.5 GeV/u. For the Run'18 the gun will be retuned to operating at a harmonic of RHIC revolution frequency e.g. 78 kHz. During the last run, the photo-injector demonstrated excellent performance, which showed significant improvements compared to the results of the Run'16, which was

challenged by the presence of strong multipacting (MP) barriers.

Multipacting

Multipactor discharge was a major limiting factor during the previous year of commissioning. We observed that vacuum activity due to the MP would significantly increase in the presence of the external magnetic field of the first solenoid (especially for a magnetic field of about 400 Gs). The most dangerous MP level was found to be at 40 kV of accelerating voltage, which would become worse when the CsK₂Sb photocathode was inserted into the cavity. This MP level would lead to serious vacuum excursions, which were rather damaging to the quantum efficiency of the photocathode—it would deteriorate from 2-8 % to 0.01-0.1 %.

After a comprehensive study of the MP in the gun using Track3P [6], it was confirmed that the external magnetic field increases the strength of MP in the gap of the fundamental power coupler (FPC), with stable trajectories moving from the cavity side of the gun towards the bellow (see Fig. 1). The simulation results showed that the stubborn MP level at 40 kV is localized in the front rounding of the cavity and is a 1st-order multipactor discharge. See [7, 8] for a more detailed discussion of the simulation results.

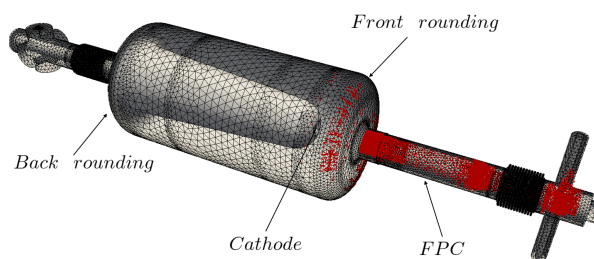


Figure 1: Geometry of the CeC photo-injector. Areas of the cavity affected by MP are shown in red.

With the knowledge of the main MP levels and their locations, operation of the gun became very intuitive. When bringing the cavity to the operating voltage, we would keep the first solenoid at zero current, and insert the FPC into position with the maximum achievable coupling using full 4 kW of available RF power in order to overcome the 40 kV MP level. After passing a voltage of about 100 kV there was no significant MP activity, and we were able to bring the cavity to the operational level by adjusting coupling via FPC position in a phase-lock loop mode.

* ipetrushina@bnl.gov

Content from this work may be used under the terms of the CC BY 3.0 licence (© 2018). Any distribution of this work must maintain attribution to the author(s), title of the work, publisher, and DOI.

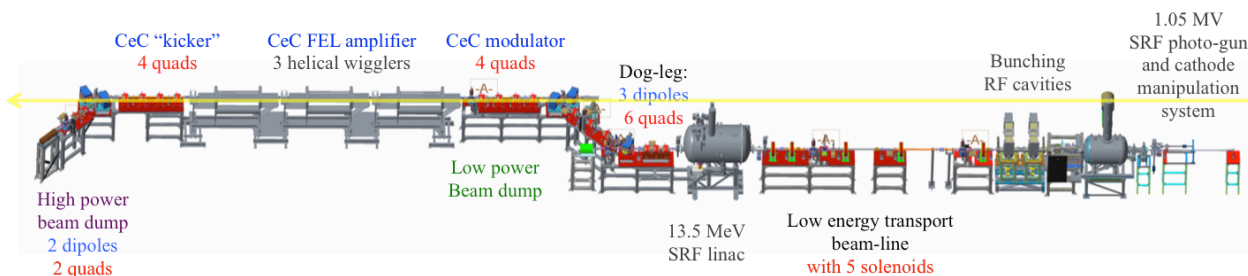


Figure 2: Schematic of the CeC experiment.

In cases when the cavity was caught onto the 40 kV MP level, the gun was turned off immediately, and left idle for about 30 minutes. We assume that this time is needed to oxidize Cs released from the surface of the cathode by the stray electron bombardment during the MP.

Overall, the gun performance during the Run' 17 was stable with the photocathode maintaining high quantum efficiency and being replaced only once during 5 months of operation.

Self-Consistent Simulation

Since the photo-injector is the very first step in the beam acceleration, it is important to perform the simulations of the beam-cavity interactions taking into account the fact that it is dominated by space charge effects. One of the tools that can perform self-consistent simulations of this kind is Pic3P [6]. Pic3P solves the complete set of Maxwell-Lorentz equations self-consistently and includes space charge, retardation, and boundary effects from the first principles.

The first attempt of the simulation was performed for the 3D simplified geometry of the gun (bellows were excluded) using a mesh of about 2.2M tetrahedral elements, with enhanced mesh distribution along the beam path—meshcell size of about 0.8 mm. Initial parameters of the beam are shown in Table 1.

Table 1: Beam Parameters for the Self-Consistent Simulation of the Gun

Parameter	Value
Total charge, nC	0.5
Number of particles	50 000
Initial velocity β_z	0.003
Radial distribution	Uniform
Radius, mm	1.5
Longitudinal distribution	Flattop
Duration of the flattop, ns	0.5
Rise/drop time, ns	0.05

The simulation did not include the external magnetic field of the first solenoid, and focusing of the beam was only provided by the electric field distribution in the gun due to the cathode puck being recessed by 6 mm relative to the "nose" of the cavity. The preliminary results of the simulation

are shown in Fig. 3-6. In order to obtain an accurate solution of the self-consistent problem, we still need to perform a mesh convergence study, and analyze the dependence of the solution on the primary number of particles in the beam, the time step and the order of curved tetrahedral elements.

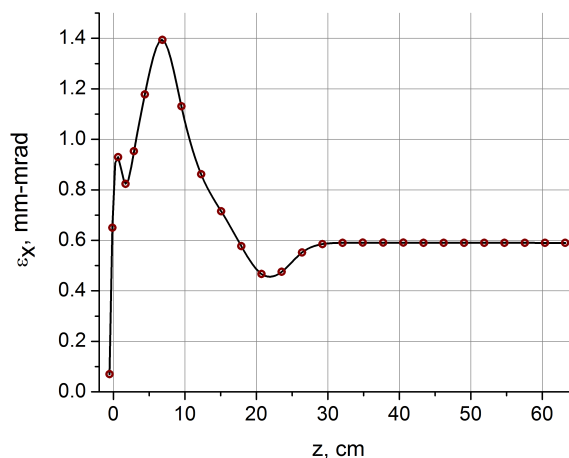


Figure 3: Normalized transverse RMS emittance as a function of the beam position in the gun. Cathode is recessed by 6 mm.

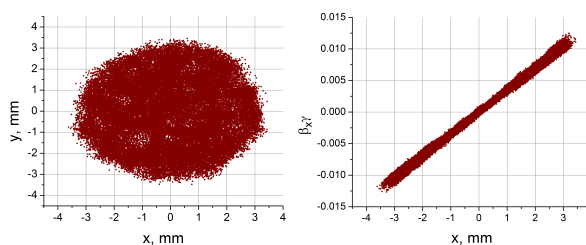


Figure 4: Transverse distribution and trace space of the bunch at $z=60$ cm from the cathode surface.

BEAM DYNAMICS STUDY

One of the critical processes in beam dynamics is a ballistic compression of the electron bunches from hundreds of picoseconds to about 20 psec. The required energy chirp is provided by the 500 MHz room-temperature cavities. The compressed beam is then propagated to the dogleg, where

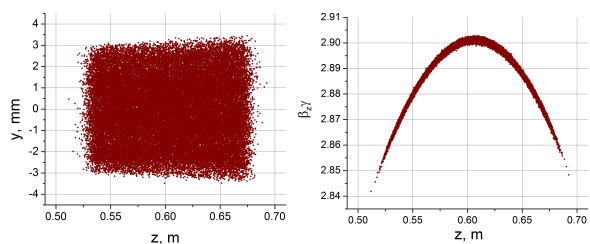


Figure 5: Longitudinal distribution and trace space of the bunch at $z=60$ cm from the cathode surface.

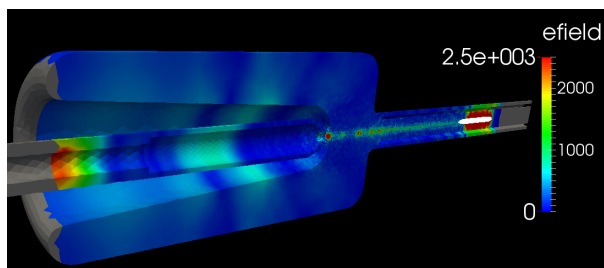


Figure 6: Electromagnetic fields induced by the electron beam in the SRF gun.

horizontal dispersion is used to analyze the beam energy spread and the bunch duration. A YAG profile monitor was used for this purpose, and the horizontal dispersion function was measured by changing the dipole magnet current. To study the longitudinal bunch structure we generated correlations between energy and time by operating the linac at ± 15 degrees off-crest. Hence, the combination of the off-crest acceleration and horizontal dispersion allowed us to utilize an improvised “streak camera”. The quadrupole triplet in front of the dipole magnet was used to focus “betatron motion” of the electrons at the YAG screen. An example of a measured longitudinal profile for the 1.2 nC bunch charge is shown in Fig. 7. One can see that part of the bunch has a periodic micro-bunching with a period of about 1.5 psec. Several factors can be responsible for such time structure: it can originate from the time structure of the initial laser pulse, space-charge driven micro-bunching instability or from wakefields induced by the beam in the transport channel.

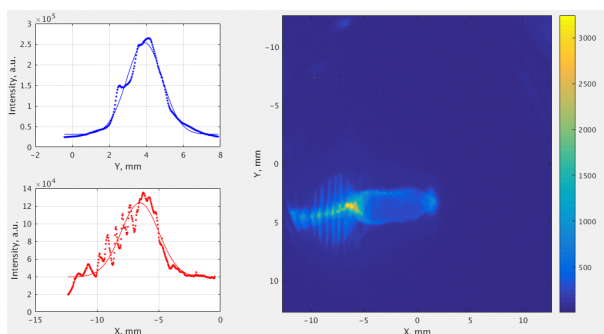


Figure 7: Periodic beam structure in the dogleg.

Numerous studies of the beam dynamics for the CeC beamline were performed throughout the years, but none of them had self-consistent simultaneous inclusion of space charge and wakefields [9, 10]. There are a number of sources of wakefields in the CeC beamline: bellows, beam diagnostics, mirrors and laser cross chamber, and other transitions in the size and shape of the vacuum chamber. We are in the process of simulating these wakefields and taking them into account in the beam dynamics simulations. With existing software for 3D simulations, such as CST Microwave Studio [11] and ACE3P [6], wakefields are calculated in non-symmetrical structures, and the resulting fields can be imported into the programs for the beam dynamics simulations. Our current plan is to perform a comprehensive wakefield study in the entire CeC system, and include the resulting fields into the IMPACT-T [12] calculations in order to see the influence of the wakefields on the beam structure.

CONCLUSION

The CeC accelerating system was successfully commissioned during this year’s run. With better understanding of the multipacting events in the SRF gun, we achieved a stable operational regime, and utilized only two CsK₂Sb photocathodes during the 5 months of operation.

As a part of preparation for next year, our goal is to perform a self-consistent simulation of the SRF gun, including space charge effects and wakefields, and study the influence of the wakefields and space charge on the beam dynamics throughout the whole system.

ACKNOWLEDGEMENT

The authors would like to thank Lixin Ge and Cho-Kuen Ng from SLAC for helpful discussions and useful tips on using ACE3P.

This research used resources of the National Energy Research Scientific Computing Center, which is supported by the Office of Science of the U.S. Department of Energy under Contract No. DE-AC02-05CH11231.

Work is supported by Brookhaven Science Associates, LLC under Contract No. DEAC0298CH10886 with the U.S. Department of Energy, DOE NP office grant DE-FOA-0000632, and NSF grant PHY-1415252.

REFERENCES

- [1] V. N. Litvinenko and Y. S. Derbenev “Coherent Electron Cooling”, *Phys. Rev. Lett.*, vol. 102, p. 114801, March 2009.
- [2] I. Pinayev *et al.*, “Commissioning of CeC PoP accelerator”, in *Proc. North American Particle Accelerator Conf. (NAPAC’16)*, Sheraton Grand, Chicago, IL, USA, 2016.
- [3] S. Belomestnykh *et al.*, “Superconducting 112 MHz QWR electron gun”, in *Proc. 15th Int. Conf. on RF Superconductivity (SRF’11)*, Chicago, IL, USA, 2011 paper MOPMN002, pp. 223.
- [4] S. Belomestnykh *et al.*, “Developing of superconducting RF guns at BNL”, in *Proc. 26th Int. Linear Accelerator Conf.*

- (LINAC'12), Tel-Aviv, Israel, 2012 paper MOPB064, pp. 324–326.
- [5] J. C. Brutus *et al.*, “Mechanical design of 112 MHz SRF gun FPC for CeC PoP experiment”, in *Proc. North American Particle Accelerator Conf. (NAPAC'13)*, Pasadena, CA, USA, 2013 paper WEPAC07, pp. 802–804.
- [6] L. Ge *et al.*, “Advances in parallel finite element code suite ACE3P”, in *Proc. 6th Int. Particle Accelerator Conf. (IPAC'15)*, Richmond, VA, USA, 2015 paper MOPMN002, pp. 702–704.
- [7] T. Xin *et al.*, “Experimental and simulational results of multipactors in 112 MHz QWR injector”, in *Proc. 6th Int. Particle Accelerator Conf. (IPAC'15)*, Richmond, VA, USA, 2015 paper TUPMA048, pp. 1938–1940.
- [8] I. Petrushina *et al.*, “Multipacting behavior study for the 112 MHz superconducting photo-electron gun”, in *Proc. 8th Int. Particle Accelerator Conf. (IPAC'17)*, Copenhagen, Denmark, 2017 paper MOPVA140, pp. 1180–1183.
- [9] Yuan Hui Wu *et al.*, “Beam dynamics studies for coherent electron cooling experiment”, in *Proc. 7th Int. Particle Accelerator Conf. (IPAC'16)*, Busan, Korea, 2016 paper WEPOY023, pp. 3032–3035.
- [10] J. Owen, “Simulation of Electron Beam Dynamics in the 22 MeV Accelerator for a Coherent Electron Cooling Proof of Principle Experiment”, MA thesis, Phys. Dept., Stony Brook University, Stony Brook, NY, USA 2013.
- [11] CST, <http://www.cst.com>
- [12] J. Qiang, “A 3D parallel beam dynamics code for modeling high brightness beams in photoinjectors”, in *Proc. Particle Accelerator Conf. (PAC'05)*, Knoxville, TN, USA, 2005 paper WPAP055, pp. 3316–3318.

Content from this work may be used under the terms of the CC BY 3.0 licence (© 2018). Any distribution of this work must maintain attribution to the author(s), title of the work, publisher, and DOI.

CSR WAKE FIELDS AND EMITTANCE GROWTH WITH A DISCONTINUOUS GALERKIN TIME DOMAIN METHOD*

D. A. Bizzozero[†], H. De Gersem, E. Gjonaj

Institut für Theorie Elektromagnetischer Felder, TU Darmstadt, Germany

Abstract

Coherent synchrotron radiation (CSR) is an essential consideration in modern accelerators and related electromagnetic structures. We present our current method to examine CSR in the time domain. The method uses a 2D Discontinuous Galerkin (DG) discretization in the longitudinal and transverse coordinates (z, x) with a Fourier decomposition in the transverse coordinate y . After summation over modes, this treatment describes all electromagnetic field components at each space-time coordinate (z, x, y, t). Additionally, by alignment of mesh element interfaces along a source reference orbit, DG methods can handle discontinuous or thin sources in the transverse x direction. We present an overview of our method, illustrate it by calculating wake functions for a bunch compressor, and discuss a method for estimating emittance growth from the wake fields in future work.

PROBLEM STATEMENT

In a continuation of earlier work [1–3], we examine the generation of CSR by an ultra-relativistic electron bunch in a vacuum chamber of rectangular cross-section. For a simplified model, we only consider motion of the bunch in a planar orbit with Cartesian coordinates (Z, X, Y) in the midplane $Y = 0$. Additionally, we only model vacuum chambers with planar horizontal boundaries at $Y = \pm h/2$ where h is the height of the chamber and only consider perfectly electrically conducting (PEC) boundary conditions on the chamber walls. An example of a chamber with a planar orbit is shown in Figure 1 (top), corresponding to the bunch compressor DESY BC0.

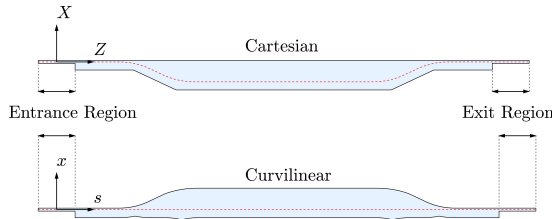


Figure 1: DESY BC0 vacuum chamber domain in (Z, X) (top) or (s, x) (bottom) coordinates with reference orbit (red dashed). The entrance region is the same in both systems.

To study CSR wake fields, we seek to time-evolve the Maxwell field equations for \mathbf{E} and \mathbf{H} inside the chamber:

$$\frac{\partial \mathbf{E}}{\partial \tau} = Z_0 \nabla \times \mathbf{H} - Z_0 \mathbf{j}, \quad \frac{\partial \mathbf{H}}{\partial \tau} = -\frac{1}{Z_0} \nabla \times \mathbf{E}, \quad (1)$$

* Work supported by DESY.

[†] bizzozero@temf.tu-darmstadt.de

where $\tau = ct$, with speed of light c , vacuum impedance Z_0 , and current density \mathbf{j} .

Given a smooth reference orbit parametrized by its arc length $\mathbf{R}_r(s) = (Z_r(s), X_r(s), 0)$, we transform the (Z, X, Y) coordinate system to a curvilinear system (s, x, y) with the inverse transformation of:

$$\begin{aligned} Z(s, x, y) &= Z_r(s) - xX_r'(s), \\ X(s, x, y) &= X_r(s) + xZ_r'(s), \\ \text{and } Y(s, x, y) &= y, \end{aligned} \quad (2)$$

using the signed curvature: $\kappa(s) = Z_r''(s)X_r'(s) - Z_r'(s)X_r''(s)$ and length scale factor: $\eta(s, x) = 1 + x\kappa(s)$. In the (s, x, y) coordinate system, the reference orbit is the straight line $(x, y) = (0, 0)$. Furthermore, this coordinate mapping is well-defined if $\eta > 0$ throughout the domain; where the transformation is unique. See Figure 1 (bottom) for a depiction of the curvilinear transformation of the geometry in the case of DESY BC0.

In the (s, x, y) coordinate frame, we assume a current density of the form: $\mathbf{j} = (qc\lambda(s - \tau)\delta(x)G(y), 0, 0)$ with Gaussian longitudinal and transverse distributions λ and G , and a Dirac distribution in the x -coordinate. We choose σ_s , the bunch length, such that the bunch is supported only in the entrance region to machine precision at $\tau = 0$.

We now use the parallel plate geometry of $y = \pm h/2$ to introduce a Fourier decomposition in y for all fields:

$$\begin{aligned} f(s, x, y, \tau) &= \sum_{p=1}^{\infty} f_p(s, x, \tau) \phi(\alpha_p(y + h/2)) \\ \text{and } f_p(s, x, \tau) &= \frac{2}{h} \int_{-h/2}^{h/2} f(s, x, y, \tau) \phi(\alpha_p(y + h/2)) dy, \end{aligned} \quad (3)$$

with $\alpha_p = \pi p/h$, f representing $E_s, E_x, E_y, H_s, H_x, H_y$ or G , and $\phi(\cdot)$ is $\sin(\cdot)$ for E_s, E_x, H_y, G or $\cos(\cdot)$ for E_y, H_s, H_x . If the initial fields and $G(y)$ are symmetric about $y = 0$, then the even p modes for all fields vanish. We denote the Fourier series modes with the subscript p .

To numerically treat the singularity at $x = 0$ in the current \mathbf{j} term on the right-hand-side of (1), we apply an additional transformation on the H_{yp} field component: $\tilde{H}_{yp} = H_{yp} - qcG_p\lambda(s - \tau)\Theta(x)$ where $\Theta(x)$ is the Heaviside function. Additional transformations can be made to transform the source to arbitrary degree of smoothness [4]; however, for a DG method with element edges which align along the discontinuity, this is not required.

Applying the curvilinear coordinate transformation in (2), the Fourier series decomposition in (3), and the transforma-

tion for H_{yp} , to (1) yields:

$$\frac{1}{Z_0} \frac{\partial E_{sp}}{\partial \tau} = \frac{\partial \tilde{H}_{yp}}{\partial x} + \alpha_p H_{xp}, \quad (4a)$$

$$\frac{1}{Z_0} \frac{\partial E_{xp}}{\partial \tau} = -\alpha_p H_{sp} - \frac{1}{\eta} \frac{\partial \tilde{H}_{yp}}{\partial s} + S_E, \quad (4b)$$

$$\frac{1}{Z_0} \frac{\partial E_{yp}}{\partial \tau} = \frac{1}{\eta} \frac{\partial H_{xp}}{\partial s} - \frac{\partial H_{sp}}{\partial x} - \frac{\kappa}{\eta} H_{sp}, \quad (4c)$$

$$Z_0 \frac{\partial H_{sp}}{\partial \tau} = \alpha_p E_{xp} - \frac{\partial E_{yp}}{\partial x}, \quad (4d)$$

$$Z_0 \frac{\partial H_{xp}}{\partial \tau} = \frac{1}{\eta} \frac{\partial E_{yp}}{\partial s} - \alpha_p E_{sp}, \quad (4e)$$

$$Z_0 \frac{\partial \tilde{H}_{yp}}{\partial \tau} = \frac{\partial E_{sp}}{\partial x} + \frac{\kappa}{\eta} E_{sp} - \frac{1}{\eta} \frac{\partial E_{xp}}{\partial s} + S_H, \quad (4f)$$

where the source terms $S_E = -qcG_p \lambda'(s - \tau)\Theta(x)/\eta(s, x)$ and $S_H = qZ_0cG_p \lambda'(s - \tau)\Theta(x)$ arise from \mathbf{j} after the H_{yp} transformation.

To initialize the time-evolution of the system in (4) we consider all fields inside the vacuum chamber to be zero initially except for the entrance region. In this region, where the reference orbit is a straight line in (Z, X, Y) with $\kappa = 0$, $\eta = 1$; the solution for a centered beam about $x = 0$ with entrance region chamber width $2d$ satisfying the PEC boundary conditions is given by:

$$\begin{aligned} E_{sp0} &= 0, & H_{sp0} &= 0, \\ E_{xp0} &= -qZ_0cG_p \lambda(s)\Phi_p(x), & H_{xp0} &= -E_{yp0}/Z_0, \\ E_{yp0} &= -qZ_0cG_p \lambda(s)\Psi_p(x), & H_{yp0} &= E_{xp0}/Z_0, \end{aligned} \quad (5)$$

and

$$\begin{aligned} \Phi_p(x) &= \frac{\sinh(\alpha_p d)}{\sinh(2\alpha_p d)} \cosh(\alpha_p(x + d)) - \cosh(\alpha_p x)\Theta(x), \\ \Psi_p(x) &= \frac{\sinh(\alpha_p d)}{\sinh(2\alpha_p d)} \sinh(\alpha_p(x + d)) - \sinh(\alpha_p x)\Theta(x). \end{aligned}$$

However, in implementation, we use a numerical DG Poisson solver in computing the initial fields on the mesh to reduce parasitic charge effects. Lastly, the beam pipes in the entrance and exit regions are also enclosed with PEC conditions since the simulation is set to halt once the electron bunch reaches midway into the exit region of the chamber. If longer wake field simulations are desired, this exit region may be extended with little additional computational effort since the cross-sectional width is small.

DISCONTINUOUS GALERKIN METHOD

In this section we briefly outline the DG scheme used for our time-evolution of (4). Our approach follows the nodal DG foundation given in [5]. To begin, we partition the vacuum chamber domain in (s, x) into K triangular elements, with curved elements along the boundary as needed. Additionally, we impose that the reference orbit $x = 0$ lies strictly along interfaces of elements and does not bisect any element.

For a given element D^k , for $k \in \{1, \dots, K\}$, we approximate each field by sums of Lagrange polynomials of N th order denoted by $\ell_j^k(s, x)$ with $N_p = (N+1)(N+2)/2$ nodes: (s_i^k, x_i^k) where $\ell_j^k(s_i^k, x_i^k) = \delta_{ij}$, for $i, j \in \{1, \dots, N_p\}$. For a field component u on element D^k , its polynomial approximation is given by:

$$u^k(s, x, \tau) = \sum_{i=1}^{N_p} u_i^k(\tau) \ell_i^k(s, x). \quad (6)$$

We next construct residuals \mathcal{R}^k for each of the fields u^k from (4) which each have the form:

$$\mathcal{R}^k(s, x, \tau) = \frac{\partial u^k}{\partial \tau} - a \frac{\partial v^k}{\partial s} - b \frac{\partial w^k}{\partial x} - cw^k - f. \quad (7)$$

For example, for equation (4c): $u = E_{yp}$, $v = \tilde{H}_{xp}$, $w = H_{sp}$, $a = Z_0/\eta$, $b = -Z_0$, $c = -Z_0\kappa/\eta$, and $f = 0$. For a Galerkin scheme, we require the residuals to be orthogonal to the same polynomial space spanned by ℓ_j^k on the element. However, a numerical flux must be introduced to couple the elements together along their edges. This flux term is a single-valued function depending on interior and exterior values along the interface. We choose an upwind flux for our hyperbolic system of equations (4). A thorough derivation of the resulting system of discrete equations is given in [2] with DG constructions detailed in [5].

With the discrete DG equations for (4) combined over all K elements, we obtain a system of $6N_p K$ equations. We evolve these equations in τ with a fourth-order low-storage explicit Runge-Kutta scheme [6].

WAKE FIELDS AND POST PROCESSING

We present simulation results for computing the longitudinal wake field by integrating E_s along the reference orbit. We define the longitudinal wake function on the orbit by:

$$\begin{aligned} w_s(z) &= \frac{-1}{q} \int_0^T E_s(\tau - z, 0, 0, \tau) d\tau \\ &= \frac{-1}{q} \sum_{p=1}^{p_{\max}} \sin\left(\frac{\pi p}{2}\right) \int_0^T E_{sp}(\tau - z, 0, \tau) d\tau. \end{aligned} \quad (8)$$

We denote z as the distance with respect to the center of the bunch along the reference orbit, not the Cartesian coordinate Z . Evaluation of E_{sp} is done while time-stepping (4) by averaging the field along $x = 0$ using the elements' DG N th-order polynomial representation as in (6). We set T/c to be the time when the bunch is midway into the exit region.

For the transverse wake function $w_x(z)$, we replace E_s by $(E_x - Z_0 H_y)$ and for the wake function $w_y(z)$ we replace E_s by $(E_y + Z_0 H_x)$ in equation (8).

We also define the loss factor by:

$$L = - \int_{-\infty}^{\infty} w_s(z) \lambda(z) dz. \quad (9)$$

In our first example, we consider a straight orbit such that $(s, x) = (Z, X)$ where the bunch passes through a rectangular beam taper. While no CSR is generated, the narrowing width of the chamber generates a longitudinal wake in Figure 2. This test is used to compare wake fields to CST Particle Studio™ [7] and PBCI [8]. The discrepancy in wake functions behind the bunch at $z \approx -50\text{mm}$ is due to the difference in wake function integration methods, and diminishes as T increases. The loss factor relative error between our DG method and CST is $|L_{\text{DG}} - L_{\text{CST}}|/|L_{\text{CST}}| = 7.87 \times 10^{-5}$.

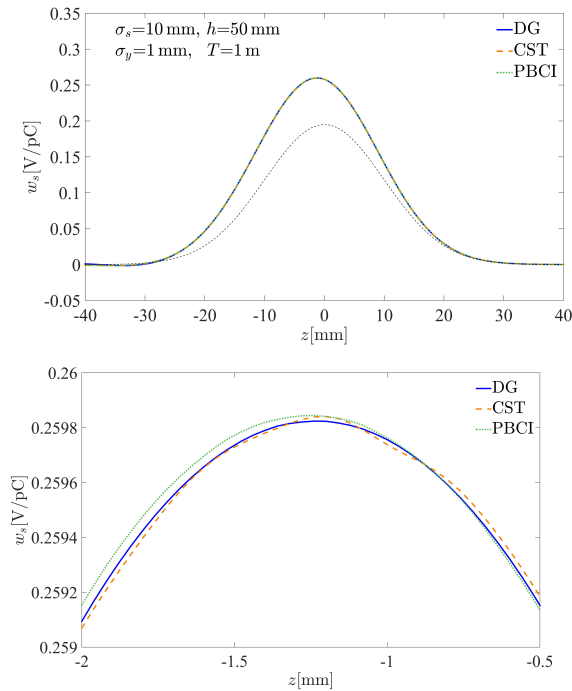


Figure 2: (Top) Wake function $w_s(z)$ shown using $N = 8$, $K = 27544$, and $p = 1, 3, 5$ modes for the tapered rectangular beam transition using our DG method, CST Particle Studio™, and PBCI. (Bottom) An enlarged view of $w_s(z)$ near $z = 0$. The thin dashed line shows the bunch profile $\lambda(z)$ scaled to the figure. The loss factor is $L = -1.847 \times 10^{-1} \text{ V/pC}$.

In our second example, we use the full DESY BC0 geometry as shown in Figure 1. In Figure 3, we plot the longitudinal wake generated by CSR and the geometry after the bunch travels along the chicane orbit comprised of straights and arcs of circles with constant curvature $\kappa = 1 \text{ m}^{-1}$.

CONCLUSION AND FUTURE WORK

In this study, we computed CSR fields generated in a bunch compressor vacuum chamber using DG finite elements in the time domain. We also presented a method to compute the longitudinal wake field and loss factors.

Our next application of this DG method will study the evolution of particle distributions by importing field maps into a particle tracking code to study emittance growth. Additionally, we will investigate the use of the Panofsky-Wenzel theorem [9] in curvilinear coordinates as an alternative

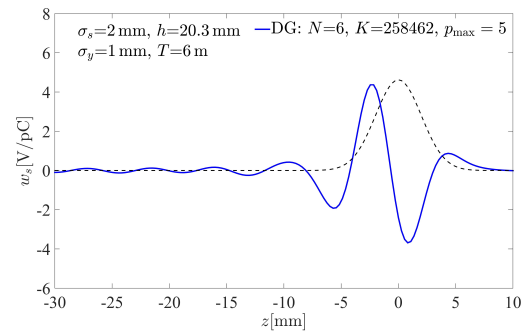


Figure 3: Wake function $w_s(z)$ for the DESY BC0 vacuum chamber. The thin dashed line shows the bunch profile $\lambda(z)$ scaled to $w_s(z)$. The loss factor is $L = 1.485 \times 10^{-5} \text{ V/pC}$.

approach to obtaining the transverse wake functions. We also will compare our results to paraxial frequency-domain methods [10] and other CSR codes such as CSRtrack [11].

REFERENCES

- [1] D. A. Bizzozero, H. De. Gerssem, and E. Gjonaj, “Coherent Synchrotron Radiation and Wake Fields With Discontinuous Galerkin Time Domain Methods”, in *Proceedings of IPAC 2017*, Copenhagen, Denmark, May 2017.
- [2] D. A. Bizzozero, *Studies of Coherent Synchrotron Radiation with the Discontinuous Galerkin Method*, Ph.D. Dissertation, Applied Math, University of New Mexico, 2015.
- [3] B. E. Billinghamurst et al., “Observation of Wakefields and Resonances in Coherent Synchrotron Radiation”, *Phys. Rev. Lett.* 114, 204801, 2015.
- [4] R. L. Warnock and D. A. Bizzozero, “Efficient Computation of Coherent Synchrotron Radiation in a Rectangular Chamber”, *Phys. Rev. Accel. Beams* 19, 090705, 2016.
- [5] J. Hesthaven and T. Warburton, *Nodal Discontinuous Galerkin Methods* New York: Springer, 2008.
- [6] J. C. Butcher, *The Numerical Analysis of Ordinary Differential Equations: Runge-Kutta and General Linear Methods*, New York: Wiley & Sons, 2003.
- [7] CST AG (2016), Bad Nauheimer Str. 19, 64289 Darmstadt, Germany. Retrieved from <http://www.cst.com>.
- [8] E. Gjonaj, T. Lau, S. Schnepf, F. Wolfheimer, and T. Weiland, “Accurate Modelling of Charged Particle Beams in Linear Accelerators”, *New J. Phys.* Vol 8, November 2006.
- [9] W. K. H. Panofsky and W. A. Wenzel “Some Considerations Concerning the Transverse Deflection of Charged Particles in Radio-Frequency Fields”, *Rev. Sci. Instrum.* 27, pp. 967, 1956.
- [10] D. Zhou, K. Ohmi, K. Oide, L. Zang, and G. Stupakov, “Calculation of Coherent Synchrotron Radiation Impedance for a Beam Moving in a Curved Trajectory”, *Jpn. J. Appl. Phys.* 51, 016401, 2012.
- [11] M. Dohlus and T. Limberg, “CSRtrack: Faster Calculation of 3-D CSR Effects”, in *Proceedings of FEL 2004*, Trieste, Italy, August 2004.

EXPERIMENTS IN ELECTRON BEAM NANOPATTERNING*

C. Zhang[†], W.S. Graves, L.E. Malin and J.C.H. Spence, ASU, Tempe, USA
 R.K. Li, E.A. Nanni, X. Shen, S.P. Weathersby and J. Yang, SLAC, Menlo Park, USA
 D. Cesar, J. Maxson, P. Musumeci and A. Urbanowicz, UCLA, Los Angeles, USA

Abstract

We report on experiments in nanopatterning electron beams from a photoinjector as a first step toward a compact XFEL (CXFEL). The nanopatterning is produced by Bragg diffraction of relativistic electron beams through a patterned Si crystal consisting of alternating thick and thin strips to produce nanometer-scale electron density modulations. Multi-slice simulations show that the target can be oriented for a two-beam condition where nearly 80% of the elastically scattered electron beam is diffracted into the 220 Bragg peak. An experiment at the two-beam condition measurement has been carried out at the SLAC UED facility showing this effect with 2.26 MeV electrons. We successfully proved a large portion of the main beam is diffracted into 220 spot by tuning the orientation of the sample. Future plans at UCLA are to observe the nanopatterned beam, and to investigate various grating periods, crystal thicknesses, and sample orientations to maximize the contrast in the pattern and explore tuning the period of the modulation. The SLAC measurement results will be presented along with design of the UCLA experiments.

INTRODUCTION

Research to develop compact XFEL [2, 3] based on inverse Compton scattering are being carried on at ASU. We proposed to use a Si grating to generate nanometer scale bunched beam [7, 9] which can be an ideal source for seeding a room-size XFEL. The method depends on diffracting electrons through a thin silicon grating structure to produce a transverse modulation, and then transferring this modulation into the time domain via emittance exchange [5]. The high reproducibility and determinability of electron bunches generated by grating diffraction method will greatly improve the coherence of X-ray output. Proof-of-principle experiments [4, 6] have been performed at SLAC's UED facility [8], and new experimental data presented here shows a close match of simulation and experiment showing that the photoinjector beam quality and the stability of the accelerator are adequate to achieve nanopatterning.

We present the results of these studies and discuss plans to carry out grating diffraction experiments at UCLA's Pegasus laboratory in the near future, and study associated beam dynamics.

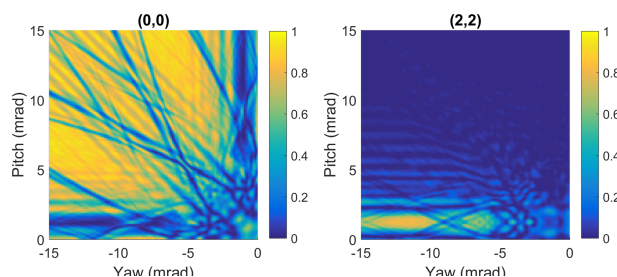


Figure 1: Simulated intensity maps of 200 nm thick planar Si membrane. The color of each pixel represents the normalized intensity of the selected beam. Left is the intensity map of (000) beam, right is the map of (220) beam.

SLAC RESULTS

Previous simulation of Si crystal electron diffraction using multislice method [4] showed a possibility to find a two-beam condition where 80% of the diffracted electron beam is in a single Bragg peak. In the laboratory frame we use pitch and yaw angles with respect to the horizontal electron beam to denote the angular deviation of the beam from the [001] normal to the silicon crystal. The aim of these experiments is to measure the variation in the transmitted (000) and (220) Bragg beams as the diffraction conditions are varied around the exact (220) Bragg condition. To determine the relation between pitch/yaw angle and diffraction intensity, 2D intensity maps shown in Fig. 1 have been created to predict the exact position where we can find the two-beam condition. To create the maps, scans of the pitch (rotation about x-axis) and yaw (rotation about the y-axis) angles have been performed while recording the diffraction pattern and then we processed the images to find the intensity of different Bragg spots as maps of pitch and yaw.

The (000) beam intensity map in Figure 1 shows a dark gap near pitch = 1 mrad, yaw = -12 mrad which is corresponding to the bright strips in the (220) beam map where the direct beam has been mainly diffracted into Bragg spots.

To make a precise measurement, careful calibrations of all rotation angles of the system are needed. The roll angle of the sample corresponding to holder pitch and yaw has been mounted less than 1 degree. Then the sample is aligned in both pitch and yaw angle within ± 0.02 degrees to normal position.

A fine 2D scan over the area of interest was performed to search for the two-beam condition. Figure 2 shows representative patterns of a two-beam condition where the majority of electron beam are scattered into either the forward (000)

* This work was supported by NSF Accelerator Science awards 1632780 and 1415583, NSF BioXFEL STC award 1231306, and DOE contract DE-AC02-76SF00515.

[†] czhan178@asu.edu

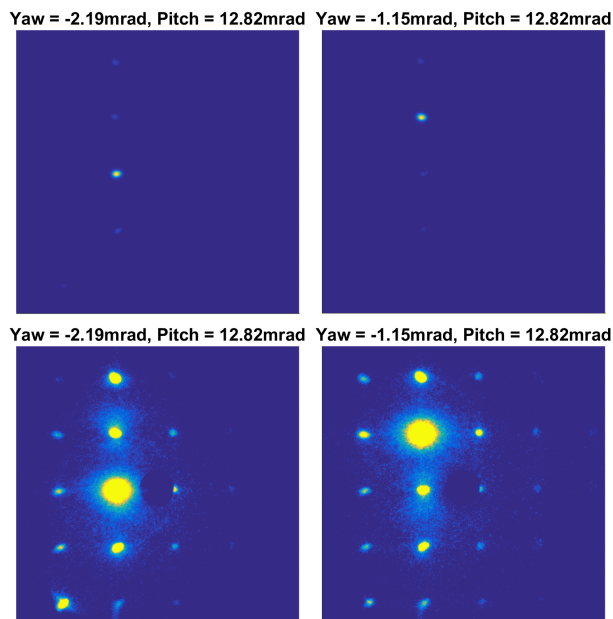


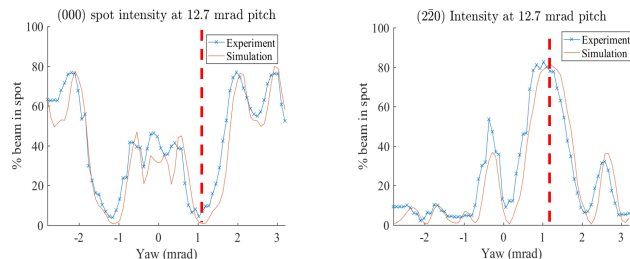
Figure 2: Original and contrast-enhanced Si electron diffraction patterns from SLAC UED facility. Central dark disk is a hole in the YAG:CE scintillator detector. Left column shows the condition where 80% of the forward beam is scattered into (000) spot. Right column shows 80% of the beam diffracting into the (220) beam.

beam or the diffracted (220) beam. Further data analyzing in Fig. 3(a) shows a lineout at pitch = 12.7 mrad illustrating how the intensity varies as a function of yaw. The vertical red dashed line calls attention to yaw = 1.1 mrad where the (000) intensity is nearly zero and the (220) intensity is about 80%, indicating the main beam is diffracted into (220) Bragg spot. Figure 3 (b) and (c) are the simulation and experimental 2D intensity maps of (000) and (220) spot showing a strong agreement between simulation and experiment.

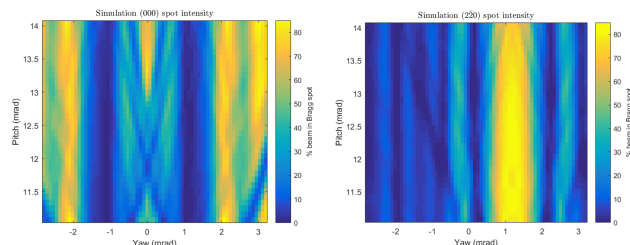
UCLA SETUP

The concept to form a nanopatterned beam is based on two-beam manipulation using a grating. The structure used to pattern the beam will consist of alternating strips of single-crystal silicon and cut through gaps running perpendicular to the beam. Prototype Si gratings are shown in Fig. 4. At the two-beam condition, the cut-through gaps will let all electrons pass through and result in a strong forward beam while other parts of the grating will diffract the beam mainly into the (220) Bragg spot, reducing the intensity of the forward beam. By blocking this forward beam, a grating patterned Si crystal with alternative gaps and thick strips will thus form a density modulated pattern like the grating itself.

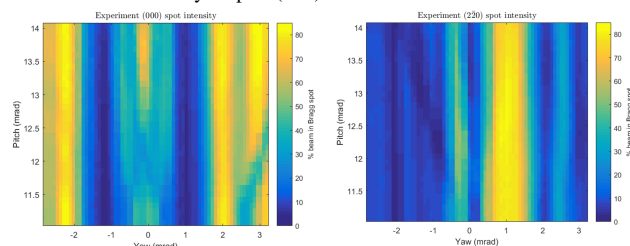
Figure 5 shows a schematic of the concept of nanopatterned beam. We first diffract forward beam at the sample plane by a Si grating, separate forward and diffracted beam by blocking either of them and then magnify or demagnify the pattern with conventional electron optics to get the pattern at image plane.



(a) 1D yaw scan of (000) and (220) spots at pitch equal to 12.7 mrad.



(b) Left is the simulated 2D intensity map of (000) beam, right is the simulated 2D intensity map of (220) beam.



(c) Left is the experimental 2D intensity map of (000) beam, right is the experimental 2D intensity map of (220) beam.

Figure 3: Experiment data and simulation comparison.

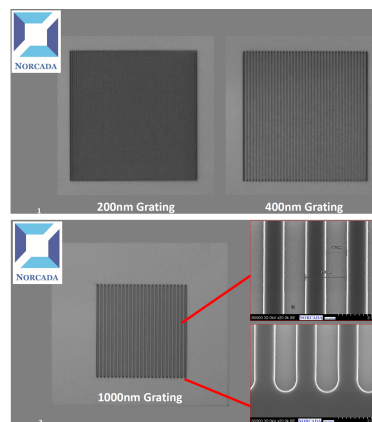


Figure 4: Prototype Si gratings at various pitches. Gratings have a 200 nm thickness and cut-through gaps.

We will take the advantage of UCLA's Pegasus Laboratory's permanent magnet quadrupole (PMQ) triplet which is capable of imaging relativistic electrons [1] to perform next grating diffraction experiment to generate nanometer scale bunched electron beam. The PMQ can be remotely inserted or removed and distance adjusted to change focal length. Their current sample holder setup offers a translational motion and alignment in both x and y. Two rotational stages will be installed to help us get a full scan range to search for

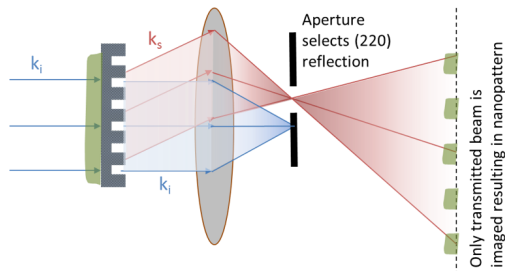


Figure 5: Concept of nanopatterned beam.

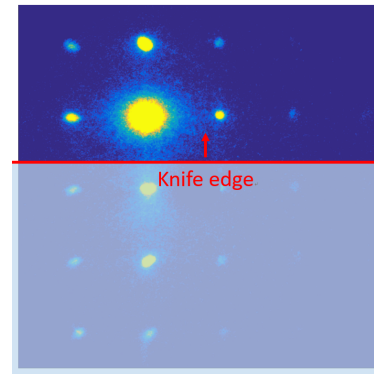


Figure 6: A knife-edge moving in one direction to block direct beam.

Content from this work may be used under the terms of the CC BY 3.0 licence (© 2018). Any distribution of this work must maintain attribution to the author(s), title of the work, publisher, and DOI.

two beam condition. A second PMQ will be installed in the image system to give a magnification up to 900X.

As UCLA's UED/UEM facility is capable of imaging the diffracting sample itself, as well as its diffraction pattern, we will mount our sample with the PMQ removed to get the system in a diffraction mode and perform the same alignment procedures as we did in SLAC. Finding the two-beam condition by making 2D pitch/yaw scanning, we choose the spot where the contrast of the forward beam and Bragg-diffracted beam are maximized as optimized working point. After that, a knife-edge is introduced as shown in fig. 6 to block direct beam and let the bright Bragg-diffracted beam go through. Then we add PMQ back to image the pattern. The flexibility of UCLA setup will also allow us to test different modulation period of electron bunched by changing magnification and multiple contrast choices by changing pitch/yaw settings.

CONCLUSION

We presented crystal diffraction results at SLAC UED facility as a method of beam manipulation. By precisely controlling crystal thickness, orientation and rotation angle, one can tune the contrast between main forward beam and Bragg-diffracted beam within a considerable intensity range. Our results show single spot excitation can be predicted through modeling, and is experimentally achievable and repeatable. Further work at UCLA will focus on producing the spatial modulated electron beam with grating Si membrane and test different sample orientation to maximize the contrast between the bright and dark strips. Through EEX, the transform transverse pattern can be transformed into a longitudinal one, this work will provide an ideal bunched electron beam to seed an XFEL using inverse Compton scattering.

ACKNOWLEDGEMENT

We gratefully acknowledge support from the National Science Foundation Division of Physics (Accelerator Science) award 1632780, the NSF BioXFEL Science and Technology Center funded by award 1231306, and DOE grant DE-AC02-

76SF00515. The UCLA component of this work is partially supported by STROBE: A National Science Foundation Science and Technology Center under Grant No. DMR 1548924 and by DOE STTR grant No. DE-SC0013115.

REFERENCES

- [1] D. Cesar *et al.*, "Demonstration of single-shot picosecond time-resolved mev electron imaging using a compact permanent magnet quadrupole based lens," *Phys. Rev. Lett.* **117** (2016), 024801.
- [2] W. Graves, F. Kärtner, D. Moncton, and P. Piot, "Intense superradiant X-rays from a compact source using a nanocathode array and emittance exchange," *Phys. Rev. Lett.* **108** (2012), 263904.
- [3] W. Graves *et al.*, "ASU compact XFEL," *Proc. of FEL'17*, TUB03, Santa Fe, USA, August 2017.
- [4] L. Malin *et al.*, "Comparison of theory, simulation, and experiment for dynamical extinction of relativistic electron beams," *Proc. of IPAC'17*, THPAB088, Copenhagen, Denmark, 2017.
- [5] E. Nanni and W. Graves, "Aberration corrected emittance exchange," *Phys. Rev. ST Accel. Beams* **18** (2015), 084401.
- [6] E. Nanni *et al.*, "Measurements of transmitted electron beam extinction through Si crystal membranes," *Proc. of IPAC'16*, TUPMY030, Busan, Korea, 2016.
- [7] E. Nanni, W. Graves, and D. Moncton, "Nano-modulated electron beams via electron diffraction and emittance exchange for coherent x-ray generation," arXiv:1506.07053, 2015.
- [8] S. Weathersby *et al.*, "Mega-electron-volt ultrafast electron diffraction at SLAC National Accelerator Laboratory," *The Review of Scientific Instruments* **86** no. 7 (2015), 073702.
- [9] C. Zhang *et al.*, "Imaging the spatial modulation of a relativistic electron beam," *Proc. of IPAC'17*, MOPAB150, Copenhagen, Denmark, 2017.

ELECTRON BEAM REQUIREMENTS FOR COHERENT ELECTRON COOLING FEL SYSTEM*

G. Wang[#], Y.C. Jing, V. N. Litvinenko and J. Ma, BNL, Upton, NY 11973, USA.

Abstract

The proof of coherent electron cooling (CeC) principle experiment is currently on-going and due to the limitations of the 5-cell SRF accelerating LINAC, the final achievable energy of the electron beam is 15 MeV, i.e. 68% of its originally designed value, 22 MeV [1]. Consequently, all evaluations and simulation results need to be revisited for the reduced beam energy. This work focuses on the requirements of the electron beam quality in order to achieve the desired amplification from the FEL amplifier of our CeC system.

FEL AMPLIFIER OF THE PROOF OF CEC PRINCIPLE EXPERIMENT

As shown in Fig. 1, the FEL amplifier of the CeC system consists of three helical undulators. Illustrated in Fig. 2, the length of each undulator is about 2.49 meters. The separations between any two adjacent undulators are 42.25 cm where phase shifters are installed to match the phase of electrons with that of the radiation [2]. The undulator period is 4 cm and for the current set-up, the undulator field on axis is 0.134 T, which correspond to an undulator parameter of $a_w = 0.5$. The originally designed gain in the bunching factor is 100, requiring peak current about 100 A for 22-MeV electron beam with normalized RMS emittance smaller than 5 mm.mrad and RMS energy spread within 0.1%.

During RHIC run 17, the CeC system is commissioned and it is found that the cavity voltage of the 5-cell SRF LINAC is limited to 13.5 MeV and hence the maximal achievable energy of the electron beam is 15 MeV. Apart from all necessary modifications of the diagnostic system, the cooling process needs to be re-visited and here we present our preliminary studies of the requirements on the electron beam qualities for achieving the desired gain from the FEL amplifier.

*Work supported by Brookhaven Science Associates, LLC under Contract No.DE-AC02-98CH10886 with the U.S. Department of Energy.
[#] gawang@bnl.gov

TOOLS AND SIMPLIFICATIONS

Since the FEL amplifier consists of three undulators with no quadrupoles in between, the beta functions vary along the amplifier section. Figure 3 (orange) shows the designed beta functions, which give minimal variation of the electron beam size along the amplifier.

We use Genesis 1.3 to investigate what are the requirements on electron beam quality to achieve the bunching gain about 100 [3]. For a preliminary estimate, we simplify the FEL amplifier as a single undulator of 7.5-m long with the undulator period of 4 cm and undulator parameter of 0.5.

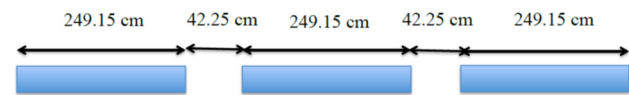


Figure 2: Illustration of the FEL amplifier of the CeC experiment.

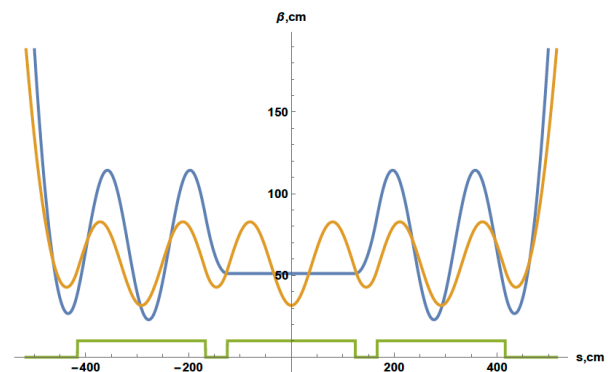


Figure 3: Variation of beta function along the FEL amplifier. Orange: the designed beta function of the amplifier, which gives minimal variation of electron beam size. Blue: one of the un-optimized lattice designs where the beta function is matched at the middle undulator but the overall variation of beam size is large.

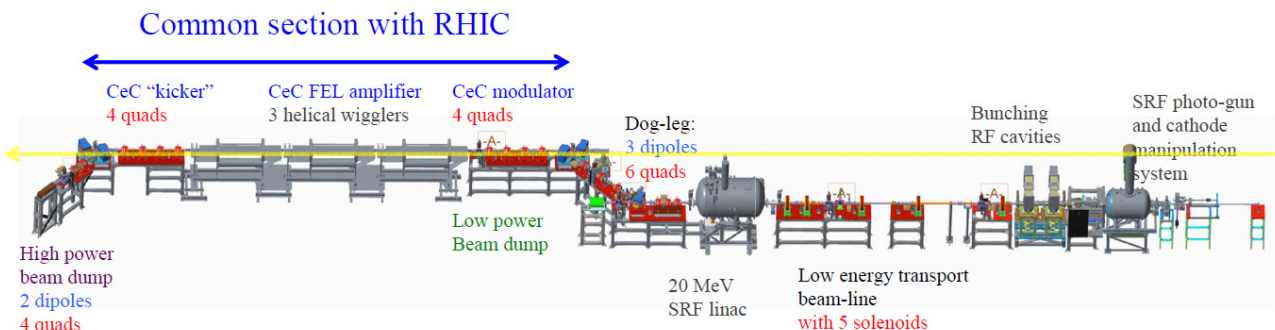


Figure 1: Layout of the proof of CeC principle experiment at RHIC IP2.

Content from this work may be used under the terms of the CC BY 3.0 licence (© 2018). Any distribution of this work must maintain attribution to the author(s), title of the work, publisher, and DOI.

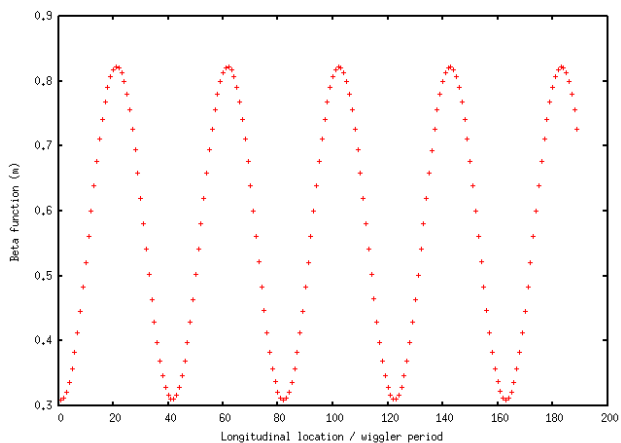


Figure 4: Beta function as calculated from the beam size variation obtained from Genesis simulation. The simulation is for a 7.5-m long undulator with 4 cm of undulator period. The initial electron beam size is chosen such that the beta function variation is similar to that of Fig. 3.

For each Genesis simulation, the initial electron beam size is chosen such that the variation of the beam size is similar to that of the designed lattice shown in Fig. 3 (orange). As shown in Fig. 4, the beta function calculated from the beam size variation in the simulation varies from 0.3 meters to 0.8 meters, successfully mimicking that of the Fig. 3 design.

To obtain the wave-packet created by density modulation of a single ion, we mostly run Genesis with quiet start and putting the expected initial bunching factor, i.e. $1e-6$, into one slice of the electron beam. To ensure the FEL works in the linear region, we run separate simulations with shot noise on and check whether the exponential growth of the bunching factor reaches saturation.

SIMULATION RESULTS

In order to investigate how the peak current influences the FEL gain, we start the simulation with uniform current distribution. Figure 5 shows the profile of the wave-packet induced by an initial modulation located at zero. The amplitude of the initial bunching factor is $1e-6$, as what expected from the CeC modulation of a single ion. As the longitudinal velocity of the electrons are slower than that of the ion inside the undulator, the ion slips forward with respect to the initial modulation. At the exit of the undulator, the slippage is given by:

$$\Delta L = N_u \lambda_0 \frac{a_w^2}{1 + a_w^2} .$$

where N_u is the length of the undulator divided by undulator period, λ_0 is the optical wavelength, and a_w is the undulator period. For $N_u = 188$ and $a_w = 0.5$, the ion slips

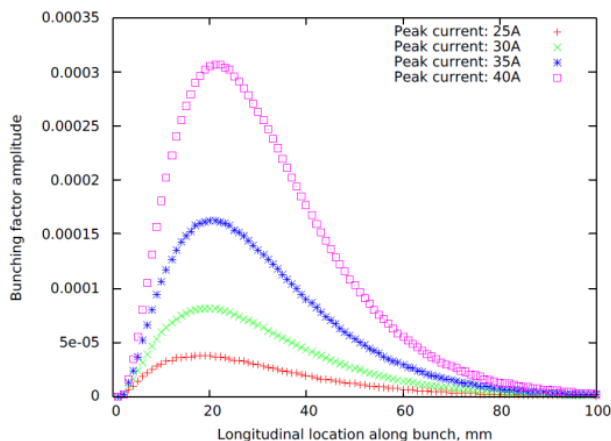


Figure 5: Amplitude of bunching factors along the wave-packet at the exit of the FEL amplifier. The initial modulation is at origin with amplitude of $1e-6$. The electron beam has uniform longitudinal profile with various peak current as shown in the plot. The normalized RMS emittance is 5 mm.mrad and the RMS energy spread is 0.1%.

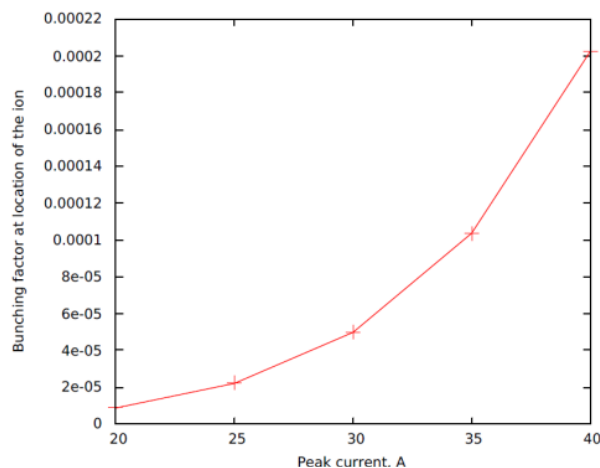


Figure 6: Amplified bunching factor at the location of the ion for various electron beam peak current.

37 optical wavelengths with respect to the location of the initial modulation.

Figure 6 shows how the amplified bunching factor at the location of the ion varies with the peak current of the electron beam. Simulations show that to achieve the desired gain of 100, the required peak current is 35 A. In order to check at what limit of peak current, the FEL saturates from shot noise, we run Genesis with shot noise turned on. Figure 7 shows that for peak current up to 40 A, the maximal bunching factor grows exponentially and the FEL works in the linear region. For peak current above 45 A, the variation of maximal bunching factor starts to deviate from exponentially growing, indicating the onsite of saturation.

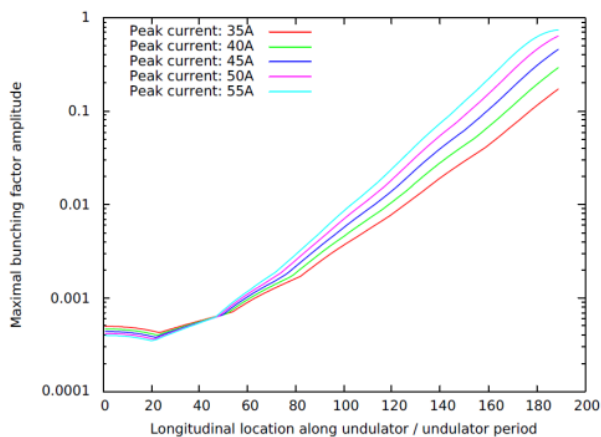


Figure 7: Growth of the maximal bunching factor along the undulator for various electron beam peak current.

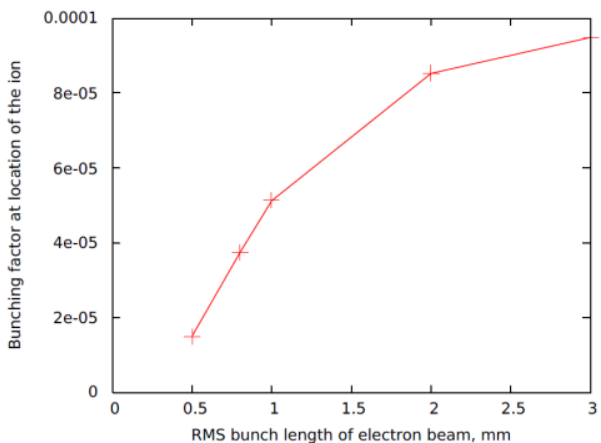


Figure 8: The amplitude of the amplified bunching factor at the location of the ion for various electron RMS bunch length. The peak current is 35 A and the longitudinal profile of the electron beam is Gaussian. The RMS normalized emittance is 5 mm.mrad and the RMS energy spread is 0.1%.

As the FEL instability relies on the coherent interaction of the radiation and the electrons, the electron bunch should be long enough to sustain such interaction. In order to investigate the influence of electron bunch length, we then run Genesis with Gaussian profile with various RMS bunch length. As shown in Fig. 8, the FEL amplification reduces by more than 20% once the RMS bunch length is longer than 2 mm.

The FEL amplification is also affected by the emittance of the electron beam. As shown in Fig. 9, the emittance should be kept under 6 mm.mrad to avoid substantial reduction (more than 30%) in FEL gain.

As expected, the most significant influences of FEL gain come from the energy spread. Figure 10 shows that the FEL gain reduces by a factor of two as the energy spread increases from 0.1% to 0.15%. Consequently, the RMS energy spread should not be larger than 0.1%.

SUMMARY

By running Genesis with a simplified model for the FEL amplifier of the CeC experiment, we obtained vari-

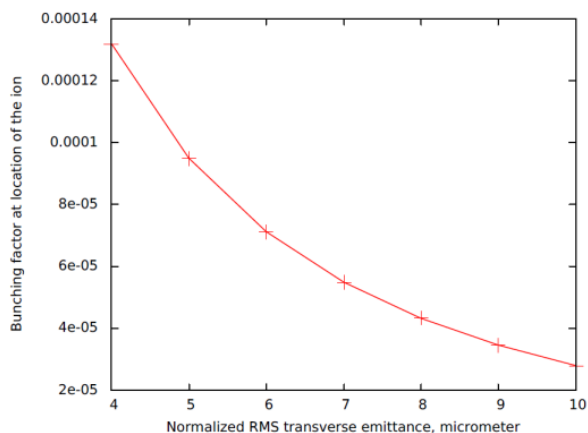


Figure 9: The amplitude of the amplified bunching factor at the location of the ion for various electron RMS emittance. The peak current is 35 A and the longitudinal profile of the electron beam is Gaussian with RMS bunch length of 3 mm. The RMS energy spread is 0.1%.

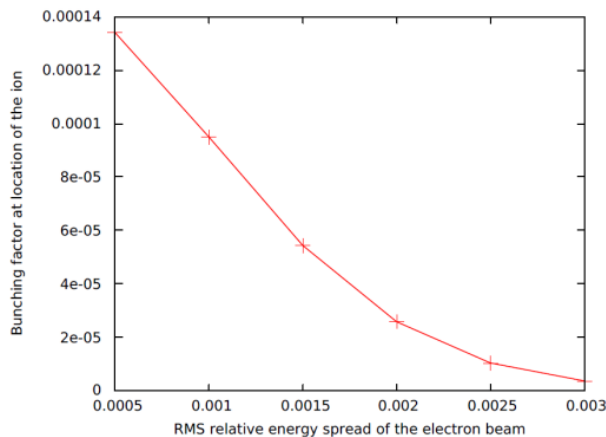


Figure 10: The amplitude of the amplified bunching factor at the location of the ion for various electron RMS energy spread. The peak current is 35 A, the RMS bunch length is 3 mm and the RMS normalized emittance is 5 mm.mrad.

ous requirements on the electron beam quality in order to achieve a gain of 100. To avoid reduction of gain by more than 30%, the electron beam peak current should be around 35 A with the RMS bunch length longer than 2 mm. The normalized RMS emittance should be smaller than 6 mm.mrad and the relative RMS energy spread should be within 0.1%.

REFERENCES

- [1] V. Litvinenko *et al.*, "Commission of FEL-based coherent electron cooling system", presented at FEL'17, MOP041.
- [2] Y. Jing *et al.*, "Simulation of phase shifters between FEL amplifiers in coherent electron cooling", presented at FEL'17, TUP072.
- [3] S. Reiche, "Introduction on Genesis 1.3", available at: http://genesis.web.psi.ch/download/documentation/genesis_talk.pdf, 2002.

DETERMINATION OF THE SLICE ENERGY SPREAD OF ULTRA-RELATIVISTIC ELECTRON BEAMS BY SCANNING SEEDED COHERENT UNDULATOR RADIATION*

J. Bödewadt[†], R. Aßmann, M. M. Kazemi, C. Lechner, DESY, Hamburg, Germany
 L. L. Lazzarino, T. Plath[‡], J. Roßbach, University of Hamburg, 22671 Hamburg, Germany

Abstract

Modern high-gain free-electron lasers make use of the high-brightness ultra-relativistic electron beams. The uncorrelated energy spread of these beams is, upon creation of the beam, in the sub-permille range and below the resolution of state-of-the-art diagnostics. One method to determine the slice energy spread is to use an external seed laser to imprint a coherent microbunching structure that gives rise to coherent radiation processes different than radiation sources such as transition radiation, synchrotron radiation, or undulator radiation and others. Here, we present a method and show measurements to determine the slice energy spread using an external seed laser with a 266 nm wavelength to produce coherent undulator radiation at higher harmonics. The distribution of these harmonics allows to retrieve the electron beams slice energy spread with high precision.

INTRODUCTION

The invention of the high-gain x-ray free-electron laser has enabled the study of the dynamics and structure of matter on the atomic and molecular level and for time scales on the order of atto- and femtoseconds [1–4]. As these devices are driven by high-brightness ultra-relativistic electron beams, the operation requires sophisticated beam and bunch diagnostics in order to be able to measure and control the properties of the electron beam parameter. One of the crucial beam parameter for the performance of an FEL is the uncorrelated energy spread σ_E . Modern high-brightness electron sources are known to generate electron bunches with uncorrelated energy spread in the order of one keV. The direct measurement of this parameter is extremely challenging as typical diagnostic tools are resolution limited at a few keV. Nevertheless, processes which directly depend on σ_E can be used to indirectly determine this value. At the SDUV-FEL facility in Shanghai, a method using laser-seeded radiation with coherent harmonic generation (CHG) was used to determine the slice energy spread [5]. Here, the seed laser power and the longitudinal dispersion of the bunching chicane of the CHG setup was scanned in order to retrieve the local energy spread using the second harmonic of the initial seed laser wavelength. Similar to that, it is possible to scan the harmonic number instead of changing the dispersion and laser power. Fitting the measurements to simulation data by using the energy spread σ_E and modulation amplitude ΔE

as free parameter, we are able to retrieve these values in a similar way. The measurements were performed at the experimental seeding setup sFLASH at the free-electron laser user facility FLASH at DESY.

METHOD

Imprinting a periodic modulation of the longitudinal current density to the electron bunches allows the production of coherent radiation at harmonics of the fundamental frequency. The radiating process can e.g. be synchrotron radiation from a dipole, diffraction or transition radiation from screens, or undulator radiation. By overlapping an external laser pulse (wavelength λ) with the electron beam of beam energy E_0 and with a slice energy spread σ_E inside an undulator, it is possible to induce a periodic modulation of the beam energy with modulation amplitude ΔE . Transporting this energy-modulated beam through a section with longitudinal dispersion (R_{56}), a periodic current modulation forms. A Fourier analysis of the current density is used to extract the bunching coefficients for higher harmonic orders [6]:

$$b_n = \exp\left[-\frac{1}{2}n^2 B^2\right] \cdot J_n(-nAB) \quad (1)$$

where $A = \Delta E / \sigma_E$ is the normalized modulation amplitude, $B = 2\pi\sigma_E R_{56} / (\lambda E_0)$ the normalized dispersive strength of the chicane, and n the harmonic number. For a laser pulse with an electric field envelope $\mathcal{E}(t)$, the modulation amplitude also will be a function of time $\Delta E(t)$. Assuming a constant energy spread along the modulated fraction of the electron bunch we can calculate the bunching distribution $b_n(t)$ after the chicane. Sending the electron beam with this bunching distribution through an undulator of length L_u tuned to the n^{th} harmonic will lead to the emission of coherent undulator radiation with a power profile proportional to $\rho_{FEL} |b_n(t)|^2 L_u^2$ [7]. For simplicity, we assume that the initial bunch current is low enough to neglect exponential FEL amplification. Integrating the power profile over time we can now calculate the photon pulse energy from the coherent harmonic generation for different harmonic numbers.

SIMULATION

For accurate simulation of the CHG process, the time-dependent FEL simulation code *GENESIS1.3* has been used [8]. The simulation parameter are similar to the experimental settings summarized in table 1. Figure 1 exemplary shows the result of the simulated bunching distributions for different harmonic numbers n and for an energy spread of

* Supported by the Federal Ministry of Education and Research of Germany under contract 05K13GU4, 05K13PE3, and 05K16PEA

[†] contact: joern.boedewadt@desy.de

[‡] present address: TU Dortmund University, Dortmund, Germany

Table 1: Experimental Parameters

	parameter	value
modulator	period length	0.2 m
	effective length	1.2 m
	max. K_{peak}	10.8
radiator	period length	31.4 mm
	effective length	2 m
	max. K_{peak}	2.7
chicane C2	R_{56}	100 μm
electron beam	energy	680-700 MeV
	peak current	160 A
	charge	0.4 nC
seed beam	wavelength	266 nm
	pulse energy	<280 μJ
	NIR pulse duration	~ 50 fs (FWHM)
	UV pulse duration	250-280 fs (FWHM)
	UV Rayleigh length	1.6 m

$\sigma_E = 20$ keV and a modulation amplitude of $\Delta E = 495$ keV. A set of 6552 time-dependent *GENESIS1.3* runs has been performed with a range of the slice energy spread from 2 to 25 keV (in steps of 1 keV) and modulation amplitude from 250 to 350 keV (in steps of 5 keV) and for the harmonic numbers $n = 7 \dots 19$.

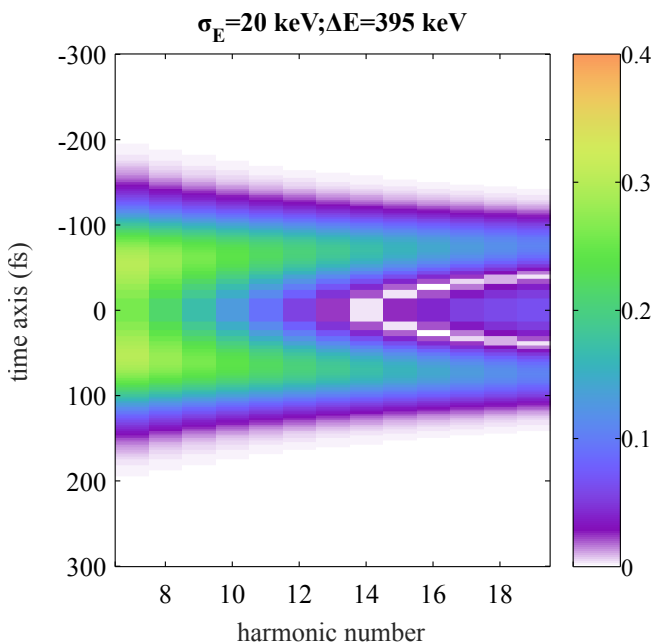


Figure 1: Distribution of the bunching factors (color coded) for different harmonic numbers $n = 7 \dots 19$.

EXPERIMENT

Setup and Procedure

The parameters of the experimental setup are summarized in Table 1. Figure 2 shows a schematic layout of the CHG

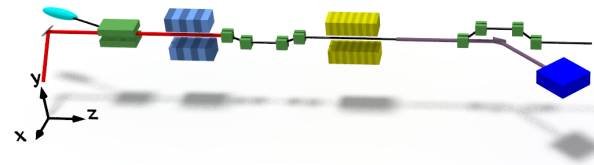


Figure 2: Schematic of the experimental setup. The seed laser is injected at the last dipole of the energy collimator section.

seeding experiment with it modulator undulator, the chicane and one radiator undulator module. An XUV spectrometer as well as an micro-channel plate (MCP) based detector are used to measure the CHG pulse energy and spectrum. The 266-nm seed pulses are generated by third-harmonic generation (THG) of near-infrared (NIR) Ti:sapphire laser pulses. The electron bunch compression settings were chosen such that a sufficient CHG signal is detectable in the photon diagnostic section but without starting exponential FEL gain within 2 meters of undulator length. Once the laser-electron overlap has been established, the undulator gap is scanned and the generated radiation is recorded by the MCP detector and the spectrometer.

Measurements

Figure 3 shows the result of the scan of the undulator gap. The CHG pulse energy was recorded up to the 19th harmonic of the 267-nm seed laser for a fixed MCP gain voltage (blue data points). Extending the range of the gap scan towards even higher harmonics was performed for higher gain voltages (red data points). The inset of the figure shows the integrated spectrum for the maxima of the harmonics. The measurement proves that the MCP indeed shows radiation at the particular harmonic and is not effected by other signals.

RESULTS

The maxima of the CHG signal for each harmonic number n was used to compare the measurement with simulation data. Figure 4 shows the calibrated energy measurements for each harmonic as a function of n . A least square fit was used in order to find the $(\sigma_E, \Delta E)$ -set of simulation which fits best to the measurement data. The red solid line corresponds to the best fit and the dashed lines indicate the $1-\sigma$ error band. The retrieved values for the energy spread the modulation amplitude are:

$$\sigma_E = 13 \pm 3 \text{ keV} \quad (2)$$

$$\Delta E = 315 \pm 10 \text{ keV} \quad (3)$$

The results are well in line with the predicted values for the energy spreads given by $\sigma_E = 100 \frac{\text{keV}}{\text{kA}} \cdot I$ with I being the peak current in kA. As the compression factor for the experiment was about 8, we can conclude that the slice energy spread from the FLASH photo-injector is in the order of 1.5 keV. This value is also close the results measured

Content from this work may be used under the terms of the CC BY 3.0 licence (© 2018). Any distribution of this work must maintain attribution to the author(s), title of the work, publisher, and DOI.

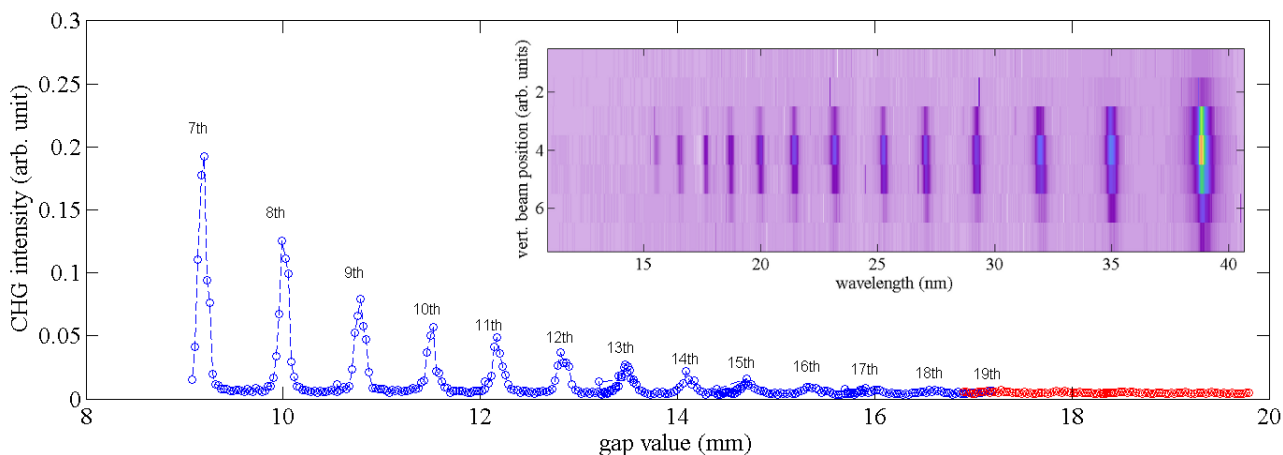


Figure 3: Coherent harmonic generation signal from a 2-m-long variable-gap undulator as a function of the gap value. By scanning the gap from 9 to 20 mm the undulator is resonant to the different harmonics of the 266 nm seed laser. The inset shows an integrated spectrum of the complete scan.

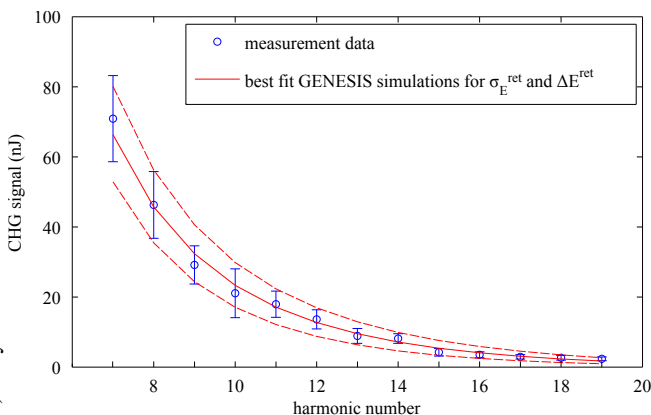


Figure 4: Measured energy maxima for scanning the harmonic number and the result of the best fit from the numerical model to the data.

at the DUV-FEL facility in Shanghai of 1.2 keV [5]. The modulation amplitude has been characterized independently using a transversely deflecting structure and fits within the measurement error to the retrieved values using this method.

SUMMARY

The slice energy spread of the FLASH electron beam has been retrieved by comparing simulation and measurements of seeded coherent undulator radiation by coherent harmonic generation. For a peak current of $I = 160$ A and a beam energy of 690 MeV we found the slice energy spread to be $\sigma_E = 13 \pm 3$ keV.

OUTLOOK

The measurements are planned to be repeated for several sets of bunch compressions and for varying laser-electron

timings. That way the energy spread profile along the electron bunch distribution can be characterized.

ACKNOWLEDGMENTS

Without the help from many groups at DESY, the preparation and commissioning of all components of this experiment would not have been conceivable. Their support is gratefully acknowledged. This work is supported by the Federal Ministry of Education and Research of Germany within FSP-302 under FKZ 05K13GU4, 05K13PE3, and 05K16PEA and the German Research Foundation within GrK 1355.

REFERENCES

- [1] W. Ackermann *et al.*, *Nature Photonics*, vol. 1, p. 336, 2007.
- [2] E. Allaria *et al.*, *Nature Photonics*, vol. 6, p. 699, 2012.
- [3] P. Emma *et al.*, *Nature Photonics*, vol. 4, p. 641, 2010.
- [4] T. Ishikawa *et al.*, *Nature Photonics*, vol. 6, p. 540, 2012.
- [5] C. Feng *et al.*, *Phys. Rev. ST Accel. Beams*, vol. 14, p. 090701, 2011.
- [6] L.-H. Yu *Phys. Rev. A*, vol. 44, p. 5178, 1991.
- [7] E. Jaeschke *et al.*, *Synchrotron Light Sources and Free-Electron Lasers*, (New York: Springer International Publishing, 2016), 207.
- [8] S. Reiche, *Nucl. Instrum. Methods Phys. Res., Sect. A*, vol. 429, p. 243, 1999.

INTERFERENCE-BASED ULTRAFAST POLARIZATION CONTROL AT FREE ELECTRON LASERS

S. Serkez*, G. Geloni, European XFEL GmbH, Schenefeld, Germany
 E. Saldin, DESY, Hamburg, Germany

Abstract

X-Ray Free Electron Lasers (XFELs) provide short high power pulses of X-rays with a high degree of polarization, where polarization properties are determined by the undulator magnetic field. Fast control of these properties would allow for unique experiments. Here we propose a scheme to modulate the polarization of FEL radiation (polarization shaping) or generate on average non-polarized radiation with FELs. This scheme is based on “crossing” APPLE-X helical undulators.

INTRODUCTION

X-ray Free Electron Lasers (XFELs) opened up the possibility of obtaining polarized X-ray pulses with unprecedented power and femtosecond-order duration. In recent years there has been a growth of demand for pump-probe schemes that deliver FEL radiation for both pump and probe with variable wavelength and delay.

At the LCLS the generation of two pulses with variable polarization and delay was demonstrated after installation of a helical undulator, following the main planar undulators [1]. In the current paper we propose another, alternative scheme to shape the polarization of FEL radiation on 100-femtosecond timescale and exemplify it for the SASE3 beamline of the European XFEL. This scheme does not require any special hardware, but only the components already being proposed for installation at this facility, namely:

- Emittance spoiler (slotted foil).
- Soft X-ray Self-Seeding monochromator (optional).
- Corrugated structure located upstream the SASE3 undulator.
- Two APPLE-X helical undulators located downstream the baseline SASE3 undulator, separated by a phase shifter.

The main elements of the proposed setup are the two helical APPLE-X undulators [2], tuned to the same resonant frequency ω , but with opposite polarization direction (as a basis for reasoning, the first undulator is tuned to produce radiation with right-handed circular polarization as defined from the point of view of the source (negative helicity), while the second one - left-handed (positive helicity).

PROPOSED METHOD

Two radiation beams with mutually orthogonal polarizations can be generated and naturally overlapped by propagating an electron beam through two planar undulators with the

orthogonal polarization planes located one after the other. If the electron beam is delayed by $\lambda/4$ between these undulators, the combined radiation would be circularly polarized, as illustrated on Fig. 1, first column. This was studied in [3] for synchrotron facilities. Later this approach was extended for FELs [4], experimentally demonstrated [5] and is currently referred to as the “crossed undulator technique”.

We consider the case, when, instead of linearly polarized radiation, two circularly polarized pulses with equal intensities, opposite helicity and a phase shift $\Delta\phi$ with respect to each other are generated. Then the resulting radiation will be always linearly polarized, with a polarization plane depending on the phase shift value $\Delta\phi$ (see Fig. 1, second column).

When the carrier frequency of the second pulse is shifted by $\Delta\omega$, then the phase difference $\Delta\phi$ varies linearly along the radiation pulses. In other words, one pulse has linear phase chirp with respect to the other. Then the polarization plane of the resulting linearly polarized radiation would gradually and periodically change its orientation (i.e. rotate) with frequency $\Delta\omega/2$, as schematically shown on Fig. 1, third column.

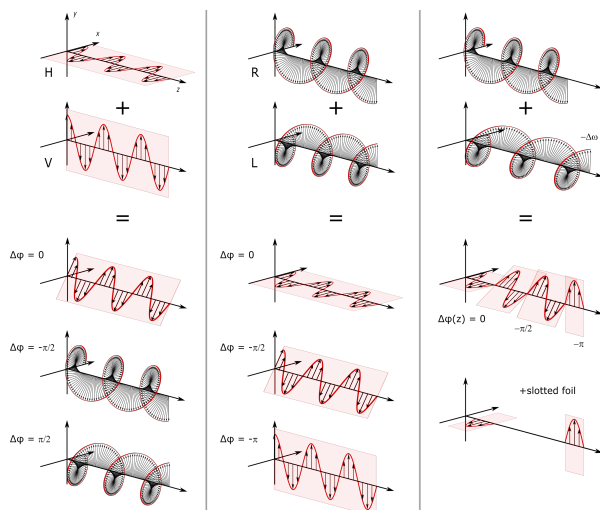


Figure 1: Combination of radiation pulses with different polarization: two linearly polarized (left column), two circularly polarized (central column), and two circularly polarized with linear phase chirp (right column). Note that for illustration purposes the depicted radiation carrier frequency is small, while the actual frequency would be much higher compared to rate of the polarization plane rotation. The same remark applies to radiation after slotted foil introduction.

On the large timescales this radiation is not polarized, since due to rotation of the Stokes vector its averaged length

* svitozar.serkez@xfel.eu

Content from this work may be used under the terms of the CC BY 3.0 licence (© 2018). Any distribution of this work must maintain attribution to the author(s), title of the work, publisher, and DOI.

approaches zero, i.e. the polarization is “scrambled”. Let us consider a nominal electron beam microbunched at frequency ω entering two consecutive helical undulators. The microbunching can be obtained in an upstream FEL section by applying for example, inverse tapering [6, 7].

In order to obtain radiation with shaped polarization, the bunching frequency of the electron beam should be shifted by a finite $\Delta\omega$ upstream the second helical undulator. This frequency shift would take place naturally if the modulated electron beam has an energy chirp and passes through a dispersive environment (as illustrated on Fig. 2).

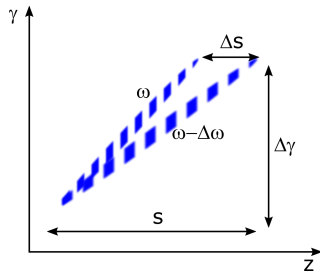


Figure 2: Longitudinal phase space of a linearly chirped electron beam with coherent density modulation at frequency ω . This frequency is shifted by $\Delta\omega$ upon propagation through dispersive environment.

Undulators have dispersive properties, given by $R_{56} = -2N\lambda$, where R_{56} is momentum compaction factor, N denotes a number of undulator periods, and $\lambda = 2\pi c/\omega$ is a resonant undulator wavelength. This means, that while propagating through an undulator, the total length of a linearly chirped electron beam is modified.

Dispersion in the undulator is too small to significantly affect the amplitude of the electron density modulation, but is sufficient to change its frequency proportionally to the final electron beam elongation $\Delta s = -R_{56}\Delta\gamma/\gamma$:

$$\frac{\Delta\omega}{\omega} = -\frac{\Delta s}{s} = \frac{R_{56}\Delta\gamma}{\gamma s}.$$

One may see that the resulting bunching frequency shift $\Delta\omega$ does not depend on the resonance frequency ω :

$$\Delta\omega = -4\pi cN \frac{\Delta\gamma}{\gamma s}.$$

The crossed undulator scheme implies that the radiation from the first undulator does not interact with the electron beam in the second, i.e. the radiation from the first undulator does not “seed” the second one.

In the case of crossed planar undulators this is always true, since the projection of the electric field of the “seed” onto the transverse electron velocity in the second undulator is always zero. In case of helical undulators this projection is not zero, but it is not constant along the undulator length. Therefore, no synchronism takes place and *on average* the “seed” does not interact with the electron beam.

Let us now consider an electron beam with positive energy chirp that enters an inverse tapered undulator, as illustrated

in Fig. 3. This energy chirp in the electron beam can be achieved by installing the corrugated structure upstream the main undulator [8].

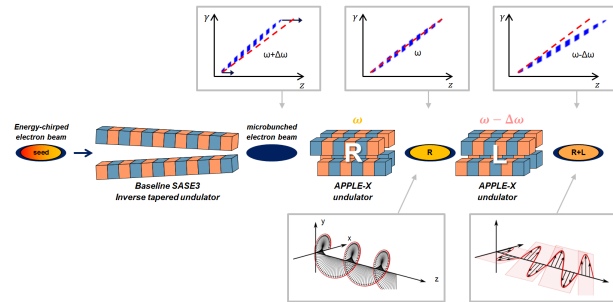


Figure 3: Illustration of the proposed scheme.

For the sake of argument, we define the bunching frequency at the center of the beam immediately after the first helical undulator as ω . The radiation emitted by this part of the beam has therefore carrier frequency ω . After propagation of the electron beam through the second undulator, the frequency of the bunching will be shifted by $\Delta\omega$. Therefore the same frequency shift $\Delta\omega$ should be expected in the carrier frequency of the radiation emitted in the second undulator. As long as the chirp in the electron beam is linear, the same frequency shift applies along the entire radiation pulse independently of the longitudinal position.

We performed numerical simulations with GENESIS code. To model the helical undulators we assume APPLE-X segments with 9 cm periods and 22 periods per segment. For simulations we used a model 30 μm -long electron beam. Its energy in terms of Lorentz factor was varying from 16500 at the tail to 16700 at the head, while the other values remained constant: current (4 kA), normalized emittances (1 mrad) and beta functions (20 m). Results of the numerical simulations are presented in Fig. 4-(b).

For pump-probe experiments it may be necessary to select only two regions of the resulting pulse with desired polarization plane. Lasing in the electron beam can be selectively inhibited by introducing slotted foil into the last bunch compressor in LINAC. Using aluminum foil with two slots, the transverse emittance of the electron beam may be spoiled except for two short 2 μm lasing windows, separated by 10 μm along the bunch. In the scheme considered above it corresponds to nearly quarter of the polarization plane rotation or half the rotation of the Stokes vector. The two resulting pulses would have high degree of linear polarization (96 %) with planes orthogonal with respect to each other, see Fig. 4-(c).

There are 3 degrees of freedom to independently control state of polarization of the two resulting pump and probe pulses: the gap of the corrugated structure, distance between slots in the slotted foil and delay of the electron beam introduced in phase shifter between the two helical undulators.

Polarization plane of the both pulses can be simultaneously changed by varying the delay in the phase shifter. The

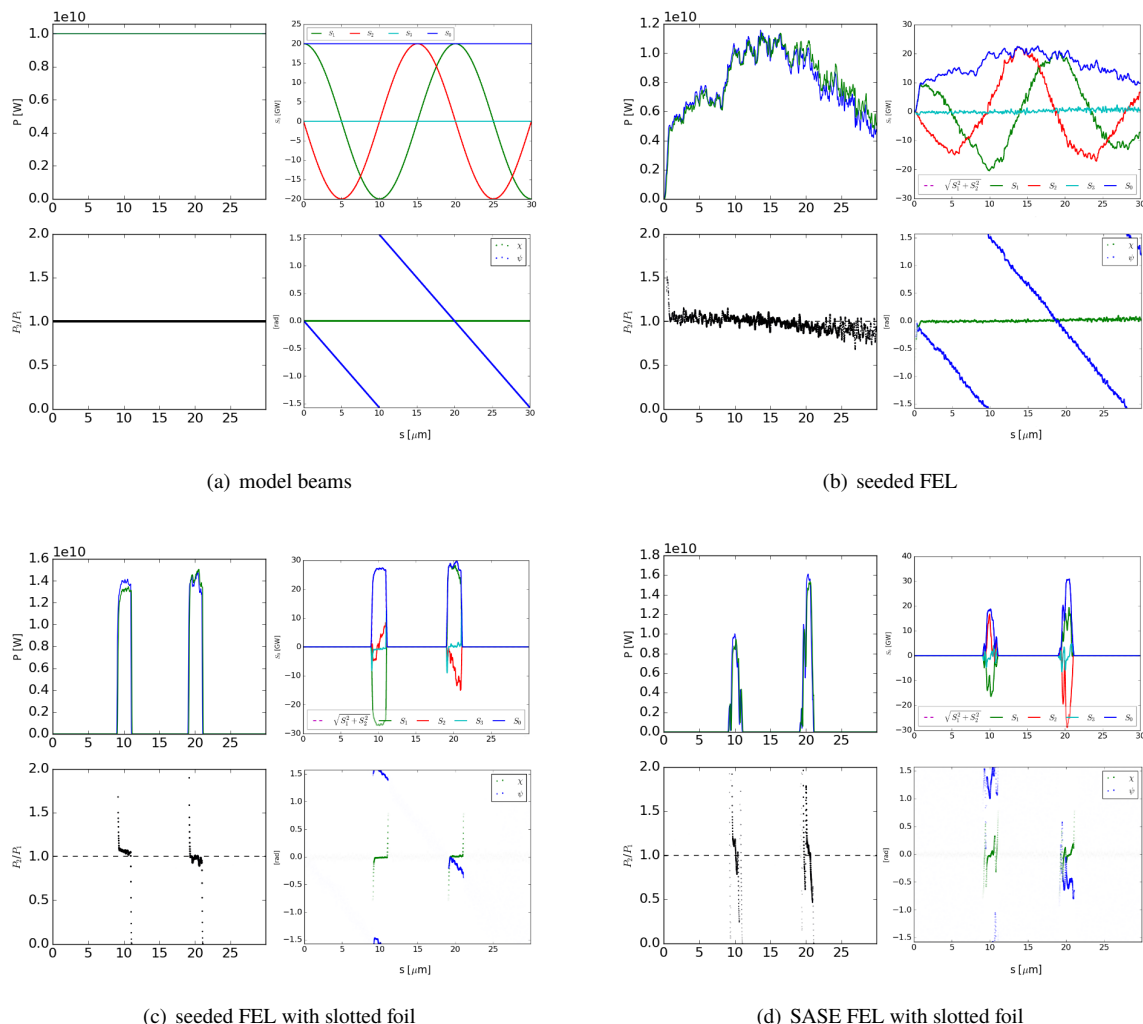


Figure 4: Result of polarization modulation in case of combining two model pulses is illustrated on subfig. (a). Genesis simulation results for the seeded FEL without, and with slotted foil are presented on subfigs. (b) and (c) correspondingly. Both pulses in subfig. (c) yield 96% of linear polarization. Simulation results without seed (subfig. (d)) show 87% and 92% degree of polarization. The top left plots show the power of combined pulses, bottom left plots show the ratios of the pulse power, top right plots show Stokes parameters of the resulting radiation and bottom right plots - spherical coordinates of the Stokes vector.

delay between these pulses can be changed by varying both the separation between the slots of the slotted foil and gap in the corrugates structure.

It is worth noting that the scheme proposed above also works if the crossed undulators are planar. In that case the polarization of the resulting radiation will be alternating between right- a left-handed circular polarizations with an intermediate state of linear polarization with 45° tilt, as in Fig. 1 (first column).

Measurement the polarization properties at the sample location (between two waists of right-handed and left-handed polarized radiation), would show that they depend on the transverse offset from the optical axis. In our case the sample is located, where the radiation with the left-handed circular polarization has passed the waist and is diverging, while the radiation with the right-handed polarization is still converg-

ing for the waist located downstream the sample. The phase difference between the two beams grows nearly quadratically as a function of the distance from optical axis, hence the resulting state of polarization varies. This effect is interesting by itself and may possibly yield to some applications. At the same time it causes degradation of the degree of polarization at the sample from 96% down to 70%. In order to account for this effect one may increase Rayleigh length of the image waists. The easiest way to accomplish it is to introduce an aperture at the location of the focusing element (lens or mirror). We have numerically propagated the radiation wavefronts with OCELOT code [9] and have found that by blocking half of the radiation intensity with the square aperture upstream the mirror it is possible to improve the transversely integrated degree of polarization up to 95%, almost reaching the on-axis value of 96%.

In Fig. 4-(d) we present Stokes parameters for the case when no temporal coherence is introduced to the density modulation of the electron beam. Both radiation pulses exhibit temporal structure of SASE radiation and, when combined, show degree of linear polarization around 90%. This value may potentially be improved by either decreasing the total radiation slippage (installing shorter helical undulators) or by increasing the coherence time with, for example, pSASE technique [10]

It may be beneficial to utilize twin bunch technique [11] instead of combination of corrugated structure and slotted foil to obtain comparable results.

The extensive study of the proposed method will be published elsewhere.

CONCLUSION

In this paper we presented a method to modulate the polarization state of the FEL radiation pulse along its position. It can be achieved by introducing the microbunched electron beam with a linear energy chirp into two helical undulators located one after another. If magnetic field of the undulators is tuned to emit right- and left-handed circular polarization, then the resulting radiation would be linearly polarized with polarization plane changing along the pulse, i.e. polarization-shaped. If magnetic field in the undulators is tuned to generate the linearly polarized radiation with orthogonal polarization planes, the resulting radiation will be alternating between right and left circular polarization. This method allows to scramble the polarization of FEL radiation with rate of several Tera-radians per second.

Two short pulses with polarization-of-interest may be selected by introducing a slotted foil in the accelerator. Both pulses will be naturally overlapped and synchronized. One can independently control their polarization state and temporal separation by varying: magnetic field of the phase-shifter between the helical undulators, distance between the slots in the slotted foil and the corrugated structure gap.

Degradation of polarization degree due to transverse effects can be accounted for by introducing apertures at focusing mirror locations.

REFERENCES

[1] A. A. Lutman *et al.*, “Polarization control in an X-ray free-electron laser”. In *Nat. Photonics* 10.7 (2016), pp. 468–472.

doi: 10.1038/nphoton.2016.79

- [2] P. Li *et al.*, “Magnetic design of an Apple-X afterburner for the SASE3 undulator of the European XFEL”. In *Nucl. Instruments Methods Phys. Res. Sect. A Accel. Spectrometers, Detect. Assoc. Equip.* 870.May (2017), pp. 103–109. doi: 10.1016/j.nima.2017.07.023.
- [3] K. J. Kim, “A synchrotron radiation source with arbitrarily adjustable elliptical polarization”. In *Nucl. Instruments Methods Phys. Res.* 219.2 (1984), pp. 425–429. doi: 10.1016/0167-5087(84)90354-5
- [4] K.-J. Kim, “Circular polarization with crossed-planar undulators in high-gain FELs”. In *Nucl. Instruments Methods Phys. Res. Sect. A Accel. Spectrometers, Detect. Assoc. Equip.* 445.1-3 (2000), pp. 329–332. doi: 10.1016/S0168-9002(00)00137-6.
- [5] H. Deng *et al.*, “Polarization switching demonstration using crossed-planar undulators in a seeded free-electron laser”. In *Phys. Rev. Spec. Top. - Accel. Beams* 17.2 (2014), pp. 1–5. doi: 10.1103/PhysRevSTAB.17.020704.
- [6] E. A. Schneidmiller and M. V. Yurkov, “Obtaining high degree of circular polarization at x-ray free electron lasers via a reverse undulator taper”. In *Phys. Rev. Spec. Top. Accel. Beams* 16 (2013), p. 110702. doi: 10.1103/PhysRevSTAB.16.110702.
- [7] S. Serkez *et al.*, “Circular polarization opportunities at the SASE3 undulator line of the European XFEL”. arXiv: 1608.08175.
- [8] I. Zagorodnov, G. Feng, and T. Limberg, “Corrugated structure insertion for extending the SASE bandwidth up to 3% at the European XFEL”. arXiv: 1607.07642v1
- [9] I. Agapov *et al.*, “OCELOT: A software framework for synchrotron light source and FEL studies”. In *Nucl. Instruments Methods Phys. Res. Sect. A* 768 (2014), pp. 151–156. doi: 10.1016/j.nima.2014.09.057.
- [10] D. Xiang *et al.*, “Purified self-amplified spontaneous emission free-electron lasers with slippage-boosted filtering”. In *Phys. Rev. Spec. Top. Accel. Beams* 16.1 (2013), pp. 1–7. doi: 10.1103/PhysRevSTAB.16.010703.
- [11] A. Marinelli *et al.*, “High-intensity double-pulse X-ray free-electron laser”. In *Nat. Commun.* 6 (2015), p. 6369. doi: 10.1038/ncomms7369.

BEAM DRIVEN ACCELERATION AND RF BREAKDOWN IN PHOTONIC BAND GAP TRAVELLING WAVE ACCELERATOR STRUCTURES

J. Upadhyay and E. Simakov

Los Alamos National Laboratory, Los Alamos, NM 87545, U.S.A.

Abstract

We report the results of an experiment to demonstrate excitation of wakefields and wakefield acceleration in a photonic band gap (PBG) accelerating structure. The experiment was conducted at Argonne Wakefield Accelerator (AWA) facility. For modern X-ray Free Electron Lasers (FELs), preservation of the electron beam quality during the beam acceleration is of crucial importance. Therefore, new accelerating structures must be designed with careful attention paid to the suppression of wakefields. PBG structures are widely studied due to their ability to exclude higher order modes. A 16-cell travelling-wave normal conducting PBG structure operating at 11.7 GHz is installed at the AWA beam line. We passed a high-charge single bunch and a multiple bunch train through the structure that generated wakefields and evaluated the effect of these wakefields on a low charge witness beam.

INTRODUCTION

Photonic band gap (PBG) structures are periodic structures (metallic, dielectric or both) which confine the drive mode and damp higher order modes. PBG structures have great potential in reducing higher order modes (HOM) and long range wakefields. The problem associated with the high beam current accelerators needed for the future light sources and high luminosity colliders are the wakefields and HOM related beam breakup instabilities. PBG structures might be the technology needed for a compact and inexpensive high beam current accelerators. This raises the needs for the test of acceleration and wakefield suppression in PBG structures. To date only one test of the acceleration in a PBG structure was performed [1].

TWO-BEAM COLLINEAR WAKEFIELD ACCELERATION EXPERIMENTAL SETUP

The experiment is conducted at Argonne Wakefield Accelerator (AWA) at Argonne National Lab. In AWA facility, an L-band photocathode rf electron gun is used to produce electron beam. The electron gun uses a cesium-telluride photocathode. Six seven-cell accelerating structures are used to raise the electron energy up to 65 MeV. The beam can be split into different bunches and bunch charge of each bunch can be varied. This is achieved by splitting the laser pulse used in electron gun and varying the energy of the laser pulse. In our experiment, a high bunch-charge beam is used to excite the longitudinal wakefield in the PBG structure and hence is referred to as

a drive beam, while low charge beam used to probe the field excited by the drive beam is known as a witness beam. When the drive and witness beams travel through the same structure, it is called a collinear configuration. More details of the facility are given in [2].

A normal temperature traveling-wave PBG accelerating structure operating at 11.7 GHz was built and successfully tested for wakefield suppression at Argonne Wakefield Accelerator. This structure has 9 times the operational frequency of the AWA facility. The PBG structure is electroformed and could not be brazed due to internal stresses, a vacuum compatible epoxy was used to attach the components. Due to the use of epoxy, the vacuum chamber containing the PBG structure could not reach ultra-high vacuum to isolate and protect the Cesium telluride photocathode used in the photo injector in AWA facility, the vacuum chamber containing the PBG structure is separated from the beamline with a thin Beryllium (Be) window of the thickness of 178 microns. The experiment on wakefield suppression was conducted at AWA [3].

In the wakefield-suppression experiment [3], a good fraction of electron beam was hitting the front of the PBG structure and not entering the beam pipe of PBG structure due to high thickness of Be window. In order to understand how to send the beam through the PBG structure a series of experiment were done at AWA facility with three different thickness (30, 75, and 127 micron) Be windows. The beam size was measured before and after these windows with different charges and different beam energies. Based on these experiments, a 30-micron Be window was chosen. This 30-micron thick Be window was used during our two-beam collinear wakefield acceleration experiment.



Figure 1: The experimental setup on the beam line at Argonne Wakefield Accelerator (AWA).

Content from this work may be used under the terms of the CC BY 3.0 licence (© 2018). Any distribution of this work must maintain attribution to the author(s), title of the work, publisher, and DOI.

We are powering the PBG structure with a drive beam and measuring the beam energies of drive and witness beams after the structure in a spectrometer placed after the PBG structure. The experimental setup is shown in Fig. 1. There are three quadrupole magnets placed before the PBG structure to focus the beam towards PBG structure. As the beam tube diameter of the PBG structure is 6.31 mm while diameter of the Be window is 9.0 mm, we need a strong focusing of beams in order for the beam to pass through the structure. There is an Inductive Current Transformer (ICT) placed after the PBG structure, which measures the beam charge passed through the structure. The beam after the spectrometer is projected on a YAG screen which shows the change in energy. The phase separation between the witness beam and the drive beam is obtained by changing the path length of the laser pulse used to produce the witness beam. As the PBG structure has 9 times frequency of the AWA accelerating structure, 40-degree phase changes in the AWA main Linear Accelerator (linac) amount to 360-degree phase change in the PBG accelerator.

EXPERIMENTAL RESULTS

We optimized for the maximum charge transfer through the PBG structure with the help of quadrupole magnets placed before the PBG chamber. By measuring the charge with the ICT placed after PBG structure we found out that approximately 5-7 nC of charge can be passed through the PBG structure in single bunch. However, for the witness bunch we chose the charge to be 0.1 nC.

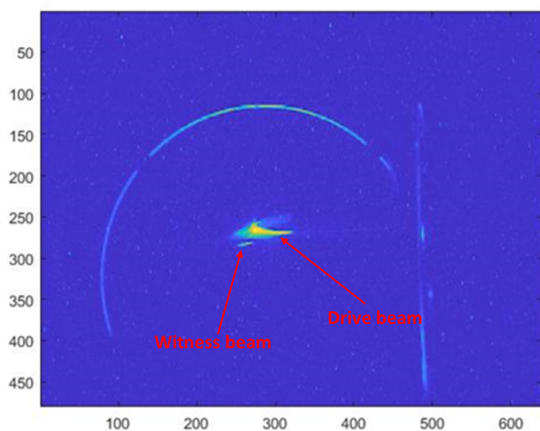


Figure 2: Both the drive and the witness beam energy on the spectrometer placed before the PBG structure.

We also measure the energy of both the beam by a spectrometer placed before the PBG structure and saw that the energy is same as shown in Fig. 2. The horizontal axis displays the energy, if both beams are at the same horizontal positions it means they have the same energy. The shift to the left shows decrease in the energy while shift to the right shows increase in energy. The energy of the electron beams is approximately 65 MeV, and various

experimental parameters used during the experiments are given in Table 1.

Table 1: Experimental Parameters at AWA

Frequency of main linac in AWA	1.3 GHz
Frequency of PBG structure	11.7 GHz
Charge in the drive beam bunch	5-7 nC
Charge in the witness beam bunch	0.1 nC
Thickness of Be window	30 micron
Diameter of the Be window	9.0 mm
Diameter of the beam tube of PBG structure	6.31 mm
Energy of the electron beam	65 MeV

Once the drive beam passes through the PBG structure, it creates the longitudinal wakefield. The magnitude of generated power in the PBG structure is proportional to the transmitted charge through the PBG structure. The effect of this generated wakefield is felt by the witness beam depending on the phase of the witness beam. When witness beam is in phase we see maximum deceleration. In Fig. 3, we show the witness beam and the drive beam after the PBG structure. Which shows that witness beam is getting decelerated due to drive beam.

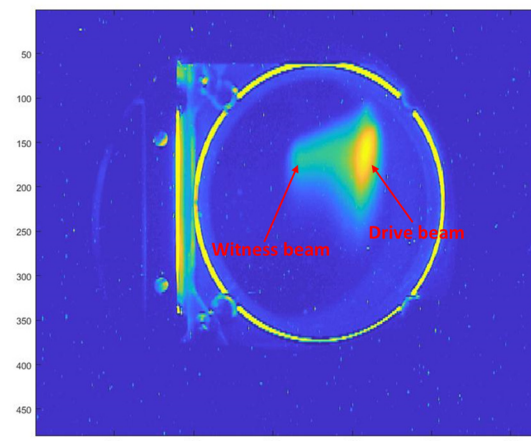


Figure 3: Both the drive and the witness beam energy on the spectrometer placed after the PBG structure.

The charge of the witness beam is small (0.1 nC) compared to the drive beam (5-7 nC). Thus, it is not very visible on the YAG screen. We varied the phase of the witness beam and saw the max deceleration but we could not see the acceleration produced by the wakefield of the drive beam. There may be problem with the phase variation as when we are changing the phase of the witness beam it is getting out of phase with the klystron and that might be creating an error in energy of both beams before the PBG itself or there is a wakefield effect of the 1.3-GHz long linac itself which might be undermining the energy gain in the PBG structure.

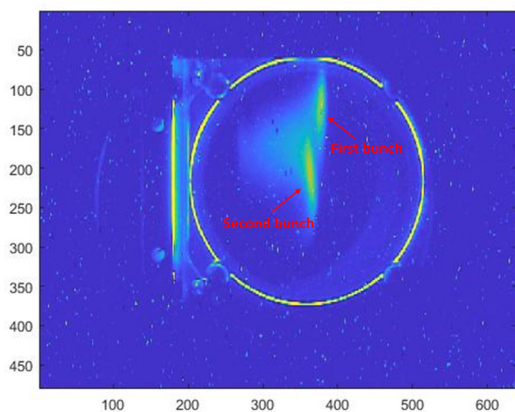


Figure 4: Two-bunch separation on spectrometer placed after the PBG structure.

We also send two and four bunches with charges of 5-7 nC each through the PBG structure and measured their energy afterwards with the spectrometer. There was no phase variation experiment done with these bunch charges. Second bunch of the charge feels the wakefield of the first bunch of the charge. The image on the YAG screen for the two bunches is shown in Fig. 4.

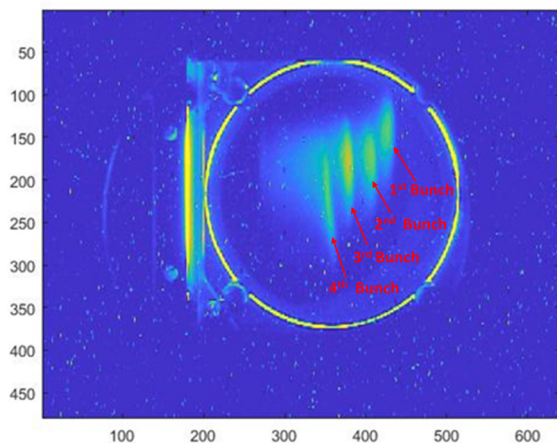


Figure 5: Four-bunch separation on spectrometer placed after the PBG structure.

The result for the four-bunch experiment is shown in Fig. 5. This fits well with the prediction that the last bunch will see the cumulative effect of all the three previous bunches and all the four bunches are equally separated on the energy scale though having the same energy at the beginning. Our future plan is to vary the phase variation more carefully and measure for all bunches energy before and after the PBG structure with the help of the spectrometer.

CONCLUSION

We conducted a collinear wakefield acceleration experiment in a 16-cell travelling wave PBG structure in AWA. We varied the phase of the low charge witness beam with respect to the high charge drive beam. We did experiment with a single bunch high charge drive beam and a multiple bunch high charge drive beam. We measured the energy of beams with a spectrometer placed after the PBG structure. We measured the witness beam energy with the drive beam on and off. We saw clearly the deceleration of the witness beam caused by the drive beam. We did not observe acceleration. A comprehensive computational beam simulation in OPAL for AWA beam line and an experiment with fine phase variation is planned for future. We are also building a normal-conducting PBG structure with reduced magnetic field by improving the design parameters of rods inside the PBG structure and we will test this PBG structure for rf breakdown at SLAC [5].

ACKNOWLEDGMENT

This work is supported by the Office of High Energy Physics, Office of Science, U.S. Department of Energy.

REFERENCES

- [1] E. I. Smirnova, A. S. Kesar, I. Mastovsky, M. A. Shapiro, and R. J. Temkin, *Phys. Rev. Lett.* **95**(7) 074801 (2005).
- [2] M. E. Conde *et al.*, *Proceedings of IPAC'15*, Richmond, VA, USA.
- [3] E. Simakov *et al.*, *Phys. Rev. Lett.* **116** 064801 (2016).
- [4] C. Jing *et al.*, *Phys. Rev. ST Accel. Beams* **12** 121302 (2009).
- [5] J. Upadhyay and E. Simakov, in *Proceedings of NAPAC'16*, Chicago, IL, USA.

THE ACHIP EXPERIMENTAL CHAMBERS AT PSI

Eugenio Ferrari*¹, Rasmus Ischebeck, Nicole Hiller, Simona Borrelli, Franziska Frei, Cigdem Ozkan-Loch, Micha Dehler, Eduard Prat, Simona Bettoni, Sven Reiche, Albert Romann, Jörg Raabe, Blagoj Sarafinov, Saha Susmita, Marco Calvi, Terence Garvey, Volker Schlott, Vitaliy A. Guzenko, Christian David, Martin Bednarzik, Hans-Heinrich Braun, Leonid Rivkin¹, Paul Scherrer Institut, Villigen PSI, Switzerland
Joshua McNeur, Peter Hommelhoff, FAU Erlangen Nurnberg, Erlangen, Germany
¹also at École Polytechnique Fédérale de Lausanne EPFL, Lausanne, Switzerland

Abstract

The Accelerator on a Chip International Program (ACHIP) is an international collaboration, funded by the Gordon and Betty Moore Foundation, whose goal is to demonstrate that laser-driven accelerator on a chip can be integrated to fully build an accelerator based on dielectric structures. PSI will provide access to the high brightness electron beam of SwissFEL to test structures, approaches and methods towards achieving the final goal of the project. In this contribution, we will describe the two interaction chambers installed on SwissFEL to perform the proof-of-principle experiments. In particular, we will present the positioning system for the samples, the magnets needed to focus the beam to sub-micrometer dimensions and the diagnostics to measure beam properties at the interaction point.

INTRODUCTION

With the potential of delivering acceleration of particles with gradients in excess of more than one order of magnitude larger than conventional RF technology, dielectric laser acceleration (DLA) [1] represents one of the most promising candidates for the realization of table top accelerators and for reducing the dimensions of future high energy colliders. The technique is based on the interaction between charged particles and the electric field of a laser, mediated by a dielectric microstructure. It is capable of exceeding the conventional technology as it implies dielectrics instead of metals. Dielectric materials are capable of supporting much higher electrical fields before breakdown happens.

The Accelerator on a Chip International Program (ACHIP) [2], an international collaboration between seven Universities, three National Laboratories and a private company, has been established with the support of the Gordon and Betty Moore Foundation to advance the DLA technology. The final goal is the realization of an all-on-a-chip particle accelerator. The role of EPFL/PSI in the collaboration is to investigate DLAs at relativistic electron beam energy and perform proof-of-principle experiments, in particular using the electron beam of SwissFEL [3].

Our goal is to demonstrate gradients in excess of 1 GV/m for a dielectric length of 1 mm, resulting in an acceleration of 1 MeV [4] for the electrons.

INJECTOR CHAMBER

Installed at meter 89 of the SwissFEL injector [5] is a chamber dedicated to experiments, see Fig. 1 where a breakout 3D representation of the setup is shown. It is composed of in vacuum manipulator, operated through a feedthrough by a stepper motor for the vertical translation and equipped with a camera box for detecting the electron beam signal on the screens (blue box on the left). Two different targets for transverse beam measurements (YAG:Ce and OTR foil) are installed on the manipulator as well as four different sample holders for the samples. Using the manipulator the samples can be inserted into the SwissFEL electron beam depending on the request of the different experiments.

A load-lock pre-chamber allows for installation of the samples on the sample holders without breaking the accelerator vacuum. A summary of the relevant parameters is reported in Table 1. Notice that in the low energy chamber the installation of a laser is not planned, hence the DLA studies are focused on the investigation of the wakefields induced by the microstructures on the electron beam and on assessing the radiation hardness of the materials used for the microstructures.

The chamber has been successfully commissioned and has been already used to perform a number of different experiments (see in the following).

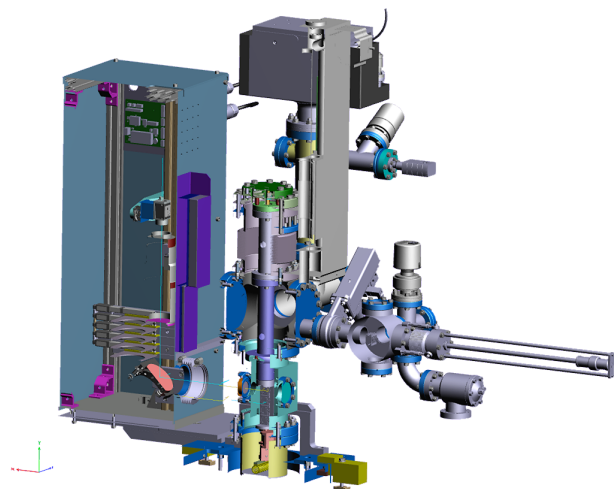


Figure 1: 3D breakout model of the ACHIP injector chamber.

* eugenio.ferrari@psi.ch

Table 1: Parameters for the Experiments in the Injector (Second Column) and in the Switchyard (Third Column). Notice that in the present installation no laser is foreseen in the injector chamber.

	Injector	Switchyard
Electron beam		
Energy	350 MeV	3 GeV
Charge	0.5 – 200 pC	1 pC
Beam size (rms)	1.4 – 25 μm	< 1 μm
Laser		
Wavelength		2 μm
Pulse energy	Not Available	500 μJ
Pulse duration		100 fs
DLA structure		
Length	3 mm	3 GeV
Gradient	0.75 GV/m	> 1 GV/m
Opening	90 μm x 500 μm	1.2 μm x 7 μm

SWITCHYARD CHAMBER

A further dedicated experimental chamber is planned to be installed in the higher energy section of the machine, in the switchyard transfer line to the ATHOS beamline. The manufacturing vacuum chamber has started and we plan to have it installed at beginning of 2018 during one of the planned shutdowns of SwissFEL. It will be placed on one of the existing girders to ensure adequate vibration stability. The relevant parameters for the experiment are summarized in Table 1.

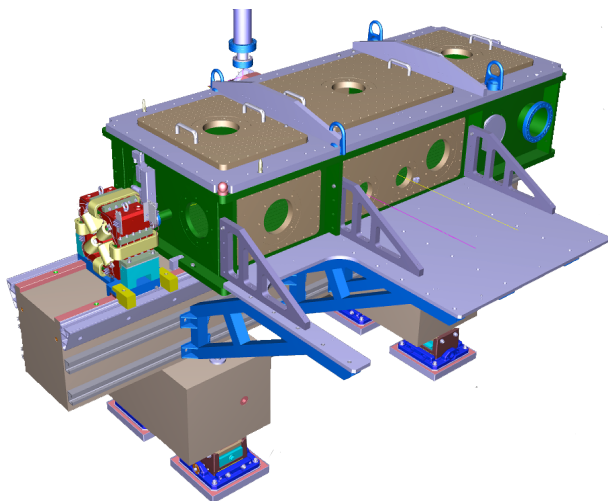


Figure 2: 3D model of the ACHIP chamber in the SwissFEL switchyard.

Chamber Design

A 3D model of the vacuum chamber is shown in Fig. 2. The pressure in the chamber will be 10^{-6} mbar, adequate to satisfy the beam transport requirements. Differently from the injector chamber, a dedicated Ti:Sa laser equipped with

an optical parametric amplifier will be installed in a laser room above the experiment. Its photon beam, transported through a low-vacuum transfer line, will be available to perform acceleration experiments. To accommodate for the enlarged interaction length of 1 mm between the laser and the electron beam, we are planning a pulse front tilt with an angle of 45 degrees between the intensity and phase fronts of the laser, via a dispersive reflective grating [6].

In the chamber, a hexapod manipulator will be installed, allowing for 6-dimensional alignment of the DLA microstructure with respect to the incoming electron beam. On the same sample mount we foresee to install different profile monitors, including a YAG:Ce scintillator, a sub- μm resolution wire-scanner, as well as an OTR target. These will enable to diagnose the beam size along the propagation direction and to ensure the superposition, both longitudinal and transverse, between the electron beam and the laser. Symmetrically with respect to the interaction point there will be two permanent quadrupole triplets to obtain the required electron beam optics for the smallest beam size at IP and transport to the second half of the switchyard, where the last bending magnet can be used as a spectrometer to detect the interaction of e-beam and laser.

The quadrupoles, whose geometrical strength will be -25.89 m^{-2} and 38.73 m^{-2} , will be installed on two translation stages each, so that their position can be controlled remotely. The horizontal translation stage will have a longer travel range to enable a complete removal of the quadrupoles from the beam path to allow the normal beamline operation. The size of the quadrupole will be approximately $15 \times 15 \times 10 \text{ cm}^3$ inclusive of the mounting support, with opening of 5 mm.

Electron Beam

Using elegant [7] and ASTRA [8] the electron beam of the first foreseen experiments has been simulated, in Fig. 3 we report the optics along the lattice and in Fig. 4 the longitudinal and transverse phase space. The β -functions at IP are 1 cm and 1.8 cm in the horizontal and vertical directions, respectively. This, combined with the reduced emittance of the SwissFEL electron beam leads to expected (rms) beam sizes of 0.26 μm and 0.36 μm for the horizontal and vertical planes. Such beam sizes are adequate for full transmission of the electron beam through the DLA structure, cfr. Table 1.

FIRST EXPERIMENTS IN THE INJECTOR CHAMBER

Radiation Hardness Testing of Dielectrics

To consider dielectric structures as the basis for a linear electron accelerator of significant current, the effect of sending a high-power electron beam through the micron-scale apertures typical in optical scale dielectric accelerators must be fully understood. In addition to the effects of wakefields and Coulomb repulsion on the beam, the beam-induced damage on the dielectric material itself needs to be studied.

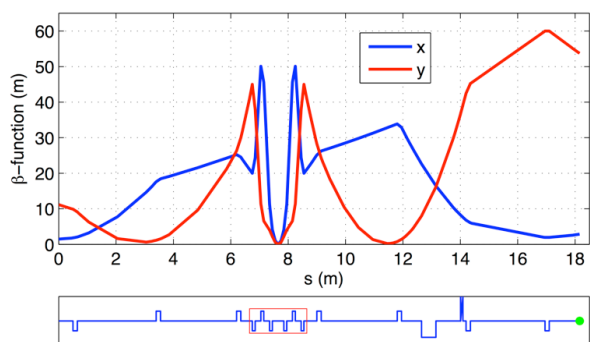


Figure 3: Horizontal (blue) and vertical (red) β -functions for the DLA experiment at the switchyard of SwissFEL. The lower sketch shows the corresponding magnetic lattice. The smaller rectangles mark the quadrupole magnets, the larger one shows the position of the dipole magnet before the profile monitor, indicated by a green circle. Image reproduced from [4].

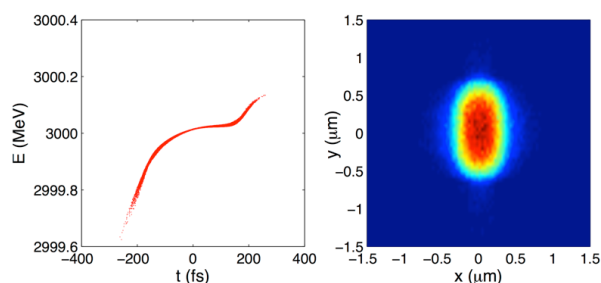


Figure 4: Longitudinal phase-space (left) and transverse profile (right) of the simulated electron beam at the experiment location. The rms pulse duration is 92 fs, the rms energy spread is 42 keV, and the rms beam sizes are $0.26 \mu\text{m}$ (horizontal) and $0.36 \mu\text{m}$ (vertical) Image reproduced from [4].

Therefore, the 350 MeV electron beam at the SwissFEL injector chamber has been used to study the radiation hardness of the materials proposed to be the components of DLAs, e.g. Al_2O_3 , SiC, and Si, by placing directly in the path of the electron beam. The materials have been examined for signs of structural damage under an optical microscope and an SEM. We are preparing an infrared spectrometer to assess the change in the optical properties of the materials.

Test of Wire-Scanners with Sub-Micron Resolution

This experiment is aimed at testing the prototype of a wire scanner with sub-micrometer spatial resolution. The geometrical resolution of a standard wire scanner depends on the wire width: the smaller the width, the higher the resolution. Instead of metallic wires stretched onto a wire-fork, the prototypes were fabricated using nanotechnology fabrication techniques based on electron beam lithography on a Silicon chip with a central Si_3N_4 membrane. On this membrane two metal (Au or Ni) wires are electroplated. The improvement of the resolution is critical for the ACHIP project as in the high-energy chamber experiment the electron beam will have sub- μm size. In the experiments in the injector

chamber we tested UH-vacuum and radiation robustness, as well as performing transverse profile measurements with the smallest beam sizes possible. Comparison with a traditional $5 \mu\text{m}$ Tungsten wire has also been performed [9].

Beam-double Pillar Structure Interaction

Transmitting an electron beam through the small aperture of the dielectric structures proposed for the ACHIP project is an experiment in itself. We will use a suitably expanded structure and low energy electrons to test the ability to fully transmit the electron beam through it. As wakefields could potentially seriously degrade the electron beam quality, we will evaluate the effect of the interaction of the electron beam with the double pillar structure, by measuring the emittance and energy distribution after the interaction, for different bunch charges and electron beam lengths.

Processional Magnetization Reversal of Ferromagnets

Modern magnetic recording technology demands operational speeds far beyond the nanosecond regime, which require the investigation of magnetic excitations on a time scale much shorter than the spin lattice relaxation time ($\sim 100 \text{ ps}$). The goal of this experiment is to provide a visual demonstration of switching on picosecond timescales for in-plane and out of plane magnetic nanostructures, by using the electron beam field as the magnetic pulse excitation. After exposure to the electron beam, the samples will be measured using scanning transmission X-ray microscopy (STXM) and X-ray magnetic circular dichroism (XMCD). The samples inserted in the SwissFEL electron beam were 25 nm thick in-plane magnetized $\text{Ni}_{80}\text{Fe}_{20}$ Py islands of length 500 nm and width 250 nm.

CONCLUSION

We presented the two experimental chambers for the ACHIP experiments in SwissFEL. A first chamber, installed in the injector part of the machine, has been commissioned and is presently available for experiments. A second chamber in the high energy part of the machine is in advanced construction phase and we plan to install it beginning of 2018.

ACKNOWLEDGEMENT

We would like to acknowledge the support of all the groups at PSI involved in the project, in particular Diagnostics, AMI, Controls and Operations. This work is supported by the Gordon and Betty Moore Foundation.

REFERENCES

- [1] R.J. England, *et al.*, *Rev. Mod. Phys.* 86 (2014) 1337.
- [2] <http://achip.stanford.edu>
- [3] R. Ganter (ed.), PSI Report No.10-04, 2012.
- [4] E. Prat, *et al.*, "Outline of a dielectric laser acceleration experiment at SwissFEL", *Nucl. Instrum. Methods Phys. Res.*, Sect. A 865, 87–90 (2017).

Content from this work may be used under the terms of the CC BY 3.0 licence (© 2018). Any distribution of this work must maintain attribution to the author(s), title of the work, publisher, and DOI.

- [5] T. Schietinger, *et al.*, "Commissioning experience and beam physics measurements at the SwissFEL Injector Test Facility", *Phys. Rev. Accel. Beams*, 19, 10, 100702 (2016).
- [6] T. Plettner and R. L. Byer, *Phys. Rev. ST Accel. Beams* 11, 030704 (2008).
- [7] M. Borland, *APS LS Note* No.287, 2000.
- [8] K. Floettmann, *ASTRA User's Manual*, 2000.
- [9] S. Borrelli, *et al.*, to be published.

PREPARATIONS FOR INSTALLATION OF THE DOUBLE EMITTANCE-EXCHANGE BEAMLINE AT THE ARGONNE WAKEFIELD ACCELERATOR FACILITY*

G. Ha¹, J. G. Power², M. Conde², D. S. Doran², W. Gai²

¹Pohang Accelerator Laboratory, Pohang, Korea

²Argonne National Laboratory, Argonne, USA

Abstract

Preparations to upgrade the single EEX beamline at the Argonne Wakefield Accelerator (AWA) facility to a double EEX beamline are underway. The single EEX beamline recently demonstrated exchange-based longitudinal bunch shaping (LBS) which has numerous applications including high energy physics linear colliders, X-ray FELs, and intense radiation sources. The exchange-based method can generate arbitrary LBS in the ideal case but has limitations in the real case. The double EEX beamline was proposed as a means to overcome the limitations of single EEX due to transverse jitter and large horizontal emittance. In this paper, we present the current status of beamline design and installation and simulation results for the planned experiments: collinear wakefield acceleration with tailored beams and tunable bunch compression without the double-horn feature.

DOUBLE EEX BEAMLINE AT AWA

The Argonne Wakefield Accelerator (AWA) is an accelerator facility dedicated for future accelerator R&D [1]. This facility consists of three RF photoinjector beamlines for carrying out future accelerator research; wakefield applications [2-4], beam manipulation [5], field emission study [6] etc. The main beamline has a 1.5 cell RF gun generating a very high charge beam (up to 100 nC for single bunch) and 6 accelerating cavities to accelerate the beam up to 70 MeV. Downstream of the beamline is a flexible experimental area including a straight section and a single emittance exchange (EEX) beamline.

The EEX beamline was recently used to demonstrate property exchange and longitudinal profile shaping (LPS) [5]. Although the experiment was successful, the single EEX beamline has two important limitations [7] for practical usage. First, the single EEX beamline exchanges the (typically) large longitudinal emittance for the small transverse yet most applications benefit from a small transverse emittance. Second, both initial timing and energy jitters become a horizontal offset jitter after the single EEX beamline.

These limitations can be overcome with a double EEX beamline where a second EEX beamline is added after the first (Fig. 1). The first EEX exchanges transverse and longitudinal phase spaces; this enables the manipulation of the longitudinal phase space by altering the transverse beam properties in the middle section. Afterward, the second EEX exchanges these phase spaces again to return the emittances. Upstream longitudinal jitters become transverse jitters after the first EEX, but go back to longitudinal jitters after the second one [7,8].

The double EEX (DEEX) beamline at the AWA is going to have two double dogleg type EEX beamlines [5] with ~3 m separation for the transverse manipulation using quadrupoles and masks. Each dogleg uses 20 degree bending angle and 1.5 m separation between dipoles. The dispersion of the dogleg is ~0.77 m, and the corresponding deflecting cavity (TDC) strength needed is 1.3 m⁻¹. This beamline also has many YAG screens for transverse measurements, ICTs for the charge level, and two TDCs for longitudinal diagnostic. A single dipole magnet is followed by each TDC to measure the longitudinal phase space. Approximately a 1-m space is reserved at the upstream, middle, and downstream of the double EEX beamline for various EEX applications (e.g. THz radiation [9], wakefield applications [10], etc.).

In the remainder of the paper, we present a study of the CSR-effect in EEX and some preliminary simulation results for applications.

CSR SUPPRESSION IN DOUBLE EEX BEAMLINE

CSR is a well-known limitation for dispersive beamlines (e.g. chicane) and it comes as no surprise that it strongly impacts the DEEX beamline which consist of eight dipole magnets with large bending angles and (some) applications that require a high charge beam. We have found a simple method to partially suppress the CSR-effect for some applications [11], but we still have significant emittance growth along the beamline [7].



Figure 1: AWA drive beamline configuration with a double EEX beamline.

Content from this work may be used under the terms of the CC BY 3.0 licence (© 2018). Any distribution of this work must maintain attribution to the author(s), title of the work, publisher, and DOI.

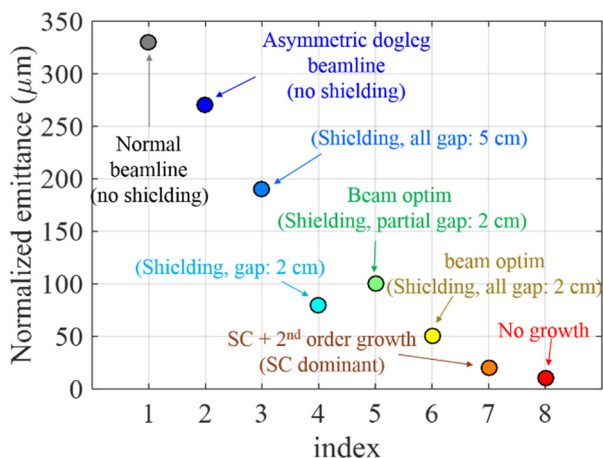


Figure 2: Final horizontal emittance after the double EEX beamline. The 5-nC beam is accelerated up to 50 MeV.

We studied three methods to reduce emittance growth from CSR: (1) asymmetric dogleg, (2) shielding, and (3) transverse beam tuning, summarized in Fig. 2. The y-axis is the final horizontal emittance after the DEEX beamline and each color corresponds to each trial. Start-to-end simulations are used (GPT [12]) to simulate the beam transport, and CSR is included using the CSR-module from Ref. [13]. A 5-nC beam is accelerated to 50 MeV with four accelerating RF cavities, which provides a normalized horizontal emittance at the end of the linac of 10 μm . This is the initial emittance to DEEX. This emittance increases to $\sim 30 \mu\text{m}$ after the DEEX due to nonlinear fields from magnets and cavities and space-charge effect but without CSR. Once CSR is included, the final emittance increases from 30 μm to 330 μm , demonstrating that CSR is the major factor limiting DEEX.

The first method studied to suppress the CSR effect was the asymmetric dogleg method that uses two different angles for the two doglegs in the EEX beamline [11]. Although it is effective in suppressing the CSR effect on the LPS, the final emittance is still enhanced to 270 μm . Since this method requires a long space compared to identical doglegs and the suppression was not effective enough, we dropped this option for the current DEEX design.

The second method studied used to suppress the CSR-effect uses two shielding plates to suppress CSR (CSR shielding [14,15]). We compared cases where the shielding gap was applied to the entire DEEX beamline to ones where the gap was only applied at key locations. When the gap is applied to the entire beamline, a 5-cm gap reduced the final emittance from 330 μm to 190 μm whereas a 2-cm gap reduced it to 70 μm . This is because the 5-cm gap only cuts a small portion of low-frequency CSR spectrum [16]. Since it is difficult to apply the 2-cm gap to entire beamline, due to the beam transport, we choose to apply it only in the dipole vacuum chambers use our normal 5 cm gap in the rest of the DEEX beamline. This point is labeled “partial gap” in Fig. 2.

Finally, we studied a third method to suppress the CSR-effect that uses transverse beam tuning. When CSR in-

creases the longitudinal emittance in the bend, it becomes entangled with the horizontal beam properties (e.g. beam size, slope, and emittance). Therefore, it is possible to minimize the CSR effect by tuning the transverse beam property [7]. Figure 2 shows the 2-cm gap for the entire beamline generated 70 μm without beam tuning. However, when the 2-cm gap is combined with the tuning method, the emittance is further decreased to 50 μm .

Our beamline design will use the partial gap (2 cm) combined with the tuning method to achieve 100 μm for the high charge case (5 nC). This design is very effective at suppressing the CSR-effect at low charge ($\sim 100 \text{ pC}$). The emittance of 1.05 micron is increased to 1.75 micron without shielding while the current design can suppress it to 1.15 micron. It is possible to preserve the emittance with 1-cm gap for the whole beamline or 2-cm gap for the whole beamline with a low bending angle (5 degree) [7].

PRELIMINARY RESULTS OF DOUBLE EEX APPLICATIONS

In this section, we present preliminary simulations and/or experiment results for two DEEX applications. The first application uses LPS to achieve a high transformer ratio, and the second application is bunch compression to overcome several disadvantages of the chicane compressor.

Current Profile Shaping

Collinear type wakefield accelerators are attractive options for the XFEL or other linac-based light sources since these accelerators may provide a high gradient and low construction cost compared to conventional accelerating cavities [17]. One obstacle to realize it is the transformer ratio, defined by the ratio of the maximum decelerating field inside the drive beam to the maximum accelerating field behind the drive beam. Since this factor is related to the efficiency of the wakefield acceleration, it is important to achieve a high value.

Beam with symmetric current profiles are limited to a transformer ratio of 2 [18], but asymmetric current profiles (e.g. triangle) can achieve a high transformer ratio (greater than 2) [19]. Various asymmetric profiles were recently demonstrated at AWA [5] and a high transformer ratio from a quadratic profile was also measured very recently [20]. This experiment demonstrated that we can achieve a transformer ratio of ~ 5.1 which is even higher than previous record (3.5) with shaping by another method [21].

We plan to demonstrate the shaping using the double EEX beamline. At the same time, we are going to prove the relationship between the current profile and the transformer ratio as predicted by theory. The final goal in terms of transformer ratio is more than 10.

Particle tracking simulations support the feasibility of this experiment. The DEEX beamline can generate various current profiles listed in Ref. [18] and [19]. Since the longitudinal phase space measurement is available at AWA [20], we can observe the wakefield pattern for

Content from this work may be used under the terms of the CC BY 3.0 licence (© 2018). Any distribution of this work must maintain attribution to the author(s), title of the work, publisher, and DOI.

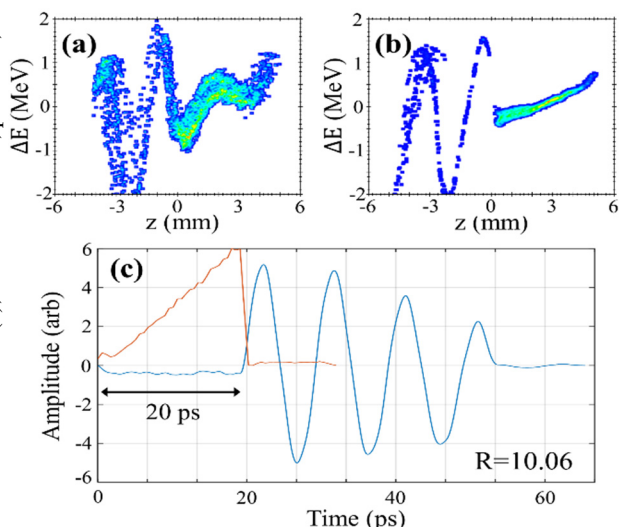


Figure 3: Reconstructed longitudinal phase space of (a) triangle and (b) special head-and-triangle drive beam with a long witness beam. (c) Wakefield pattern estimated from the simulated current profile. Estimated transformer ratio is 10 (ideal is 12).

different drive profiles as shown in Fig. 3. In this figure, (a) and (b) show reconstructed longitudinal phase spaces from different current profiles. The structure introduced in Ref. [10] is used for the simulation, and these are S2E simulation results. The transformer ratio can be calculated from the measured longitudinal phase space or a numerical estimation from the measured current profile, as illustrated in Fig. 3(c).

By optimizing the head shape of the triangle profile, transformer ratio of 10.06 is achieved in simulation and it is very close to the ideal value of 12 under this condition.

EEX as Bunch Compressor

While the magnetic chicane is clearly today's state-of-the-art bunch compression system [22] it still has a few minor limitations. First, a chicane compressor requires a negative longitudinal incident chirp since the momentum compaction of the chicane and the chirp together determine the compression ratio. Therefore, changing the compression ratio is not easy. Second, the strong compression normally generates a double-horn feature on the current profile that can affect the performance of the XFEL as well as radiation safety. Finally, it is necessary to remove this energy chirp after the chicane with a de-chirping beamline or operating a linac off-phase.

An EEX compressor may be able to overcome these limitations. While the chicane relies on the path-length difference of different energies, compression using EEX uses the transverse focusing and the transverse-to-longitudinal exchange. Ref. [22] presents preliminary simulations to show the advantages from EEX compres-

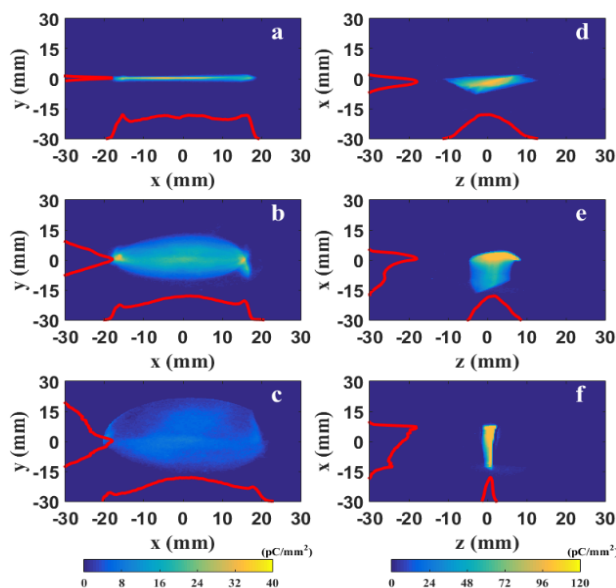


Figure 4: (a-c) Electron-beam images at the YAG screen after a single EEX, showing the impact of an upstream quadrupole, Q1. (a-c) show transverse image as Q1 was set to (a) -0.7 T/m, (b) 0 T/m, and (c) $+0.7$ T/m. (d-f) utilize a deflecting cavity to measure bunch length, with Q1 set to (d) -0.5 T/m, (e) 0 T/m, and (f) $+0.5$ T/m.

sors. Since the compression ratio is determined by the horizontal focusing in the middle section (shown in Fig. 1), the compression ratio is easily tunable; even bunch lengthening and bunch shaping are possible. Second, the transverse focusing cannot introduce double horn features for initially smooth phase space. Even though the double horn feature is introduced by the kink on the initial longitudinal phase space, it may be cancelled by third order momentum kick from a single octupole magnet. Finally, the longitudinal chirp at the exit of the DEEX beamline depends on the quadrupole setting in the middle section again. Both negative and positive chirps can be generated and be controlled in reasonable range.

The tunable compression ratio described above was partially demonstrated during the single EEX shaping experiment last year. When the quadrupole in front of the EEX beamline focused/defocused the beam vertically (shown in Fig. 4 (a-c)), the horizontal beam size after the EEX beamline does not change (a-c) while the bunch length changed from 1.4 mm to 5.0 mm (d-f). Compared to the zero quadrupole case (3.2 mm), negative and positive quadrupole gradients compressed and lengthened the bunch length.

We plan to demonstrate this tunable compression ratio using the double EEX beamline. Based on the simulation, we expect to see the bunch length shorter than 0.05 mm. Also, we plan to explore other advantages, double horn and chirp control, during this experiment.

CONCLUSION

We presented the current status of the double EEX (DEEX) upgrade at AWA. A DEEX beamline is a powerful phase space manipulator and it has numerous applications. We introduced preliminary simulation results for two promising applications: shaping and compression. Various EEX applications will soon be demonstrated at AWA. On the other hand, the DEEX beamline at AWA has a big emittance growth issue due to (1) many dipole magnets, (2) large bending angles and (3) high charge applications. We explored three simple methods to suppress CSR effects, and CSR shielding combined with beam matching is the most promising method found so far but we are still exploring other avenues to handle CSR in the EEX beamline.

ACKNOWLEDGEMENT

This work is supported by Department of Energy, Office of Science, under Contract No. DE-AC02-06CH11357.

REFERENCES

- [1] M. Conde *et al.*, “Research program and recent results at the Argonne Wakefield Accelerator Facility (AWA)”, in *Proc. IPAC’17*, Copenhagen, Denmark, paper WEPAB132, pp. 2885-2887.
- [2] J. Shao *et al.*, “Recent two-beam acceleration activities at Argonne Wakefield Accelerator Facility”, in *Proc. IPAC’17*, Copenhagen, Denmark, paper WEPVA022, pp. 3305-3307.
- [3] W. Dan *et al.*, “Interaction of an ultrarelativistic electron bunch train with a W-band accelerating structure: high power and high gradient”, *Phys. Rev. Lett.*, vol. 116, p. 054801, 2016.
- [4] E. I. Simakov *et al.*, “Observation of wakefield suppression in a photonic-band-gap accelerator structure”, *Phys. Rev. Lett.*, vol. 116, p. 064801, 2016.
- [5] G. Ha *et al.*, “Precision control of the electron longitudinal bunch shape using an emittance-exchange beam line”, *Phys. Rev. Lett.*, vol. 118, p. 104801, 2017.
- [6] J. Shao *et al.*, “In situ observation of dark current emission in a high gradient rf photocathode gun”, *Phys. Rev. Lett.*, vol. 117, p. 084801, 2016.
- [7] G. Ha *et al.*, “Limiting effects in double EEX beamline”, *J. Phys. Conf. Ser.*, vol. 874, p. 012061, 2017.
- [8] A. A. Zholents and M. S. Zolotarev, “A new type of bunch compressor and seeding of a short wave length coherent radiation”, Report No. ANL/APS/LS-327, ANL, Argonne, USA, May 2011.
- [9] Y.-E. Sun *et al.*, “Tunable subpicosecond electron-bunch-train generation using a transverse-to-longitudinal phase-space exchange technique”, *Phys. Rev. Lett.*, vol. 105, p. 234801, 2010.
- [10] G. Ha *et al.*, “Simultaneous generation of drive and witness beam for collinear wakefield acceleration”, *J. Phys. Conf. Ser.*, vol. 874, p. 012027, 2017.
- [11] G. Ha *et al.*, “Perturbation-minimized triangular bunch for high-transformer ratio using a double dogleg emittance exchange beam line”, *Phys. Rev. ST Accel. Beams*, vol. 19, p. 121301, 2016.
- [12] GPT, <http://www.pulsar.nl/gpt/>
- [13] I. V. Bazarov and T. Miyajima, “Calculation of coherent synchrotron radiation in general particle tracer”, in *Proc. EPAC’08*, Genoa, Italy, paper MOPC024, pp. 118-120.
- [14] R. Kato *et al.*, “Suppression and enhancement of coherent synchrotron radiation in the presence of two parallel conducting plates”, *Phys. Rev. E*, vol. 57, p. 3454, 1988.
- [15] V. Yakimenko *et al.*, “Experimental observation of suppression of coherent-synchrotron-radiation-induced beam-energy spread with shielding plates”, *Phys. Rev. Lett.*, vol. 109, p. 164802, 2012.
- [16] D. Sagan *et al.*, “Extended one-dimensional method for coherent synchrotron radiation including shielding”, *Phys. Rev. ST Accel. Beams*, vol. 12, p. 040703, 2009.
- [17] A. Zholents *et al.*, “A preliminary design of the collinear dielectric wakefield accelerator”, *Nucl. Instrum. and Methods Phys. Res. Sect. A*, vol. 829, p. 190, 2016.
- [18] K. L. F. Bane, P. Chen, and P. B. Wilson, “On collinear wakefield acceleration”, Report No. SLAC-PUB-3662, SLAC, Menlo Park, USA, Apr. 1985.
- [19] F. Lemery and P. Piot, “Tailored electron bunches with smooth current profiles for enhanced transformer ratios in beam-driven acceleration”, *Phys. Rev. ST Accel. Beams*, vol. 18, p. 081301, 2015.
- [20] Q. Gao *et al.*, unpublished note.
- [21] S. Antipov *et al.*, “Transformer ratio enhancement with triangular beam”, *AIP Conference Proceedings*, vol. 1777, p. 070005, 2016.
- [22] G. Ha *et al.*, “Preliminary simulations on chirp-less bunch compression using double-EEX beamline”, in *Proc. IPAC’17*, Copenhagen, Denmark, paper THPAB062, pp. 3862-3864.

MEASUREMENT OF SHORT-WAVELENGTH HIGH-GAIN FEL TEMPORAL COHERENCE LENGTH BY A PHASE SHIFTER

G. Zhou^{1,2,3†}, J. Wu^{1‡}, M. Yoon^{1,4}, C-Y. Tsai¹, C. Yang^{1,5},
 W. Liu^{1,5}, W. Qin^{1,6}, B. Yang⁷, T. Raubenheimer¹

¹SLAC National Accelerator Laboratory, Menlo Park, U.S.A

²Institute of High Energy Physics, Chinese Academy of Science, Beijing, China

³University of Chinese Academy of Science, Beijing, China

⁴Department of Physics, Pohang University of Science and Technology, Pohang, Korea

⁵University of Science and Technology of China, Hefei, Anhui, China

⁶Peking University, Beijing, China

⁷University of Texas at Arlington, Arlington, USA

Abstract

Short-wavelength high-gain free-electron lasers (FELs) are now well established as ultra-fast, ultra-bright, longitudinally partial coherent sources. Since coherence is one of the fundamental properties of a light source, continuous efforts on high-gain free electron laser coherence measurements are made. In this work, we propose a possible approach, employing a phase shifter to induce electron beam delay to measure the temporal coherence length. Simple analysis, numerical simulation and preliminary experimental results are presented. This approach can be robust and independent of frequency.

INTRODUCTION

Free-electron lasers (FELs) greatly benefit fundamental research in physics, chemistry, materials science, biology, and medicine by producing intense tunable radiation ranging from the infrared to hard x-ray region [1]. Approaches like coherent x-ray diffraction imaging (CXDI), x-ray holography and nano-crystallography promise important new insights in biology, condensed matter physics and atomic physics [2]. Therefore, coherence property plays an important role in these experiments. Furthermore, [3-4] indicate that small deviations from perfect coherence can be considered in the CXDI method if the degree of coherence is known. Thus, a pre-knowledge of FEL coherence properties would help.

Young's experiment [5] is one of the most widely used methods for characterization of coherence, the transverse coherence properties could be measured with the interference pattern. Previous work regarding measurements of transverse coherence properties of FEL sources has been done earlier [6-8]. The other important statistical characteristic of the FEL radiation is its temporal coherence. Due to the FEL instabilities leading to partial coherence, the FEL pulses are not fully coherent in the time domain.

In addition, the slippage effect in FEL results in the radiation pulse consisting of several spikes with a width of about the temporal coherence length. These longitudinal modes can be correlated and interfere with each other, which affects the temporal coherence length, which was recently observed experimentally [9]. Several optical methods are proposed to measure the FEL temporal coherence length. In the extreme ultraviolet regime, the feasibility of autocorrelation methods using laser beam splitter has been proved in [10]. Experimental measurement employing two-beam interference, analyzing the contrast of these interference fringes to get the temporal coherence length has been reported [11].

In this paper, we make use of high-gain FEL process to measure temporal coherence length. By introducing phase difference between the radiation field and the electron beam, the resultant radiation field can be represented by two waves with a constant phase difference, in which two-wave temporal interference should be expected [see Theory Section]. Based on this analysis, we propose a possible approach to measure the FEL temporal coherence length. In the theory part, we obtain solutions of high-gain FEL including phase shift in time domain. We further prove the feasibility of our approach with supports of numerical simulation. In the on-going experiment part, preliminary experimental results at Linac Coherent Light Source (LCLS) are presented and further experimental investigation is on our schedule.

THEORY

Following [12], we start from a one-dimension linear model described by:

$$\frac{\partial A(\bar{z}, \bar{s})}{\partial \bar{z}} + \frac{\partial A(\bar{z}, \bar{s})}{\partial \bar{s}} = B(\bar{z}, \bar{s}), \quad (1)$$

$$\frac{\partial B(\bar{z}, \bar{s})}{\partial \bar{z}} = P(\bar{z}, \bar{s}), \quad (2)$$

$$\frac{\partial P(\bar{z}, \bar{s})}{\partial \bar{z}} = iA(\bar{z}, \bar{s}). \quad (3)$$

*Work supported by the US Department of Energy (DOE) under contract DE-AC02-76SF00515 and the US DOE Office of Science Early Career Research Program grant FWP-2013-SLAC-100164

†gzhou@SLAC.Stanford.EDU

‡jhwu@SLAC.Stanford.EDU

In these equations, $\bar{z} = z/l_g$, $\bar{s} = -c(t-z/v_z)/l_c$, where z is the coordinate along the undulator axis, \bar{s} is the scaled position along the bunch, v_z is the electron velocity in the z direction, and $l_g = \lambda_u/4\pi\rho$ and $l_c = \lambda_s/4\pi\rho$ are the gain length and the cooperation length, respectively. The other quantities are: λ_u , the wiggler period; λ_s , the radiation wavelength (satisfying the well-known resonance relation $\lambda_s = \lambda_u(1+a_u^2)/2\gamma^2$); A , the dimensionless field amplitude $E_0/(4\pi mc^2\gamma_0 n_e \rho)^{1/2}$ (which uses the average initial electron energy $mc^2\gamma_0$, beam density $n_e = I/ec\sigma$, and FEL parameter ρ [13]); B , the bunching parameter $\langle e^{-i\theta} \rangle$ (where the electron phase $\theta_j = (k_s + k_u)z - ck_s t_j$); and P , the average momentum $\langle \eta e^{-i\theta} \rangle$ (where η_j is the normalized energy deviation $(\gamma_j - \gamma_0)/\rho\gamma_0$).

Note that Eqs. (1-3) have been obtained from linearizing the Compton FEL equations [13], based on coasting beam approximation, and describe the exponential growth of the signal in the high-gain regime prior to saturation.

To solve Eqs. (1-3), we first Fourier transform \bar{s} to Δ ,

$$\frac{\partial a(\bar{z}, \Delta)}{\partial \bar{z}} + i\Delta a(\bar{z}, \Delta) = b(\bar{z}, \Delta), \quad (4)$$

$$\frac{\partial b(\bar{z}, \Delta)}{\partial \bar{z}} = p(\bar{z}, \Delta), \quad (5)$$

$$\frac{\partial p(\bar{z}, \Delta)}{\partial \bar{z}} = ia(\bar{z}, \Delta), \quad (6)$$

where $a(\bar{z}, \Delta)$, $b(\bar{z}, \Delta)$ and $p(\bar{z}, \Delta)$ are the Fourier transform of $A(\bar{z}, \bar{s})$, $B(\bar{z}, \bar{s})$ and $P(\bar{z}, \bar{s})$ respectively. By assuming that $a(\bar{z}, \Delta)$ is proportional to $e^{i\mu\bar{z}}$, we obtain the cubic equation,

$$\mu^3 - \Delta\mu^2 + 1 = 0. \quad (7)$$

Solving the eigenvalue in Eq. (7) to the first order of Δ and considering that the exponential gain will dominate the process, we obtain that $\mu = \frac{-\sqrt{3}}{2}i + \frac{1}{2} + \frac{\Delta}{3}$. After some proper approximation, the solution of these equations in frequency domain should be:

$$a(\bar{z}, \bar{s}) = \frac{1}{3} \left[a(0, \Delta) + \left(-\frac{1}{2}i + \frac{\sqrt{3}}{2}\right) b(0, \Delta) + \left(\frac{1}{2} - \frac{\sqrt{3}}{2}i\right) p(0, \Delta) \right] e^{\frac{\sqrt{3}}{2}\bar{z} + \left(\frac{\Delta}{3} + \frac{1}{2}\right)i\bar{z}}. \quad (8)$$

With inverse Fourier transform, we obtain the radiation field in time domain,

$$A(\bar{z}, \bar{s}) = \frac{1}{3} \left[A(0, \bar{s} + \frac{\bar{z}}{3}) + \left(-\frac{1}{2}i + \frac{\sqrt{3}}{2}\right) B(0, \bar{s} + \frac{\bar{z}}{3}) + \left(\frac{1}{2} - \frac{\sqrt{3}}{2}i\right) P(0, \bar{s} + \frac{\bar{z}}{3}) \right] e^{\frac{\sqrt{3}}{2}\bar{z} + \frac{i}{2}\bar{z}}. \quad (9)$$

The electric field at position (\bar{z}, \bar{s}) is driven by the initial electric field A , bunching B , energy modulation P , at $\bar{s} + \bar{z}/3$ with exponential gain and $l_c = l_c\bar{z}/3 = N\lambda_s/3$ is the approximate temporal coherence length, where N is total number of undulator periods.

To add a phase shifter located at z_0 , we assume that a sudden slippage is induced at z_0 . Mathematically, this can be regarded as $B(\bar{z}, \bar{s})$ and $P(\bar{z}, \bar{s})$ in Eqs. (1-3) replaced by $B(\bar{z}, \bar{s} + \delta\bar{s})$ and $P(\bar{z}, \bar{s} + \delta\bar{s})$, so that we can get the equations to describe the FEL process including a phase shifter:

$$\frac{\partial A(\bar{z}, \bar{s})}{\partial \bar{z}} + \frac{\partial A(\bar{z}, \bar{s})}{\partial \bar{s}} = B(\bar{z}, \bar{s} + \delta\bar{s}), \quad (10)$$

$$\frac{\partial B(\bar{z}, \bar{s} + \delta\bar{s})}{\partial \bar{z}} = P(\bar{z}, \bar{s} + \delta\bar{s}), \quad (11)$$

$$\frac{\partial P(\bar{z}, \bar{s} + \delta\bar{s})}{\partial \bar{z}} = iA(\bar{z}, \bar{s} + \delta\bar{s}). \quad (12)$$

Similarly, we can solve Eqs. (10-12) to obtain the solution of radiation field in time domain:

$$A(\bar{z}, \bar{s}) = \frac{1}{3} \left\{ A(\bar{z}_0, \bar{s} + \frac{\bar{z}}{3}) + \left[\left(-\frac{1}{2}i + \frac{\sqrt{3}}{2}\right) B(\bar{z}_0, \bar{s} + \frac{\bar{z}}{3}) + \left(\frac{1}{2} - \frac{\sqrt{3}}{2}i\right) P(\bar{z}_0, \bar{s} + \frac{\bar{z}}{3}) \right] e^{ik_s\delta\bar{s}} \right\} e^{\frac{\sqrt{3}}{2}\bar{z} + \frac{i}{2}\bar{z}}. \quad (13)$$

For Eq. (13), we can regard $A(\bar{z}, \bar{s})$ as two waves with a constant phase difference $k_s\delta\bar{s}$. It is expected that there exists an interference phenomenon. If we change the phase difference within a small range, e.g. within 2π , we could find the radiation power oscillates with respect to the phase difference. However, if the phase difference is too large (greater than the temporal coherence length), the phase correlation between the two waves is destroyed. In this case, the two waves are no longer coherent. Therefore, by continuous scanning the phase difference and measuring the radiation power, we can obtain the FEL temporal coherence length. We could expect that the envelope of FEL power as a function of phase difference should gradually shrink.

NUMERICAL SIMULATION

In the previous section, we propose a possible approach to measure the temporal coherence length by tuning the phase shifter. To further investigate the feasibility, we have done some numerical simulations with GENESIS, a well-benchmarked, three dimensional, time-dependent FEL simulation code [14]. To more precisely simulate the FEL process with relatively large phase shift, we made some modifications on its source code. Because the large-scale GENESIS time-dependent simulations are computational intensive, we only sample five points ($0, \pi/2, \pi, 3\pi/2, 2\pi$) within 2π (induced slippage is one wavelength) and then skip 32 wavelengths to sample another five points. In the simulation, we use LCLS parameters [15]

Content from this work may be used under the terms of the CC BY 3.0 licence (© 2018). Any distribution of this work must maintain attribution to the author(s), title of the work, publisher, and DOI.

listed in Table 1. Schematic LCLS undulator system is illustrated in Fig. 1 and hard x-ray self-seeding (HXRSS) chicane at Section 16 is employed as the phase shifter. The simulation results are shown in Fig. 2, in which the interference pattern can be clearly seen.

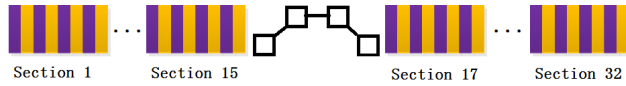


Figure 1: LCLS undulator system, the phase shifter is placed at Section 16.

Table 1: Main Parameters of LCLS for simulation

Parameter	Value
Radiation wavelength	0.2755 nm
Electron beam energy	10.1 GeV
RMS Undulator parameter	2.475
RMS Relative energy spread	1.29×10^{-4}
Normalized emittance	4×10^{-7} m
Undulator period	3 cm
Peak current	3.5kA

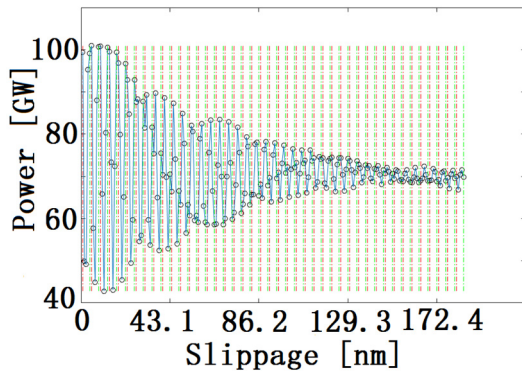


Figure 2: The radiation power as a function of slippage length. Every five points illustrate a wavelength, which is zoomed in. The wavelengths that we did not scan are zoomed out, shown as the space between the green line and red line.

In our case, the temporal coherence length is about $N\lambda_s/3 \sim 151.53$ nm, where N is total number of undulator periods. At the end of the 15th undulator, N is equal to 1650. From Fig. 2, we can find that the temporal coherence length is roughly about 150 nm.

ON-GOING EXPERIMENTAL EFFORTS

Since the analysis and simulation results are quite promising, we have done some preliminary experiments. Based on LCLS machine parameters shown in Table 1, we use HXRSS chicane as phase shifter and gas-detector to measure the FEL pulse energy. We change the magnetic

field strength of the chicane to scan phase difference and measure multi-shot averaged FEL pulse energy. Figure 3 shows the experimental results.

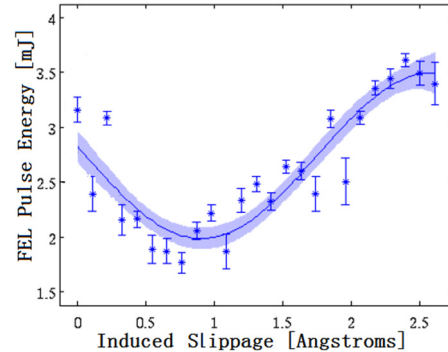


Figure 3: The FEL pulse energy as a function of slippage length.

At this point in time, we have scanned the phase difference within 2π . The experimental results agree with our analysis and simulation well. It is worth to point out that this approach is frequency-independent.

SUMMARY AND OUTLOOK

In this paper, we have presented a simple analysis of FEL including a phase shifter in time domain. We find that when phase difference is quite small, FEL power oscillates with respect to the electron beam delay. However, when the phase difference is greater than the temporal coherence length, the radiation would not change much. Based on the analysis, we propose an approach to measure the FEL temporal coherence length by scanning the electron beam delay. Numerical simulation and preliminary experiments at LCLS show that this approach can be potentially developed to measure the FEL temporal coherence length. Effects of the momentum compact factor R_{56} on temporal coherence will be presented in further studies and the experiments using this approach to measure the FEL temporal coherence length at LCLS is on our schedule. Also, this study will help us understand the performance of slippage enhanced SASE.

REFERENCES

- [1] E. Hemsing, G. Stupakov, D. Xiang, and A. Zholents, *Rev. Mod. Phys.*, vol. 86, p. 897, 2014.
- [2] A. Singer *et al.*, "Spatial and temporal coherence properties of single free-electron laser pulses," *Opt. Express*, vol. 20, p. 17480-17495, 2012.
- [3] L.W. Whitehead *et al.*, "Diffractive imaging using partially coherent X-rays", *Phys. Rev. Lett.*, vol. 103, p. 243902, 2009.
- [4] B. Abbey *et al.*, "Lensless imaging using broadband x-ray sources", *Nat. Photon*, vol. 5, p. 420-424, 2011.
- [5] J. W. Goodman, *Statistical Optics*, New York, NY, USA: Wiley, 1985.

- [6] A. Singer *et al.*, “Transverse-coherence properties of the free-electron-laser FLASH at DESY”, *Phys. Rev. Lett.*, vol. 101, p. 254801, 2008.
- [7] I. A. Vartanyants, A. P. Mancuso, A. Singer, O. M. Yefanov, and J. Gulden, “Coherence measurements and coherent diffractive imaging at FLASH”, *J. Phys. B: At., Mol. Opt. Phys.*, vol. 43, p. 194016, 2010.
- [8] S. Roling *et al.*, “Temporal and spatial coherence properties of free-electron-laser pulses in the extreme ultraviolet regime”, *Phys. Rev. ST Accel. Beams*, vol. 14, p. 050703, 2011.
- [9] W. F. Schlotter *et al.*, “Longitudinal coherence measurements of an extreme-ultraviolet free-electron laser”, *Opt. Lett.*, vol. 35, p. 372-374, 2010.
- [10] S. Roling *et al.*, “Temporal and spatial coherence properties of free-electron-laser pulses in the extreme ultraviolet regime”, *Phys. Rev. ST Accel. Beams* 14, 080701, 2011.
- [11] I. A. Vartanyants, “Coherence properties of individual femtosecond pulses of an X-ray free-electron laser”, *Phys. Rev. Lett.*, vol. 107, p. 144801, 2011.
- [12] R. Bonifacio, L. De Salvo, P. Pierini, N. Piovella, and C. Pellegrini, “Spectrum, temporal structure, and fluctuations in a high-gain free-electron laser starting from noise”, *Phys. Rev. Lett.*, vol. 73, p. 70, 1994.
- [13] R. Bonifacio, C. Pellegrini, and L. Narducci, *Opt. Commun.*, vol. 50, p. 313, 1984.
- [14] S. Reiche, *Nucl. Instrum. Methods Phys. Res., Sect. A*, vol. 429, p. 243, 1999.
- [15] J. Arthur *et al.*, “Linac Coherent Light Source (LCLS) Conceptual Design Report”, SLAC, USA, SLAC-R-593, UC-414, April 2002.

SLIPPAGE-ENHANCED SASE FEL*

Juhao Wu^{1†}, Kun Fang^{1‡}, Claudio Pellegrini^{1§}, Tor Raubenheimer¹, Guanqun Zhou^{1¶},
 Axel Brachmann¹, Agostino Marinelli¹, Cheng-Ying Tsai¹, Chuan Yang^{1||}, Moohyun Yoon^{1**},
 Heung-Sik Kang^{2††}, Gyu Jin Kim², Inhyuk Nam², Andrew Chen³,
 Claire Davidson-Rubin⁴, Alexandra Li⁵, Nancy Munoz⁶, Bo Yang⁷

¹SLAC, Stanford University, Stanford, CA, USA,

²PAL-XFEL, Pohang University of Science and Tech., Pohang, Korea,

³Mission San Jose High School, Fremont, CA, USA,

⁴UC San Diego, La Jolla, CA, USA,

⁵Saratoga High School, Saratoga, CA, USA,

⁶Texas Tech University, Lubbock, TX, USA

⁷UT Arlington, Arlington, TX, USA

Abstract

High-brightness XFELs are in demand for many users, in particular for multiple types of imaging applications. Seeded FELs including self-seeding XFELs were successfully demonstrated. Alternative approaches by enhancing slippage between the x-ray pulse and the electron bunch were also demonstrated. This class of Slippage-enhanced SASE (SeSASE) schemes can be unique for FEL spectral range between 1.5 keV to 4 keV where neither grating-based soft x-ray self-seeding nor crystal-based hard x-ray self-seeding can easily access. SeSASE can provide high-brightness XFEL for high repetition rate machines not suffering from heat load on the crystal monochromator. We report start-to-end simulation results for LCLS-II project and preliminary experimental results for PAL-XFEL project.

SLIPPAGE-ENHANCED SASE (SESASE)

Free electron lasers (FEL) are perceived as the next-generation light source for many frontier scientific researches. Ultra-fast hard-X-ray FEL pulses, providing atomic and femtosecond spatial-temporal resolution, makes them a revolutionary tool attracting world-wide interest [1,2]. While an FEL provides high spatial coherence due to gain selection, *i.e.*, only the transverse mode which has the highest gain will dominate at the end of the undulator; the temporal coherence is rather poor. The temporal structure is spiky with coherent spikes with random relative phase among them [3]. In the high-gain region, the FEL group velocity

is $v_g = \omega_0 / (k_0 + 2k_u/3)$ and the electron longitudinal velocity is $v_l = \omega_0 / (k_0 + k_u)$ where $\omega_0 = k_0 c = 2\pi c / \lambda_0$ with c speed of light in vacuum, λ_0 the FEL resonance wavelength; and $k_u = 2\pi / \lambda_u$ with λ_u the undulator period. So, the coherent spike duration, the cooperation duration, is only $\tau_s \approx N_u \lambda_0 / (3c)$ where N_u is the total undulator period for the FEL to reach saturation. The so-called cooperation length is $Z_c = \tau_s c$. For the LCLS 1.5-Å FEL, $N_u \approx 2000$ to reach saturation, so $\tau_s \approx 0.3$ fs, which is much shorter than the electron bunch duration on the order of 10 to 100 fs.

To improve the temporal coherence, seeding approaches: both external [4,5] and self-seeding [6,7] have been actively pursued. Another approach along this line is to try to increase the slippage between the electron bunch and the FEL pulse. Such Slippage-enhanced SASE (SeSASE) [8–11] can produce bandwidth much narrower than that of a conventional SASE. The first preliminary experimental results was reported in Ref. [10].

ONE-DIMENSIONAL THEORY

To understand the SeSASE mechanism, let us work with a 1-D theory here. Such analysis is very similar to those developed in Refs. [12–14].

The coupled Maxwell-Vlasov equations for the FELs can be written as [14]:

$$\left(\frac{\partial}{\partial z} - 2ik_u \eta v \right) F(v, \eta, z) = \kappa_1 A(v; z) \frac{\partial}{\partial \eta} V(\eta), \quad (1)$$

$$\left(\frac{\partial}{\partial z} - i\Delta v k_u \right) A(v; z) = \kappa_2 \int F(v, \eta; z) d\eta, \quad (2)$$

where z is the coordinate along the undulator system; $\eta = (\gamma - \gamma_0) / \gamma_0$ the relative energy deviation with γ_0 the electron resonant energy; $v = \omega / \omega_0$ with ω the radiation frequency which is different from the FEL resonant frequency ω_0 ; $\Delta v = v - 1$ the detuning parameter; $F(v, \eta, z)$ is the electron bunch bunching factor; $A(v; z)$ is the slow varying envelop function of the FEL field, and $V(\eta)$ is the

* Work was supported by the US Department of Energy (DOE) under contract DE-AC02-76SF00515 and the US DOE Office of Science Early Career Research Program grant FWP-2013-SLAC-100164.

† jhwu@slac.stanford.edu

‡ Now at Wells Fargo & Co., San Francisco, CA, USA

§ Also as UCLA., Los Angeles, CA, USA

¶ Visiting Ph.D. student from Institute of High Energy Physics, and UCAS, Chinese Academy of Sciences, Beijing, China

|| Visiting Ph.D. student from NSRL, University of Science and Technology of China, Hefei, Anhui, China

** On sabbatical leave from Department of Physics, Pohang University of Science and Technology, Pohang, Korea

†† hskang@postech.ac.kr

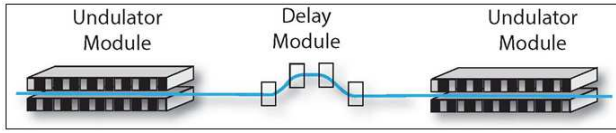


Figure 1: Schematics of an one-stage SeSASE FEL.

electron bunch initial energy spread distribution function. The coefficients κ_1 and κ_2 define the FEL parameter ρ [15]:

$$\kappa_1 \kappa_2 = k_u^2 \rho^3. \quad (3)$$

Passing through an undulator gap providing a distance of D , both the FEL field and the electron bunching factor acquire an additional phase:

$$A(\nu; z + D) = A(\nu; z) e^{i\Delta\nu k_u D}, \quad (4)$$

$$F(\nu, \eta; z + D) = F(\nu, \eta; z) e^{i\Delta\theta}. \quad (5)$$

One-stage SeSASE

Now let us discuss an undulator system with two undulator sections interrupted by a phase shifter in-between as shown in Fig. 1.

The analysis here is similar to Ref. [16]. The first stage is a SASE process with the initial conditions:

$$E_{1\nu}(0) = 0, \quad \int F_{1\nu}(0) = \frac{1}{N_\lambda} \sum_{j=1}^{N_e} e^{i\nu\omega_{10}t_j(0)}, \quad (6)$$

where $\nu = \omega_1/\omega_{10}$ with $\omega_1 = k_1 c = 2\pi c/\lambda_1$ the radiation frequency and ω_{10} the resonant radiation frequency in the first undulator; N_λ is the number of electrons in one radiation wavelength; and $t_j(0)$ is the random arrival time of the j^{th} electron at the entrance of the first undulator. The first undulator will be operating in the exponential growth region, generating a SASE FEL with a bandwidth of

$$\mathcal{S}(\nu) = \frac{1}{\sqrt{2\pi}\sigma_\nu} \exp\left[-\frac{(\nu-1)^2}{2\sigma_\nu^2}\right], \quad (7)$$

where σ_ν is the rms bandwidth.

Now the electron bunch and the FEL field pass the phase shifter and restart the FEL amplification in the second undulator.

Short second undulator If the second undulator is short, then resulting FEL field is mostly from coherent emission after the transient startup, which can leads to interference. The field is:

$$E_{2\nu}(z) = E_{1\nu}(L_1) \left[e^{-i\psi} (1 - \mathcal{B}e^{i\Delta\theta}) + \mathcal{B}e^{i\Delta\theta} \right], \quad (8)$$

where z is now the distance starting from the entrance of the second undulator, L_1 is the first undulator length, and

$$\psi = \Delta\nu k_u z, \quad (9)$$

$$\mathcal{B} \equiv \frac{2\rho}{\Delta\nu\mu_g^2} \left(1 - \mu_g e^{i\alpha} \rho k_u z \right), \quad (10)$$

with the growth mode:

$$\mu_g = e^{i2\pi/3} + \frac{\Delta\nu}{6\rho} - e^{i\pi/3} \left(\frac{\Delta\nu}{6\rho} \right)^2. \quad (11)$$

Long second undulator If on the other hand, the second undulator is long and supports high-gain exponential growth, which will also lead to interference. The FEL field reads:

$$E_{2\nu}(z) \approx \frac{e^{-i2\rho\mu_g k_u z} E_{1\nu}(L_1)}{(\mu_g - \mu_o)(\mu_g - \mu_d)} \left(\mu_g^2 - \frac{2e^{i\Delta\theta}}{\mu_g} \right), \quad (12)$$

where, besides the exponential growth mode defined in Eq. (11), we also have the oscillating mode:

$$\mu_o = 1 + \frac{\Delta\nu}{6\rho} + \left(\frac{\Delta\nu}{6\rho} \right)^2, \quad (13)$$

and the decay mode:

$$\mu_d = -e^{i\pi/3} + \frac{\Delta\nu}{6\rho} + e^{i2\pi/3} \left(\frac{\Delta\nu}{6\rho} \right)^2. \quad (14)$$

Spectrum narrowing Neglecting the optical-klystron type power enhancement, we find that at the exit of the second undulator, the temporal field is:

$$E_2(t) = \int \frac{\omega_1 d\nu}{\sqrt{2\pi}} E_{2\nu}(L_2) e^{i\Delta\nu[(k_1+k_u)L_2-\omega_1 t]}, \quad (15)$$

where L_2 is the second undulator length.

We can now computing the SeSASE bandwidth:

$$|R(\nu)|^2 \mathcal{S}(\nu), \quad (16)$$

where $\mathcal{S}(\nu)$ is the SASE spectrum in Eq. (7). The frequency filter function is:

$$R(\nu) = \frac{1 - \int d\xi \frac{dV(\xi)/d\xi}{(\mu-\xi)^2} e^{-i\rho k_1 \nu R_{56} \xi} e^{i k_1 \nu R_{56} / 2}}{1 - \int d\xi \frac{dV(\xi)/d\xi}{(\mu-\xi)^2}}, \quad (17)$$

where R_{56} is the transport matrix element, μ is the mode defined in Eq. (11), Eq. (13), and Eq. (14).

For a cold electron bunch, the frequency filter function is simplified as:

$$|R(\nu)|^2 = \frac{5 + 4 \cos(k_1 R_{56} \nu / 2)}{9}. \quad (18)$$

Now, with this frequency filter function, for multi-stage SeSASE, we can step-by-step multiple the $|R(\nu)|^2$. Shown in Fig. 2, the red curve is for the baseline SASE. The blue is for the case of 5 phase shifters, each provides 2 cooperation length slippage: $2Z_c$. The green is to add 5 phase shifters each providing 4 cooperation length. The yellow is for a geometrically increasing configuration, the 5 phase shifters provide 1, 2, 4, 8, and 16 cooperation length slippage.

As this point, we want to comment that, the above analysis is very crude; however, it illustrates the bandwidth narrowing effect with slippage-enhanced scheme.

Content from this work may be used under the terms of the CC BY 3.0 licence (© 2018). Any distribution of this work must maintain attribution to the author(s), title of the work, publisher, and DOI.

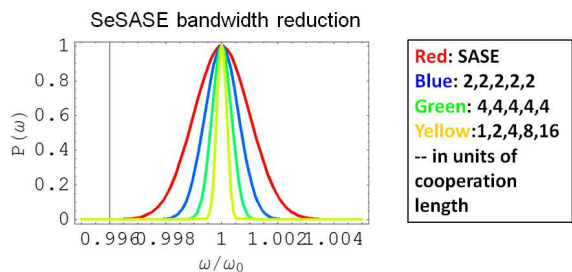


Figure 2: FEL bandwidth reduction with different slippage configuration.

SeSASE FOR FEL PROJECTS

As mentioned above, self-seeding is a demonstrated approach to generate coherent seed to improve the FEL temporal coherence. For soft X-ray it is normally grating-based. For such monochromators, it is very difficult to reach FEL energy higher than 1.5 keV. While for hard X-ray, normally, we can adopt thin crystal monochromator, like diamond. However, due to the strong absorption, it is very difficult to produce coherent seed below 4 keV. So, in short, self-seeding is difficult to access the FEL energy range of 1.5 keV to 4 keV. Besides, for the high repetition rate FELs, like the LCLS-II, or the Euro-XFEL, the thermal load, the vibration effect, the stress and strain effects on the thin crystal monochromator where the FEL pulses impinge on can cause large detrimental effects on the coherent seed generation. Therefore, SeSASE scheme can be an alternative.

LCLS-II

Here, we show some preliminary results for LCLS-II project. As we mentioned about, we are interested in the FEL energy range between 1.5 keV to 4 keV. Figure 3

presents the results of the 3.25 keV FEL (or FEL wavelength $\lambda_1 = 3.15 \text{ \AA}$). We develop two-options for LCLS-II using new hardware (Stanford Linear Collider Damp Ring-based chicane) and no new hardware (detuned undulator only).

Case A In this option, we will introduce new hardware. We will introduce 4-dipole chicanes in three undulator slots: the 5th, the 8th, and the 16th. According to the LCLS-II baseline design, the 16th has been planned for 1-stage hard X-ray self-seeding and the 8th has been reserved for 2-stage hard X-ray self-seeding.

Case B In this option, we will not introduce new hardware, but use detuned undulator in the 5th and the 8th slot. So there is only a chicane in the 16th undulator slot, which will be there anyway for the hard X-ray self-seeding.

Preliminary results indicate that with Case B, the SeSASE bandwidth can be 4 to 5 times narrower than that of the baseline SASE FEL. With additional two new chicanes in the 5th and the 8th undulator slot, *i.e.*, Case A, there is another factor of 3 to 4 reduction in the bandwidth. A single-shot spectrum is shown in Fig. 3 just to illustrate the bandwidth narrowing.

PAL-XFEL

We conducted SeSASE experimental study on the Soft X-Ray undulator line in PAL-XFEL. There are 7 undulators total. There is a phase shifter in each undulator interruption, *i.e.*, there are total of 6 phase shifters. Each phase shifter can provide a maximum of $50\lambda_1$ slippage. In the experiment, we turn the 6 phase shifters all to the maximum strength to produce a total of $300\lambda_1$ slippage. With this enhanced slippage, the SeSASE FEL bandwidth is about 3 times nar-

- Example: $\lambda_{\text{FEL}} = 3.815 \text{ \AA}$ FEL

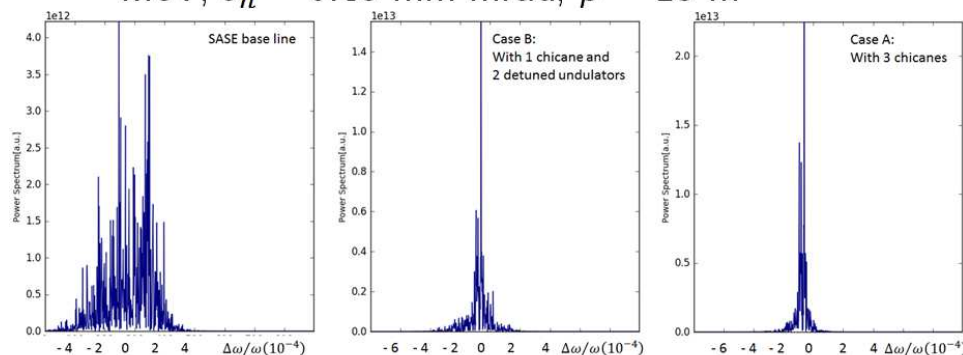
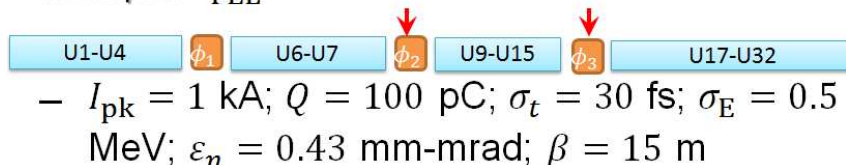


Figure 3: SeSASE FEL study for LCLS-II.

rower than the SASE baseline bandwidth. The details of the experimental results are still being analyzed and will be reported in the near future.

CONCLUSION

To improve the SASE FEL temporal coherence, one can introduce phase shifters in-between the undulator section to increase the slippage between the FEL pulse and the electron bunch. We call these schemes as SeSASE. We developed a simple 1-D theory for the SeSASE FEL operation mode. We conducted *Genesis* [17] simulations for LCLS-II project and show that a factor of 20 reduction in bandwidth is possible with three-chicane configuration. We also conducted experimental work in PAL-XFEL. With very limited 300 wavelength total slippage, the SeSASE bandwidth is 3 times narrower than the SASE baseline bandwidth.

REFERENCES

- [1] P. Emma *et al.*, “First lasing and operation of an ångstrom-wavelength free-electron laser”, *Nature Photonics* **4**, 641-647 (2010).
- [2] T. Ishikawa *et al.*, “A compact X-ray free-electron laser emitting in the sub-ångstrom region”, *Nature Photonics* **6**, 540-544 (2012).
- [3] R. Bonifacio, L. De Salvo, P. Pierini, N. Piovela, and C. Pellegrini, “Spectrum, temporal structure, and fluctuations in a high-gain free-electron laser starting from noise”, *Phys. Rev. Lett.* **73**(1), 70 (1994).
- [4] L.-H. Yu *et al.*, “High-gain harmonic-generation free-electron laser”, *Science* **289**, 932-934 (2000).
- [5] G. Stupakov, “Using the beam-echo effect for generation of short-wavelength radiation”, *Phys. Rev. Lett.* **102**, 074801 (2009).
- [6] J. Feldhaus *et al.*, “Possible application of X-ray optical elements for reducing the spectral bandwidth of an X-ray SASE FEL”, *Opt. Commun.* **140**, 341-352 (1997).
- [7] G. Geloni, V. Kocharyan, and E. Saldin, “A novel self-seeding scheme for hard X-ray FELs”, *J. Mod. Opt.* **58**, 1391-1403 (2011).
- [8] B. McNeil, N. Thompson, and D. Dunning, “Transform-limited X-ray pulse generation from a high-brightness self-amplified spontaneous-emission free-electron laser”, *Phys. Rev. Lett.* **110**, 134802 (2013).
- [9] J. Wu, A. Marinelli, and C. Pellegrini, “Generation of longitudinally coherent ultra-high power X-ray FEL pulses by phase and amplitude mixing”, *Proceedings of the 34th International Free Electron Laser Conference (FEL'12)*, Nara, Japan, 2012 (JACoW, Nara, Japan, 2012), p. 237.
- [10] J. Wu *et al.*, “X-ray spectra and peak power control with iSASE”, *Proceedings of the 4th International Particle Accelerator Conference (IPAC'13)*, Shanghai, China (JACoW, Shanghai, China, 2013), p. 2068.
- [11] D. Xiang, Y. Ding, Z. Huang, and H. Deng, “Purified self-amplified spontaneous emission (pSASE) free-electron lasers with slippage-boosted filtering”, *Phys. Rev. ST Accel. Beams* **16**, 010703 (2013).
- [12] N.A. Vinokurov, “Multisegment wigglers for short wavelength FEL”, *Nuclear Instruments and Methods in Physics Research Section A: Accelerators, Spectrometers, Detectors and Associated Equipment* **375**(1-3), 264-268 (1996).
- [13] K.-J. Kim, M. Xie, and C. Pellegrini, “Effects of undulator interruptions on the performance of high-gain FEL amplifiers”, *Nuclear Instruments and Methods in Physics Research Section A: Accelerators, Spectrometers, Detectors and Associated Equipment* **375**(1-3), 314-316 (1996).
- [14] K.-J. Kim, “Undulator interruption in high-gain free-electron lasers”, *Nuclear Instruments and Methods in Physics Research Section A: Accelerators, Spectrometers, Detectors and Associated Equipment* **407**, 126-129 (1998).
- [15] A. Bonifacio, C. Pellegrini, and Narcucci, “Collective instabilities and high-gain regime in a free electron laser”, *Opt. Commun.* **50**(6), 373 (1984).
- [16] Y. Ding and Z. Huang, “Statistical analysis of crossed undulator for polarization control in a self-amplified spontaneous emission free electron laser”, *Phys. Rev. ST Accel. Beams* **11**, 030702 (2008).
- [17] S. Reiche, “Genesis 1.3: a fully 3d time-dependent fel simulation code”, *Nuclear Instruments and Methods in Physics Research Section A: Accelerators, Spectrometers, Detectors and Associated Equipment* **429**(1), 243-248 (1999).

ALTERNATIVE ELECTRON BEAM SLICING METHODS FOR CLARA AND X-RAY FELS

D. J. Dunning*, D. Bultrini, H. M. Castañeda Cortés, S. P. Jamison,
T. A. Mansfield, N. R. Thompson, D. A. Walsh
STFC Daresbury Laboratory and Cockcroft Institute, Daresbury, UK

Abstract

Methods to generate ultra-short radiation pulses from X-ray FELs commonly slice a relatively long electron bunch to feature one (or more) short regions of higher beam quality which then lase preferentially. The slotted foil approach spoils the emittance of all but a short region, while laser-based alternatives modulate the electron beam energy, improving potential synchronisation to external sources. The CLARA FEL test facility under development in the UK will operate at 100-400 nm, aiming to demonstrate FEL schemes applicable at X-ray wavelengths. We present laser-based slicing schemes which may better suit the wavelength range of CLARA and provide options for X-ray facilities.

INTRODUCTION

CLARA is a new FEL test facility being developed at STFC Daresbury Laboratory in the UK [1], which will operate with 250 MeV maximum energy and $\lambda_r=100\text{-}400$ nm fundamental FEL wavelength. Commissioning is underway on the front-end while design of the later stages is still being finalised. An overview of the facility layout and FEL schemes is given in [2] but briefly the aim is to demonstrate novel FEL capabilities that could be applied at X-ray FEL facilities such as high-brightness SASE [3], mode-locking [4], mode-locked afterburner [5], optically slicing a single SASE spike [6] and others. It will have a flexible design that can accommodate new ideas and future changes.

A common feature of many FEL schemes including [4–6] is so called ‘slicing’ of the electron beam. It refers to applying a longitudinal variation in electron beam properties such that one (or more) short regions of the bunch lase preferentially, thereby generating shorter photon pulses for use in experiments. For example, the slotted foil method [7, 8] spoils emittance in all but a short section of the beam, while [6] defines the lasing part of the beam via a specific energy chirp.

Given the aims of CLARA it is desirable to keep the focus on wavelength-independent aspects of the FEL concepts and so minimise wavelength-specific difficulties where possible. For example, to suit single-shot temporal diagnostics it is proposed to study short pulse generation for FEL wavelengths in the range 250-400 nm. A similar argument applies for the seed/modulating lasers. Initially it was planned that both mode-locking and slicing with chirp/taper would be carried out with an applied energy modulation of period $\lambda_{\text{mod}} \approx 50 \mu\text{m}$ [1]. However it has since been recognised

that wavelengths outside the range $20 \mu\text{m} \lesssim \lambda_{\text{mod}} \lesssim 70 \mu\text{m}$ would require less laser R&D to deliver suitable sources.

Modeling shows that mode-locking can be achieved with $\lambda_{\text{mod}} = 20 \mu\text{m}$ while the transverse apertures of the modulation section have been specified to transport wavelengths up to $100 \mu\text{m}$ to retain these options. However, another option could be to use a shorter wavelength seed (e.g. 800 nm) to replace some of the functionality of the $20 \mu\text{m} \lesssim \lambda_{\text{mod}} \lesssim 100 \mu\text{m}$ range - this paper reports studies of two such methods.

MODE-LOCKING WITH BEAT MODULATION

The mode-locked FEL concept [4] uses chicane delays between undulator sections to allow pulses with duration much shorter than the FEL co-operation length, $l_c = \lambda_r/4\pi\rho$ (where the FEL parameter $\rho \approx 10^{-4}\text{-}10^{-3}$), which is a lower limit for many schemes. The number of optical cycles in the pulse can be reduced from hundreds to approximately the number of periods in an undulator module, $N = 27$ for CLARA. The electron beam energy (or other electron-beam properties [9] such as current [10]) needs to be modulated with period $\lambda_{\text{mod}} = S_e N \lambda_r$, where a slippage enhancement factor [4] $S_e \approx 4\text{-}8$ has commonly been used, corresponding to $\sim 30\text{-}60 \mu\text{m}$ for CLARA. While it might not be straightforward to deliver a suitable laser source operating in this range, it might nevertheless be possible to modulate the electron beam energy on this scale through a laser induced beating modulation, as has already been demonstrated for various purposes at the FERMI FEL [11].

Modulation Stage

For initial studies the modulation stage was approximated by directly applying a superposition of two sinusoidal energy modulations of different period to the electron beam. Wavelengths of $\lambda_1 = 800$ nm and $\lambda_2 = 816$ nm were used to give a beat modulation period $\lambda_{\text{beat}} = 40 \mu\text{m}$ as shown in Fig. 1. This is plotted alongside a typical sinusoidal energy modulation (with $\lambda_{\text{mod}} = 40 \mu\text{m}$) as would normally be used. In both cases it would be expected for FEL pulses to develop at $s = 20/60/100 \mu\text{m}$, etc. where the energy variation is minimised. The beat modulation case can in fact be anticipated to give cleaner output since the normal sinusoidal modulation generates secondary spikes at the maxima of the energy modulation where the energy chirp is also minimised [9].

* david.dunning@stfc.ac.uk

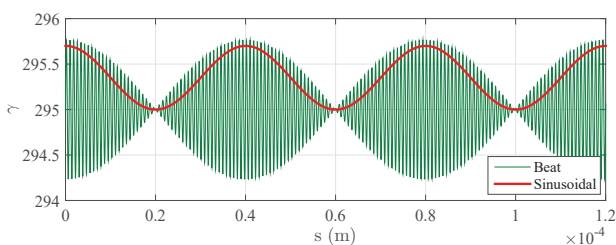


Figure 1: Electron beam energy variation with longitudinal bunch position for a beat modulation case comprising two sinusoidal wavelengths of $\lambda_1 = 800$ nm and $\lambda_2 = 816$ nm to give $\lambda_{\text{beat}} = 40$ μm and a sinusoidal modulation with $\lambda_{\text{mod}} = 40$ μm as typically used in mode-locked FEL simulations.

Mode-Locked FEL Simulation Results

The modulated electron beam was entered into a mode-locked FEL simulation using the ‘beamfile’ method (a list defining electron beam slice properties) in Genesis 1.3 [12]. The electron beam parameters of the CLARA long-bunch mode [13] were used and the undulator parameters were set for $\lambda_r = 266$ nm. In addition to an undulator slippage of $27\lambda_r$, chicane slippage of $123\lambda_r$ was applied (assuming no dispersion), such that the total slippage per undulator-chicane module matched the modulation period. The modulation amplitude was scanned and the temporal profile and spectrum of the FEL radiation near to saturation (at the end of the 15th radiator module) are shown in Fig. 2 for the optimum case, alongside the current profile.

The beat modulation on the electron beam energy is seen to work well in giving a well defined temporal pulse profile and discrete modes in the spectrum. Individual pulse durations of ~ 30 fs FWHM correspond to ~ 27 cycles as expected from the earlier discussion. The envelope of the temporal profile and noise in the spectrum show the usual effects of SASE. As anticipated there are no sub-spikes (i.e. interleaved pulses at the minima/maxima) as is observed in the normal energy modulation case [1].

Studies are underway to model the modulation stage using Genesis 1.3 with a simple two-colour seed. Preliminary results indicate that the peak power for the modulating laser should be of the order 10^{8-9} W and that a suitable variation in energy spread can be achieved while the fine structure of the energy modulation appears washed out.

SLICING A SINGLE SASE SPIKE

In [6] simulations of the chirp and taper method were carried out at a hard x-ray resonant FEL wavelength of $\lambda_r = 0.15$ nm in combination with an 800 nm modulating laser pulse and an isolated SASE spike with 200 as FWHM duration was predicted, corresponding to sub-cycle scale of the 800 nm modulation. For operation on CLARA at $\lambda_r = 266$ nm the modulating laser should be approximately 40 μm [1] though $\lambda_r = 400$ nm and $\lambda_{\text{mod}} \approx 70$ μm may be

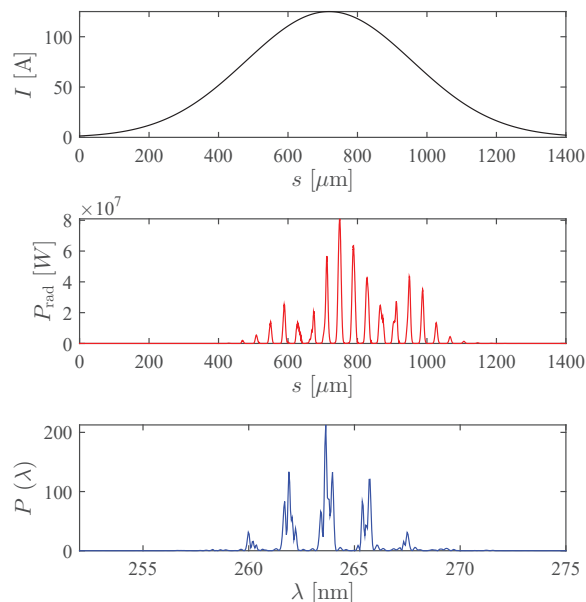


Figure 2: Current profile (top), temporal profile of the FEL power after 15 undulator modules (middle) and corresponding spectrum (bottom).

preferable to deliver a suitable modulating laser. In both cases this is a less straightforward source to generate and requires much larger apertures for transport than for 800 nm.

Another approach has recently been demonstrated [14, 15], in which the temporal profile of the laser pulse used in the laser heater is shaped to have a short dip in intensity, such that the laser heater increases the energy spread of the beam everywhere except a short region. Compression of the bunch downstream of the laser heater and prior to the FEL means that the region of the bunch for lasing is further shortened compared to the feature imposed by the laser. This optical pulse shaping is expected to have advantages over the slotted foil method in terms of applicability at high repetition rates and in terms of flexibility and is an area that could be studied in detail on CLARA - here we report the first studies.

Modulation Stage

A laser heater is not included in the baseline design for CLARA since microbunching studies indicate it is not essential for FEL lasing, however space is reserved as it may enable useful experiments in future [16]. The FEL scheme has therefore been assessed for CLARA using modulator 1 tuned to be resonant with an 800 nm seed. Further studies in combination with start-to-end simulations would be of interest to determine the optimum location in terms of achievable pulse duration, synchronisation etc.

The long-bunch mode of CLARA [13] was again used for simulations but with the energy increased from 150 MeV to 190 MeV to allow the modulator to be resonant at 800 nm while operating at 266 nm in the radiator (this will also apply to the mode-locked FEL study). A preliminary study was

Content from this work may be used under the terms of the CC BY 3.0 licence (© 2018). Any distribution of this work must maintain attribution to the author(s), title of the work, publisher, and DOI.

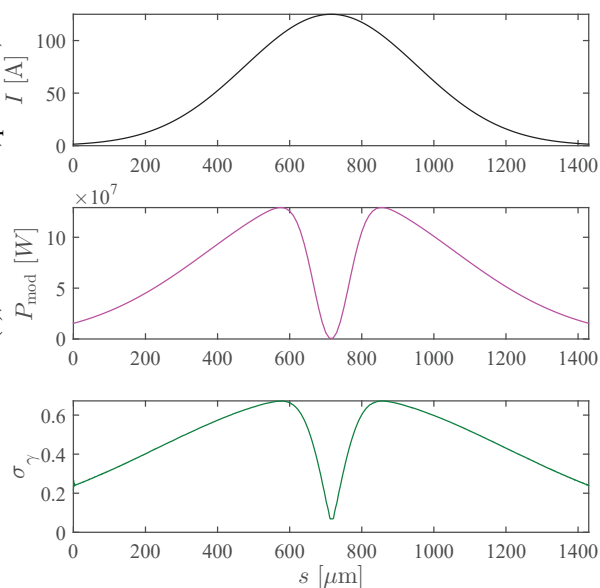


Figure 3: Current profile (top), temporal profile of the modulating laser pulse (middle) and corresponding induced energy spread at the end of the modulator (bottom).

carried out to determine how increasing the energy spread reduces the FEL power at the nominal saturation point. An energy spread of $\sigma_\gamma = 0.7$ was selected in order to reduce the maximum output power by around 3 orders of magnitude compared to the nominal $\sigma_\gamma = 0.05$. The modulation step was then modeled in Genesis 1.3 using the ‘radfile’ input method (a list of temporal slice properties of the laser pulse). The Gaussian temporal envelope of the modulating laser pulse was set to have duration slightly longer than the electron bunch. The peak power of the laser pulse was set to deliver the required energy spread increase from the earlier study. The width of the Gaussian dip in the radiation power was optimised to pick out a single SASE spike. The radiation power profile and the resulting energy spread profile are shown in Fig. 3 alongside the current profile. The modulating laser pulse energy should be $\sim 300 \mu\text{J}$. Similar results were found assuming a $3 \mu\text{m}$ modulating laser, however 800 nm is preferable.

FEL Output

The modulated electron beam distribution was exported from the first stage and imported into a second Genesis simulation to model the CLARA radiator (initialising the shot noise at 266 nm). The FEL process starts up from noise so the scheme was first optimised for a single shot noise realisation then repeated for the optimum case using OCELOT [17] to automate runs. Several iterations of this process were carried out and the optimum results (temporal profile and spectrum at saturation) are shown in Fig. 4 and can be compared to a baseline case without any slicing effect shown in Fig. 5. An isolated pulse of duration $\sim 200 \text{ fs}$ FWHM is selected, corresponding to ~ 200 cycles at 266 nm . This is ~ 4 times longer than studies of the chirp and taper scheme

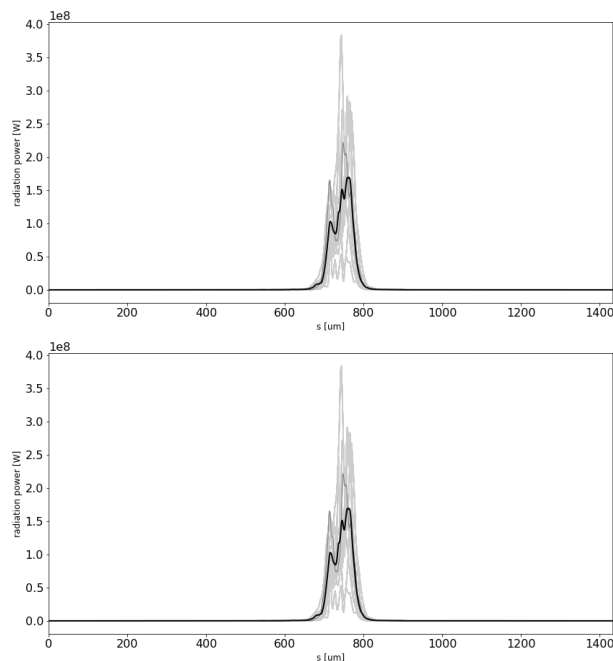


Figure 4: 800 nm sliced case power (top) and spectrum (bottom) for 10 shot noise cases (grey) and the average (black).

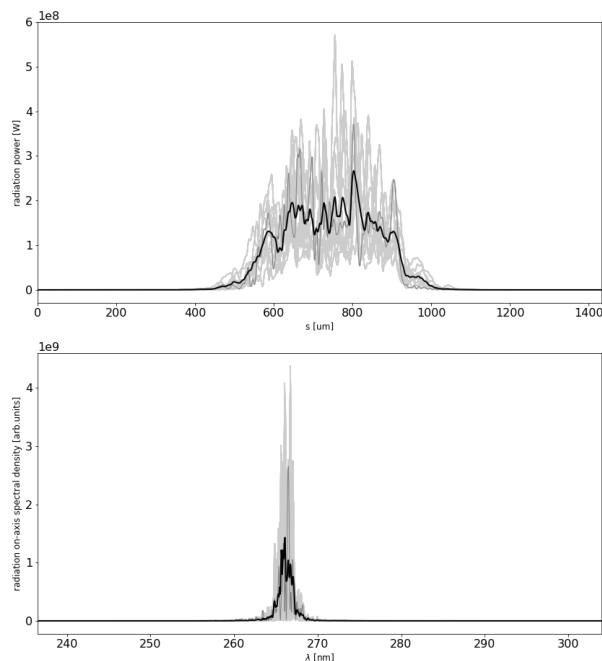


Figure 5: Nominal case power (top) and spectrum (bottom) for 10 shot noise cases (grey) and the average (black).

for CLARA [1], albeit with somewhat different parameters, indicating that further optimisation may be possible.

SUMMARY

Two methods have been investigated in which some functionality of difficult to realise longer wavelength sources required for CLARA could be replaced with a more readily available and configurable 800 nm source. The results of

both are promising and will be considered in further studies. In particular, for the case of slicing a single SASE spike further work is required to assess how the ultimate potential of the temporal dip scheme compares to the chirp and taper scheme in terms of delivering short pulses at X-ray facilities.

REFERENCES

- [1] J. A. Clarke *et al.*, “CLARA conceptual design report,” *Journal of Instrumentation*, vol. 9, no. 05, p. T05001, 2014, <https://doi.org/10.1088/1748-0221/9/05/T05001>.
- [2] D. J. Dunning *et al.*, “CLARA facility layout and FEL schemes,” presented at FEL’17, Sante Fe, NM, USA, paper MOP054, this conference.
- [3] B. W. J. McNeil, N. R. Thompson, and D. J. Dunning, “Transform-limited X-ray pulse generation from a high-brightness self-amplified spontaneous-emission free-electron laser,” *Phys. Rev. Lett.*, vol. 110, p. 134802, 2013, <https://doi.org/10.1103/PhysRevLett.110.134802>.
- [4] N. R. Thompson and B. W. J. McNeil, “Mode locking in a free-electron laser amplifier,” *Phys. Rev. Lett.*, vol. 100, p. 203901, 2008, <https://doi.org/10.1103/PhysRevLett.100.203901>.
- [5] D. J. Dunning, B. W. J. McNeil, and N. R. Thompson, “Few-cycle pulse generation in an x-ray free-electron laser,” *Phys. Rev. Lett.*, vol. 110, p. 104801, 2013, <https://doi.org/10.1103/PhysRevLett.110.104801>.
- [6] E. L. Saldin, E. A. Schneidmiller, and M. V. Yurkov, “Self-amplified spontaneous emission FEL with energy-chirped electron beam and its application for generation of attosecond X-ray pulses,” *Phys. Rev. Spec. Top. Accel. Beams*, vol. 9, no. 5, pp. 1–6, 2006. Available at: <https://doi.org/10.1103/PhysRevSTAB.9.050702>.
- [7] P. Emma *et al.*, “Femtosecond and subfemtosecond x-ray pulses from a self-amplified spontaneous-emission-based free-electron laser,” *Phys. Rev. Lett.*, vol. 92, p. 074801, 2004. Available at: <https://link.aps.org/doi/10.1103/PhysRevLett.92.074801>.
- [8] Y. Ding *et al.*, “Femtosecond x-ray pulse characterization in free-electron lasers using a cross-correlation technique,” *Phys. Rev. Lett.*, vol. 109, p. 254802, 2012. Available at: <https://link.aps.org/doi/10.1103/PhysRevLett.109.254802>.
- [9] D. J. Dunning, “Methods for the generation of ultra-short free-electron laser pulses,” Ph.D. dissertation.
- [10] E. Kur, D. J. Dunning, B. W. J. McNeil, J. Wurtele, and A. A. Zholents, “A wide bandwidth free-electron laser with mode locking using current modulation,” *New J. Phys.*, vol. 13, 2011. Available at: <https://doi.org/10.1088/1367-2630/13/6/063012>.
- [11] E. Roussel *et al.*, “New scenarios of microbunching instability control in electron linacs and free electron lasers,” in *Proc. of IPAC’17*, pp. 3642–3644. Available at: <http://accelconf.web.cern.ch/AccelConf/ipac2017/papers/thya1.pdf>.
- [12] S. Reiche, “GENESIS 1.3: a fully 3D time-dependent FEL simulation code,” *Nucl. Instr. Meth. Phys. Res. Sect. A*, vol. 429, p. 243, 1999. Available at: [https://doi.org/10.1016/S0168-9002\(99\)00114-X](https://doi.org/10.1016/S0168-9002(99)00114-X).
- [13] P. H. Williams *et al.*, “Developments in the CLARA FEL Test Facility accelerator design and simulations,” in *Proc. of IPAC’16*, pp. 797–800. Available at: <http://accelconf.web.cern.ch/AccelConf/ipac2016/papers/mopow037.pdf>.
- [14] A. Marinelli *et al.*, “Optical shaping of x-ray free-electron lasers,” *Phys. Rev. Lett.*, vol. 116, p. 254801, 2016. Available at: <https://link.aps.org/doi/10.1103/PhysRevLett.116.254801>.
- [15] V. Grattoni *et al.*, “Control of the seeded FEL pulse duration using laser-heater pulse shaping,” in *Proc. of IPAC’17*, 2017. Available at: <http://accelconf.web.cern.ch/AccelConf/ipac2017/papers/wepab034.pdf>.
- [16] A. D. Brynes *et al.*, “Inducing microbunching in the CLARA FEL test facility,” presented at FEL’17, Sante Fe, NM, USA, paper WEP026, this conference.
- [17] I. Agapov, G. Geloni, S. Tomin, and I. Zagorodnov, “Ocelot: a software framework for synchrotron light source and FEL studies,” *Nuclear Instruments and Methods in Physics Research Section A: Accelerators, Spectrometers, Detectors and Associated Equipment*, vol. 768, pp. 151 – 156, 2014. Available at: <http://dx.doi.org/10.1016/j.nima.2014.09.057>.

STUDY OF THE ELECTRON TRANSPORT IN THE COXINEL FEL BEAMLINE USING A LASER-PLASMA ACCELERATED ELECTRON BEAM*

T. Andre[†], I. Andriyash, F. Blache, F. Bouvet, F. Briquez, M.-E. Couprie, Y. Dietrich,
J.-P. Duval, M. El-Ajjouri, A. Ghaith, C. Herbeaux, N. Hubert, C. Kitegi, M. Khojayan,
M. Labat, N. Leclercq, A. Lestrade, A. Loulergue, O. Marcouillé, F. Marteau,
P. Ngotta, P. Rommeluere, E. Roussel, M. Sebdaoui, K. Tavakoli, M. Valléau

SOLEIL, Gif-sur-Yvette, France

S. Corde, J. Gautier, J.-P. Goddet, G. Lambert, B. Mahieu, V. Malka, K. Ta-Phuoc, C. Thaury
LOA, Palaiseau, France

S. Bielawski, C. Evain, C. Szwaj, PhLAM/CERLA, Villeneuve d'Ascq, France

Abstract

The ERC Advanced Grant COXINEL aims at demonstrating free electron laser (FEL) at 200 nm, based on a laser-plasma accelerator (LPA). To achieve the FEL amplification a transport line was designed to manipulate the beam properties. The 10-m long COXINEL line comprises a first triplet of permanent-magnet variable-strength quadrupoles (QUAPEVA), which handles the large divergence of LPA electrons, a magnetic chicane, which reduces the slice energy spread, and finally a set of electromagnetic quadrupoles, which provides a chromatic focusing in a 2-m undulator. Electrons were successfully transported through the line from LPA with ionization-assisted self-injection (broad energy spectra up to 250 MeV, few-milliradian divergence).

INTRODUCTION

Today, LPAs [1–3] can deliver over few millimeters of acceleration distances, relativistic electron beams with energies from hundreds MeV to few GeV [4] of few femtosecond durations and high peak currents in the multi-kiloAmps range. While transported and accelerated in the laser wake field, electrons acquire significant spread of the transverse and longitudinal momenta, leading to degradation of beam quality ($\sigma_{x'} \approx 1$ mrad and $\sigma_{\delta} \approx 1\%$ [5]). So far LPA-based undulator radiation has been observed [6–10] but application of such beams for FEL remains very challenging. The large divergence can be handled by means of high gradient quadrupoles or plasma lens [11, 12], while the energy spread can be reduced using a demixing magnetic chicane [13, 14] or being compensated in a Transverse Gradient Undulator [15, 16]. Among other LPA-based FEL projects [13, 17, 18], COXINEL [19–22] is part of the French FEL project LUNEX5 [23–25]. A transport line was designed to handle the large divergence of LPA electrons thanks to strong permanent magnet quadrupoles, a magnetic chicane permits to reduce the slice energy spread and a chro-

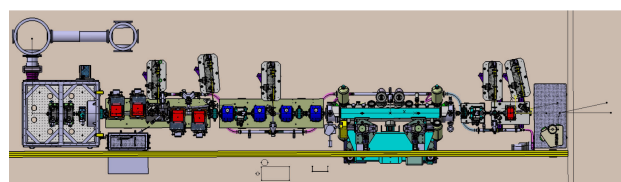


Figure 1: General top view of the COXINEL LPA demonstration set-up. From left to right: LPA chamber (gray) with the first set of quadrupoles, magnetic chicane dipoles (red), quadruplet of quadrupoles (blue), undulator (2-m U18 shown), dipole for beam dump (red), and UV-spectrometer (brown).

matic focusing in the undulator was developed to improve FEL performance [26].

TRANSPORT LINE DESCRIPTION

The transport line was designed, build and characterized at SOLEIL, then installed and aligned with the laser line of the “Salle Jaune” laser system of Laboratoire d’Optique Appliquée (see Fig. 1).

The laser plasma acceleration is performed with a Ti:Sa laser system that delivers 800 nm, 30 fs (FWHM), 30 PW pulses. A first triplet of quadrupoles, called QUAPEVA [27], is immediately installed after the source. These quadrupoles are built with permanent magnets, but have an original design for gradient variation and magnetic center adjustment for flexible refocusing [28, 29]. The beam is then manipulated in a magnetic chicane composed of four electromagnetic dipoles followed by a set of four electromagnetic quadrupoles (QEM) to provide electron beam focusing inside a cryo-ready U18 undulator [30, 31]. Electron diagnostics such as turbo-Integrated Current Transformer, cavity Beam Position Monitors, and multiple scintillating screens, are installed every 1–2 m along the beam line [32]. Two photons diagnostic devices, an under vacuum CCD camera and a photon spectrometer, are installed at the exit of the undulator.

* Work supported by ERC COXINEL (340015).

[†] thomas.andre@synchrotron-soleil.fr

Table 1: Properties of the Magnetic Equipment for Modeling the Beam Line for Central Energy of $E = 176$ MeV

Equipment	Properties	Values	
		Chromatic Matching	Strong Focusing
QUAPEVAs	Gradient (QUAPEVA1)	102.8 [T/m]	101.9 [T/m]
	Gradient (QUAPEVA2)	-101.2 [T/m]	-99.97 [T/m]
	Gradient (QUAPEVA3)	88.17 [T/m]	88.82 [T/m]
Dipoles	r_{56}	4.3 [mm]	
	$B\rho$ @ 176 MeV	0.60 [T.m]	
Quadrupoles	Gradient (QEM 1)	-2.43 [T/m]	0 [T/m]
	Gradient (QEM 2)	3.98 [T/m]	0 [T/m]
	Gradient (QEM 3)	-5.76 [T/m]	0 [T/m]
	Gradient (QEM 4)	2.14 [T/m]	0 [T/m]
Undulator	Period	18 [mm]	
	Peak Field (5-mm gap)	1.156 [T]	
	Magnetic Length	2	
	K (5-mm gap)	1.94	

MODELING OF THE LINE

Here, numerical simulations, using a hand-made Matlab code [33, 34], are done for a more realistic case than the reference one [19]. A deteriorated LPA beam with an energy spread of 5%, a divergence of $\sigma'_x = \sigma'_z = 3$ mrad and an emittance: $\epsilon = 1$ mm.mrad, for a reference energy of 176 MeV is considered. Table 1 summarizes the characteristics of the magnetic equipment composing the beam line.

Energy spread has a significant impact on the FEL amplification and should be lower than the Pierce parameter ($\sigma_\delta \ll \rho_{\text{FEL}}$) [35]. A strategy to reduce the large energy spread of LPA beam ($\approx 1\%$) is to stretch it longitudinally in a chicane where a correlation between the longitudinal position and energy is created. The stretching factor is defined by:

$$C = \frac{1}{1 + h \cdot R_{56}} \quad \text{and} \quad h = \frac{\Delta E}{E_0} \cdot \frac{1}{l_b},$$

where R_{56} is the strength of the chicane, ΔE is the uncorrelated energy spread of the beam, E_0 is the nominal energy and l_b is bunch length at the entrance of the chicane. The length of the stretched bunch is given by:

$$\sigma_s = \frac{l_b}{C}, \quad (1)$$

Figure 2 shows the phase-space of the beam before and after the chicane for a strong R_{56} value. In the simulation shown in Fig. 2, $E = 176$ MeV, $\sigma'_x = \sigma'_z = 3$ mrad, $\sigma_\delta = 5\%$, $N_p = 10^6$, $q = 34$ pC, and $R_{56} = 4.3$ mm. Machine parameters match the values listed in Table 1. The longitudinal beam size input is $5 \mu\text{m}$. With an energy spread of 5%, the stretching factor is $C = 0.0227$, leading to a beam size at the exit of the chicane of $220.3 \mu\text{m}$, which is in a good agreement with the numerical result of $220.5 \mu\text{m}$. In this configuration the energy spread is well reduced.

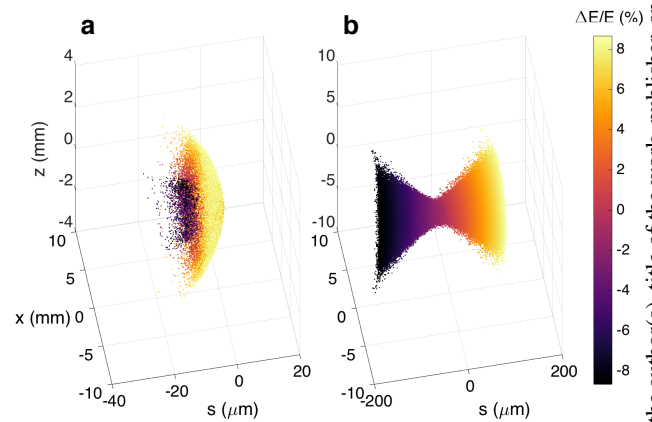


Figure 2: Simulated beam phase space (a) before chicane and (b) after chicane.

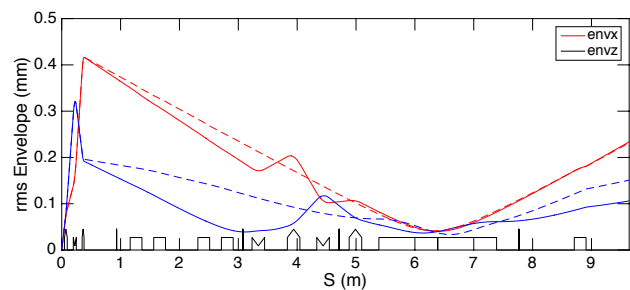


Figure 3: Beam envelopes for a 176-MeV reference energy, using different optics in COXINEL: strong focusing (dashed lines) or chromatic focusing (solid lines).

The lengthening of the beam size process can also be combined with a chromatic focusing (CF) to enhance the FEL amplification process [26]. In this configuration, the set of four quadrupoles before the undulator, is used to focus each slice of the beam at a specific location inside the undulator.

Figure 3 compares the beam dynamics using this chromatic focusing to one without using electromagnetic quadrupoles, known as Strong Focusing (SF). Due to the large divergence of the electron beam, the transverse beam sizes increase dramatically in the first centimeters. Thanks to the strong quadrupoles, the beam can be controlled all along the line.

Figure 4 shows a comparison of the transverse phase-space in the middle of the undulator for these two focusing settings. This comparison uses the same beam and machine parameters as before: $E = 176$ MeV, $\sigma'_x = \sigma'_z = 3$ mrad, $\sigma_\delta = 5\%$, $N_p = 10^6$, $q = 34$ pC, $R_{56} = 4.3$ mm, and the machine parameters listed in Table 1. The tilt of the beam in phase-space shown in Fig. 4 (a) and (b) informs about the slice focusing. In this case only the central energy is well focused in the middle of the undulator compared to CF optics where all the slices are focused in a specific location.

For low energy spread and low divergence, the transmission of the beam line is 100%, but when considering more realistic beam parameters the transmission of the beam line is reduced (see Fig. 5). In both CF and SF cases, losses start

Content from this work may be used under the terms of the CC BY 3.0 licence (© 2018). Any distribution of this work must maintain attribution to the author(s), title of the work, publisher, and DOI.

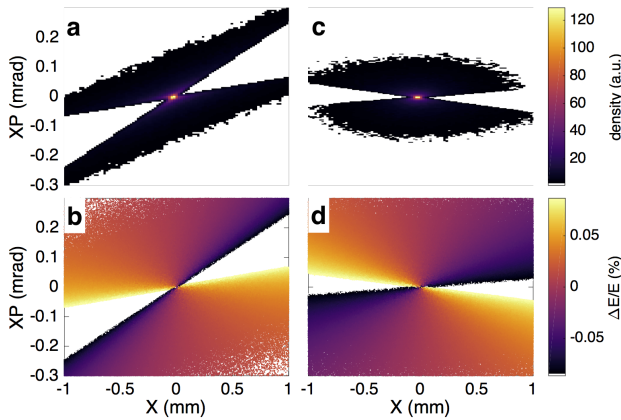


Figure 4: Beam phase-space in the middle of the undulator: The left plots present the xx' phase space in (a) density and (b) energy representation using SF optics; the right plots present the xx' phase space in (c) density and (d) energy representation using CF optics.

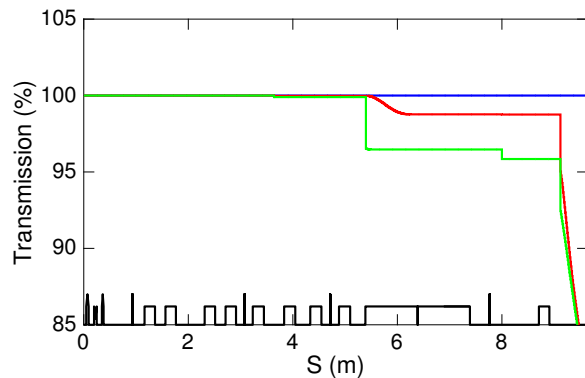


Figure 5: Transmission of the beam line using different optics: Chromatic focusing with $\sigma'_x = \sigma'_z = 1$ mrad, $\sigma_\delta = 1\%$ (blue). Chromatic focusing with $\sigma'_x = \sigma'_z = 3$ mrad, $\sigma_\delta = 5\%$ (red). Strong focusing with $\sigma'_x = \sigma'_z = 3$ mrad, $\sigma_\delta = 5\%$ (green).

to appear after the chicane but in the SF case, the losses are greater due to the optics properties.

TRANSPORT RESULTS

For reliability of electron production, the first experiments were done using self-injection and ionization injection mechanisms [36] where the laser is focused on a spot of 10–15 μm size in a supersonic jet of a gas mixture composed of 99% helium and 1% nitrogen. This method of production creates an electron beam with high divergence and a wide energy spectrum (50–250 MeV). In this configuration, the beam properties are far from the reference case, but a proper tuning of the equipment allowed us to transport the electron beam all along the COXINEL line, down to the beam dump and control its properties.

CONCLUSION

The experimental observations confirm that it is possible to properly transport the electron beam and control its properties. Comparison of the simulations and experiments are in good agreement. Despite the significant difference of the electron beam parameters in the realistic and reference cases, the handle of the transport open the way to the observation of spontaneous emission of the undulator, a first step towards FEL amplification.

ACKNOWLEDGEMENT

The authors are grateful to the support of the European Research Council for COXINEL (340015, P.I. M.-E. Couprie) and X-Five advanced grants (339128, P.I. V. Malka), the “Triangle de la Physique” for the QUAPEVA valorisation contract and to J. L. Lancelot, F. Forest and O. Cosson from Sigmaphi for their involvement in the project.

REFERENCES

- [1] T. Tajima and J. M. Dawson, “Laser electron accelerator”, *Physical Review Letters*, vol. 43 pp. 267, Jul. 1979.
- [2] E. Esarey, C. Schroeder, and W. Leemans, “Physics of laser-driven plasma-based electron accelerators”, *Reviews of Modern Physics*, vol. 81, no. 3, pp. 1229, 2009.
- [3] V. Malka *et al.*, “Laser-driven accelerators by colliding pulses injection: A review of simulation and experimental results,” *Physics of Plasmas (1994-present)*, vol. 16, no. 5, pp. 056703, 2009.
- [4] W. P. Leemans, *et al.*, “Multi-GeV electron beams from capillary-discharge-guided sub-petawatt laser pulses in the self-trapping regime,” *Physical Review Letters*, vol. 113, p. 245002, Dec 2014.
- [5] C. Rechatin *et al.*, “Controlling the Phase-Space Volume of Injected Electrons in a Laser-Plasma Accelerator”, *Physical Review Letters*, vol. 102, no. 16, pp. 164801, 2009.
- [6] H.-P. Schlenvoigt *et al.*, “A compact synchrotron radiation source driven by a laser-plasma wakefield accelerator,” *Nature Physics*, vol. 4, no. 2, pp. 130–133, 2008.
- [7] M. Fuchs *et al.*, “Laser-driven soft-X-ray undulator source,” *Nature Physics*, vol. 5, no. 11, pp. 826–829, 2009.
- [8] M. P. Anania *et al.*, “The ALPHA-X beam line: toward a compact FEL,” in *Proc. of IPAC'10*, vol. 5, paper TUPE052.
- [9] G. Lambert *et al.*, “Progress on the generation of undulator radiation in the UV from a plasma-based electron beam,” in *Proc. of FEL'12*, Nara, Japan, paper THPD47.
- [10] “Plasma accelerator produces first X-rays”, http://www.desy.de/news/news_search/index_eng.html?openDirectAnchor=1261&two_columns=0
- [11] C. Thauray *et al.*, “Demonstration of relativistic electron beam focusing by a laser-plasma lens,” *Nature Communications*, vol. 6, Apr. 2015.
- [12] N. Nakanii *et al.*, “Transient magnetized plasma as an optical element for high power laser pulses,” *Physical Review Special Topics – Accelerators and Beams*, vol. 18, no. 2, pp. 021303, 2015.

- [13] A. Maier *et al.*, “Demonstration scheme for a laser-plasma-driven free-electron laser,” *Physical Review X*, vol. 2, no. 3, pp. 031019, 2012.
- [14] M.-E. Couprie, A. Loulergue, M. Labat, R. Lehe, and V. Malka, “Towards a free electron laser based on laser plasma accelerators,” *Journal of Physics B: Atomic, Molecular and Optical Physics*, vol. 47, no. 23, pp. 234001, 2014.
- [15] T. Smith, J. Madey, L. Elias, and D. Deacon, “Reducing the sensitivity of a free-electron laser to electron energy,” *Journal of Applied Physics*, vol. 50, no. 7, pp. 4580–4583, 1979.
- [16] Z. Huang, Y. Ding, and C. B. Schroeder, “Compact X-ray free-electron laser from a laser-plasma accelerator using a transverse-gradient undulator,” *Physical Review Letters*, vol. 109, no. 20, pp. 204801–204805, 2012.
- [17] C. B. Schroeder *et al.*, “Application of Laser Plasma Accelerator beams to Free-Electron Laser,” in *Proc. of FEL’12*, Nara, Japan, paper THPD57.
- [18] M.P. Anania *et al.*, “An ultrashort pulse ultra-violet radiation undulator source driven by a laser plasma wakefield accelerator,” *Applied Physics Letters*, vol. 104, no. 26, pp. 264102, 2014.
- [19] M.-E. Couprie *et al.*, “An application of laser–plasma acceleration: towards a free-electron laser amplification,” *Plasma Physics and Controlled Fusion*, vol. 58, no. 3, pp. 034020, 2016.
- [20] M.-E. Couprie *et al.*, “Towards free electron laser amplification to qualify laser plasma acceleration”, *The Review of Laser Engineering*, 45(2):94–98, 2017.
- [21] M.-E. Couprie *et al.*, “Experiment preparation towards a demonstration of laser plasma based free electron laser amplification”, in *Proc. of FEL’14*, Basel, Switzerland, paper TUP086.
- [22] T. Andre *et al.*, “First electron beam measurements on CONIXEL”, in *Proc. of IPAC’16*, Busan, Korea, paper MOPOW005.
- [23] M.-E. Couprie *et al.*, “The LUNEX5 project in France”, *Journal of Physics: Conference Series*, vol. 425, no. 7, pp. 072001, 2013.
- [24] M.-E. Couprie *et al.*, “Progress of the LUNEX5 project,” in *Proc. of FEL’13*, New York, NY, USA, paper WEP505.
- [25] M.-E. Couprie *et al.*, “Strategies towards a compact XUV free electron laser adopted for the LUNEX5 project,” *Journal of Modern Optics*, pp. 1–13, 2015.
- [26] A. Loulergue *et al.*, “Beam manipulation for compact laser wakefield accelerator based free-electron lasers,” *New Journal of Physics*, vol. 17, no. 2, pp. 023028, 2015.
- [27] F. Marteau *et al.*, “Variable high gradient permanent magnet quadrupole (quapeva)”,. arXiv preprint arXiv:1706.04355, 2017.
- [28] C. Benabderrahmane, M.-E. Couprie, F. Forest, and O. Cosson, “Multi-pôle magnétique réglable,” Patent 2016, WO2016034490 (10/3/2016).
- [29] C. Benabderrahmane, M.-E. Couprie, F. Forest, and O. Cosson, “Adjustable magnetic multipole,” Patent 2016. Europe: PCT/EP2015/069649 (27/08/2015), WOBL14SSOQUA/CA.
- [30] C. Benabderrahmane *et al.*, “Development and operation of a $\text{pr}_2\text{fe}_{14}\text{B}$ based cryogenic permanent magnet undulator for a high spatial resolution x-ray beam line.” *Physical Review Special Topics – Accelerators and Beams*, 20:033201, Mar 2017.
- [31] A. Ghaith *et al.*, “Progress of PrFeB Based Hybrid Cryogenic Undulators at SOLEIL”, presented at IPAC’17, this conference.
- [32] M Labat *et al.*, “Electron beam diagnostics for CONIXEL”, in *Proc. of FEL’14*, paper THP087.
- [33] M. Khojayan *et al.*, “Transport studies of LPA electron beam towards the FEL amplification at COXINEL,” *Nuclear Instruments and Methods in Physics Research Section A: Accelerators, Spectrometers, Detectors and Associated Equipment*, 2016. <http://dx.doi.org/10.1016/j.nima.2016.02.030>
- [34] J. Payet *et al.*, “Beta code,” CEA, SACLAY.
- [35] Z. Huang and K.-J. Kim, “Review of X-ray free-electron laser theory,” *Physical Review Special Topics – Accelerators and Beams*, vol. 10, no. 3, pp. 034801, 2007.
- [36] C. McGuffey *et al.*, “Ionization induced trapping in a laser wakefield accelerator,” *Physical Review Letters*, vol. 104, no. 2, pp. 025004, 2010.

ELECTROMAGNETIC AND MECHANICAL ANALYSIS OF A 14 MM 10-PERIOD NBTI SUPERCONDUCTING UNDULATOR*

F. Trillaud[†], Instituto de Ingeniería, UNAM, CDMX, 04510, Mexico

G.A. Barraza-Montiel, Facultad de Ingeniería, UNAM, CDMX, 04510, Mexico

M. Gehlot, and G. Mishra, IDDL, Devi Ahilya University, Indore, MP 452001, India

Abstract

A 14 mm - 10 period NbTi superconducting undulator for the next generation of Free Electron Laser has been studied. The optimum electromagnetic pre-design was carried out using RADIA, an extension module of the commercial software Mathematica. For this pre-design, a variable gap was considered. Additionally, a thermo-mechanical study of one eighth of the superconducting undulator was conducted. This study utilized a thermal and mechanical contact model between the pancake coils and the carbon steel core. This coupled model allowed estimating the minimum pre-loading of the coil. This pre-loading ensures that the coil would remain stuck to its pole during cooling. Numerical results are presented for both studies.

INTRODUCTION

The new generation of light sources are expected to achieve greater luminosity benefiting from the advances in superconducting wires and tapes [1]. In the past 15 years, an increasing body of research has been dedicated to the development of superconducting insertion devices making use of state of the art commercial Low Temperature Superconductors operated in liquid helium [2]. Over the years, a few prototypes have been built and installed showing the applicability of the technology [3]. As the superconductivity gets more and more reachable to countries such as India which operates light sources, there is an increasing interest in exploring new technologies to upgrade their existing facilities [4]. It should be noted that the Mexican scientific community, users of light sources, have recently expressed their interest in the construction of a first light source in Mexico [5]. Addressing both interests in light sources and new technological developments for greater brightness, a small program to develop a first Indian 14 mm-10 period superconducting undulator operated in boiling liquid helium at 4.2 K has been launched in 2015 [6, 7], a technology that will certainly benefit the Mexican light source as well.

SCU are superconducting electromagnets wound on two ferromagnetic cores separated by a gap. The electromagnets are made of series-connected, impregnated coils with alternative winding to provide an oscillating magnetic field on axis [8]. The magnitude of the field is adjusted by the current intensity fed to the coils. Additionally, as the superconductor can carry large amount of currents without

losses, it is possible to achieve greater field allowing the construction of shorter period undulators at a greater brightness than any of the conventional technologies [9]. They are clear advantages over more conventional technologies such as permanent magnets (PPM) and hybrid undulators (HU).

The following work reports pre-studies carried out on a NbTi undulator to be operated at 4.2 K and its structure. The choice of the conductor was made on the basis of its well-understanding and its malleability compared to other technologies such as Nb₃Sn or the High Temperature Superconductors (HTS) [10, 11]. The electromagnetic pre-design, the conceptual design of the mechanical structure and cryogenic system needed to test the SCU and a mechanical pre-analysis to operate safely the device are presented. The current margin of the superconducting electromagnet and the pre-compression to ensure that the coils would not delaminate from their support were estimated. It is a first step allowing understanding the technology to be completed by more in depth studies.

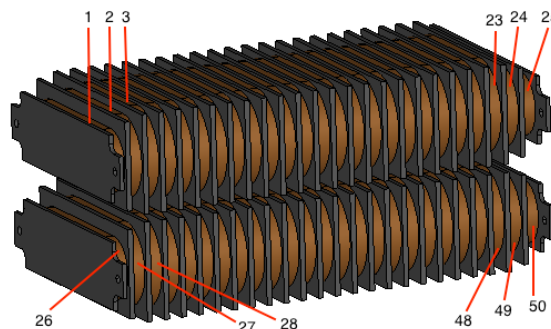


Figure 1: SCU structure with coil packs.

ELECTROMAGNETIC PRE-DESIGN

The NbTi superconducting undulator (SCU) is composed of two separated carbon steel cores, referred to as poles as it is shown in Fig. 1. Each pole holds 25 epoxy-impregnated racetrack coils connected in series with alternative winding. The coils are numbered from 1 to 50 over both poles (1-25 and 26-50). The first and last two coils of each pole are graded to smoother the magnetic flux density and lower the kick. The first and last coils (1 and 25, 26 and 50) are 1/4th of the height and width of the regular coil whereas the second and the penultimate coils (2 and 24, 27 and 49) are 3/4th. The regular coils, 3-23 and 28-48, have same dimensions along the pole length to generate a regular oscillating magnetic field. Figure 2 provides the dimensions of a regular coil and

* Work supported by the Dirección General Asuntos del Personal Académico (DGAPA) of the Universidad Nacional Autónoma de México (UNAM) under grant PAPIIT TA100617 and from SERB, India.

[†] ftrillaudp@iingen.unam.mx

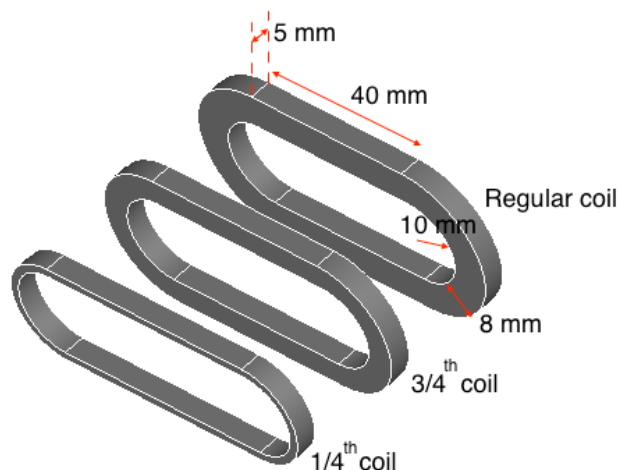


Figure 2: Dimensions of the regular coil. The 3/4th and 1/4th have same cross-section but their length and width are scaled down.

shows the scale of the graded coils compared to this same regular coil. Each coil is separated by a 2 mm thick carbon steel wall whose widths and heights are the same as the coil ones.

The module RADIA of the commercial software Mathematica [12] was used to provide a first estimation of the current margin of the superconducting electromagnet. The geometry of the SCU was meshed and the magnetic flux density was computed on axis and off axis at the surface of the coil. The results provided the choice of the commercial superconductor and the distance between the ferromagnetic cores to ensure a safe operation of the SCU at 4.2 K. Amongst some of the most relevant results are given in Figs. 3 and 4. The former shows the engineering current density flowing through the SCU as a function of the magnetic flux density on the coil and the latter 4 shows the evolution of the magnitude of the magnetic flux density on axis. Using both figures, an insulated rectangular 1 mm x 0.5 mm conductor with a copper-to-superconductor ratio equal to 1.5 was chosen to reach a target of 1 T on axis with a current margin on the superconductor larger than or equal to 10% at a gap of 5 mm for an engineering current density in the superconductor of 800 A/mm² [7].

CONCEPTUAL DESIGN OF THE MECHANICAL STRUCTURE AND CRYOGENIC SYSTEM

Figure 5 shows the conceptual design of the cryogenic experimental setup to test the proposed SCU in liquid helium (LHe) at 4.2 K. The experimental setup is composed of a LHe cryostat surrounded by a liquid nitrogen jacket (LN₂). A top flange, which seals the cryostat, houses two vapor-cooled current leads, sealed connectors for data transfer, LHe level sensor, a LHe inlet and a relief valve for safety purposes. Four non-magnetic rods, screwed to the top flange, hold the SCU in a vertical position. Cu plates and a styrofoam ring are used to scatter the convection heat transfer and are

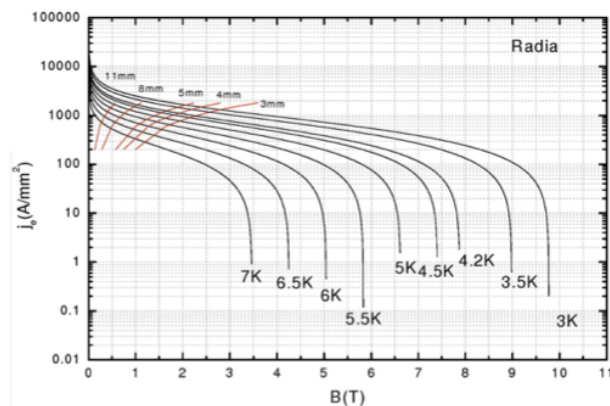


Figure 3: Current margin on the superconductor at different gaps [7].

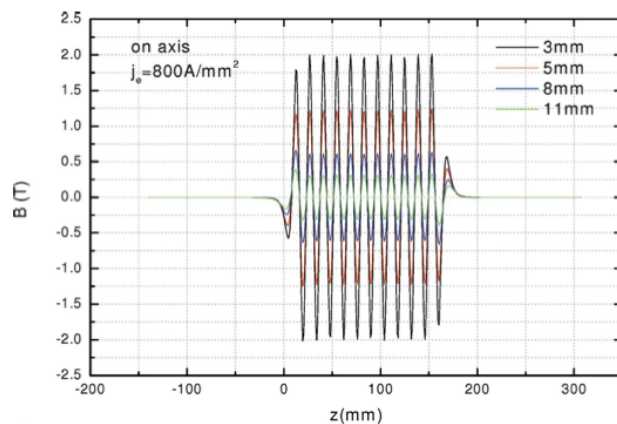


Figure 4: Pattern of the magnetic flux density generated by the SCU. By grading the coils, the kick is smoothed allowing a stable entrance and exit of the electron beam [7].

held by the same rods supporting the undulator. A G10 plate allows centering the experiment and guiding the rods. Spring-like supports at the extremities of the SCU poles will be considered to ensure that the gap remains equal to 5 mm during cooling and energizing. Various thermal sensors, labeled T₁ through T₄ will be installed at key locations to monitor the cooling of the system. A 5-V, 600-A power supply feeds the vapor-cooled current leads connected to the undulator winding, producing an adequate magnetic field in the gap between the undulator poles.

A magnetic rig, consisting of an infinite screw linear positioner and an array of Hall probes, will allow to measure the magnetic field between the undulator poles. This feature will slide along the undulator gap to perform the field mapping at different locations. A crane will help holding the top flange and a special stand is used to help positioning the undulator so that the operator can easily connect the undulator to the rods and the current leads. Once the undulator is attached to the experimental holder (top flange and its components) and connected to the current leads, the holder is dipped into the cryostat using the crane. The cryostat is then slowly filled up with LHe meanwhile the temperature across the system is monitored.

Content from this work may be used under the terms of the CC BY 3.0 licence (© 2018). Any distribution of this work must maintain attribution to the author(s), title of the work, publisher, and DOI.

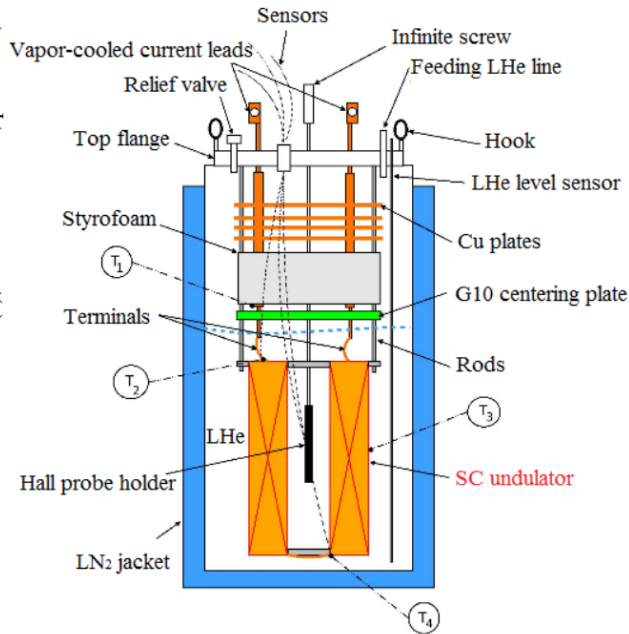


Figure 5: Conceptual design of the experiment setup to test the proposed SCU.

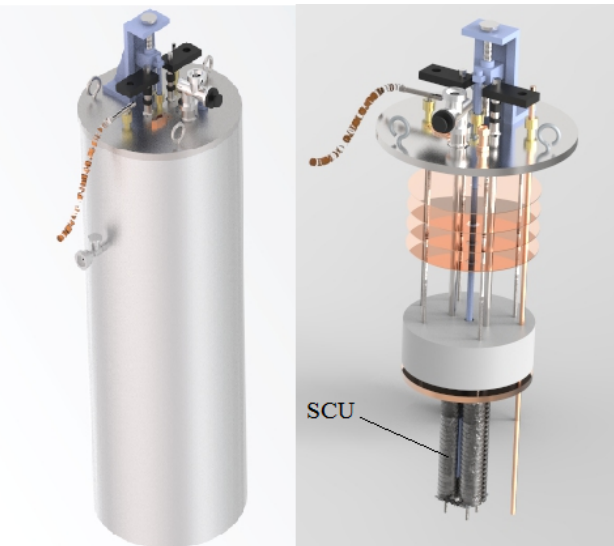


Figure 6: 3D CAD of the experimental setup showing detailed engineered parts and the SCU.

Figure 6 shows the corresponding 3D solid model of the SCU experiment. This setup is expected to be built upon grant approval.

THERMO-MECHANICAL ANALYSIS

A coupled thermo-mechanical 3D Finite Element Analysis (FEA) of the SCU was conducted using the electromagnetic pre-design as geometrical input. The model assumed non-ideal thermal and mechanical contacts between the coils and their pole. For each time step, the temperature distribu-

tion was first computed assuming a cooling speed of 30 min. Then, the mechanical strains and stresses were calculated from the thermal induced deformation. A pre-compression was added to the mechanical model to simulate the winding tension and an eventual additional wrapping on top of the coils. Such a wrapping can be made of aluminum having a larger thermal contraction than the coil winding providing an adjustable pre-loading. In the model, the magnitude of the pre-compression is tuned so that the coils remain in contact to the surface of the core.

Thermal Model

The heat balance equation to solve the temperature field of the SCU is given by

$$\nabla \cdot [k \nabla (T)] = \rho c_p \frac{\partial T}{\partial t} \quad (1)$$

where T is the temperature, ρ the mass density, k the thermal conductivity and c_p the specific heat capacity, both depending on temperature. To model the thermal properties of the winding, it is necessary to take into account the properties of the different materials: superconductor, Cu matrix, insulation and epoxy. To that end, a mixture rule was applied to obtain an isotropic, homogeneous equivalent material property of the coils. In addition, the thermal contact between coils and poles was added to the model through an equivalent thermal heat exchange coefficient h so that

$$\Delta \Phi_{j,i} = h (T_j - T_i) \quad (2)$$

is the exchanged heat flux in W/m^2 between the surfaces i and j in contact. The value of the equivalent thermal heat exchange coefficient was chosen equal to $2580 \text{ W/m}^2\text{-K}$ [13].

To simulate the cooling down of the device from room temperature to 4.2 K, a time varying boundary condition was applied to the external surfaces of the SCU model. The expression of the boundary temperature T_b is given by

$$T_b(t) = (T_{lh} - T_0)e^{-\beta t} + T_0 \quad (3)$$

where T_0 is equal to 300 K and T_{lh} represents the liquid helium temperature equal to 4.2 K. β is a parameter associated with the cooling speed in s^{-1} . This parameter was chosen as 0.0045 s^{-1} to provide a slow cooling of 30 min, an achievable cooling speed for the dimensions of the cryogenic system.

Mechanical Model and Thermo-Mechanical Coupling

One of the requirements to ensure a reliable SCU's operation and performance is to avoid a large coil deformation during the different phases of the device operation. These phases include cooling, energizing and warming. In the present work, the focus is on the cooling step where the difference in thermal expansion coefficient between the coil and its support may lead to the loss of contact between the two. This loss of contact may lead to early quenches. It is

worth mentioning that during the current loading of the magnet, deformations arising from the Lorentz forces are also expected to occur. This effect will be studied later on. To minimize the risk of coil delamination, a classic strategy is to apply a pre-loading if the winding tension is not enough.

Addressing only the issues related to the cooling phase, the mechanical equation that defines the displacement field $\mathbf{u} = [u, v, w]$ due to the thermal load, is given by

$$G\nabla^2 \mathbf{u} + \frac{G}{1-2\nu} \nabla(\nabla \cdot \mathbf{u}) - \frac{E}{1-2\nu} \alpha \nabla(T) = \rho \ddot{\mathbf{u}} \quad (4)$$

where E is the Young's Modulus (210 GPa for the carbon steel and 120 GPa for the winding pack), ν is the Poisson's ratio (0.3), $G = E/2(1 + \nu)$ is the shear modulus and α is the thermal expansion coefficient ($17 \times 10^{-6} \text{ K}^{-1}$ for the carbon steel and $9.8 \times 10^{-6} \text{ K}^{-1}$ for the winding pack). The contact is modeled through an elastic relation between the displacement of the nodes composing the surface of the material facing each other. No interpenetration is allowed.

The coupling is carried out by adding the thermal strain to the equation of the displacement field (4). The thermal strain depends directly on the coefficient of thermal expansion α and the temperature gradient. This coefficient is similarly obtained by a mixture rule.

The clamping of the SCU to the support rod is modeled through a spring-like boundary condition (spring foundation).

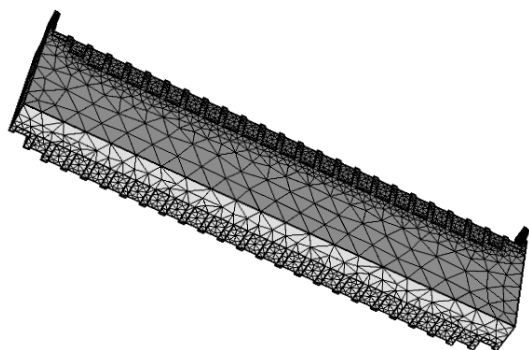


Figure 7: Meshing of 1/8th of the SCU. A denser mesh is used around the coil to provide a better resolution of the temperature and displacement fields. The same mesh was used for the thermal and mechanical problems.

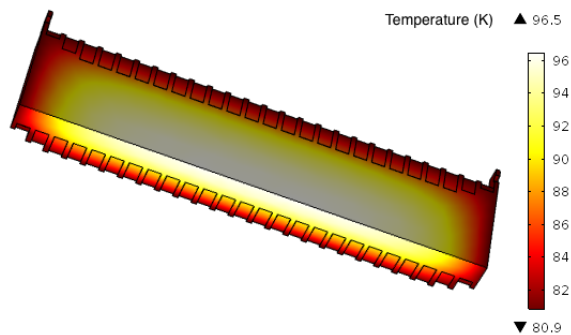


Figure 8: Temperature distribution at 300 s at the beginning of the cooling phase.

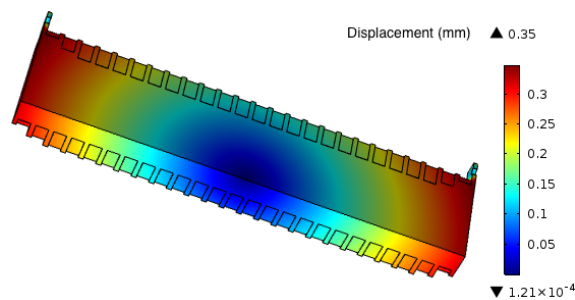


Figure 9: Displacement field at 300 s corresponding to the temperature distribution shown in Fig. 8.

FEA Model and Solver

To solve the 3D coupled temperature and displacement fields, the authors used the commercial FEA software COMSOL Multiphysics[®] version 5.2. Benefiting from the symmetry of the problem, only one eighth of the SCU was modeled, representing a quarter of a pole. Figure 7 shows the mesh used for the coupled analysis. A small gap exist between the coil and the pole meshes to model both the thermal and mechanical contacts.

The heat balance and field displacement equations are solved sequentially. First, the temperature distribution is obtained, then the thermal strain is computed and added to the mechanical model. The same mesh was used for both the thermal and mechanical models. At each time step, both the temperature and the displacement fields are obtained until steady state is reached.

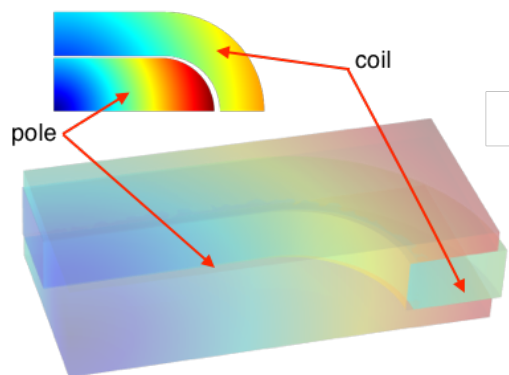


Figure 10: Detail of the coil separation from the ferromagnetic core. The displacement is amplified by a factor of 15.

THERMO-MECHANICAL RESULTS AND DISCUSSION

At first, the whole SCU is at 300 K. For this analysis, it is assumed that the SCU is homogeneously cooled by LHe. As the boundary temperature follows (3), a thermal gradient develops inside the SCU. This thermal gradient vanishes rapidly after the boundary reached 4.2 K. Figures 8 and 9 show the temperature distribution and the displacement field after 300 s at the beginning of the cooling phase, respectively. Because of the discrepancies in the material

REFERENCES

- [1] N. Mezentsev, "Survey of superconducting insertion devices for light sources," in *Proceedings of PAC'05*, Knoxville, Tennessee, pp. 256–260, 2006.
- [2] C.S. Hwang, J.C. Jan, C.S. Chang, S.D. Chen, C.H. Chang, and T.M. Uen, "Development trends for insertion devices of future synchrotron light sources," *Physical Review Special Topics - Accelerators and Beams*, vol. 14, no. 044801, 2011.
- [3] E. Moog and Y. Ivanyushenkov, "Developments in superconducting insertion devices," in *Proceedings of PAC'11*, New York, NY, USA, pp. 2077–2081, 2012.
- [4] H. Winick, "Synchrotron light sources in developing countries," in *APS March Meeting 2017*, New Orleans, Louisiana, USA, vol. 62, 2017.
- [5] A. Antillón, J. Jiménez and M. Moreno, "Momentum gathers towards a Mexican light source," <https://www.aps.org/units/fip/newsletters/201509/mexico.cfm>. Forum on International Physics, 2015.
- [6] M. Gehlot, G. Mishra, F. Trillaud, G. Sharma, "Magnetic design of a 14 mm period prototype superconducting undulator," *Nuclear Instruments and Methods in Physics Research A*, vol. 846, pp. 13–17, 2017.
- [7] G. Mishra, M. Gehlot, G. Sharma, and F. Trillaud, "Magnetic design and modelling of a 14 mm-period prototype superconducting undulator," *Journal of Synchrotron Radiation*, vol. 24, pp. 1–7, 2017.
- [8] S. Prestemon, D. Dietderich, S. Marks, and R. Schlueter, "NbTi and Nb3Sn superconducting undulator designs," in *AIP Conference Proceedings*, vol. 705, pp. 294–300, 2004.
- [9] J. Bahrtdt and Y. Ivanyushenkov, "Short period undulators for storage rings and free electron lasers," in *Journal of Physics: Conference Series*, vol. 425, p. 032001, 2013.
- [10] P. Emma *et al.*, "A plan for the development of superconducting undulator prototypes for LCLS-II and future FELs," in *Proceedings of FEL'14*, Basel, Switzerland, 2014.
- [11] I. Kesgin, C. Doose, M. Kasa, Y. Ivanyushenkov, and U. Welp, "Design of a REBCO thin film superconducting undulator," in *IOP Conference Series: Materials Science and Engineering*, vol. 101, p. 012053, 2015.
- [12] O. Chubar, P. Elleaume, and J. Chavanne, "A 3D magnetostatics computer code for insertion devices," *Journal of Synchrotron Radiation*, vol. 5, pp. 481–484, 1998.
- [13] E. Gmelin, M. Asen-Palmer, M. Reuther, and R. Villar, "Thermal boundary resistance of mechanical contacts between solids at sub-ambient temperatures," *Journal of Physics D: Applied Physics*, vol. 32, no. 6, p. R19, 1999.
- [14] I.R. Dixon, R.P. Walsh, W.D. Markiewicz, and C.A. Swenson, "Mechanical properties of epoxy impregnated superconducting solenoids," *IEEE Transactions on Magnetics*, vol. 32, no. 4, pp. 2917–2920, 1996.

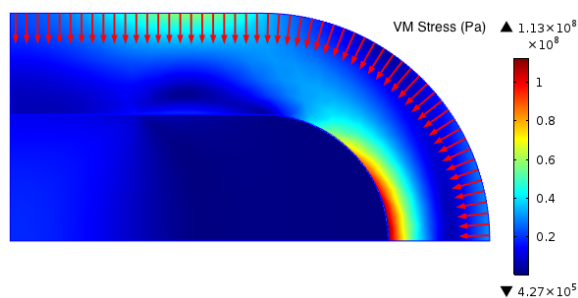


Figure 11: A pre-compression of 25 MPa allows the contact between the inner surface of the coil and its pole. The maximum stress generated at the coil is equal to 113 MPa.

thermal shrinkage, a thermal strain develops that can be ultimately compensated by a pre-loading (or the winding tension). Without pre-loading, if the coil is poorly bonded to its carbon steel support, it is likely to delaminate as shown in Fig. 10. As a result, an overall maximum separation of 0.05 mm occurs at the circular portion of the racetrack coil meanwhile, over the straight section, the separation amounts to a maximum of 0.024 mm. By applying a pre-loading of about 25 MPa as shown in Fig. 11, this separation disappears and the maximum Von Mises stress developed in the coil still reaches an admissible value of 113 MPa [14]. Since the deformations of the coil and the pole remain small, the elastic model provides a good first approximation. However, it should be noted that this model, elastic in its most basic assumption, does not include phenomena such as cracks and fractures. Therefore, the resulting deformation once the temperature of the SCU reached 4.2 K is independent of the cooling velocity. It is a limitation of the model which can difficultly be overcome without experimental data.

CONCLUSION

A preliminary mechanical and magnetic study has been conducted to build a NbTi superconducting undulator prototype to be tested at 4.2 K in liquid helium. This first Indian superconducting prototype is expected to be tested at the Insertion Device Development and Measurement Lab of the Devi Ahilya University. The electromagnetic pre-design targets a 1 T magnetic flux density on axis for a gap of 5 mm. On the basis of field requirement, a rectangular commercial NbTi wire has been chosen which provides a safe temperature and current margin to reach the nominal magnetic field on axis. To avoid the possibility of delamination of the coils during cooling, the magnitude of the pre-compressing force (pre-loading) was estimated. Further works are still necessary to take into the mechanical behavior of the SCU poles during energization. In addition to the thermal forces, the Lorentz force will be added to the mechanical model to get the proper pre-loading.

DIELECTRIC LASER ACCELERATION SETUP DESIGN, GRATING MANUFACTURING AND INVESTIGATIONS INTO LASER INDUCED RF CAVITY BREAKDOWNS*

M. Hamberg[†], E. Vargas Catalan, M. Karlsson, D. Dancila, A. Rydberg, J. Ögren, M. Jacewicz,
Uppsala University, Uppsala, Sweden
M. Kuittinen, I. Vartiainen, Institute of Photonics, University of Eastern Finland, Finland

Abstract

Dielectric laser acceleration (DLA) is the technique utilizing strong electric fields in lasers to accelerate electrons in the proximity of nanoscaled dielectric gratings. The concept was recently demonstrated in experimental studies. Here, we describe the experimental DLA investigation setup design including laser system and scanning electron microscope (SEM). We also present the grating manufacturing methods as well as investigations into vacuum breakdowns occurring at RF accelerating structures.

INTRODUCTION

Accelerator physics plays an exponentially increasing role within the fields of natural sciences though the technology is generally spacious and expensive which hampers scientific progress [1]. Electrical breakdown inside of the acceleration cavities are limiting them in field strength and, therefore, size. Typical gradients are on the order of 10-50 MVm⁻¹ [2], which is less than the structures developed by the Compact Linear Collider (CLIC) collaboration, which operate up to 100 MVm⁻¹ [3]. To overcome these limits, alternative methods should be investigated.

Dielectric materials have proven superior properties regarding damage threshold of strong electric fields. Therefore, dielectric laser acceleration (DLA) where the strong electric fields from lasers are used for acceleration of charged particles at nanofabricated dielectric structures is a promising alternative [4]. The method has recently been proven in proof of principle studies for a large interval of energies ranging from non-relativistic and with acceleration gradients up to 690 MVm⁻¹ [4-7].

The technology is under development and promising, with gradients 10-100 times higher than current state of the art. Such increase in gradients would result in the corresponding size reduction and effectively more inexpensive accelerators rendering in higher scientific output when more accelerators can be built up. Challenges include timing, manufacturing of the dielectric structures regarding material and layout.

In this paper, we describe manufacturing of acceleration gratings made of diamond, construction of an acceleration test setup and how this setup can be utilized for vacuum breakdowns by high electric fields in metallic accelerator cavities (this is also previously described in [8]).

*Work supported by Stockholm-Uppsala Centre for Free Electron Laser Research.

[†]mathias.hamberg@physics.uu.se

DIAMOND GRATING MANUFACTURING AND LASER DAMAGE INVESTIGATIONS

For the dielectric acceleration grating structures we choose to work with 10 mm diameter and 300 μm thick polycrystalline diamond substrates from Element Six Ltd and Diamond Materials GmbH.

Recently, co-authors demonstrated an improved process utilizing electron-beam lithography, nano-replication using solvent assisted micro molding (SAMIM) [9,10]. The result of this process are replicas with line widths close to identical to the master grating pattern. The method furthermore includes inductively coupled plasma etching (ICP-RIE) with pure oxygen resulting in a lower sidewall angle [9].

As a first suitability test laser damage investigations of unprocessed diamond substrates were undertaken Friedrich-Alexander Universität (FAU) in Erlangen, Germany. The substrates were irradiated by a 1MHz laser with a wavelength of 1.93 μm, 600-fs pulse duration, and a 4-GVm⁻¹ peak field. No visible damage on the substrates was identified which motivated proceeding with the subsequent manufacturing steps.

Once the diamond structures are ready they will be tested for acceleration at FAU.

SEM TEST SETUP

We are constructing a DLA test bench based on a scanning electron microscope (SEM) Philips XL-30 (Fig. 1), with a similar design as at FAU. Such device can provide a well determined and precisely tuneable electron beam. Furthermore, the electron energies are typically in the tens of keV which arguably a very important energy range for investigation.

The design scheme in Fig. 2, illustrates where the electron beam passes near the acceleration grating. A laser beam is irradiating in transverse direction, exciting near fields which accelerate electrons in the right phase. An alignment microscope is used to read out the position of the laser spot on the diamond grating. Finally, an energy spectrometer is used for reading out the effect of the acceleration. It consists of two electrostatic plates bending the electron beam onto a micro channel plate (MCP).

The inside of the SEM of ~Ø300x200 mm leaves room for movable sample mount and energy spectrometer. The sample mount consists of three vacuum compatible

Content from this work may be used under the terms of the CC BY 3.0 licence (© 2018). Any distribution of this work must maintain attribution to the author(s), title of the work, publisher, and DOI.



Figure 1: Installation of lasers in front of SEM at the Ångström Laboratory clean room.

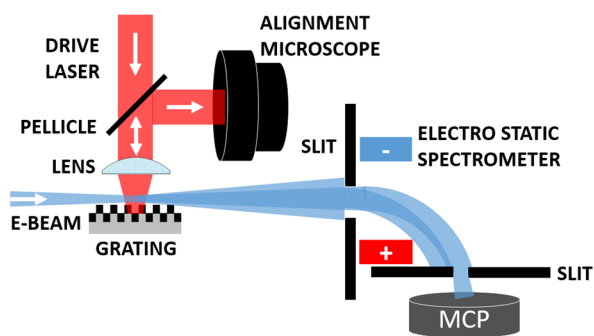


Figure 2: Design scheme of the DLA test setup. The electron beam is emitted from a SEM and is then subsequently passing the acceleration grating and an energy spectrometer.

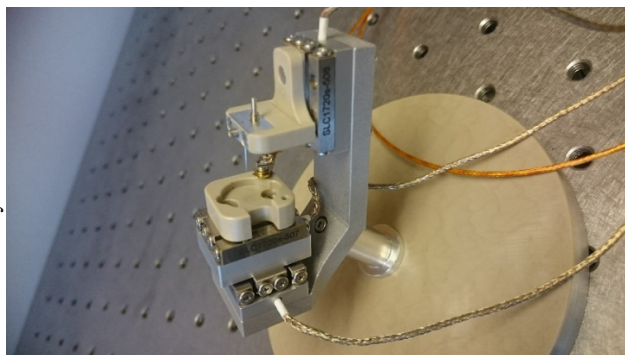


Figure 3: XYZ-control through nm resolution linear piezo stages and tungsten tip.

Smaract SLC1720 linear piezo translation stages as shown in Fig. 3. Each stage has better than 1-nm resolution and the sample mount can be further adapted at the Ångström Laboratory workshop for the forthcoming experiments.

LASER SETUP

The experimental setup includes Spectra Physics Tsunami Ti:Sapphire laser used for the acceleration. It runs with 80 MHz repetition rate, wavelength of 720-850 nm, better than 100-fs pulse duration, and with a peak field of approximately 800 MVm^{-1} .

The emitted light passes a periscope, vacuum viewport into the SEM where a positive lens is used to focus the beam onto the acceleration substrate. An additional positive lens mounted on a XY manual micrometer translation stage is used to direct the beam after reading out the position on an alignment microscope from a part of the reflected light, as shown in Fig. 2.

SURFACE HARDENING THROUGH LASER INDUCED CONDITIONING

CLIC uses normal-conducting, high-gradient copper accelerating structures [3] and due to the high gradient of 100 MVm^{-1} , breakdown of the radio-frequency fields (RF) is an issue and a limiting factor for achieving high luminosity. There are many aspects of RF breakdown (BD), vacuum discharges, conditioning and field-emission that are not fully understood.

The classical BD theory, where BD onset starts at a local surface defect e.g. a nano-protrusion or a scratch on the surface, assumes that the electric field is enhanced at the defect location and can become sufficiently high to start field emission from that site. What follows is heating of the material, evaporation of the neutrals and ionization by field emitted electrons resulting in formation of plasma and finally of an arc.

The results from conditioning of the high-gradient RF structures show that situation is even more complicated. This mechanism can explain the behaviour at lower field values, but when structure is reaching surface fields well above 100 MVm^{-1} it is believed that a more ultimate physical limit is reached. At these fields one starts to see evidence of field generated features not just on the surface but rather forming below the surface and being connected with dynamics of dislocations, which are imperfection of the crystal lattice that are being generated and are moving around due to operated field. Evidence indicates that the conditioning is a pulse-by-pulse process, depending not on the number of RF breakdowns but rather the total number of RF pulses [11].

It is therefore theorized that the repetitive action of a RF field forms an array of new dislocations that move and interlock with each other reducing the possibility of further movement within the bulk. Only when this happens the breakdown rate reduces to sufficiently low levels as required by CLIC [12].

We have a setup for in-situ SEM studies of electrical discharges where a metallic sample and a tungsten tip are mounted on the movable stage driven by piezo-motors (Fig. 3) [13]. This allows for precise control of the gap distance between the tip and surface and location on the surface. High voltage is applied over the gap and with a Keithley electrometer 6517A the field emission currents can be measured.

The setup allows for studies of surface changes due to field emission under DC field, however exact correlation of the results with situation in RF is not fully possible. With the laser setup described earlier we now have the possibility to study laser-induced conditioning phenomena which perhaps can resemble situation with RF more closely. Interesting effects of laser-induced faceting and growth [14] have been studied before and the importance of collective motion inside crystal lattice in the context of accelerating structures has been pointed out [15].

CONCLUSION

The field of accelerator physics is expanding strongly and more efficient acceleration cavities are needed for a faster and less expensive scientific progress. DLA is an attractive concept which recently was demonstrated, and should be further investigated and developed. We are designing diamond gratings which will be tested at the FAU SEM test setup and subsequently in Sweden on a new setup built up at Uppsala University. This setup can also be used for investigation towards laser induced conditioning of the metallic surface.

ACKNOWLEDGEMENT

We thank FAU (group of P. Hommelhoff) for helpful discussions and performing the damage threshold test.

REFERENCES

- [1] B. McNeil and N. Thompson, *Nat. Photon.* 4, p. 814, 2010.
- [2] A. W. Chao *et al.*, *Reviews of Accelerator Science and Technology*, vol. 5, World Scientific, 2012.
- [3] S. Stapnes (Ed.), *The CLIC Programme: Towards a Staged e+e- Linear Collider Exploring the Terascale*, CERN-2012-005, Geneva, 2012.
- [4] J. Breuer and P. Hommerhoff, *Phys. Rev. Lett.* 111, p. 134803, 2013.
- [5] K. Koyama *et al.*, *Proc. of IPAC'16*, TUPMY017.
- [6] E. A. Peralta *et al.*, *Nature* 503, p. 91, 2013.
- [7] K. P. Wootton *et al.*, *Opt. Lett.* 41, p. 2696, 2016.
- [8] M. Hamberg *et al.*, *Proc. of IPAC'17*, WEPVA016.
- [9] E. Catalan *et al.*, *Diamond Relat. Mater.* 63, p. 60, 2016.
- [10] E. King *et al.*, *Adv. Mat.* 9, p. 651, 1997.
- [11] A. Degiovanni, W. Wuensch, and J. Navarro, "Comparison of the conditioning of high gradient accelerating structures," *Phys. Rev. ST - Accel. and Beams.* 19, p. 032001, 2016.
- [12] W. Wuensch, "Ultimate Field Gradient in Metallic Structures," *Proc. of IPAC'17*, MOYCA1.
- [13] J. Ögren, V. Ziemann, S. Jafri, and K. Leifer, *Proc. of IPAC'16*, p. 2083.
- [14] H. Yanagisawa, *et al.*, "Laser-induced asymmetric faceting and growth of a nano-protrusion on a tungsten tip," *APL Photonics* 1, p. 091305, 2016.
- [15] C. Z. Antoine, *et al.*, "Erratum to: Electromigration occurrences and its effects on metallic surfaces submitted to high electromagnetic field: a novel approach to breakdown in accelerators," *Nucl. Inst. and Methods A* 670, p. 79, 2012.

LUMINOSITY INCREASE IN LASER-COMPTON SCATTERING BY CRAB CROSSING*

Y. Koshiba[†], T. Takahashi, S. Ota, M. Washio, RISE, Waseda University, Tokyo, Japan
 K. Sakaue, WIAS, Waseda University, Tokyo, Japan
 T. Higashiguchi, Utsunomiya University, Tochigi, Japan
 J. Urakawa, KEK, Ibaraki, Japan

Abstract

Laser-Compton scattering X-ray (LCS-X) sources has been expected as a compact and powerful source, beyond X-ray tubes. It will enable laboratories and companies, opening new X-ray science. It is well known that luminosity depends on the collision angle of laser and electron beam. Head-on collision is ideal in the point of maximizing the luminosity, though difficult to create such system especially with optical enhancement cavity for laser. In collider experiments, however, crab crossing is a promising way to increase the luminosity. We are planning to apply crab crossing to LCS, to achieve a higher luminosity leading to a more intense X-ray source. Electron beam will be tilted to half of the collision angle using an rf-deflector. Although crab crossing in laser-Compton scattering has been already proposed [1], it has not been demonstrated yet anywhere. The goal of this study is to experimentally prove the luminosity increase by adopting crab crossing. In this conference, we will report about our compact accelerator system at Waseda University, laser system favorable for crab crossing LCS, and expected results of crab crossing LCS.

INTRODUCTION

Laser-Compton scattering (LCS) has been expected as an attractive X-ray source for years. Brilliance of almost 10^{10} has been achieved [2], and exceeding 10^{12} has been designed [3]. Comparing with magnetic undulators, LCS could be explained as “laser undulator”, which the undulator period equivalent to laser wavelength (~ 1 μm) while magnetic undulator is the order of cm. Figure 1 shows the comparison of undulator radiation and LCS.

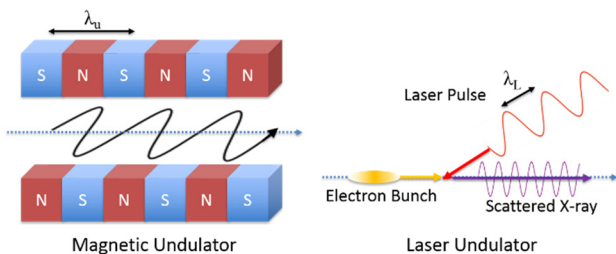


Figure 1: Comparison of undulator radiation and LCS.

* Work supported by Grant-in-Aid for JSPS Research Fellow.
[†] email address: advanced-yuya@asagi.waseda.jp

In order to produce 1- \AA photons, LCS needs to provide a beam of 25-MeV energy, assuming 6 GeV for undulator radiation ($K = 1$, $\lambda_u = 2$ cm) and 4 GeV for synchrotron radiation ($\rho = 12$ m). Low required beam energy enable the whole system compact and low cost so that laboratories and hospitals may take care. The schematic drawing of LCS is shown in Fig. 2.

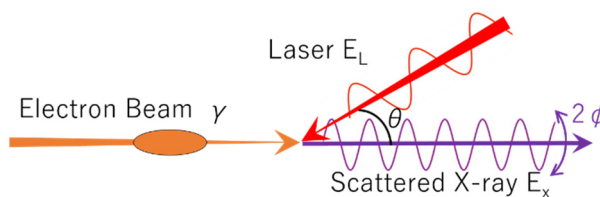


Figure 2: Schematic drawing of LCS.

In Fig. 2, γ , E_L , E_x , θ , ϕ represents the Lorentz factor of electron beam, energy of laser photon, energy of scattered X-ray, colliding angle, and scattering angle, respectively. The maximum X-ray energy E_x^{MAX} would be obtained along the electron beam axis $\phi=0$ and written as:

$$E_x^{MAX} \approx 2\gamma^2(1 + \beta \cos \theta)E_L, \quad (1)$$

where β is the velocity of electrons relative to the speed of light. We can see in Eq. (1) that scattered photon energy is tunable by controlling the beam energy or the collision angle.

The number of scattered photons is given by the product of cross section and luminosity:

$$N = \sigma L = \sigma P G. \quad (2)$$

Since the total cross section is unchangeable once the laser wavelength and beam energy is decided, it is necessary to increase the luminosity as much as possible. Luminosity can be expressed as the product of power factor (P) and geometric factor (G) as seen in Eq. (2). Power factor is the product of the number of electrons in a bunch and the number of photons in a laser pulse. Geometric factor is written as Eq. (3) when assuming Gaussian for both electron bunch and laser pulse. Here σ_x , σ_y , σ_z represents the electron bunch sizes of horizontal, vertical, and longitudinal respectively, and prime ones are those of laser pulse. We substitute our beam parameters, shown in Table 1, into the equation for the geometric factor,

Content from this work may be used under the terms of the CC BY 3.0 licence (© 2018). Any distribution of this work must maintain attribution to the author(s), title of the work, publisher, and DOI.

$$G = \frac{1 + \beta \cos \theta}{2\pi \sqrt{\sigma_y^2 + \sigma'_y{}^2} \sqrt{\sigma_x^2 (\beta + \cos \theta)^2 + \sigma'_x{}^2 (1 + \beta \cos \theta)^2 + \left(\sigma_z^2 + \sigma'_z{}^2\right) \sin^2 \theta}} \quad (3)$$

Table 1: Parameters of Electron Beam and Laser Pulse

	Electron Beam	Laser Pulse
Energy	4.2 MeV	1.2 eV (1030 nm)
Intensity	40 pC	10 mJ
Transverse Size	40 μm	50 μm
Duration	3 ps (rms)	0.43 ps (rms)

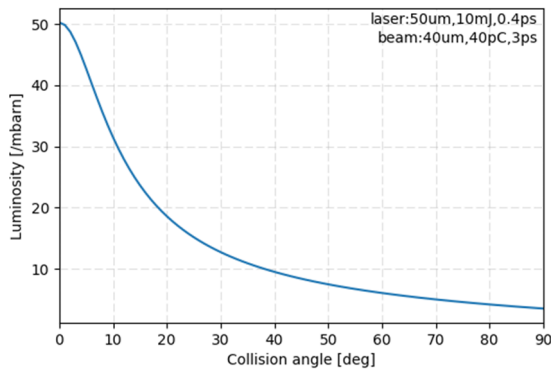


Figure 3: Luminosity as a function of collision angle.

For these values, the luminosity depends on collision angle as depicted in Fig. 3.

We can see that the luminosity is maximum when collision angle is zero, i.e. head-on collision and monotonically decrease as collision angle increase. Despite this fact, head-on collision is hard to realize especially with an optical enhancement cavity [4], considering the interference of cavity mirrors and electron beam path. In addition, scattered X-ray must get across a mirror. This might cause damages to the mirror. Due to these facts, quite a few LCS X-ray sources have a certain colliding angle which causes luminosity loss [5]. One method to overcome this problem is the crab crossing.

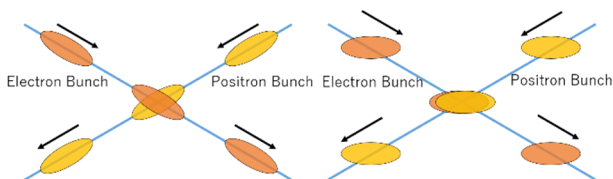


Figure 4: Schematic drawing of crab crossing.

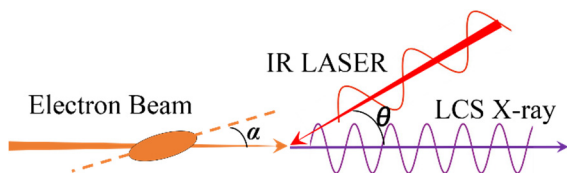


Figure 5: Schematic of crab crossing LCS.

CRAB CROSSING LCS

Effect of Crab Crossing

Crab crossing is a proven technique in colliders that allows an angle crossing without luminosity loss. Figure 4 depicts the schematic of crab crossing.

Luminosity is increased by tilting the bunch. In LCS, since it is a collision of electron bunch and laser, we are planning to tilt only the electron beam with an rf-deflector. Figure 5 shows the schematic of crab crossing LCS. Luminosity is maximized when the tilt angle α is half of collision angle [1]. The enhancement ratio between ordinary crossing and crab crossing would be:

$$\frac{G_{\text{crab}}}{G_{\text{non-crab}}} = \sqrt{\frac{(\sigma_x^2 + \sigma'_x{}^2) \cos^2 \frac{\theta}{2} + (\sigma_z^2 + \sigma'_z{}^2) \sin^2 \frac{\theta}{2}}{\sigma_x^2 + \sigma'_x{}^2 \cos^2 \frac{\theta}{2} + \sigma_z^2 \sin^2 \frac{\theta}{2}}} \quad (4)$$

Using those parameters listed in Table 1, the enhancement ratio (crab ratio) in our system is shown in Fig. 6.

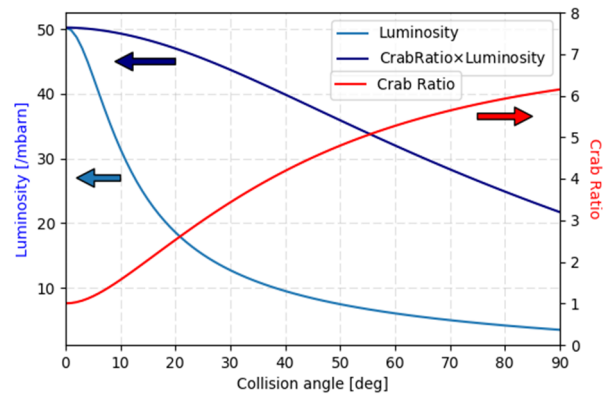


Figure 6: Enhancement ratio of crab crossing.

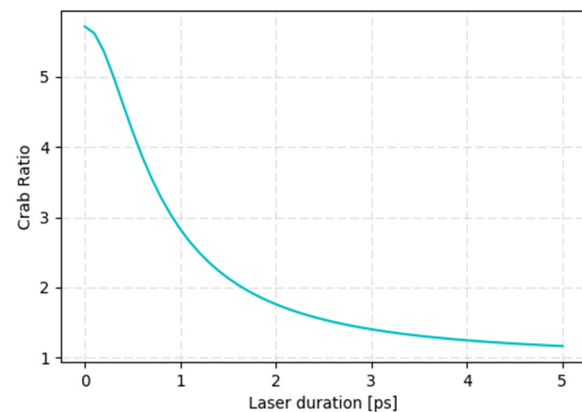


Figure 7: Pulse duration and enhancement ratio.

Content from this work may be used under the terms of the CC BY 3.0 licence (© 2018). Any distribution of this work must maintain attribution to the author(s), title of the work, publisher, and DOI.

We are planning to conduct the proof of principle experiment at 45 degrees and the expected enhancement ratio is 4.15. By comparing the blue lines, we can say that the luminosity is compensated by crab crossing.

The effect of pulse duration of colliding laser is shown in Fig. 7. Short and intense pulse makes crab crossing more effective. We are developing a laser system based on Yb fiber oscillator and Yb:YAG thin-disk regenerative amplifier for crab crossing LCS.

CAIN Simulation

The expected spectra were calculated by a Monte-Carlo code, CAIN. Figure 8 shows the calculation of ordinary 45 degrees crossing (blue), 45 degrees crossing with crab crossing (green), and ideal head-on crossing (red).

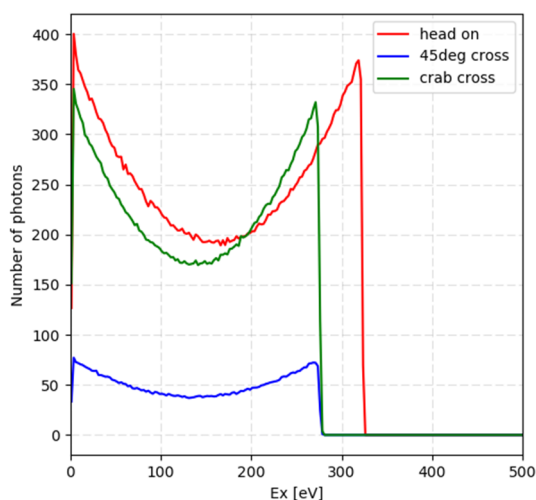


Figure 8: Calculated spectra by CAIN.

It is clear that the number of photons increase by crab crossing. We can also see that the maximum energy, i.e. the Compton edge does not change by crab crossing. The number of photons is listed in Table 2.

Table 2: Scattered Photons Calculated by CAIN

(θ, α)	Number of Photons
(0, 0)	32900
(45, 0)	5573
(45, 22.5)	24940

We can confirm that the total number of generated photons in crab crossing is more than 4 times larger than that of ordinary crossing. Furthermore, crab crossing enables almost 76 % of head-on likeness, while ordinary crossing is only 17 %.

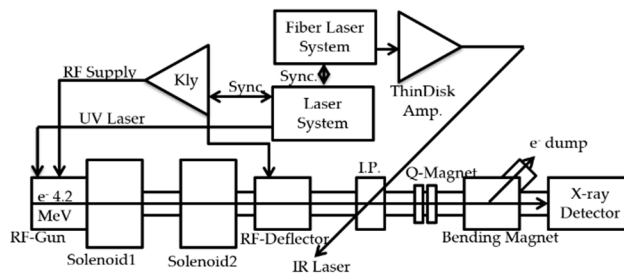


Figure 9: Experimental Setup for crab crossing LCS.

EXPERIMENTAL SETUP

The experimental setup for crab crossing LCS is shown in Fig. 9. A 1.6-cell rf-gun with CsTe photocathode will generate a 4.2-MeV, 40-pC, 3-ps electron bunch. It will be focused at the interaction point (I.P.) by a solenoid magnet to maximize the luminosity. The rf-deflector will give tilt to the bunch for crab crossing. The bending magnet is necessary to separate the scattered X-rays from the electron beam. Finally, the MCP (Micro-Channel Plate) will be used as the X-ray detector. We have already done background measurement (transporting electron beam without laser collision) and confirmed it was sufficiently low. We are now developing a colliding laser system suitable for crab crossing LCS, based on fiber laser and thin-disk regenerative amplifier.

CONCLUSION

We are planning to demonstrate the crab crossing LCS in our compact accelerator system in Waseda University. Luminosity increase is likely to be more than fourfold when the colliding angle is 45 deg. Encouraged by such good prospects, we are now concentrating on constructing the thin disk regenerative amplifier as a colliding laser, favorable for the crab crossing LCS.

REFERENCES

- [1] A. Variola *et al.*, "Luminosity optimization schemes in Compton experiments based on Fabry-Perot optical resonators", *Phys. Rev. ST Accel. Beams*, vol. 14, p. 031001, 2011.
- [2] E. Egl *et al.*, "The Munich compact light source: initial performance measures" *Journal of synchrotron radiation*, vol. 23, p. 1137-1142, 2016.
- [3] W. S. Graves *et al.*, "Compact x-ray source based on burst-mode inverse Compton scattering at 100 kHz" *Phys. Rev. ST Accel. Beams*, vol. 17, 2014.
- [4] K. Sakaue *et al.*, "Laser-compton scattering X-ray source based on normal conducting linac and optical enhancement cavity", in *Proc. IPAC'15*, Richmond, Virginia, USA, paper TUPJE011.
- [5] T. Akagi *et al.*, "Narrow-band photon beam via laser Compton scattering in an energy recovery linac", *Phys. Rev. ST Accel. Beams*, vol. 19, p. 114701, 2016.

STUDY ON CHERENKOV LASER OSCILLATOR USING TILTED ELECTRON BUNCHES *

K. Sakaue[†], WIAS, Waseda University, Tokyo, Japan

M. Brameld, Y. Tadenuma, R. Yanagisawa, M. Washio, RISE, Waseda University, Tokyo, Japan

R. Kuroda, Y. Taira, AIST, Ibaraki, Japan

J. Urakawa, KEK, Ibaraki, Japan

Abstract

We have been studying a coherent Cherenkov radiation by using tilted electron bunches. Bunch tilting can enhance the radiation power about 10 times due to the wavefront matching of radiations. Recently, we investigated that this technique can produce high peak power THz pulses with sufficient pulse energy. The resulting pulse energy was more than 30 nJ/pulse and peak power was about 10 kW. Introducing the oscillator cavity with two concave mirrors can achieve lasing using tilted electron bunches. In the calculation we present, 1 μ J/micro-pulse and 100 μ J/macro-pulse broadband THz pulses are expected to achieve, which is powerful THz source compared with the existing THz FELs. In this conference, we will report the experimental results of coherent Cherenkov radiation, calculated results towards lasing and future prospective.

INTRODUCTION

Radiation in the terahertz (THz) frequency range is recognized to be useful for material science, medical use and other applications. The most useful feature of THz radiation its absorption spectrum of particular materials. This is the absorption of the vibration and/or rotation of molecules. Recently, the high peak power THz pulse was found to be useful for transforming the surface molecular using specific absorption [1]. The accelerator based THz source has an advantage in high peak power THz pulse generation with monochromatic and wavelength tunability. have useful properties. The photon energy of the THz radiation is several meV so that our electron accelerator system based on photocathode rf gun with 5-MeV energy is enough for the THz generation.

We have been studying on the coherent THz generation with Cherenkov radiation process [2]. In order to enhance the THz radiation power, we employed an electron bunch tilting. The relativistic electrons radiate a Cherenkov radiation when the velocity of electron is faster than the light in the medium at certain angle. Fig. 1 shows the schematic of Cherenkov radiation from electron (left) and tilted electron bunch (right), radiation from different points of the medium can coherently overlap and enhance the pulse intensity [2].

* This work was supported by a research granted from The Murata Science Foundation and JSPS KAKENHI 26286083.

[†] kazuyuki.sakaue@aoni.waseda.jp

We successfully measured and enhanced the THz power, then started to design the oscillator cavity for lasing by Cherenkov radiation. This paper reports on the experimental results of coherent Cherenkov radiation, design and calculated results for constructing a laser, and future prospective.

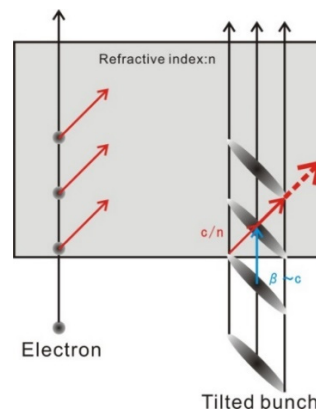


Figure 1: Generation of Cherenkov radiation from a tilted electron bunch.

EXPERIMENTS OF COHERENT CHERENKOV RADIATION

Experimental setup

Figure 2 shows the experimental setup of coherent Cherenkov radiation by electron bunch tilting. Electron bunch is produced by photocathode rf electron gun with energy of 4.5 MeV. Electron bunch is passed through the solenoid magnet for emittance compensation and focused by the quadrupole magnets. The focus size is the key parameter of the form factor in this experiment. After the quadrupole magnets, we installed an rf transverse deflecting cavity for tilting the bunch. Tilting angle can be controlled by regulating the rf power for the rf deflector.

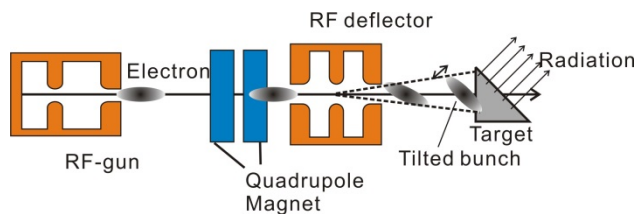


Figure 2: Experimental setup of coherent Cherenkov radiation by electron bunch tilting.

Content from this work may be used under the terms of the CC BY 3.0 licence (© 2018). Any distribution of this work must maintain attribution to the author(s), title of the work, publisher, and DOI.

After the rf deflector, the target medium of Cherenkov radiation is installed. We employed the target made by TOPAS [3], which has transmittance and uniform refractive index in THz range. The refractive index of TOPAS is 1.52 in the THz frequency. The resulting Cherenkov angle is 48.9 degrees. The radiation is extracted through the vacuum window and guided to the measurement system. We used a schottky barrier diode (SBD), the THz power meter and the time domain spectroscopy (TDS) system using EO sampling method [4].

Experimental results

Here we show the measurement results of coherent Cherenkov radiation experiment. Firstly, we detected the THz pulses by SBD. Figure 3 shows the measured THz waveform.

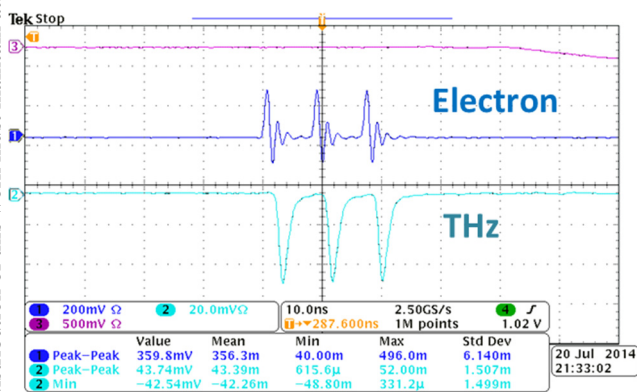


Figure 3: THz waveform detected by SBD (aqua) and electron bunch waveform by a current transformer (blue).

As shown in Fig. 3, three electron bunches produced three THz pulses. Our accelerator system can produce multi-bunch beam up to 200 bunches/train so that introducing oscillator cavity will realize the lasing.

As a next step, we measured the pulse energy of THz pulse. The resolution of the THz power meter is in the μW range, thus we used the multi-bunch beam to measure the average power and then divided by the number of pulses. Table 1 shows the results of this measurement.

Table 1: Results of Pulse Energy Measurement by THz Power Meter

	Tilted	Untilted
Total band	33.2 nJ	4.5 nJ
0.3±10% THz	10.6 nJ	-
0.6±10% THz	4.0 nJ	-

Comparing the total band pulse energy, electron bunch tilting increased the pulse energy more than 7 times. The other columns are the measurement using band pass filters (BPFs). These results indicate that the THz pulse has

a broad band spectrum and larger intensity in the low frequency part.

In order to confirm the THz spectrum, we employed a TDS system using EO sampling method. TDS systems measure the waveform of the THz pulse directly and its Fourier transformation corresponds to the spectrum of the THz pulse. The detail of the TDS system utilized in our experiment is can be found in [4]. We used ZnTe crystal as an EO crystal and a Yb fiber laser as a probe. Figure 4 shows the measured results in the time domain (top) and frequency domain (bottom).

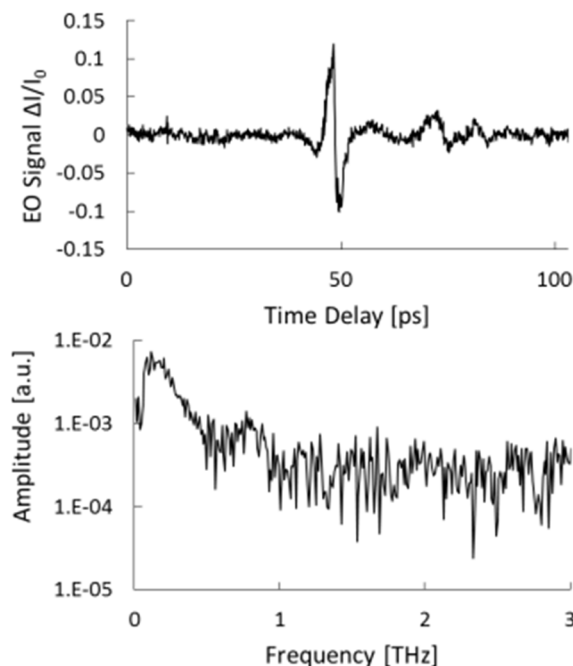


Figure 4: Measurement results of TDS system in time domain (top) and frequency domain (bottom).

The waveform in time domain has the single cycle property, a broad band spectrum. In the frequency domain, the THz pulse has a broad band spectrum up to 1 THz, the upper limit of the frequency determined by the system configuration. A combination of ZnTe 1 mm thick and Yb fibre laser would limit the sensitivity up to 1 THz. From the beam size before tilt, we expect that the THz pulse may include frequency content up to 3 THz.

CALCULATIONS OF CHERENKOV LASER OSCILLATOR

After the successful results of coherent Cherenkov radiation via electron-bunch tilting, we designed two different systems that could lase using an oscillator cavity. The first type is a normal TOPAS target with an output coupler oscillator. A sketch of this configuration, called NORMAL, is shown in Figure 5. The other is a high peak-power type with low losses and can extract a single pulse though a laser-plasma mirror. A sketch of this configuration, called HIPEAK, is shown in Figure 6.

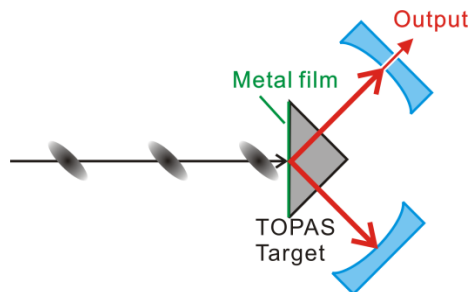


Figure 5: Designed laser oscillator type NORMAL.

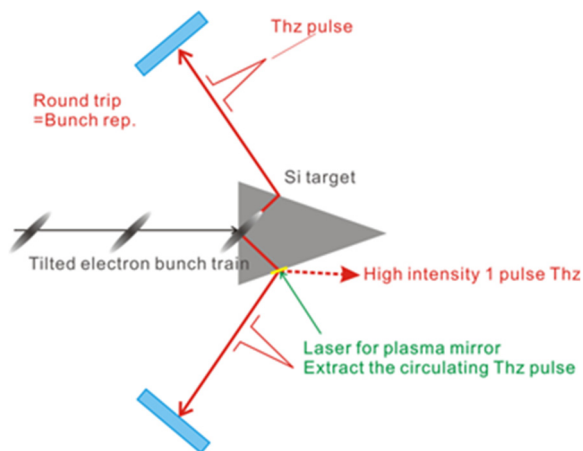


Figure 6: Designed laser oscillator type HIPEAK.

For a normal type oscillator, we employed TOPAS target as we used in the experiment. In order to make a closed loop, one surface of the TOPAS has metal coat. The refractive index of TOPAS is not high so that we simply configured the oscillator. The output coupler is employed for one mirror to match with the round-trip loss of the oscillator. We assumed one pass energy gain is 33 nJ as we measured above. The calculated result is shown in Fig. 7.

Considering the practical use of THz pulses, high peak power THz radiation is the most useful. Thus, we designed the high peak power oscillator. Figure 6 illustrates the configuration of HIPEAK oscillator. We employed a Si target, which is low absorption in the medium. In addition, the THz pulse is extract/inject to the medium by a Brewster's angle in order to minimize the loss. The round-trip loss is less than 2%.

The key point of this oscillator is the extraction by the laser. We use the Si semiconductor target and the injection is not perpendicular to the medium. If we make mirror surface at the time which the oscillator is saturation, the maximum pulse energy can be extracted. The laser plasma mirror is a well-known technique for the semiconductors [5]. Then we can obtain the single, high peak-power THz pulse using the HIPEAK oscillator. It should be noted that we assumed in the calculation that the single pass gain of Si was same with TOPAS.

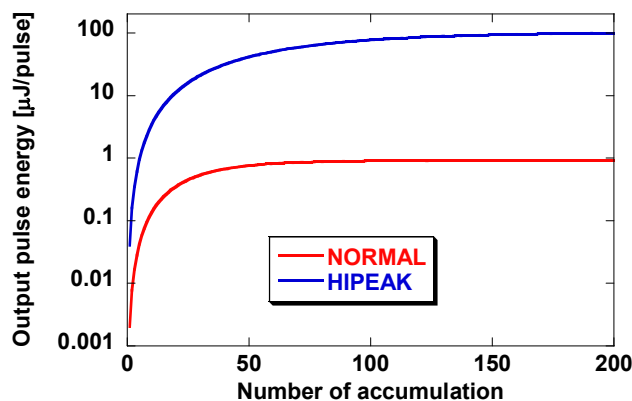


Figure 7: Calculated results of lasing by coherent Cherenkov radiation by two types of oscillator.

Figure 7 shows the calculated results of lasing by two types of oscillator shown in Figs 5 and 6. In Fig. 7, the red line shows the result of NORMAL oscillator. We used 200 multi-bunch beams for the calculation. The NORMAL type utilizes the output coupler, so the oscillator is saturated around 100 bunches. The resulting pulse energy was about 1 μJ. The output THz pulse is multi-pulse so that the macro pulse energy will be more than 100 μJ. The blue line in Figure 7 shows the result of HIPEAK oscillator. The vertical axis indicates the single pulse energy extracted by the plasma mirror. The output pulse energy exceeds about 100 μJ around 200 pulse stacks in the oscillator. This pulse energy would be one of the most powerful THz pulse, which is produced by the accelerator consists of the rf electron gun alone.

CONCLUSIONS

We demonstrated the coherent Cherenkov radiation via electron-bunch tilting. A THz pulse of about 10 kW peak power was obtained by this technique. This technique can be utilized for lasing using an oscillator cavity. A calculation of the oscillator cavity is presented in this paper. We designed two types of oscillator which can achieve as much as 100-μJ pulse energy by the electron gun alone. We are planning to construct the oscillator and expect to realize the very high peak-power THz source in the near future.

REFERENCES

- [1] H. Hoshina *et al.*, *Sci. Rep.*, vol. 6, p. 27180 (2016).
- [2] K. Sakaue *et al.*, in *Proc. of IPAC'17*.
- [3] P. D. Cunningham *et al.*, *J. Appl. Phys.*, vol. 109 (2011) 043505.
- [4] R. Yanagisawa *et al.*, in *Proc. of IPAC'17*, THPAB119.
- [5] A. Y. Elezzabi *et al.*, *Opt. Lett.*, vol. 19, p. 898 (1994).

SIMULATING BEAM DYNAMICS IN COHERENT ELECTRON-COOLING ACCELERATOR WITH WARP

K. Shih[†], V. N. Litvinenko, I. Pinayev, Y. Jing, G. Wang, I. Petrushina, K. Mihara,
Brookhaven National Laboratory, New York, USA
Stony Brook University, SUNY, USA

Abstract

Coherent Electron Cooling (CeC) [1] is a novel cooling technique based on amplification of interaction between hadrons and electron by an FEL. If proven, this CeC could bring a revolution in hadron and electron-hadron colliders. A dedicated CeC proof-of-principle experiment is under way at RHIC collider (BNL) using a sophisticated SRF accelerator for generating and accelerating electron beam. This paper is dedicated to studies of beam dynamics in the CeC accelerator and specifically to emittance preservation in its ballistic compressions section. Two 500-MHz RF cavities are used for generating the necessary energy chirp leading in 1.56-MeV, 0.5-nsec-long electron bunched to compress them to 25-psec duration downstream. During the commissioning of the CeC accelerator we noticed that beam emittance can be strongly degraded when electron beam passes these 500 MHz RF cavities off-axis. We used a full 3D PIC code WARP to simulate effect of the off-axis beam propagation through these cavities.

INTRODUCTION

The CeC PoP experiment [2] is divided into two sections, the accelerator section and the cooling section (see Fig. 1). In the accelerator section, 1.05-MeV electron beam is first generated by a 113 MHz SRF gun. This electron beam is then “bunched” by two 500 MHz RF cavities and accelerated by a 704-MHz RF cavity to about 14.6 MeV. This acceleration provides the CeC electron beam with enough speed to match up with the RHIC’s hadron beam. After passing through a dogleg, electron beam will enter the cooling section.

The first part of the cooling section is the modulator, where the electron – hadron interaction takes place, the CeC electron beam will carry the density imprints of the RHIC’s hadron beam which will then be amplified by the

FEL undulators. At the end of cooling section, the electron beam will be allowed to merge with RHIC’s hadron beam and perform coherent electron cooling.

During the commissioning of CeC PoP machine, we allowed a 1.05-MeV electron off-axis electron beam to pass through two 500-MHz RF cavities. The cavities were aiming to provide an energy chirp for compressing a 0.5-nsec electron beam to 25 psec downstream. While we varied the phase of these cavities, a correlation between the phase and transverse positions of the off-axis electron beam following the cavities was observed. The data of transverse position of the off-axis electron beam was recorded by a beam-center position monitor (bpm) about 2 meters after the second 500 MHz RF cavity. The phase of both cavities was changed linearly in time, while a sine-wave like pattern of bpm readings were shown (see Fig. 2). This whole event was simulated by using the full-3D PIC code WARP. In WARP, an electron beam with the same initial condition to the experiment was used. It passed through two 500 MHz RF cavities with multiple offset values in the y-direction. The control comparison was also performed by allowing the same electron beam to pass through the same cavities at the center of the cavities. Details are shown in the next section.

ANALYSIS

We first simulated the effect of a single 500 MHz RF cavity to an off-axis electron beam. The beam had the same initial condition as with that of the experiment. The phase of cavity was set into zero-crossing (The phase with no total kinetic energy gain for the beam, but energy chirp). This was the default setting for the experiment. During the simulation, we allowed both the off-axis beam and the centered beam (electron beam without offset to the cavity center) to pass through this RF cavity. Multiple beam profiles

[†] kshih@bnl.gov

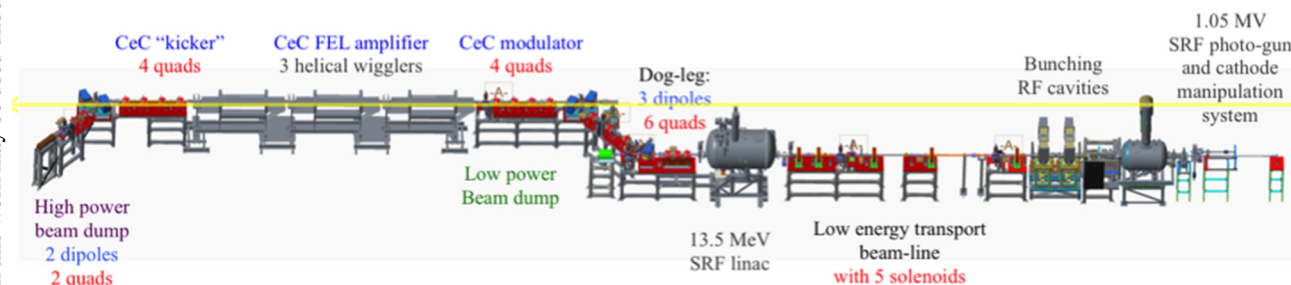


Figure 1: Schematic drawing of the CeC PoP Experiment machine. CeC electron beam travels from right to left.

Content from this work may be used under the terms of the CC BY 3.0 licence (© 2018). Any distribution of this work must maintain attribution to the author(s), title of the work, publisher, and DOI.

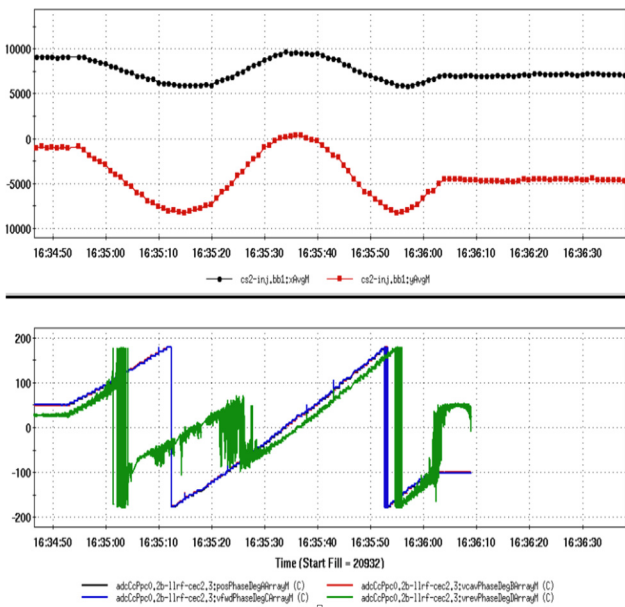


Figure 2: Experimental data of beam position monitor reading and 500-MHz cavity phase with off-axis electron beam.

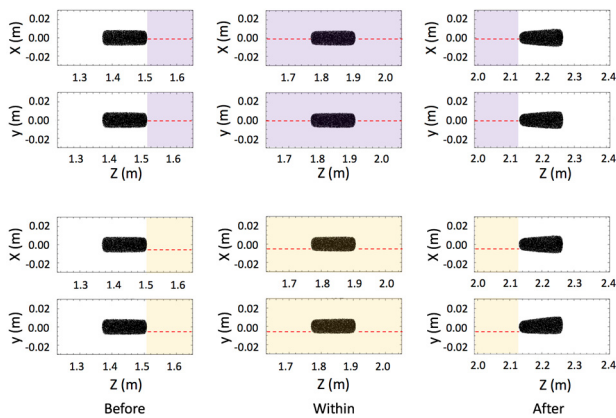


Figure 3: 2D beam profile comparison in (x,z) space. Purple and yellow region indicates the location of centered RF cavity and 5-mm +y off-axis RF cavity.

were recorded for both cases in the positions of before, inside, and after the RF cavity (see Figs. 3–6). Compared to the centered beam case (upper half of Figs. 3–5), an asymmetrical pattern was introduced to the off-axis beam after it passed through the RF cavity.

This pattern was in the same axis of the initial beam position offset relative to the cavity center, that being the y-axis (see Fig. 4). Also, this asymmetry in transverse phase space is affecting the beam center position significantly. Resulting a beam center position gain. However, the same effect had not been observed in the longitudinal direction (see Fig. 6). From this result, we can conclude that off-axis RF cavity dose create a transverse kick to the beam, in the same axis with the initial beam center position offset.

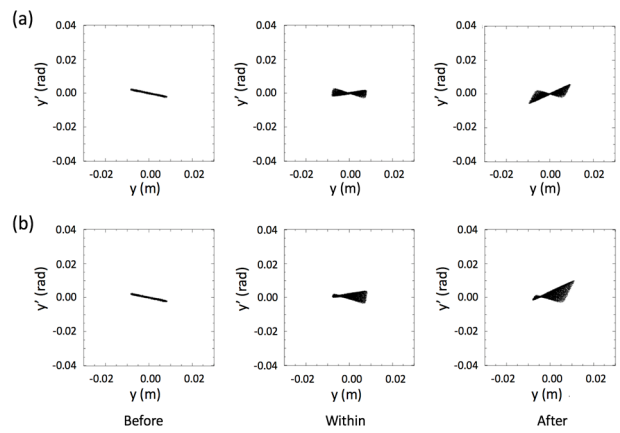


Figure 4: Beam phase-space $(y-y')$ comparison, starting with (a) a centered beam phase space, or (b) an off-axis beam phase space.

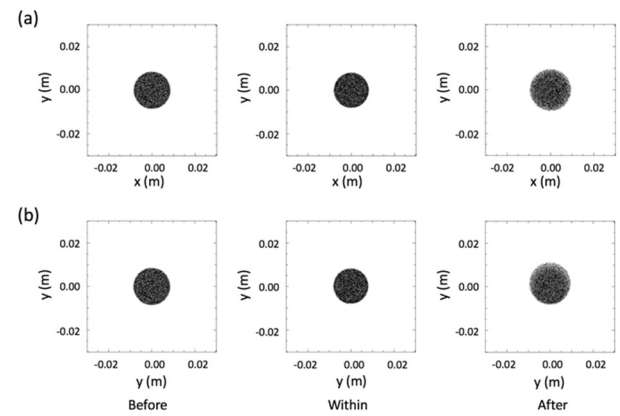


Figure 5: Two-dimensional $(x-y)$ beam profile comparison, starting with (a) a centered beam profile, or (b) an off-axis beam profile.

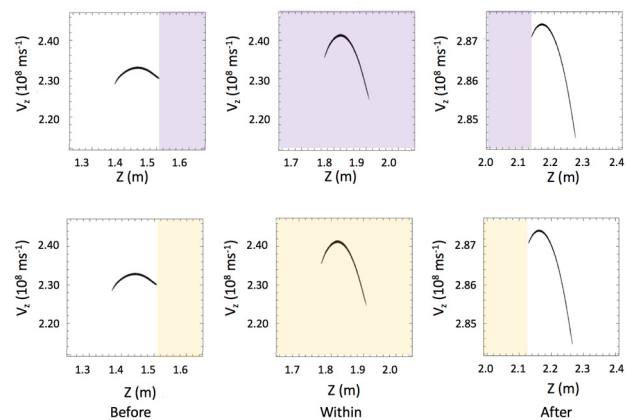


Figure 6: Longitudinal beam phase space $(z-v_z)$ comparison. Purple and yellow region indicates the location of centered RF cavity and 5-mm +y direction off-axis RF cavity.

Content from this work may be used under the terms of the CC BY 3.0 licence (© 2018). Any distribution of this work must maintain attribution to the author(s), title of the work, publisher, and DOI.

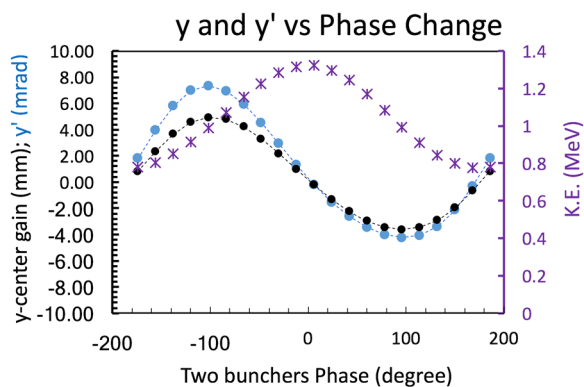


Figure 7: WARP simulation result on CeC electron beam passed through two 5-mm +y off-axis 500 MHz RF cavities.

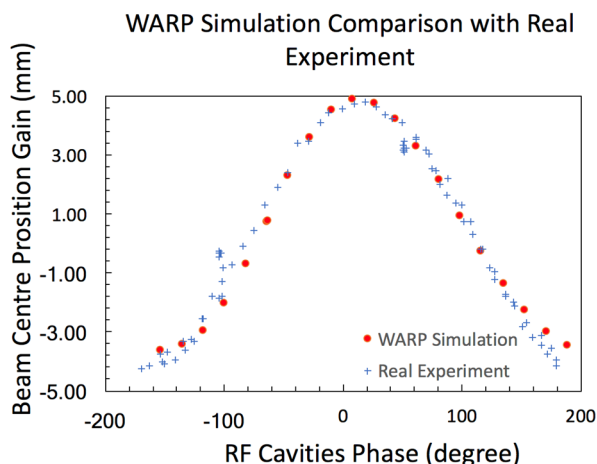


Figure 8: Comparison of WARP simulation with real experiment data of commissioning.

RESULTS

In the next simulation, the same off-axis electron beam was allowed to pass through two 500 MHz RF cavities, a recreation of the real experiment. The resulting beam center position gain was plotted against the RF phase change (see Fig. 7). Not only the beam center position gain, but also the final beam angle had a periodic oscillation while the RF cavities phase were changing. This result clearly indicates a similar sine-wave pattern as of that in (Fig. 1). However, it should be notice that the values of phase angle in (Fig. 7) is a dummy. Only the relative phase between data points carry meanings. After a constant shift in the phase data in (Fig. 7), we put on a comparison of WARP simulation (5 mm +y direction off-axis RF cavities) with the real experiment data (see Fig. 8).

The result shows a great agreement between WARP simulation and real experiment data. Beam center position after the RF cavities in WARP was drifting as expected in the experiment.

Moreover, according to the simulation, the drifting magnitude of both position and angle depend on the initial offset of the beam position, relative to the cavity's center (see

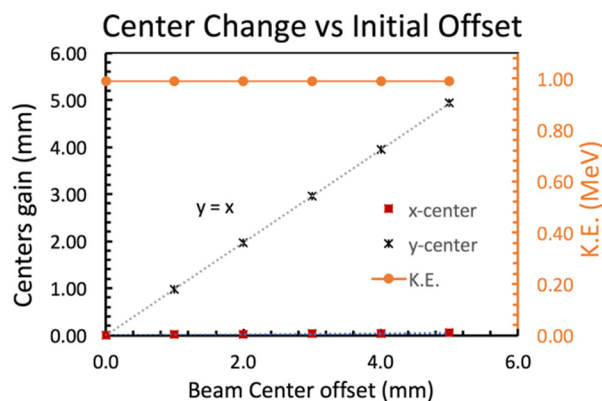


Figure 9: WARP Simulation result, showing final beam position offset for a given initial beam position offset.

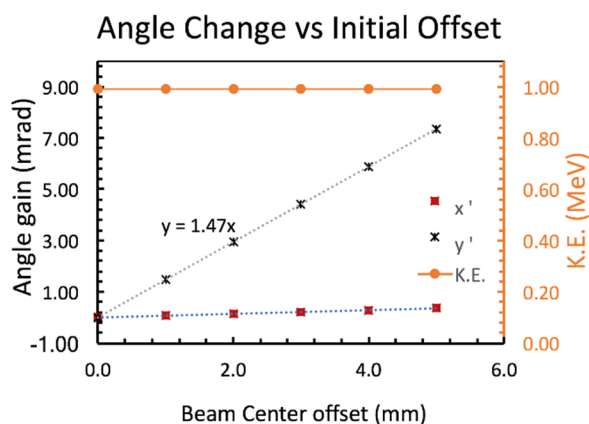


Figure 10: WARP Simulation result, showing final beam angle for a given initial beam position offset.

Figs. 9 and 10). If we change the initial beam center position offset in a fixed RF phase, the final beam position and beam angle change linearly. Therefore, scanning RF phase of cavities will have no effect on the final beam center position and beam angle for an initially centered electron beam.

SUMMARY

In summary, WARP simulation on off-axis RF cavities had a great agreement with the real experiment during the CeC PoP machine commissioning. The final beam position and angle were modified along the same axis of the beam initial offset (between the initial beam center and the cavity center), by the phase of the RF cavities. At some phase angle, this offset can be canceled. While it can also be magnified in pluses or minus direction at certain phase angles. Resulting beam final center position and angle oscillate with the RF phase angle. Moreover, the magnitude of this oscillation depends linearly to the value of initial beam position offset. Larger the initial offset, larger the oscillation amplitude. There will be no oscillation for initial centered beam.

In the future, we will use WARP to construct a full start to end simulation of CeC PoP machine. This not only can establish a new numerical model for the experiment, but also proof the capability of WARP simulation.

ACKNOWLEDGEMENT

Work is supported by Brookhaven Science Associates, LLC under Contract no. DEAC0298CH10886 with the U.S. Department of Energy, DOE NP office grant DE-FOA-0000632, and NFS grant PHY-1415252.

REFERENCES

- [1] V. Litvinenko and Y. Derbenev, "Coherent electron cooling," *Physical Review Letters* 102.11, 114801, 2011.
- [2] V. Litvinenko *et al.* "Proof-of-principle experiment for FEL-based coherent electron cooling," no. BNL-96405-2011-CP. Brookhaven National Laboratory (BNL) Relativistic Heavy Ion Collider, 2011.

DEVELOPMENT OF MID-INFRARED PHOTOACOUSTIC SPECTROSCOPY SYSTEM FOR SOLID SAMPLES AT KYOTO UNIVERSITY FREE ELECTRON LASER FACILITY

J. Okumura[†], H. Zen, T. Kii, and H. Ohgaki,
Institute of Advanced Energy, Kyoto University, Uji, Japan

Abstract

A Photoacoustic Spectroscopy (PAS) system for solid samples using a Mid-Infrared Free Electron Laser (MIR-FEL) with a high-resolution grating monochromator is under development at Kyoto University Free Electron Laser Facility. Our target is to achieve 0.2% resolution in 10 μm . We designed a PAS cell whose internal volume was small for reducing the loss of the acoustic energy and by using cups for the sample holder to exchange the samples easily. We also conducted experiments to check the sensitivity of the developed PAS system using powdered $\text{CaSO}_4 \cdot 2\text{H}_2\text{O}$ and CaCO_3 as samples. The monochromator had the wavelength resolution of 0.015 μm (0.15% at 10- μm wavelength) in the experiments. As the result, we obtained quite high S/N ratio PAS signals with the FEL beam whose expected spectral width was 0.15% and whose power was reduced to one-eightieth by the monochromator.

INTRODUCTION

When material (whether solid, liquid or gas) is illuminated by light, acoustic wave is generated. This is called Photoacoustic effect. Especially with solid, this phenomenon is explained by RG Theory [1]. According to this theory, light is absorbed by the sample and its energy is converted to a thermal energy. The thermal energy causes the temperature distribution at the circumambient gas of the sample, and a pressure variation is arisen. Thus, the acoustic pressure wave is produced. Since the intensity of the acoustic pressure wave depends on the light absorption of the sample, we can directly obtain the absorption spectrum of the sample by measuring the intensity of pressure wave as the function of the illumination wavelength. This method is called Photoacoustic Spectroscopy (PAS).

When we use a pulsed infrared (IR) laser, PAS enables us IR absorption spectrum measurements of solid samples without pre-processing of samples such as the KBr pellet preparation and fine polish to very small thickness. As a feature of the PAS, its sensitivity and resolution depend on the intensity and spectral width of the IR light, respectively. Since a mid-infrared Free Electron Laser (MIR-FEL) is an intense, quasi-monochromatic and tunable laser in MIR region, the method of PAS with MIR-FEL (FEL-PAS) was proposed [2, 3]. In these previous works on the FEL-PAS, the spectral resolution was limited be

cause the used FEL beam had the spectral width of 1%. Therefore, they could not resolve sharp peaks in previous experiments. The spectral resolution can be significantly improved by inserting a monochromator on the optical path of the PAS system.

In order to realize this idea and targeting 0.02 μm resolution in 10 μm wavelength region, a high-resolution PAS system for solid samples using an MIR-FEL with a monochromator is under development at Kyoto University Free Electron Laser Facility (KU-FEL). We designed a new PAS cell and conducted demonstration experiments using this system to evaluate the system performance. In this paper, the outline of PAS system and demonstration experiments are briefly reported.

HIGH-RESOLUTION PAS SYSTEM

Figure 1 shows the outline of a high-resolution PAS system for solid samples. As the light source, we use KU-FEL [4]. A grating monochromator (DK240, CVI) whose grating was 75 groove/mm was put into the optical path. The monochromator had the wavelength resolution of 0.015 μm when the entrance and exit slit were adjusted to 0.3 mm. The FEL beam after passing through the monochromator was injected to a parabolic mirror and converted to the quasi-parallel beam. Then the FEL beam was split into two by a beam splitter. The transmitted light was monitored by a pyroelectric detector and the reflected light was focused on the sample within the PAS cell by the focusing mirror.

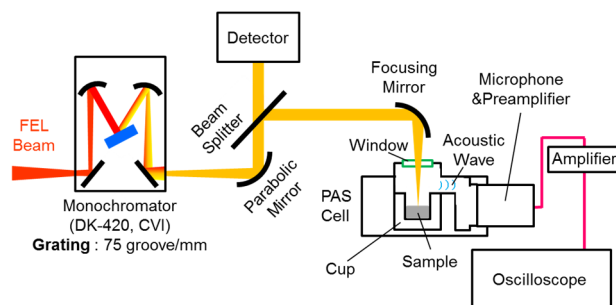


Figure 1: The outline of a high-resolution PAS system for solid samples using KU-FEL and monochromator.

[†] okumura.jumpei.24c@st.kyoto-u.ac.jp

Content from this work may be used under the terms of the CC BY 3.0 licence (© 2018). Any distribution of this work must maintain attribution to the author(s), title of the work, publisher, and DOI.

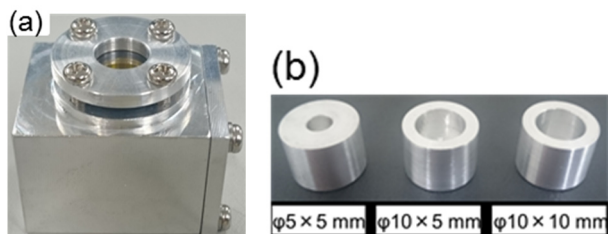


Figure 2: (a) The PAS cell made of aluminium and containing a ZnSe window. (b) Three cup-type sample holders which was detachable from the cell structure. Left one: $\phi 5 \times 5$ mm, Middle one: $\phi 10 \times 5$ mm, Right one: $\phi 10 \times 10$ mm.

The PAS cell was made of aluminium and it had an uncoated ZnSe window to transmit the FEL light. The internal volume of this cell was designed as small as possible (about 0.98 cm^3) to reduce the loss of the acoustic energy. The solid samples in the new PAS cell can be easily exchanged by using cup type sample holders which was detachable from the cell structure (Fig. 2 (b)). The acoustic wave was detected by the microphone (MI-1233, Ono Sokki), and converted into a voltage signal and amplified by a preamplifier (MI-3110, Ono Sokki), and sensor amplifier (SR-2200, Ono Sokki).

We conducted two demonstration experiments using standard samples to check the sensitivity of the developed PAS system. We measured the signal in wider wavelength region from 8.0 to 11.0 μm with 0.5 μm step in the first experiment, and in narrower region from 8.0 to 9.5 μm with 0.1 μm step in the second experiment, respectively.

DEMONSTRATION EXPERIMENTS

The experimental setup is shown in Fig. 3. The typical parameters of the FEL beam used in this experiment are shown in Table 1. The macro-pulse energy was reduced to one-eightieth after the monochromator, and the expected spectral width was 0.015 μm (0.15% at 10 μm). Powdered $\text{CaSO}_4 \cdot 2\text{H}_2\text{O}$ and CaCO_3 were used as standard samples, because $\text{CaSO}_4 \cdot 2\text{H}_2\text{O}$ has the strong IR absorption peak at the range from 8.0 to 11.0 μm , whereas CaCO_3 does not have such peak [5].

The transmittance spectra of those samples measured by FT-IR are shown in Fig. 4. In addition, powdered carbon samples (called Carbon Black) was used in order to normalize the signal. The gain of sensor amplifier was set to +30 dB. The sampling rate and the number of data points of the oscilloscope used for recording the voltage waveform from the microphone were set to 500 kHz and 10^5 , respectively. At one measurement condition, we recorded the voltage signal waveform 100 times for each sample and took an average.

Parameter	Value
Macro-pulse duration	$\sim 2 \mu\text{s}$
Macro-pulse repetition rate	2 Hz
Macro-pulse energy (before the monochromator)	$\sim 24 \text{ mJ}$
Macro-pulse energy (after the monochromator)	$\sim 0.3 \text{ mJ}$
Expected spectral width	$\sim 0.015 \mu\text{m}$ at 10 μm

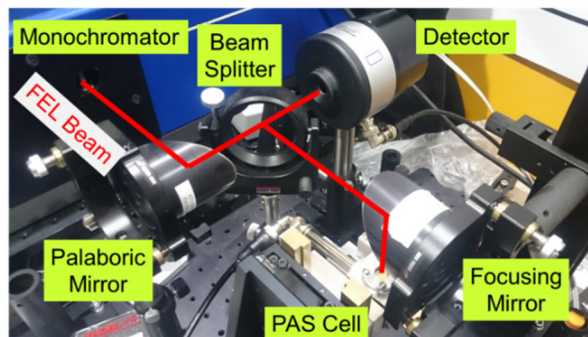


Figure 3: Key components of the experimental setup.

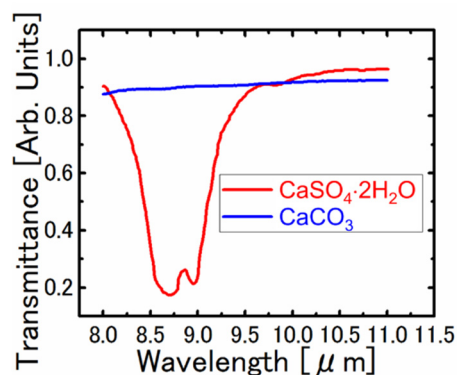


Figure 4: The IR transmittance spectra of $\text{CaSO}_4 \cdot 2\text{H}_2\text{O}$ and CaCO_3 [5].

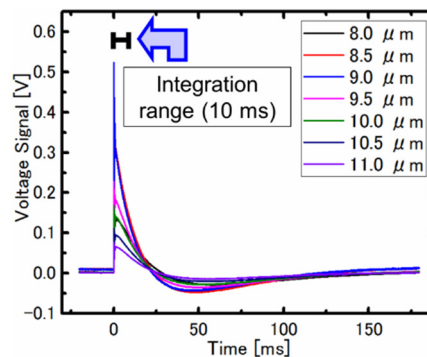


Figure 5: The voltage signal waveforms for $\text{CaSO}_4 \cdot 2\text{H}_2\text{O}$ from 8.0 to 11.0 μm with the interval of 0.5 μm .

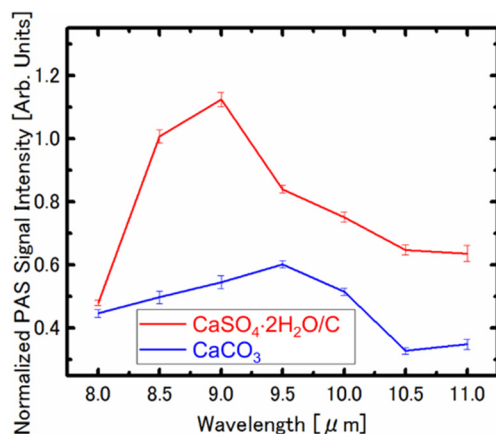


Figure 6: The wavelength dependence of the integrated voltage signal waveforms for $\text{CaSO}_4 \cdot 2\text{H}_2\text{O}$ and CaCO_3 . They are normalized by FEL intensity and Carbon Black. The specific peaks at 8.5 and 9.0 μm were observed in $\text{CaSO}_4 \cdot 2\text{H}_2\text{O}$. The error bars represent the standard deviation of 100 samples.

Figure 5 shows the waveforms of the averaged voltage signal for $\text{CaSO}_4 \cdot 2\text{H}_2\text{O}$ at different excitation wavelength. According to this graph, it was confirmed that a high S/N ratio voltage signal could be measured. The integrals of the voltage signal waveform in the time range from 0.06 to 10.06 ms (for 10 ms) were calculated and normalized by the FEL intensity measured by the reference detector for each sample. The normalized integrated values of $\text{CaSO}_4 \cdot 2\text{H}_2\text{O}$, CaCO_3 were also normalized by that of Carbon Black. Figure 6 shows the wavelength dependence of the PAS signal from $\text{CaSO}_4 \cdot 2\text{H}_2\text{O}$ and CaCO_3 . As is shown in the figure, the specific peaks at 8.5 and 9.0 μm were observed in $\text{CaSO}_4 \cdot 2\text{H}_2\text{O}$. This result is consistent with the reported IR transmittance spectrum (Fig. 4) [5]. Therefore, we successfully measured the PAS signals (the voltage signals) by using the developed system.

In Fig. 7, the frequency power spectra of the voltage signal waveforms for $\text{CaSO}_4 \cdot 2\text{H}_2\text{O}$ is shown at the frequency range from 0 to 20000 Hz, because the frequency response range of the microphone is from 20 to 20000 Hz. In this graph, a strong peak is observed at around 4000 Hz, and small peak was observed at around 13000 Hz. These peaks are considered as the primary and tertiary order resonant frequency of PAS cell, respectively.

Next, PAS measurement of $\text{CaSO}_4 \cdot 2\text{H}_2\text{O}$ sample in the wavelength region from 8.0 to 9.5 μm with the interval of 0.1 μm . As same as the first experiment, we measured the voltage signal waveform (the PAS signal) 100 times, and take an average. The integral of the voltage signal waveform was calculated at the same range and normalized by the FEL intensity and the PAS signal of Carbon Black. The result is shown in Fig. 8 which is also consistent with the reported IR spectrum (Fig. 4) [5]. In this result, it was confirmed that the small dip at 8.8 μm , which is also visible in the transmittance spectrum shown in Fig. 4, can be recognized in the obtained PAS spectrum.

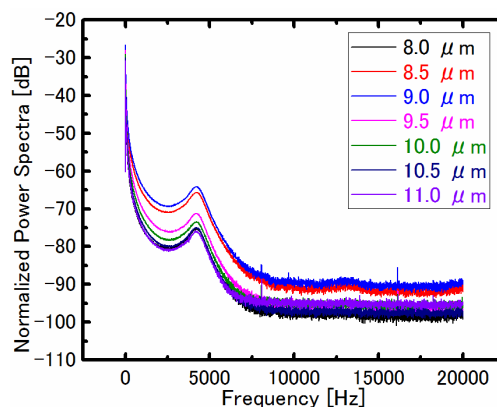


Figure 7: The frequency power spectra of the voltage signal waveforms for $\text{CaSO}_4 \cdot 2\text{H}_2\text{O}$. A strong peak was observed at around 4000 Hz, and small peak was observed at around 13000 Hz.

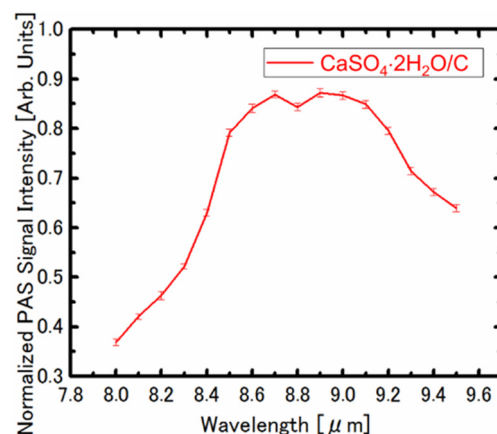


Figure 8: The wavelength dependence of the integrated voltage signal waveforms for $\text{CaSO}_4 \cdot 2\text{H}_2\text{O}$ from 8.0 to 9.5 μm by 0.1 μm step. They are normalized by FEL intensity and Carbon Black. The error bars represent the standard deviation of 100 samples.

In order to confirm whether the developed system has expected resolution (0.15%) or not, we should measure a reference sample which has narrower absorption peak to confirm the resolution of this system. In addition, the S/N ratio of PAS signal is quite high, so we will evaluate the minimum required number of samples for PAS measurement.

CONCLUSION

A high-resolution PAS system for solid samples is under development at Kyoto University Free Electron Laser Facility. We aim to achieve 0.2% resolution in 10 μm . A PAS cell which has a small internal volume with cup type sample holders to exchange the sample easily has been designed and fabricated. In order to evaluate the system performance, two demonstration experiments have been conducted. One was a PAS measurement of $\text{CaSO}_4 \cdot 2\text{H}_2\text{O}$ and CaCO_3 in wider wavelength region with a 0.5- μm

Content from this work may be used under the terms of the CC BY 3.0 licence (© 2018). Any distribution of this work must maintain attribution to the author(s), title of the work, publisher, and DOI.

step. The other was a PAS measurement of $\text{CaSO}_4 \cdot 2\text{H}_2\text{O}$ in a narrower wavelength region and with 0.1- μm step. As the result, the PAS signals with high S/N ratio and the reasonable wavelength dependences were observed for both $\text{CaSO}_4 \cdot 2\text{H}_2\text{O}$ and CaCO_3 , even though the FEL beam power was reduced to one-eightieth by the monochromator which had the wavelength resolution of 0.15% at 10- μm wavelength.

ACKNOWLEDGEMENT

The authors deeply thank Dr. Yasumoto, AIST, for his kind support and suggestions on this study.

REFERENCES

- [1] A. Rosenzwaig and A. Gersho, *J. Appl. Phys.*, **47**, pp. 64-69, 1976.
- [2] M. Yasumoto *et al.*, *Proc. of FEL'04*, pp. 703-705.
- [3] M. Yasumoto *et al.*, *Eur. Phys. J. Special Topics*, **153**, pp. 37-40, 2008.
- [4] H. Zen *et al.*, *Physics Procedia*, **84**, pp. 47-53, 2016.
- [5] Coblenz Society, Inc., "Evaluated Infrared Reference Spectra" in *NIST Chemistry WebBook, NIST Standard Reference Database 69*, eds. P.J. Linstrom and W.G. Mallard, National Institute of Standards and Technology, Gaithersburg MD, doi:10.18434/T4D303.

STUDY ON SECOND HARMONIC GENERATION IN SiC USING INFRARED FEL

S. Tagiri[†], H. Zen, T. Kii, and H. Ohgaki,
 Institute of Advanced Energy, Kyoto University, Uji, Japan

Abstract

Mode-selective phonon excitation (MSPE) is an attractive method for studying the lattice dynamics (e.g. electron-phonon interaction and phonon-phonon interaction). In addition, MSPE can control electronic, magnetic, and structural phases of materials. In 2013, we have directly demonstrated MSPE of a bulk material (6H-SiC) with MIR-FEL (KU-FEL) by anti-Stokes (AS) Raman scattering spectroscopy. Recently, we have certified that the Sum Frequency Generation (SFG) also occurs with AS Raman scattering. For distinguishing between the AS Raman scattering and SFG, we need to know the nonlinear susceptibility and the transmittance. The coefficients can be measured by the Second Harmonic Generation (SHG) spectroscopy. This paper outlines of the measurement system and reports preliminary results with a 6H-SiC sample.

INTRODUCTION

The electron-phonon interaction influences physical properties of solid-state materials. Thus, the clarification of the interaction is required for understanding basic physical properties of solid-state materials and developing high-performance devices [1,2]. To clarify the interaction, it is important to understand the relation between the electronic state and the excitation of a particular lattice vibration (phonon). Mode-selective phonon excitation (MSPE) is one of the attractive methods in the solid-state physics because it can be a powerful tool for the study of ultrafast lattice dynamics (e.g. electron-phonon interaction and phonon-phonon interaction). Not only for that, but MSPE can control electronic, magnetic, and structural phases of ma-

terials [3-5]. By irradiating a mid-infrared pulse laser tuned to the resonant wavelength of a specific phonon, the direct excitation of a specific phonon mode is available [3,5].

We have developed a technique which can directly observe the vibration of a particular phonon mode by using AS Raman scattering spectroscopy (Fig. 1) [6]. By using the technique, the MSPE induced by MIR-FEL has been directly demonstrated with a bulk material of 6H-SiC (Fig. 2)[7]. However, we have certified that SFG also occurs together with AS Raman scattering. For distinguishing between the AS Raman scattering and SFG, we need to know the nonlinear susceptibility and the transmittance. In the previous study at FHI-FEL [8], the wavelength dependence of nonlinear susceptibilities $\tilde{\chi}^{(2)}$ of 4H-SiC and 3C-SiC in MIR region have been experimentally characterized by the SHG spectroscopy.

The SHG intensity scales linearly with nonlinear polarization P , which can be given by the formula [9],

$$\vec{P}(2\omega) = \tilde{\chi}^{(2)}(2\omega, \omega, \omega) : \left(\vec{L}_1(\omega) \vec{E}_1(\omega) \right) \left(\vec{L}_2(\omega) \vec{E}_2(\omega) \right),$$

where ω denotes frequency of incident light. The frequency of SHG is twice as great as it of incident light. $\vec{L}_{1(2)}$ are the Fresnel transmission tensors for two incident beams representing the macroscopic local field corrections [10], and $\vec{E}_{1(2)}$ are the incident electric field vectors. The Fresnel transmission tensor can be evaluated by theoretical calculation. The nonlinear susceptibility must be experimentally determined by the equation of SHG spectroscopy in the reference [8]. The reflected second harmonic intensity is given by projecting the nonlinear polarization onto the field direction of the reflected [10].

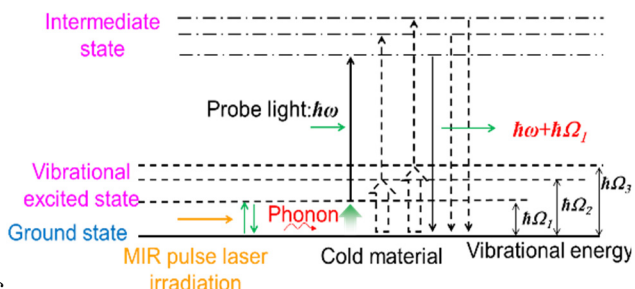


Figure 1: Schematic of the principle of demonstration experiment of MSPE induced by MIR-FEL irradiation. The anti-Stokes-Raman scattering was utilized to observe the excited state [3].

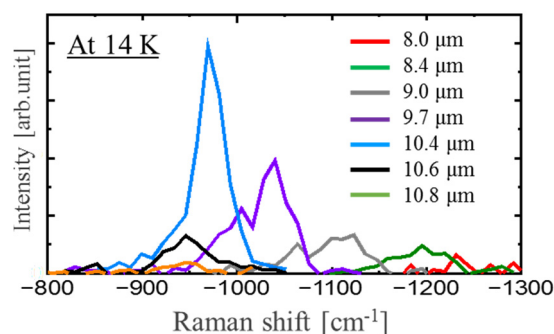


Figure 2: Anti-Stokes Raman scattering spectra measured with MIR-FEL and pico-second laser at 14K [7].

[†] tagiri.shunsuke.53a@st.kyoto-u.ac.jp

Content from this work may be used under the terms of the CC BY 3.0 licence (© 2018). Any distribution of this work must maintain attribution to the author(s), title of the work, publisher, and DOI.

In this study, a SHG spectroscopy system has been developed at a MIR-FEL facility, KU-FEL, for determining the nonlinear susceptibility of 6H-SiC. The preliminary experimental results are reported in this paper.

CALCULATION

We calculate Fresnel transmission coefficient $L_{xx(yy/zz)}$ of 6H-SiC based on the equations in the previous report [8]. The equations are as follows:

$$L_{xx}(\omega, \theta^i) = \frac{2k_{z,e}^{SiC}(\omega, \theta^i)}{\epsilon_{\perp}(\omega)k_z^{air}(\omega, \theta^i) + k_{z,e}^{SiC}(\omega, \theta^i)} \quad (1)$$

$$L_{yy}(\omega, \theta^i) = \frac{2k_z^{air}(\omega, \theta^i)}{k_z^{air}(\omega, \theta^i) + k_{z,o}^{SiC}(\omega, \theta^i)} \quad (2)$$

$$L_{zz}(\omega, \theta^i) = \frac{\epsilon_{\perp}(\omega)}{\epsilon_{\parallel}(\omega)} \frac{2k_z^{air}(\omega, \theta^i)}{\epsilon_{\perp}(\omega)k_z^{air}(\omega, \theta^i) + k_{z,e}^{SiC}(\omega, \theta^i)} \quad (3)$$

$$\epsilon_{\perp}(\omega) = \epsilon_{\perp}^{\infty} \left(1 + \frac{\omega_{LO,\perp}^2 - \omega_{TO,\perp}^2}{\omega_{TO,\perp}^2 - \omega^2 - i\omega\gamma_{TO,\perp}} \right) \quad (4)$$

$$\epsilon_{\parallel}(\omega) = \epsilon_{\parallel}^{\infty} \left(1 + \sum_{j=0,1} \frac{\omega_{LO,\parallel j}^2 - \omega_{TO,\parallel j}^2}{\omega_{TO,\parallel j}^2 - \omega^2 - i\omega\gamma_{TO,\parallel j}} \right) \quad (5)$$

$$k_{z,o}^{SiC}(\omega, \theta^i) = \frac{2\pi\omega}{c_0} \sqrt{\epsilon_{\perp}(\omega) - \sin^2(\theta^i)} \quad (6)$$

$$k_{z,e}^{SiC}(\omega, \theta^i) = \frac{2\pi\omega}{c_0} \sqrt{\epsilon_{\perp}(\omega) - \frac{\epsilon_{\perp}(\omega)}{\epsilon_{\parallel}(\omega)} \sin^2(\theta^i)} \quad (7)$$

The parameters used to calculate the Fresnel transmission coefficient are listed in Table 1.

Result of calculation of the Fresnel transmission coefficients are shown in Fig. 3. L_{xx} and L_{yy} have a peak at 970–980 cm^{-1} . On the other hand, L_{zz} has a peak at 1055 cm^{-1} . In this wavenumber region, the nonlinear susceptibility of 6H-SiC is not expected to have any peak similar to 3C-SiC and 4H-SiC [8]. Therefore, it is expected that the observed peaks of SHG at 975 cm^{-1} and 1055 cm^{-1} are due to the high Fresnel transmission coefficient.

Table 1: Parameters Used to Calculate the Fresnel Transmission Coefficient of 6H-SiC [8,11-14]

	ω_{TO}	ω_{TO}	ω_{TO}	ϵ_{∞}
Planar strong	797 cm^{-1}	3.5 cm^{-1}	969.9 cm^{-1}	6.58
Axial strong	788 cm^{-1}	3.5 cm^{-1}	965 cm^{-1}	6.72
Axial weak	775 cm^{-1}	1.85 cm^{-1}	889 cm^{-1}	-

EXPERIMENT CONDITIONS AND SETUP

We used a 6H-SiC sample which is the same sample used in the previous studies [6, 7, 15]. It was a commercially available semi-insulator type 6H-SiC (Xlamen Powerway Advanced Material Co., LTD) with dimension of 15 mm × 15 mm × 0.33 mm and the crystal orientation of (0001). The known phonon modes of 6H-SiC around 10 μm are listed in Table 2 [11].

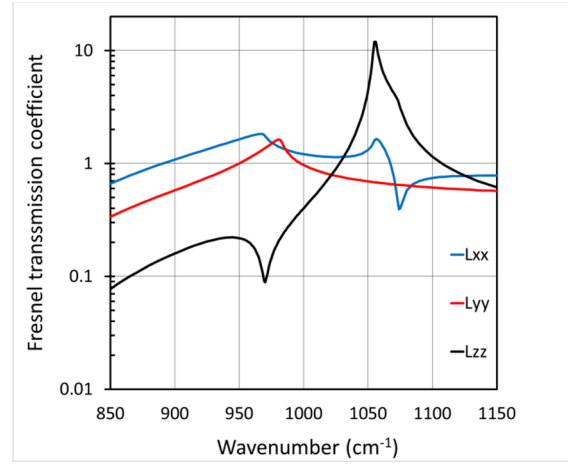


Figure 3: Calculated Fresnel transmission coefficient of 6H-SiC by the reference experiment [7].

Table 2: Phonon Modes of 6H-SiC [11]

wavenumber (wavelength)	infrared	Raman
965 cm^{-1} (10.4 μm)	active	active
797 cm^{-1} (12.5 μm)	active	inactive
787 cm^{-1} (12.7 μm)	inactive	active
767 cm^{-1} (13.0 μm)	inactive	active

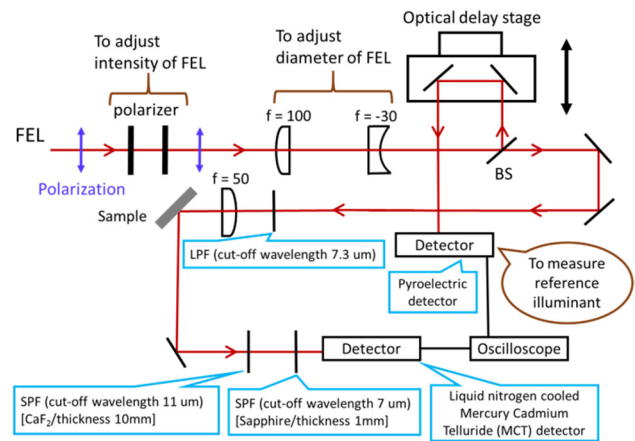


Figure 4: Schematic of the experimental setup.

Content from this work may be used under the terms of the CC BY 3.0 licence (© 2018). Any distribution of this work must maintain attribution to the author(s), title of the work, publisher, and DOI.

The schematic of the experimental setup is illustrated in Fig. 4. To adjust the intensity of FEL irradiated on the 6H-SiC sample, two wire-grid polarizers were used. In order to keep the polarization angle of FEL beam on the sample, the angle of second polarizer was kept constant and that of first polarizer was varied for changing the total attenuation of this polarizer pair. A telescope was used to reduce the beam size by one third.

We split FEL beam into two with a beam splitter and simultaneously measured the SHG and incident FEL intensities. SHG was measured by a highly sensitive liquid nitrogen cooled MCT detector (J15D12, Judson). A long pass filter was used to block the harmonic components inherently included in FEL. The FEL beam was focused on the sample using a focusing lens. The fundamental beam was blocked by a 10-mm thick CaF₂ plate and a 1-mm thick sapphire plate so as to inject only SHG beam on to the MCT detector. The polarization of incident light was adjusted to P-polarization, because P-polarization was used in the previous MSPE experiments [6,7,15].

At first, we confirmed the relationship between the intensity of irradiated pulse and MCT signal with changing FEL intensity. Next, relative SHG efficiencies as the function of the incident FEL wavelength were measured.

RESULTS AND DISCUSSION

The measured relationship between the intensity of incident FEL pulse and the signal intensity measured by the MCT detector at the wavelength of 8.0 μm is shown in Fig. 5. The fitting curve whose function is $y = ax^2 + b$ (red line) is also plotted in Fig. 5. The observed MCT signal intensity follows a quadratic dependence on the intensity of the incident FEL. As the result, it was confirmed that the measured signal is SHG generated on the 6H-SiC sample.

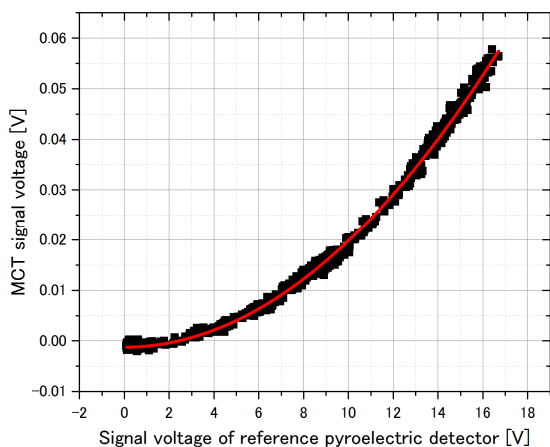


Figure 5: Relationship between the intensity of FEL pulse and the signal intensity measured by the MCT detector. Black dots represent the measured data. Red line represents the fitting curve with the function of $y = ax^2 + b$.

Next, the second-order coefficients of FEL intensity dependences at each FEL wavelength were measured to determine the SHG efficiency dependence on the wavelength. We adjusted the angle of the mirror arranged after the sample by fundamental beam without the CaF₂ and sapphire plates. The result of the second-order coefficient dependence on the FEL wavelength is shown in Fig. 6. In this case, single weak peak was observed at 970 cm⁻¹ while the highest second-order coefficient was observed at 1111 cm⁻¹.

After that, we adjusted the mirror after the sample to have the highest SHG signal on the MCT detector at each FEL wavelength. The measured dependence of the second-order coefficient on the FEL wavenumber is shown in Fig. 7. In this case, two peaks around 970 cm⁻¹ and 1050 cm⁻¹ were observed. This result suggested that the angular distribution of SHG has strong wavelength dependence, because we needed to adjust the mirror angle to obtain the maximum intensity for each wavelength. Under the assumption that $\chi^{(2)}$ possesses no peak in this wavenumber region as reported [9], a small peak expected to appear around 970 cm⁻¹, and a large peak expected to appear around 1055 cm⁻¹ from the calculated result of the Fresnel transmission coefficient shown in Fig. 3. Figure 7 indicates two peaks in these corresponding wavenumbers.

As a result, we successfully observed SHG signal from 6H-SiC. We could deduce that the angular distribution of the SHG depends on the FEL wavelength from the comparison of the second-order coefficients shown in Figs. 6 and 7. The measured SHG dependence on the FEL wavelength was not sharp as 4H-SiC and 3C-SiC as reported [8]. Further investigation of the developed measurement system need to be performed.

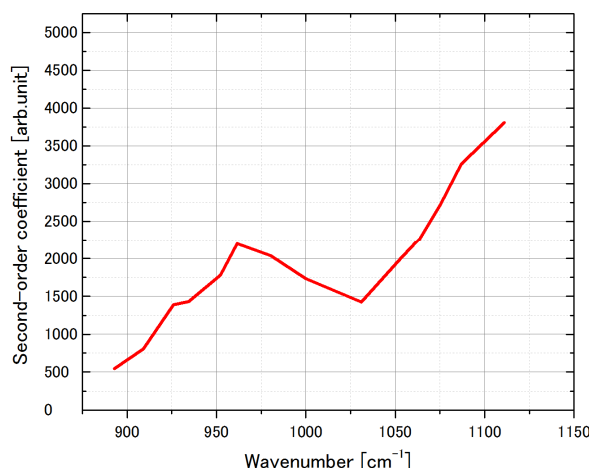


Figure 6: The second-order coefficient when we adjusted optical axis by fundamental wave and fixed optical axis.

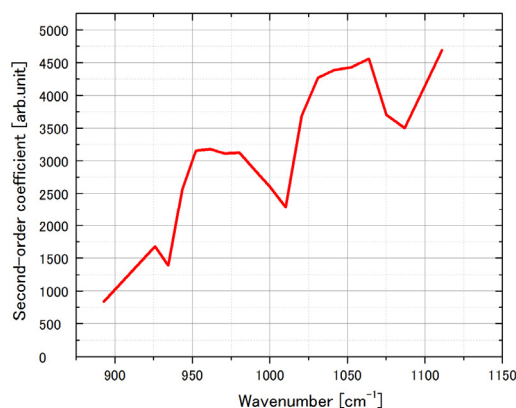


Figure 7: The second-order coefficient when we adjusted the angle of a mirror after the sample at each wavelength to get maximum SHG signals.

CONCLUSION

A SHG spectroscopy system has been developed to measure the second-order nonlinear susceptibility of 6H-SiC in the MIR region. It was confirmed that the SHG generated on the 6H-SiC sample can be measured by the developed system. The wavelength dependence of SHG intensity had some similarity with the calculated Fresnel transmission. The spatial distribution of the SHG depends on the wavelength.

REFERENCES

- [1] K. Kato *et al.*, *J. Appl. Phys.* 111, 113520 (2012).
- [2] T. Sonobe *et al.*, *AIP Conf. Proc.* 1214, 23 (2010).
- [3] M. Rini *et al.*, *Nature* 449, 72-74 (2007).
- [4] M. Först *et al.*, *Phys. Rev. B* 84, 241104 (2011).
- [5] D. Fausti *et al.*, *Science* 331, 189 (2011).
- [6] K. Yoshida *et al.*, *Appl. Phys. Lett.* 103, 182103 (2013).
- [7] T. Murata, thesis for Masters degree, Kyoto University, (2016).
- [8] A. Paarmann *et al.*, *Phys. Rev. B* 94, 134312 (2016).
- [9] A. Paarmann *et al.*, *Appl. Phys. Lett.* 107, 081101 (2015).
- [10] Y.R. Shen, *Annu. Rev. Phys. Chem.* 40, 327 (1989).
- [11] S. Nakashuma and H. Harima, *Phys. Stat. Sol. A* 162, 39 (1997).
- [12] H. Mutschke, A. Andersen, D. Clement, T. Henning, and G. Peiter, *Astron. Astrophys.* 345, 187 (1999).
- [13] F. Engelbrecht and R. Helbig, *Phys. Rev. B* 48, 15698 (1993).
- [14] J. Bluet, K. Chourou, M. Anikin, and R. Madar, *Materials Science and Engineering B* 61-62, 212 (1999).
- [15] T. Katsurayama *et al.*, *Proc. of IRMMW-THz'16*, T5P.25.05.

SIMULATION OF PHASE SHIFTERS BETWEEN FEL AMPLIFIERS IN COHERENT ELECTRON COOLING*

Yichao Jing^{†,1}, Vladimir N. Litvinenko^{1,2}, Igor Pinayev¹

¹Collider-Accelerator Department, Brookhaven National Laboratory, Upton, NY, USA

²Physics Department, Stony Brook University, NY, USA

Abstract

Coherent electron Cooling (CeC) [1] is a proposed advanced beam cooling method that has the potential of reducing the ion beam emittance in significantly shorter amount of time compared to existing cooling methods. A high gain FEL, composed of three permanent magnet helical wigglers, is acting as an amplifier of the ion's signals picked up by electron beam in CeC. A self-consistent simulation which takes the space and possible phase shifts between wigglers into account is crucial in determining the performance of the FEL. The authors developed an algorithm based on the well-used GENESIS [2] code to treat the propagation of particles and radiations in between wigglers and predicted the FEL performance with different beamline layouts. The authors will present their simulation setup and results.

INTRODUCTION

The CeC beamline (Figure 1) consists of low energy beam transport (where electron beam is prepared and accelerated to a total energy of 14.6 MeV), a dogleg section to transport the beam to a common section where the electron beam is co-propagating with the hadron beam. In the common section, the electron beam is picking up information from hadron beam in modulator section (consists of four quadrupoles for beam optics tuning). Then the information is amplified in the FEL section and reacts back to the hadron beam with proper phase adjustment to cool the hadron beam, i.e., to reduce the hadron beam's energy spread and phase space areas. The performance of the CEC is highly dependent on the FEL gain and phase preservation. Thus, a self-consistent simulation of the FEL section is crucial in determining the required electron beam properties and in predicting the machine setups to characterize the cooling.

The FEL section consists of three helical wigglers composed of permanent magnets. The magnetic length for each wiggler is about 250 cm while the wigglers are separated by a drift space of about 42 cm. A schematic drawing of the detailed FEL can be found in Fig. 2 [3]. In between two wigglers, a three pole C-type chicane is used to properly delay the phases of the electron beam (to match

with the phases of the radiation fields) and potentially to change the gain of the FEL and thus to adjust the cooling time of the CeC. In the following section of this paper, the authors will explain a method to simulate the three wigglers together with the drifts in between wigglers. The authors will examine how to maximize the beam-field matching using the phase shifter. The authors will also discuss how this study is affecting the understanding of the gain and performance of the cooling.



Figure 1: Engineering drawing of CeC beamline (electron beam travels from right to left).

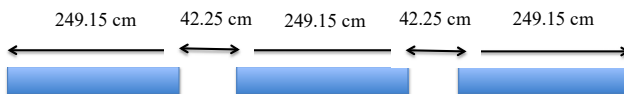


Figure 2: Schematic drawing of CeC FEL section (consisting of three wigglers and drifts in between).

FEL SIMULATION SETUP

The authors used GENESIS for the FEL process simulation. It is to our interest that the pondero-motive phases could be adjusted so that the relative phasing between the electron beam and the laser fields could be varied and FEL gain of signal could be studied under various beamline setups. In order to simulate such effect, the phase needs to be changed in a small fraction of the radiation wavelength. In GENESIS, the drifts and chicane models all result in integer steps of the radiation wavelength (tracking results are calculated and exported in steps of the radiation wavelength). Thus, for our study, the distributions of both electrons and fields at the end of each wiggler needs to be exported and reused as inputs for next section of wiggler simulation.

A transport which calculates the phase shifting for both particles and fields is fulfilled with external C++ code which reads in the binary files (.dpa and .dfl files) and generates new binary files with proper phase propagated in between the wiggler gaps. The electron beam parameters used in GENESIS for the studies in this paper is listed in Table 1 [4].

* Work is supported by Brookhaven Science Associates, LLC under Contract No. DEAC0298-CH10886 with the U.S. Department of Energy, DOE NP office grant DEFOA-0000632, and NSF grant PHY-1415252.

[†] yjing@bnl.gov

Table 1: Beam Parameters used in GENESIS Simulations

Beam energy (MeV)	14.66
Beam current, peak (A)	50
Norm. emittance (mm-mrad)	5
Momentum spread (σ_p/p)	1×10^{-3}
Undulator period (cm)	4
Radiation wavelength (μm)	30

In the GENESIS setup, we sliced the electron bunch into 400 slices and each slice contains 16384 macro particles. We generated random shot noises in GENESIS and simulated the evolution of the bunch along with the EM wave “with” and “without” a small δ -function-like perturbation, which is located at the middle of the bunch, i.e., slice # 200.

The FEL response on the perturbation was calculated by subtracting it from the bunching factor in the presence of perturbation (“with”) and in the case of the pure shot noise (“without”). Being the difference between two complex numbers, such a FEL response is a complex function, i.e., it is described both by the amplitude, and the phase. In the following section, we will discuss our treatment of such FEL responses for the drifts in between wigglers.

PHASE SHIFTER MODEL AND RESULTS

As mentioned above, in between two wigglers, there is a C-type chicane which delays the electron bunch to adjust the pondero-motive phase between particles and fields. We exported the particle and field distribution at the end of each wiggler. Shifting particle distribution is rather simple, since it is merely to modify the complex bunching factor by $\exp(ikx)$, where k is the wave number of the radiation.

The manipulation on radiation field, however, must take into account that the envelope is changing over the distance, i.e., Rayleigh length is not infinity. In the code, we fulfill this phase shift on fields by performing shifts in the 2D Fourier transformed EM fields. To be more specific, we shifted the EM fields transversely and then performed 2D Fourier transform. After we added the phase shifts, we performed inverse Fourier transform and shifted the EM fields transversely back to where they were.

By doing this, we considered the longitudinal variance of the EM fields. Figure 3 shows evolution of the gain (amplification of the perturbation stated above) of the signal in the FEL under two different phase shifter settings. The phase shifter strength is converted to microns, where 0 μm indicates the electrons and the radiation fields are perfectly in phase at the entrance of next wiggler. On the other hand, when we shifted the electrons with respect to the fields by 6 μm , about 1/5 of the wavelength, the gain of signal in the FEL drops from 100 to about 80.

A full-blown study of the 2D parametric space (two phase shifters between three wigglers) can be seen in Figure 4, which indicates that we have the ability to tune the gain of CeC FEL to cover a wide range ($\sim 60 - 120$) by varying the phase shifter settings. In reality, a 77-ampere current in the phase shifter is correspondent to shifting the beam by entire wavelength and we will have 10% margin in power supplies to tune the FEL gain by adjusting phase shifters [5].

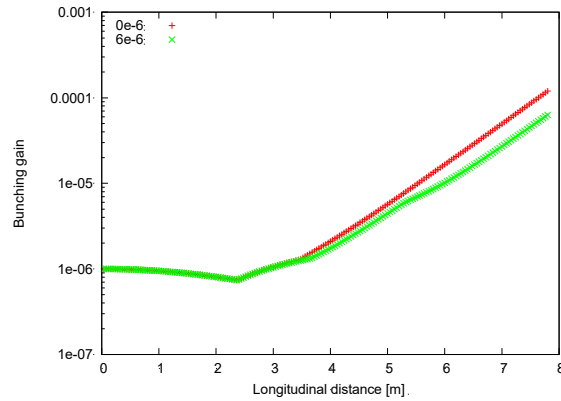


Figure 3: Evolution of gain of a perturbation in existence of shot noise in CeC FEL. When phase shifter is set to perfectly align the electrons and radiation, the gain (~ 100) is higher than the gain when the phase shifter is shifting the electrons by 1/5 of the radiation wavelength (~ 80).

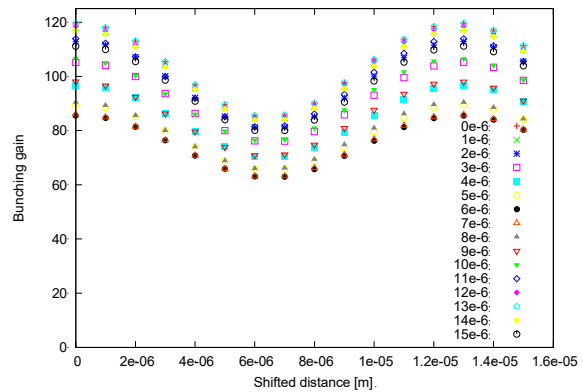


Figure 4: A 2D scan of phase shifter setup results in changing the gain of FEL amplification by a factor of two ($\sim 60-120$), which could be easily distinguishable by the change of cooling time of CeC.

If we compare the electron envelope in the FEL for two cases: a) three wigglers with phase shifters; b) one continuous long wiggler, we could find that the longitudinal variation of EM fields may play an important role, i.e., our Rayleigh length is not significantly larger than the drift space in between wigglers. Detailed study of the causes of this difference is underway. The electron envelope for both cases can be found in Figure 5.

Content from this work may be used under the terms of the CC BY 3.0 licence (© 2018). Any distribution of this work must maintain attribution to the author(s), title of the work, publisher, and DOI.

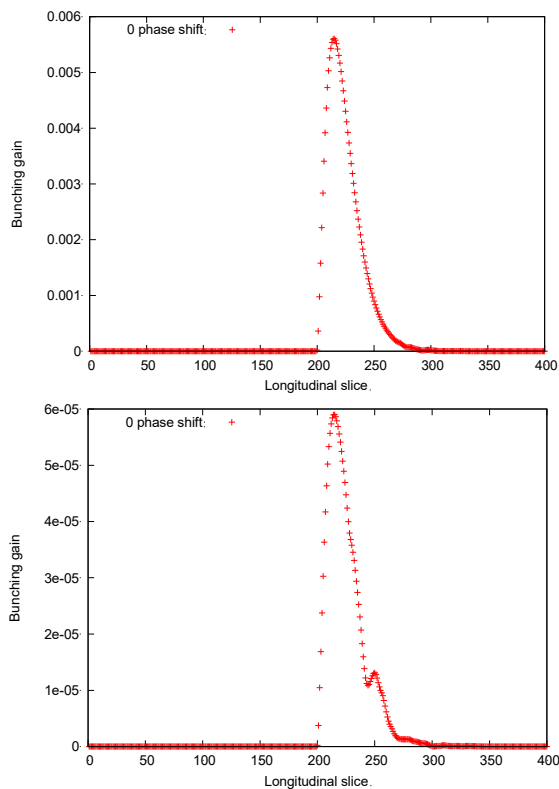


Figure 5: Electron envelope at 6 m in the CeC FEL for one continuous wiggler (top) and three wigglers separated by a ~ 0.4 -m drift space (bot), suggesting the longitudinal variation of radiation could affect the shape of electron envelope, thus affecting the FEL gain the hadron beam sees if not sitting on the top of the curve.

CONCLUSION

We modelled CeC FEL section while taking the drift space in between wigglers into account. The simulation results suggest that by varying the strengths of phase shifters, we can control the FEL gain in a relatively wide range ($\sim 60 - 120$). The change in the electron envelope may arise from the limited Rayleigh length of the radiation, and we are currently studying this connection.

REFERENCES

- [1] V. N. Litvinenko and Y. S. Derbenev, *Phys. Rev. Lett.* 102, p. 114801 (2009).
- [2] S. Reiche, Genesis 2.0 manual, available at: <http://genesis.web.psi.ch/>
- [3] V. N. Litvinenko, private communication.
- [4] G. Wang, Y. Jing, V. N. Litvinenko, and J. Ma, presented at FEL'17, paper TUP039.
- [5] V. N. Litvinenko, private communication.

EUROPEAN XFEL INJECTOR COMMISSIONING RESULTS*

B. Beutner[†], DESY, Hamburg, Germany

on behalf of the European XFEL Accelerator Consortium and Commissioning Team

Abstract

In the first commissioning phase of the European XFEL SASE FEL driver linac, we demonstrated the design goals for the injector section. These goals include reliable operation of sub-systems and feasible beam parameters like emittance and bunch length of the beam produced by the RF gun. Of particular interest is the operation of long bunch trains with up to 2700 bunches with a 4.5 MHz repetition rate. In this presentation we will provide an overview of our experiences from the injector commissioning run including beam dynamics studies, diagnostics, and system performance.

INTRODUCTION

The European XFEL aims at delivering X-rays from 0.25 to up to 25 keV out of 3 SASE undulators lines [1, 2]. These undulators are driven by a superconducting linear accelerator based on TESLA technology [3]. European XFEL is build in an international collaboration of eleven countries.

In this paper we summarize results from the commissioning run of the injector in the first half of 2016, building on a previous report [4]. Results from the commissioning of the downstream part off the machine are summarised in [5].

The injector of the European XFEL consists of (compare Fig. 1) the RF gun, an booster and a lineariser accelerating module, a laser heater, and a diagnostic section. The main

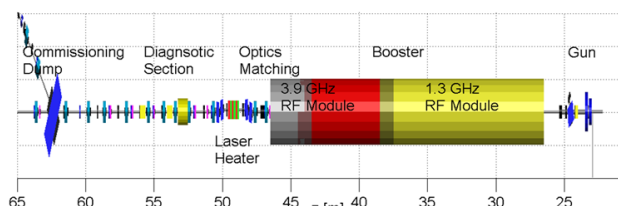


Figure 1: Injector of the European XFEL. Two RF stations (A1 at 1.3 GHz, and the AH1 at 3.9 GHz) are used for acceleration and longitudinal phase space shaping.

task of the injector is the production of low emittance beam at various charges ranging from 20 pC to 1 nC and the generation of a suitable longitudinal phase space correlation for downstream bunch compression. Nominal beam energy in the injector is 130 MeV.

As summarised in Table 1 we were able to demonstrate the design performance of the injector.

Time Structure

The unique feature of superconducting RF systems is the ability to generate long RF pulses and thus long bunch trains.

* Work supported by the respective funding agencies of the contributing institutes; for details please see <http://www.xfel.eu>

[†] bolko.beutner@desy.de

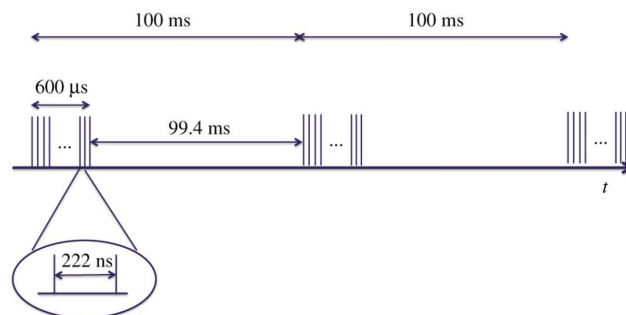


Figure 2: Time structure of the European XFEL bunch trains.

As visualised in Fig. 2 trains of up to 600 μ s are generated with a 10 Hz repetition rate. With an intra train rate of up to 4.5 MHz the linac can deliver up to 2700 bunches per pulse. With a total of up to 473 kW beam power at full beam energy of 17.5 GeV. These bunches can be send to different undulator lines using fast kicker systems to allow flexible timing patterns for the user stations.

RF GUN

Gun Operation

During the injector run we restricted gun operation to limit the stress on the RF window. Either the gradient is driven to the maximum, for optimum emittance, or the pulse length is set to the design to demonstrate long train operation maintaining reasonable emittance. The parameters are shown in Table 2. These limitations are mainly imposed by the RF window. At PITZ¹ a setup with two RF windows is in operation allowing full design operation. For the time being we do not risk operation, however a later upgrade to a two-window setup is considered.

Fast Gun Start-up

Long RF pulses in the gun are challenging for gun operation. Up to 50 kW heat load are deposited in this normal conducting copper cavity from the RF. While the temperature stability requirements to keep the cavity on resonance is on the order of 0.05 deg C. Especially during startup the resonator is detuned since the RF load typically reacts much faster than the water regulation. The traditional solution to this problem is a slow increase of RF power. In such a operation, however, the startup takes about an hour with a risk of trips during the process. The process can be significantly accelerated by inducing an dynamic phase slope on the RF input signal. Such a slope is an effective frequency shift of the drive signal. A control system server is updating this phase slope according the determined detuning minimising the reflected RF power in the process [6]. With this

¹ Photo-injector test stand in DESY Zeuthen.

Table 1: Injector Performance Defined in the Technical Design Report (TDR) Compared with Demonstrated Parameters during the Commissioning of the Injector

Quantity	TDR	achieved
Macro pulse repetition rate	10 Hz	10 Hz
RF pulse length (flat top)	650 μ s	670 μ s
Bunch repetition frequency within pulse	4.5 MHz	4.5 MHz
Bunch charge	20 pC–1 nC	20 pC–1 nC
Slice emittance (50 MV/m, 500 pC)	0.6 mm mrad	0.6 mm mrad

Table 2: Operation Modes of the RF Gun during the Injector Commissioning Run

	maximum pulse length	maximum gradient
forward power	4.2 MW	6.61 MW
pulse length	650 μ s	50 μ s
gradient	50 MV/m	60 MV/m

procedure we can startup or recover gun operation in a few minutes instead of at least an hour significantly increasing machine availability.

PHASE SPACE STUDIES

Diagnostics Section

Phase space studies are done in a diagnostic section downstream of the laser heater. This section includes four-screen stations, a spectrometer arm, and a transverse deflecting RF structure (TDS) for longitudinal resolved studies. A unique feature of this diagnostics layout are fast kicker systems to kick individual bunches on off-axis screens [7]. In this configuration individual bunches out of the train can be analysed while the remaining bunches continue eventually to the SASE user stations. In Fig. 3 the operation of such semi-parasitic measurements is illustrated.

Projected Emittance

An important part of the injector commissioning was the demonstration of sufficient beam quality for the upcoming FEL commissioning. The focus these emittance optimisa-

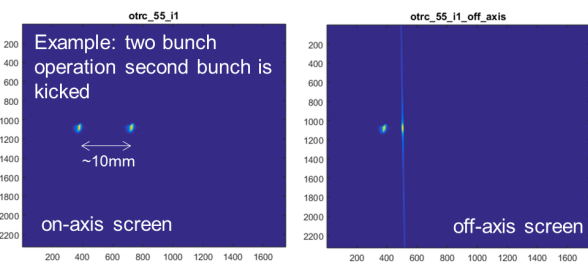


Figure 3: Semi-parasitic diagnostic operation. Two bunches are on the train. the second bunch is kicked using the kicker system. On the left hand side the full screen is inserted and both bunches are visible. Inserting the off-axis screen (right hand side) only the second bunch is visible while the first bunch continues through the beam dump.

tions was on the 500 pC operation mode. The other modes, namely th 50, 100, and 1000 pC options were studied with lower priority. The results of these optimisation runs are summarised in Table 3.

The measured optimised emittance results are quite symmetric in the horizontal and vertical plane. This, however, is by choice. If we measure the emittance as function of the solenoid strength (an example is shown in Fig. 4) we observe an asymmetry between the planes. We choose the solenoid strength which minimises the geometric average $\sqrt{\epsilon_x \cdot \epsilon_y}$.

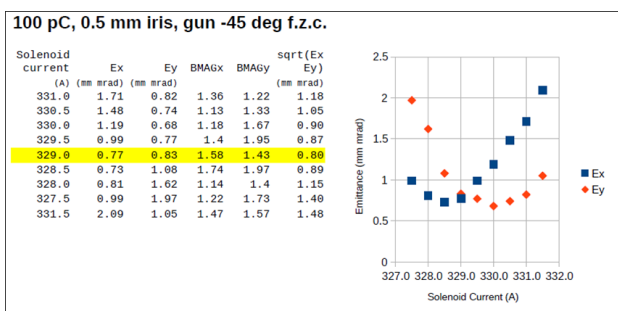


Figure 4: Summary of an emittance optimisation study. Normalised emittances in both planes are measured as a function of the solenoid current.

In 2017 corrector quads in the normal and skew direction are installed. Such correctors were studied at PITZ and are a promising tool to mitigate such asymmetries [8–10].

The discrepancies between the measured and simulated values in Table 3 have two main explanations. First of all most effort in terms of beam-time was put in the 500 pC mode, it is possible and to some extent expected, that modes with significantly different charge are not as well optimised.

Another reason for discrepancies, especially for lower bunch charges than 500 pC are issues with the screens for small beam spot sizes.

Transverse beam sizes are measured with scintillating screens (LYSO). Resolution of the screens is measured to be of the order of a few micron [11]. Typical transverse beam sizes to be resolved range from 40 to 100 μ m, and are thus well above the resolution limit of the screens. Nevertheless, emittance measurements give unreasonable results at small beam sizes below about 50 μ m, as they appear in four-screen sections. Only multi-quadrupole scans with enlarged beta-functions at the screen position give reliable results. This effect is under investigation.

Content from this work may be used under the terms of the CC BY 3.0 licence (© 2018). Any distribution of this work must maintain attribution to the author(s), title of the work, publisher, and DOI.

Table 3: Optimised Projected Normalised Emittances for the Different Bunch Charges Compared with Beam Dynamics Simulations. Uncertainties are the propagated statistical beam size measurement errors. Simulations are done with ASTRA [12].

charge	horizontal	vertical	simulation
50 pC	(0.56 ± 0.01) mm mrad	(0.64 ± 0.01) mm rad	0.27 mm rad
100 pC	(0.77 ± 0.02) mm mrad	(0.83 ± 0.03) mm rad	0.31 mm rad
500 pC	(1.28 ± 0.02) mm mrad	(1.23 ± 0.03) mm rad	1.15 mm rad
1 nC	(2.95 ± 0.02) mm mrad	(2.81 ± 0.03) mm rad	1.83 mm rad

Slice Emittance

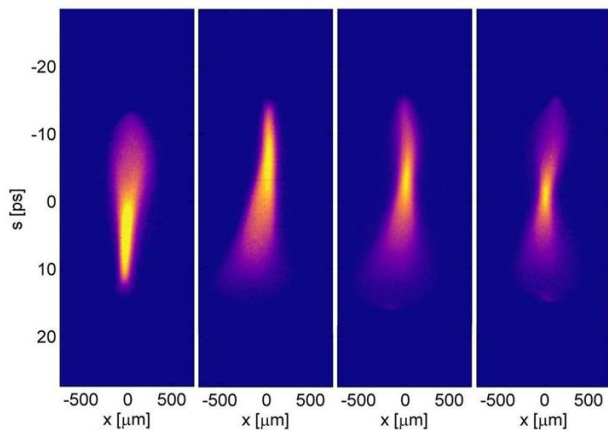


Figure 5: An example of a slice emittance measurement using the four-screen setup, as described for the projected measurements, in combination with a transverse deflecting structure

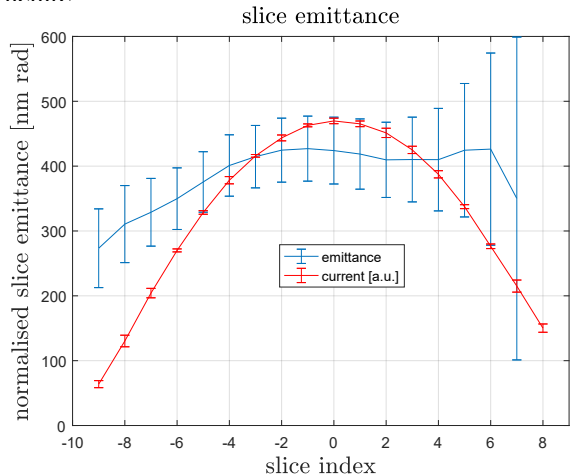


Figure 6: An example slice emittance measurement. 200 pC beam accelerated with 60 MV/m in the gun. The current profile as well as the slice emittance is plotted.

In the described diagnostics layout a TDS is used for longitudinal resolved measurements (see Figures 5, 6, 7). This allows for studies of the emittance of individual slices. Such slices are still much longer than the corporation length but still a very good approximation to this relevant number for the FEL gain. In contrast to the projected emittance results shown earlier here the agreement with the expected results from calculations is much better. This is another indication for issues with the diagnostics of small beam spots.

horizontal phase space

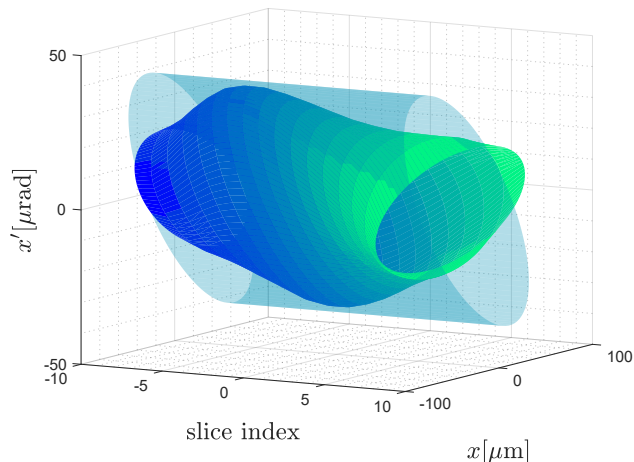


Figure 7: A representation of the Twiss phase space ellipses of the data shown in Fig. 6. The design optics is indicated by the transparent "tube".

Using not only the spot size to fit the phase-space beam moments but include the slice centroid positions as well we can determine the centroid position of each slice in phase-space. This allows us to recover the projected emittance from the slice measurements (see Fig. 8). This values have some uncertainty, since non-uniformities in the kicker fields

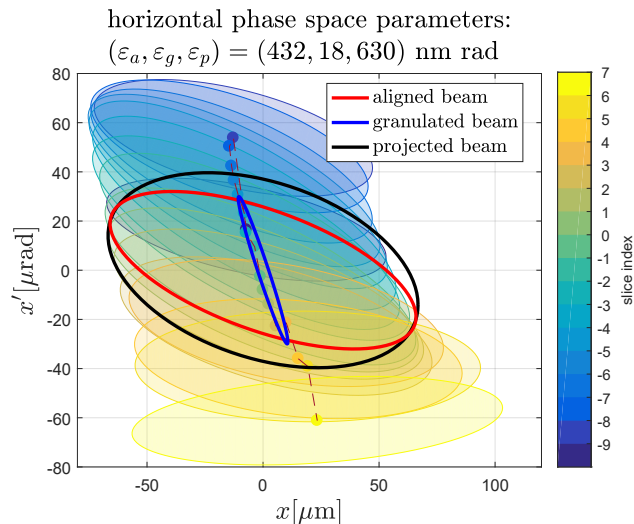


Figure 8: From the data in Fig. 6 we reconstructed the projected beam parameters. The relative "rotation" as well as centroid shifts in phase space needs to be taken into account [13, 14].

Content from this work may be used under the terms of the CC BY 3.0 licence (© 2018). Any distribution of this work must maintain attribution to the author(s), title of the work, publisher, and DOI.

were only partially included, but still the agreement with the expected projected emittance is good.

The measurements discussed so far utilised the fast-kicker system diagnostic section in semi-parasitic operation. These measurements are fast and very well suited for scans of parameter spaces for machine optimisation. However, better results can be achieved by multi-quadrupole scans on a single screen. In such scans the beam spot size is chosen much larger than in the FODO configuration avoiding resolution issues and the longitudinal resolution of the TDS setup can be optimised. In addition more than four data points are

available increasing the accuracy of the beam moment fit. With measurements using this technique we achieved normalised emittances down to 0.4 mm mrad slice emittance for 500 pC for moderate gun gradients (compare Fig. 9).

Phase Space Tomography

More detailed phase-space beam dynamics studies are possible by using not only the beam spot-sizes but the profile information from a modified multi-quad scan [15]. With tomographic methods the phase-space density distribution can be recovered (compare Fig. 10). While the phase-space dynamics in the injector are relatively straightforward we

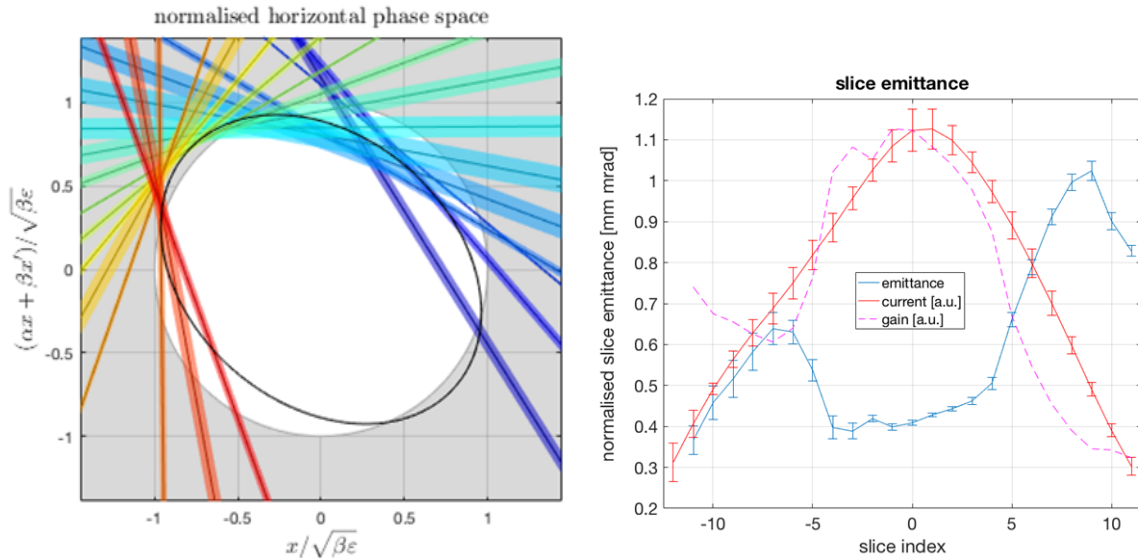


Figure 9: An example of an optimised 500 pC beam at 53 MV/m gun gradient using a multi-quad scan. The phase space fit indicated on the left hand side corresponds to the core slice of the bunch.

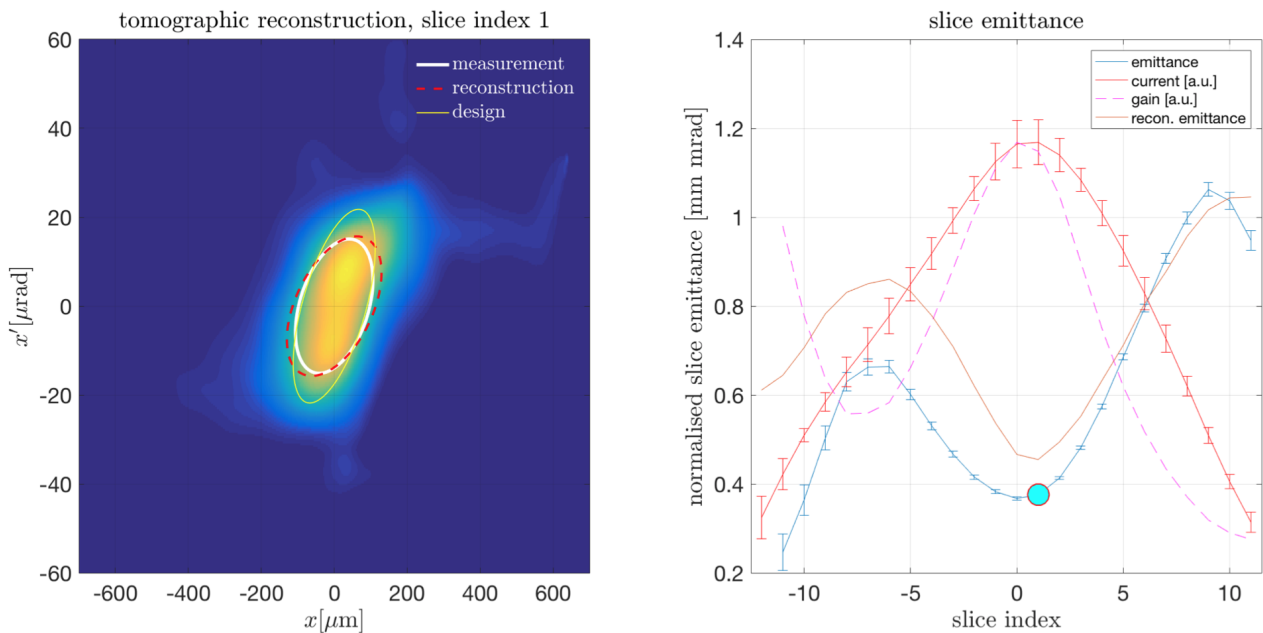


Figure 10: Tomographic reconstruction of the core slice from a slice emittance measurement. The phase space density distribution is shown in the left hand plot together with the design and reconstructed Twiss ellipses. On the right hand side the corresponding emittances are shown along the bunch.

expect more interesting studies with this techniques in the bunch compressor sections downstream of the injector.

SUMMARY AND OUTLOOK

In summary we report that the injector of the European XFEL was commissioned to design performance. However optimisations are still possible. Especially the operation at full gun gradient with long bunch trains needs to be established for long-train user operation foreseen for 2018. On the beam dynamics and diagnostic side issues with the emittance measurements, namely the overestimation of small beam sizes is under investigation and will be worked on in the future.

Another topic which was not covered in this discussion is the laser heater system. Even though we have first demonstrations of its utility (see [16]) systematic studies during FEL beam delivery are foreseen in the future.

ACKNOWLEDGEMENTS

The fabrication, testing and installation of the injector components were only possible with a tremendous effort from all partners - and still it is needed from the operators and scientists doing the commissioning. The author likes to thank the complete team for their work and support.

REFERENCES

- [1] M. Altarelli *et al.* Ed., "The European X-Ray FreeElectron Laser - Technical Design Report", DESY, Hamburg, Germany, Rep. DESY 2006-097, July 2007.
- [2] R. Brinkmann *et al.* Ed., "TESLA XFEL Technical Design Report Supplement", DESY, Hamburg, Germany, Rep. DESY 2002-167, March 2002.
- [3] R. Brinkmann *et al.* Ed., "TESLA Technical Design Report - Part II: The Accelerator", DESY, Hamburg, Germany, Rep. DESY 2001-011, March 2001.
- [4] F. Brinker, "Commissioning of the European XFEL Injector", in *Proc. IPAC2016*, Busan, Korea, 2016, <https://doi.org/10.18429/JACoW-IPAC2016-TU0CA03>
- [5] W. Decking and H. Weise, "Commissioning of the European XFEL Accelerator", in *Proc. IPAC2017*, Copenhagen, Denmark, 2017, <https://doi.org/10.18429/JACoW-IPAC2017-M0XAA1>
- [6] Y. Renier *et al.*, "Fast Automatic Ramping of High Average Power Guns", in *Proc. IPAC2017*, Copenhagen, Denmark, 2017, <https://doi.org/10.18429/JACoW-IPAC2017-TUP1K052>
- [7] C. Wiebers *et al.*, "Scintillating Screen Monitors for Transverse Electron Beam Profile Diagnostics at the European XFEL", in *Proc. IBIC2013*, Oxford, UK, paper WEPF03, 2013.
- [8] M. Scholz and B. Beutner, "Studies of the Transverse Beam Coupling in the European XFEL Injector", presented at FEL 2017, Santa Fe, NM, USA, paper TUP005, 2017.
- [9] M. Krasilnikov *et al.*, "Electron Beam Asymmetry Compensation with Gun Quadrupoles at PITZ", presented at FEL2017, Santa Fe, NM, USA, paper WEP007, 2017.
- [10] Q. Zhao, M. Krasilnikov *et al.*, "Beam Asymmetry Studies with Quadrupole Field Errors in the PITZ Gun Section", presented at FEL2017, Santa Fe, NM, USA, paper WEP010, 2017.
- [11] G. Kube *et al.*, "Transverse Beam Profile Imaging of few-Micrometer Beam Sizes Based on A Scintillator Screen", in *Proc. IBIC2015*, Melbourne, Australia, 2015, <https://doi.org/10.18429/JACoW-IBIC2015-TUPB012>
- [12] Y. Kot, private communication.
- [13] C. Mitchell, "A General Slice Moment Decomposition of RMS Beam Emittance", arXiv:1509.04765v1[physics.acc-ph], 2015.
- [14] V. Balandin, private communication.
- [15] M. Scholz and B. Beutner, "Electron Beam Phase Space Tomography at the European XFEL Injector", in *Proc. IPAC2017*, Copenhagen, Denmark, May 2017, <https://doi.org/10.18429/JACoW-IPAC2017-WEPAB024>
- [16] M. Hamberg *et al.*, "Electron Beam Heating with the European XFEL Laser Heater", presented at FEL2017, Santa Fe, NM, USA, paper WEP018, 2017.

MODEL OF PHOTOCATHODE FOR CW ELECTRON GUN

P. W. Huang[†], W. H. Huang, C. X. Tang, Tsinghua University, Beijing, China

Abstract

The rapid development of X-ray Free Electron Lasers (XFEL) requires continuous wave (CW) electron guns to provide high brightness electron bunch. Most of the proposed CW gun for free electron laser use semiconductors as photocathodes due to their high quantum efficiency and potentially low thermal emittance. We manage to establish a model to explain the photoemission of semiconductors with incident photon energy above or below the theoretical threshold and derive the expression for quantum efficiency and thermal emittance. For the incident photon energy near or below the threshold of the cathode, things will be subtle and we should be careful to consider the details we used to neglect. The results of quantum efficiency and thermal emittance agree well with the published work.

INTRODUCTION

The next generation of the XFEL is the most powerful scientific instrument for cutting edge research areas, such as material science and biology. To achieve the desired x-ray performance, many researches have been dedicated to making XFELs with high brightness and high repetition rate. This will give a great challenge to the fabrication and conditioning of the photocathode. High quantum efficiency (QE) is required to achieve high repetition rate. Thermal emittance is now of greater importance to high brightness, for it has gradually become the dominant term for beam emittance due to the development of electron gun technologies. Both characters are closely related to the photoemission of the cathode. Therefore, understanding the mechanism of photoemission will be helpful to the design of the cathode. Recently, some researchers [1, 2] have discovered that it is possible to obtain extremely low thermal emittance from semiconductors with photon energy lower than the emission threshold. These results cannot be explained by the previous model. In this paper, we would like to establish our photoemission model to explain the experimental results and explore the subtle nature near the threshold region.

MODEL OF SEMICONDUCTOR PHOTOCATHODE

Our model is shown in Fig. 1. We consider the photoelectrons provided by defect level and valance band. First, we define n_d as the ratio between the density of defect level and valance band. To estimate the value of n_d , we can do the following derivation. The electrons at defect level should follow the Fermi-Dirac statistics as

$$f(E_A) = \frac{1}{1 + 2 \exp((E_A - E_F) / k_B T)}, \quad (1)$$

where E_A is the energy of a defect level beyond the bottom of the valance band, and E_F is the Fermi energy. The factor 2 is required in the expression for defect levels or impurities, representing two spins. The electrons occupied at the defect level can be calculated as

$$N_{\text{defect}} = N_A \times f(E_A), \quad (2)$$

where N_A is the density of acceptors. To estimate the electron density of the valance band, we use the effective mass approximation. The energy of electrons can be transferred to the free particle form near the bottom or top of the band. The density of states $g(E)$ can be defined as

$$\frac{2}{8\pi^3} \int d^3k = \frac{1}{2\pi^2} \left(\frac{2m_e^*}{\hbar^2} \right)^{\frac{3}{2}} \int \sqrt{E} dE = \int g(E) dE. \quad (3)$$

Based on the expression of the density of states, we can normalize the contribution of the defect level as

$$n_d = \frac{N_{\text{defect}}}{(2m_e^* / \hbar^2)^{\frac{3}{2}} / 2\pi^2}. \quad (4)$$

Thus, the distribution of excited electrons with regard to the energy can be expressed as

$$N(E) = n_d \sqrt{E} \delta(E - \hbar\omega + E_g - E_A) + \sqrt{E(E - \hbar\omega + E_g)}. \quad (5)$$

When the photon energy is below the threshold, the contribution from defect level will become remarkable. The formation of defect level starts from the vacancies of atoms, which is very universal during the fabrication process. If the atom happens to be a positive ion, then the vacancy behaves as a negative charge. It will attract a hole

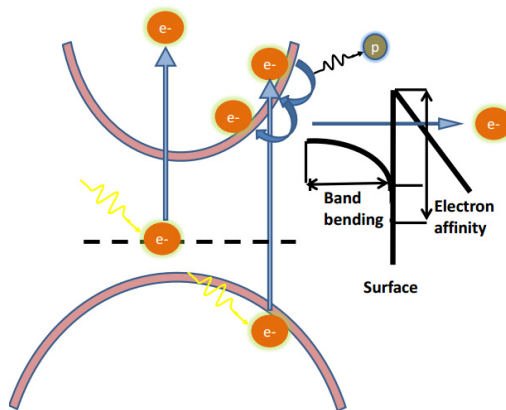


Figure 1: Model of photoemission for semiconductors.

[†] hpw17@mails.tsinghua.edu.cn

Content from this work may be used under the terms of the CC BY 3.0 licence (© 2018). Any distribution of this work must maintain attribution to the author(s), title of the work, publisher, and DOI.

and form the defect level. In this case, the defect level is the acceptor level. If the initial atoms are negative ions, the defect level will be the same as the donor level. As shown in Fig. 1, the electrons from the defect level will always have higher energy than those from the valance band. This will considerably influence the value of the thermal emittance.

When the photon energy is lower than the threshold energy, the electrons from the valance band can still emit into the vacuum because the band bending at the surface reduces the effective electron affinity. The band bending is formed by the interaction between the surface state and the bulk. If the surface state is n-typed while the bulk is p-typed, which is usually the case for photocathodes, then the abundant electrons at the surface will move toward the bulk. Therefore, a p-n junction will form and the surface electric field is built. The electron traversing the band bending region will obtain extra energy in the longitudinal direction. We can estimate the band bending energy by assuming all the holes in the band bending region are occupied with electrons such that

$$E_b = \frac{N_A e d^2}{2 \epsilon \epsilon_0}. \quad (6)$$

Absorbing a photon, some of excited electrons will move towards the surface for emission. They will experience scattering during the process. For semiconductors, electron-phonon scattering is dominant rather than the electron-electron scattering in metals. One collision will induce the electron to emit a phonon and lose energy E_{ph} . The direction of electron movement tends to maintain because it prefers to small angle scattering [3]. Therefore, it is a good assumption that the photoelectrons follow ballistic transport. We can calculate the transporting time as

$$t = \frac{s}{x \times \sqrt{2E/m}}, \quad (7)$$

where x is $\cos\theta$ and θ is the angle between the direction of electron movement and the normal direction of the surface, and s is the distance from surface.

The phonon scattering is mainly of two kinds, one is optical phonon scattering, the other is inter-valley scattering. The former can happen to all electrons with any energy while the latter can only happen when the electron have higher energy than the bottom of the other valley. The scattering rate $\lambda(E)$ is much higher for inter-valley scattering than for optical phonon scattering. This means the high energy electrons will lose energy more quickly than the low energy ones. The scattering rate $\lambda(E)$ can be calculated by the methods described by Fawcett [4]. Therefore, the energy loss ΔE can be expressed as

$$\Delta E = t \times \lambda(E) \times E_{ph}. \quad (8)$$

When the electrons arrive at the surface, they have some probability to tunnel through the vacuum barrier. We consider the triangle barrier model. This consideration is necessary, for when the photon energy is below the threshold,

a large part of the excited electrons do not have enough energy to overcome the barrier. If we still use the step function, many photoelectrons will be deleted artificially and the analysis will result in a serious deviation from the reality. Therefore, we should carefully deal with the tunnel probability and take the expression for triangle barrier derived in the previous work [5]:

$$D(E) = \frac{4\sqrt{EH(E)}}{2\sqrt{EH(E)} + (H(E) + E)(e^{\theta(E)} - \frac{1}{4}(1 - e^{-\theta(E)}))}, \quad (9)$$

$$H(E) = \sqrt{(E - E_a)^2 + \left(\frac{p_0^2 \hbar^2 (e\beta\xi)^2}{2m}\right)^{\frac{3}{2}}}, \quad (10)$$

and

$$\theta(E) = \begin{cases} 0 & E > E_a \\ \frac{2}{e\hbar\beta\xi} \sqrt{2m(E - E_a)^3} & E < E_a \end{cases}, \quad (11)$$

where ξ is the electric field, m is the electron mass, and p_0 is equal to 0.51697. The field enhancement factor β is considered for the electric field in the expression $D(E)$.

Under the above assumptions and derivations, we can derive the expression of the QE for semiconductors:

$$QE = (1 - R(\omega)) \frac{\iiint N(E)F(s)T(E, s, x, \lambda(E))dEdsdx}{\int N(E)dE \int_{-1}^1 dx}, \quad (12)$$

$$T(E, s, x, \lambda(E)) = D\left(E - \frac{s}{x\sqrt{2E/m}} \times \lambda(E) \times E_{ph}\right) x^2 + E_{bend}, \quad (13)$$

and

$$F(s) = \alpha(\omega)e^{-\alpha(\omega)s}, \quad (14)$$

where $T(E, s, \cos\theta, \lambda(E))$ is the emission possibility of electrons excited from the depth s with energy E and direction θ . $\alpha(\omega)$ represents the light-absorption factor and $R(\omega)$ is the reflectivity.

To derive the thermal emittance, we can calculate MTE first and obtain the thermal emittance through

$$\varepsilon_n = \frac{1}{m_0 c} \sqrt{\langle x^2 \rangle \langle p_x^2 \rangle} = \sigma_x \sqrt{\frac{MTE}{m_0 c^2}}. \quad (15)$$

It has been supposed that the transverse position is irrelevant to the transverse momentum. Surface roughness is believed to have some unfavourable effect on the thermal emittance, but we will neglect its contribution in the following discussion and there exists fabrication methods to minimize the roughness. We assume the conservation of transverse momentum at the interface. Thus, the MTE can be expressed as

$$MTE = \frac{\iiint N(E)F(s)T(E, s, x, \lambda(E))(1 - x^2)EdEdsdx}{\iiint N(E)F(s)T(E, s, x, \lambda(E))dEdsdx}. \quad (16)$$

Content from this work may be used under the terms of the CC BY 3.0 licence (© 2018). Any distribution of this work must maintain attribution to the author(s), title of the work, publisher, and DOI.

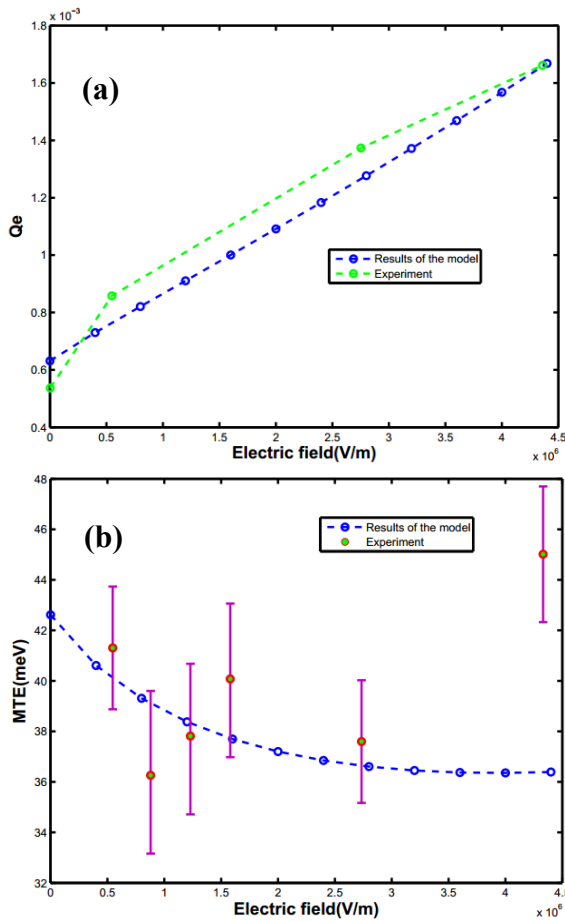


Figure 2: Comparison between calculation results of our model and the published data [1] in (a) QE and (b) MTE.

RESULTS

Our model succeeds in explaining the performance of the cathode when the incident photon energy is lower than the threshold. We take cesium antimonide with an incident photon energy of 1.8 eV as an example. The applied electric field is taken as a variable. We can see the calculation results fit well with the published work [1] for both QE and MTE. There exists an initial decrease for MTE with the enhancement of electric field. This is because the rise of the electric field enables the low energy valance band electrons to tunnel through the barrier with higher probability and reduce the ratio of defect level, resulting in the decrease of the average energy. Therefore, the participation of valance band is important to obtain low thermal emittance.

If we fabricate a perfect crystal, *i.e.* without any defect level, it will exert great influence on the thermal emittance. We take the applied electric field as a variable and calculate the situation with and without the consideration of defect level respectively. The results are shown in Fig. 3. We can see that the MTE will generally be larger with the consideration of defect level. This phenomenon is more visible at the low electric field. This is because the electrons from defect level have higher energy than those from valance

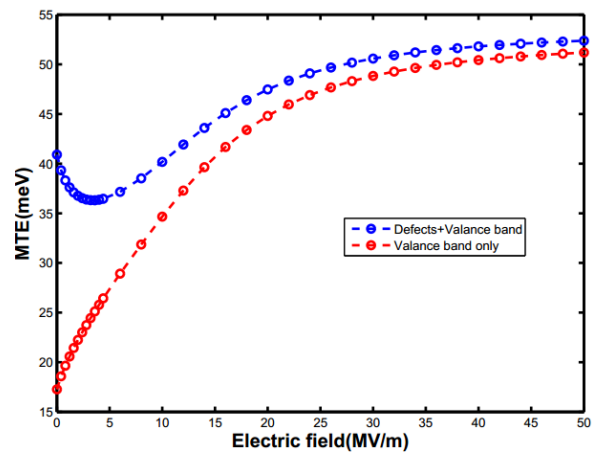


Figure 3: The difference in MTE with and without consideration of defect level.

band. When the electric field is low, the valance band electrons have little chance to tunnel through the barrier. But the defect level electrons are hardly affected. Therefore, the defect level electrons account for a large part of photoelectrons at the low gradient.

With the enhancement of the electric field, the effective electron affinity decreases and valance band electrons gradually become the dominant part of the photoelectrons. Thus, both lines have similar trends and values at large gradient. The case without defect level is similar to the situation at low temperature, for at that time the electron density is quite low at defect level and can be neglected.

CONCLUSION

In conclusion, we propose a model of photoemission of semiconductors and derive the expressions for QE and MTE. We take Cs_3Sb as an example and the results given by this model agree well with the published work. We also discover that perfect crystal may have lower thermal emittance at low electric field, but this advantage will be small at high gradient.

REFERENCES

- [1] L. Cultrera *et al.*, “Cold electron beams from cryocooled, alkali antimonide photocathodes”, *Physical Review Special Topics–Accelerators and Beams* 18(11), 113401, 2015.
- [2] J. Maxson *et al.*, “Measurement of the tradeoff between intrinsic emittance and quantum efficiency from a NaKSb photocathode near threshold”, *Applied Physics Letters* 106(23), p. 234102, 2015.
- [3] L. X. Ye, Semiconductor physics. Higher Education Press, Beijing, p. 307 (in Chinese), 2001.
- [4] W. Fawcett, W. *et al.*, “Monte-Carlo determination of electron transport properties in gallium arsenide”, *Journal of Physics & Chemistry of Solids* 31(9), pp. 1963-1990, 1970.
- [5] K. Jensen, “Electron emission theory and its application: Fowler–Nordheim equation and beyond”, *Journal of Vacuum Science & Technology B* 21(4), pp. 1528-1544, 2003.

NOVEL CONCEPTS OF A HIGH-BRIGHTNESS PHOTOINJECTOR RF GUN

S.V. Kuzikov^{†,2,3}, O.A. Ivanov, A.A. Vikharev, A.L. Vikharev,

Institute of Applied Physics, Russian Academy of Sciences, Nizhny Novgorod, Russia

S. Antipov, Euclid Techlabs LLC, Bolingbrook, IL, USA

²Euclid Techlabs LLC, Bolingbrook, IL, USA

³Lobachevsky University of Nizhny Novgorod, Nizhny Novgorod, Russia

Abstract

We propose here a program to design and manufacture a high performance, advanced source of electrons having high beam brightness (over 10^{16} A/m²) and high bunch charge (~100 pC). Three innovations are being considered: (1) the use of a high peak cathode field, short-pulse RF gun; (2) the use of multi-layered diamond photocathode at low temperature; and (3) the utilization of THz ultrafast field emission gating. High peak cathode field is necessary to achieve a high brightness (low emittance) beam to be accelerated to relativistic energies before space-charge effects lengthen the bunch. The multilayered diamond photocathode is needed to obtain high QE with long wavelength laser in the first doped layer, beam cooling in the next layer, and negative electron affinity at the emission layer. High field single cycle THz pulses, produced by means of laser light rectification in a nonlinear crystal, allow to avoid a UV laser, provide high field emission charge (up to 1 nC) and ~1 GV/m pre-acceleration of sub picosecond bunches.

HIGH CATHODE-FIELD RESONATORS

A natural way to enhance brightness of beams emitted in a photoinjector gun is increasing of cathode fields in order to mitigate space charge effects [1,2]. The necessary high fields can be obtained avoiding a breakdown and a pulse heating by means of short high-power RF pulses. Because high brightness is extremely important parameter for XFEL applications, a possible solution could be to use an additional RF gun which emits short bunch train producing short high-power RF pulse. In recent experiments, it was shown that ~300 MW, 10 ns of RF power can be taken away from bunch train in ANL gun [3]. It is important that RF power in this case is phase locked with a laser of the first “driving” RF gun. The same laser can service the second high-brightness RF gun.

Note that high fields are necessary at near cathode area only because in the rest part of the resonator a flying beam is already relativistic one. That is why, we suggest a scheme of a gun consisted of two uncoupled cells powered independently (Figure 1). To obtain ~500 MV/m on the cathode surface in X-band, a large portion of RF power, about 70 MW, is directed into the half-cell section that has quality factor $Q \approx \pi \cdot f \cdot \tau$ of 370 ($f=11.7$ GHz, $\tau=10$ ns). RF is coupled in using a coaxial coupler and a choke

reflector. Approximately 20% of the power fed into the first section is required for the second 1-cell section to achieve an acceleration field of 150 MV/m. The power splitting between the two sections is done using a variable power attenuator and a variable phase shifter. The field structures in cells are shown in Figure 1.

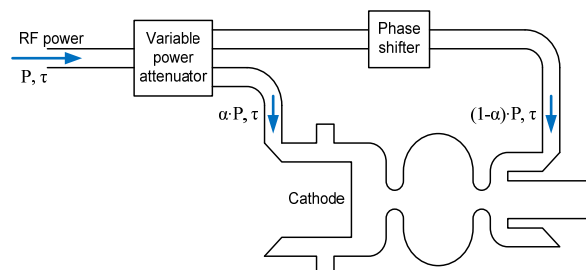


Figure 1: A schematic of the proposed two-cell photoinjector.

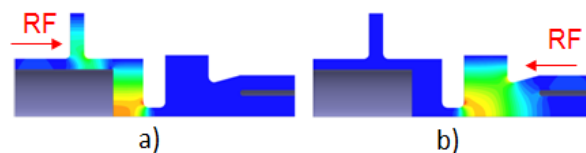


Figure 2: Field distribution in the first half-cell (a) and in the second cell (b).

ULTRAFAST FIELD EMISSION GATING

Another idea is to build a high brightness gun based on a gated picosecond flat field-emission cathode. Laser-based single-cycle THz pulse production by optical rectification and semiconductor switching yields high intensity, ~1 ps long THz pulses [4]. The 1 GV/m field strength of the THz pulse, combined with the RF gun accelerating field of ~100 MV/m, results in the emission of a short current pulse from the cathode. Compared to a standard photocathode, the beam brightness is increased due to the high additional accelerating field provided by the THz pulse. The proposed injection scheme does not require a UV laser, high emission charge (up to 1 nC) is emitted due to field emission at high THz fields for sub-picosecond bunch lengths.

In order to obtain the highest emission fields the THz pulse that is generated will be focused to the smallest possible size at the cathode by means of a parabolic mirror

[†] sergeykuzikov@gmail.com

Content from this work may be used under the terms of the CC BY 3.0 licence (© 2018). Any distribution of this work must maintain attribution to the author(s), title of the work, publisher, and DOI.

(Figure 3). Such scheme is well suitable to use the described THz emitter in a conventional RF gun. The mentioned parabolic mirror allows efficient focusing of the broadband THz pulse. In Figure 4 the incident pulse shown on the left, the field at the time correspondent to maximum of focusing is shown on the right. Field increasing near focal point is close to ~ 10 (Figure 5). Note that transverse magnetic field (Figure 6) in this time is close to zero so that the emitted electron bunch is not laterally deflected.

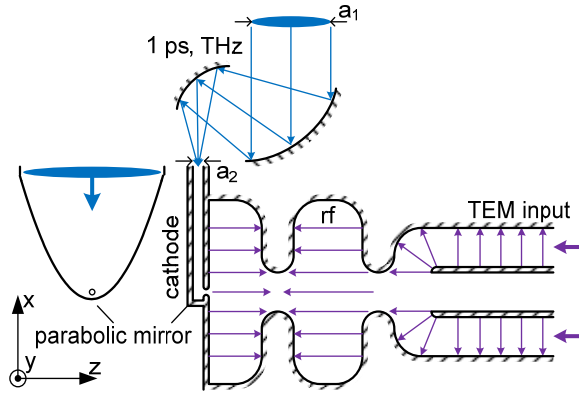


Figure 3: RF gun wherein electron emission is controlled by a picosecond THz pulse irradiating a metallic cathode.

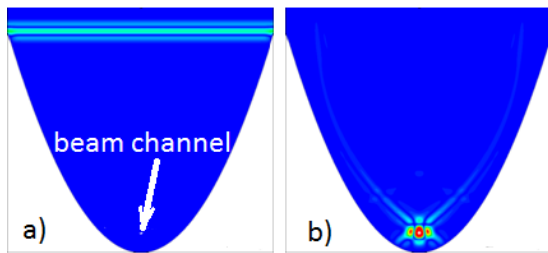


Figure 4: Field distributions at the parabolic mirror while focusing the short THz pulse, for the time correspondent to beginning of focusing at $t=5$ ps (a) and for time when focusing is close to maximum at $t=33$ ps (b).

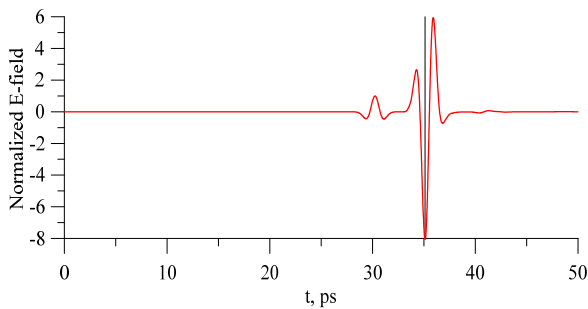


Figure 5: Electric field components at the focus of the parabolic mirror.

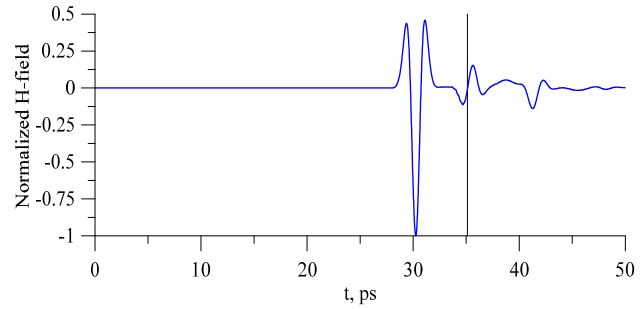


Figure 6: Magnetic field components at the focus of the parabolic mirror.

The anticipated parameters of the THz injector are summarized in the Table 1.

Because THz part of the gun has length $\sim 100 \mu\text{m}$ electrons are able to increase energies up to energy of the rest level only. In a multi-cell structure consisted of sector waveguides with parabolic mirror at bottom (like in Figure 4) bunches can be accelerated to much higher energy due to Cherenkov synchronism with incoming portions of THz radiation. The incident pulse is shown in Figure 7a, fields and accelerated bunch are shown in Figure 7b.

Table 1: Anticipated Parameters of the THz-gated Injector

Parameters	Value
Cathode field, GV/m	8
Bunch length, ps	0.13
Cathode radius, mm	8×10^{-3}
Bunch charge, pC	25
ϵ_{th} , mm \times mrاد	9×10^{-4}
ϵ_{sc} , mm \times mrاد	0.13
ϵ_{RF} , mm \times mrاد	7×10^{-3}
Brightness, (A/m ² \times rad ²)	2.2×10^{16}

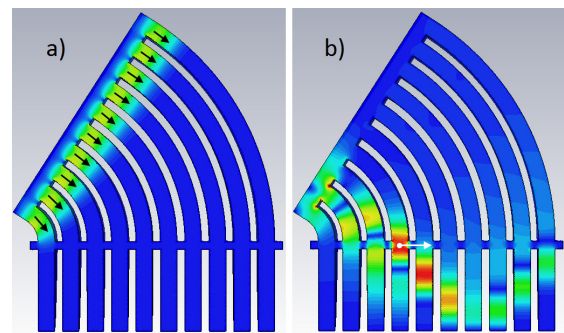


Figure 7: Concept for particle acceleration by a single picosecond THz pulse propagating in periodic accelerating gaps.

DIAMOND PHOTOCATHODE

Diamond is considered as a prospective candidate for high-brightness photocathode. We propose an n -type conductivity, negative-electron-affinity diamond terminated on the surface with hydrogen (n -D:H) which is robust in air [5]. The photocathode is assumed to be cryogenically cooled to generate high charge bunches that have significantly reduced energy spreads and emittances. A key element of this injector will be a specialty 3-layer diamond photocathode cooled to 80 K (Figure 8) [6].

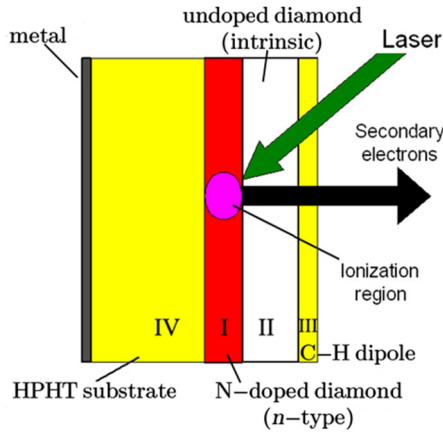


Figure 8: A basic sketch of diamond photocathode.

The layer I is a heavily n -doped diamond (i.e. it conducts electrons). n -doping can be obtained via introducing nitrogen or phosphorous impurities in the diamond lattice at concentrations of 10^{19} - 10^{20} cm^{-3} . Most importantly, n -doping allows for the use of a longer wavelength laser (over 150–200 nm) due to the existence of impurity states in the bandgap of diamond that have electron activation energies (1.6 eV for N and 0.6 eV for P) much lower than the diamond bandgap of 5.5 eV. The layer II (undoped intrinsic diamond) will transmit electrons to the surface in an external RF field while removing excess electron energy to achieve the smallest energy spread and emittance. The layer III (C-H electric dipole formed after diamond surface hydrogenation) will enable high efficiency electron emission into vacuum.

Dynamics of free carriers in the described photocathode is shown in Figure 9. Three sequent snapshots are illustrated showing phenomena taken place in the layers.

Because the space charge induced emittance is inversely proportional to the cathode surface field, we assume to use feeding scheme based on short high-power RF pulses which was analyzed in the first paragraph.

The anticipated parameters of the diamond photocathode are shown in the Table 2 for two laser pulse lengths.

Note that diamond has indirect zone structure. Nevertheless, the cooled electrons in conducting band, being near minimum in the energy-momentum diagram (ε - p), move with close to zero velocity $v = d\varepsilon/dp$ [7]. So, these electrons at a low temperature T can be emitted with near to zero velocity ($v = (2kT/m)^{1/2}$) independently on particular orientation of a crystal with respect to emitting surface.

Cooling of electrons occurs mainly due to scattering by acoustic phonons. Several so-called optical phonons with typical energy ~ 0.17 eV in the diamond is negligibly small at the cryogenic temperatures.

In order to compensate possible positive charge arisen after emission, a so-called Schottky diode (metal n -doped diamond) is planned to be created at the backing removing accumulated charge between pulses. At emission side the trapped electrons can be removed using Boron-doped layer which does not contradict with the projected surface hydrogenation.

Table 2: Diamond Photocathode Performance and Anticipated Parameters of the 11.7 GHz Gun

Parameter	Version1	Version 2
Pulse duration, ps	0.1	0.5
Cathode radius, mm	3	3
Bunch charge, pC	100	100
Cathode field, MV/m	500	500
ε_{th} , mm \times mrad (80 K)	0.17	0.17
ε_{sc} , mm \times mrad	0.2	0.2
ε_{RF} , mm \times mrad	1.4×10^{-2}	0.35
Brightness, (A/m $^2 \times$ rad 2)	2.9×10^{16}	2.1×10^{15}

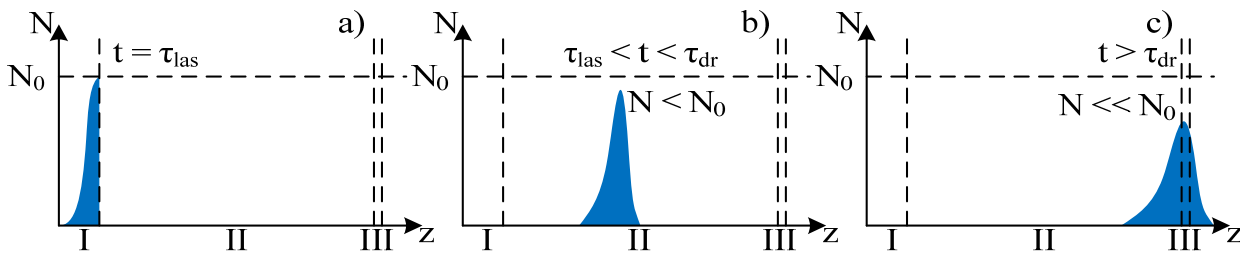


Figure 9: Free carrier packet dynamics in the layered diamond. Three snapshots are illustrated: (a) just-formed electron pulse upon the absorption of the laser pulse (b) electron pulse drift in the external electric field toward the NEA surface, and (c) onset of emission into vacuum.

CONCLUSION

Three concepts were suggested: (1) to apply short-pulse, high-power RF sources maintaining high cathode fields; (2) to use ultrafast terahertz gating providing preliminary acceleration of bunches; (3) to apply cold diamond photocathode producing low-emittance bunches. These concepts are able to provide $\sim 10^{16}$ A/m²×rad² beam brightness.

REFERENCES

- [1] J. B. Rosenzweig *et al.*, “Next-generation high-brightness electron beams from ultra-high field cryogenic radiofrequency photocathode sources”, arXiv:1603.01657 (2016).
- [2] S.V. Kuzikov, S. Shchelkunov, and A.A. Vikharev, “Concepts for a short-wavelength RF gun”, AIP Conference Proceedings 1812, 080005 (2017).
- [3] C. Jing, submitted to *Phys. Rev. Accelerators Beams*.
- [4] C. Vicario *et al.*, “Generation of mJ pulses in the 0.1-5 THz gap with electric field exceeding 80 MV/cm,” *Optics Letters* 39, 6632 (2014).
- [5] K.J. Pérez Quintero, S. Antipov, A.V. Sumant, C. Jing, S.V. Baryshev, “Planar ultra-nanocrystalline diamond field emitter in accelerator radio-frequency electron injector: performance metrics”, *Applied Physics Letters* 105, 123103 (2014).
- [6] A.L. Vikharev *et al.* “Nanometric diamond delta doping with boron”, *Physica status solidi (RRL) - Rapid Research Letters* 10, 324 (2016).
- [7] L.D. Landau and L.M. Lifshitz, *Course of Theoretical Physics: Statistical Physics*, Part 2, 55, Pergamon Press, 1981, p.227.

HIGHER FIELDS AND BEAM ENERGIES IN CONTINUOUS-WAVE ROOM-TEMPERATURE VHF RF GUNS*

F. Sannibale†, J. Byrd, D. Filippetto, M. Johnson, D. Li, T. Luo, C. Mitchell, J. Staples, S. Virostek, Lawrence Berkeley National Laboratory, 94720 Berkeley, CA,

Abstract

The development/proposal in the last decade of MHz-class repetition rate free electron lasers (FELs), inverse Compton scattering sources, and ultrafast electron diffraction and microscopy (UED/UEM), required the development of new gun schemes capable of generating high brightness beams at such high rates. The VHF-Gun, a 186 MHz room-temperature continuous wave RF photogun developed at the Lawrence Berkeley Lab (LBNL) was one of the answer to that need. The VHF-Gun was constructed and tested in the APEX facility at LBNL successfully demonstrating all design parameters and the generation of high brightness electron beams. A close version of the APEX VHF-Gun is in the final phase of fabrication at LBNL to operate as the electron source for the LCLS-II, the new SLAC X-ray FEL. The recently approved upgrade of the LCLS-II towards higher energies (LCLS-II HE), and the always brightness-starving UED and UEM applications, would greatly benefit from an increased brightness of the electron source. Such performance upgrade can be obtained by raising the electric field at the cathode and the beam energy at the gun exit. In this paper, we present and discuss possible upgrade options that would allow to extend the VHF-Gun performance towards these new goals.

INTRODUCTION

The last decade has been characterized by the formidable and successful development of several X-ray free electron laser (FEL) facilities capable to generate peak brightness of up to 9 orders of magnitude higher than the ones generated by 3rd generation light sources based on storage rings. More recently, a number of new FEL facilities were proposed targeting a similar dramatic performance increase also in terms of average brightness using superconducting RF (SRF) linacs operating in continuous wave (CW) mode. These facilities are designed to increase the repetition rate of the original FELs from hundreds of Hz to MHz. Among those, the LCLS-2 at SLAC was funded and it is now in the construction phase [1], and very recently, the Shanghai Coherent Light Facility (SCLF) project was approved in China [2].

The electron source is a key component in linac-based applications where it ultimately determines the maximum electron beam brightness and the facility overall performance. A high-repetition rate, high-brightness electron source was not readily available and several groups around the world started to propose and develop

new schemes or upgrades for electron guns that could address that need.

It is worth to remark that the availability of such a high-repetition rate, high-brightness source would also dramatically benefit other electron beam applications such as inverse Compton Scattering sources and ultrafast electron diffraction and microscopy (UED/UEM).

In response to that need, our group at the Lawrence Berkeley Laboratory (LBNL) developed in the framework of the Advanced Photoinjector EXperiment (APEX), the VHF-Gun, a room-temperature RF photo-gun resonating at 186MHz in the VHF frequency range and designed to operate in CW mode [3, 4]. During its commissioning, the gun successfully demonstrated reliable continuous wave RF operation at the design parameters [5] generating MHz electron beams with transverse emittances, longitudinal phase space and charge suitable for the operation of a high-repetition rate X-ray FEL such as the LCLS-II [6]. Also importantly, the APEX VHF-gun also demonstrated the low vacuum pressures required to operate high quantum efficiency semiconductor cathodes (Cs₂Te and CsK₂Sb) with acceptable lifetimes [7, 8].

At the present time, a close version of the APEX gun is in the final phase of fabrication at LBNL to serve in the LCLS-II injector, while the original APEX gun is now in operation as the electron source for HiRES, the LBNL high repetition-rate UED experiment [9].

In spite of these positive developments, there are already several high repetition-rate applications that would strongly benefit from an even further increase in beam brightness at high repetition rates. A notable example is the LCLS-II HE, the higher energy upgrade of the SLAC FEL [10], which already received CD-0 (the 1st approval level by the US Department of Energy. LCLS-II HE would require for its main mode of operation at 100 pC bunch charge, a normalized transverse emittance approaching 0.1 μm rms for further extending its lasing spectrum in the hard X-ray region. This is an about two-fold reduction with respect to the present LCLS-II emittance requirement. The additional electron beam coherence offered by the higher brightness would also greatly benefit UED/UEM applications.

The successful performance of the APEX VHF-Gun pushed our group to investigate the possibility of extending the VHF technology towards higher beam brightness while maintaining the operational functionality and reliability demonstrated by the present VHF-gun. In this paper, we present several concepts for possible gun configurations with the capability of achieving the desired enhanced performance. We will refer to these upgraded gun versions as the APEX-2.

*Work supported by the Director of the Office of Science of the US Department of Energy under Contract no. DEAC02-05CH11231

†fsannibale@lbl.gov

FROM APEX TO APEX-2

In upgrading the APEX gun to the APEX-2 evolution, we want to increase the brightness and the energy of the beam at the gun while adopting as much as possible the mechanical, vacuum and RF solutions that ensured the successful performance of APEX.

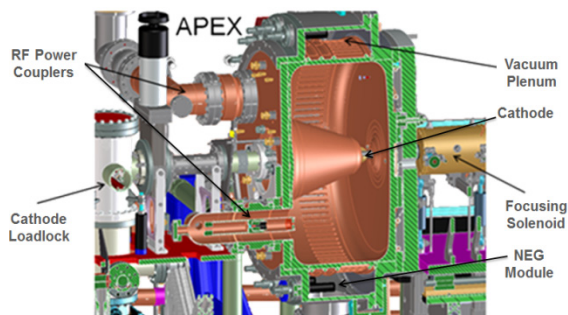


Figure 1: CAD cross-section view of the existing APEX VHF-Gun with main components in evidence. The two main RF couplers, the pumping slots on the cavity wall, and the vacuum plenum where up to 20 NEG modules can be located are visible. The photo-cathode plug is located on the tip of the nosecone and is inserted and removed without breaking vacuum by the loadlock system located in the back of the gun.

The brightness augmentation requires the increase of the accelerating electric field at the cathode during the electron emission [11, 12], and of the beam energies at the gun exit to reduce space charge forces that can degrade the quality of the beam phase space.

In order to preserve the APEX reliability, the APEX-2 design effort to maximize the cathode peak field and beam energy, is done maintaining the RF thermal heating at manageable levels by minimizing the power density on the cavity walls. This can be done by lowering the frequency of the gun from the 186 MHz (1/7th of 1.3 GHz) of APEX to the 162.5 MHz (1/8th of 1.3 GHz) of APEX-2. The lower frequency decreases the surface resistivity of the cavity copper wall, allowing for higher fields at the cathode for same surface power density. The new frequency is also convenient for the availability of commercial RF sources, and for its compatibility with existing superconducting linac cavities at 325 MHz, 650 MHz, and 1.3 GHz.

Table 1 shows a comparison between the present APEX gun parameters and the target values for APEX-2. The significantly higher field targeted at the cathode is justified by the operational experience at APEX, where no evidence of voltage breakdown was observed (with fields at the cathode of up to ~ 22 MV/m), and extremely low dark current values were measured (less than a nA at the nominal field). The maximum RF power choice for APEX-2 allows using four APEX-type RF couplers and RF waveguide configurations used and demonstrated at APEX. The value is also compatible with existing commercially available solid state RF sources.

Table 1: APEX vs. APEX-2 main design parameters

Parameter	APEX	APEX-2
Frequency [MHz]	186.7 (1300/7)	162.5 (1300/8)
Mode of operation	CW	CW
Technology	Room-temp. Cu	Room-temp. Cu
Number of cells	1	1 or 2
Peak power density [W/cm ²]	22	< 35
Max RF power [kW]	120	< ~ 250
Launching field at photocathode [MV/m]	20	~ 35
Beam energy [MV]	0.75	1.5-2.0

Several upgrade configurations for APEX-2 were considered. In one case, two APEX-like re-entrant-nose RF cavities are put back-to-back to create a two-cell structure where the cathode is inserted into the nosecone of one cell and the beam is extracted from the nosecone of the other cell. In this design, visible in Fig. 2, most of the APEX mechanical, RF and vacuum solutions are directly adopted. The two cells are extremely weakly coupled and can be operated with arbitrary RF phase difference enabling a flexible control over the beam exit energy and emittance preservation. This design uses about 250 kW of RF power divided between the 4 couplers to generate ~ 34 MV/m field at the cathode and ~ 2 MeV beams at the gun exit. The peak wall power density assumes a moderate value of 30 W/cm², and the cell inner radius increases from the 35 cm of APEX to 47.5 cm.

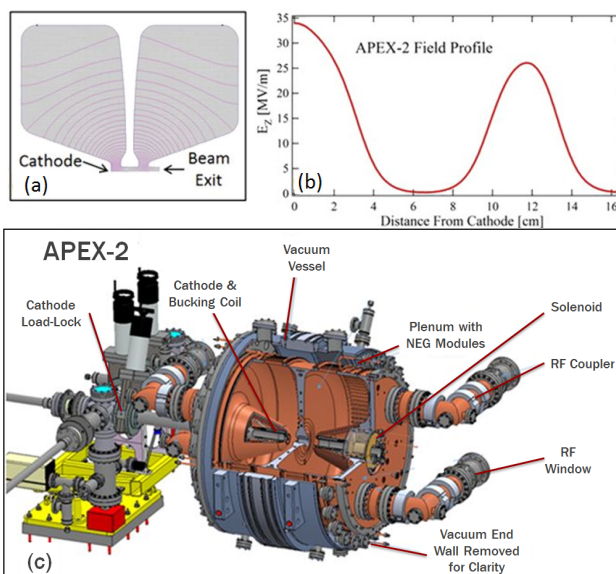


Figure 2: (a): Superfish [13] calculation showing the electric field geometry in (half) the cavity for the two-cell geometry of APEX-2. (b): accelerating field intensity along the gun axis. (c): 3-D CAD view of a preliminary mechanical design for the two-cell geometry with main components in evidence.

Content from this work may be used under the terms of the CC BY 3.0 licence (© 2018). Any distribution of this work must maintain attribution to the author(s), title of the work, publisher, and DOI.

Alternate configurations were also studied. By removing the central wall between the two cells visible in Fig. 2, the cavity assumes a single-cell dual-nose re-entrant geometry. Removing the wall reduces the overall heating losses (no more losses on the removed wall) increasing the beam energy for fixed RF power, but also decreasing the peak electric field at the cathode. A third geometry, which recovers the field at the cathode and at the same time allows for a higher RF efficiency, is obtained by inserting a drift tube in the middle of the gap. Initial design indicates that fields at the cathode of up to 35 MV/m can be reached with ~200 kW of RF power. The preliminary electric field configurations for both these single-cell options are visible in Fig. 3.

Cryogenic operation for APEX-2 could be also considered to alleviate thermal loading and improve efficiency. Recent experiments also showed that at cryo temperatures the increased copper rigidity can reduce the RF breakdown rate [14].

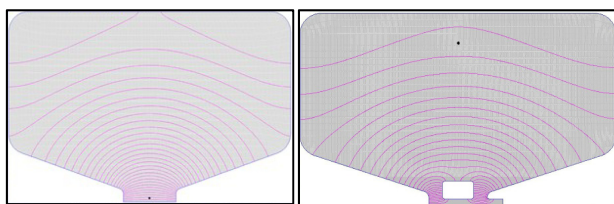


Figure 3: Superfish calculations showing the electric field geometry inside (half of) the cavity. Left: case of a single-cell dual-re-entrant nose geometry. Right: same design with the addition of a drift tube in the center of the gap.

INITIAL BEAM DYNAMICS STUDIES

Beam dynamics simulations using the ASTRA code [15] were done to evaluate the beam dynamics performance of two of the different APEX-2 geometries, the dual-cell and the single-cell dual-re-entrant nose without drift tube. An APEX-like injector layout [6] was used replacing the original APEX gun with the two different versions of the APEX-2 gun.

Figure 4 shows the preliminary results of a genetic algorithm optimization for 100 pC charge per bunch minimizing normalized emittance and rms bunch length at the end of the injector for the two gun configurations. The field at the cathode was kept fixed at 34 MV/M for both cases. The very similar solution fronts indicate that for fixed field at the cathode, the performance is essentially independent on the gun geometry. In order to keep computing time reasonable, the simulations shown in Fig. 4 used 10k macro-particles. Accurate simulations (with 250k macro-particles) using several solutions taken from the fronts systematically showed emittances ~15-20% smaller than the ones in the figure. In the bunch length range of interest for an FEL like the LCLS-II (0.8 to 1.2 mm rms), the simulated emittances for 100% of the beam are between ~0.12 to 0.144 μm . This is about a factor 2 better than in APEX approaching the desired 0.1 μm goal for 95% of the particles.

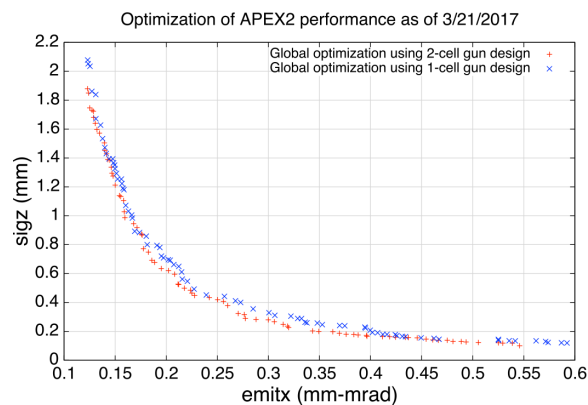


Figure 4. Fronts of solutions (trading between emittance and rms bunch length) for injector layouts using two of the APEX-2 gun geometries. See text for more details.

CONCLUSIONS

Demand from existing/proposed high-repetition rate facilities for higher brightness electron beams is pushing the design/upgrade of CW guns with higher fields and beam energies. Preliminary studies indicated the possibility of upgrading the successful room-temperature VHF-gun technology to higher fields at the cathode and beam energies, while preserving the reliability and vacuum performance demonstrated by the VHF-gun at the APEX project at LBNL. Several possible upgrade options were studied at the conceptual level and no show-stoppers were found. Initial simulations showed a brightness performance very close to the desired goal.

REFERENCES

- [1] J. Galayda, in *Proc. IPAC'14*, Dresden, Germany, pp. 935 (2014).
- [2] Zhentang Zhao, private communication.
- [3] J. Staples, F. Sannibale, and S. Virostek, CBP Tech. Note 366, 2006, LBNL-1003792, available at https://publications.lbl.gov/publication_search
- [4] R. Wells, *et al*, *Rev. of Sci. Instr.* **87**, 023302 (2016).
- [5] F. Sannibale, *et al.*, *PRST-AB* **15**, 103501 (2012).
- [6] F. Sannibale, *et al.*, in *Proc. IPAC'16*, Busan, South Korea, pp. 1041 (2016).
- [7] D. Filippetto, H. Qian, and F. Sannibale, *Appl. Phys. Lett.* **107**, 042104 (2015).
- [8] CsK₂Sb cathode tests at APEX. To be published.
- [9] D. Filippetto, and H. Qian, *J. Phys. B: At. Mol. Opt. Phys.* **49**, 104003 (2016).
- [10] https://portal.slac.stanford.edu/sites/conf_public/lclsiih2016/Documents/Forms/AllItems.aspx
- [11] I. Bazarov, *et al.*, *Phys. Rev. Letters* **102**, 104801 (2009).
- [12] D. Filippetto, *et al.*, *Phys. Rev. ST-AB* **17**, 024201 (2014).
- [13] LANL, http://laacg1.lanl.gov/laacg/services/download_sf.phtml.
- [14] Rosenzweig, J. B., *et al.* arXiv:1603.01657 (2016).
- [15] K. Flottman, ASTRA: A Space Charge Tracking Algorithm, <http://www.desy.de/~mpyflo>.

R&D AT SLAC ON NANOSECOND RANGE MULTI MW SYSTEMS FOR ADVANCED FEL FACILITIES*

A. Krasnykh[†], A. Benwell, T. Beukers, and D. Ratner, SLAC, Menlo Park, CA, USA

Abstract

A nanosecond range, multi MW system containing TEM mode electrodynamic structures fed by controllable pulsers are needed for (1) an array of FEL beamlines powered by superconducting linear accelerators operating with close MHz bunch repetition rate and (2) fast injection systems in multi-bend achromat upgraded (MBA-U) storage rings. The R&D effort covers both: type (1) and (2) layouts.

INTRODUCTION

L-Band CW linacs with approximately MHz bunch trains powered by a photoinjector are a fundamental to next generation FELs [1]. Such FEL projects require MW peak power spreader kicker systems of a nanosecond range. These systems have to distribute GeV bunches from the superconducting CW linac into beamlines with independently configurable undulators. In the ideal case, such systems allow the option to pick out bunches with arbitrary time pattern from a MHz bunch train. This technology optimizes the flexibility of the FEL for end users.

US Storage Ring Upgrades [2] are another example where nanosecond range multi-MW peak pulsers are required. They are necessary for the injection/extraction system to swap “bad” bunches with the new ones without shaking up the neighbours. Similar requirements were specified for the injection/extraction system of the ILC damping rings [3]. A main difference between [2] and [3] pulser specification is repetition rates. The repetition rate to swap bunches in the storage ring is approximately four orders of a magnitude lower compared to the ILC damping rings pulser.

The MaRIE complex [4] with pRad, XFEL, and eRad beamlines and switchyards is discussed presently. The electron bunch trains of the XFEL and eRad SC linacs will be unevenly spaced during 100 μ s. The spacing between micro pulses is governed by the radiographic experiments. The unevenness in the bunch train formed in the photoinjector is a source of transients in the high Q accelerating structures. To avoid unwanted effects during accelerating mode, the MaRIE linac ends may contain a fast kicker system. The kicker system allows controlling the 12 GeV pulse train with the arbitrary bunch pattern. Pulses with fast rise/fall shapes are needed to knock out the unneeded bunches from the 100 μ s train.

Discussed above are motivations for MW peak power systems of a nanosecond range in the future. However, beamlines built now at SLAC LCLS-II XFEL may incorporate the pump-probe experiments with two bunches. A separation between bunches is approximately 10 ns. A

fast kicker system is required to control the bunch destination. The beamline layout is illustrated in Fig. 1.

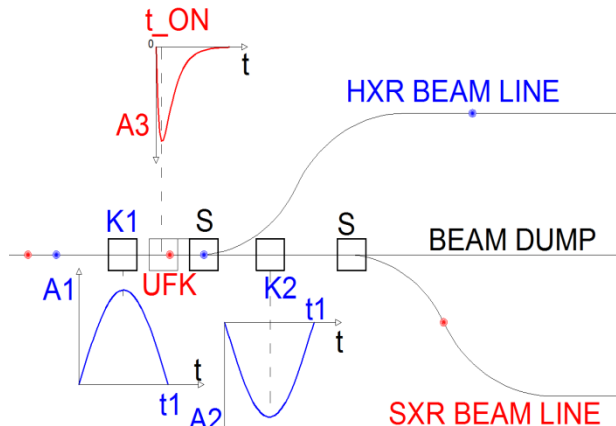


Figure 1: LCLS-II beamline scenario for pump-probe experiments. Red and blue dots represent two bunches, which propagate from the left to the right. K1 and K2 boxes are “slow” kicker magnets. Their transverse force (A1 and A2) vs. time (t) is shown in the blue curves. Two septum magnets (S) direct bunches into the hard or soft X-ray beamlines. The “fast” kicker system (UFK) is introduced into this beamline for the pump-probe experiments. The transverse force peak (A3) of the UFK vs. time (t) is shown in the red curve and cancels the kick K1. The system is activated when the separation between bunches is approximately 10 ns. The resulting x-rays, of different color, would be recombined for pump-probe experiments.

Figure 1 illustrates one possible scenario with a fast kick ON time (t_{ON}) and slow decay. The reader can find other scenarios with the fast kicker system in [5] where fast kick OFF time is discussed too.

GENERAL SPECIFICATIONS FOR FAST KICKER SYSTEM

Table 1 shows a general requirement for fast kicker system.

Table 1: Required Specifications

Parameter	Requirement	Unit
Deflection	0.75	mrad
Bunch Energy	4.0	GeV
Aperture	10	mm
Rise or/and Fall time	10.8 is good, 5.4 is better	ns
Repeatability	100	ppm rms
Availability	Low	
Pre-pulse/Post-	5	% of peak

* Work supported by US DoE contract DE-AC02-76SF00515

[†] e-mail address: krasnykh@slac.stanford.edu

pulse		pulse
Residual field at the time of the next duplet	0.01 is good 0.02 I is manageable	G*m
Rate	10 (more is better 1 ok to start)	kHz

POTENTIAL ENGINEERING SOLUTIONS

A TEM mode kicker system is an attractive concept for advanced FEL facilities due to the ability to select individual bunches as needed. The electrodynamic kicker structure represents a broadband transmission line. The structure is very well studied and broadly used in the accelerator field. Our main R&D effort is focused on the pulser technology. Potential engineering solutions of multi-MW nanosecond pulsers were broadly discussed in the frame of R&D activities for the ILC damping rings ten years ago [6]. The 2006 Cornell Workshop in this regard selected: (1) inductive adder pulser concept (LNLL/SLAC), (2) pulsers based on Drift Step Recovery Diodes (SLAC), (3) commercial available pulsers from FID, Inc., (4) pulsers from Kentech, Inc., (5) pulsers from Behlke Inc. etc. All solutions are still valid for discussed advanced FEL facilities. An array of fast MOSFETs is used in (1). Several groups around world adopted this concept successfully. All needed components are available from industry. The FID, Inc. (and Megaimpulse) pulsers are effective solution from a cost and peak power point of view. However their technical solutions are based on proprietary technology. “Know-how” solutions are employed in their products. Several institutions successfully tested the FID pulsers for accelerator applications.

The R&D activity at SLAC adopts two well-known approaches to realize a multi-MW nanosecond peak power at resistive load. In both cases a non-linear media is used to assist a commercially available “slow” switch. The magnetic permeability of a ferromagnetic material and the conductance of semiconductors are common parameters that can be used to “speed up” a “slow” primary switch. A di/dt rate for all high-power switches (gas filled and solid state) shows that the current rise rate is reduced vs. switching current amplitude. It is known that the transmission line with ferromagnetic material may behave in an opposite way: a current rise rate on the output of a transmission line is an inversely proportional to the acting current amplitude. Such lines can assist the industry available switches to generate a high di/dt. Theory and engineering issues for a NTL design was developed in 60th [6].

Formation of solid state plasma and fast ionization processes in Si-base materials are the second approach where di/dt speed may be dramatically higher than takes place in the primary “slow” switch. A fast change of conductivity is limited by the saturated velocity of carrier in the solid-state semiconductor. For example, the saturated speed in Si-based semiconductor is approximately 10⁻² cm/ns. So,

the semiconductor thickness of 0.1 mm can change the conductivity during a 1 ns interval. Theory and engineering issues for this mode operation in semiconductors were developed in the 1980s [7]. The technology of DSRD fabrication was developed in the former USSR. The DSRD user community is not large and that is why there has not been a western supplier of similar devices in the past. This statement is not accurate for present-day, because the DSRD production capability has been transferred to the USA in the period from 2006 to 2013 under the SBIR DoE Phase I and II grant.

TABLE-TOP PULSE DEMONSTRATORS

Simplified circuit layouts for table-top demonstrators are shown in Fig. 2.

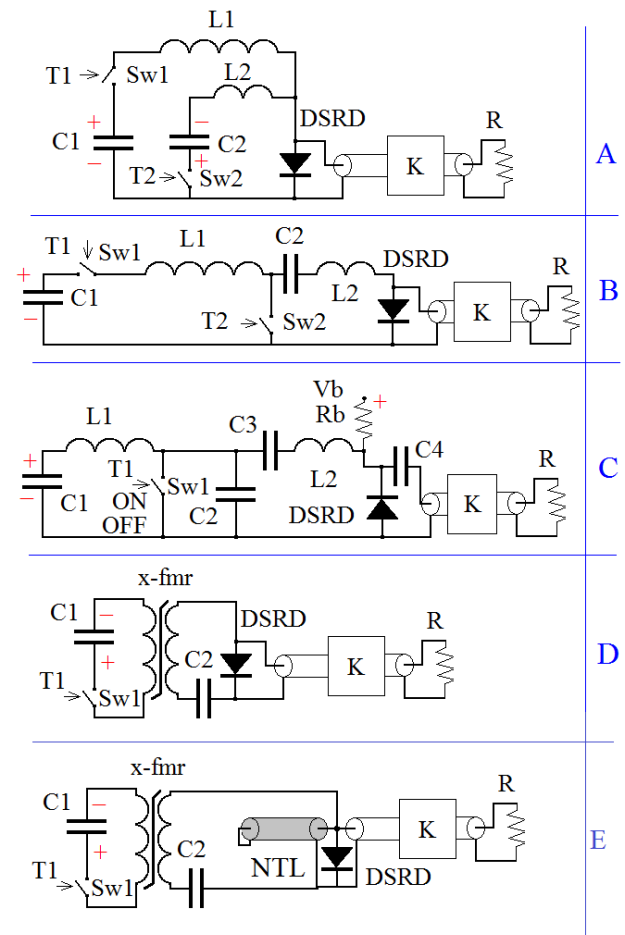


Figure 2: Simplified circuit diagrams for table-top demonstrators. Sw1 and Sw2 are primary “slow” switches governed by the external trigger (T1 and/or T2). DSRD and NTL are assisting “slow” switch.

The “A” and “B” layouts required two ON-type switches (Sw1 and Sw2) that are synchronized independently via T1 and T2. A DSRD is a two-terminal dynamic OFF switch that works with high current densities. The DSRD conductance is controlled by space charge effects in the p-n junction during pumping of semiconductor in forward

Content from this work may be used under the terms of the CC BY 3.0 licence (© 2018). Any distribution of this work must maintain attribution to the author(s), title of the work, publisher, and DOI.

Content from this work may be used under the terms of the CC BY 3.0 licence (© 2018). Any distribution of this work must maintain attribution to the author(s), title of the work, publisher, and DOI.

and reverse directions. Amplitudes I_{FWD} and I_{RE} depend upon charging voltages, and circuit parameters. The “C” and “D” topologies employ only one primary switch (Sw1). However, the “C” topology uses the ON/OFF primary switch. The “D” circuit diagram is planning to be used for UFK pulser in LCLS-II for the pump-probe experiments. Figure 3 shows the pulser output waveform, and Fig. 4 shows the lab table-top Demonstrator #1 setup.

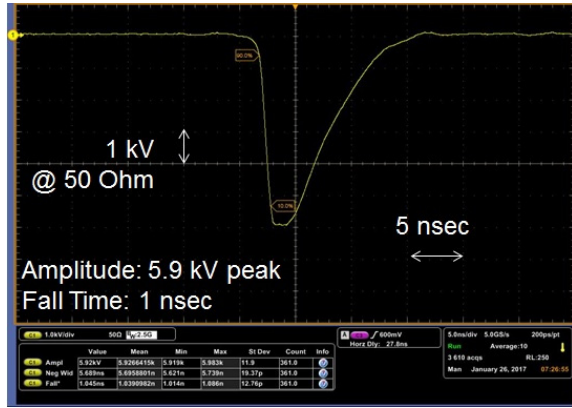


Figure 3: Output waveform with 1 ns fall time.

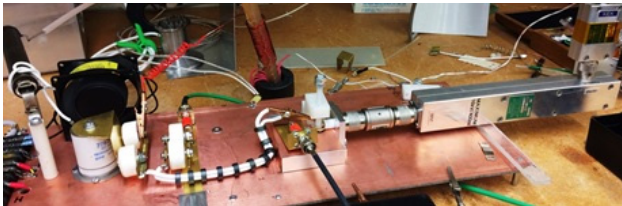


Figure 4: Lab table-top demonstrator #1.

The “E” circuit topology was used to demonstrate a multi-MW nanosecond pulse for the injection/extraction system. The output waveform is shown in Fig. 5.

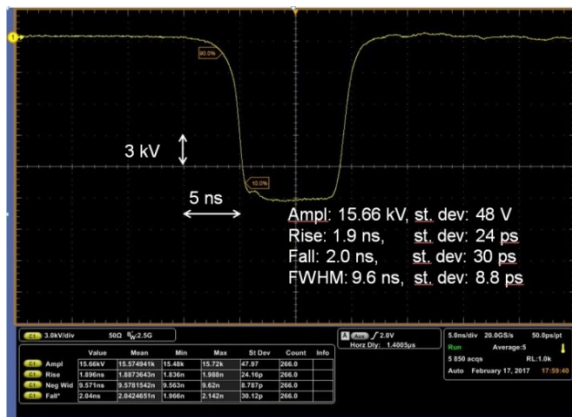


Figure 5: Output waveform with 2 ns rise and fall time.

In this case the HY-3189 thyatron was employed as a primary “slow” switch. A table-top Demonstrator #2 is shown in Fig. 6.

An evaluation of a field rigidity shows that Demonstrator #2 produces approximately 70+ G-m kick with a 100 cm TEM kicker structure. Advanced TEM kicker structure is shown in Fig. 7.

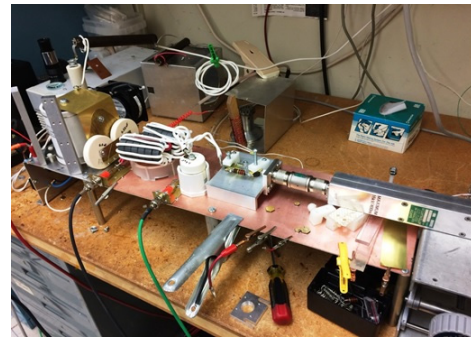
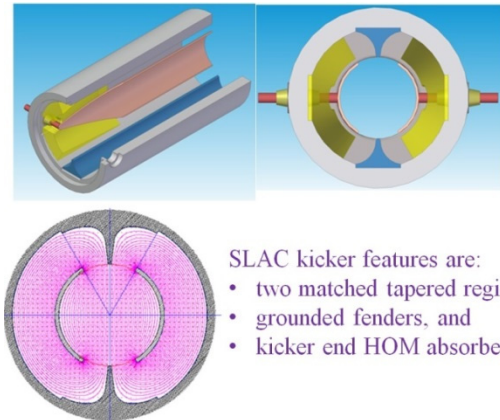


Figure 6: Lab table-top Demonstrator #2.



SLAC kicker features are:

- two matched tapered regions,
- grounded fenders, and
- kicker end HOM absorbers

Figure 7: Proposed in the 2002 TEM kicker structure for ILC DR [8] may be used in the advanced FEL facilities.

CONCLUSION

Our R&D results show that the known pulser concepts based on the assistance of non-linear materials (ferromagnetic and semiconductor) are attractive, promising, and a cost-effective solution for employment in the advanced FEL installations. A particular application of immediate research is a kicker for LCLS-II which requires <10 ns transit times such that two electron bunches can be utilized to generate different color X-rays for pump-probe experiments.

REFERENCES

- [1] BESAC Report on Facility Upgrades, June 9, 2016, <https://science.energy.gov>
- [2] Available at <https://science.energy.gov/aso/projects/>
- [3] F. Arntz, *et al.*, *Proc. of PAC07*, THPMN111, Albuquerque, NM, 2007.
- [4] Available at <http://www.lanl.gov/science-innovation/science-facilities/marie/accelerator-systems.php>
- [5] Available at <http://slac.stanford.edu/pubs/slacwps/wp07/slac-wp-131.pdf>
- [6] I. Katayev, “Electromagnetic Shock Waves”, Ed. D.L. Jones, 1963.
- [7] I. Grekhov, *et al.*, *Sov. Tech. Phys. Letters*, 9, 1983.
- [8] A. Krasnykh, *et al.*, SLAC-PUB-17099, 2017.

LASER-TO-RF SYNCHRONIZATION WITH FEMTOSECOND PRECISION

T. Lamb*, Ł. Butkowski, E. Felber, M. Felber, M. Fenner, S. Jablonski,
T. Kozak, J. Müller, P. Prędki, H. Schlarb, C. Sydlo, M. Titberidze,
F. Zummack, Deutsches Elektronen-Synchrotron (DESY), Hamburg, Germany

Abstract

Optical synchronization systems are already in regular operation in many FELs, or they will eventually be implemented in the future. In FLASH and the European XFEL, phase-stable optical reference signals are provided by a pulsed optical synchronization system in order to achieve low timing jitter FEL performance. The generation of phase-stable RF signals from a pulsed optical synchronization system is still a field of active research. The optical reference module (REFM-OPT), designed at DESY for operation in both FELs, employs a laser-to-RF phase detector, based on an integrated Mach-Zehnder interferometer. The phase drift of the 1.3 GHz RF reference signals with respect to the optical pulses is measured and actively corrected within the REFM-OPT at multiple locations in the accelerator. Therefore the REFM-OPT provides phase stable 1.3 GHz RF reference signals at these locations. The short-term and long-term performance in the accelerator tunnel of the European XFEL is presented and carefully reviewed.

INTRODUCTION

Femtosecond stability has become a key requirement in modern large-scale free-electron lasers (FELs). Optical synchronization systems for femtosecond synchronization have been developed and built over the past years. The most recent application for such an optical synchronization system is the remote RF synchronization. RF reference signals are distributed and used as the phase reference for many accelerator sub-systems at the European XFEL and FLASH at DESY. Their performance requirements are driven by the low-level RF (LLRF) system, where the stability of the accelerating fields in the superconducting cavities depends on them. The field stability requirement of 0.01° at 1.3 GHz (or about 20 fs) leads to a stability requirement of the reference signals of about 10 fs [1].

An active system had to be implemented due to the size of the European XFEL and the number of devices connected. RF amplifiers are required to compensate cable losses. The phase stability of the RF reference signals is disturbed during their transport through the accelerator due to temperature and humidity induced drifts of the installed RF cables, amplifiers and auxiliary components. The 10 fs stability can therefore – especially in large scale FELs like the European XFEL – not be reached by conventional RF transport. The optical synchronization system however can supply laser pulse trains with femtosecond stability to any point in the

accelerator. A Laser-to-RF phase detector within the REFM-OPT is used to measure the phase drift of the 1.3 GHz RF reference signals with respect to the optical reference at dedicated locations. These drifts are actively corrected and the REFM-OPT can therefore supply RF reference signals with femtosecond stability.

THE OPTICAL SYNCHRONIZATION SYSTEM

The central component of the optical synchronization system is the redundant master laser oscillator (MLO) which generates a low jitter, 216.66 MHz repetition rate optical pulse train at a wavelength of 1550 nm. It is tightly phase-locked to the RF master oscillator of the facility. The MLO is located in a central synchronization laboratory close to the injector laser. Environmental parameters like temperature and humidity are carefully controlled in this synchronization laboratory.

The laser pulses are subsequently distributed to individual link stabilization units (LSUs) from where the fiberlinks to the individual end stations launch. The fiberlink stabilization is based on balanced optical cross-correlation. The length changes of the optical fibers are compensated by a piezo driven fiber stretcher for fast changes and an optical delay line for slow long-term drift correction. Thirteen stabilized fiberlinks are currently in permanent operation at the European XFEL. More information on the optical synchronization system can be found in [2]. The optical synchronization system supplies reference signals to three different types of end stations.

The bunch arrival time monitors (BAMs) are used to measure the electron bunch arrival time with femtosecond precision at dedicated locations along the accelerator. A more detailed description of the BAM system can be found at [3]. A feedback system to the LLRF controllers allows to stabilize the electron bunch arrival time based on the BAM measurement.

Laser-to-Laser synchronization using balanced two-color optical cross-correlation is employed to synchronize laser systems along the FEL to the optical synchronization system. This is especially crucial for the pump-probe lasers which need to be tightly synchronized to the FEL but it is also foreseen for the injector lasers. Further details on Laser-to-Laser synchronization is available at [4].

The third and newest application is the Laser-to-RF synchronization. The key component of the REFM-OPT is the Laser-to-RF phase detector. It is based on a commercial integrated Mach-Zehnder modulator in which the phase dif-

* Thorsten.Lamb@desy.de

Content from this work may be used under the terms of the CC BY 3.0 licence (© 2018). Any distribution of this work must maintain attribution to the author(s), title of the work, publisher, and DOI.

ference between the 1.3 GHz RF signal and the phase stable laser pulses from the optical synchronization system leads to a proportional amplitude modulation of the optical pulse train. The principle of the Laser-to-RF phase detector has been evaluated and analyzed in [5].

The REFM-OPT is an engineered and fully integrated, remote controllable 19" unit built to be operated directly in the accelerator tunnel. Requirements for the REFM-OPT were driven by the architecture of the RF distribution system. The REFM-OPT for example includes six RF outputs with an output power level of 21 dBm each, such that all local components of the LLRF system plus the neighboring stations can be connected without requiring any further external components. An overview over the internals of the REFM-OPT and its engineering has been published in [6].

THE RF REFERENCE DISTRIBUTION SYSTEM

The conventional RF distribution system of the European XFEL is based on heliax cables. It starts at the 1.3 GHz RF master oscillator (RF-MO) in the injector building. The layout is presented in Figure 1. The fiberlinks which provide the optical reference signals with femtosecond precision to the REFM-OPTs are shown in red.

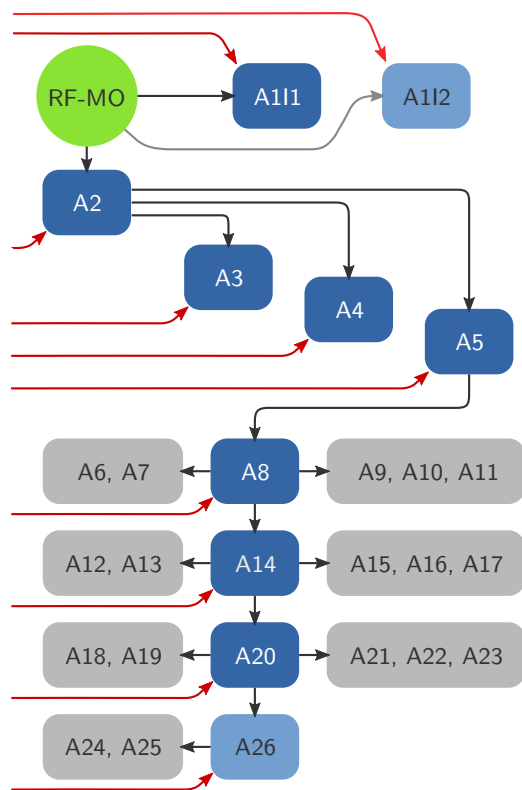


Figure 1: Layout of the RF reference distribution system including the optical reference signals (red). LLRF stations equipped with a REFM-OPT are presented in blue.

The RF distribution system is currently stabilized by a total of eight (final expansion stage is ten) REFM-OPTs within

dedicated LLRF stations (printed in blue). Each REFM-OPT delivers femtosecond-stable RF signals to the connected systems. Every LLRF master station up to the third magnetic chicane, which is located downstream of the LLRF station A5, is equipped with a REFM-OPT. These are the LLRF stations with the most demanding phase stability requirements. Further downstream of the bunch compressor the stability requirements are relaxed such that a single REFM-OPT supplies up to six LLRF stations with a local subdistribution. LLRF stations without a REFM-OPT are printed in gray. As a future upgrade, it is planned to stabilize this subdistribution (up to 150 m of distance) with RF interferometers for residual cable drift suppression [7].

The injector LLRF system (A111) is connected directly to the RF-MO and also phase stabilized by a REFM-OPT. The second injector (A112) has not been built yet and the REFM-OPT at the LLRF station A26 has not been installed up to now (both shown in light blue).

MEASUREMENT DATA

Until now only the REFM-OPTs in the injector (A111) and at the LLRF stations A3, A4 and A8 have been operated permanently. The remaining stations have already been commissioned but not regularly operated because their Firmware can only be updated to the newest version after a cabling modification which requires hardware access. The tunnel positions of the operated stations are 247 m for A3 and 295 m for A4. The station A8 is located at 611 m. The phase-locked-loops (PLL) within the REFM-OPTs have been established with a bandwidth of a few hundred Hz in order to correct slow drifts of the 1.3 GHz RF reference signals.

The measurement presented in Figure 2 has been started at the end of a maintenance day and it lasts one week. The bottom plot shows temperatures which were measured within the accelerator tunnel. The tunnel heats up after operation has been resumed. The LLRF stations A3 and A4 are located in the L2 area while the station A8 is located in the L3 area. The RF cables from the RF-MO are guided two stories down through media shafts and along the accelerator tunnel from L1 over L2 to L3. The peak-to-peak RF phase drift which was corrected at the station A8 amounts to 14.2 ps. The plot shows that the majority of the corrected phase drift of all three stations is common mode which indicates that it is induced already upstream of A3.

The largest temperature change after the maintenance occurs during the first 3 days. The temperature variations afterwards are much smaller. The peak-to-peak corrected phase change at A8 from day four to the end of the measurement amounts for example only to 2.9 ps while the stations A3 corrects in this time period already 2.2 ps of peak-to-peak phase drifts. The peak-to-peak temperature variation in this time in L2 is 0.26 °C while the temperature in L3 only varies about 0.18 °C. It is only an approximation to correlate single point temperature measurements with the phase drifts of the long RF connections. One can however estimate that even during the last four days of the measurement about 1 ps of

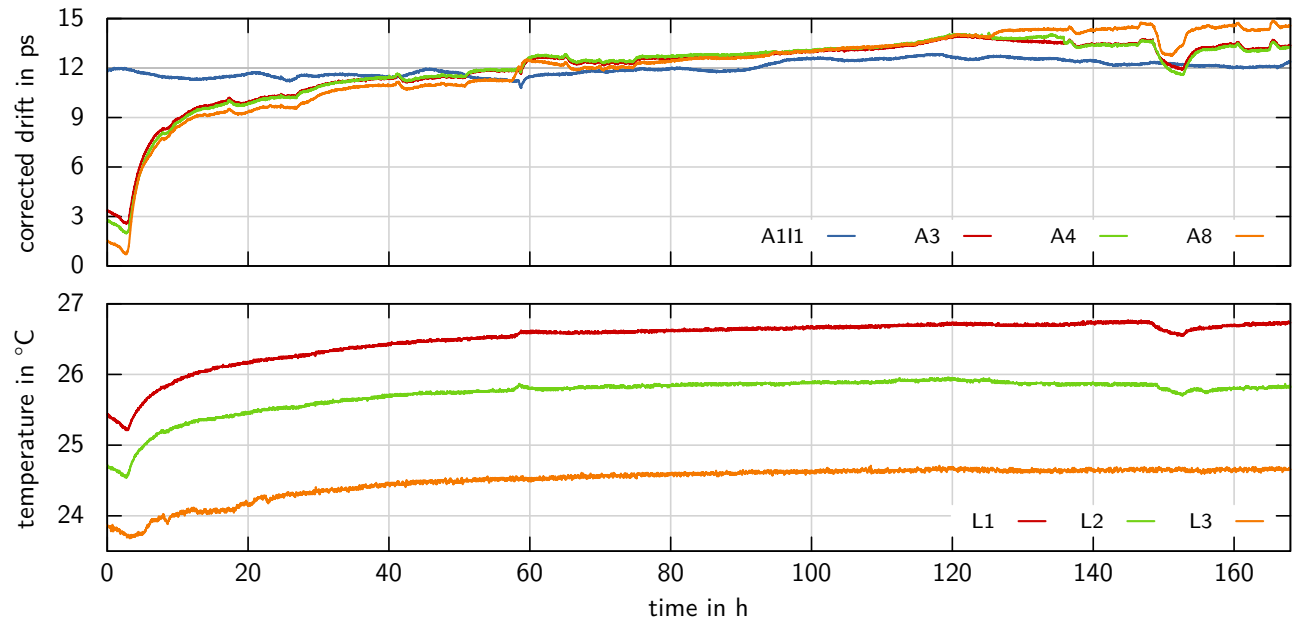


Figure 2: Cable drifts corrected by REFm-OPTs during regular FEL operation following a maintenance day. The remaining in-loop jitter amounts to 9.5 fs (1 Hz to 125 kHz).

common mode phase drifts might not have originated in the tunnel but elsewhere in the injector building.

The next REFm-OPT to be permanently operated is therefore the REFm-OPT at A2 in order to prove the above assumptions. The LLRF station A2 is located at 131 m. It should be possible to correct most of the phase drifts from Figure 2 at this station such that the consecutive REFm-OPTs see greatly reduced phase drifts.

The injector (A1I1) is connected by a dedicated cable directly from the RF-MO. It is shorter and guided through a different area. The peak-to-peak corrected phase drift at the REFm-OPT at A1I1 amounts to 2.1 ps. This is in the same order as the phase drifts in the accelerator tunnel - if one disregards the heat up after the maintenance day which is not applicable for the injector.

The short-term performance of the REFm-OPT at A3 is presented in Figure 3. Within the locking bandwidth of about 200 Hz the integrated detector noise floor amounts to 55 as while the in-loop jitter is 1 fs. There is still a large jitter contribution visible in the noise bump around 7 kHz which originates from the RF power-amplifier in the RF-MO and is outside the locking bandwidth of the REFm-OPT. This amplifier is about to be exchanged which should improve the performance of the 1.3 GHz RF reference signals by at least a few femtoseconds.

CONCLUSION

The quality of the RF reference signals throughout the facility can now be analyzed and monitored online with femtosecond precision through the REFm-OPT. Without the REFm-OPT the RF reference phase stability at the European XFEL would be in the order of a few ps peak-to-peak during normal operation and more than 10 ps peak-to-peak after

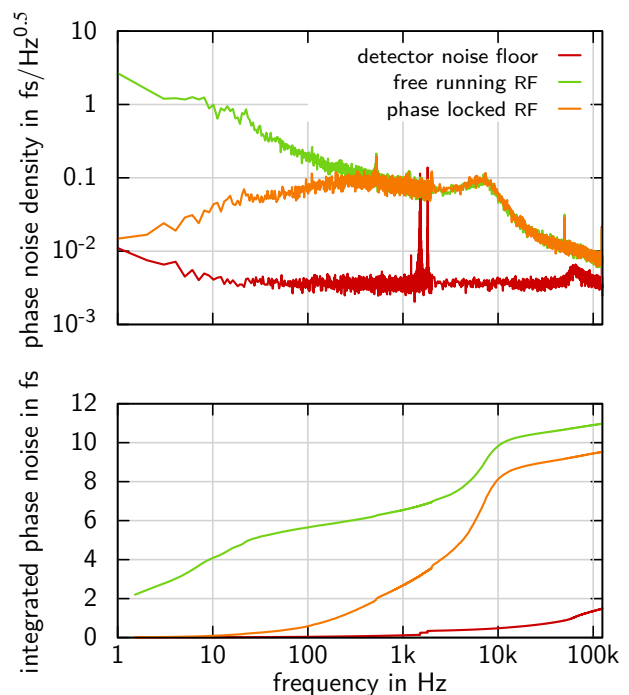


Figure 3: Short term performance of the REFm-OPT at A3.

maintenance days. With the REFm-OPT in operation, the phase drifts are corrected and the residual phase jitter of the 1.3 GHz RF in a bandwidth from 1 Hz to 125 kHz amounts to 9.5 fs. The specification of 10 fs phase stability is therefore fulfilled.

The next crucial step is to finally establish permanent operation of all installed REFm-OPTs and to further improve their performance.

REFERENCES

- [1] J. Branlard *et al.*, “The European XFEL LLRF system”, in *Proceedings of IPAC2012*, New Orleans, LA, USA, May 2012, paper MOOAC01, pp. 55–57.
- [2] C. Sydlo *et al.*, “Femtosecond optical synchronization system for the European XFEL”, in *Proceedings of IPAC2017*, Copenhagen, Denmark, May 2017, paper THPAB108, pp. 3969–3971. doi: 10.18429/JACoW-IPAC2017-THPAB108.
- [3] M. Viti *et al.*, “Recent upgrades of the bunch arrival time monitors at FLASH and the European XFEL”, in *Proceedings of IPAC2017*, Copenhagen, Denmark, May 2017, paper MOPIK072, pp. 695–697. doi: 10.18429/JACoW-IPAC2017-MOPIK072.
- [4] J. Müller *et al.*, “All-optical synchronization of pulsed laser systems at FLASH and XFEL”, in *Proceedings of IPAC2015*, Richmond, VA, USA, May 2015, paper MOPHA032, pp. 854–857.
- [5] T. Lamb, “Laser-to-RF phase detection with femtosecond precision for remote reference phase stabilization in particle accelerators”, Phd thesis, Technische Universität Hamburg-Harburg, Hamburg, Germany, 2016. doi: 10.3204/PUBDB-2017-02117.
- [6] T. Lamb *et al.*, “Design and operation of the integrated 1.3 GHz optical reference module with femtosecond precision”, in *Proceedings of IPAC2017*, Copenhagen, Denmark, May 2017, paper THPAB105, pp. 3963–3965. doi: 10.18429/JACoW-IPAC2017-THPAB108.
- [7] K. Czuba *et al.*, “Overview of the RF synchronization system for the European XFEL”, in *Proceedings of IPAC2013*, Shanghai, China, May 2013, paper WEPME035, pp. 3001–3003.

OPTIMIZATION OF SUPERCONDUCTING UNDULATORS FOR LOW REPETITION RATE FELS

J. A. Clarke, K. Marinov, B. J. A. Shepherd, and N.R. Thompson,
STFC Daresbury Laboratory and Cockcroft Institute, Sci-Tech Daresbury, Warrington, UK
V. Bayliss, J. Boehm, T. Bradshaw, A. Brummitt, S. Canfer, M. Courthold, B. Green, T. Hayler,
P. Jeffery, C. Lockett, and D. Wilsher, STFC Rutherford Appleton Laboratory, Didcot, UK
S. Milward and E. C. M. Rial, Diamond Light Source, Didcot, UK

Abstract

Superconducting undulators (SCUs) optimized for storage rings and MHz-level FELs require an intermediate beam screen to intercept the power deposited by the electron beam, due to resistive wall wakefields, to prevent magnet quenching. This beam screen increases the magnet gap by around 2 mm which is a significant increase when compared to the typical electron beam aperture of around 5 mm. However, lower repetition rate FELs only deposit of the order of tens of mW/m and so the beam screen is no longer needed resulting in a significant reduction in undulator magnet gap. We have investigated the impact of this reduced magnet gap and found that the magnetic field level increases greatly. For example, an SCU with a 15-mm period and 5-mm aperture optimized for a low repetition rate FEL instead of a storage ring will generate a field of 2.1 T compared to 1.4 T. Such a major increase in undulator performance could have a significant impact on the optimization of FELs. This paper describes how an SCU optimized for application in a FEL will be able to generate magnetic field levels far beyond those currently foreseen for any other magnet technology.

INTRODUCTION

Despite the ongoing improvements in permanent magnet undulators (PMUs), there is still a clear margin in performance advantage to be gained through the application of superconducting materials and it is for this reason that several groups around the world have been actively pursuing the detailed development of short period, high field SCUs for light source applications over the past ten years or more [1]. This research and development effort has led to the construction of a few SCUs which are now installed and in daily use on storage ring light sources in Germany [2] and USA [3]. These particular examples have exhibited very good operational performance in terms of reliability, stability, and user experience and this has increased confidence within the accelerator community that national FEL light source facilities, such as LCLS-II, should carefully assess employing SCUs rather than permanent magnet alternatives in their baseline configurations [4].

This paper explores how and when the engineering of SCUs can be significantly simplified for FELs compared to storage rings and the impact this will have on the available undulator parameters compared against the most advanced PMU options today.

SCU OPTIMIZATION FOR FELS

International efforts on SCU developments have primarily focussed upon storage ring applications which have different constraints to FELs. One clear difference is the accelerator vacuum requirement which is radically different between a stored beam facility and a single pass facility, with the former being far more demanding. Another difference is the relatively large good field region required in the storage ring undulators to maintain an adequate dynamic aperture and to enable efficient off-axis injection. Neither of these issues is of importance for single pass FELs, enabling narrower good field regions to be fit for purpose and potentially further simplifying the engineering.

However, the most significant difference between the two types of facility is the heating due to the electron beam in the SCU itself. In a storage ring care must be taken to ensure no synchrotron radiation from upstream dipoles can impinge on the SCU cold surface which is not an issue in FELs. More importantly though, in a storage ring there is significant beam heating due to resistive wall wakefields (RWW) within the SCU. This power level is too high for the 4K undulator magnet to handle without quenching and so all storage ring SCUs employ an intermediate beam screen between the magnet poles, held at between 10 and 20K, to absorb this power safely. This beam screen also acts as the beam vacuum chamber, which is essential to separate the machine vacuum from the magnet's thermal insulating vacuum. Significant engineering efforts are made to make this vacuum vessel have as little impact on the SCU magnet gap as possible but even with wall thicknesses of ~0.5mm and similar insulating spacing between this surface and the SCU coils and poles the magnet gap is increased by typically ~2.0mm compared to the aperture needs of the electron beam itself.

Since the power deposited by these wakefields scales linearly with the number of bunches passing through the SCU, it is clear that as the bunch repetition rate is reduced there will be a point at which the SCU will not suffer from significant beam heating and the internal vacuum chamber can be completely removed from the design and instead be replaced by a thin high conductivity copper liner similar to that employed by all permanent magnet in-vacuum undulators (IVU).

Content from this work may be used under the terms of the CC BY 3.0 licence (© 2018). Any distribution of this work must maintain attribution to the author(s), title of the work, publisher, and DOI.

Wakefield Calculations

We use the standard expression relating the longitudinal wakefield impedance of the beam pipe to the surface impedance of the beam pipe material at cryogenic temperatures [5]. The latter is a result of the anomalous skin effect (ASE) theory in metals [6, 7]. At room temperature, the classical skin depth is much larger than the mean free path of the conduction electrons in the metal and the ASE theory reproduces the surface impedance value obtained under normal skin effect assumptions. At cryogenic temperatures, however, the mean free path could greatly exceed the classical skin depth value. If, in addition, the bunch length is much greater than the critical length $\sigma_0 \approx 10$ fs (for copper) the ASE theory approaches the extreme anomalous skin effect regime (EASE) where the surface impedance only weakly depends on the temperature [8]. We consider an internal copper liner of circular cross-section with room temperature conductivity of 5.7×10^7 S/m, mean free path of 35.6 nm and relaxation time of 22.3 fs [5]. The residual resistance ratio (RRR) is set to 10, which is a conservative assumption. As the validity of the EASE approximation relies upon bunch lengths greatly exceeding σ_0 , the longitudinal loss factor calculation is performed in the framework of the full ASE theory. Gaussian bunch profiles have been assumed.

From the calculated longitudinal loss factor the energy deposited within the SCU per bunch per meter has been calculated for two different representative FEL bunch charges and this is plotted in Fig. 1 for three alternative apertures. Note that we have also calculated the loss factors for two parallel plates, representing a flat copper liner mounted on the magnet pole surface, and found the results to be broadly similar to those of the circular aperture given here. The loss factor increases rapidly as the bunch length approaches 1 fs but we expect that this bunch length regime is only significant for low charge FEL operation (typically 20 pC) and so in fact the higher charge mode (assumed here to be 250 pC) has the highest energy loss per bunch at its shortest operational bunch length, presumed here to be 10 fs.

Figure 2 plots the power loss per meter within the SCU as a function of bunch repetition rate, or more strictly speaking the number of bunches per second, for two representative FEL bunches. Note that we have carried out similar calculations for the power loss per meter in the SCU designed for the Diamond Light Source and although the energy loss per bunch is orders of magnitude less due to the relatively long bunches (~15–20 ps depending upon the operating mode), the actual power loss per meter is ~1 W/m due to the high average beam current when compared to FELs. This storage ring SCU power level from RWW is similar to that calculated and observed at the APS [9]. We estimate, based upon our long experience of SCU development and cryogenic systems in general, that a cryocooler-based cooling system for the SCU will comfortably operate at 0.1 W/m. From this we see from Fig. 2 that even the extreme FEL bunch of 250 pC with an rms bunch length of 10 fs (~10 kA peak

current) will comfortably sustain several hundred Hz repetition rate, at an aperture of only 3 mm. If longer bunches and/or lower bunch charges are acceptable then bunch repetition rates in excess of 10 kHz are feasible.

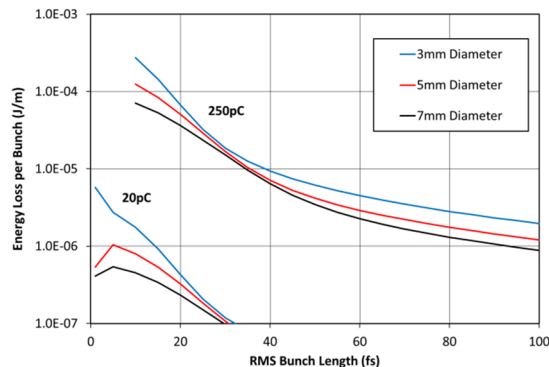


Figure 1: Energy deposited per bunch per meter, for two different bunch charges, in the SCU at 4K due to RWW as a function of electron bunch length and beam aperture.

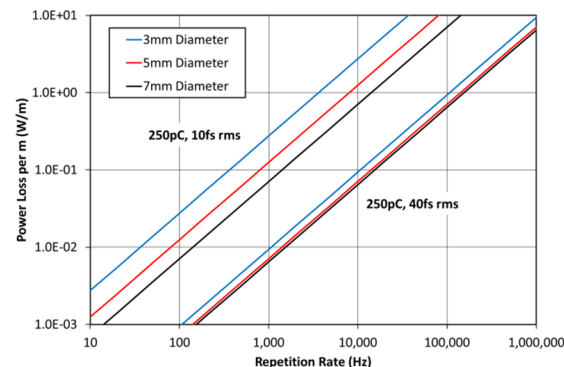


Figure 2: Power loss per meter, for two different bunch lengths, in the SCU at 4K due to RWW as a function of repetition rate and beam aperture.

SCU PARAMETERS

To compare the two types of SCU, one with the internal vacuum vessel and one with only a thin copper liner we have modelled the peak magnetic field in the undulator as a function of electron beam aperture and period using Opera 3D [10] for thirty separately optimized cases. The magnetic modelling assumes commercially available rectangular cross-section NbTi superconductor with a safety margin of 10%, operating at 1.8K. Each model has been individually optimized for the number of discrete windings per layer and for the number of layers. For models at 4K instead of 1.8K we typically observe a 10% reduction in peak field. For the case with the internal vacuum vessel (storage ring SCU) the magnet pole gap is 2.0 mm larger than the electron beam aperture (2 x 0.5 mm vacuum wall thickness plus 2 x 0.5 mm separation between the 20 K vessel and the 1.8 K magnet steel former and windings) and for the alternative case (FEL SCU) the magnet pole gap is only 0.2 mm larger than the electron beam aperture (2 x 0.1 mm copper liner mounted on the pole surface). A summary of the modelling results

is given in Fig. 3 for an example 15 mm period device. Also included for comparison is a state of the art cryogenic permanent magnet undulator (CPMU) utilising $\text{Pr}_2\text{Fe}_{14}\text{B}$ with a remnant field of 1.57 T at 77 K [11] and the SwissFEL Aramis IVU [12], the most advanced undulator technology so far in an operating FEL. At a typical FEL beam aperture of 5 mm the Aramis IVU generates 0.8 T ($K = 1.12$), the CPMU will generate 1.1 T ($K = 1.54$), the storage ring SCU 1.4 T ($K = 1.96$) and the FEL SCU 2.1 T ($K = 2.94$).

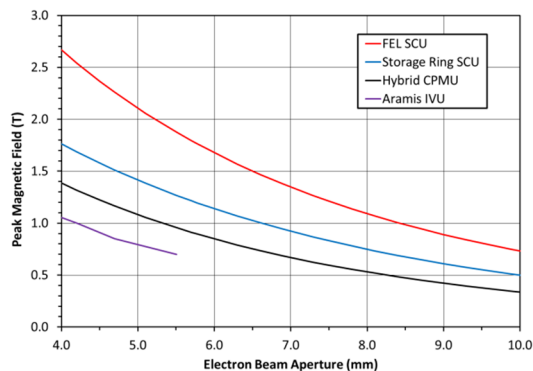


Figure 3: Peak magnetic field for a 15 mm period undulator as a function of electron beam aperture for both types of SCU, a state of the art hybrid CPMU and the Aramis IVU.

Fig. 4 shows how the peak field varies with period at a fixed electron beam aperture of 5 mm. Even at a period of 10 mm, the peak field is 1.2 T ($K = 1.12$) for the FEL SCU.

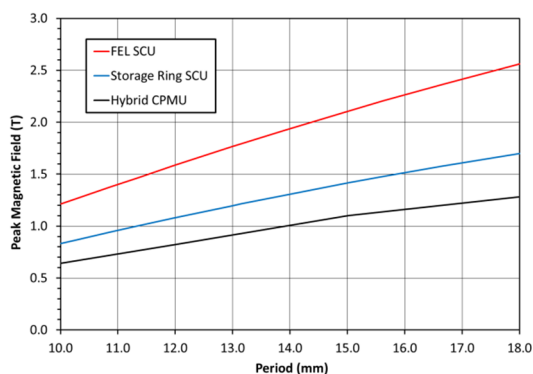


Figure 4: Peak magnetic field for a 5-mm electron beam aperture as a function of period for both types of SCU and a state of the art hybrid CPMU.

IMPACT OF ENHANCED SCU PERFORMANCE

In this section, we look at the impact of the enhanced performance offered by this new type of SCU on the fundamental parameters of an X-ray FEL. We take the SwissFEL Aramis hard X-ray FEL as an example. The Aramis FEL has an output wavelength range between 0.1 and 0.7 nm and this tuning range is enabled by adjusting the electron beam energy, not the undulator K value since it is assumed that $K = 1.2$ is a minimum value for sufficient FEL coupling. If we follow the same philosophy of

optimization then the period of the undulator reduces to 10.3 mm from 15.0 mm and the maximum required electron beam energy is only 4.8 GeV cf 5.8 GeV, a saving of ~17% in beam energy, a key cost driver for all FEL user facilities. In addition, the saturation length of the FEL reduces by more than 20%. As an alternative optimization, we have maintained the period at 15.0 mm but now our maximum K value of 2.9 allows significant wavelength tuning at a fixed electron energy and the minimum energy required to reach the longest wavelengths is significantly higher meaning higher beam powers and so higher FEL output power. A summary of the two SCU options considered compared against the Aramis FEL is given in Table 1.

Table 1: Comparison of FEL performance for two FEL SCU optimizations (5.0 mm electron beam aperture) and the implemented IVU for the Aramis FEL (4.7 mm aperture). Assumes peak current = 3kA, emittance = 0.4 mmrad, absolute rms energy spread = 350keV.

	Aramis IVU	FEL SCU Option 1	FEL SCU Option 2	
Period (mm)	15.0	10.3	15.0	
K	1.2	1.2	1.2 to 2.9	
Energy (GeV)	5.8	4.8	5.8	3.8
Wavelength (nm)	0.1 - 0.7	0.1 - 0.7	0.1 - 0.3	0.23 - 0.7
L_{sat} (m)	27.9 - 15.5	22.0 - 12.3	27.9 - 17.2	24.4 - 13.4
P_{sat} (GW)	10.2 - 7.6	7.4 - 5.4	10.2 - 17.3	9.1 - 15.1

CONCLUSIONS AND FURTHER WORK

There are significantly different design constraints on an SCU when it is optimized for an FEL instead of a storage ring. The most important change is that no internal vacuum chamber is required when the power levels due to RWW heating fall below ~100 mW/m. This constraint holds for FELs operating in the kHz regime and below and so is generally applicable to all normal conducting RF and plasma driven FELs.

Without the internal vacuum chamber the SCU magnet gap reduces by ~1.8 mm, leading to magnetic field levels far beyond those currently foreseen for any other magnet technology and opening up new FEL facility optimization possibilities. Whilst this paper has been wholly focussed upon planar devices, the conclusions also hold for helical SCUs which can achieve similar field levels in each plane to those predicted for the planar option and also offer enhanced FEL coupling. Indeed, we have successfully constructed a short period, high field helical SCU for a different application in the past [13].

We are currently constructing a short planar FEL SCU prototype in the UK and plan to test it with beam on the CLARA FEL Test Facility [14] in 2018.

REFERENCES

- [1] J. Clarke and T. Bradshaw, "Superconducting Undulator Workshop Report," *ICFA Beam Dynamics Newsletter* 65, p. 148 (2014).
- [2] S. Casalbuoni *et al.*, "Recent Developments on Superconducting Undulators at ANKA," *Proceedings of IPAC'15*, Richmond, VA, p. 2485 (2015).
- [3] Y. Ivanyushenkov *et al.*, "Development and Performance of 1.1-m Long Superconducting Undulator at the Advanced Photon Source," *Proceedings of IPAC'15*, Richmond, VA, p. 1794 (2015).
- [4] P. Emma *et al.*, "A Plan for the Development of Superconducting Undulator Prototypes for LCLS-II and Future FELs," *Proceedings of FEL'14*, Basel, Switzerland, p. 649 (2014).
- [5] G. Stupakov, K. L. F. Bane, P. Emma and B. Podobedov, *PRST-AB* 18, 034402 (2015). doi:10.1103/PhysRevSTAB.18.034402.
- [6] G. E. H. Reuter and E. H. Sondheimer, *Proc. R. Soc. A* 195, 336 (1948). doi:10.1098/rspa.1948.0123.
- [7] R. Dingle, *Physica* 19, 311 (1953). [https://doi.org/10.1016/S0031-8914\(53\)80035-2](https://doi.org/10.1016/S0031-8914(53)80035-2).
- [8] B. Podobedov, *PRST-AB* 12, 044401 (2009) doi:10.1103/PhysRevSTAB.12.044401.
- [9] Y. Ivanyushenkov *et al.*, "Development and operating experience of a short-period super-conducting undulator at the Advanced Photon Source," *PRST-AB* 18, 040703 (2015).
- [10] Opera magnetic modelling software, from Cobham: <http://operafea.com/>
- [11] A. Ghaith *et al.*, "Report on state-of-the-art short period undulators," EuPRAXIA Report, Del 6.1, Oct 2016.
- [12] SwissFEL "Conceptual Design Report," PSI Bericht 10-04, April 2012.
- [13] D. J. Scott *et al.*, "Demonstration of a High-Field Short-Period Superconducting Helical Undulator Suitable for Future TeV-Scale Linear Collider Positron Sources," *Phys. Rev. Lett.* 107, 174803 (2011).
- [14] J. A. Clarke *et al.*, "CLARA Conceptual Design Report," *JINST* 9, T05001 (2014).

UPDATE ON THE LIFETIME OF Cs₂Te CATHODES OPERATED AT THE FLASH FACILITY

S. Schreiber*, S. Lederer, DESY, Hamburg, Germany

L. Monaco, D. Sertore, P. Michelato, INFN Milano - LASA, Segrate (MI), Italy

Abstract

The photoinjector of the free-electron laser facility FLASH at DESY (Hamburg, Germany) uses Cs₂Te photocathodes. We give an update on lifetime and quantum efficiency of cathodes operated at FLASH during the last years. At the time of the conference, cathode 73.3 has been operated with a record of 933 days with a stable quantum efficiency of in average 8.8 %.

INTRODUCTION

Since 2005, FLASH [1–4], the free-electron laser user facility at DESY (Hamburg, Germany), successfully delivers high brilliance femtosecond short XUV and soft X-ray SASE radiation pulses to photon experiments.

A unique feature of FLASH is its superconducting accelerating technology. It allows to accelerate several thousand electron bunches per second. The bunches come in bursts with a repetition rate of 10 Hz. The maximal burst duration is 0.8 ms, the smallest distance between single bunches is 1 μs allowing a maximum number of 800 bunches per burst or 8000 bunches per second with a single bunch charge between 20 pC and a bit more than 1 nC. With a beam time of more than 8000 h per year, a maximum of about 200 C would be extracted from the cathode per year. In practice, not all users require maximum charge and maximum number of bunches per second so that the charge actually extracted is much lower and depends on the experimental requirements. The cathode of the electron source has to cope with these requirements.

THE ELECTRON SOURCE

The electron source of FLASH is a photoinjector based on a normal conducting L-band 1.5 cell RF-gun (1.3 GHz). [5] The RF-gun is version 3 (G3.1) with the usual race-track spring RF-contact between the gun backplane and the cathode. The RF-gun was built in 2005, conditioned at the PITZ facility (DESY, Zeuthen) in 2006 and finally installed in April 2013 as a preemptive maintenance measure replacing gun G4.1. The gun is operated with an RF power of 5 MW corresponding to a maximal accelerating field at the cathode of 52 MV/m, which leads to a beam momentum of 5.6 MeV/c. The gun is designed to provide the same RF-pulse length as the superconducting accelerator: the RF pulse flat top duration is up to 800 μs with a repetition rate of 10 Hz. The average RF power of 40 kW is efficiently cooled away by a dedicated water cooling system [6] keeping the gun temperature within 0.02 K [7].

* email: siegfried.schreiber@desy.de

The RF-gun and cathode system vacuum is pumped with several ion-getter pumps (IGP) most of them with a pumping speed of 60 l/s each. A few IGP's are equipped with an additional titanium-sublimation pump (TSP) adding 1000 l/s. The vacuum set-up is very similar to Fig. 4 in [5]. The base pressure without RF is kept below 2×10^{-10} mbar, with RF, the pressure increases roughly by a factor of 2. Note, that the pressure is not measured inside the gun body nor at the cathode surface.

To generate thousands of bunches per second with a charge in the nC-scale, we use a high quantum efficiency cathode. Cesium telluride (Cs₂Te) has been proven to be a reliable and stable cathode material with an excellent quantum efficiency (QE) for a laser wavelength around 260 nm [8–10]. The bunch charge required for FLASH operation is between 20 pC (for ultra-short SASE pulse operation) and a bit more than 1 nC (for efficient THz-generation).

Typical numbers are illustrated in the following example: We extract a charge of 1 nC with a laser pulse energy of 50 nJ having a QE of the Cs₂Te cathode of 10 %. The laser wavelength is 262 nm. For a burst of 800 pulses with 1 MHz and 10 bursts per second, this corresponds to a burst laser power of 50 mW. The laser pulse duration is 6.5 ps (sigma) leading to a peak power of 3 kW only. The laser spot shape is a truncated Gaussian with a diameter of 1.2 mm yielding a fluence in the burst of 4.4 mJ/cm², far away from typical damage thresholds of a few J/cm². These are all reasonable low laser power values which eases the design of the laser system and, damages or ablations of optical components or of the cathode thin film itself are avoided. The laser is sent to the cathode through a high quality fused-silica vacuum window [11] and is reflected to the cathode with a custom made mirror [12] inside the vacuum. For details on the FLASH injector laser systems, the reader is referred to [13] and references therein.

QUANTUM EFFICIENCY

For practical reasons, we define the quantum efficiency (QE) as the ratio of number of photons impinging the photocathode and the number of electrons emitted – while the RF-gun is operated at its nominal working point.

The nominal working point of the RF-gun is at a forward power of 5 MW which yields in an on-crest accelerating field of 52 MV/m. The launch phase is set to of 38° from the zero-crossing point. This phase has been chosen years ago and has been kept as a reference phase for all QE-data presented since then. The launch phase for SASE-operation is usually around 45°.

Content from this work may be used under the terms of the CC BY 3.0 licence (© 2018). Any distribution of this work must maintain attribution to the author(s), title of the work, publisher, and DOI.

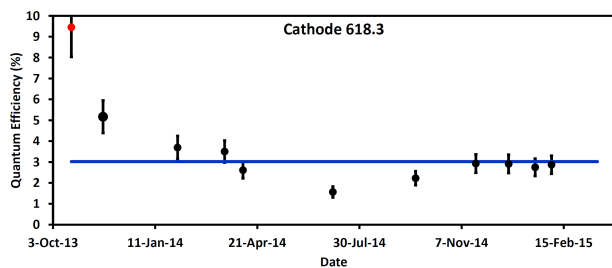


Figure 1: Quantum efficiency (QE) of cathode 618.3 during operation at FLASH. The cathode was in operation for 439 days. The blue line shows the average QE of 3 %. The red dot indicated the QE measured immediately after production with a Hg-lamp in May 2013.

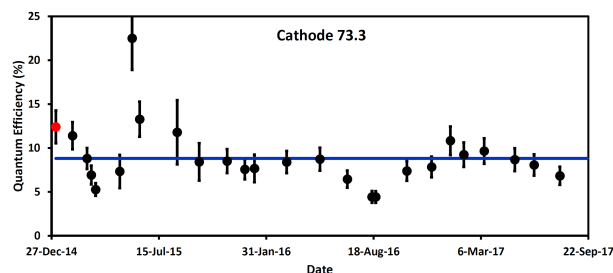


Figure 2: Quantum efficiency (QE) of cathode 73.3 during operation at FLASH. By the time of the conference, the cathode is in operation for 933 days. The blue line shows the average QE of 8.8 %. The red dot indicated the QE measured immediately after production with a Hg-lamp in June 2013.

The extracted charge is measured with a toroid at the RF-gun exit, the laser energy with a joulemeter [14] in front of the vacuum window. The transmission of the vacuum window and the reflectivity of the in-vacuum mirror is taken into account. However, a possible long-term degradation of transmission of the vacuum window due to radiation or a degradation of the reflectivity of the in-vacuum mirror has not been taken into account for this study.

The charge is measured as a function of laser energy while the laser energy is varied using a combination of a half wave-plate with a polarizer. The QE is always measured at the center of the cathode with laser spot diameters of 1 and 1.2 mm, while the cathode diameter is 5 mm. Usually a laser spot of 1.2 mm is used for SASE-operation.

Finally the QE is obtained by a linear fit on the data points not yet in saturation. From a certain laser energy density on, space charge effects reduce the amount of emitted electrons. For an example of such a fit, the reader is referred for instance to [15, 16]. The measurement error is in the order of 15 %.

Longterm Operation of Cs₂Te Cathodes

In the early years of RF-gun operation at the TESLA Test-Facility and FLASH, 1998 to 2013, many different cathodes have been in use, mostly for a short time only. For more information on lifetime of various cathodes, the reader is referred to [9, 15–21].

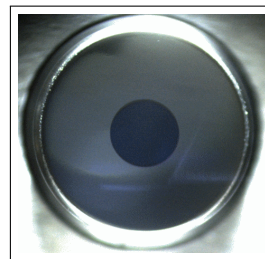


Figure 3: Picture of a cathode plug in a transport chamber. The molybdenum-plug has a diameter of 16 mm, the Cs₂Te thin film of 5 mm. The Cs₂Te film has in this example a dark blueish color.

Since November 2013, only two different photocathodes have been in operation at FLASH: cathode 618.3 produced at DESY in May 2013 and 73.3 produced at LASA, Milano in June 2013.

The cathodes have been produced with the usual recipe. A thin film of Cs₂Te with a diameter of 5 mm is deposited on a polished molybdenum plug. Figure 3 shows a picture of a cathode. Cathodes 618.3 and 73.3 have the 3rd thin-film of Cs₂Te deposited onto plug 618 and 73 resp. For details on the production of cathodes see [16, 18].

In February 2015, cathode 618.3 has been exchanged with 73.3 after 439 days of stable operation at a QE of 3 % (Fig. 1). The reason for the change was nor low quantum efficiency nor any other defect. We simply wanted to verify, that cathode 73.3 stored for almost 2 years was still good – since it was, we kept it in.

The lifetime of both cathodes is remarkable. Cathode 618.3 already showed a lifetime record of more than 400 days, cathode 73.3 surpassed this with 933 days of continuous operation – by the time of the conference. FLASH usually runs more than 8000 hours per year thus the cathode has a small idle time of 10 % of the yearly operation time. Cathode 73.3 is still in operation with a QE average of 8.8 ± 1.3 % (Fig. 2). The total amount of charge extracted by cathode 618.3 was 3.2 C, by cathode 73.3 18 C up to now.

The drop of QE of cathode 618.3 when firstly operated – compared to the initial QE after production – is explained by a small vacuum leak developed in October 2013 at the gun RF-window of 10^{-8} mbar l/s. The leak had only been discovered later and was repaired in April 2014 by exchanging the RF-window. This explains the low but stable quantum efficiency around 3 % of cathode 618.3. During conditioning time of the new window from April to June 2014 the QE dropped further to 2 % and recovered later due to the improved vacuum pressure when a stable operation with the new window has been achieved.

This shows, that the key for a long lifetime is to maintain a good vacuum pressure in the RF-gun. Also cathode 73.3 has partially suffered from vacuum leaks in the beamline section downstream the RF-gun and on the RF-window (July 2016). In contrast to 618.3, these leaks have been discovered early

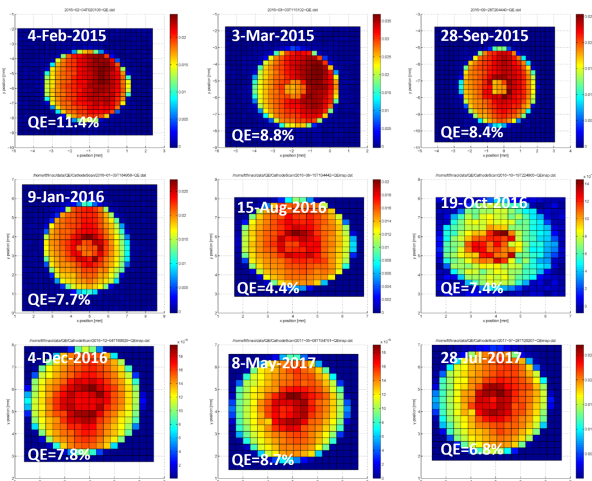


Figure 4: QE-map evolution of cathode 73.3 from February 2015 to July 2017. Each map shows the measured charge as a function of the horizontal and vertical position of the laser beam spot on the cathode surface. The charge is color coded and is given in nC. The QE value measured in the center of the cathode is indicated in the lower left corner of each map.

and could be repaired in a timely manner, so that the QE has not suffered too much and recovered quickly.

As to remind the reader, previous studies e.g. [22] have already shown, that the QE strongly depends on vacuum conditions and that pollution with oxygen or other molecules containing oxygen has to be avoided. The same study also showed, that partial recovery of the initial QE by UV light exposure is possible.

QE-Map Evolution

A QE-map is obtained by scanning a laser beam with constant energy over the cathode. The size of the laser beam is 100 μm in diameter ($\sigma = 25 \mu\text{m}$) obtained with a hard edge aperture imaged onto the cathode. The scanning step size is 85 μm . We use calibrated linear translation stages moving beamline mirrors in horizontal and vertical direction. For each scan point, the charge is measured with a toroid right after the RF-gun. The single bunch charge is adjusted to a maximum of 10 to 30 pC, small enough to avoid space charge related saturation effects.

Figure 4 shows a series of QE-maps of cathode 73.3 measured during the last 900 days of operation.

Initially the QE degrades at the cathode center where the laser hits. The cathode has a diameter of 5 mm, while the laser spot during FLASH operation is 1.2 mm (flat top). The surrounding QE reduces slowly but steadily with time. Due to non-perfect vacuum conditions, we expect a slow reduction of the overall QE.

The QE at the cathode center remains stable at a high level of 8%. We explain this by laser cleaning of the cathode surface. A similar behavior has been observed with cathode 618.3 [10]. This again confirms the result of previous pollution studies [22].

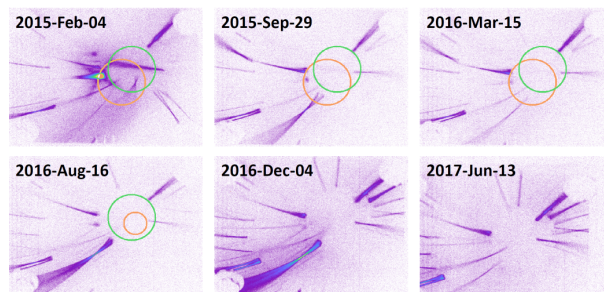


Figure 5: Darkcurrent emitted by cathode 73.3. The images are taken between February 2015 and Jun 2017. The green circle indicates the approximate position of the Cs_2Te film, the orange circle is a marker for another purpose not discussed here. The darkcurrent point sources appear as streaks due to the field of the gun solenoid (180 mT).

DARKCURRENT

Darkcurrent which is transported with the beam is usually emitted by particles close to or on the cathode [23, 24]. The RF-gun has been cleaned with dry-ice reducing the darkcurrent emitted at the gun backplane by an order of magnitude. Even though care is being taken to avoid particle contamination, contamination due to cathode handling cannot be totally excluded. The cathode is produced in a preparation chamber (at LASA or DESY). A stack of four fresh cathodes sitting in a carrier is transferred to a so-called transport box – maintaining ultra-high vacuum conditions all time. The transport box is shipped to FLASH where it is connected to the load-lock system of the RF-gun. One cathode plug is pulled out of the carrier and inserted into the gun. Due to this handling, contamination with emitting particles may occur.

Figure 5 shows images of darkcurrent taken from February 2015 to June 2017 with cathode 73.3. We use a screen of Ce:YAG powder about 1.6 m from the cathode downstream the RF-gun. For all images, the RF-gun is operated with standard parameters (see above), and a solenoid field of 180 mT. Since the emitted darkcurrent has a large energy spread, streaks develop due to the focusing solenoid field. The camera settings and RF-pulse length have been equal for all images so that the relative strength of the darkcurrent emitters can be compared. The absolute darkcurrent measured with a Faraday cup at the same location and with the same size as the screen is 5 μA . The uncertainty of the current measurement is 20%.

The first image of Fig. 5 shows the darkcurrent of the freshly inserted cathode. A strong emitter is present, which disappeared later. A few other smaller emitters disappeared with time until a new emitter started mid 2016. The darkcurrent increased by a factor of 2 during this incident. The emitter was conditioned away by normal operation by January 2017. Since then the situation is stable again, the darkcurrent is back to the usual 5 μA level.

What the operation of the RF-gun is concerned, the tracking of darkcurrent images is a useful tool to detect defects at

the gun backplane and the RF-contact between the cathode and the gun. In the past, at several occasions damages have been observed forcing a change of the cathode or even the gun body itself. Moreover, high darkcurrent leads to serious activation of beamline components in the accelerator and is also a cryogenic load, which needs to be avoided. We use a kicker/collimator system to suppress darkcurrent to a large amount after the RF-gun at 5.6 MeV.

CONCLUSION

A Cs₂Te cathode has been operated at FLASH with a lifetime record of more than 900 days with a stable quantum efficiency of in average 8.8 ± 1.3 %. The cathode is operated with beam 90 % of the year and has extracted a total of 18 C of charge up to now. The QE maps show a quick reduction of quantum efficiency of the fresh cathode at the place where the laser hits. The overall QE of the whole cathode degrades with time as expected. In contrast, the QE at the cathode center remains stable due to laser cleaning effects. The long lifetime is clearly connected to a very good ultra-high vacuum being maintained in the RF gun. The darkcurrent from the cathode is stable at a low 5 μ A level. A few emitters of the fresh cathode have been successfully conditioned away.

ACKNOWLEDGMENT

We would like to acknowledge our colleagues from LASA, Milano, Italy and from DESY Hamburg and Zeuthen for their support in cathode preparation and vacuum equipment.

REFERENCES

- [1] W. Ackermann *et al.*, “Operation of a free-electron laser from the extreme ultraviolet to the water window”, *Nature Photonics* **1**, 336 (2007).
- [2] S. Schreiber and B. Faatz, “The free-electron Laser FLASH”. In: High Power Laser Science and Engineering, **3**, e20 (2015).
- [3] B. Faatz *et al.*, “Simultaneous operation of two soft x-ray free-electron lasers driven by one linear accelerator”, *New J. Phys* **18**, 062002 (2016).
- [4] K. Honkavaara *et al.*, “Status of the FLASH FEL User Facility at DESY”, presented at the 38th Int. Free Electron Laser Conf., Santa Fe, NM, USA, 2017, paper MOD02, this conference.
- [5] F. Stephan *et al.*, “Detailed characterization of electron sources yielding first demonstration of European X-ray Free-Electron Laser beam quality”, *Phys. Rev. ST Accel. Beams* **13** (2010) 020704.
- [6] K. Kruppa *et al.*, “High Precision Temperature Control for Injector Components of a Free-Electron Laser”, in Simulation and Modeling Methodologies, Technologies and Applications, Advances in Intelligent Systems and Computing, **442**, 2016 Ed. M.S. Obaidat, J. Kacprzyk, T. Oeren, J. Filipe, Springer Int. Publ., Switzerland
- [7] S. Pfeiffer *et al.*, “Precision feedback control of a normal conducting standing wave resonator cavity”, *Phys. Rev. Accel. Beams*, to be published.

- [8] D. Sertore *et al.*, “First operation of cesium telluride photocathodes in the TTF injector RF gun”, *Nucl. Instr. Meth. A* **445**, 422 (2000).
- [9] S. Schreiber *et al.*, “On the Photocathodes used at the TTF Photoinjector”, in *Proc. 2003 Particle Acc. Conf.*, Portland, Oregon, USA, 2003, p. 2071, WPAB016.
- [10] S. Schreiber and S. Lederer, “Lifetime of Cs₂Te Cathodes Operated at the FLASH Facility”, in *Proc. 37th Int. Free Electron Laser Conf.*, Daejeon, Korea, 2015, paper TUP042, p. 464.
- [11] MPF Products Inc., fused silica viewport, Corning 8655 Grade AA, Class 0.
- [12] LT Ultra-Precision Technology GmbH, planar mirror, aluminum coated stainless steel.
- [13] S. Schreiber *et al.*, “Simultaneous Operation of Three Laser Systems at the FLASH Photoinjector”, in *Proc. 37th Int. Free Electron Laser Conf.*, Daejeon, Korea, 2015, paper TUP041, p. 459.
- [14] Moletron, J-5, <http://lasers.coherent.com>
- [15] S. Schreiber *et al.*, “Cathode Issues at the FLASH Photoinjector”, in *Proc. 30th Int. Free-Electron Laser Conf.*, Gyeongju, Korea, 2008, paper FRAAU05, p. 552.
- [16] S. Lederer *et al.*, “Photocathode Studies at FLASH”, in *Proc. 11th European Particle Acc. Conf.*, Genoa, Italy, 2008, paper MOPC072, p. 232.
- [17] S. Schreiber, “Performance status of the RF-gun based injector of the TESLA Test Facility Linac,” in *Proc. 7th European Particle Acc. Conf.*, Vienna, Austria, 2000, paper THOAF203, p. 309.
- [18] D. Sertore *et al.*, “Review of the Production Process of TTF and PITZ Photocathodes”, in *Proc. 2005 Particle Acc. Conf.*, Knoxville, Tennessee, USA, 2005, paper MOPB009, p. 671.
- [19] D. Sertore *et al.*, “High QE photocathodes at FLASH,” in *Proc. 10th European Particle Acc. Conf.*, Edinburgh, Scotland, UK, 2006, paper WEPLS052, p. 2496.
- [20] L. Monaco *et al.*, “High QE Photocathodes Performance during Operation at FLASH/PITZ Photoinjectors,” in *Proc. 22th Particle Acc. Conf.*, Albuquerque, NM, USA, 2007, paper THPMN025, p. 2763.
- [21] S. Lederer *et al.*, “Photocathodes at FLASH”, in *Proc. 33th Int. Free Electron Laser Conf.*, Shanghai, China, 2011, paper THPA19, p. 511.
- [22] P. Michelato *et al.*, “Cs₂Te Photocathodes Robustness Studies”, in *Proc. 11th European Particle Acc. Conf.*, Genoa, Italy, 2008, paper MOPC075, p. 241.
- [23] J.H. Han *et al.*, “Dark Current and Multipacting in the Photocathode RF Guns at PITZ”, in *Proc. 2005 Particle Acc. Conf.*, Knoxville, Tennessee, USA, 2005, paper WPAP004, p. 895.
- [24] L. Monaco *et al.*, “Dark Current Investigation of FLASH and PITZ RF Guns”, in *Proc. 10th European Particle Acc. Conf.*, Edinburgh, Scotland, UK, 2006, paper WEPLS051, p. 2493.

CALCULATIONS FOR A THz SASE FEL BASED ON THE MEASURED ELECTRON BEAM PARAMETERS AT PITZ

P. Boonpornprasert*, M.Krasilnikov, F. Stephan, DESY, Zeuthen, Germany

Abstract

The Photo Injector Test facility at DESY, Zeuthen site (PITZ), develops high brightness electron sources for modern linac-based Free Electron Lasers (FELs). The PITZ accelerator can also be considered as a suitable machine for the development of an IR/THz source prototype for pump-probe experiments at the European XFEL. Calculations of THz radiation by means of a SASE FEL based on the simulated and the measured beam profiles at PITZ for the radiation wavelength of 100 μm were performed by using the GENESIS1.3 code. The results of these simulations are presented and discussed in this paper.

INTRODUCTION

The Photo Injector Test facility at DESY, Zeuthen site (PITZ) has been established to develop, study and optimize high-brightness electron sources for modern linac-based short-wavelength Free-Electron Lasers (FELs) like FLASH [1] and the European XFEL [2].

The concept of generating IR/THz radiation by electron bunches from a "PITZ-like" accelerator for pump and probe experiments at the European XFEL was presented in [3]. PITZ has been considered as an ideal machine for the development of such IR/THz source. Start-to-end (S2E) simulations of the SASE FEL from a PITZ-like accelerator were performed and presented in [4]. An electron beam with 4 nC bunch charges was used for the FEL generation. Experimental optimization and characterization of 4 nC electron beams including time-resolved measurements were done and presented in [5].

In this paper, we present results of beam dynamics simulation using the actual PITZ beamline layout together with the results of electron beam measurements. Then, we performed SASE FEL simulations based on the simulated and the measured beam profiles for a radiation wavelength of 100 μm by using the GENESIS1.3 code. The initial seed for the random number generator used for particle phase fluctuation in the GENESIS1.3 code was scanned in order to simulate the FEL pulse energy fluctuation during the SASE FEL process.

BEAM DYNAMICS SIMULATION

Since works in [4] were studied by using only a PITZ-like beamline layout, the beam dynamics simulations with the actual PITZ layout were re-done. The actual PITZ beamline plus an extension for simulation studies for an IR/THz SASE FEL at the end of the beamline is shown in Fig. 1. The layout consists of a 1.6-cell L-band photocathode RF gun

surrounded by main and bucking solenoids, a CDS booster, a TDS cavity, screen stations, quadrupole and dipole magnets and an APPLE-II type undulator which is assumed to be placed at the end of the beamline. Dispersive sections (LEDA, HEDA1 and HEDA2) are used for electron beam momentum and longitudinal phase space (LPS) measurements.

The ASTRA code [6] is used for simulation of the electron beam with 4 nC bunch charge from the cathode to the undulator entrance. Space-charge effects were included in the simulation as well. Machine parameters used in this simulation are shown in Table 1. The RF gun phase was adjusted for the maximum mean momentum and the booster phase was adjusted for the minimum momentum spread. The quadrupole magnets along the beamline were used for beam transport and matching. The simulated beam parameters at the undulator entrance are listed in Table 2.

Table 1: Machine Parameters Used in Beam Dynamics Simulations and Measurements. PC means Photocathode.

Parameter	Sim.	Meas.
PC laser long. pulse shape	Flat-top	Gaussian
PC laser pulse duration (FWHM) [ps]	~20	~11
PC laser diameter on the cathode [mm]	5.0	3.7
Peak E-field in the gun [MV/m]	60.5	60.5
Peak E-field in the booster [MV/m]	9.8	9.8

Table 2: Electron Beam Parameters Resulted from Beam Dynamics Simulation and Measurements

Parameter	Sim. [§]	Meas. [†]
Bunch charge [nC]	4.0	4.0
Average momentum [MeV/c]	15.1	15.2
Momentum spread [keV/c]	134.7	50.9
Average slice momentum spread [keV/c]	6.2	28.5
Projected $\varepsilon_{n,x}$ [μm]	7.9	7.1
Projected $\varepsilon_{n,y}$ [μm]	7.6	11.1
Average slice $\varepsilon_{n,x}$ [μm]	3.1	10.9
Average slice $\varepsilon_{n,y}$ [μm]	3.1	-
Peak current [A]	195	183
Bunch length [mm]	2.0	3.0

[§] The simulated beam parameters at the undulator entrance

[†] The measured beam parameters at the measurement stations

* prach.boonpornprasert@desy.de

Content from this work may be used under the terms of the CC BY 3.0 licence (© 2018). Any distribution of this work must maintain attribution to the author(s), title of the work, publisher, and DOI.

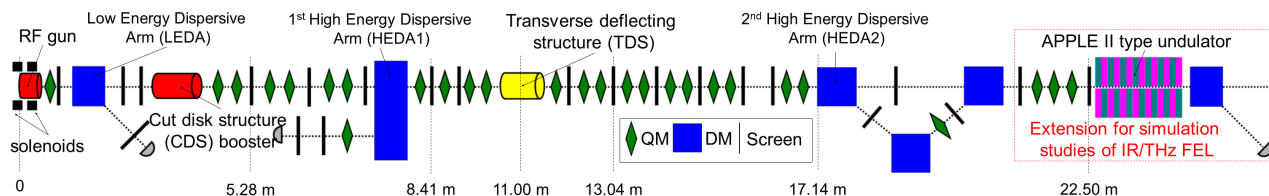


Figure 1: Layout of the actual PITZ beamline plus an extension for an IR/THz FEL for simulation studies. Here QM, DM and screen represent quadrupole magnets, dipole magnets and screen stations for monitoring of beam transverse profiles, respectively. The numbers represent the distance from the photocathode location ($z = 0$).

BEAM MEASUREMENTS

Machine parameters used for the 4 nC beam measurements are also listed in Table 1. Different from the simulation, a photocathode laser pulse with Gaussian temporal shape was used because this profile was the only one available at that time due to technical reasons. The laser diameter on the cathode was also reduced to 3.7 mm in order to have an acceptable uniform transverse laser profile on the cathode. Similar to the simulation, the RF gun phase was adjusted for the maximum mean momentum measured by LEDA and the booster phase was adjusted for the minimum momentum spread measured by HEDA1.

Some parameters of the 4 nC electron beams which are necessary for SASE FEL calculations were measured including, projected momentum profile, transverse phase space, current profile, slice transverse emittance and slice momentum spread. Details about the measurements of the 4 nC electron beams are presented and discussed in [5]. The measured beam parameters are listed in Table 2 together with the parameters from the beam dynamics simulation. Note that measured beam parameters are parameters at their measurement stations. By transporting the electron beam to the location of the undulator entrance, these parameters may have been changed. However, in this work we assumed that they are parameters at the undulator entrance for comparison of FEL simulation results from both cases.

SASE FEL CALCULATIONS

The GENESIS1.3 code [7] is used for simulations of the SASE FEL radiation. An APPLE-II undulator in helical mode [8] with period length of 40 mm and total length of 5 m (125 periods) is used as the radiator. The simulations were performed for a radiation wavelength of 100 μm using a 15 MeV/c beam. We assumed that the simulated and measured beam parameters in Table 2 are those at the undulator entrance. The Twiss parameters of the beams were assumed to be matched for beam transport along the undulator.

In order to simulate the FEL pulse energy fluctuation during the SASE FEL process, the initial seed for the random number generator used for particle phase fluctuation [9,10] in the GENESIS1.3 code was scanned from 1 to 100. Figure 2 shows results of the simulated FEL pulse energy averaged from the 100 simulations along the undulator axis (black lines). The grey areas are shadows of all plots from the 100 simulations. The blue dot-lines show the fluctuation

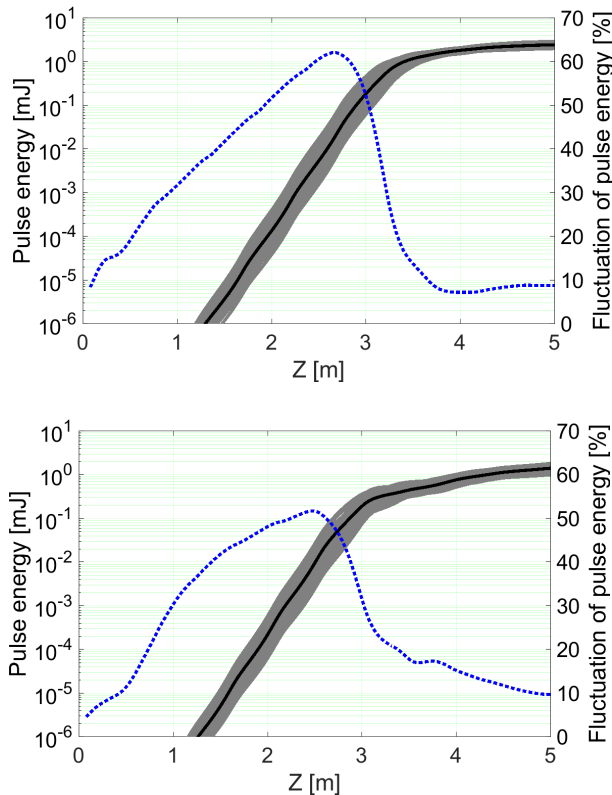


Figure 2: Simulated FEL pulse energy averaged from the 100 simulations along the undulator axis (black lines) based on the simulated (top) and measured (bottom) electron beam parameters. The grey area shows shadows of all plots from the 100 simulations. The blue dot-line shows the fluctuation of the pulse energy along the undulator axis.

of the pulse energy along the undulator axis which is a ratio between standard deviation of the pulse energy and the averaged pulse energy at each position along the undulator. For the case based on the simulated beam parameters, the pulse energy at the undulator axis reaches 2.7 mJ with 8.4% fluctuation. While for the case based on the measured beam parameters, the pulse energy at the undulator axis reaches 1.7 mJ with 10.2% fluctuation.

Figure 3 shows temporal profiles of the radiation pulses averaged from the 100 simulations at the undulator exit ($z = 5$ m), while the spectrum profiles are shown in Fig. 4. The grey areas in these figures are also shadows of all plots from the 100 simulations. They cover quite big areas which mean

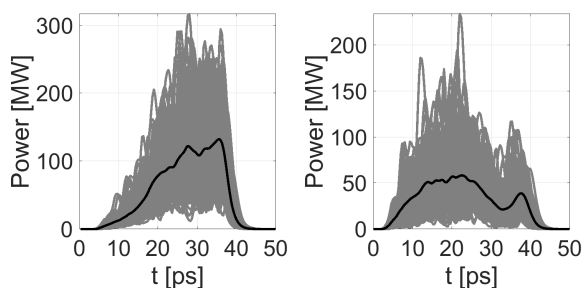


Figure 3: Simulated temporal profiles averaged from the 100 simulations (black lines) of the FEL radiation pulse at the undulator exit based on the simulated (left) and measured (right) electron beam parameters. The grey area shows shadows of all plots from the 100 simulations.

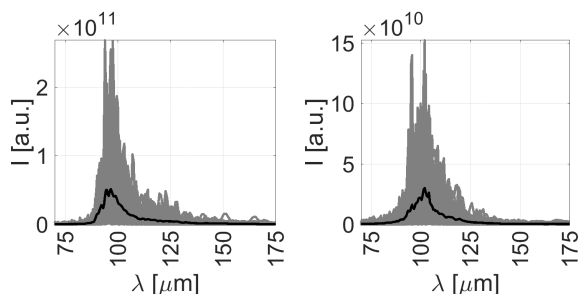


Figure 4: Simulated spectral profiles averaged from the 100 simulations (black lines) of the FEL radiation pulse at the undulator exit based on the simulated (left) and measured (right) electron beam parameters. The grey area shows shadows of all plots from the 100 simulations.

the radiation pulses fluctuate a lot. This behavior is natural for the SASE FEL process.

SUMMARY AND OUTLOOK

SASE FEL simulations for the radiation wavelength of 100 μm using the GENESIS1.3 code were performed for 2 cases of input electron beam parameters; based on the S2E beam dynamics simulation and based on the measured electron beam profiles. Different 100 initial seeds for the random number generator were used in the FEL simulations in order to simulate the fluctuations of the radiation pulse. The results show that, for both case, a radiation pulse energy of about 2 mJ can be achieved within a undulator length of 5 m with about 10% fluctuation. However, the temporal and spectral profiles of the radiation pulse fluctuate a lot which is a natural behavior of the SASE FEL process.

This fluctuation can be significantly reduced by using seeding FEL methods. General ideas of the seeding methods are presented in [11]. There are few interesting options to generate a pre-modulated electron beam for the seeding FEL

at PITZ; using of a modulated photocathode laser pulse [12], using of wakefields from a corrugated pipe [13] and from a dielectric-lined waveguide [14, 15]. Studies on these options are ongoing.

REFERENCES

- [1] W. Ackermann *et al.*, "Operation of a free-electron laser from the extreme ultraviolet to the water window," *Nature Photonics*, vol. 1, pp. 336-342, 2007.
- [2] M. Altarelli *et al.*, "The European x-ray free-electron laser technical design report," DESY, Hamburg Report No. DESY 2006-097, 2007.
- [3] E. Schneidmiller *et al.*, "Tunable IR/THz source for pump probe experiment at European XFEL," in *Proc. FEL2012*, Nara, Japan, 2012, pp. 503-506.
- [4] P. Boonpornprasert *et al.*, "Start-to-End simulations for IR/THz undulator radiation at PITZ," in *Proc. FEL2014*, Basel, Switzerland, 2014, pp. 153-158.
- [5] P. Boonpornprasert *et al.*, "Experimental optimization and characterization of electron beams for generating IR/THz SASE FEL radiation with PITZ," *Proc. IPAC2017*, Copenhagen, Denmark, 2017, pp. 2650-2653.
- [6] K. Flöttmann, ASTRA particle tracking code, available: <http://www.desy.de/~mpyf1o/>.
- [7] S. Reiche, GENESIS 1.3 code, available: <http://genesis.web.psi.ch/>.
- [8] C. J. Boccheta *et al.*, "Conceptual Design Report (CDR) for the FERMI@Elettra project," Sincrotrone Trieste, Trieste, ST/F-TN-07/12, 2007, pp. 230-232.
- [9] S. Reiche, "Numerical studies for a single pass high gain free-electron laser," PhD thesis, Universitt Hamburg, 1999.
- [10] S. Reiche, "GENESIS 1.3 User Manual" 2004.
- [11] S. Reiche, "Overview of seeding methods for FELs," *Proc. IPAC2013*, Shanghai, China, 2013, pp. 2063-2067.
- [12] M. Boscolo *et al.*, "Laser comb: simulations of pre-modulated E-beams at the photocathode of a high brightness RF photoinjector," *Proc. EPAC2006*, Edinburgh, Scotland, 2006, pp. 98-100.
- [13] P. Emma *et al.*, "Experimental demonstration of energy-chirp control in relativistic electron bunches using a corrugated pipe," *Phys. Rev. Lett.* 112, 034801, 2014.
- [14] F. Lemery and P. Piot, "Ballistic bunching of photoinjected electron bunches with dielectric-lined waveguides," *Phys. Rev. ST Accel. Beams* 17, 112804, 2014.
- [15] F. Lemery *et al.*, "Experimental demonstration of ballistic bunching with dielectric-lined waveguide at PITZ," *Proc. IPAC2017*, 2017, pp. 2857-2860.

COAXIAL COUPLER RF KICK IN THE PITZ RF GUN

Y. Chen[†], H. Qian, M. Krasilnikov, I. Isaev, Q. Zhao¹, P. Boonpornprasert, J. Good, H. Huck, A. Oppelt, Y. Renier and F. Stephan, DESY, Platanenallee 6, 15738 Zeuthen, Germany
W. Ackermann, H. De Gerssem, TEMF, Technische Universität Darmstadt, Schlossgartenstraße 8, 64289 Darmstadt, Germany
M. Dohlus, DESY, Notkestraße 85, 22607 Hamburg, Germany

Abstract

We investigate a transverse RF kick induced by the transition between rectangular waveguide and coaxial line of the RF coupler in the 1.6-cell L-band normal conducting (NC) RF gun at the Photo Injector Test Facility at DESY, Zeuthen site (PITZ). A three-dimensional electromagnetic simulation shows the disturbed RF field distributions in the fundamental accelerating mode. Based on the 3D RF field map, an electron beam based characterization and quantification of the coaxial coupler RF kick in the PITZ gun is simulated. The current status of the investigation is presented.

INTRODUCTION

As a high brightness photoelectron source required for the operation of TESLA technology based FELs, the 1.6-cell 1.3-GHz NC RF gun at PITZ has been used at FLASH [1] and the European X-ray Free Electron Laser (XFEL) [2]. The RF power in the PITZ gun is supplied by a 10 MW multi-beam klystron. The power is coupled from the input waveguide (WG) via the door-knob transition into the rotationally symmetric coupler and the gun cavity. This is illustrated in Fig. 1. For a thorough description of the PITZ gun and its supporting RF system, the interested reader is referred to [3-6].

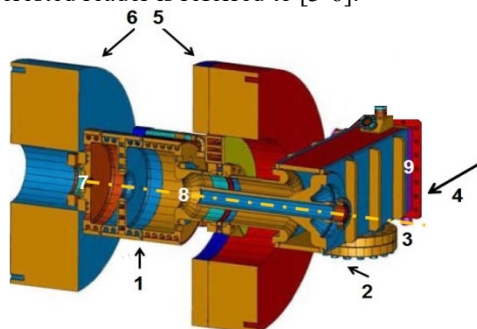


Figure 1: Sketch of the PITZ gun with coaxial RF coupler: 1-gun cavity, 2-door-knob transition, 3-cavity axis, 4-RF feeding direction, 5-main solenoid, 6-bucking solenoid, 7-cathode, 8-end of coaxial line and 9-reference position of WG port for simulations. Note that this sketch is rotated by 90 degrees compared to the computational model used in the follow-up simulations.

The rotationally symmetric coupler at PITZ is designed as a coaxial input coupler that couples to the gun cavity on the cavity axis [7-8]. The axial symmetry of the cavity thus stays undisturbed. Compared to the conventional input coupler aside the cavity [9], the asymmetric electromagnetic modes are strongly suppressed. This inhibits the emittance growth due to the RF field distortions caused by these asymmetric modes. The evanescent dipole modes, however, are not avoidable to be generated at the door-knob transition (see 2 in Fig. 1). The dipole modes may not be fully decayed till the end of the coaxial line and thus can disturb the cylindrical symmetry of the fundamental mode. The induced RF field asymmetries may create a transverse kick onto the electron bunch [10-11]. This occurs, more specifically, when the bunch is leaving the cavity through the inner conductor of the coaxial line (see 8 in Fig. 1). To first clarify the RF field asymmetries, three-dimensional electromagnetic field simulations are performed using CST Microwave Studio® (CST-MWS®) [12].

RF FIELD ASYMMETRY

The RF field in the gun is simulated using the frequency domain solver in CST-MWS®. To enable excitation, a standard WG port condition is applied at the boundary of the input WG. Based on a so-called mono-frequency excitation method, two principal matching conditions (i.e., broadband matching from WG to coaxial line and narrowband matching from coaxial line to cavity) are satisfied by slightly tuning the length of the inner conductor. This results in a reflection coefficient lower than -30 dB at the WG port position. The RF field is then calculated under such optimized conditions of the gun at its resonance frequency. Surface losses are taken into account. Based on the field simulation, a 3D RF field map is also extracted for later particle tracking simulations in ASTRA [13].

In Fig. 2, the RF field asymmetries are exemplarily visualized in the close vicinity of the coaxial coupler. One can recognize these asymmetries from the electric and magnetic field strength variation around the inner conductor, as well as from the on-axis zero-crossing positions of the fields.

[†] ye.lining.chen@desy.de

¹ on leave from IMP/CAS, Lanzhou, China

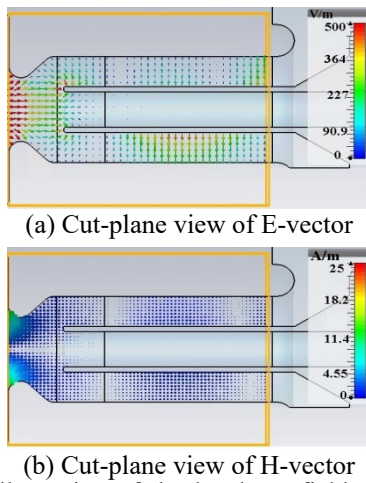


Figure 2: Illustration of the local RF field asymmetries. The colour maps are adjusted for a better visualization.

Figure 3 shows the distribution of the transverse magnetic field component (H_x) along the cavity axis. Note that the magnetic field starts to rise at about the end of the gun cavity. It reaches the peak value somewhere in the transition between the end of the coaxial line and the cavity. The field distribution is decaying into the inner conductor of the coaxial line. Furthermore, the field is compared to the same field component calculated by a simulation without the door-knob transition and the rectangular waveguide in the computational model. One can see that the resulting H_x component in this case is almost zero. For this comparison, the maximum accelerating electric field in both cases are normalized to 60 MV/m.

In our simulation frame, such an existing horizontal magnetic component (red curve) can kick the electron bunch vertically. In order to know the correlation of the vertical kick with time, particle tracking simulations are performed at different RF phases of the gun using an extracted 3D RF field map.

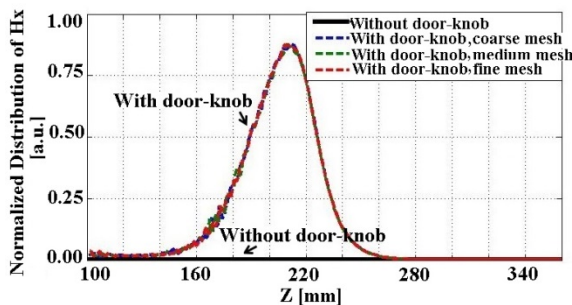


Figure 3: Distribution of the magnetic field component along the cavity axis and the comparison with the same field calculated by a simulation without the door-knob transition and the rectangular waveguide in the computational model. Different curves in colours represent gradual steps for mesh refinements in the simulations.

BEAM-BASED CHARACTERIZATION OF THE RF KICK

The kick characterization is conducted by scanning the RF start-phase of the gun in particle tracking simulations.

The beam centroid is initially placed at the center of the cathode plane. It is tracked through the gun cavity till close vicinity of the door-knob transition. The whole calculation domain is covered by the RF field map.

In Fig. 4, the particle offset from the axis on the transverse plane and corresponding transverse momentum are calculated at different longitudinal positions along the cavity axis. A vertical kick is identified starting from the transition of the full cell of the gun to the coaxial line (see (d) in Fig. 4). The kick strength is, furthermore, depending on the start-phase of the gun. At the Maximum Mean Momentum Gain (MMMGM) phase (i.e., 40 degrees), this leads to a transverse kick of about 0.65 mrad. A vertical offset of 55 μm is found at 0.3 meters downstream from the photocathode. However, there is almost no considerable kick in the horizontal direction for a large range of the RF phase w.r.t. the MMMGM phase of the gun.

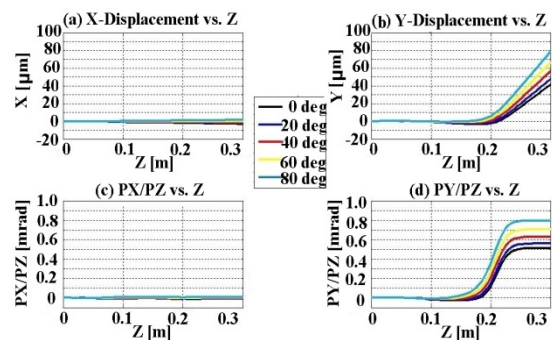


Figure 4: Off-center distance on the transverse plane and corresponding transverse momentum of the beam centroid for the RF start-phases.

In Fig. 5, the kick strength and the particle offset from the axis at $z = 0.3$ m are plotted as a function of the gun phase. The red star denotes the MMMGM phase of the gun. Note that, a nominal electron bunch of 20 ps FWHM (full width half maximum) at PITZ corresponds to about 10 degrees gun phase at the resonant frequency of 1.3 GHz. Consequently, the head and tail of the electron bunch may see a kick slope (see (b) in Fig. 5) due to the time dependency of the RF kick. This results in a kick difference of about 0.05 mrad around the MMMGM phase at a RF power level of 6.5 MW in the gun. However, the presence of the imperfect solenoid fields may further complicate the beam dynamics in a nonlinear manner.

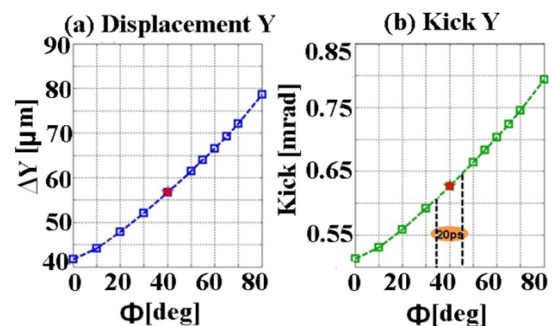


Figure 5: Vertical displacement at $z = 0.3$ m and kick strength as a function of the gun phase.

MULTIPOLE-EXPANSION BASED QUANTIFICATION OF THE KICK

To clarify the multipole composition and quantify their strengths in the integral kick, the transverse momentum of the beam particle is presumably decomposed in a dipole component, a normal and a skew quadrupole component according to

$$P_X = P_{0x} + (K_{RF} + K_N)X + K_S Y \quad (1)$$

and

$$P_Y = P_{0y} + (K_{RF} - K_N)Y + K_S X. \quad (2)$$

Here, X and Y are the particle offsets from the axis at the location of the integral kick, respectively. The terms P_X and P_Y represent the particle transverse momenta in the horizontal and vertical direction, respectively. The parameters P_{0x} and P_{0y} characterize the dipole kick while K_{RF} describes the RF focusing strength of the cylindrical symmetric mode. The values K_N and K_S denote the normal and skew quadrupole kick strength, respectively.

The kick strengths of the multipole components in (1-2) are quantified based on the tracking simulations for a grid of macroparticles initially placed on the cathode plane (see Fig. 6). These particles are tracked through the gun cavity passing by the end of the coaxial coupler till the door-knob transition. The whole calculation domain is covered by a 3D RF field map. The simulation results are shown in Fig. 7. The integral transverse RF kick at $z = 0.3$ m is plotted as a function of the vertical and horizontal displacements at $z = 0.18$ m for all the simulation particles. A vertical kick is seen in Fig. 7 (b). The transverse momentum in Fig. 7 (a) and (d) is nearly linear proportional to the displacement at the kick location.

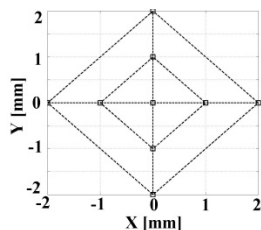


Figure 6: Beam centroid positions on the cathode plane used in the simulations for kick quantification.

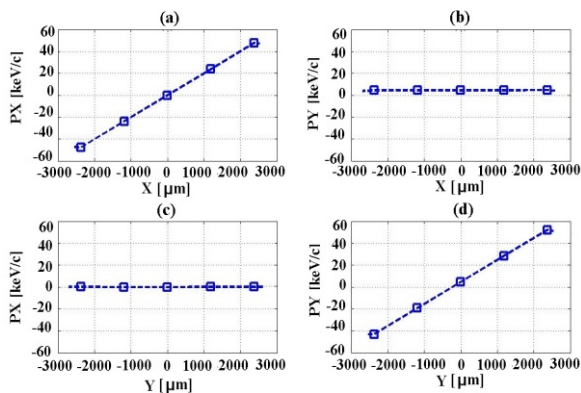


Figure 7: Particle tracking simulation results for multipole-expansion based quantification of the integral kick.

Based on the simulation results in Fig. 7, the multipole-expansion forms (1-2) are numerically fitted. This renders a pronounced vertical dipole kick (P_{0y}) of 4.576 keV/c. The horizontal dipole kick strength (P_{0x}) is almost zero. For the normal quadrupole component, the kick strength K_N is estimated as 1.0e-5 keV/c/ μ m. The skew quadrupole component is calibrated by K_S as 5.0e-6 keV/c/ μ m.

Furthermore, to cross-check the kick quantification, an electron bunch of 20 ps is used for tracking simulations, instead of beam centroids. Fig. 8 shows the vertical kick strength as a function of the longitudinal position for the electron bunch distribution at $z \approx 0.33$ m (blue dots). To visualize the kick variation in time, the whole bunch is treated slice by slice (dashed black lines). Within each slice, the mean kick strength is calculated. The inset provides a closer look at the trend of the kick slope along the bunch. One can see that the mean kick strength is 0.65 mrad, and also that the bunch tail sees higher kick strength than the head by about 0.05 mrad. This is consistent with the results shown in Figs. 4 and 5.

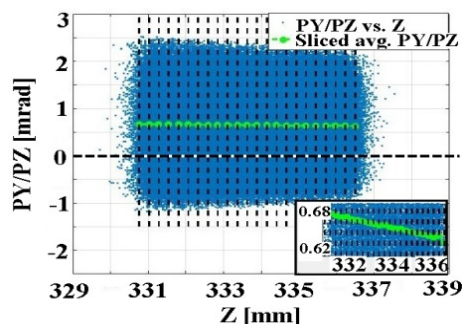


Figure 8: Bunch distribution at $z \approx 0.33$ m in terms of the vertical kick strength versus z -positions.

SUMMARY AND OUTLOOK

In this paper, RF fields with rotational symmetry disturbed by the transition from the input rectangular waveguide to the coaxial coupler of the PITZ gun are shown. The resulting RF kick to the electron bunch is vertical and time-dependent. The latter characteristic can introduce a kick slope along the bunch. The integral kick is, furthermore, quantified in the form of its multipole components using the results of particle tracking simulations. This gives a main vertical dipole kick of about 0.65 mrad at the MMMG phase of the gun for a gun RF power of 6.5 MW. A small normal and skew quadrupole component is found to be 1.0e-5 and 5.0e-6 keV/c/ μ m, respectively. Further studies are foreseen to investigate the impacts of the kick on beam dynamics when space charge effect is included. Note that, to explain the asymmetries in measured transverse phase spaces of the electron bunch at PITZ, other effects, such as the imperfect solenoid symmetry are also under investigation [14-16].

ACKNOWLEDGEMENT

The authors would like to thank Klaus Flöttmann and Frank Brinker from DESY for very useful advices and comments on this topic.

REFERENCES

- [1] W. Ackermann *et al.*, “Operation of a free-electron laser from the extreme ultraviolet to the water window”, *Nat. Photon.* 1, 336 (2007).
- [2] M. Altarelli *et al.*, Report No. DESY 2006-097, DESY (2006).
- [3] F. Stephan *et al.*, “Detailed characterization of electron sources yielding first demonstration of European X-ray Free-Electron Laser beam quality”, *PRST-AB* 13, 020704 (2010).
- [4] M. Krasilnikov, F. Stephan *et al.*, “Experimentally minimized beam emittance from an L-band photoinjector”, *PRST-AB* 15, 100701 (2012).
- [5] Y. Renier *et al.*, “Statistics on high average power operation and results from the electron beam characterization at PITZ”, *Proc. IPAC'17*, Copenhagen, Denmark, TUPIK051 (2017).
- [6] F. Stephan and M. Krasilnikov, “High Brightness Photo Injectors for Brilliant Light Sources”, in *Synchrotron Light Sources and Free-Electron Lasers*, Springer International Publishing Switzerland, ISBN 9783319143941 (2016).
- [7] B. Dwersteg *et al.*, “RF gun design for the TESLA VUV Free Electron Laser”, *NIM A*393, p. 93-95 (1997).
- [8] A. Oppelt *et al.*, “Tuning, conditioning, and dark current measurements of a new gun cavity at PITZ”, *Proc. FEL'06*, Berlin, Germany, THPPH023, p. 609 (2006).
- [9] M. Krasilnikov *et al.*, “Impact of the RF-Gun Power Coupler on Beam Dynamics,” *EPAC'02*, Paris, France, p. 1640 (2002).
- [10] M. Dohlus *et al.*, “Coupler kick for very short bunches and its compensation”, *Proc. EPAC'08*, Genoa, Italy, p. 580 (2008).
- [11] H. Qian *et al.*, “Design of a 1.3 GHz Buncher for APEX”, *Proc. IPAC'14*, Dresden, Germany, THPRI066, p. 3924 (2014).
- [12] CST Computer Simulation Technology AG, <https://www.cst.com/>.
- [13] K. Flöttmann, ASTRA particle tracking code, <http://www.desy.de/~mpyflo/>.
- [14] M. Krasilnikov *et al.*, “Investigations on Electron Beam Imperfections at PITZ”, *Proc. LINAC'16*, East Lansing, MI, MOPLR013 (2016).
- [15] M. Krasilnikov *et al.*, “Electron beam asymmetry compensation with gun quadrupoles at PITZ”, presented at FEL'17, WEP007.
- [16] Q. Zhao *et al.*, “Beam asymmetry studies with quadrupole field errors in the PITZ gun section”, presented at FEL'17, WEP010.

PRELIMINARY ON-TABLE AND PHOTOELECTRON RESULTS FROM THE PITZ QUASI-ELLIPSOIDAL PHOTOCATHODE LASER SYSTEM

J. Good[#], G. Asova[†], P. Boonpornprasert, Y. Chen, M. Gross, H. Huck, I. Isaev, O. Lishilin, D. Kalantaryan, X. Li, G. Loisch, M. Kraslinikov, D. Melkumyan, A. Oppelt, Y. Renier, H. Qian, T. Rublack, F. Stephan, Q. Zhao[¶], Deutsches Elektronen-Synchrotron, Zeuthen, Germany
I. Hartl, S. Schreiber, Deutsches Elektronen-Synchrotron, Hamburg, Germany
A. Andrianov, E. Gacheva, E. Khazanov, S. Mironov, A. Poteomkin, V. Zelenogorsky, Institute of Applied Physics, IAP, Nizhny Novgorod, Russia
E. Syresin, JINR, Dubna, Moscow Region, Russia

Abstract

High brightness photoinjectors for superconducting linac-based FELs are developed, optimized and characterized at the Photo Injector Test facility at DESY in Zeuthen (PITZ). Simulations have previously shown that homogeneous ellipsoidal photocathode laser pulses allow the production of high brightness electron bunches with minimized emittance.

Correspondingly, a new prototype photocathode laser system capable of producing quasi-ellipsoidal laser pulses was installed last year and brought into active electron beam operation at the start of this year.

Several electron beam measurements have been made with pulse shaping. It was possible to show a beam quality improvement equivalent to that of conventional beam shaping techniques such as pulse stacking and beam shaping apertures. Further improvements were constrained due to a number of systematic limitations which are to be addressed in the redesign currently under construction.

INTRODUCTION

Low-emittance beams have been obtained using a flat-top temporal laser profile with 60 MV/m gradient in the RF gun [1], more recently with a Gaussian temporal laser profile and 53 MV/m [2]. In earlier simulations, it was found that uniform ellipsoidal charge distributions with sharp charge transition boundaries would produce even higher beam quality. Furthermore, it was shown that such electron bunches should also be less sensitive to machine parameter jitter [3] and therefore increase the reliability and stability – crucial parameters for single-pass FELs such as FLASH and the European XFEL.

QUASI-ELLIPSOIDAL PHOTOCATHODE LASER SYSTEM

Naturally, a homogenous ellipsoidal photocathode laser pulse is a first approximation to produce such charge distributions. Consequently, such a laser system has been developed for PITZ by the Institute of Applied Physics in Nizhny Novgorod, under the framework of a joint German-Russian research activity [4].

[#] james.david.good@desy.de

[†] on leave from BAS INRNE, 1784 Sofia, Bulgaria

[¶] on leave from IMP/CAS, 730000 Lanzhou, China

The system produces quasi-ellipsoidal laser pulses in the infrared through spatio-spectral amplitude masking of chirped Gaussian laser pulses.

The shaper is implemented by locating a modulator at the Fourier plane of a 4f - zero-dispersion stretcher-compressor. In this case the modulator is a Spatial Light Modulator (SLM) to act as an amplitude mask in the transverse-temporal domains (Fig. 1).

The pulses are passed through the shaping unit, rotated 90° about their propagation axis before being passed back through the shaper, and are then coupled out for frequency conversion to the ultraviolet.

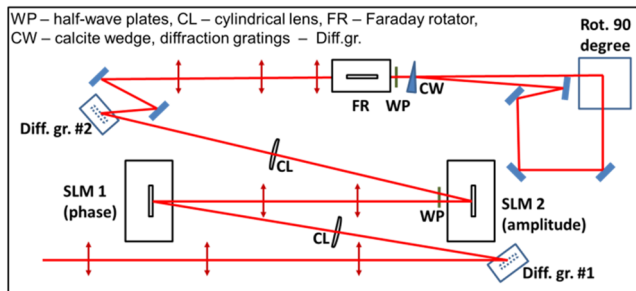


Figure 1: Schematic overview of the 3D shaper (phase mask currently omitted).

A number of diagnostic tools are implemented to characterize the laser pulses. The temporal envelope of the laser pulses is characterized by cross-correlator coupled cameras in the both the infrared, prior to frequency conversion, and in the ultraviolet afterwards. Furthermore, a slit-scanning spectrometer is used to acquire spectrographs of the pulses and reconstruct their profiles.

Finally, the laser is coupled into a shared laser transport beamline. A uTCA-based feedback loop is used to ensure synchronization to the RF systems which permitted the first electron beam quality measurements with the new laser system at PITZ.

SIMULATIONS

Simulations were done using the ASTRA [5] code to compare and contrast various pulse distributions (Fig. 2) for the 9.5 ps FWHM pulse durations which are currently available. These were done for the operating parameters of 0.5 nC bunch charge, 6.5 MeV/c momentum in the gun, and 22.3 MeV/c after the CDS booster.

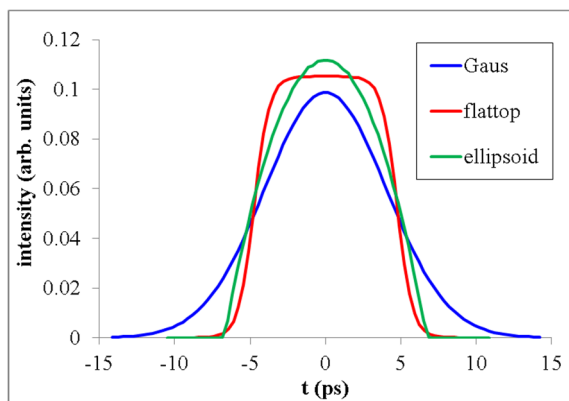


Figure 2: Used pulse profiles for the three types of photocathode pulse envelopes.

For these parameters, and of three shapes of the photocathode laser all with 9.5 ps FWHM, the minimized emittance for the EMSY station located 5.277 m downstream of the gun was found (Table 1).

Table 1: ASTRA Simulation Results

Pulse shape→	cylindrical		ellipsoid
	Gaussian	Flattop	
Projected normalized emittance [mm·mrad]	0.80	0.64	0.35
Average slice emittance [mm·mrad]	0.49	0.57	0.33
Bunch length (rms) [mm]	1.44	1.20	1.34
Peak current [A]	35.4	39.5	37.8
Longitudinal emittance [mm keV]	34	22	12.5

ELECTRON BEAM MEASUREMENTS

Preliminary electron beam measurements with the new photocathode laser system utilized a “truncated” beam owing to the imperfect transport of the laser to the cathode resulting in a large transverse spot size on the cathode. This could be observed with a camera (VC2) placed at a virtual plane with an optically equivalent distance to that of the real beam path. As the new photocathode laser system “piggybacks” onto the already existing laser transport beamline it was possible to achieve the desired dimensions by cropping the beam with the pre-existing Beam Shaping Aperture (BSA) in the tunnel. The diameter was then set to 1.2 mm (Fig. 3).

A SLM mask was manually fitted by observation of the IR cross-correlation to obtain a 10-12 ps FWHM distribution as a first approximation. The unusual shape of the temporal envelope can be explained by the laser spectrum, shown in Fig. 4.

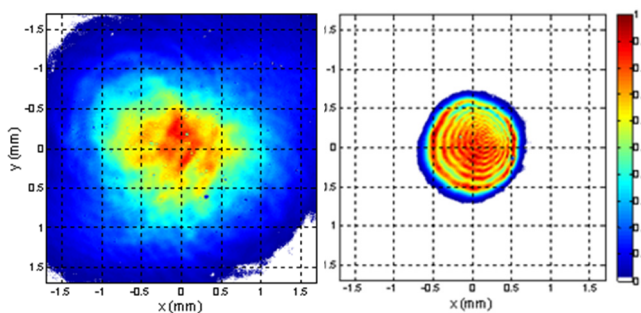


Figure 3: Transverse laser profile at a virtual cathode plane without (left) and with (right) a beam shaping aperture.

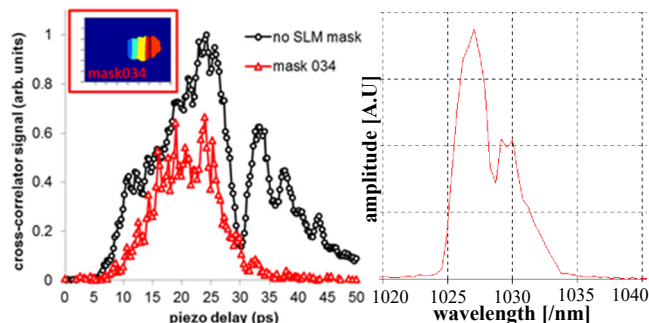


Figure 4: Laser temporal envelope obtained by infrared cross-correlation (left), and the laser spectrum (right).

The emittance of the generated electron beam was measured, under the machine parameters given in the simulation section, as a function of solenoid current in comparison to the simulations above. The measured beam emittance is shown in Fig. 5 together with the rms beam sizes as a function of main solenoid current.

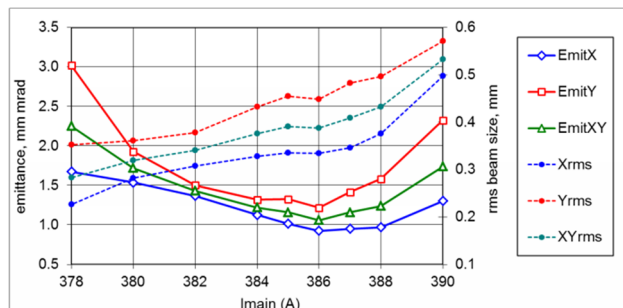


Figure 5: Measured electron bunch emittance and spot size as a function of main solenoid current.

The normalized transverse emittance at the optimum solenoid current (386 A/225 mT) was found to be $\epsilon_{nx} = 0.93$ mm mrad, $\epsilon_{ny} = 1.22$ mm mrad, and a geometric mean of $\epsilon_{nxy} = 1.06$ mm mrad.

These values are on par with measurements undertaken for the nominal flat-top photocathode laser pulses. The beam was also observed on a transverse deflecting cavity and seen to have a close-to parabolic current density (Fig. 6) and a roughly ellipsoidal shape on the temporal-transverse x coordinate plane (Fig. 6 insert).

Content from this work may be used under the terms of the CC BY 3.0 licence (© 2018). Any distribution of this work must maintain attribution to the author(s), title of the work, publisher, and DOI.

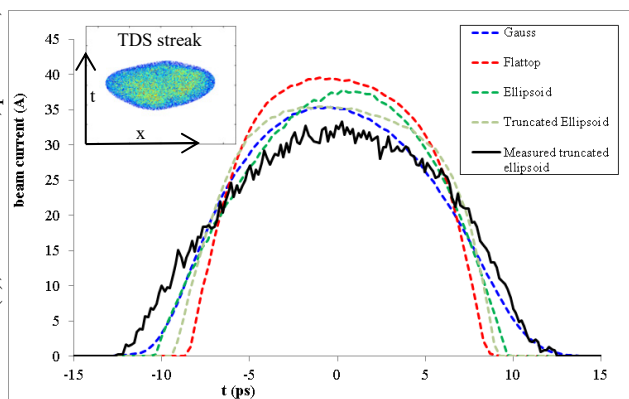


Figure 6: Measured beam current profile with a TDS compared to simulated profiles for various laser pulse envelopes.

The measurements do not meet the theoretical values predicted by simulation (Table 1) due to limited spectral quality, beam stability and transport issues. As can be seen in Fig. 4, the pulse spectrum is masked very short due to the absorption band slightly off-center in the spectrum. This also results in even shorter pulses after frequency conversion than in simulation. The long-term stability suffers due to poor opto-mechanical stability which leads to drifting throughout the system. Finally, piggybacking the laser onto the pre-existing laser transport designed for magnification brings issues because the new laser system prefers demagnification. The transversely cut laser distribution on the photocathode is far from the optimal case studied in simulation.

REDESIGN

Through operation of the laser a number of systematic limitations have been identified and are foreseen to be corrected with a simplified redesign centred around a single high-power, oscillator-amplifier laser system. The new system is a 1 MHz solid-state Yb:KGW Pharos laser from Light Conversion capable of producing 20 μ J chirped laser pulses whose energy inversely scales with decreasing repetition rate up to 200 μ J.

This system is seen to be the backbone of a linear, highly robust, stable, and flexible laser pulse shaping system based on the same zero-dispersion stretcher-compressor concept as the old design with two independent, high resolution shaping units utilizing the maximum chip area on dichroic Hamamatsu SLMs for each spatio-spectral plane.

A significant reduction in optical path length and the number of optical elements was achieved and the inclusion of detectors for on-line parasitic observation at every stage was included, as shown in Fig. 7. The linear scheme also simplifies troubleshooting and alignment.

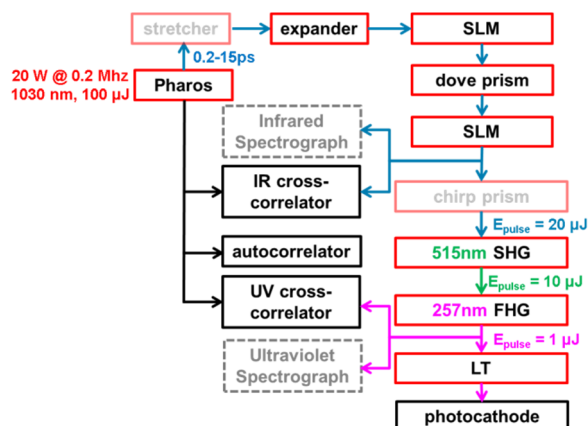


Figure 7: Schematic overview of the new photocathode laser system under construction.

CONCLUSION

Owing to the implementation of uTCA-based synchronization system in the last year it became possible to generate photoelectron bunches with modulated three-dimensional profiles and measure their beam properties.

These photoelectron bunches have displayed improved properties in relation to that of unshaped pulses, and a quality on par with conventional pulse shaping techniques. Several systematic limitations prevented realization of photocathode laser pulses with the desired beam shape.

A redesign of the laser system was done based on a commercial, high power oscillator-amplifier laser while keeping the concept of the pulse shaper. It is expected that this should solve most of the systematic limitations in the near future.

It is anticipated with the simplified redesign based around a single-stage photonic source that most of the systematic limitations shall be eliminated in the near future.

REFERENCES

- [1] M. Krasilnikov *et al.*, Experimentally minimized beam emittance from an L-band photoinjector, PRST-AB 15, 100701 (2012).
- [2] G. Vashchenko *et al.*, Emittance measurements of the electron beam at PITZ for the commissioning phase of the European X-FEL, Proc. FEL'15, Daejeon, Korea.
- [3] M. Khojyan *et al.*, Optimization of the PITZ photoinjector towards the best achievable beam quality, Proc. FEL'14, Basel, Switzerland.
- [4] A. Poteomkin *et al.*, Cross-correlator for the diagnostics of 3D ellipsoidal shaped UV laser pulses for the future XFEL low-emittance photo-injector, CLEO EUROPE/IQEC, Munich (2013).
- [5] ASTRA, A Space Charge Tracking Algorithm, <http://www.desy.de/~mpyflo/>

ELECTRON BEAM ASYMMETRY COMPENSATION WITH GUN QUADRUPOLES AT PITZ

M. Krasilnikov*, I. Isaev, G. Amatuni¹, G. Asova², P. Boonpornprasert, Y. Chen, J. Good, B. Grigoryan¹, M. Gross, H. Huck, D. Kalantaryan, X. Li, O. Lishilin, G. Loisch, D. Melkumyan, A. Oppelt, H. Qian, Y. Renier, F. Stephan, Q. Zhao³, DESY, Zeuthen, Germany

¹on leave from CANDLE, Yerevan, Armenia

²on leave from INRNE, Sofia, Bulgaria

³on leave from IMP/CAS, Lanzhou, China

Abstract

The electron beam asymmetry observed at the Photo Injector Test Facility at DESY in Zeuthen (PITZ) was traced back to multipole kicks in the gun section, namely around the location of the coaxial power coupler and the main solenoid. Several dedicated studies have been performed to quantify the kick location and strength. Based on these studies, two designs of correction quadrupole coils were proposed. The coils were fabricated and tested with an electron beam. The second updated design implies a two-quadrupole setup on a frame installed around the gun coaxial coupler close to the main solenoid centre location. Skew and normal quadrupole magnets are powered independently, enabling flexibility in electron beam manipulations. By means of this setup, a more symmetric beam was obtained at several screens. This led also to more equal measured horizontal and vertical phase spaces and to even smaller overall emittance values. Some details of the gun quadrupole designs, magnetic measurements, and results of electron beam measurements including emittance optimization will be reported.

INTRODUCTION

Several dedicated experiments to investigate the observed asymmetry in the transverse distribution of electron beams in the rotationally symmetric PITZ photo injector have been performed. One of them, the so-called “Larmor angle experiment” [1] yielded a possible location of the kick onto the transverse phase space at the longitudinal position of ~ 0.2 m from the photocathode. A 45° orientation of the kick corresponds to a skew quadrupole-like impact. Additional studies were performed in order to characterize this source considering RF gun power coupler [2] and main solenoid aberrations due to anomalous quadrupole fields [3] as major candidates responsible for the observed distortions in the transverse electron beam shape. These studies yielded also the second location of the possible kick – namely around $z \sim 0.4$ m from the cathode [3].

In order to compensate the assumed kick integrally by a static quadrupole field, two sets of gun quadrupoles were designed and fabricated. The first are quadrupole air coils on an aluminium frame, tested at PITZ for both orientations – normal and skew. No universal settings of these coils were found to compensate the beam asymmetry for

both solenoid polarities. The second design consists of a pair of quadrupoles – normal and skew on the same frame. They were connected to two independent power supplies and were able to deliver symmetric beams for both solenoid polarities. Two parameter scans of the beam images at YAG screens as functions of the normal and skew gun quadrupoles currents were performed resulting in slightly different settings for various screens. Emittance measurements were performed for 0.5 nC beams without and with found settings of gun quadrupoles.

GUN QUADRUPOLES

The gun quadrupole design is based on an air coil concept, consisting of eight individual coils that form two separate quadrupoles: normal (Gun.Quad1) and skew (Gun.Quad2). Such combination of the skew and normal quadrupole fields provides an opportunity to perform a virtual rotation of the quadrupole field. Both quadrupole magnets are placed on the same aluminium frame of 108 mm inner diameter and 36 mm width. Each of eight air coils consists of 140 windings of 0.56 mm copper wire. The coils are powered independently by currents $I_{\text{Gun,Quad1}}$ and $I_{\text{Gun,Quad2}}$, respectively, with up to ± 3 A.

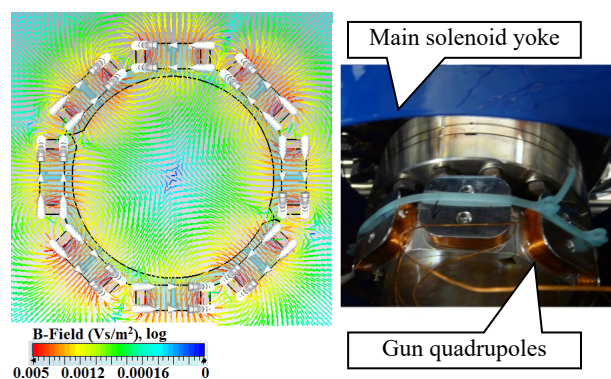


Figure 1: Compensating gun quadrupoles consisting of two air quadrupole coils: normal and skew. Magnetic field simulated with CST EM Studio for $I_{\text{Gun,Quad1}} = -0.5$ A and $I_{\text{Gun,Quad2}} = -0.6$ A (left). Photo of the quadrupole installed in the PITZ injector (right).

Before quadrupoles fabrication magnetic simulations using the CST EM Studio [4] were performed (Fig. 1, left). Thermal load for the maximum currents was estimated as well resulting in a maximum temperature of 75-

* mikhail.krasilnikov@desy.de

Content from this work may be used under the terms of the CC BY 3.0 licence (© 2018). Any distribution of this work must maintain attribution to the author(s), title of the work, publisher, and DOI.

79°C. Two thermal switchers are installed with 80°C threshold. The simulated gradient of a single quadrupole is 0.012 T/m/A, the effective length is 0.0627 m. The gun quadrupoles were fabricated and installed in the PITZ beamline at the longitudinal position of ~0.32 m from the photocathode. This location is determined by very strong space constraints in the gun area. The frame is mounted around the gun coaxial coupler inside the main solenoid (Fig. 1, right)

It should be noticed that the first design of the gun quadrupole had a similar geometry but consists of only one quadrupole. Tests with this gun quadrupole option have revealed that the beam asymmetry can be compensated only for a one solenoid polarity. Other polarity case needed the quadrupole orientation change (from normal to skew).

Tests with the second design of the gun quadrupoles (Fig. 1) demonstrated a possibility to compensate the electron beam asymmetry by a tuning of the quadrupole currents $I_{\text{Gun,Quad1}}$ and $I_{\text{Gun,Quad2}}$.

Nevertheless, there is still remaining asymmetry while optimizing the electron beam transverse shape at many screens along the beamline for the same machine settings. One of the reasons for this is the transient character of the RF coupler kick which cannot be fully compensated by a static magnetic field. Another reason could be that fact that two locations of the possible kick ($z \sim 0.4$ m additionally to $z \sim 0.2$ m) were found from dedicated studies [3] and the current gun quadrupole is installed between them. Presence of other multipole components (not quadrupole) can be also responsible for the remaining electron beam asymmetry.

EMITTANCE MEASUREMENTS

In order to study the possibility to symmetrize horizontal and vertical phase spaces of electron beams the standard procedure for emittance optimization was used. The projected emittance was measured for the 0.5 nC beam as a function of the main solenoid current which is one of major tuning tool for the PITZ photo injector. The photocathode laser with Gaussian temporal profile of ~11 ps FWHM was used. A quasi-flattop transverse distribution was obtained by applying the beam shaping aperture of 1.2 mm diameter. Figure 2 shows the transverse laser distribution measured with a UV sensitive CCD camera placed at a location which is optically equivalent to the real cathode position. The laser transverse distribution deviates from a homogeneous radial distribution and also contributes to the electron beam asymmetry.

The RF peak power in the gun was tuned to ~6.6 MW yielding a maximum mean momentum of 6.5 MeV/c at the gun exit. The booster was operated on-crest at ~3 MW peak power delivering the final beam mean momentum of 22.3 MeV/c.

The emittance for space charge dominated beams is measured at PITZ using the slit-scan technique [5] at the first measurement station located at $z=5.27$ m from the photocathode (which is also location of the screen

HIGH1.Scr1). The beamlets are collected at the screen HIGH1.Scr4 located 3.133 m downstream the slit mask.

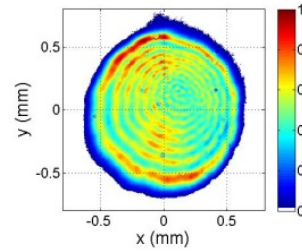


Figure 2: Transverse distribution of the photocathode laser. A beam shaping aperture of 1.2 mm diameter is applied yielding horizontal and vertical rms spot size of 0.29 mm and 0.30 mm, respectively.

Two series of measured emittance data have been taken: first, with no gun quadrupoles applied ($I_{\text{Gun,Quad1,2}} = 0\text{A}$) and the second, with gun quadrupoles tuned to $I_{\text{Gun,Quad1}} = -0.6\text{A}$ and $I_{\text{Gun,Quad2}} = -0.5\text{A}$ (Corresponding magnetic field distribution is shown in Fig.1, left plot). These gun quadrupole settings were obtained from the two parameter scans ($I_{\text{Gun,Quad1}}, I_{\text{Gun,Quad2}}$) at screens HIGH1.Scr1 and HIGH1.Scr4 compromising a round beam at both screens. Measured rms spot sizes at HIGH1.Scr1 and projected normalized emittance are shown in Figure 3 for both gun quadrupole cases. Such gun quadrupole optimization procedure is rather empirical and needs more systematic studies including four dimensional phase space reconstruction.

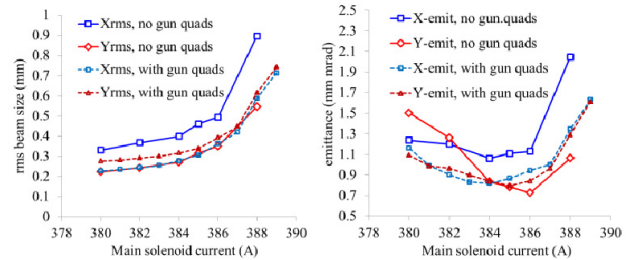


Figure 3: Transverse rms beam size (left) and projected normalized emittance (right) measured for 0.5 nC electron beam as a function of the main solenoid current for the case without gun quadrupoles and with gun quadrupoles tuned to $I_{\text{Gun,Quad1/2}} = -0.6\text{A}/-0.5\text{A}$, respectively.

Besides more round beam (w.r.t. rms horizontal and vertical beam sizes) more equal horizontal and vertical emittances were obtained. Main results of projected transverse phase space measurements for the main solenoid currents delivering the minimum transverse emittance ($\epsilon_{x,n} \times \epsilon_{y,n}$)^{1/2} are summarized in Table 1. Errors of emittance measurements are estimated to be ~0.04 mm mrad. Besides the emittance values also corresponding Twiss parameters for horizontal and vertical planes are getting more equal.

Electron beam transverse distributions at screens HIGH1.Scr1 and HIGH1.Scr4 for both cases of the experiment are shown in Figure 4. Whereas the beam asymmetry (tail structure) is almost completely corrected by the gun quadrupoles at HIGH1.Scr1 a remaining structure

is still observed at HIGH1.Scr4. Besides that also a small tilt is still present in the electron beam transverse distributions. This remaining coupling between x and y planes is most probably due to the rather empirical correction procedure mentioned above. Systematic coupling studies are ongoing now at PITZ and are under preparation at XFEL and FLASH.

Table 1: Transverse Phase-Space Measurements

	No Gun Quadrupoles	With Gun Quadrupoles
I_{main}	386 A	384 A
$I_{\text{gun,quad1}}$ (normal)	0 A	-0.5 A
$I_{\text{gun,quad2}}$ (skew)	0 A	-0.6 A
σ_x (HIGH1.Scr1)	0.50 mm	0.28 mm
σ_y (HIGH1.Scr1)	0.35 mm	0.32 mm
$\epsilon_{x,n}$	1.13 mm mrad	0.82 mm mrad
$\epsilon_{y,n}$	0.73 mm mrad	0.84 mm mrad
β_x	6.53 m	3.18 m
β_y	6.49 m	3.24 m
γ_x	0.56 mrad	0.32 mrad
γ_y	0.16 mrad	0.31 mrad

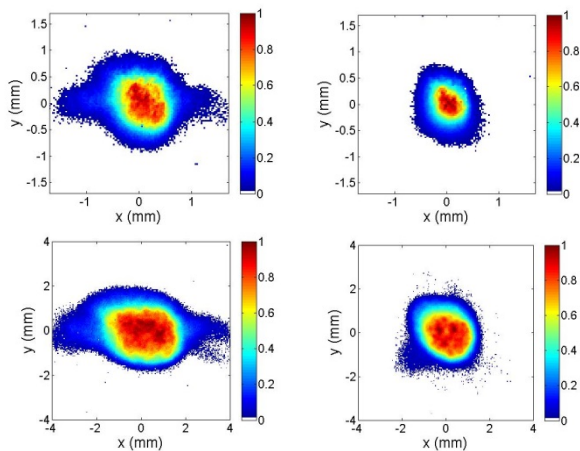


Figure 4: Transverse electron beam distributions at screens HIGH1.Scr1 (upper row) and HIGH1.Scr4 (bottom row) for the case without gun quads (left column) and with applied gun quads (right column).

Corresponding measured transverse phase spaces are shown in Figure 5. It should be noticed that for the case without gun quadrupoles the beam was diverging in the horizontal and converging in the vertical plane. After the application of the gun quadrupoles correction a more similarity is clearly observed between both transverse planes.

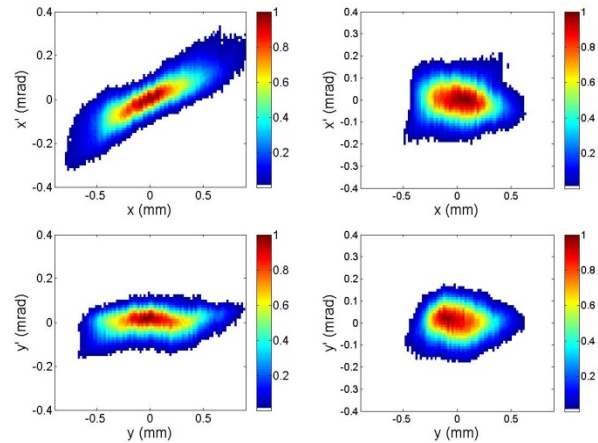


Figure 5: Horizontal (upper row) and vertical (bottom row) phase space measured without gun quadrupoles (left column) and with gun quadrupoles tuned for a symmetric beam (right column).

CONCLUSIONS

Regular (tail) structure in the electron beam transverse distributions observed at PITZ was correlated with the main solenoid polarity. Using the Larmor angle concept and tracking back the tails enabled to localize a location of the kick onto the transverse phase space at the distance of ~ 0.2 m from the photocathode. Two main factors were considered as reasons of the kick: the RF coupler kick and the main solenoid aberrations due to anomalous quadrupole fields. A single quadrupole installed at this location was not able to compensate the beam asymmetry for both polarities of the main solenoid. The final design of the gun compensating coils consists of two quadrupoles (normal and skew) on the same aluminium frame installed around the coaxial power coupler close to the solenoid centre position. First experiments with applied gun quadrupoles demonstrated the capability to produce a rotationally symmetric 0.5-nC electron beam with almost equalized horizontal and vertical emittances. The mean value of the transverse emittance $(\epsilon_{x,n} \epsilon_{y,n})^{1/2}$ was reduced from 0.91 ± 0.04 to 0.83 ± 0.04 mm mrad.

REFERENCES

- [1] M. Krasilnikov *et al.*, “Investigations on electron beam imperfections at PITZ”, in *Proc. LINAC’16*, East Lansing, USA, paper MOPLR013.
- [2] Y. Chen *et al.*, “Coaxial coupler RF kick in the PITZ RF Gun”, presented at *FEL’17*, Santa Fe, NM, USA, paper WEP005.
- [3] Q. Zhao *et al.*, “Beam asymmetry studies with quadrupole field errors in the PITZ gun section”, presented at *FEL’17*, Santa Fe, NM, USA, paper WEP010.
- [4] CST, <https://www.cst.com/>.
- [5] M. Krasilnikov *et al.*, “Experimentally minimized beam emittance from an L-band photoinjector”, *PRSTAB’15*, 100701, 2012.

BEAM BRIGHTNESS IMPROVEMENT BY ELLIPSOIDAL LASER SHAPING FOR CW PHOTOINJECTORS

H. Qian[#], M. Krasilnikov, F. Stephan, DESY, Zeuthen, Germany

Abstract

High brightness photoinjectors operating in continuous wave (CW) mode are enabling many advanced applications, such as CW X-ray free electron laser (FEL), ERL light source, electron coolers for hadron beams and electron-ion colliders and so on. Now, three types of CW electron guns are available: DC gun, SRF gun, and normal conducting RF gun. Compared to pulsed guns, the CW gun beam brightness is compromised due to a lower acceleration gradient at the cathode. Flattop laser shaping and ‘cigar beam’ photoemission have been applied in CW guns to improve beam emittance. In this paper, ellipsoidal laser shaping is studied to further improve the beam brightness for CW photoinjectors towards $\sim 0.1 \mu\text{m-rad}$ at 100 pC.

INTRODUCTION

X-ray free electron lasers (XFEL) have seen great success in the past decades, increasing peak brightness of X-ray beams over synchrotron X-ray sources by as much as 11 orders of magnitude [1]. While all current XFELs are low repetition rate pulsed machines, with advances of CW SRF linac technology, new XFEL machines in CW mode are under design [2, 3]. The gradient of a CW SRF linac is lower than a pulsed linac, and thus CW XFEL linac energy is expected to be lower. To lase at the shortest photon wavelength with lower linac energy, an even brighter electron source is required, e.g. 100 pC bunch charge with $\sim 0.1 \mu\text{m-rad}$ transverse emittance and ~ 20 A peak current is wished [4].

The electron source brightness is limited by photoemission at the cathode, which can be described as [5, 6]:

$$B_{\perp}^{\text{pancake}} \propto \frac{E_0}{\sigma_{p_{\perp}}^2}. \quad (1)$$

$$B_{\perp}^{\text{cigar}} \propto \frac{E_0^{3/2} t_{\text{laser}}}{\sqrt{R} \sigma_{p_{\perp}}^2}. \quad (2)$$

where $B_{\perp}^{\text{pancake}}$ and B_{\perp}^{cigar} are the transverse beam brightness for pancake photoemission and cigar photoemission, resp., E_0 is the gradient at photoemission, t_{laser} is the cathode laser pulse duration, R is the laser spot radius on the cathode, and $\sigma_{p_{\perp}}$ is the RMS transverse momentum after photoemission. Current CW guns, such as DC guns, SRF guns, and normal conducting guns, have a relatively low accelerating gradient at the cathode compared to pulsed guns. This makes it more difficult to

achieve a better beam brightness at CW guns. According to Eq. (1) and (2), to improve the electron source brightness with a relatively low gun gradient, low $\sigma_{p_{\perp}}$, i.e. a low thermal emittance cathode becomes extremely important. Besides, for cigar beam photoemission, a long laser pulse duration and a smaller laser spot size can increase the transverse beam brightness by relaxing the peak current. This might be recovered by velocity or magnetic compression downstream the gun. Both methods have been applied in state of the art CW photoinjector designs.

Even with an optimized emittance at the gun, emittance growth along the linac has to be kept at a minimum. Without careful control of space charge effects, both the projected emittance growth due to slice mismatch and the slice emittance growth easily go beyond $0.1 \mu\text{m-rad}$. Flattop laser shaping has been used to improve space charge linearization in both pulsed and CW guns. An emittance of $\sim 0.2 \mu\text{m-rad}$ has been achieved at ~ 200 pC [7, 8]. To further increase the beam brightness, laser shaping for a uniform ellipsoidal beam has been proposed for 3D space charge linearization. Experimental realizations of an ellipsoidal beam have made a lot of progress in the past, both in the pancake beam regime through blowout emission and in the cigar beam regime through direct laser shaping [9-11].

In simulations, uniform ellipsoidal laser shaping has shown an emittance reduction of $\sim 30\%$ for a 1 nC beam compared to flattop laser shaping in high gradient pulsed guns [12]. In this paper, uniform ellipsoidal laser shaping will be applied in CW photoinjectors to check its benefit in improving the transverse emittance of a 0.1 nC beam for XFEL applications.

OPTIMIZATION TOOL

As shown in Eq. (2), the transverse beam brightness can be increased by relaxing the peak current. Besides, in CW photoinjector designs based on a DC gun or a normal conducting VHF gun, a buncher is used to control the beam peak current, trading transverse emittance.

Transverse emittance and bunch length are two compromising goals in photoinjector optimization, and a group of non-dominating optimal solutions of transverse emittance and bunch length form the Pareto front, which can be solved by multi objective genetic algorithm (MOGA) [13]. In this paper, a MOGA tool developed at LBNL is used to drive ASTRA simulations for photoinjector optimization [14]. 10000 macro particles are used in MOGA simulations, and interesting solutions are refined with 100000 macro particles in ASTRA for detailed analysis.

[#] houjun.qian@desy.de

NC VHF GUN BASED CW PHOTOINJECTOR

A CW normal conducting VHF gun has been developed at LBNL, demonstrating a cathode gradient of 20 MV/m and a gun voltage of 750 kV. Based on the LBNL VHF gun, a CW photoinjector has been designed for the LCLS-II project. Its layout is shown in Fig. 1 [14, 15].



Figure 1: Normal conducting VHF gun based CW photoinjector for LCLS-II.

The LCLS-II injector has been optimized with a flattop laser and a conservative thermal emittance of 1 $\mu\text{m}/\text{mm}$. Both injector transverse emittance and peak current, satisfy LCLS-II injector specs. In this part, uniform ellipsoidal laser shaping is applied to such an injector design to further improve the beam brightness for the 100 pC case. A group of injector parameters, similar to Table 1 in Ref [15], were varied during MOGA optimizations, and optimal solutions of the Pareto fronts are shown in Fig. 2.

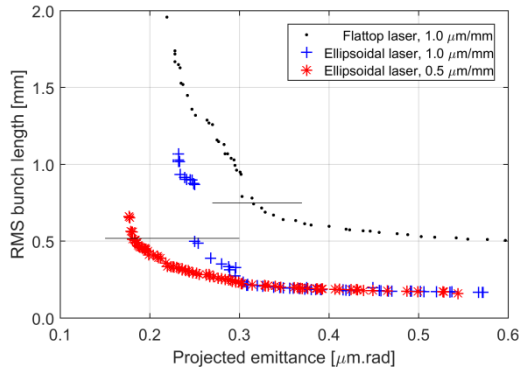


Figure 2: Pareto fronts for LCLS-II injector based on different cathode laser shaping and cathode thermal emittance with 100 pC bunch charge (10k macro particle ASTRA simulations), 20 A peak current solutions marked.

The solutions in Fig. 2 with 20 A peak current are further refined with 100k macro particle simulations. Beam projected and sliced parameters are shown in Fig. 3 and Table 1. Ellipsoidal laser shaping reduces both projected emittance and slice emittance by $\sim 30\%$. With a smaller thermal emittance of 0.5 $\mu\text{m}/\text{mm}$, another 30% reduction on emittance is achieved, making $\sim 0.1 \mu\text{m}\text{-rad}$ emittance with 20 A peak current within reach at 100 pC bunch charge. Besides emittance reduction, current profiles in Fig. 3 show, longitudinal profile distortion due to nonlinear space charge energy chirp and velocity bunching dynamics are reduced with an ellipsoidal beam. Also, the RMS bunch length for 20 A peak current is reduced from 2.5 ps to 1.7 ps.

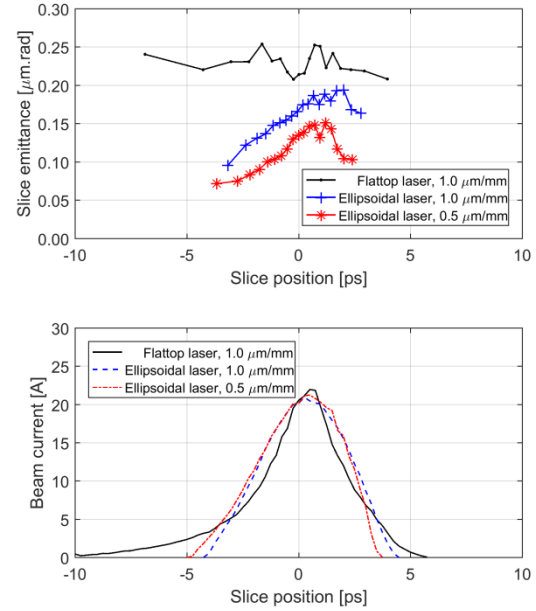


Figure 3: Slice emittance and current profile of the 20 A peak current solutions in Fig. 2 (100k macro particle simulations, each slice has 5k macro particles).

Table 1: Emittance decomposition for solutions shown in Fig. 3 ($\epsilon_{100\%}$ is 100 % projected emittance, $\epsilon_{95\%}$ is 95% projected emittance, $\langle \epsilon_{\text{slice}} \rangle$ is average slice emittance, ϵ_{th} is thermal emittance, $\Delta \epsilon_{\text{mis}}$ is projected emittance growth due to longitudinal slice mismatch, $\Delta \epsilon_{\text{slice}}$ is slice emittance growth w.r.t. thermal emittance)

	Flattop 1 $\mu\text{m}/\text{mm}$	Ellipsoidal 1 $\mu\text{m}/\text{mm}$	Ellipsoidal 0.5 $\mu\text{m}/\text{mm}$	Unit
$\epsilon_{100\%}$	0.28	0.19	0.12	μm
$\epsilon_{95\%}$	0.22	0.14	0.09	μm
$\langle \epsilon_{\text{slice}} \rangle$	0.23	0.16	0.11	μm
ϵ_{th}	0.18	0.14	0.09	μm
$\Delta \epsilon_{\text{slice}}$	0.15	0.09	0.07	μm
$\Delta \epsilon_{\text{mis}}$	0.16	0.09	0.04	μm

Emittance decompositions of the optimal solutions according to Ref. [16] are listed in Table 1, showing the main emittance contributions and residual emittance growth. The projected emittance is decomposed as,

$$\epsilon_{100\%} = \sqrt{\epsilon_{th}^2 + \Delta \epsilon_{\text{slice}}^2 + \Delta \epsilon_{\text{mis}}^2}. \quad (3)$$

Emittance growth due to slice phase space centroid misalignment is zero in this case, because situations such as slice dependent kicks are not considered in these simulations. Table 1 shows that all solutions are dominated by thermal emittance, and that emittance growth due to slice mismatch and slice emittance growth can be reduced below 0.1 $\mu\text{m}\text{-rad}$ with ellipsoidal laser.

SRF GUN BASED CW PHOTOINJECTOR

Superconducting (SC) RF is a natural CW technology. SRF guns for CW XFEL and ERL applications have been under development and great progress has been made towards high gradient operation and towards compatibility with high QE cathodes [17]. Figure 4 shows a classical photoinjector layout consisting of a 1.5 cell L-band SRF gun and an 8-cavity CW superconducting module. A superconducting solenoid is positioned at 0.5 meter from the cathode. Such an injector is used to check the effect of ellipsoidal laser shaping on the transverse emittance at 100 pC.



Figure 4: L-band superconducting RF gun based CW photoinjector layout (preliminary example, not optimal).

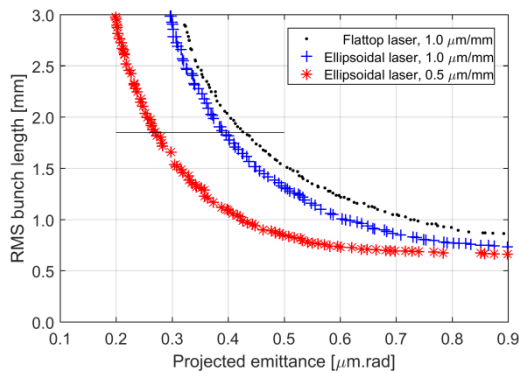


Figure 5: Pareto fronts for the CW injector in Fig. 4 with 100 pC bunch charge, 5 A peak current solutions marked.

Velocity bunching is not used in such an injector not only for simplicity but also for minimizing the longitudinal beam distortion which occur with velocity bunching. Beam bunch length is controlled by either cathode laser pulse duration or magnetic bunch compression after the harmonic cavity (see European XFEL injector [18]). During MOGA optimizations, cathode laser pulse duration and radius, solenoid strength, and SC cavity gradients can be varied for optimal solutions. The gun is set to 40 MV/m peak cathode gradient and maximum energy gain phase. Such a high field in SRF guns is still to be demonstrated in reality. On axis peak acceleration gradients of SC cavities are up to 32 MV/m, following the LCLS-II parameters [19], and the cavity phases are set to on-crest. Pareto fronts of the above injector are shown in Fig. 5, and refined 100k particle simulations are in Fig. 6 and Table 2.

Emittance decompositions of the 5 A peak current solutions show that emittance growth due to slice mismatch is negligible, which means a very good emittance compensation. Emittance growth for all three cases is dominated by slice emittance growth, caused by solenoid spherical aberration [20]. In the current setup, both the Pareto fronts and specific solutions show the

ellipsoidal laser shaping effect on emittance improvement is small. With an improved solenoid design and injector layout optimization, the effect of ellipsoidal laser shaping will be further investigated.

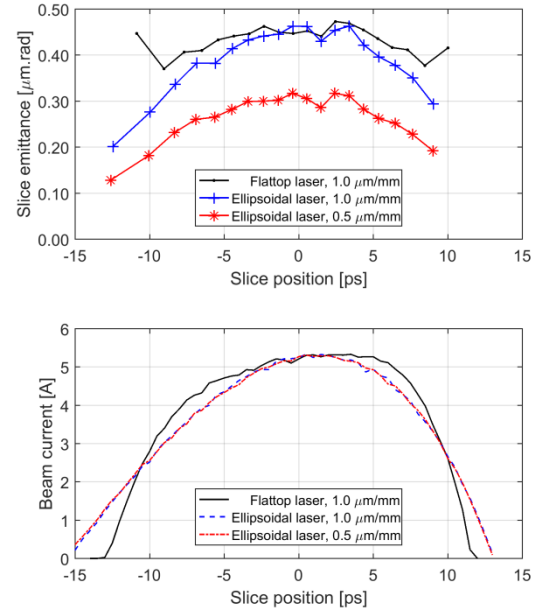


Figure 6: Slice emittance and current profile of the 5 A peak current solutions in Fig. 5.

Table 2: Emittance decomposition for solutions in Fig. 6

	Flattop 1 μm/mm	Ellipsoidal 1 μm/mm	Ellipsoidal 0.5 μm/mm	Unit
$\epsilon_{100\%}$	0.44	0.39	0.26	μm
$\epsilon_{95\%}$	0.35	0.31	0.21	μm
$\langle \epsilon_{slice} \rangle$	0.43	0.38	0.26	μm
ϵ_{th}	0.28	0.28	0.18	μm
$\Delta \epsilon_{slice}$	0.33	0.26	0.19	μm
$\Delta \epsilon_{mis}$	0.08	0.05	0.03	μm

CONCLUSION

In this paper, beams from uniform ellipsoidal shaped lasers are simulated for CW photoinjectors based on a VHF gun and an L-band SRF gun for the 100 pC case. In the case of LBL type VHF gun with a peak gradient of 20 MV/m at cathode, ellipsoidal laser shaping can improve both emittance and longitudinal current profile distortions at 20 A peak current based on the LCLS-II injector. For the L-band 1.5 cell SRF gun with a 40 MV/m cathode gradient and a SC solenoid 0.5 meter from cathode, simulations show slice emittance growth is dominated by solenoid spherical aberrations. Further improvements of CW solenoid design or injector layout are needed for showing the effect of ellipsoidal laser shaping.

REFERENCES

- [1] W.A. Barletta *et al.*, Nucl. Instr. Meth., 618, 69, 2010.

- [2] J.N. Corlett *et al.*, in *Proc. IPAC'11*, pp. 775.
- [3] T.O. Raubenheimer., in *Proc. IPAC'15*, pp. 2434.
- [4] Report of the Basic Energy Sciences Workshop on the Future of Electron Sources, 2016, https://science.energy.gov/~media/bes/pdf/reports/2017/Future_Electron_Source_Worskhop_Report.pdf
- [5] Ivan V. Bazarov *et al.*, PRST AB 102, 104801, 2009.
- [6] D. Filippetto *et al.*, PRST AB 17, 024201, 2014.
- [7] M. Krasilnikov *et al.*, PRST AB 15, 100701, 2012.
- [8] T. Schietinger *et al.*, PRST AB 19, 100702, 2016.
- [9] P. Musumeci *et al.*, PRL 100, 244801, 2008.
- [10] Yuelin Li *et al.*, PRST AB 12, 020702, 2009.
- [11] J. Good *et al.*, “Preliminary On-Table and Photoelectron Results from the PITZ Quasi-Ellipsoidal Photocathode Laser System”, presented at FEL'17, Santa Fe, NM, Aug. 2017, paper WEP006, this conference.
- [12] M. Khojayan *et al.*, in *Proc. FEL'13*, pp. 298.
- [13] Ivan V. Bazarov *et al.*, PRST AB 8, 034202, 2005.
- [14] C. F. Papadopoulos *et al.*, in *Proc. FEL'14*, pp. 864.
- [15] C. Mitchell *et al.*, in *Proc. IPAC'16*, pp. 1699.
- [16] C. Mitchell, arXiv:1509.04765.
- [17] J. Sekutowicz, in *Proc. SRF'15*, pp. 994.
- [18] F. Brinker, in *Proc. IPAC'16*, pp. 1044.
- [19] D. Gonnella *et al.*, in *Proc. IPAC'17*, pp. 1156.
- [20] Ivan V. Bazarov *et al.*, PRST AB 8, 034802, 2005.

A CRYOCOOLED NORMAL-CONDUCTING AND SUPERCONDUCTING HYBRID CW PHOTOINJECTOR

H. Qian[#], M. Krasilnikov, F. Stephan, DESY, Zeuthen, Germany

Abstract

Continuous wave (CW) photoinjectors have seen great progress in the last decades, such as DC gun, superconducting RF (SRF) gun and normal conducting (NC) VHF-band gun. New developments of CW guns are aiming higher acceleration gradient and beam energy for higher beam brightness. While a SRF gun being the natural CW gun technology for better performance, it has been technically limited by the compatibility between normal conducting high QE cathodes and superconducting (SC) cavity. In this paper, a high gradient and low voltage cryocooled CW NC gun is proposed to house the high QE cathode, and a half cell SRF cavity immediately nearby gives further energy acceleration. Preliminary RF design of the NC gun and ASTRA simulations of such a hybrid photoinjector are presented.

INTRODUCTION

Electron sources of both high peak brightness and high average brightness are wished for a lot of advanced applications [1]. Pulsed electron guns enjoy a high cathode gradient (60-200 MV/m), enabling electron beams with high 6D-brightness possible right at the cathode. Such high gradients are difficult to extend to a CW gun, due to cooling concerns, dark current, and other concerns. Current CW RF guns operate at cathode gradient around 20 MV/m [2,3], and beam transverse brightness are optimized by relaxing peak current at photoemission, which is recovered by velocity bunching or magnetic bunch compression [4,5]. To achieve higher beam brightness, higher cathode gradient and beam energy is wished [1]. The next generation of normal conducting VHF-band gun with over 30-MV/m cathode gradient is under study, and a major challenge is thermal loading (over 100 kW)[6].

Based on such a gun design, ASTRA simulations have shown that the emittance of a 100-pC beam can be improved towards $\sim 0.1 \mu\text{m}\cdot\text{rad}$ [6,7]. Besides, SRF guns have made great progress in the past decade, showing the possibility of high cathode gradient up to 60 MV/m [8]. The compatibility of a high-QE cathode and a high gradient SRF cavity is still a technical challenge. In most of cases, the SRF gun gradient is greatly reduced once a high QE photocathode is present inside the cavity. Besides, multipacting inside the gun can also kill the high QE cathode [9]. While engineering improvements have been implemented in the design of cathode insertion channels of SRF guns to mitigate multipacting and to avoid cathode contamination to SRF cavity surface, risks still exist due to the high sensitivity of SRF cavity surface.

Other special SRF gun designs are also under development. The DESY 1.5-cell L-band SRF gun uses superconducting metal cathodes, eliminating the gap between SRF cavity and NC high QE cathodes for potentially high-gradient performance [8]. The DC-SRF gun developed at Peking University puts the high-QE cathode inside the DC gun just before the SRF cavity, preventing the complex cathode channel design and cathode contamination to SRF cavity. The DC-SRF gun has demonstrated an average current of $\sim \text{mA}$ for CW operation [10].

Inspired by the DC-SRF gun, the DC acceleration of the hybrid gun is proposed to be replaced by a high-gradient NC-CW RF gun, forming a NC-SRF gun, so that beam brightness is not limited by the low cathode gradient. In this paper, the preliminary concept and RF design of such a gun is described, and the engineering considerations are not discussed. Based on the proposed NC-SRF gun concept, a CW photoinjector is optimized by ASTRA simulations.

NC-SRF GUN CONCEPT

The high gradient NC RF cavity is proposed to house the high QE cathode and support high brightness photoemission with high cathode gradient, and the main acceleration is still in the SRF cavity. The compatibility between high gradient NC RF cavity and high QE cathode has been well demonstrated in both pulsed and CW NC guns [11,12]. Since the NC cavity voltage is supposed to be low, to maintain the beam brightness from the NC cavity, the SRF cavity should be as close to the NC cavity as possible, same as in the DC-SRF gun. Since the NC cavity and SRF cavity will stay in the same cryomodule, the NC cavity should be cryocooled, and then the NC cavity RF heating should be minimized. The NC cavity should be high gradient with low cavity voltage, i.e. a thin gap cavity. A re-entrant cavity shape is considered for such a thin gap cavity. Scaling from the existing LBL VHF gun parameters [3], i.e. $\sim 100 \text{ kW}$ for 800 kV, the gun is assumed to be $\sim 1 \text{ kW}$ for 80 kV. Since the NC cavity will be cryocooled, the cavity quality factor will increase, and the RF heating will be even lower. Several cryocooled NC guns have been proposed for the purpose of ultrahigh gradient operation [13,14]. Microwave measurements at cryogenic temperature (20 K) has shown RF surface-resistance reduction of a factor of ~ 5 compared to room temperature at both S-band and C-band frequencies [15,16]. Applying the same reduction ratio to the assumed 80 kV NC cavity, the RF heating, i.e. cryogenic load at 20 K will be reduced from $\sim 1 \text{ kW}$ to $\sim 200 \text{ W}$.

[#]houjun.qian@desy.de

To keep the NC cavity RF heating low and RF energy curvature small for a sub-100 ps beam, a low frequency cavity, i.e. sub-harmonic of 1.3 GHz, is designed. To have a thin gap low frequency cavity with compact cavity size, the re-entrant cavity shape is used. The SRF cavity for main acceleration has many options, such as single cell or multi cell, 1.3 GHz or its sub harmonic. For the first design, a half-cell 1.3-GHz SRF cavity is used. Both the low frequency NC cavity and the half-cell SRF cavity are designed using the SUPERFISH code.

Figure 1 shows a preliminary physics design without engineering realizations, and both cavity designs are not fully optimized yet from RF and beam dynamics perspectives. The separation between the two cavities is chosen arbitrarily without consulting engineers, and the half-cell SRF cavity front wall is 37.3 mm from cathode.

The NC cavity frequency is 325 MHz, and shunt impedance is 4.27 M Ω at room temperature. With a 30 MV/m gradient on the cathode, the cavity voltage is \sim 80 kV, and the cavity RF heating at room temperature is \sim 1.5 kW, which is a bit worse than the scaling from the LBL VHF cavity (185.7 MHz) [3]. With further cavity optimizations, the cavity shunt impedance is expected to increase. The on-axis electric field maps of both cavities are shown in Fig. 2. If both the NC and SC cavity peak gradients are assumed to be 30 MV/m, the total beam energy acceleration is \sim 1.4 MeV.

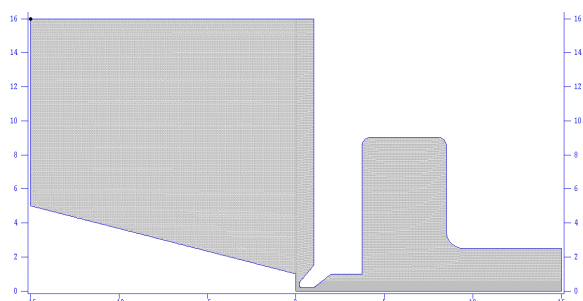


Figure 1: Preliminary SUPERFISH model of a NC-SRF gun, consisting of a re-entrant NC cavity (325 MHz) and a half-cell SRF cavity (1.3 GHz).

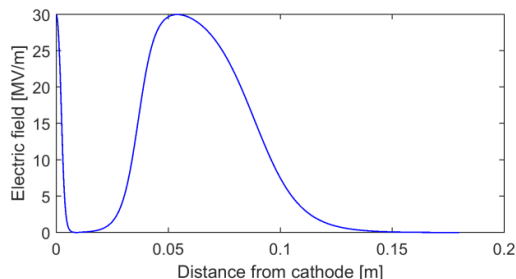


Figure 2: On-axis electric field of the NC-SRF gun in Fig. 1. The two cavities are de-coupled, and the field amplitudes in the plot are preliminary assumptions.

Further RF optimizations have to be done, and beam dynamics verifications of such a gun concept are shown in the next section.

BEAM DYNAMICS OPTIMIZATION

A classical photoinjector layout based on the NC-SRF gun is shown in Fig. 3, consisting of the gun, a SC solenoid, and an 8-cavity cryomodule (CM). Other photoinjector layouts, including a dedicated buncher cavity and two solenoids, are not yet tested in this paper.

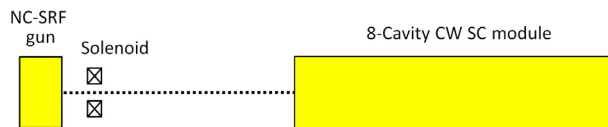


Figure 3: Preliminary photoinjector layout.

The photoinjector is optimized using a multi-objective genetic algorithm (MOGA). A code developed at LBL can be used to drive ASTRA simulations for searching optimal solutions of both good emittance and short bunch length [17]. In this paper, only emittance is optimized, no constraint on bunch length is done in the optimizations for simplicity. Two cases are simulated with a 100 pC bunch charge. In the first case, phase of cavity #1 in the 8-cavity CM is allowed to vary for velocity bunching. In the 2nd case, phase of cavity #1 is set to on-crest.

The peak gradients of the NC and SC cavity are fixed at 30 MV/m, which are a bit higher than current operating cavities (\sim 20 MV/m). The 2nd and 3rd cavities in the 8-cavity CM are OFF, following the LCLS-II injector experience [18]. The 4th cavity amplitude is variable, and all the other cavities in the module are set to fixed amplitudes of 32 MV/m with on-crest phases. The laser is a quasi-flat-top distribution. The transverse distribution is a Gaussian distribution with 1-sigma cut, and the longitudinal distribution is a flat-top with 2-ps rising and falling edges. The cathode thermal emittance is assumed to be 0.5 μ m.rad/mm.

There are 9 variable parameters during the optimization for the case with velocity bunching by cavity #1 in CM, which are listed in Table 1. For the 2nd case without velocity bunching, there are 8 variables, excluding the cavity #1 phase.

Content from this work may be used under the terms of the CC BY 3.0 licence (© 2018). Any distribution of this work must maintain attribution to the author(s), title of the work, publisher, and DOI.

Table 1: Nine Variable Parameters During Photoinjector Optimizations (for the case including velocity bunching)

Parameter	Range	Unit
SC cavity phase	[-10, 10]	degree
Solenoid peak field	[0, 0.1]	T
Solenoid position	[0.55, 1.5]	m
1 st cavity position in CM	[2, 5]	m
1 st cavity amplitude	[0, 32]	MV/m
1 st cavity phase	[-90, 0]	degree
4 th cavity amplitude	[0, 32]	MV/m
Laser radius	[0.1, 1.5]	mm
Laser pulse duration	[10, 70]	ps

Two solutions with best emittance results at the end of photoinjector are found, without touching the hard limits in Table 1. The emittance results are listed in Table 2. The current profiles and slice emittances are shown in Fig. 4 and Fig. 5. The longitudinal phase spaces after removing linear and quadratic energy chirps are plotted in Fig. 6.

Although the emittance values from the two optimal solutions are low, many other aspects of the beam indicate the injector is still not optimum. Emittance decompositions [19], in Table 2, show both beams are not thermal emittance dominated, which should be a feature of state of the art photoinjector optimizations [20]. Emittance growth from slice mismatch and slice emittance growth are large compared to thermal emittance. In the longitudinal phase space, both beam current profiles are highly distorted, and the higher order energy spread of the beam with velocity bunching is high. Both transverse and longitudinal phase space analysis show the injector is still not optimum. Both the NC-SRF gun and the injector layout need further optimizations.

Table 2: Emittance decomposition for solutions shown in Figs. 4 and 5. $\epsilon_{100\%}$ is 100% projected emittance, $\epsilon_{95\%}$ is 95% projected emittance, $\langle \epsilon_{\text{slice}} \rangle$ is average slice emittance, ϵ_{th} is thermal emittance, $\Delta \epsilon_{\text{mis}}$ is projected emittance growth from longitudinal-slice mismatch, and $\Delta \epsilon_{\text{slice}}$ is slice emittance growth w.r.t. thermal emittance.

	No chirp in Cav 1	Chirp in Cav 1	Unit
$\epsilon_{100\%}$	0.31	0.20	μm
$\epsilon_{95\%}$	0.24	0.13	μm
$\langle \epsilon_{\text{slice}} \rangle$	0.23	0.13	μm
ϵ_{th}	0.08	0.06	μm
$\Delta \epsilon_{\text{slice}}$	0.22	0.12	μm
$\Delta \epsilon_{\text{mis}}$	0.20	0.15	μm

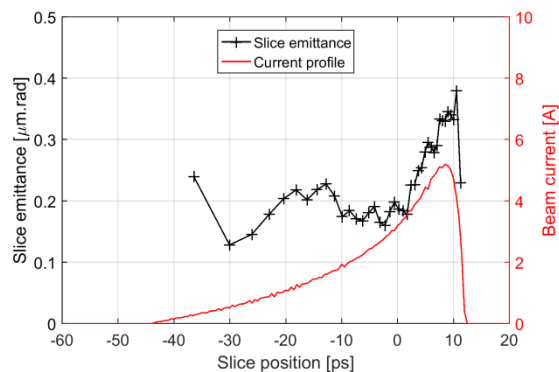


Figure 4: Slice emittance and current profile for 100 pC beam based on the injector in Fig. 3, no velocity bunching by cavity #1 of 8-cavity CM.

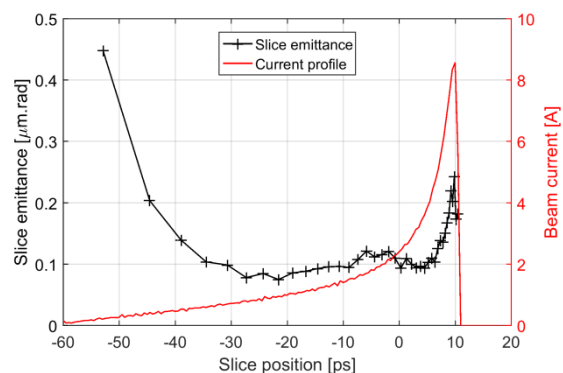


Figure 5: Slice emittance and current profile for 100 pC beam based on the injector in Fig. 3, with velocity bunching by cavity #1 of 8-cavity CM.

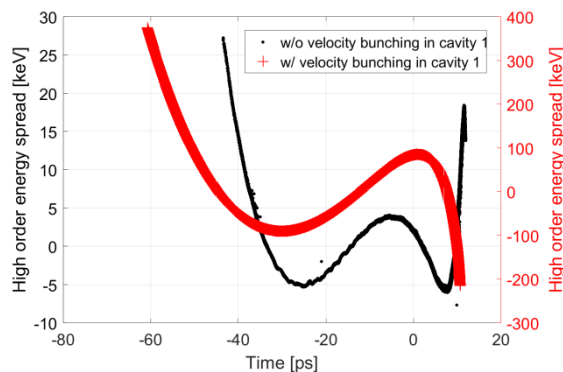


Figure 6: Longitudinal phase space of the two solutions in Figs. 4 and 5 after removing the linear and quadratic energy chirps, showing a 4.4-keV (rms) higher-order energy spread for the case w/o velocity bunching (left axis), and a 76-keV (rms) higher-order energy spread for the case w/ velocity bunching (right axis).

Although the injector is still not optimized, the low thermal emittances in both solutions indicate high transverse beam brightness from photoemission, which supports the considerations of a high gradient but low voltage cathode cell design.

CONCLUSION

In this paper, a cryocooled NC-SRF gun concept is proposed. A high gradient and low voltage NC cathode cell not only simplifies the normal conducting high QE cathode compatibility issues in SC gun, but also supports the high transverse brightness photoemission. A SC cavity immediately nearby will do the main acceleration to damp the space charge effect and conserve the beam brightness from the cathode cell. The two cavities are decoupled.

A preliminary gun concept is designed by SUPERFISH code. Preliminary beam dynamics optimizations based on such a gun with 30 MV/m in both the NC cathode cell and SC cell are presented for a bunch charge of 100 pC. Although low emittance values are found, analysis of both transverse and longitudinal phase spaces show the injector is still not optimum. Both the gun concept and the injector layout need further developments.

REFERENCES

- [1] *Report of the Basic Energy Sciences Workshop on the Future of Electron Sources*: https://science.energy.gov/~media/bes/pdf/reports/2017/Future_Electron_Source_Worskhop_Report.pdf
- [2] R. Xiang, in *Proc. IPAC'17*, p. 500.
- [3] F. Sannibale *et al.*, *PRST-AB* 15, 103501 (2012).
- [4] I. Bazarov *et al.*, *PRST-AB* 8, 034802 (2005).
- [5] D. Filippetto *et al.*, *PRST-AB* 17, 024201 (2014).
- [6] F. Sannibale *et al.*, in *Proc. IPAC'17*, p. 542.
- [7] H. Qian *et al.*, presented at FEL'17, this conference.
- [8] J. Sekutowicz, in *Proc. SRF'15*, p. 994.
- [9] I. Petrushina *et al.*, in *Proc. IPAC'17*, p. 1180.
- [10] K. Liu *et al.*, presented at FEL'17, this conference.
- [11] D. Filippetto *et al.*, *Appl. Phys. Lett.* 107 042104 (2015).
- [12] M. Krasilnikov *et al.*, *PRST-AB* 15, 100701 (2012).
- [13] V. Vogel *et al.*, in *Proc. IPAC'11*, p. 77.
- [14] J. Rosenzweig *et al.*, arXiv:1603.01657.
- [15] A. Cahill *et al.*, in *Proc. IPAC'16*, p. 487.
- [16] T. Tanaka *et al.*, in *Proc. IPAC'17*, p. 518.
- [17] C. F. Papadopoulos *et al.*, in *Proc. FEL'14*, p. 864.
- [18] C. Mitchell *et al.*, in *Proc. IPAC'16*, p. 1699.
- [19] C. Mitchell, arXiv:1509.04765.
- [20] C. Gulliford *et al.*, *Appl. Phys. Lett.* 106, 094101 (2015).

BEAM ASYMMETRY STUDIES WITH QUADRUPOLE FIELD ERRORS IN THE PITZ GUN SECTION

Q. Zhao^{†,1}, M. Krasilnikov, I. Isaev, H. Qian, P. Boonpornprasert, G. Asova², Y. Chen, J. Good, M. Gross, H. Huck, D. Kalantaryan, X. Li, O. Lishilin, G. Loisch, D. Melkumyan, A. Oppelt, Y. Renier, T. Rublack, C. Saisa-Ard³, F. Stephan, DESY, Zeuthen, Germany

Abstract

The Photo Injector Test Facility at DESY, Zeuthen site (PITZ) was built to test and optimize high brightness electron sources for Free Electron Lasers (FELs) like FLASH and the European XFEL. Although the beam emittance has been optimized and experimentally demonstrated to meet the requirements of FLASH and XFEL, transverse beam asymmetries, such as wing structures and beam tilts were observed during many years of operation with different generations of guns. These cannot be explained by simulations with the rotationally symmetric gun cavities and symmetric solenoid fields. Based on previous coupler kick, solenoid field imperfection studies and coupling beam dynamics, the beam asymmetries most probably stem from anomalous quadrupole field error in the gun section. A thin lens static quadrupole model is applied in the RF gun section simulations to fit the position and intensity of quadrupole field errors by comparing the beam asymmetry directions in experiments and ASTRA simulations. Furthermore, by measuring the laser position movement at the photocathode and the corresponding beam movement at downstream screens, the integrated quadrupole field strength can also be extracted.

INTRODUCTION

The RF gun of PITZ is a rotationally symmetric 1.6 cell L-band cavity. The electron beam is generated at the cathode by a laser and then accelerated by gun cavity RF fields and focused by the solenoid field. From beam dynamics simulation with $E_z(z)$ and $B_z(z)$ field map in ASTRA [1], the beam transverse distribution is symmetric anywhere downstream the gun cavity, which is not exactly matching to the experimental results. During several years of operation with different generations of guns, the imperfect beams were always observed from experiments [2-3], such as beam tilt from transverse images, beam wing structures, asymmetric x and y phase space distributions and not round beam transverse distributions observed during emittance measurements. One of the most obvious asymmetric features is the beam wing structure shown in Figure 1 from experiment. For Figure 1 the experiment results were taken at High1.Scr1 ($z = 5.277$ m from cathode) with beam momentum of 6.18 MeV/c, bunch charge 480 pC and two polarities of the main solenoid (I_{main}) but the same current. The beam wings are at

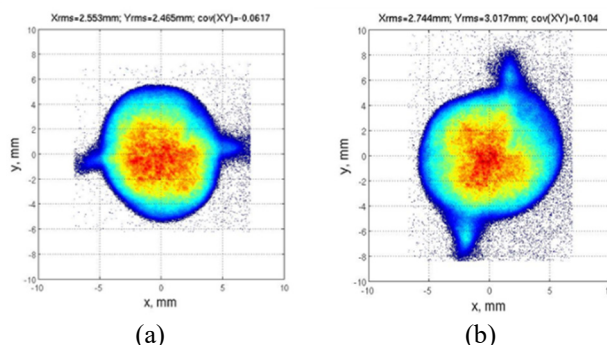


Figure 1: Beam images at High1.Scr1 (a) normal solenoid polarity ($I_{\text{main}} = -360$ A) and (b) opposite solenoid polarity ($I_{\text{main}} = +360$ A).

different orientations due to different rotation angle caused by different solenoid polarity.

From previous studies [4-5], the PITZ gun RF coupler kick was found from RF field simulations. In the transition region from the coupler to the gun, the RF field distribution is not uniform. The RF coupler kick optics can be modelled as a rotated quadrupole with focal length and rotation angle given in terms of complex voltage kicks. A rotated quadrupole near the coupler is effective at compensating for the coupler kicks, cancelling both the coupling emittance and the astigmatic focusing [6-7]. Another source of the beam asymmetries may come from solenoid field imperfections. Beam asymmetries from photo gun are also observed in other labs [8]. The feature of the beam transverse coupling from rotated quadrupoles can be observed from beam transverse distributions in experiment like the beam tilt in Figure 1. Linear coupling can be compensated in principle by additional rotated quadrupoles, but the beam dynamics for coupling effects must be known to perform a proper compensation [9].

QUADRUPOLE FIELD ERROR POSITION AND ROTATION ANGLE ESTIMATION

Experiments for Beam Wings Studies

For beam asymmetry studies, some dedicated experiments were done with different RF power in the Gun4.2 and solenoid current scan. Three values of power 5 MW, 3 MW and 1.5 MW in the gun were used. The beam wings appeared at High1.Scr1 by solenoid current scan and the clearest signals of beam wings are seen for I_{main} at 360 A, 290 A, 219 A respectively and other I_{main} s have shown the beam tilted images for both polarities. The

[†] quantang.zhao@desy.de

¹ on leave from IMP/CAS, Lanzhou, China

² on leave from INRNE, Sofia, Bulgaria

³ on leave from Chiang Mai University, Chiang Mai, Thailand

beam images with beam wing structure are shown in Figure 2 row 3 for different gun power. For each gun power, when changing the polarity of the solenoid, the beam wing directions are changed. The experiment settings and beam parameters are shown in Table 1.

Table 1: Experimental Settings for Beam Wings Studies

Power (MW)	Gradient (MV/m)	I _{main} (A)	Charge (pC)	Maximum Momentum (MeV/c)
5	54.2	360	502	6.18
3	42.2	290	502	4.86
1.5	31.4	219	334	3.69

Beam Wings Directions Fitting by Simulations with Rotated Quadrupole Model

For RF power of 5 MW in the gun, the beam wings appeared in different directions with both solenoid polarities. With I_{main} = -360 A, the beam wings are at about 12 degrees with respect to the anticlockwise direction and for I_{main} = 360 A the beam wings are at about 78 degrees. A rotated quadrupole model is added in simulations with scanning both the quadrupole positions along the beam line, the rotation angle and the strength. The rotation

angle is scanned from 0 to 360 degrees with a step of 5 degrees for each position in order to fit the beam wings direction to that of the experimental images. The quadrupole model parameters are shown in Figure 2, with an effective length of 0.01 m. The simulated beam images at High1.Scr1 are investigated with both solenoid polarities as a function of the quadrupole rotation angle at the assumed kick location position. The quadrupole positions scanning range covered the whole possible area where a quadrupole like field could exist due to field imperfection reason. The range is from 0.12 m to 0.38 m at a step of 0.02 m. By fitting the beam wings direction for both solenoid current polarities from the simulation to experiment, two possible positions and corresponding rotation angles of the quadrupoles were found. One is shown at z = 0.18 m, with skew type (rotation angle 135 degree); another one is at z = 0.36 m, with normal type (rotation angle 0 degree). The simulated image results are shown in Figure 2, in row 4 and row 6. The beam wings structure appeared from simulation with quadrupole fields. The beam wings directions could fit to the experiment results very well with found quadrupole positions and rotation angle. For the skew quadrupole at z = 0.18 m, when change the solenoid polarity, the quadrupole polarity did not change, but for the normal quadrupole at z = 0.36 m, the quadrupole polarity changes together with the main solenoid polarity.

I _{main}	-360 A	+360 A	-290 A	+290 A	-219 A	+219 A
Beam momentum from experiment	5 MW in the gun 6.18 MeV/c		3 MW in the gun 4.86 MeV/c		1.5 MW in the gun 3.69 MeV/c	
Experiment: Beam at High1.Scr1 at z = 5.277 m						
Simulation: High1.Scr1 with skew quad (rotation angle 135 degree) at z = 0.18 m						
K _{skew} (m ⁻²)	-0.6	-0.6	-1.0	-1.0	-2.0	-2.0
Simulation: High1.Scr1 with normal quad (rotation angle 0 degree) at z = 0.36 m						
K _{normal} (m ⁻²)	0.2	-0.2	0.3	-0.3	1.0	-1.0

Figure 2: Experimental beam images (row 3) and simulation results, with skew quadrupole located at z = 0.18 m (row 4) and with normal quadrupole located at z = 0.36 m (row 6). The row (5) and (7) are the quadrupole strength used in simulation when the beam wings structure appeared.

Content from this work may be used under the terms of the CC BY 3.0 licence (© 2018). Any distribution of this work must maintain attribution to the author(s), title of the work, publisher, and DOI.

QUADRUPOLE FIELD ERRORS STRENGTH ESTIMATION

Principle and Method for Estimating the Rotated Quadrupole Field Strength

In the PITZ gun section, because of the overlap of the RF and solenoid fields, also couplings from solenoid and quadrupoles field error are both existing, which causes the coupling problem to be more complicated. If we track the beam in a solenoid induced coordinate system, the coupling due to beam rotation induced by the main solenoid can be neglected. Beam transport in a solenoid will be rotated and the rotation angle can be defined by:

$$\phi = -\frac{1}{2} \int_{z_0}^z S(z) dz, \quad S(z) = \frac{e}{P(z)} B_s(z), \quad (1)$$

where the solenoid field $B_s(z)$ starts from z_0 . In the gun section, the beam momentum $P(z)$ increases along the beam line, so the rotation angle along the gun section beam line depends not only on the solenoid field profile but also on the RF field profile. By varying the laser position at the cathode and observing the corresponding electron beam movements at downstream screens, the integrated quadrupole field strength can be extracted. The principle is shown in Figure 3: (a) laser positions at the cathode, (b) beam positions at the downstream screens in lab coordinate (x, y) , (c) beam positions at downstream screens in solenoid induced rotation coordinate (x', y') without any other x - y coupling, (d) beam positions at downstream screens in solenoid induced rotation coordinate (x', y') with other x - y coupling (rotated quadrupole, et al). The beam relative positions in lab coordinate system transform to the solenoid induced coordinate system. By fitting the simulation results to experiment, the rotated quadrupole strength can be estimated.

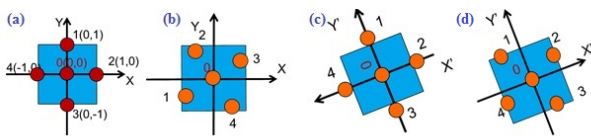


Figure 3: Sketch map of beam positions in different coordinate system.

Rotated Quadrupoles Strength Estimation for Gun with Solenoid

One important parameter for transforming the coordinates from the lab coordinate frame to the solenoid induced coordinates is the rotation angle induced by the solenoid field. So a beam imaging experiment by grid transverse shaping the laser beam at the cathode [3] was done to check the rotation angle with simulation. The experiment was taken with Gun4.2 operated at 5 MW

with focusing solenoid currents. Laser RMS size is 0.3 mm and the bunch charge is 500 pC. The laser relative positions are as following: 10, (0.018, 1.001) mm, 20, (0.98, -0.001) mm, 30, (-0.008, -1.066) mm, 40, (-1.015, 0.073) mm, where 10 means laser relative position with laser position at 1 (up ~1 mm) minus laser position at 0 (nominal running position), other positions 20, 30, and 40 are in a similar way. The laser positions at VC2 (virtual cathode camera) and the beam positions at Low.scr3 ($z = 1.708$ m from cathode) are shown in Figure 4. We moved the laser to five positions, up and down, left and right and zero positions shown in Figure 4 (a) and observed the corresponding beam positions at Low.scr3 shown in Figure 4(b).

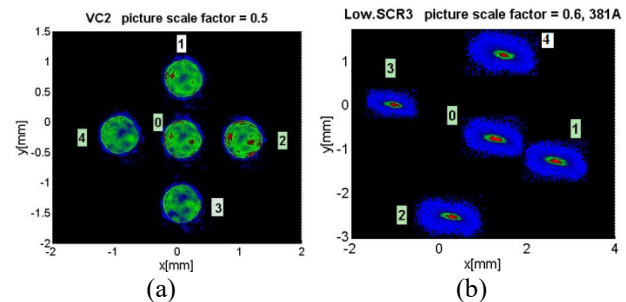


Figure 4: The laser positions at VC2 (a) and beam positions at Low.scr3 ($I_{\text{main}} = -381$ A) (b) in lab coordinate from experiment.

From the previous studies, we found two possible locations of kicks: skew quadrupole at $z = 0.18$ m and normal quadrupole at $z = 0.36$ m. So these two quadrupoles were used for changing the beam relative positions from simulation and try to fit to the experimental results, by which the quadrupoles strength can be estimated. The results are shown in Table 2 for two solenoid currents. It is shown with normal and skew quadrupoles the simulated beam relative positions are changed much closer to the experiment results, especially for laser position 30 fitting very well. The quadrupole strength was estimated to be: $g_{\text{skew}} = -0.01$ T/m, $g_{\text{normal}} = 0.04$ T/m for $I_{\text{main}} = -356$ A and $g_{\text{skew}} = -0.01$ T/m, $g_{\text{normal}} = 0.09$ T/m for $I_{\text{main}} = -381$ A, the quadrupole effective length is assumed to be 1 cm in simulation. In Table 2, the italic numbers are the fitting positions between experiment and simulation results with the rotated quadrupoles mentioned above, other non-italic numbers still have big discrepancy from simulation and experiment. Due to the source of the quadrupole error field are expected from gun coupler and solenoid field imperfections, there are anomalous quadrupoles and the field distribution is irregular. But in simulation we use regular quadrupole fields. Therefore in simulation we cannot fit all four positions to experiment at the same time with one group of normal and skew quadrupoles. By fitting position 30 and several other positions, the estimated quadrupole strength is still reasonable.

Content from this work may be used under the terms of the CC BY 3.0 licence (© 2018). Any distribution of this work must maintain attribution to the author(s), title of the work, publisher, and DOI.

Table 2: Experimental and simulated (with quadrupoles) beam relative positions in solenoid induced coordinate system.

P	-356A		-381A	
	Simulation (x,y)(mm)	Experiment (x,y)(mm)	Simulation (x,y)(mm)	Experiment (x,y)(mm)
10	(-0.11, -1.18)	(0.12, -0.73)	(-0.20, -2.21)	(-0.17, -1.49)
20	(-1.08, -0.11)	(-0.93, 0.35)	(-1.97, -0.20)	(-1.97, 0.57)
30	(0.11, 1.18)	(0.10, 1.12)	(0.20, 2.21)	(0.21, 2.44)
40	(1.08, 0.11)	(1.02, -0.13)	(1.97, 0.20)	(1.91, 0.26)

CONCLUSION

The beam tilt and wing structure observed from experiments can be reproduced by ASTRA simulations including a rotated quadrupoles model for different gun power and solenoid current and the wings directions can be fit rather good. These simulations were done with parameters completely the same as the experimental machine running settings. Two positions of the quadrupole-like error fields were found, one is at $z = 0.18$ m, which is most probably from the RF coupler field asymmetry and its polarity does not depend on the solenoid polarity, another one is at $z = 0.36$ m, which is most probably from the solenoid field imperfection and its polarity changes when changing the solenoid polarity. From moving the laser spot at the photocathode experiment, the method for estimating the rotated quadrupoles strength is validated and confirmed by simulation.

Combining experimental and simulated results, the skew and normal quadrupoles strengths can be estimated to be on the orders of 10^{-4} T and it is also found that these quadrupole error fields are not regular and have anomalous distribution. These results are helpful for the further beam asymmetries compensation and optimization studies [10].

REFERENCES

- [1] K. Floettmann, ASTRA particle tracking code, <http://www.desy.de/~mpyflo/>.
- [2] M. Krasilnikov *et al.*, „Experimentally minimized beam emittance from an L-band photoinjector”, *PRST-AB* 15, 100701, 2012.
- [3] M. Krasilnikov, Q. Zhao, *et al.*, “Investigations on electron beam imperfections at PITZ”, *Proc. of LINAC’16*, East Lansing, MI, USA, 2016.
- [4] I. Isaev, “RF field asymmetry simulations for the PITZ RF Photo Gun”, DPG-Frühjahrstagung Wuppertal, 9 March 2015.
- [5] Y. Chen *et al.*, “Coaxial Coupler RF Kick in the PITZ RF Gun”, presented at FEL’17, this conference.
- [6] M. Dohlus *et al.*, “Coupler kick for very short bunches and its compensation”, *Proc. of EPAC’08*, pp. 580-582, Genoa, Italy.
- [7] D. Dowell, “Analysis and cancellation of RF coupler-induced emittance due to astigmatism”. Report no. LCLS-2 TN-15-05, SLAC, 2015.
- [8] J. Schmerge, “LCLS gun solenoid design considerations”, Report no. SLAC-TN-10-084, SLAC, 2010.
- [9] H. Wiedemann, Particle Accelerator Physics, Third Edition, pp 605-620.
- [10] M. Krasilnikov, *et al.*, “Electron beam asymmetry compensation with gun quadrupoles at PITZ”, presented at FEL’17, this conference.

A 2.45 GHz PHOTOINJECTOR GUN FOR AN FEL DRIVEN BY LASER WAKEFIELD ACCELERATED BEAM*

S. V. Kuzikov[†], S. A. Bogdanov, E. I. Gacheva, E. V. Ilyakov, D. S. Makarov,
S. Yu. Mironov, A. K. Potemkin, A. P. Shkaev, A. A. Vikharev,
Institute of Applied Physics, Russian Academy of Sciences, Nizhny Novgorod, Russia

Abstract

The photoinjector of short electron bunches is a key element of investigations aimed on particle acceleration by pulses of the subpetawatt laser PEARL (10 J, 50-70 fs)[1]. Projected parameters of the photoinjector are the following: an electron energy of 5 MeV, charge >0.1 nC, bunch length of about 3 mm, transverse emittance no worse than $1\text{ mm}\times\text{mrad}$, and an energy spread no more than $\sim 0.1\%$. The photoinjector is based on a 2.45-GHz klystron (model KIU-111 built by Toriy), with output power ~ 5 MW, pulse length ~ 7 μs , efficiency $\sim 44\%$, power gain ~ 50 dB. This klystron will feed a standard 1.5-cell gun resonator with removable photocathode. The gun will be driven by a third harmonic of a Ti:Sa laser with 100- μJ energy in a picosecond pulse. The photocathode will be made of CVD diamond film which has high QE, long lifetime and is robust with respect to the vacuum conditions.

RF GUN DESIGN

The gun has classical design based on bunch acceleration in 1.5-cell cavity fed by a KIU-111 klystron, built by Toriy, operating at 2.45 GHz [2-3]. The klystron radiation is synchronized with laser system based on third harmonics of Ti:Sa laser.

Klystron

The klystron, shown in Fig. 1, generates output power up to 5 MW over a pulse duration of 7 μs . It provides 10-40% efficiency and 50 dB power gain at a frequency band of 10 MHz. Its repetition rate can reach 1 kHz. In our RF gun the repetition rate is planned to be as high as only 10 Hz. The klystron requires a 55-kV power supply supporting 250 A of current. In order to deliver the necessary 100-200 W of input RF power to klystron, we are going to use a so-called preamplifier which has been already produced.

Laser

We carried out experiments to generate 10-ps, 0.1- μJ laser pulses (at third harmonics of 1030 nm wavelength) with cylindrical and 3D ellipsoidal distributions of the intensity [4]. The system setup is shown in Fig. 2. Two methods were exploited. In both methods, the fact was

used that for pulses with essential linear frequency modulation the spectra distribution follows for intensity distribution in time, and that control for spectrum shape corresponds to the control of the intensity distribution. The first method is based on using of pulse compressor with zero frequency dispersion and a programmed mirror SLM (Spatial Light Modulator). This method allowed to generate quasi-ellipsoidal laser pulses with 90° axial symmetry. The second method is based on a use on SLM matrix and the profiled volume Bragg grating. The Bragg grating was written inside ellipsoidal volume and is absent outside it at all. By means of SLM laser pulses were formed with cylindrical intensity distribution in a space and were guided to the Bragg grating. The reflected radiation also had the ellipsoidal intensity distribution in a space.

We have performed a project of an original system for synchronization of the klystron KIU-111 with the laser.



Figure 1: The klystron KIU-111.

*This work was supported by the Russian Scientific Foundation (grant #16-19-10448).

[†]sergeykuzikov@gmail.com



Figure 2: Laser system.

1.5-Cell Cavity

The accelerating cavity has axisymmetric coaxial coupler which excites the TM_{01} (π -type) mode at 2.450 GHz, shown in Fig. 3. The Q-factor in copper cavity at room temperature is more than 1.4×10^4 . The klystron, producing 5 MW of RF power, allows obtaining maximum cathode field of approximately 70 MV/m. Field distribution of the operating mode is shown in Fig. 4. This mode is separated of the so-called 0-mode by 150 MHz. The coupling factor of the operating mode is close to 1.

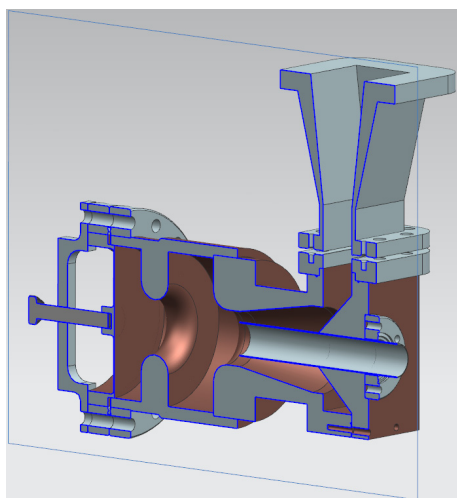


Figure 3: 1.5-cell RF cavity.

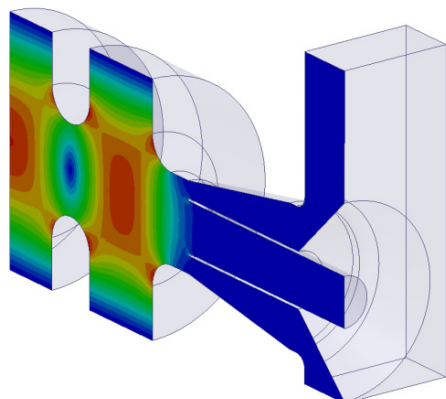


Figure 4: Field distribution in the cavity.

In Fig. 5, the reflection by the cavity is plotted. One can see that at resonant frequency (2.45 GHz) the reflection is less than -20 dB.

Transmission Line

Transmission line from the klystron to RF resonator is based on 90×45 mm² rectangular cross-section waveguide. It includes ferrite isolator, in order to isolate the klystron from reflection, directional couplers, and an additional window made of quartz.

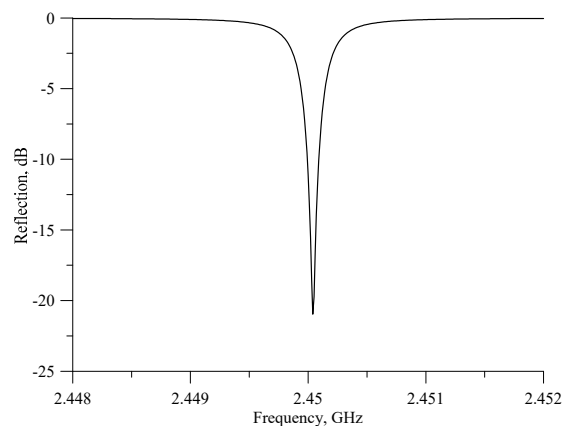


Figure 5: Reflection by the cavity.

Diamond Photocathode

Diamond photocathodes are able to provide high quantum efficiency ($\sim 10^{-3}$) as well as a low sensitivity to contaminations and vacuum quality [5]. We carried out a precipitation of the nano-crystal diamond films on a surface of the molybdenum cathodes of different shapes (cylindrical and plane) by means of precipitation from gas phase (CVD). For the precipitation, the modernized plasma-chemical reactors on a base of CW gyrotron at frequency 30 GHz with power up to 12 kW and a reactor based on 2.45 GHz magnetron of 3 kW power were used. It was found out that morphology and film structure crucially depend on a particular precipitation regime that can be influential on emission cathode properties.

BEAM SIMULATIONS

Bunch dynamics was simulated using particle in cell method. Typically, total number of particles exceeded 500. A motion of each particle in given RF fields was calculated by means of relativistic equations with Coulomb fields of particles itself taken into account.

Results of calculations are illustrated by Figs. 6-8. In Fig. 6, one can see energy of the particles in dependence on distance from cathode. Because power of the klystron is limited by 5 MW, particle's energy gain does not exceed 4 MeV. The length of the first cell was chosen so that bunch arrives to the first iris at near to zero electric field. In these simulations, we assumed Gaussian laser wavebeam shape along all coordinates.

Content from this work may be used under the terms of the CC BY 3.0 licence (© 2018). Any distribution of this work must maintain attribution to the author(s), title of the work, publisher, and DOI.

We carried out calculations of the main solenoid as well as backing coil, which compensates the field at cathode, both operating in CW regime with DC water cooling. Magnetic field amplitude and distribution of the magnetic field of the solenoid along longitudinal coordinate were optimized in order to get minimum of transverse beam emittance. The result of the mentioned optimization is that we can reach 1.4 mm×mrad transverse emittance in accordance with the plot shown in Fig. 7, where the emittance is plotted in dependence on time elapsed since bunch injection. In Fig. 6, time $t = 0.5$ ns corresponds to time when the bunch has already left the second cell.

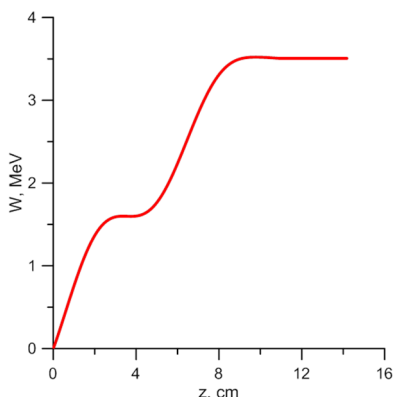


Figure 6: Energy of particles vs. distance from cathode.

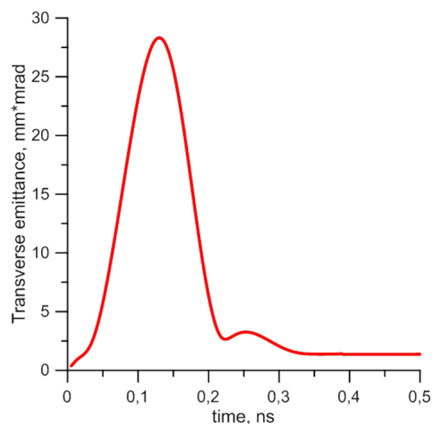


Figure 7: Transverse emittance vs. time.

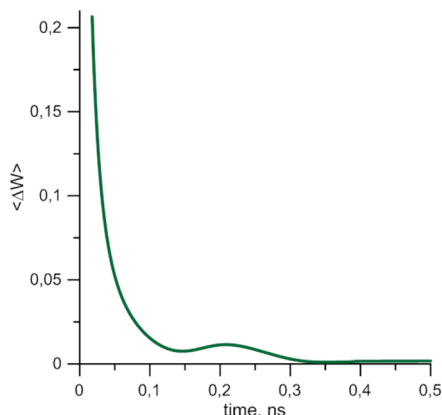


Figure 8: Normalized energy spread of particles vs. time.

For experiments on laser acceleration of electrons in a bubble it is important to produce bunches with small energy spread. For our RF gun project, we optimized an injection phase in order to obtain the energy spread as small as ~0.1%. Figure 8 shows the normalized energy spread in dependence on time elapsed since bunch injection.

Key parameters of RF photoinjector (to be finally produced in 2018) are summarized in the Table 1.

Table 1: Specification of Key Parameters

Parameters	Value
Frequency	2.45 GHz
Cavity length	11.74 cm
Laser pulse duration	10 ps
Magnetic field	1.07 T
Bunch charge	100 pC
Laser spot radius at cathode	1 mm
Cathode field	70 MV/m
Injection phase	-40°
Average energy	3.5 MeV
Transverse emittance	1.4 mm×mrad
Energy spread	0.2%

CONCLUSION

Preliminary calculations show that necessary parameters of RF gun for laser wakefield acceleration experiment are achievable. Commissioning is scheduled in the fall of 2018.

REFERENCES

- [1] <http://www.xcels.iapras.ru/img/site-xcels.pdf>
- [2] J.G. Power, "Overview of photoinjectors", in *Proc. of 14th Advanced Accelerator Concept Workshop*, edited by S.Gold and G.S.Nusinovich, Annapolis, USA, 2010.
- [3] D.H. Dowell *et al.*, "The development of the linac coherent light source RF gun", *ICFA Beam Dynamics Newsletter*, no. 46, Aug. 2008.
- [4] S.Yu. Mironov *et al.*, "Generation of 3D ellipsoidal laser beams by means of a profiled volume chirped Bragg grating", *Laser Physics Letters*, vol. 13, no. 5, 2016.
- [5] K.J.P. Quintero *et al.*, "High quantum efficiency ultrananocrystalline diamond photocathode for photoinjector applications", *Appl. Phys. Lett.*, vol. 105, p. 123103, 2014. <http://dx.doi.org/10.1063/1.4896418>.

PULSE DURATION MEASUREMENT OF PICO-SECOND DUV PHOTO-CATHODE DRIVING LASER BY AUTOCORRELATION TECHNIQUE USING TWO-PHOTON ABSORPTION IN BULK MATERIAL*

H. Zen[†], T. Nakajima, T. Kii, K. Masuda, and H. Ohgaki, Institute of Advanced Energy, Kyoto University, Uji, Japan

Abstract

Photocathode RF guns have been used for generating high brightness electron beams. Measurement of the pulse duration of photocathode driving laser in deep-ultraviolet (DUV) wavelength is quite important to estimate the electron beam properties generated from the RF gun. The autocorrelation technique has been commonly used for pulse duration measurement of laser pulses. Two-photon absorption has been utilized as the nonlinear process in the autocorrelation measurement of ultrashort pulse laser beams in DUV region. In this study, DUV autocorrelator utilizing the two-photon absorption in a sapphire plate as the nonlinear process was developed. The developed autocorrelator was used to measure the pulse duration of ps-DUV laser pulses which has been used for driving photocathode RF guns in the free electron laser facility at Institute of Advanced Energy, Kyoto University. As the result, the pulse duration of deep-UV laser pulse was measured as 5.8 ± 0.2 ps-FWHM.

INTRODUCTION

Recently, photocathode RF guns are widely used for generation of high brightness electron beams. At the Institute of Advanced Energy, Kyoto University, a 4.5-cell RF gun with a LaB₆ thermionic cathode used for driving mid-infrared free electron laser (MIR-FEL) has been operated with laser induced photoelectron emission [1]. And the MIR-FEL performance, especially for the peak power, has been significantly increased with the photocathode operation. In parallel, a compact THz coherent undulator radiation source using a 1.6-cell photocathode RF gun has been developed [2]. For driving those RF guns, a multi-bunch picosecond-deep-ultraviolet (ps-DUV) photocathode driving laser system has been developed [3]. The pulse duration of DUV photocathode driving laser is so important parameter, which determines the initial electron pulse duration at the cathode. Therefore, measurement of its pulse duration is so important to estimate the available electron beam parameter. In many electron accelerator facilities, streak cameras have been used for measuring the pulse structure of DUV laser pulses. However, the streak camera is so expensive and not easy to use. As an alternative method, some facilities using photocathode RF guns have been developed cross correlator which uses femto-second near infrared (fs-NIR) laser as a probe to measure the cross correlation between the ps-DUV laser and the fs-NIR laser using difference frequency generation [4, 5].

* Work supported by Collaboration Program of the Laboratory for Complex Energy Processes, Institute of Advanced Energy, Kyoto University
[†] e-mail address zen@iae.kyoto-u.ac.jp

The cross correlation method is only available in the facilities where the fs-NIR lasers are available.

In the ultrafast laser community, an autocorrelation technique utilizing a two-photon absorption (TPA) in a bulk material has been developed for measuring the pulse duration of ultrashort UV and DUV pulses [6, 7]. In this study, an autocorrelator using TPA in a sapphire crystal was developed and used for measuring the pulse duration of photocathode driving laser at the Institute of Advanced Energy, Kyoto University. The measurement principle, the developed autocorrelator, and measured results are reported in this paper.

MEASUREMENT PRINCIPLE

In general, intensity autocorrelation technique is used for measuring the pulse duration of short pulse lasers. The basic setup of the intensity autocorrelator is shown in Fig. 1. At first, the laser beam is divided into two pulses by a beam splitter. Those two beams are focused by a focusing optics on a nonlinear material. The arrival time difference of the two pulses is controlled by an optical delay inserted in one side of the optical beam path. The nonlinear signal generated at the nonlinear crystal as the function of the arrival time difference is recorded to obtain the information of overlap of those two pulses. Finally, by analyzing the recorded result, the pulse duration of injected laser beam is determined. In the visible and infrared region, second harmonic generation crystals are normally used as the nonlinear crystal and then the intensity of second harmonic light is measured by photodetectors.

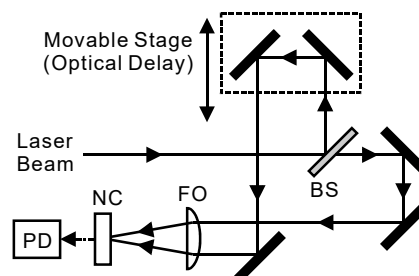


Figure 1: Schematic diagram of basic setup of the intensity autocorrelator used for laser pulse duration measurements. BS: Beam Splitter, FO: Focusing Optics, NC: Nonlinear Crystal, PD: Photodetector.

The laser pulses with the wavelength shorter than 300 nm were mainly used for photoelectron generation in photocathode RF guns. In our case, the laser wavelength is 266 nm and its second harmonic wavelength is 133 nm. The second harmonic wavelength (133 nm) is in the vac-

Content from this work may be used under the terms of the CC BY 3.0 licence (© 2018). Any distribution of this work must maintain attribution to the author(s), title of the work, publisher, and DOI.

uum UV region and absorption by the atmosphere is high. Therefore, it is not a good idea to use the second harmonic generation as the nonlinear phenomena for the laser beam with the wavelength of 266 nm. Therefore, TPA has been utilized as the nonlinear phenomena to measure the pulse duration of UV and DUV pulses [6, 7]. In this method, the laser beam is divided into an intense (pump) beam and a weak (probe) beam. The variation of transmittance of probe beam as the function of arrival time difference of those two pulses is recorded. In the case of TPA, the phase matching condition, which is normally required for second harmonic generation and sometimes limits the shortest pulse duration can be measured, does not need to be achieved or considered. The autocorrelation using TPA simply requires spatial overlap of pump and probe beams. Theoretical study of the TPA intensity and the measurable shortest pulse duration for various bulk materials has already been done so far [7]. Based on the theoretical study, we selected a sapphire crystal because of its high TPA intensity at DUV region and good availability.

EXPERIMENTAL SETUP

The schematic diagram of TPA autocorrelator developed for this study is shown in Fig. 2. A small fraction (around 10%) of the DUV laser beam injected to this device was reflected by a beam sampler (BS: BSF10-UV, Thorlabs) and injected to a reference detector (Ref. PD: DET25K/M, Thorlabs) to monitor the intensity of incident laser beam. The transmitted beam through the beam sampler was then injected to another beam sampler and divided into the intense transmitted (pump) and weak reflected (probe) beams. Those two beams were reflected by two mirrors and focused on a sapphire plate (SP) by a focusing lens (FL). The probe beam after passing through the sapphire plate was injected to a signal detector (Sig. PD: DET25K/M, Thorlabs). Focusing lenses were arranged in front of the two detectors to reduce the influence of the pointing instability. The laser intensity both on

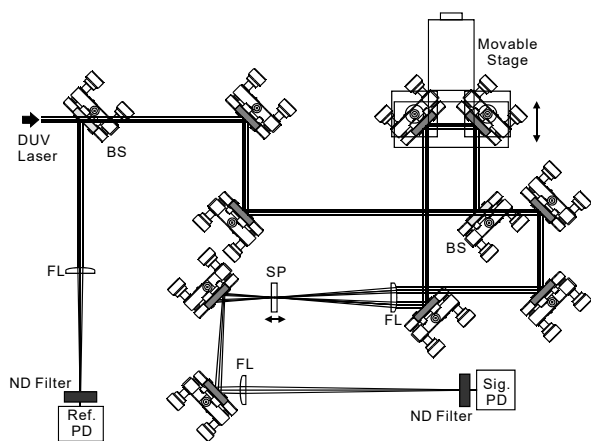


Figure 2: Schematic diagram of UV autocorrelator utilizing the two-photon absorption in a sapphire plate as the nonlinear process. BS: Beam Sampler, FL: Focusing Lens, SP: Sapphire Plate, ND: Neutral Density Filter, PD: Photodiode.

the reference and signal detectors are attenuated by ND filters to avoid saturation of those detectors. The laser intensity measured by the signal detector was divided by that measured by the reference detector to cancel out the variation of the intensity of the incident laser beam. The arrival time difference of the pump and probe pulses was varied by changing the condition of the optical delay line which was inserted in the optical path of the probe beam. The sapphire plate was placed on a linear translation stage for changing the focusing condition and the fluence of the laser beam on the sapphire plate.

RESULTS

In this study, the pulse duration of photocathode drive ps-DUV laser developed at the Institute of Advanced Energy, Kyoto University [3] was measured. The laser was developed for multi-bunch electron beam generation for oscillator FEL. The laser system was operated at the single pulse condition with the repetition rate of 2 Hz.

Before autocorrelation measurements, direct TPA of pump beam as the function of the longitudinal position of the sapphire plate was measured. The measured results for a 2-mm thick sapphire plate with the laser pulse energy of 2.5 and 18 μ J are shown in Figure 3.

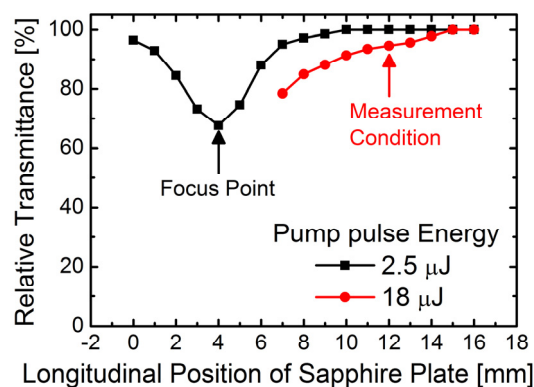


Figure 3: Variation of pump laser transmittance as the function of the longitudinal position of a sapphire plate (2 mm thick) with two different pulse energy conditions.

As one can obviously see in the figure, the relative transmittance of the pump beam strongly depended on the longitudinal position of the sapphire plate, i.e. fluence of the laser beam on the sapphire plate. The observed maximum transmittance change in the case of 2.5- μ J condition was 32% at the focus point of the DUV laser. In the case of 18- μ J condition, the ablation of the sapphire plate was observed at the focus point. The longitudinal position of the sapphire plate and the pulse energy of the pump beam in the autocorrelation measurement were adjusted to 12 mm and 18 μ J, respectively. In this condition, the sapphire plate is placed on the off focus condition to have larger laser beam size and to ease the difficulties of spatial overlap of pump and probe pulses.

For autocorrelation measurements, the probe beam position was adjusted to have the largest TPA of the probe

beam at the zero delay condition of the pump and probe pulses. After the good overlap of the pump and probe pulses were achieved, TPA autocorrelation measurements were performed. The typical result for a 2-mm thick sapphire plate is shown in Fig. 4. The least square fitting of measured autocorrelation trace with the Gaussian function was performed and then the width of autocorrelation trace was determined as 9.9 ps-FWHM. The laser pulse duration was evaluated as 7.0 ps-FWHM with the assumption of the Gaussian laser pulse shape, i.e. the conversion factor of $1/\sqrt{2}$. Same measurements were performed for sapphire plates with the thickness of 1 and 0.5 mm. For each condition, measurements were performed 5 times to check the reproducibility. The measured pulse durations were summarized in Fig. 6 and Table 1. The data points represent the averaged value of 5-times measurement and the error bars represent the standard deviation of 5-times measurement.

The shortest measured result (5.8 ± 0.2 ps-FWHM) was obtained when the 1-mm thick sapphire plate was used. In the case of 0.5-mm sapphire plate, the measured pulse duration was longer than that with the 1-mm plate. And the reproducibility was poor. It was because of low signal to noise ratio and weak TPA in the sapphire plate. The result with the 2-mm thick sapphire plate was 1 ps longer than the 1-mm thick one. The previous theoretical study [6] reported that the measurable shortest pulse duration with a 200- μ m sapphire plate at the wavelength of 266 nm was around 15 fs. Then the measurable shortest pulse duration for a 2-mm thick sapphire plate expected to be 150 fs. Our result was not consistent with the theoretical expectation. In the theoretical work, only a pulse elongation effect due to the dispersion inside in the sapphire was taken into account. For thicker sample and/or longer pulse duration, additional side effects may limit the performance of the TPA autocorrelator.

The obtained pulse duration (5.8 ± 0.2 ps-FWHM) was slightly shorter than the designed pulse duration (7.5-ps FWHM) of Nd:YVO₄ mode-locked oscillator which used in the laser system [3]. The pulse duration could be shortened by wavelength conversion from NIR to DUV using second and fourth harmonic generation crystals.

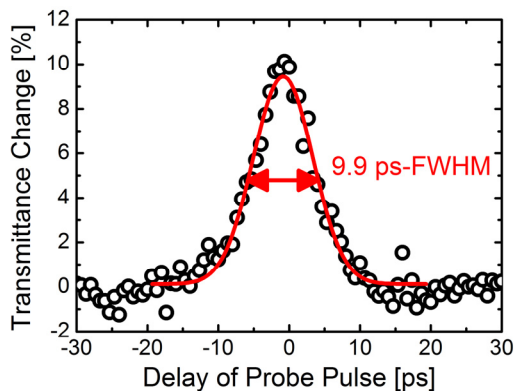


Figure 4: Typical measured results of autocorrelation measurement of DUV ps-laser at the Institute of Advanced Energy, Kyoto University.

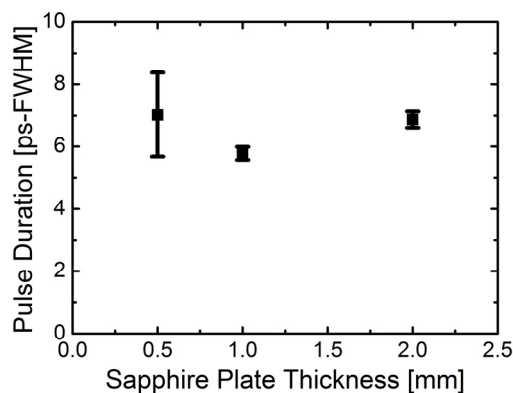


Figure 5: Measured pulse duration of ps-DUV laser with different thickness of the sapphire plates.

Table 1: Measured pulse duration of ps-DUV laser with different thickness of the sapphire plate

Thickness of Sapphire Plate	Measured Pulse Duration
0.5 mm	7.0 ± 1.3 ps
1.0 mm	5.8 ± 0.2 ps
2.0 mm	6.8 ± 0.3 ps

SUMMARY

In order to measure the pulse duration of DUV laser pulse used for driving photocathode RF guns at the Institute of Advanced Energy, Kyoto University, an autocorrelator utilizing the two-photon absorption has been developed. The DUV laser pulse duration was measured as 5.8 ± 0.2 ps-FWHM by using the sapphire plate with the thickness of 1 mm as the two-photon absorbing material at the wavelength of 266 nm. The measured pulse duration was slightly shorter than the specification of mode-locked Nd:YVO₄ oscillator (7.5 ps-FWHM). The wavelength conversion from NIR to DUV using second harmonic and fourth harmonic generation crystals may cause the pulse shortening.

REFERENCES

- [1] H. Zen *et al.*, *Proc. of IPAC2016*, pp.754-756 (2016).
- [2] S. Sikharin *et al.*, *Proc. of IPAC2016*, pp.1757-1759 (2016).
- [3] H. Zen *et al.*, *Proc. of FEL2014*, pp.828-831 (2015).
- [4] L. Yan *et al.*, *Proc. of PAC'07*, pp. 1052-1054, (2007).
- [5] C. Kim, *et al.*, *Journal of Korean Physical Society*, 50, pp.1427-1430 (2007).
- [6] J. I. Dadap, *et al.*, *Optics Letters*, 16, pp.499-501 (1991).
- [7] C. Homann, *et al.*, *Applied Physics B*, 104, 783 (2011).

CURRENT EXPERIMENTAL WORK WITH DIAMOND FIELD-EMITTER ARRAY CATHODES

H. L. Andrews[†], B. K. Choi, R. L. Fleming, J. L. Lewellen, K. Nichols, D. Yu. Shchegolkov,
E. I. Simakov, Los Alamos National Laboratory, Los Alamos, USA

Abstract

Diamond Field-Emitter Array (DFEA) cathodes are arrays of micron-scale diamond pyramids with nanometer-scale tips, thereby providing high emission currents with small emittance and energy spread. To date they have been demonstrated in a “close-diode” configuration, spaced only a few hundred microns from a solid anode, and have shown very promising results in terms of emittance, energy spread, and per-tip emission currents. We present recent results investigating DFEA performance in a large-gap configuration, such that the cathodes are a few millimeters from a solid anode, and show that performance is the same or better as the close-diode geometry previously studied. However, array performance is still limited by anode damage. We are redesigning our cathode test stand to overcome the inherent limitations of a solid anode, allow for transport of the emitted beam, and further explore real-world DFEA performance.

INTRODUCTION

Diamond Field-Emission Array (DFEA) cathodes are arrays of exquisitely sharp diamond pyramids [1]. They are a promising cathode option for a wide range of applications. DFEAs are particularly relevant to FELs because they can produce high-current, low emittance beams. LANL is currently investigating using DFEAs as the cathode for a dielectric laser accelerator (DLA), which can achieve acceleration gradients of GV/m in a structure where the transverse and longitudinal dimensions of the accelerating field are on the order of the laser wavelength [2]. The promise of DLAs is that they can be orders of magnitude more compact than conventional linacs driven by RF sources. We are currently working to characterize DFEA emission in order to understand how to gate, focus, and collimate beams from a single or few tips. The experimental work presented here is supported by a theoretical modelling effort [3].

DFEAs emit in high or low vacuum, can be transported in air, and have good thermal conductivity that allows for very high per tip current emission without failure. We fabricate DFEAs using standard silicon wafer fabrication processes, so that they can be fabricated in any array configuration. Individual pyramid base sizes range from 25 micrometers to 2 micrometers.

DFEAs were first fabricated at Vanderbilt University, but are now used at several institutions. Originally (see Fig. 1), the diamond was highly conductive and yielded

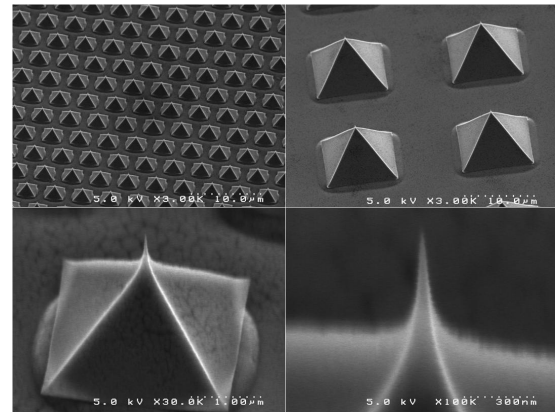


Figure 1: DFEA pyramids at four magnifications, showing the exquisitely sharp tip. (Vanderbilt University).

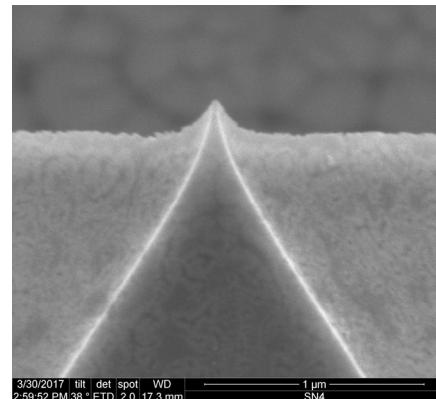


Figure 2: An SEM image of a recent DFEA tip. It has a diameter of around 50 nm.

exquisitely sharp tips, however more recent DFEAs consist of less conductive diamond and exhibit the blunter tips shown in Figure 2. The overall emission properties of the two types of diamond appear similar. We hope to investigate these differences more in the future.

EXPERIMENTAL SETUP

Our cathode characterization experiments are conducted in a vacuum test stand that is equipped with several diagnostics and shown in Figure 3. The test chamber has an ion gauge mounted adjacent to the cathode and anode. The chamber is also equipped with an RGA to analyse constituent gasses. The high-voltage is supplied by a negative 60-kV supply connected to the cathode mount. Experiments are typically conducted at 40 kV, allowing us

* Work supported by the LDRD program at LANL. LA-UR-17-27451.

[†] hlac@lanl.gov

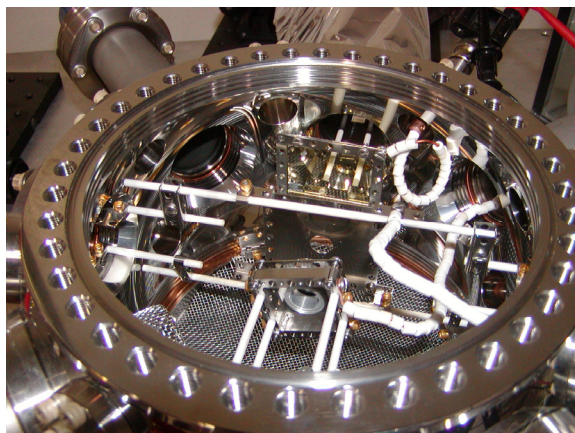


Figure 3: Image from the top of the small experiment chamber. The cathode holder, mesh anode, and phosphor are in line from close to far in this image.

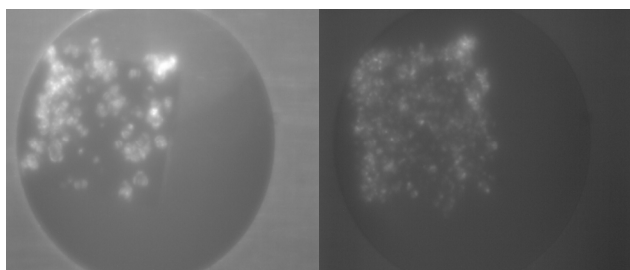


Figure 4: Emission imaged on an AZO screen from a dense array (5 mm x 5 mm, 20- μ m base, 30- μ m pitch) after about 30 minutes of conditioning (left) and after about 2 hours of conditioning at about 11-MV/m field and 250- μ A total current (right).

to operate the DFEAs with an anode-cathode spacing of a few millimeters. The cathode is mounted on a fine linear actuator. This actuator is used to precisely adjust the field applied to the cathode. The anode-cathode gap can be adjusted from zero to 25 mm. We use either a AZO (ZnO:Al₂O₃) coated sapphire or diamond substrate or a stainless-steel plate with a mesh welded across a 0.4-inch hole as the anode.

With a mesh anode we either image the beam on the AZO coated substrate (screen), or dump the beam onto a flat stainless-steel plate that acts as a Faraday cup. Both the anode and screen or Faraday cup are connected to ground through current-viewing resistors. Typically, we operate the experiment as follows: with a large anode-cathode gap we turn up the voltage to 40 kV, then slowly bring the cathode closer to the anode. After taking measurements of emission current and pictures of the spot if using a screen at various gap distances, we bring the cathode away from the anode, continuing to record data.

We are in the process of commissioning a new experiment chamber that will include all the measurement features of the small chamber. The main feature of the new chamber is that it is large enough to contain electron focusing and collimating optics and diagnostics.



Figure 5: Image of the dense array above in the AZO coating. We suspect in this case the insulating diamond substrate charged and damaged the coating during discharge.

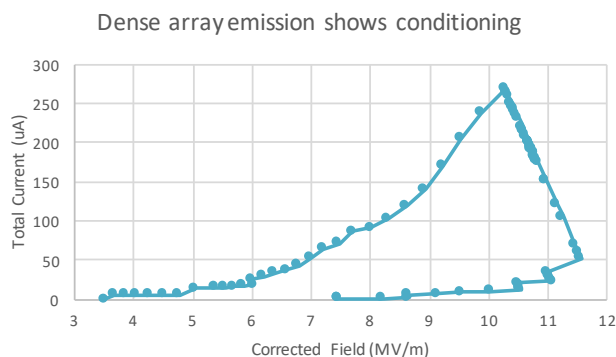


Figure 6: Emission from the dense array shown above.

EMISSION FROM A DENSE ARRAY

Even operating at a relatively large anode-cathode gap of about 4 mm, we still damage the AZO screen. Any anode damage inevitably leads to cathode damage through ion back-bombardment. Recently we were able to operate a dense cathode, observing very nice conditioning data, and also extensive AZO screen anode damage from the process.

Figure 4 shows the image of a dense array (5 mm x 5 mm square, 20- μ m base, 30- μ m pitch) both initially (left), and after about 2 hours of conditioning at 11 MV/m and 250- μ A total current (right).

Figure 5 shows the image of the dense array burned into the AZO coating material. We suspect in this case that the insulating diamond substrate charged during operation and damaged the AZO on discharge. Potentially we could get around this by using a conductive diamond substrate, however we have observed burn marks in the AZO coating from moderate current beams so it is not clear that increased substrate conductivity would help much.

Figure 6 shows the emission from the dense array shown above. The corrected field is the voltage/gap minus the voltage drop across the 20 M Ω ballast resistor. In this run the array turned on around 7.5 MV/m, we turned the field up to about 11.5 MV/m, the array conditioned (increasing current at constant voltage), then we opened the

Content from this work may be used under the terms of the CC BY 3.0 licence (© 2018). Any distribution of this work must maintain attribution to the author(s), title of the work, publisher, and DOI.

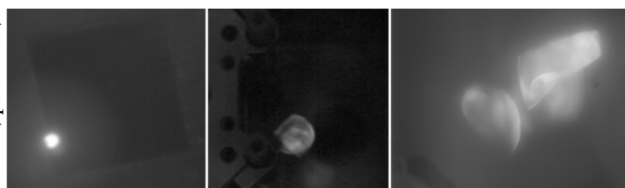


Figure 7: Emission shown on an AZO screen without (left) and with (middle, right) a mesh anode.

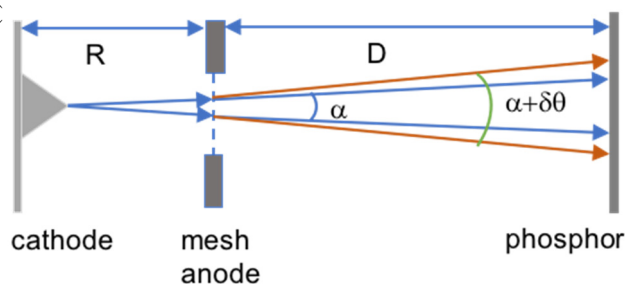


Figure 8: Diagram showing inherent beam divergence (blue) and the contribution of divergence from the mesh anode (orange).

gap slowly, dropping the field to 3.5 MV/m at which point the array turned off. The behavior of the turn-off field lowering after conditioning seems to be characteristic of the lower conductivity diamond arrays and we would like to explore this behavior further.

CHARACTERIZING THE EFFECT OF A MESH ANODE

The advantage of using an imaging screen to view the beam is that, for sparse arrays, we can see how many tips are emitting and measure their spot size in order to find the inherent divergence of the beams. The significant disadvantages are that we cannot do anything else with the beam, and that even at moderate per-tip currents we can burn the AZO coating. In order to address both these issues we are characterizing the effect that a mesh anode has on beam divergence.

Figure 7 shows images of an emission spot on an AZO screen under three conditions. In the left image, the screen is acting as the anode spaced about 4 mm from the cathode. In the middle image, the anode is a 50-line/inch mesh with a 0.49-mm square aperture welded across a 0.4-inch diameter hole in a stainless-steel plate, and the screen is placed about 19 mm back from the anode. In the right image, the set-up is the same as the middle image, but the camera magnification is increased to show the spot structure. It is possible that this structure is due to a few closely spaced emitting tips, or from a few emission sites on one tip. We need a proper single-tip cathode in order to fully understand what has been observed.

Table 1: Summary of Estimated and Measured Beam Divergence and Resulting Spot Sizes.

Quantity	Estimated	Measured
A-K gap		4 mm
Beam divergence	7 degrees	
Mesh contribution	0.7 degrees	
Spot on screen anode		0.5 mm
Spot on screen at 19.7 mm from anode	3.3 mm	2.9 mm
Spot on screen at 29.8 mm from anode	4.6 mm	4.6 mm

The spot sizes we see on an AZO screen anode, at a distance of about 4 mm, are about 0.5 mm. This suggests a divergence angle of about 7 degrees. Theory suggests that the mesh contribution to electron beam divergence should be $\delta\theta \sim h/(8R)$ where h is the mesh aperture and R is the anode-cathode spacing [4]. For our mesh, we estimate that this quantity is about 0.7 degrees. Figure 8 shows a rough diagram of beam divergence (blue) and mesh contribution (orange).

We are now measuring the spot sizes at a range of D (anode-screen distance) in order to determine α and $\delta\theta$. Table 1 shows a rough first look at a comparison of estimated and measured spot sizes for two anode-screen distances. A significant difference between what we are attempting now and prior work is that previously the emittance was measured for an entire array [5]. Here we are interested in divergence of a single beamlet.

Although we have not attempted to estimate the error bars on this data yet because of many complicating factors including differing emission current levels and possibly multiple closely spaced emitting tips, it is encouraging that there is a rough agreement between our measurements and estimates.

SUMMARY AND PATH FORWARD

We continue working towards using a DFEA as the cathode for a DLA. One step in this project is to understand how to focus and guide the beam from a single or few tips. Working at a relatively large gap, we still observe AZO coating damage at moderate tip currents. We expect to have a new batch of cathodes, both sparse arrays and single tips, for testing in the next month. These cathodes will help us make reliable measurements of inherent beam divergence and mesh contribution to beam divergence. Reliable measurements also require that we take data at similar current levels for various anode-screen distances. Current can be hard to control day-to-day, but will hopefully be easier if we can condition the cathode using a mesh anode and metal Faraday cup in place of the AZO screen.

REFERENCES

- [1] J. D. Jarvis *et al.*, “Uniformity conditioning of diamond field emitter arrays,” *J. Vac. Sci. Technol. B*, vol. 27, p. 2264, 2009.
- [2] K. P. Wootton *et al.*, “Demonstration of acceleration of relativistic electrons at a dielectric microstructure using femtosecond laser pulses,” *Opt. Lett.*, vol. 41, pp. 2696–2699, 2016.
- [3] C.-K. Huang *et al.*, “Modeling of diamond field-emitter arrays for high-brightness photocathode applications,” presented at FEL’17, Santa Fe, USA, August 2017, paper WEP016.
- [4] J. Feng *et al.*, “A novel system for the measurement of the transverse electron momentum distribution from photocathodes,” *Rev. Sci. Instr.*, vol. 86, p. 015183, 2015.
- [5] J. D. Jarvis *et al.*, “Emittance measurements of electron beams from diamond field emitter arrays,” *J. Vac. Sci. Technol. B*, vol. 30, p. 042201, 2012.

MODELING OF DIAMOND FIELD-EMITTER ARRAYS FOR HIGH-BRIGHTNESS PHOTOCATHODE APPLICATIONS*

C.-K. Huang[†], H. L. Andrews, B. K. Choi, R. L. Fleming, T. J. T. Kwan, J. W. Lewellen, D. C. Nguyen, K. Nichols, V. Pavlenko, A. Piryatinski, D. Shchegolkov, E. I. Simakov, Los Alamos National Laboratory, Los Alamos, 87544, USA

Abstract

Dielectric Laser Accelerators (DLA) are capable of generating high output power for an X-ray free-electron laser (FEL), while having a size 1-2 orders of magnitude smaller than existing Radio-Frequency (RF) accelerators. A single Diamond Field-Emitter (DFE) or an array of such emitters (DFEA) can be employed as high-current ultra-low-emittance photocathodes for compact DLAs. We are developing a first principle semi-classical Monte-Carlo (MC) emission model for DFEAs that includes the effects of carriers' photoexcitation, their transport to the emitter surface, and the tunnelling through the surface. The electronic structure size quantization affecting the transport and tunnelling processes within the sharp diamond tips is also accounted for. These aspects of our model and their implementation and validation, as well as macroscopic electromagnetic beam simulation of DFE are discussed.

INTRODUCTION

DLAs can achieve acceleration gradients of GV/m in a structure that is orders of magnitude more compact than conventional metallic linacs driven by RF sources. To accelerate high current-density electron beams in DLAs, where the transverse and longitudinal dimensions of the accelerating field structure are on the order of the laser wavelength, new cathodes capable of producing small divergence, low emittance beams with dimensions matching the aperture of DLA need to be developed. DFEAs (Fig. 1), manufactured from the mold-transfer process and Microwave Plasma Chemical Vapor Deposition, are promising candidates for such a high-brightness cathode. These DFEAs consist of micron-scale diamond pyramids, together with nanometer-scale tips (Fig. 1) sharpened by an oxide layer in the mold process. DFEAs may produce tightly focused high-current bunched beams ideal for DLAs under suitable photo excitation. The effect and the required conditions of photoemission from a DFEA cathode are being studied at LANL [1].

DFEAs have already been demonstrated experimentally for the field emission [2]. Recently, DFEA field emission test is carried out at LANL with a variable anode-cathode (A-K) gap at a fixed voltage of 40 kV. The measured current is shown in Fig. 1 for the cases of most robust emission (A-K gap $d < 7.2$ mm, greater than ~60% emitters emit). Note the average current I per emitter may be fitted by $I \propto d^{-5.8}$, as compared to d^{-2} (d^m , $m \sim 1.1-1.2$) for the space-charge limited emission from a flat (sharp) metallic surf-

ace. This result indicates that the material and complex geometry/features of the DFE, as well as possible space-charge effect may play important roles in emission.

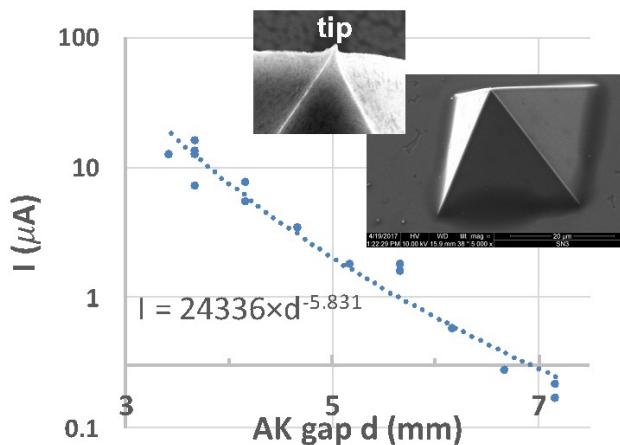


Figure 1: Averaged current (dots) per emitter as a function of A-K gap distance and their fit (dashed). The cathode has a 5×5 emitter array and each emitter has a 20 μ m×20 μ m base and is separated by 500 μ m. Insets show the pyramid base and the sharp tip of a DFE.

SIMULATION MODEL

Since diamond is a semiconductor material (with a band gap E_g approximately 5.5 eV), its field- and photo-emission properties will depend on the charge carrier excitation (mostly electrons in the absence of impact ionization process) and subsequent transport and tunnelling processes in the emitter. Furthermore, the dielectric property of the DFEA, the geometric field enhancement at the top of the emitter and its nm-scale tip can change the field distribution over the surface. Additionally, the electronic structure size quantization effect should modify the transport and emission at the tip. A simulation model, integrating (1) carrier transport within the diamond pyramid and the surface tunnelling, (2) the quantum-size effects in the tip, and (3) the space charge effects of the emitted electrons, is essential to understand DFEA electron emission, to predict conditions favouring efficient photoemission and for the production and transport of tightly focused electron beams to a DLA. We develop such a model by combining the semi-classical MC device simulations with the electromagnetic simulations. The model components along with some preliminary results are presented below.

* Work supported by the LDRD program at LANL.

[†] huangck@lanl.gov

Content from this work may be used under the terms of the CC BY 3.0 licence (© 2018). Any distribution of this work must maintain attribution to the author(s), title of the work, publisher, and DOI.

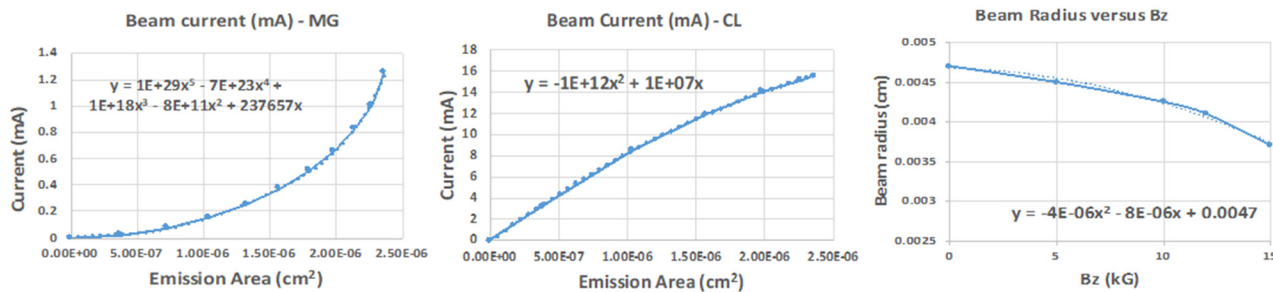


Figure 2: Simulation results using the Murphy-Good (MG, left) and Child-Langmuir (CL, middle) and their analytic fits. The right panel shows the magnetic field effect on the beam radius.

EM Simulation of Pyramid Field Emission

The fully electromagnetic relativistic code LSP was used to numerically model the electron emission process of the diamond pyramid, using the space-charge-limited and the Murphy-Good (MG) models. 2D simulations in the cylindrical (r,z) geometry, in which the pyramid is modelled as a cone, are used to study its emission scaling and the effect of external magnetic field on the beam size. The nm-scale tip is not modelled in the current EM simulation but will be added once our nanowire model (described below) is fully developed. The A-K gap between the base of the cone and the anode foil is set to 35 μm , and the voltage set to 0.4 kV, resulting in an electric field of 114 kV/cm at the cathode surface, similar to the experimental field strength with an A-K gap of ~ 3.4 mm. The simulation resolution is typically 0.5 μm and our convergence study shows it is adequate for these diode simulations. Our simulations show a significantly higher current for the space-charge-limited model in all cases. Furthermore, the current has a strong dependence on the allowed area of electron emission from the cathode surface. The simulation data and the fitted analytic forms are shown in Fig. 2. Comparison to experimental data (~ 12 $\mu\text{A}/\text{emitter}$) indicates that the electron emission may have occurred in a very small area ($\sim 3\%$) near the cone tip and is more consistent with the MG model (~ 1.3 mA/emitter). The effect of an external magnetic field on the electron beam trajectory are also investigated. The beam radius at 75 μm from the base of the cathode is shown in Fig. 2 with its analytic fit. The effect is only noticeable for magnetic field of 10 to 15 kG which can be challenging to implement. Design of a Pierce diode can possibly facilitate the extraction of the electron beam.

MC Model for Charge Transport/Emission

The semi-classical MC method has been widely used to model transport problems in semiconductors [3]. In the MC method, the equation of motion for charge carrier's trajectory \mathbf{r} and crystal momentum $\hbar\mathbf{k}$ accounts for the energy dispersion relation. Lattice, defect and carrier-carrier scattering mechanisms can be incorporated in the resulting Boltzmann equation. Associated mean free times $\tau(E)$ are

evaluated using the corresponding cross-sections. During $\tau(E)$, a carrier experiences free-flight until a random scattering event changes its momentum. At the emission surface, a carrier may tunnel through the surface potential barrier and be emitted as a free electron. The emission probability can be calculated via the Transfer-Matrix (TM) approach. This assumes a 1D electron tunnelling under a potential barrier with its profile approximated by a piece-wise function. The MC model together with the TM surface tunnelling model, have been used to study charge transport in a diamond amplifier for photocathodes. Here we adopt a similar approach for the electron transport/emission in a DEFA pyramid, while the tip will be modelled as a nanowire (NW). The photo excitation processes will be added subsequently.

Transport in the Pyramid

Our MC model employs the following simplifications: (1) In high purity diamond, the conduction band electron transport is predominantly controlled by lattice scattering. Hence, in our model, we ignore the defect and carrier-carrier scattering; (2) Both the intra-valley acoustic and inter-valley phonon scattering processes are included; (3) For intra-valley acoustic phonon scattering, a deformation potential $E_1=8.7$ eV is used; (4) Due to the symmetry selection rules, only the longitudinal optical (LO) phonons are allowed for inter-valley g-type (between parallel valleys) scattering. For f-type (between perpendicular valleys) scatterings, the longitudinal acoustic (LA) and transverse optical (TO) phonons are involved; (5) The g-type and f-type inter-valley scatterings are calculated for transitions between points of the energy minima with the following phonon spectrum: 0.16 eV (1900 K, LO, g3 mode); 0.13 eV (1560 K, LA, f1 mode); 0.15 eV (1720 K, TO, f2 mode).

With the above simplifications to the MC model, the electron drift velocity in the bulk diamond and its temperature dependence due to externally applied electric field is calculated and compared to available simulation result from VORPAL (Fig. 3) [4]. These results are also in good agreement with experimental measurement.

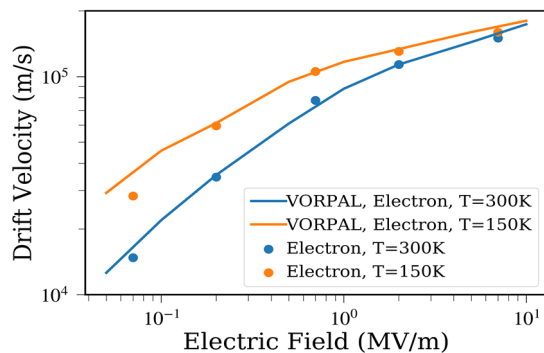


Figure 3: Electron drift velocity in an external electric field for two temperatures, $T=150, 300$ K. Dots are our MC results and solid lines are from VORPAL.

By combining the LSP electromagnetic simulation and the MC model, we also conduct simulation test of the electron transport in the pyramid. Figure 4 shows the longitudinal (E_z) and transverse (E_r) electric fields near the pyramid (cone) in the (r, z) LSP simulation. At $t = 0$, a thermal (in z direction) population of electrons at $T = 300$ K is initialized at the base of the pyramid (denoted by the green box in the E_z plot). The electrons' energy and longitudinal spatial distributions are shown in Fig. 4 for $t = 10$ ps and 30 ps. In Fig. 4, it can be clearly seen that electrons drift and diffuse as they are attracted to the top of the pyramid due to the electric field inside that is mostly longitudinal. They would gain energy in the electric field due to the drift motion, however, there is no substantial energy gain for the bulk energy distribution but a higher energy thermal tail is developed due to the scatterings.

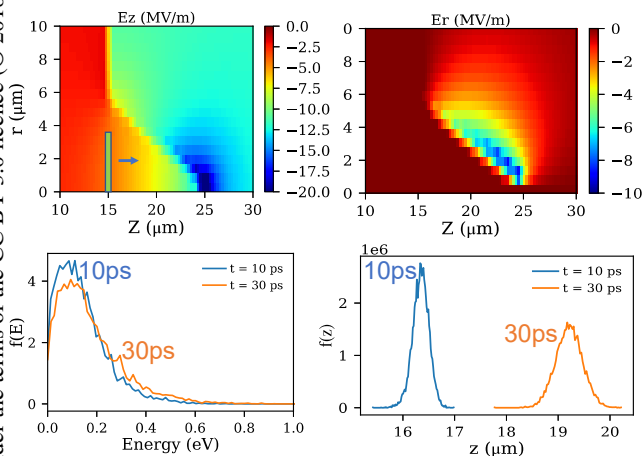


Figure 4: (Top) Electric fields inside and near a dielectric DFE pyramid with an average A-K electric field of 114 kV/cm. These fields are used to transport thermal electrons initially located at the green box. (Bottom) Electrons' energy and longitudinal spatial distributions.

Surface Emission Probability

The emission probability is evaluated by solving a 1D tunnelling problem with a spatially varying electron mass. The TM method, which treats each segment in a piece-wise surface potential profile as a constant barrier, is used to simplify the calculation. Spatial variation and anisotropy of the electron mass is considered at the crystal-vacuum interface only. Under 1D approximation, transverse momentum conservation essentially suppresses the electron emission from perpendicular valleys and also impacts the transmission from parallel valleys as shown in Fig. 5.

Tip Transport Model

To model transport via the tip of a pyramid, we approximate tip geometry by a sequence of NW segments of gradually decreasing radii (Fig. 6). Each segment is assumed to have length exceeding electron mean-free path so that Boltzmann equation can be used. Size-quantization results in a set of coupled 1-D Boltzmann equations for each energy sub-band. The coupling occurs due to the electron-phonon scattering processes. Each junction between two NW segments is accounted for via boundary condition for the Boltzmann equation.

Our scattering theory calculations show that the mismatch in the radii of NW segments at each junction corresponds to the redistribution of the sub-band population via electron forward (through the junction) scattering and back scattering, as illustrated in Fig. 6. The tunnelling outside the NW segment occurs along the tip axis at each NW junction through the interfaces with vacuum. It is to be accounted for via the TM formalism combined with our scattering theory.

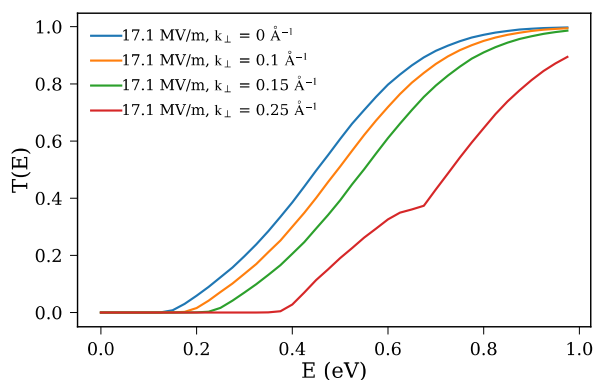


Figure 5: Energy and transverse momentum dependent transmission probability in a Fisher-type potential barrier with an external field.

Content from this work may be used under the terms of the CC BY 3.0 licence (© 2018). Any distribution of this work must maintain attribution to the author(s), title of the work, publisher, and DOI.

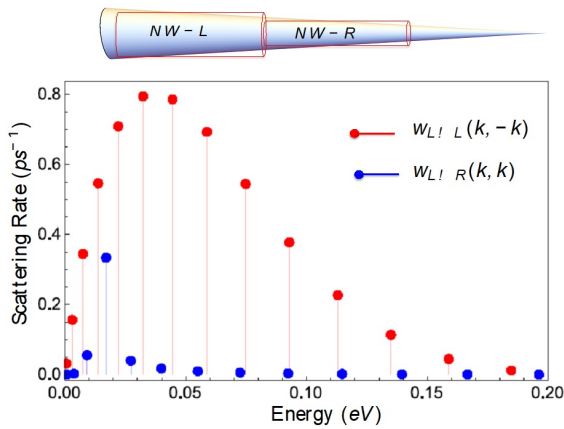


Figure 6. (Top) Partitioning of the tip into NW segments. (Bottom) Forward (L→R) and back (L→L) scattering rates from sub-band 4 into different sub-bands calculated for a junction between NW segments of radii 10 nm (NW-L) and 9 nm (NW-R). The electron incident kinetic energy is set to 0.2 eV and the mean-free path to 1 nm.

CONCLUSION

DFEAs are being characterized experimentally for photocathode applications relevant to DLAs and FELs. We have used electromagnetic beam simulations and are developing MC models to investigate electron transport, emission and beam dynamics issues related to the field-emission yield and the beam properties. By incorporating the NW model for DEFA tips and photo-excited electrons from electronic structure calculation, simulations will be essential for optimizing DEFA in these applications.

ACKNOWLEDGMENT

We would like to acknowledge the helpful discussions with Dr. D. A. Dimitrov and Dr. J. R. Cary regarding the diamond MC model and relevant results.

REFERENCES

- [1] H. L. Andrews *et al.*, “Current experimental work with diamond field-emitter array cathodes,” presented at FEL’17, Santa Fe, USA, August 2017, paper WEP015.
- [2] J. D. Jarvis *et al.*, “Uniformity conditioning of diamond field emitter arrays,” *J. Vac. Sci. Tech. B* 27, pp. 2264, 2009.
- [3] C. Jacoboni *et al.*, “The Monte Carlo method for the solution of charge transport in semiconductors with applications to covalent materials,” *Rev. Mod. Phys.* 55, pp. 645, 1983.
- [4] D. A. Dimitrov *et al.*, “Multiscale three-dimensional simulations of charge gain and transport in diamond,” *J. Appl. Phys.* 108, pp. 073712, 2010.

ELECTRON BEAM HEATING WITH THE EUROPEAN XFEL LASER HEATER*

M. Hamberg[†], Uppsala University, Uppsala, Sweden
 F. Brinker, M. Scholz, B. Manschwetus, S. Koehler, L. Winkelmann, I. Hartl,
 DESY, Hamburg, Germany

Abstract

The Laser Heater of the European XFEL is installed and is in commissioning phase. In this paper, results of heating in the injector section with an additional laser amplifier is discussed.

INTRODUCTION

The European X-ray Free Electron laser (EU-XFEL) will produce fs photon flashes in the interval of 0.05 to 4.7 nm. The setup is based on a 3.4-km long electron accelerator. Longitudinal micro bunch instabilities may occur in the electron beam and hamper the X-ray power level [1]. To overcome such problems a Laser Heater (LH) is installed as in LCLS and FERMI [2-3]. In the LH, a NIR laser is overlapping the electron bunches when they pass a 0.7-m magnetic undulator situated in a chicane section 23-m downstream of the electron gun. The undulator is tuned to resonance which cause a phase space modulation which subsequently is transferred into a net heating effect while leaving the chicane. This heating decreases the instability effects without hampering the FEL performance.

The EU-XFEL LH is a Swedish in-kind contribution which previously has been described [4-8]. Here we report results of injector section measurements after implementation of a NIR laser amplifier [9].

PRECONDITIONING

As described in ref. 6 and 7 overlap of the NIR laser over the electron beam was created in transverse direction in an iterative procedure by readout from Cromox screens. The temporal overlap was adjusted by a fine delay line made up by moving a retro reflector installed on a μm resolution 210 mm linear stage and simultaneously observing heating of the electron bunches as increase in beam width in the dispersive dump section at the injector with an Lyso screen. The accelerator optics was optimized for large dispersion and small beta function at the Lyso screen location to increase the resolution.

The undulator gap was tuned to 42.4 mm to fulfill the resonance condition at the electron energy of 130 MeV with a NIR laser wavelength of (λ_L) of 1030 nm and undulator period (λ_u) of 7.4 cm according to:

$$B_u = \frac{2\pi m_e c}{q_e \lambda_u} \cdot \sqrt{2 \left(\frac{\lambda_L}{\lambda_u} \cdot 2 \cdot \gamma^2 - 1 \right)}.$$

A NIR laser amplifier was installed [9], increasing the NIR laser energy from $\sim 4 \mu\text{J}$ to a maximum of $\sim 200 \mu\text{J}$ per pulse inside of the undulator. The standard deviation radius

of the electron and laser beams were both tuned to approximately $\sigma \approx 0.3 \text{ mm}$ whereas the temporal FWHM of the UV cathode laser and LH NIR laser was tuned to $\sim 12 \text{ ps}$ and $\sim 36 \text{ ps}$, respectively. Since they derive from the same oscillator they are inherently temporally locked.

HEATING

As in previous tests the temporal overlap was adjusted through scan of a linear stage made by a $\sim \mu\text{m}$ stepsize linear stage with an implemented retro reflector and simultaneous readout of the STD beam width on the downstream Lyso screen in the dispersive section. Such measurement is illustrated in Fig. 1 when using a NIR pulse energy of $\sim 35 \mu\text{J}$. The horizontal axis corresponds to temporal offset whereas the vertical axis indicates the STD beam width in mm increasing from $150 \mu\text{m}$ to $325 \mu\text{m}$ which corresponds to an energy spread increase from $\sim 11 \text{ keV}$ to $\sim 31 \text{ keV}$. This should be compared to previous results without amplifier (and therefore a limited NIR pulse energy of $\sim 4 \mu\text{J}$) of $\sim 14 \text{ keV}$ to $\sim 18 \text{ keV}$ [8].

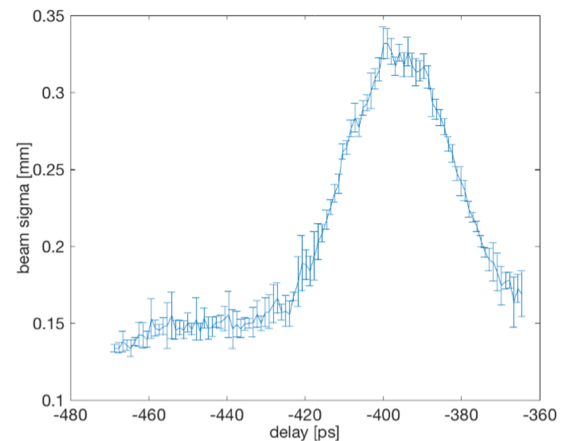


Figure 1: The fine delay scan illustrating the beam size standard deviation in mm versus temporal delay of the cathode laser relative to the beam.

Furthermore, the transverse deflecting structure (TDS) was used to illustrate the effect of the heating. The vertical direction corresponds to longitudinal direction of the electron bunch whereas the horizontal direction corresponds to the energy and therefore illustrate the energy spread at each part of the bunch. An example can be seen in Fig. 2 where the NIR laser is off (top) and partly overlapping (bottom) respectively. It is clear that the whole bunch is strongly heated. The upper part of the heated (bottom figure) bunch is more heated than the lower part.

Content from this work may be used under the terms of the CC BY 3.0 licence (© 2018). Any distribution of this work must maintain attribution to the author(s), title of the work, publisher, and DOI.

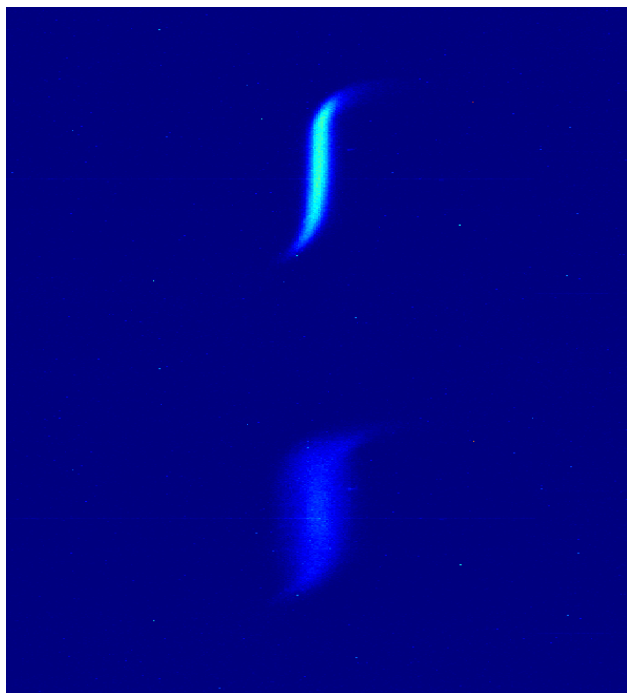


Figure 2: Readout of TDS trace from OTR screen in the dispersive section before the dump when the NIR laser is off (top) and partly temporally overlapping respectively (bottom).

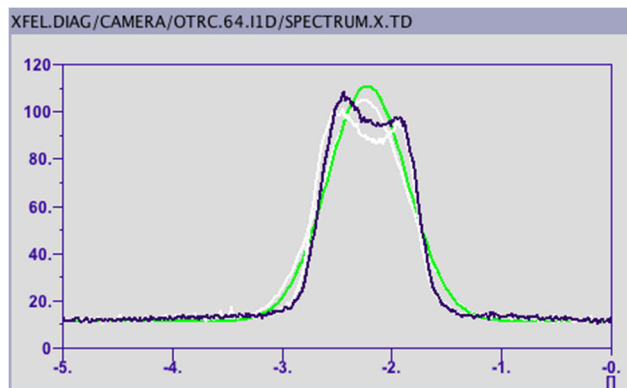


Figure 3: The horizontal projection of the screen intensity in the dispersive section indicating that the energy of the electrons is shifted to higher and lower energies by the LH as predicted for a matched laser beam.

Additionally, the heating effect is illustrated in Fig. 3 indicating that the electron beam is divided into two beams at the dispersive section thanks to the LH accelerating / decelerating part of the electrons respectively, when the NIR laser is fully overlapping with matched beams and on full energy at $\sim 200 \mu\text{J}$.

CONCLUSION AND OUTLOOK

The EU-XFEL Laser Heater demonstrated heating with the additional NIR laser amplifier implemented. The measurements were conducted in the injector section.

The upcoming test will be investigation of the impact of the laser heater on the EU-XFEL SASE, power and stability. Additionally, the following tests will include a fine scan of the power level which will be conducted to reveal any trickle heating effects. Of interest is also to further investigate the heating effect of longer bunches.

ACKNOWLEDGEMENT

Mathias Hamberg thank DESY and Olle Engkvist Foundation for financial support, and all involved DESY groups for excellent support.

REFERENCES

- [1] E. L. Saldin *et al.*, *NIM*, A528, 355-359, 2004.
- [2] Z. Huang *et al.*, *Phys. Rev. ST Accel. Beams*, 13, 020703, 2013.
- [3] S. Spampinati *et al.*, *Phys. Rev. ST Accel. Beams*, 17, 120705, 2014.
- [4] M. Hamberg and V. Ziemann, *Proc. of FEL'13*, New York, NY, USA, TUPSO25.
- [5] M. Hamberg and V. Ziemann, *Proc. of IPAC'14*, Dresden, Germany, THPRO024.
- [6] M. Hamberg and V. Ziemann, *Proc. of FEL'15*, Daejeon, South Korea, paper TUP038.
- [7] M. Hamberg *et al.*, *Proc. of IBIC'16*, Barcelona Spain, WEPG32.
- [8] M. Hamberg *et al.*, *Proc. of IPAC'17*, Copenhagen, Denmark, WEPVA016.
- [9] F. Moglia *et al.*, *EuroPhoton 2016*, Vienna, Austria.

HIHG STABLE PULSE MODULATOR FOR PAL-XFEL*

Soung Soo Park[†], Heung-Sik Kang, Sang-Hee Kim, Heung-Soo Lee
 Pohang Accelerator Laboratory, Pohang City, Korea

Abstract

The construction of Pohang Accelerator Laboratory X-ray Free Electron Laser (PAL-XFEL) was completed by the end of 2015. The commissioning began in April 2016, and the lasing of the hard X-ray FEL was achieved on end of 2016. The PAL-XFEL needs a highly stable electron beam. The very stable beam voltage of a klystron-modulator is essential to provide the stable acceleration field for an electron beam. Thus, the modulator system for the XFEL requires less than 50 ppm beam voltage stability. To get this high stability on the modulator system, the inverter type HVPS is a pivot component. And the modulator needs lower noise and more smart system. We report the stability of the pulse voltage and the test results of the pulse modulator.

INTRODUCTION

PAL-XFEL is a 4th generation light source, a coherent X-ray free electron laser (XFEL). The RF stability is a key issue to get stable FEL output. The reasonably stable output requests the RF stability of 0.02% (rms) for both RF phase and amplitude. The modulator systems consist of 46 sets of 80 MW klystrons and 200 MW modulators to achieve 10 GeV energy for PAL XFEL. To get the RF phase stability of < 0.05 degree, the required beam voltage stability of the PAL XFEL will be < 50 ppm (rms). This requires that we need to use an ultra precision inverter power supply and a fine controller of feedback signal of the charging voltage in order to stabilize the PFN charging level. The proper conditioning of feedback signal with a thermally stable probe is necessary to realize an ultra stable charging performance [1]. And the modulator needs lower noise level and the heater power of the klystron and thyratron was trigger synchronised to the cluster part where the change was small.

PULSE MODULATOR SYSTEM

The pulse modulator system uses a constant current source such as an inverter power supply type.

High Power Klystron and Modulator

An inverter power supply is called capacitor charging power supply (CCPS) because it supplies constant current into the capacitors. In the CCPS, to turn off a thyratron switch in the modulator safely after every discharge, the next charging schedule, digitally safe system, is under short-circuit condition due to the current limit feature. With this CCPS, the modulator system will be naturally compact.

These features are well matched to the next generation modulator for PAL XFEL facility. The CCPS power rating is 120 kJ/s. Total charging time is about 14 ms. The specifications of the modulator are output power of 200 MW, beam voltage of 400 kV, beam current of 500 A, pulse width of 8 μ s and repetition rate of 60 Hz. To achieve those demands, we adopted the fine CCPS as well as the coarse CCPS. Table 1 summarizes the specification of the modulator. As a load s-band E37320 80 MW klystron will be matched to the modulator system. Fig. 1 shows the circuit diagram of a modulator using CCPS.

Table 1: PAL-XFEL Modulator Specifications

Discription	Unit	Value
Peak Power	MW max.	200
Repetition Rate	Hz (normal)	60
Pulse Voltage Stability	ppm	>50
Pulse Peak Voltage	kV	400
Pulse Peak Current	A	500
Pulse Width	μ s	7.5
PFN Impedance	Ω	2.63
Main CCPS Power	kJ/s	120

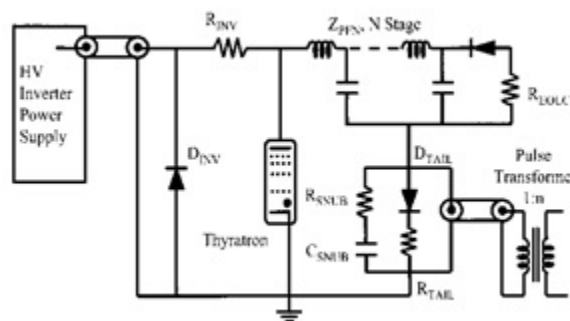


Figure 1: Circuit diagram of a modulator with a CCPS.

Inverter High Voltage Power Supply

To meet specifications of Table 1, two different types of current charging power supply (CCPS) are employed. One is a fine CCPS which is a high precision type (< 50 ppm) and the other is a coarse CCPS (< 1000 ppm). The coarse charging and fine charging is arranged to get the regulation with optimum power sharing. Figure 2 shows the charging schedule with parallel operation of inverters [2]. Total charging time T_c and charging voltage V_o are given by

$$\begin{aligned} (m+n) t_o &= T_c, m(D+d) + n d = V_o, \\ n d &= V_o - V = j D, \\ m+n &= a, m^2 - a m + (a+b) j = 0, \end{aligned}$$

* Work supported by Ministry of Science, ICT(Information/Communication Technology) and Future Planning.

[†] sspark@postech.ac.kr

Content from this work may be used under the terms of the CC BY 3.0 licence (© 2018). Any distribution of this work must maintain attribution to the author(s), title of the work, publisher, and DOI.

where inverter switching time $t_o = 1/f_s$, T_c is total charging time, m is total switching number of coarse charging, n is total switching number of fine charging, $a = T_c / t_o$, fine charging step $d = I_f t_o / C$, coarse charging step $D = (I_c + I_f) t_o / C$, C is a load capacitance, I_f is charging current of a fine inverter, I_c is charging current of a coarse inverter.

Typical parameters for PAL XFEL modulator are PRR = 60 Hz, $f_s = 50$ kHz, $V_o = 50$ kV, $C = 1.4$ μ F, $b = 10,000$. Then $T_c = 16.7$ ms, $t_o = 20.0$ μ s, $a = 835$, $P_{av} = 120$ kJ/s.

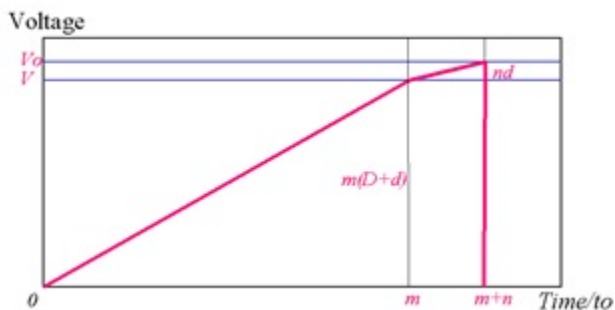


Figure 2: Charging Scheme in Parallel Operation.

Paraday Cage Type Modulator and Klystron

We used a faraday cage circuit to reduce EMI noise. The modulator and klystron are configured in one faraday cage form in order to remove the noise generated by the switching of the thyatron. Fig. 3 shows a faraday cage consisting of modulator and klystron.

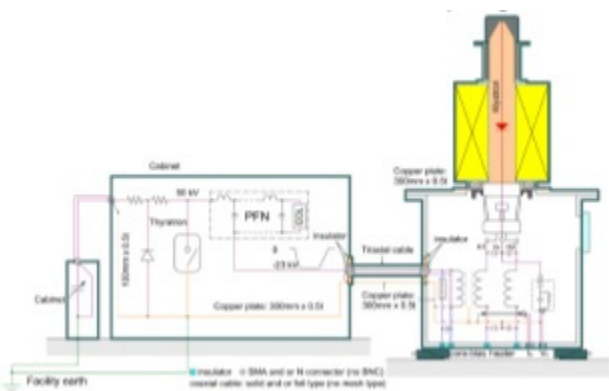


Figure 3: Faraday cage consisting of modulator and klystron.

Stability Measurement

The 50 ppm beam voltage stability measurement setup is shown in Fig. 4. The beam voltage signal was obtained at 10,000:1 CVD installed in insulating oil cooling with cooling water. On the beam voltage waveform, the zero offset is defined by a differential amplifier (DA1855A, Lecroy) setting a band width of 1 MHz [2,3]. To display the histogram, an oscilloscope (DPO7104, Tektronix) equipped with a high resolution mode (11bit) in an acquisition mode is used. The beam voltage stability measurement test is performed at 42kV, maximum voltage of modulator and 1 hour later, sufficient time for temperature of

modulator panel inside to saturate. Test environments are as following;

- 1) oscilloscope, differential amplifier, trigger generator : warming up 1hour,
- 2) CCPS, master controller: warming up 1 hour (60Hz @ 35kV),
- 3) maximum PFN voltage is 42 kV and repetition rate 60 Hz at ambient temperature: 20~25°C and humidity: 10~25%,
- 4) trigger signal synchronized with AC line frequency at thyatron AC heater power.

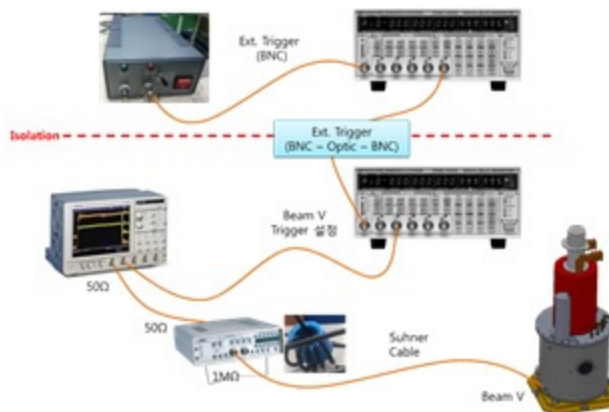


Figure 4: Beam voltage stability measurement setup.

RESULTS OF TEST

The experimental setup is shown in Figure 5 for the 200 MW modulator system with 80 MW klystron load. The used DC source power supply consists of 3 coarse CCPSs (each 30 kJ/s) and 1 coarse and fine CCPS (35 kJ/s) controlled by a digital signal processing (DSP). The operation condition of the modulator is repetition rate 60 Hz, PFN charging voltage 42 kV, pulse width 7.5 μ s.



Figure 5: Experiment setup for the modulator system.

Figure 6 shows the waveform of the PFN voltage when it is charging. The blue line indicates PFN charging voltage and the green line shows resonant current. The total capacitance is 1.4 μ F.

Content from this work may be used under the terms of the CC BY 3.0 licence (© 2018). Any distribution of this work must maintain attribution to the author(s), title of the work, publisher, and DOI.

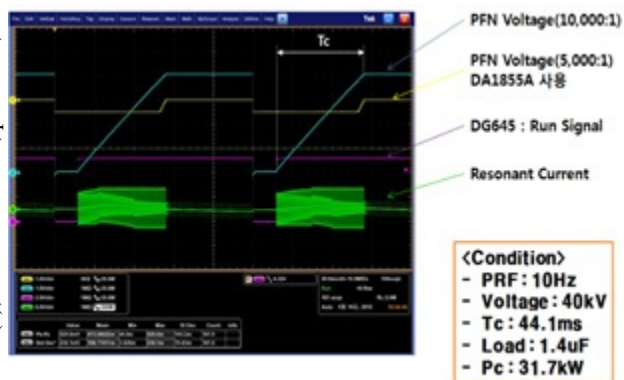


Figure 6: PFN charging voltage waveform and resonant current.

Figure 7 shows detailed charging waveform of each bucket. The size of average charging voltage step is 34 V from the coarse CCPS. The resonant switching frequency is 40 kHz. The waveform in the lower part of the right figure shows charging voltage step by means of coarse CCPS, fine CCPS in pulse width modulation and fine CCPS in high regulation mode subsequently. In the regulation mode, the charging voltage step is about 2 V.

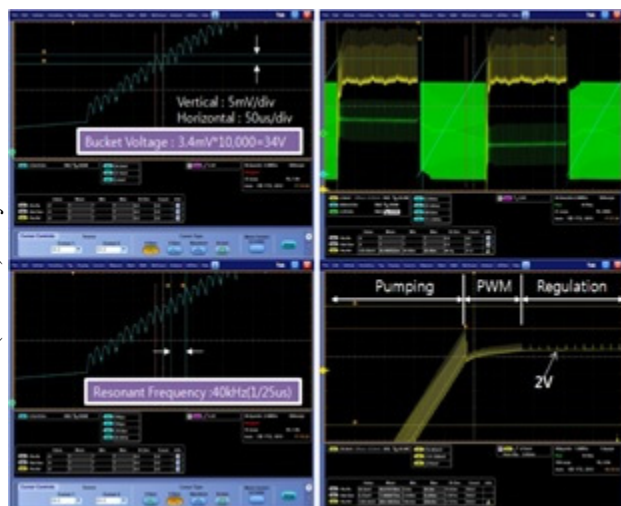


Figure 7: Detail waveform of PFN charging voltage (one bucket voltage of 34 V, resonant frequency of 40 kHz, regulation voltage of 2 V)

Figure 8 shows the stability measurement waveform of the beam voltage. The measurement value of beam voltage is 21.53 ppm at 42 kV PFN voltage, 60 Hz repetition rate.

Figure 9 shows the variation of beam voltage stability measured 8 times, which is measured as about 3.8 ppm. The stability test conditions of the modulator were 60 Hz, 42 kV PFN charging voltage.

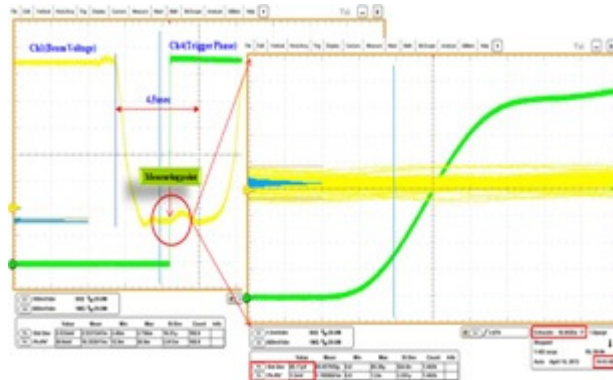


Figure 8: Stability measurement of the beam voltage (1 mV/div, 5 ns/div) 21.53 ppm (85.17 V/39.554 V=21.53 ppm).

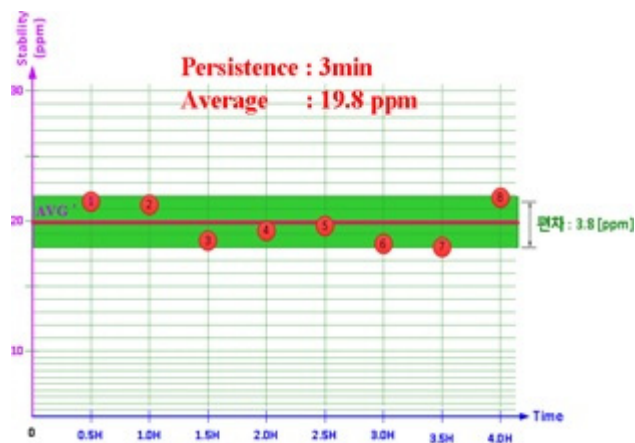


Figure 9: Beam voltage Stability of the modulator (Standard deviation 3.8 ppm).

SUMMARY

PAL developed DC source power supply consists of 3 coarse CCPSs (each 30 kJ/s) and 1 coarse and fine CCPS (35 kJ/s) controlled by a digital signal processing (DSP). The CCPS system was applied to the 200 MW modulator in order to obtain highly stable beam voltage with a repetition rate of 60 Hz. The result of the beam voltage stability was < 50 ppm satisfying the requirement.

REFERENCES

- [1] J.S. Oh, J.H. Suh, Y.G. Son, S.D. Jang, S.J. Kwon, E.H. Song, "Stabilization of a Klystron Voltage at 100 ppm Level for PAL XFEL," in *Proc. FEL2007*, Novosibirsk, Russia, 2007, pp. 424-427.
- [2] J.S. Oh, S.S. Park, Y.J. Han, I.S. Ko, W. Namkung, "Design Considerations for the Stability Improvement of Klystron-modulator for PAL XFEL," in *Proc. PAC2005* Knoxville, TN, USA, 2005, pp. 1165-1167.
- [3] T. Shintake, T. Inagaki, K. Shirasawa, C. Kondo, T. Sakurai, "Compact Klystron Modulator for XFEL/SPring-8," in *Proc. IPAC'10*, Kyoto, Japan, 2010, pp. 3287-3289

PRELIMINARY RESULTS OF THE DARK CURRENT MODELLING FOR THE POLFEL SUPERCONDUCTING LEAD PHOTOCATHODE

Karol Szymczyk, Jerzy Andrzej Lorkiewicz, Robert Nietubyć, NCBJ, Świerk, Poland
Jacek Sekutowicz, DESY, Hamburg, Germany

Abstract

Preparation for the construction of the Polish Free Electron Laser (POLFEL) has been launched at NCBJ. POLFEL is a 4th generation light source driven by a continuous wave or long pulse operating superconducting electron accelerator. The concept includes all-superconducting injector, with a thin-film lead superconducting photocathode, dedicated for generation of low-current ($\sim 25 \mu\text{A}$), low-emittance beam.

One of the issues which emerges in connection with operation of high gradient electron guns furnished with dismountable photocathode plugs is the dark current (DC) emitted from the cathode plug edges and surface inhomogeneities, which degrade the accelerator performance.

The purpose of this paper is to present an approach to dark current investigation and the preliminary results obtained. Specific features of the geometric configuration like rounded plug edges, a gap between the plug and back wall as well as surface roughness have been taken into account for the electron emission and RF field calculations.

THz SOURCE

The POLFEL will consist of a linear accelerator that will deliver 30 MeV (100 MeV in the second step) electron beam, used to emit a THz-IR ranged electromagnetic radiation in plane, variable gap undulator.

The construction of the first Polish FEL is planned for 3 years. The POLFEL will be used in two parallel experimental end-stations that will foster major advances from materials studies such as diffraction imaging with spatial and temporal resolution, spectral investigations of photoionized plasmas by direct or multiphoton ionization of molecules.

DARK CURRENT

One of the main problems of a dismountable photocathode plug is dark current. Incoherently propagating electrons may collide with photocurrent beam, load the cryogenic system, may cause activation or damage of accelerator components and induce cavity quenches. Moreover, dark current caused by field emission limits lifetime of photocathodes.

The main dark current sources of the RF gun cavity are:

- the photocathode plug,
- the cavity backplane close to the cathode,
- the irises because of the strong surface field.

The dark current is preferably emitted from the rough fragments of arc deposited lead layer, and from the plug bends. The intensity of dark current depends on the cavity and photocathode surface finishing.

There are developed dark current reduction methods:

- Suppressing field emission by improved surface preparation.
- Lowering RF gradient at the cathode.
- Applying a collimator.

The main topic of this publication is modeling of surface roughness and its influence on the DC generation. Special attention was paid for RF field calculation, taking into account specific features of the geometric configuration like rounded plug edges, a gap between the plug and back wall as well as surface roughness.

At the FLASH [1] injector, the normal conducting RF gun operated at the nominal gradient of 40–44 MV/m, produces a steady DC electron flux of 200–300 μA as measured with a Faraday cup near the exit of the gun structure. The dark current rises exponentially, regards to the max RF field at the cathode (see Fig.1).

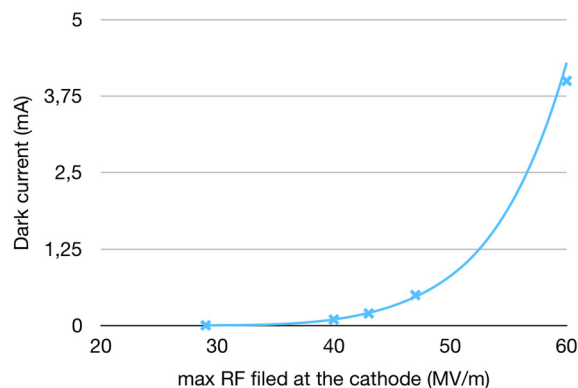


Figure 1: Relationship of dark current to RF field.

CALCULATION METHOD

The main part of calculation was performed using: Astra (A Space Charge Tracking Algorithm) [2] and FEM [3] codes. The FEM uses finite element approximation based on the mesh optimised to map curvilinear boundary of gun resonator. It was used to calculate the RF field in the cavities. For the particles tracking simulation, the Astra program was used.

RESULTS

Work was performed in following steps. Firstly, the RF field distribution with the FEM program, was calculated inside the gun cavities, with the flat back wall surface. Fig. 2 and 3. The programme calculates two-dimensional field distribution assuming cylindrical symmetry relative to the longitudinal z axis.

Content from this work may be used under the terms of the CC BY 3.0 licence (© 2018). Any distribution of this work must maintain attribution to the author(s), title of the work, publisher, and DOI.

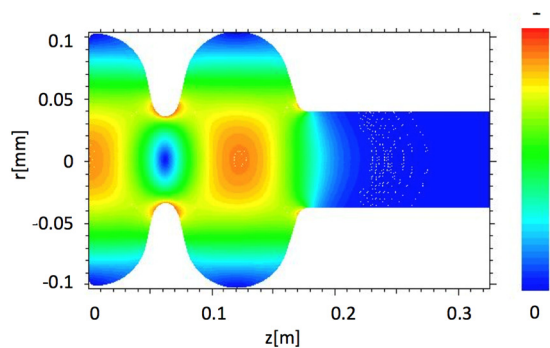


Figure 2: Simulated magnitude of the electric field in the e-gun cavities.

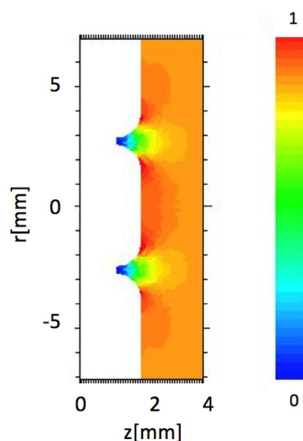


Figure 3: Magnitude of the electric field in the vicinity of the cathode plug.

In the second step, the RF field near the bumps –representing roughness and potential dark current emitters of 50 and 30 μm radii, was modelled. To keep accuracy of the result and overcome program limit in the number of nodes, only selected part of the cavity was simulated. For an optimal FEM mesh density, resonator transverse dimension was matched to various bump sizes. Fig. 4 presents mesh of photocathode surface, bump in the middle, with 50 μm radius and two rings with 30 μm elevation.

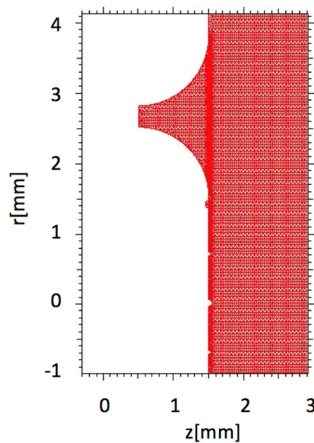


Figure 4: Mesh of photocathode in FEM program.

The results of the calculation show that the electric field is the most enhanced in the arches and on the top of the bumps, as shown in Fig. 5. It was also observed that reduction of the bump dimension reduces field perturbation in the cavity.

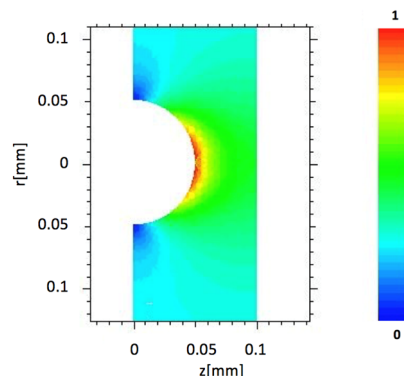


Figure 5: Normalized contour of electric field amplitude in POLFEL gun on the 50 μm bump.

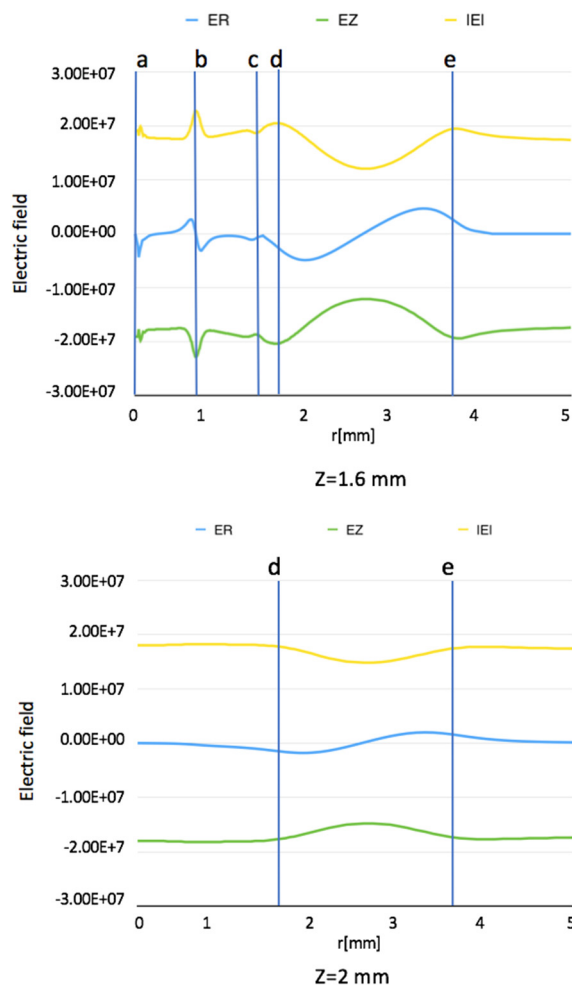


Figure 6: Electric field on the r-axis for different planes in the z-axis: $z = 1.6 \text{ mm}$ (upper plot) and $z = 2 \text{ mm}$ (lower plot). Individual points represent roughness on the surface: a) 50- μm bump, b) 30- μm bump, c) 30- μm bump, d) and e) the photocathode RF gun arc.

Based on the FEM simulation, the dependence of the electric field on r-axis was determined for different planes in the z direction. It can be seen on the plot in Fig. 6, which presents the electric field at $z = 1.6$ mm and $z = 2$ mm plain in the r-axis. The electric field disturbance, caused by the surface roughness, is negligible at the distance of 0.5 mm from the surface. In Ref. [1], the dark current onset is for the field $E > 30$ MV/m, (Fig. 1) which is 75% of the gradient specified for the superconducting cathode. Gun operation frequency is 1.3 GHz, therefore wave period is 770 ps, which means that the dark current is generated for 152 ps in every cycle.

In the next step, a special script in the R-language was written to reflect the shape and roughness of the photocathode, with the DC emitters on the surface Fig. 7. The script file was used as input file for Astra. Based on the RF-field simulations, the areas with the local maximum RF field were assumed as the most probably locations of the dark current generation. Electric field input parameters used in Astra simulator are presented in Table 1.

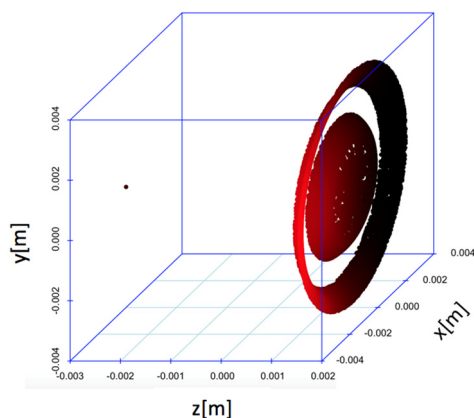


Figure 7: Visualization of DC emitters on the cathode implemented in R-language.

In the Astra simulation, the rounded plugs of the cathode with the flat surface were modeled. Roughness on the cathode surface will be implemented in the further work.

Dark current is generated unevenly during time interval, from the cathode arcs -where the electric field is the largest. Generated electrons have a delay in time and space in the z direction. During acceleration, the bunch of electrons is not coherent, as illustrated in Figure 8. It can be seen that the dark-current distribution is getting spread about 10 cm.

Table 1: Cavity Field in Astra Simulation

Frequency	1.30	GHz
Maximum gradient	40.00	MV/m

Table 2: Particle Statistic in Astra Simulation

Total number of particles on stack	21000	
Active Particle	89.56	%
Backward traveling particles	0.14	%
Particle lost on aperture	10.30	%

Particle statistics is displayed in Table 2. 89.56% particles (black points) contribute to the DC propagating along the linac, 10.3% of total number of electrons are lost on aperture (red points) and 0.14% of electrons are traveling back-ward to the photocathode (blue points).

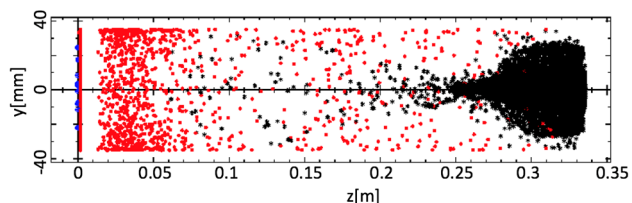


Figure 8: The Astra result.

CONCLUSION

In this paper, the preliminary DC modelling results were presented. Specific features of the geometric configuration like rounded plug edges, a gap between the plug and back wall as well as surface roughness have been taken into account for the electron emission and RF field calculations. The modelling confirms that surface roughness has significant influence on the local RF field. It was proven that local change of the RF field affects the generation of dark current which is distributed in time as space, disturbing the accelerating field.

The subsequent works will focus on the dark current generation depending on the RF field phase and more detailed calculations.

ACKNOWLEDGEMENT

I am grateful to Marcin Staszczak for his help and valuable comments relating to the simulations in Astra and FEM program.

REFERENCES

- [1] J.-H. Han, "Dark current at the XFEL injector", DESY Technical Note, Hamburg, Germany, 2006.
- [2] K. Floettmann, "ASTRA: A Space Charge Tracking Algorithm Version 3.0", DESY Technical Note, Hamburg, Germany, 1997.
- [3] J. Sekutowicz, "FEM-2D: FEM code with third-order approximation for rf cavity computation", in *Proc. LINAC '94*, Tsukuba, Japan.

DESIGN AND RESEARCH OF A MICRO-PULSE ELECTRON GUN

D. Y. Yang, J. F. Zhao, B. T. Li, Y. J. Yang, K. Zhao, X. Y. Lu[†], Z. Q. Yang, W. W. Tan, L. Xiao
State Key Laboratory of Nuclear Physics and Technology at Peking University, Beijing, China

Abstract

Micro-pulse electron guns (MPG) are a novel electron source which can produce narrow-pulse, high-repetition rate electron current. Theoretical and experiment work have been done to study physical properties and steady operating conditions of MPG. Proof-of-principle work has been finished and the next work is to research the parameters of the MPG electron beam and understand the MPG properties. Thus, a high-voltage accelerating platform which can supply 100 kV direct voltage was designed. Furthermore, electromagnetic and mechanism designs were operated to adapt the high voltage platform and measure beam parameters.

INTRODUCTION

The multipactor, based on a secondary electron emission (SEE) [1], is often destructive to the microwave device such as waveguide, coupler, RF resonant cavity [2-3], and its avoidance has been a major task for sic-tech workers.

The underlying mechanism behind the multipactor has been studied deeply [4-7]. But before the publications of this theoretical work, the first electron gun based on multipacting was made by Gallagher in 1969 [8]. Among those publications, the beam self-bunching effect attracted the attention of Mako, who gave the concept of the micro-pulse electron gun (MPG) and obtained important conclusions about MPG [9-11]. After the initial work of Mako, many other research institutions have made their contributions to the development of MPG [12-14].

MPG could produce a narrow-pulse electron beam due to the self-bunching effect. In addition, simple structure and high tolerance to contamination make it a potential electron source for accelerators and microwave systems [15]. However, no records on the applications of MPG have been reported until now. One of the reasons to explain the limitation of the MPG applications may be the bad stability of MPG operation.

In our previous work, a prototype electron gun has been designed, tested and the steady operation of MPG has been obtained [15]. Yet several problems remained. For instance, the steady operation time cannot meet the demands of MPG applications as a novel electron source, the beam parameters such as energy spread, intrinsic emittance need to be detected and the former system doesn't have the ability to do this job. Our goal is to design and build a new MPG test system at the basis of previous work in addition to detect the beam parameters and study the principle of MPG steady operation.

This paper presents the electromagnetic design and test of a MPG which works for high voltage accelerator plat

form. In the second section, basic concepts of MPG are introduced and several types of gun shape are compared. The third section gives the fabrication of the new gun, and brief introduction of HV platform. Finally, primary experiment results are presented.

THE MPG MODEL

Working Principle of MPG

The MPG shown in Figure 1 consists of three parts in general: RF cavity which works at TM010 mode, cathode with the secondary electron yield (S.E.Y) of δ_1 grid anode with the S.E.Y of δ_2 .

The initial electrons in the RF cavity which are caused by field emission move from cathode to grid anode by means of their interaction with electromagnetic fields, and they impact the anode after odd multiple of half period and generate secondary electrons. The triggered secondary electrons traverse back and forth between the electrons until saturation.

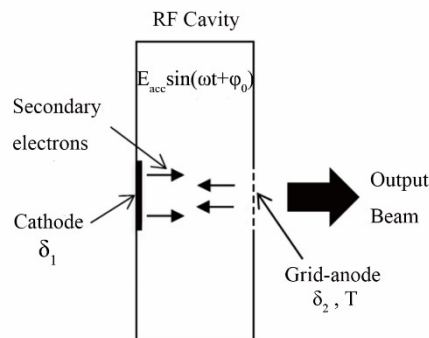


Figure 1: The schematic diagram of the MPG model.

The Choice of Cavity Shape

The general cavity type for TM010 mode is pill-box cavity. Figure 2 shows the comparison of three pill-box like cavities. (a) is the general pill-box cavity, (b) is the concave cavity that equivalent to pill-box with a part cut inside, (c) is the convex cavity that shapes like a pill-box added two parts. Figure 3 demonstrates the electric field distribution of three different cavities. a1/a2 are three-dimensional diagrams and pseudo-color maps of general pill-box cavity. b1/b2, c1/c2 are have the same meaning for concave cavity and convex cavity separately. Concave cavity has the sharpest peak among these three cavities. What's more, there is a 'flat roof' in the centre electric field of concave cavity and it helps decrease the electron transverse energy difference.

Content from this work may be used under the terms of the CC BY 3.0 licence (© 2018). Any distribution of this work must maintain attribution to the author(s), title of the work, publisher, and DOI.

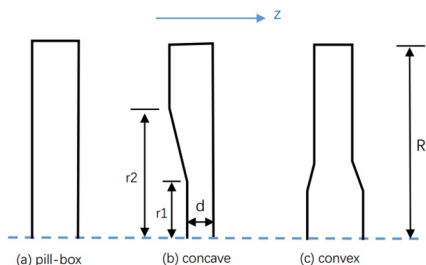


Figure 2: The schematic diagram of three types cavity.

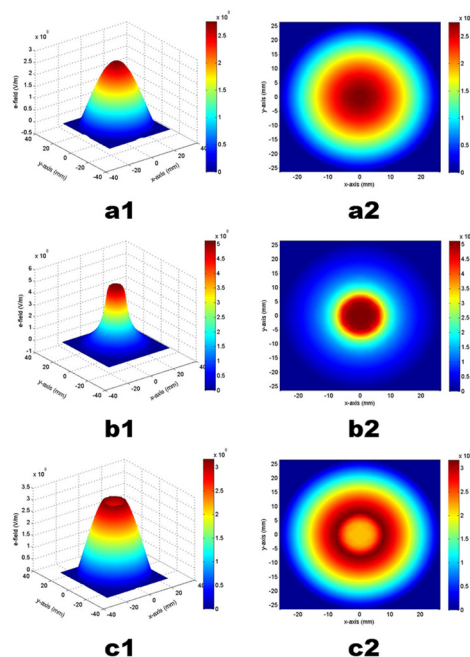


Figure 3: Electric field distribution of different cavities.

After the cavity shape was chosen, we optimised the dimensions of the concave cavity, and Figure 4 shows the final electromagnetic field distribution. The maximum electric field is located in the centre ‘flat roof’ and the maximum magnetic field is at $x=13\text{mm}$.

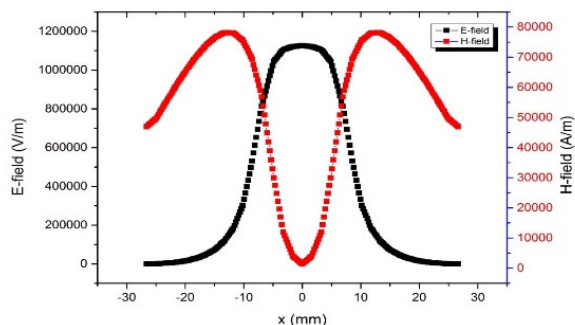


Figure 4: Electromagnetic field distribution of the optimized concave cavity. Maximum of electric field is in the centre of the cavity ($x=0$, black dash), and a centre ‘flat roof’ is clearly demonstrated. Magnetic field is at a maximum at $x\sim 13\text{mm}$.

HIGH VOLTAGE PLATFORM

The high-voltage accelerating platform consists of two distinct parts:

- MPG-II which could produce high repetition rate, narrow pulse electron beam;
- 100KV high voltage system.

MPG-II

The RF cavity is made of stainless steel. The cathode is made of Cu-Al-Mg alloy and the grid anode is made of oxygen-free copper. Figure 5 shows the details of MPG-II. Magnetic coupling was chosen and the external Q changes from 140 to 244 with the coupling loop angle changes from 0° to 90° . Table 1 shows the test RF parameters of MPG-II.

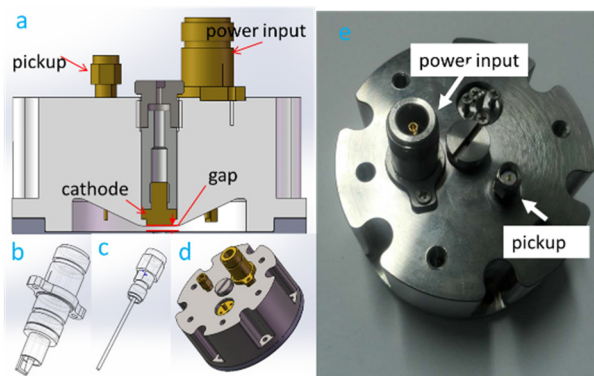


Figure 5: Details of MPG-II. The cutaway of MPG-II (a), coupling loop (b), pick-up antenna (c), MPG-II pictures of design (d) and physical (e).

Table 1: RF Parameters of MPG-II

RF parameters	Test value
f_0	2856MHz
d	1.75mm
Q_0	157
Γ_{shunt}	0.036M Ω

High Voltage Platform

The key components include the ceramics, MPG-II, pump and all those components have been fabricated tested. These are exhibited in Fig 6.

The Glassman high voltage source could supply 100KV. The ceramic (pink part) has the length of 200mm, inside radius of 190mm. The white part of ceramic’s length is 400mm and inside radius is 120mm.

EXPERIMENTAL RESULTS

The information of output current which is obtained by faraday cup is showed in the oscilloscope. Figure 7 shows the output signal of electron beam. The yellow line is the current signal and blue line is the pickup signal. Table 2 demonstrates the details of output current.

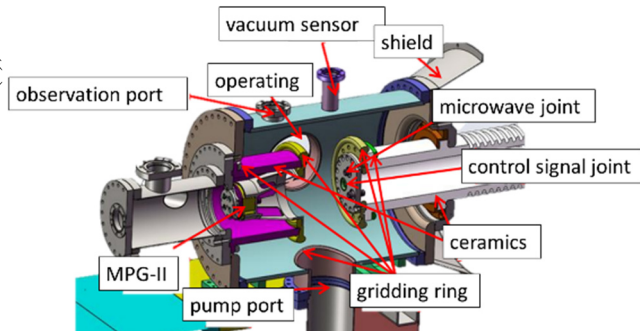


Figure 6: Components of high-voltage accelerating platform, shown in cutaway view.

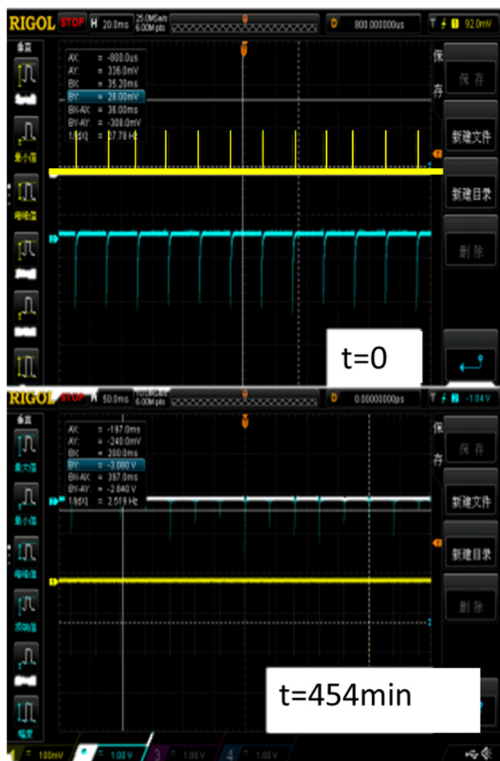


Figure 7: Schematic of current signal. The output current at $t=0$ (up), at $t=454\text{min}$ (down).

Table 2: Current Parameters

Parameters	Value
Current	~10mA
Life time	~454min
Pulse length	10us

In the study of MPG, lifetime limitations are the biggest challenge. In our experiment, the pulse length jitter was observed not only the current decrease. The time evolution of beam current and pulse-length is shown in Figure 8. Current at this experiment is 1.08mA and the life time is about 600min. But the pulse length jitter occurred in $t=150\text{min}$ before the decrease of amplitude. With the input power increases, the jitter amplitude decreases.

Figure 9 shows the comparison of surface morphology between initial and after bombardment. Dose effect was observed in Henrist's work [16], which is related to the electron bombardment influence to the material surface. The color of grid anode changed after the electron bombardment.

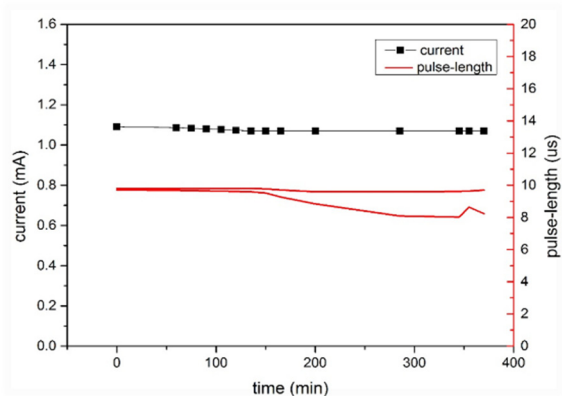


Figure 8: Time evolution of beam current and pulse-length over 360 minutes.

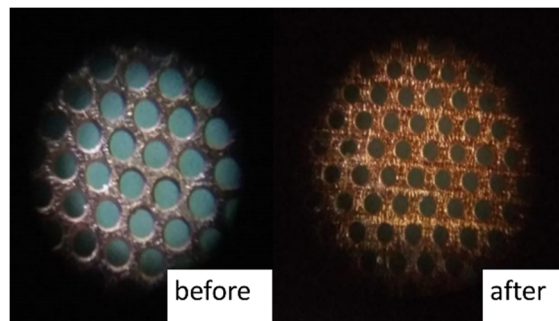


Figure 9: Comparison of surface morphology between initial and after bombardment.

CONCLUSION

At the high voltage platform, the MPG-II beam output experiment has been operated. The key point of MPG-II application, lifetime, is 454mins. In addition, the pulse length jitter and dose effect were also observed. In our next work, the S.E.Y. of material in different conditions will be tested and the relationship between pulse length jitter and power input will be studied.

Content from this work may be used under the terms of the CC BY 3.0 licence (© 2018). Any distribution of this work must maintain attribution to the author(s), title of the work, publisher, and DOI.

REFERENCES

- [1] R. A. Kishek *et al.*, *Phys. Plasmas* 5, 2120 (1998), and references therein.
- [2] R. Boni *et al.*, “Reduction of multipacting in an accelerator cavity,” *IEEE Transactions on Nuclear Science*, vol. NS-32, no.5, pp. 2815-2817 (1985).
- [3] R. L. Geng *et al.*, “Suppression of multipacting in rectangular coupler waveguides,” *Nuclear Instruments and Methods in Physics Research A*, 508 pp. 227-238 (2003).
- [4] J. Rodney *et al.*, “Multipactor,” *IEEE Transactions on Electron Devices*, vol. 35, no. 7, pp. 1172-1180 (1988).
- [5] S. Riyopoulos *et al.*, “Effect of random secondary delay times and emission velocities in electron multipactors,” *IEEE Transactions on Electron Devices*, vol. 44, no. 3, pp. 489-497 (1997).
- [6] S. Riyopoulos, “Multipactor saturation due to space-charge-induced debunching,” *Phys. Plasmas* 4(5), pp. 1448-1462 (1997).
- [7] A. Valfells *et al.*, “Frequency response of multipactor discharge,” *Phys. Plasmas* 5(1), pp. 300-304 (1998).
- [8] W. Gallagher, “The multipactor electron gun.” *Proceedings of the IEEE* 57(1): pp. 94-95 (1969).
- [9] F. M. Mako and W. Peter, “A High-Current Micro-Pulse Electron Gun,” *Proc. PAC’93*, pp. 2702-2704.
- [10] L. K. Len and F. M. Mako, “Self-bunching electron guns,” *Proc. PAC’99*, pp. 70-74.
- [11] S. Guharay, L. Len, and F. Mako. “X-band high-current micro-pulse electron gun for accelerators,” *Proc. IVEC’02*, pp. 174-175.
- [12] J. Zhai, C. Tang, and S. Zheng, “Multipactor electron gun with CVD diamond cathodes,” *Proc. EPAC’06*, 6 pp. 3203.
- [13] M. Zhong, S. Zheng, and C. Tang, “The primary experiment of multipactor electron-gun-based accelerator,” *Proc. PAC’09*, FR5REP091.
- [14] L. Liao *et al.*, “Novel Design of a Micro-Pulse Electron Gun,” *Nuclear Instruments and Methods in Physics Research Section A* 729, pp. 381–86 (2013). doi:10.1016.
- [15] L. Kui *et al.*, “Study on the Steady Operating State of a Micro-Pulse Electron Gun,” *Review of Scientific Instruments* 85, no. 9 93304 (2014). doi:10.1063/1.4895604.
- [16] B. Henrist *et al.*, “The variation of the secondary electron yield and of the desorption yield of copper under electron bombardment: origin and impact on the conditioning of the LHC,” *Proc. EPAC’02*, WEPD014.

EMITTANCE MEASUREMENTS AND SIMULATIONS FROM SRF GUN IN CEC ACCELERATOR

Kentaro Mihara, Vladimir N. Litvinenko¹, Irina Petrushina

Center for Accelerator and Science and Education, Department of Physics and Astronomy,
 Stony Brook University, New York, USA

Igor Pinayev, Gang Wang, Yichao Jing

Collider-Accelerator Department, Brookhaven National Laboratory, New York, USA

¹also at Collider-Accelerator Department, Brookhaven National Laboratory, New York, USA

Content from this work may be used under the terms of the CC BY 3.0 licence (© 2018). Any distribution of this work must maintain attribution to the author(s), title of the work, publisher, and DOI.

Abstract

In this paper, we report on extremely good performance of 113 MHz SRF CW gun. This gun is a part of the system built to test coherent electron cooling concept and was aimed to generate trains of 78 kHz pulses with large 1 nC to 5 nC charge per bunch. While it was not built for attaining record low emittances, the machine can achieve very low normalized emittances ~ 0.3 mm mrad with 0.5 nC charge per bunch using CsK2Sb photocathode. In addition to excellent performance, this gun provides for very long lifetime of these high QE photocathodes, with a typical using time of 2 months.

INTRODUCTION

Coherent electron Cooling (CeC) is a novel technique promising high cooling rates for high energy hadron beams [1], BNL's future electron-ion collider, eRHIC especially concerns its feasibility [2]. We found CeC efficiency to outperform other cooling methods such as electron cooling or stochastic cooling by orders of magnitude. Since CeC is untested method, it will need to be tested by cooling a single bunch of gold ions circulating in RHIC [1]. The proof-of-principle experiment is conducted at BNL to demonstrate this technique. The dedicated accelerator, shown in Fig.1, comprising of 113 MHz SRF electron gun, two 500 MHz room-temperature bunching cavities and 704 MHz SRF linac built for this purpose has been commissioned and now is fully operational [3].

Since CeC SRF accelerator uses cryogenic system supplied by RHIC, it is able to operate only during RHIC runs. The SRF electron gun with CsK2Sb photo-cathode is operating for third season and generates electron beams with kinetic energy of 1.05-1.15 MeV and to 3.9 nC charge per

bunch. In this paper, we pre-sent selected simulation and experimental results focused on the transverse beam emittance.

SRF GUN AND PARMELA SIMULATIONS

The electrons in the SRF gun are generated from CsK2Sb photocathode by illumination from green 532 nm laser generating pulses with 0.25-nsec to 0.5-nsec duration. After accelerating to kinetic energy of 1.05 MeV (total energy 1.56 MeV), the beam propagates through the gun solenoid (located $z = 0.65$ m from the cathode, further in the text all distances are from the cathode surface), the bunching cavities (turned off for this measurements) and first transport solenoid (LEBT1, at $z = 3.65$ m) before it can be observed at YAG profile monitor ($z = 4.28$ m). The arrangement of this beamline is shown in Fig. 2. Being a low energy beam, its beam dynamics is strongly influenced by space charge starting from charge per bunch of few hundreds of pC. The particle tracking code PARMELA [4] has been used to simulate the beam dynamics.

We simulated the evolution of projected emittance and attempt to optimize strength of the gun and LEBT1 solenoids as well as the laser spot size on the cathode. Table 1 summarizes the parameters used in this optimization and result is summarized in Fig. 3. Cathode is located without recession in this simulation.

Table 1: Parameters Used for Optimization

Laser spot [mm]	Pulse length [ps]	Bunch charge [nC]	Energy gain [MeV]
1.25 ~ 2.5	300	0.1~0.5	1.05

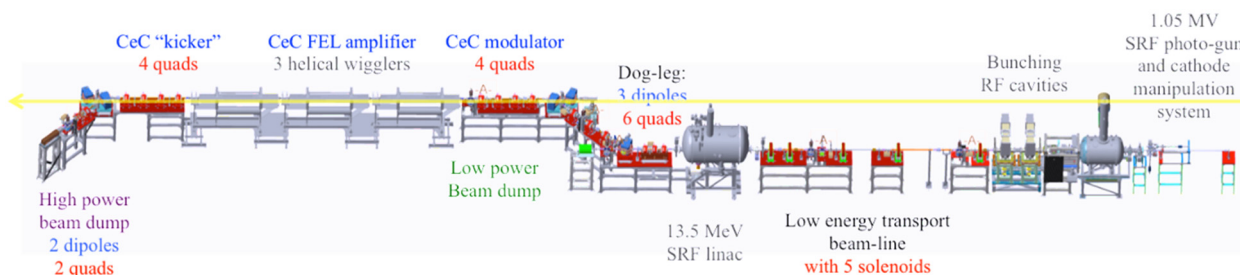


Figure 1: The layout of CeC experiment.

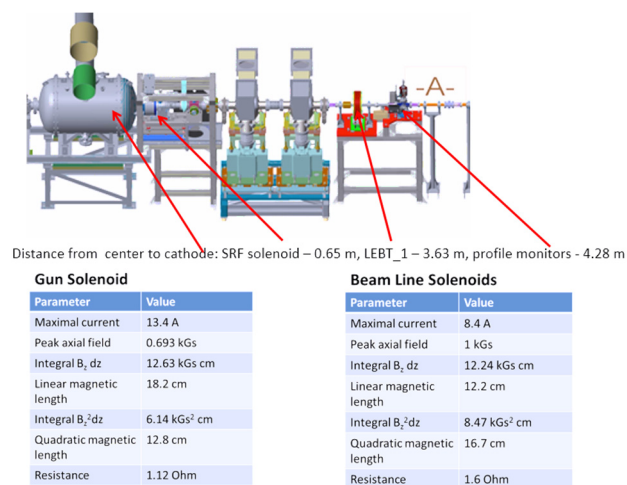


Figure 2: The SRF electron gun, the gun and LEPT1 solenoids and the YAG profile monitor.

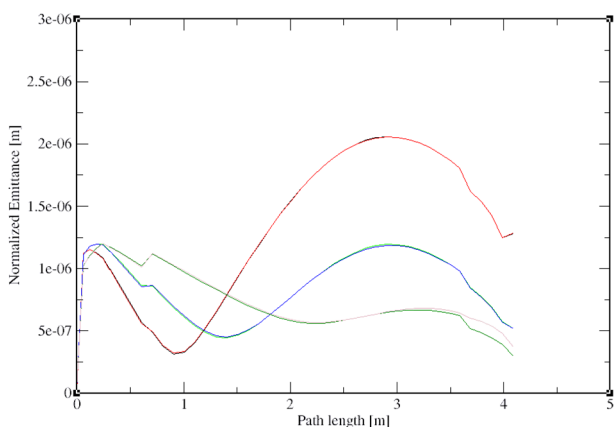


Figure 3: Evolution of the beam normalized emittance for various laser spot sizes: red curve is 1.25 mm, blue curve is 1.8 mm, and green curve is 2.5 mm.

Oscillations of normalized emittance along the beam line, known as emittance compensation, are shown in Fig. 3. Using PARMELA, emittance compensation was simulated to indicate the numerically feasible normalized emittance after the Gun solenoid for different charges.

Optimization has been done by scanning the Gun solenoid or LEPT1 solenoid aiming of minimizing the projected emittance by aligning all the phase space slices as much as possible. We used flat top and beer can-like distribution for the laser pulse and shape [5]. Simulations summarized in Fig. 4 showed that in the beam normalized emittance can be manipulated under one mm-mrad by proper choice of solenoid strength by help of emittance compensation.

Also, the 1.5-mm laser spot size showed relatively better emittance compensation outcome than the 1.0-mm spot size. Therefore, it is found that larger spot size prevents emittance growth in the gun.

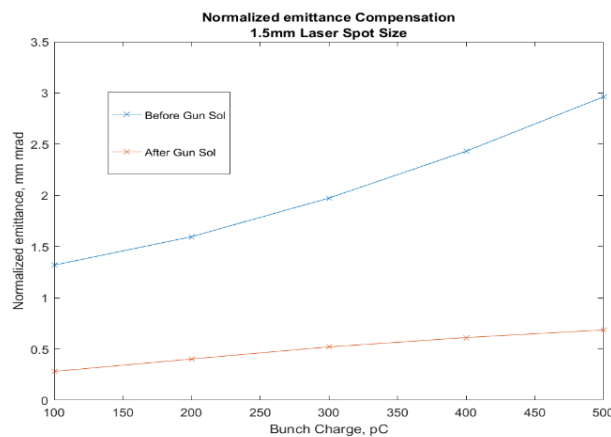
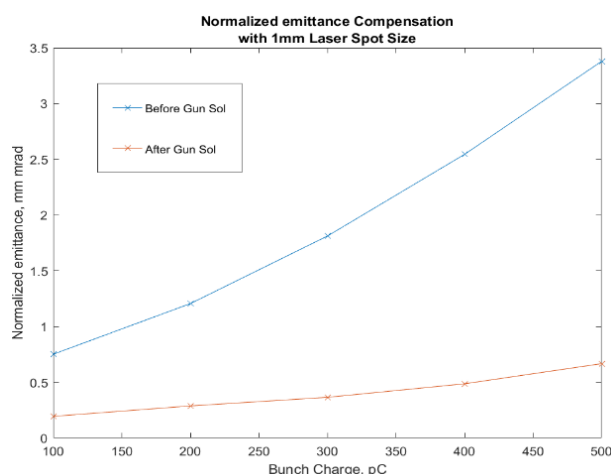


Figure 4: Relationship between emittance-compensation effect by Gun solenoid and bunch charge for 1.0-mm laser spot size (top), 1.5-mm (bottom): blue curve - normalized emittance before the Gun solenoid, red curve - normalized emittance after the Gun solenoid.

The emittance growth due to the nonlinear force inside of the gun is inevitable effect for our system. The different location of the cathode was simulated to test the relationship between the recessed cathode and achievable normalized emittance. The results are shown in Fig. 5. Here, the cathode position, mm, indicates the amount of cathode recession from the cathode nose.

The result showed that the focusing effect inside of the Gun depends on the cathode position. Hence, for certain cathode positions, beam radius at the Gun solenoid gets so tiny that solenoidal focusing becomes less effective compared with the beam of other cathode positions. This would be useful giving us a good estimation of cathode position because fine cathode position adjustment is necessary to have better emittance as shown in Fig. 5.

Content from this work may be used under the terms of the CC BY 3.0 licence (© 2018). Any distribution of this work must maintain attribution to the author(s), title of the work, publisher, and DOI.

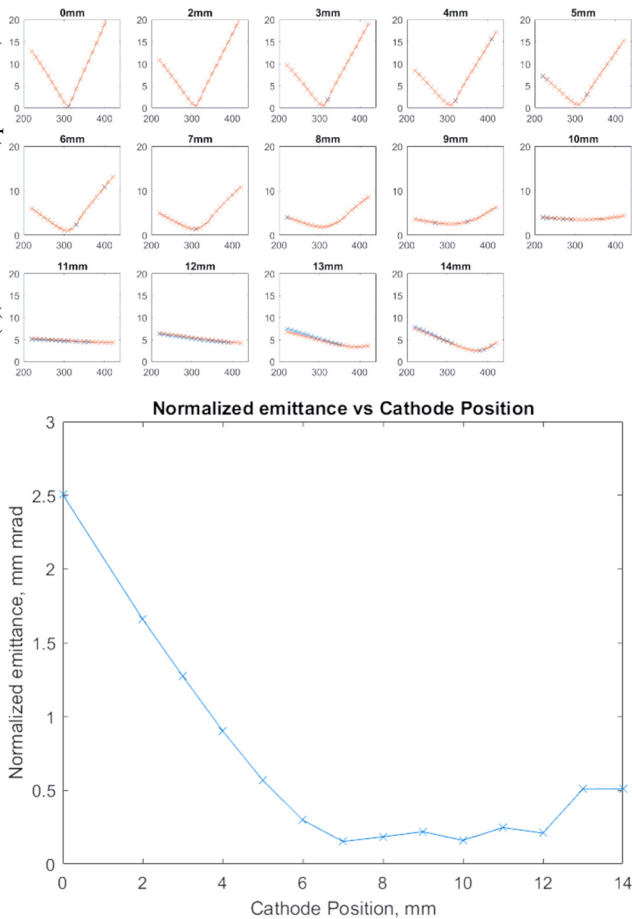


Figure 5: The result of Gun solenoid scan on YAG profile monitor1 for different cathode positions (top) and achievable compensated normalized emittance at YAG profile monitor 1 for each cathode position.

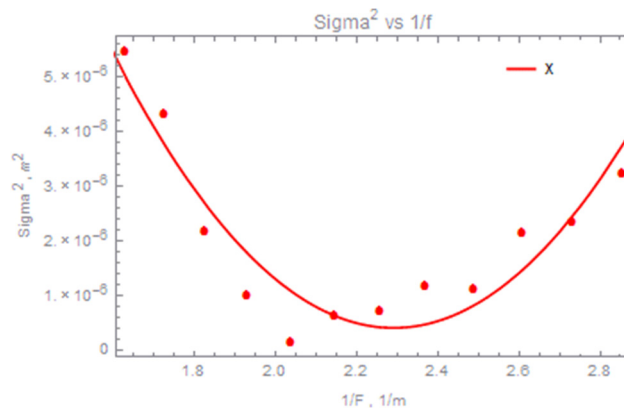
EXPERIMENTAL RESULTS

Experimentally beam emittances were measured using system and script detailed in Fig. 5.

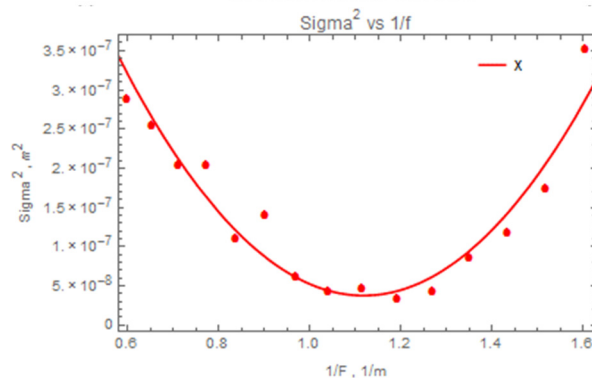
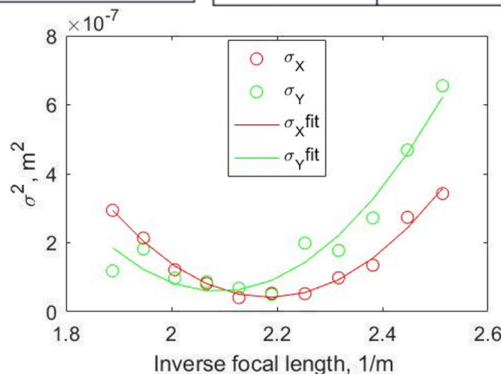
Measurements had been done in three configurations:

- 1) Gun solenoid scan and YAG1 profile monitor.
- 2) LEBT1 solenoid and YAG1 profile monitor.
- 3) LEBT3 solenoid and YAG2 profile monitor.

In all case, the SRF gun voltage was at 1.05 MV and the charge per bunch was larger than 100 pC. Some of experimental results of the emittance measurements by the above solenoid's scan are shown in Fig. 6. Measured normalized emittances in horizontal plane were 0.48, 0.95, 0.58 mm mrad for horizontally, correspondingly.



fit	ax^2+bx+c	β_x [m]	5.00816
a	0.0000104474	α_x [rad]	-10.0929
b	-0.0000478713	ϵ_x [m rad]	1.58662×10^{-7}
c	0.0000552547	ϵ_{xn} [m rad]	4.8468×10^{-7}



fit	ax^2+bx+c	β_x [m]	5.29172
a	1.05177×10^{-6}	α_x [rad]	-0.752514
b	-2.35158×10^{-6}	ϵ_x [m rad]	1.89218×10^{-7}
c	1.35199×10^{-6}	ϵ_{xn} [m rad]	5.77651×10^{-7}

Figure 6: Results of three emittance measurements performed using three different solenoid's scans: (a) the gun solenoid and YAG1 profile monitor with 500pC; (b) the LEBT1 solenoid and YAG1 profile monitor with 300pC; (c) LEBT3 solenoid and YAG2 profile monitor with 100pC.

Possible explanation of larger value of the beam emittance measured using LEPT1 solenoid is its close proximity to the YAG 1 profile monitor and limited resolution of the later. We plan to continue detailed studies of the beam emittance from our unique SRF gun.

CONCLUSIONS

All the experimental results indicate that our SRF gun is generating electron bunches with normalized emittance at submicron scale for bunch charges ~ 0.5 nC. Therefore, the 113 MHz SRF gun is capable of generating CW beam (in our case 78 kHz rep-rate provided by the laser) with high charge per bunch and sub-micron normalized emittances. Our experimental results also reflect the simulation results done by PARMELA with good agreements, but we will pursue further verification and more detailed comparison. As PARMELA predicts, the fine adjustment of laser spot size is necessary to minimize the normalized emittance and its estimation can be done by Gun solenoid scan. In our low energy transport beamline, we have a “pepper pot” system located in front of the YAG2 profile monitor, which we plan to use for further measurements and analysis our beam.

ACKNOWLEDGMENTS

Work is supported by Brookhaven Science Associates, LLC under Contract No. DEAC0298CH10886 with the U.S. Department of Energy, DOE NP office grant DE-FOA-0000632, and NSF grant PHY-1415252.

REFERENCES

- [1] V. N. Litvinenko and Y. S. Derbenev, *Phys. Rev. Lett.* 102, 114801 (2009).
- [2] V. N. Litvinenko, “Electron-Ion Collider eRHIC” in “Challenges and goals for accelerators in the XXIst century”, edited by S. Myers and O. Bruning, World Scientific Publishing Co, 2016. ISBN #9789814436403, p. 523.
- [3] V. N. Litvinenko *et al.*, in *Proc. of IPAC'14*, Dresden, Germany, paper MOPRO013, 2014.
- [4] Parmela, <http://1aacg.1anl.gov/>
- [5] Yuan Hui Wu and V. N. Litvinenko, in *Proc. of IPAC'16*, Busan, Korea, paper WEPOY, 2016.

Content from this work may be used under the terms of the CC BY 3.0 licence (© 2018). Any distribution of this work must maintain attribution to the author(s), title of the work, publisher, and DOI.

INDUCING MICROBUNCHING IN THE CLARA FEL TEST FACILITY

A. D. Brynes*

STFC Daresbury Laboratory & Cockcroft Institute, Warrington, UK

Abstract

We present simulation studies of the laser heater interaction in the CLARA FEL test facility using a non-uniform laser pulse. The microbunching instability, which manifests itself as correlated energy or density modulations in an electron bunch, can degrade the performance of an FEL. Most x-ray free electron lasers (FELs) utilise a so-called laser heater system to impose a small increase in the uncorrelated energy spread of the bunch at low energy to damp the instability – this technique involves imposing a laser pulse on the bunch while it is propagating through an undulator in a dispersive region. However, if the instability can be controlled, the electron bunch profile can be manipulated, yielding novel applications for the FEL, or for generation of THz radiation. Control of the microbunching instability can be achieved by modulating the intensity profile of the laser heater pulse to impose a non-uniform kick along the electron bunch. We have simulated this interaction for various laser intensity profiles and bunch compression factors.

INTRODUCTION

The quality of a photon beam produced by an FEL, in terms of spatial and temporal coherence, is strongly dependent on the electron bunch parameters. One important factor which can degrade the quality of an electron bunch in an FEL is the influence of collective effects, such as coherent synchrotron radiation (CSR) [1], or the microbunching instability [2]. This instability arises from density or energy variations in the bunch at low energies (due to factors such as shot noise [3], or longitudinal space charge [4]), and can become amplified due to CSR in dispersive regions, for example in bunch compressors [5]. Upon reaching the FEL undulator section, the electron beam can develop a correlated energy spread, which can limit the performance of x-ray FELs. The most commonly implemented solution to this is the laser heater [6].

Laser heater systems have proven to be crucial in improving the performance of x-ray FELs [7–9]. Recent results have also shown that, through modulating the temporal profile of the laser pulse used in the laser heater, it is possible to achieve a greater degree of control over the longitudinal profile of the electron bunch, yielding novel applications in the production of multi-colour FEL beams, or the production of THz radiation via a bunch with induced microbunching [10]. This technique is similar to the echo-enabled harmonic generation scheme [11], but it can achieve similar results in a shorter space, as it does not require multiple modulators before the FEL radiator section. In this paper we investigate the possibility of providing a tunable longitudinal profile of the

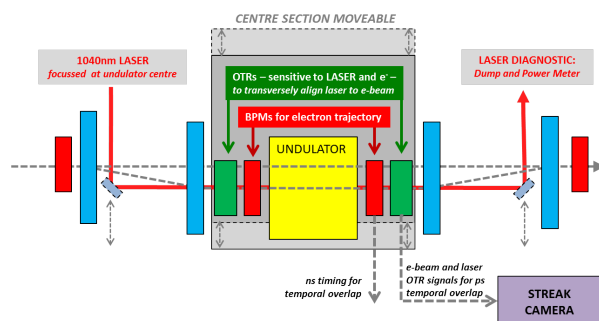


Figure 1: Schematic of laser heater system. Dipoles are shown in blue.

electron beam in the CLARA FEL test facility [12], which is currently under construction at Daresbury Laboratory.

THE CLARA LASER HEATER

In a typical laser heater system, an unmodulated Gaussian laser pulse is propagated with the bunch in the undulator, and any small-scale modulation is removed through the uncorrelated energy spread increase and the R_{52} parameter of the second half of the chicane. A schematic of the CLARA laser heater system is shown in Fig. 1, and the laser heater system parameters are given in Table 1; further details can be found in [13]. Simulations have shown that, while the microbunching instability is not expected to have a large impact on the nominal CLARA modes of operation, it would still be useful to install a laser heater in order to investigate potential methods of utilising the laser heater in novel configurations in order to achieve flexible control of the electron bunch properties. Current profiles and longitudinal distributions up to the exit of the CLARA accelerating section, at 240 MeV, have been simulated using the Elegant code [14] (with CSR and longitudinal space charge included) for the nominal laser heater operating mode, and with the laser heater off are shown in Fig. 2. In the nominal laser heating operating mode, sufficient power will be available to damp any small-scale structure in the electron bunch. Simulations have shown that a small increase in the RMS energy spread of 25 keV, or 0.1 % of the final beam energy, should be sufficient to heat the beam without greatly degrading the quality of the FEL – for this nominal operating mode of the laser heater, a pulse energy of around 48 μ J is required.

CHIRPED-PULSE BEATING

There are various ways of using modified laser pulses to modulate the longitudinal profile of an electron bunch. One method for achieving this is through chirped-pulse beating [15] of the laser heater pulse. The pulse is stretched

* alexander.brynes@stfc.ac.uk

Content from this work may be used under the terms of the CC BY 3.0 licence (© 2018). Any distribution of this work must maintain attribution to the author(s), title of the work, publisher, and DOI.

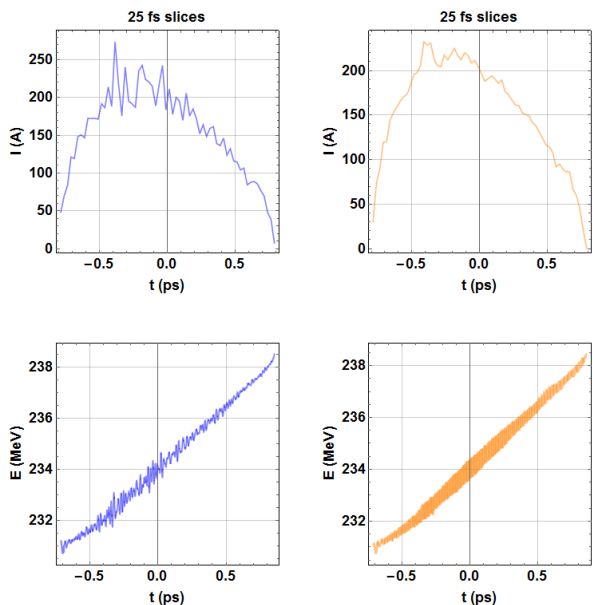


Figure 2: Current profiles at full energy for: Left: laser heater off; Right: laser heater at nominal settings.

Table 1: Laser Heater System Parameters

BEAM TRANSPORT	
Chicane magnet length	10 cm
Chicane magnet bend angle	0 – 5 °
Beam energy	100 – 200 MeV
Emittance	0.5 mm–mrad
UNDULATOR	
Period	60 mm
Number of full periods	8
Total length inc. end terminations	585 mm
Minimum undulator gap	24 mm
Undulator parameter	0.8 – 3.0
LASER	
Wavelength	1040 nm
Spot size σ_{rad} at undulator centre	$\leq 500 \mu\text{m}$
Pulse energy	80 μJ

temporally (or chirped), then split in a Michelson interferometer, one arm of which has a variable length. The two laser pulses are recombined, and they overlap in the temporal domain. By varying the length of the interferometer arm, a delay between the two pulses can be created, giving rise to a laser pulse with a beat frequency that is directly related to the delay parameter τ . The intensity profile of such a laser pulse is given by:

$$I_{\text{tot}}(t) = I^+(t) + I^-(t) + E_0^2 \left(\frac{\sigma}{\sigma_n} \right) \times \exp\left(\frac{-2t^2 - \tau^2}{\sigma_n^2} \right) \cos\left(\frac{2t\tau}{\sigma_n\sigma} + \omega_0\tau \right), \quad (1)$$

with E_0 the field strength of the initial pulse, σ the Gaussian half-width of the initial pulse, σ_n the stretched pulse half-

width, ω_0 the centre of the optical pulse spectrum, and $I^\pm = E_0^2 \frac{\sigma}{2\sigma_n} \exp(-2(t \pm \frac{\tau}{2})^2 / \sigma_n^2)$. For a frequency chirp rate of μ , the beat frequency of the modulated laser is given by $f(\tau, \mu) \approx \mu\tau/2\pi$ [15]. We can take the parameters for the CLARA photoinjector laser pulse stretcher as an example: the initial laser pulse, with an rms duration of 76 fs will be stretched to a length of 1–8 ps. The longer laser pulse should provide consistent overlap with the electron bunch, which has a FWHM duration of 4 ps in the laser heater section.

The interaction of such a modulated laser pulse with an electron bunch undergoing periodic motion can cause the bunch to develop longitudinal structure, thus inducing the microbunching instability. Taking the parameters for the CLARA laser heater and applying the chirped-pulse beating technique, we can obtain a range of longitudinal intensity profiles, as shown in Fig. 3. The flexibility of laser intensity modulations provided by this technique could lead to the generation of a range of customisable longitudinal electron beam profiles.

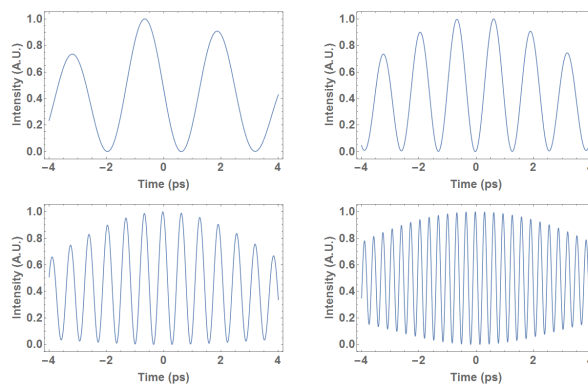


Figure 3: Calculated intensity profiles of modulated laser pulses for: Top left: 1 ps; top right: 2ps delay; bottom left: 4ps delay; bottom right: 8ps delay.

LASER HEATER SIMULATIONS

The interaction of a modulated laser pulse with the electron bunch in the CLARA laser heater chicane has been modelled using the Elegant simulation code [14], which allows the user to implement custom laser fields in a laser-electron interaction. Scans of a number of laser heater parameters have been performed in order to determine the optimal settings for inducing the largest density/energy variations in the bunch. After the laser heater interaction, which occurs at around 130 MeV, the bunch is shortened in a magnetic compression chicane and accelerated to its full energy of 240 MeV. As shown in [5], any perturbations in the bunch density or energy can be amplified in a bunch compressor, and so we should expect to observe a more pronounced microbunching effect after compression.

A number of operating modes have been specified for CLARA, depending on the electron bunch length and the energy [16]; here we simulate the chirped-pulse beating interaction for the Short bunch mode at 240 MeV. Parameter scans over modulation wavelength and bunch compressor

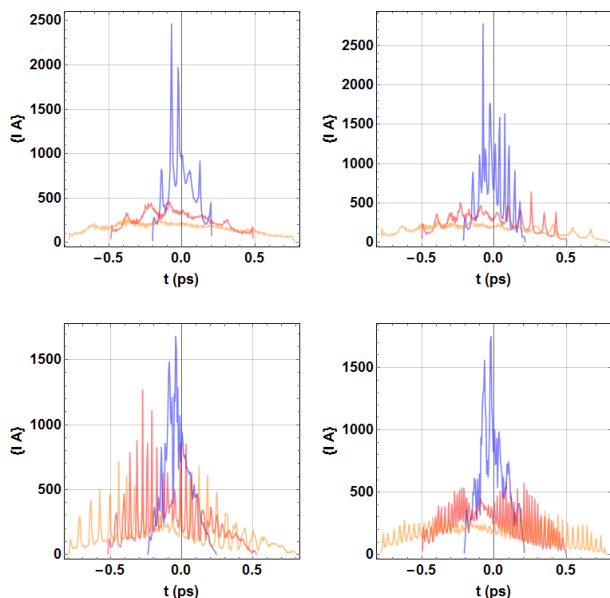


Figure 4: Current profiles for scans of bunch compression factor for the laser intensity profiles given in Fig. 3: Blue: 1.4; Red: 3.0; Orange: 4.6.

angle have been performed in simulations in order to determine the effects of varying these parameters on the energy and longitudinal profile of the bunch. The laser intensity profiles shown in Fig. 3 correspond to modulation wavelengths of $376\ \mu\text{m}$, $188\ \mu\text{m}$, $94\ \mu\text{m}$ and $47\ \mu\text{m}$. The bunch compressor angle was set to $104\ \text{mrad}$, $104.5\ \text{mrad}$ and $105\ \text{mrad}$ (the nominal setting for the short bunch operating mode), corresponding to compression factors of 1.4, 3.0, and 4.6, respectively. Current profiles for various bunch compression factors and modulation wavelengths are shown in Fig. 4. We see that, as the modulation wavelength decreases, the electrons become more tightly (micro-)bunched. As the compression factor increases, we see much larger peaks in the current profile as the bunch becomes maximally compressed, but with fewer peaks due to the shorter bunch length. In Fig. 5 we show the bunch energy profiles only for the maximally compressed bunch at the wavelengths given above, as this is where the energy modulations are most pronounced; at most other bunch compression factors, the R_{52} parameter of the laser heater chicane was sufficient to remove longitudinal energy variations along the bunch. These energy profiles show that it may be possible to use this method to produce multi-colour FEL light in CLARA (similar to [10]), but further simulations are needed to confirm this.

From these simulations we can see that, by varying the modulation wavelength of the laser heater, we can induce a variation in the current profile of the electron bunch. The flexibility that the chirped-pulse beating technique affords in terms of the laser pulse beating frequency, in addition to the variable bunch compression factor, could increase the range of FEL pulse characteristics that CLARA can provide.

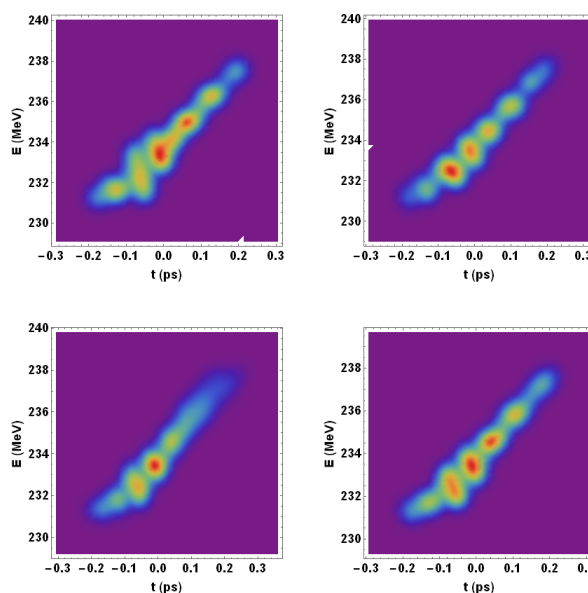


Figure 5: Energy profiles for the laser intensity profiles given in Fig. 3 near maximal bunch compression factor.

SUMMARY

We have proposed a method of inducing small-scale structure on bunches in the CLARA FEL test facility via the interaction with a frequency-modulated laser. The flexibility of the frequency modulations offered by the chirped-pulse beating method, along with the variation of the laser heater parameters and the bunch compression schemes, may provide a range of new modes of operation for the FEL. Further work will include simulations of these modulated electron bunches in the CLARA undulator section, to investigate the applicability of this technique to novel FEL schemes, and the potential for the generation of THz radiation.

REFERENCES

- [1] E.L. Saldin *et al.* On the coherent radiation of an electron bunch moving in an arc of a circle. *Nucl. Instrum. Meth. A*, 398(2):373 – 394, 1997.
- [2] D. Ratner *et al.* “Time-resolved imaging of the microbunching instability and energy spread at the Linac Coherent Light Source”. *Phys. Rev. ST Accel. Beams*, 18:030704, 2015.
- [3] D. Ratner *et al.* “Three dimensional analysis of longitudinal space charge microbunching starting from shot noise”. *SLAC-PUB-13392*, 2008.
- [4] J. Rosenzweig *et al.* “Space-charge oscillations in a self-modulated electron beam in multi-undulator free-electron lasers”. *TESLA FEL Reports 1996-15*.
- [5] Z. Huang & K.-J. Kim. “Formulas for coherent synchrotron radiation microbunching in a bunch compressor chicane”. *Phys. Rev. ST Accel. Beams*, 5:074401, 2002.
- [6] Z. Huang *et al.* “Suppression of microbunching instability in the linac coherent light source”. *Phys. Rev. ST Accel. Beams*, 7:074401, 2004.

- Content from this work may be used under the terms of the CC BY 3.0 licence (© 2018). Any distribution of this work must maintain attribution to the author(s), title of the work, publisher, and DOI.
- [7] Z. Huang *et al.* “Measurements of the linac coherent light source laser heater and its impact on the x-ray free electron laser performance”. *Phys. Rev. ST Accel. Beams*, 13:020703, 2010.
 - [8] S. Spampinati *et al.* “Laser heater commissioning at an externally seeded free-electron laser”. *Phys. Rev. ST Accel. Beams*, 17:120705, 2014.
 - [9] J. Lee *et al.* “PAL-XFEL laser heater commissioning”. *Nucl. Instrum. Meth. A*, 2016.
 - [10] E. Roussel *et al.* “New scenarios of microbunching instability control in electron linacs and free electron lasers”. *Proceedings of IPAC17, Copenhagen, Denmark*, 2017.
 - [11] G. Stupakov. “Using the beam-echo effect for generation of short-wavelength radiation”. *Phys. Rev. Lett.*, 102:074801, 2009.
 - [12] J. A. Clarke *et al.* “CLARA conceptual design report”. *Journal of Instrumentation*, 9(05):T05001, 2014.
 - [13] A. D. Brynes *et al.* “Laser heater design for the CLARA FEL test facility”. *Proceedings of IPAC17, Copenhagen, Denmark*, 2017.
 - [14] M. Borland. “elegant: A flexible SDDS-compliant code for accelerator simulation”. *Proceedings of ICAP'00, Darmstadt, Germany*, 2000.
 - [15] A. S. Weling & D. H. Auston. “Novel sources and detectors for coherent tunable narrow-band terahertz radiation in free space”. *Journal of the Optical Society of America B*, 13(12):2783, 1996.
 - [16] P. H. Williams *et al.* “Developments in the CLARA FEL test facility accelerator design and simulations”. *Proceedings of IPAC16, Busan, Korea*, 2016.

NUMERICAL STUDY OF CHERENKOV RADIATION FROM THIN SILICA AEROGEL*

H. Hama[†], K. Nanbu, H. Saito, Y. Saito,

Research Center for Electron Photon Science, Tohoku University, Sendai, Japan

Abstract

Vavilov-Cherenkov radiation, usually just Cherenkov radiation (CR), is commonly used in high energy charged particle and cosmic rays detectors. We have studied CR emitted from very low refractive index material such as silica-aerogel and found it may be useful tool for electron beam diagnostics since the opening angle (Cherenkov angle) is small, then the CR can be transported onto a detector located far from the radiator. We have prepared a thin (1 mm thick) hydrophobic silica-aerogel having refractive index of 1.05 that has been developed at Chiba University. Since the intensity of CR is much stronger than that of optical transition radiation, the CR is a better light source for low intensity beam diagnostics. In order to apply the CR to measurement of bunch length of electron beams, we have investigated properties of CR by numerical simulation study based on the Liénard-Wiechert potentials. In addition, possibility of intense THz source is also discussed.

CHERENKOV RADIATION

Frank-Tamm theory [1] explaining properties of the Vavilov-Cherenkov radiation [2,3] without charged particle (de-)acceleration is based on the assertion that a charge moving uniformly in a dielectric medium with the velocity faster than the velocity of light in the medium radiates spherical electromagnetic waves from each point of its trajectory, it is the so-called “Cherenkov ring”. Although the CR property seemed to be mostly understood because Tamm’s first consideration was in 1939, it is however very interesting that we can find some theoretical works regarding “Tamm Problem” arising from an instantaneous acceleration and deceleration of a charge at the beginning and termination of its motion [4,5].

The opening angle, Cherenkov angle θ_C , is in general characterized by the refractive index n and the particle velocity β as

$$\cos\theta_C = 1/(n\beta). \quad (1)$$

Therefore, the radiation does not occur when $n\beta < 1$. Photon numbers of CR between the wavelengths λ_1 and λ_2 is given as [1]

$$N_{\text{photon}} = 2\pi\alpha z \left| \frac{1}{\lambda_1} - \frac{1}{\lambda_2} \right| \sin^2\theta_C, \quad (2)$$

*This work supported by JSPS KAKENHI: Grant numbers JP15K13394 and JP17H01070.

[†]hama@lms.tohoku.ac.jp

where α and z are the fine structure constant and the radiator thickness, respectively. Although common e-beam diagnostics, transition radiation is often employed, the photon number of it is poorly small. Since CR is a significant effect, the study has probed the potential ability of CR for beam diagnostics. For example, yield of 500-nm photons with 1% bandwidth from relativistic electron is ~ 0.5 per electron for a 1-mm thick radiator having $n = 1.5$.

NUMERICAL EVALUATION

We start our analysis with the well-established Liénard-Wiechert potential [6]

$$\frac{dI}{d\omega d\Omega} = \frac{1}{4\pi\epsilon_0} \frac{e^2}{4\pi^2 c(\omega)} \omega^2 \times \left| \int \mathbf{n} \times (\mathbf{n} \times \boldsymbol{\beta}(\omega)) e^{i\omega \left(t' - \frac{\mathbf{n} \cdot \mathbf{r}(t')}{c(\omega)} \right)} dt' \right|^2 \quad (3)$$

where $c(\omega)$ is the speed of light in the medium and $\boldsymbol{\beta}(\omega)$ is a particle speed with respect to $c(\omega)$. A vector \mathbf{n} denotes a unit vector to the observing point from the particle located at $\mathbf{r}(t')$. Assuming a charge travelling in a straight line at a velocity and the velocity of light in the medium is

$$c(\omega) = 1/\sqrt{\epsilon(\omega)\mu_0}, \quad (4)$$

then eq. (3) becomes

$$\frac{dI}{d\omega d\Omega} = \frac{\mu_0}{4\pi} \frac{e^2}{4\pi^2 c(\omega)} \omega^2 v^2 \sin^2\theta \left| \int e^{i\omega(1-\boldsymbol{\beta}(\omega)\cos\theta)} dt' \right|^2. \quad (5)$$

After some mathematical treatment, it can be shown that

$$\int e^{i\omega(1-\boldsymbol{\beta}(\omega)\cos\theta)} dt' = 2\pi\delta[\omega(1-\boldsymbol{\beta}(\omega)\theta)]. \quad (6)$$

Thus, we obtain

$$\frac{dI}{d\omega d\Omega} = \frac{\mu_0}{4\pi} \frac{e^2 \omega^2}{4\pi^2 c(\omega)} \sin^2\theta \left(\frac{\sin\alpha}{\alpha} \right)^2 (dz)^2, \quad (7)$$

where

$$\alpha = \frac{1}{2} [1 - \boldsymbol{\beta}(\omega)\cos\theta] \omega \Delta t, \quad (8)$$

and Δt denotes the time passing through the medium.

Content from this work may be used under the terms of the CC BY 3.0 licence (© 2018). Any distribution of this work must maintain attribution to the author(s), title of the work, publisher, and DOI.

Hereafter we have used a refractive index $n = 1.05$ for the radiator medium and an electron energy of 30 MeV for numerical evaluations. Spatial distributions of the Cherenkov ring from single electron calculated for the wavelengths of $3 \mu\text{m}$ and $30 \mu\text{m}$ is shown in Fig. 1. The observed angular range is -0.5 rad to $+0.5 \text{ rad}$ in both horizontal and vertical planes while the Cherenkov angle is 0.31 rad (17.75°). It should be noted that the calculated angular distributions of air CR using presented parameters in Figs. 2 and 4 of Ref. [5] mostly corresponds to the exact solutions given in the article. As one notices that the Cherenkov ring of longer wavelength is getting fat. It is because of laxly interference condition.

The phenomenon is much more clearly seen in Fig. 2. In addition, since the intensity of CR is inversely proportional to the square of the wavelength, even the shorter bunch length such as 100 fs, coherent enhancement of the radiation intensity is not much impressive (see Fig. 3).

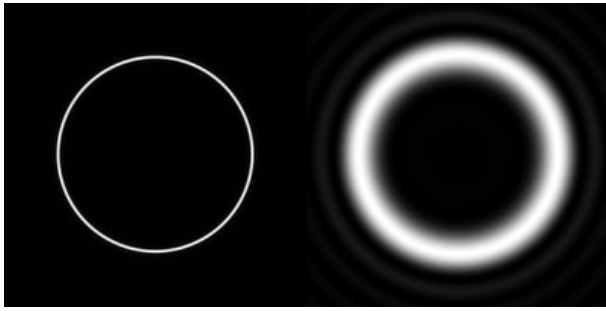


Figure 1: Calculated Cherenkov rings for the wavelengths of $3 \mu\text{m}$ (left) and $30 \mu\text{m}$ (right).

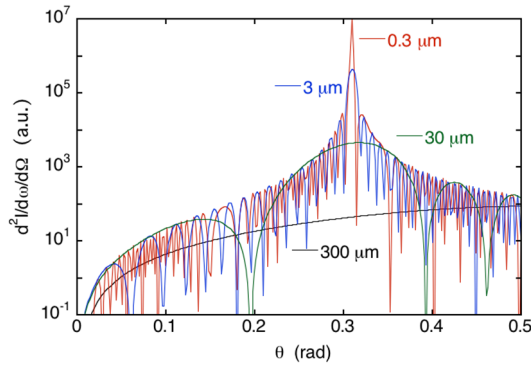


Figure 2: Angular distributions of CR for various wavelengths.

BUNCH LENGTH MEASUREMENT

As indicated in Fig. 4, observable bunch length is possibly observed as

$$\sigma_{\text{observed}} = \sqrt{(\sigma_L \cos \theta_C)^2 + (\sigma_T \sin \theta_C)^2}. \quad (9)$$

Note the radiator thickness does not affect the temporal structure ideally.

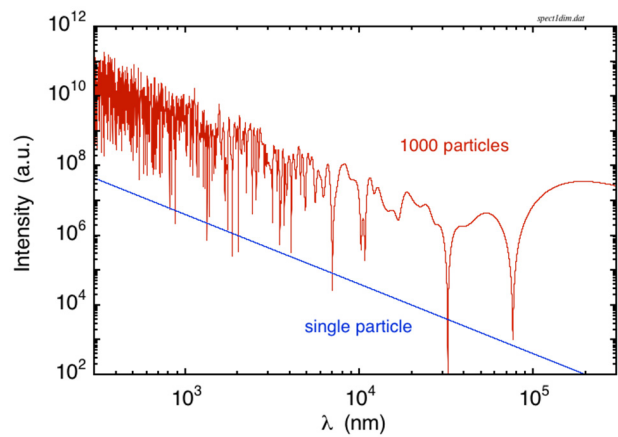


Figure 3: Calculated CR intensities. For the 1000 particle simulation, the bunch length employed is 100 fs (rms).

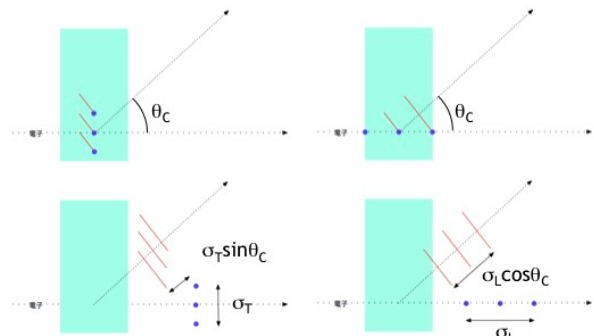


Figure 4: Schematics for bunch length measurement.

By using the approximation $n = 1 + \delta$, we obtain

$$\cos \theta_C = \frac{1}{n\beta} \approx 1 - \frac{\theta_C^2}{2} = \frac{1}{1 + \delta} \approx 1 - \delta, \quad (10)$$

and

$$\sin \theta_C = \sqrt{1 - \cos^2 \theta_C} \approx \sqrt{1 - (1 - \delta)^2} \approx \sqrt{2\delta}. \quad (11)$$

Thus, the effect of the transverse beam size on the observed bunch length is expected to be:

$$\frac{\sigma_T \sin \theta_C}{\sigma_L \cos \theta_C} = \frac{\sigma_T \sqrt{2\delta}}{\sigma_L (1 - \delta)}. \quad (12)$$

If we use a radiator of $n = 1.05$, a ratio of transverse size and bunch length in observed bunch length is ~ 0.33 . It can be concluded that the transverse beam size must be focused onto three times of the bunch length at least.

Looking at wavelengths short enough such as visible region, the radiator thickness affects the width of the Cherenkov ring Γ . It can be expressed by a convolution of radiator thickness and beam transverse size. Using the radiator thickness $2t$ and the beam size projection onto propagation axis $\sigma (= \sigma_T \cos \theta_C)$, we obtain

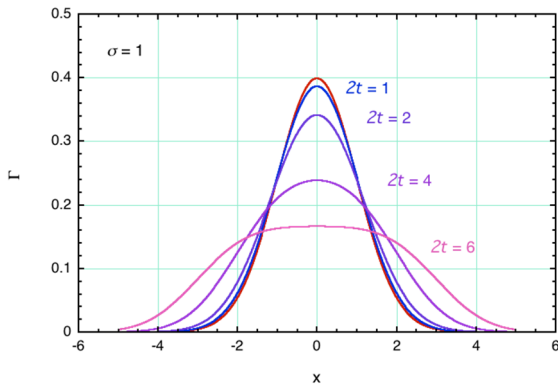


Figure 5: Calculated width of the Cherenkov ring normalized to the transverse beam size.

$$\Gamma = \frac{1}{2t\sqrt{\pi}} \times \left(\sum_n \frac{(-1)^n \left[\frac{1}{\sqrt{2\sigma}}(x+t) \right]^{2n+1}}{n!(2n+1)} - \sum_n \frac{(-1)^n \left[\frac{1}{\sqrt{2\sigma}}(x-t) \right]^{2n+1}}{n!(2n+1)} \right) \quad (13)$$

We can see the effect of the radiator thickness if the beam size is approximately three times larger than the radiator thickness.

TEST EXPERIMENT

A silica aerogel film produced by hydro-phobic treatment for which the refractive index does not change in the vacuum was provided by Chiba University [7,8]. In a test experiment, we used a light extraction system shown in Fig. 6 (upper), and a photograph of the Cherenkov ring is shown in Fig. 6 (lower).

A Cherenkov ring is clearly seen. In order to suppress the Cherenkov angle for light transportation, we employed the minimum refractive index silica aerogel available at the moment ($n = 1.05$).

SUMMARY OF FUTURE PROSPECTS

We have studied properties of the Cherenkov radiation from a thin silica aerogel by numerical evaluation. An accelerator test facility, t-ACTS at Tohoku University is capable of providing 100-fsec electron pulses with a beam energy of 30 MeV [9] while employing a velocity-bunching scheme [10]. A thin silica aerogel with water-free hydrophobic treatment is used as Cherenkov radiator. A complete Cherenkov ring emitted from the 1-mm-thick silica aerogel having low refractive index was already observed. Various experiments with Cherenkov light may start soon. Currently, we are developing a specially designed axicon-mirror system to transport the Cherenkov radiation for long distance.

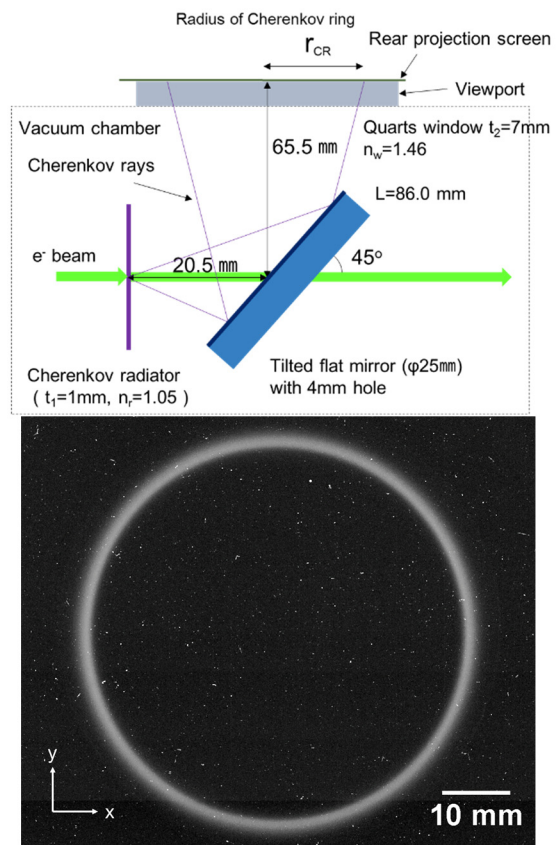


Figure 6: Apparatus of a test experiment (upper) and observed Cherenkov ring (lower) using a 50 MeV electron beam.

REFERENCES

- [1] I. Frank and I. Tamm, *Dokl. Akad. Nauk SSSR*, vol. 14, p. 109 (1937).
- [2] P. A. Cherenkov, *Dokl. Akad. Nauk SSSR*, vol. 2, p. 451 (1934).
- [3] S. I. Vavilov, *Dokl. Akad. Nauk SSSR*, vol. 2, p. 457 (1934).
- [4] G. A. Afanasiev and V. M. Shilov, *J. Phys. D: Appl. Phys.*, vol. 35, p. 854 (2002).
- [5] C. W. James, *AIP Conf. Proc.* vol. 1535, p. 152 (2013).
- [6] J. D. Jackson, *Classical Electrodynamics* (3rd Ed), John Wiley & Sons, New York, 1998.
- [7] M. Tabata *et al.*, *Nucl. Instr. and Meth. A*, vol. 623, p. 339 (2010).
- [8] M. Tabata, I. Adachi, H. Kawai, T. Sumiyoshi, and H. Yokogawa, *Nucl. Instr. and Meth. A*, vol. 668, p. 64 (2012).
- [9] H. Hama *et al.*, *Energy Procedia*, vol. 9, p. 391 (2011).
- [10] L. Serafini and M. Ferrario, *AIP Conf. Proc.*, vol. 581, p. 87 (2001).

RECENT EXPERIMENTAL RESULTS ON HIGH-PEAK-CURRENT ELECTRON BUNCH AND BUNCH TRAINS INTERACTING WITH A THz UNDULATOR*

Xiaolu Su, Lixin Yan[†], Dan Wang, Yifan Liang, Lujia Niu, Qili Tian,
 Dong Wang, Yingchao Du, Wenhui Huang, Chuanxiang Tang,
 Department of Engineering Physics, Tsinghua University, Beijing, China

Abstract

In this paper, experimental results based on THz undulator with widely tunable gap installed at Tsinghua Thomson scattering X-ray (TTX) beamline are introduced. This is a planar permanent magnetic device with 8 regular periods, each 10-cm long. The undulator parameter varies from 9.24–1.39 by changing the magnetic gap from 23 mm to 75 mm. The coherent undulator radiation can be used as a narrow-band THz source with central frequency ranging from 0.4 THz to 10 THz. The bunch length was determined from the radiation intensity at different undulator gaps, agreeing well with simulations. Furthermore, slice energy modulation was directly observed when high-peak-current bunch trains based on nonlinear longitudinal space charge oscillation passed through the undulator. The demonstrated experiment in the THz regime provides a significant scaled tool for FEL mechanism exploration owing to the simplicity of bunch modulation and diagnostics in this range.

INTRODUCTION

High-peak-current electron bunch and bunch trains have many important applications in accelerator research. Ultrashort bunches are widely used in high-gain free electron lasers (FEL) [1], wake-field acceleration [2], ultrafast electron diffraction (UED) [3] and high-power coherent radiation in the terahertz (THz) spectral range [4]. The resonant excitation of wakefield accelerators [5] and production of narrow-band terahertz radiation [6] rely on the development of bunch trains with a large number of equally spaced electron micro bunches. The measurement of ultrashort bunch length and bunch train distribution is of vital importance for these frontier applications.

the electron-bunch form factor, defined as:

$$F(\omega) = \left| \int_{-\infty}^{\infty} e^{i\omega z/c} S(z) dz \right|^2 \quad (1)$$

is derived from the Fourier transform of the longitudinal electron density in the bunch, where $S(z)$ is the distribution function for particles in the bunch, measured relative

to the bunch centre, c is light velocity in vacuum. Form factor is closely related to the bunch longitudinal distribution, both for ultrashort bunch and bunch trains. There have been several methods for bunch form factor or longitudinal distribution measurement. Deflecting cavity is one of the most useful tool for beam diagnostics, converting the longitudinal distribution into transverse coordinate [7]. Electro-optic method can measure bunch length with temporal resolution limited to sub-ps level [8]. Moreover, spectrum and intensity of coherent radiation are used for bunch longitudinal distribution diagnose or monitoring, including coherent diffraction radiation (CDR), coherent transition radiation (CTR) [9], and coherent Smith-Purcell radiation [10]. In this paper, ultrashort bunch length and bunch train distribution are derived from THz radiation energy of a tunable-gap undulator.

Moreover, radiation spectrum and energy from the tunable-gap undulator were measured, which is an intense narrow-band THz source. Terahertz sources have many potential applications in biophysics, medical, industrial imaging, nanostructures, and metal science [11]. Intense THz radiation has been utilized as probes of low-frequency excitations, which is a powerful tool to improve the fundamental understanding of matter. THz sources based on relativistic electrons are usually with high power and have various properties based on emission mechanisms. Coherent undulator radiation is naturally narrow-band, which is of great advantage for scientific research. The resonant frequency is defined as:

$$f = \frac{2\gamma^2 c}{(1 + K^2/2)\lambda_u}, \quad (2)$$

where γ is the Lorentz factor, K is the undulator parameter, and λ_u is the period.

When electron bunch train with the same period passes through undulator, the radiation from bunch tail slips ahead the bunch and interact with the electron ahead. Furthermore, if the resonant wavelength is the same with bunch train period, the radiation from micro bunches add coherently and interact with electron bunch. Bunch energy modulation was observed at Terahertz spectrum during the experiment. The beamline and experimental results are introduced in the following sections.

*Work supported by the National Natural Science Foundation of China (NSFC Grants No. 11475097) and the National Key Scientific Instrument and Equipment Development Project of China (Grants No. 2013YQ12034504).

[†]yanlx@mail.tsinghua.edu.cn

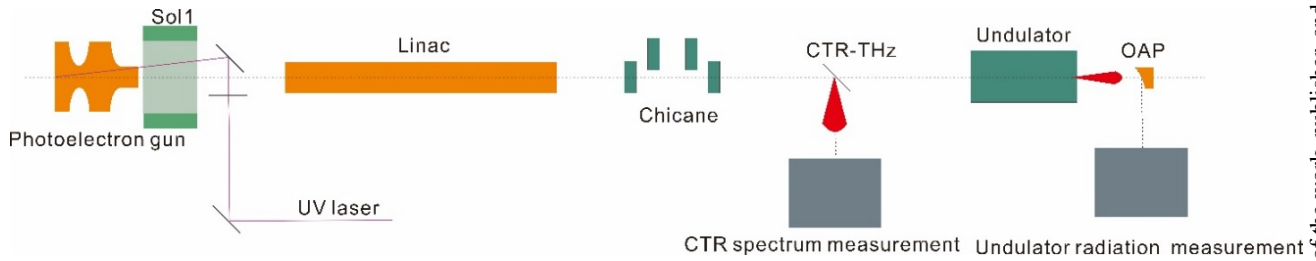


Figure 1: Layout of the Tsinghua beam line and THz system.

EXPERIMENTAL LAYOUT

The experiment was performed at Tsinghua Thomson scattering X-ray (TTX) beamline, which is illustrated in Figure 1. A Ti:sapphire laser system generates ultraviolet driving laser for the photocathode radio-frequency (RF) gun. For ultrashort bunch generation, the laser is a 10-ps quasi flat-top distribution and the bunch train is generated by modulated driving laser from laser stacking using birefringent α -BBO crystals. Bunch charge varies from a few pC to ~ 1 nC according to the laser energy. After acceleration by a 3-m SLAC-type traveling wave accelerating section, the bunch energy increases up to 45 MeV. The bunch is compressed by a magnetic chicane to change bunch length or period of electron bunch train.

The undulator is installed downstream the chicane, and it is an widely tunable permanent magnetic planar undulator with eight regular periods, each of which are 10 cm long. The magnetic gap is widely tunable from 23 to 75 mm. According to Halbach's fitting equation, the peak magnetic field is:

$$B_0 [T] = 3.0255 \times e^{-5.2255(\frac{g}{\lambda_u}) + 1.6202(\frac{g}{\lambda_u})^2}, \quad (3)$$

where g is the magnetic gap. The undulator parameter,

$$K = \frac{eB_0\lambda_u}{2\pi mc} = 0.934\lambda_u [cm] B_0 [T], \quad (4)$$

varies from 9.24 to 1.39 continuously. The undulator parameter is plotted as a function of undulator magnetic gap in Figure 2.

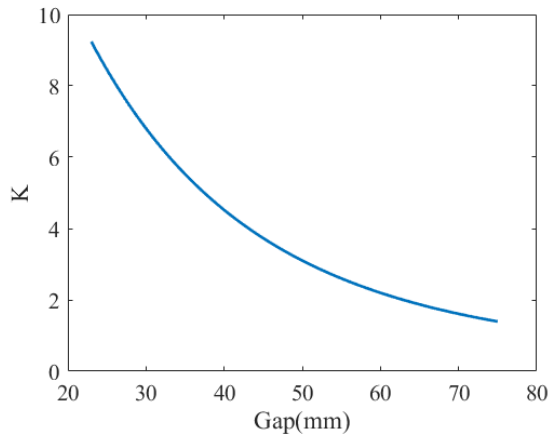


Figure 2: Undulator parameter as a function of undulator magnetic gap.

EXPERIMENTAL RESULTS

Radiation Energy and Spectrum Measurement

An ultrashort Gaussian bunch was generated by 10-ps quasi-flat-top driving laser and compressed by chicane. The radiation energy was collected by off-axis parabolic mirrors and measured by Golay cell detector. The radiation spectrum was measured by Michelson interferometer. The measured autocorrelation curve and corresponding energy spectrum, when undulator gap was 30 mm and bunch energy 28 MeV, are shown in Figure 3. The central frequency is about 0.73 THz, which agrees well with theoretical calculation. The measured energy was μJ level depending on central frequency and bunch properties.

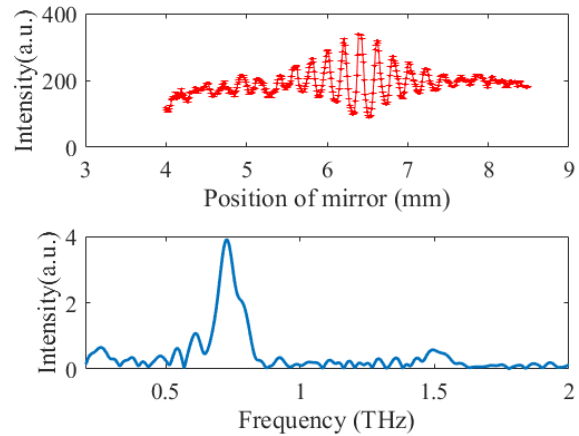


Figure 3: Measured autocorrelation curve (top) and the converted radiation spectrum (bottom).

Bunch Length Measurement

Coherent radiation intensity is closely related to form factor, which is determined by bunch length. For undulator radiation, the radiated energy is mainly influenced by diffraction effects at low central frequency but limited by form factor at high frequency. The radiation energy curve was measured as we scanned undulator gap continuously. The curve shape is determined by bunch length, as shown in Figure 4. The bunch length was delivered from fitting of Gaussian bunch radiation energy. From the radiation energy curve, the ultrashort bunch length was 110 fs. The resolution is determined by bunch energy and undulator parameters.

CONCLUSION

Recent experimental results on high-peak-current electron bunch and bunch trains interacting with a THz undulator are introduced in this paper. The narrow-band THz radiation energy and spectrum were measured. Bunch length were delivered from energy undulator gap curve. Furthermore, bunch trains based on nonlinear longitudinal space charge oscillation were generated and passed through the tunable-gap undulator. Slice energy modulation were observed directly, providing a significant scaled tool for FEL mechanism exploration.

ACKNOWLEDGMENT

The authors are grateful to Dr. Hai-Xiao Deng and Dr. Huihua Lu's group for their help in the experiment.

REFERENCES

- [1] P. Emma *et al.*, "First lasing and operation of an ångstrom-wavelength free-electron laser," *Nature Photonics*, 2010, 4(9): 641-647.
- [2] A. Pukhov and J. Meyer-ter-Vehn, "Laser wake-field acceleration: the highly non-linear broken-wave regime," *Applied Physics B: Lasers and Optics*, 2002, 74(4): 355-361.
- [3] V. Lobastov *et al.*, "Ultrafast Electron Diffraction," *Ultrafast Optics IV*, Springer, New York, 2004: 419-435.
- [4] G. Carr *et al.*, "High-power terahertz radiation from relativistic electrons," *Nature*, 2002, 420(6912): 153.
- [5] C. Jing *et al.*, "Observation of enhanced transformer ratio in collinear wakefield acceleration," *AIP Conference Proceedings*, 2006, 877(1): 511-519.
- [6] Y. Li and K.-J. Kim, "Nonrelativistic electron bunch train for coherently enhanced terahertz radiation sources," *Applied Physics Letters*, 2008, 92(1): 014101.
- [7] R. Akre *et al.*, "Bunch length measurements using a transverse RF deflecting structure in the SLAC linac," *Proc. EPAC'02*.
- [8] X. Yan *et al.*, "Subpicosecond electro-optic measurement of relativistic electron pulses," *Physical Review Letters*, 2000, 85(16): 3404.
- [9] A. Murokh *et al.*, "Bunch length measurement of picosecond electron beams from a photoinjector using coherent transition radiation," *Nuclear Instruments and Methods in Physics Research Section A: Accelerators, Spectrometers, Detectors and Associated Equipment*, 1998, 410(3): 452-460.
- [10] D. Nguyen, "Measuring short electron bunch lengths using coherent smith-purcell radiation," U.S. Patent 5,889,797, 1999-3-30.
- [11] M. Kemp, "Millimetre wave and terahertz technology for detection of concealed threats-a review," *Infrared and Millimeter Waves, 2007 and the 2007 15th International Conference on Terahertz Electronics. IRMMW-THz. Joint 32nd International Conference on. IEEE*, 2007: 647-648.
- [12] Z. Zhang *et al.*, "Tunable high-intensity electron bunch train production based on nonlinear longitudinal space charge oscillation," *Physical Review Letters* 2016, 116(18): 184801.

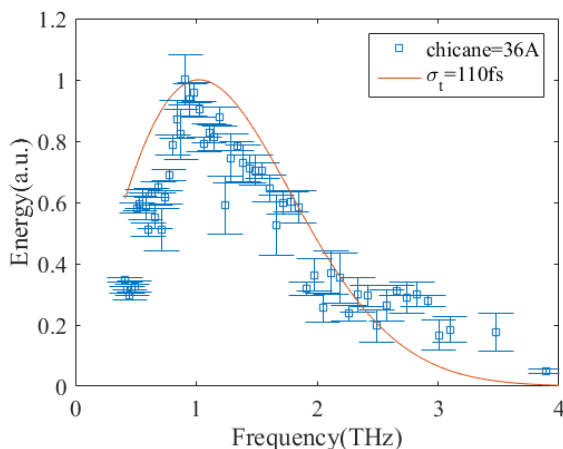


Figure 4: Radiation energy as a function of central frequency. The square was measured and solid line was from theory.

Observation of Bunch-Train Energy Modulation

A high-intensity electron bunch train, based on a nonlinear longitudinal space charge oscillation, was generated with about 1-ps separation (corresponding to a frequency of 1 THz) [12]. If the undulator resonant frequency was close to bunch train separation, the radiation from micro bunch in the tail slipped ahead per resonant wavelength every undulator period. The slipped radiation added coherently with radiation from the micro bunch ahead and interacted with the bunch, resulting in much higher radiation energy due to coherence and bunch modulation from beam and field interaction. The measured energy spectrum was presented in Figure 5, when radiation from micro bunches added coherently, the bunch in the head is modulated obviously.

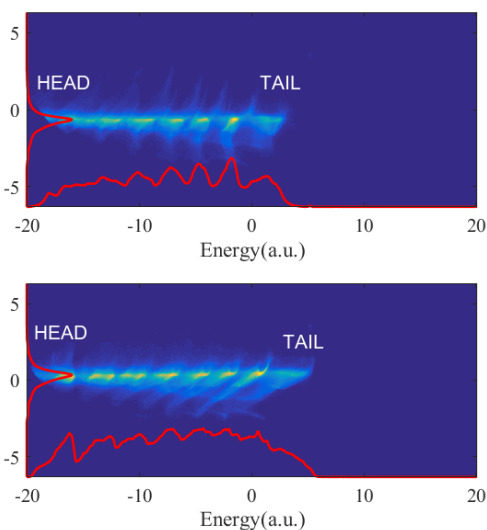


Figure 5: Energy spectrum when radiation from micro bunches added (Top) uncoherently and (Bottom) coherently.

Content from this work may be used under the terms of the CC BY 3.0 licence (© 2018). Any distribution of this work must maintain attribution to the author(s), title of the work, publisher, and DOI.

LARGE-SCALE TURNKEY TIMING DISTRIBUTION SYSTEM FOR NEW GENERATION PHOTON SCIENCE FACILITIES

K. Şafak[†], H. P. H. Cheng, J. Derksen, A. Berlin, E. Cano, A. Dai, D. Forouher, W. Nasimzada, M. Neuhaus, P. Schiepel, E. Seibel, Cycle GmbH, Hamburg, Germany
 A. Kalaydzhyan, J. Meier, D. Schimpf, A. Berg, T. Tilp, F. X. Kärtner¹, CFEL, Hamburg, Germany
¹also at RLE, MIT, Cambridge, Massachusetts, USA

Abstract

We report a large-scale turnkey timing distribution system able to satisfy the most stringent synchronization requirements demanded by new generation light sources such as X-ray free-electron lasers and attoscience centers. Based on the pulsed-optical timing synchronization scheme, the system can serve 15 remote optical and microwave sources in parallel via timing stabilized fiber links. Relative timing jitter between two link outputs is less than 1 fs RMS integrated over an extended measurement time from 1 μ s to 2.5 days. The current system is also able to generate stabilized microwaves at the link outputs with 25-fs RMS precision over 10 h, which can be easily improved to few-femtosecond regime with higher quality VCOs.

INTRODUCTION

Low-noise transfer of time and frequency standards over large distances provides high temporal resolution for ambitious scientific explorations such as sensitive imaging of astronomical objects using multi-telescope arrays [1], comparison of distant optical clocks [2] or gravitational-wave detection using large laser interferometers [3]. In particular, rapidly-emerging new generation light sources such as X-ray free-electron lasers (FELs) [4] and attoscience centers [5] have the most challenging synchronization requirements on the order of few femtoseconds or below to generate ultrashort X-ray pulses for the benefit of creating super-microscopes with sub-atomic spatiotemporal resolution. The critical task in these facilities is to synchronize various pulsed lasers and microwave sources across multi-kilometer distances as required for seeded FELs and attosecond pump-probe experiments.

Recently, it has been shown that the pulsed-optical timing synchronization scheme based on balanced optical cross-correlators (BOCs) and balanced optical-microwave phase detectors (BOMPDs) can deliver sub-femtosecond precision between remotely synchronized lasers and microwave sources in laboratory environment [6,7]. Here, we transform this experimental system into a large-scale turnkey timing distribution system (TDS) that is able to serve 15 remote optical and microwave sources via timing stabilized fiber links. The system exhibits less than 1-fs RMS timing jitter at the outputs of the fiber links over 2.5 days of operation. The current system is able to serve remote microwave devices with 25-fs RMS precision over 10 h which can be easily improved to few femtoseconds with higher quality VCOs.

In this paper, we describe the layout of the TDS together with its dedicated control system. We also discuss the characterization measurements of the timing stabilized fiber links and the remote microwave synchronization.

SYSTEM LAYOUT AND ARCHITECTURE

Figure 1 shows the layout of the TDS capable of serving 15 remote clients. The optical master oscillator (OMO) is a low-noise mode-locked laser operating at 1550-nm center wavelength with a free-running timing jitter of 0.4 fs RMS integrated between 1 kHz and 1 MHz [8]. A BOMPD (i.e., BOMPD-OMO in Fig. 1) is employed to lock the OMO to an external RF master oscillator in order to ensure the TDS operates synchronously with the facility's RF reference (e.g., low-level RF system). Then the output of the OMO is split into 15 separate polarization maintaining (PM) fiber links. In order to preserve the low noise properties of the OMO during the delivery to remote locations, fiber link stabilizers (FLS) are developed. Each FLS contains a BOC to detect the time-of-flight fluctuations of the optical pulses during fiber-link transmission with attosecond precision. Then, the integral control elements of the FLS (i.e., a fiber stretcher and a motorized delay line) are activated to stabilize the arrival time of the delivered optical pulses at the fiber link output. Once the fiber links are stabilized, two-color BOCs (TCBOCs) and BOMPDs are activated to synchronize ultrafast lasers and microwave sources to the link outputs at remote locations. The TCBOC detects the timing error between the two optical pulse trains, emanating from the fiber link output and the remote slave laser. The voltage response of the TCBOC is then used as a feedback signal to control the frequency of the remote slave laser via its

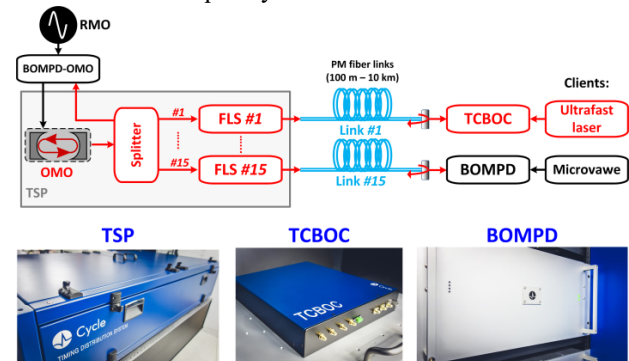


Figure 1: Layout of the timing distribution system (top sketch) and its individual modules as built in the lab (bottom pictures). RMO: RF master oscillator; OMO: optical master oscillator; TSP: temperature-stabilized platform; FLS: fiber link stabilizer; TCBOC: two-color balanced optical cross-correlator; BOMPD: balanced optical-microwave phase detector.

[†] kemal.shafak@cyclelasers.com

Content from this work may be used under the terms of the CC BY 3.0 licence (© 2018). Any distribution of this work must maintain attribution to the author(s), title of the work, publisher, and DOI.

intracavity Piezo actuators. The BOMPD, on the other hand, relies on an optoelectronic-phase-detection scheme between the optical and microwave inputs where the timing error is converted into an intensity modulation of the optical pulse train. The intensity modulation is detected by a balanced detector which generates a voltage signal that is proportional to the phase error between the microwave signal and the optical pulse repetition rate. The voltage signal (or the error signal) is fed back to the microwave source, e.g., to a voltage controlled oscillator (VCO) to correct for its phase error with respect to the optical pulse train.

We have also developed a cost-effective and reliable control system based on the Xilinx hardware platform, with FPGA for fast signal processing, and an ARM core for interfacing and high-level processing. The hardware platform is distributed, with individual control processor dedicated to each element in the TDS (e.g., BOC, TCBOC, etc.). Operation signals are digitized with low-noise, high-bandwidth ADCs, and sampled by the FPGA. These signals can then be processed and output directly to high bandwidth DACs, or passed onto the ARM core, which runs the Linux and EPICS interfaces. Since the hardware description and software development are carried out in the Xilinx-Vivado architecture, the existing control system can be transferred easily to other hardware platforms such as ATCA and MicroTCA.

Figure 2 shows the overview panel of the graphical user interface (GUI) developed for the easy supervision of the TDS where all subsystems can be automatically started and observed. Advance settings of the individual synchronization modules can also be accessed via the TDS-GUI; for instance, to optimize the feedback parameters of the FLS, TCBOC and BOMPD.

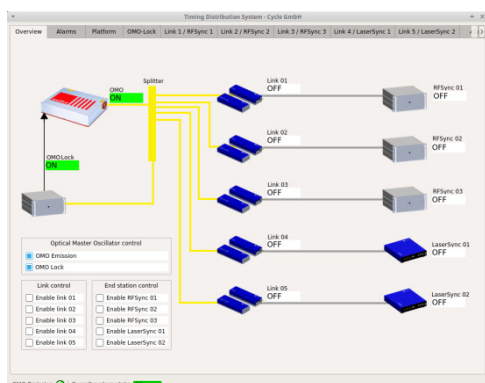


Figure 2: Interactive overview panel of the TDS-GUI.

Another significant development in the control system is the Digital Synchronization Unit (DSU), which is specifically designed to aid the slave oscillator synchronization of the TDS. The DSU carries out a low-noise digital microwave locking that pre-locks the slave optical and microwave oscillators so that the BOC- or the BOMPD-locks can be initiated automatically. The DSU has also an FPGA interface for programmability and offers three important features. First, it can divide the input frequency, so that a frequency can be locked to its (sub-) harmonic. Second, it provides a clock synthesis option. It can generate various low-

voltage locking signals with low latency and jitter, which can be a (sub-) harmonic of the reference input. Third, it has the ability to delay one of the input signals allowing a digitally controlled delay scan between the two sources.

PERFORMANCE CHARACTERIZATION

Timing-stabilized fiber link

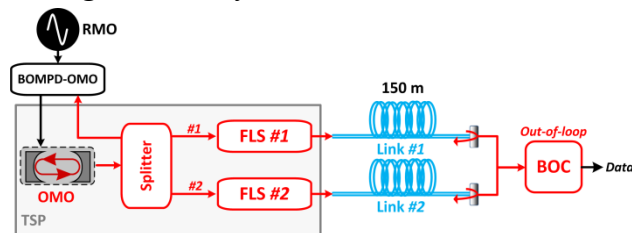


Figure 4: Performance characterization setup of the timing-stabilized fiber links.

The first set of measurements is performed to characterize the relative timing jitter of the fiber links with the setup shown in Fig. 3. Two 150-m long PM fiber links are stabilized with two FLS units where roundtrip delay fluctuations are detected by the BOCs and fed back to the motorized delay lines and the fiber stretchers. Once the control system is activated, it performs an automatic search and locks the fiber links to the zero-voltage crossing of the BOC error signal. Then, the outputs of these two fiber links are combined into a free-running BOC serving as the out-of-loop timing detector.

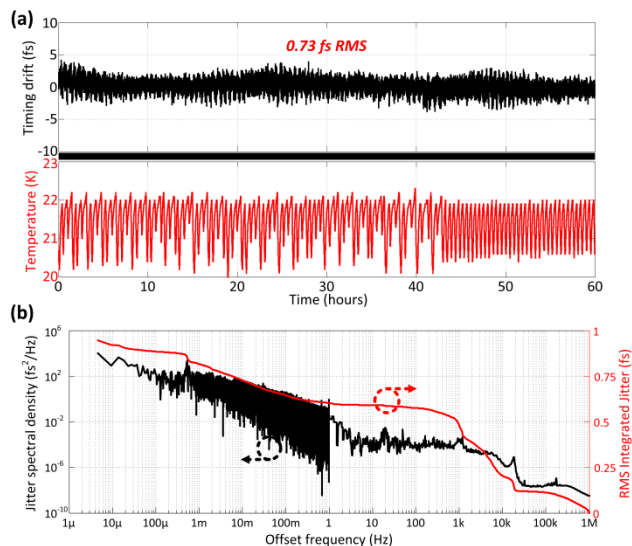


Figure 5: Performance measurements of the timing-stabilized fiber links. (a) Long-term timing drift and environmental temperature. (b) Timing jitter spectral density and integrated timing jitter between 4.6 μ Hz and 1 MHz.

Stabilization of the two fiber links is operated for 60 h without any interruption. The black curve in Fig. 4(a) shows the residual timing drift between the two link outputs measured with 2-Hz sampling, whereas the red curve underneath shows the environmental temperature outside the TSP where the fiber links are placed. Even though the environmental temperature is modulated by 2°C peak-to-

peak with a period of 30 mins, the TDS is able to keep the system synchronized continuously without showing any locking volatility. The out-of-loop timing drift is only 0.73 fs RMS measured over 60 h between the two link outputs. Figure 5(b) shows the timing jitter spectral density between 4.6 μ Hz and 1 MHz. The links exhibit a total integrated timing jitter of less than 1 fs RMS where high frequency noise above 1 Hz amounts to 0.6 fs RMS proving both long-term and short-term sub-femtosecond operation precision of the TDS.

Microwave generation at link ends

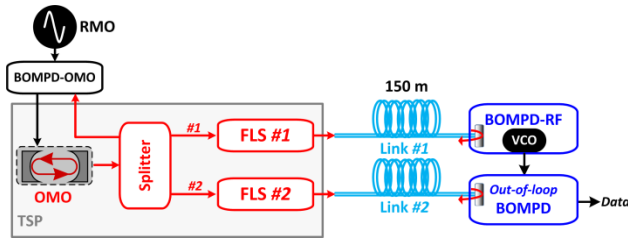


Figure 6: Performance characterization setup of the microwave generation at link ends.

Next, we perform remote microwave synchronization experiments with the setup illustrated in Fig. 5. At the remote of ends of two fiber links, two BOMPDS are constructed which use the timing-stabilized pulse trains of the fiber links as their optical input signals. The first BOMPD (i.e., BOMPD-RF in Fig. 5) contains an integral VCO whose frequency (i.e., 2.856 GHz) is locked to the Link #1 output. The second BOMPD, on the other hand, is used as a free-running detector to measure the out-of-loop timing jitter between the remotely synchronized VCO and the link #2 output.

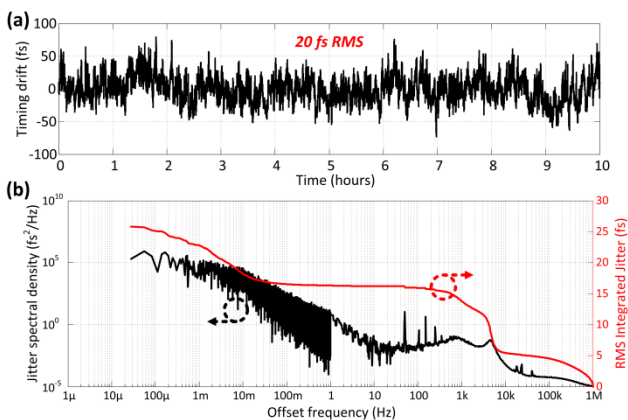


Figure 7: Performance measurements of the microwave generation at link ends. (a) Long-term timing drift sampled at 2 Hz. (b) Timing jitter spectral density and integrated timing jitter between 28 μ Hz and 1 MHz.

Figure 7 shows the long- and short-term stability measurements of the generated microwave with respect to the second fiber link. Out-of-loop timing drift is \sim 20 fs RMS over 10 h (see Fig. 6(a)), whereas total timing jitter integrated from 28 μ Hz to 1 MHz is \sim 25 fs RMS (see

Fig. 6(b)). As can be inferred from the red curve in Figure 7(b), there are two frequency regions where the remote microwave acquires excess noise. First, high frequency noise above 1 kHz amounts to \sim 15 fs RMS which is mainly limited by the inherent noise of the VCO. High frequency performance could be easily improved to few-femtosecond regime by employing higher quality VCOs. Second, low frequency noise below 0.03 Hz (i.e., 33 s) cause the main timing drift contribution with \sim 20 fs RMS. Uncompensated fiber paths used for the intensity modulation of the optical pulse train is quite susceptible to the environmental fluctuations. Long-term performance of the remote microwave synchronization could be also improved by isolating or minimizing such fiber paths.

CONCLUSION & OUTLOOK

The TDS discussed here could enable sub-femtosecond precision synchronization of optical lasers and microwave sources in X-ray photon-science facilities. The current system can serve 15 separate clients via timing stabilized fiber links which exhibit less than 1-fs RMS timing jitter integrated over an extended measurement time from 1 μ s to 2.5 days. Microwave synchronization experiments at the link outputs show \sim 25-fs RMS jitter for the frequency range of 28 μ Hz - 1 MHz. Higher quality VCOs and better environmental isolation of the BOMPD would improve the microwave precision to few femtoseconds. We are currently working also on the remote synchronization of pulsed-laser systems using TCBOCs, which is essential for highly time-resolved pump-probe experiments in new generation light sources.

REFERENCES

- [1] J.-F. Cliche and B. Shillue, "Precision timing control for radioastronomy: maintaining femtosecond synchronization in the Atacama large millimeter array", *IEEE Control Systems*, vol. 26, no. 1, pp. 19-26, 2006.
- [2] C. Lisdat *et al.*, "A clock network for geodesy and fundamental science", *Nat. Commun.*, vol. 7, no. 12443, 2016.
- [3] I. Bartos *et al.*, "The advanced LIGO timing system", *Class. Quantum Grav.*, vol. 27, no. 084025, pp. 1-9, 2010.
- [4] P. Emma *et al.*, "First lasing and operation of an angstrom wavelength free-electron laser", *Nat. Photonics*, vol. 4, pp. 641-647, 2010.
- [5] G. Mourou and T. Tajima, "More intense, shorter pulses", *Science*, vol. 331, pp. 41-42, 2011.
- [6] M. Xin *et al.*, "Attosecond precision multi-kilometer laser microwave network", *Light Sci. Appl.*, vol. 6, e16187, 2017.
- [7] M. Xin *et al.*, "Breaking the femtosecond barrier in multi-kilometer timing synchronization systems", *IEEE J. Sel. Top. Quantum Electron.*, vol. 23, no. 3, 2017.
- [8] K. Şafak, M. Xin, P. T. Callahan, M. Y. Peng, and F. X. Kärtner, "All fiber-coupled, long-term stable timing distribution for free-electron lasers with few-femtosecond jitter", *Struct. Dyn.*, vol. 2, 041715, 2015.

USING A NEURAL NETWORK CONTROL POLICY FOR RAPID SWITCHING BETWEEN BEAM PARAMETERS IN AN FEL

A. L. Edelen^{†*}, Colorado State University, Fort Collins, CO
S.G. Biedron¹, Element Aero, Chicago, IL

J. P. Edelen, Fermi National Accelerator Laboratory, Batavia, IL

S.V. Milton, Los Alamos National Laboratory, Los Alamos, NM

P. J. M. van der Slot, University of Twente, Enschede, The Netherlands

¹also at University of Ljubljana, Ljubljana Slovenia and
University of New Mexico, Albuquerque, NM

Abstract

FEL user facilities often must accommodate requests for a variety of beam parameters. This usually requires skilled operators to tune the machine, reducing the amount of available time for users. In principle, a neural network control policy that is trained on a broad range of operating states could be used to quickly switch between these requests without substantial need for human intervention. We present preliminary results from an ongoing study in which a neural network control policy is investigated for rapid switching between beam parameters in a compact THz FEL.

INTRODUCTION

Free-electron laser (FEL) user facilities often must accommodate requests for a variety of beam parameters. This usually requires skilled human operators to tune the machine manually, thus reducing the amount of available up time for the users. In principle a neural network control policy that is trained on a broad range of operating states could be used to quickly switch between these requests without substantial need for human intervention [1]. Additionally, this policy could be updated concurrently to machine operation as new states are visited or as drift occurs in the system. It also provides a relatively compact way of storing the information (as compared to, e.g., a database of previous settings and measured output). We are exploring this approach using simulations of a compact THz FEL design based on the Twente/Eindhoven University FEL (TEU-FEL) [2]. This an appealing system for this study because it has a relatively small number of components, yet it exhibits non-trivial beam dynamics.

Here, we focus on an initial study: injector and beam-line tuning to achieve specific electron beam parameters at the entrance of the undulator. In this case, changing the operating state consists of specifying a change in energy and then choosing the appropriate injector settings and beamline settings such that the match of the beam into the undulator is preserved and emittance is minimized.

The way the neural network controller is trained is similar to how one might try to do it for a real machine. First, we train a neural network model based on data from a

priori simulations of the machine, with noise added. This creates a surrogate for the simulation that in principle contains the relevant physics of the machine and can execute quickly to facilitate controller training. We then train a reinforcement learning [3] controller via interaction with the learned model. Interaction directly with the simulation can then be used to fine-tune the controller.

We first give an overview of the FEL. This is followed by a discussion of our initial study. We then discuss our current efforts on a comprehensive study that includes start-to-end matching and minimizing the emittance, and we conclude with our future plans for this effort.

FEL LAYOUT AND SIMULATION

The FEL is designed to produce light with a wavelength that is tunable between 200 μm and 800 μm . It consists of a 5.5-cell, 1.3-GHz photocathode RF gun, a beam transport section, and a fixed-gap THz undulator with an undulator parameter K equal to 1. More details on this machine can be found in [4], and Fig. 1 shows the relevant components for this study.

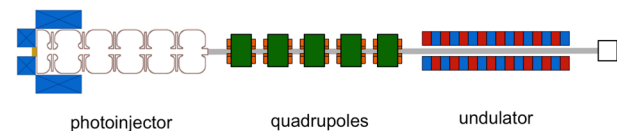


Figure 1: Layout of the accelerator showing the 5.5-cell photoinjector with its bucking coil and solenoid, the quadrupoles, the undulator, and the beam dump. There also are steering coils, but these are excluded, as the simulated electron beam is generated on-axis.

Beam Dynamics Considerations

While this machine is comparatively simple in terms of the number of components and interacting systems, the beam dynamics exhibit some subtleties that if not addressed properly will result in decreased performance of the FEL. Because the bunch charge can be as large as 5 nC and the beam energy is low (3–6 MeV), space-charge effects will be significant both in the photoinjector and in the beamline. A solenoid is typically used to compensate for space-charge effects by matching the beam to the invariant envelope [5]. This can easily be done in long (more than ~ 10 cells) accelerating structures or with in-

Content from this work may be used under the terms of the CC BY 3.0 licence (© 2018). Any distribution of this work must maintain attribution to the author(s), title of the work, publisher, and DOI.

*A.L.E. is partially supported by a scholarship from the Directed Energy Professional Society

†auralee.l.morin@gmail.com

jectors that have a short (e.g. 1.5-cell) gun followed by a drift and a secondary accelerating stage. The TEU-FEL photoinjector, with 5.5 cells, is neither a long gun nor a short gun with a secondary accelerating structure. This decreases the ability to perform adequate compensation of space-charge-induced emittance growth. Additionally, due to physical space constraints there is not enough room to allow the emittance to fully damp before the matching section into the undulator, and because the beam is low-energy, space-charge forces will continue to impact the emittance along the beamline. This complicates the task of focusing the beam even after initial space-charge compensation is performed by the solenoid, which in turn complicates the task of matching the beam into the FEL. Thus, a full study where the gun parameters and the beamline parameters are optimized simultaneously is needed to achieve optimal FEL performance.

PARMELA Simulation

A simulation model of the TEU-FEL injector and beamline was constructed using SUPERFISH [6] for the RF fields and PARMELA [7] for the beam dynamics. Because the coupling between the cells of the cavity is not axially symmetric, a full simulation of the gun geometry could not be conducted using SUPERFISH. Therefore, we approximated the geometry by simulating each of the individual cell types and splicing them together in PARMELA to create the proper field geometry. When compared with measurements of the field geometry this approach performs reasonably well [8]. The solenoid and bucking coil assembly were modelled using PANDRIA [6] using the nominal current settings in the solenoid. The bucking coil was then scaled to cancel the magnetic field on the cathode. The combined field map is then scaled in PARMELA in order to tune the space-charge compensation. The PARMELA simulations were performed using 5000 macro-particles with a 0.1° phase integration step. This was determined to be well within the stable region for reasonable estimation of bulk parameters [8]. In order to achieve proper matching into the undulator, the beam is focused to a waist at the entrance, which means the alpha parameter $\alpha_{x,y} = 0$. The good magnetic field region for equal focusing in both planes requires the beam size to be less than 4 mm [9]. We chose to optimize the beamline, which contains 5 quadrupoles (Q1–Q5), with the same beta function ($\beta_{x,y}$) value at the entrance of the undulator for each electron beam energy: $\beta_{x,y} = 0.106$ [m/rad]. This corresponds to a beam size that is within the optimal field region of the undulator for all energies.

INITIAL BEAMLIN STUDY

For the initial study the aim was to set the quadrupole settings such that specific $\alpha_{x,y}$ and $\beta_{x,y}$ are achieved at the entrance of the undulator for a given electron beam energy. Limited adjustment of the RF power, phase, and solenoid strength is also included.

Neural Network Model

The model was trained to predict the Twiss parameters at the entrance of the undulator, given the RF power, the RF phase, the solenoid strength, and the quadrupole settings. The general setup is shown in Figure 2, and in this case the extraneous outputs are not used during training.

The training set consisted of the output from each iteration of simplex optimization of the quadrupole settings for 12 different beam energies. This looks similar to what one might see in the data archive of an operational accelerator: a lot of tuning around roughly optimal settings. In order to reduce the overall optimization time and simplify the initial problem for the neural network, the gun and the beamline were optimized separately, with the knowledge that the match may not be fully optimized for FEL performance. This training data includes the following variable ranges: -2.14 to 2.11 rad for α_x , -5.76 to 1.45 for α_y , 0.058 to 1.86 m/rad for β_x , 0.074 to 3.65 m/rad for β_y , -0.98 to 0.83 T/m for Q1, 0.65 to 1.98 T/m for Q2, -2.24 to -1.07 T/m for Q3, 0.89 to 2.26 T/m for Q4, -1.90 to -0.23 T/m for Q5, 0.67 to 1.05 for solenoid strength (normalized units), and 10.3° to 21.4° for RF phase.

For the validation set, the optimization data for the 5.7-MeV electron beam was used. The performance of the model in terms of mean absolute error (MAE) and standard deviation (STD) is shown in Table 1. A representative plot from the validation set is shown in Figure 3.

The neural network architecture consists of four hidden layers containing 50, 50, 30, and 30 nodes, respectively. Each node in the hidden layers uses a hyperbolic tangent activation function and a dropout [10] probability of 10%.

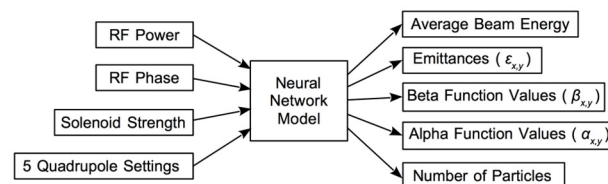


Figure 2: General setup for the neural network model. Output parameters are at the entrance of the undulator.

Content from this work may be used under the terms of the CC BY 3.0 licence (© 2018). Any distribution of this work must maintain attribution to the author(s), title of the work, publisher, and DOI.

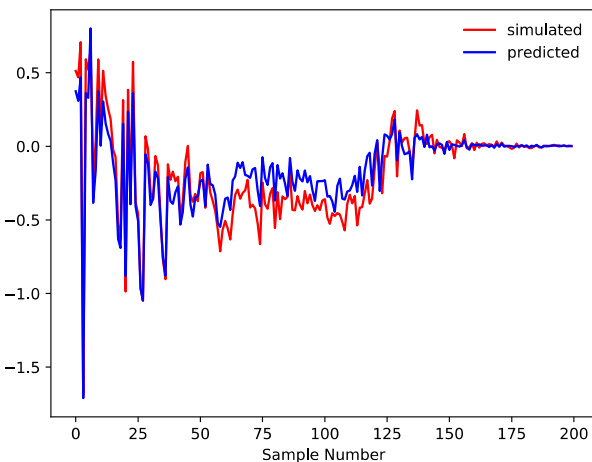


Figure 3: Neural network model predictions and simulated values for α_x on the validation data set for the initial study, with a beam energy of 5.7 MeV.

Table 1: Model Performance

Variable	Train MAE	Val. MAE	Train STD	Val. STD
α_x [rad]	0.018	0.067	0.042	0.091
α_y [rad]	0.022	0.070	0.037	0.079
β_x [m/rad]	0.004	0.008	0.009	0.012
β_y [m/rad]	0.005	0.012	0.011	0.017

Neural Network Controller

The controller was trained via reinforcement learning by allowing it to interface with the model. For the controller, random desired beam energy values between 3.1 and 6.2 MeV were specified, along with a target set of $\alpha_{x,y}$ and $\beta_{x,y}$ values. Larger quadrupole settings were penalized proportionally. This time, energy values between 4.8 and 5.2 MeV were excluded from training and used exclusively for the validation set. The controller network architecture consists of three hidden layers, with 30, 30, 20, and 20 nodes, respectively. As before, a hyperbolic tangent activation function and a dropout probability of 10% for each node was used.

Given random requested energy values within 3–6 MeV, Table 2 shows the performance in reaching the desired Twiss parameters ($\alpha_{x,y} = 0$ rad, $\beta_{x,y} = 0.106$ m/rad) in one iteration. This shows that for a given energy, the controller will immediately reach the desired beam size to within about 10% and the beam will be close to a waist, requiring minimal further tuning to reach the target values. The maximum absolute errors for the energy range seen in the training data set were 0.063 rad, 0.023 m/rad, 0.067 rad, and 0.041 m/rad for α_x , β_x , α_y ,

and β_y respectively. The maximum absolute errors for the validation set were 0.141 rad, 0.140 m/rad, 0.008 rad, and 0.038 m/rad for α_x , β_x , α_y , and β_y respectively.

Table 2: Ability to achieve $\alpha_{x,y} = 0$ rad and $\beta_{x,y} = 0.106$ m/rad for 3–6 MeV electron beams in one iteration.

Variable	Train MAE	Val. MAE	Train STD	Val. STD
α_x [rad]	0.012	0.075	0.011	0.046
α_y [rad]	0.013	0.079	0.012	0.045
β_x [m/rad]	0.008	0.004	0.006	0.002
β_y [m/rad]	0.014	0.011	0.011	0.011

FULL PHOTOINJECTOR AND BEAMLINE STUDY

Based on the encouraging results from the initial study, we have been conducting a more comprehensive version of it that also includes the task of minimizing the emittance at the entrance of the undulator. As this requires finer adjustment of the RF phase, RF power, and solenoid strength in conjunction with the quadrupole settings, additional data sets consisting of the output from start-to-end optimizations and parameter scans were collected that include fine adjustment of these parameters. In this case, the neural network model inputs and outputs are as shown in Figure 2. This time the controller takes in desired beam energy, Twiss parameters, emittances, and transmission at the entrance of the undulator and sets the RF power, RF phase, solenoid strength, and quadrupole settings needed to achieve them. Figure 4 shows an example of the model’s performance on the validation set, which consisted of start-to-end optimization data for 3.5 MeV

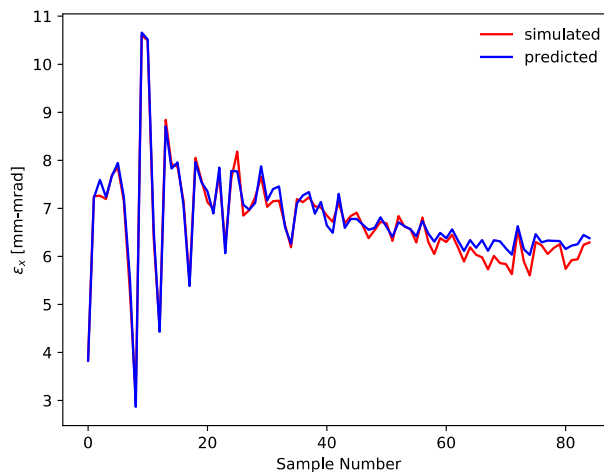


Figure 4: Neural network model predictions and simulated values for normalized ϵ_x on the new validation data set at 3.5 MeV for full the photoinjector and beamline study.

CONCLUSIONS AND FUTURE WORK

We have shown encouraging results from an initial beamline tuning study, indicating that in one iteration the controller can set up the machine to achieve close to the correct Twiss parameters for arbitrary beam energies between 3–6 MeV. This is a successful first step toward the development of a neural network reinforcement learning controller that will facilitate fast switching between operational parameters along with fine-tuning. The TEU-FEL presents a good platform to explore this technique because of its relative simplicity in terms of the number of control parameters and its nonlinear beam dynamics. Our next steps are to (1) finish the full photoinjector and beamline study and (2) incorporate FEL simulations and train the controller based on FEL output. While the true merit of the approach won't be clear until it is tested experimentally, we can optimistically say that with some further R&D a neural network control policy may well be an expedient way of switching between operating states in an FEL.

REFERENCES

- [1] A. L. Edelen *et al.*, “Neural networks for modeling and control of particle accelerators,” *IEEE Transactions on Nuclear Science*, vol. 63, no. 2, pp. 878-897, Apr. 2016.
- [2] G. J. Ernst *et al.*, “Status of the TEU-FEL project,” *Nuclear Instruments and Methods in Physics Research A*, vol. 318, no. 1-3, 1992.
- [3] R. S. Sutton and A.G. Barto, *Reinforcement Learning: An Introduction*. MIT Press, Cambridge, MA, 1988.
- [4] S. Milton *et al.*, “Colorado State University Accelerator and FEL,” *Proc. IPAC 2014*, Dresden, Germany, THPRI074.
- [5] L. Serafini and J. B. Rosenzweig, “Envelope analysis of intense relativistic quasilaminar beams in RF photoinjectors: a theory of emittance compensation,” *Phys. Rev. E*, vol. 55, pp. 7565, 1997.
- [6] J. Billen, “Poisson Superfish Codes,” Los Alamos National Laboratory, Copyright 1985-2005.
- [7] L. Young, “PARMELA Codes,” Los Alamos National Laboratory, Copyright 1985-2005.
- [8] J. P. Edelen, “Design and simulation of the Colorado State University linear accelerator system,” M.S. Thesis, Colorado State University, Fort Collins, CO, 2014.
- [9] J. Verschuur, G. J. Ernst, and W. J. Witteman, “The TEU-FEL undulator,” *Nuclear Instruments and Methods in Physics Research A*, vol. 318, pp. 847-852, 1992.
- [10] N. Srivastav *et al.*, “Dropout: a simple way to prevent neural networks from overfitting,” *Journal of Machine Learning Research*, vol. 15, pp. 1929-1958, 2014.

DIAGNOSTICS UPGRADES FOR INVESTIGATIONS OF HOM EFFECTS IN TESLA-TYPE SCRF CAVITIES*

A.H. Lumpkin[#], D. Edstrom Jr., J. Ruan, R. Thurman-Keup Y. Shin, P. Prieto, N. Eddy
Fermilab Accelerator Laboratory, Batavia, IL 60510 USA

B.E. Carlsten^{**}, Los Alamos National Laboratory, Los Alamos, NM 87545 USA

Abstract

We describe the upgrades to diagnostic capabilities on the Fermilab Accelerator Science and Technology (FAST) electron linear accelerator that will allow investigations of the effects of high-order modes (HOMs) in SCRF cavities on macropulse-average beam quality. We examine the dipole modes in the first pass-band generally observed in the 1.6-1.9 GHz regime for TESLA-type SCRF cavities due to uniform transverse beam offsets of the electron beam. Such cavities are the basis of the accelerators such as the European XFEL and the proposed MaRIE XFEL facility. Preliminary HOM detector data, prototype BPM test data, and first framing camera OTR data with ~20-micron spatial resolution at 250 pC per bunch will be presented.

INTRODUCTION

There are current Free-Electron Laser (FEL) initiatives that will be enabled by the use of the TESLA-type SCRF cavities in Europe (the European XFEL) and proposed in the USA (the MaRIE facility). One of the challenges is the control of the high-order modes (HOMs) that develop in these cavities due to transverse beam offsets. Diagnostic capabilities are being upgraded on the Fermilab Accelerator Science and Technology (FAST) facility [1] that will allow investigations of the effects of high-order modes (HOMs) in SCRF cavities on macropulse-average beam quality. We focus on the dipole modes in the first pass-band generally observed in the 1.6-1.9 GHz regime in TESLA-type SCRF cavities due to beam offsets. Such cavities are the basis of the accelerators for the European XFEL and the proposed MaRIE XFEL facility. Raw HOM data indicate that the mode amplitudes oscillate for ~10 μ s after the micropulse enters the cavity. With a 3-MHz pulse train, we expect transverse centroid shifts will then occur during the macropulse resulting in a blurring of the beam-size image averaged over the macropulse.

To evaluate these effects, upstream corrector magnets were tuned to steer the beam off axis upon entering the first of the two cavities. From there, several parameters were tracked, including the two HOM detector signal strengths for each cavity, the average transverse beam positions from rf beam position monitors (BPMs), and the

average beam size using intercepting screens and imaging. Preliminary efforts demonstrated reduction of the HOM signals by beam steering. Our initial data from an optical transition radiation (OTR) source indicated a framing camera mode can provide ~20-micron spatial resolution at ~250 pC per bunch while the prototype rf BPM required higher charge to approach this resolution for single-bunch beam position. The preliminary HOM detector data, prototype BPM test data, and framing camera data will be presented later in this paper.

EXPERIMENTAL ASPECTS

The FAST Linac

The FAST linac is based on the L-band rf photocathode (PC) gun which injects beam into two superconducting rf (SCRF) capture cavities denoted CC1 and CC2, followed by transport to a low energy electron spectrometer. A Cs₂Te photocathode is irradiated by the UV component of the drive laser system described elsewhere [2]. The basic diagnostics for the HOMs studies include the rf BPMs located before, between, and after the two cavities as shown in Fig. 1. These are supplemented by the imaging screens at X107, X108, X121, and X124. The HOM couplers are located at the upstream and downstream ends of each SCRF cavity, and these signals are processed by the HOM detector circuits with the output provided online through ACNET, the Fermilab accelerator controls network. The upgrades will include optimizing the HOM detectors' bandpass filters, reducing the 1.3 GHz fundamental with a notch filter, converting the rf BPMs electronics to bunch-by-bunch capability with reduced noise, and using the C5680 streak camera in a rarely-used framing mode for bunch-by-bunch spatial information.

The Streak Camera System

In an initial framing camera study [3] we observed the green component remaining from UV-conversion at 3 and 9 MHz micropulse frequencies with the laser lab streak camera. We have also recently applied the principle to optical transition radiation (OTR) from an Al-coated Si substrate with subsequent transport to a beamline streak camera that views OTR from the X121 screen location. Commissioning of the streak camera system was facilitated through a suite of controls centered around ACNET. This suite includes operational drivers to control and monitor the streak camera as well as Synoptic displays to facilitate interface with the driver. Images are

* Work supported under Contract No. DE-AC02-07CH11359 with the United States Department of Energy.

** Work at LANL supported by US Department of Energy through the LANL/LDRD Program.

lumpkin@fnal.gov

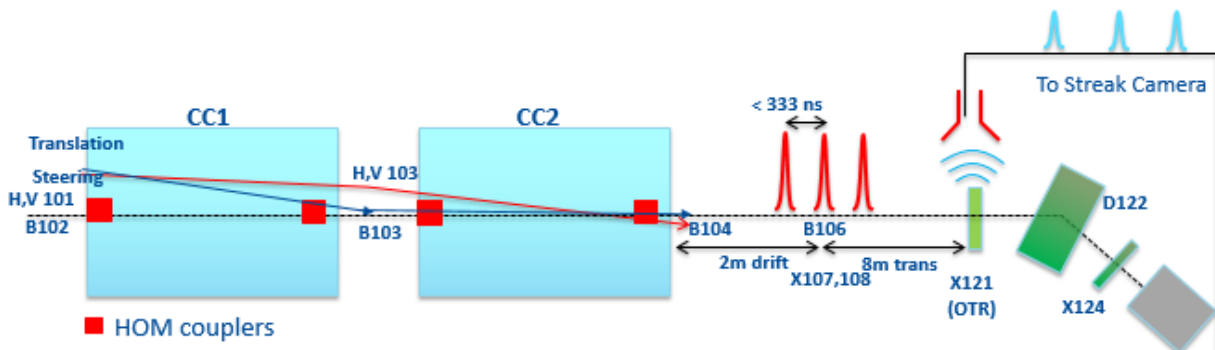


Figure 1: Schematic of the FAST beamline layout showing the capture cavities, correctors, rf BPMs, HOM couplers, X121 OTR screen, spectrometer, and path to streak camera.

captured from the streak camera using the readout cameras, Prosilica 1.3 Mpixel cameras with 2/3" format, and may be analyzed both online with a Java-based ImageTool and an offline MATLAB-based ImageTool processing program [4,5]. Bunch-length measurements using these techniques have been reported previously from the A0 Facility [6] and FAST first system streak camera commissioning at 20 MeV [7].

The streak camera stations each include a Hamamatsu C5680 mainframe with S20 PC streak tube and can accommodate vertical sweep plugin units and either a horizontal sweep unit or a blanking unit. The UV-visible input optics allow the assessment of the 263-nm component as well as the amplified green component or IR components converted to green by a doubling crystal. The framing mode studies required replacing the M5675 synchroscan unit with the M5677 slow vertical sweep unit (5-ns to 1-ms ranges) [8]. The M5679 dual axis plugin which provides a horizontal sweep with selectable ranges had already been installed for the previous dual sweep synchroscan tests. A second set of deflection plates in the streak tube provides the orthogonal deflection for the slower time axis in the 100-ns to 10-ms regime. These plates are driven by the dual-axis sweep unit which was also commissioned during previous studies.

EXPERIMENTAL RESULTS

Initial HOM Detector Data: 3 MHz

The basic tests involved the HOM couplers installed in the upstream and downstream ends of the capture cavities, CC1 and CC2. These are designed to damp the HOMs, but in addition their signals can be filtered, processed, amplified, and digitized. In our initial tests, we used a bandpass filter at 1.7-1.8 GHz to select some of the dipole modes that are seen when the beam transits the cavities off axis. We used the settings, as found, for steering through the cavities. Sample waveforms are shown in Fig. 2 for the steering normally used during the Summer of 2016. However, we show that the CC1 detector signals can be reduced and minimized by a factor of 5 by steering with 1.15 A in corrector H101 as seen in Fig. 3. We subsequently steered H and V 103 to minimize the HOMs

in CC2 as well. When these new corrector settings were then used a few days later, the observed x,y emittances were reduced by 20-30%. In the upgrade, we are using a notch filter at 1.3 GHz to reduce it by 10,000, wider bandpass filters at 1.6-1.9 GHz for the dipole modes, and a shortpass filter at 2.2 GHz to reduce any signal from the monopole modes in the cavities.

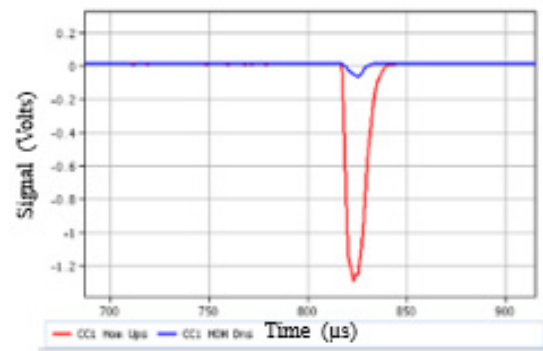


Figure 2: Digitized signal envelopes from the CC1 upstream (red) and downstream (blue) detectors with 750 pC per bunch and a 25- μ s-long pulse train.

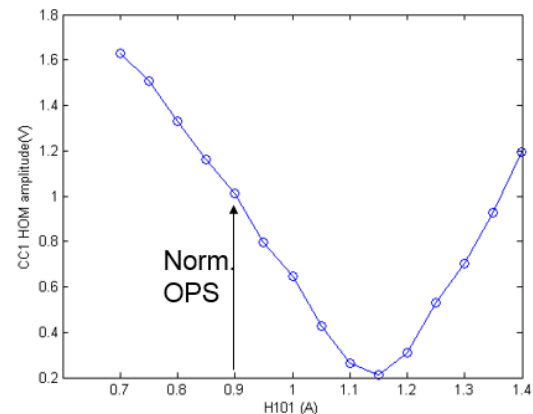


Figure 3: CC1 HOM detector 1 peak signal variation with H101 corrector settings.

Another preliminary trajectory study was performed by adjusting the corrector H101 located ~0.5 m upstream of the first capture cavity CC1. We tracked the average rf BPM readings in B102, B103, B104, and B106 as a

Content from this work may be used under the terms of the CC BY 3.0 licence (© 2018). Any distribution of this work must maintain attribution to the author(s), title of the work, publisher, and DOI.

function of the H101 corrector current settings. The data in Fig. 4 indicate that the normal setting of 0.9 A corresponded to a 1.4-mm offset at B102 as beam enters CC1. The B103 readings are somewhat insensitive to these entrance values due to the focusing effects by cavity fields in CC1. More significant mm-scale offsets are seen after CC2, and one would expect stronger HOMs in CC2.

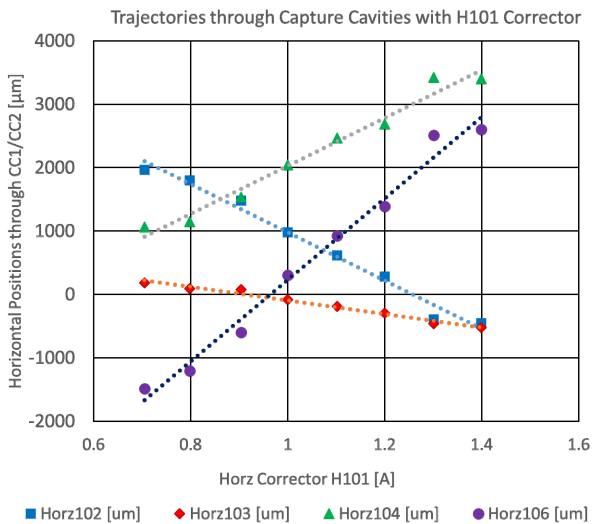


Figure 4: Sample of tracking of the average beam centroids through CC1 and CC2.

Bunch-by-Bunch rf BPM

The upgrades in the prototype rf BPM electronics board included noise reduction which enabled an improved spatial resolution for a given charge. At 2 nC per micropulse, the rms noise was found to be 25 μm in x and 15 μm in y in B101 in the August 29, 2016 test with 4.5-MeV beam from the gun. The firmware to allow the tracking of the beam positions bunch by bunch was also implemented. An example of the tracking of the 50 micropulses in a macropulse train is shown in Fig. 5 before the low-noise revision was employed. Both noise-reduction and bunch-by-bunch capabilities are needed for the proposed HOM long-range wakefield studies in which the mode oscillations are anticipated to kick different micropulses varying amounts depending on the amplitude.

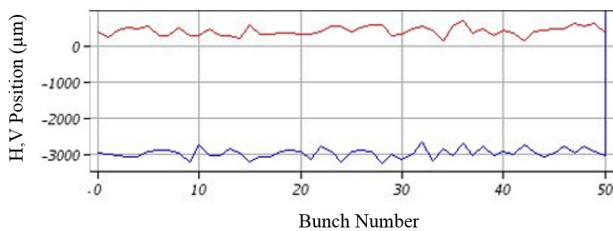


Figure 5: Sample of the tracking of the beam centroids bunch by bunch for 50 micropulses.

Initial Green Component Studies: 3 MHz

The basic principles are illustrated with the Laser Lab Streak Camera. In Fig. 6, a 10- μs vertical sweep shows

each of the 20 micropulses from the incident laser macropulse. The vertical projected profiles for the region of interest (ROI) would show all 20 micropulses at a 3-MHz rate. Such an image could track bunch-by-bunch centroid motion as well, particularly in the horizontal plane as it is perpendicular to the sweep direction. To obtain more pulse separation vertically, one can reduce the coverage to 1 μs with a faster deflection and add the horizontal sweep to cover more micropulses.

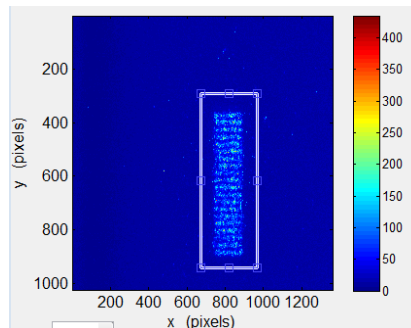


Figure 6: Vertical slow sweep image of 20 micropulses with 10- μs sweep range. Green at 3 MHz.

Linac Beamline Streak Camera with OTR

The beamline streak camera is installed in an optical enclosure outside of the beamline enclosure with transport of OTR from the instrumentation cross at beamline location 121 (X121) as described [9]. The all-mirror transport minimizes the chromatic temporal dispersion effects for bunch length measurements. The same transport can be used for the framing-mode tests. In this case, we only used the horizontal sweep to separate the micropulses at 3 MHz. The input image was apertured by the entrance slits to provide $\sigma_x=135 \mu\text{m}$ and $\sigma_y=25 \mu\text{m}$ effective sizes for the demonstration shown in Fig. 7. The spatial resolution for the system is ~ 10 to 15 μm with an effective calibration factor of 6.6 $\mu\text{m}/\text{pixel}$. The OTR signal from the initial micropulse charge of $\sim 300 \text{ pC}$ was reduced by the apertures for the camera images. This proof of principle of the framing technique using OTR can be applied to HOM dipole mode effects within the e-beam macropulse and turn-by-turn OSR effects in IOTA.

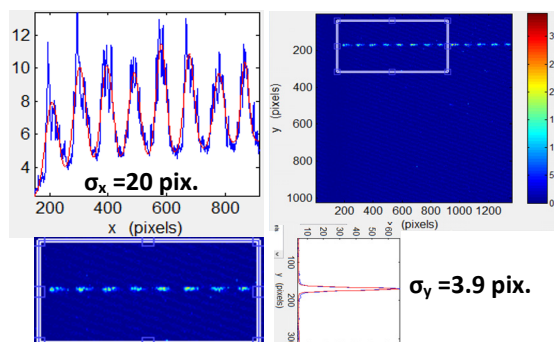


Figure 7: Semi-framing-camera mode with X121 OTR from the electron beam pulse train at 3 MHz.

SUMMARY

In summary, a series of preliminary observations were made using the HOM detectors, the rf BPMs, and the Laser Lab streak camera configured in framing mode to track beam size and position at 3 MHz. The framing mode was also applied to OTR from X121, demonstrating viability for HOM-effect measurements upon individual e-beam micropulses. Optical synchrotron radiation sources in IOTA [10] are calculated to be brighter turn by turn than the OTR from a single micropulse in the electron beamline so we have established the proof of principle for that application as well.

ACKNOWLEDGMENTS

The authors acknowledge the support of A. Valishev, D. Broemmelsiek, and R. Dixon, all at Fermilab. They also acknowledge support from the rest of the FAST/IOTA group and Electrical, Mechanical, Controls, and Cryogenic departments.

REFERENCES

- [1] "The ASTA User Facility Proposal," Fermilab-TM-2568, October 2013.
- [2] J. Ruan, M. Church, D. Edstrom, T. Johnson, and J. Santucci, *Proc. of IPAC'13*, WEPME057.
- [3] A. H. Lumpkin, D. Edstrom, and J. Ruan, "Initial demonstration of 9-MHz framing camera rates on the FAST drive laser pulse trains", *Proc. of NAPAC'16*, TUPOA25.
- [4] J. Diamond, "Online Java-based ImageTool," Internal FNAL Report (2013).
- [5] R. Thurman-Keup, "Offline MATLAB-based ImageTool," Internal FNAL Report (2011).
- [6] A.H. Lumpkin, J. Ruan, and R. Thurman-Keup, *Nucl. Instr. and Meth. A* **687**, 92-100 (2012).
- [7] A. H. Lumpkin *et al.*, *Proc. of FEL'14*, MOP021, Basel, Switzerland.
- [8] Bingxin Yang *et al.*, "Characterizing transverse beam dynamics at the APS storage ring using a dual-sweep streak camera," *Proc. of BIW'98*, AIP Conf. Proc. 451 (1999).
- [9] A. H. Lumpkin *et al.*, *Proc. of NAPAC'16*, TUPOA26.
- [10] R. Thurman-Keup, private communication, May 2016.

ADAPTIVE FEEDBACK FOR AUTOMATIC PHASE-SPACE TUNING OF ELECTRON BEAMS IN ADVANCED XFELS

A. Scheinker*, Los Alamos National Laboratory, Los Alamos, USA
D. Bohler†, SLAC National Accelerator Laboratory, Menlo Park, USA

Abstract

Particle accelerators are extremely complex devices having thousands of coupled, nonlinear components which include magnets, laser sources, and radio frequency (RF) accelerating cavities. Many of these components are time-varying. One example is the RF systems which experience unpredictable temperature-based perturbations resulting in frequency and phase shifts. In order to provide users with their desired beam and thereby light properties, LCLS sometimes requires up to 6 hours of manual, experience-based hand tuning of parameters by operators and beam physicists, during a total of 12 hours of beam time provided for the user. Even standard operational changes can require hours to switch between user setups. The main goal of this work is to study model-independent feedback control approaches which can work together with physics-based controls to make overall machine performance more robust, enable faster tuning (seconds to minutes instead of hours), and optimize performance in real time in response to un-modeled time variation and disturbances.

INTRODUCTION

While existing and planned free electron lasers (FEL) have automatic digital control systems, they are not controlled precisely enough to quickly switch between different operating conditions. Existing controls maintain components at fixed set points, which are set based on desired beam and light properties, such as, for example, the current settings in a bunch compressor's magnets. Analytic studies and simulations initially provide these set points. However, models are not perfect and component characteristics drift in noisy and time-varying environments; setting a magnet power supply to a certain current today does not necessarily result in the same magnetic field as it would have 3 weeks ago. Also, the sensors are themselves noisy, limited in resolution, and introduce delays. Therefore, even when local controllers maintain desired set points exactly, performance drifts. The result is that operators continuously tweak parameters to maintain steady state operation and spend hours tuning when large changes are required, such as switching between experiments with significantly different current, beam profile (2 color, double bunch setups), or wavelength requirements. Similarly, traditional feed-forward RF beam loading compensation control systems are limited by model-based beam-RF interactions, which work extremely well for perfectly known RF and beam properties, but in practice are limited by effects which include un-modeled drifts and fluc-

tuations and higher order modes excited by extremely short pulses. These limitations have created an interest in iterative (beam-based feedback), machine learning, and adaptive techniques.

The focus of this work is on minimizing the lengthy (1-10 hours) suboptimal manual tuning is required when beam parameters are changed between experiments, especially when settings of the low energy beam sections (<500 MeV) are changed. The sources of tuning difficulty include complex effects such as: space charge and coherent synchrotron radiation, which depend on many machine settings simultaneously, unobservable parameters, which are not well controlled, and time varying, drifting components. Such difficulties will only increase as existing and future light are exploring new and exotic schemes such as two-color operation (LCLS, LCLS-II) and next generation light sources seek to provide brighter, shorter wavelength (0.1nm at PAL, 0.05 nm at EuXFEL, and 0.01 nm at MaRIE), more coherent light [1]. To achieve their performance goals, new machines face unique challenges, such as requiring extremely low electron beam emittance and energy spread. LCLS-II requires <0.01% rms energy stability, which is >10x more than the existing LCLS linac [2]. EuXFEL requires < 0.001 %/deg rms RF amplitude and phase errors, respectively (current state of the art is 0.01) [3]. Existing and future accelerators will benefit from an ability to quickly tune between experiments and to compensate for extremely closely spaced electron bunches, such as might be required for MaRIE, requiring advanced controls and approaches such as droop correctors [4,5].

The type of tuning problems that we are interested in have recently been approached with powerful machine learning methods [6, 7], which are showing very promising results. Our approach to this problem is complementary to other machine learning methods in that instead of learning over long periods of time, we attempt to respond quickly in real time, based on very limited measurements. One possible limitation of our approach is that being a real time, local feedback, it may become trapped in a local minimum. Future plans exist for combining the work discussed here with machine learning. We utilize a novel model-independent extremum seeking (ES) based feedback scheme, which operates based only on noisy measurements without dependence on accurate system models [8, 9] and is closely related to vibrational control [10]. The advantages of this approach are:

* ascheink@lanl.gov

† dbohler@slac.stanford.edu

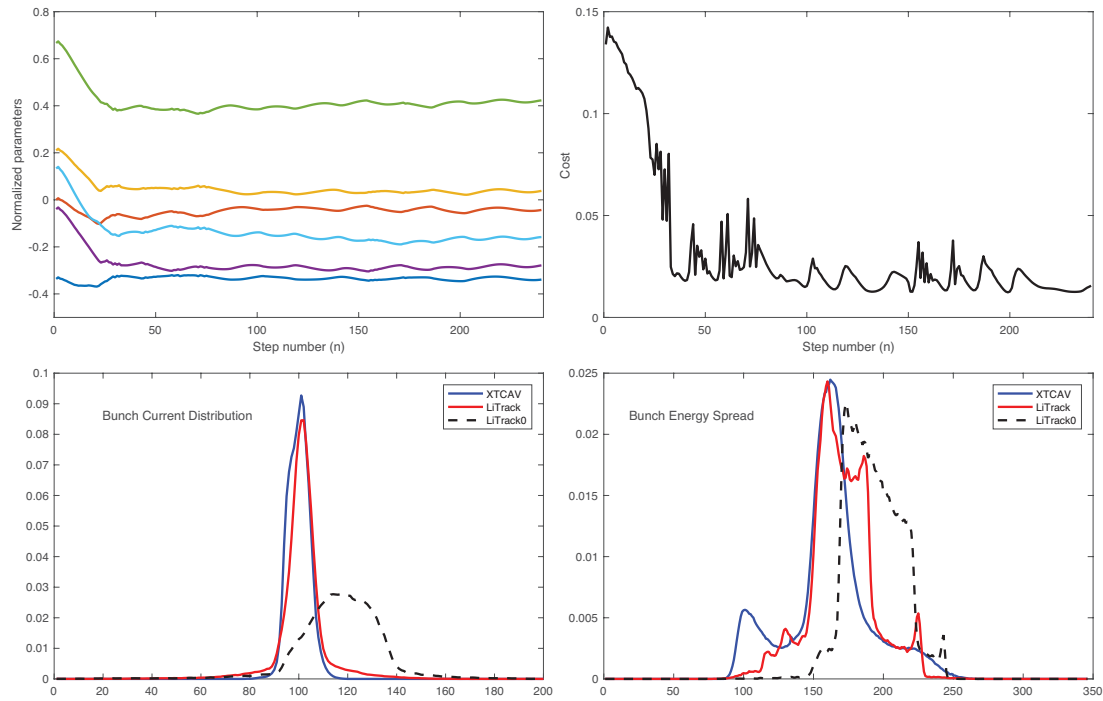


Figure 1: Parameter convergence and cost minimization for matching desired bunch length and energy spread profiles.

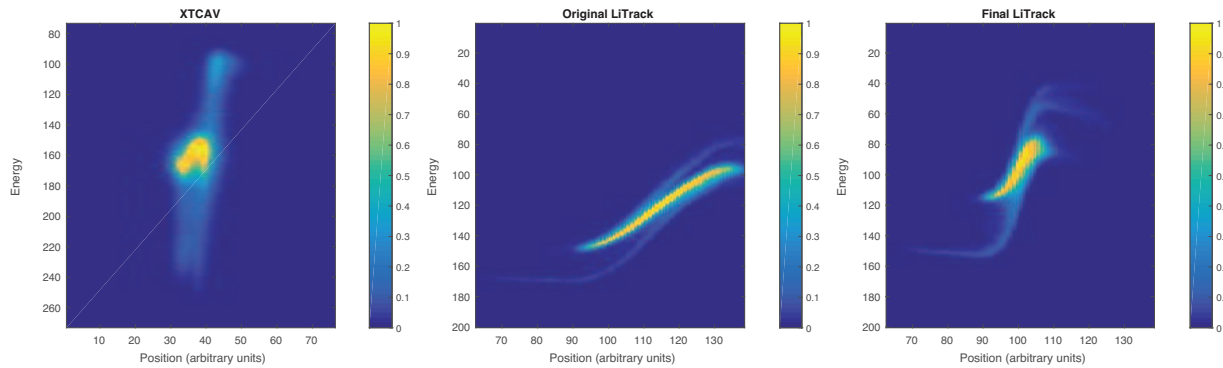


Figure 2: Measured XTCAV, original LiTrack and final, converged LiTrack energy vs position phases space of the electron bunch shown.

1. Multiple parameters tuned simultaneously.
2. The method is incredibly robust to noise, as has been demonstrated in hardware for tuning magnets [14].
3. Unlike genetic algorithms or simulation-based learning approaches, ES acts as a feedback directly on the actual system, adapting as things vary with time, and has analytically proven robustness, stability, and convergence rate estimates.
4. The parameter settings and update rates have analytically known, user-chosen bounds.

ITERATIVE EXTREMUM SEEKING

The ES method has been utilized in software and in hardware for automated particle accelerator tuning [11], electron bunch length prediction at FACET [13], in-hardware tuning

of RF systems at LANSCE [12, 15], and automated tuning of magnets in a time-varying lattice to continuously minimize betatron oscillations at SPEAR3 [14].

For the work described here, a measured XTCAV image was utilized and compared to the simulated energy and position spread of an electron bunch at the end of the LCLS as simulated by LiTrack. The electron bunch distribution is given by a function $\rho(\Delta E, \Delta z)$ where $\Delta E = E - E_0$ is energy offset from the mean or design energy of the bunch and $\Delta z = z - z_0$ is position offset from the center of the bunch. We worked with two distributions:

$$\text{XTCAV measured : } \rho_{\text{XTCAV}}(\Delta E, \Delta z),$$

$$\text{LiTrack simulated : } \rho_{\text{LiTrack}}(\Delta E, \Delta z).$$

These distributions were then integrated along the E and z projections in order to calculate 1D energy and charge

distributions:

$$\begin{aligned} \rho_{E,\text{TCAV}}(\Delta E), \quad \rho_{z,\text{TCAV}}(\Delta z), \\ \rho_{E,\text{LiTrack}}(\Delta E), \quad \rho_{z,\text{LiTrack}}(\Delta z). \end{aligned}$$

Finally, the energy and charge spread distributions were compared to create cost values:

$$C_E = \int [\rho_{E,\text{TCAV}}(\Delta E) - \rho_{E,\text{LiTrack}}(\Delta E)]^2 d\Delta E, \quad (1)$$

$$C_z = \int [\rho_{z,\text{TCAV}}(\Delta z) - \rho_{z,\text{LiTrack}}(\Delta z)]^2 d\Delta z, \quad (2)$$

whose weighted sum was combined into a single final cost:

$$C = w_E C_E + w_z C_z. \quad (3)$$

Iterative extremum seeking was then performed via finite difference approximation of the ES dynamics:

$$\frac{\mathbf{p}(t + dt) - \mathbf{p}(t)}{dt} \approx \frac{d\mathbf{p}}{dt} = \sqrt{\alpha\omega} \cos(\omega t + kC(\mathbf{p}, t)), \quad (4)$$

by updating LiTrack model parameters, $\mathbf{p} = (p_1, \dots, p_m)$, according to

$$p_j(n + 1) = p_j(n) + \Delta\sqrt{\alpha\omega_j} \cos(\omega_j n \Delta + kC(n)), \quad (5)$$

where the previous step's cost is based on the previous simulation's parameter settings,

$$C(n) = C(\mathbf{p}(n)). \quad (6)$$

Machine tuning work has begun with general analytic studies as well as simulation-based algorithm development focused on the LCLS beam line, using SLAC's LiTrack software, a code which captures most aspects of the electron beam's phase space evolution and incorporates noise representative of operating conditions. The initial effort focused on developing ES-based auto tuning of the electron beam's bunch length and energy spread by varying LiTrack parameters in order to match LiTrack's output to an actual TCAV measurement taken from the accelerator by tuning bunch compressor energies and RF phases. The results are shown in Figures 1 and 2. Running at a repetition rate of 120 Hz, the simulated feedback would have converged within two seconds on the actual LCLS machine.

CONCLUSIONS

Preliminary results have demonstrated that ES is a powerful tool with the potential to automatically tune an FEL between various bunch properties such as energy spread and bunch length requirements by simultaneously tuning multiple coupled parameters, based only on a TCAV measurement at the end of the machine. Although the simulation results are promising, It remains to be seen what the limitations of the method are in the actual machine in terms of getting stuck in local minima and time of convergence. We plan on exploring the extent of parameter and phase space through which we can automatically move.

REFERENCES

- [1] J. Bradley III, D. Rees, A. Scheinker, and R. L. Sheffield, "An Overview of the MaRIE X-FEL and electron radiography LINAC RF systems," in Proceedings of the International Particle Accelerator Conference, Richmond, Virginia, USA, 2015.
- [2] T. O. Raubenheimer, "Technical challenges of the LCLS-II CW X-RAY FEL," in Proceedings of the International Particle Accelerator Conference, Richmond, VA, USA, 2015.
- [3] C. Schmidt *et al.*, "Recent developments of the European XFEL LLRF system," in Proceedings of the International Particle Accelerator Conference, Shanghai, China, 2013.
- [4] R. L. Sheffield, "Enabling cost-effective high-current burst-mode operation in superconducting accelerators," *Nuclear Instruments and Methods in Physics Research Section A: Accelerators, Spectrometers, Detectors and Associated Equipment* 785, pp.197-200, 2015.
- [5] J. Bradley III, A. Scheinker, D. Rees, and R. L. Sheffield, "High power RF requirements for driving discontinuous bunch trains in the MaRIE linac," in Proceedings of the LINAC Conference, East Lansing, MI, USA, 2016.
- [6] A. L. Edelen *et al.*, "Neural networks for modeling and control of particle accelerators." *IEEE Transactions on Nuclear Science* 63.2, pp. 878-897, 2016.
- [7] A. L. Edelen *et al.*, "Neural network model of the PXIE RFQ cooling system and resonant frequency response," arXiv preprint arXiv:1612.07237, 2016.
- [8] A. Scheinker and D. Scheinker, "Bounded extremum seeking with discontinuous dithers," *Automatica*, vol. 69, pp. 250-257, 2016.
- [9] A. Scheinker and D. Scheinker, "Constrained extremum seeking stabilization of systems not affine in control," *International Journal of Robust and Nonlinear Control*, DOI: 10.1002/rnc.3886, to appear 2017.
- [10] R. Bellman, J. Bentsman, and S. Meerkov, "Vibrational control of nonlinear systems: vibrational stabilizability," *IEEE Transactions on Automatic control* 31.8, pp. 710-716, 1986.
- [11] A. Scheinker, X. Pang, and L. Rybarczyk, "Model-independent particle accelerator tuning," *Physical Review Special Topics-Accelerators and Beams*, 16.10, 102803, 2013.
- [12] A. Scheinker, S. Baily, D. Young, J. Kolski, and M. Prokop, "In-hardware demonstration of model-independent adaptive tuning of noisy systems with arbitrary phase drift," *Nuclear Instruments and Methods in Physics Research A*, vol.756, pp.30-38, 2014.
- [13] A. Scheinker and S. Gessner, "Adaptive method for electron bunch profile prediction" *Physical Review Special Topics-Accelerators and Beams*, 18.10, 102801, 2015.
- [14] A. Scheinker, X. Huang, and J. Wu, "Minimization of betatron oscillations of electron beam injected into a time-varying lattice via extremum seeking," *IEEE Transactions on Control Systems Technology*, DOI: 10.1109/TCST.2017.2664728, 2017.
- [15] A. Scheinker, "Application of extremum seeking for time-varying systems to resonance control of RF cavities" *IEEE Transactions on Control Systems Technology*, 25.4, pp. 1521-1528, 2017.

SUB-FEMTOSECOND TIME-RESOLVED MEASUREMENTS BASED ON A VARIABLE POLARIZATION X-BAND TRANSVERSE DEFLECTION STRUCTURE FOR SwissFEL

P. Craievich*, M. Bopp, H.-H. Braun, R. Ganter, M. Pedrozzi, E. Prat,
 S. Reiche, R. Zennaro, Paul Scherrer Institut, Villigen-PSI, Switzerland
 A. Grudiev, N. Catalan Lasheras, G. Mcmonagle, W. Wuensch, CERN, Geneva, Switzerland
 B. Marchetti, R. Assmann, F. Christie, R. D'Arcy, D. Marx, DESY, Germany

Abstract

The SwissFEL project, under commissioning at the Paul Scherrer Institut (PSI), will produce FEL radiation for soft and hard X-rays with pulse durations ranging from a few to several tens of femtoseconds. A collaboration between DESY, PSI and CERN has been established with the aim of developing and building an advanced X-Band transverse deflection structure (TDS) with the new feature of providing variable polarization of the deflecting force. As this innovative CERN design requires very high manufacturing precision to guarantee highest azimuthal symmetry of the structure to avoid the deterioration of the polarization of the streaking field, the high-precision tuning-free assembly procedures developed at PSI for the SwissFEL C-band accelerating structures will be used for the manufacturing. Such a TDS will be installed downstream of the undulators of the soft X-ray beamline of SwissFEL and thanks to the variable polarization of the TDS it will be possible to perform a complete characterization of the 6D phase space. We summarize in this work the status of the project and its main technical parameters.

INTRODUCTION

The SwissFEL project at PSI consists out of a 6 GeV accelerator complex and two undulator beam lines. The Aramis beam line, presently under commissioning, covers the energy photon ranges from 12.4 to 1.8 keV [1], while the Athos beam line the range from 1.9 to 0.25 keV [2]. The Athos line will operate in parallel to the Aramis line and, actually consists of a fast-kicker magnet, a dog-leg transfer line, a small linac and 16 APPLE undulators. It is designed to operate in advanced modes of operation slightly different to standard SASE operation and will produce soft X-rays FEL radiation with pulse durations ranging from a few to several tens of femtoseconds [3]. Electron beam diagnostic based on a transverse deflection structure (TDS) placed downstream of the undulators (post-undulator TDS) in conjunction with an electron beam energy spectrometer can indirectly measure the pulse length of these ultra-short photon beam analysing the induced energy spread on the electron bunch due to the FEL process [4, 5]. Furthermore, a complete characterization of the electron beam 6D phase space by means of measurements of the bunch length, energy and of the transverse slice emittances (vertical and horizontal) are important tasks for

commissioning and optimization of FEL process [6–9]. In this context, the design of an innovative X-band TDS structure, including a novel variable polarisation feature, has been proposed by CERN [10, 11]. In order to avoid the rotation of the polarization of the dipole fields along the structure, a high-precision tuning-free assembly procedure developed for the C-band linac at PSI will be used for the fabrication of the TDSs [12]. This procedure has been used to fabricate 120 cavities for the SwissFEL linac and it is currently being used for the fabrication of the tuning free X-band structure prototypes for CLIC [13]. Several experiments at DESY (FLASH2, FLASHForward, SINBAD) and PSI (Athos) are interested in the utilization of high gradient X-band TDS systems for high resolution longitudinal diagnostics. In this context a collaboration between DESY, PSI and CERN has been established with the aim of developing and building an advanced X-Band transverse deflection structure (TDS) with the new feature of providing variable polarization of the deflecting field [14]. In this paper we summarize the specifications of the TDS system for the Athos line and we also introduce some details of the mechanical design of the first prototype that will be compatible with the requests from DESY and PSI [14].

TDS DIAGNOSTIC LINE

Table 1 contains the electron beam parameters at Athos post-undulator diagnostic section that have been used for the following calculations. Layout and more details on the Athos line are in [2].

Table 1: Beam and optical parameters involved in the streaking process at ATHOS post-undulator diagnostic section.

Parameter	Sy.	Value	Unit
Beam energy	E	2.9-3.4	GeV
Charge	Q	10-200	pC
Bunch length	σ_t	2-30	fs
β @TDS	$\beta_x = \beta_y$	50	m
Emittance	$\gamma\epsilon_x = \gamma\epsilon_y$	0.1-0.3	μm
Rep. rate		100	Hz

Figure 1 shows a schematic layout of the post-undulator diagnostic section. Beam slice emittance in both transverse planes will be investigated by a multi-quadrupole scan technique combined with the TDS. By means of the TDS, the

* paolo.craievich@psi.ch

Content from this work may be used under the terms of the CC BY 3.0 licence (© 2018). Any distribution of this work must maintain attribution to the author(s), title of the work, publisher, and DOI.

beam is vertically and horizontally streaked and a multi-quadrupole scan is performed in the horizontal or vertical direction, respectively, with the constraint of keeping the vertical/horizontal beam size constant over the whole scan [15]. For this purpose, five quadrupoles are foreseen to be placed downstream of the TDS. Reconstruction of the longitudinal phase space will be performed by means of the spectrometer line.

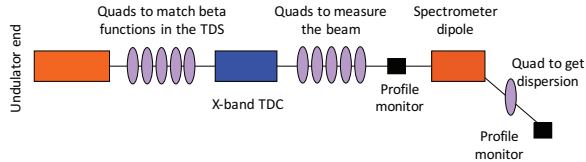


Figure 1: Concept of the post-undulator diagnostic section.

Figure 2 shows the β -functions of the beam lattice optics in the post-undulator diagnostic section. The locations of the deflectors are highlighted with a green circle and the β -functions are the same for the two polarization ($\beta_x = \beta_y = 50$ m). The rms energy spread resolution at the spectrometer is less than 180 keV. Moreover, if we also consider the minimum rms beam size that can be measured at the screen, corresponding to 150 keV, then adding the two contributions in quadrature we obtain a resolution of less than 234 keV.

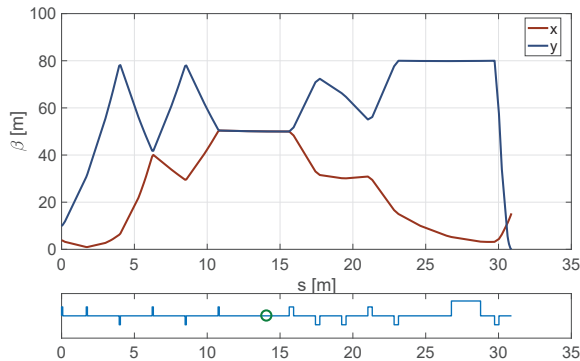


Figure 2: (Top) The β -function of the beam lattice optics for the post-undulator diagnostic section. $s=0$ corresponds to the end of the last Athos undulator. (Bottom) Locations of the quadrupoles and dipole are indicated with vertical lines while the TDS are highlighted with a green circle where $\beta_x = \beta_y = 50$ m.

The well-known formulas, i.e. contained in [9], describing the dynamics of the bunch deflection as a function of the TDS parameters and of the optical Twiss parameters are used here. Figure 3 shows the time resolution (up), the induced energy spread (middle) and the rms centroid jitter induced by the RF jitter (bottom) as a function of the integrated deflecting voltage. The time resolution is on sub-fs scale if the deflecting voltage is more than 45 MV with a $\beta_d = 50$ m. Such time resolutions allow the characterization of the shortest beam profile pulse indicated in Table 1 with approximately 2-3 slices. The uncorrelated energy spread in-

duced by the TDS is 500 keV with $\beta_d = 50$ m. Considering the RF phase jitters indicated in Fig. 3 (bottom) and a deflecting voltage of 45 MV, the expected shot-to-shot centroid jitter of the streaked beam is approximately 200-700 μ m (rms). This is in the same order of magnitude as the beam size of the streaked beam on the screen for the longer pulse ($\sigma_y = 450 \mu$ m) while it is an order of magnitude higher for the shortest pulse ($\sigma_y = 30 \mu$ m).

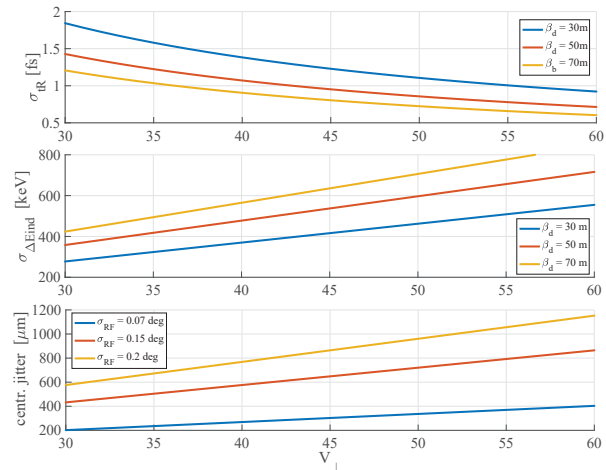


Figure 3: Time resolution (up) and rms induced energy spread (middle) as a function of the integrated deflecting voltage. Sub-fs resolution with $V_{\perp} > 45$ MV and $\beta_d = 50$ m in both transverse planes. Centroid jitter (bottom) as a function of the integrated deflecting voltage. Centroid jitter is estimated considering three different values of the RF phase jitters for $\beta_d = 50$ m.

TDS RF PARAMETERS

Two versions of constant-impedance and backward traveling wave TDS are under study. A short version, 960-mm long, and a longer and more efficient structure about 1.2 m long. Table 2 lists the RF parameters for both versions. The shortest version, matching the space constraints at FLASH2 at DESY [14, 16], will be fabricated as first prototype. Table 2 also lists the RF parameters if a RF pulse compressor, as a Barrel Open Cavity (BOC) or SLED systems, will be adopted. It is worthwhile noting that the iris aperture was fixed at 8 mm based on some considerations about the photon beam transmission through the TDS system on one side and based on the maximisation of the cell shut impedance on the other side. The distance between the first undulator stage and the TDS system is about 40 m and the worst case is the two color operation with the first undulator stage tuned to the longest wavelength of 5 nm [3]. In this case, the divergence is approximately 25 μ rad providing an rms photon beam radius of 1 mm at the TDS location that is enough for the photon beam transmission.

Mechanical design

The mechanical design is very similar to that of the Swiss-FEL C-band structure [12], with the main difference in the

input/output couplers. They are E-Rotator-type in order to provide a linearly polarized mode out of the two circularly polarized input waves [10]. The orientation of the linearly polarized mode can be varied by changing the phase between the two input waveguide, as shown in Fig. 4 (left and middle).

Table 2: RF parameters for short and long X-band TDS. Both structures are constant impedance and backward traveling wave structures. t_k is the klystron pulse width.

Cell parameter		Unit
Frequency	11995.2	MHz
Phase advance/cell	120	°
Iris radius	4	mm
Iris thickness	2.6	mm
Group velocity	-2.666	%c
Quality factor	6490	
Shunt impedance	50	MΩ/m

TDS parameter	Short	Long	Unit
n. cells	96	120	
Filling time	104.5	129.5	ns
Active length	800	1000	mm
Total length	960	1160	mm
Power-to-voltage	5.225	6.124	MV/MW ^{0.5}

TDS + BOC	Short	Long	Unit
BOC Q ₀	150000	150000	
BOC β @ $t_k=1.5\mu s$	8.7	8	
Power-to-voltage	11.958	13.528	MV/MW ^{0.5}

Figure 4 (right) also shows the basic disk in copper which has a T-shape. Thanks to the absence of any tuning feature, machining of the half cell will be subsequently performed on both side with the aim of having the brazing plane in the middle of the cell. An important advantage of this solution is to have a double rounding of the cells and to thus avoid that the braze alloy can flow into the structure through capillary action. The brazing alloy in copper-silver will be placed in two brazing grooves. Furthermore, sharp edges are foreseen in the cells in order to eventually hold the melted brazing material back from flowing into the cells. However, the size of the brazing groove has been experimentally optimized to provide the best reproducibility of the brazing material distribution. The cooling circuits are integrated in the cups as shown in Fig. 4. From the tolerance study [18], the inner profiles of the cups should be within the tolerance of ± 3 m with an average surface roughness R_a below 25 nm.

WAVEGUIDE NETWORK (CONCEPT)

The linearizer system at the SwissFEL injector is equipped with a Scandinova K2-3X solid state modulator and a 50 MW, 100 Hz X-band klystron. A first preliminary idea is to reproduce a similar RF plant for the TDS system in order to eventually use it as spare parts for the injector plant. Figure 5 shows a preliminary sketch of the X-band TDS power

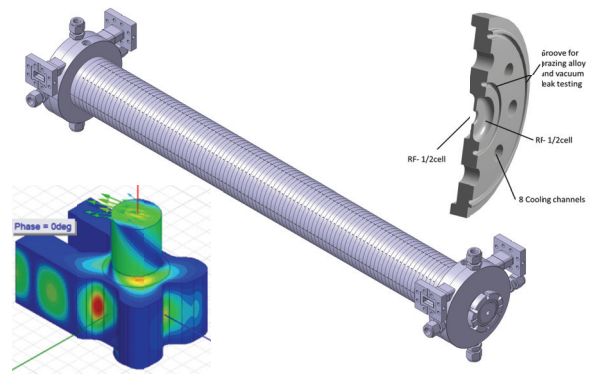


Figure 4: Left: detail of the input/output coupler. Middle: whole TDS prototype. Right: basic disk.

distribution system. The main RF parameters of the TDS and pulse compressor are summarized in Table 2.

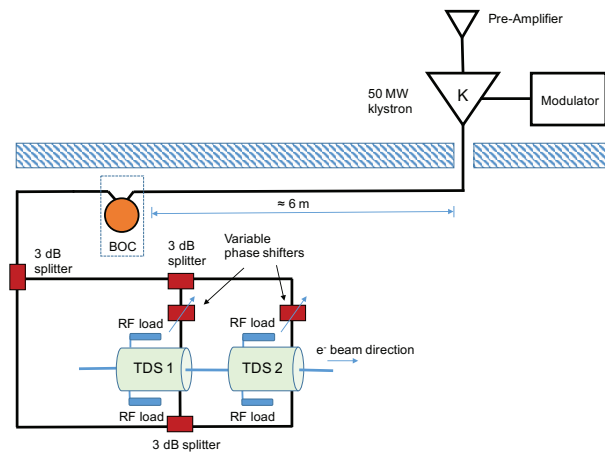


Figure 5: First concept for RF power feeding scheme with a 50 MW CPI klystron for two long TDS. If a pulse compressor will be adopted then a short TDS can be just used.

Considering the waveguide attenuation and insertion losses of the waveguide components then for Athos a deflecting voltage of 45 MV can be achieved with a RF power from the klystron of 36 MW and a set of two long TDSs without pulse compressor. On the other hand, a Barrel Open Cavity (BOC) pulse compressor scaled from the C-band linac may be adopted to increase RF power for the TDS [17]. Thus, for Athos a deflecting voltage of 45 MV can be also achieved with a RF power from the klystron of 19 MW and only a single TDS.

CONCLUSION

In this paper we have presented the X-band TDS system for the Athos diagnostic line. We also introduced some details of the mechanical design of the first prototype that will be compatible with the requests from DESY and PSI.

REFERENCES

- [1] C. J. Milne *et al.*, “SwissFEL: The Swiss X-ray Free Electron Laser”, *Appl. Sci.*, vol. 7, no. 720, July 2017.
- [2] R. Ganter *et al.*, “Overview of the soft X-ray line ATHOS at SwissFEL”, presented at the 38th Int. Free Electron Laser Conf. (FEL2017), Santa Fe, USA, August 2017, paper MOP038, this conference.
- [3] J. Alex *et al.*, “Athos Conceptual Design Report”, PSI Report, in press, 2017.
- [4] V. A. Dolgashev *et al.*, *Phys. Rev. ST Accel. Beams*, vol. 17, p. 102801, October 2014.
- [5] C. Behrens *et al.*, *Nature Communications*, vol. 5, no. 3762, April 2014.
- [6] D. Alesini *et al.*, *Nucl. Instrum. Meth. Phys. Res., A* 568 (2006), pp. 488–502.
- [7] R. Akre *et al.*, in *Proc. PAC’01*, Chicago, IL, USA, 2001, pp. 2353-2355.
- [8] H. Ego *et al.*, *Nucl. Instrum. Meth. Phys. Res., A* 795 (2015), pp. 381–388.
- [9] P. Craievich *et al.*, *IEEE Transact.on Nucl. Science*, vol. 62, no. 1, 2015.
- [10] A. Grudiev, “Design of compact high power rf components at X-band”, CERN, Geneva, Switzerland, Rep. CLIC Note 1067, May 2016.
- [11] A. Grudiev, “RF Design of X-band TDS with variable polarization”, presented at *CLIC Workshop 2017*, CERN, Geneva, Switzerland, March 2017.
- [12] U. Ellenberger *et al.*, “Status of the manufacturing process for the SwissFEL C-band accelerating structures”, in *Proc. FEL’13*, New York, USA, paper TUPSO17, pp. 246–249.
- [13] R. Zennaro *et al.*, “High power tests of a prototype X-band accelerating structure for CLIC”, in *Proc. IPAC’17*, Copenhagen, Denmark, May 2017, paper THPIK097, pp. 4318–4320.
- [14] B. Marchetti *et al.*, “X-Band TDS project”, in *Proc. IPAC’17*, Copenhagen, Denmark, May 2017, paper MOPAB044, pp. 184–187.
- [15] E. Prat and M. Aiba, *Phys. Rev. ST Accel. Beams*, vol. 17, p. 052801 (2014).
- [16] F. Christie, J. Roensch-Schulenburg, S. Schreiber, and M. Vogt, “Generation of ultra-short electron bunches and FEL pulses and characterization of their longitudinal properties at FLASH2”, in *Proc. IPAC2017*, Copenhagen, Denmark, May 2017, paper WEPAB017, pp. 2600–2603.
- [17] R. Zennaro *et al.*, in *Proc. IPAC’13*, Shanghai, China, paper WEPFI059, pp. 2827–2829.
- [18] A. Grudiev, P. Craievich, and B. Marchetti, Internal note, to be published.

HLS TO MEASURE CHANGES IN REAL TIME IN THE GROUND AND BUILDING FLOOR OF PAL-XFEL, LARGE-SCALE SCIENTIFIC EQUIPMENT*

Hyojin Choi[†], Sangbong Lee, Hong-Gi Lee, Jang Hui Han, Seung Hwan Kim, Heung-Sik Kang
 Department of Accelerator, PAL-XFEL, Pohang, Korea

Abstract

A variety of parts that comprise large-scale scientific equipment should be installed and operated at accurate three-dimensional location coordinates X, Y, and Z through survey and alignment in order to ensure optimal performance. However, uplift or subsidence of the ground occurs over time and consequently this causes the deformation of building floors. The deformation of the ground and buildings cause changes in the location of installed parts, and eventually that leads to alignment errors (ΔX , ΔY , and ΔZ) of components. As a result, the parameters of the system change and the performance of large-scale scientific equipment is degraded.

Alignment errors that result from changes in building floor height can be predicted by real-time measurement of changes in building floors. This produces the advantage of reducing survey and alignment time by selecting the region where great changes in building floor height are shown and re-aligning components in the region in a short time. To do so, HLS (hydrostatic levelling sensor) with a resolution of 0.2 μm and a waterpipe of 1000 meters are installed and operated at the PAL-XFEL building. WPS (wire position sensor) with a resolution of 0.1 μm is installed at undulator section where the changes in the location of equipment should be measured with two-dimensional coordinates (vertical Y and horizontal X). This paper introduces the installation and operation status of HLS.

INTRODUCTION

As shown in Figure 1, if the ground and the floor of a building changes, the location of equipment changes accordingly and the performance of the PAL-XFEL is degraded [1]. To measure the displacement of building floors in a real time, an ultrasonic-type HLS, which was manufactured by Budker Institute of Nuclear Physics (BINP) of Russia, was installed as shown in Figure 2 [2-3].

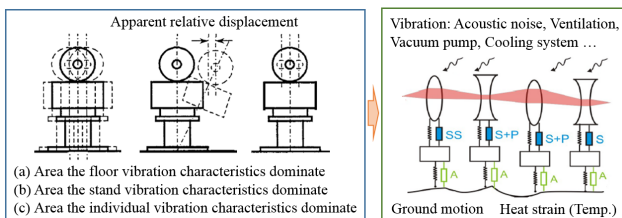


Figure 1: Three vibration patterns which generate relative displacement [1].

*Work supported by Ministry of the Science, ICT and Future Planning
[†]choihyo@postech.ac.kr

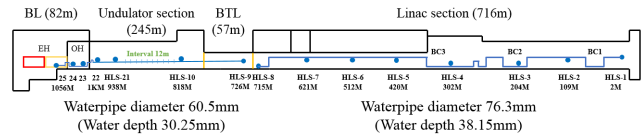


Figure 2: Locations where HLS of PAL-XFEL is installed.

SOURCES OF GROUND VIBRATION

In the section ‘Between model and reality, Part I’ (pp. 237-244) of the Beam Diagnostic textbook published by CERN Accelerator School [4], beam-orbit instability-inducing elements were classified in categories depending on the time scale as shown in Table 1. In addition to geological changes, various vibrations generating inside and outside the buildings affect the equipment and cause beam orbit instability. The CAS textbook describes the elements and countermeasure of beam orbit instability in detail [4].

Table 1: Instability Classified by Time Scale

Instability	Time Scale
Long term	Weeks to years - sun and moon motion - ground settlement - seasonal ground motion
Medium term	Minutes to days - weather (rain, hot, dry, cold, etc.) - diurnal temperature - thermal drift
Short term	Milliseconds to seconds - ground vibration - cooling water flow vibration - machinery vibration (chillers, air conditioners, vacuum pumps, etc.)
Very short term	Higher frequency or shorter periods

Some instability elements described in the CAS textbook are observed on HLS data as shown in Figure 3. Temperature variation is included in the instability elements. The temperature on the HLS was measured to correct the thermal deformation of instruments according to temperature variation.

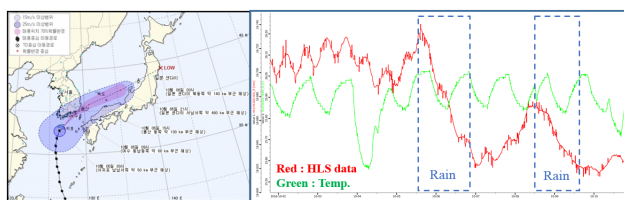
Content from this work may be used under the terms of the CC BY 3.0 licence (© 2018). Any distribution of this work must maintain attribution to the author(s), title of the work, publisher, and DOI.

Content from this work may be used under the terms of the CC BY 3.0 licence (© 2018). Any distribution of this work must maintain attribution to the author(s), title of the work, publisher, and DOI.

HLS SAMPLING RATE

According to the Nyquist sampling theory, the sampling frequency should be at least twice the highest frequency contained in the signal. The sampling rate of HLS should be increased to measure various external vibrations. As HLS was designed to the water level of waterpipes, it may be short-lived or broken down owing to the principle of measurement and electronic structures if the sample rates increase too high. If the water level oscillates by the influence of vibration, some errors occur in HLS measurements that are recorded as randomized vibration on HLS data.

PAL-XFEL records measurements from the HLS every two minutes. If it is intended to measure vibration, installing triaxial vibration sensors will be helpful to measuring accurate high frequency and monitoring vibration from all directions (X, Y, and Z).



Observation of ground motion due to typhoon storm @ 5 Oct. 2016
 Figure 3: HLS data (tide wave, rain, and vibration)



Figure 4: Condition of installed waterpipes and HLSs (Linac on the left and Undulator on the right).

PRESENT CONDITION OF HLS INSTALLATION

As the floor height of undulator building is 1 meter lower than that of the Linac building, waterpipes were installed in the Linac section and Undulator section respectively as shown Figure 2. As shown in Figure 4, as it was impossible to install waterpipes on the floor of the Linac section due to the circumstances, they were installed to the acceleration tube girder. In case of undulator section, waterpipes and HLS were installed on the floor of the building.

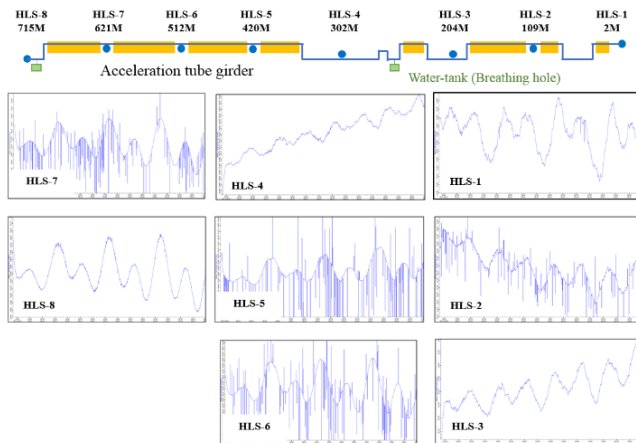


Figure 5: HLS measurements in the Linac section.

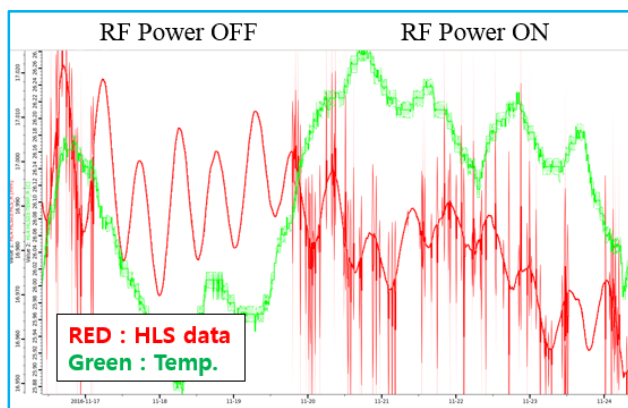


Figure 6: HLS data when RF Power ON and OFF.

In the Linac section, vibration was generated in waterpipes owing to a 80-MW pulse klystron RF power transmitted to the acceleration tube and 1 to 12- μ m of randomized vibration was detected by the four HLSs (HLS-2, 5, 6, and 7) installed on the girder as shown in Figure 5. It means that some shock wave energy vibrates water in the waterpipes randomly through the girder after pulse RF energy was transmitted to the acceleration tube but doesn't mean that it vibrates firmly-fixed acceleration tube and girder. As shown in Figure 6, when the RF output of Klystron was switched off, no randomized vibration was observed. Some vibration-proof pads are planned to be installed on the waterpipe mounts in order to reduce vibration. No vibration was observed on the three HLS attached to the wall side of modulator gallery (HLS-3, 4, 8) and on HLS-1, 7 meters away from the girder. Vibration from LCW (low-conductivity water), which keeps flowing to cool the acceleration tube, was not observed on the HLS measurement.

Table 2: Waterpipe Improvements

Date	Work Content
19 Sep. 2016	Start HLS measurement - no water-tank (no breathing hole): waterpipe is in enclosed state - no tide wave observed in HLS-1 - Tide wave is not visible exactly in HLS-2, 3, 4, 5 - vibration observed in HLS that waterpipe installed at the Linac girder
6 Jan. 2017	Confirm that HLS-1 measurement value is atmospheric pressure change (cause unknown)
15 Jan. 2017	The pressure inside the sealed waterpipe rises and water leaks (waterpipe needs a breathing hole to solve internal pressure problem)
Feb. 2017	Install two water-tanks (breath hole) - HLS connection transparent hose improvement - waterpipe height alignment - no atmospheric pressure observed in HLS-1, but tide wave is not visible exactly
July 2017	Check the water flow of waterpipe - Linac section water flow delayed (Need a breathing hole near to HLS-1)

HLS REFERENCE: WATERPIPE

The flow of waterpipes which provides reference is very important in HLS measurement. A waterpipe the diameter of which was determined in consideration of its length was installed, as shown in Figure 2, so that water flow may be complete within one hour in PAL-XFEL [2]. Table 2 shows the features and improvements resulting from operation of HLS after waterpipes were installed.

The flow of waterpipe was obtained by measuring through HLS the time taken until the water height of waterpipe becomes level after water was injected or drained. As the flow is very fast in the waterpipe of undulator section, the water height becomes level within one hour. As shown in Figure 7, it took more than 2 hours for the water height to become level in the Linac section. In case of HLS-1, it took more than 12 hours for the water height to become level. As the Linac section has eighteen 90 degree curves, it is believed that they interrupt the flow of air and fluids. As HLS-1 is installed at the end of waterpipe, 240 meters away from the breathing hole, it is difficult for air and fluids to flow in an opposite direction at the same time. Therefore, it takes long time for them to flow within the waterpipe. To reduce the water leveling time of HLS-1, some more breathing holes are planned to be installed near to HLS-1.

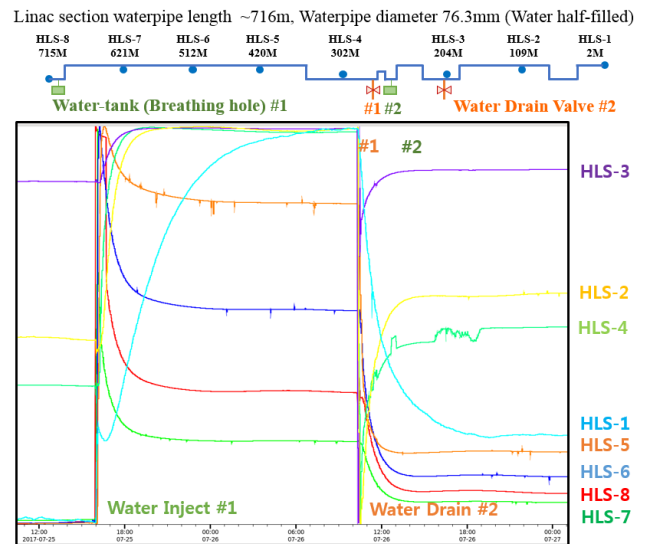
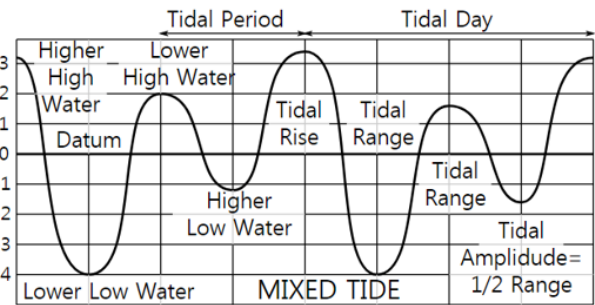


Figure 7: Flow measurements in the Linac section (HLS value axis scales are not same).



Copy from Wikipedia - Tide
 Figure 8: Distribution of tidal phase.

The flow of waterpipe should be fast to monitor HLS in a real time and the tide wave of HLS data be observed at the time-synchronized form. If HLS data are not time-synchronized, the average on tidal periods should be taken as shown in Figure 8.

PRESENT CONDITION OF HLS OPERATION

HLS program was built on the NI-PXI system by using NI LabVIEW [5]. Real-time HLS data can be checked on the operator interface (OPI) screen in the PAL-XFEL operation room. Figure 9 shows the ground variations measured by using HLS data on a weekly basis.

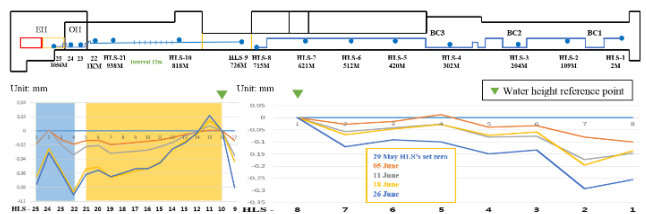


Figure 9: Observation of ground variations by HLS.

Content from this work may be used under the terms of the CC BY 3.0 licence (© 2018). Any distribution of this work must maintain attribution to the author(s), title of the work, publisher, and DOI.

CONCLUSION

The waterpipe design providing reference for HLS measurement is very important and should meet the Table 3 conditions for real-time measurement.

Table 3: Conditions for Real-Time HLS Measurement

- The flow of waterpipe should be fast so that it may become level within one hour.
- The tide wave of all HLS should be time-synchronized.
- All tidal amplitudes should be identical or similar.
- HLS data should have no vibration elements or a small amount of them.

REFERENCES

- [1] Kazuyoshi Katayama *et al.*, “The investigation of vibration of LINAC at KEK”, IWAA’90, pp. 333-342.
- [2] Hyojin Choi *et al.*, “Introduction to BINP HLS to measure vertical changes on PAL-XFEL buildings and ground”, *IPAC’15*, paper MOPTY028.
- [3] Hyojin Choi *et al.*, “The BINP HLS to measurement vertical changes on PAL-XFEL buildings and ground”, FEL’15, paper MOP047.
- [4] *Beam Diagnostics*. CERN-2009-005, Geneva, 2009.
- [5] Hyojin Choi *et al.*, “LabVIEW EPICS program for measuring BINP HLS of PAL-XFEL”, ICAL-EPCS’15, paper WEPGF115.

TUNE-UP SIMULATIONS FOR LCLS-II

M. W. Guetg*, P. J. Emma

SLAC National Accelerator Laboratory, Menlo Park, CA 94025, USA

Abstract

The planned superconducting LCLS-II linac poses new operational constraints with respect to the existing copper linac currently operated for LCLS. We present the results of exhaustive accelerator simulations, including realistic machine errors and exploring beam tune-up strategies. Specifically, these simulations concentrate on longitudinal and transverse beam matching as well as orbit and dispersion control through the new linac and up to the hard x-ray FEL. Dispersion control is achieved by a novel method presented within this paper. The results confirm that the beam diagnostics in the current scheme are sufficient for tune-up, yet identify the importance of dispersion control leading to minor changes in the lattice to further improve performance.

INTRODUCTION

The planned FEL upgrade LCLS-II includes a variety of new subsystems. The complex interplay of all the systems requires good electron beam diagnostics to guarantee beam quality and thus FEL performance. This proceeding outlines three key aspects to evaluate tune-up performance through simulations:

- ▶ Identify redundancy and lack of diagnostics
- ▶ Asses tolerances
- ▶ Test tune-up algorithms

All simulations were done using Elegant 29.0 [1]. The simulations start off with machine settings as present after preliminary phasing of the cavities and initial steering to establish partial transmission and simulate tune-up using readouts as available from LCLS-II diagnostics (Figure 1)

only. Low probability corner cases were covered by repetitions of the simulation using newly generated machine and beam imperfections for each run. Simulated machine imperfections include misalignments of magnets, cavities and beam position monitors (BPMs) as well as strength errors of magnets and cavities. Non-static imperfections like shot-to-shot fluctuations and machine drifts are expected to be small and were neglected. The beam was simulated with a standard setup of 750 A final peak current, 100 pC bunch charge and 4 GeV final beam energy, but initially off momentum and displaced in space for all 3 dimensions, optics and charge. All initial values but the beam optics parameters were randomly drawn from normal distributions with standard deviations as summarized in Table 1. The beam optics error is expressed by the mismatch parameter [2], which was simulated with constant magnitude but random phase drawn independently for both transverse planes. To ensure validity of these studies, the assumed errors are larger than what is expected after initial RF machine phasing and beam based alignment.

The main components of beam misalignment are orbit offsets, dispersion and transverse and longitudinal mismatches. Orbit offsets may arise from various effects. With increasing offset the following effects manifest: Quadrupole magnets will kick the beam and thereby generate dispersion, small apertures (RF cavities, etc) excite transverse wakefields and the beam halo will be lost along the machine. Core beam losses are not assumed for the simulation as the collimation and machine protection system would prevent prolonged operation in this condition [3] and initial phasing and steering is expected to establish transmission.

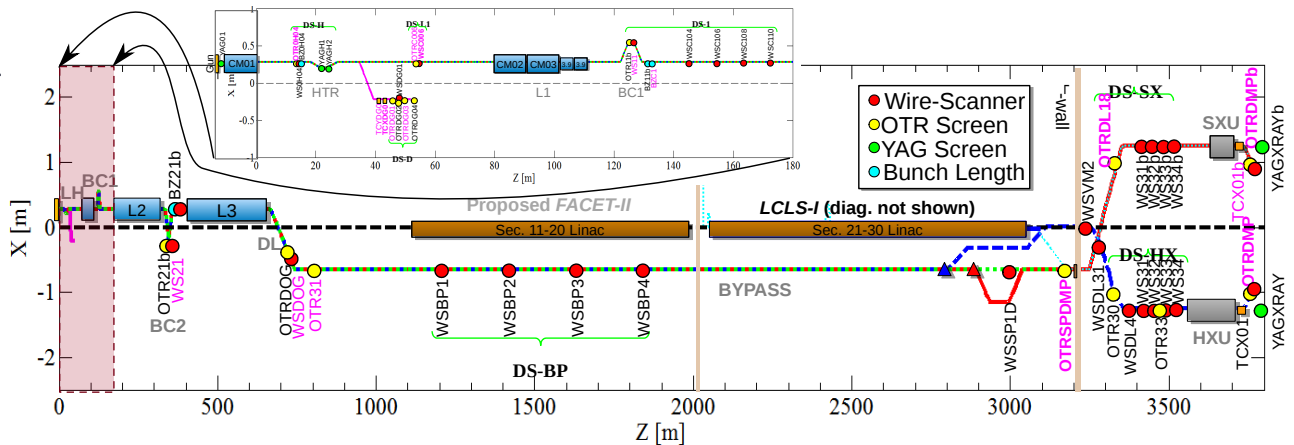


Figure 1: Schematic setup of LCLS-II highlighting locations where the bunch profile can be measured. Not shown on the scheme are BPMs and bunch length monitors

* marcg@slac.stanford.edu

Content from this work may be used under the terms of the CC BY 3.0 licence (© 2018). Any distribution of this work must maintain attribution to the author(s), title of the work, publisher, and DOI.

Uncorrected dispersion increases not only the projected emittance but also the discrepancy between slice and projected optics. It leads to a slice mismatch if only the projected optics can be measured, which is the case for LCLS-II baseline design. Therefore, dispersion control is a major issue. Strong sources of dispersion include dipole strength errors and quadrupole strength errors in dispersive sections and off-center BPMs that are included in an orbit steering.

Transverse matching along the beam line is important to reduce chromaticity and limit adverse effects from transverse wakefields and CSR [4]. Final matching prior to entering the undulator line is critical for good FEL performance.

Simulated collective effects include Coherent Synchrotron Radiation (CSR), transverse and longitudinal wakefields and resistive wall wakefields. While space charge is a major driver of micro-bunching for LCLS-II, it can be neglected with respect to the evaluation of the electron diagnostics and tune-up effectiveness [5] and was therefore not considered here. The presented figures show results after completed tune-up recorded for a typical simulation run.

Table 1: Assumed RMS Error Used for Tuning Simulation Assuming a Normal Distribution. * While the absolute mismatch was kept constant the mismatch phase was altered randomly. The mismatch was introduced prior to QCM01

Item	rms
BPM transverse offset	300 μm
Dipole strength error	1‰
Quadrupole transverse offset	300 μm
Quadrupole longitudinal offset	3 mm
Quadrupole strength error	1‰
RF amplitude error	1‰
RF phase error	5°
RF transverse offset	300 μm
Initial mismatch* ($\xi = \frac{\beta\gamma_0 + \gamma\beta_0 - 2\alpha_0}{2}$)	1.5
Initial centroid offset	1 mm
Initial angular offset	100 μrad
Charge error	5‰
Momentum error	5 MeV

RESULTS

We run tune-up algorithms to improve orbit and dispersion control as well as longitudinal and transverse beam matching within the simulations. First, orbit offsets were corrected given their severe effects and the relative ease of correction using a simplex algorithm relying on the available orbit correctors and BPMs. The resulting orbit offset with respect to the machine center was kept well below 1 mm along the machine, indicating that the available BPMs are sparse but sufficient for tuning.

Next, dispersion was reduced. Dispersion can be measured by correlating orbit with energy fluctuation. The electron central momentum is measured within bunch compres-

sors and the final dogleg. Orbit fluctuations are measured by the over 220 BPMs along the beam line. Given the low shot-to-shot energy jitter expected in LCLS-II (0.01% rms) [6] the sensitivity of energy measurements is not sufficient to calculate dispersion with enough resolution for correction, which thus requires a scan of energy. Dispersion is corrected for by either changing the BPMs offsets and steering the orbit to relative zero within the BPMs, or changing the strength of quadrupole magnets within the dispersive sections. The required correction values are calculated by the pseudo inverse of the dispersion response. Iteration redresses non-linearities and measurement errors. Figure 2 shows the response of dispersion as measured with BPMs to changes in perturbation values (BPMs and quadrupoles) in both transverse directions for the beam line past the bypass line. The values in the upper right and lower left quadrants correspond to offsets in the elements within the 60° rotated transfer line, indicating that this rotated linac turns the correction into a true 4D problem. With this method dispersion errors throughout the machine were reduced below cm level from initial meter size levels.

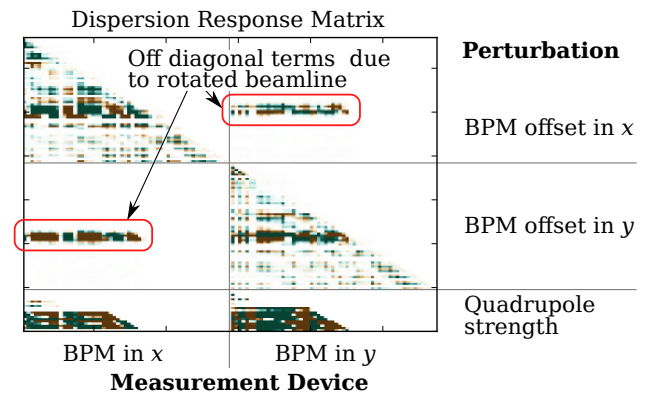


Figure 2: Magnitude of dispersion response to BPM offsets and dispersive quadrupole strengths. Vertical: quadrupoles with altered strengths or BPMs that were offset. Horizontal: BPMs at which dispersion was measured. Each BPM was offset in both transverse directions and dispersion was measured in both directions as well.

Finally, transverse and longitudinal matching along the beam line was accomplished. Initial difficulties in transverse matching were over-come by the dispersion correction. The beam is matched in the following locations:

- ▶ Prior to the laser heater (1 Wire scanner)
- ▶ After the second Bunch compressor (1 Wire scanner)
- ▶ After the dogleg (4 Wire scanner)
- ▶ Within the LTU (4 Wire scanner)

Each matching station is equipped with 4, or more, matching quadrupole magnets. Beam sizes are measured by wire scanners. The matching quadrupole magnets at the bunch compressor are located prior to the chicane ensuring a good match in the critical fourth bending magnet. Correction to mismatch values of $\xi < 1.01$ were achieved for all cases. For longitudinal matching, peak current and energy were tuned using RF phase and amplitude at both bunch compressors and the dogleg (for energy only). The simplex algorithm

readily converged for all cases resulting in final longitudinal beam parameters which are only limited by detector resolution.

The performed simulations showed good tune-up capabilities. Figure 3 shows the projected emittance along the lattice after orbit correction only (top) and a fully tuned run (bottom). In the first case the main contributor to emittance is unclosed dispersion. The simulations showed good preservation of the projected emittance after complete tune-up. The residual emittance increase after the bunch compressors originates from Coherent Synchrotron Radiation (CSR) resulting in transverse offsets along the longitudinal slices. Baseline correction capabilities allow to correction scheme this beamtilt [7].

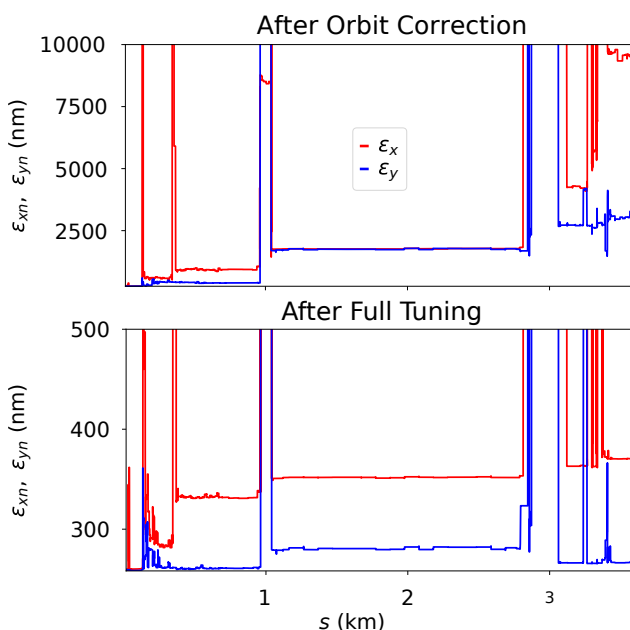


Figure 3: Projected emittance along the beam line for a typical simulation run. Top: Emittance after orbit correction only. Bottom: Emittance after complete tuning.

Figure 4 shows that the slice parameters at the undulator entrance are preserved after complete tune-up. This indicates that there are no major transverse problems, save for centroid slice offsets due to CSR. However, the simulations did not include space charge after the first cryo module. These effects [8] would decrease the resolution of the beam towards the measured sensitivities but increase the values of the slice parameters as compared to the presented results. Impact simulations specifically taking into account space charge were done elsewhere [8].

DISCUSSION

This study shows that both longitudinal and transverse correction and diagnostic as present in LCLS-II are sufficient to match the beam even for tolerances looser than expected in the real machine. Both the projected and slice final beam parameters are more than sufficient for good lasing [9]. The applied correction algorithms performed well and converged

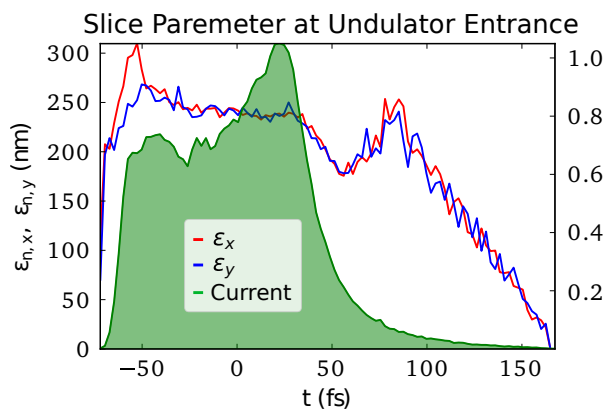


Figure 4: Slice emittance at the undulator entrance of the hard X-ray line.

for all 10 simulated cases. Furthermore, this study highlights the importance of dispersion correction despite the low energy jitter as present in LCLS-II. In consequence, to further empower the presented method for dispersion control, the power supply layout has been updated to allow individual tuning of the quadrupole magnets within the dogleg area enabling better dispersion control.

The authors thank Micheal Borland, Jim Welch, Mark Woodley and Feng Zhou for fruitful discussions. This work has been supported by DOE contract #DE-AC02-76SF00515.

REFERENCES

- [1] M. Borland, "Elegant: A flexible SDDS-compliant code for accelerator simulation," Argonne National Lab., IL (US), Tech. Rep., 2000. [Online]. Available: http://www.osti.gov/bridge/product.biblio.jsp?osti_id=761286
- [2] M. Sands, "A beta mismatch parameter," SLAC, Stanford, CA, Tech. Rep. SLAC-AP-85, Apr. 1991.
- [3] M. Guetg, P. Emma, M. Santana-Leitner, J. Welch, and F. Zhou, "Collimation System Design for LCLS-II," in *Proc. of International Particle Accelerator Conference (IPAC'16)*, Busan, Korea, 2016, paper THPMY043, pp. 3755–3758. [Online]. Available: <http://jacow.org/ipac2016/papers/thpmy043.pdf>
- [4] S. Di Mitri, M. Cornacchia, and S. Spampinati, "Cancellation of coherent synchrotron radiation kicks with optics balance," *Phys. Rev. Lett.*, vol. 110, p. 014801, Jan 2013. [Online]. Available: <http://link.aps.org/doi/10.1103/PhysRevLett.110.014801>
- [5] C. Mitchell, J. Qiang, and P. Emma, "Longitudinal pulse shaping for the suppression of coherent synchrotron radiation-induced emittance growth," *Physical Review Special Topics-Accelerators and Beams*, vol. 16, no. 6, p. 060703, 2013.
- [6] LINAC Coherent Light Source II (LCLS-II), "Final design report," SLAC, Tech. Rep., 2015.
- [7] M. W. Guetg, B. Beutner, and E. P. S. Reiche, "Optimization of free electron laser performance by dispersion-based beam-tilt correction," *Phys. Rev. ST Accel. Beams*, vol. 18, p. 030701, Mar. 2015.

- Content from this work may be used under the terms of the CC BY 3.0 licence (© 2018). Any distribution of this work must maintain attribution to the author(s), title of the work, publisher, and DOI.
- [8] J. Qiang *et al.*, “Start-to-end simulation of the LCLS-II beam delivery system with real number of electrons,” in *Proc. of Free Electron Laser Conference (FEL14)*, Basel, Switzerland.
- [9] G. Marcus and J. Qiang, “LCLS-II SCRF start-to-end simulations and global optimization as of September 2016,” 2017.

BEAM LOSS MONITOR FOR UNDULATORS IN PAL-XFEL*

H. Yang[†] and D. C. Shin
 Pohang Accelerator Laboratory, Pohang 790-784, Korea

Abstract

PAL-XFEL consists of a hard x-ray line, based on a 4-10-GeV electron beam, and a soft x-ray line, based on a 3-3.5 GeV electron beam. The HX line consists of 20 undulators and the SX line consists of 7 undulators. The permanent magnets in an undulator should be protected from the radiation-induced demagnetization. We develop a beam loss monitor (BLM) for undulators in PAL-XFEL. It consists of a detector part (head) and an ADC part. The BLM head consists of two fused quartz rods, two photo-multiplier tube (PMT) modules, and an LED bulb. It is based on the Cherenkov radiator: two fused quartz rods are used for radiators. Two sets of the radiator and PMT module are installed up and down the beam tube. An LED bulb is between the radiators for the heartbeat signal. The ADC part digitizes the output signal of the PMT module. It measures and calculates the beam loss, background, and heartbeat. One ADC processes the signal from 6-8 heads. The BLM system generates interlock to the machine interlock system for over-threshold beam loss. The 28 BLM heads are installed downstream of each undulator. Those are calibrated by the heartbeat signal and operated in the electron beam transmission with 150 pC.

INTRODUCTION

PAL-XFEL produces 0.1 – 1 nm FEL with 4 – 10 GeV electron beam in the hard x-ray (HX) line and 1–10 nm FEL with 3 – 3.5 GeV electron beam in soft x-ray (SX) line. 20 and 7 undulators are installed respectively in the HX line and the SX line. Undulators made with permanent magnets are used for the FEL generation in the XFEL machines [1-3]. Since there is the radiation-induced demagnetization for the permanent magnet, it is important to prevent the electron beam irradiation in the undulator [4]. This irradiation is occurred unintentionally by the electron beam loss in the undulator region caused by abnormal beam orbit and beam size. The beam operation should be blocked until the system is recovered in the normal condition.

We develop the SLAC type Beam Loss Monitor (BLM) system for interlock of the undulator region [5]. The system consists of the BLM head (detector part) and the ADC part. The BLM heads are based on Cherenkov radiators. They are installed after each undulator and measure the beam loss occurred at the drift in each undulator. The beam loss signal is digitized in the ADC system. It calculates the beam loss and generates interlock signal for over threshold beam loss. In this paper, we present the design of the BLM head and ADC system. Also, we present the details of the installation, calibration, and operation of this system.

* work supported by MSIP, Korea.

[†] highlong@postech.ac.kr

BLM HEAD

The BLM head converts Cherenkov radiation by the electron loss into electric signal. It is located in the 1-m long intersection of the undulator region (Fig. 1(a)). It consists of radiators, PMT modules, an LED bulb, and a case (Fig. 2). The radiators are located at up and down of the beam tube (Fig. 1(b)) and the PMT should receive photons from two radiators. Since the width of the BLM head should be minimized for installation of other components in the intersection, we used two PMT modules with small size for each radiator.

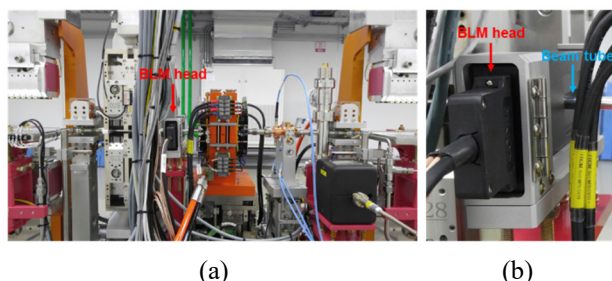


Figure 1: (a) Location of the BLM head at the intersection in the undulator region. (b) Location of the BLM head and the beam tube.

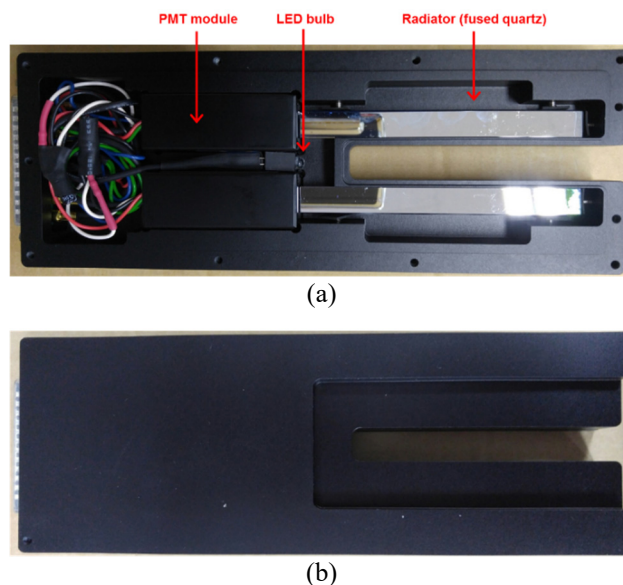


Figure 2: Structure of (a) the inside and (b) the back of the BLM head.

Content from this work may be used under the terms of the CC BY 3.0 licence (© 2018). Any distribution of this work must maintain attribution to the author(s), title of the work, publisher, and DOI.

The model of the PMT module is Hamamatsu H10722-110. It has 230 – 700-nm spectral response range, 1-V/ μ A conversion factor at 1-V control voltage, and 8-mm-diameter effective area. The radiators are the fused quartz rods with 11-mm \times 11-mm \times 110-mm size (Fig. 3). When the lost electrons enter the radiator, the Cherenkov radiation is emitted in random direction along the incidence angle of electrons. In order to transmit the radiation to the PMT with less loss, a pure aluminium film was coated onto 5 faces of the radiators for the reflector and an AR coating layer with 400 – 500-nm penetration wavelength was coated in the face to meet the PMT module for more penetration of light (Fig. 3). The additional AR coating layer was coated in the corner of one longer face for penetration of light from the LED bulb (Fig. 3).

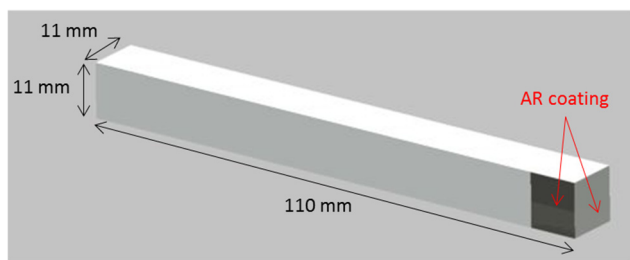


Figure 3: Drawing of the fused quartz rod.

The LED bulb with 5-mm diameter and 480 – 520-nm wavelength is for the heartbeat signal. It checks operation of the PMT module by its pulsed operation after electron beam time. The case is a rectangular shape with 24.7-mm \times 85-mm \times 236-mm size, and made of aluminium. There is a groove with 13-mm height and 105-mm length for the beam tube (Fig. 2). Since the inner area of the BLM head should be darkroom to reduce the background noise of PMT, the surface of case was anodized (Fig. 2). The empty space in the back of the BLM head (Fig. 2(b)) is for installation of other material with upper atomic number than aluminium. Since it makes more secondary electrons for lost electrons, the measuring resolution of the beam loss can be improved.

ADC SYSTEM

ADC system for BLM is divided into the power unit and the VME system (Fig. 4). The power unit consists of the Single Board Computer (SBC), FPGA, 16-channel DAC, and power module (Fig. 5). The SBC with EPIC IOC controls digital/analogue signal, FPGA, and the data acquisition. The FPGA generate the heartbeat signal from the input trigger. It has 8-output channels. PMT gain voltage is controlled 0.1 – 1.1 V by the 16-channel DAC.

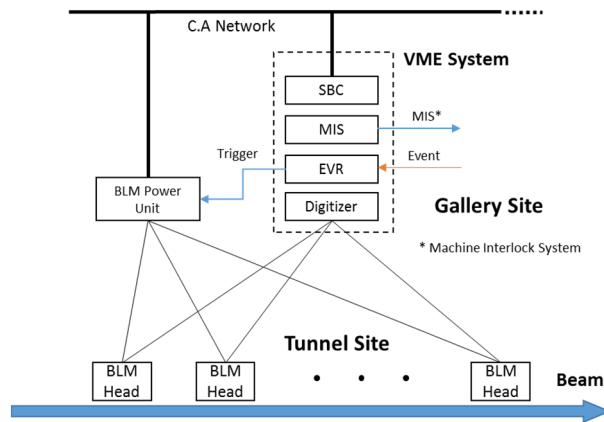


Figure 4: ADC system for the BLM.

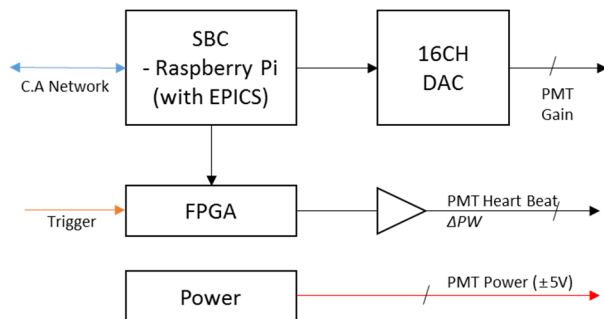


Figure 5: Power unit for the ADC system.

The VME system consists of the digitizer, Event Receiver (EVR), SBC, and Machine Interlock System (MIS) card (Fig. 6). The digitizer has 14-bit resolution and \pm 5-V input voltage range. We can switch its sampling frequency with 0.78, 1.56, 3.125, 6.25, 12.5, 25, 50, and 100 MS/s. We use 0.78 MS/s in the BLM operation and the one-time unit for the AD is about 1.28 μ s. The EVR receive the event data from the Event Generator (EVG) and generates the trigger and event cord for the BLM system. The MIS card link the BLM to MIS system. When the beam loss over the threshold is occurred, the MIS card send the interlock signal and the MIS system block the laser shutter in the electron gun. The details of devices for the ADC system is shown in Table 1.

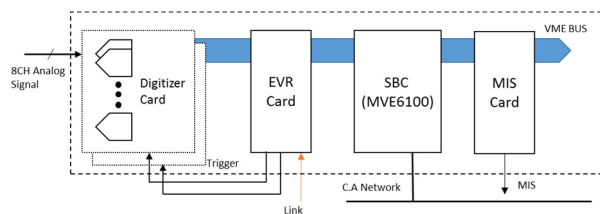


Figure 6: VME system for the ADC system.

Table 1: The Details of Devices for the VME System

Device	Specification
SBC	Raspberry Pi, Linux OS, with EPICS IOC
FPGA	8-channel output
DAC	16-channel output
Power module	PMC15E-3 (COSEL)
Digitizer	V1724 (CAEN), 14bit, +/-5V, 8 S/F (MS/s) (0.78, 1.56, 3.125, 6.25, 12.5, 25, 50, 100)
EVR	for event trigger and cord
SBC	EMVME6100 (EMERSON)
MIS card	8-channel output, self-development

The event timing for the BLM system has a dual-class time trigger and a triple-class time window (Figs. 7 and 8). The triggers are divided the digitizer trigger for the beam signal and the heartbeat trigger. The time windows consist of the beam-loss, background, and heartbeat. The beam-loss window is for measuring the beam loss signal. The background window is located between the beam-loss and heartbeat windows for measuring the background noise. The heartbeat trigger is generated 1150 μ s after the digitizer trigger and the heartbeat window start at the same time. The range of whole time window is about 1300 μ s (1024 time unit for the AD) for one pulse. We can control the timing of the triggers and windows freely in this range (Fig. 8).

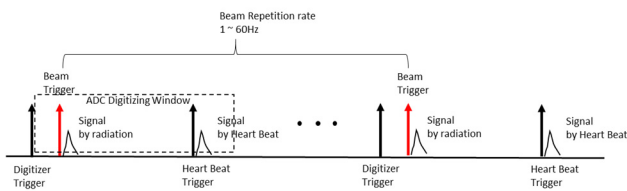


Figure 7: Event trigger for the BLM system.

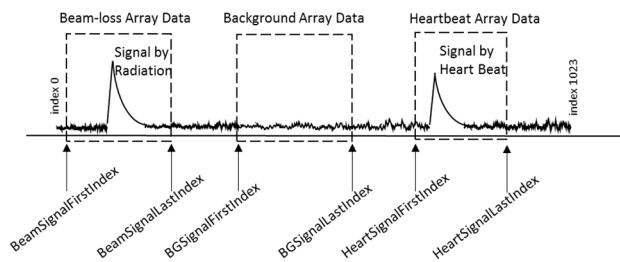


Figure 8: Timing window and data acquisition for the BLM system.

INSTALLATION, CALIBRATION, AND OPERATION

Twenty BLM heads were installed in the intersection for the HX line and 7 ones were installed for the SX line. Three ADCs were installed for the HX line and an ADC was installed for the SX line. The first ADC was connected to the first six BLM heads, the second one was connected the next six heads, and the third one was connected to the final eight heads in the HX line. Figure 9 shows the operation program for one BLM head. It can control the time windows of beam-loss, background, and heartbeat, the PMT control voltage, thresholds, and the pulse width of heartbeat signal. The beam loss (L_{beam}) is calculated by

$$L_{beam} = \frac{\int (\text{loss signal})}{\Delta t_{beam}} - \frac{\int (\text{background signal})}{\Delta t_{back}}, \quad (1)$$

where Δt_{beam} is the time window of beam loss and Δt_{back} is the time window of background. The unit of time is about 1.28 μ s (1/AD frequency).

If L_{beam} exceeds the threshold of beam loss, the BLM system generates interlock to machine interlock system (MIS) and the MIS close the laser shutter in the injector. Also, when the heartbeat signal is less than the heartbeat threshold because of problems in the PMT module, interlock signal is generated.

When the large beam loss occurs, the beam loss signal affects the signal in the time window of background. Therefore, we use the threshold of background – if the background ($\int(\text{background signal})/\Delta t_{back}$) is larger than the threshold of background, the threshold of background is applied for the calculation of L_{beam} (Fig. 10).

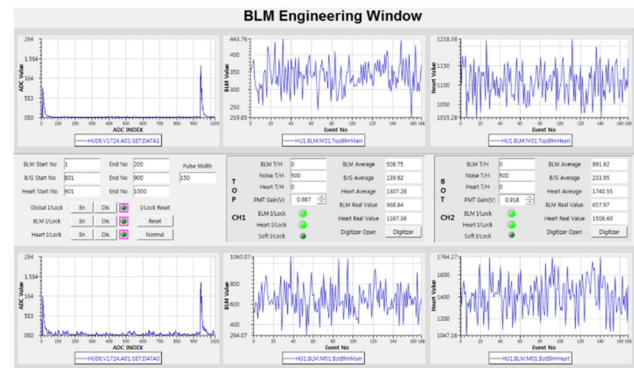


Figure 9: Operation program for the BLM system.

Content from this work may be used under the terms of the CC BY 3.0 licence (© 2018). Any distribution of this work must maintain attribution to the author(s), title of the work, publisher, and DOI.

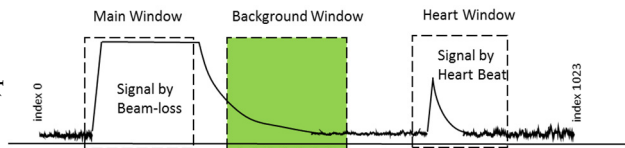


Figure 10: Timing window for the BLM system. When the beam loss affects in the time window of background, the threshold of the background is used.

Since there are different sensitivity in each PMT, the PMT gain (G_{PMT}) were calibrated. We use the heartbeat signal for the criterion of the calibration because the intensities of LEDs and the inner structure of BLM heads are uniform. We applied the heartbeat signal with about 5-V amplitude and 0.9-ms pulse width and adjusted the control voltage until the flat top of the heartbeat signal became 10000 time unit of AD (Fig. 11(a)). We got the calibrated control voltage (V_{cal}) and set that $V_{cal} + 0.6$ V. The relation function between G_{PMT} and control voltage (V_{ctrl}) is

$$G_{PMT,n} = a_n \cdot V_{ctrl,n}^{8.6}, \quad (2)$$

where a_n is a constant for each BLM. The pulse width of heartbeat signal reset 190 μ s for operation (Fig. 11(b)). The time window settings are 1 – 200 for the beam-loss, 801 – 900 for the background, and 901 – 1000 for the heartbeat (Fig. 10). We conduct the beam based alignment, beta matching, and orbit correction for the undulator region. Therefore, we achieve the beam transport with less loss in 4 – 10-GeV, 150-pC e-beam condition.

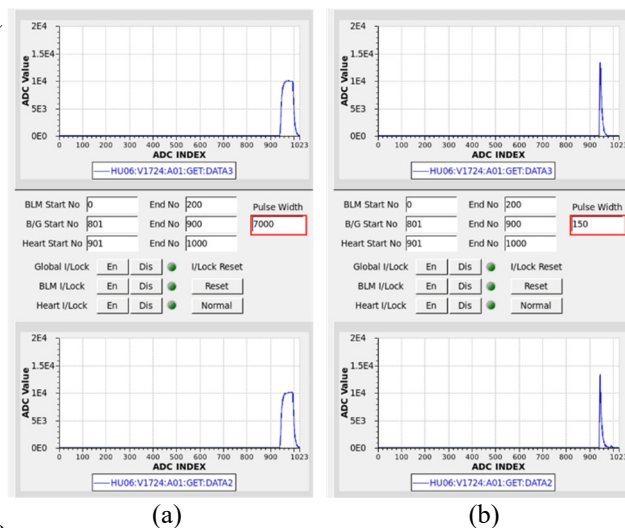


Figure 11: Parameters setting of the BLM system for the (a) calibration and (b) operation.

SUMMARY AND FUTURE WORK

We developed the BLM system to prevent the radiation-induced demagnetization of undulators. It consists of the BLM head and ADC system. The BLM head is based on the Cherenkov radiator. Two fused quartz rods were used for the radiator and located up and down of beam tube. The Cherenkov radiation by the beam loss is measured by PMT module with 230 – 700-nm spectral response range. The PMT signal is digitized in the ADC system and the beam loss calculated from beam-loss and background signal. The heartbeat signal from the LED bulb in the BLM head is also calculated for indicating the BLM system operation.

The ADC system consists of the power unit and the VME system. The power unit supply the gain voltage for the PMT module and the operation power for all sub devices. All analogue signals are digitized to 0.78 MS/s sampling frequency and the time triggers and windows is controlled in the VME system. When the beam loss exceeds the threshold, an interlock signal is sent to the MIS system and it blocks the e-beam generation. 20 BLM heads were installed in the intersection for the HX line and 7 ones were installed for the SX line. 3 ADC were installed for the HX line and one ADC was installed for the SX line. Since there are different sensitivity in each PMT, the PMT gain were relatively calibrated by the heartbeat signal from the LED operation of 5-V and 0.9-ms pulse width.

The integrated value of BLM signal relates the accumulated radiation dose of undulators. If one wants to get the absolute accumulated radiation dose from the BLM signal, the BLM should be calibrated by the dosimetry. We plan this calibration to install the TLD in front of radiators in the BLM head and measure the dose during one FEL operation shift. We expect the correct quantification of the beam loss by this calibration. Also, we expect that it used effectively for the maintenance and replacement of the undulators.

REFERENCES

- [1] J. Arthur *et al.*, “Conceptual design report: Linac Coherent Light Source (LCLS),” SLAC-R-593, 2002.
- [2] S. Gota *et al.*, “XFEL/SPring-8 beamline technical design report,” SPring-8 Technical Document, 2010.
- [3] D. E. Kim *et al.*, in *Proceedings of IPAC’12*, New Orleans Louisiana, USA, p. 1738.
- [4] J. Alderman *et al.*, “Radiation-induced demagnetization of Nb-Fe-B permanent magnets,” LS-290, 2000.
- [5] W. Berg *et al.*, in *Proceedings of LINAC’08*, Victoria, BC, Canada, p. 492.

COHERENT UNDULATOR RADIATION FROM A KICKED ELECTRON BEAM

J. P. MacArthur*, A. A. Lutman, J. Krzywinski, Z. Huang,
SLAC National Accelerator Laboratory, Menlo Park, USA

Abstract

The properties of off-axis radiation from an electron beam that has been kicked off axis are relevant to recent Delta undulator experiments at LCLS. We calculate the coherent emission from a microbunched beam in the far-field, and compare with simulation. We also present a mechanism for microbunches to tilt toward a new direction of propagation.

INTRODUCTION

During the commissioning of the Delta undulator at LCLS, a highly circularly polarized beam was produced by kicking the electron beam prior to the Delta undulator [1]. This situation is depicted in Figure 1. With the right detune in the Delta undulator parameter K , a large angular separation between linear light produced prior to the Delta and circular light produced in the Delta was observed. This result is non-intuitive because, as seen in Figure 1, the microbunches don't realign themselves in the direction of propagation.

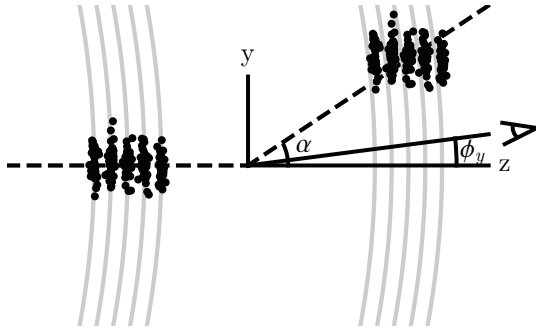


Figure 1: Microbunched electrons traveling left to right (black) are kicked by an angle $\alpha \ll 1$ in the y direction. The microbunches drift relative to the extant electric field (gray). An observer examines the far-field power at an angle ϕ_y .

Here the coherent radiation from a kicked beam is analyzed from a classical synchrotron radiation perspective. The motion of an electron in a diffracting electric field is also investigated.

COHERENT EMISSION FROM ANGLED MICROBUNCHES

The electric field in the paraxial approximation from a single electron traveling on axis and with no transverse velocity in an undulator of length L_u is [2]

$$\mathcal{E}_{v,j}^0(\phi, z = L_u) \propto e^{i\omega t_j} \int_0^{L_u} e^{ikz'\phi^2/2} e^{i(\nu-1)k_u z'} dz', \quad (1)$$

* jmacart@slac.stanford.edu

where $\mathcal{E}_{v,j}^0(\phi, z)$ is the field at an angle ϕ and wavenumber $k = \omega/c = \nu k_1$, t_j is the electron arrival time at $z = 0$, and k_1 is the wavenumber resonant to an undulator of period $\lambda_u = 2\pi/k_u$. The frequency of interest is detuned by an amount $\Delta\nu = \nu - 1 = (k - k_1)/k_1$ from the undulator resonant frequency.

The electric field from an electron with position \mathbf{x}_j , transverse velocity $d\mathbf{x}_j/dz = \mathbf{x}'_j$, and energy deviation from resonance $\eta_j = (\gamma - \gamma_r)/\gamma_r$ is [2]

$$\mathcal{E}_{v,j}(\phi, L_u) = e^{-ik\phi \cdot \mathbf{x}_j} \mathcal{E}_{\nu-2\eta_j,j}^0(\phi - \mathbf{x}'_j, L_u). \quad (2)$$

In order to calculate the power from the kicked beam shown in Figure 1, we sum and square the contributions from all N_e electrons,

$$P(\phi, L_u) = \sum_j^{N_e} |\mathcal{E}_{v,j}|^2 + \sum_j^{N_e} \sum_{k \neq j}^{N_e} \mathcal{E}_{v,j} \mathcal{E}_{v,k}^*. \quad (3)$$

The first sum is inconsequential for a bunched beam, while the double sum is typically converted into a double integral over the electron probability distribution, $f(\mathbf{x}_j, \mathbf{x}'_j, \eta_j, t_j)$.

For simplicity we assume that all variables are independent and therefore f is separable. The expression for the power takes a simple form when the beam has no spread in energy ($\eta_j = 0$), and no spread in angle ($\mathbf{x}'_j = 0$). These assumptions eliminate the emittance effects discussed in Ref [3], but other effects become more apparent. To match Figure 1, we set $\mathbf{x}'_j = (0, \alpha)$. The explicit form of the longitudinal distribution $f(t_j)$ is not important for this calculation, so we set

$$\int e^{i\omega t} f(t) dt = b. \quad (4)$$

After integrating over \mathbf{x} and t , the power is seen to be

$$P(\phi_x, \phi_y) \propto |b|^2 |\tilde{f}(\phi_x, \phi_y)|^2 \times \text{sinc}^2 \left[\pi N_u \left(\Delta\nu + \gamma_z^2 \phi_x^2 + \gamma_z^2 (\phi_y - \alpha)^2 \right) \right], \quad (5)$$

where

$$\tilde{f}(\phi_x, \phi_y) = \int d\mathbf{x} f(x, y) e^{ik\phi \cdot \mathbf{x}} \quad (6)$$

is the spatial transform of the transverse distribution, $N_u = L_u/\lambda_u$ is the number of oscillations in the wiggler, and $\gamma_z^2 = \gamma^2/(1 + K^2)$. Expressions similar to Equation 5 are derived elsewhere [3–5]. If \mathbf{x} is normally distributed around zero with rms spread σ ,

$$P(\phi_x, \phi_y) \propto |b|^2 e^{-k^2 \sigma^2 (\phi_x^2 + \phi_y^2)} \times \text{sinc}^2 \left[\pi N_u \left(\Delta\nu + \gamma_z^2 \phi_x^2 + \gamma_z^2 (\phi_y - \alpha)^2 \right) \right], \quad (7)$$

Examining Equation 7, the far-field intensity may be maximized by setting the argument of the sinc function equal to zero with $\phi = 0$. The detune $\Delta\nu^*$ required to correct for a tilt α is

$$\Delta\nu^* = -\gamma_z^2 \alpha^2. \quad (8)$$

This prediction is compared to Genesis simulation results in a subsequent section.

Another point of interest is the angle ϕ_y , at which the maximum radiation intensity occurs for a non-optimal detune $\Delta\nu$ and kick α . In order to arrive at a compact expression, we approximate the sinc² function as a Gaussian centered at 0 with the appropriate width, $\text{sinc}^2(x) \approx e^{-x^2/3}$. With this simplification the angle ϕ_y^* of maximum emission is the only real solution to

$$6N\phi_y^* = (\alpha - \phi_y^*)\pi N_u \left(\gamma_z^2 (\alpha - \phi_y^*)^2 + \Delta\nu \right), \quad (9)$$

where $N = k\sigma^2/L_u$ is the electron beam Fresnel number [4]. This simplification ignores the local maxima of the sinc function that occur away from the origin, though similar equalities could be written for these maxima. Equation 9 is compared to Genesis simulation results with LCLS-like parameters in a subsequent section.

For beams with a large transverse size, $N \rightarrow \infty$, and therefore $\phi_y^* \rightarrow 0$. Such a beam will only radiate perpendicular to its microbunches.

For beams of small transverse size, $N \rightarrow 0$, and therefore $\phi_y^* \rightarrow \alpha + (\alpha\Delta\nu/|\alpha\Delta\nu|)|\Delta\nu|^{1/2}/\gamma_z$. In this regime, radiation at or beyond the kick angle α is possible.

The number of wiggle periods N_u is important in the intermediate regime where N is close to unity. N_u governs how sharp the sinc² function is. Thus, a long undulator will have more concentrated off-axis emission.

A MECHANISM TO TILT MICROBUNCHES

The previous section showed that off-axis emission from a tilted microbunch is predicted from classical radiation theory. In this section, however, we show that a microbunch kicked off-axis is expected to realign towards the new direction of travel. This effect is not large, but may be large enough to extend the off-axis radiation farther off axis. This realignment is the result of an interaction with an extant electric field.

For simplicity we consider the dynamics of an electron moving in a diffracting Gaussian field E are described by the FEL pendulum equations [2],

$$\frac{d\theta}{dz} = 2k_u\eta \quad (10)$$

$$\frac{d\eta}{dz} = 2\chi_1 E(y, z) \quad (11)$$

$$E(y, z) = \frac{E_0 w_0}{w(z)} e^{-y(z)^2/w(z)^2} \cos(\psi(z) + \theta), \quad (12)$$

where θ is the electron phase, $\eta = (\gamma - \gamma_0)/\gamma_0$ is the energy deviation, $\chi_1 = Ke/\sqrt{2}\gamma_0 mc^2$, w_0 is the beam waist size, $w(z)^2 = w_0^2(1 + z^2/z_r^2)$, $z_r = \pi w_0^2/\lambda$ is the Rayleigh range, and

$$\psi(z) = \tan^{-1}\left(\frac{z}{z_r}\right) - \frac{ky(z)^2}{2z(1 + z_r^2/z^2)}. \quad (13)$$

The FEL resonance condition eliminates the $kz - \omega t$ phase accrual in an electric field, but the Gouy phase $\tan^{-1}(z/z_r)$ and the off-axis term in $\psi(z)$ cannot be accounted for by a wiggler with a constant K value. Equation 12 is written with $z = 0$ corresponding to the Gaussian beam waist. While the actual beam waist is behind the end of an undulator, we argue momentarily that the curvature of the field not critical under LCLS-like conditions, and the exponential drop-off in intensity plays a more important role. The FEL pendulum equations are usually written with a third differential equation relating the field growth to the bunching. In this analysis we ignore this effect, and therefore the result is not self-consistent. We believe the model still provides some understanding of the phenomena observed in simulation, so we proceed. In analogy to Figure 1, only the radiation from undulators upstream of the kick will affect the particle dynamics discussed here.

We will also assume that the transverse position of the electron is simply

$$y(z) = \alpha z + y_0. \quad (14)$$

This trajectory ignores undulator focusing and transverse field effects. Equations 10-12 can easily be solved numerically, but insight is gained from making two assumptions.

The first simplification is that the electron is kicked far beyond a beam waist after propagating a distance z_r ,

$$\alpha \gg \frac{w_0}{z_r} = \frac{\lambda}{\pi w_0}. \quad (15)$$

During Delta experiments, this criterion is weakly satisfied. Typical values for α are around 30–60 μrad , while matching simulations at 850 eV tells us that $\lambda/(\pi w_0) \approx 15 \mu\text{rad}$.

The assumption in Equation 15 means the exponential factor in Equation 12 will have turned off any interaction long before an electron travels a Rayleigh range. Therefore, the phase factor

$$\psi(z) = \tan^{-1}\left(\frac{z}{z_r}\right) - \frac{k(y_0 + \alpha z)^2}{2z(1 + z_r^2/z^2)} \quad (16)$$

is zero for the duration of interaction when $y_0 = 0$.

A corollary is $y_0 \ll \alpha z_r$, generalizing the previous statement to include non-zero y_0 . This follows directly from Equation 15 since a typical electron transverse starting position is of the same order as w_0 .

The second assumption is that the phase θ in Equation 12 may be treated as constant. This may be justified by requiring that the phase, θ_e , accumulated over the distance

at which $E(y, z)$ is decreased by $1/e$ is small. It follows from Equations 10-12 that, for $y_0 = 0$,

$$|\theta_e| < 2\chi_1 |E_0| k_u \frac{w_0^2}{\alpha^2} \left(\frac{1}{e} - 1 + \sqrt{\pi} \text{Erf}(1) \right), \quad (17)$$

where $\text{Erf}(x)$ is the error function. Since $|y_0| \lesssim w_0$, this argument still holds for nonzero y_0 . For the LCLS-like situation analyzed in the subsequent section, the left hand side of the inequality evaluates to 0.26.

With these two assumptions, Equations 10 and 11 take a much simpler form,

$$\frac{d\theta}{dz} = 2k_u \eta \quad (18)$$

$$\frac{d\eta}{dz} = 2\chi_1 E_0 e^{-(y_0+\alpha z)/w_0^2} \cos \theta_0. \quad (19)$$

These equations have simple solutions expressed in terms of the error function. Of interest here is the microbunch angle, $\alpha_b = -(k)^{-1} d\theta/dy$ at a particular location z . The on-axis ($y_0 = 0$) angle is

$$\alpha_{b,y_0=0} = \frac{E_0 \chi_1 w_0}{\alpha^2 \gamma_z^2} \left(2 \frac{z\alpha}{w_0} - \sqrt{\pi} \text{Erf} \left(\frac{z\alpha}{w_0} \right) \right) \cos \theta_0. \quad (20)$$

The scaling with z is somewhat hidden by the error function, but the rate at which the slope changes with z is more elucidating,

$$\left. \frac{d\alpha_b}{dz} \right|_{y_0=0} = \frac{2E_0 \chi_1}{\alpha \gamma_z^2} \left(1 - e^{-z^2 \alpha^2 / w_0^2} \right) \cos \theta_0. \quad (21)$$

Evidently after a quick energy modulation for $z \lesssim w_0/\alpha$, the microbunches continue to shear. The shearing continues indefinitely in this model, similar to the first step in the EEHG scheme [6]. However, a non-zero energy spread and emittance, not included here, will also rapidly debunch the beam.

Another feature of note is the importance of the initial phase, θ_0 . When operating the Delta undulator, a phase shifter immediately before the wiggler allows for a particular phase, and therefore tilt.

A quantitative comparison of Equation 20 with Genesis simulations are shown in the next section.

COMPARISON WITH SIMULATION

In this section we compare the predictions of the previous sections with Genesis [7] simulations. The simulation conditions, seen in Table 1, were chosen to match experiments done at LCLS. In order to generate a useful test, a pre-microbunched beam is sent through a 3.2-m helical afterburner.

The beam is pre-microbunched in a reverse tapered LCLS-like undulator 9 undulator segments in length. This reverse tapered undulator generates a microbunched beam and 0.34 GW of background, linearly polarized radiation. This background field is decomposed into right and left circular components, and sent into a helical afterburner with variable K .

Table 1: Simulation Parameters

Parameter	Value
Beam energy	4.37 GeV
Energy spread	1.8 MeV
Photon energy	850 eV
Peak current	2.5 kA
Emittance	0.4 μm
Afterburner length	3.2 m

The predicted detune required for maximum power, Equation 8, is compared with the radiation produced in the helical afterburner in Figure 2. The coherent radiation model matches simulation even though the afterburner is more than a gain length long. The prediction (dashed) is compared with Genesis results (solid) for $\alpha = 30 \mu\text{rad}$ and $\alpha = 60 \mu\text{rad}$. A 0- μrad K -scan is shown for comparison.

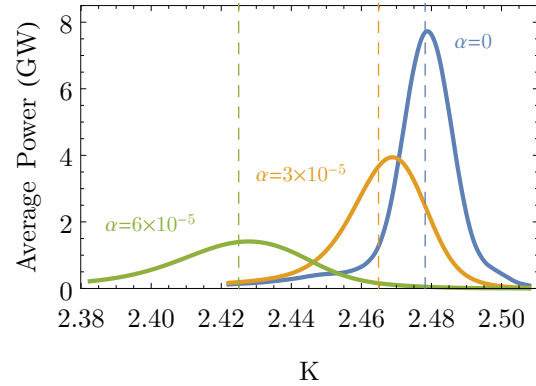


Figure 2: The average power from a Genesis simulation output as a function of afterburner K . A kick of $60 \mu\text{rad}$ (green), $30 \mu\text{rad}$ (orange), and $0 \mu\text{rad}$ (blue) are plotted along with the prediction from Equation 8.

Figure 3 compares the predicted angle at which the power is maximized, Equation 9, with the simulated angle at which power is maximized for $\alpha = 30 \mu\text{rad}$. The prediction fails at a large positive detune because the sinc^2 function's secondary local maxima are ignored in Equation 9.

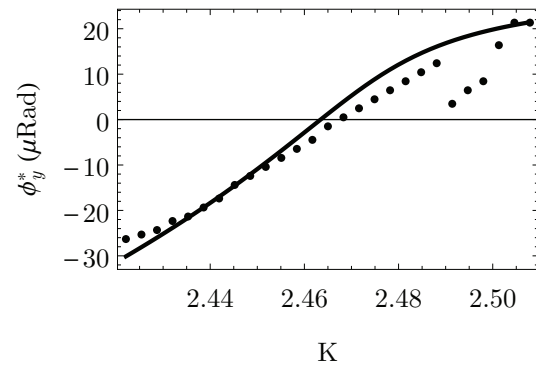


Figure 3: The angle of maximum emission as a function of K value is plotted for $\alpha = 30 \mu\text{rad}$. Genesis results are dots, while the solid line is Equation 9.

Figure 4 compares the predicted microbunch angle, Equation 20, with the microbunch angle observed in Genesis simulations after a 30- μ rad kick. The phase is set to $\theta_0 = 0$ for comparison. The microbunch angle is calculated from the Genesis output file by performing an angular transform on the complex bunching factor for each output slice, and averaging over all slices. In this way the average angle is automatically weighted by the strength of the bunching in a given slice.

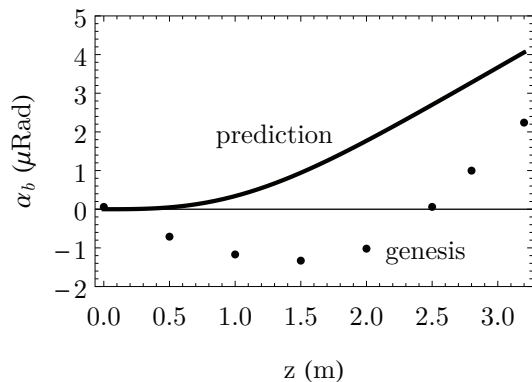


Figure 4: The predicted microbunch angle (solid) is plotted against the microbunch angle calculated from a Genesis output (dots).

REFERENCES

- [1] A. A. Lutman *et al.*, “Polarization control in an X-ray free-electron laser,” *Nat. Photon.*, vol. 10, p. 468, May 2016.
- [2] K. Kim, Z. Huang, and R. Lindberg, *Synchrotron Radiation and Free-Electron Lasers*. Cambridge, UK: Cambridge University Press, 2017.
- [3] T. Tanaka, H. Kitamura, and T. Shintake, “Consideration on the BPM alignment tolerance in X-ray FELs,” *Nucl. Instr. Meth. Phys. Res.*, vol. 528, p. 172, Aug. 2004.
- [4] E. L. Saldin, E. A. Schneidmiller, and M. V. Yurkov, “A simple method for the determination of the structure of ultrashort relativistic electron bunches,” *Nucl. Instr. Meth. Phys. Res.*, vol. 539, p. 449, Mar. 2005.
- [5] G. Geloni, V. Kocharyn, and E. Saldin, “On radiation emission from a microbunched beam with wavefront tilt and its experimental observation,” arXiv 1706.10185, Jun. 2017.
- [6] G. Stupakov, “Using the beam-echo effect for generation of short-wavelength radiation,” *Phys. Rev. Lett.*, vol. 539, p. 449, Mar. 2005.
- [7] S. Reiche, “GENESIS 1.3: a fully 3D time-dependent FEL simulation code,” *Nucl. Instr. Meth. Phys. Res.*, vol. 102, p. 074801, Feb. 2009.

HELICAL UNDULATORS FOR COHERENT ELECTRON COOLING SYSTEM*

P. Pinayev[†], Y. Jing, R. Kellerman, V.L. Litvinenko, J. Skaritka, G. Wang,
 BNL, Upton, NY 11973, U.S.A.
 I. Ilyin, Yu. Kolokolnikov, S. Shadrin, V. Shadrin, P. Vobly, V. Zuev,
 Budker INP, Novosibirsk, Russia

Abstract

In this paper, we present the description and results of the magnetic measurements and tuning of helical undulators for the Coherent electron Cooling system (CeC). The FEL section of the CeC comprises three 2.5-m long undulators separated by 40-cm drift sections, where BPMs and phase-adjusting 3-pole wigglers are located. We present design, tuning techniques and achieved parameters of this system.

INTRODUCTION

Coherent electron cooling proof-of-principle (CeC PoP) experiment is conducted at relativistic hadron collider (RHIC) in the Brookhaven National Laboratory (USA) to test the basic physical principles underlying coherent electronic cooling [1]. The coherent electron cooling is based on the electrostatic interaction between electrons and hadrons, when density modulation of the electron bunch induced by the hadrons is amplified by a high-gain single pass free-electron laser (FEL) structure and is subsequently used to reduce the energy spread of the hadron beam [2].

The requirements on the wiggler parameters shown Table 1 are defined by the CeC PoP physics and are set to obtain high gain in the FEL. The high gain requirement contributed to the choice of the helical undulator as well. The undulator have fixed gap which simplifies design, manufacturing and tuning.

The undulator gap is rather large to accommodate hadron beams circulating in RHIC. The hadron beams have vertical separation of 10 mm at the location of the FEL to prevent their collision. Therefore, we decided to make undulator vacuum chamber square and rotated by 45°. Although gap is fixed the undulator design should provide capability for opening for insertion the vacuum chambers.

Table 1: Undulator Specifications

Parameter	Value
Wiggler parameter, a_w	0.5 +0.05/-0.1
Undulator gap	32 mm
Period	40±1 mm
RMS Phase Error	< 1° (3° peak-to-peak)
1 st field integral	< 30 Gs·cm
2 nd field integral	< 300 Gs·cm ²

* Work supported by the US Department of Energy under contract No. DE-SC0012704.

[†] pinayev@bnl.gov

DESIGN AND MANUFACTURING

The undulator body was made from the aluminum alloy, which has sufficient stiffness and no magnetic properties. Its magnetic structure is pure permanent magnet [3]. A design allows for the correction of the magnetic field at any point of the undulator.

The magnetic structure of the undulator comprises of two types of magnets. The first one has longitudinal magnetization, and the second type has transverse magnetization. Since a magnet with longitudinal magnetization has zero first integral, the error correction can be performed only by a magnet with transverse magnetization. The size and configuration of magnets with transverse magnetization is chosen such that a magnetic force of 10 kg pushes them out of the groove and presses the magnet to adjusting screws, and magnets with longitudinal magnetization are pushed back against the cassette slot with a force of 6 kg (see Fig. 1).

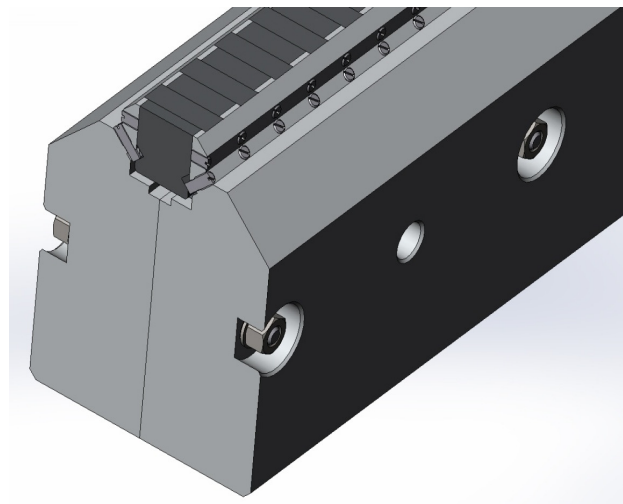


Figure 1: Cassette design. Cassette comprises two precisely machined halves bolted together. The magnets are inserted after cassette assembly and are hold in place with adjusting and fixing screws made of the stainless steel.

At the entrance to the undulator has such a distribution of the magnetic field that the electron beam, when entering the regular structure of the undulator, begins to perform symmetrical oscillations with respect to the longitudinal axis of the undulator. Figure 2 schematically shows the arrangement of magnets that satisfies this requirement as well as magnetic field and its integrals.

Content from this work may be used under the terms of the CC BY 3.0 licence (© 2018). Any distribution of this work must maintain attribution to the author(s), title of the work, publisher, and DOI.

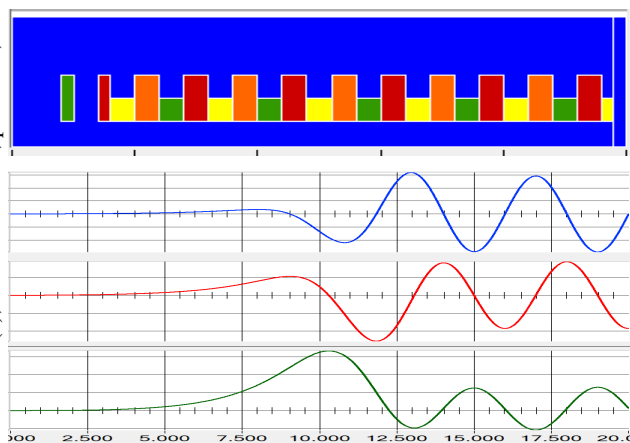


Figure 2: Magnetic structure of the undulator entrance. Red and orange magnets have vertical magnetization, and yellow and green longitudinal magnetization. Blue curve shows vertical component of the magnetic field, red curve corresponds to the first integral, and the green curve corresponds to the second integral.

The beam leaving the undulator should not have a transverse mixing and has zero angle with respect to the central axis. Figure 3 schematically shows the longitudinal distribution of magnets at the exit from the undulator and the longitudinal distribution of the vertical field, as well as the first and second integral of the magnetic field at the output from the undulator.

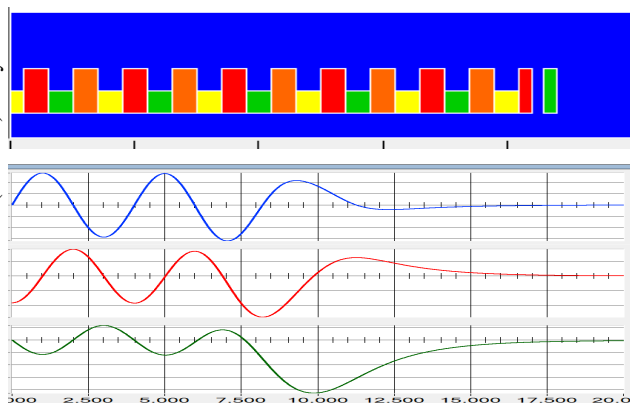


Figure 3: The magnetic structure of the undulator exit. Red and orange magnets have vertical magnetization, and yellow and green longitudinal magnetization. Blue curve shows vertical component of the magnetic field, red curve corresponds to the first integral, and the green curve corresponds to the second integral.

Before choosing the final design of helical undulators, a short prototype with a length of 0.5 meters was built. It served also for verification of the procedure for the fine tuning of the undulator after its assembly.

The prototype is shown in Fig. 4. Four cassettes hold in the aluminum frame. The undulator gap can be closed and opened with a help of the manually driven lead screws. Gap is established by the inserts between the frame and the cassettes. Helicity of the undulator is provided by the longitudinal shifts of the cassettes.

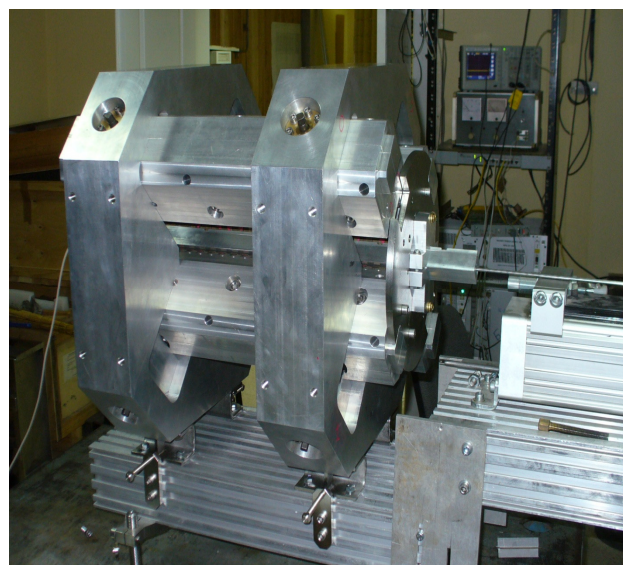


Figure 4: Undulator prototype has 10.5 periods. It shown on the stand for pulsed wire measurement.

During the production of undulator in the shop particular attention was paid to the accuracy of manufacturing long cassettes. In addition to machine precision, since the ratio of the cross-sectional dimensions of the cassette to their length was small the residual deformation has a strong effect on their straightness after removing the cassettes from the machine. The final measurements of the cassettes showed that the deviations from straightness along the entire length of the cassette did not exceed 20 microns.

Prior to the installation of permanent magnets into the cassettes, their magnetic parameters were measured with accuracy at the level of 10^{-4} . The scatter of the magnetization was found of the order of 6%, which is about an order of magnitude greater than magnets usually used for the production of magnets for accelerators. Based on the results of measurements, it was decided to employ a selective installation of magnets into the cassettes, since it greatly reduces the magnitude of errors in the distribution of the field in the undulator.

After insertion of the magnets into the cassettes, their vertical position is adjusted for equalization of the magnetic field amplitude over the entire length of the cassette. The magnetic field amplitude is measured with the Hall carriage with the magnetic mirror, and then the corrections for the field amplitude of each pole was calculated. The distance from the pole to the magnetic mirror at the time of measurement is equal to half the vertical gap in the undulator. This procedure took only a few hours. The combination of two individually pre-tuned cartridges greatly reduces the initial spread of the amplitudes and makes the magnetic potential in the undulator axis equal to zero, thus making the fine tuning of the undulator much easier.

The pre-tuning was followed by insertion of the cassettes into the frames and mounting them onto the support structure as shown in Fig. 5.



Figure 5: Assembled undulator. The extensions at the ends of the cassettes are installed for magnetic measurements.

TUNING

The tuning of the undulator field was done using a 2D Hall probe mounted on the special cartridge. The cartridge was pulled through the undulator with closed gap using saw-tooth plastic belt shown in Fig. 6. The cartridge position was monitored with laser interferometer. Custom-designed VME-based system for high-precision magnetic measurements with Hall probes was used for the tuning [4].

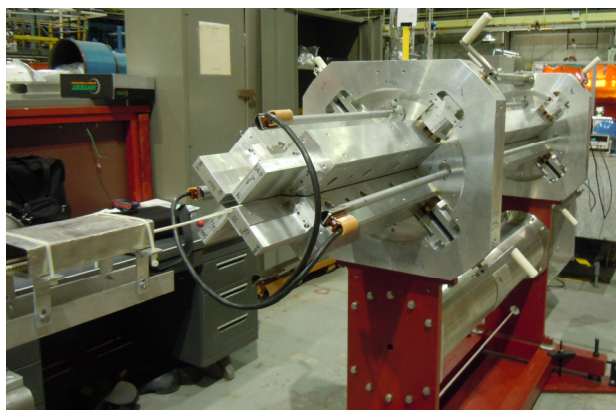


Figure 6: Assembled undulator during measuring of the magnetic field map. The extensions of the cassettes support the carriage during the scan of the undulator ends. On the left side, there is a zero-field chamber.

After the measurement of the magnetic field in the undulator is done two opposite cassettes are opened to provide access to the tuning screws. The carriage is moved from pole to pole and field is adjusted by increment/decrement found from the scan. Then the operation is repeated with the orthogonal plane. It was found that due to the ambient temperature variations we need to relax and tight the lead screws prior each measurement to relax the mechanical tension in the system.

Having adjusted amplitude of the pole fields we need to correct the field integrals. The entrance position and angle were adjusted using matching section of the undulator. The second integral was adjusted by correcting one-two poles in the location where “orbit” receives the kick or start significantly deviating from the axis. The first integral was finally correcting with exit section. After the end of the magnetic measurements, the amplitude is repeatedly adjusted, but only of one sign, for example positive. At this stage, the amplitude adjustment should be done as accurately as possible. The field of all three tuned undulators is shown in Fig. 7.

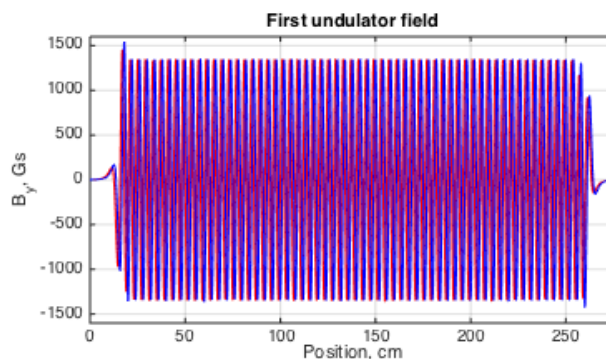


Figure 7: Field profiles of the first undulator after tuning. Two traces (blue and red) show fields for orthogonal planes. Other two undulators have similar fields with equal amplitudes.

CONCLUSION

We have successfully designed, built, and tuned three helical undulator for the coherent electron cooling proof-of-principle experiment. The tight requirements on the field quality were achieved with magnets having substantial distribution of field errors.

REFERENCES

- [1] V. N. Litvinenko *et al.*, “Proof-of-principle experiment for FEL-based coherent electron cooling,” in *Proc. PAC’11*, New York, U.S.A., March 2011, paper THOBN3.
- [2] V. N. Litvinenko and Ya. S. Derbenev, “Coherent Electron Cooling,” *PRL* 102, 114801 (2009).
- [3] P. Vobly *et al.*, “Helical wigglers for relativistic heavy ion collider (RHIC) at Brookhaven National Laboratory,” in *Proc. 20th National Conference on Synchrotron Radiation Utilization (SR-2014)*, Novosibirsk, Russia, July 2014.
- [4] A. Batrakov *et al.*, “The new VME-based system for magnetic measurements with Hall sensors,” in *Proc. RuPAC’06*, Budker INP, Novosibirsk, Russia, October 2006, paper THDO07.

Content from this work may be used under the terms of the CC BY 3.0 licence (© 2018). Any distribution of this work must maintain attribution to the author(s), title of the work, publisher, and DOI.

THE MAGNETIC FIELD INTEGRAL HYSTERESIS ON THE EUROPEAN XFEL GAP MOVABLE UNDULATOR SYSTEMS

F. Wolff-Fabris[†], Y. Li, J. Pflüger, European XFEL GmbH, 22869 Schenefeld, Germany

Abstract

Magnetic field hysteresis effects between opening and closing the gap of an undulator or phase shifter of the Undulator System of the European X-ray FEL may have an impact on the radiation properties. Using the moving wire technique the hysteresis between opening and closing the magnetic gap has been measured with high accuracy. Within the measurement accuracy undulator segments show negligible magnetic hysteresis between opening and closing the gap so that no effect on beam operation is to be expected. In contrast, about 2/3 of the phase shifters show a small hysteresis of the first field integrals of a few G.cm. In one direction of the gap movement they exceed field integral specifications. However the hysteresis is very reproducible. All phase shifters are magnetically tuned so that they fully satisfy magnetic specifications for beam operation when the gap is opened.

INTRODUCTION

The European XFEL (XFEL.EU) is designed to use three gap movable SASE Undulator Systems to produce FEL radiation tunable from 0.05 to 5.2 nm and pulse lengths of less than 100 fs [1,2]. The radiation wavelength can be tuned while selecting the e-beam energy between 8.5 to 17.5 GeV and / or changing the gap of the undulator systems. A total of 91 so called undulator cells are built and each is composed of a 5-metre long undulator segment equipped with two horizontal/vertical air coil correctors on both ends and a 1.1-metre long intersection unit containing a phase shifter (PS), a quadrupole mover with quadrupole magnet, the vacuum system and the beam position monitor. All undulator segments and phase shifters [3] for the XFEL.EU are built using NdFeB hard magnets. All devices were magnetically tuned to tight specifications in order to optimize the SASE effect (see Table 1).

The quality of the produced SASE radiation is essentially influenced by the global electron trajectory while traveling through the whole SASE System. At either end of an undulator segment there might occurs entrance and exit kicks, which are related to imperfections in the magnetic structures. They are compensated by using the air coils correctors. Similarly, small field integrals in the phase shifters [4] are required to guarantee minimum FEL power loss and no beam wander in between undulator segments. While tuning the wavelength and changing the gaps of the permanent magnet undulator systems, the presence of hysteresis effects on the magnetic field integrals while opening or closing the gaps may result in

uncorrected compensation for the end kicks or mismatch of the e-beam phase between undulator cells. As a consequence the global trajectory of the electron beam and the quality of the produced SASE radiation is deteriorated. These considerations gave the motivation to investigate and monitor the presence of hysteresis of magnetic field integrals on undulators and phase shifters during the serial production.

Table 1: XFEL.EU Magnetic Specifications

Undulators	SASE1-2	SASE3
# of Segments	35	21
K-parameter @10mm	≥ 3.9	≥ 8.0
End kicks B_y and B_z (T.mm)	$ \leq 0.15 $	$ \leq 0.15 $
RMS Phase jitter (degrees)	≤ 8	≤ 8
Phase shifters		
# of Phase Shifters		95
Magnetic Field at gap = 10.5 mm		≥ 1.26 T
Phase Integral at gap = 10.5 mm		≥ 25000 T ² m ³
First Field Integrals (T.mm or 10 ³ G.cm)	Gap (mm)	\pm Tolerance
	16	± 0.004
	15	± 0.007
	14	± 0.009
	13	± 0.012
	12	± 0.014
	11	± 0.017
	10.5	± 0.018

EXPERIMENTAL METHODS AND FIELD INTEGRAL PROPERTIES

Direct field integral measurement techniques provide much higher accuracy [5–7] than Hall sensor measurements for the evaluation of total first and second field integral properties. The stretched wire (SW) method [5] was chosen and two dedicated moving wire (MW) systems [8] were built. The first, so-called “short MW”, is designed to measure first field integrals in short devices such as phase shifters or air coils with sub-G.cm accuracy. The “long MW” system is focused to measure both first and second field integrals of the 5-metre long undulator segments and to determine the end kicks and their respective compensations. In both systems the first and second

[†] f.wolff-fabris@xfel.eu

field integrals are calculated based on the integrated induced voltage $V(t)$ over a time t when the N strand wire moves by Δx as follows:

$$I_{1y,z} = \frac{\Delta\Phi_1}{\Delta x} = \frac{\int_{t_1}^{t_2} V(t)dt}{N\Delta x} \quad (\text{parallel motion}) \quad (1)$$

and

$$I_{2y,z} = \frac{L}{2} I_{1y,z} - \frac{L \int V(t)dt}{2N\Delta x} = \frac{L}{2} I_{1y,z} - F_{2y,z} \quad (\text{anti-parallel motion}), \quad (2)$$

where the so-called measured integrated voltage $F_{2y,z}$ is obtained while performing anti-parallel movements of the stretched wire ends [5,8]. Therefore, the second field integrals $I_{2y,z}$ are estimated from direct measurements of magnetic flux when moving the stretched wire in parallel and anti-parallel directions.

Typical results for the first field integral measurements of a batch of 31 phase shifters are shown in Fig. 1A. First and second integrals of a representative undulator segment with air coil correction are shown in Fig. 1B. The gaps were moved from closed to open for these measurements. Figure 1A demonstrates that the field integrals of all phase shifters are well within inside XFEL.EU specifications and Fig. 1B shows that the field integrals of an undulator segment can be properly compensated by the air coil correctors. Very similar results are obtained for all phase shifters and undulator segments of the serial production.

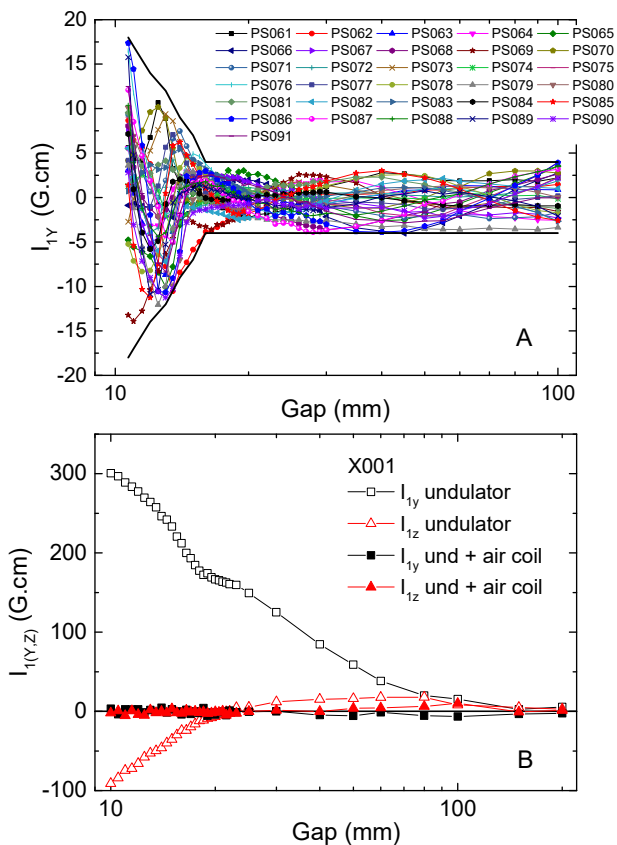


Figure 1: First field integrals of a Phase shifter batch (1A) and of an undulator segment (1B).

Hysteresis effects were measured by first carrying out measurements when the gaps are opened followed by measurements when the gaps are closed. The measurements ranged between 10.0 and 200mm gaps for the undulator segments and between 10.7 and 100mm for the phase shifters.

HYSTERESIS IN UNDULATORS

Hysteresis measurements were made on several undulator segments. The gap dependent vertical first field integrals taken for gaps closed \rightarrow open \rightarrow closed for two representative segments are shown in Fig. 2A. Curves coincide within linewidth. No clear evidence of magnetic hysteresis is observed.

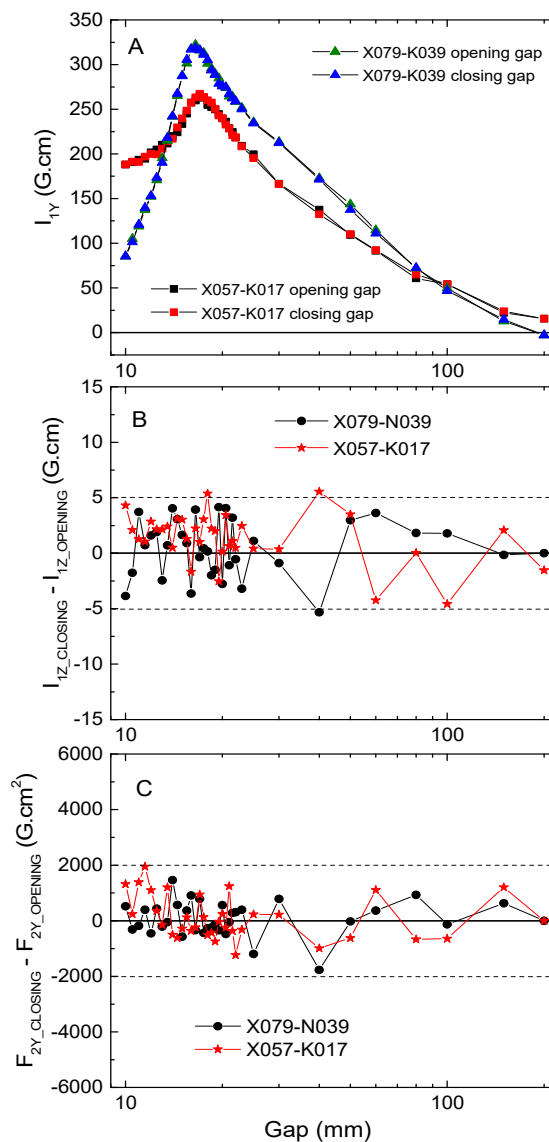


Figure 2: The vertical first field integral for two undulator segments (2A) and differences between closing and opening gap measurements (2B) and (2C).

Content from this work may be used under the terms of the CC BY 3.0 licence (© 2018). Any distribution of this work must maintain attribution to the author(s), title of the work, publisher, and DOI.

The differences between the open and close direction measurements, for the horizontal first integral and the vertical F_{2y} , are shown in Fig. 2B and Fig. 2C. Within measurement accuracy no magnetic hysteresis is seen. The differences seen in Fig. 2B and Fig. 2C are determined by the accuracy of the first and second field integrals of 5 G.cm and 2000 G.cm², respectively. Based on these magnetic measurements it is assumed that within measurement accuracy the undulator segments can be operated equally well in both directions.

HYSTERESIS IN PHASE SHIFTERS

The vertical field integral of a phase shifter when measured in open, close, and again open direction is shown in Fig. 3A. A clear magnetic hysteresis between opening and closing the gaps is seen. Such characteristic closed loop behaviour has been seen in about 60 out of a total 95 phase shifters of the serial production. This was also observed in prototypes where no mechanical hysteresis was present [9,10] and in electromagnetic phase shifters [11]. The difference between opening and closing the gap (Fig. 3B) amounts 10-20 G.cm and exceed the specifications by about 10 G.cm. This hysteretic behaviour is very reproducible and open direction measurements agree well (Fig. 3A and Fig. 3B).

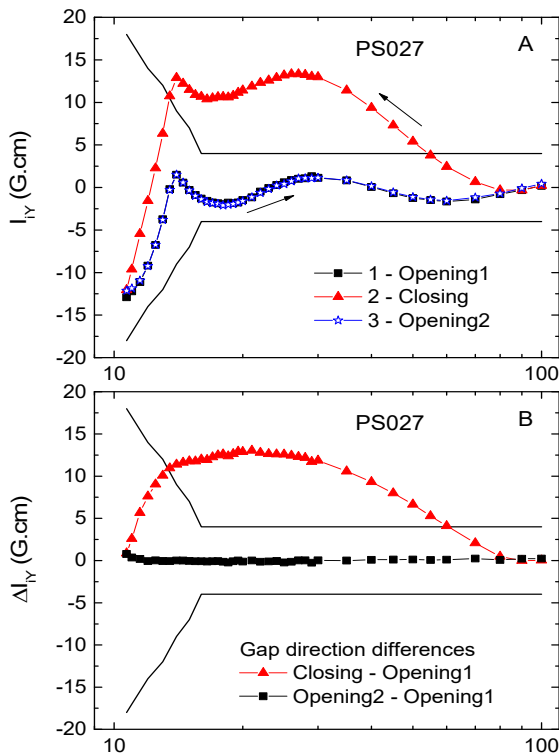


Figure 3: One representative closed loop magnetic hysteresis of the vertical integrals as seen for 60 phase shifters. The close → open direction is outside the XFEL.EU specification window.

On the other hand, magnetic hysteresis is not observed in horizontal field integral (not shown here) due to the much smaller magnetic fields in this direction. Nevertheless, we emphasize that all 95 phase shifters which were built for XFEL.EU are tuned inside the specification window on the close → open direction.

The hysteretic behaviour on the phase shifters is explained by a small remanent magnetization of the iron yoke which engages the permanent magnet components and reduces fringe fields [3]. Although only a selected iron grade was used and magnetic annealing at 850°C after machining was applied a small remanence was still observed. Without the magnetic annealing the effect would be significantly larger.

SUMMARY AND CONCLUSION

The magnetic hysteresis of the field integrals of the undulators and phase shifters for the XFEL.EU were investigated using the moving wire method.

Within the measurement accuracy of about 5 G.cm and 2000 G.cm² for the first and second field integrals, respectively, the undulator segments were found to have no magnetic hysteresis.

A closed loop hysteresis is found on the vertical field integrals of 60 phase shifters of the serial production. It is, however, very reproducible. The open direction of gap movement is well within specifications, while the close direction may exceed specs by up to 20 G.cm. Therefore for the best performance with lowest field integral errors the phase shifters should be operated when the gap is opened.

REFERENCES

- [1] M. Altarelli *et al.*, “The European x-ray free electron laser – technical design report”, Desy, Hamburg, Germany, Rep. DESY 2006-097, July 2007.
- [2] E. Schneidmiller *et al.*, “Photon beam properties at the European XFEL”, Desy, Hamburg, Germany, Rep. DESY 2011-152, Sep. 2011.
- [3] H. H. Lu *et al.*, in *Proc. FEL’08*, pp. 356-358.
- [4] Y. Li *et al.*, “Tuning method for phase shifters with very low first field integral errors for the European X-ray free electron laser”, *Phys. Rev. ST Accel. Beams*, vol. 18, p. 030703, 2015.
- [5] D. Zangrando *et al.*, “A stretched wire system for accurate integrated magnetic field measurements in insertion devices”, *Nucl. Instr. Meth. A*, vol. 376, p. 275, 1996.
- [6] Z. Wolf, “Undulator field integral measurements”, LCLS, Stanford, USA, Rep. LCLS-TN-05-22, Aug. 2005.
- [7] J. Xu *et al.*, in *Proc. IPAC’05*, IEEE 1808, 2005.
- [8] F. Wolff-Fabris *et al.*, “High accuracy measurements of magnetic field integrals for the European XFEL undulator systems”, *Nucl. Instr. Meth. A*, vol. 833, pp. 54-60, 2016.
- [9] I. Moya *et al.*, in *Proc. LINAC’12*, pp. 1029-1031.
- [10] H. G. Lee *et al.*, in *Proc. IPAC’13*, pp. 3564-3566.
- [11] M. Tischer *et al.*, in *Proc. IPAC’14*, pp. 2010-2012.

TAPERED FLYING RADIOFREQUENCY UNDULATOR*

S. V. Kuzikov^{†,2}, A. V. Savilov, A. A. Vikharev

Institute of Applied Physics, Russian Academy of Sciences, Nizhny Novgorod, Russia

S. Antipov, A. Liu, Euclid Techlabs LLC, Bolingbrook, IL, USA

²Euclid Techlabs LLC, Bolingbrook, IL, USA

Abstract

We propose an efficient XFEL consisting of sequential RF undulator sections using: 1) tapered flying RF undulators, 2) short pulse, high peak-power RF and 3) driving undulator sections by spent electron beam. In a flying RF undulator, an electron bunch propagates through a high-power, nanosecond, co-propagating RF pulse. Helical waveguide corrugation supports a space harmonic with a negative propagation constant, providing a large Doppler up-shift. The undulator tapering technique improves FEL efficiency by 1-2 orders of magnitude in comparison with other facilities by decreasing the undulator period so that particles are trapped in the combined field of the incident x-ray and undulator field. We develop a so-called non-resonant trapping regime not requiring phase locking for feeding RF sources. Simulations show that by decreasing the corrugation periodicity one can vary an equivalent undulator period by 15%. The spent electron beam can be used to produce wakefields that will drive the RF undulator sections for interaction with the following beam. We have already manufactured and tested the 30-GHz simplified version of the 50-cm long undulator section for cold measurements and currently start low-power test of the tapered prototype.

FLYING-RF UNDULATOR

The RF undulator based on a travelling wave benefits from a Doppler up-shift when the electron beam interacts with oncoming microwaves. In [1] an RF pulse co-propagating (with the electron beam) was proposed where a benefit of the Doppler up-shift of Compton scattering is not lost due to the mode having strong -1^{st} spatial harmonic transverse fields at axis of a helical corrugated waveguide (Figure 1). In this “flying” undulator the effective interaction length L_{eff} of a pulse with length τ and group velocity v_{gr} is proportional to $(1-v_{\text{gr}}/c)^{-1}$. For a large group velocity L_{eff} can be much larger than the pulse length.

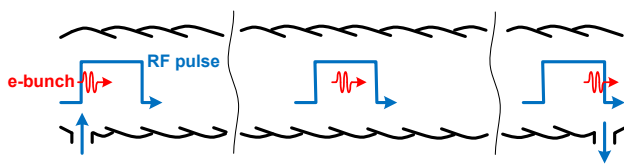


Figure 1: Flying RF undulator geometry (helical corrugation) and interaction timing structure.

*This work was supported by DoE Small Business Innovative Research Phase I Grant #DE-SC0017145.

[†]sergeykuzikov@gmail.com

In [1-2], a 30 GHz, 10 ns, 1 GW relativistic backward wave oscillator powers a 10-m long RF undulator with effective undulator strength $K = 0.3$ and undulator period $\lambda_u \approx 5$ mm. There are high power Ka-band BWO's which are good candidates for powering of the proposed flying undulator [3-4].

Figure 2 shows the dispersion characteristic of the operating mode of the TE_{11} - TM_{01} - TM_{11} RF undulator for the following geometrical parameters: $R_0 = 6.1$ mm, periodicity $D = 6$ mm and corrugation depth $a = 0.3$ mm (red solid curve). The dashed curve is the dispersion characteristic of the same mode in the waveguide with smaller corrugation period, 5.4 mm. Therefore, a tapered undulator can be built near 34 GHz using adiabatic variation of corrugation period so that the effective undulator period change is as high as 10%.

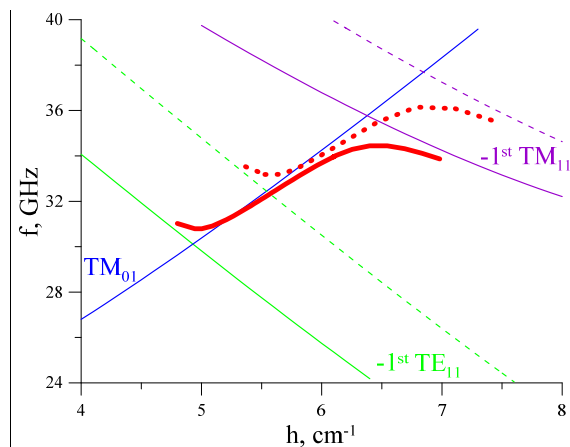


Figure 2: Dispersion of the operating mode (red solid curve) of the helical undulator with period of corrugation 6 mm and dispersion of this mode (red dashed curve) of the undulator with period of corrugation 5.4 mm.

HIGH-EFFICIENCY, TAPERED FLYING-RF UNDULATOR

For a high efficiency free electron laser we consider a string of tapered flying undulators (Figure 3). Each RF undulator section is assumed to be a helical corrugated structure with periodicity and corrugation depth changing as a function of z (coordinate along electron beam propagation).

Content from this work may be used under the terms of the CC BY 3.0 licence (© 2018). Any distribution of this work must maintain attribution to the author(s), title of the work, publisher, and DOI.

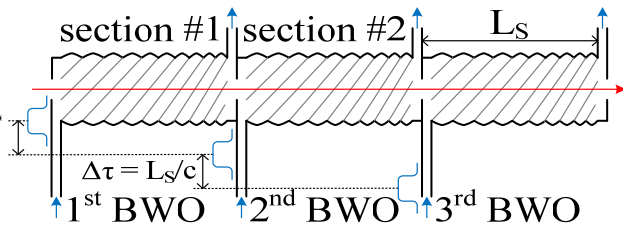


Figure 3: FEL scheme based on tapered RF undulators with decreasing equivalent undulator period.

In each undulator section geometrical parameters are varied to maintain the resonant condition ($\lambda \approx \lambda_u/2\gamma^2$) with particles losing their energy from γ_0 to γ_{\min} , which defines the maximum efficiency $\eta = \Delta\gamma/(\gamma-1)$. The electron beam enters each undulator section at such time that it ends up in the tail of the RF pulse. As electrons travel along the undulator at virtually the speed of light they pass the RF pulse which has a group velocity slower than speed of light.

By the time the electron beam reaches the head of the RF pulse it has arrived at the exit of the undulator section. Electrons interact with both the RF field of the undulator and x-ray field generated by the electrons themselves. This interaction in a tapered undulator section can be represented in a phase space as a typical pendulum behavior with stationary buckets in which electrons are trapped (have finite trajectories). The center of the bucket corresponds to a resonant energy, and its size in energy is proportional to a current undulator parameter $K(z)$ as well as x-ray wave amplitude. Due to a finite signal rise and fall time electron beam sees initially a very small bucket due to low RF field. As it passes the RF pulse, at the exit of the undulator the bucket collapses again due to RF field roll off.

In the traditional resonant trapping scheme, considered for XFELs, electrons were assumed to be trapped in the bucket and stay in the same bucket the whole time, decreasing their energy from γ_0 to γ_{\min} . For resonant trapping with RF undulators all undulator sections have to be at the same RF phase, meaning that all RF sources have to be phase locked. As it was proven in the experiment [4], phase locking of the mentioned BWOs is possible, but it dramatically increases cost of the XFEL.

We propose a so-called *non-resonant* trapping of electrons to relieve the stringent requirements on phase locking [5, 6]. In this scenario, not all electrons fall into the bucket at the entrance of the section. The ones that are trapped in a bucket stay trapped, and collapse inside the bucket, decreasing their energy due to radiation. The energy of other electrons does not change and they do not radiate. In the following sections another portion of electrons are trapped and decelerated. Going from section to section most of the electrons will end up decelerated.

Let us consider an example of XFEL calculations on a base of the described principles. In this example we take a 600 MeV ($\lambda \approx 2$ nm), 100 pC electron bunch of 0.167 ps length and 30 μm diameter. The energy spread is 0.1%. According to 1D FEL theory, Pierce parameter is as high as $\rho = 5 \times 10^{-4}$ (gain length $L_g \approx 0.5$ m). The FEL consists of 16 sections, each 10 m long, each section has sine-like tapering of the corrugation amplitude with undulator parameter $K_{\max} = 0.25$ in maximum. In Figure 4, one can see variations of undulator period along the XFEL. The first two sections (first 20 m) with $\lambda_u = 5.5$ mm are necessary to excite initial x-ray wave which is to be amplified in next sections. All other sections are tapered ones. In these sections the magnitude of tapering increased along the distance. The further a given section from the entrance, the stronger it's tapering magnitude.

This law is necessary because in the beginning of the FEL the x-ray amplitude is rather small so that effective trapping of particles is not available. As the amplitude of the x-ray wave grows up the stronger tapering becomes possible which promises higher efficiency. In the considered example the last 16th section has 10% variation of the undulator period. The efficiency of the FEL was calculated using 1D theory equations. In Figure 5, the black curve (#1) corresponds to the simulation where all sections were phase locked. In this simulation, the highest efficiency (0.8%) was obtained.

Other simulations (curves #2-6) were performed with only the first two sections being phase locked and all other 14 sections had a uniform $[0-2\pi]$ random distribution of RF phases from one section to another section. Note that calculated in these cases efficiencies are high, in the worst case (curve #4) the efficiency is approximately 15% less than in the best case (curve #1).

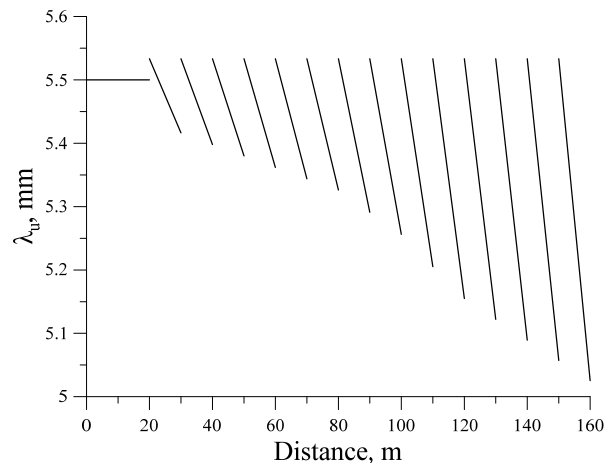


Figure 4: Dependence of effective undulator period in FEL consisted of individually tapered sections.

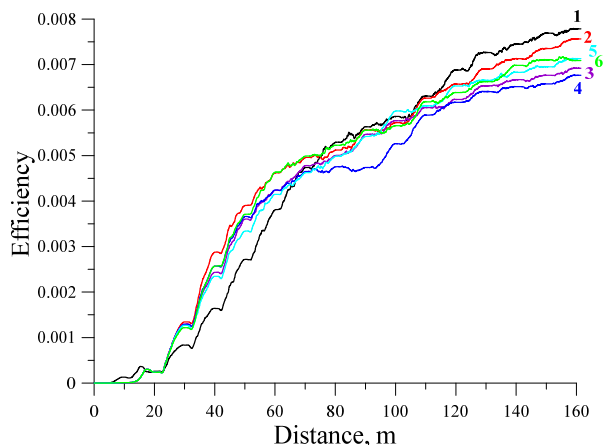


Figure 5: Efficiency of lasing along FELs for in-phase undulator sections (black curve #1) and for 5 different sets of sections with randomly distributed phases (curves 2-6).

Figure 6 represents particle distributions in the entrance of the simulated XFEL (blue dots) and in the exit (red dots). It is well seen that energies of most particles considerably reduced.

Note that the suggested principle of the non-resonant trapping allows further increase of the efficiency. The longer the XFEL, the higher efficiency could be reached. In the non-resonant trapping case, electrons that missed the bucket because of phase, frequency or amplitude drift are not lost completely as they have a chance to be trapped in the following section.

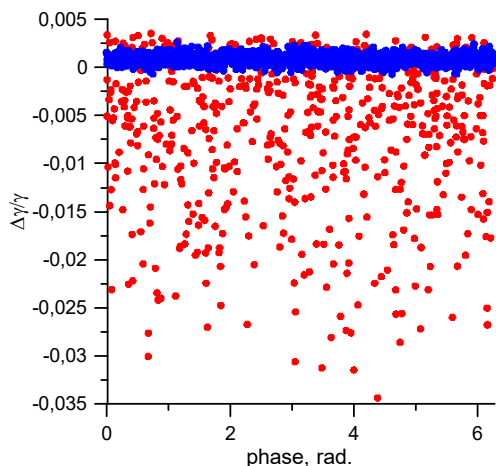


Figure 6: Energy-phase distribution of particles in the entrance of FEL (blue) and in its exit (red).

One more assertion follows from the calculations. According to Figure 6, the energy spread from section to section increased. Therefore, non-resonant trapping is well suitable for XFELs driven by bunches having large energy spread. In particular, bunches produced by means of laser-plasma acceleration technique can be used. We are working to develop GENESIS simulation of lasing in the flying RF undulator.

LOW-POWER TEST

For low-power test we produced two prototypes of RF undulator sections made of aluminium using 3D printing technology. One is the described 20 cm long TE_{11} - TM_{01} - TM_{11} section with sine-like corrugation amplitude along section and 10% linear variation of undulator period (Figure 7). The second one is TE_{11} - TE_{21} - TM_{11} section with the same corrugation amplitude change law and 15% linear variation of the period (Figure 8).



Figure 7: A 34 GHz TE_{11} - TM_{01} - TM_{11} RF undulator.



Figure 8: A 34-GHz TE_{11} - TE_{21} - TM_{11} RF undulator and a low-power experimental setup.

The low-power test is necessary to prove the desired tapering in a single RF undulator section. To obtain this goal we are going to use a scheme exploiting bead pull measurements of transverse fields along the longitudinal axis. In the mentioned undulator TE_{11} - TM_{21} - TM_{11} there are no any fields of 0th harmonics at axis that is why, it is more convenient for measurements. For the test we first excite the rotating on azimuth TE_{21} mode by means of a mode converter consisted of two bends and a polarizer. Second, we feed the undulator by a standing wave produced by means of a Bragg reflector which reverses rotation of the TE_{21} mode (Figure 9). As a result, we can measure the standing wave field structure at axis and easily to compare undulator period in the beginning and in the end of the tested section correspondingly.

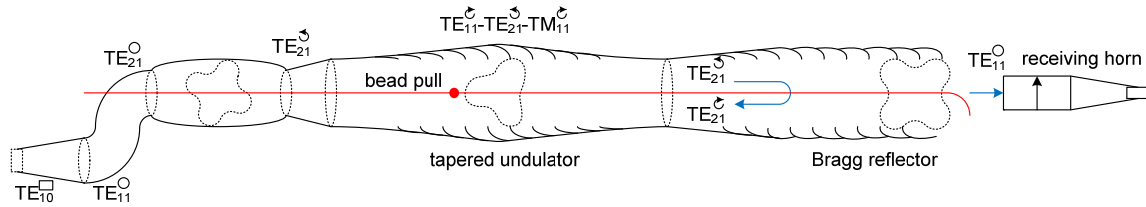


Figure 9: Scheme of low-power measurements.

CONCLUSION

Calculations show that high efficiency $\sim 1\%$ are achievable in a XFEL driven by 600 MeV bunches having 0.1% energy spread. The considered FEL consists of tapered undulator sections with varied waveguide period and operates basing on non-resonant trapping of particles. The proposed Ka-band RF undulators, fed by gigawatt level BWOs, allow keeping the mentioned efficiency of the XFEL even for non phase locked RF sources.

REFERENCES

- [1] S. V. Kuzikov, A. V. Savilov, and A. A. Vikharev, "Flying radio frequency undulator", *Applied Physics Letters* 105, 033504 (2014). doi: 10.1063/1.4890586.
- [2] E. B. Abubakirov *et al.*, "Microwave undulators and electron generators for new-generation free-electron lasers", *Radiophysical Quantum Electronics* 58, p. 755 (2016). doi:10.1007/s11141-016-9648-z.

- [3] S. D. Korovin *et al.*, "Generation of Cherenkov superradiance pulses with a peak power exceeding the power of the driving short electron beam", *Physical Review E* 74, 016501 (2006).
- [4] V. V. Rostov, A. A. Elchaninov, I. V. Romanchenko, and M. I. Yalandin, "A coherent two-channel source of Cherenkov superradiance pulses", *Applied Physical Letters* 100, 224102 (2012).
- [5] A. V. Savilov, "Cyclotron resonance maser with a tapered magnetic field in the regime of 'nonresonant' trapping of the electron beam", *Physical Review E* 64, p. 066501 (2001).
- [6] A. V. Savilov, I. V. Bandurkin, N. Yu. Peskov, "Regime of non-resonant trapping in an FEM-amplifier", *Nuclear Instruments and Methods in Physics Research, Section A: Accelerators, Spectrometers, Detectors and Associated Equipment*, 507 (1-2), pp. 158-161 (2003).

EFFECT OF BEAM TRANSVERSE ANGLE DEFLECTION IN TGU ON FEL POWER

G. Zhou^{1,2,3†}, J. Wu^{1‡}, J. Yi², J. Wang²,

¹SLAC National Accelerator Laboratory, Menlo Park, California, U.S.A

²Institute of High Energy Physics, Chinese Academy of Science, Beijing, China

³University of Chinese Academy of Science, Beijing, China

Abstract

Recent study shows that electron beams with constant dispersion together with the transverse-gradient undulator (TGU) can reduce the sensitivity to energy spread for free-electron laser (FEL). By inducing dispersion function, electrons with different energy are placed at different positions corresponding to proper magnetic fields. Thus, FEL resonant condition can be kept for electrons with different energy. In this paper, we mainly studied: 1. The effects of electron beam angle deflection at the entrance of the TGU on the radiation power. 2. The utility of a kicker to introduce an angle deflection of electron beam to improve the FEL radiation power.

INTRODUCTION

Free-electron lasers (FELs) greatly benefit fundamental research in physics, chemistry, materials science, biology, and medicine by producing intense tunable radiation ranging from the infrared to hard x-ray region [1]. However, the FEL facilities are usually large and costly. Efforts have been made to develop compact FELs with similar radiation properties but smaller size. One optional way is to use laser-plasma accelerators (LPAs) to drive a high-gain FEL instead of conventional linear accelerator (LINAC) [2].

Compared to traditional LINAC, LPAs have much higher accelerating field gradient, smaller size and less cost but larger electron beam energy spread. At present, LPA can produce high energy (~ 1 GeV), high peak current (~ 10 kA), and low emittance ($\sim 0.1 \mu\text{m}$) electron beam with a relatively large energy spread about 1% experimentally [3, 4]. Such a relatively large energy spread, compared to conventional LINAC, terribly interferes the FEL gain process, which hinders LPAs from driving a high-gain FEL, which can be understood from the FEL resonance condition,

$$\lambda_r = \frac{1 + K_0^2 / 2}{2\gamma^2} \lambda_u, \quad (1)$$

where $K_0=0.934\lambda_u[\text{cm}]B[\text{T}]$, λ_u is the undulator period, B is the peak field of the undulator, γ is the electron beam energy in unit of the rest energy. Energy spread would lead to a spread of the above equation, leading to a weak

radiation power adverse to diffraction imaging experiments [5]. To overcome the impediment caused by electron beam energy spread in the FEL gain process, approaches, such as transverse gradient undulator (TGU) [6] and decompression [7], have been proposed and studied in detail. Recent study on TGU for high-gain FEL driven by LPAs points out that electron beam with a proper dispersion cooperating with TGU would increase the output radiation power significantly, about two orders, more effective than decompression [2].

TGU was proposed to reduce the sensitivity to the electron beam energy spread [2, 6]. By canting the magnetic poles, a linear transverse dependence of undulator field can be generated, like

$$\frac{\Delta K}{K} = \alpha x, \quad (2)$$

where α is the transverse gradient of the undulator. For an electron beam dispersed horizontally according to its energy, we get $x=\eta_0\delta$, where η_0 is the electron beam dispersion. Properly choosing the dispersion

$$\eta_0 = \frac{2 + K_0^2}{\alpha K_0^2}, \quad (3)$$

and keeping it constant along the TGU, the spread in electron beam's energy would be compensated. Note that, in this paper, we only consider the electron beam dispersed in x direction.

In this paper, we study the effect of beam transverse angle deflection on radiation power. We first analyse the case that the electron beam has an angle deflection at the entrance of TGU. Numerical simulation scan has been done to further quantitatively study the power decrease caused by angle deflection. Then, we study the case that the angle deflection induced at proper position in TGU. By comparing this case with linear tapered undulator, we find that it is possible to make use of angle deflection to improve the radiation power simply with an additional kicker. Multi-dimension optimization has been done and we find that the radiation power improves significantly. Simulations are done based on GENESIS, a 3D FEL simulation software, presenting reliable FEL process, proved by experiments [8].

* The work was supported by the US Department of Energy (DOE) under contract DE-AC02-76SF00515 and the US DOE Office of Science Early career Research Program grant FWP-2013-SLAC-100164

†gzhou@SLAC.Stanford.EDU

‡jhwu@SLAC.Stanford.EDU

BEAM ANGLE DEFLECTION VERSUS RADIATION POWER

In this section, we investigate the sensitivity of radiation power to transverse angle deflection at the entrance of TGU. Since the electron beam is dispersed in x direction, it is expected that TGU-FEL is more sensitive to angle deflection in x direction.

TGU-FEL makes use of beam dispersion to distribute the electrons with different energy along x direction so that together with TGU the off-resonance electrons could satisfy the resonance condition. And the key is to match the electrons with different energy to proper K . Therefore, TGU-FEL is sensitive to angle deflection at the entrance of TGU. Supposing that, the electron beam enters TGU with a small transverse velocity v_x ($v_x \ll v_z$), which means that the electron beam deviate from its designed trajectory, which is illustrated in Fig. 1. We find that with the electron beam traveling along the TGU, the transverse offset has a linear increase, shown as below,

$$x = \frac{v_x}{v_z} z = \tan \theta_x z \approx \theta_x z \quad (4)$$

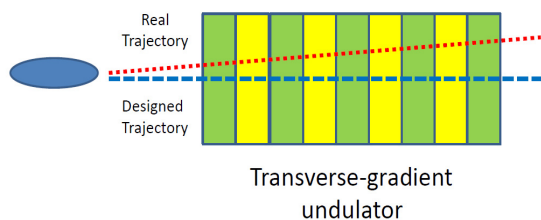


Figure 1: Schematic illustration for beam angle deflection at the entrance of TGU.

From Eqs. (1-3), we can obtain that

$$\frac{1 + K_0^2 / 2}{(1 + \rho)^2} < 1 + K_0^2 (1 + \frac{\alpha v_x}{v_z} z)^2 / 2 < \frac{1 + K_0^2 / 2}{(1 - \rho)^2} \quad (5)$$

Thus, when v_x is large enough, with the electron beam traveling along the TGU, the electron beam will be out of the gain bandwidth. To further investigate this phenomenon, we did numerical simulation using GENESIS (steady state) with parameters shown in Table 1, listed as below,

Table 1: Parameters for Numerical Simulation

Parameter	Value
Beam energy	500 MeV
Norm. transv. Emittance	0.1 μ m
Peak current	5000 A
Rel. rms energy spread	2 %
Undulator period	2 cm
Undulator parameter	1.93
Undulator length	10.0 m
Resonant wavelength	30 nm
Transverse gradient	43 m^{-1}

By scanning the angle deflection in x and y direction, we obtain simulation results shown in Fig. 2, which indicates that the radiation power of TGU-FEL is much more sensitive to θ_x . Roughly, in our case, tolerance for θ_y is 0.1 mrad but for θ_x is 0.01 mrad.

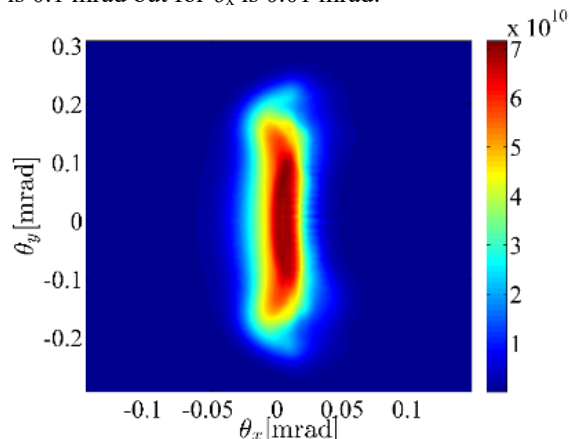


Figure 2: Radiation power as a function of (angle deflection in x direction) and θ_y (angle deflection in y direction).

ANGLE DEFLECTION AND POWER IMPROVEMENT

In the last section, we find that electron beam angle deflection at the entrance of TGU would lead to radiation power decrease. However, if we use a kicker to induce an angle deflection at a proper position in the TGU, we can even improve the radiation power of TGU-FEL. It is expected to perform like a linear tapered undulator. From Eq. (2) and Eq. (4), we can obtain that,

$$K(z) = K_0 (1 + \frac{\alpha v_x}{v_z} z) \quad (6)$$

which is quite similar to the form of a tapered undulator,

$$K(z) = K_0 (1 + \frac{k}{L} z) \quad (7)$$

where k is the taper ratio, L is the length of the tapered part.

Furthermore, we did optimization for TGU-FEL with kicker and without kicker via numerical simulation. Basic parameters are the same as those in Table 1. Considered Twiss parameter, detune, kicker location and kicker strength (induced angle deflection), we have done multi-dimension optimization with GENESIS steady-state simulation and the result is shown in Table 2. The optimizer is robust conjugate direction search (RCDS), a both efficient and robust optimization algorithm [9].

From the optimization result, we can find that the radiation power increases significantly (more than two times) with a kicker added and the electron beam centre transverse offset at end of the undulator would not influence too much (much smaller than the width of pipe). We also have done time-dependent simulation with the

optimized parameters in Table 2 and the temporal radiation profiles are plotted in Fig. 3. The max power in the radiation pulse almost doubled and the pulse energy increases more than two times.

Table 2: The Optimization Result for TGU with/without Kicker

Parameter	Without kicker	With kicker
Kicker location	-	4.72 m
Angle deflection θ_x	-	0.1732 mrad
Twiss α_x	3.093	2.992
Twiss α_y	-0.064	-0.359
RMS beam size σ_x	49.41 μm	32.68
RMS beam size σ_y	15.94 μm	12.46
K/K_0	0.995	0.999
Detune P	7.00 GW	18.37 GW
Offset Δx	-0.62 μm	-0.89 μm

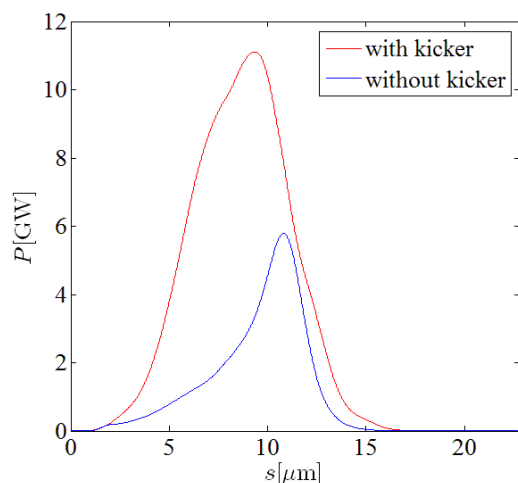


Figure 3: Temporal radiation profile of TGU with/without a kicker.

SUMMARY AND OUTLOOK

In this paper, we present the sensitivity of radiation power to the angle deflection in TGU-FEL. At the entrance of TGU, transverse angle deflection always decreases the radiation power. Since the dispersion is induced in x direction (in our case), the radiation power is more sensitive to angle deflection in this direction. Moreover, if we induce an angle deflection at a proper location together with optimized value, the TGU will perform like a linear tapered undulator (transverse-gradient preserved), which significantly improves the radiation power. Detailed study about beam transport analysis, optimization considering time-dependent effects will be presented in further studies.

REFERENCES

- [1] Erik Hemsing, Gennady Stupakov, Dao Xiang and Alexander Zholents, *Rev. Mod. Phys.*, 86, 897, 2014.
- [2] Zhirong Huang, Yuantao Ding and Carl B. Schroeder, *Phys. Rev. Lett.*, 109, 204801, 2012.
- [3] E. Esarey, C. Schroeder, and W. Leemans, *Rev. Mod. Phys.*, 81, 1229, 2009.
- [4] V. Malka, *Phys. Plasmas*, 19, 055501, 2012.
- [5] A. Aquila *et al.*, “The linac coherent light source single particle imaging road map”, *Struct. Dyn.*, 2, 041701, 2015.
- [6] T. Smith, J. M. J. Madey, L. R. Elias, and D. A. G. Deacon, *J. Appl. Phys.*, 50, 4580, 1979.
- [7] A. R. Maier, A. Meseck, S. Reiche, C. B. Schroeder, T. Seggebrock, and F. Gruner, *Phys. Rev. X*, 2, 031019, 2012.
- [8] S. Reiche, *Nucl. Instrum. Methods Phys. Res. A*, 429, 243, 1999.
- [9] X. Huang *et al.*, *Nucl. Instrum. Methods Phys. Res. A*, 726, 77–83, 2013.

DESIGN OF A COMPACT HYBRID UNDULATOR FOR THE THz RADIATION FACILITY OF DELHI LIGHT SOURCE (DLS)

S. Tripathi[†], S. Ghosh, R. K. Bhandari, D. Kanjilal,
 Inter-University Accelerator Centre (IUAC), New Delhi, India
 M. Tischer, Deutsches Elektronen-Synchrotron (DESY), Hamburg, Germany
 U. Lehnert, Helmholtz Zentrum Dresden Rossendorf (HZDR), Dresden, Germany

Abstract

A compact Free Electron Laser (FEL) facility to produce coherent THz radiation is in the development stage at Inter-University Accelerator Centre (IUAC), New Delhi, India [1-3]. The facility is named the Delhi Light Source (DLS). It is planned to produce an 8-MeV electron beam from a photo-cathode RF gun, and the electron beam will be injected into a compact undulator to generate the radiation. To produce THz radiation in the range of 0.15 to 3.0 THz, the electron beam energy and the undulator gap will be varied from 4 to 8 MeV and 20 to 45 mm, respectively. The variable-gap undulator of 1.5-m length will consist of NdFeB magnets with vanadium permendur poles. The magnet design and dimensions are optimised by using code 3D RADIA [4]. The detailed design of the compact hybrid undulator is presented in this paper.

INTRODUCTION

The compact light source project at IUAC named as Delhi Light Source (DLS) is in the developmental stage [2]. In the first phase (Phase I) of the DLS, a normal conducting (NC) photocathode electron gun will be used to generate the pre-bunched electron beam which will be injected in to a compact undulator magnet to produce THz radiation. The layout of the facility is shown in Figure 1. Permanent magnet technology, both pure permanent magnet and hybrid design, is most common for undulators of several-cm period length, while electromagnetic devices are usually built for longer period length. For DLS, we decided to go for a hybrid permanent magnet design as it will provide the biggest magnetic field. It is, however, a little more demanding in terms of field tuning than a pure permanent magnet structure due to the nonlinear behaviour of the iron poles.

THE 50 MM HYBRID UNDULATOR

An undulator is a spatially periodic magnetic structure and can be explained as pack of dipole magnets making alternating direction of magnetic fields. The magnetic field in a planar undulator is of the form $B_0 \sin(2\pi y/\lambda_u)$, where λ_u is the period length of the undulator.

When an electron passes through such magnetic fields, it will undergo a sinusoidal path with a certain period length and release synchrotron radiation as the electron

changes its direction. This radiation has high intensity and the radiation concentrates into a narrow band spectrum at the fundamental wavelength of

$$\lambda = \frac{\lambda_u}{2\gamma^2} \left(1 + \frac{K^2}{2} + \gamma^2 \theta^2 \right),$$

where λ_u is the period length of the undulator, γ is the Lorentz factor, and θ is the observation angle. The undulator parameter K , representing the undulator strength, can be written as $K = 0.934 \times B_0 [T] \times \lambda_u [cm]$, where B_0 is magnetic field at the undulator mid-plane.

The undulator for the Delhi Light Source (U50-DLS) has a period length of 50 mm in an antisymmetric configuration and optimised using the code RADIA. The undulator has magnet block of 80 mm wide, 55-mm high and 19-mm thick with 5 mm \times 5 mm square cuts at the corners for clamping the block with the holders. The vanadium permendur poles are 60-mm wide, 45-mm high and 6-mm thick. The end sections are designed and optimised with the configuration of 1/4 : 3/4 : 1 in terms of end pole strength [5].

A full five-period model undulator is shown in Figure 2. The end section consists of two magnet blocks and two end poles separated by air spaces. The inner 2nd last end magnet block has the same shape as the full-size blocks but the thickness is reduced to 75% of the thickness of the full-size blocks while the last end magnet has 25% of thickness as compared to regular magnet block. There is an air space between the second last magnet block and the second last end pole as well as between last magnet & last pole. The shape of both end poles is the same as for the full-size poles. In Table 1, the specifications of U50-DLS are summarised.

Table 1: Specification of U50-DLS Undulator

Technology	Hybrid planar, anti-symmetric
Magnet	Permanent NdFeB magnet ($B_r = 1.21T$)
Pole	Vanadium permendur
Magnetic gap	20 - 45 (mm)
Period length	50 mm
No of Periods	28 (full)
Magnetic field	0.62 - 0.11 (T)
Undulator parameter (K)	2.89 - 0.61
Device length	~1.5 m

[†] stri_29sep@yahoo.co.in

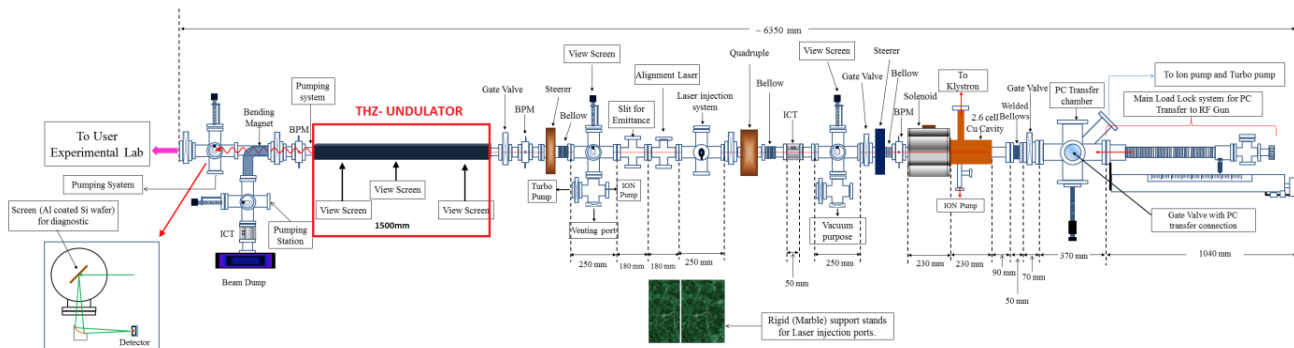


Figure 1: The beamline layout of Phase-I of DLS.

The mechanical design for the magnet/the pole holders and the support body system is in progress. For magnets and poles, we will design period holders that will be mounted on aluminum girders. The girder movement will be done by a system of two motors. To achieve accuracy in μm level while adjusting the gap, we will use absolute linear encoders.

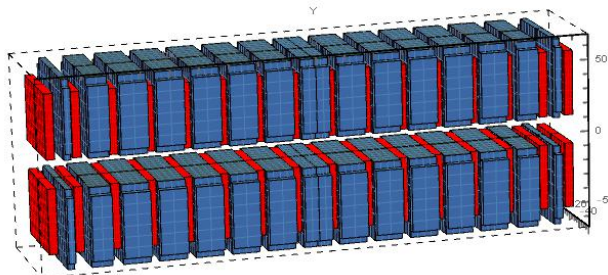


Figure 2: RADIA model of full five period U50-DLS.

RESULTS AND DISCUSSION

The design and optimisation of the hybrid undulator to be developed for DLS has been done with RADIA [4]. The magnetic field profile for the minimum gap (20 mm) as well as for the maximum gap (45 mm) is shown in Figure 3. The undulator has been designed in an anti-symmetric configuration, i.e. the ends have opposite sign, so that their nonlinearities and errors will cancel as good as possible. While the first field integral will cancel to zero in an ideal magnet structure, the second field integral needs to be zeroed by proper configuration of the end field termination. The vertical second field integral will change with the undulator gap as we can see for maximum and minimum gaps in Figure 4. A further optimisation can still reduce this small trajectory offset. Final remaining kick errors of the real device will be corrected by small air coils on both sides of the undulator. Small trim magnets (magic fingers) at the end structures will be applied for correction of multipole errors.

The transverse field roll-off depends strongly on the transverse width of the undulator. A flat transverse roll-off reduces the higher order integrated multipoles over the

good field region and reduces the effect of dynamic field integrals. In this design the width of the magnet and pole has been selected to assure a good-field region of ± 10 mm about the central axis of the undulator as recommended by the beam optics calculation. The percentage of the roll-off with respect to the on-axis field at transverse positions of ± 5 mm, ± 10 mm, and ± 20 mm is 0.05, 0.25, 2.92 and 0.30, 1.39, 8.74 percent at the closed (20 mm) and open (45 mm) gaps, respectively. Figure 5 shows the transverse roll-off over the full undulator width at (a) the minimum gap of 20 mm and (b) the maximum gap of 45 mm. The field variation of magnetic field B_0 over the working gap range 20–45mm is plotted and is shown in Figure 6.

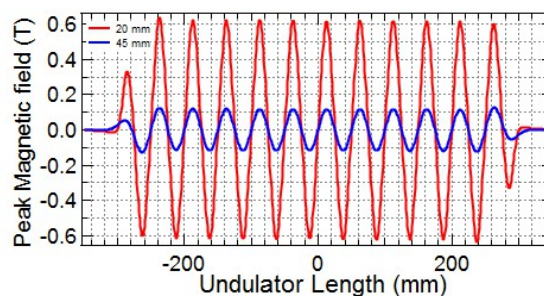


Figure 3: Field plot for the ten-full period model of U50-DLS at the minimum (20 mm) and maximum (45 mm) gaps.

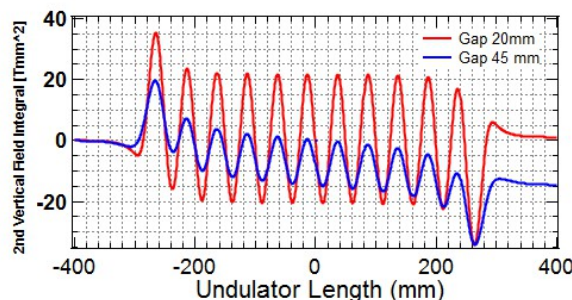


Figure 4: Vertical second field integral (trajectory) plots for the ten-full period model of U50-DLS at the minimum (20 mm) and maximum (45 mm) gaps.

Content from this work may be used under the terms of the CC BY 3.0 licence (© 2018). Any distribution of this work must maintain attribution to the author(s), title of the work, publisher, and DOI.

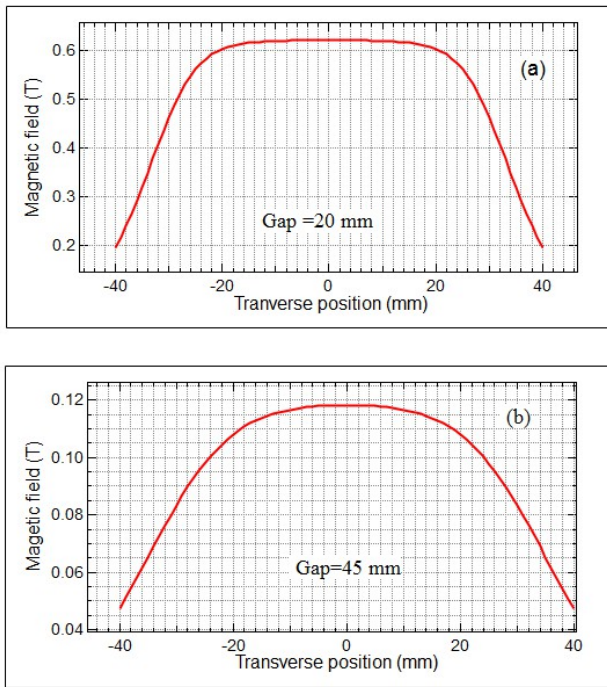


Figure 5: Transverse roll-off plot in magnetic mid-plane.

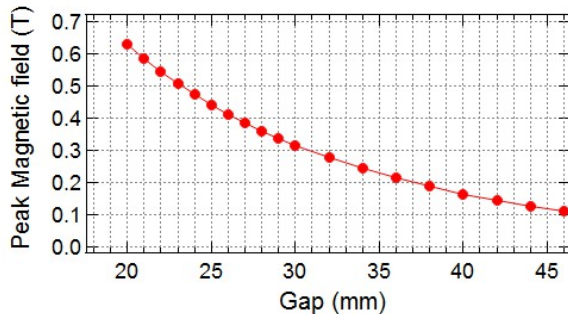


Figure 6: Variation of magnetic peak field as function of undulator gap.

CONCLUSION

A compact hybrid planar undulator for THz radiation production at DLS facility, New Delhi, is designed and optimised successfully with code 3D RADIA. The mechanical design of the undulator is going to be carried out shortly, and then the device will be fabricated, assembled and tested. As per the schedule of the DLS project at IUAC, the device should be installed in the beamline at the beginning of 2019 and the production of THz is expected to be demonstrated by the end of the same year.

ACKNOWLEDGEMENT

One of the authors, S. Tripathi (PH/16-17/0029) would like to acknowledge University Grant Commission (UGC) New Delhi, India for financial support through the D. S. Kothari Postdoctoral fellowship. The authors also sincerely acknowledge the help received from Pavel Vagin from DESY, Hamburg, Germany.

REFERENCES

- [1] S. Ghosh *et al.*, *Proc. of FEL'14*, Basel, Switzerland, 596.
- [2] S. Ghosh *et al.*, *NIM-B*, 402 (2017) 358–363.
- [3] S. Ghosh *et al.*, presented at FEL'17, this conference.
- [4] RADIA, available at: [http://www.esrf.eu/Accelerators/groups/Insertion Devices/Software/Radia](http://www.esrf.eu/Accelerators/groups/Insertion%20Devices/Software/Radia).
- [5] J. A. Clarke, “The science and technology of undulators and wigglers”, Oxford Press, Oxford, 2004.

CHARACTERIZING SUB-FEMTOSECOND X-RAY PULSES FROM THE LINAC COHERENT LIGHT SOURCE

S. Li*, R. Coffee, K. Hegazy, Z. Huang, A. Natan¹, T. Osipov, D. Ray, J. Cryan¹, and A. Marinelli,
SLAC National Laboratory, Menlo Park, United States

¹also at Stanford PULSE Institute, Menlo Park, United States

Z. Guo, Stanford University, Stanford, United States

Abstract

The development of sub-femtosecond x-ray capabilities at the Linac Coherent Light Source requires the implementation of time-domain diagnostics with attosecond (as) time resolution. Photoelectrons created by attosecond duration x-ray pulses in the presence of a strong-laser field are known to suffer an energy spread which depends on the relative phase of the strong-laser field at the time of ionization. This phenomenon can be exploited to measure the duration of these ultrashort x-ray pulses. We present an implementation which employs a circularly polarized infrared laser pulse and novel velocity map imaging design which maps the phase dependent momentum of the photoelectron onto a 2-D detector. In this paper, we present the novel co-linear VMI design, simulation of the photoelectron momentum distribution, and the reconstruction algorithm.

INTRODUCTION

Electron motion in atoms and molecules is the essential key to understanding the earliest processes involved in chemical changes. Electrons move across a molecular bond in 0.1 to 1 femtosecond (fs), a time scale of which direct measurement was impossible until recently when high harmonic generation [1, 2] became a widely used tool to synthesize light pulse in the extreme ultra-violet regime with sub-femtosecond duration. Extending the photon wavelength to the soft x-ray regime, the enhanced self-amplified spontaneous emission (eSASE) from x-ray free electron lasers enables the production of high intensity attosecond pulses [3]. The method of eSASE is currently being implemented experimentally at the linac coherent light source (LCLS) [4]. The electron bunch goes through an emittance spoiler which destroys the bunch except for a femtosecond duration beam core. The unspoiled core then interacts with an optical laser which imprints energy modulation on to the beam. Going through a dispersive section, the energy modulation turns into a single current spike with sub-femtosecond duration. The current spike goes through the undulator which emits coherent attosecond x-ray pulses.

Therefore, in order to measure the temporal profiles of sub-femtosecond x-ray pulses we employ a variant of the well known “attosecond streak camera” technique [5]. Our variation, which is closely related to the “atto-clock” technique [6], exploits the correlation between optical-cycle phase and streaking direction in a circularly polarized laser pulse. The

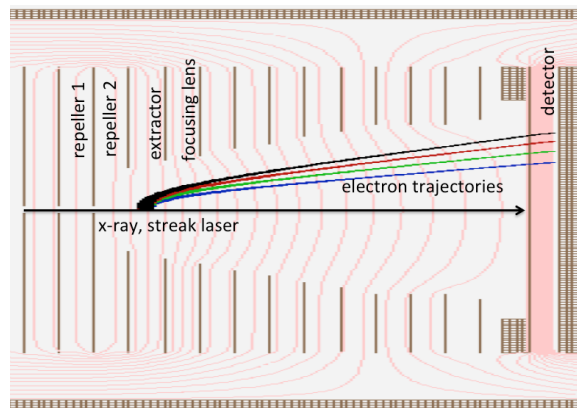


Figure 1: Side view of the cVMI design, with the linearly polarized x-ray pulse and circularly polarized streaking laser pulse propagating co-linearly. Picture taken in SIMION-8.0.

photoelectrons generated by the attosecond x-ray pulse interacting with gas molecules in the presence of a strong laser field experience an energy spread which depends on the duration of these ultrashort x-ray pulses. With a circularly polarized streaking laser, we provide a kick to the photoelectrons momentum distribution, and the angle and the strength of the momentum shift contains timing information of the x-ray pulse. Similar work has been done with longer x-ray pulses and a detector that measures a slice of the photoelectron momentum distribution [7]. With our novel co-linear velocity map imaging (cVMI), we will measure a 2-D projection of the 3-D momentum distribution of electrons generated by the linearly polarized attosecond x-ray pulse and the circularly polarized IR streaking pulse.

We develop an algorithm to reconstruct the x-ray pulse from the 2-D photoelectron momentum distribution. We use the von Neumann representation [8] to decompose the x-ray pulse into a set of basis functions. The fitting algorithm searches for the complex coefficients related to the basis functions by minimizing the difference between the measurement image and the fitted image. We demonstrate that we can successfully reconstruct attosecond x-ray pulses generated from free electron laser simulations.

VMI DESIGN

A VMI spectrometer has the advantages of high collection efficiency and high angular resolution. The critical requirement for a VMI to work is to image the charged particles with the same momentum onto the same position on the

* siqili@slac.stanford.edu

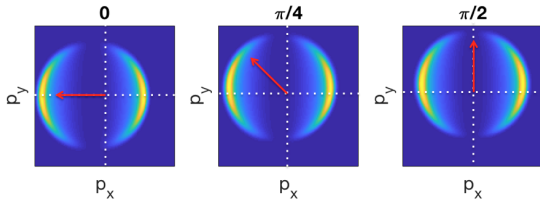


Figure 2: Simulation of the measured VMI image with a FWHM 300as x-ray pulse streaked by a 1.3 μ m laser. From left to right we vary the relative phase between the x-ray pulse and the streaking laser pulse to be 0, $\pi/4$, and $\pi/2$ respectively. The red arrows illustrate the direction of the momentum kick relative to the center of the image.

two-dimensional detector, regardless of the particles' initial position. This is achieved by arranging the metal plates with specific voltages in the spectrometer to create electro-static field that images the photoelectrons. Our co-linear VMI design follows a similar procedure as described in [9]. Instead of a traditional VMI configuration [10], we include a focusing lens plate and several subsequent plates for enhancing energy resolution to treat the novel setup where the x-ray and streaking laser propagate co-linearly. We use an ion-tracking program, SIMION-8.0, to simulate electron motions in the VMI. Figure 1 is a side view of the cylindrically-symmetric spectrometer.

The energy resolution of the VMI is determined by simulating trajectories of groups of charged particles with different central energy, 0.3 standard deviation in energy, and a uniformly-distributed initial momentum direction. Our cVMI design is capable of distinguishing 3% energy difference among the particle groups. For the purpose of diagnosing photoelectrons generated by attosecond pulses which necessarily have a large bandwidth, above 3eV, our VMI design provides sufficient energy resolution.

STREAKING SIMULATION

We base our simulation of the streaking process on the Lewenstein model [11]. Under the strong field approximation, the governing equation to calculate the transition amplitude as a function of photoelectron's final momentum, $b(\vec{p})$, of the continuum states of atoms in the presence of strong laser field is expressed as follows,

$$b(\vec{p}) = -i \int_{-\infty}^{+\infty} dt \vec{E}(t) \cdot \vec{d}(\vec{p} + \vec{A}(t)) \exp\{i\Phi(t)\}, \quad (1)$$

and

$$\Phi(t) = - \int_t^{+\infty} dt' [(\vec{p} + \vec{A}(t'))^2 / 2 + I_p]. \quad (2)$$

In Eq. 1 and 2, \vec{E} is the total electric field, \vec{d} is the dipole moment for the transition to the continuum states, \vec{A} is the vector potential of the streaking laser, and I_p is the ionization potential of the atom. The integral in the exponential starts from the time of ionization, t , to ∞ , and the outer integral expands entire time to allow any time of ionization. Because

the x-ray pulse contains much higher frequency components compared to the streaking laser pulse, only the x-ray field contributes to the outer integral to compensate for the fast oscillating phase Φ . We can replace the total electric field \vec{E} with the x-ray electric field \vec{E}_X . Note that Eq. 1 calculates the transition amplitude as a function of a photoelectron's final 3-D momentum, $b(p_x, p_y, p_z)$. However, what we measure with a VMI spectrometer is the probability distribution of a photoelectron's 2-D momentum,

$$B(p_x, p_y) = \int dp_z \left| b(p_x, p_y, p_z) b^*(p_x, p_y, p_z) \right|. \quad (3)$$

An important feature of angular streaking is that the circularly polarized streaking laser imposes a momentum kick to the photoelectrons as a function of time. The strength and the angle of the kick is determined by the relative phase between the x-ray pulse and the streaking laser pulse. In Fig. 2 we demonstrate the simulated photoelectron momentum distribution projected onto a 2-D VMI detector, while varying the relative phase between the x-ray pulse and the streaking laser pulse. The apparent double-arc shape comes from the dipole moment \vec{d} in Eq. 1.

RECONSTRUCTION ALGORITHM

Traditionally VMI images are analyzed with inverse Abel transform due to cylindrical symmetry [12]. This is not possible for our VMI design because angular streaking breaks the cylindrical symmetry. However, since we know the physics of the streaking process, we can limit the reconstruction to a small subset of all possible momentum distributions.

The basic idea of our reconstruction algorithm is to decompose the measured VMI image into "basis images" and the complex coefficients corresponding to each basis give the reconstructed x-ray pulse. As shown in Eq. 1, the transition amplitude is linearly proportional to the x-ray electric field, $b(\vec{p}) \propto \vec{E}_X(t)$. If we decompose $\vec{E}_X(t)$ into a sum of basis functions, then we can write $b(\vec{p}) = \sum_n c_n b_n(\vec{p})$, where we allow the coefficients c_n to be complex. The measured 2-D momentum distribution becomes

$$\begin{aligned} B(p_x, p_y) &= \sum_n \sum_m \int dp_z c_n^* c_m b_n^*(\vec{p}) b_m(\vec{p}) \\ &= \sum_n \sum_m c_n^* c_m B_{nm}(p_x, p_y), \end{aligned} \quad (4)$$

where \vec{p} denotes the 3-D momentum, and $B_{nm}(p_x, p_y)$ is what we refer to as the "basis image".

To decompose the electric field, we choose the von Neumann representation to describe the x-ray electric field [8], which includes the intensity and phase information of the x-ray pulse in both the time and the frequency domain. The von Neumann basis function is

$$\alpha_{\omega_i t_j}(t) = \left(\frac{1}{2\alpha\pi} \right)^{\frac{1}{4}} \exp \left[- \frac{1}{4\alpha} (t - t_j)^2 - it\omega_i \right], \quad (5)$$

where t_i and ω_j are the time and frequency axis in the von Neumann representation, α is a constant determined by the

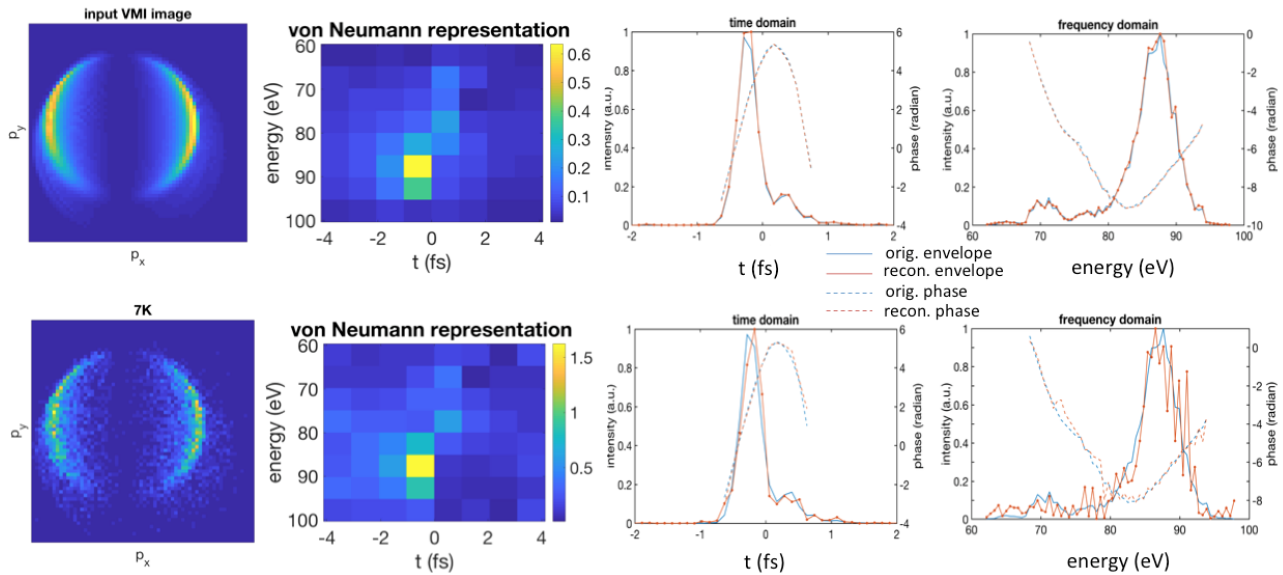


Figure 3: Example reconstruction of an attosecond x-ray pulse from genesis simulation. Top row from left to right: input 2-D momentum distribution; results of the nonlinear fitting algorithm to describe the x-ray pulse in the von Neumann representation; time domain reconstruction of the x-ray intensity; frequency domain reconstruction of the x-ray intensity. The bottom row is to show count statistics by sampling the simulated VMI image with Poisson noise of 7K particles.

time and frequency window, and i, j are indices that expand the frequency and time axes respectively (see details in [8]). We then obtain the basis functions $b_n(\vec{p})$ by plugging $\alpha_{\omega;t_j}(t)$ into Eq. 1, and obtain B_{nm} using Eq. 3. Note that the index for the basis function n and m each spans the entire parameter space in time and frequency. In other words, $n = ij$, and it is the same for m . The von Neumann coefficients $Q_{i,j}$ are obtained by rearranging the 1-D coefficients c_n into a 2-D representation, where one axis is for time and the other is for frequency. The reconstructed x-ray electric field is $\vec{E}_{\text{recon}} = \sum_{i,j} Q_{i,j} \alpha_{\omega;t_j}$.

Therefore the reconstruction problem is reduced to solving for the complex coefficients c_n . We define the cost function to be

$$\text{cost} = \sum_{p_x, p_y} \left| M(p_x, p_y) - B(p_x, p_y) \right|^2, \quad (6)$$

where $M(p_x, p_y)$ is the measured photoelectron 2-D momentum distribution. We use Matlab's `fminunc` function to search for the complex coefficients c_n by minimizing the cost function. Figure 3 illustrates an example of the reconstruction result. We obtain the input pulse from a GENESIS simulation which has intricate substructures in the time and frequency domain. The algorithm successfully and completely reconstructs these structures. With count statistics of 7K particles sampled via Poisson noise, the algorithm is robust enough to still reconstruct the x-ray pulse in time and frequency domain.

It is worth noting the intricate structures in the GENESIS pulse which shows up as a second peak in time domain as well as frequency domain. The effect of the second bump in the x-ray pulse on the VMI detector image is an interference pattern of the photoelectron wave packet, which then

is reflected in the interference fringes in the 2-D momentum distribution [13] (see the lower left corner of the VMI image in Fig. 3 for an example). Our reconstruction algorithm is capable of decoding such complicated quantum mechanical effects thanks to the complex coefficients that contain the phase information of the pulse. Further discussions on the algorithm's convergence, robustness, and limitations will be found in a future publication.

CONCLUSIONS

In this paper we discussed the working mechanism of angular streaking as diagnostic for attosecond x-ray pulses. We presented the novel co-linear VMI design with 3% energy resolution to measure photoelectron momentum distribution in the presence of a circularly polarized streaking laser. We showed the simulation results of the streaking process based on the Lewenstein model. Moreover, we described the nonlinear fitting algorithm that takes advantage of the von Neumann representation of any electric field. We demonstrated successful reconstruction of an attosecond x-ray pulse in both time and frequency domain. The outlook of this work is to utilize the angular streaking technique with experimentally produced attosecond x-ray pulses generated at LCLS.

ACKNOWLEDGEMENTS

This work was supported by the US Department of Energy, Office of Science, Basic Energy Sciences, Chemical Sciences, Geosciences, and Biosciences Division, under contract number DE-AC02-76SF00515 and DOE-BES Field Work Proposal 100317.

REFERENCES

- [1] P. B. Corkum, and F. Krausz, "Attosecond science," *Nature Physics* 3.6 (2007): 381.
- [2] P. M. Paul *et al.*, "Observation of a train of attosecond pulses from high harmonic generation," *Science* 292.5522 (2001): 1689-1692.
- [3] A. Zholents, "Method of an enhanced self-amplified spontaneous emission for x-ray free electron lasers." *Physical Review Special Topics-Accelerators and Beams* 8.4 (2005): 040701.
- [4] J. MacArthur *et al.*, "High power sub-femtosecond X-ray pulse study for the LCLS." Proceedings of 8th Int. Particle Accelerator Conf.(IPAC'17), Copenhagen, Denmark, 14 - 19 May, 2017. (JACOW, Geneva, Switzerland, 2017.)
- [5] J. Itatani *et al.*, "Attosecond streak camera," *Physical Review Letters* 88.17 (2002): 173903.
- [6] P. Eckle *et al.*, "Attosecond angular streaking," *Nature Physics* 4.7 (2008): 565-570.
- [7] N. Hartmann, G. Hartmann, and W. Helml, "Angle-resolved streaking for complete attosecond FEL pulse characterization," manuscript in preparation.
- [8] S. Fechner *et al.*, "The von Neumann picture: a new representation for ultrashort laser pulses," *Optics Express* 15.23 (2007): 15387-15401.
- [9] N. G. Kling *et al.*, "Thick-lens velocity-map imaging spectrometer with high resolution for high-energy charged particles," *Journal of Instrumentation* 9.05 (2014): P05005.
- [10] A. T. J. B. Eppink and D. H. Parker, "Velocity map imaging of ions and electrons using electrostatic lenses: Application in photoelectron and photofragment ion imaging of molecular oxygen," *Review of Scientific Instruments* 68.9 (1997): 3477-3484.
- [11] M. Lewenstein *et al.*, "Theory of high-harmonic generation by low-frequency laser fields," *Physical Review A* 49.3 (1994): 2117.
- [12] C. J. Dasch, "One-dimensional tomograttosecondaphy: a comparison of Abel, onion-peeling, and filtered backprojection methods," *Applied Optics* 31.8 (1992): 1146-1152.
- [13] A. K. Kazansky *et al.*, "Interference effects in angular streaking with a rotating terahertz field," *Physical Review A* 93.1 (2016): 013407.

THERMAL STRESS ANALYSIS OF A THIN DIAMOND CRYSTAL UNDER REPEATED FREE ELECTRON LASER HEAT LOAD*

Bo Yang[†], Department of Mechanical and Aerospace Engineering,
 University of Texas at Arlington, Arlington, TX 76019, USA

Juhao Wu[‡], SLAC National Accelerator Laboratory, Menlo Park, California, 94025, USA

Abstract

Thin crystals are used as many important optical elements in XFELs, such as monochromators and spectrometers. To function properly, they must survive the ever-increasing heat load under repeated pulses. Here, we conduct a thermal stress analysis to examine the crystal lattice distortion due to the thermal load under various rep rates from 0.1 to 1 MHz. The thermal field is obtained by solving the transient heat transfer equations. The temperature-dependent material properties are used. It is shown that for pulse adsorption energy around tens of μJ over a spot size of $10\ \mu\text{m}$, the thermal response of diamond is sensitive to rep rate. The thermal strain components are very different in the in- and out-of-plane directions, due to different constraint conditions. It suggests complicated strain effects in the Bragg and Laue diffraction cases.

INTRODUCTION

XFELs generate high peak-power pulses with atomic and femtosecond scale resolution, impacting high-frontier scientific research [1,2]. Thin crystals are used in several important elements, such as monochromators [3,4], single-shot spectrometers [5–7], and other applications [8]. In pursuit of high-brightness XFELs, the power has been increased by orders of magnitude, so the thin crystals will experience much increased heat load. Thus, it is important to understand their photo-thermo-mechanical behaviours at higher temperature. Here, we perform a thermal stress analysis to elucidate the deformation field in a thin diamond crystal subjected to repeated heat load of XFEL pulses. The stress/strain field is obtained with a thermal field as a loading source by solving the static equilibrium equation. The thermal field is modelled by solving transient heat transfer equations and material properties, such as the thermal expansion, heat capacity [9] and thermal conductivity [10] valid up to temperatures $\sim 3000\ \text{K}$. The problem is solved with a finite volume method [11,12]. The case of a $40\text{-}\mu\text{m}$ thick plate with a Gaussian beam of FWHM of $20\ \mu\text{m}$ is studied with rep rates from 0.1 to 1 MHz. For a pulse depositing tens of μJ energy, the temperature that a next pulse sees ratchets up slowly at 0.1-0.2 MHz, but upsurges at higher rep rates. At 1 MHz, a runaway increase of temperature is found after a few pulses. It is because the heat relaxation rate through con-

duction decreases with temperature due to decreasing heat conductivity. The thermal stress/strain fields are analysed with a residual thermal field as a loading source. The strain components are different, implying complicated strain effects in Bragg and Laue diffractions.

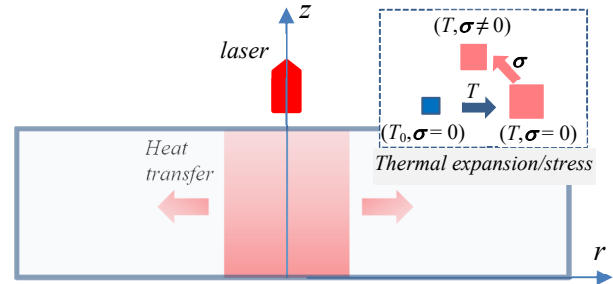


Figure 1: Schematics of instantaneous heating and subsequent heat transfer upon laser energy deposition in a thin crystal. The inset on the upper-right shows the thermal expansion and the stress to be built up due to constraint. The cylindrical coordinate with axisymmetry is used.

PROBLEM FORMULATION

Governing Equations

An XFEL impinging on a crystal would interact with the electrons and deposit a part of energy first onto the electrons [13]. Later the energy is transferred to the lattice raising the temperature. This process occurs at the pico-to-nano second scale. Then, the thermalized lattice expands emitting stress waves at the nano-to-tens-of-nano second scale at the sound speed [14]. The thermal diffusion will start, but not become effective until hundreds of nanoseconds. During this time, the stress waves would have bounced back and forth between boundaries for tens of times. If passive damping is instated, the inertia effect will soon become trivial. Thus, we assume that the specimen is in the mechanical equilibrium despite the transient heat transfer. The thermal field will significantly affect the deformation field, but the effect of deformation on thermal field is trivial. We analyse the processes of transient heat transfer and resulting thermal stress field. A cylindrical coordinate system (r, θ, z) is used with z -axis normal to the crystal surface as in Fig. 1. Only a pulse perpendicular to the crystal surface is studied.

The equilibrium equation without body forces is:

$$\nabla \cdot \boldsymbol{\sigma} = 0, \quad (1)$$

where $\boldsymbol{\sigma}$ is the stress tensor. Assuming the isotropic thermoelasticity, the constitutive law is given by [15]:

*Work supported by the US Department of Energy (DOE) under contract DE-AC02-76SF00515 and the US DOE Office of Science Early Career Research Program grant FWP-2013-SLAC-100164.

[†]boyang@uta.edu

[‡]jhwu@slac.stanford.edu

$$\boldsymbol{\sigma} = 2G \left(\boldsymbol{\varepsilon} - \frac{1}{3} \text{tr}(\boldsymbol{\varepsilon}) \mathbf{I} \right) + 3K_b \left(\frac{1}{3} \text{tr}(\boldsymbol{\varepsilon}) - \varepsilon_T \right) \mathbf{I}, \quad (2)$$

where G is the modulus of rigidity, K_b the bulk modulus, $\boldsymbol{\varepsilon}$ the strain tensor, ε_T the thermal strain, \mathbf{I} the identity matrix, and $\text{tr}(\boldsymbol{\varepsilon})$ the trace of $\boldsymbol{\varepsilon}$.

The equation of energy conservation is given by

$$\frac{dU_T}{dt} = -\nabla \cdot (-\kappa \nabla T), \quad (3)$$

where T is the temperature, $U_T (= \int \rho C_v dT)$ the thermal energy density, κ the thermal conductivity, ρ the mass density, and C_v the specific heat.

The initial temperature is $T_0 = 300\text{K}$. The FEL pulse energy is partially absorbed raising the temperature. The FEL pulse is assumed to be Gaussian. It impinges perpendicularly to the crystal surface, assumed so that the problem can be reduced to be axisymmetric. The change of thermal energy density as a function of r and z is

$$\Delta U_T(r, z) = \frac{2I_0}{\pi a^2 L} e^{-\frac{2r^2}{a^2}} e^{-\frac{z}{L}}, \quad (3)$$

where I_0 is the FEL pulse energy, a the transverse FWHM of the Gaussian beam in the radial direction, and L the attenuation length. The temperature increase is determined from the relationship of U_T to T . The thermal insulation and traction-free boundary conditions are applied.

Material Properties

The thermal strain and specific heat capacity of diamond are taken from Ref.⁹. The thermal strain is given by

$$\varepsilon_T = \sum_{i=1}^3 \frac{X_i \theta_i}{\exp\left(\frac{\theta_i}{T}\right) - 1}, \quad (4)$$

where θ_i and X_i are constants, given by $\theta_1 = 200\text{K}$, $\theta_2 = 880\text{K}$, $\theta_3 = 2137.5\text{K}$, $X_1 = 0.4369 \times 10^{-7} \text{K}^{-1}$, $X_2 = 15.7867 \times 10^{-7} \text{K}^{-1}$, $X_3 = 42.5598 \times 10^{-7} \text{K}^{-1}$. The linear thermal expansion coefficient is $\alpha_T = \partial \varepsilon_T / \partial T$. The U_T is obtained through $\int \rho C_v dT$ with tabulated values of C_v up to $T = 3000\text{K}$. The thermal conductivity is $\kappa = 2200 \text{Wm}^{-1}\text{K}^{-1}$ for diamond at 300K . Yet, it decreases rapidly with increasing temperature, to be $100 \text{Wm}^{-1}\text{K}^{-1}$ at $T = 2000\text{K}$. The data of Ref. 10 from 300K to 2000K are averaged and fit to a power law: $\kappa = 23.9 \times 10^6 T^{-1.63}$. Other materials constants are given as density $\rho = 3.51 \text{g/cm}^3$, shear modulus $G = 508 \text{GPa}$, and bulk modulus $K_b = 678 \text{GPa}$.

RESULTS AND DISCUSSION

Simulations were carried out at four rep rates: 0.1, 0.2, 0.5, and 1 MHz. The FWHM of the Gaussian beam is $a = 20\ \mu\text{m}$. The pulse energy $I_0 = 100\ \mu\text{J}$. The attenuation length $L = 50\ \mu\text{m}$, corresponding to $\sim 4\text{keV}$ X-ray. The crystal plate thickness $h = 40\ \mu\text{m}$. In this case, the laser energy is about 55 % absorbed by the crystal. As the laser energy decreases, it raises the internal energy at the front

(entry) surface about 2.2 times that at the back (exit) surface. This amount of energy is added to the system each pulse according to the rep rates. Eleven equal divisions are used to discretize the domain in the thickness direction. An adaptive mesh is used in the radial direction, with 10 equal divisions in near $10\ \mu\text{m}$ distance, and 200 unequal divisions with increasing size outwards by gradient 1.015 in following $1490\ \mu\text{m}$ distance, from the center. The time step is 10 ns. For each repetition rate, the simulation was run longer than 0.1 ms. Selected results are presented in Figs. 2–6. Figures 2(a)–(d) show the temperature evolution on the front surface ($z = 0$) at three radial distances $r = 0, 20, 50\ \mu\text{m}$ for the four rep rates. Figures 3(a)–(d) show the temperature profiles along the radial direction on the front surface for the four cases. Figures 4(a)–(d) show the corresponding three normal strain components, ε_r , ε_θ and ε_z . Figures 5(a)–(d) and 6(a)–(d) show the same profiles as in Figs. 3 and 4, but on the middle plane of the layer. Based on the above results, some observations are made and discussed as follows.

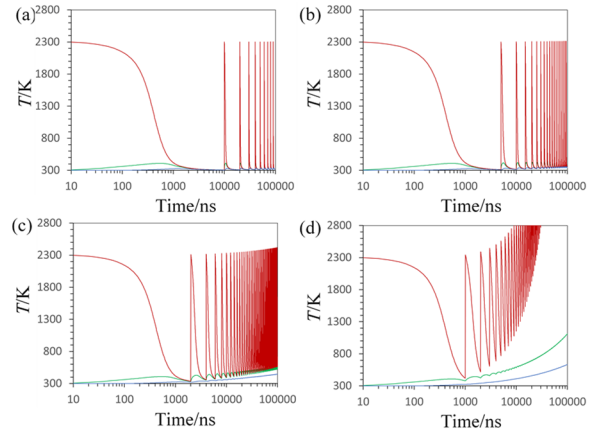


Figure 2: Temperature evolution at three radial distance $r = 0$ (red), 20 (green), 50 (blue) μm on the surface ($z = 0$) under repetition rates: (a) 0.1; (b) 0.2; (c) 0.5; (d) 1 MHz.

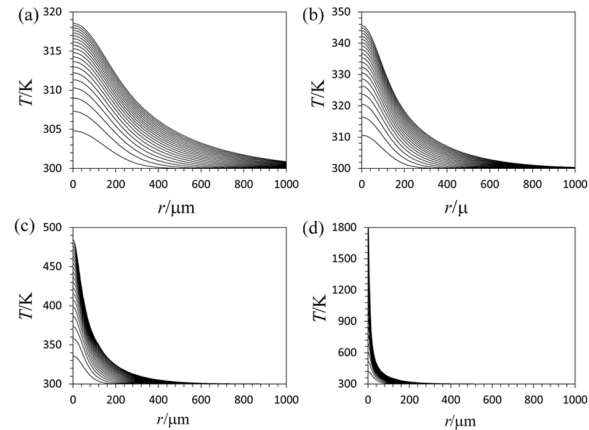


Figure 3: Temperature profiles along the radial axis at the front surface ($z = 0$) at times before a next pulse strikes under repetition rate: (a) 0.1; (b) 0.2; (c) 0.5; (d) 1 MHz. Twenty pulses are plotted in each case.

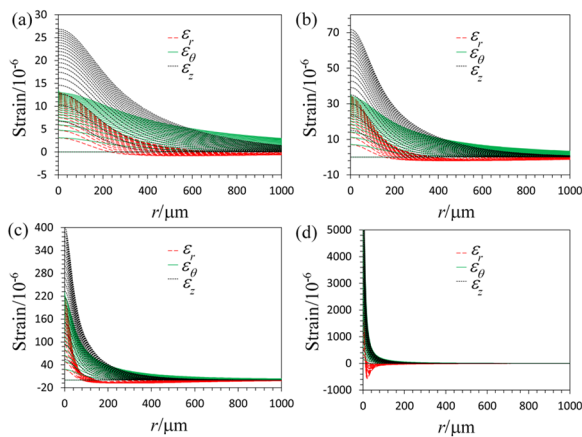


Figure 4. Profiles of strain components ε_r (red), ε_θ (green) and ε_z (black) along the radial axis at the front surface ($z = 0$) at times before a next pulse strikes under repetition rate: (a) 0.1; (b) 0.2; (c) 0.5; (d) 1 MHz. Twenty pulses are plotted in each case.

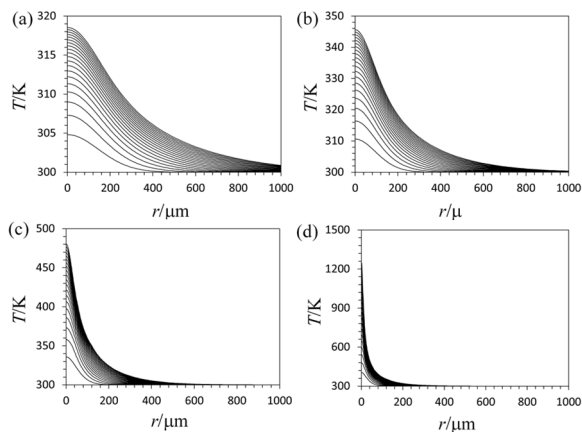


Figure 5. Temperature profiles along the radial axis at the middle plane ($z = 20 \mu\text{m}$) at times before a next pulse strikes under repetition rate: (a) 0.1; (b) 0.2; (c) 0.5; (d) 1 MHz. Twenty pulses are plotted in each case.

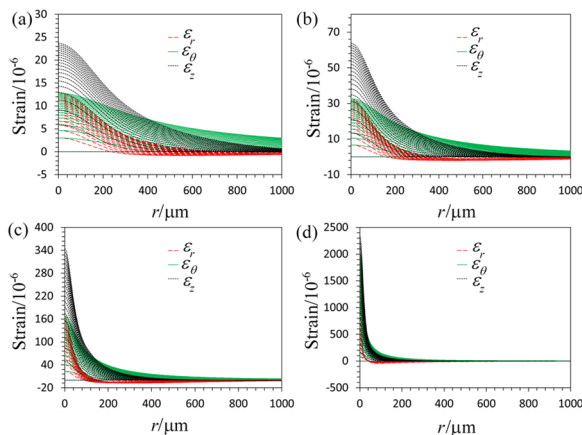


Figure 6. Profiles of strain components ε_r (red), ε_θ (green) and ε_z (black) along the radial axis at the middle plane ($z = 20 \mu\text{m}$) at times before a next pulse strikes under repetition rate: (a) 0.1; (b) 0.2; (c) 0.5; (d) 1 MHz. Twenty pulses are plotted in each case.

It may be seen from Figs. 2, 3, and 5 that the thermal response of diamond is sensitive to repetition rate when it gets near 1 MHz at the energy deposition of tens of μJ per pulse over a spot size around $10 \mu\text{m}$. At 100 – 200 kHz, the temperature increases with each pulse, but slowly. At 500 kHz, the temperature ratchets up much more quickly. At 1 MHz, a runaway of temperature is observed only after a few pulses. At 100 – 200 kHz, the temperature is nearly uniform across thickness upon relaxation after each pulse and before the next pulse. In contrast, at the higher rep rates, the temperature rises so high and the thermal diffusivity drops so significantly that the thermal equilibrium cannot be established across the thickness between pulses. At 1 MHz, the runaway thermal spike occurs near the front surface where the laser beams strike. At low temperatures, the strain resulting from thermal expansion is proportional to the temperature change with a coefficient about $1 \times 10^{-6} \text{ K}^{-1}$, indicating that diamond is an excellent material against thermal expansion. At higher temperatures, its strong lattice force constants soften, leading to much increased linear thermal expansion coefficient. It quickly reaches $4 \times 10^{-6} \text{ K}^{-1}$ at $\sim 1000 \text{ K}$ and keeps rising though at a slower rate, similarly to how its specific heat varies with temperature. The spatial variation of strain follows that of temperature as in these figures. The strain fields are also somewhat different at the surface and inside the layer due to three-dimensional effect across the thickness and along the radial direction.

Due to the different constraint conditions, the strain components ε_r , ε_θ and ε_z turn out to be very different. ε_r and ε_θ are equal to each other along the center line ($r = 0$) of the FEL spot, as in Figs. 4 and 6. This is consistent with the corresponding analytical result demonstrating the validity of the present numerical solution. Importantly, it is seen that ε_z is nearly twice the other two normal components. Since the Bragg and Laue cases of diffraction use reflection planes ranging from parallel to the surface to tilted by a large angle from the surface, it becomes complicated how the strain field affects them. It necessitates a detailed thermomechanical study to understand the thermal effect on diffraction. The present study and alike provide the 3-D strain field in a thin crystal under heat load. The relationship of thin-crystal-based optical element sensitivity to strain is yet to be established.

SUMMARY

Transient heat transfer and static thermal stress analyses are performed for a thin diamond crystal under repeated FEL heat load. The formulation is phenomenological. The problem is solved with a finite volume method [14,16]. The realistic material properties of diamond from room temperature to elevated temperature are used. The range of rep rates from 0.1 to 1 MHz is considered. For deposition energy of tens of μJ per pulse over a spot size of $10 \mu\text{m}$, the thermal response of diamond is found

to be quite sensitive to the repetition rate. The instantaneous maximum temperature due to a single pulse can reach over 2000 K. It relaxes to a certain extent before a next pulse. The temperature and hence the thermal strain field ratchet up with pulses, slowly at 0.1–0.2 MHz, but much accelerated at 0.5 MHz and above. At 1 MHz, a runaway increase of temperature is observed after only a few pulses. Meanwhile the temperature increases, the thermal conductivity drops. It slows down the thermal relaxation in the radial direction and across the thickness. Finally, it is shown that the strain components are very different in the in- and out-of-plane directions. It implies complicated strain effect in the Bragg and Laue diffractions. The present analysis and alike using realistic material properties are necessary to understand the limits to using diamond in the optical elements for XFEL's under high rep rate.

REFERENCES

- [1] Emma, P. *et al.*, “First lasing and operation of an ångstrom-wavelength free-electron laser.” *Nature Photonics* **4**, 641–647 (2010).
- [2] Ishikawa, T. *et al.*, “A compact X-ray free-electron laser emitting in the sub-ångstrom region.” *Nature Photonics* **6**, 540–544 (2012).
- [3] Geloni, G., Kocharyan, V. and Saldin, E., “A novel self-seeding scheme for hard X-ray FELs.” *Journal of Modern Optics* **58**, 1391–1403 (2011).
- [4] Amann, J. *et al.*, “Demonstration of self-seeding in a hard-X-ray free-electron laser.” *Nature Photonics* **6**, 693–698 (2012).
- [5] Yabashi, M. *et al.*, “Single-shot spectrometry for X-ray free-electron lasers.” *Physical Review Letters* **97**, 084802 (2006).
- [6] Zhu, D. *et al.*, “A single-shot transmissive spectrometer for hard x-ray free electron lasers.” *Applied Physics Letters* **101**, 034103 (2012).
- [7] Rehanek, J. *et al.*, “The hard X-ray photon single-shot spectrometer of SwissFEL—initial characterization.” *Journal of Instrumentation* **12**, A07001 (2017).
- [8] Shvyd'ko, Y., Blank, V. and Terentyev, S., “Diamond x-ray optics: transparent, resilient, high-resolution, and wavefront preserving.” *MRS Bulletin* **42**, 437–444 (2017).
- [9] Reeber, R. R. and Wang, K., “Thermal expansion, molar volume and specific heat of diamond from 0 to 3000K.” *Journal of Electronic Materials* **25**, 63–67 (1996).
- [10] Wei, L., Kuo, P., Thomas, R., Anthony, T. and Banholzer, W., “Thermal conductivity of isotopically modified single crystal diamond.” *Physical Review Letters* **70**, 3764 (1993).
- [11] LeVeque, R. J., “Finite volume methods for hyperbolic problems.” vol. 31, Cambridge University Press, 2002.
- [12] Versteeg, H. K. and Malalasekera, W., “An introduction to computational fluid dynamics: the finite volume method.” Pearson Education, 2007.
- [13] Von der Linde, D., Sokolowski-Tinten, K. and Bialkowski, J., “Laser–solid interaction in the femtosecond time regime.” *Applied Surface Science* **109**, 1–10 (1997).
- [14] Yang, B., Wang, S. and Wu, J., “Transient thermal stress wave and vibrational analyses of a thin diamond crystal for X-ray FELs under high-repetition-rate operation.” *Journal of Synchrotron Radiation* (under review).
- [15] Shorr, B. F., “Thermal integrity in mechanics and engineering.” Springer, 2015.
- [16] Yang, B., Wu, J., Raubenheimer, T. O. and Feng, Y., “Fluid dynamics analysis of a gas attenuator for X-ray FELs under high-repetition-rate operation.” *Journal of Synchrotron Radiation* **24** (2017).

OPTICAL BEAM QUALITY ANALYSIS OF THE CLARA TEST FACILITY USING SECOND MOMENT ANALYSIS

H. M. Castañeda Cortés*, D. J. Dunning, M. D. Roper and N. L. Thompson
 ASTeC, Cockcroft Institute, STFC, Daresbury Laboratory, Warrington, United Kingdom

Abstract

We studied and characterised the FEL optical radiation in simulations of the CLARA FEL test facility under development at Daresbury Laboratory in the UK. In particular, we determined the optical beam quality coefficient, waist position and other source properties corresponding to different potential FEL operating modes via wavefront propagation in free space using OPC (Optical Propagation Code) and second moment analysis. We were able to find the operation mode and undulator design for which the optical beam has the optimum quality at highest brightness. Furthermore, we studied the way that different properties of the electron bunches (emittance, peak current, bunch length) affect the optical beam. We are now able to understand how the optical beam will propagate from the end of the undulator and through the photon transport system to the experimental stations. This knowledge is necessary for the correct design of the photon transport and diagnostic systems.

INTRODUCTION

The CLARA FEL test facility, currently under construction at Daresbury Laboratory [1], will have different operation modes in order to probe and test several advanced FEL concepts, such as high brightness SASE, mode-locking and afterburner schemes [2]. An aspect of fundamental interest in the design of CLARA is the assessment of the radiation properties obtained at the end of the FEL process. It is extremely important to optimise the design of the facility so that the optical beam quality does not degrade as the beam is transported through the optical beamline. This paper summarises the studies of optical beam quality carried out for the long bunch operation mode, assessing the different design parameters which could degrade or enhance it. The spatial source properties are calculated by using second moment analysis.

SECOND MOMENT ANALYSIS

The M^2 analysis states that the second moment of the optical beam profile follows a quadratic free-space propagation rule in terms of the propagating distance z as [3]

$$\sigma_i^2 = \sigma_{i0}^2 + \left(\frac{M_i^2 \lambda}{4\pi\sigma_{i0}} \right)^2 (z - z_0)^2, \quad \text{where } i = x, y. \quad (1)$$

The M^2 parameter compares the beam quality of the propagated beam to the free-space propagation of a TEM₀₀ Gaussian beam ($M_i^2 = 1$). The rms size at the beam waist is σ_{i0} and z_0 the waist position. M_i^2 , σ_{i0} and z_0 can be calculated

from fitting the evolution of the optical beam profile (defined as $\sigma_i^2(z) = C_2 z^2 + C_1 z + C_0$) to the measured values of second moments, [4],

$$M_i^2 = \frac{2\pi}{\lambda} \sqrt{4C_0 C_2 - C_1^2}, \quad (2)$$

$$z_0 = -\frac{C_1}{2C_2}, \quad \text{and} \quad (3)$$

$$\sigma_{i0} = \sqrt{C_0 - \frac{C_1^2}{4C_2}}. \quad (4)$$

The optical code OPC [5, 6] was used to perform the free-space propagation of the calculated radiation at the end of the undulator. Time-dependent FEL simulations were carried out in GENESIS 1.3 [7] to obtain the radiation field.

PRELIMINARY STUDY

The long bunch operation mode in CLARA is designed to demonstrate FEL schemes generating radiation pulses significantly shorter than the electron bunch length. It will have between 150 and 250 MeV beam energy, 250 pC bunch charge, $\sigma_t = 800$ fs, peak current of 125 A, 0.5 mm-mrad normalised emittance and 25 keV energy spread. Planar variable gap undulators will have a 2.5 cm period and maximum rms of the undulator parameter of 1.4, allowing resonant wavelengths between 100 and 400 nm. A comparison of steady state and time-dependent simulations in GENESIS 1.3 was done to have a rough estimate of the source properties and demonstrate the validity of time-dependent approach for beam quality calculations. Previous CLARA undulator values were used, as given in Table 2. The radiation wavelength defined for the simulations is set to be 266 nm (the shortest wavelength for single-shot temporal diagnostics).

Table 1: Comparison Between Optical Beam Parameters Obtained from Steady State and Time-Dependent Simulations.

Parameter	Steady State		Time-Dependent	
	x	y	x	y
M^2	3.8	3.6	3.6	3.5
z_0 (m)	-1.85	-1.93	-1.27	-1.27
σ_{z_0} (μm)	283	273	274	278

Second moment analysis was performed via the wavefront propagation code FOCUS (for steady state simulations) [8] and OPC (for time-dependent simulations). The obtained source properties for both scenarios (following Eqs. (2), (3), and (4)) are shown in Table 1. The M^2 parameters obtained

* hector.castaneda@stfc.ac.uk

Table 2: Undulator parameters chosen for the preliminary study in last section and each undulator module length case. There are 1.5 undulator periods end pieces for all cases, per end.

Parameter	Previous Study	Undulator module length		
		0.5 m	0.75 m	1 m
Und. period [m]	0.0275	0.025	0.025	0.025
Active periods	28	17	27	37
Number of periods drift	18	23	23	23
Break sections [m]	0.4125	0.5	0.5	0.5
Quad length [m]	0.055	0.05	0.05	0.05
x/y quad. gradient [T/m]	8/10	13/13	10/10	9/9

for the steady state and time-dependent simulations are quite close to each other with a relative difference of 5.2% and 2.8% in x and y, respectively. Therefore, the time-dependent simulations are suitable in order to find the radiation source properties. However, the M^2 obtained for both steady state and time-dependent simulations deviates from $M^2 = 1$, corresponding to a TEM₀₀ Gaussian beam.

IMPACT OF UNDULATOR MODULE LENGTH

As a follow-up to the previous study, three different undulator module lengths (0.5, 0.75 and 1 m) were chosen in order to find the radiation source properties for each undulator length (characterised by the number of undulator segments (n_{sec}) in GENESIS 1.3). Table 2 shows the undulator parameters chosen for each simulated undulator module length (compared to the ones used in the previous section).

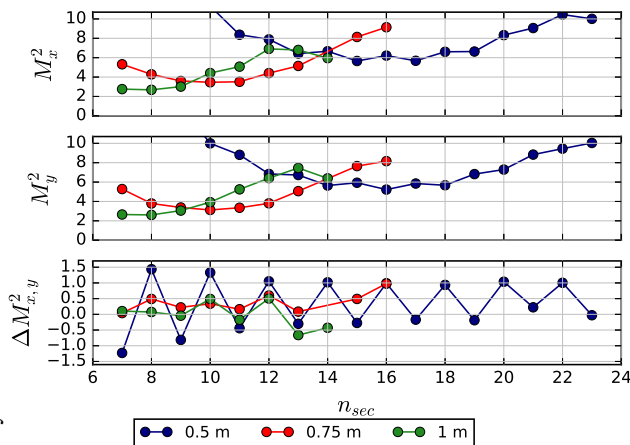


Figure 1: M^2 in x (top) and y (middle) and their difference $\Delta M_{x,y}^2 = M_x^2 - M_y^2$ (bottom) in terms of the number of undulator segments (for 0.5, 0.75 and 1 m modules).

Fig. 1 shows that a parabolic function can be fitted around the minimum value of M^2 as a function of n_{sec} for the three

chosen modules. The minimum M^2 coefficient for the 0.5 m module length (in Table 3) has the largest M^2 of all modules (2.1 and 2.3 times larger than the smallest value obtained for the 1 m module in x and y, respectively). As it is desired to have a M^2 as close to the TEM₀₀ Gaussian mode as possible for higher beam quality, this module can be discarded as a possibility.

The difference between M^2 in x and y, $\Delta M_{x,y}^2$, (in Fig. 1) in terms of n_{sec} fluctuates around a non-zero value due to the focusing and defocusing of the electron beam while traversing the FODO cell. It shows an asymmetry in beam quality due to the difference in focusing for both transversal directions. For larger undulator lengths, the difference in focusing and defocusing is more significant (especially deep into saturation) and the difference in beam quality between x and y increases.

Table 3: Comparison Between Source Parameters at n_{sec} Corresponding to the Minimum of M^2 for the Three Proposed Undulator Module Lengths

L (m)	M_x^2	M_y^2	z_{0x} [m]	z_{0y} [m]	$\sigma_{z_{0x}}$ [μ m]	$\sigma_{z_{0y}}$ [μ m]
0.5	5.65	5.93	-1.3	-1.19	350	351
0.75	3.46	3.12	-1.1	-1.11	229	229
1	2.68	2.6	-1.21	-1.1	202	211

To get a complete picture of how impactful the change in the undulator design is, we consider the beam brightness, defined in terms of the M^2 coefficient as [9]

$$B_{x,y} = 16P_{n_{sec}} / (\lambda^2 (M_{x,y}^2)^2). \quad (5)$$

Here λ is the radiation wavelength and $P_{n_{sec}}$ is the peak power at the end of the n_{sec} undulator segment.

It can be seen in Fig. 2 that the brightness has its maximum value at a number of undulator segments larger than the one that corresponds to the minimum M^2 . We, therefore, choose the undulator length associated with the highest brightness as the most feasible comparison scenario for the three undulator modules. This case approximately corresponds to the onset of saturation of the FEL.

The results in Table 4 show the source properties calculated at the number of the undulator segments where the brightness is maximum. The 0.75 and 1 m modules have the best results at maximum brightness. When compared, the relative difference between the beam quality coefficients shows that the beam quality for those undulator modules is similar (relative difference less than 1% in x and 3.1% in y). The 0.75 m module is chosen for compatibility with the novel schemes to be tested in the facility, such as mode locking and HB-SASE.

IMPACT OF BEAM PARAMETERS

Different electron beam scenarios were proposed to study the impact of electron beam properties on the beam quality: (A) Increased emittance bunch (from 0.5 to 0.8 mm-mrad),

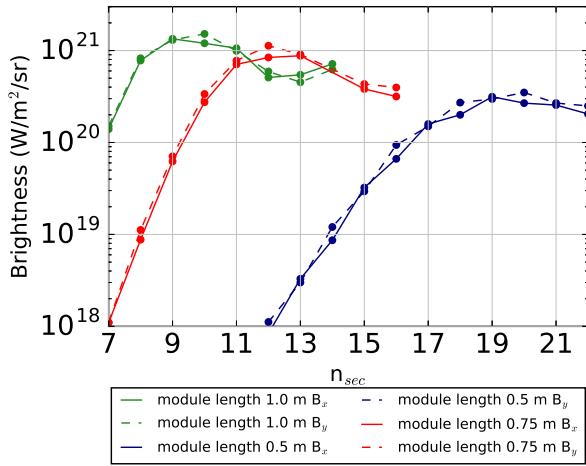


Figure 2: Brightness for the three undulator module lengths as a function of n_{sec} .

Table 4: Comparison Between Optical Beam Parameters at n_{sec} Corresponding to Maximum Brightness for the Three Proposed Modules

L (m)	M_x^2	M_y^2	z_{0x} [m]	z_{0y} [m]	σ_{z0x} [μ m]	σ_{z0y} [μ m]
0.5	8.32	7.29	-1.99	-2.1	509	471
0.75	4.40	3.80	-1.41	-1.50	300	287
1	4.41	3.92	-1.86	-1.97	348	329

(B) reduced quad strength (from 10 to 2 T/m, so that the electron beam is much bigger in one plane), (C) symmetric undulator focusing (by artificially setting the undulator to be helical in GENESIS 1.3, it can be guaranteed that the focusing in both planes will be the same) and (D) electron beam with double peak current and half the bunch length.

A summary of the calculated source properties for the n_{sec} at which M^2 to be minimum and at which the brightness is maximum can be found in Table 5. The brightness as a function of number of undulator segments for each scenario is shown in Fig. 3.

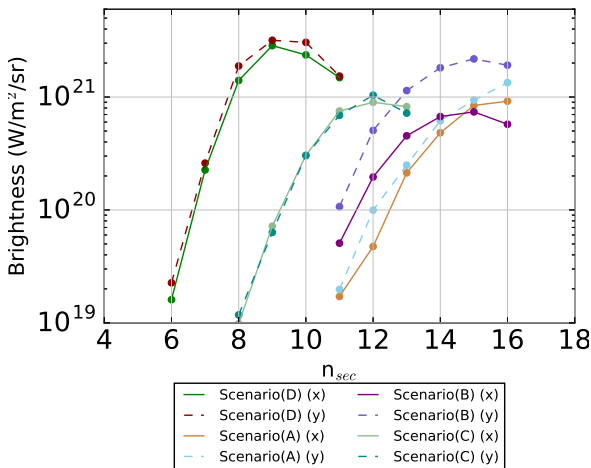


Figure 3: Brightness as a function of the undulator length (for the electron beam case studies).

Table 5: Optical Beam Parameters at n_{sec} Corresponding to the Minimum M^2 and Maximum Brightness for the Electron Beam Scenario

Scenario	Minimum M^2		Maximum Brightness	
	M_x^2	M_y^2	M_x^2	M_y^2
Scenario (A)	3.61	3.34	4.65	3.86
Scenario (B)	3.67	2.31	4.76	2.77
Scenario (C)	3.54	3.57	4.41	4.11
Scenario (D)	3.04	2.69	3.38	3.21

Considering only the calculated values at maximum brightness, the comparison of M^2 for the larger emittance scenario parameters shows degradation in the beam quality with respect to the nominal 0.75 m module (relative difference of M^2 in x around 5.7% and 1.5% in y). The M^2 parameter in y for the reduced quad strength scenario is the smallest of all considered proposals (2.77 for the y direction in Table 5), making the beam less divergent in that direction. The relative difference of M^2 with respect to the nominal 0.75 m module case in x shows degradation in beam quality (around 8.2%) but an important improvement of beam quality in y (27%). The symmetric focusing scenario does not show any improvement of beam quality in either of the planes. The M^2 is indeed more symmetric between the two planes. Finally, the electron beam with twice the peak current and half the bunch length has the minimum M^2 of all proposed cases. When comparing the obtained parameters to the results in Table 4, an improvement in the beam quality is achieved, with a M^2 reduced to 0.77 and 0.84 of the nominal case in x and y, respectively. Thus, the beam quality is improved for both planes. A large difference of the M^2 in x and y shows an asymmetry in the beam profile. In particular, the reduced quad strength scenario favours the beam quality on one coordinate of the transversal plane (stronger focusing in one plane).

Similarly to that studied previously, the beam quality was assessed for undulator designs which produces coherent radiation with wavelength of 100 and 400 nm. The M^2 at maximum brightness were calculated for the 100 nm and 400 nm. A slight improvement of beam quality in x and y can be observed for the 400 nm with respect to the nominal 0.75 m module length ($M_x^2 = 4.28$ and $M_y^2 = 3.38$ with relative difference of 2.7% and 11% in x and y, respectively). The 100 nm scenario shows improvement in beam quality for both transversal planes with respect to the 0.75 m module length, providing the best optical beam quality of the studied cases (2.87 and 2.77 in x and y respectively).

SUMMARY

Following the second moment analysis, the beam quality coefficient M^2 and main source properties were calculated for the long bunch mode at the CLARA test facility. Three different module lengths (0.5, 0.75 and 1 m) were assessed to determine the impact of the undulator design on the beam

Content from this work may be used under the terms of the CC BY 3.0 licence (© 2018). Any distribution of this work must maintain attribution to the author(s), title of the work, publisher, and DOI.

quality. The source properties were determined per module as a function of the undulator length. The M^2 parameter used for comparison was chosen to be the one corresponding to the undulator length at the largest brightness. It was shown that choosing an undulator module length of 0.75 m, optimum for the different R&D topics proposed, does not degrade the beam quality compared to longer modules.

REFERENCES

- [1] J. A. Clarke *et al.*, “CLARA conceptual design report”, *JINST*, Vol. 9, pp. T05001, 2014.
- [2] D.J. Dunning, “CLARA Facility Layout and FEL Schemes”, presented at FEL2017, Santa Fe, USA, Aug. 2017, paper MOP054, this conference.
- [3] A. E. Siegman, “How to (Maybe) Measure Laser Beam Quality”, in DPSS (Diode Pumped Solid State) Lasers: Applications and Issues, M. Dowley, ed., Vol. 17 of OSA Trends in Optics and Photonics (Optical Society of America), paper MQ1, 1998.
- [4] M. D. Roper, “Matching a variable-included-angle grating monochromator to the properties of a soft X-ray FEL source to achieve a controlled temporal stretch”, *Nucl. Instrum. Methods A*, Vol. 635, pp. S80–S87, 2011.
- [5] J. Karssenberg *et al.*, “Modelling paraxial wave propagation in free-electron laser oscillators”, *J. App. Phys.*, Vol. 100, 093106, 2006.
- [6] P.J.M. van der Slot, “Recent Updates to the Optical Propagation code OPC”, in *Proceedings of the Int. FEL Conference Conf. (FEL'14)*, Basel, Switzerland, Aug. 2014, paper TUP021, pp. 412-415.
- [7] S. Reiche, “Genesis 1.3: a fully 3D time-dependent FEL simulation code”, *Nucl.Instrum.Methods A*, Vol. 429, pp. 243–248, 1999.
- [8] M.A. Bowler and S. P. Higgins, “FOCUS – A new Wavefront Propagation Code”, presented at the SMEXOS Conference, Grenoble, France, Feb. 2009, <http://www.esrf.eu/files/live/sites/www/files/events/conferences/2009/SMEXOS/talkBowler.pdf>.
- [9] G. Machavariani, N. Davidson, Y. Lumer, I. Moshe, A. Meir, and S. Jackel, “New methods of mode conversion and beam brightness enhancement in a high-power laser”, *Opt. Mater.*, Vol. 30, pp. 1723–1730, 2008.

Content from this work may be used under the terms of the CC BY 3.0 licence (© 2018). Any distribution of this work must maintain attribution to the author(s), title of the work, publisher, and DOI.

The proposed design has following features:

- (a) The basic structure is mirror symmetric therefore the magnetic forces is better balanced than traditional undulators.
- (b) Overall width (~1.3m) is almost same as the existing single-sided undulators.
- (c) Distance between beam centers is about 0.96 m, enough for two lines of components in parallel.
- (d) Enough space between undulators for transport and installation work near the tunnel walls. The space of 1.5 m width between undulator lines is available for transporting undulators and 0.9 m between tunnel wall and outer undulator magnet for component installations.
- (e) The short distance between two photon beams makes it easier to bring them to the same end-station for pump-probe or other kinds of experiments with completely independent controlled X-ray pulses. There are large flexibilities in choosing wavelength, polarization, coherence, intensity and pulse duration, etc.
- (f) With this type of undulator design each tunnel with 5.9m-diameter may accommodate up to four independent undulator lines, as can be observed in Figure 5.

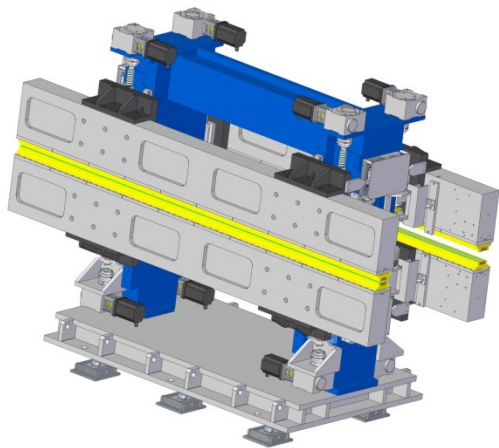


Figure 4: Overall view of the proposed 3-meter prototype undulator.

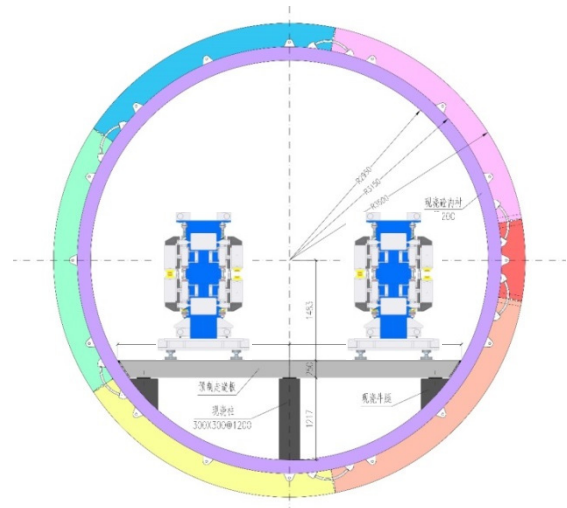


Figure 5: Cross section of the undulator tunnel with two undulators.

The new layout with two-in-one type undulator in the SCLF tunnels shows that it is feasible to install two such undulator lines therefore four FEL lines with independent tuning capabilities of the photon properties.

On the other hand, one usually needs to diverse photon beams from two-in-one undulators to the different end-stations. Also it is obvious that two undulator lines must have the identical length for each unit including undulator magnet and components between the adjacent undulators.

In order to verify the robustness and study mechanical performance of this type of concept, an engineering design of a full-size prototype undulator has been completed [4]. Figure 6 shows the final engineering layout. The order is placed to a company for manufacturing a 3-meter-long full size prototype undulator frame for further studies.

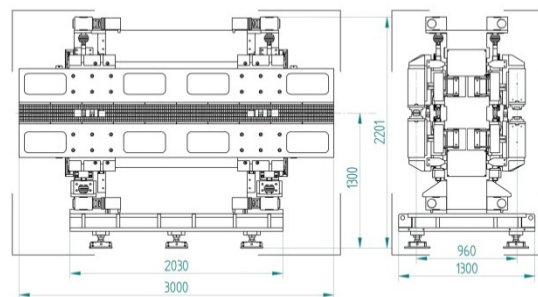


Figure 6: Engineering design of the type of undulator in the SINAP.

CONCLUSION

A concept of two-in-one undulator magnet is proposed to utilize the space in tunnel more efficiently. The concept has several advantages on achieving independently tuning flexibilities of two different XFEL photon beams within comparable spaces to the conventional out-vacuum undulators, which may pave the way of maximizing the capabilities of photon beamlines of future high rep rate X-ray Free Electron Lasers.

ACKNOWLEDGEMENT

Authors would like to thank L. Yin, B. Liu and other colleagues in SINAP for useful discussions. This work is supported by National Program on Key Basic Research Project (No. 2016YFA0401900), the Ministry of Science and Technology of China.

REFERENCES

- [1] M. Altarelli *et al.* Ed., “The European X-Ray Free-Electron Laser – Technical Design Report”, Rep. DESY 2006-097, DESY (2007).
- [2] “LCLS-II Final Design Report”, Report No. LCLSII-1.1-DR-0251, SLAC (2015).
- [3] K. Li and H. Deng, “Systematical design of X-ray FEL oscillator for the Shanghai Coherent Light Facility”, *Journal of Synchrotron Radiation*, arXiv:1706.06338 (2017).
- [4] Z. Jiang *et al.*, to be submitted.

TUNABLE HIGH-GRADIENT QUADRUPOLES FOR A LASER-PLASMA ACCELERATION-BASED FEL*

A. Ghaith[†], F. Marteau, P. N'gotta, M. Valléau, J. Veteran, F. Blache, C. Kitegi, M. E. Couprie, Synchrotron SOLEIL, Gif-sur-Yvette, France
 C. Benabderrahmane, ESRF, Grenoble, France
 O. Cosson, F. Forest, P. Jivkov, J. L. Lancelot, SigmaPhi, Rue des Freres Montgolfier, Vannes, France

Abstract

The magnetic design and characterization of tunable high gradient permanent magnet based quadrupole, or so-called QUAPEVAs, are presented. To achieve a high gradient field with a compact structure, permanent magnets are chosen rather than usual electro-magnets due to their small aperture. The quadrupole structure consists of two superimposed quadrupoles capable of generating a gradient of 210 T/m. The first quadrupole is composed of permanent magnets in a Halbach configuration shaped as a ring which attains a constant gradient of 160 T/m, and the second is composed of four permanent magnet cylinders surrounding the ring and capable of rotating around their axis in order to achieve a gradient tunability of ± 50 T/m. Each tuning magnet is connected to a motor and is controlled independently, enabling the gradient to be tuned with a rather good magnetic center stability (20 μ m and without any field asymmetry). Seven quadrupoles have been built with different magnetic lengths in order to fulfill the integrated gradient required. A set of QUAPEVA triplet are now in use, to focus a high divergent electron beam with large energy spread generated by a laser plasma acceleration source for a free electron laser application [1].

INTRODUCTION

Accelerator physics and technology have recently seen tremendous developments especially in the synchrotron radiation domain, which is actively investigating low emittance storage rings with multibend achromat optics for getting closer to the diffraction limit and providing a high degree of transverse coherence [2]. In addition, Laser Plasma Acceleration (LPA) can now generate a GeV beam within a very short accelerating distance, with high peak current of ~ 10 kA, but the high divergence (on the order of a few mrad) and large energy spread (a few percent) can present problems.

All these recent developments require high gradient quadrupoles that can not be provided by usual room temperature electro-magnet technology. To achieve a high gradient, one is more likely to choose either superconducting or permanent magnet [3] technologies. Permanent Magnets (PMs)

can be arranged in the so-called Halbach configuration [4], to provide a quadrupolar field. Interest in permanent magnet quadrupoles has been recently renewed because of their compactness and their capability of reaching high field gradient, alongside the absence of power supplies, letting them to be a solution for future sustainable green society.

DESIGN

The QUAPEVA is composed of two superimposed quadrupoles, one placed at the center following a Halbach configuration, surrounded by another that consists of four rotating cylindrical magnets to provide the gradient variability, illustrated in Fig. 1). Figure 1 also shows three particular configurations of the tuning magnets; (a) maximum gradient: tuning magnets easy axis towards the central magnetic poles, (b) intermediate gradient: the tuning magnets are in the reference position, *i.e.* their easy axis is perpendicular to the central magnetic poles, (c) minimum gradient: tuning magnets easy axis is away from the central magnetic poles. Table 1 shows the QUAPEVA parameters alongside the characteristics of the magnets and poles.

Table 1: QUAPEVA Parameters.

Parameters	Value	Unit
Gradient (G)	110 - 210	T/m
Remanent Field (B_r)	1.26	T
Coercivity (H_{cj})	1830	kA/m
Good-Field Region	4	mm
$\Delta G/G$	< 0.01	at 4 mm

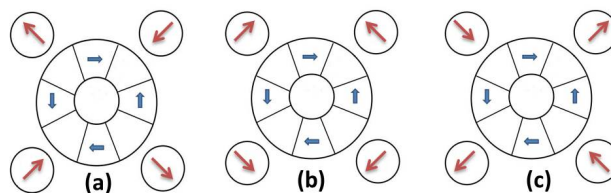


Figure 1: (a) maximum gradient, (b) intermediate gradient, (c) minimum gradient.

* Synchrotron SOLEIL

[†] amin.ghaith@synchrotron-soleil.fr

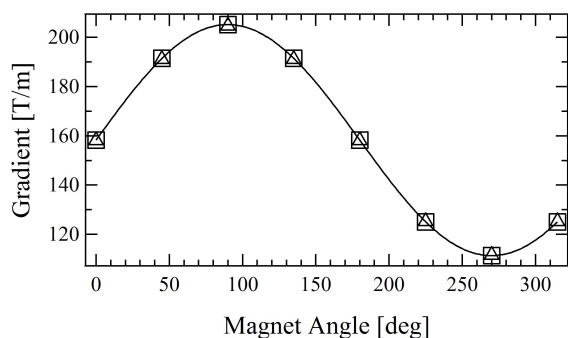


Figure 2: Magnetic field gradient computed as the cylindrical magnets are rotating for the 100 mm magnetic length of the QUAPEVA. (□) RADIA, (△) TOSCA.

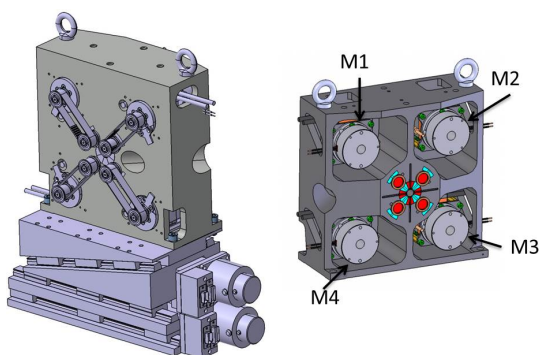


Figure 3: QUAPEVA design mounted on a translation table.

In order to optimize the geometry and magnetic parameters, QUAPEVAs are modeled using two numerical tools: RADIA, a magnetostatic code based on the boundary integral method where materials are meshed [5], and TOSCA, a finite element magnetostatic code [6].

Figure 2 shows the gradient computed as the cylindrical magnets rotate in the case of the 100-mm magnetic length system. The intermediate gradient is ~ 160 T/m, and due to the rotating magnets it can be increased by $\sim 50\%$ up to 210 T/m.

The motors have sufficient torque to counteract the magnetic forces induced by the magnetic system, are very compact ($48.5 \times 50 \times 50 \text{ mm}^3$), and have an encoder within a $31\text{-}\mu\text{rad}$ resolution. The magnetic system is mounted on an Aluminum frame and the motors are placed at the four corners of the frame to avoid perturbations of the magnetic field as shown in Fig. 3. A non-magnetic belt transmits the rotation movement from the motor to the cylindrical magnets. Each magnet is connected to one motor to allow for a precise positioning of each magnet and minimizes the magnetic center shift at different gradients. The quadrupole is mounted on a translation table (horizontal and vertical displacement) used to compensate any residual magnetic axis shift when varying the gradient, to perform electron beam based alignment or for the magnetic measurements benches.

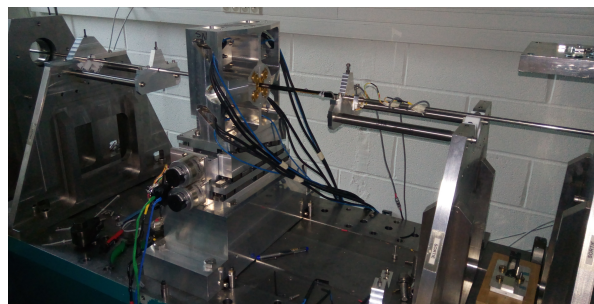


Figure 4: Rotating coil bench installed at SOLEIL.

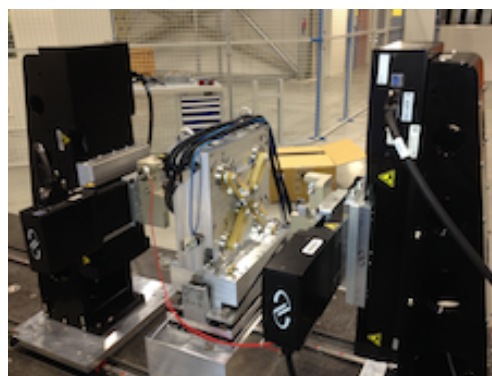


Figure 5: Stretched wire bench at ESRF.

MAGNETIC MEASUREMENTS

Displayed in Fig. 4, a dedicated 10-mm diameter, radially rotating coil was built for the SOLEIL magnet characterization bench [7], to fit the quadrupole inner diameter of 10.5 mm. In order to qualify the accuracy of the rotating coil, a permanent magnet quadrupole with a 76-mm diameter bore has been measured first with a reference coil and then with the 10-mm diameter coil. The geometrical parameter of the new coil has been determined in order to find the same harmonic content with both coils at 4 mm.

The integrated gradient of the seven systems with different magnetic lengths is measured with the rotating coil and compared to the simulations of RADIA and TOSCA, where they showed good agreement with a difference no larger than 4%.

The stretch-wire bench developed at ESRF [8] has been used for magnetic field integral measurements (see Fig. 5). The wire is positioned inside the magnet gap and its resonance frequency is tuned. Its sag depends on its tension. A voltage proportional to the variation of magnetic flux is induced and measured with a Keithley nanovoltmeter, resulting in the first field integral. A granite table supports the linear stages and the measured magnet. The stretched wire bench enables fast measurements to be performed with good precision and good repeatability.

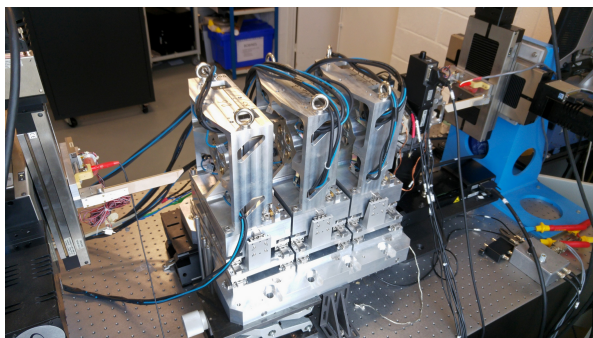


Figure 6: Pulsed wire system setup with three QUAPEVAs (26 mm, 40.7 mm, and 44.7 mm mechanical lengths).

This method has been used to calculate the magnetic center excursion as the gradient is varied. The center stability is found to be within $\pm 10 \mu\text{m}$.

The pulsed-wire method has been used to align the magnetic center of the three QUAPEVAs (see Fig. 6) before their installation at COXINEL transport line [9]. It is based on applying a square current pulse through a wire placed in a magnetic field, which induces an interaction due to the Lorentz force. This force leads to wire displacement which is measured using a motion laser detector [10].

A first triplet of QUAPEVA was checked with the pulsed wire technique in view of the COXINEL application. The three QUAPEVA were directly installed on the bench, with a medium gradient value setting and with random values for the horizontal and vertical positions of the translation stage. The pulse wire measurements for such a deviation show deviations of the magnetic axis from the axis. Then, the three QUAPEVA were centered one by one, starting from the 40.7 mm, then the 44 mm and finally the 26 mm. Such an adjustment had been performed with only two iterations for each quadrupole: the first measurement is performed for the actual position and the second one while the quadrupole has been displaced $250 \mu\text{m}$ in the vertical and horizontal planes. As the field is proportional to the displacement, the new positions are calculated from these two measurements to recover the center position. The pulsed wire technique was thus used for checking the final alignment and the absence of cross talk between the magnets.

COXINEL

A first triplet (26-mm, 40.7-mm, and 44.7-mm mechanical length) is used for focusing the electron beam produced by laser plasma acceleration at Laboratoire d'Optique Appliquée in view of electron qualification with a Free Electron Laser application. The results from the pulsed wire measurement have been used for QUAPEVA alignment during COXINEL experiment. Figure 7 shows the electron beam, using a lanex screen placed 3 m away from the electron source, with and without the triplet. The large divergent beam is well focused.

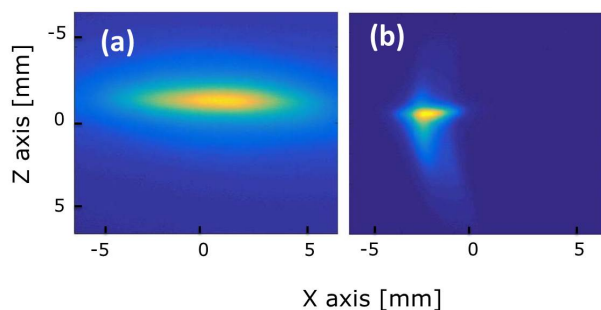


Figure 7: Measured electron beam on a Lanex screen placed 3 m away from the electron source. (a) without QUAPEVAs, (b) with QUAPEVAs.

CONCLUSION

The design and magnetic measurements of a permanent magnet based quadrupole of variable strength have been presented. A high gradient ($\sim 210 \text{ T/m}$) with a wide tuning range ($\sim 100 \text{ T/m}$) is obtained with such a design. The measurement using different methods are consistent and in good agreement between themselves and the simulations. The quadrupoles have been installed successively at COXINEL beam line, and are able to achieve good focusing with a highly divergent large energy spread beam.

ACKNOWLEDGEMENT

The authors are very grateful to the European Research Council for the advanced grant COXINEL (340015) and also to the Fondation de la Coopération Scientifique for the Triangle de la Physique / valorisation contract QUAPEVA (2012-058T). The authors are very thankful for the COXINEL team. The authors also acknowledge the Laboratoire d'Optique Appliquée team led by V. Malka for the generation of the electron beam by laser plasma acceleration, enabling to use the QUAPEVA.

REFERENCES

- [1] M. E. Couprie, A. Louergue, M. Labat, R. Lehe, and V. Malka, "Towards a free electron laser based on laser plasma accelerators," *Journal of Physics B: Atomic, Molecular and Optical Physics*, 47(23):234001, 2014.
- [2] Y. Cai, K. Bane, R. Hettel, Y. Nosochkov, M.-H. Wang, and M. Borland, "Ultimate storage ring based on fourth-order geometric achromats," *Physical Review Special Topics-Accelerators and Beams*, 15(5):054002, 2012.
- [3] K. Halbach, "Physical and optical properties of rare earth cobalt magnets," *Nuclear Instruments and Methods in Physics Research*, vol. 187, no. 1, pp. 109–117, 1981.
- [4] K. Halbach, "Conceptual design of a permanent quadrupole magnet with adjustable strength," *Nuclear Instruments and Methods in Physics Research*, vol. 206, no. 3, pp. 353–354, 1983.

- [5] O. Chubar, P. Elleaume, and J. Chavanne, "A three-dimensional magnetostatics computer code for insertion devices," *Journal of Synchrotron Radiation*, vol. 5, no. 3, pp. 481–484, 1998.
- [6] J. Simkin and C. Trowbridge, "Three-dimensional nonlinear electromagnetic field computations, using scalar potentials," in *IEE Proceedings B-Electric Power Applications*, vol. 127, pp. 368–374, IET, 1980.
- [7] A. Madur, *Contribution à la métrologie magnétique des multipôles d'accélérateurs: les quadripôles du Synchrotron SOLEIL*. PhD thesis, Vandoeuvre-les-Nancy, INPL, 2006.
- [8] G. Le Bec, J. Chavanne, and C. Penel, "Stretched wire measurement of multipole accelerator magnets," *Physical Review Special Topics – Accelerators and Beams*, vol. 15, no. 2, p. 022401, 2012.
- [9] M. E. Couprie *et al.*, *et al.*, "An application of laser-plasma acceleration: towards a free-electron laser amplification," *Plasma Physics and Controlled Fusion*, vol. 58, no. 3, p. 034020, 2016.
- [10] D. W. Preston and R. W. Warren, "Wiggler field measurements and corrections using the pulsed wire technique," *Nuclear Instruments and Methods in Physics Research Section A: Accelerators, Spectrometers, Detectors and Associated Equipment*, vol. 318, no. 1-3, pp. 794–797, 1992.

CRYOGENIC PERMANENT MAGNET UNDULATOR FOR AN FEL APPLICATION*

A. Ghaith[†], M. Valléau, F. Briquez, F. Marteau, M. E. Couprie, P. Bertheaud, O. Marcouillé,
 T. Andre, I. Andriyash, M. Labat, E. Roussel, M. Tilmont, K. Tavakoli, N. Bechu,
 C. Herbeaux, M. Sebdaoui, Synchrotron SOLEIL, Gif-sur-Yvette, France

Abstract

Cryogenic Permanent Magnet Undulator (CMPU) is capable of achieving high brightness radiation at short wavelengths, by taking advantage of the permanent magnet's enhanced performance at low temperature. A CPMU of period 18 mm (U18) that has been built at Synchrotron SOLEIL is used for the COXINEL project to demonstrate Free Electron Laser (FEL) at 200 nm using a laser plasma acceleration source. Another undulator of period 15 mm (U15) is currently being built to replace U18 undulator for FEL demonstration at 40 nm. A new method is also introduced, using SRWE code, to compute the spectra of the large energy spread beam (few percent) taking into account the variation of the Twiss parameters for each energy slice. The construction of U18 undulator and the magnetic measurements needed for optimization, as well as the mechanical design of U15, are presented.

INTRODUCTION

Third generation synchrotron radiation has been used widely in different applications, due to the intense brightness produced ranging from infrared to x-rays. This intensity is generated by the use of a low emittance beam and an insertion device most commonly known as undulator. An undulator consists of periodic arrangements of dipole magnets generating a periodic sinusoidal magnetic field, and is capable of producing an intense and concentrated radiation in narrow energy bands as relativistic electrons are traversing it. The emitted radiation wavelength observed is expressed as $\lambda_R = (\lambda_u/2\gamma^2)[1 + K^2/2]$, where λ_u is the magnetic period, $K = 93.4\lambda_u[m]B[T]$ the deflection parameter, and B the peak field. Fourth generation sources, such as Free Electron Laser (FEL) based experiments, exceed the performance of previous sources by one or more orders of magnitude in important parameters such as brightness, coherence, and shortness of pulse duration. The future FEL based projects relies on the compactness of the machine. Hence, compact undulators are needed for such developments.

Permanent magnet undulators are able to function at room temperature and attain a fair magnetic field depending on the magnet material. Most pure permanent magnet undulators use the Halbach geometric design [1], and by replacing poles with the vertically magnetized magnets making it a hybrid type [2] and enhances its magnetic peak field. In order to achieve a more compact undulator with sufficient field, one has to decrease the size of magnets which will reduce

the peak field. So the idea was proposed at SPring-8 [3] to cool down the undulator to cryogenic temperature and enhancing the performance of the permanent magnets. The Cryogenic Permanent Magnet Undulator (CPMU) design is easily adapted to the in-vacuum undulator, achieving a high peak field with a shorter period length making it suitable for compact FEL based applications.

MAGNETIC AND MECHANICAL DESIGN

The prototypes design has been done using RADIA [4] as shown in Fig. 1. The magnets used are $Pr_2Fe_{14}B$ [5] and Vanadium Permendur poles, and their characteristics are presented in Table 1 for both CPMUs, period 18 mm (U18) and period 15 mm (U15).

Figure 2 shows the field computed for the two cryogenic undulators at both room and cryo temperature. The field is increased by ~12% from room temperature to cryo temperature. The minimum gaps reached by U15 and U18 are 3 mm and 5 mm respectively.

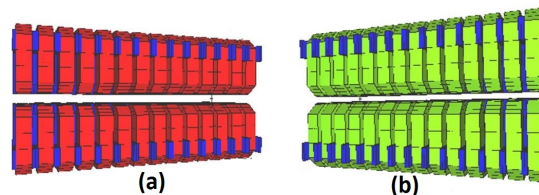


Figure 1: (a) prototype design of the undulator U18 and (b) of U15 with 7 periods, using RADIA code with IGOR Pro as front end.

Table 1: U18 prototype characteristics.

Parameters	Value	Unit
Magnet dimension (U18)	50 x 30 x 6.5	mm ³
Magnet dimension (U15)	50 x 30 x 5.5	mm ³
Pole dimension (U18)	33 x 26 x 2.5	mm ³
Pole dimension (U15)	33 x 26 x 2	mm ³
B_r @ RT	1.32	T
B_r @ CT	1.57	T

The mechanical design consists of a carriage with a metallic base where the frame is welded, two out-vacuum (external) girders fixed on the frame that can move vertically thanks to two series of sliders. The magnetic system components are fixed on two in-vacuum girders connected to the

* Synchrotron SOLEIL

[†] amin.ghaith@synchrotron-soleil.fr

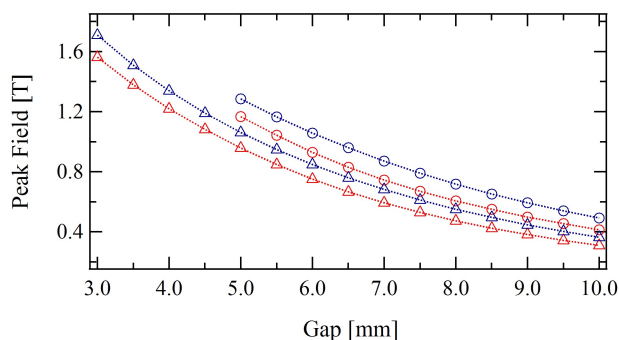


Figure 2: Peak field computed by RADIA versus magnetic gap. (blue) at cryogenic temperature, (red) room temperature, (o) U18, (Δ) U15.

external ones by 24 rods in U18 (Fig. 3-a) case and 36 rods in U15 (Fig. 3-b). The in-vacuum girders are separated by a gap to let the electron beam pass through the undulator. The gap variation is enabled by two steps motors Berger Lahr VRDM3910, and a third one to move vertically the undulator in order to align the magnetic axis in the vertical direction with the electron beam axis.

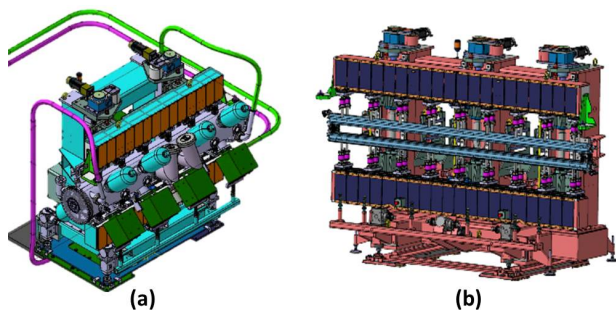


Figure 3: Mechanical design, (a) U18, (b) U15.

MAGNETIC MEASUREMENTS AND OPTIMIZATION

The brightness of the radiation emitted as the electrons traverse the undulator should be as intense as possible. Also the beam dynamics should not be disturbed especially in the case of a storage ring. The figures of merit during the assembly and corrections are the field integrals, the trajectory straightness, and the phase error. They have to be minimized to reduce the impact of the magnetic errors on the undulator performance in terms of photon spectrum and beam dynamics. The assembly and the magnetic corrections of the CPMU are performed at room temperature with a standard magnetic bench allowing Hall probe and flip coil measurements [6]. An optimization software called ID-Builder developed at SOLEIL [7] has been used at all steps of the undulator construction: magnets sorting, period assembly, shimming (vertical displacement of magnets and poles to correct the field integrals and the phase error), and multipole shim magnets also known as magic fingers (small magnets

installed at the extremities of the undulator to correct the field integrals). For U18 the phase error RMS was 12.5° after assembly and has been corrected (using shims) to reach 2.5° .

Figure 4 shows the optimization of the field integrals, which are proportional to the angle and trajectory of the electrons as they propagate through the undulator, using multipole trim magnets also known as magic fingers.

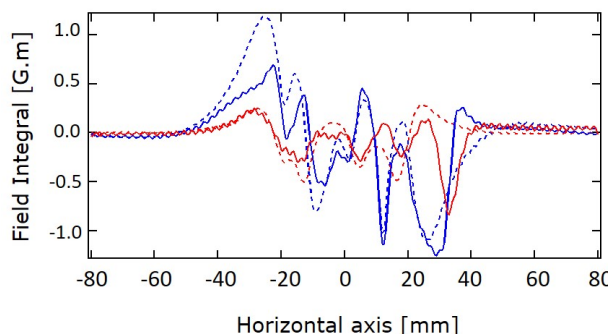


Figure 4: Field integrals across the transverse planes before and after applying the magic fingers. (blue) horizontal axis, (red) vertical axis, (dashed) before magic fingers, (line) after magic fingers.

SPECTRAL FLUX

The undulator radiation calculation is not completely straightforward in the case of COXINEL [8, 9] due to high energy spread leading to chromatic effects. One now takes into account the transmission of the line as in electron beam energy, charge, and their Twiss parameters inside the undulator. Thus a new approach has been done on simulating the spectrum radiation using SRWE code [10], in the case of 5% rms energy spread, by taking slices of the beam energy, get the spectrum of each slice and add them up.

Figure 5 shows the variation of the Twiss parameters versus electron energy, and Fig. 6 presents the result of the spectra computed using these values compared to an average case. The method has been also used for the broad energy case ($\sim 30\%$ energy spread rms), where it showed a very different spectrum compared to the average case.

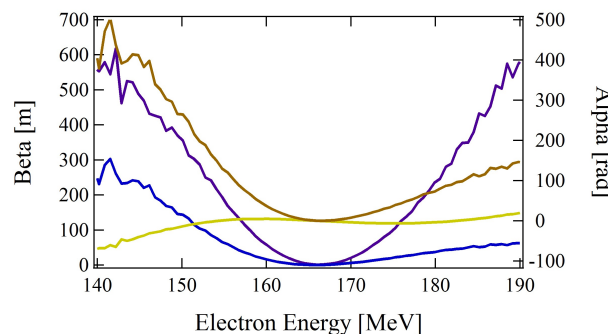


Figure 5: Twiss parameters for each energy slice. (Purple) horizontal beta, (Blue) vertical beta, (Yellow) horizontal alpha, (Brown) vertical alpha.

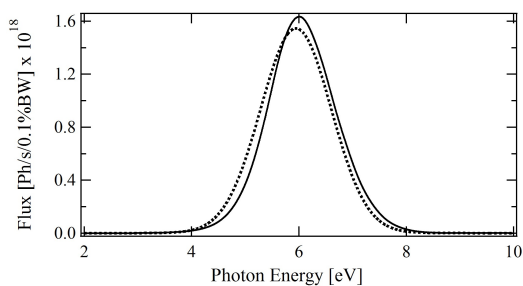


Figure 6: Spectral flux of the first harmonic. Gap = 5.5 mm, Peak field = 0.98 T. (...) average case taking into account an average value of the Twiss parameters and emittance, (—) slicing method taking into account the variation of the Twiss parameters and emittance for each energy slice.

INSTALLATION AND COMMISSION

U18 has been installed at COXINEL as shown in Fig. 7, it is operating at room temperature due to infrastructure reasons. A Coupled Charged Device (CCD) camera is installed 3 m after the undulator exit, and the transverse beam shape has been measured and showed good agreement with the simulated one, after 8 m of controlled transport line.

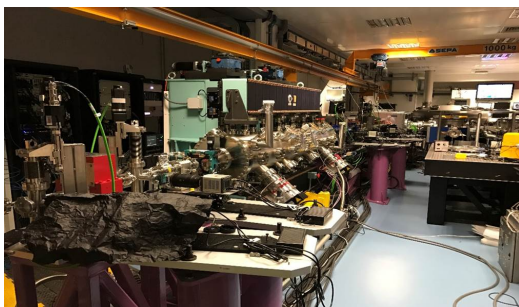


Figure 7: U18 undulator installed at LOA operating at room temperature. A CCD camera is installed downstream the undulator 3 m away.

CONCLUSION

A CPMU of period 18 mm has been successfully installed at COXINEL and synchrotron radiation were detected using a CCD camera installed 3 m away from the undulator. Another CPMU of period 15 mm is still under progress and its mechanical design allows for a minimum gap of 3 mm. An original method using SRWE has been developed to compute the spectrum for a broad energy spread case.

ACKNOWLEDGEMENT

The authors are very grateful to the European Research Council for the advanced grant COXINEL (340015). The authors also acknowledge the Laboratoire d'Optique Appliquée team led by V. Malka for the generation of the electron beam by laser plasma acceleration, and the Swedish-VR-French collaboration for U15 undulator development.

REFERENCES

- [1] K. Halbach, "Permanent magnet undulators", *J. Phys. Colloques*, no. 44, 1983.
- [2] K. E. Robinson *et al.*, "Hybrid undulator design considerations", *Nuclear Instruments and Methods A*, vol. 250, no. 1 pp. 100–109, 1986.
- [3] T. Hara *et al.*, "Cryogenic permanent magnet undulators", *Physical Review Special Topics – Accelerators and Beams* vol. 7, no. 5, 050702, 2004.
- [4] O. Chubar, P. Elleaume and J. Chavanne, "A three-dimensional magnetostatics computer code for insertion devices", *Journal of Synchrotron Radiation*, vol. 5, no. 3, pp. 481–484, 1998.
- [5] H. Hiroyoshi *et al.*, "High-field magnetization and crystalline field of r2fe14b and r2co14b," *Journal of Magnetism and Magnetic Materials*, vol. 70, no. 1-3, pp. 337–339, 1987.
- [6] C. Benabderrahmane *et al.*, "Development and operation of a Pr 2 Fe 14 B based cryogenic permanent magnet undulator for a high spatial resolution x-ray beam line." *Physical Review Accelerators and Beams* vol. 20, no. 3, 033201, 2017.
- [7] O. Chubar, O. Rudenko, C. Benabderrahmane, O. Marcouille, J. Filhol, and M. Couprie, "Application of genetic algorithms to sorting, swapping and shimming of the SOLEIL undulator magnets", *Proc. SRI'07* vol. 879, no. 1, pp. 359–362.
- [8] M.-E. Couprie, A. Loulergue, M. Labat, R. Lehe, and V. Malka, "Towards a free electron laser based on laser plasma accelerators," *Journal of Physics B: Atomic, Molecular and Optical Physics*, vol. 47, no. 23, p. 234001, 2014.
- [9] M. Couprie *et al.*, "An application of laser-plasma acceleration: towards a free-electron laser amplification," *Plasma Physics and Controlled Fusion*, vol. 58, no. 3, p. 034020, 2016.
- [10] O. Chubar and P. Elleaume, "Accurate And Efficient Computation Of Synchrotron Radiation In The Near Field Region", *Proc. EPAC'98*, pp. 1177–1179.

LIE MAP FORMALISM FOR FEL SIMULATION*

Kilean Hwang[†], Ji Qiang, Lawrence Berkeley National Laboratory, Berkeley, USA

Abstract

Undulator averaging and non-averaging are in compromise between computational speed and reliability. It is hard to catch the advantages of the both methods simultaneously. In this report, we present a method that compromises between the averaging and non-averaging methods through Lie map formalism.

INTRODUCTION

In a more general sense, the method of averaging can be viewed by an instance of the re-formulation of the equations of particle and field motion to a numerically or analytically simpler form. Performance of such methods are based on analytic capability of producing accurate but simple enough equations and corresponding solutions that can alternatively describe the original system. A simple averaging can overlook the coupling between the betatron and wiggling motion, nonlinear and high order field strength. This coupling can be important when the undulator fringe field at entrance is not well tapered so that the averaged closed orbit is offset by half of the undulator oscillation amplitude. On the other hand, if one can obtain re-formulated equations that can describe the original system to a good accuracy, then it can have both advantages of averaging and non-averaging method. Such a robust set of equations can be derived using perturbative Lie map. Since the map over undulator period integrate out the fast undulator oscillation, the numerical performance can be as good as the method of averaging.

OVERVIEW

To start with, we briefly review the perturbative Lie map method.

Lie Map Perturbation

Let the Hamiltonian be decomposed with slow S , fast F and radiation field potential V , i.e. $H(z) = S(z) + F(z) + V(z)$ where z is the longitudinal coordinate used as a time variable. Then, the map of the Hamiltonian system can be written by [1]

$$\mathcal{H}(z|z_0) = \mathcal{V}(z|z_0)\mathcal{F}(z|z_0)\mathcal{S}(z|z_0), \quad (1)$$

where z_0 is the starting location of the integrator, $\mathcal{S} \equiv e^{\mathcal{G}_S}$, $\mathcal{F} \equiv e^{\mathcal{G}_F}$, $\mathcal{V} \equiv e^{\mathcal{G}_V}$ are slow, fast, field map respectively,

and the generators of each map are

$$\begin{aligned} \mathcal{G}_S &= -\int_{z_0}^z dz : S : + \frac{1}{2} \int_{z_0}^z dz_1 \int_{z_0}^{z_1} dz_2 :: S_2 : S_1 : + \dots \\ \mathcal{G}_F &= -\int_{z_0}^z dz : F^{\text{int}} : + \frac{1}{2} \int_{z_0}^z dz_1 \int_{z_0}^{z_1} dz_2 :: F_2^{\text{int}} : F_1^{\text{int}} : + \dots \\ \mathcal{G}_V &= -\int_{z_0}^z dz : V^{\text{int}} : + \frac{1}{2} \int_{z_0}^z dz_1 \int_{z_0}^{z_1} dz_2 :: V_2^{\text{int}} : V_1^{\text{int}} : + \dots, \end{aligned} \quad (2)$$

where the interaction picture potentials are

$$\begin{aligned} F_i^{\text{int}} &\equiv \mathcal{S}(z_i|z_0)F(z_i) \\ V_i^{\text{int}} &\equiv \mathcal{F}(z_i|z_0)\mathcal{S}(z_i|z_0)V(z_i). \end{aligned} \quad (3)$$

Field Model

In order to calculate the field map \mathcal{G}_V for particle motion, one need to know the force field priori. Therefore, the method we are presenting involves field modeling and requires the field solver to solve for the model field. This is a generalization of the spectral method. Since, we expect narrow-band and slowly varying envelope radiation, we model the radiation vector potential normalized by e/mc as

$$a_r \equiv \Re \sum_{h=1}^5 [\mathbb{K}_h + (z - z_0) \partial_z \mathbb{K}_h] e^{ih(\theta - k_u z)}, \quad (4)$$

where $\theta = k_s(z - ct) + k_u z$ is the ponderomotive phase of radiation k_s and undulator k_u wave numbers. $\mathbb{K}_h(x, y, \theta)$ is the model field envelope at each integration step. Note that dependence of field amplitude on z is removed while the longitudinal gradient $\partial_z \mathbb{K}_h$ is included based on slowly varying envelope approximation. The gradient term and can be important for fast growth mode when the pre-unched beam is seeded [3], and thus can be beneficial for both averaging and non-averaging method. The order of magnitude of the normalized field strength is roughly about $\mathbb{K}_1 \sim 10^{-6}$ at saturation estimated using $P_{\text{rad}} \sim 1.6\rho P_{\text{beam}}$ and LCLS parameters [2].

Effective Hamiltonian

In general, the solution of the perturbed map \mathcal{V} is not available, so it is hard to build a high order map out of the perturbed Lie map. On the other hand, an effective Hamiltonian can be obtained using Baker-Campbell-Hausdorff (BCH) formula.

$$\begin{aligned} H_{\text{eff}} &= -\frac{1}{L} (\mathcal{G}_S + \mathcal{G}_F + \mathcal{G}_V) \\ &\quad -\frac{1}{2L} (: \mathcal{G}_S : \mathcal{G}_F + : \mathcal{G}_S : \mathcal{G}_V + : \mathcal{G}_F : \mathcal{G}_V) + \dots \end{aligned} \quad (5)$$

Since the fast oscillating motion is already integrated out, re-concatenation of the perturbed Lie map through BCH formula can be well truncated within few orders.

* Work supported by the Director of the Office of Science of the US Department of Energy under Contract no. DEAC02-05CH11231

[†] kilean@lbl.gov

SLOW MAP

The normalized Hamiltonian for a particle in planar undulator is

$$H(x, p_x, y, p_y, \theta, \gamma/k_s; z) \quad (6)$$

$$= -\sqrt{\gamma^2 - 1 - (p_x - a_x)^2 - (p_y - a_y)^2} + (k_u + k_s) \frac{\gamma}{k_s},$$

where γ is the normalized energy, and $a_{x,y} = eA_{x,y}/mc$ are normalized vector potentials. In a planar undulator the vector potentials are

$$a_x = K \cosh(k_x x) \cosh(k_y y) \cos(k_u z) + a_r$$

$$a_y = K \frac{k_x}{k_y} \sinh(k_x x) \sinh(k_y y) \cos(k_u z),$$

where K is the normalized undulator peak (not r.m.s.) strength and $k_u^2 = k_x^2 + k_y^2$. Here $\cos(k_u z)$ is used instead of $\sin(k_u z)$ assuming the undulator fringe field is tapered so that the averaged closed orbit is on-axis. We define the averaged Hamiltonian Eq. (6) as slow Hamiltonian,

$$S \equiv \frac{k_u}{k_s} \gamma + \frac{1}{2\gamma} \left[1 + p_x^2 + p_y^2 + \frac{K^2}{2} (1 + k_x^2 x^2 + k_y^2 y^2) \right]$$

$$+ \frac{K^2}{4\gamma} \left[\frac{1}{3} (k_x^4 x^4 + k_y^4 y^4) + k_x^2 k_u^2 x^2 y^2 \right]$$

$$+ \frac{1}{(2\gamma)^3} \left(1 + K^2 + \frac{3}{8} K^4 \right). \quad (7)$$

Note that γ^{-3} term is about same order of magnitude with the field potential when $\mathbb{K}_1 \sim O(10^{-6})$ and $\gamma \sim O(10^3)$. We truncated Hamiltonian at $O(10^{-12})$ assuming $k_x x, k_y y, p_x, p_y \sim O(10^{-2})$ and $\gamma \sim O(10^3)$. Since the slow Hamiltonian is autonomous, the Lie map generator is simply

$$\mathcal{G}_S(L) = -SL. \quad (8)$$

FAST MAP

We define the fast Hamiltonian by non-averaged part of the Hamiltonian independent of the radiation field, i.e., $F \equiv [H - S]_{\mathbb{K}_h=0}$. After integrations, the generator of the fast map become

$$\mathcal{G}_F = -L \frac{K^3 k_x^2}{k_u^2 \gamma^3} \left(\frac{K}{16} - \frac{p_x}{3} \right) \quad (9)$$

where we assumed the initial location z_0 and step size L are multiple of undulator period and included 3rd order of Magnus series not shown in Eq. (2). Although, it is as small as γ^{-3} , it is about same order of magnitude with radiation field potential when $\mathbb{K}_1 \sim O(10^{-6})$ and $\gamma \sim O(10^3)$.

FIELD MAP

The interaction picture potential of the radiation field for each harmonic h is

$$V^{\text{int}} = - \left(\frac{K_{\text{eff}}}{\gamma} \cos(k_u z) + \frac{p_x}{\gamma} \right) K_h^{\text{int}} \sum_{l,m}^{[-\infty, \infty]} J_l^{h\xi} J_m^{h\xi} e^{ih\psi_s^{\text{int}}}$$

$$\psi_s^{\text{int}} \equiv h\theta + h\dot{\theta}\delta z - (2l + m + h) k_u z$$

$$K_h^{\text{int}} = \mathbb{K}_h + \left(\frac{K_{\text{eff}}}{k_u \gamma} \sin(k_u z) + \frac{p_x}{\gamma} \delta z \right) \frac{\partial \mathbb{K}_h}{\partial x}$$

$$+ \frac{p_y}{\gamma} \delta z \frac{\partial \mathbb{K}_h}{\partial y} + \delta z \partial_z \mathbb{K}_h, \quad (10)$$

where J_n^a is the Bessel function of order n with argument a , $\delta z \equiv z - z_0$, and

$$\dot{\theta} \equiv k_u - \frac{k_s}{2\gamma^2} \left(1 + p_x^2 + p_y^2 + \frac{K_{\text{eff}}^2}{2} \right)$$

$$K_{\text{eff}} \equiv K \left(1 + k_x^2 \frac{x^2}{2} + k_y^2 \frac{y^2}{2} \right).$$

Then, the Lie map generator can be written by the following form

$$\mathcal{G}_V = L \left(\frac{K_{\text{eff}}}{\gamma} \int_C + \frac{p_x}{\gamma} \int_0 \right) \mathbb{K}_h e^{ih\theta}$$

$$+ L \left[\frac{K_{\text{eff}}^2}{k_u \gamma^2} \int_{SC} + \frac{K_{\text{eff}} p_x}{\gamma} \int_{1C} + \frac{1}{k_u} \int_S \right] \partial_x \mathbb{K}_h e^{ih\theta}$$

$$+ L \frac{K_{\text{eff}}}{\gamma} \int_{1C} \left(\frac{p_y}{\gamma} \partial_y \mathbb{K}_h + \partial_z \mathbb{K}_h \right) e^{ih\theta}, \quad (11)$$

where \int_i are integration parameters. Due to limited space in this paper, we write down few terms of the leading order integration parameter,

$$\int_C \equiv \frac{e^{-ih\theta}}{L} \int_0^L d(\delta z) \cos \psi_u e^{ih\psi_s^{\text{int}}}$$

$$= \frac{1}{2} \left(J_{-\frac{h+1}{2}}^{h\xi} + J_{\frac{1-h}{2}}^{h\xi} \right) + \frac{h\dot{\theta}}{4k_u} \left(J_{-\frac{h+1}{2}}^{h\xi} - J_{\frac{1-h}{2}}^{h\xi} \right)$$

$$+ \sum_{l \neq -\frac{h+1}{2}, \frac{1-h}{2}} \frac{h\dot{\theta}}{k_u} \frac{(2l+h) J_l^{h\xi R}}{(2l+h+1)(2l+h-1)}$$

$$+ \dots \quad (12)$$

The first term is so-called coupling factor. Although $\dot{\theta}/k_u$ is small due to resonance condition, it is as important as the coupling factor contribution on $d\theta/dz$ as can be seen from Eq. (13)

$$-\frac{\partial \mathcal{G}_V}{\partial \gamma} \propto \frac{1}{2\gamma^2} \left(J_{-\frac{h+1}{2}}^{h\xi} + J_{\frac{1-h}{2}}^{h\xi} \right) - \frac{hk_s}{4\gamma^4 k_u} \left(J_{-\frac{h+1}{2}}^{h\xi} - J_{\frac{1-h}{2}}^{h\xi} \right) + \dots \quad (13)$$

COMPARISON

Here, we present comparison between our method and and GENESIS pusher [4]. We take the particle tracking using

original Hamiltonian Eq. (6) with small enough time step to represent exact solution. In order to compare the particle pusher independent of the field solver, the radiation field is modeled by transversely Gaussian envelope of rms size same with the electron beam. Undulator parameters used are $K = 1.5$, $k_x = k_y = k_u/\sqrt{2}$, $\lambda_u = 2.5$ cm. We prepare initially matched Gaussian electron beam truncated at 3σ with normalized emittance $1\mu\text{m}$ and $\sigma_\gamma/\gamma = 0.01$. In order to quantify the error, we use $|\theta - \theta_{\text{exact}}|/2\pi$ and record the error for each particles. Integration step size is chosen by one undulator period at which the numerical error due to large step size showed convergence. In other words, the error shown in figures originates from the inaccuracy of the re-formulated equations by averaging or Lie map method. Figure 1 shows the error in the absence of the radiation field showing an order of magnitude better accuracy. Figure 2 shows the error under radiation field whose normalized strength is $\mathbb{K} = 10^{-6}$ which corresponds to the field strength near saturation in case of LCLS. Figure 3 shows the error under exponentially growing radiation field with growth rate $L_G \sim 10^2 \lambda_u$ and initial strength $\mathbb{K} = 10^{-8}$. Inclusion longitudinal field gradient in Eq. (10), made the accuracy as good as the zero radiation case of Fig. 1. This can be especially important when much shorter gain length $< 10^2 \lambda_u$ is achieved.

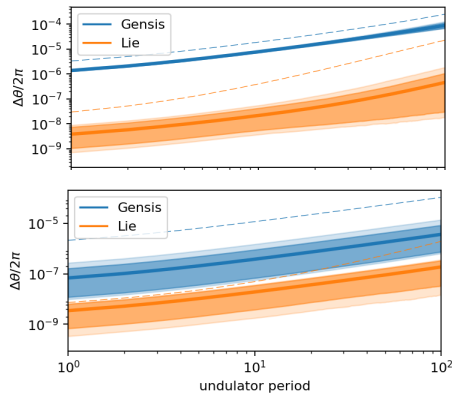


Figure 1: Ponderomotive phase error in the absence of the radiation field. Top and bottom corresponds to $\gamma = 10^3$ and $\gamma = 10^4$ respectively. Thick line represent the average, shadowed area corresponds to the error of 90% and 95% population for lighter and darker shade. The dashed line corresponds to the maximum error.

CONCLUSION

A compromised method between averaging and non-averaging method is presented and tested. More robust equations of motion than undulator averaging is derived using perturbative Lie map. Simulation result shows good improvement on the accuracy while the computation time was only about 1.3 times of the method of averaging. In order to build a Lie map, we had to model the radiation field. The modeled field ansatz is what we need to solve in field solver which is our next research plan.

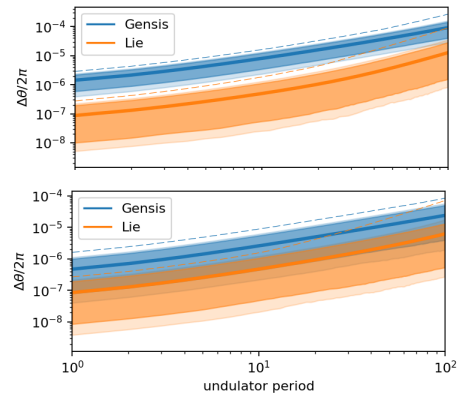


Figure 2: Ponderomotive phase error at radiation field strength $\mathbb{K} = 10^{-6}$. Top and bottom corresponds to $\gamma = 10^3$ and $\gamma = 10^4$ respectively.

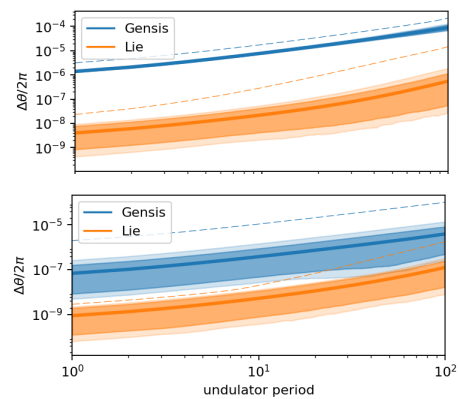


Figure 3: Ponderomotive phase error at initial radiation field strength $\mathbb{K} = 10^{-8}$ and exponentially growing by rate $L_G \sim 10^2 \lambda_u$. Top and bottom corresponds to $\gamma = 10^3$ and $\gamma = 10^4$ respectively.

ACKNOWLEDGEMENT

We appreciate valuable discussion with Gregory Penn. This work is supported by the Director of the Office of Science of the US Department of Energy under Contract no. DEAC02-05CH11231

REFERENCE

- [1] A. Dragt, "Lie Methods for Nonlinear Dynamics", <http://www.physics.umd.edu/dsat>
- [2] https://portal.slac.stanford.edu/sites/lclscore_public/Accelerator_Physics_Published_Documents/LCLS-parameters-3-22-17.pdf
- [3] L. H. Yu., "Generation of intense uv radiation by subharmonically seeded single-pass free-electron lasers", *Phys. Rev. A*, vol. 44, p. 5178–5193, 1991.
- [4] S. Reiche, "GENESIS 1.3: A fully 3D time-dependent FEL simulation code", *Nucl. Instrum. Methods Phys. Res., Sect. A*, vol. 429, p. 243, 1999.

SIMULATIONS OF THE DEPENDENCE OF HARMONIC RADIATION ON UNDULATOR PARAMETERS*

G. Penn[†], LBNL, Berkeley, CA 94720, USA

Abstract

The flux and bandwidth of radiation produced at harmonics of the fundamental are very sensitive to the undulator parameter, and thus the beam energy or undulator period. We look at high-energy XFELs with parameters relevant to the MaRIE FEL design. Both SASE and seeded FELs are considered.

INTRODUCTION

One method to extend the photon energy reach of free electron lasers (FELs) is to radiate at harmonics of the resonant wavelength. There are two main versions of this technique. Nonlinear harmonic gain [1, 2] occurs as the fundamental radiation enters saturation; the microbunching becomes sufficiently strong to include a significant component at harmonics of the fundamental. This is most prominent for planar FELs, which can couple to the microbunching at odd harmonics to produce strong, forward-directed radiation. There is also linear harmonic gain, where radiation at wavelengths shorter than resonance self-amplifies. In this case the amplification process almost requires a planar undulator and use of an odd harmonic. Strong radiation at the fundamental wavelength tends to interfere with linear harmonic gain, but there are methods to overcome this [3] and, for an FEL seeded at a harmonic, that harmonic can reach saturation well before the fundamental.

Linear harmonic gain can reach much higher power than nonlinear harmonic gain. However, it imposes greater demands on the electron beam and other systems. This paper will mostly focus on nonlinear harmonics.

IMPORTANCE OF THE UNDULATOR PARAMETER

For nonlinear harmonic generation in a planar undulator, ignoring transverse effects such as the angular and energy spread of the electrons, the ratio of the third harmonic radiation to the fundamental near saturation has been calculated as [2]:

$$\frac{P_3}{P_1} \approx 0.094 \frac{J_1(3\xi) - J_2(3\xi)}{J_0(\xi) - J_1(\xi)}, \quad (1)$$

where the J_i are Bessel functions, $\xi \equiv 0.5 a_u^2 / (1 + a_u^2)$, and a_u is the rms undulator parameter. For undulator parameters close to unity, there is a strong improvement in this ratio as a_u is increased. As the undulator parameters becomes $\gg 1$, the ideal ratio saturates close to 2.1%. The power of the fundamental also improves with the undulator parameter,

but the term defined above varies more rapidly. The scaling with undulator parameter is shown in Fig. 1.

This effect is multiplied by the “3D” effects corresponding to beam emittance and energy spread. The third harmonic can only tolerate roughly 1/3rd of the energy spread or emittance, and so it can be strongly suppressed by changes which only slightly affect the fundamental.

For undulators tuned to a fundamental photon energy of 14 keV, the undulator parameter $a_u \geq 2$, and the harmonic is not sensitive to small changes in the undulator parameter.

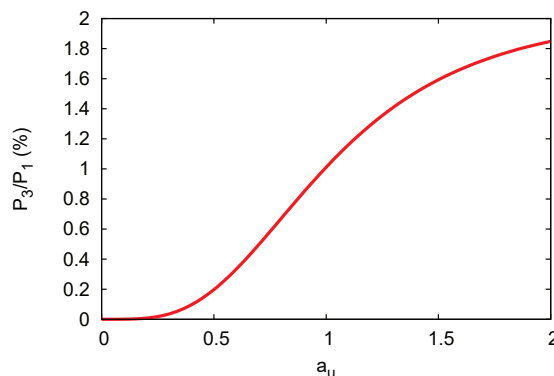


Figure 1: Scaling of the ratio of nonlinear third harmonic to fundamental radiation near saturation, for ideal beams.

BEAM PARAMETERS AND CONFIGURATION

The beamline parameters are modeled loosely after those of the MaRIE X-FEL [4] as summarized in Table 1. A self-seeding stage uses undulators tuned to 14 keV to produce not only strong SASE radiation at the fundamental but also a significant 3rd harmonic component. This harmonic component is then put through a monochromator. At this point, there can be a fresh-slice [5] or multi-bunch stage to allow for unperturbed electrons to interact with the narrow-bandwidth 40-keV radiation. This radiation is then amplified and can be used to produce third harmonic radiation in turn.

The undulator sections used for the final stage are taken to each be 3.6 m in length. Breaks in between sections are either 0.9 m or 1.26 m in length. Undulator periods in the range of 15 mm to 20 mm have been considered, corresponding to undulator parameters of 1.10 to 0.81. The corresponding ideal ratio P_3/P_1 ranges from 1.16% to 0.69%. Superconducting undulators with a 15-mm period are consistent with a beam pipe diameter of roughly 9 mm, if a large tuning range is not required. PPM undulators with an 18-mm period are consistent with a beam pipe diameter of roughly 5 mm. Advanced designs such as superconducting

* This work was supported by the Director, Office of Science, Office of Basic Energy Sciences, U.S. Department of Energy under Contract No. DE-AC02-05CH11231.

[†] gepenn@lbl.gov

or in-vacuum undulators would be helpful in improving the performance, allowing for more beam clearance, and reducing wake fields.

Table 1: Beam Parameters

Energy	12 GeV
Energy spread	1.2 MeV
Peak current	3 kA
Emittance	0.2 μm
Beta function	15 m
Radiation wavelength	0.01, 0.03, 0.09 nm
Undulator period	15 — 20 mm
Undulator section	3.6 m

SIMULATION RESULTS

The self-seeding stage to yield 40-keV photons is not simulated; instead, the beam is assumed to be unperturbed, possibly using the fresh-slice or multi-bunch technique, and the radiation is taken to be monochromatic with a peak power of 100 kW. The precise value of this power is mostly important in determining the length of the amplification stage, although for realistic beams the bandwidth will tend to grow as variations in the slice energy lead to phase shifts. The seeded power must also be well above noise levels. From there, nonlinear harmonic generation of the third harmonic is simulated using the GENESIS simulation code [6].

Although linear amplification of the 40-keV photons in undulators tuned to 14 keV is a possibility, the gain length using this method is close to and slightly longer than the gain length for undulators tuned to a fundamental of 40 keV. Furthermore, the saturated power is significantly lower. As there is no advantage to using this scheme, results for this case are not shown. For different electron beam parameters the ratio of gain lengths could be more promising. Similarly, linear amplification of the third harmonic in undulators tuned to 40 keV is suppressed by the beam emittance and energy spread. Thus, the focus is on direct amplification of 40 keV radiation, and the production of 120-keV photons by nonlinear harmonic generation.

The undulator strength was not tapered from section to section, which could improve performance. However, the average energy loss due to incoherent synchrotron radiation was removed, which has the effect of a fixed linear undulator taper.

The results are shown in Figs. 2 and 3 for the power radiated at the 40-keV fundamental and the third harmonic, respectively. For the fundamental, there is a modest improvement in power near saturation both as the undulator period is made shorter and as the breaks between undulator sections are made shorter. The third harmonic shows almost an order of magnitude improvement with shorter undulator period (and thus larger undulator parameter), while the impact of reducing the break between undulators is mostly to reduce the distance required to reach saturation. The third harmonic

continues to grow past saturation, even without undulator taper. The impact of tapering should be explored.

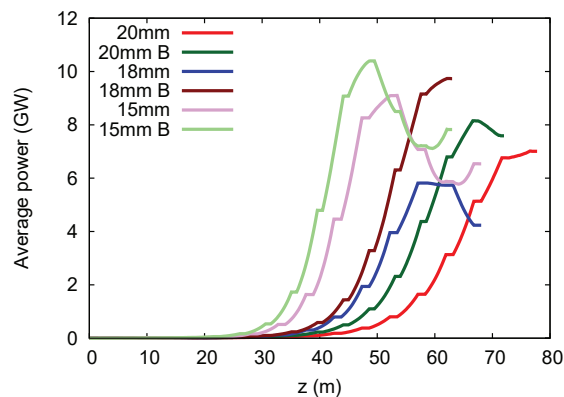


Figure 2: Radiation at the fundamental tuned to 40 keV starting with a seed having peak power of 100 kW, for various undulator choices. Curves marked with a “B” have a smaller break between undulator sections.

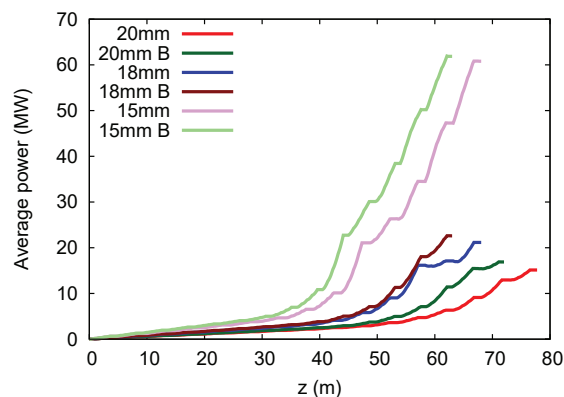


Figure 3: Radiation at the third harmonic for undulators tuned to a fundamental of 40 keV, starting with a seed having peak power of 100 kW, for various undulator choices. Curves marked with a “B” have a smaller break between undulator sections.

The radiated power at the third harmonic is mostly produced in the final undulators after the fundamental has reached saturation. Thus, it should be possible initially to use longer period undulators, and only switch to shorter period undulators near the end of the undulator line. In Fig. 4, the power at the third harmonic is shown for the case of larger breaks between undulators, where the initial undulator period is 18 mm and is then switched to undulators with a 15-mm period after either 49 m or 58 m. The cases of uniform undulator lines with periods of 15, 18, or 20 mm are shown for comparison. By changing over after 49 m, the power produced after 80 m almost matches that of the case where all undulators have a 15-mm period. Waiting until after 58 m to switch undulators yields a final power that is roughly in the middle of the output from undulators that are all 15-mm or all 18-mm period.

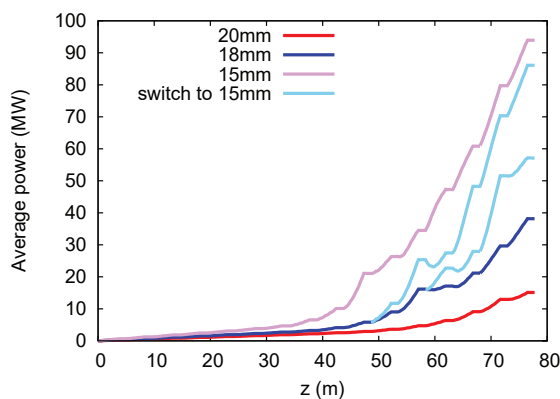


Figure 4: Radiation at the third harmonic for undulators tuned to a fundamental of 40 keV, ending around 80 m after the self-seeding monochromator. Various undulator periods are considered, including switching from 18-mm to 15-mm period for the final sections.

CONCLUSION

For generating harmonics through nonlinear harmonic gain, the undulator parameter is an important quantity to optimize. Besides changing the undulator period, the undulator parameter can be increased by going to higher electron energy. For example, changing the beam energy to 14 GeV will raise the resonant a_u for an 18-mm period undulator from 0.92 to 1.23. The “fill fraction”, or percentage of the undulator line that is taken up by active undulators instead of drift sections, does not seem to have as strong an effect, although the fill fraction was only varied from 74% to 80%.

Another important impact on radiation at harmonics is the electron beam energy spread. A fresh-slice or fresh-bunch stage before reaching saturation of the fundamental could increase the final power radiated at the third harmonic. If

the fresh-slice technique is used for the self-seeding, and the unperturbed part of the bunch could be made twice as long as the initial radiating part, a simple delay line could move the seeded portion of the radiation to a reasonably unperturbed part of the bunch. To maintain good spectral quality, microbunching and wake fields need to be minimized. The use of energy spread heating to control microbunching will be limited by tight tolerances on the energy spread to allow for good coupling to the third harmonic.

REFERENCES

- [1] R. Bonifacio, L. De Salvo and P. Pierini, “Large harmonic bunching in a high-gain free-electron laser,” *Nucl. Instr. Meth. A*, 293:627–629, 1990. doi:10.1016/0168-9002(90)90334-3.
- [2] E.L. Saldin, E.A. Schneidmiller and M.V. Yurkov, “Properties of the third harmonic of the radiation from self-amplified spontaneous emission free electron laser,” *Phys. Rev. ST Accel. Beams*, 9:030702, 2006. doi: 10.1103/PhysRevSTAB.9.030702.
- [3] E.A. Schneidmiller and M.V. Yurkov, “Harmonic lasing in x-ray free electron lasers,” *Phys. Rev. ST Accel. Beams*, 15:080702, 2012. doi: 10.1103/PhysRevSTAB.15.080702.
- [4] J.W. Lewellen, K.A. Bishofberger, B.E. Carlsten, *et al.*, “Status of the MaRIE X-FEL accelerator design,” in *Proc. 6th Int. Particle Accelerator Conf.*, Richmond, VA, USA, 2015. TUPMA026.
- [5] A.A. Lutman, T.J. Maxwell, J.P. MacArthur, M.W. Guetg *et al.*, “Fresh-slice multicolour X-ray free-electron lasers,” *Nature Photonics*, 10:745–750, 2016. doi:10.1038/NPHOTON.2016.201.
- [6] S. Reiche, “GENESIS 1.3: a fully 3D time-dependent FEL simulation code,” *Nucl. Instr. Meth. A*, 429:243–248, 1999. doi:10.1016/S0168-9002(99)00114-X.

PERIOD-AVERAGED SYMPLECTIC MAPS FOR THE FEL HAMILTONIAN*

S. D. Webb[†], RadiaSoft, LLC, Boulder, USA

Abstract

Conventional treatments of synchrotron radiation in electron beams treat the radiation as a non-Hamiltonian aspect to the beam dynamics. However, the radiation can be modeled with an electromagnetic Hamiltonian. We present a period-averaged treatment of the FEL problem which includes the Hamiltonian aspects of the coupled electron-radiation dynamics. This approach is then applied to two problems: a 3D split-operator symplectic integrator, and a 1D single-mode FEL treated using Hamiltonian perturbation theory.

SYMPLECTIC MAP TREATMENT

Symplectic maps are useful for computing invariants in Hamiltonian systems and deriving symplectic integration schemes (among others) in single- or few-particle systems. Recent work has highlighted their use for studying many-body systems and self-consistent electromagnetic algorithms. Maps can also be applied to the period-averaged free-electron laser problem, using the factored map formalism and a first order Magnus expansion.

We begin with the Lagrangian for a system of relativistic electrons in a mix of external and self-consistent electromagnetic fields [1–3]:

$$\mathcal{L} = \sum_j -mc^2 \sqrt{1 - \left(\frac{\dot{\mathbf{x}}_j}{c}\right)^2} - e\phi(\mathbf{x}_j) + \frac{e}{c} \dot{\mathbf{x}}_j \cdot \mathbf{A}(\mathbf{x}_j) + \frac{1}{8\pi} \int d\mathbf{x} \left(\frac{1}{c} \frac{\partial \mathbf{A}}{\partial t} - \nabla \phi \right)^2 - (\nabla \times \mathbf{A})^2. \quad (1)$$

It is convenient to use s , the longitudinal variable, as the independent variable. We can do this by noting that the action integral $\mathcal{A} = \int dt \mathcal{L}$, and that $dt = (dt/ds)ds$ is a valid transformation of the integral as long as $ds/dt \neq 0$. This allows us to change the independent variable to the s -dependent Lagrangian \mathcal{S} as

$$\mathcal{S} = \sum_j -mc^2 \sqrt{\left(\frac{1}{c} \frac{d\tau_j}{ds}\right)^2 - \left(\frac{(\mathbf{x}_\perp)_j'}{c}\right)^2} + \frac{e}{c} \tau_j' \phi(\mathbf{x}_j) + \frac{e}{c} (\mathbf{x}_j')_\perp \cdot \mathbf{A}_\perp(\mathbf{x}_j) + \frac{e}{c} A_s(\mathbf{x}_j) - \frac{1}{8\pi c} \int d\mathbf{x}_\perp d\tau \left(\frac{\partial \mathbf{A}}{\partial \tau} + \nabla \phi \right)^2 - (\nabla \times \mathbf{A})^2 \quad (2)$$

* Work supported by the United State Department of Energy, Office of Scientific Research, under SBIR contract number DE-SC0017161.

[†] swebb@radiasoft.net

where the prime denotes total differentiation with respect to s and we have defined $\tau = -ct$ for dimensional convenience, so all the generalized coordinates have the same units. The action integral remains unchanged.

The scalar potential comes purely from self-consistent source terms – there are no electrostatic elements in our beamline – and \mathbf{A} can be broken into external and self-consistent components. We need not worry about the dynamics of the external vector potentials. For simplicity, we can make the choice that $A_s^{(sc)} = 0$ (equivalent to the Weyl gauge $\phi = 0$ when we use t as the independent variable) and assume that $\phi = 0$ which neglects space charge effects. This leaves $\mathbf{A}_\perp = \mathbf{A}_\perp^{(ext.)} + \mathbf{A}_r$ and $A_s = A_s^{(ext.)}$, which captures the undulator fields and any external focusing elements like quadrupoles or dipoles, as well as the self-consistent radiation field.

We write the radiation field as

$$\mathbf{A}_r = \frac{mc}{e} \mathbf{e}_p \sum_\sigma u_\sigma e^{ik_\perp^{(\sigma)} \cdot \mathbf{x}_\perp + ik_0^{(\sigma)} \tau} + c.c. \quad (3)$$

for a fixed, generally complex, polarization vector $\mathbf{e}_p = p_x \hat{\mathbf{x}} + p_y \hat{\mathbf{y}}$ with unit norm $|p_x|^2 + |p_y|^2 = 1$, and a range of perpendicular k -vectors and τ -components. The individual $u_\sigma(s)$ give the complex amplitude of a given radiation mode as a function of s . This gives the Lagrangian in terms of the individual mode amplitudes for the radiation, the external fields, and the particles to be:

$$\mathcal{S} = \sum_j -mc \sqrt{(\tau_j')^2 - ((\mathbf{x}'_\perp)_j)^2} + \frac{e}{c} (\mathbf{x}'_\perp)_j \cdot (\mathbf{A}_\perp^{(ext.)}(\mathbf{x}_j) + \mathbf{A}_r) + \frac{e}{c} A_s(\mathbf{x}_j) - \frac{1}{8\pi c} \left(\frac{mc}{e}\right)^2 \sum_\sigma \left((k_0^{(\sigma)})^2 - |p_y k_x^{(\sigma)} - p_x k_y^{(\sigma)}|^2 \right) |u_\sigma|^2 - |u_\sigma'|^2 \quad (4)$$

which then gives the canonical momenta for the electrons as well as for the individual modes as:

$$p_\tau = \frac{mc\tau'}{\sqrt{\tau'^2 - 1 - (\mathbf{x}'_\perp)^2}}, \quad (5)$$

$$\mathbf{p}_\perp = \frac{mc\mathbf{x}'_\perp}{\sqrt{\tau'^2 - 1 - (\mathbf{x}'_\perp)^2}} - \frac{e}{c} (\mathbf{A}_\perp^{(ext.)}(\mathbf{x}_j) + \mathbf{A}_r)$$

and

$$\mathcal{P}_\sigma = -\frac{1}{4\pi c} \left(\frac{mc}{e}\right)^2 u_\sigma'^* \quad (6)$$

for each individual particle and mode.

To compute symplectic maps, we must compute the Hamiltonian for this system, which is taken through the usual Legendre transformation over the j particle indices and the σ mode indices. The resulting Hamiltonian is given by:

$$\begin{aligned} \mathcal{H} = & - \sum_j \sqrt{\left(p_\tau^{(j)}\right)^2 - \left(\mathbf{p}_\perp^{(j)} - \frac{e}{c}(\mathbf{A}_\perp^{(ext.)}(\mathbf{x}_j) + \mathbf{A}_r)\right)^2} - m^2 c^2 \\ & + \frac{e}{c} A_s(\mathbf{x}_j) + \sum_\sigma \frac{1}{2} \frac{4\pi}{c} \left(\frac{e}{mc}\right)^2 |\mathcal{P}_\sigma|^2 \\ & + \frac{1}{2} \frac{c}{4\pi} \left(\frac{mc}{e}\right)^2 \left((k_0^{(\sigma)})^2 - |p_y k_x^{(\sigma)} - p_x k_y^{(\sigma)}|^2 \right) |u_\sigma|^2. \end{aligned} \quad (7)$$

Assuming that p_τ is the dominant momentum component, which it usually is, we can Taylor expand the radical in powers of $1/p_\tau$ to get the approximate Hamiltonian for high energy electrons:

$$\begin{aligned} \mathcal{H} \approx & \sum_j -p_\tau^{(j)} + \frac{1}{2} \frac{m^2 c^2}{p_\tau^{(j)}} + \frac{1}{2} \frac{\left(\mathbf{p}_\perp^{(j)} - \frac{e}{c}(\mathbf{A}_\perp^{(ext.)}(\mathbf{x}_j) + \mathbf{A}_r)\right)^2}{p_\tau^{(j)}} + \\ & \frac{e}{c} A_s + \sum_\sigma \frac{1}{2} \frac{4\pi}{c} \left(\frac{e}{mc}\right)^2 |\mathcal{P}_\sigma|^2 + \frac{1}{2} \frac{c}{4\pi} \left(\frac{mc}{e}\right)^2 \Omega_\sigma^2 |u_\sigma|^2, \end{aligned} \quad (8)$$

with $\Omega_\sigma^2 = (k_0^{(\sigma)})^2 - |p_y k_x^{(\sigma)} - p_x k_y^{(\sigma)}|^2$ being the natural frequency of the σ mode.

We can then break up $\mathbf{A}_\perp^{(ext.)}$ into the on-axis wiggler field and the off-axis wiggler field as

$$\mathbf{A}_\perp^{(ext.)} = \mathbf{A}_w(s) + \mathbf{A}_f(x, y, s), \quad (9)$$

which allows us to expand the perpendicular momentum term and break the Hamiltonian into the sum of the one-dimensional FEL Hamiltonian and the transverse focusing Hamiltonian.

The transverse canonical momentum term expands to

$$\begin{aligned} \left(\mathbf{p}_\perp - \frac{e}{c}(\mathbf{A}_w + \mathbf{A}_f + \mathbf{A}_r)\right)^2 = & \left(\mathbf{p}_\perp - \frac{e}{c}\mathbf{A}_f\right)^2 + \\ & \left(\mathbf{p}_\perp - \frac{e}{c}\mathbf{A}_f\right) \cdot (\mathbf{A}_w + \mathbf{A}_r) + \\ & |\mathbf{A}_w|^2 + 2\mathbf{A}_w \cdot \mathbf{A}_r + |\mathbf{A}_r|^2. \end{aligned} \quad (10)$$

The first term represents the finite transverse emittance dynamics and the undulator focusing terms. The second term is the dot product of the average transverse velocity with the undulator and radiation fields, and averages to zero. $|\mathbf{A}_r|^2$ will introduce the ponderomotive force on the average transverse particle motion, and this is also negligible.

Dropping these negligible terms leaves the FEL Hamiltonian as

$$\begin{aligned} \mathcal{H} \approx & \sum_j -p_\tau^{(j)} + \frac{1}{2} \frac{m^2 c^2}{p_\tau^{(j)}} + \\ & \frac{1}{2} \frac{\left(\mathbf{p}_\perp^{(j)} - \frac{e}{c}\mathbf{A}_f\right)^2 + (e/c)^2 |\mathbf{A}_w|^2 + 2(e/c)^2 \mathbf{A}_w \cdot \mathbf{A}_r}{p_\tau^{(j)}} + \\ & \frac{e}{c} A_s + \sum_\sigma \frac{1}{2} \frac{4\pi}{c} \left(\frac{e}{mc}\right)^2 |\mathcal{P}_\sigma|^2 + \frac{1}{2} \frac{c}{4\pi} \left(\frac{mc}{e}\right)^2 \Omega_\sigma^2 |u_\sigma|^2. \end{aligned} \quad (11)$$

This is the Hamiltonian for relativistic particles in a radiation field and an undulator, with potential external focusing forces. At this point, more approximations are possible, such as linearizing $p_\tau^{(j)} = -\gamma_0 mc - \delta^{(j)}$ with $\delta \ll \gamma_0 mc$. We can also break the Hamiltonian up, for formal convenience, into \mathcal{H}_0 , \mathcal{H}_\perp and \mathcal{V}_I for the electromagnetic, longitudinal, and transverse dynamics, respectively:

$$\begin{aligned} \mathcal{H}_0 = & \sum_j -p_\tau^{(j)} + \frac{1}{2} \frac{m^2 c^2}{p_\tau^{(j)}} + \frac{1}{2} \left(\frac{e}{c}\right)^2 \frac{|\mathbf{A}_w|^2}{p_\tau^{(j)}} + \\ & \sum_\sigma \frac{1}{2} \frac{4\pi}{c} \left(\frac{e}{mc}\right)^2 |\mathcal{P}_\sigma|^2 + \frac{1}{2} \frac{c}{4\pi} \left(\frac{mc}{e}\right)^2 \Omega_\sigma^2 |u_\sigma|^2, \\ \mathcal{H}_\perp = & \frac{1}{2} \sum_j \frac{\left(\mathbf{p}_\perp^{(j)} - \frac{e}{c}\mathbf{A}_f\right)^2}{p_\tau^{(j)}} + \frac{e}{c} A_s, \\ \text{and} \\ \mathcal{V}_I = & 2 \left(\frac{e}{c}\right)^2 \frac{\mathbf{A}_w \cdot \mathbf{A}_r}{p_\tau^{(j)}}. \end{aligned} \quad (12)$$

The combination $\mathcal{H}_0 + \mathcal{V}_I$, if we assume $\mathbf{k}_\perp^{(\sigma)} = 0$, is the one-dimensional FEL Hamiltonian. \mathcal{H}_\perp captures the transverse dynamics, assuming as we have that there is no space charge – if we were to include space charge in this treatment there would be a self-consistent A_s or ϕ and these would also contribute to the transverse and longitudinal dynamics.

We are now in a position to compute symplectic maps over a single wiggler period, $\mathcal{M}_{s \rightarrow s+l_w}$.

The symplectic map satisfies the operator differential equation

$$\mathcal{M}' = \mathcal{M} : -\mathcal{H} : \quad (13)$$

where $:-\mathcal{H}:$ is the Hamiltonian Lie operator [4–6], which generates s transformations on the particle-field coupled phase space. There are multiple applications to this map: (1) we can compute a map for the one-dimensional FEL problem that includes the field terms; (2) we can derive symplectic integrators for the 1D and 3D FEL Hamiltonians, especially for tapering and other more schemes; (3) we can compute invariants for the 1D (and, less likely, but possibly) the 3D FEL Hamiltonians.

For the 1D FEL problem, we have that

$$\mathcal{M}'_{1D} = \mathcal{M}_{1D} : -\mathcal{H}_0 - \mathcal{V}_I : \quad (14)$$

where \mathcal{H}_0 is exactly integrable – it is the radiation modes as harmonic oscillators with mass $m\sqrt{c}/4\pi e$ and frequency Ω_σ and motion in a drift where $|\mathbf{A}_w|^2$ may have some s -dependence for a planar undulator, for example.

Using the factored map formalism, we can write $\mathcal{M}_{1D} = \mathcal{M}_{1D}^{(I)} \mathcal{M}_{1D}^{(0)}$, where

$$(\mathcal{M}_{1D}^{(0)})' = \mathcal{M}_{1D}^{(0)} : -\mathcal{H}_0 : \quad (15)$$

and

$$(\mathcal{M}_{1D}^{(I)})' = \mathcal{M}_{1D}^{(I)} \left(\mathcal{M}_{1D}^{(0)} : -\mathcal{V}_I : (\mathcal{M}_{1D}^{(0)})^{-1} \right). \quad (16)$$

The transformation of \mathcal{V}_I integrates along the unperturbed trajectory, as the similarity transformation on the Lie operator passes through the colons and gives that

$$\mathcal{M}_{1D}^{(0)} : -\mathcal{V}_I : (\mathcal{M}_{1D}^{(0)})^{-1} = : -\mathcal{M}_{1D}^{(0)} \mathcal{V}_I :. \quad (17)$$

The unperturbed trajectory ends up giving the transformed interaction potential as

$$\begin{aligned} \mathcal{M}_{1D}^{(0)} \mathcal{V}_I &= \frac{2e^2}{\gamma_0 m c^3} \mathbf{A}_w \times \\ &\mathbf{e}_p \frac{m c}{e} \sum_\sigma \sum_j \left(u_\sigma + \frac{e}{m c} \mathcal{P}_\sigma^* \right) e^{i\Omega^{(\sigma)} s} \times \\ &e^{i\mathbf{k}_\perp^{(\sigma)} \cdot \mathbf{x}_\perp^{(j)} + i k_0^{(\sigma)} (\tau^{(j)} - \psi^{(j)}(s))} + c.c. \end{aligned} \quad (18)$$

where

$$\psi(s) = -s - \frac{1}{2} \frac{m^2 c^2}{(p_\tau^{(j)})^2} s - \frac{1}{2} \frac{m^2 c^2}{(p_\tau^{(j)})^2} \left(\frac{e}{c} \right)^2 \int_{s_0}^s ds' |\mathbf{A}_w|^2 \quad (19)$$

is the unperturbed drift trajectory.

To first order in a Magnus expansion [7, 8], we can compute the interaction map to be given by

$$\mathcal{M}_{1D}^{(I)} \approx \exp \left\{ - \int_{s_0}^s ds' : \mathcal{M}_{1D}^{(0)} \mathcal{V}_I : + \mathcal{O}(s^2) \right\}. \quad (20)$$

This begins to introduce the 1D FEL resonance condition, as the exponent of the map is proportional to just s if the resonant condition is satisfied. A full analysis of $\mathcal{M}_{1D}^{(I)}$ is beyond the scope of this proceeding, as it contains the entire FEL interaction including saturation, if it is taken to sufficiently long s .

We can also consider the 3D FEL problem numerically by using a split-operator approach. We can approximate the full map as the symmetric product of partial maps:

$$\mathcal{M}_{s_0 \rightarrow s_0+l_2} \approx \mathcal{M}_{(s_0 \rightarrow s_0+l_2)/2}^{(\perp)} \mathcal{M}_{1D} \mathcal{M}_{(s_0 \rightarrow s_0+l_2)/2}^{(\perp)} \quad (21)$$

where $\mathcal{M}_{(s_0 \rightarrow s_0+l_2)/2}^{(\perp)}$ integrates the perpendicular Hamiltonian weighted by a factor of a half from s_0 to $s_0 + l$. We can carry over the 1D map, and approximate the perpendicular map using the same first order Magnus expansion:

$$\begin{aligned} \mathcal{M}_{(s_0 \rightarrow s_0+l_w)/2}^{(\perp)} &\approx \\ \exp \left\{ - \frac{1}{2} \int_{s_0}^{s_0+l_w} ds' : \sum_j \frac{(\mathbf{p}_\perp^{(j)} - \frac{e}{c} \mathbf{A}_f)^2}{2p_\tau^{(j)}} + \frac{e}{c} A_s : l_w \right\}. \end{aligned} \quad (22)$$

If we assume that A_s has no explicit s dependence over the range of integration and that $\int_{s_0}^{s_0+l_w} \mathbf{A}_f = 0$, which is the case if \mathbf{A}_f is periodic with the wiggler period and l_2 is the undulator period, then this maps becomes

$$\begin{aligned} \mathcal{M}_{(s_0 \rightarrow s_0+l_2)/2}^{(\perp)} &\approx \\ \exp \left\{ - \frac{1}{2} : \sum_j \frac{(\mathbf{p}_\perp^{(j)})^2 - \left(\frac{e}{c} \right)^2 \langle \mathbf{A}_f^2 \rangle}{2p_\tau^{(j)}} + \frac{e}{c} A_s : l_w \right\} \end{aligned} \quad (23)$$

where we have averaged \mathbf{A}_f^2 over the wiggler period. This map can then be split in half again as a drift-kick map, giving the correct trajectories to order l_w^3 .

CONCLUSION

In this report, we have highlighted a derivation of symplectic maps as can be applied to the one-dimensional or three-dimensional free-electron laser problem. These maps could be applied to computing invariants and saturation effects in one-dimensional free-electron lasers or for computing second-order symplectic integrators for the three-dimensional free-electron laser. It remains to apply these approaches and determine the applicability of these symplectic maps.

REFERENCES

- [1] F. E. Low, "A lagrangian formulation of the boltzmann-vlasov equation for plasmas," *Proc. R. Soc. London Ser. A. Math. Phys. Sci.*, vol. 248, num. 1253, pp. 282-287, 1958.
- [2] E. Evstatiev and B. A. Shadwick, "Variational formulations of particle algorithms for kinetic plasma simulations," *J. Comp. Phys.*, vol. 245, pp. 376-398, 2013.
- [3] S. D. Webb *et al.*, "A spectral symplectic algorithm for cylindrical electromagnetic plasma simulations," *ArXiv e-prints, Submitted for publication*, 2016.
- [4] A. Dragt and J. Finn, "Lie series and invariant functions for analytic symplectic maps," *J. Math. Phys.*, vol. 17, num. 12, 1976.
- [5] A. Dragt, "A method of transfer maps for linear and nonlinear beam elements," *IEEE Trans. Nucl. Sci.*, vol. NS-26, num. 3, 1979.
- [6] A. Dragt, "Lectures on nonlinear orbit dynamics," in *Physics of High Energy Particle Accelerators*, AIP Publishing, 1982, pp. 147-313.
- [7] W. Magnus, "On the exponential solution of differential equations for a linear operator," *Commun. Pure Appl. Math.*, vol. VII, pp. 649-673, 1954.
- [8] J. A. Oteo and J. Ros, "The magnus expansion for classical hamiltonian systems," *J. Phys. A: Math. Gen.*, vol. 24, pp. 5751-5762, 1991.

NON-STANDARD USE OF LASER HEATER FOR FEL CONTROL AND THZ GENERATION

E. Allaria[†], M. B. Danailov, S. Di Mitri, D. Gauthier, L. Giannessi, G. Penco, M. Veronese, P. Sigalotti, L. Badano, M. Trovo¹, S. Spampinati, A. Demidovich, E. Roussel¹, Elettra Sincrotrone Trieste S.C.p.A., 34149 Basovizza, Italy
¹now at SOLEIL, Paris, France

Abstract

The laser heater system is currently used at various FEL facilities for an accurate control of the electron beam energy spread in order to suppress the micro-bunching instabilities that can develop in high brightness electron beams. More recently, studies and experiments have shown that laser-electron interaction developing in the laser heater can open new possibilities for tailoring the electron beam properties to meet special requirements. A suitable time-shaping of the laser heater pulse opened the door to the generation of (tens of) femtosecond-long FEL pulses.

Using standard laser techniques it is also possible to imprint onto the electron bunch, energy and density modulations in the THz frequency range that, properly sustained through the accelerator, can be exploited for generation of coherent THz radiation at GeV beam energies.

In this report, recent results at the FERMI FEL are presented together with near future plans.

INTRODUCTION

Modern linear accelerators that opened the era of X-ray Free Electron Lasers (X-FELs) [1–5] are required to generate very high peak current and high-quality electron beams in order for them to sustain the FEL process. The high peak current is generally achieved with the compression of the electron bunch in magnetic chicanes. Due to the very high density that electrons reach in the 6-D phase space, the beam develops collective effects, such as the microbunch instability, that can deteriorate the electron beam properties [7]. This instability can be driven by longitudinal space charge (LSC) [8] and coherent synchrotron radiation (CSR) [9]. These instabilities can introduce into the electron beam very strong energy modulations [10] that are a limitation for the operation of X-FELs at short wavelengths and in particular for seeded FELs because they produce a reduction of the longitudinal coherence [11, 12].

In order to fight the development of the microbunch instability, the so-called laser heater (LH) has been proposed [7] and is currently used in most FELs [13,14]. By using a resonant interaction between the electron beam and an external laser, the LH introduces a controlled spread in energy of the uncompressed beam and at low energy. This process can be optimized to suppress the microbunch instability [7]. As a result of the LH, the

FEL intensity can be increased significantly [13,14]. In addition, specifically for seeded FELs, it has been shown that the LH is essential to produce narrow-bandwidth FEL radiation [11,12].

NON-GAUSSIAN ENERGY DISTRIBUTION

The optical energy modulation introduced to the beam by the interaction with the laser is removed by the LH chicane who is designed to smear out short wavelength modulations. This lead to an uncorrelated energy spread on the beam. It has been shown that the shape of distribution of the energy spread can be controlled acting on the relative transverse size of the laser and electron beam in the interaction region [13]. In particular the use of a laser with a transverse mode significantly larger than the electron beam can lead to distributions that differ significantly from a Gaussian and can become a double horn distribution [15].

Having the possibility to control the shape of the electron energy distribution is important in the case of seeded FELs. Indeed, the use of non-Gaussian distributions can lead to a more efficient bunching process at higher harmonics.

Figure 1 reports the results of numerical simulations showing the advantage of using a non-Gaussian distribution for wavelengths shorter than 16 nm. For details about the parameters in the simulations refer to [16].

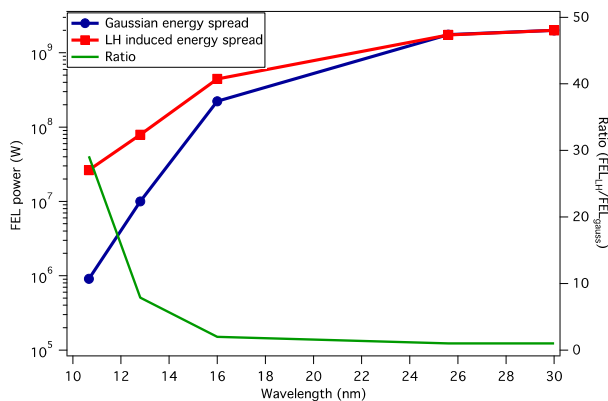


Figure 1: Simulations results of FEL power vs wavelength for standard Gaussian energy spread and LH induced non-Gaussian energy spread [16].

Content from this work may be used under the terms of the CC BY 3.0 licence (© 2018). Any distribution of this work must maintain attribution to the author(s), title of the work, publisher, and DOI.

[†]enrico.allaria@elettra.eu

TEMPORAL SHAPE CONTROL

For standard operation modes LH has a laser pulse that is much longer than the electron beam. This allows producing a uniform energy spread along the whole beam that can be entirely used for generating FEL radiation. However it is possible to control the energy-spread profile by acting on the temporal shape of the LH laser. This possibility can be exploited to control the shape of the FEL pulse length since the FEL process critically depends on the energy spread. This optical shaping of the e-beam [17] has been proposed as an alternative scheme to the emittances spoiler used at SLAC for shortening the FEL pulse [18].

A preliminary experiment has been performed at FERMI for controlling the temporal shape of the electron beam energy spread [18]. The laser pulse has been temporally shaped as reported in Fig. 2 by chirping the laser pulse and using a 4-f system, where an amplitude mask is placed in the Fourier-plane.

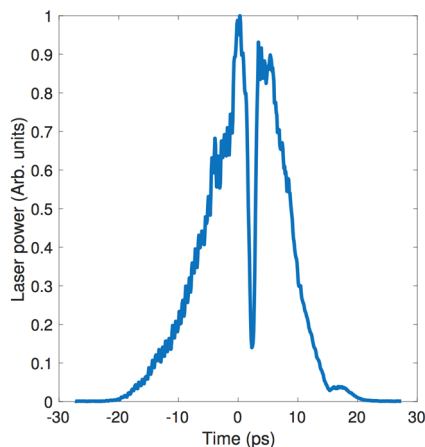


Figure 2: Cross correlation curve of the LH laser pulse with the temporal shaping. A narrow region in the centre of the pulse is characterized by low intensity.

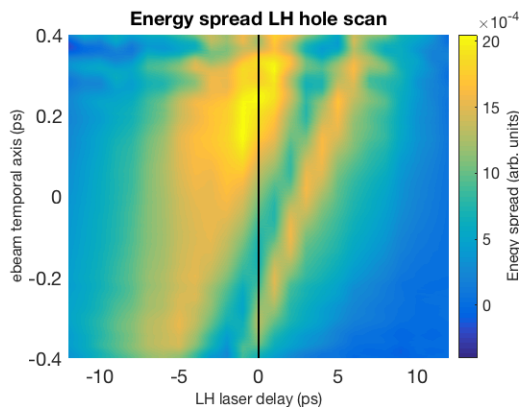


Figure 3: False colour plot representing the slice energy spread produced by the LH laser as a function of the laser delay with respect to the electron beam.

The shaped laser has been used in LH and the beam compressed and propagated as usual [19] to the end of the linac. There a transverse deflecting cavity has been used to measure the slice energy spread.

Figure 3 reports the result of the measurements of the electron-beam slice energy-spread along the beam axis (vertical axis) as the delay between e-beam and the laser has been changed (horizontal axis). Data clearly show the presence of a cold region of the beam that moves as the relative delay is changed.

A future upgrade in the transport system for the LH laser will be used for a sharper profile that combined with the seeding would allow the generation at FERMI FEL pulses at the 20-nm spectral range as short as 10 fs [18].

LONG WAVELENGTH PERIODIC MODULATION

An additional possibility is to introduce in the LH laser an amplitude modulation at much longer wavelength than the optical one. This has been done by taking advantage that the LH laser is generally strongly chirped. The superposition of two chirped laser pulses produced a pulse with a strong amplitude modulation that depends on the relative delay (Fig. 4) [19].

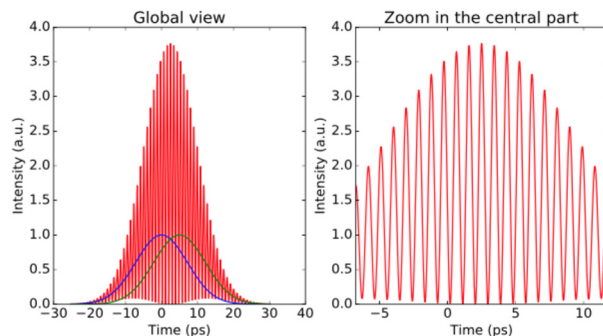


Figure 4: Amplitude modulated laser pulse obtained with the beating from two chirped pulses with a small relative delay.

It has been shown at FERMI that this long wavelength modulation can be transferred to the electron beam as energy spread amplitude modulation and it is not washed out by the LH chicane. The laser beating wavelength can be adjusted to enter the gain bandwidth of the micro-bunching instability, so that the small modulation introduced into the beam in the LH can be amplified through the accelerator and create significant energy and current modulation to the beam. Those modulations can be controlled to be in the few-THz frequency range.

This seeded micro-bunching gives the possibility to control electron beam properties that can be exploited for special FEL operational modes or for coherent THz emission.

CONCLUSION

We discussed new interesting possibilities offered by the laser heater for controlling specific properties of the electron beam. Results already obtained at FERMI and new planned experiments have been presented.

ACKNOWLEDGEMENT

This work resulted from the activities of the FERMI machine physics group at Elettra-Sincrotrone Trieste. The authors are grateful to all the FERMI team for the valuable support.

REFERENCES

- [1] W. Ackermann *et al.*, *Nat. Photonics* **1**, 336 (2007).
- [2] P. Emma *et al.*, *Nat. Photonics* **4**, 641 (2010).
- [3] T. Ishikawa *et al.*, *Nat. Photonics* **6**, 540 (2012).
- [4] E. Allaria *et al.*, *Nat. Photonics* **6**, 699 (2012).
- [6] W. Decking, *Proc. IPAC'17*, Copenhagen, Denmark, MOXAA1.
- [7] M. Borland *et al.*, *Nucl. Instrum. Methods Phys. Res. A* **483**, 268 (2002).
- [8] E.L. Saldin *et al.*, *Nucl. Instrum. Methods Phys. Res. A* **528**, 355 (2004).
- [9] E.L. Saldin *et al.*, *Nucl. Instrum. Methods Phys. Res. A* **490**, 1 (2002).
- [10] D. Ratner *et al.*, *Phys. Rev. ST Accel. Beams* **18**, 030704 (2015).
- [11] Z. Zhang *et al.*, *Phys. Rev. ST – Accel. Beams* **19**, 050701 (2016).
- [12] E. Allaria, *Proc. SPIE 10237- 14, SPIE Optics and Optoelectronics*, Prague, April 2017.
- [13] Z. Huang *et al.*, *Phys. Rev. ST – Accel. Beams* **13**, 020703 (2010).
- [14] S. Spampinati *et al.*, *Phys. Rev. ST – Accel. Beams* **17**, 120705 (2014).
- [15] Z. Huang *et al.*, *Phys. Rev. ST – Accel. Beams* **7**, 074401 (2004).
- [16] E. Ferrari *et al.*, *Phys. Rev. Lett.* **112**, 114802 (2014).
- [17] A. Marinelli *et al.*, *Phys. Rev. Lett.* **116**, 254801 (2016).
- [17] P. Emma *et al.*, *Phys. Rev. Lett.* **92**, 074801 (2004).
- [18] V. Grattoni *et al.*, *Proc. IPAC'17*, Copenhagen, Denmark, WEPAB034.
- [19] E. Roussel *et al.*, *Phys. Rev. Lett.* **115**, 214801 (2015).

TIME-DOMAIN ANALYSIS OF ATTOSECOND PULSE GENERATION IN AN X-RAY FREE-ELECTRON LASER

P. Baxevanis, Z. Huang and A. Marinelli,
 SLAC National Accelerator Laboratory, Menlo Park, CA 94025, USA

Abstract

The method of enhanced self-amplified spontaneous emission (eSASE) is one of the strongest candidates for the generation of sub-femtosecond X-ray pulses in a free-electron laser. The optimization of an eSASE experiment involves many independent parameters, which makes the exploration of the parameter space with 3-D simulations computationally intensive. Therefore, a robust theoretical analysis of this problem is extremely desirable. We provide a self-consistent, analytical treatment of such a configuration using a one-dimensional, time-dependent FEL model that includes the key effects of linear e-beam chirp and linear undulator taper. Verified via comparison with numerical simulation, our formalism is also utilized in parameter studies that seek to determine the optimum setup of the FEL.

INTRODUCTION

Because of their attractiveness to users, the generation of ultrashort X-ray pulses is one of the main objectives of research into advanced operation modes in a modern FEL facility. One of the more prominent schemes for generating sub-fs X-rays in an FEL is eSASE [1] (enhanced Self-Amplified Spontaneous Emission). This technique involves the interaction of an electron beam with an optical laser pulse in the presence of a short wiggler, prior to the beam being sent into a conventional undulator. This process relies on some intense manipulation of the longitudinal phase space of the e-beam, after which the strongly chirped beam typically has to travel through a tapered undulator in order to achieve lasing with the required properties. Apart from a significant improvement in the performance of the FEL, this method provides an attractive scheme for generating X-ray pulses in the attosecond range.

In this paper, we provide a self-consistent, analytical treatment of such a configuration using a simple, one-dimensional (1D) FEL model that includes the effects of startup from noise (SASE), slippage, electron beam chirp (linear and nonlinear) and undulator taper. 3D effects such as radiation diffraction, emittance and focusing are excluded. This allows us to calculate various key properties of the FEL radiation in the latter stage of the exponential gain regime. After verifying its validity through comparison with the output of a 1D FEL simulation code, our analysis is also utilized in parameter studies that seek to determine the optimum setup of the FEL. This enables us to obtain a more thorough understanding of the physics behind the experimental method.

1D FEL ANALYSIS

In this section, we outline the main results of our theoretical analysis, leaving the details of the derivation for another publication. In the context of our model, the main properties of the radiation can be extracted from a slowly-varying complex amplitude $a(\theta, z)$, which can be related to the actual electric field through the relation $E_{\text{rad}} = a(\theta, z)e^{ik_r(z-ct)}/2 + \text{c.c.}$. Here, $k_r = 2\pi/\lambda_r$ is the radiation wave number and $\theta = k_u z + k_r(z - ct)$ is the ponderomotive phase ($k_u = 2\pi/\lambda_u$, where λ_u is the undulator period). The θ variable also satisfies the relation $\theta = k_r s$, where s is an internal bunch coordinate. The main FEL parameters satisfy the resonance condition $\lambda_r = \lambda_u(1 + K_0^2/2)/(2\gamma_0^2)$, where λ_r is the radiation wavelength, K_0 is the (initial) undulator parameter and γ_0 is the average relativistic factor of the beam. The longitudinal phase space coordinates are (θ, η) , where $\eta = \gamma/\gamma_0 - 1$ is the energy deviation variable.

As far as the key properties of the e-beam are concerned, we assume that the current is given by $I(\theta) = I_0\chi(\theta)$, where $0 \leq \chi(\theta) \leq 1$ is a scaled profile and I_0 is the peak current, while the correlated energy (chirp) profile is $\eta = -\mu(\theta - \theta_m) - \Upsilon(\theta)$. Here, $\theta_m = \theta_b/2$ is the phase corresponding to the middle of the bunch (we have $\chi(0) = \chi(\theta_b) = 0$), μ is a constant linear chirp coefficient and the Υ function represents a nonlinear chirp component (we assume zero uncorrelated energy spread). For our purposes, we select a parabolic current profile of the form $\chi(\theta) = 1 - (\theta - \theta_m)^2/\theta_m^2$ and a nonlinear chirp profile given by $\Upsilon(\theta) = \mu_3(\theta - \theta_m)^3$, though the formalism can also accommodate the general case. The logic of this particular selection will be justified later on. Finally, we also assume a linear taper profile of the form $K = K_0(1 + \epsilon z)$.

We follow the self-consistent analysis of Ref. [2]. In the linear regime of the interaction, we can show that the complex radiation amplitude can be expressed as

$$a(\theta, z) \propto \sum_j e^{-i\theta_j} G(\theta, \theta_j, z), \quad (1)$$

where θ_j are the random initial electron phases (at $z = 0$) and $G(\theta, \theta_j, z)$ is a Green's function. The latter is non-zero only when $0 < \theta - \theta_j < k_u z$, in which case it is given in contour integral form (up to a phase term) by

$$G = -\frac{1}{2\pi i} \int_{-\infty+iy}^{+\infty+iy} \frac{d\hat{\lambda}}{\hat{\lambda}} \exp(-i\hat{\lambda}[\bar{z} - (\hat{\theta} - \hat{\theta}_j)] - i \int_{\hat{\theta}_j}^{\tau(\hat{\theta})} dt \times \hat{\chi}(t)[\hat{\lambda} + \hat{\Delta}_0(t - \hat{\theta}_j) + \hat{\mu}_3\{(t - \hat{\theta}_m)^3 - (\hat{\theta}_j - \hat{\theta}_m)^3\}]^{-2}). \quad (2)$$

Content from this work may be used under the terms of the CC BY 3.0 licence (© 2018). Any distribution of this work must maintain attribution to the author(s), title of the work, publisher, and DOI.

In the above equation, we have introduced the following scaled variables: $\bar{z} = 2\rho k_u z$, $\hat{\theta} = 2\rho\theta$, $\hat{\theta}_j = 2\rho\theta_j$, $\hat{\theta}_m = 2\rho\theta_m$ (where ρ is the dimensionless FEL (or Pierce) parameter), $\hat{\mu}_3 = \mu_3/(8\rho^4)$ and $\hat{\Delta}_0 = (\mu - \bar{a}_1)/(2\rho^2)$, where $\bar{a}_1 = a_1/(2k_u^2)$ and $a_1 = -2\epsilon k_u K_0^2/(2 + K_0^2)$. Moreover, y is a real constant that is larger than the imaginary part of all the integrand singularities.

Apart from the current profile itself, finite pulse effects are reflected in the function $\tau(\hat{\theta})$, which is equal to $\hat{\theta}$ for $0 \leq \hat{\theta} \leq \hat{\theta}_b = 2\hat{\theta}_m$ and $\hat{\theta}_b$ for $\hat{\theta} > \hat{\theta}_b$. For the case of zero taper and zero nonlinear chirp ($a_1 = 0$, $\mu_3 = 0$), the above expressions reduce to the Green's function for the case of linear chirp [3]. On the other hand, we can easily show that taking $\hat{\Delta}_0 = 0$ reproduces the well-known compensation condition between linear chirp and linear taper [4]. In any case, calculation of the Green's function via the contour integral is facilitated by the stationary phase approximation, which is accurate enough in the latter stage of the linear regime. It is worth noting that, for the case of parabolic current/cubic chirp, the t -integral in Eq. (2) can be determined analytically.

Given the Green's function, we can determine various properties of the radiation, the most important of which is the radiation power. This quantity, averaged over a large number of shots (i.e. ensembles of random phases), is given by (see [5] and [1])

$$P_{\text{rad}}(\hat{\theta}, \bar{z}) = 2\gamma_0 m c^3 k_r \rho^2 \int d\hat{\theta}_j \hat{\chi}(\hat{\theta}_j) |G(\hat{\theta}, \hat{\theta}_j, \bar{z})|^2. \quad (3)$$

Moreover, we can also quantify the state of the e-beam by calculating the bunching factor $b = |\langle e^{-i\theta_j} \rangle_{\Delta}|$, where the Δ -index refers to average within a radiation wavelength. The shot-averaged version of this quantity is, in turn, given by

$$\langle b^2(\hat{\theta}, \bar{z}) \rangle_{\text{shot}} = \frac{4\pi\rho}{n_0\lambda_r} \int d\hat{\theta}_j \hat{\chi}(\hat{\theta}_j) |G_b(\hat{\theta}, \hat{\theta}_j, \bar{z})|^2 / \hat{\chi}^2(\hat{\theta}), \quad (4)$$

where $n_0 = I_0/(ec)$ is the peak number density and $G_b = (\partial/\partial\bar{z} + \partial/\partial\hat{\theta})G$ is a derivative Green's function (unlike G , G_b is non-zero only within the electron bunch).

Finally, we note the relationship between the nonlinear chirp coefficient μ_3 and the linear chirp μ . Though these two parameters are - in principle - independent, we correlate them in the following way: since the chirp profile of the beam is shaped by space charge effects before the amplification process, it can be modeled by the θ -derivative of the actual current profile, which is closer to a Gaussian. Thus, we have

$$\eta = -\mu(\theta - \theta_m) - \mu_3(\theta - \theta_m)^3 \propto \frac{d}{d\theta} \exp\left(-\frac{(\theta - \theta_m)^2}{2\sigma_\theta^2}\right), \quad (5)$$

up to third order terms in $\theta - \theta_m$. This yields the relation $\mu_3 = -\mu/(2\sigma_\theta^2)$. As far as σ_θ is concerned, we can either choose it in an ad-hoc way or derive it by matching the parabolic and Gaussian current profiles up to second order in $\theta - \theta_m$. The latter manipulation yields $\sigma_\theta = \theta_m/\sqrt{2}$. Though not entirely self-consistent, this strategy allows us to adequately model the space-charge induced chirp while

preserving some degree of analyticity as far as the Green's function is concerned.

NUMERICAL RESULTS

In what follows, we present a brief numerical illustration of the theory outlined in the previous section. We select a parameter set that roughly approximates a plausible configuration of the X-LEAP eSASE experiment at SLAC. This involves the generation of 800 eV photons ($\lambda_r = 1.55$ nm) with a standard LCLS undulator ($\lambda_u = 3$ cm, $K_0 = 3.5$) and a 4.24 GeV beam with a peak current of 4.5 kA. The average beta function is about 10 m, which corresponds to an rms beam size of approximately $25 \mu\text{m}$ (for a transverse normalized emittance of $0.5 \mu\text{m}$). The ρ -parameter is about 2×10^{-3} , while we also assume zero uncorrelated energy spread. In the first case we consider, μ is given by $\mu = -(\Delta\gamma/\gamma_0)/\theta_b$, where $\Delta\gamma = \Delta E/mc^2$ and $\Delta E = 30$ MeV is the total energy variation due to the linear chirp. This leads to a negative linear chirp, which is compensated by the appropriate (reverse) taper, leaving only the cubic component contribution.

In Figs. 1 and 2, we plot the (shot-averaged) radiation power and bunching factor (the latter defined as $\sqrt{\langle b^2 \rangle_{\text{shot}}}$) as functions of the position s along the bunch. The theoretical values are calculated by Eqs. (3) and (4) while the simulation values are obtained from a 1D FEL simulation code (some details in Ref. [2]). Reasonable agreement is observed between the two approaches, which helps us build up confidence in the formalism.

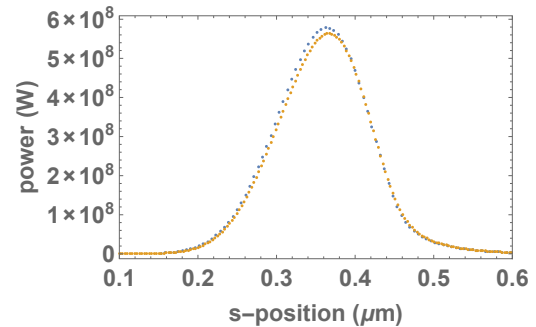


Figure 1: Shot-averaged radiation power along the bunch ($z = 11.45$ m, $0.5 \mu\text{m}$ bunch length, $\sigma = \sigma_\theta/k_r = 160$ nm, $\Delta E = 30$ MeV, 400 shot average, matched linear chirp). The blue/brown curve represents theory/simulation data.

Moving on, we scan the electron pulse duration t_e while keeping constant both the peak current I_0 and the product $\mu \times t_e$. According to our previous discussion, the latter is proportional to the total energy variation ΔE , which is fixed at 35 MeV. Using the Green's function, we obtain the power profiles for the pure, matched linear chirp case (red data in Figs. 3-4) and for the case with the added nonlinear chirp component (blue data). In Fig. 3, we plot these two profiles for a bunch length of 1.5 fs. A power suppression due to the cubic chirp is immediately evident. Moreover, we find that the radiation full-width-at-half-maximum (FWHM) is *also reduced*. This is made explicit in Fig. 4, where the FWHM

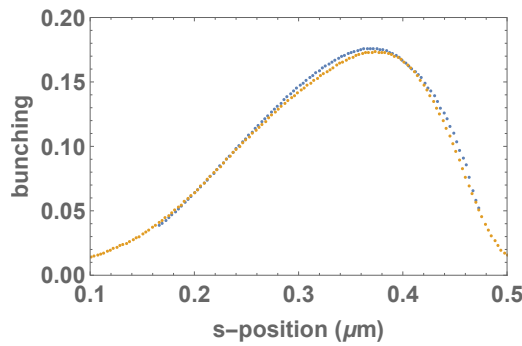


Figure 2: Shot-averaged bunching factor along the bunch (same parameters/color convention as in Fig. 1).

is plotted as a function of t_e . A marked *linear dependence* is observed, along with what appears to be a constant vertical shift (reduction) due to the cubic chirp.

The former feature can actually be obtained in a heuristic way by the following simple argument: since the ρ -parameter scales according to $L_g^{-1} \sim \rho \sim I^{1/3}$, we can define a θ -dependent ρ by plugging in the parabolic profile $\chi(\theta) = 1 - (\theta - \theta_m)^2/\theta_m^2$ (recall that $I \sim \chi(\theta)$). Combining this with the power growth relation $P = P_0 \exp(z/L_g)$, we find a power profile of the form $\exp(-(z/L_0)(\theta - \theta_m)^2/(3\theta_m^2))$, where $L_0 = \lambda_u/(4\pi\sqrt{3}\rho)_{I \rightarrow I_0}$ is the basic (minimum) value for the power gain length L_g (about 0.70 m for our parameters). This predicts maximization of the radiation power in the middle of the electron bunch, which is not very accurate (in fact, it happens closer to the head of the beam, see Fig. 3). On the other hand, the FWHM is simply $t_e \times \sqrt{3} \log 2/(z/L_0)$, a result which also exhibits linear dependence with a slope of about 0.35. This is very close to the value calculated from the Green's function data (0.32), even though the simple model does not take into account detuning effects etc. This scaling may be of some use when doing back-of-the-envelope calculations involving attosecond-style pulses.

In conclusion, we also point out that the Green's function formalism allows us to get a sense of what the optimum setup of the FEL configuration is. Apart from determining the proper matching strategy involving the linear chirp and taper, we can study the interplay of power suppression and

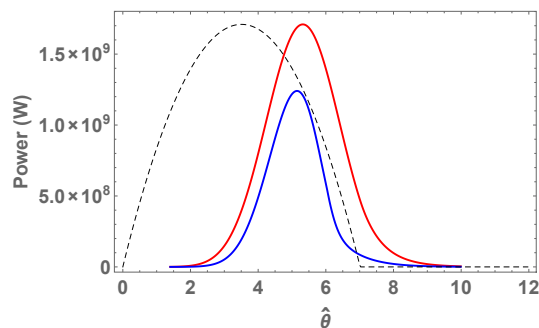


Figure 3: Power profiles for a matched linear chirp with or without the cubic chirp component (blue and red curves, respectively). The dashed line denotes the current profile.

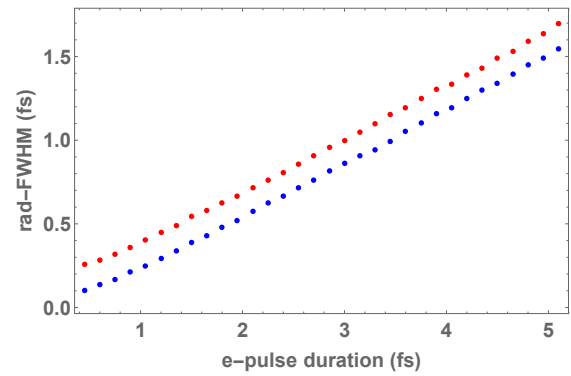


Figure 4: Radiation FWHM vs the electron bunch length (same color convention as in Fig. 3). All of the data shown in Figs. 3-4 have been calculated assuming that $z = 12.3$ m.

FWHM reduction due to the nonlinear chirp in order to find a suitable working point. Though our results are only one-dimensional, the essential conclusions remain valid in a more complicated (3D) setup.

CONCLUSIONS

We have developed a one-dimensional, time-dependent theory which can adequately model an eSASE-based FEL. Our formalism includes startup from noise, radiation slippage, e-beam chirp (linear and nonlinear) and undulator linear taper. Using a Green's function approach, we are able to determine the basic properties of the radiation pulse prior to the onset of saturation. As part of our derivation, we can provide a rigorous proof of the well-known compensation condition between linear chirp and taper. Reasonable agreement is observed between our semi-analytical treatment and the output of a 1D FEL code. Moreover, our technique is robust enough to allow us to perform simple parameter studies, which show some interesting features like the pulse-shortening effect due to nonlinear chirp.

REFERENCES

- [1] A. Zholents, "Method of an enhanced self-amplified spontaneous emission for x-ray free electron lasers", *Phys. Rev. ST Accel. Beams*, vol. 8, p. 040701, 2005.
- [2] Z. Huang and K. J. Kim, "Effects of bunch density gradient in high-gain free-electron lasers", *Nucl. Instrum. Meth. A*, vol. 445, p. 105, 2000.
- [3] Z. Huang and S. Krinsky, "Frequency chirped self-amplified spontaneous-emission free-electron lasers", *Phys. Rev. ST Accel. Beams*, vol. 6, p. 050702, 2003.
- [4] E. L. Saldin, E. A. Schneidmiller and M. V. Yurkov, "Self-amplified spontaneous emission FEL with energy-chirped electron beam and its application for generation of attosecond x-ray pulses", *Phys. Rev. ST Accel. Beams*, vol. 9, p. 050702, 2006.
- [5] S. Krinsky, "Transient analysis of free-electron lasers with discrete radiators", *Phys. Rev. E*, vol. 59, p. 1171, 1999.

DYNAMICS OF SUPERRADIANT EMISSION BY A PREBUNCHED E-BEAM AND ITS SPONTANEOUS EMISSION SELF-INTERACTION*

R. Iancu†, Shenkar College, Ramat Gan, Israel and University of Tel-Aviv, Tel-Aviv

A. Gover, University of Tel-Aviv, Tel-Aviv, Israel

A. Friedman, Ariel University, Ariel

C. Emma, P. Musumeci, UCLA, Los Angeles

Abstract

In the context of radiation emission from an electron beam, Dicke's superradiance (SR) is the enhanced "coherent" spontaneous radiation emission from a pre-bunched beam, and Stimulated-Superradiance (ST-SR) is the further enhanced emission of the bunched beam in the presence of a phase-matched radiation wave. These processes are analyzed for Undulator radiation in the framework of radiation field mode-excitation theory. In the nonlinear saturation regime the synchronism of the bunched beam and an injected radiation wave may be sustained by wiggler tapering: Tapering-Enhanced Superradiance (TES) and Tapering-Enhanced Stimulated Superradiance Amplification (TESSA). Identifying these processes is useful for understanding the enhancement of radiative emission in the tapered wiggler section of seeded FELs. The nonlinear formulation of the energy transfer dynamics between the radiation wave and the bunched beam fully conserves energy. This includes conservation of energy without radiation reaction terms in the interesting case of spontaneous self-interaction (no input radiation).

INTRODUCTION

In the context of radiation emission from an electron beam, Dicke's superradiance (SR) [1] is the enhanced "coherent" spontaneous radiation emission from a pre-bunched beam, and Stimulated-Superradiance (ST-SR) is the further enhanced emission of the bunched beam in the presence of a phase-matched radiation wave [2]. These processes are analyzed for Undulator radiation in the framework of radiation field mode-excitation theory. In the nonlinear saturation regime the synchronism of the bunched beam and an injected radiation wave may be sustained by wiggler tapering: Tapering-Enhanced Superradiance (TES) and Tapering-Enhanced Stimulated Superradiance Amplification (TESSA) [3]. In section II we present the radiation modes expansion formulation (in the spectral Fourier frequency formulation) [2] and explain the radiation cases. In section III we derive the radiation from a single bunch and from a finite train of bunches in the spectral Fourier frequency formulations. In section IV we present the single frequency formulation of the radiation field mode-excitation, and calculate the power radiated by an infinite train of bunches, and in section V we derive an energy-conserving non linear model which results in a couple of differential equations and

present numerical results of those equations for some cases of interest.

SUPERRADIANCE AND STIMULATED SUPERRADIANCE IN SPECTRAL FORMULATIONS

As a starting point we review the theory of superradiant (SR) and stimulated superradiant (ST-SR) emission from free electrons in a general radiative emission process. In this section we use a spectral formulation, namely, all fields are given in the frequency domain as Fourier transforms of the real time-dependent fields. We use the radiation modes expansion formulation of [2], where the radiation field is expanded in terms of an orthogonal set of eigenmodes in a waveguide structure or in free space (eg. Hermite-Gaussian modes):

$$\{\tilde{\mathbf{E}}_q(\mathbf{r}), \tilde{\mathbf{H}}_q(\mathbf{r})\} = \{\tilde{\mathbf{E}}_q(\mathbf{r}_\perp), \tilde{\mathbf{H}}_q(\mathbf{r}_\perp)\} e^{ik_q z}$$

$$\check{\mathbf{E}}(\mathbf{r}, \omega) = \sum_{\pm q} \check{C}_q(z, \omega) \tilde{\mathbf{E}}_q(\mathbf{r})$$

$$\check{\mathbf{H}}(\mathbf{r}, \omega) = \sum_{\pm q} \check{C}_q(z, \omega) \tilde{\mathbf{H}}_q(\mathbf{r})$$

The amplitude coefficients \check{C}_q have dimensions of time, are in units of sec V/m and sec A/m.

The excitation equations of the mode amplitudes is:

$$\frac{d\check{C}_q(z, \omega)}{dz} = \frac{-1}{4\mathcal{P}_q} \int \check{\mathbf{J}}(\mathbf{r}, \omega) \cdot \tilde{\mathbf{E}}_q^*(\mathbf{r}) d^2\mathbf{r}_\perp. \quad (1)$$

where the current density $\check{\mathbf{J}}(\mathbf{r}, \omega)$ is the Fourier transform of $\mathbf{J}(\mathbf{r}, t)$.

The above is formally integrated and given in terms of the initial mode excitation amplitude and the currents:

$$\check{C}_q(z, \omega) - \check{C}_q(0, \omega) = -\frac{1}{4\mathcal{P}_q} \int \check{\mathbf{J}}(\mathbf{r}, \omega) \cdot \tilde{\mathbf{E}}_q^*(\mathbf{r}) dV,$$

where

$$\mathcal{P}_q = \frac{1}{2} Re \iint (\tilde{\mathbf{E}}_q \times \tilde{\mathbf{H}}_q) \cdot \hat{e}_z d^2\mathbf{r}_\perp = \frac{|\tilde{\mathbf{E}}_q(\mathbf{r}_\perp = 0)|^2}{2Z_q} A_{emq} \quad (2)$$

and Z_q is the mode impedance ($\sqrt{\mu_0/\epsilon_0}$ in free space). In the case of a narrow beam passing on axis near $\mathbf{r}_\perp = 0$, Eq. (2) defines the mode effective area A_{emq} in terms of the field of the mode on axis $\tilde{\mathbf{E}}_q(\mathbf{r}_\perp = 0)$.

* Partial support by US-Israel Binational Science Foundation (BSF) and by Deutsche-Israelische Projektkooperation (DIP).

† riancon@gmail.com

For the Fourier transformed fields we define the total spectral energy (per unit of angular frequency) based on Parseval theorem as

$$\frac{dW}{d\omega} = \frac{2}{\pi} \sum_q \mathcal{P}_q |\check{C}_q(\omega)|^2.$$

This definition corresponds to positive frequencies only: $0 < \omega < \infty$. Considering now one single mode q ,

$$\frac{dW_q}{d\omega} = \frac{2}{\pi} \mathcal{P}_q |\check{C}_q(\omega)|^2.$$

For a particulate current (an electron beam):

$$J(\mathbf{r}, t) = \sum_{j=1}^N -e\mathbf{v}_j(t)\delta(\mathbf{r} - \mathbf{r}_j(t)).$$

The field amplitude increment appears as a coherent sum of contributions (energy wavepackets) from all the electrons in the beam:

$$\check{C}_q^{out}(\omega) - \check{C}_q^{in}(\omega) \equiv \sum_{j=1}^N \Delta\check{C}_{qj}(\omega) = -\frac{1}{4\mathcal{P}_q} \sum_{j=1}^N \Delta\check{W}_{qj}, \text{ or}$$

$$\Delta\check{W}_{qj} = -e \int_{-\infty}^{\infty} \mathbf{v}_j(t) \cdot \tilde{\mathbf{E}}_q^*(\mathbf{r}_j(t)) e^{i\omega t} dt. \quad (3)$$

The contributions can be split into a spontaneous part (independent of the presence of radiation field) and stimulated (field dependent) part:

$$\Delta\check{W}_{qj} = \Delta\check{W}_{qj}^0 + \Delta\check{W}_{qj}^{st}.$$

We do not deal in this section with stimulated emission; however, we note that, in general, the second term $\Delta\check{W}_{qj}^{st}$ is a function of $\check{C}_q(z)$ through $\mathbf{r}_j(t)$ and $\mathbf{v}_j(t)$ and therefore $\Delta\check{W}_{qj}^{st}$ cannot be calculated explicitly from the integral in Eq. 3. Its calculation requires solving the electron force equations together with the wave excitation equation in Eq. 1.

Assuming a narrow cold beam where all particles follow the same trajectories, we may write $\mathbf{r}_j(t) = \mathbf{r}_j^0(t - t_{0j})$ and $\mathbf{v}_j(t) = \mathbf{v}_j^0(t - t_{0j})$, change variable $t' = t - t_{0j}$ in Eq. (3) [5], so that the spontaneous emission wavepacket contributions are identical, except for a phase factor corresponding to their injection time t_{0j} :

$$\Delta\check{W}_{qj}^0 = \Delta\check{W}_{qe}^0 e^{i\omega t_{0j}},$$

where

$$\Delta\check{W}_{qe}^0 = -e \int_{-\infty}^{\infty} \mathbf{v}_e^0(t) \cdot \tilde{\mathbf{E}}_q^*(\mathbf{r}_e^0(t)) e^{i\omega t} dt. \quad (4)$$

The radiation mode amplitude at the output is composed of a sum of wavepacket contributions including the input field contribution (if any):

$$\check{C}_q^{out}(\omega) = \check{C}_q^{in}(\omega) + \Delta\check{C}_{qe}^0(\omega) \sum_{j=1}^N e^{i\omega t_{0j}} \quad (5)$$

so that the total spectral radiative energy from the electron pulse is

$$\begin{aligned} \frac{dW_q}{d\omega} &= \frac{2}{\pi} \mathcal{P}_q |\check{C}_q^{out}(\omega)|^2 \\ &= \frac{2}{\pi} \mathcal{P}_q \left\{ |\check{C}_q^{in}(\omega)|^2 \right. \\ &\quad \left. + \left| \Delta\check{C}_{qe}^0(\omega) \right|^2 \left| \sum_{j=1}^N e^{i\omega t_{0j}} \right|^2 \right. \\ &\quad \left. + \left[\check{C}_q^{in*}(\omega) \Delta\check{C}_{qe}^0(\omega) \sum_{j=1}^N e^{i\omega t_{0j}} + c.c. \right] \right\} \\ &= \left(\frac{dW_q}{d\omega} \right)_{in} + \left(\frac{dW_q}{d\omega} \right)_{sp/SR} + \left(\frac{dW_q}{d\omega} \right)_{ST-SR}. \end{aligned}$$

The first term in the $\{\}$ parentheses (“in”) represents the input wave spectral energy. The second term (“sp/SR”) is the spontaneous emission, which may also be superradiant in case that all contributions add in phase. The third term has a very small value (averages to 0) if the contributions add randomly, so it is relevant only if the electrons of the beam enter in phase with the radiated mode. It is thus dependent on the coherent mode complex amplitude \check{C}_q^{in} , and therefore it is marked by the subscript “ST-SR”, i.e. “zero-order” stimulated superradiance.

SINGLE BUNCH AND FINITE TRAIN OF BUNCHES

Using Eq. (4) for a single tight bunch one obtains the spectral energy per unit of angular frequency at the exit of the undulator for SR

$$\left(\frac{dW_q}{d\omega} \right)_{SR} = \frac{N^2 e^2 Z_q}{16\pi} \left(\frac{\bar{a}_w}{\beta_z \gamma} \right)^2 \frac{L_w^2}{A_{em}} \text{sinc}^2(\theta L_w/2),$$

and for ST-SR

$$\begin{aligned} \left(\frac{dW_q}{d\omega} \right)_{ST-SR} &= |\check{C}_q^{in}(\omega)| \frac{Ne}{2\pi} \left(\frac{\bar{a}_w}{\beta_z \gamma} \right) \sqrt{\frac{2Z_q \mathcal{P}_q}{A_{em}}} L_w \\ &\quad \times \text{sinc}(\theta L_w/2) \cos(\varphi_{qb0} - \theta L_w/2), \end{aligned}$$

where L_w is the undulator length.

Similarly, for a train of N_M tight bunches, one obtains

$$\begin{aligned} \left(\frac{dW_q}{d\omega} \right)_{SR} &= \frac{N^2 e^2 Z_q}{16\pi} \left(\frac{\bar{a}_w}{\beta_z \gamma} \right)^2 \\ &\quad \times \frac{L_w^2}{A_{em}} |M_M(\omega)|^2 \text{sinc}^2(\theta L_w/2), \end{aligned}$$

$$\begin{aligned} \left(\frac{dW_q}{d\omega} \right)_{ST-SR} &= |\check{C}_q^{in}(\omega)| \frac{Ne}{2\pi} \left(\frac{\bar{a}_w}{\beta_z \gamma} \right) \sqrt{\frac{2Z_q \mathcal{P}_q}{A_{em}}} L_w |M_M(\omega)| \\ &\quad \times \text{sinc}(\theta L_w/2) \cos(\varphi_{qb0} - \theta L_w/2), \end{aligned}$$

where

$$M_M(\omega) = \frac{\sin(N_M \pi \omega / \omega_b)}{N_M \sin(\pi \omega / \omega_b)}.$$

INFINITE TRAIN OF BUNCHES IN SINGLE FREQUENCY ANALYSIS

In the single frequency analysis, the radiation modes expansion formulation is expressed by the following equations:

$$\tilde{\mathbf{E}}(\mathbf{r}) = \sum_q \tilde{C}_q(z) \tilde{\mathbf{E}}_q(\mathbf{r})$$

$$\tilde{\mathbf{H}}(\mathbf{r}) = \sum_q \tilde{C}_q(z) \tilde{\mathbf{H}}_q(\mathbf{r})$$

$$\mathcal{P}_q = \frac{1}{2} Re \iint (\tilde{\mathbf{E}}_q \times \tilde{\mathbf{H}}_q) \cdot \hat{e}_z d^2 \mathbf{r}_\perp = \frac{|\tilde{\mathbf{E}}_q(\mathbf{r}_\perp = 0)|^2}{2Z_q} A_{emq}$$

$$\frac{d\tilde{C}_q(z)}{dz} = \frac{-1}{4\mathcal{P}_q} \int \tilde{\mathbf{J}}(\mathbf{r}) \cdot \tilde{\mathbf{E}}_q^*(\mathbf{r}) d^2 \mathbf{r}_\perp$$

$$P = \sum_q \mathcal{P}_q |\tilde{C}_q(\omega)|^2$$

representing the radiated power. We can again use the excitation as described in Eq. (5):

$$\tilde{C}_q^{\text{out}}(\omega) - \tilde{C}_q^{\text{in}}(0) = -\frac{1}{4\mathcal{P}_q} \int \tilde{\mathbf{J}}(\mathbf{r}) \cdot \tilde{\mathbf{E}}_q^*(\mathbf{r}) dV.$$

Applying this to an infinite train of tight bunches results in the SR radiated power

$$P_{SR} = \frac{1}{32} Z_q \frac{N^2 e^2 \omega_0^2 |\tilde{\beta}_w|^2}{\pi^2 \beta_z^2} \frac{L_w^2}{A_{emq}} \text{sinc}^2(\theta L_w/2),$$

and the ST-SR radiated power

$$P_{ST-SR} = \frac{1}{4} |\tilde{C}_q(0)| \frac{N e \omega_0 |\tilde{\beta}_w|}{\pi \beta_z} \sqrt{\frac{2Z_q \mathcal{P}_q}{A_{emq}}} L_w \times \cos(\varphi_{qb0} - \theta L_w/2) \text{sinc}(\theta L_w/2).$$

DYNAMICS OF A PERIODICALLY BUNCHED BEAM INTERACTING WITH RADIATION FIELD

In this section we include the influence of the radiated field on the charged bunches, and include this influence in the calculation of the radiated power.

The power of the electron bunches

$$N_b m c^2 \frac{d\gamma}{dt} = Q_b \mathbf{v} \cdot \mathbf{E}(\mathbf{r}, t),$$

combined with the excitation equation

$$\frac{d\tilde{C}_q}{dz} = \frac{-1}{4\mathcal{P}_q} \int \tilde{\mathbf{J}} \cdot \tilde{\mathbf{E}}_q^* d^2 \mathbf{r}_\perp,$$

using the definition

$$\psi \equiv -[\varphi_b(z) - \varphi_q(z) - \pi/2] = -\int_0^z \theta(z') dz' + \psi(0),$$

results in a Shifted-Pendulum equation:

$$\frac{d|\tilde{C}_q|}{dz} = B \sin \psi$$

$$\frac{d\delta\gamma}{dz} = -\frac{\beta_{zr}^3 \gamma_{zr}^2 \gamma_r}{k_0} K_s^2(z) [\sin \psi - \sin \psi_r]$$

$$\frac{d\psi}{dz} = \frac{k_0}{\beta_{zr}^3 \gamma_{zr}^2 \gamma_r} \delta\gamma + \frac{B}{|\tilde{C}_q|} \cos \psi,$$

where $0 < \psi_r < \pi/2$. We use the parameters of the NO-CIBUR experiment [6] assuming idealized tight bunching and moderate tapering. In the following figures we show phase-space results for different cases of uniform or tapered wiggler. In all following figures panel (a) shows the phase-space diagram $\psi - \theta$, where the black line shows the separatrix at the end of the trajectory and panel (b) shows the radiation power change, the electron beam power change, and their sum which remains at zero.

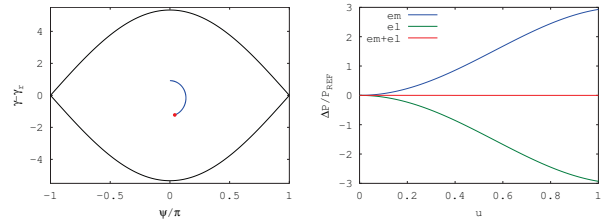


Figure 1: Uniform wiggler superradiance.

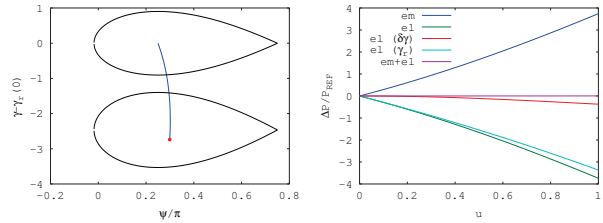


Figure 2: Tapered wiggler with initial phase ψ_r . Contributions of the tapering $\gamma_r(u)$ (cyan), synchrotron oscillation dynamics $\delta\gamma(u)$ (red), and the total beam power drop ΔP_{el} (green).

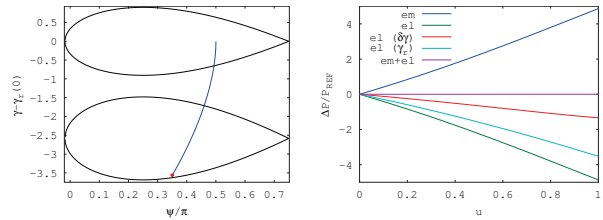


Figure 3: Same as Figure 2 with initial phase $\pi/2$.

CONCLUSION

We showed in this work a simplified approach for including the force on the charged bunches in the calculation of the

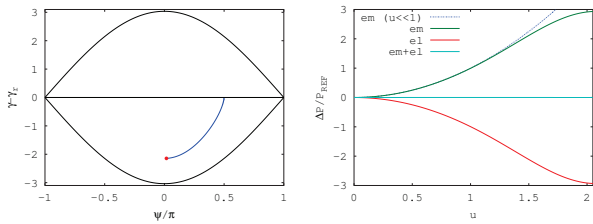


Figure 4: Uniform wiggler self interaction.

radiation. The simplification is in assuming perfectly tight bunches, and infinite train of bunches, in the single frequency approach. In spite of those simplifications, the method is useful for better understanding the tapering mechanism and improve it.

REFERENCES

[1] R. H. Dicke, "Coherence in Spontaneous Radiation Processes". *Physical Review* 93 (1): 99-110, (1954).

[2] A. Gover, "Superradiant and stimulated-superradiant emission in prebunched electron-beam radiators: I. Formulation" *Phys. Rev. ST-AB* 8, 030701 (2005).

[3] J. Duris, A. Murokh, and P. Musumeci, "Tapering enhanced stimulated superradiant amplification", *New J. Phys.* 17 063036, 2015.

[4] A. Gover, E. Dyunin, Y. Lurie, Y. Pinhasi, and M. V. Krongauz, "Superradiant and stimulated-superradiant emission in prebunched electron-beam radiators. II. Radiation enhancement schemes", *Phys. Rev. ST-AB* 8, 030702 (2005).

[5] R. Ianculescu, E. Hemsing, A. Marinelli, A. Nause and A. Gover, "Sub-Radiance and Enhanced-Radiance of undulator radiation from a correlated electron beam", *Proc. FEL'15*, August 23-28, Daejeon, Korea, MOP078.

[6] N. Sudar *et al.*, "Very high efficiency energy extraction from a relativistic electron beam in a strongly tapered undulator", *Phys. Rev. Letters* 117, 174801 (2016).

CANONICAL FORMULATION OF 1D FEL THEORY REVISITED, QUANTIZED AND APPLIED TO ELECTRON EVOLUTION*

Petr M. Anisimov[†], Los Alamos National Laboratory, Los Alamos, USA

Abstract

An original free-electron laser (FEL) paper relied on quantum analysis of photon generation by relativistic electrons in alternating magnetic field [1]. In most cases, however, the system of pendulum equations for non-canonical variables and the theory of classical electromagnetism proved to be adequate. As x-ray FELs advance to higher energy photons, quantum effects of electron recoil and shot noise has to be considered. This work presents quantization procedure based on the Hamiltonian formulation of an x-ray FEL interaction in 1D case. The procedure relates the conventional variables to canonical coordinates and momenta and does not require the transformation to the Bambini-Renieri frame [2]. The relation of a field operator to a photon annihilation operator reveals the meaning of the quantum FEL parameter, introduced by Bonifacio, as a number of photons emitted by a single electron before the saturation takes place [3]. The quantum description is then applied to study how quantum nature of electrons affects the startup of x-ray FEL and how quantum electrons become indistinguishable from a classical ensemble of electrons due to their interaction with a ponderomotive potential of an x-ray FEL.

INTRODUCTION

A one dimensional free-electron laser (FEL) theory has played a dominate role in understanding how FELs generate electromagnetic radiation in an undulator with a strength parameter $K = eB_0/k_u m_0 c^2$, which is given in CGS units here, and period λ_u . This theory allows for an universal scaling that only depends on the FEL parameter $\rho = (1/\gamma)(K\Omega_P/4ck_u)^{2/3}$ [4] and predicts that in a helical undulator, electrons with energy γ in $m_0 c^2$ units generate radiation at a wavelength $\lambda = \lambda_u/2\gamma^2(1+K^2)$. This generation is driven by electron bunching and is governed by the first order equation deduced from Maxwell's equations:

$$\frac{dA}{dz} = \frac{1}{N} \sum_{\alpha=1}^N e^{-i\theta_\alpha}, \quad (1)$$

where the field amplitude A is measured in terms of the saturation value $E_s = (m_0 c/e)\Omega_P \sqrt{\rho\gamma}$, time is replaced by the distance along the undulator $z = ct/L_{g0}$ measured in the units of the gain length $L_{g0} = (2k_u \rho)^{-1}$, and $\theta_\alpha = (k + k_u)z_\alpha - \omega t$ is a ponderomotive phase of the α^{th} electron out of N with respect to the radiation. The electron bunching by the generated radiation is described by the pendulum equations [5, 6] derived most often from the Lorentz force

equation:

$$\frac{d\theta_\alpha}{dz} = \eta_\alpha \quad (2a)$$

$$\frac{d\eta_\alpha}{dz} = -2\text{Re} \left(E e^{i\theta_\alpha} \right), \quad (2b)$$

where $\eta_\alpha = (\gamma - \gamma_r) / \rho\gamma_r$ is the relative energy detuning.

Future x-ray FEL designs, that reduce energy of electrons for a given energy of x-ray photons by reducing the undulator period, will require the quantum theory of FEL operation [7]. The equations above are not suitable for a quantum description since they assume that one can specify the exact ponderomotive phase, energy detuning and the field amplitude simultaneously at any point in time. Yet, the principle of stationary action S , which is an attribute of the dynamics of a physical system, from which the equations of motion of the system can be derived is better suited for generalizations. Moreover, it is best understood within quantum mechanics, where a system does not follow a single path but its behavior depends on all imaginable paths.

The principle of stationary action is a variational principle $\delta S = 0$ that was best formulated by W. R. Hamiltonian in 1834. It has been used on an occasion to describe electrons in a helical undulator [8] but not the generated radiation, which was described by Maxwell's equations. R. Feynman has demonstrated how this principle can be used in quantum calculations by introducing path integrals [9]. We however will use this principle for an FEL system consisting of relativistic electrons and generated radiation in order to derive a non-relativistic Hamiltonian without the Bambini-Renieri frame [2]. We will then generalize the Hamiltonian principle to quantum mechanics through Poisson brackets for canonical variables. We will finally apply this result to the study of quantum evolution of electrons in an FEL in order to determine if quantum uncertainty of an electron's position can reduce the electron bunching and degrade FEL performance.

HAMILTONIAN PRINCIPLE

The Hamiltonian principle is W. R. Hamilton formulation of the principle of stationary (least) action. It states that the dynamics of a physical system is determined by a variational problem for a functional based on a single function, the Lagrangian:

$$\delta S[\mathbf{q}(t)] = \delta \int_{t_1}^{t_2} L(\mathbf{q}(t), \dot{\mathbf{q}}(t), t) dt = 0. \quad (3)$$

One can use it to obtain equations of motion when applied to the action of a mechanical system such as electrons in an FEL but can be also used to derive Maxwell's equations.

* Work supported by LDRD-ER

[†] petr@lanl.gov

First, we write the action function for N relativistic electrons interacting with an electromagnetic field [10]:

$$S = - \sum_{\alpha=1}^N \int m_0 c ds_{\alpha} - \int \frac{A_k j^k}{c^2} d\Omega - \int \frac{F_{ik} F^{ik}}{16\pi c} d\Omega, \quad (4)$$

where ds_{α} is the proper time interval for the α^{th} electron; $A_k = (0, -\mathbf{A}_u - \mathbf{A}_r)$ is the four-vector potential in radiation gauge; j^k is the current four-vector, which is the product of the charge density,

$$\rho_e = -e \sum_{\alpha=1}^N \delta(\mathbf{r} - \mathbf{r}_{\alpha}(t)),$$

and the four-velocity vector $u^k = (c, \dot{\mathbf{r}})$; and $d\Omega = c dt d^3\mathbf{r}$ is the proper volume. Finally, $F^{ik} = (\partial\mathbf{A}_r/c\partial t, \nabla \times \mathbf{A}_r)$ is the electromagnetic field tensor in a short-hand notation.

Second, we determine the Lagrangian for the whole system $S = \int_{t_1}^{t_2} (L_e + L_{\text{int}} + L_r) dt$ after integrating Eq. (4) over interaction volume V . The first two terms are standard and describe N relativistic electrons in the presence of an undulator field and generated radiation:

$$L_e + L_{\text{int}} = - \sum_{\alpha=1}^N \left[m_0 c^2 \sqrt{1 - \frac{\dot{\mathbf{r}}_{\alpha}^2}{c^2}} + \frac{e}{c} (\mathbf{A}_u^{\alpha} + \mathbf{A}_r^{\alpha}) \dot{\mathbf{r}}_{\alpha} \right], \quad (5)$$

where the vector potentials \mathbf{A}_u^{α} and \mathbf{A}_r^{α} are evaluated at the position of the α^{th} electron.

The last term in the Lagrangian describes the generated radiation and is necessary for deriving Maxwell's equations but can be used for deriving the growth equation 1 instead. Let us focus on 1D theory and neglect the dependence of the generated radiation on transverse coordinates x and y in our choice of the vector potential:

$$\mathbf{A}_r(z, t) = -\frac{i}{2k} E(t) e^{ikz - i\omega t} + c.c., \quad (6)$$

where ϵ is a polarization vector and $E(t)$ is a complex, slowly-varying amplitude, which equation of motion we are interested in finding. The corresponding Lagrangian for such a specific radiation in a volume V is

$$L_r = i \frac{VE^*}{4\pi\omega} \dot{E}, \quad (7)$$

where dt integration by parts on terms containing \dot{E}^* has been carried out; and the term proportional to $\ddot{E}(t)/\omega^2$ has been neglected according to the slowly-varying amplitude approximation.

Finally, the Hamiltonian principle for a 1D FEL can now be written as:

$$\delta \int_{\mathbf{q}(t_1)}^{\mathbf{q}(t_2)} p_E dE + \sum_{\alpha=1}^N (\mathbf{p}_{\alpha} d\mathbf{r}_{\alpha} - H_{\alpha} dt) = 0, \quad (8)$$

where the conjugate momenta have been found from $p \stackrel{\text{def}}{=} \partial L / \partial \dot{q}$ such that

$$p_{\alpha} = \frac{m\dot{\mathbf{r}}_{\alpha}}{\sqrt{1 - \dot{\mathbf{r}}_{\alpha}^2/c^2}} - \frac{e}{c} (\mathbf{A}_u^{\alpha} - \mathbf{A}_r^{\alpha})$$

and

$$p_E = i \frac{V}{4\pi\omega} E^*,$$

and H_{α} is the standard Hamiltonian of an electron in an electromagnetic field obtained as a result of the Legendre transformation of the Lagrangian: $H = \mathbf{p}\dot{\mathbf{q}} - L(\mathbf{q}(t), \dot{\mathbf{q}}(t), t)$.

It is common, at this point, to perform the Lorentz transformation from the laboratory frame of reference to the moving frame introduced by Bambini and Renieri in order to obtain a non-relativistic Hamiltonian [2]. In contrast to this approach, we will employ canonical transformations that generate FEL variables and obtain the Bambini-Renieri Hamiltonian for electrons that are near an FEL resonance. This is similar to the approach discussed in Ref. [11] yet it will be carried out in the context of a planar undulator.

CANONICAL TREATMENT OF PLANAR UNDULATOR

We will assume a near-axis magnetic field of a planar undulator to be $\mathbf{B} = -B_0 \sin(k_u z) \hat{\mathbf{e}}_y$. The Hamiltonian equations of motion immediately imply that the components $p_x = 0$ and $p_y = 0$ are constants of motion. Hence, a single electron Hamiltonian becomes

$$H_{\alpha} = c \sqrt{p_{\alpha}^2 + m^2 c^2} \left[1 + \frac{K^2}{2 + K^2} \cos(2k_u z_{\alpha}) \right], \quad (9)$$

where $H_{\alpha} = \gamma_{\alpha}(0) m_0 c^2$ is the energy of an electron at an undulator entrance, $m^2 = m_0^2 (1 + K^2/2)$ is a mass of an "undulator" electron that incorporates the transverse degrees of freedom such that $\gamma_{z,\alpha} = \gamma_{\alpha}(0) / \sqrt{1 + K^2/2}$ with $K = 0.934 B_0[\text{T}] \lambda_u[\text{cm}]$, and p_{α} is a projection of the canonical momentum, which is no longer a constant of motion, on z -axis.

In the limit of $K/\gamma \ll 1$, the projection of the canonical momentum on the axis of a planar undulator has two separate terms:

$$p \approx \bar{p} - \frac{1}{2\bar{p}} \frac{m^2 c^2 K^2}{2 + K^2} \cos(2k_u z), \quad (10)$$

with $\bar{p} = mc \sqrt{\gamma_z^2 - 1}$ as an undulator averaged part of the canonical momentum. The complexity of a planar undulator description comes from the oscillating term so we will remove it by introducing a new canonical momentum with the help of the following generating function

$$\begin{aligned} F_2(z, \bar{p}) &= \int p dz \\ &= z\bar{p} - \frac{1}{4k_u \bar{p}} \frac{m^2 c^2 K^2}{2 + K^2} \sin(2k_u z), \end{aligned} \quad (11)$$

that generates a new canonical coordinate as follows:

$$\bar{z} = \frac{\partial}{\partial \bar{p}} F_2(z, \bar{p}) = z + \frac{1}{4k_u \bar{p}^2} \frac{m^2 c^2 K^2}{2 + K^2} \sin(2k_u z). \quad (12)$$

This leads to a new Hamiltonian $H_{\alpha} \approx c \sqrt{m^2 c^2 + \bar{p}_{\alpha}^2}$ where \bar{p}_{α} is a constant of motion.

Generation of electromagnetic radiation perturbs this Hamiltonian such that:

$$H_\alpha = c\sqrt{m^2c^2 + \bar{p}_\alpha^2} + V(z_\alpha, E) + O(E^2), \quad (13)$$

with an interaction potential

$$V(z_\alpha, E) = \frac{K}{\gamma_\alpha(0)} \text{Im} \left[\frac{eE}{k} \cos(kz_\alpha) e^{ikz_\alpha - i\omega t} \right] \quad (14)$$

being still dependent on the old coordinate, z_α . We need to use Jacobi-Anger expansion

$$\exp(iY \sin \Phi) = \sum_{n=-\infty}^{\infty} J_n(Y) \exp(in\Phi), \quad (15)$$

in order to write the interaction potential in terms of the new coordinate \bar{z}_α

$$V(\bar{z}_\alpha, E) = \frac{K}{2\gamma_\alpha(0)} \sum_{n=-\infty}^{\infty} \widehat{J}J_n \text{Im} \left[\frac{eE}{k} e^{ik_n\bar{z}_\alpha - i\omega t} \right], \quad (16)$$

where $k_n = k + (2n + 1)k_u$ and $\widehat{J}J_n \approx J_n[Y_+] + J_{n+1}[Y_-]$ with $J_n[\]$ being Bessel functions of the first kind and $Y_\pm = -((k \pm k_u)/2k_u\gamma_z^2) \times (K^2/4 + 2K^2)$.

We finally say that an FEL interaction is resonant if $k_n\bar{z}_\alpha - \omega t$ does not depend on time, which is fulfilled if $k = (2n + 1)k_u\dot{\bar{z}}_\alpha (c - \dot{\bar{z}}_\alpha)^{-1}$. A fundamental mode corresponds to the case of $n = 0$, which results in the interaction potential similar to the one, a relativistic electron experiences in a helical undulator:

$$V_0(\bar{z}_\alpha, E) = \frac{\hat{K}}{2\gamma_\alpha(0)} \text{Im} \left[\frac{eE}{k} e^{i(k+k_u)\bar{z}_\alpha - i\omega t} \right] \quad (17)$$

where $\hat{K} = \widehat{J}J_0K$ is a modified undulator parameter.

INTRODUCING FEL NOTATIONS

It has been pointed out in the previous section that the ponderomotive phase $\theta_\alpha = (k + k_u)\bar{z}_\alpha - \omega t$ of the α^{th} electron with respect to the radiation is what affects the FEL generation. Hence, we will introduce it as a new canonical coordinate with the help of the following generating function, $F_2(\bar{z}_\alpha, p_\theta) = p_\theta [(k + k_u)\bar{z}_\alpha - \omega t]$ that generates a new conjugate momentum $\bar{p} = (k + k_u)p_\theta$ and a new Hamiltonian:

$$H_\alpha = c\sqrt{m^2c^2 + (k + k_u)^2 p_{\theta,\alpha}^2} - \omega p_{\theta,\alpha} + V_0(\theta_\alpha, E), \quad (18)$$

which becomes a conserved quantity. The resonance condition, $\dot{\theta}_\alpha = 0$, now implies that $\partial H_\alpha / \partial p_{\theta,\alpha} = 0$ from the corresponding Hamiltonian equation so that the energy of a resonant electron is $\gamma_r m_0 c^2 = mc^2 (k + k_u) / \sqrt{k_u (2k + k_u)}$. The later condition corresponds to the velocity of a resonant electron being $\dot{\bar{z}}_r = \omega / (k + k_u)$, which is in accordance with the resonance condition of the previous section.

The resonant condition also implies that the system is near the minimum of the Hamiltonian. Assuming that any

departure due to the interaction potential from the resonance is small, we expand the Hamiltonian near this minimum:

$$H_\alpha = H_r + \frac{k_u (k + k_u)^2}{k\gamma_r m_0} \Delta p_{\alpha,\theta}^2 + \frac{\hat{K}}{2\gamma_r} \text{Im} \left[\frac{eE}{k} e^{i\theta_\alpha} \right], \quad (19)$$

and obtain a non-relativistic Hamiltonian without resorting to the transformation into the Bambini-Renieri frame.

We are finally ready to introduce the FEL parameter ρ as a fraction of total electron energy transferred into electromagnetic energy, $\rho\gamma_r m_0 c^2 N = (E_s^2/4\pi)V$, upon saturation. We will also introduce a new independent variable $\tau = 2\rho k_u c t$ that rescales the Hamiltonian as $H = 2\rho k_u c H_{\text{new}}$ so that

$$H_\alpha = \frac{\Delta p_{\alpha,\theta}^2}{2M} + \frac{em_0 \hat{K} E_s}{4M k_u k^2} \text{Im} [A e^{i\theta_\alpha}], \quad (20)$$

where an effective mass, $M \approx \rho\gamma_r m_0 c/k$, and a normalized amplitude $A = E/E_s$ have been introduced, and a constant contribution to the Hamiltonian has been omitted. By comparing the first Hamiltonian equation with Eq. (2a), we can identify that $\eta_\alpha = \Delta p_{\alpha,\theta}/M$ such that the second Hamiltonian equation becomes

$$\frac{d\eta_\alpha}{d\tau} = -\frac{em_0 \hat{K} E_s}{4M^2 k_u k^2} \text{Re} [A e^{i\theta_\alpha}]. \quad (21)$$

Comparing this equation with Eq. (2b), one obtains that the FEL parameter is $\rho = (1/\gamma_r)(\hat{K}\Omega_P/8\omega_u)^{2/3}$ in terms of an electron's plasma frequency $\Omega_P^2 = 4\pi e^2 n_e/m_0$ for electron density $n_e = N/V$. The resulting Hamiltonian:

$$H = \sum_{\alpha=1}^N \left(\frac{\Delta p_{\alpha,\theta}^2}{2M} + 2M \text{Im} [A e^{i\theta_\alpha}] \right), \quad (22)$$

leads to the final equation of the 1D FEL theory Eq. (1) via its derivative with respect to the conjugate moment $p_A = iMNA^*$.

QUANTIZATION PROCEDURE

In order to quantize the FEL Hamiltonian we note that, since it is related to the original Hamiltonian principle Eq. (8) via canonical transformations, commutation relations are preserved: $[\hat{\theta}, \hat{p}_\theta] = i\hbar$ and $[\hat{A}, \hat{p}_A] = i\hbar$. These relationships can now be used to derive Heisenberg equations for operators, which are visually identical to the classical 1D equations Eqs. (1) and (2).

From the first commutator relationship, one can derive the Heisenberg uncertainty for the electron operators that reads in the FEL notations as:

$$\Delta\theta\Delta\eta \geq \frac{\hbar}{2M} = \frac{1}{2\bar{\rho}}, \quad (23)$$

where $\bar{\rho}$ is the quantum FEL parameter introduced in Ref. [3]. In the limit when the quantum FEL parameter is large, the ponderomotive phase and the energy detuning can be exactly specified at any point in time. Thus, the quantum FEL parameter single-handedly determines how quantum electrons are.

For radiation operators \hat{A} and \hat{A}^\dagger , the commutator is $[\hat{A}, \hat{A}^\dagger] = (N\bar{\rho})^{-1}$, which is always small due to a large number of participating electrons, N . The photon annihilation and creation operators never commute since $[\hat{a}, \hat{a}^\dagger] = 1$. Comparing two commutators, one can introduce the photon annihilation operator as $\hat{a} = \sqrt{\bar{\rho}N}\hat{A}$ such that a physical meaning of the quantum FEL parameter becomes apparent since $\langle \hat{a}^\dagger \hat{a} \rangle = \bar{\rho}N|A|^2$. It is the number of photons emitted by a single electron before saturation.

ELECTRON EVOLUTION

A 1D quantum FEL theory can now be used to study the quantum state evolution of electrons in an FEL. In the case of an FEL with 12 GeV electrons that can generate 120 keV photons, the quantum FEL parameter $\bar{\rho} = 10$ for a typical FEL parameter $\rho = 10^{-4}$. In this case the Heisenberg uncertainty principle states that $\Delta\theta_H \geq 0.05$ for $\Delta\eta = 1$, which is the highest energy uncertainty for an FEL to laze. Therefore, an electron is no longer a point particle but a wave packet. It means that a well-localized electron does not stay localized for long if there is no trapping potential since the free space dispersion causes the wave packet to spread [12].

Let us represent the state of a quantum electron at an FEL entrance by a Gaussian of width σ :

$$\Psi_{\theta_0, p_0}(\theta, 0) = \frac{1}{\sqrt{\sqrt{2\pi}\sigma}} e^{-\frac{(\theta-\theta_0)^2}{4\sigma^2} + i\frac{p_0}{\hbar}\theta}, \quad (24)$$

where θ_0 and p_0 are initial position and momentum of an electron. The wave packet spreading means that position uncertainty of an electron increases according to

$$\sigma^2(\tau) = \sigma^2 + \frac{\tau^2}{4\bar{\rho}^2\sigma^2}, \quad (25)$$

where the quantum FEL parameter controls the free space dispersion. Since it takes $\tau = 4\pi$ for an FEL to reach saturation, the minimum position uncertainty at saturation is expected to be $\sigma_s = \sqrt{4\pi/\bar{\rho}} \approx 3.5\bar{\rho}^{-1/2}$. It is achieved if an electron started with $\sigma_m = \sigma_s/\sqrt{2}$, which corresponds to $\Delta\eta_0 = 1/\sqrt{8\pi\bar{\rho}}$ initially [13]. This position uncertainty is higher than the one expected from the Heisenberg uncertainty principle, $\Delta\theta_H$.

Assuming that the radiation field amplitude A is a c-number that is equal to the solution of the classical 1D FEL theory equations, the quantum evolution of this wave packet can be described by the Schroedinger equation:

$$i\frac{\partial\Psi}{\partial\tau} = \left\{ -\frac{1}{2\bar{\rho}}\frac{\partial^2}{\partial\theta^2} + 2\bar{\rho}\text{Im}[A(\tau)e^{i\theta}] \right\} \Psi(\theta, \tau), \quad (26)$$

where the coordinate representation of the Hamiltonian operator has been used.

The radiation field, which determines properties of the interaction potential, grows exponentially $A(\tau) \propto e^{(i+\sqrt{3})/2\tau}$. Its magnitude determines the strength of the interaction potential while the phase determines its relative position. The

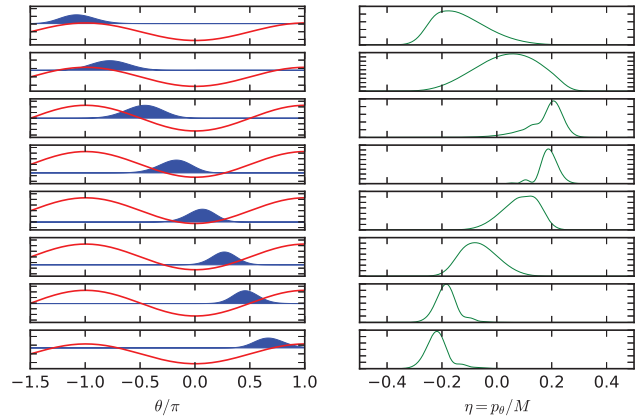


Figure 1: Family of initially stationary wave packets, $p_0 = 0$, with $\sigma_m = 0.354$ and θ_0 in the range from $-\pi$ to 0.75π (blue) after spending $\tau = 3\pi$ in the interaction potential with $A(0) = 10^{-4}$ and $\bar{\rho} = 50$ (red). The wave packets are presented as $|\Psi|^2$ where a vertical offset corresponds to an average energy of an electron $\langle \hat{H} \rangle = \int_{-\infty}^{\infty} \Psi^* \hat{H} \Psi d\theta$ that finally places them below the top of the interaction potential. The momentum distributions (green) are no-longer centered at zero, which leads to a net displacement of wave packets and onset of bunching. The wave packet displacements are still masked by the spreading.

linear growth of the phase implies that the interaction potential is moving with a speed $v = -0.5$. Therefore, a stationary electron has a momentum $\Delta p_\theta = -M/2 = -\hbar\bar{\rho}/2$ with respect to the potential, which corresponds to the kinetic energy $\hbar^{-1}\tilde{K} = \bar{\rho}/8$ that places the electron above the potential for as long as $|A| < 0.0625$. This critical magnitude of the radiation field amplitude is reached at $\tau = \tau_s - \pi$ in accordance with the magnitude growth $\exp((\sqrt{3}/2)(\tau_s - \pi))$ and $|A_s| = 1$.

Numerical solutions of the Schroedinger equation with $\bar{\rho} = 50$ as in the case of MaRIE x-ray FEL, after interaction time $\tau = 3\pi$ are presented in Figure 1 for a family of initially stationary wave packets, which are uniformly distributed in the range from $-\pi$ to $3\pi/4$. They clearly illustrate our theoretical expectations outlined above. Here, the interaction potential is shifted from its original position by $\psi_A(3\pi) = 3\pi/2$ and is finally strong enough to trap most of the electrons, $\langle \hat{H} \rangle < 2\bar{\rho}|A(3\pi)|$. At this point, some electrons have already emitted up to 20% of the maximum number of photons yet some of them have absorbed as much thus resulting in $|A(3\pi)|^2 = 0.4\%$ net emission.

The interaction potential is expected to significantly modify evolution of an electron for $\tau > 3\pi$. The electron placed at the most right in Figure 1 will emit the most photons as it continues to increase its negative momentum, which is associated with recoil. Reflection of the positive slope, which moves to the left, will compress that wave packet as well as accelerate it by pushing on it. Thus an electron surfs the ponderomotive wave as it gains momentum.

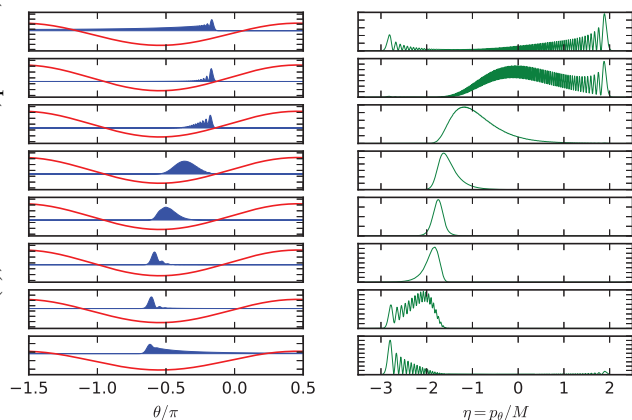


Figure 2: Electron's wave packets (blue) after spending $\tau = 4\pi$ in the interaction potential with $A(0) = 10^{-4}$ and $\bar{\rho} = 50$ (red). At this point, the radiation amplitude reaches its maximum value of $A(4\pi) \approx 1$ that corresponds to the radiation field at saturation. Ensemble averaging of the quantum bunching is $\frac{1}{N} \sum_{\alpha=1}^N \langle e^{-i\theta_{\alpha}} \rangle = 0.76$, which is equal to the classical bunching.

The wave packets of electrons at saturation are presented in Figure 2. They have been obtained by numerical integration of the Schroedinger equation with $\bar{\rho} = 50$ till the radiation field amplitude has reached its maximum. Here, one can see that the wave packets are no longer Gaussian and may even have long tails that extend beyond a single ponderomotive bucket. The ensemble, however, is bunched within 25% of a single bucket width. Although this bunching is not perfect, $\frac{1}{N} \sum_{\alpha=1}^N \langle e^{-i\theta} \rangle = 0.76$, it is not due to the wave packet spreading but due to different initial positions of electrons as they evolve in the interaction potential.

CONCLUSION

This manuscript provides canonical formulation of the 1D FEL theory in a planar undulator instead of a helical one. This formulation does not require usage of the Bambini-Renieri frame in order to end up with a non-relativistic Hamiltonian. We have also showed that the growth equation for the generate field amplitude can be derived using Hamiltonian principle instead of Maxwell's equations.

The canonical nature of the theory allows immediate generalization of the Hamiltonian principle to quantum mechanics through Poisson brackets for canonical variables and their relationship to commutators for quantum operators. The quantum analysis of the electron operators identifies the importance of the quantum FEL parameter $\bar{\rho}$ that determines whether a ponderomotive phase and electron's energy can be known exactly at the same time. The quantum analysis of the field operators identifies the physical meaning of the quantum FEL parameter as number of photons emitted by a single electron before saturation.

Finally, the manuscript discusses the quantum state evolution of an electron in an interaction potential created by

a classical radiation numerically calculated based on the classical 1D FEL theory. During the first three fourth of the undulator length, the interaction potential is too weak to affect the quantum evolution of an electron state. In the remaining undulator length, the interaction potential dominate the quantum evolution of the electron state, which has been demonstrated by numerically solving the Schroedinger equation for in the case of $\bar{\rho} = 50$ until the radiation amplitude has reached maximum. At this point, electrons are bunched within a 25% of a bucket width by the action of the interaction potential. We thus conclude that reduced bunching cannot be attributed to the wave packet spreading but to different initial positions of electrons with respect to the interaction potential.

REFERENCES

- [1] J. M. J. Madey, "Stimulated emission of bremsstrahlung in a periodic magnetic field," *J. Appl. Phys.*, vol. 42, no. 5, p. 1906, 1971.
- [2] A. Bambini and A. Renieri, "Free-electron laser – single-particle classical-model," *Let. Nuovo Cimento*, vol. 21, no. 11, pp. 399–404, 1978.
- [3] R. Bonifacio, N. Piovella, G. R. M. Robb, and A. Schiavi, "Quantum regime of free electron lasers starting from noise," *Phys. Rev. ST Accel. Beams*, vol. 9, no. 9, p. 090701, 2006.
- [4] R. Bonifacio, C. Pellegrini, and L. M. Narducci, "Collective instabilities and high-gain regime in a free-electron laser," *Opt. Commun.*, vol. 50, no. 6, pp. 373–378, 1984.
- [5] W. B. Colson, "One-body electron dynamics in a free-electron laser," *Phys. Lett. A*, vol. 64, no. 2, pp. 190–192, 1977.
- [6] W. H. Louisell, J. F. Lam, D. A. Copeland, and W. B. Colson, "Exact classical electron dynamic approach for a free-electron laser-amplifier," *Phys. Rev. A*, vol. 19, no. 1, pp. 288–300, 1979.
- [7] C. Pellegrini, A. Marinelli, and S. Reiche, "The physics of x-ray free-electron lasers," *Rev. Mod. Phys.*, vol. 88, no. 1, p. 55, 2016.
- [8] R. Bonifacio, F. Casagrande, and C. Pellegrini, "Hamiltonian model of a free-electron laser," *Opt. Commun.*, vol. 61, no. 1, pp. 55–60, 1987.
- [9] R. Feynman and A. Hibbs, *Quantum mechanics and path integrals*. McGraw-Hill, 1965.
- [10] L. D. Landau and E. M. Lifshitz, *The classical theory of fields; 3rd ed.*, ser. Course of theoretical physics. Oxford: Pergamon, 1971, Eq. (28.6).
- [11] W. Becker and J. K. McIver, "Many-particle quantum theory for a class of free-electron devices," *Physics Reports*, vol. 154, no. 4, pp. 205–245, 1987.
- [12] H. P. Freund and T. M. Antonsen, *Principles of Free-Electron Lasers*. Springer US, 1996, page 14, Eq. (1.26).
- [13] P. Anisimov, "Quantum nature of electrons in classical x-ray FELs," in *Proc. 37th Int. Free-Electron Laser Conf. (FEL'15)*, 2015, pp. 338–341.

WIDE BANDWIDTH, FREQUENCY MODULATED FREE ELECTRON LASER

L.T. Campbell^{1,2}, B.W.J. McNeil¹

¹SUPA, Department of Physics, University of Strathclyde, Glasgow, G4 0NG and
 Cockcroft Institute, Warrington, WA4 4AD, UK

²ASTeC, STFC Daresbury Laboratory, Warrington, WA4 4AD, UK

Abstract

It is shown via theory and simulation that the resonant frequency of a Free Electron Laser (FEL) may be modulated to obtain an FEL interaction with a frequency bandwidth which is at least an order of magnitude greater than normal FEL operation. The system is described in the linear regime by a summation over exponential gain modes, allowing the amplification of multiple light frequencies simultaneously. Simulation in 3D demonstrates the process for parameters of the UK's CLARA FEL test facility currently under construction. This new mode of FEL operation has close analogies to Frequency Modulation in a conventional cavity laser. This new, wide bandwidth mode of FEL operation scales well for X-ray generation and offers users a new form of high-power FEL output.

The Free Electron Laser (FEL) is currently the world's brightest source of X-rays by many orders of magnitude [1–3]. The FEL consists of a relativistic electron beam injected through a magnetic undulator with a co-propagating resonant radiation field. Initially, co-propagating radiation will occur due to incoherent spontaneous noise emission from the electron beam and may be supplemented by an injected seed laser. The electrons can interact cooperatively with the radiation they emit and become density modulated at the resonant radiation wavelength. This coherently modulated oscillating electron beam exponentially amplifies the co-propagating radiation field in a positive feedback loop. In the single-pass high-gain mode, the energy of the initial incoherent, spontaneous X-rays may be amplified by around ten orders of magnitude. With such an increase in brightness over other laboratory sources, the X-ray FEL has unique applications across a wide range of the natural sciences. FEL science is, however, still under development, and the creation of novel and improved output from the FEL is still an active topic of research.

For example, it has been shown via simulations that equally spaced frequency modes may be generated in a single-pass FEL amplifier [4,5] by introducing a series of delays to the electron beam with respect to the co-propagating radiation field (e.g. by using magnetic chicanes placed between undulator modules). These radiation modes are formally identical to those created in an oscillator cavity. Analogously with a mode-locked conventional laser oscillator, a modulation of the electron beam energy [4,5] or current [6] at the mode spacing can phase-lock the modes and amplify them to generate a train of short, high power pulses.

Multiple colours may also be excited by directly tuning each undulator module to switch between 2 (or more) dis-

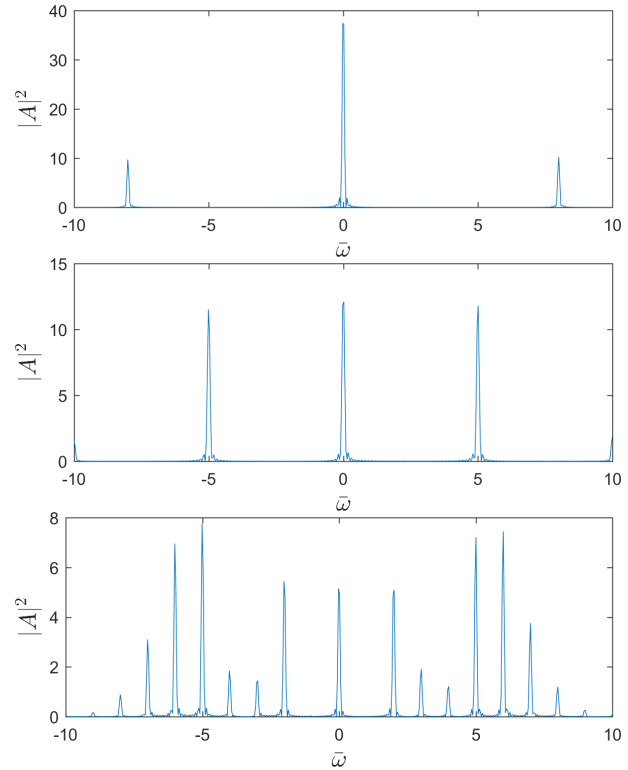


Figure 1: Result of analytic solution in equation (5) using the sinusoidal frequency modulation. The plots show the 1D scaled power spectrum (in arbitrary units) of a single electron radiating in a modulated wiggler with parameters $\rho = 0.001$ and modulation amplitude $\kappa = 0.014$, for 3 different values of modulation frequency \bar{k}_M . Values are, from top to bottom, $\bar{k}_M = 8$; $\bar{k}_M = 5$; and $\bar{k}_M = 1$, corresponding to modulation index $\mu = 0.875$, 1.4 and 7 respectively. Note how, as the modulation frequency is reduced, more modes are within the bandwidth described by the frequency modulation amplitude.

ting colours [7]. This colour switching may also excite and amplify modes via a resulting gain modulation [8].

In what follows, the resonant frequency of the FEL is continuously modulated by varying the magnetic undulator field, as opposed to either a continual temporal modulation of e.g. the beam energy, or a spatial variation between two distinct colours.

Control of the resonant frequency of the FEL ω_r , may be achieved by varying the electron beam energy γ_0 , the undulator wavenumber k_u , or undulator magnetic field strength B_u ,

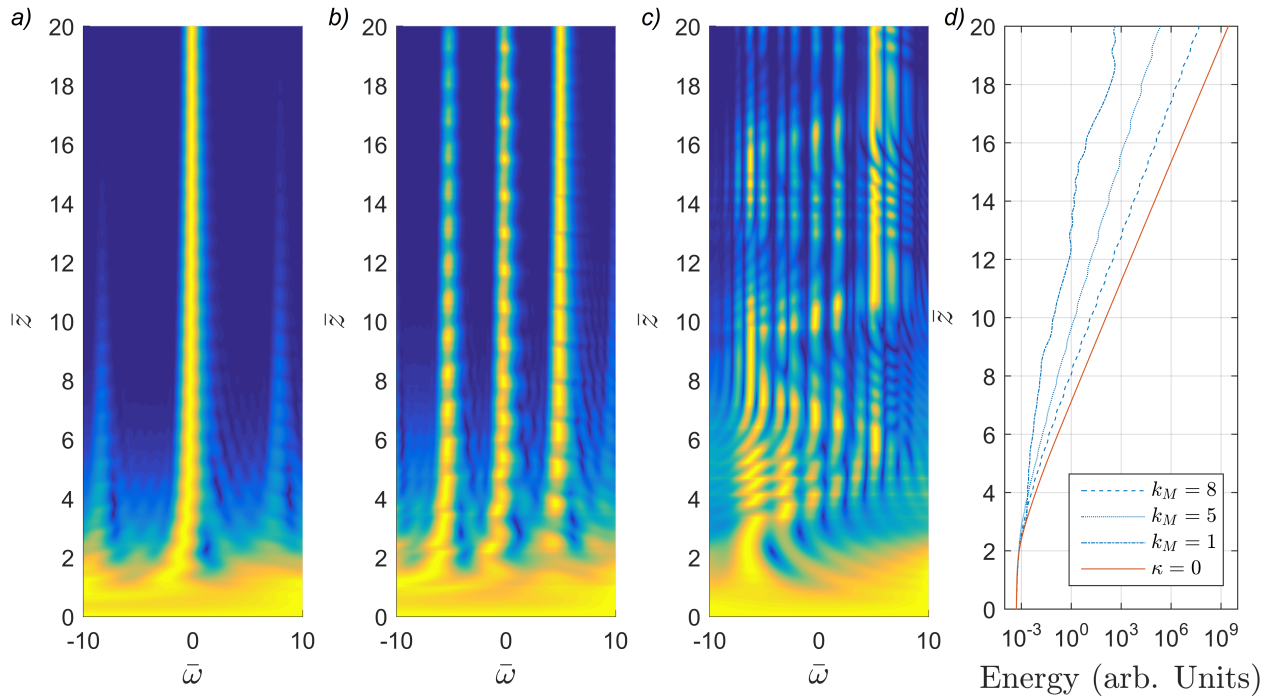


Figure 2: Result of numerical solution of the linear system in equations (2-4) using the sinusoidal frequency modulation, for $\rho = 0.001$ and $\kappa = 0.014$. The plots show the evolution of the normalised spectral intensity profile of the field from an initial broad bandwidth seed, constant for all frequencies. Each horizontal slice in \bar{z} is normalised to its maximum: a) $\bar{k}_M = 8$, b) $\bar{k}_M = 5$ and c) $\bar{k}_M = 1$, corresponding to modulation index $\mu = 0.875, 1.4$ and 7 respectively.

via the resonance relation:

$$\omega_r = \frac{2\gamma_0^2 c k_u}{(1 + \bar{a}_u^2)}, \quad (1)$$

where the mean undulator parameter $\bar{a}_u \propto B_u \lambda_u$, the product of its magnetic field and period respectively and γ_0 is the mean electron beam Lorentz factor. The undulator parameter \bar{a}_u may be varied to change the resonant frequency as a function of the scaled propagation distance through the undulator $\bar{z} = z/l_g$ where $l_g = \lambda_u/4\pi\rho$ is the gain length of the FEL interaction and ρ is the FEL parameter [9].

In this letter a periodic modulation of the FEL resonant frequency is made along the undulator length by varying \bar{a}_u . The spectral output is composed of equally spaced frequency modes, and it is found that the modulation amplitude extends the range of frequencies which may be amplified, allowing a control of the bandwidth within which the modes are amplified. This may be extended to orders of magnitude above the typical FEL amplification bandwidth, at the cost of lengthening the characteristic FEL gain length. The temporal radiation profile is seen to exhibit rapid temporal phase/frequency changes.

A system of linearised equations was used in [10] to investigate the efficiency of a tapered undulator FEL. Here a similar linear model is used but with a modulated undulator. Defining the undulator parameter to be $\bar{a}_u(\bar{z}) = \bar{a}_{u0}(1 + \epsilon(\bar{z}))$, where the constant $\bar{a}_{u0} \gg 1$ and $|\epsilon(\bar{z})| \ll 1$, the following system of fourier-transformed, linearised FEL equations in terms of the collective variables $\tilde{b}(\bar{z}, \bar{\omega})$, $\tilde{P}(\bar{z}, \bar{\omega})$ and $\tilde{A}(\bar{z}, \bar{\omega})$

are obtained:

$$\frac{\partial \tilde{b}}{\partial \bar{z}} = -i\tilde{P} \quad (2)$$

$$\frac{\partial \tilde{P}}{\partial \bar{z}} = -\tilde{A} \quad (3)$$

$$\frac{\partial \tilde{A}}{\partial \bar{z}} = \tilde{b} - i(\bar{\omega} + \epsilon(\bar{z}))\tilde{A}, \quad (4)$$

where $\bar{\omega} = (\omega/\omega_{r0} - 1)/2\rho$ is the scaled radiation frequency, with ω_{r0} the radiation frequency for $\bar{a}_u = \bar{a}_{u0}$. Note that $\bar{\omega}$ is then in units of the usual SASE FEL bandwidth.

A modulation of the resonant frequency may be achieved within the above limits of validity via a sinusoidal modulation of the undulator parameter by setting $\epsilon(\bar{z}) = \kappa \sin(\bar{k}_M \bar{z})/2$, where \bar{k}_M defines the modulation period, to give $\omega_r(\bar{z})/\omega_{r0} \approx 1 - \kappa \sin(\bar{k}_M \bar{z})$.

The spontaneous single electron output for such a modulated undulator, i.e. with no FEL interaction, may be derived exactly and the solution for the scaled spectral power written as a sum over frequency modes with spacing \bar{k}_M : $|\tilde{A}(\bar{z}, \bar{\omega})|^2 = \bar{z}^2 M M^*/2\pi$ where:

$$M = \sum_{n=-\infty}^{\infty} i^n e^{i\frac{\omega_n \bar{z}}{2}} J_n \left(\frac{\omega}{\omega_{r0}} \mu \right) \text{sinc} \left(\frac{\bar{\omega}_n \bar{z}}{2} \right), \quad (5)$$

with $\bar{\omega}_n \equiv \bar{\omega} + n\bar{k}_M$ describing a system of modes of scaled frequency spacing \bar{k}_M . Here, a modulation index $\mu = \kappa/2\rho\bar{k}_M$ appears explicitly, equivalent to that defined in conventional frequency-modulated lasers [11]. The modulation index gives an approximate upper limit to $|n|$ in equa-

tion (5) of those modes that fall within the modulated bandwidth, so that the number of modes present is $N_M \approx 2\mu + 1$ (as shown in Fig. 1).

Performing a Laplace transform on (2-4), ($\hat{A}(s, \bar{\omega}) = \mathcal{L}\{\hat{A}(\bar{z}, \bar{\omega})\}$, etc) yields the following recursive solution of exponential modes in s :

$$\hat{A}_n = \frac{s_n^2}{s_n^2(s_n + \bar{\omega}) + 1} \left(\frac{\kappa}{4\rho} (\hat{A}_{n-1} - \hat{A}_{n+1}) - \tilde{A}_i \right) \quad (6)$$

where $s_n \equiv s + n\bar{k}_M$, $\hat{A}_n \equiv \hat{A}(s_n, \bar{\omega})$ and $\tilde{A}_i \equiv \tilde{A}(0, \bar{\omega})$. When $\kappa = n = 0$, this reduces to the well-known cubic relation for the characteristic equation [9].

The linear solution, Eqn. 6, indicates that the frequency modes of the radiation are not directly coupled – each frequency evolves independently. Seeding just one of the radiation modes does not therefore couple to the other modes (although it should be noted that this model does not take into account coherent spontaneous emission [12]). However, the *spatial* exponential modes (in s) are coupled, and result in a spatial gain modulation for each frequency mode.

Taking the inverse Laplace transform of (6), the complex field envelope may be expressed as a convolution in \bar{z} of the usual FEL gain function $G(\bar{z}, \bar{\omega})$ with the frequency modulation:

$$\tilde{A} = -iG * \tilde{A} \frac{\kappa}{2\rho} \sin(\bar{k}_M \bar{z}) + G\tilde{A}_i, \quad (7)$$

where:

$$G(\bar{z}, \bar{\omega}) = \sum_{\text{residues}} \frac{s^2 e^{is\bar{z}}}{s^3 + \bar{\omega}s^2 + 1} \quad (8)$$

is the usual FEL gain function for a radiation seed. The ‘steady-state’ FEL solution of [9] is recovered for $\kappa = 0$.

Results of numerical solutions of the linear system (2-4) are shown in Fig. 2 for three values of \bar{k}_M and a range of the modulation index μ which covers few to several radiation modes. The system was seeded with a homogeneous broadband seed $\tilde{A}_i = 10^{-3}$. It is noted that the general form of the radiation emission of Fig. 2 is similar to that of the single particle emission of equation (5) which has a rich structure as a function of \bar{z} and $\bar{\omega}$. The undulator modulation generates radiation frequency modes spaced at the modulation frequency \bar{k}_M . For more than one set of sidebands within the modulated bandwidth the modulation index $\mu > 1$. Furthermore, for the radiation modes to span a range greater than the usual FEL gain bandwidth, which is of interest in this letter, the modulation bandwidth $\kappa > 2\rho$, or equivalently, $\mu\bar{k}_M > 1$. Hence, as \bar{k}_M decreases, more modes may fall within the extended bandwidth. Radiation pulse energy oscillations of period $2\pi/\bar{k}_M$ in \bar{z} are seen to occur. For the $\bar{k}_M = 5$ case of Fig. 2, each of the 3 modes have a period in \bar{z} of $\bar{\lambda}_M \approx 1.26$.

Note that for the more extreme case of a modulation index of $\mu = 7$ shown in Fig. 2 c), exponential FEL gain occurs across many frequency modes. However, gain is not evenly

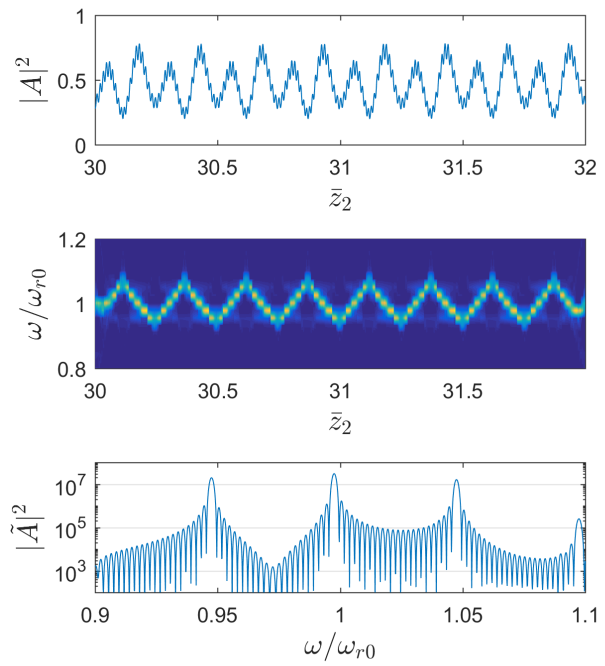


Figure 3: Puffin simulation using a sinusoidal undulator modulation, for $\rho = 0.001$, $\kappa = 0.06$ and $\bar{k}_M = 25$ at $\bar{z} = 13.2$. Each mode is seeded with a scaled intensity $|A|^2 = 10^{-4}$. Top - scaled intensity vs \bar{z}_2 , showing an almost CW profile, Middle - wavelet transform showing corresponding scaled frequency modulation, Bottom - fourier transform showing modal output. Note that radiation frequencies span 50 times the usual FEL spectral bandwidth.

distributed across the modes and being spread out over the many modes, occurs at a reduced rate from that of the usual unmodulated SASE case. Of course, this linear solution does not model saturation effects and in non-linear simulations using Puffin [13], for the many mode cases examined, saturation was seen to occur at around twice the undulator length of the unmodulated SASE case.

In linear solutions of multi-mode cases one mode appears to dominate for $\bar{z} \gg 1$. It also appears that frequency modes are driven even when non-resonant with the electrons as defined by the usual FEL relation (1). In non-linear models, saturation usually occurs before a single mode can completely dominate, leaving a modal structure with characteristic asymmetric Bessel-like ‘horns’ familiar from conventional frequency modulated laser systems [11].

Figure 3 shows the radiation output from a 1D Puffin simulation in the non-linear regime with $\rho = 0.001$, $\kappa = 0.06$ and $\bar{k}_M = 25$ (modulation index $\mu = 1.2$) close to saturation at $\bar{z} \approx 13.2$. The scaled temporal coordinate $\bar{z}_2 = (ct - z)/l_c$ is used here, scaled to the 1D FEL cooperation length. The initial temporal structure of the radiation seed is composed of short pulses ($\ll l_c$) due to the interference of the different modes, but the modes do not have a fixed phase relationship during the FM-FEL lasing. As the system saturates, the contrast of the radiation spikes reduces and their power structure briefly becomes more continuous with a strong frequency modulation, as seen in Fig. 3. This is

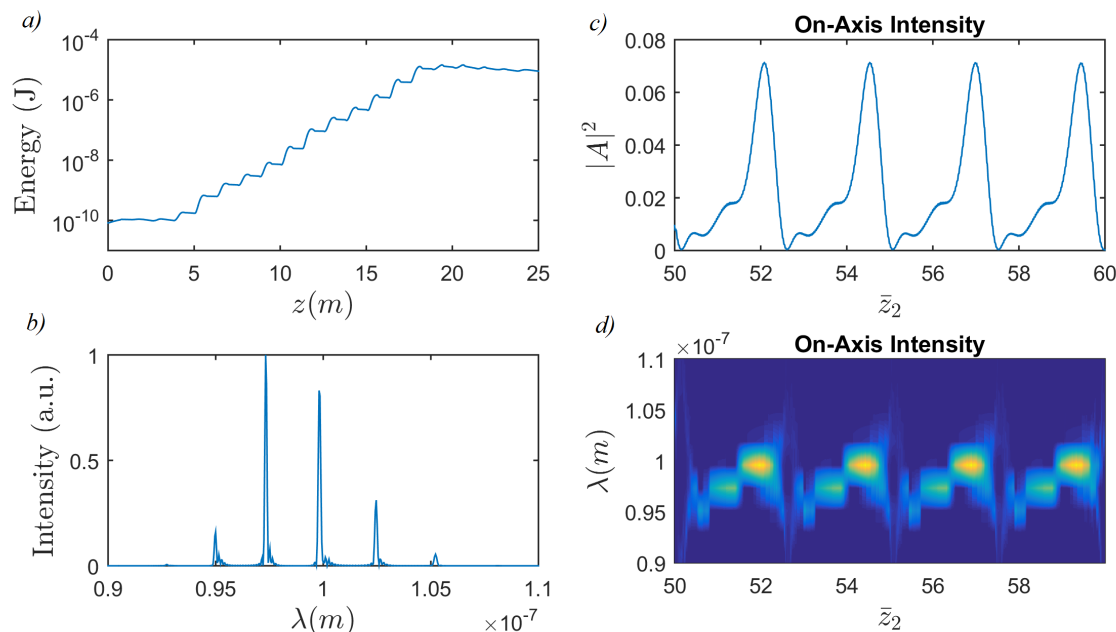


Figure 4: a) Radiated energy as a function of distance through the undulator line from CLARA simulation with modulated linear undulator tapers. The regions of no growth correspond to the spaces between undulator modules for the FODO focussing quadrupoles. Plots b), c), and d) are respectively the spectrum, temporal power, and wavelength-temporal intensity correlation (by wavelet analysis) of on-axis radiation, just before saturation at $z \approx 17$ m. The frequency modes have a spacing of $\approx 5\rho$, within a bandwidth spanning $\approx 20\rho$.

similar to that observed in a conventional FM laser [11]. Post saturation, the pulsed output is seen to return, with a frequency modulation which further evolves in \bar{z} . The large bandwidth of the amplified modes spans $\sim 100\rho$ but is achieved with a variation in \bar{a}_u of only 3%. For the X-rays, where more typically the FEL parameter is reduced to $\rho \sim 10^{-4}$, a similar amplification bandwidth may be achieved with variations of $\bar{a}_u < 1\%$.

The sinusoidal modulation applied here may be difficult to realise at a current typical FEL facility. For a more practical application, a periodic linear modulation to the undulator parameter \bar{a}_u may be applied which has the same rate of frequency change for all frequencies. This version of the method is more easily realized at a short wavelength FEL facility, where the undulator is composed of many undulator modules, each of which would require the ability to be linearly tapered. A simulation of this method using Puffin is shown in Fig. 4. The parameters used are similar to the those of the future UK FEL test-facility CLARA [14], lasing at a wavelength $\lambda \approx 100$ nm. The electron beam has energy $E = 230$ MeV, normalised emittance $\epsilon_n = 0.5$ mm-mrad, and a flat-top current profile of duration $\sigma_t = 250$ fs and peak current $I_{pk} = 400$ A. The planar undulators each have 25 periods of $\lambda_u = 2.75$ cm and mean undulator parameter $\bar{a}_{u0} = 0.78$. The Puffin simulations are in 3D, include a FODO focusing lattice to maintain a mean beam radius of ~ 60 μ m. The FEL interaction is seeded at each of the modes by an external radiation source of scaled intensity $|A|^2 = 10^{-4}$. The radiation has a relatively short Rayleigh range of ≈ 0.23 m, corresponding to approximately $1/3$

of an undulator module length, and therefore allowing a good test of the robustness of the method to 3D effects. Each undulator module is linearly tapered from over a range $0.7 \leq \bar{a}_u \leq 0.85$. As seen from the figure, 3D effects do not appear to adversely affect the frequency modulation in this simulation. Multiple modes are seen to be excited and amplified within a frequency bandwidth of approximately 20ρ . The analysis of the linear system of equations showed that modes are driven even when strictly non-resonant. It would appear that there are diffractive guiding effects similar to that which occurs in normal, single frequency FEL operation. The wavelet analysis of Fig. 4 d) shows a clear correlation of the radiation frequency to the temporal power profile.

The FM-FEL has been shown to exhibit similar properties to that of its conventional laser counterpart. It is a more complex system to study due to the temporal slippage of the radiation field through the co-propagating, amplifying electron beam. The general concepts and methodology used here may also be valid, at least within certain limits, to similar cooperative many-body systems, such as the Collective Atomic Recoil Laser (CARL) instability [15]. FM-FEL operation appears to scale well in the X-ray regime, where only relatively small changes of the undulator parameter within each undulator module are required for a notable extension of the mode-amplification bandwidth over that of a typical FEL. In order to demonstrate the rich behaviour of the FM-FEL, multi-coloured radiation seeds were used in the simulations to avoid noise in the output spectra which would mask the underlying physics. Note that such seeds could be provided

Content from this work may be used under the terms of the CC BY 3.0 licence (© 2018). Any distribution of this work must maintain attribution to the author(s), title of the work, publisher, and DOI.

by an HHG seed source in the soft X-rays. In principle it may be possible to seed the FM-FEL interaction via e.g. Echo-Enabled Harmonic Generation (EEHG) [16], or other future methods, in which the bunching spectra exhibits a plateau of harmonics/modes. The use of chicanes [4] between the tapered undulator modules may also allow further control of the the modes, such as independent control of both the amplification bandwidth of modes and the mode spacing. These methods could lead to a powerful, tunable, broadband source of many-coloured coherent radiation into the hard X-ray regime.

We gratefully acknowledge support of the Science and Technology Facilities Council Agreement Number 4163192 Release #3; ARCHIE-WeSt HPC, EPSRC grant EP/K000586/1; EPSRC Grant EP/M011607/1; and John von Neumann Institute for Computing (NIC) on JUROPA at Jülich Supercomputing Centre (JSC), under project HHH20.

REFERENCES

- [1] P. Emma *et al.*, *Nat. Photonics* **4**, 641 (2010).
- [2] H. Tanaka *et al.*, *Nat. Photonics* **6**, 540 (2012).
- [3] B.W.J. McNeil and N. R. Thompson, *Nat. Photonics* **4**, 814 (2010).
- [4] N.R. Thomson and B.W.J. McNeil, *Phys. Rev. Lett.* **100**, 203901 (2008).
- [5] B.W.J. McNeil, N.R. Thompson and D.J. Dunning, *Phys. Rev. Lett.* **110**, 134802 (2013).
- [6] E. Kur, D.J. Dunning, B.W.J. McNeil, J. Wurtele and A.A. Zholents, *New J. Phys.* **13**, 063012 (2011).
- [7] L.T. Campbell, B.W.J. McNeil and S. Reiche, *New J. Phys.* **16**, 103019 (2014).
- [8] A. Marinelli *et al.*, *Phys. Rev. Lett.* **111**, 134801 (2013)
- [9] R. Bonifacio, C. Pellegrini and L.M. Narducci, *Opt. Comm.* **50**, 373 (1984).
- [10] R. Bonifacio, F. Casagrande, M. Ferrario, P. Pierini and N. Piovella, *Opt. Comm.* **66**, 133 (1988).
- [11] A.E. Siegman, *Lasers*, University Science Books, Sausalito, 1986.
- [12] B.W.J. McNeil, G.R.M. Robb and D.A. Jaroszynski, *Nucl. Instrum. Methods Phys. Res. A* **445** 72-76 (2000).
- [13] L.T. Campbell and B.W.J. McNeil, *Phys. Plasmas* **19**, 093119 (2012).
- [14] J.A. Clarke *et al.*, *JINST* **9** T05001 (2014).
- [15] R. Bonifacio and L. De Salvo, *Nucl. Instrum. Methods Phys. Res. A* **341**, 360 (1994).
- [16] G. Stupakov, *Phys. Rev. Lett.* **102**, 074801 (2009).

List of Authors

Bold papercodes indicate primary authors; ~~crossed-out~~ papercodes indicate 'no submission'

— A —	
Abhilash, S. R.	MOP046
Ackermann, W.	WEP005
Allaria, E.	MOD04, THB02
Altinbas, Z.	MOP041
Amann, J.W.	TUB02
Amatuni, G.A.	WEP007
Amstutz, Ph.	MOP028
Anderson, R.	MOP041
Andersson, J.	TUP010, TUP013
André, T.	TUP061 , WEP065
Andrews, H.L.	WEP015 , WEP016
Andrianov, A.V.	WEP006
Andriyash, I.A.	TUP061, WEP065
Anisimov, P.M.	FRB04
Antipov, S.P.	TUP015, WEA04, WEP055
Anton, J.W.J.	MOP001
Aryshev, A.	MOP046, MOP047
Asano, Y.	WEC05
Aschikhin, A.	MOP043
Asova, G.	WEP006, WEP010, WEP007
Äßmann, R.W.	MOP003, MOP042, TUP042, WEP040
Azima, A.	MOP003, MOP042

— B —	
Badano, L.	MOD04, THB02
Bae, S.	MOP048
Baek, I.H.	WEB02
Bahns, I.	MOP064, TUC02
Balandin, V.	TUP003
Bane, K.L.F.	TUC03, TUC05, TUP023
Barnes, C.W.	MOD06
Barraza Montiel, G.A.	TUP062
Baxevanis, P.	FRB01
Bayliss, V.	WEC02
Béchu, N.	WEP065
Bednarzik, M.	TUP053
Behrens, C.	MOP043
Belomestnykh, S.A.	MOP041
Benabderrahmane, C.	WEP064
Bencivenga, F.	MOD04, THA02
Benediktovitch, A.I.	TUP015
Benwell, A.L.	WEB03
Berg, A.	WEP030
Berlin, A.	WEP030
Berrah, N.	FRA01
Berteaud, P.	WEP065
Bettoni, S.	MOP038, TUP053, THB04
Beukers, T.G.	WEB03
Beutner, B.	TUP002, TUP003, TUP005, WEA01

Bhandari, R.K.	MOP046, MOP047, WEP057
Biedron, S.	WEP031
Bielawski, S.	TUP061
Bischofberger, K.	TUP016
Bizen, T.	WEC05
Bizzozero, D. A.	TUP035
Björklund Svensson, J.	TUP010 , TUP013
Blache, F.	TUP061, WEP064
Blank, V.D.	MOP001, MOP008, TUC03
Blau, J.	MOP066
Bödewadt, J.	MOP003, MOP028, MOP042, TUP042
Boehm, J.	WEC02
Bogdanov, S.A.	WEP012
Bohlen, S.	MOP043
Bohler, D.K.	WEP036
Boonpornprasert, P.	WEP004 , WEP005, WEP006, WEP007, WEP010
Bopp, M.	WEP040
Borowiec, P.B.	MOP051
Borrelli, S.	TUP053
Boulware, C.H.	MOP041
Bouvet, F.	TUP061
Brachmann, A.	TUP058
Bradshaw, T.W.	WEC02
Brameld, M.	TUP067
Brandin, M.	TUP013
Braun, H.-H.	MOP038, TUP053, WEP040
Brinker, F.	WEP018
Briquez, F.	TUP061, WEP065
Brown, K.A.	MOP041
Bruhwieler, D.L.	MOP011, TUP022
Brummitt, A.J.	WEC02
Brutus, J.C.B.	MOP041
Brynes, A.D.	WEP026
Bultrini, D.	TUP059
Butkowski, Ł.	WEB04
Byrd, J.M.	WEA05
Büsing, B.	MOP027

— C —	
Callegari, C.	MOD04
Calvi, M.	MOP038, TUP053
Campbell, L.T.	MOP016, FRB02, FRB05
Canfer, S.J.	WEC02
Cano, E.	WEP030
Capotondi, F.	MOD04, THA02
Carlsten, B.E.	TUP016, WEP034
Castaneda Cortes, H.M.	TUP059, WEP062
Catalán Lasheras, N.	WEP040
Cesar, D.B.	TUP038
Chao, A.	FRA04

Content from this work may be used under the terms of the CC BY 3.0 licence (© 2018). Any distribution of this work must maintain attribution to the author(s), title of the work, publisher, and DOI.

Chaudhari, G.K. **MOP046**
 Chen, J.E. **WEA03**
 Chen, J.P.J. **TUB03**
 Chen, S. **MOC04**
 Chen, Y. **WEP005, WEP006, WEP007, WEP010, WEP030**
 Cheng, H.P.H. **WEA03**
 Cheng, W. **WEA03**
 Chmielewski, K. **MOP051**
 Choi, B.K. **WEP016, WEP015**
 Choi, H. J. **WEP041**
 Chorowski, M. **MOP051**
 Chou, M.C. **MOP052, TUP031**
 Christie, F. **WEP040**
 Cilento, F. **MOD04**
 Cinquegrana, P. **MOD04**
 Clarke, J.A. **WEC02**
 Cocco, D. **WEC03**
 Coffee, R.N. **TUB01, WEP060, FRA01**
 Cohn, K. R. **MOP066**
 Colocho, W.S. **TUP023**
 Colson, W.B. **MOP066**
 Conde, M.E. **TUP054**
 Corde, S. **TUP061**
 Coreno, M. **MOD04**
 Cosson, O. **WEP064**
 Couprie, M.-E. **MOP026, TUP061, WEP064, WEP065**
 Courthold, M.J.D. **WEC02**
 Craievich, P. **MOP038, WEP040**
 Cryan, J. **WEP060**
 Cucini, R. **THA02**
 Cudin, I. **MOD04**
 Curbis, F. **TUA02, TUP010, TUP013**
 Curcio, A.J. **MOP041**

— D —

D’Arcy, R.T.P. **MOP043, WEP040**
 D’Auria, G. **MOD04**
 Dai, A. **WEP030**
 Dai, D.X. **MOC04**
 Dale, J. **MOP043**
 Danailov, M.B. **MOD04, THB02**
 Dancila, D.S. **TUP065**
 David, Ch. **TUP053**
 De Gerssem, H. **TUP035, WEP005**
 De Monte, R. **MOD04**
 De Ninno, G. **MOD04**
 Decker, F.-J. **TUA03, TUP023**
 Decking, W. **MOC03, MOP008, TUP002, TUP003, TUP004**
 Dehler, M.M. **TUP053**
 Delgiusto, P. **MOD04**
 Demidovich, A.A. **MOD04, THB02**
 Deng, H.X. **MOBB01, WEP063**
 Derksen, J. **WEP030**

Di Fraia, M. **MOD04**
 Di Lieto, A. **MOP041**
 Di Lucchio, L. **MOP043**
 Di Mitri, S. **MOD04, THB02**
 Dietrich, Y. **TUP061**
 Ding, Y. **MOP013, MOP014, MOP061, TUA03, TUA05, TUC03, TUC05, FRA01**
 Diviacco, B. **MOD04**
 Dohlus, M. **MOP003, WEP005**
 Dong, X. **MOP008**
 Doran, D.S. **TUP054**
 Drescher, M. **MOP003, MOP042**
 Du, Y. C. **WEP029**
 Duda, M. **MOP051**
 Duda, P. **MOP051**
 Dunning, D.J. **MOP054, TUP059, WEP062**
 Dunning, M.P. **MOP017**
 Duris, J.P. **MOP061, FRA01**
 Duval, J.P. **TUP061**
 Dyunin, E. **TUC04**

— E —

Eddy, N. **WEP034**
 Edelen, A.L. **WEP031**
 Edstrom, D.R. **WEP034**
 Ekanayake, N. **MOP003, MOP028**
 El Ajjouri, M. **TUP061**
 Elias, L.R. **MOA01**
 Emma, C. **TUB02, FRA01, FRB03**
 Emma, P. **MOD01, TUC03, WEP043, WET01**
 Engling, C. **MOP008**
 Evain, C. **TUP061, MOP026**

— F —

Faatz, B. **MOP031**
 Fabian, R. **WEB02**
 Fabris, A. **MOD04**
 Fabris, R. **MOD04**
 Falgari, P. **FRB02**
 Fang, G.P. **MOD05**
 Fang, K. **TUP058**
 Fawley, W.M. **MOD04, TUC03, TUB01**
 Felber, E.P. **WEB04**
 Felber, M. **MOP043, WEB04**
 Feng, C. **MOC04, MOP023, MOP024, FRA04**
 Feng, G. **MOP003, TUP004**
 Feng, L.W. **WEA03**
 Feng, Y. **MOP018, MOP061, TUA05, TUB01**
 Fenner, M. **WEB04**
 Ferianis, M. **MOD04**
 Ferrari, E. **TUP053, FRA02**
 Feurer, T. **WEB01**

Filippetto, D. **WEA05**
 Fleming, R.L. **WEP015, WEP016**
 Fletcher, L.B. **THA03**
 Foglia, L. **THA02**
 Follath, R. **MOP038**
 Folz, C. **MOP041**
 Forest, F. **WEP064**
 Forouher, D. **WEP030**
 Foster, B. **MOP043**
 Frei, F. **TUP053**
 Freund, H. **FRB02**
 Friedman, A. **FRB03**
 Fröhlich, L. **TUP003**
 Fromme, P. **TUB03**
 Fukami, K. **TUA04**
 Fukuda, M.K. **MOP046**
 Fukuda, S. **MOP046**
 Furlan Radivo, P. **MOD04**
 Fydrych, J. **MOP051**

— G —

Gacheva, E. **WEP006, WEP012**
 Gai, W. **TUP054, WEP029**
 Gaio, G. **MOD04**
 Galyamin, S.N. **TUP015**
 Ganter, R. **MOP038, WEP040**
 Garcia, B.W. **MOP010, MOP016, MOP017,**
TUB01, TUP024
 Garvey, T. **TUP053, WEB01**
 Garzella, D. **MOP026**
 Gassner, D.M. **MOP041**
 Gauthier, D. **MOD04, THB02**
 Gautier, J. **TUP061**
 Gehlot, M. **TUP062**
 Gelmetti, F. **MOD04**
 Geloni, G. **MOP008, MOP037, TUP004,**
TUP045
 Gewinner, S. **MOP059**
 Ghaith, A. **MOP026, TUP061, WEP064,**
WEP065
 Ghosh, S. **MOP046, MOP047, WEP057**
 Giannessi, L. **MOD04, MOP005, TUB05,**
THB02
 Gjonaj, E. **TUP035**
 Glowinkowski, J. **MOP051**
 Goldberg, L. **MOP043**
 Golubeva, N. **MOP008, TUP003**
 Good, J.D. **WEP005, WEP006, WEP007,**
WEP010
 Gottschalk, S.C. **MOP066**
 Gough, C.H. **MOP038**
 Gover, A. **TUC04, FRB03**
 Gołębiewski, Z. **MOP051**
 Grabowski, W.C. **MOP051**
 Grattoni, V. **MOP042**
 Graves, W.S. **TUB03, TUP038**

Green, B. **WEC02**
 Grigoryan, B. **WEP007**
 Grimm, T.L. **MOP041**
 Grimminck, D.L.A. **FRB02**
 Grizolli, C. **TUC03**
 Groß, M. **WEP006, WEP007, WEP010**
 Grudiev, A. **WEP040**
 Gruse, J.-N. **MOP043**
 Grzegory, P. **MOP051**
 Gu, M. **MOD05**
 Gu, Q. **MOD05**
 Gudkov, B.A. **MOP048, WEB02**
 Guetg, M.W. **TUA03, TUB02, WEP043,**
FRA01
 Guo, G. **WEP060**
 Guzenko, V. **TUP053**

— H —

Ha, G. **TUP054**
 Halavanau, A. **TUP015**
 Hall, C.C. **MOP011, TUP022**
 Hama, H. **WEP027**
 Hamberg, M. **TUP065, WEP018**
 Han, B. **WEB02**
 Han, J.H. **WEP041**
 Hao, H. **TUC01**
 Hao, J.K. **WEA03**
 Hara, T. **TUA04, WEC05**
 Hardin, C.L. **WEC03**
 Hartl, I. **MOP003, MOP042, WEP006,**
WEP018
 Hasegawa, T. **WEC05**
 Hasegawa, T. **TUA04**
 Hast, C. **MOP017**
 Hastings, J.B. **TUB01, TUC03**
 Hayati, M. **WEB01**
 Hayes, T. **MOP041, TUP034**
 Hayler, T. **WEC02**
 Hegazy, K.H. **WEP060**
 Hellert, T. **TUP002**
 Hemsing, E. **MOP010, MOP017, TUA05,**
TUB01
 Henderson, J. **FRB02**
 Heo, H. **MOC01**
 Herbeaux, C. **TUP061, WEP065**
 Higashiguchi, T. **TUP066**
 Hiller, N. **TUP053**
 Hillert, W. **MOP042**
 Holl, M.R. **TUB03**
 Hommelhoff, P. **TUP053**
 Hong, K.-H. **TUB03**
 Honkavaara, K. **MOD02**
 Hsu, K.T. **MOP052**
 Hsu, S.Y. **MOP052**
 Hu, Z. **MOP043**
 Huang, C. **WEP016**

Content from this work may be used under the terms of the CC BY 3.0 licence (© 2018). Any distribution of this work must maintain attribution to the author(s), title of the work, publisher, and DOI.

Huang, N.Y. **MOP052, TUP031**
 Huang, P.W. **WEA02**
 Huang, S. **MOP013, MOP014, TUA05, TUC01, TUC05, WEA03**
 Huang, W.-H. **WEA02, WEP029**
 Huang, X. **TUB04**
 Huang, Z. **MOP013, MOP014, MOP061, TUA03, TUA05, TUB01, TUC03, TUC05, WEP048, WEP060, THB03, FRA01, FRB01**
 Hubert, N. **TUP061**
 Huck, H. **WEP005, WEP006, WEP007, WEP010**
 Hulsart, R.L. **MOP041**
 Hwang, C.-S. **MOP052**
 Hwang, J.-Y. **MOP052**
 Hwang, K. **WEP073**

— I —

Ianconescu, R. **FRB03**
 Iazzourene, F. **MOD04**
 Ihee, H. **WEB02**
 Iluk, A. **MOP051**
 Ilyakov, E.V. **WEP012**
 Ilyin, I.V. **WEP051**
 Inacker, P. **MOP041**
 Inagaki, T. **TUA04**
 Isaev, I.I. **WEP005, WEP006, WEP007, WEP010**
 Isaksson, L. **TUP013**
 Ischebeck, R. **TUP053, WEB01**
 Itoga, T. **WEC05**
 Ivanov, O.A. **WEA04**

— J —

Jabłoński, S. **WEB04**
 Jacewicz, M. **TUP065**
 Jacobson, B.T. **MOP053**
 Jamilkowski, J.P. **MOP041**
 Jamison, S.P. **TUP059**
 Jan, J.C. **MOP052**
 Jang, K.H. **MOP048, WEB02**
 Jeffery, P. **WEC02**
 Jeong, Y.U. **MOP048, WEB02**
 Jezabek, M. **MOP051**
 Jiang, Z. **WEP063**
 Jing, Y.C. **MOP041, TUP034, TUP039, TUP069, TUP072, WEP025, WEP051**
 Jivkov, P. **WEP064**
 Johnson, M.J. **WEA05**
 Joshi, V.J. **MOP046, MOP047**

— K —

Kabiraj, D. **MOP046**
 Kärtner, F.X. **WEP030**
 Kagamihata, A. **WEC05**
 Kalantaryan, D.K. **WEP006, WEP007, WEP010**
 Kalaydzhyan, A. **WEP030**
 Kan, K. **THB03**
 Kang, H.-S. **MOC01, MOP001, TUP058, WEC04, WEP019, WEP041**
 Kanjilal, D. **MOP046, MOP047, WEP057**
 Karabekyan, S. **MOP008**
 Karlsson, M. **TUP065**
 Karmakar, B. **MOP046, MOP047**
 Karmakar, J. **MOP046, MOP047**
 Karstensen, S. **MOP043**
 Kasprzak, K. **MOP051**
 Kayran, D. **MOP041, TUP034**
 Kearney, S.P. **MOP001, MOP056, TUC03**
 Kellermann, R. **MOP041, WEP051**
 Khan, D. **TUP027, TUP028, TUP030**
 Khan, S. **MOP003, MOP027, MOP028, MOP042**
 Khazanov, E. **WEP006**
 Khizhanok, A. **MOP053**
 Khojoyan, M. **TUP061**
 Kida, Y. **WEC05**
 Kiessling, R. **MOP059**
 Kii, T. **MOP049, MOP050, TUP070, TUP071, WEP014**
 Kim, C. **MOC01**
 Kim, D.E. **WEC04**
 Kim, G. **MOC01, TUP058**
 Kim, H.W. **WEB02**
 Kim, J. **WEB02**
 Kim, K.-J. **MOP001, MOP056, MOP061, MOP062, TUC03, TUC05**
 Kim, K.W. **WEB02**
 Kim, S.H. **WEP019**
 Kim, S.H. **WEP041**
 Kim, Y.-C. **WEB02**
 Kinjo, R. **WEC05**
 Kirian, R. **TUB03**
 Kitegi, C.A. **TUP061, WEP064**
 Knetsch, A. **MOP043**
 Ko, I.S. **WEC04**
 Kocharyan, V. **MOP008, MOP037, TUP004**
 Koehler, S. **WEP018**
 Kolodziej, T. **MOP001, MOP056, TUC03**
 Kolokolnikov, Y. **WEP051**
 Kondo, C. **TUA04**
 Kononenko, O. S. **MOP043**
 Koshiba, Y. **TUP066**
 Kosinski, K. **MOP051**
 Kostrzewa, K. **MOP051**
 Kotarba, A. **MOP051**
 Kotur, M. **TUP010, TUP013**

Kozak, T. **WEB04**
 Krainara, S. **MOP049, MOP050**
 Krasilnikov, M. **WEP004, WEP005, WEP006,**
WEP007, WEP008, WEP009,
WEP010
 Krasnykh, A.K. **WEB03**
 Krause, B. **MOP008**
 Krawczyk, F.L. **TUP016**
 Krawczyk, P. **MOP051**
 Krecic, S. **MOD04**
 Krejciak, P. **WEB01**
 Krzysik, K. **MOP051**
 Krzywinski, J. **MOP061, TUA05, TUB02,**
TUC03, WEP048, FRA01
 Kuan, C.K. **MOP052**
 Kudla, I.M. **MOP051**
 Kuhlmann, M. **MOP031, MOP036**
 Kuittinen, M. **TUP065**
 Kumar, N. **MOP046, MOP047**
 Kumar, S. **MOP046**
 Kuroda, R. **TUP067**
 Kuzikov, S.V. **WEA04, WEP012, WEP055**
 Kwan, T.J. **WEP016**

— L —

Laarmann, T. **MOP003, MOP028, MOP042**
 Labat, M. **TUP061, WEP065**
 Lamb, T. **WEB04**
 Lambert, G. **TUP061**
 Lambiase, R.F. **MOP041**
 Lancelot, J.L. **WEP064**
 Lang, T. **MOP003**
 Lau, W.K. **MOP052, TUP031**
 Lazzarino, L.L. **MOP028, MOP042, TUP042**
 Le Pimpec, F. **MOP044**
 Lechner, C. **MOP003, MOP028, MOP042,**
TUP042
 Leclercq, N. **TUP061**
 Lederer, S. **MOP008, WEP003**
 Lee, A.P. **MOP052, TUP031**
 Lee, H.-G. **WEP041**
 Lee, H.-S. **WEP019**
 Lee, K. **MOP048, WEB02**
 Lee, S.B. **WEP041**
 Leemans, W. **WEB01**
 Lehé, R. **WEB01**
 Lehnert, U. **MOP046, MOP047, WEP057**
 Leng, Y.B. **MOD05**
 Lensch, T. **TUP003**
 Lestrade, A. **TUP061**
 Lewellen, J.W. **WEP015, WEP016**
 Li, B.T. **WEP024**
 Li, D. **WEA05**
 Li, J.L. **TUC01**
 Li, R.K. **TUP038**
 Li, S. **WEP060**

Li, X. **WEP006, WEP007, WEP010**
 Li, Y. **WEP054**
 Liang, C.C. **MOP052**
 Liang, Y.F. **WEP029**
 Libov, V. **MOP043**
 Limborg-Deprey, C. **TUB03**
 Lin, L. **WEA03**
 Lindau, F. **TUP010, TUP013**
 Lindberg, R.R. **MOP056, MOP061, MOP062,**
TUC03, TUC05
 Lishilin, O. **WEP006, WEP007, WEP010**
 Litvinenko, V. **MOP041, TUP034, TUP039,**
TUP069, TUP072, WEP025,
WEP051, TUC01
 Liu, A. **WEP055**
 Liu, B. **MOD05, MOP023**
 Liu, K.X. **MOP013, MOP014, TUC05,**
WEA03
 Liu, S. **MOP008, TUP003, TUP004**
 Liu, W. **TUP015**
 Liu, W. **TUP057**
 Lockett, C. **WEC02**
 Lockmann, N.M. **MOP027, MOP042**
 Löhl, F. **MOP038**
 Loisch, G. **WEP006, WEP007, WEP010**
 Lonza, M. **MOD04**
 Lorkiewicz, J.A. **MOP051, WEP021**
 Loulergue, A. **MOP026, TUP061**
 Lu, X.Y. **WEP024**
 Ludwig, K. **MOP043**
 Lumpkin, A.H. **TUP016, WEP034**
 Lundh, O. **TUP010**
 Luo, G.-H. **MOP052**
 Luo, T.H. **WEA05**
 Lurie, Yu. **TUC04**
 Lutman, A.A. **TUA03, TUA05, TUB02,**
TUP023, WEP048, FRA01

— M —

Ma, J. **TUP039**
 Maag, C.P. **MOP064, TUC02**
 MacArthur, J.P. **WEP048, FRA01**
 Maesaka, H. **TUA04**
 Mahieu, B. **TUP061**
 Mahler, G.J. **MOP041**
 Mahne, N. **MOD04**
 Mai, C. **MOP027**
 Maier, A.R. **MOP043**
 Makarov, D.S. **WEP012**
 Malcher, K. **MOP051**
 Malin, L.E. **TUB03, TUP038**
 Malka, V. **TUP061**
 Maltezopoulos, Th. **MOP003, MOP028**
 Malvestuto, M. **MOD04**
 Malyzhenkov, A. **WEB05**
 Manschwetus, B. **WEP018**

Content from this work may be used under the terms of the CC BY 3.0 licence (© 2018). Any distribution of this work must maintain attribution to the author(s), title of the work, publisher, and DOI.

Mansfield, T.A. TUP059
 Mansten, E. TUP010, TUP013
 Mapes, M. MOP041
 Marchetti, B. WEP040
 Marcouillé, O. TUP061, WEP065
 Marcus, G. MOP010, MOP016, MOP061,
 TUB01, TUC03, TUC05,
 THB03
 Marinelli, A. M0BB02, TUA05, TUP058,
 WEP060, FRA01, FRB01
 Marinov, K.B. WEC02
 Markowski, P. MOP051
 Marks, H. S. TUC04
 Marksteiner, Q.R. TUP009
 Marteau, F. TUP061, WEP064, WEP065
 Martinez de la Ossa, A. MOP043
 Marusic, A. MOP041
 Marutzky, F. MOP043
 Marx, D. WEP040
 Masciovecchio, C. MOD04, THA02
 Masuda, K. MOP050, WEP014
 Maxson, J.M. TUP038
 Maxwell, T.J. MOP061, TUA03, TUA05,
 TUC03, TUC05, FRA01
 Mazza, T. MOP037
 McMonagle, G. WEP040
 McNeil, B.W.J. MOP016, FRB02, FRB05
 McNeur, J.C. TUP053
 Mehrling, T.J. MOP043
 Meier, J. WEP030
 Meisel, M. MOP043
 Meissner, K. MOP051
 Melkumyan, D.M. WEP006, WEP007, WEP010
 Meng, W. MOP041
 Mernick, K. MOP041
 Meyer auf der Heide, A. MOP027
 Meyer, M. MOP037
 Michalski, G. MOP051
 Michel, P. MOP046
 Michelato, P. WEP003
 Michnoff, R.J. MOP041
 Miginsky, S.V. WEB02, MOP048
 Mihalcea, D. TUP015, MOP053
 Mihara, K. MOP041, TUP034, TUP069,
 WEP025
 Mikhailov, S.F. TUC01
 Miller, T.A. MOP041
 Milloch, M. MOD04
 Miltchev, V. MOP028, MOP042
 Milton, S.V. WEP031
 Milward, S. WEC02
 Min, C.-K. M0C01, MOP001
 Mincigrucci, R. THA02
 Minty, M.G. MOP041
 Mirian, N.S. MOD04, MOP005
 Mironov, S. WEP006, WEP012

Mishra, G. TUP062
 Mitchell, C.E. WEA05, THB01
 Moeller, S.P. FRA01
 Mohammad Kazemi, M.M. MOP042, TUP042
 Monaco, L. WEP003
 Moncton, D.E. TUB03
 Morimoto, O. TUA04
 Morton, D.S. WEC03
 Müller, J.M. WEB04
 Mun, J. MOP048
 Murokh, A.Y. MOP011, MOP053, TUP022,
 FRA03
 Musumeci, P. M0A02, MOP011, TUP022,
 TUP038, FRA03, FRB03

— N —

N'gotta, P. TUP061, WEP064
 Nagaitsev, S. FRA03
 Naik, V. MOP046
 Nakajima, T. WEP014
 Nakazawa, S. TUA04
 Nam, I.H. TUP058
 Nam, J.H. WEB02
 Nanbu, K. WEP027
 Nanni, E.A. TUB03, TUP038
 Narayan, G. MOP041, TUP034
 Nasimzada, W. WEP030
 Natan, A. WEP060
 Neuhaus, M. WEP030
 Neveu, N.R. TUP015
 Neyman, P.J. MOP066
 Nguyen, D.C. MOP061, TUB02, WEP016
 Nichols, K.E. WEP015, WEP016
 Nicolás, J. WEC03
 Niemczyk, R. MOP027
 Nietubyć, R. WEP021
 Niknejadi, P. MOP043

— O —

Oang, K.Y. WEB02
 Ögren, J. TUP065
 Oh, B.G. MOP001
 Ohgaki, H. MOP049, MOP050, TUP070,
 TUP071, WEP014
 Okumura, J. MOP050, TUP070
 Ollmann, Z. WEB01
 Olsson, D. TUP013
 Oppelt, A. WEP005, WEP006, WEP007,
 WEP010
 Orfin, P. MOP041
 Osipov, T. WEP060
 Osterhoff, J. MOP043
 Ota, S. TUP066
 Otake, Y. TUA04
 Ozkan Loch, C. TUP053

— P —

Paarmann, A.	MOP059
Palmer, C.A.J.	MOP043
Pandey, A.	MOP046
Paraliev, M.	MOP038
Park, K.-H.	WEC04
Park, S.	WEB02
Park, S. H.	MOP048
Park, S.S.	WEP019
Park, Y.	MOP011, TUP022
Parmigiani, F.	MOD04, TUP01
Patra, P.	MOP046
Patthey, L.	MOP038
Pavlenko, V.N.	WEP016
Pedersoli, E.	THA02
Pedrozzi, M.	MOP038, WEP040
Pellegrini, C.	TUB02, TUP058
Penco, G.	MOD04, THB02
Penn, G.	MOP010, TUB01, WEP074
Perucchi, A.	MOD04
Petrov, A.	MOP008
Petrushina, I.	MOP041, TUP034, TUP069, WEP025
Pflüger, J.	WEP054
Phillips, D.	MOP041
Pinayev, I.	MOP041, TUP034, TUP069, TUP072, WEP025, WEP051
Piot, P.	MOP053, TUP015
Piryatinski, A.	WEP016
Pivetta, L.	MOD04
Plath, T.	MOP003, MOP042, MOP028, TUP042
Plawski, E.P.	MOP051
Plekan, O.	MOD04
Poder, K.	MOP043
Polinski, J.	MOP051
Popov, V.	TUC01
Poteomkin, A.	WEP006, WEP012
Pourmousavi, P.	MOP043
Power, J.G.	TUP015, TUP054
Prat, E.	MOP038, TUP053, WEB01, WEP040, THB04, FRA02
Prędko, P.	WEB04
Predonzani, M.	MOD04
Prieto, P.S.	WEP034
Principi, E.	MOD04, THA02
Przystawik, A.	MOP042

— Q —

Qi, Z.	MOP023
Qian, H.J.	WEP005, WEP006, WEP007, WEP008, WEP009, WEP010
Qiang, J.	WEP073, THB01
Qin, W.	MOP013, MOP014, TUC03, WEA03, MOP062, TUC05, TUP057

Quan, S.W.	WEA03
Quast, M.	MOP043

— R —

Raabe, J.	TUP053
Raimondi, L.	MOD04
Rao, T.	MOP041, MOP046
Ratner, D.F.	MOP061, TUB01, TUB02, WEB03
Raubenheimer, T.O.	MOP017, MOP018, MOP061, TUB01, TUB04, TUP024, TUP027, TUP028, TUP030, TUP057, TUP058, THB05
Ravikumar, D.	MOP041
Ray, D.	WEP060
Rebernik Ribič, P.	MOD04
Reich, J.	MOP041
Reiche, S.	MOC02, MOP016, MOP038, TUP053, WEB01, WEP040, THB04, FRA02
Renier, Y.	WEP005, WEP006, WEP007, WEP010
Rial, E.C.M.	WEC02
Riemann, B.	MOP027
Rivkin, L.	TUP053
Robert-Demolaize, G.	MOP041
Rodrigues, G.O.	MOP046
Röckemann, J.-H.	MOP043
Röckemann, J.-H.	MOP043
Rönsch-Schulenburg, J.	MOP031
Romann, A.	TUP053
Rommelue, P.	TUP061
Roper, M.D.	WEP062
Roser, T.	MOP041
Roßbach, J.	MOP003, MOP028, MOP042, MOP064, TUC02, TUP042
Rossi, F.	MOD04
Roussel, E.	MOD04, THB02, MOP026, TUP061, WEP065
Roy, A.	MOP046
Ruan, J.	MOP053, TUP016, WEP034
Rublack, T.	WEP006, WEP010
Rumiz, L.	MOD04
Rusinski, E.	MOP051
Rydberg, A.	TUP065
Ryne, R.D.	TUP024

— S —

Sahu, B.K.	MOP046
Saisa-ard, C.	WEP010
Saito, H.	WEP027
Saito, Y.	WEP027
Sakaue, K.	TUP066, TUP067
Saldin, E.	MOP008, MOP037, TUP045
Samoylova, L.	MOP008
Sannibale, F.	WEA05, THB01

Content from this work may be used under the terms of the CC BY 3.0 licence (© 2018). Any distribution of this work must maintain attribution to the author(s), title of the work, publisher, and DOI.

Sarafinov, B.	TUP053		TUC03
Savilov, A.V.	WEP055	Sigalotti, P.	MOD04, THB02
Sawadski, B.	MOP027	Simakov, E.I.	TUP050, WEP015, WEP016
Scafuri, C.	MOD04	Simoncig, A.	THA02
Schaffran, J.	MOP043	Sinn, H.	MOP008, MOP064, TUC02
Schaper, L.	MOP043	Sitek, M.	MOP051
Scheinker, A.	TUB04, WEP036	Skaritka, J.	MOP041, WEP051
Schiepel, P.	WEP030	Sleziona, V.	TUC02
Schietinger, T.	FRA02	Smart, L.	MOP041
Schimpf, D.	WEP030	Smith, K.S.	MOP041, TUP034
Schlarb, H.	MOP043, WEB04	Snydstrup, L.	MOP041
Schlott, V.	TUP053, WEB01	Soria, V.	MOP041
Schmidt, B.	MOP043	Spampinati, S.	MOD04, THB02, MOP005
Schmidt, K.E.	TUB03	Spence, J.	TUB03, TUP038
Schmidt, T.	MOP038	Spezzani, C.	MOD04
Schneidmiller, E.	MOBA01, MOBA02, MOP031, MOP032, MOP033, MOP035, MOP036, TUA01	Staples, J.W.	WEA05
Schöllkopf, W.	MOP059	Stefan, P.	WEC03
Schoenlein, R.W.	TUB01	Steinke, S.	WEB01
Scholz, M.	TUP005, WEP018	Stephan, F.	WEP004, WEP005, WEP006, WEP007, WEP008, WEP009, WEP010
Schreiber, S.	MOP031, MOP043, TUA01, WEP003, WEP006	Stodulski, M.	MOP051
Schroeder, C.B.	MOP043	Stoupin, S.	MOP056, TUC03
Schröder, S.	MOP043	Streeter, M.J.V.	MOP043
Schwinkendorf, J.-P.	MOP043	Stupakov, G.	MOP017
Sebdaoui, M.	TUP061, WEP065	Su, X.L.	WEP029
Seberg, S.K.	MOP041	Sudar, N.S.	MOP011
Seibel, E.	WEP030	Sun, Y.	MOP011, TUP022
Seike, T.	WEC05	Suphakul, S.	MOP049, MOP050
Sekutowicz, J.K.	MOP051, WEP021	Suski, M.	MOP027
Serkez, S.	MOP008, MOP037, TUP004, TUP045	Susmita, S.	TUP053
Serpico, C.	MOD04	Svärd, R.	TUP013
Sertore, D.	WEP003	Svandriik, M.	MOD04
Setiniyaz, S.	MOP048, WEB02	Świerbleski, J.	MOP051
Setya, I.	FRB02	Sydlo, C.	WEB04
Severino, F.	MOP041, TUP034	Syresin, E.	WEP006
Shafak, K.	WEP030	Szewiński, J.	MOP051
Sharma, A.	MOP046	Szwaj, C.	TUP061
Shchegolkov, D.Y.	WEP015, WEP016	Szymczyk, K.	WEP021
Sheehy, B.	MOP041		
Sheeran, B.	MOP043		
Sheffield, R.L.	MOD06		
Shen, X.	TUP038		
Sheng, I.C.	MOP052		
Shepherd, B.J.A.	WEC02		
Sheppard, J.C.	TUP023		
Shi, X.	TUC03		
Shih, K.	MOP041, TUP034, TUP069		
Shin, D.C.	WEP044		
Shin, Y.-M.	WEP034, TUP016		
Shkaev, A.	WEP012		
Shu, D.	MOP001, MOP008, MOP056, TUC03		
Shvyd'ko, Yu.	MOP001, MOP056, MOP061,		

— T —

Ta Phuoc, K.	TUP061
Tadenuma, Y.	TUP067
Tagiri, S.	TUP071, MOP050
Taira, Y.	TUP067
Takahashi, T.	TUP066
Tan, W.W.	WEP024
Tanaka, H.	MOD03, TUA04
Tanaka, T.	WEC05
Tang, C.-X.	WEA02, WEP029
Tapia, J.P.	MOD06
Tarkeshian, R.	WEB01
Tauscher, G.E.	MOP043
Tavakoli, K.T.	TUP061, WEP065
Terentiev, S.	MOP001, MOP008, TUC03
Terunuma, N.	MOP046

Than, R. MOP041
 Thaury, C. TUP061
 Theisen, C. MOP041
 Thiessen, P. MOP064, TUC02
 Thompson, N. TUP059, MOP039, WEC02, WEP062
 Thorin, S. TUP010, TUP013
 Thurman-Keup, R.M. TUP016, WEP034
 Tilmont, M. WEP065
 Tilp, T. WEP030
 Tischer, M. MOP031, MOP046, WEP057
 Titberidze, M. WEB04
 Todd, A.M.M. MOP066
 Togawa, K. TUA04
 Tono, K. THA01
 Torgasin, K. MOP050
 Trillaud, F. TUP062
 Tripathi, S. MOP046, MOP047, WEP057
 Trovò, M. MOD04, THB02
 Tsai, C.-Y. MOP018, TUP058, MOP020, MOP021, TUP057
 Tuozzolo, J.E. MOP041
 Tyukhtin, A.V. TUP015

— U —

Underhill, M. TUB03
 Ungelenk, P. MOP027
 Upadhyay, J. TUP050
 Urakawa, J. MOP046, TUP066, TUP067
 Urbanowicz, A. TUP038

— V —

Valléau, M. TUP061, WEP064, WEP065
 van der Slot, P.J.M. WEP031, FRB02
 Vargas Catalan, E. TUP065
 Vartiainen, I. TUP065
 Vascotto, A. MOD04
 Veronese, M. MOD04, THB02
 Vétéran, J. WEP064
 Vikharev, A.A. WEA04, WEP012, WEP055
 Vikharev, A.L. WEA04
 Vinokurov, N.A. TUC01, WEB02
 Virostek, S.P. WEA05
 Visintini, R. MOD04
 Vobly, P. WEP051
 Vodnala, P. MOP001

— W —

Wacker, V. MOP043
 Walker, N. TUP002
 Walker, P.A. FRA05
 Walko, D. MOP056
 Walsh, D.A. TUP059
 Walsh, J. MOP041
 Wang, D. MOC04, MOD05, MOP024,

Wang, D. MOP055, WEP063
 Wang, D. WEP029
 Wang, E. MOP041
 Wang, F. WEA03
 Wang, G. MOP041, TUP034, TUP039, TUP069, WEP025, WEP051
 Wang, G.L. MOC04
 Wang, J. MOP056
 Wang, J.Q. WEP056
 Washio, M. TUP066, TUP067
 Watanabe, T. WEC05
 Weathersby, S.P. TUP038
 Webb, S.D. MOP011, TUP022, WEP078, FRA03
 Weichert, S. MOP043
 Weierstall, U. TUB03
 Weise, H. MOC03
 Weiss, D. MOP041
 Wen, Y.H. MOP052
 Werin, S. TUA02, TUP010, TUP013
 Wesch, S. MOP043
 Whiteford, C. TUP015
 Wiencek, M. MOP051
 Wilsher, D.S. WEC02
 Winkelmann, L. MOP003, WEP018
 Winkler, P. MOP043
 Winkowski, M. MOP051
 Wisniewski, E.E. TUP015
 Wik, P. MOP051
 Wohlenberg, T. MOP008
 Wojciechowski, M. MOP051
 Wojciechowski, Z. MOP051
 Wolf, M. MOP059
 Wolff-Fabris, F. WEP054
 Wrochna, G. MOP051
 Wu, G.R. MOC04
 Wu, J. MOP018, MOP019, MOP020, MOP021, MOP062, TUB04, TUP031, TUP057, TUP058, WEP056, WEP061
 Wu, Y.K. TUC01
 Wuensch, W. WEP040
 Wunderlich, S. MOP043
 Wurth, W. MOP003

— X —

Xiang, D. MOP017
 Xiao, B. P. MOP041
 Xiao, L. WEP024
 Xie, H.M. WEA03
 Xin, T. MOP041
 Xu, W. MOP041

— Y —

Yampolsky, N.A. WEB05
 Yan, J. TUC01

Content from this work may be used under the terms of the CC BY 3.0 licence (© 2018). Any distribution of this work must maintain attribution to the author(s), title of the work, publisher, and DOI.

Yan, L.X.	WEP029	Zatsepin, N.A.	TUB03
Yanagisawa, R.	TUP067	Zelenogorsky, V.	WEP006
Yang, B.	MOP018, MOP019, TUP057, TUP058, WEP061	Zemella, J.	MOP043, MOP064, TUC02, TUC03, FRA01
Yang, C.	MOP018, MOP020, MOP021, TUP057, TUP058	Zen, H.	MOP049, MOP050, TUP070, TUP071, WEP014
Yang, D.Y.	WEP024	Zeng, L.	MOP013, MOP014
Yang, H.	MOC01, WEP044	Zennaro, R.	WEP040
Yang, H.	WEB02	Zhang, C.	TUB03, TUP038
Yang, J.	TUP038	Zhang, K.Q.	MOP024
Yang, X.	TUB05	Zhang, M.	MOC04
Yang, X.M.	MOC04	Zhang, W.Q.	MOC04
Yang, Y.	WEP024	Zhang, W.Y.	MOP023
Yang, Z.H.	MOP055	Zhang, Z.	THB03
Yang, Z.Q.	WEP024	Zhao, G.	MOP013, MOP014
Yin, L.	MOD05, MOP055	Zhao, J.	WEP024
Yoon, M.	MOP020, MOP021, TUP057, MOP018, TUP058	Zhao, Q.T.	WEP007, WEP010, WEP005
Yoshioka, M.	TUA04	Zhao, Z.	MOP041
Yurkov, M.V.	MOBA02, MOP031, MOP032, MOP033, MOP035, MOP036, TUA01	Zhao, Z.T.	MOC04, MOP023, MOP024, MOP055, FRA04
— Z —			
Zagorodnov, I.	MOP003, TUP004	Zhentang, Z.T.	MOD05
Zaltsman, A.	MOP041	Zholents, A.	MOP011, TUP022, FRA03
Zandonella, A.Z.	MOP038	Zhou, G.	MOP020, MOP021, TUP057, WEP056, MOP018, TUP058
Zangrando, D.	MOD04	Zhou, K.	WEP024
Zangrando, M.	MOD04, WEC01	Zhu, D.	TUA05
		Zhu, F.	WEA03
		Zummack, F.	WEB04

Institutes List

AES

Medford, New York, USA

- [Todd, A.M.M.](#)

AIST

Tsukuba, Ibaraki, Japan

- [Kuroda, R.](#)
- [Taira, Y.](#)

ALBA-CELLS Synchrotron

Cerdanyola del Vallès, Spain

- [Nicolás, J.](#)

ANL

Argonne, Illinois, USA

- [Antipov, S.P.](#)
- [Anton, J.W.J.](#)
- [Conde, M.E.](#)
- [Doran, D.S.](#)
- [Gai, W.](#)
- [Kearney, S.P.](#)
- [Kim, K.-J.](#)
- [Kolodziej, T.](#)
- [Lindberg, R.R.](#)
- [Liu, W.](#)
- [Neveu, N.R.](#)
- [Power, J.G.](#)
- [Shi, X.](#)
- [Shu, D.](#)
- [Shvyd'ko, Yu.](#)
- [Sun, Y.](#)
- [Walko, D.](#)
- [Wang, J.](#)
- [Whiteford, C.](#)
- [Wisniewski, E.E.](#)
- [Zholents, A.](#)

Ariel University

Ariel, Israel

- [Dyunin, E.](#)
- [Friedman, A.](#)
- [Lurie, Yu.](#)

Arizona State University

Tempe, USA

- [Chen, J.P.J.](#)
- [Fromme, P.](#)
- [Graves, W.S.](#)
- [Holl, M.R.](#)
- [Kirian, R.](#)
- [Malin, L.E.](#)
- [Schmidt, K.E.](#)
- [Spence, J.](#)
- [Underhill, M.](#)
- [Weierstall, U.](#)

- [Zatsepin, N.A.](#)

- [Zhang, C.](#)

ASML

Veldhoven, The Netherlands

- [Grimminck, D.L.A.](#)
- [Setya, I.](#)

BINP SB RAS

Novosibirsk, Russia

- [Ilyin, I.V.](#)
- [Kolokolnikov, Y.](#)
- [Miginsky, S.V.](#)
- [Vinokurov, N.A.](#)
- [Vobly, P.](#)

BNL

Upton, Long Island, New York, USA

- [Altinbas, Z.](#)
- [Anderson, R.](#)
- [Belomestnykh, S.A.](#)
- [Brown, K.A.](#)
- [Brutus, J.C.B.](#)
- [Curcio, A.J.](#)
- [Di Lieto, A.](#)
- [Folz, C.](#)
- [Gassner, D.M.](#)
- [Hayes, T.](#)
- [Hulsart, R.L.](#)
- [Inacker, P.](#)
- [Jamilkowski, J.P.](#)
- [Jing, Y.C.](#)
- [Kayran, D.](#)
- [Kellermann, R.](#)
- [Lambiase, R.F.](#)
- [Litvinenko, V.](#)
- [Mahler, G.J.](#)
- [Mapes, M.](#)
- [Marusic, A.](#)
- [Meng, W.](#)
- [Mernick, K.](#)
- [Michnoff, R.J.](#)
- [Miller, T.A.](#)
- [Minty, M.G.](#)
- [Narayan, G.](#)
- [Orfin, P.](#)
- [Phillips, D.](#)
- [Pinayev, I.](#)
- [Rao, T.](#)
- [Ravikumar, D.](#)
- [Reich, J.](#)
- [Robert-Demolaize, G.](#)
- [Roser, T.](#)
- [Seberg, S.K.](#)
- [Severino, F.](#)
- [Sheehy, B.](#)
- [Skaritka, J.](#)

- Smart, L.
- Smith, K.S.
- Snydstrup, L.
- Soria, V.
- Than, R.
- Theisen, C.
- Tuozzolo, J.E.
- Walsh, J.
- Wang, E.
- Wang, G.
- Weiss, D.
- Xiao, B. P.
- Xin, T.
- Yang, X.
- Zaltsman, A.
- Zhao, Z.

BSU

Minsk, Belarus, Belarus

- Benediktovitch, A.I.

CAEP/IAE

Mianyang, Sichuan, People's Republic of China

- Zhou, K.

CANDLE SRI

Yerevan, Armenia

- Amatuni, G.A.
- Grigoryan, B.

CEA

Gif-sur-Yvette, France

- Garzella, D.

Center for Optical Research and Education, Utsunomiya University

Utsunomiya, Japan

- Higashiguchi, T.

CERN

Geneva, Switzerland

- Catalán Lasheras, N.
- Grudiev, A.
- McMonagle, G.
- Wuensch, W.

CFEL

Hamburg, Germany

- Maier, A.R.
- Shafak, K.

Chiang Mai University

Chiang Mai, Thailand

- Saisa-ard, C.
- Suphakul, S.

Chung Buk National University

Cheongju, Republic of Korea

- Kim, K.W.

Cockcroft Institute

Warrington, Cheshire, United Kingdom

- Bultrini, D.
- Jamison, S.P.
- Thompson, N.

Compass Scientific Engineering, Compass Manufacturing Services

Fremont, USA

- Neyman, P.J.

Cornell University (CLASSE), Cornell Laboratory for Accelerator-Based Sciences and Education

Ithaca, New York, USA

- Stoupin, S.

CSU

Fort Collins, Colorado, USA

- Biedron, S.
- Edelen, A.L.
- Freund, H.
- Milton, S.V.

Cycle GmbH

Hamburg, Germany

- Berlin, A.
- Cano, E.
- Cheng, H.P.H.
- Dai, A.
- Derksen, J.
- Frouher, D.
- Nasimzada, W.
- Neuhaus, M.
- Schiepel, P.
- Seibel, E.

DELTA

Dortmund, Germany

- Büsing, B.
- Khan, S.
- Lockmann, N.M.
- Mai, C.
- Meyer auf der Heide, A.
- Niemczyk, R.
- Plath, T.
- Riemann, B.
- Sawadski, B.
- Suski, M.
- Ungelenk, P.

DESY Zeuthen

Zeuthen, Germany

- Asova, G.
- Boonpornprasert, P.
- Chen, Y.
- Good, J.D.
- Groß, M.
- Huck, H.
- Isaev, I.I.
- Kalantaryan, D.K.
- Krasilnikov, M.
- Li, X.
- Lishilin, O.
- Loisch, G.
- Melkumyan, D.M.
- Oppelt, A.
- Qian, H.J.
- Renier, Y.
- Rublack, T.
- Saisard, C.
- Stephan, F.
- Zhao, Q.T.

DESY

Hamburg, Germany

- Aschikhin, A.
- Abmann, R.W.
- Balandin, V.
- Behrens, C.
- Beutner, B.
- Bödewadt, J.
- Bohlen, S.
- Brinker, F.
- Butkowski, Ł.
- Christie, F.
- D'Arcy, R.T.P.
- Dale, J.
- Decking, W.
- Di Lucchio, L.
- Dohlus, M.
- Ekanayake, N.
- Engling, C.
- Faatz, B.
- Felber, E.P.
- Felber, M.
- Feng, G.
- Fenner, M.
- Foster, B.
- Fröhlich, L.
- Goldberg, L.
- Golubeva, N.
- Grattoni, V.
- Gruse, J.-N.
- Hartl, I.
- Hellert, T.
- Honkavaara, K.
- Hu, Z.
- Jabłoński, S.
- Karstensen, S.
- Knetsch, A.
- Kocharyan, V.

- Koehler, S.
- Kononenko, O. S.
- Kozak, T.
- Krause, B.
- Kuhlmann, M.
- Laarmann, T.
- Lamb, T.
- Lang, T.
- Lechner, C.
- Lederer, S.
- Lensch, T.
- Libov, V.
- Liu, S.
- Ludwig, K.
- Manschwetus, B.
- Marchetti, B.
- Martinez de la Ossa, A.
- Marutzky, F.
- Marx, D.
- Mehrling, T.J.
- Mohammad Kazemi, M.M.
- Müller, J.M.
- Niknejadi, P.
- Osterhoff, J.
- Palmer, C.A.J.
- Petrov, A.
- Poder, K.
- Pourmoussavi, P.
- Prędko, P.
- Przystawik, A.
- Quast, M.
- Röckemann, J.-H.
- Rönsch-Schulenburg, J.
- Saldin, E.
- Schaffran, J.
- Schaper, L.
- Schlarb, H.
- Schmidt, B.
- Schneidmiller, E.
- Scholz, M.
- Schreiber, S.
- Schröder, S.
- Schwinkendorf, J.-P.
- Sekutowicz, J.K.
- Sheeran, B.
- Streeter, M.J.V.
- Sydlo, C.
- Tauscher, G.E.
- Tischer, M.
- Titberidze, M.
- Wacker, V.
- Walker, N.
- Walker, P.A.
- Weichert, S.
- Weise, H.
- Wesch, S.
- Winkelmann, L.
- Winkler, P.
- Wohlenberg, T.
- Wunderlich, S.
- Yurkov, M.V.

- Zagorodnov, I.
- Zemella, J.
- Zummack, F.

Deutsches Elektronen Synchrotron (DESY) and Center for Free Electron Science (CFEL)

Hamburg, Germany

- Berg, A.
- Kärtner, F.X.
- Kalaydzhyan, A.
- Meier, J.
- Schimpf, D.
- Tilp, T.

Devi Ahilya University

Indore, India

- Gehlot, M.
- Mishra, G.

DICP

Dalian, People's Republic of China

- Dai, D.X.
- Wang, G.L.
- Wu, G.R.
- Yang, X.M.
- Zhang, W.Q.

DLS

Oxfordshire, United Kingdom

- Milward, S.
- Rial, E.C.M.

Elettra-Sincrotrone Trieste S.C.p.A.

Basovizza, Italy

- Allaria, E.
- Badano, L.
- Bencivenga, F.
- Callegari, C.
- Capotondi, F.
- Cilento, F.
- Cinquegrana, P.
- Coreno, M.
- Cucini, R.
- Cudin, I.
- D'Auria, G.
- Danailov, M.B.
- De Monte, R.
- De Ninno, G.
- Delgiusto, P.
- Demidovich, A.A.
- Di Fraia, M.
- Di Mitri, S.
- Diviacco, B.
- Fabris, A.
- Fabris, R.
- Fawley, W.M.
- Ferianis, M.

- Foglia, L.
- Furlan Radivo, P.
- Gaio, G.
- Gauthier, D.
- Gelmetti, F.
- Giannessi, L.
- Iazzourene, F.
- Krecic, S.
- Lonza, M.
- Mahne, N.
- Malvestuto, M.
- Masciovecchio, C.
- Milloch, M.
- Mincigrucci, R.
- Mirian, N.S.
- Parmigiani, F.
- Pedersoli, E.
- Penzo, G.
- Perucchi, A.
- Pivetta, L.
- Plekan, O.
- Predonzani, M.
- Principi, E.
- Raimondi, L.
- Rebernik Ribič, P.
- Rossi, F.
- Roussel, E.
- Rumiz, L.
- Scafuri, C.
- Serpico, C.
- Sigalotti, P.
- Simoncig, A.
- Spampinati, S.
- Spezzani, C.
- Svandrlík, M.
- Trovò, M.
- Vascotto, A.
- Veronese, M.
- Visintini, R.
- Zangrando, D.
- Zangrando, M.

EPFL

Lausanne, Switzerland

- Ferrari, E.
- Rivkin, L.

ESRF

Grenoble, France

- Benabderrahmane, C.

ESS

Lund, Sweden

- Fydrich, J.

Euclid Beamlabs LLC

Bolingbrook, USA

- Antipov, S.P.

Euclid TechLabs, LLC

- Solon, Ohio, USA
- Antipov, S.P.
 - Liu, A.

European X-Ray Free-Electron Laser Facility GmbH

- Schelefeld, Germany
- Dong, X.

FEL/Duke University

- Durham, North Carolina, USA
- Hao, H.
 - Mikhailov, S.F.
 - Popov, V.
 - Wu, Y.K.
 - Yan, J.

Fermilab

- Batavia, Illinois, USA
- Eddy, N.
 - Edstrom, D.R.
 - Lumpkin, A.H.
 - Mihalcea, D.
 - Nagaitsev, S.
 - Piot, P.
 - Prieto, P.S.
 - Ruan, J.
 - Shin, Y.-M.
 - Thurman-Keup, R.M.

FHI

- Berlin, Germany
- Gewinner, S.
 - Kiessling, R.
 - Paarmann, A.
 - Schöllkopf, W.
 - Wolf, M.

**Friedrich-Alexander Universität Erlangen-Nuernberg,
University Erlangen-Nuernberg LFTE**

- Erlangen, Germany
- McNeur, J.C.

HZDR

- Dresden, Germany
- Lehnert, U.
 - Michel, P.

IAP/RAS

- Nizhny Novgorod, Russia
- Andrianov, A.V.
 - Bogdanov, S.A.
 - Gacheva, E.
 - Ilyakov, E.V.
 - Ivanov, O.A.
 - Khazanov, E.

- Kuzikov, S.V.
- Makarov, D.S.
- Mironov, S.
- Poteomkin, A.
- Savilov, A.V.
- Shkaev, A.
- Vikharev, A.A.
- Vikharev, A.L.
- Zelenogorsky, V.

IFJ-PAN

- Kraków, Poland
- Świerblewski, J.
 - Duda, M.
 - Jezabek, M.
 - Kasprzak, K.
 - Kotarba, A.
 - Krzysik, K.
 - Stodulski, M.
 - Wienczek, M.

IHEP

- Beijing, People's Republic of China
- Li, J.L.
 - Wang, J.Q.
 - Zhou, G.

IIT

- Chicago, Illinois, USA
- Neveu, N.R.

IMP/CAS

- Lanzhou, People's Republic of China
- Zhao, Q.T.

INFN/LASA

- Segrate (MI), Italy
- Michelato, P.
 - Monaco, L.
 - Sertore, D.

INRNE

- Sofia, Bulgaria
- Asova, G.

ISIR

- Osaka, Japan
- Kan, K.

IUAC

- New Delhi, India
- Abhilash, S. R.
 - Bhandari, R.K.
 - Chaudhari, G.K.
 - Ghosh, S.
 - Joshi, V.J.
 - Kabiraj, D.

- Kanjilal, D.
- Karmakar, B.
- Karmakar, J.
- Kumar, N.
- Kumar, S.
- Pandey, A.
- Patra, P.
- Rodrigues, G.O.
- Sahu, B.K.
- Sharma, A.
- Tripathi, S.

JASRI/SPring-8

Hyogo, Japan

- Bizen, T.
- Fukami, K.
- Itoga, T.
- Kagamihata, A.
- Seike, T.
- Tono, K.
- Watanabe, T.

JINR

Dubna, Moscow Region, Russia

- Syresin, E.

KAERI

Daejeon, Republic of Korea

- Bae, S.
- Baek, I.H.
- Gudkov, B.A.
- Han, B.
- Jang, K.H.
- Jeong, Y.U.
- Kim, H.W.
- Kim, Y.-C.
- Lee, K.
- Miginsky, S.V.
- Mun, J.
- Nam, J.H.
- Park, S.
- Setiniyaz, S.

KAIST

Daejeon, Republic of Korea

- Fabian, R.
- Ihee, H.
- Kim, J.
- Oang, K.Y.
- Yang, H.

KEK

Ibaraki, Japan

- Aryshev, A.
- Fukuda, M.K.
- Fukuda, S.
- Terunuma, N.
- Urakawa, J.

Korea University Sejong Campus

Sejong, Republic of Korea

- Park, S. H.

Kriosystem

Wroclaw, Poland

- Grzegory, P.
- Michalski, G.

Kyoto Univeristy

Kyoto, Japan

- Tagiri, S.

Kyoto University

Kyoto, Japan

- Kii, T.
- Krainara, S.
- Masuda, K.
- Nakajima, T.
- Ohgaki, H.
- Okumura, J.
- Suphakul, S.
- Tagiri, S.
- Torgasin, K.
- Zen, H.

LANL

Los Alamos, New Mexico, USA

- Andrews, H.L.
- Anisimov, P.M.
- Barnes, C.W.
- Bishofberger, K.
- Carlsten, B.E.
- Choi, B.K.
- Fleming, R.L.
- Huang, C.
- Krawczyk, F.L.
- Kwan, T.J.
- Lewellen, J.W.
- Malyzhenkov, A.
- Marksteiner, Q.R.
- Nguyen, D.C.
- Nichols, K.E.
- Pavlenko, V.N.
- Piryatinski, A.
- Scheinker, A.
- Shchegolkov, D.Y.
- Sheffield, R.L.
- Simakov, E.I.
- Tapia, J.P.
- Upadhyay, J.
- Yampolsky, N.A.

LBNL

Berkeley, California, USA

- Byrd, J.M.
- Filippetto, D.

- Hwang, K.
- Johnson, M.J.
- Leemans, W.
- Lehé, R.
- Li, D.
- Luo, T.H.
- Mitchell, C.E.
- Penn, G.
- Qiang, J.
- Ryne, R.D.
- Sannibale, F.
- Schoenlein, R.W.
- Schroeder, C.B.
- Staples, J.W.
- Steinke, S.
- Virostek, S.P.

Lime BV

Eindhoven, The Netherlands

- Falgari, P.

LNLS

Campinas, Brazil

- Grizolli, C.

LOA

Palaiseau, France

- Corde, S.
- Gautier, J.
- Lambert, G.
- Mahieu, B.
- Malka, V.
- Ta Phuoc, K.
- Thauray, C.

Lund University, Division of Atomic Physics

Lund, Sweden

- Björklund Svensson, J.

Lund University

Lund, Sweden

- Björklund Svensson, J.
- Lundh, O.

MAX IV Laboratory, Lund University

Lund, Sweden

- Andersson, J.
- Brandin, M.
- Curbis, F.
- Isaksson, L.
- Kotur, M.
- Lindau, F.
- Mansten, E.
- Olsson, D.
- Svård, R.
- Thorin, S.
- Werin, S.

Mesa+

Enschede, The Netherlands

- van der Slot, P.J.M.

MIT

Cambridge, Massachusetts, USA

- Hong, K.-H.
- Moncton, D.E.

NCBJ

Świerk/Otwock, Poland

- Chmielewski, K.
- Gołębiewski, Z.
- Grabowski, W.C.
- Kosinski, K.
- Kostrzewa, K.
- Krawczyk, P.
- Kudła, I.M.
- Lorkiewicz, J.A.
- Markowski, P.
- Meissner, K.
- Nietubyć, R.
- Plawski, E.P.
- Sitek, M.
- Szewiński, J.
- Szymczyk, K.
- Wojciechowski, M.
- Wojciechowski, Z.
- Wrochna, G.

Niowave, Inc.

Lansing, Michigan, USA

- Boulware, C.H.
- Grimm, T.L.

Northern Illinois University

DeKalb, Illinois, USA

- Halavanau, A.
- Khizhanok, A.
- Mihalcea, D.
- Piot, P.
- Shin, Y.-M.
- Vodnala, P.

NPS

Monterey, California, USA

- Blau, J.
- Cohn, K. R.
- Colson, W.B.

NSRRC

Hsinchu, Taiwan

- Chou, M.C.
- Hsu, K.T.
- Hsu, S.Y.
- Huang, N.Y.
- Hwang, C.-S.

- Hwang, J.-Y.
- Jan, J.C.
- Kuan, C.K.
- Lau, W.K.
- Lee, A.P.
- Liang, C.C.
- Luo, G.-H.
- Sheng, I.C.

NTHU

Hsinchu, Taiwan

- Wen, Y.H.

PAL

Pohang, Kyungbuk, Republic of Korea

- Choi, H. J.
- Ha, G.
- Han, J.H.
- Heo, H.
- Kang, H.-S.
- Kim, C.
- Kim, D.E.
- Kim, G.
- Kim, S.H.
- Lee, H.-G.
- Lee, H.-S.
- Lee, S.B.
- Min, C.-K.
- Nam, I.H.
- Oh, B.G.
- Park, K.-H.
- Park, S.S.
- Shin, D.C.
- Yang, H.

PhLAM/CERCLA

Villeneuve d'Ascq Cedex, France

- Bielawski, S.
- Evain, C.
- Szwaj, C.

PhLAM/CERLA

Villeneuve d'Ascq, France

- Evain, C.

PKU

Beijing, People's Republic of China

- Chen, J.E.
- Cheng, W.
- Feng, L.W.
- Hao, J.K.
- Huang, S.
- Li, B.T.
- Lin, L.
- Liu, K.X.
- Lu, X.Y.
- Qin, W.

- Quan, S.W.
- Tan, W.W.
- Wang, F.
- Xiao, L.
- Xie, H.M.
- Xu, W.
- Yang, D.Y.
- Yang, Y.
- Yang, Z.Q.
- Zeng, L.
- Zhao, G.
- Zhao, J.
- Zhu, F.

POSTECH

Pohang, Kyungbuk, Republic of Korea

- Ko, I.S.
- Yoon, M.

Private Address

warrington, United Kingdom

- Spampinati, S.

PSI

Villigen PSI, Switzerland

- Bednarzik, M.
- Bettoni, S.
- Bopp, M.
- Borrelli, S.
- Braun, H.-H.
- Calvi, M.
- Craievich, P.
- David, Ch.
- Dehler, M.M.
- Ferrari, E.
- Follath, R.
- Frei, F.
- Ganter, R.
- Garvey, T.
- Gough, C.H.
- Guzenko, V.
- Hiller, N.
- Ischebeck, R.
- Löhl, F.
- Ozkan Loch, C.
- Paraliev, M.
- Patthey, L.
- Pedrozzi, M.
- Prat, E.
- Raabe, J.
- Reiche, S.
- Rivkin, L.
- Romann, A.
- Sarafinov, B.
- Schietinger, T.
- Schlott, V.
- Schmidt, T.
- Susmita, S.
- Zandonella, A.Z.

- Zennaro, R.

RadiaBeam

Santa Monica, California, USA

- Jacobson, B.T.
- Murokh, A.Y.

RadiaSoft LLC

Boulder, Colorado, USA

- Bruhwiler, D.L.
- Hall, C.C.
- Webb, S.D.

RIKEN SPring-8 Center

Hyogo, Japan

- Asano, Y.
- Hara, T.
- Hasegawa, T.
- Inagaki, T.
- Kida, Y.
- Kinjo, R.
- Kondo, C.
- Maesaka, H.
- Otake, Y.
- Tanaka, H.
- Tanaka, T.
- Togawa, K.

RISE

Tokyo, Japan

- Ota, S.
- Takahashi, T.
- Washio, M.

Saint Petersburg State University

Saint Petersburg, Russia

- Galyamin, S.N.
- Tyukhtin, A.V.

SBU

Stony Brook, New York, USA

- Ma, J.
- Shih, K.

SES

Hyogo-pref., Japan

- Hasegawa, T.
- Morimoto, O.
- Nakazawa, S.
- Yoshioka, M.

Shanghai Jiao Tong University

Shanghai, People's Republic of China

- Xiang, D.

Sigmaphi

Vannes, France

- Cosson, O.
- Forest, F.
- Jivkov, P.
- Lancelot, J.L.

SINAP

Shanghai, People's Republic of China

- Chen, S.
- Deng, H.X.
- Fang, G.P.
- Feng, C.
- Gu, M.
- Gu, Q.
- Jiang, Z.
- Leng, Y.B.
- Liu, B.
- Qi, Z.
- Wang, D.
- Yin, L.
- Zhang, K.Q.
- Zhang, M.
- Zhang, W.Y.
- Zhao, Z.T.
- Zhentang, Z.T.

SLAC

Menlo Park, California, USA

- Amann, J.W.
- Bane, K.L.F.
- Baxevanis, P.
- Benwell, A.L.
- Beukers, T.G.
- Bohler, D.K.
- Brachmann, A.
- Chao, A.
- Cocco, D.
- Coffee, R.N.
- Colocho, W.S.
- Cryan, J.
- Decker, F.-J.
- Ding, Y.
- Dunning, M.P.
- Duris, J.P.
- Emma, P.
- Fang, K.
- Fawley, W.M.
- Feng, Y.
- Fletcher, L.B.
- Garcia, B.W.
- Guetg, M.W.
- Hardin, C.L.
- Hast, C.
- Hastings, J.B.
- Hegazy, K.H.
- Hemsing, E.
- Huang, X.
- Huang, Z.
- Khan, D.
- Krasnykh, A.K.

- Krejčík, P.
- Krzywinski, J.
- Li, R.K.
- Li, S.
- Limborg-Deprey, C.
- Lutman, A.A.
- MacArthur, J.P.
- Marcus, G.
- Marinelli, A.
- Maxwell, T.J.
- Moeller, S.P.
- Morton, D.S.
- Nanni, E.A.
- Natan, A.
- Osipov, T.
- Pellegrini, C.
- Qin, W.
- Ratner, D.F.
- Raubenheimer, T.O.
- Ray, D.
- Shen, X.
- Sheppard, J.C.
- Stefan, P.
- Stupakov, G.
- Tsai, C.-Y.
- Weathersby, S.P.
- Wu, J.
- Yang, C.
- Yang, J.
- Yoon, M.
- Zemella, J.
- Zhou, G.
- Zhu, D.

Solaris National Synchrotron Radiation Centre, Jagiellonian University

Kraków, Poland

- Borowiec, P.B.

SOLEIL

Gif-sur-Yvette, France

- André, T.
- Andriyash, I.A.
- Berteaud, P.
- Blache, F.
- Bouvet, F.
- Briquez, F.
- Béchu, N.
- Couprie, M.-E.
- Dietrich, Y.
- Duval, J.P.
- El Ajjouri, M.
- Ghaith, A.
- Herbeaux, C.
- Hubert, N.
- Khojoyan, M.
- Kitegi, C.A.
- Labat, M.
- Leclercq, N.
- Lestrade, A.

- Louergue, A.
- Marcouillé, O.
- Marteau, F.
- N'gotta, P.
- Rommeluère, P.
- Roussel, E.
- Sebdaoui, M.
- Tavakoli, K.T.
- Tilmont, M.
- Valléau, M.
- Vétéran, J.

Stanford University

Stanford, California, USA

- Guo, G.

STFC/DL/ASTeC

Daresbury, Warrington, Cheshire, United Kingdom

- Brynes, A.D.
- Campbell, L.T.
- Castaneda Cortes, H.M.
- Clarke, J.A.
- Dunning, D.J.
- Jamison, S.P.
- Mansfield, T.A.
- Marinov, K.B.
- Roper, M.D.
- Shepherd, B.J.A.
- Thompson, N.
- Walsh, D.A.

STFC/RAL

Chilton, Didcot, Oxon, United Kingdom

- Bayliss, V.
- Boehm, J.
- Bradshaw, T.W.
- Brummitt, A.J.
- Canfer, S.J.
- Courthold, M.J.D.
- Green, B.
- Hayler, T.
- Jeffery, P.
- Lockett, C.
- Wilsher, D.S.

STI Optronics, Inc.

Redmond, USA

- Gottschalk, S.C.

Stony Brook University

Stony Brook, USA

- Litvinenko, V.
- Mihara, K.

SUNY SB

Stony Brook, New York, USA

- Petrushina, I.

TEMF, TU Darmstadt

- Darmstadt, Germany
- Ackermann, W.
 - Bizzozero, D. A.
 - De Gersem, H.
 - Gjonaj, E.

TISNCM

- Troitsk, Russia
- Blank, V.D.
 - Terentiev, S.

Tohoku University, Research Center for Electron Photon Science

- Sendai, Japan
- Hama, H.
 - Nanbu, K.
 - Saito, H.
 - Saito, Y.

TUB

- Beijing, People's Republic of China
- Du, Y. C.
 - Gai, W.
 - Huang, P.W.
 - Huang, W.-H.
 - Liang, Y.F.
 - Su, X.L.
 - Tang, C.-X.
 - Wang, D.
 - Yan, L.X.
 - Zhang, Z.

UCLA

- Los Angeles, USA
- Cesar, D.B.
 - Emma, C.
 - Maxson, J.M.
 - Musumeci, P.
 - Park, Y.
 - Pellegrini, C.
 - Sudar, N.S.
 - Urbanowicz, A.

UEF

- Joensuu, Finland
- Kuittinen, M.
 - Vartiainen, I.

UNAM

- México, D.F., Mexico
- Barraza Montiel, G.A.
 - Trillaud, F.

University of Connecticut

- Storrs, Connecticut, USA
- Berrah, N.

University of Erlangen-Nuremberg

- Erlangen, Germany
- Hommelhoff, P.

University of Glasgow

- Glasgow, Scotland, United Kingdom
- Bultrini, D.

University of Hamburg, Institut für Experimentalphysik

- Hamburg, Germany
- Amstutz, Ph.
 - Azima, A.
 - Bahns, I.
 - Drescher, M.
 - Hillert, W.
 - Lazzarino, L.L.
 - Maag, C.P.
 - Maier, A.R.
 - Maltezos, Th.
 - Martinez de la Ossa, A.
 - Meisel, M.
 - Miltchev, V.
 - Plath, T.
 - Roßbach, J.
 - Röckemann, J.-H.
 - Thiessen, P.
 - Wurth, W.

University of Hamburg

- Hamburg, Germany
- Wacker, V.

University of Hawaii at Manoa

- Honolulu, USA
- Elias, L.R.

University of Science and Technology of Korea (UST)

- Daejeon, Republic of Korea
- Baek, I.H.
 - Jang, K.H.
 - Jeong, Y.U.
 - Kim, H.W.
 - Lee, K.
 - Nam, J.H.
 - Vinokurov, N.A.

University of Tel-Aviv, Faculty of Engineering

- Tel-Aviv, Israel
- Gover, A.
 - Ianculescu, R.
 - Marks, H. S.

University of Texas at Arlington

- Arlington, USA
- Yang, B.

Universität Bern, Institute of Applied Physics

Bern, Switzerland

- Feurer, T.
- Hayati, M.
- Ollmann, Z.
- Tarkeshian, R.

UNN

Nizhny Novgorod, Russia

- Savilov, A.V.

Uppsala University, Department of Engineering Sciences

Uppsala, Sweden

- Karlsson, M.
- Rydberg, A.
- Vargas Catalan, E.

Uppsala University

Uppsala, Sweden

- Dancila, D.S.
- Hamberg, M.
- Jacewicz, M.
- Ögren, J.

USTC/NSRL

Hefei, Anhui, People's Republic of China

- Liu, W.
- Yang, Z.H.

USTRAT/SUPA

Glasgow, United Kingdom

- Campbell, L.T.
- Henderson, J.
- McNeil, B.W.J.

Vanderbilt University

Nashville, USA

- Choi, B.K.

VECC

Kolkata, India

- Naik, V.
- Roy, A.

Virginia Polytechnic Institute and State University

Blacksburg, Virginia, USA

- Tsai, C.-Y.

Waseda University, Waseda Institute for Advanced Study

Tokyo, Japan

- Sakaue, K.

Waseda University

Tokyo, Japan

- Brameld, M.
- Koshiba, Y.
- Tadenuma, Y.
- Washio, M.
- Yanagisawa, R.

Wroclaw Technology Park

Wroclaw, Poland

- Glowinkowski, J.
- Winkowski, M.
- Wlk, P.

WRUT

Wrocław, Poland

- Chorowski, M.
- Duda, P.
- Iluk, A.
- Malcher, K.
- Polinski, J.
- Rusinski, E.

XFEL. EU

Hamburg, Germany

- Geloni, G.
- Karabekyan, S.
- Le Pimpec, F.
- Li, Y.
- Mazza, T.
- Meyer, M.
- Pflüger, J.
- Samoylova, L.
- Serkez, S.
- Sinn, H.
- Sleziona, V.
- Wolff-Fabris, F.

Content from this work may be used under the terms of the CC BY 3.0 licence (© 2018). Any distribution of this work must maintain attribution to the author(s), title of the work, publisher, and DOI.

Luis Elias	U. Hawaii	United States
Paul Emma	SLAC	United States
Claudio Emma	SLAC	United States
Joel England	SLAC	United States
Bart Faatz	DESY	Germany
Michael Fazio	SLAC	United States
Matthias Felber	DESY	Germany
Chao Feng	SINAP	China
Lie Feng	SINAP	China
Eugenio Ferrari	PSI	Switzerland
Aaron Fetterman	LANL	United States
Ryan Fleming	LANL	United States
Luke Fletcher	SLAC	United States
Henry Freund	U. of New Mexico	United States
Wei Gai	Tsinghua U. Beijing	United States
John Galayda	SLAC	United States
Romain Ganter	PSI	Switzerland
Bryant Garcia	Stanford U.	United States
Raffaella Geometrante	Kyma	Italy
Sandy Gewinner	FHI-Berlin	Germany
Amin Ghaith	SOLEIL	France
Luca Giannessi	Trieste	Italy
James Good	DESY	Germany
Steve Gottschalk	Compass	United States
Avraham Gover	Tel-Aviv U.	Israel
Vanessa Grattoni	DESY	Germany
William Graves	ASU	United States
Marc Walter Guetg	SLAC	United States
Lalit Gupta	BHAT	India
Christopher Hall	RadiaSoft	United States
Hiroyuki Hama	Tohoku U.	Japan
Mathias Hamberg	Uppsala U.	Sweden
Toru Hara	SACLA-RIKEN	Japan
Mark Harrison	RadiaBeam	United States
Takatoshi Hasegawa	R&K Company	Japan
Stefan Hau-Riege	LLNL	United States
Thorsten Hellert	DESY	Germany
Erik Hemsing	SLAC	United States
Wolfgang Hillert	Hamburg U.	Germany
Kazuhiro Hirano	R&K Company	Japan
Mary Hockaday	LANL	United States
Mark Holl	ASU	United States
Yosuke Honda	KEK	Japan
Katja Honkavaara	DESY	Germany
Steven Hopkins	Spellman HV	United States
Tongning Hu	Huazhong U. S&T	China
Dazhang Huang	SINAP	China

Zhirong Huang	SLAC	United States
Chengkun Huang	LANL	United States
Jenny Humbert	LANL	United States
Kyung Ryun Hwang	LBNL	United States
Radu Ianconescu	Tel-Aviv U.	Israel
Erik Iseman	Compass	United States
Elvis Janezic	Instrumentation Tech	Slovenia
Kyu-Ha Jang	KAERI	South Korea
Young Uk Jeong	KAERI	South Korea
Yichao Jing	BNL	United States
Okumura Jumpei	U. Kyoto	Japan
Heinz Junkes	FHI-Berlin	Germany
Petra Kaertner	Cycle GmbH	Germany
Heung-Sik Kang	PAL	South Korea
Shaukat Khan	T.U. Dortmund	Germany
Donish Khan	SLAC	United States
Riko Kiessling	FHI-Berlin	Germany
Dong Eon Kim	PAL	South Korea
Hyun Woo Kim	KAERI	South Korea
Kwang-Je Kim	ANL	United States
Ryota Kinjo	SACLA-RIKEN	Japan
Yuya Kobayashi	R&K Company	Japan
Vitali Kocharyan	DESY	Germany
Yuya Koshiha	Waseda U.	Japan
Marija Kotur	Max Lab/Lund U.	Sweden
Siriwan Krainara	Kyoto U.	Japan
Mikhail Krasilnikov	DESY	Germany
Anatoly Krasnykh	SLAC	United States
Pawan Kumar	RKG Inst. Technology	India
Sergey Kuzikov	IAP/RAS	Russia
Thorsten Lamb	DESY	Germany
Frederic le Pimpec	DESY	France
Ulf Lehnert	HZDR	Germany
Eliane Lessner	DOE/SC	United States
John Lewellen	LANL	United States
Siqi Li	SLAC	United States
Vladimir Litvinenko	BNL	United States
Ao Liu	Euclid Tech Lab	United States
Bo Liu	SINAP	China
Kexin Liu	PKU	China
Shan Liu	DESY	Germany
Florian Loehl	PSI	Switzerland
Charles Loelius	PNNL	United States
Jerzy Lorkiewicz	National Centre for Nucl	Poland
Alex Lumpkin	Fermilab	United States
Alberto Lutman	SLAC	United States
James MacArthur	SLAC	United States

Lucy Maestas	LANL	United States
Lucas Malin	ASU	United States
Alexander Malyzhenkov	LANL	United States
Gabriel Marcus	SLAC	United States
Agostino Marinelli	SLAC	United States
Harry Marks	Tel-Aviv U.	United Kingdom
Quinn Marksteiner	LANL	United States
Ian Martin	Diamond Light Source	United Kingdom
James McVea	Thales US	United States
Marek Miciak	Agilent	United States
Daniel Mihalcea	NIU	United States
Kentaro Mihara	Stony Brook	United States
Stephen Milton	LANL	United States
Chad Mitchell	LBNL	United States
Nathan Moody	LANL	United States
Ross Muenchausen	LANL	United States
Cecile Mukerjee	Continuum Lasers	United States
Alex Murokh	RadiaBeam	United States
Pietro Musumeci	UCLA	United States
Anett Nagyvaradi	U. of Pecs	Hungary
Inhyuk Nam	PAL	South Korea
Pulak Nath	LANL	United States
Subrata Nath	LANL	United States
Derek Neben	Mich. State U.	United States
Joseph Ayala	Compass	United States
Dinh Nguyen	LANL	United States
Kimberley Nichols	LANL	United States
Robert Olivero	Spellman HV	United States
Joseph O'Toole	LANL	United States
Soung-Soo Park	PAL	South Korea
Youna Park	UCLA	United States
Fulvio Parmigiani	Trieste	Italy
Katherine Patton-Hall	NNSA	United States
Vitaly Pavlenko	LANL	United States
Gregory Penn	LBNL	United States
Irina Petrushina	BNL	United States
Martin Pieck	LANL	United States
Tim Plath	Hamburg U.	Germany
John Post	LLNL	United States
Rohit Prasankumar	LANL	United States
Eduard Prat	PSI	Switzerland
Zheng Qi	SINAP	China
Houjun Qian	LBNL	United States
Weilun Qin	SLAC	United States
Sven Reiche	PSI	Switzerland
Joerg Rossbach	Hamburg U.	Germany
Eleonore Roussel	SOLEIL/Trieste	France

Marcos Ruelas	RadiaBeam	United States
Steven Russell	LANL	United States
Robert Ryne	LBNL	United States
Shadike Saitiniyazi	KAERI	South Korea
Kazuyuki Sakaue	Waseda U.	Japan
Evan Sanchez	LANL	United States
Richard Sandberg	LANL	United States
Fernando Sannibale	LBNL	United States
Volker RW Schaa	GSI-Darmstadt	Germany
Alexander Scheinker	LANL	United States
Evgeny Schneidmiller	DESY	Germany
Wieland Schoellkopf	FHI-Berlin	Germany
Matthias Scholz	DESY	Germany
Siegfried Schreiber	DESY	Germany
Peter Schwartz	Compass	United States
Steve Searfoss	Rialtopartner	United States
Svitozar Serkez	DESY	Germany
Richard Sheffield	LANL	United States
Kai Shih	BNL	United States
Yuri Shvyd'ko	ANL	United States
Teja Cadez Sirca	Instrumentation Tech	Slovenia
Evgenya Simakov	LANL	United States
Loren Skeist	Spellman HV	United States
Todd Smith	Stanford U.	United States
Cynnamon Spain	CCS	United States
Dan Spruit	TDK-Lambda	United States
Steve Steidl	BiRa Systems	United States
Frank Stephan	DESY	Germany
Elizabeth Sturgeon	LANL	United States
Nicholas Sudar	UCLA	United States
Jonas Bjorklund Svensson	Max Lab/Lund U.	Sweden
Karol Szymczyk	National Centre for Nucl	Poland
Shunsuke Tagiri	Kyoto U.	Japan
Hitoshi Tanaka	SACLA-RIKEN	Japan
Chuanxiang Tang	Tsinghua U. Beijing	China
Takanori Tanikawa	DESY	Germany
Roxana Tarkeshian	Bern U.	Switzerland
Charles Taylor	LANL	United States
Tina Thaxton	LANL	United States
Patrick Thiessen	Hamburg U.	Germany
Sara Thorin	Max Lab/Lund U.	Sweden
Zoltan Tibai	U. of Pecs	Hungary
Benjamin Tobias	LANL	United States
Alan Todd	Compass	United States
Kensuke Tono	SACLA-RIKEN	Japan
Frederic Trillaud	UNAM (Mexico)	Mexico
Janardan Upadhyay	LANL	United States

Content from this work may be used under the terms of the CC BY 3.0 licence (© 2018). Any distribution of this work must maintain attribution to the author(s), title of the work, publisher, and DOI.

Sandra Valdez	LANL	United States
Lex van der Meer	Radboud U. Nijmegen	Netherlands
Peter JM van der Slot	Enschede U. Twente	Netherlands
Peggy Vigil	LANL	United States
Paul Andreas Walker	DESY	Germany
Richard Walker	Diamond Light Source	United Kingdom
Dong Wang	SINAP	China
Guangki Wang	DICP	China
Gang Wang	Duke U.	United States
Alexander Wass	LANL	United States
Stephen Webb	RadiaSoft	United States
Hans Weise	DESY	Germany
Sverker Werin	Max Lab/Lund U.	Sweden
Bonnie West	TDK-Lambda	United States
Joel Williams	CSU	United States
Frederik Wolff-Fabris	DESY	Germany
Juhao Wu	SLAC	United States
Ying Wu	Duke U.	United States
Dao Xiang	SJTU	China
Vyacheslav Yakovlev	Fermilab	United States
Shigeru Yamamoto	KEK	Japan
Nikolai Yampolsky	LANL	United States
Jun Yan	Duke U.	United States
Lixin Yan	Tsinghua U. Beijing	China
Deyu Yang	PKU	China
Haeryong Yang	PAL	South Korea
Xi Yang	BNL	United States
Bo Yang	U. Texas Anderson	United States
Mikhail Yurkov	DESY	Germany
Marco Zangrando	Trieste	Italy
Heishun Zen	Kyoto U.	Japan
Ling Zeng	PKU	China
Chenou Zhang	ASU	United States
Kaiqing Zhang	SINAP	China
Weiying Zhang	DICP	China
Wenyan Zhang	SINAP	China
Zhentang Zhao	SINAP	China